MEDICAL RADIOLOGY

Diagnostic Imaging

A. L. Baert
M. Knauth
K. Sartor

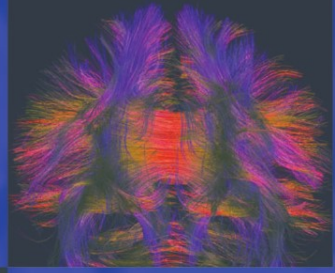

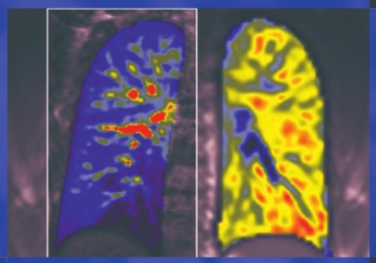

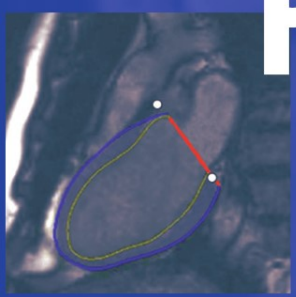

Parallel Imaging in Clinical MR Applications

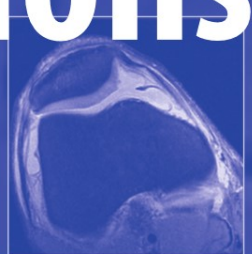

S. O. Schoenberg
O. Dietrich · M. F. Reiser
Editors

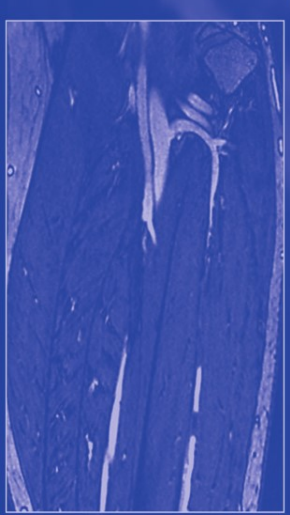

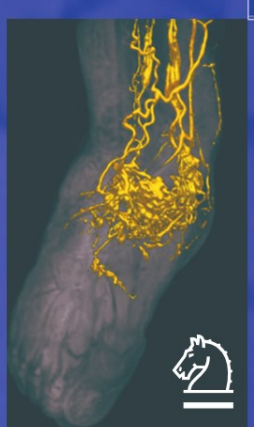

Springer

MEDICAL RADIOLOGY

Diagnostic Imaging

S. O. Schoenberg · O. Dietrich · M. F. Reiser (Eds.)

Parallel Imaging in Clinical MR Applications

With Contributions by

E. Adalsteinsson · M. Aksoy · D. Atkinson · R. Bammer · P. G. Batchelor · T. Benner
M. Bock · J. W. Casselman · O. Dietrich · R. Duensing · R. Eibel · M. Essig
C. Fink · J. P. Finn · B. Fischer · M. A. Griswold · K. A. Herrmann · R. M. Hoogeveen
A. Huber · P. Kellman · H. Kramer · K.-F. Kreitner · D. J. Larkman · T. Leiner
C. Liu · C. A. McKenzie · H. J. Michaely · K. Nael · S. Nagle · K. Nikolaou · M. Nittka
N. Oesingmann · S. B. Reeder · W. Reith · A. Reykowski · J. Rieger · B. Romaneehsen
G. P. Schmidt · S. O. Schoenberg · B. Stieltjes · L. L. Wald · R. Wang · A. M. Wallnoefer
V. J. Wedeen · O. Wieben · G. Wiggins · B. J. Wintersperger · C. J. Zech

Foreword by

A. L. Baert

With 389 Figures in 774 Separate Illustrations, 137 in Color and 37 Tables

Springer

PD Dr. med. Stefan O. Schoenberg
Dr. rer. nat. Olaf Dietrich
Prof. Dr. med. Dr. h.c. Maximilian F. Reiser
Department of Clinical Radiology
University Hospitals – Grosshadern
Ludwig Maximilian University of Munich
Marchioninistrasse 15
81377 Munich
Germany

Medical Radiology · Diagnostic Imaging and Radiation Oncology
Series Editors: A. L. Baert · L. W. Brady · H.-P. Heilmann · M. Knauth · M. Molls · K. Sartor

Continuation of Handbuch der medizinischen Radiologie
Encyclopedia of Medical Radiology

Library of Congress Control Number: 2006925090

ISBN 3-540-23102-1 Springer Berlin Heidelberg New York
ISBN 978-3-540-23102-8 Springer Berlin Heidelberg New York

Medical Editor: Dr. Ute Heilmann, Heidelberg
Desk Editor: Ursula N. Davis, Heidelberg
Production Editor: Kurt Teichmann, Mauer
Cover-Design and Typesetting: Verlagsservice Teichmann, Mauer

Printed on acid-free paper – 21/3151xq – 5 4 3 2 1 0

Foreword

The parallel imaging technique is a major technical development in MRI with a broad spectrum of clinical applications in various organs and organ systems of the human body.

This book is the first compilation to offer a comprehensive and detailed overview of the advantages and drawbacks of parallel imaging in clinical practice. It also provides a detailed description of the fundamental basic principles of this new method.

The editors of this book are internationally renowned experts in the field of MRI. Many contributions originate from the department of radiology at the Grosshadern University Hospital in Munich which, under the guidance of Prof. Dr. M. F. Reiser, has a long-standing reputation of excellence and leadership in cutting edge technology for medical imaging. Besides this group, other eminent European and overseas radiologists with outstanding knowledge and experience in new MR technology have contributed various chapters to this book.

I am very much indebted to the editors and the authors for their outstanding contributions resulting in this superb volume.

While I recommend this book to certified radiologists and radiologists in training, many other clinical disciplines involved in MR imaging will also benefit from the knowledge it offers.

I am convinced that this work will meet with great interest among our readership and that it will enjoy the same success as many other volumes previously published in our series Medical Radiology.

Leuven

Albert L. Baert

Preface

Magnetic resonance imaging (MRI) has the substantial advantage over other imaging modalities that assessment of morphology can be combined with evaluation of function and metabolism. Due to the lack of exposure to radiation or iodinated contrast agents, imaging can be multiply repeated and extended to the entire body within a single MRI scan. However, in the past this appealing comprehensive approach was highly restricted due to limitations in speed and spatial resolution of the acquisitions.

Accelerating MRI has been one of the key incentives that resulted in the enormous technical progress of MRI we have witnessed during the last two decades. While early milestones in the history of accelerated MRI were fairly general improvements such as the introduction of fast gradient-echo or turbo-spin-echo pulse sequences and of the partial-Fourier approach in the mid-1980s, subsequent developments became more and more specific and limited to certain applications. These include in particular techniques such as key-hole imaging or echo sharing that were especially designed for fast dynamic MRI applicable only with a small number of very specific pulse sequences and imaging protocols.

Parallel imaging was also motivated by the desire to accelerate MRI when it was proposed in the second half of the 1990s. In contrast to many other techniques, however, it soon turned out to provide extraordinary advantages in virtually all areas of MRI, and thus, became one of the most important technical advances in current MRI technology. This was possible since parallel imaging can be applied to practically all types of pulse sequences and imaging protocols, ranging from high-resolution morphological imaging over various functional imaging techniques to ultra-fast dynamic MRI. In addition to substantially accelerated imaging, parallel MRI has been found to increase robustness of MR examinations and to reduce blurring of single-shot acquisitions as well as susceptibility and motion artifacts.

The major challenge for the successful implementation of parallel imaging in clinical routine was the introduction of multi-channel MRI technology which initially limited its widespread use. The key hardware requirement for parallel imaging is the capability to receive data in parallel from several independent coil elements. Some MRI systems had already provided this ability when parallel imaging became generally known and since then the number of receiver channels has been substantially increased from year to year. Thus, parallel imaging can now be clinically used at the vast majority of clinical and research sites.

This book, written by leading experts world-wide, aims to provide an in-depth introduction to parallel-imaging techniques and, in particular, to the application of parallel imaging in clinical MRI. It will provide readers with a broader understanding of the fundamental principles of parallel imaging and of the advantages and disadvantages

of specific MR protocols in clinical applications in all parts of the body at 1.5 and 3 Tesla. The first part of the book explains relevant MRI physics and techniques, detailing the various parallel-imaging reconstruction algorithms, pulse-sequence design for parallel imaging, as well as hardware considerations. Special emphasis was put on communicating these technical principles in a practical and coherent way attractive for physicists and physicians, radiological technicians, and researchers.

The second part presents detailed, ready-to-use clinical protocols for morphologic, angiographic, and functional MR imaging, with special emphasis on problem-solving strategies for assessment of cardiovascular and oncological diseases. Due to the introduction of new scanner platforms, these protocols are also extended from imaging of individual organs to disease-specific evaluation of the entire body. In addition, detailed information is provided on cutting-edge techniques such as diffusion-tensor imaging, oxygen-enhanced lung imaging, and MRA with blood-pool contrast agents.

We would like to thank Albert L. Baert as the responsible editor of the series "Medical Radiology – Diagnostic Imaging", for his immediate endorsement of this book. We would also gratefully acknowledge the Springer publishers who enthusiastically supported us during the preparation of this book.

Munich

Stefan O. Schoenberg
Olaf Dietrich
Maximilian F. Reiser

Contents

Part I:
Basic Principles of Parallel-Imaging Techniques

MRI from k-Space to Parallel Imaging

1

Olaf Dietrich

CONTENTS

1.1 Introduction

Magnetic resonance imaging (MRI) is based on the principles of nuclear magnetic resonance (NMR), i.e., the excitation of the spin of the atomic nucleus by resonant electromagnetic radio frequency (RF) fields (Wehrli 1992; Gadian 1995). This physical phenomenon was discovered in the 1940s (Bloch et al. 1946; Bloch 1946; Purcell et al. 1946) and has been applied since then in a multitude of experiments and measurements, e.g., in physics, inorganic chemistry, biochemistry, biology, and medical research. A simple NMR experiment requires a strong, static magnetic field, B_0, a short RF pulse (also referred to as the B_1 field), and a sample inside the static field whose spins are excited by the RF pulse. After the excitation, the sample emits a quickly decaying RF signal, which can be received by an antenna or RF coil (Fig. 1.1); this signal can be used to analyze the chemical or physical properties of the sample.

Both RF signals, the one used to excite the spins and the one emitted by the sample afterwards, are characterized by a certain frequency, f, which typically is in the MHz range. This precession frequency, or Larmor frequency, f, is proportional to the field strength, B_0; thus, e.g., by doubling the static field strength, the Larmor frequency is also doubled. This relation can be written $f=\gamma\times B_0$ with the gyromagnetic ratio, γ, as a constant of proportionality. The gyromagnetic ratio, γ, depends on the kind of nucleus and on the chemical environment of the nucleus such that nuclei in different chemical compounds can be differentiated by analyzing the frequencies, f, they are emitting. This is the basic principle of MR spectroscopy.

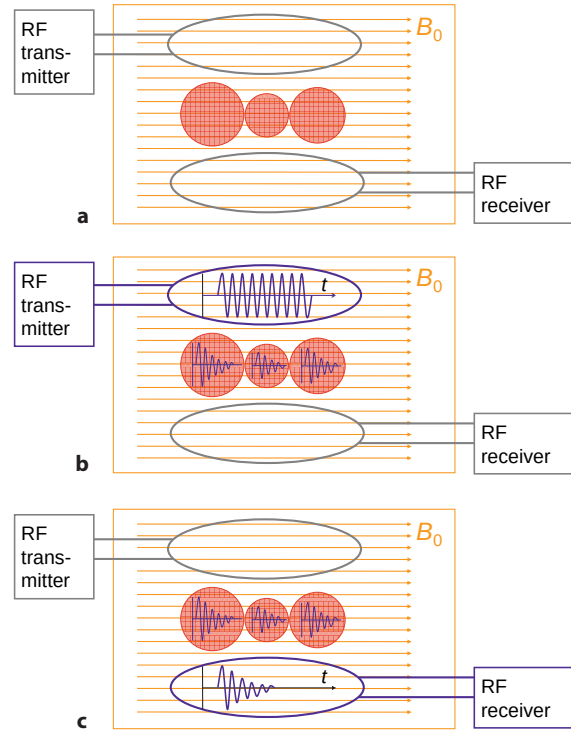

Fig. 1.1a–c. Illustration of a simple NMR experiment. **a** The sample (*three red spheres*) is placed in the static magnetic field, B_0. **b** The RF transmitter excites the spins of the sample by sending a short resonant RF pulse with the Larmor frequency. **c** The exponentially decaying RF signal emitted by the precessing spins of the sample is received.

O. Dietrich, PhD
Department of Clinical Radiology, University Hospitals – Grosshadern, Ludwig Maximilian University of Munich, Marchioninistr. 15, 81377 Munich, Germany

An important limitation of the NMR experiment described above is that the received RF signal cannot be assigned to a spatial location within the sample. Only in the 1970s were the methods developed for localized NMR, i.e., for magnetic resonance imaging (Wehrli 1992; Lauterbur 1973; Mansfield and Granell 1973). The crucial extension to the simple NMR experiment described above is the introduction of additional magnetic fields whose field strength varies linearly with the spatial position. These fields are called magnetic field gradients, or simply gradients, *G*, and they are used to distinguish the RF signals emitted at different locations. In a very simple MRI experiment, we may excite a sample as before, but then switch on a gradient during the data acquisition or readout (Fig. 1.2). Because of this gradient, the Larmor frequencies of the RF-emitting spins now depend on their location and, thus, their location can be determined by analyzing the frequencies received by our antenna. The mathematical procedure to calculate the different frequencies mixed into the received signal of all spins is called the Fourier transform and is the very basis of almost all image reconstruction in MRI.

The relation of received RF signals on the one hand and the reconstructed image data on the other hand is essential in order to understand the techniques of parallel imaging presented in this book. Especially important is the concept of signal data in the frequency domain or k-space (Paschal and Morris 2004) and the image reconstruction by Fourier transformation that are introduced in the following sections.

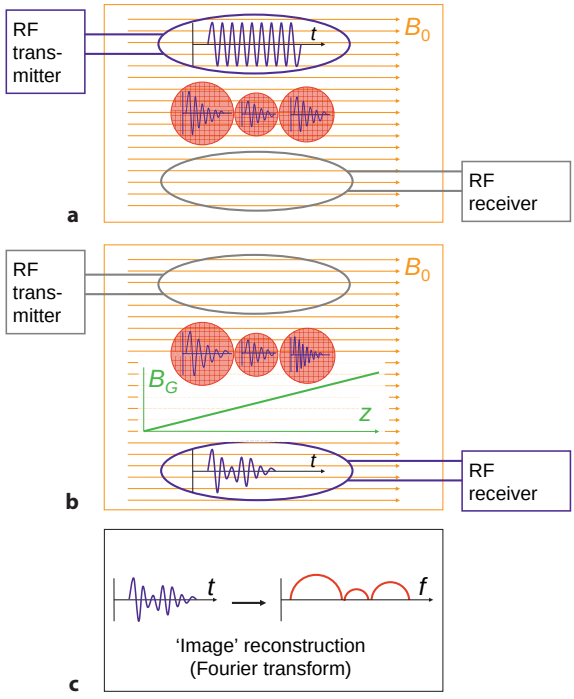

Fig. 1.2a–c. Illustration of a simple MRI experiment. **a** The spins of the sample (*three red spheres*) placed in the static magnetic field, B_0, are excited by an RF pulse. **b** A gradient is switched on, causing a linear magnetic-field dependence and, thus, linearly varying precession frequencies in the sample. The superposition of the of the RF signals is received. **c** A one-dimensional "image" of the sample is reconstructed by Fourier transforming the received signal.

1.2 Fourier Analysis and Fourier Transform

Fourier analysis and the Fourier transform can be illustrated using oscillating processes such as sound waves in acoustics or RF signals in MRI. The most basic oscillation (at least from a mathematical point of view) is a sine (or cosine) wave, which is also called a harmonic oscillation. Harmonic oscillations are characterized by their frequency, *f*; all other periodic oscillations can be described as a mixture of several harmonic oscillations with different frequencies and different amplitudes. The frequencies and amplitudes that are required to describe an arbitrary oscillation are known as the frequency spectrum of the oscillation; this relationship is illustrated in Fig. 1.3. The oscillating signal on the left-hand side is described by one or several harmonic oscillations with different amplitudes. The mathematical tool to calculate the frequency spectrum of a signal is the (discrete) Fourier transform: the signal is transformed into a series of Fourier coefficients describing the amplitude of the oscillation for each frequency, e.g., the rectangular wave with frequency *f* shown at the bottom of Fig. 1.3 can be composed from sine waves with the frequencies *f*, 3*f*, 5*f*, 7*f*… and with the amplitudes 1, 1/3, 1/5, 1/7…, respectively.

An important (but certainly not obvious) property of the discrete Fourier transform is that it can be calculated itself as a superposition of harmonic oscillations. This means, in order to determine the harmonic components of a given signal, the time course of this signal is interpreted as a series of coefficients to calculate a new mixture of oscillations. This idea is illustrated for a rectangular wave in Fig. 1.4. The right-hand side of this figure is simply a visualization of the concept of the frequency spectrum: each point in the frequency domain (shown in red) refers to an

oscillation in the time domain (small blue graphs), and the frequency spectrum defines how to superpose these temporal oscillations to yield the original signal. The (perhaps) surprising part of this figure is shown on the left-hand side and illustrates that the original signal in the time domain can also be interpreted as a spectrum of waves in the frequency space.

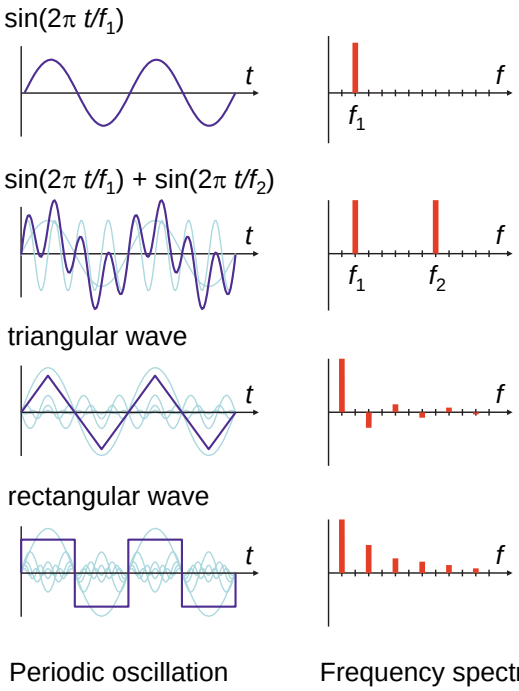

Fig. 1.3. Periodic oscillations can be described by their frequency spectrum. The amplitudes of the frequencies are the coefficients of the Fourier series of a periodic oscillation.

The mathematical background of this property is that the Fourier transform is its own inverse, i.e., it can be inverted by a second Fourier transform (neglecting normalization factors).

Finally, it should be noted that every signal that is restricted to a certain time interval, i.e., every signal of finite duration, can be regarded as a periodic signal simply by repeating it after its duration, as shown in grey in Fig. 1.4. In particular, signals in MRI are restricted either to the duration of the readout interval or to the reconstructed field of view and, thus, the properties of the discrete Fourier transform of periodic data described above are valid for MRI data.

1.3 Spatial Encoding, Gradients, and Data Acquisition

As mentioned above, a single receiving RF coil cannot distinguish where a received MR signal is emitted, but "sees" only the superposition of all radiation emitted from a sample. MRI uses magnetic field gradients to overcome this limitation. By adding a gradient field to the static B_0 field, the resulting magnetic field varies linearly in space. Hence, the Larmor frequencies, being proportional to the field, vary as well; e.g., in the one-dimensional example of Fig. 1.2, spins at the left-hand side have a lower Larmor frequency than spins at the right-hand side. All spins now emit electromagnetic radiation with a frequency corresponding to their spatial position and intensity proportional to

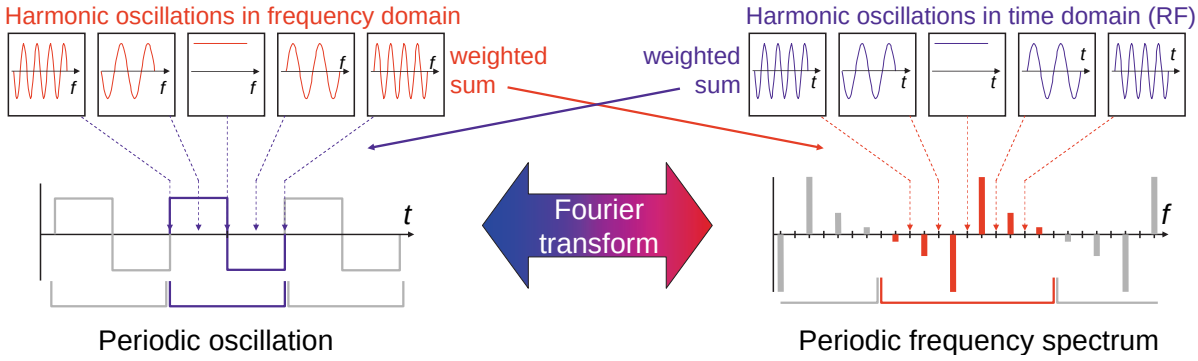

Fig. 1.4. Calculation of the Fourier transform. The discrete Fourier transform of a periodic oscillation (*blue oscillation on the left-hand side*) can be calculated as a sum of harmonic oscillations weighted by the original signal intensities. Conversely, the (inverse) Fourier transformation of the frequency spectrum (*red signal on the right-hand side*) can also be calculated as weighted sum of oscillations, i.e., the Fourier transform of a Fourier transform yields the original signal (neglecting normalization factors).

the density of spins at the different locations. Thus, spatial positions can be distinguished by means of different Larmor frequencies that contribute to the resulting RF signal.

Hence, the "analysis of the received frequency spectrum," i.e., the determination of all frequencies that are superposed within the resulting RF signal, is the fundamental problem of MR image reconstruction as illustrated in Fig. 1.5. Fortunately, this is exactly what the Fourier transform of a signal does: A mixture or superposition of harmonic oscillations with different frequencies and different amplitudes is transformed into a series of Fourier coefficients that describe the amplitude of the oscillation for each frequency. Thus, by Fourier transforming the received RF signal, the spin density is determined for each received frequency, and a one-dimensional "image" can be calculated by assigning the spatial position to each frequency. This is illustrated in Fig. 1.5a for a very simple "image" with spins at only two positions in space. In this case, only two corresponding frequencies are superposed, and the Fourier transform of the mixture of these two frequencies consists of only two non-zero coefficients. A more complicated image with a continuous spectrum of frequencies and more non-zero Fourier coefficients is shown in Fig. 1.5b. Since spatial encoding is achieved by a gradient during readout that assigns different frequencies to different spatial locations, this technique is called frequency encoding, and the gradient is referred to as the frequency-encoding gradient or readout gradient.

While the concept of one-dimensional spatial encoding by a frequency-encoding gradient during the data acquisition is relatively uncomplicated, the two- or three-dimensional spatial encoding of image data requires more explanation. First, it is important to note that all data acquisition in MRI is always dis-

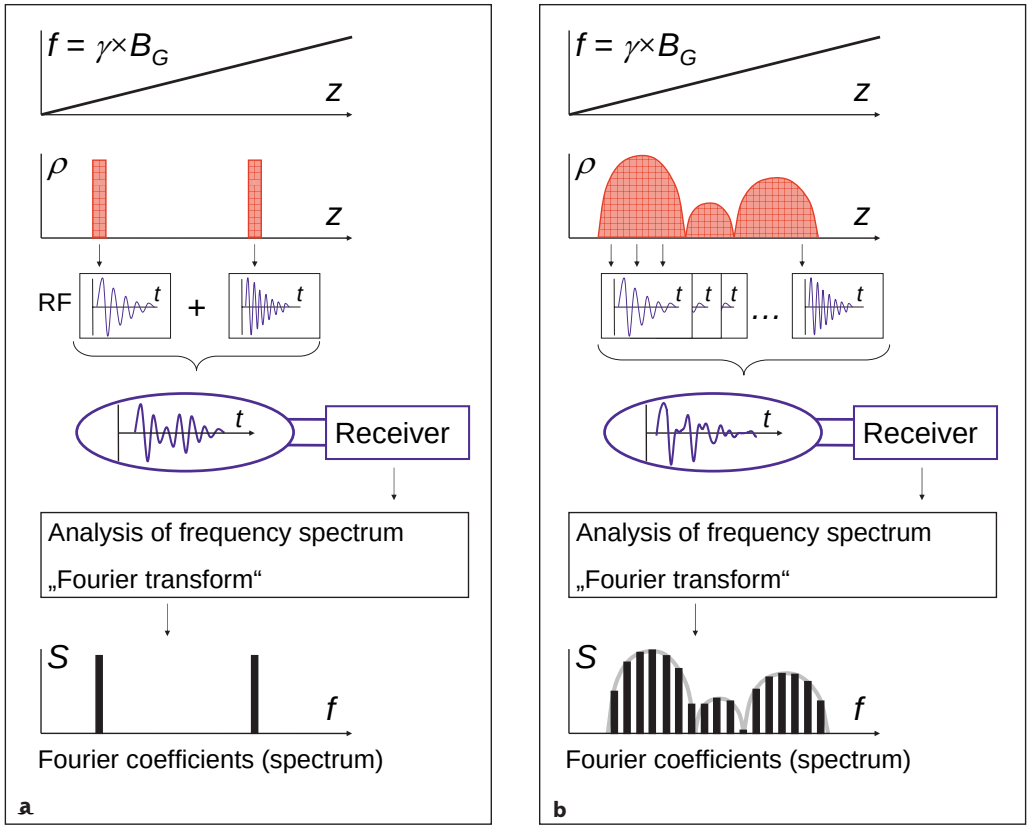

Fig. 1.5a,b. The Fourier transform of the RF signal describes the frequency spectrum of the signal and thus the spin distribution in space. **a** Simple object (*red*) with spins only at two positions in space. The Larmor frequencies of these two positions vary due to an applied gradient. The superposition of two oscillations with different frequencies is received. The calculated frequency spectrum (Fourier coefficients) corresponds to the original object. **b** The object (*red*) emits an RF signal with a continuous distribution of Larmor frequencies. As before, the calculated frequency spectrum corresponds to the original object.

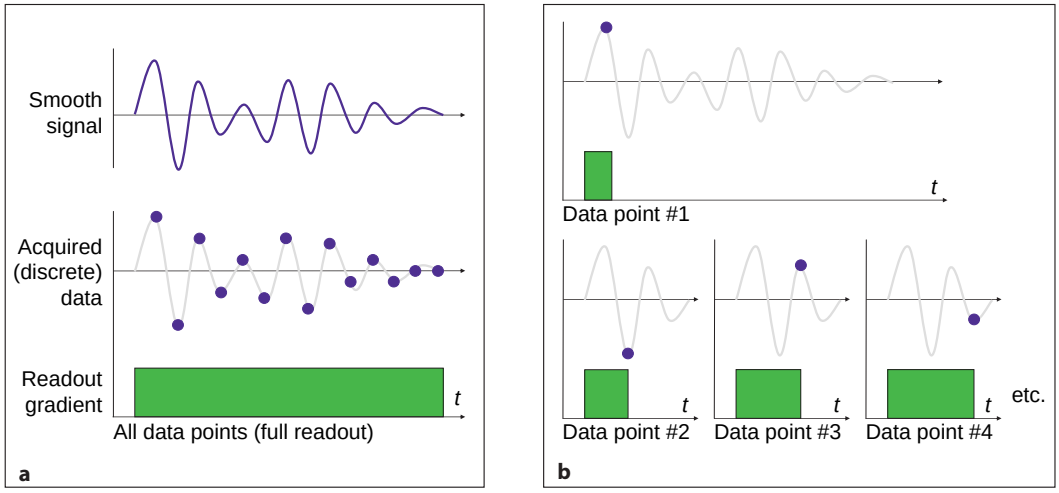

Fig. 1.6a,b. a Frequency encoding: The signal is acquired while the readout gradient is applied. The smooth signal is discretized during acquisition. **b** Phase encoding: Instead of acquisition of the complete signal during a single readout, the discrete data points can be acquired separately after applying gradients of increasing duration. The resulting series of signal intensities is the same as before.

crete, i.e., data consist of a series of separate values and not of a smooth, continuous curve (we will neglect for now that data in MRI are almost always complex data with a real and an imaginary part and show only the real part). For one-dimensional imaging, these discrete data points can be acquired during the application of the readout gradient. Thus, for each data point the readout gradient has been switched on for a certain time before its value is actually measured.

As a consequence, instead of acquiring all data points while the readout gradient is applied, it would also be possible to acquire only a single value at a time after the application of correspondingly timed gradients (see Fig. 1.6). To acquire the same signal curve as before, this procedure must be repeated after the sequence repetition time, TR, for every data point of the readout. Although it may be less obvious, the separately acquired data points describe the same superposition of different Larmor frequencies corresponding to different spatial locations as before. Thus, the spatial distribution of spins can again be calculated by Fourier transforming the signal assembled from several separate measurements. With the described technique, spins at different locations are not distinguished by their current frequency during the (now very short) readout, but by the accumulated phase acquired in the gradient interval before the readout. This technique is therefore called phase encoding and the gradient is referred to as the phase-encoding gradient.

Obviously, this technique is dramatically slower than the acquisition during a single gradient, since instead of a single readout interval of, e.g., 8 ms for all 256 data points, now 256 readouts separated by a TR of, e.g., 600 ms are required, resulting in a scan time increased from 8 ms to 153 600 ms. However, the described technique is exactly what we need in two- or three-dimensional imaging to encode the second and third spatial direction, since the fast data acquisition during the readout gradient can only be applied for a single spatial direction. The only difference in real life is that usually the amplitude of the phase-encoding gradient is modified for each phase-encoding step instead of the duration of the gradient (Fig. 1.7). The resulting data points are the same (neglecting relaxation effects), since the "area under the gradient," i.e., the product of gradient amplitude and duration is the same in both cases.

Thus, using a combination of frequency encoding for one spatial direction and phase encoding for the others, the acquired raw data have identical properties for all directions and can be reconstructed by applying Fourier transforms for all three axes. A simplified version of a three-dimensional non-selective gradient-echo pulse sequence scheme is displayed in Fig. 1.8. The displayed pulse sequence scheme acquires a single frequency-encoded line of raw data and must be repeated for each required line with different combinations of the two phase-encoding gradients. For a three-dimensional data set with a matrix size of 256×256×64, this results in 256×64=16,384 rep-

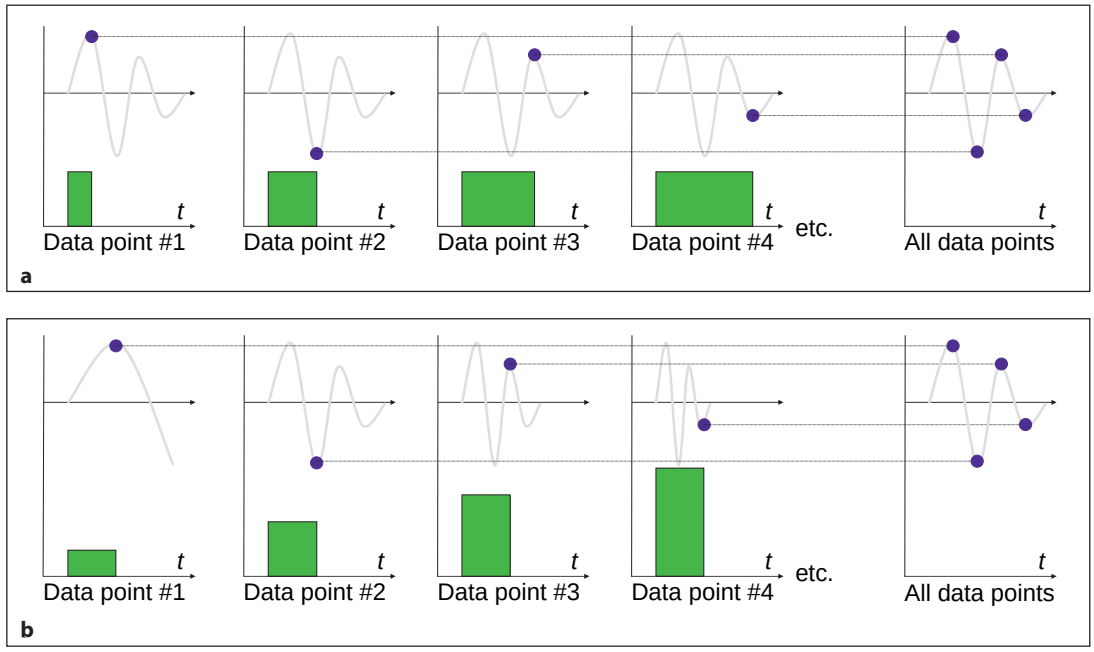

Fig. 1.7a,b. Phase-encoding gradient. **a** The signal is sampled by applying phase-encoding gradients of increasing duration. **b** The same signal can be sampled by applying phase-encoding gradients of increasing amplitude.

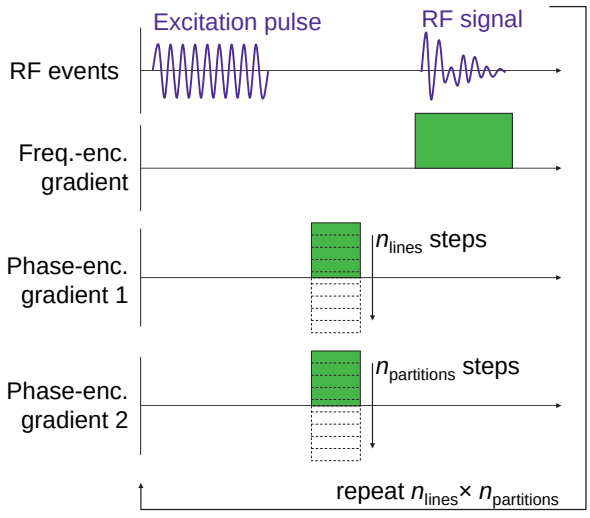

Fig. 1.8. Pulse diagram of a simplified three-dimensional gradient-echo sequence. Frequency and phase encoding are combined to acquire three-dimensional image data. The shown diagram must be repeated for all combinations of amplitudes of the two phase-encoding gradients. Not shown in this diagram is an additional "dephasing" gradient in frequency-encoding direction, which is usually inserted before the data acquisition to shift the maximum of the RF signal to the center of the readout.

etitions. In the case of a fast gradient-echo sequence with a short repetition time of TR=10 ms, the total acquisition time for the three-dimensional data set is thus 163.84 s.

1.4 k-Space and Spatial Frequencies

The complete process of one-dimensional data acquisition and image reconstruction is summarized in Fig. 1.9a. The object to be imaged is shown in red in the image space as a function $\rho(x)$ of the spatial coordinate, x. The frequency-encoding gradient is applied such that the Larmor frequency, f, of the spins becomes proportional to the spatial position, $f \sim x$; the different frequencies are illustrated in blue above the object. The received RF signal (shown in blue on the right hand side) is the sum of all Larmor frequencies weighted by the image density, $\rho(x)$. Mathematically, the received signal is the Fourier transform of the image function $\rho(x)$. At this point, the process of data acquisition is completed.

Image reconstruction is performed as the inverse process of data acquisition. The RF signal is to be

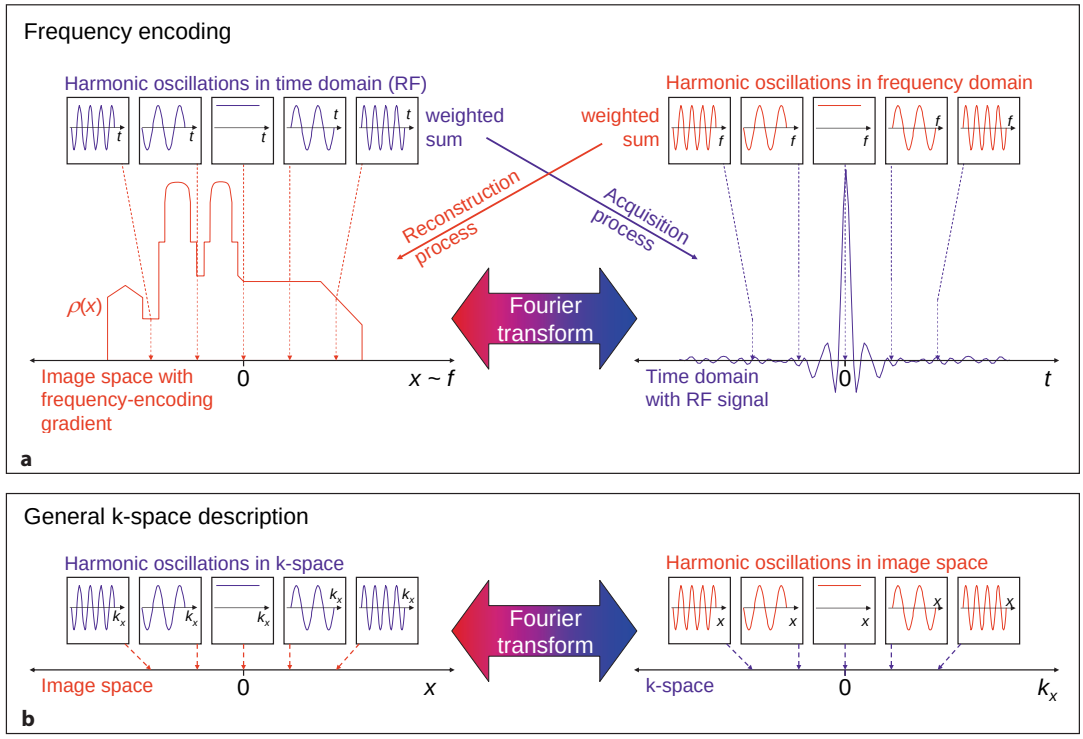

Fig. 1.9a,b. Complete illustration of data acquisition and image reconstruction in one-dimensional MRI. **a** Frequency encoding: Different spatial positions of the imaged object (shown in *red* on the left-hand side) correspond to different RF frequencies (*blue*); data acquisition is the process of acquiring the superposition of all these RF oscillations. Conversely, different points in the time domain can be identified with oscillations in the "frequency domain," and a superposition of these oscillations results in the reconstructed image in frequency (or image) space. Frequency domain and time domain are transformed into each other using the Fourier transform. **b** Generalized k-space description: Points in image space are identified with oscillations in k-space (instead of the time domain) and points in k-space with oscillations in image space (instead of the frequency domain). The latter explains why k is referred to as *spatial frequency*.

decomposed into harmonic oscillations, which again can be achieved with a Fourier transform as described above in Sect. 1.2. In summary, MR data acquisition corresponds to a Fourier transform, and MR image reconstruction corresponds to a second Fourier transform, which is the inverse transformation of the first one.

In the explanations above, one-dimensional raw data have been presented as an RF signal time course or, equivalently, as a series of intensity values as shown in Fig. 1.6. However, as demonstrated in Fig. 1.7, the signal is in general not fully characterized by a gradient duration alone, but rather by the product of duration, t, and amplitude, G, of the encoding gradient. Therefore, it has proven convenient to use the spatial frequency, $k=\gamma \times G \times t$, which is proportional to the product $G \times t$, instead of t as a coordinate for the acquired signal. According to this definition, k is proportional to the area under the gradient of amplitude G and duration t. The received RF signal is now no longer described as a signal time course, but as a function of the coordinate k. Obviously, this definition provides coordinates not only for the frequency-encoding direction, but also for the phase-encoding directions where the amplitude (and not the duration) of the gradient is varied. Thus, each data point of a one-dimensional readout is assigned to a coordinate k between $-k_{max}$ and $+k_{max}$ in k-space, and each data point of a two- or three-dimensional acquisition is described by a pair (k_x, k_y) or a triple (k_x, k_y, k_z) of coordinates in k-space, respectively (Pascal and Morris 2004).

The name spatial frequency has been chosen because each coordinate, k, i.e., each point in k-space, corresponds to a certain spatial oscillation in the image space as demonstrated in Fig. 1.9b. This

figure is a generalization of Fig. 1.9a with RF signals as functions of k_x instead of t. As mentioned above, each coordinate of the RF signal corresponds to harmonic oscillation, and in the generalized description, these are oscillations in image space (in contrast to oscillations in the frequency domain for frequency encoding or oscillations in an "inverse gradient" domain for phase encoding). Thus, the description of MR raw data and image reconstruction can be unified for all spatial directions and all kinds of spatial encodings by introducing k-space. It should finally be noted that the spatial frequency is given in units of an inverse length, e.g., in 1/cm, in analogy to the more common temporal frequencies with units of inverse time: 1 Hz=1/s.

In MRI we usually deal with two- or three-dimensional data sets and their representation in k-space. Again, each point in two-dimensional k-space corresponds to a harmonic oscillation as shown in Fig. 1.10, and image reconstruction aims at adding all these oscillations weighted with the amplitude of k-space data at this point. Mathematically, this is done by calculating the two- or three-dimensional Fourier transform of the k-space data.

Raw data in k-space have some essential properties that can be derived from Fig. 1.10 and are discussed using the MR image shown in Fig. 1.11. A first important observation is that most of the intensity of k-space data is usually found in the center of k-space. The center corresponds to low spatial frequencies, i.e., to slowly varying image intensity in the image space. This slowly varying portion usually determines the overall impression of an image, as illustrated in Fig. 1.12. Although only a very small fraction of less than 1% of all k-space data were used for reconstruction, the overall shape and contrast of

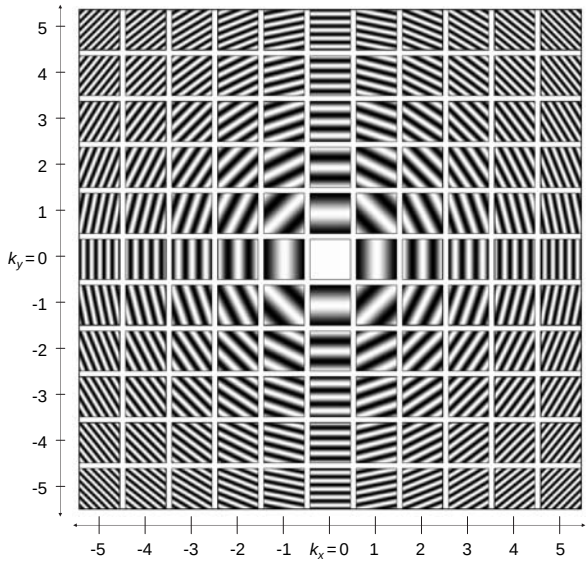

Fig. 1.10. Illustration of spatial frequencies: Each *square* illustrates a single point in (two-dimensional) k-space. These points correspond to those spatial oscillations in image space that are shown in the *squares*. Low spatial frequencies are found in the center of k-space; image intensity varies slowly in image space. High spatial frequencies correspond to peripheral points in k-space.

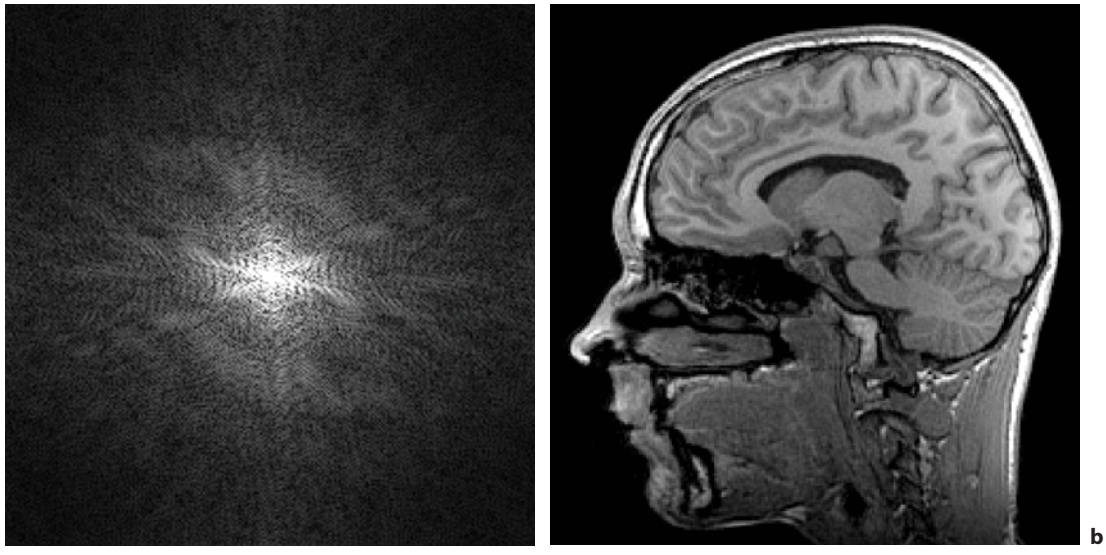

Fig. 1.11a,b. a Raw data in k-space (magnitude presentation of complex data) and **b** corresponding reconstructed MR image. Highest intensities in k-space are found in the center, corresponding to slowly varying image intensities in **b**.

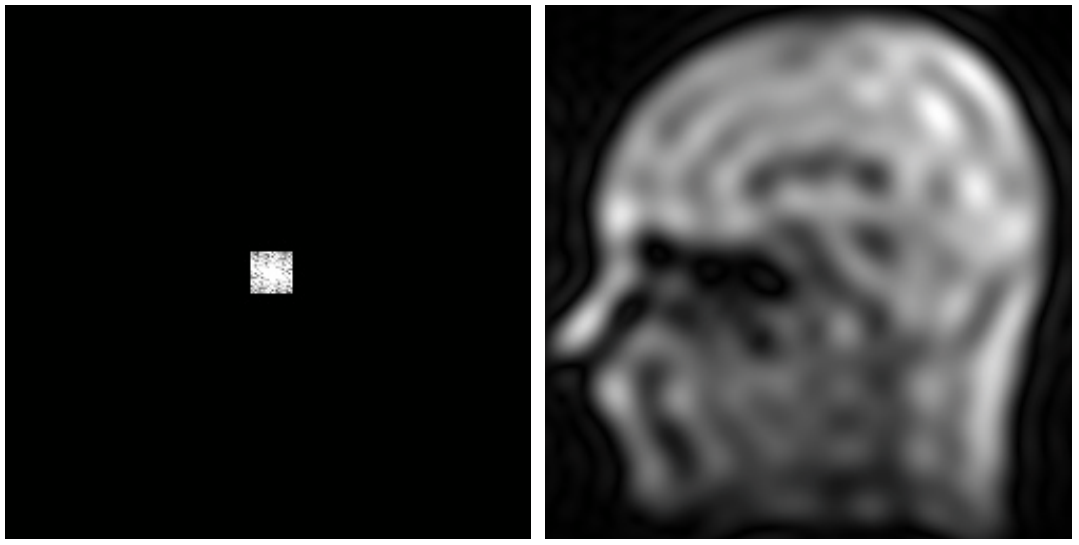

Fig. 1.12a,b. a Raw data in the center of k-space and **b** corresponding reconstructed MR image. The image appears filtered; only large-scale changes of intensity corresponding to low spatial frequencies remain.

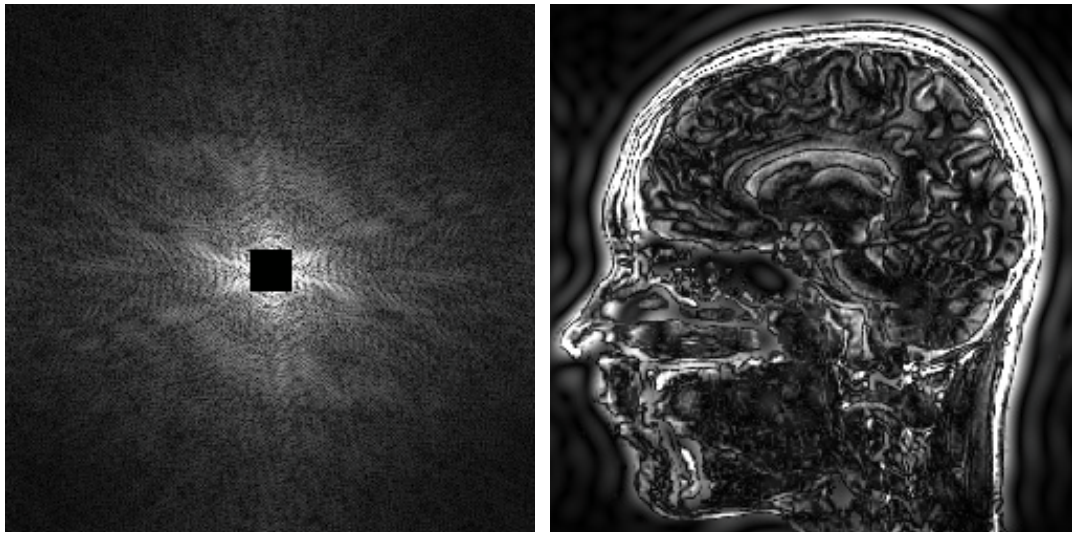

Fig. 1.13a,b. a Raw data in the periphery of k-space and **b** corresponding reconstructed MR image. The image contains information complementary to Fig. 1.12a**.** Only changes of intensity in small spatial scales corresponding to high spatial frequencies remain.

the image is still recognizable. The remaining 99% of k-space contains information about the image details, in particular about the shape of sharp edges as illustrated in Fig. 1.13. High spatial frequencies are required to describe rapid changes of signal intensity in very small areas, and the maximum spatial resolution of an image, Δx, is determined by the highest spatial frequencies acquired, i.e., by the largest coordinates, k_{max}, in k-space.

Another essential property of the Fourier transform can now be deduced from the symmetry of the Fourier transform. Since we have just seen that the image resolution, Δx, depends on the maximum value of the spatial frequency, k_{max}, in k-space, it must be also be true that the resolution in k-space, Δk, is connected with the maximum image coordinate, x_{max}. The meaning of this is illustrated in Fig. 1.14. If the resolution in k-space is reduced by doubling Δk,

then the maximum field of view of the reconstructed image is reduced to 50%. In the shown example, the field of view is now smaller than the head in the anterior-posterior direction, resulting in typical aliasing or fold-over artefacts. Although the shown image still has the same nominal size as before, it contains information in only 50% of all data rows, i.e., the right half of the image is completely identical to the left half. Further reduction of k-space sampling density is shown in Fig. 1.15, where only every fourth k-space line is acquired. Aliasing is much more severe in the reconstructed image with an effective field of view of only a fourth of the original one.

A further property of raw data is its (Hermitian) point symmetry that is employed for partial Fourier imaging as described in Chapter 7. Finally, it should

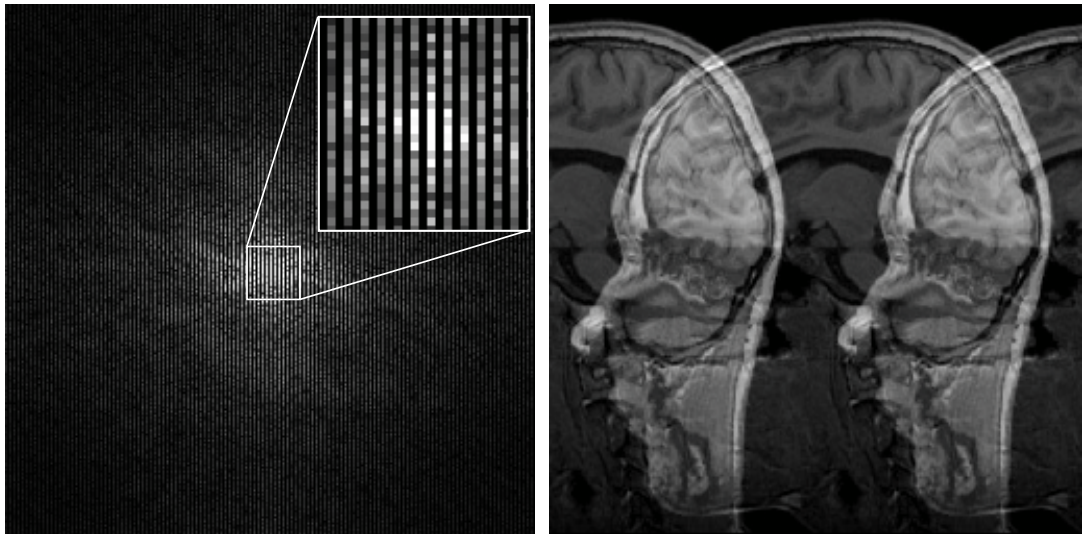

Fig. 1.14a,b. **a** Raw data after removing every other line in k-space and **b** corresponding reconstructed MR image. The effective field of view of the image is reduced to 50%, resulting in aliasing artefacts in anterior-posterior direction.

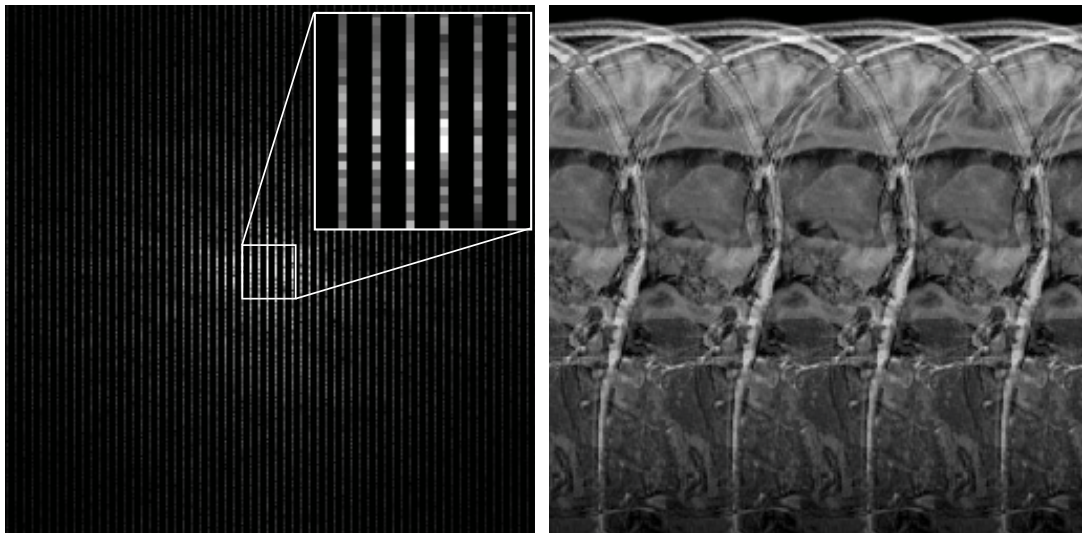

Fig. 1.15a,b. **a** Raw data after removing three of four neighboring lines and **b** corresponding reconstructed MR image. The effective field of view of the image is reduced to 25%, resulting in severe aliasing artefacts in anterior-posterior direction.

be noted that each point in k-space corresponds to an oscillation over the complete image space as demonstrated in Fig. 1.10. Thus, an erroneous data value at a single point in k-space will influence all pixels in image space, as illustrated in Fig. 1.16. The artificially added point artefact in the raw data results in a global artefact in image space.

The k-space is important to understand image reconstruction, but also to distinguish different kinds of data acquisition schemes. The simplified three-dimensional gradient-echo sequence shown in Fig. 1.8 acquires k-space data line-by-line; all lines are parallel, and their orientation is defined by the frequency-encoding gradient. However, other k-space sampling schemes can also be employed, although they are less frequently used than conventional Cartesian acquisitions. The most important alternatives are radial and spiral k-space sampling (Lauzon and Rutt 1996; Block and Frahm 2005). Both techniques typically start data acquisition in the center of k-space and cover k-space either with straight radial lines (like the spokes of a wheel) or with a single or with several spiral trajectories. To avoid image artefacts, the maximum distance, Δk, between neighboring sample points in k-space is required to be sufficiently small, similarly as in Cartesian imaging. Further details about these non-Cartesian techniques can be found in Chapter 6.

1.5 Parallel Imaging

As mentioned above, MRI acquisitions can be very time consuming since raw data are typically acquired line by line, and the pulse sequence must be repeated for each of these lines in order to build up a full data set in k-space. Even with the minimum possible echo times and repetition times, the total acquisition time of a data set may be unacceptably long for many state-of-the-art MRI applications such as dynamic MR angiographies, perfusion MRI, or MR imaging of the cardiac function. Therefore, reducing the number of k-space lines required for an acquisition is often desirable. However, it is usually not acceptable simply to acquire fewer lines in the k-space periphery since this decreases the spatial resolution of the image data, although a reduction of lines of up to almost 50% can be achieved with partial-Fourier techniques where the k-space periphery is sampled asymmetrically (King 2004). Partial-Fourier imaging and several other specific techniques to increase imaging speed are discussed in detail in Chapter 7.

Most of these techniques (with the exception of partial-Fourier imaging) are limited to a few specific MRI applications. In contrast to these specific approaches, an idea for accelerated acquisitions pro-

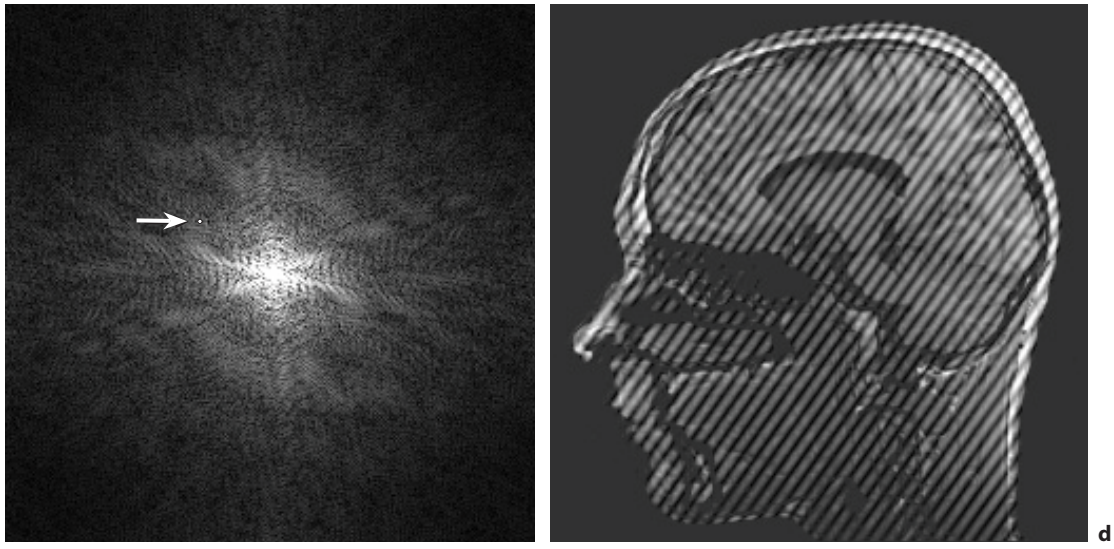

Fig. 1.16a,b. a Raw data after adding a single point with artificially increased intensity (*arrow*) and **b** corresponding reconstructed MR image. The image is affected from artefacts extending over the complete field of view.

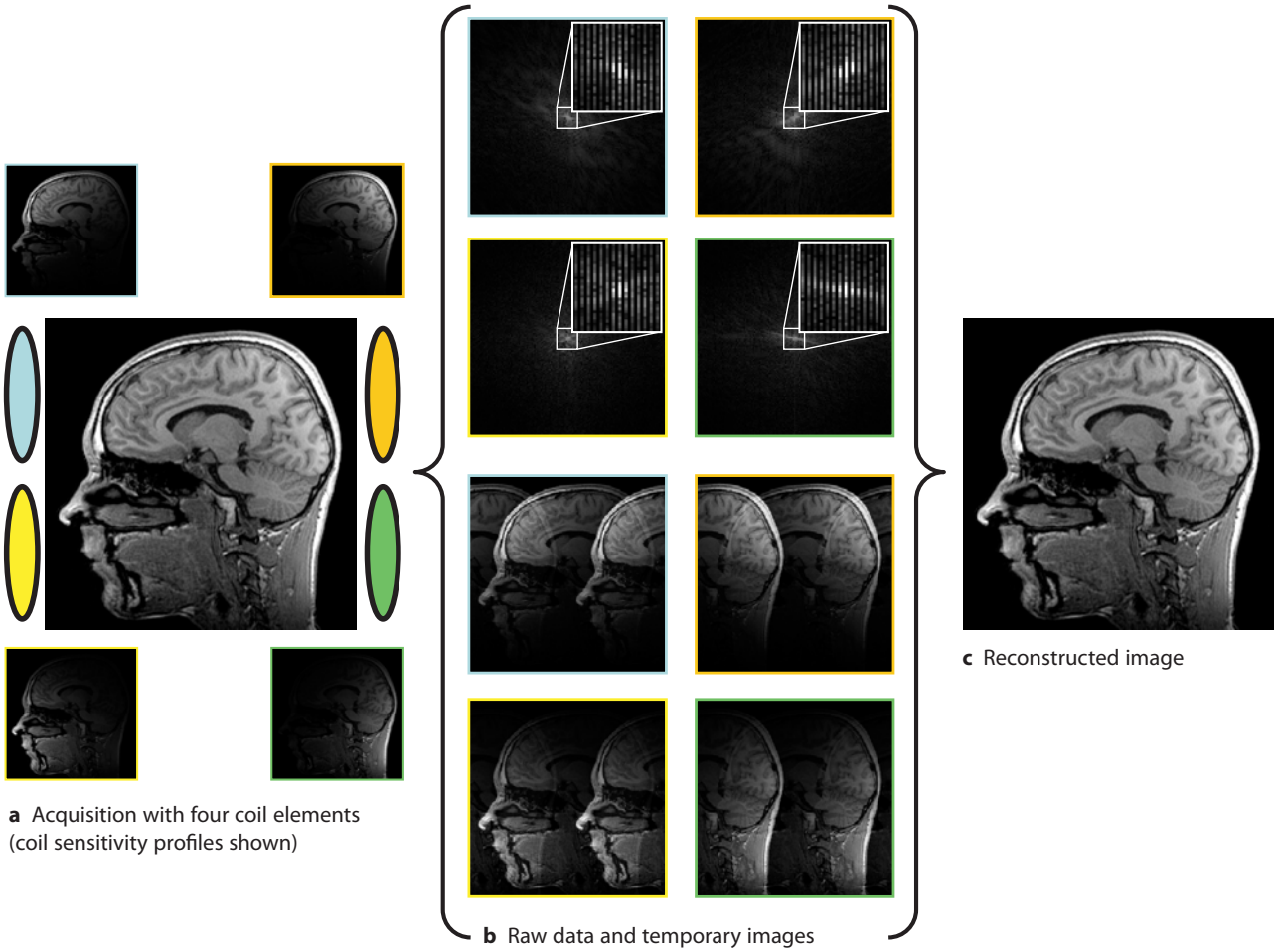

Fig. 1.17a–c. Data acquisition and image reconstruction in parallel MRI. **a** Data is acquired by four coil elements with different spatial sensitivity profiles in parallel. **b** Four sets of reduced raw data are available for image reconstruction. Each of these data sets corresponds to an aliased image from one of the coil elements. **c** Specific reconstruction algorithms are required to reconstruct the image in parallel MRI.

posed in the second half of the 1990s has found wide acceptance in virtually all areas of MRI (Dietrich et al. 2002; Heidemann et al. 2003; Bammer and Schoenberg 2004): this approach is now known as parallel imaging, parallel MRI, (partially) parallel acquisition (PPA), or parallel acquisition techniques (PAT).

The basic idea of parallel imaging is to employ several independent receiver coil elements in parallel to reduce the number of phase-encoding steps. Thus, a certain amount of the spatial encoding originally achieved by the phase-encoding gradients is now substituted by evaluating data from several coil elements with spatially different coil sensitivity profiles. The reduction of phase-encoding steps is achieved by reducing the sampling density, Δk, in k-space as illustrated in Fig. 1.17. Raw data reduction factors between 2 and 6 can typically be achieved with parallel imaging in a single direction; a combination of reduced sampling densities in two phase-encoding directions is possible in 3D MRI and results in higher total reduction factors. The maximum reduction factor is limited by the number of independent coil elements or separate receiver channels of an MRI system. Thus, the most important precondition for the applicability of parallel imaging is a multi-channel MRI system with several parallel receiver channels as well as appropriate multi-channel coil systems.

Data acquisition for parallel MRI is very similar to acquisition schemes of conventional pulse sequences. Most relevant techniques of MRI can be adapted relatively easily to parallel imaging, since the data acqui-

sition is essentially equivalent to an acquisition of a reduced (rectangular) field of view in the phase-encoding direction. Image reconstruction of parallel imaging raw data on the other hand is much more demanding than conventional Fourier-transform reconstruction, and considerable efforts have been made to develop optimized reconstruction algorithms. Today, several reconstruction techniques are used for parallel imaging (Blaimer et al. 2004); the most common approaches are known by the acronyms SENSE (Pruessmann et al. 1999), SMASH (Sodickson and Manning 1997), and GRAPPA (Griswold et al. 2002). All these approaches aim for the best compromise between minimizing localized image artefacts on the one hand and image noise on the other hand. Details about the different techniques used for parallel imaging as well as about hardware and software requirements are presented in Chapters 2 and 3.

The main motivation for the development of parallel imaging and its application in the clinical routine is the acceleration of the image acquisition. Acceleration factors of two, three, or four are achieved by sampling only every second, third, or fourth k-space line, respectively. However, several other areas of MRI also benefit from parallel imaging; in particular, parallel imaging can be efficient to reduce several kinds of image artefacts as discussed in Chapter 5.

1.6 Signal and Noise

Image noise is present in practically all MR images and is one of the major limiting factors for MRI protocols. The effect of image noise is demonstrated in Fig. 1.18: small low-contrast structures, such as, e.g., in the cerebellum, become more difficult to differentiate with increasing noise levels. The noise level is described by the noise standard deviation, σ, and its statistical distribution. The visual impression of an MR image depends on the signal-to-noise ratio (SNR), i.e., the ratio of the signal intensity and the noise standard deviation:

SNR=(signal intensity)/(noise standard deviation).

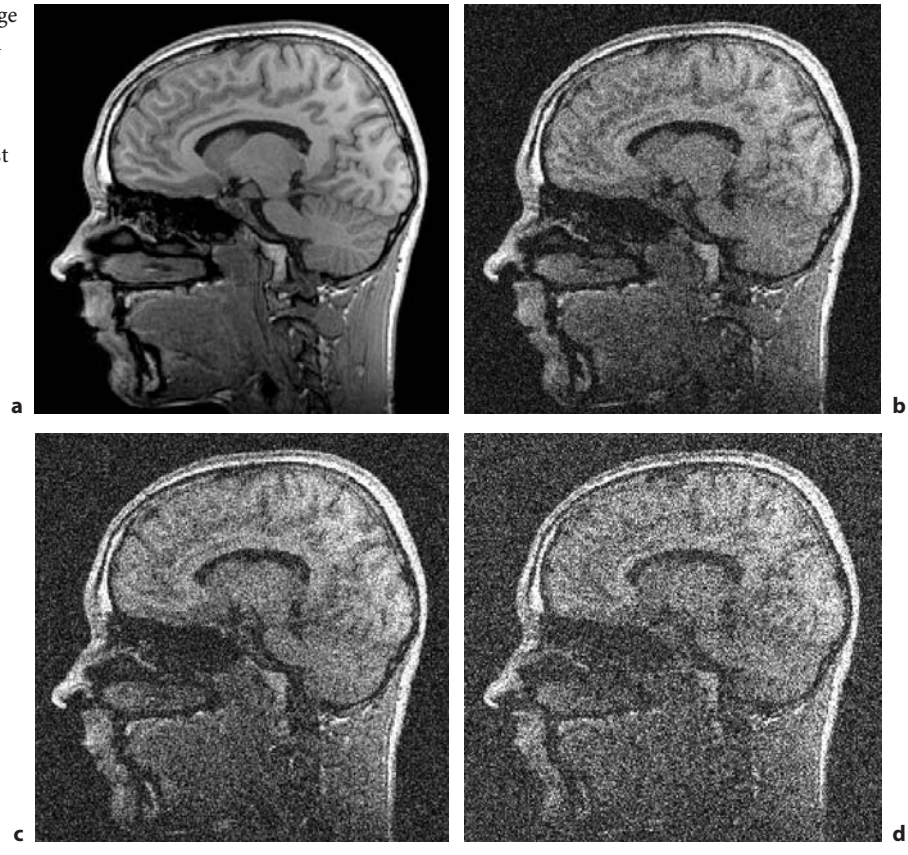

Fig. 1.18a–d. Illustration of image noise. The same MR image with increasing noise levels (from **a** to **d**) is shown. High noise levels reduce the visibility of small details and of low-contrast changes.

Typically, noise becomes a limitation in fast imaging techniques, since the noise level of an MR image is connected with its acquisition time. The dependence of the signal-to-noise ratio on the acquisition time and several other MR imaging parameters can be summarized in the formula (Edelstein et al. 1986; Haake et al. 1999):

$$\mathrm{SNR} \approx C \times \Delta x \times \Delta y \times \Delta z \times \sqrt{T_{\mathrm{receive}}} \times B_0$$

where Δx, Δy and Δz describe the dimensions size, T_{receive} is the total time of receiving RF data, B_0 is the static field strength, and C is a factor describing all other influences such as image contrast, relaxation effects, coil geometry and efficacy, coil fill factor, temperature, etc. Most important for fast imaging is the dependence on the square root of T_{receive}. The time T_{receive} is calculated as the product of the duration of a single readout, T_{readout}, and the number of all readouts of the complete raw data set, i.e., the number of phase-encoding steps, N_{phase}, times the number of averages, N_{averages}:

$$T_{\mathrm{receive}} = N_{\mathrm{phase}} \times N_{\mathrm{averages}} \times T_{\mathrm{readout}}$$

The duration of the single readout, T_{readout}, depends on the receiver bandwidth, BW, of the pulse sequence, $T_{\mathrm{readout}} \sim 1/\mathrm{BW}$. Thus, by doubling the receiver bandwidth, the SNR is reduced to $1/\sqrt{2} \approx 71\%$ of the original value. On the other hand, by increasing the number of averages from one to four, the SNR can be doubled. Similarly, increasing the field of view in a phase-encoding direction while leaving the voxel size constant, i.e., increasing the number of phase-encoding steps, N_{phase}, results in a higher SNR as well. It should be noted that the total receiving time, T_{receive}, is not the total acquisition time, T_{acq}, i.e., the duration of the pulse sequence. The latter depends on the repetition time, TR, and the pulse sequence design (e.g., single-echo vs. multi-echo sequence, etc.).

Parallel imaging reduces the number of phase-encoding steps without changing the geometry (field of view) or the voxel size of the reconstructed image. Thus, the total acquisition time, T_{acq}, and simultaneously the total receiving time, T_{receive}, can be reduced to, e.g., 50 or 25% of its original value. Consequently, the SNR is also reduced to at least 71 or 50%, respectively. This is an unavoidable side effect of parallel imaging that is discussed in detail in the following chapters. Consequently, quantification of SNR is an important issue in parallel imaging studies; however, due to the specific properties of the reconstruction algorithms used for parallel imaging, this quantification can usually not be performed in a straightforward manner (Dietrich et al. 2005). The potential difficulties and several appropriate techniques to determine the SNR in parallel imaging are presented in Chapter 4.

1.7 Conclusion

Parallel imaging is a relatively new MRI technique that employs parallel data acquisition from several receiver coil elements in order to reduce the number of phase-encoding steps and, thus, to increase imaging speed. To discuss acquisition techniques and image reconstruction algorithms used in parallel MRI, the concepts of k-space and of the Fourier transform introduced in this chapter are indispensable. Based on these concepts, parallel imaging from its historic origins to current state-of-the-art techniques is presented in the following chapters of the first part of this book.

References

Bammer R, Schoenberg SO (2004) Current concepts and advances in clinical parallel magnetic resonance imaging. Top Magn Reson Imaging 15:129–158

Blaimer M, Breuer F, Mueller M, Heidemann RM, Griswold MA, Jakob PM (2004) SMASH, SENSE, PILS, GRAPPA: how to choose the optimal method. Top Magn Reson Imaging 15:223–236

Bloch F (1946) Nuclear induction. Phys Rev 70:460–474

Bloch F, Hansen WW, Packard M (1946) Nuclear induction. Phys Rev 69:127

Block KT, Frahm J (2005) Spiral imaging: a critical appraisal. J Magn Reson Imaging 21:657–668

Dietrich O, Nikolaou K, Wintersperger BJ, Flatz W, Nittka M, Petsch R, Kiefer B, Schoenberg SO (2002) iPAT: applications for fast and cardiovascular MR imaging. Electromedica 70:133–146

Dietrich O, Reeder SB, Reiser MF, Schoenberg SO (2005) Influence of parallel imaging and other reconstruction techniques on the measurement of signal-to-noise ratios. Proc Intl Soc Mag Reson Med 13:158

Edelstein WA, Glover GH, Hardy CJ, Redington RW (1986) The intrinsic signal-to-noise ratio in NMR imaging. Magn Reson Med 3:604–618

Gadian DG (1995) NMR and its applications to living systems, 2nd edn. Oxford University Press, Oxford New York Tokyo

Griswold MA, Jakob PM, Heidemann RM, Nittka M, Jellus V, Wang J, Kiefer B, Haase A (2002) Generalized autocalibrating partially parallel acquisitions (GRAPPA). Magn Reson Med 47:1202–1210

Haacke EM, Brown RW, Thompson MR, Venkatesan R (1999) Magnetic resonance imaging: physical principles and sequence design. Wiley-Liss, New York

Heidemann RM, Ozsarlak O, Parizel PM, Michiels J, Kiefer B, Jellus V, Muller M, Breuer F, Blaimer M, Griswold MA, Jakob PM (2003) A brief review of parallel magnetic resonance imaging. Eur Radiol 13:2323–2337

King KF (2004) Partial Fourier reconstruction. In: Bernstein MA, King KF, Zhou XJ (eds) Handbook of MRI sequences. Elsevier Academic Press, London, pp 546–557

Lauterbur PC (1973) Image formation by induced local interactions: examples employing nuclear magnetic resonance. Nature 242:190–191

Lauzon ML, Rutt BK (1996) Effects of polar sampling in k-space. Magn Reson Med 36:940–949

Mansfield P, Granell P (1973) NMR 'diffraction' in solids? J Phys C 6:L422–L426

Paschal CB, Morris HD (2004) K-space in the clinic. J Magn Reson Imaging 19:145–159

Pruessmann KP, Weiger M, Scheidegger MB, Boesiger P (1999) SENSE: sensitivity encoding for fast MRI. Magn Reson Med 42:952–962

Purcell EM, Torrey HC, Pound RV (1946) Resonance absorption by nuclear magnetic moments in a solid. Phys Rev 69:37–38

Sodickson DK, Manning WJ (1997) Simultaneous acquisition of spatial harmonics (SMASH): fast imaging with radiofrequency coil arrays. Magn Reson Med 38:591–603

Wehrli FW (1992) Principles of magnetic resonance. In: Stark DD, Bradley WG (eds) Magnetic resonance imaging. Mosby-Year Book, St. Louis, pp 3–23

Basic Reconstruction Algorithms for Parallel Imaging

2

Mark A. Griswold

CONTENTS

M. A. Griswold, PhD
Department of Radiology, Case Center for Imaging Research, Case Western Reserve University School of Medicine, 11100 Euclid Avenue, Cleveland, OH 44106, USA

2.1 Introduction

The past few years has seen the rapid development of many parallel imaging methods for nearly every MR application, as demonstrated by the high-quality clinical images shown in this book. The goal of this chapter is to provide the clinician with a basic understanding of these methods, including how they were developed. Particular emphasis is placed on underlying requirements and assumptions of the various methods, since these directly relate to the potential image artefacts seen in images reconstructed with any particular parallel imaging method.

We begin with a very idealized experiment which demonstrates the basic principles and limitations involved in parallel imaging. This is followed by a short history of the development of more general parallel imaging methods and detailed descriptions of some of today's most widely used methods. Finally, some of the important emerging parallel imaging methods are briefly described.

2.2 A Simplified Example

While most modern parallel imaging methods require somewhat complex mathematical skills, most of the basic concepts and requirements can be understood from a very simple example, which is a simplification of the basic parallel imaging with localized sensitivities (PILS) method (Griswold et al. 2000).

Let us assume we are interested in imaging an axial cross section of a head with the phase-encoding direction in the left–right direction. If we use a standard head coil, we would have to image with a large enough field of view (FOV) to cover the entire width of the head. Also assume we need N_y points in the phase-encoding direction to achieve the resolu-

tion we need (see Fig. 2.1a). Assuming we acquire one echo per TR interval, this would require a time of $N_y \times$ TR to acquire the image.

Now assume we have a coil which only has sensitivity on the left half of the head. In this case, we could image just the left side of the head with half the total FOV. This would require only 0.5 N_y phase-encoding steps to achieve the same resolution, resulting in a two-times increase in our imaging speed; however, we would only have an image of one-half of the head (see Fig. 2.1c). In addition, this image would have a signal-to-noise ratio (SNR) which is reduced by $\sqrt{2}$ compared with the full acquisition, due to the reduced imaging time, however, assuming that instead of a single coil we have an array that includes another coil that can simultaneously image the right side of the head (Fig. 2.1d). In this case, each coil would only see half of the head, but used together, we could stitch together an image of the whole head (Fig. 2.1e). This would have been accomplished in half of the normal imaging time. This is the most simple version of parallel imaging, but it highlights five basic concepts of parallel imaging:

- Multiple receiver coils must be positioned so that each coil has a different sensitivity over the FOV. In this case, each coil has sensitivity on only one side of the head.
- Each receiver coil must be supplied with its own independent receiver chain, so that all coils in the array can operate simultaneously.
- A reduced number of phase-encoding steps are acquired, generally resulting in an aliased, or folded-over, image in a reduced imaging time. (Aliasing artefacts will be absent only in the special case of our simplified example involving two completely disjoint coil sensitivities.)
- The following parallel imaging reconstruction has to have knowledge of the sensitivity patterns of the individual coils in the array. In this example, we must know which coil is on the left and which one is one the right. In the most extreme cases, we must know the complex sensitivity of each coil at each pixel in the image.
- Image SNR is reduced by at least the square-root of the reduction factor used in the image acqui-

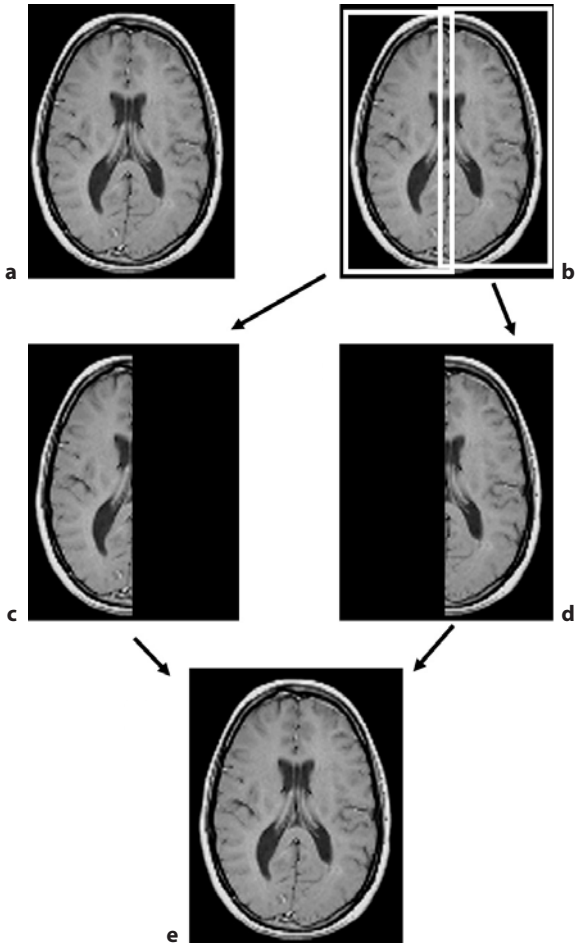

Fig. 2.1a–e. A simplified example of parallel imaging. **a** Full-field-of-view (FOV) image. **b** The two coils shown as *white boxes* each have sensitivity on only one side of the head. **c** The left coil can be used to make an image of the left side of the brain in half the imaging time. **d** The same can be done simultaneously with the right coil. **e** These two images can be combined to obtain a complete image in half the normal imaging time.

sition. As discussed in detail in the next chapter, SNR is typically reduced even more than this, and the additional reduction is referred to as geometry factor, or g-factor losses.

While this example illustrates these basic points, a method such as this is nearly useless in practice, since we typically do not have access to a coil with sharp boundaries between different regions of the object. The rest of this chapter discusses more general methods which have been developed to deal with this and other problems encountered in practice. Historically, these methods have been categorized by the path taken from the data acquisition to the reconstructed image. The image domain methods, such as SENSE (Pruessmann et al. 1999), operate, as expected, entirely in the image domain using folded images and coil sensitivity maps. On the other hand, k-space methods, such as SMASH (Sodickson and Manning 1997) or Generalized SMASH (Bydder et al. 2004a), or GRAPPA (Griswold et al. 2002a), work entirely in k-space. There are also hybrid methods which perform the reconstruction directly from the k-space data to an unaliased image. SPACERIP (Kyriakos et al. 2000) and generalized SENSE (Pruessmann et al. 1999, 2001) are examples of this type of reconstruction.

2.3 A Short History of Parallel imaging Methods

2.3.1 The First Method Started in k-Space

Carlson then at University of California, San Francisco (and later with Minemura at Toshiba), recognized early that one could accelerate image acquisition using a combination of both phase-encoding gradients and RF coils to reconstruct an image. The method that he proposed worked directly in the k-space (or raw data) domain (Carlson 1987; Carlson and Minemura 1993) using a specifically constructed head coil, which generated a homogeneous sensitivity pattern in one channel of the coil, and a linear gradient in the other channel. Using this specifically designed coil array, their reconstruction method used a Fourier series expansion to reconstruct the unfolded image data directly in k-space. This method successfully reconstructed phantom data as early as 1989 and in vivo reconstructions were acquired using this method as early as 1993 (see Fig. 2.2). Unfortunately, an abstract containing these in vivo images was rejected from the SMRM in 1994, and these images remained relatively unknown until the 2004 Second International Workshop on Parallel Imaging in Zurich (Carlson et al. 2004).

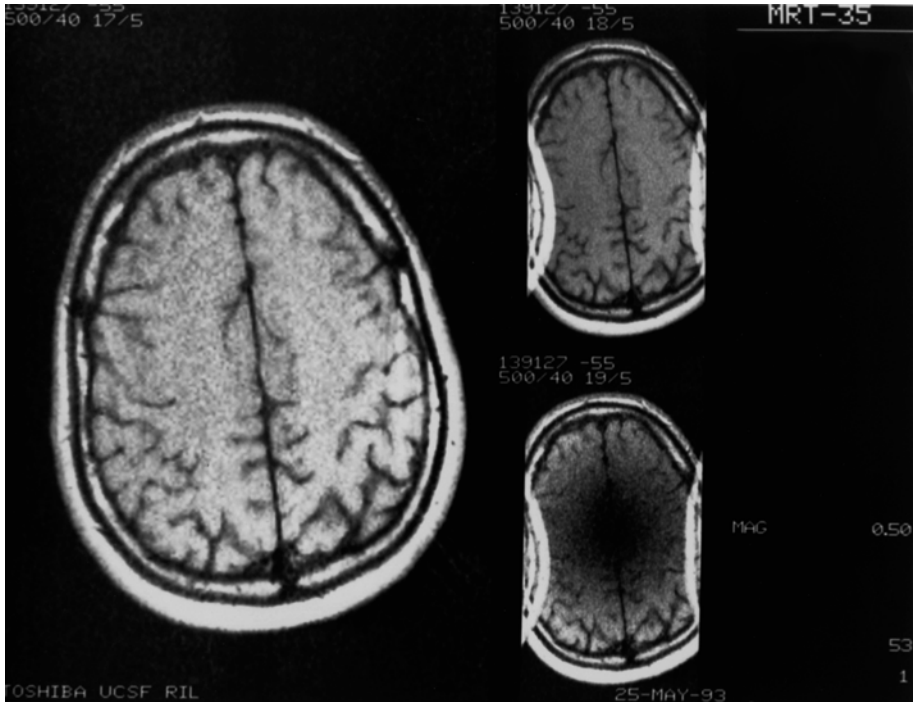

Fig. 2.2. The first known in vivo parallel imaging reconstructions. These images were reconstructed using the method of Carlson and Minemura (1993), which requires the use of one homogeneous coil (*upper right*) and one with a linear gradient sensitivity (*lower right*). The two-times accelerated image is shown on the left (Courtesy of J. Carlson, Lawrence Berkeley National Laboratory, Berkeley, Calif.).

2.3.2 Early Image-Based Methods

After several people had proposed using RF coils to essentially encode the entire image along the phase-encoding direction (e.g., Hutchinson and Raff 1988; Kwiat et al. 1991), Kelton et al. (1989) from the University of Illinois were the first to propose an image domain parallel imaging reconstruction in 1989 which used normal phase encoding in combination with partial RF coil encoding. This was accomplished by skipping some fraction of the normal phase-encoding steps followed by a matrix inversion to unalias the resulting images. Although the quality of the resulting reconstruction was not perfect (Fig. 2.3), this was the first image domain parallel imaging reconstruction in the modern sense of the term. Ra and Rim (1993) from the University of South Korea followed a few years later with a similar proposal which would work for cases when the reduction factor was less than the number of coils. Their technique was used in phantom experiments with good results, although as with Kelton et al. (1989), no in vivo data were obtained. A fundamental limitation of both of these studies was the lack of a robust method for determining the coil sensitivities needed for the reconstruction.

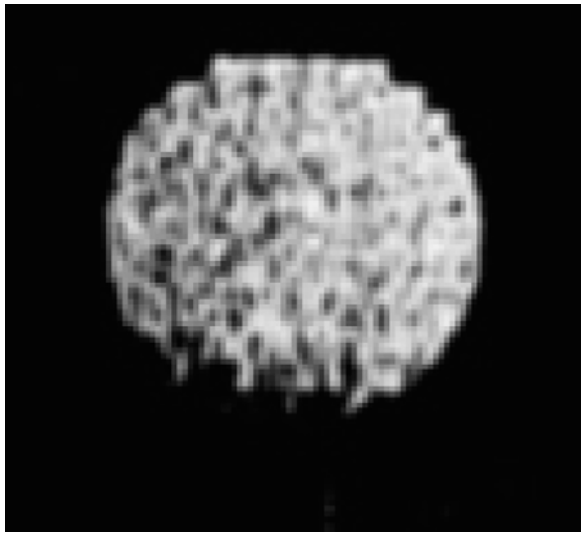

Fig. 2.3. The first known image domain parallel imaging reconstruction from the Kelton et al. (1989) poster.The two-element array setup was a saddle coil and a surface coil. The spin-echo imaging parameters were TR 750 ms and TE 70 ms, with a final image matrix of 64×256 reconstructed from two 32×256 images (Courtesy of S. Wright, Texas A&M University, College Station, Texas).

2.3.3 Why These Early Methods Did Not Catch On

While any of these methods could have started the parallel imaging revolution, no one really "took up arms", before the introduction of the SMASH method in 1997 (Sodickson and Manning 1997). In retrospect, this can be traced to several reasons, which are instructive to examine so that one can understand the important elements of modern parallel imaging methods, and why they are successful when previous methods were not. One of the primary reasons previous methods were not investigated further was actually the lack of scanners with multi-channel capability. Without this, parallel imaging is impossible. Another significant limitation was that most MRI scans at the time had low enough SNR that multiple averages had to be used, due to both the lack of an imaging array, but also due to inefficient sequences and suboptimal system electronics. In these cases, where SNR was the limiting factor, it was clearly easier to reduce the number of averages to save time compared with a complicated parallel imaging reconstruction. Half-Fourier methods could also be used to gain another factor of two in imaging speed, which typically brought most sequences to the lower limit of acceptable SNR, so further reductions in imaging time were not feasible.

These reasons hindered much of the work in this area, and left many important details unresolved. In particular, the lack of coil sensitivity mapping and the requirement of special coil arrays were significant limitations that needed to be solved before the broad acceptance of the methods could be achieved. Unfortunately, all of these groups had effectively stopped working on parallel imaging methods by the mid-1990s because of these limitations.

2.3.4 SMASH and the Advent of Modern Parallel imaging Methods

Around the mid-1990s, however, MR scanner technology was starting to change. Four- and six-channel systems were becoming standard, and with them, multi-channel array coils and better imaging sequences and improved electronics had brought with them a large increase in SNR. By this point, averaging was not needed for many scans, and the time was ripe for a revival of parallel imaging concepts to accelerate image acquisition.

The method that kicked off the modern parallel imaging era was SiMultaneous Acquisition of Spatial Harmonics, or SMASH, introduced at the ISMRM meeting in Vancouver in 1997 by Sodickson and Manning (1997) from Beth Israel Hospital in Boston. SMASH was the first technique to be successfully implemented in vivo and worked with a broad range of coil arrays. Taking an inspiration from his brother's Ph.D. work on a generalized framework to describe k-space modulations (Sodickson and Cory 1998), Sodickson proposed combining the signals from the different coils in the array to mimic the modulations (or spatial harmonics) that would normally be produced by a phase-encoding gradient. These modulations then act like a retrospective phase-encoding gradient, which can effectively generate a line shifted in the phase-encoding direction. This k-space shifting effect of surface coils was noticed very early in MRI (Jesmanowicz et al. 1987); however, at that time, this effect was viewed more as a nuisance than as something useful. SMASH uses this shifting property in a beneficial way to reconstruct missing lines in k-space.

2.3.5 SENSE and the Beginnings of Clinical Parallel Imaging

Later, in 1997, Pruessmann et al. from the ETH in Zurich proposed the SENSitivity Encoding (SENSE) method (1999). SENSE is essentially the completion of the original ideas of Kelton et al. (1989), and Ra and Rim (1993), with an SNR-optimized reconstruction along with a coil sensitivity mapping methodology that ensures that the process works robustly. Since the SENSE formalism was much more generalized than SMASH, and results in significantly higher SNR for low acceleration factors (Pruessmann et al. 1999; Sodickson et al. 1999), SENSE was the clear method of choice until the further development of the SMASH-like k-space methods. Even today the originally proposed SENSE method is still optimal in many areas of clinical imaging.

2.3.6 Autocalibrating Methods

Much of the development in parallel imaging methods since has focused on increasing the performance of k-space based methods and expanding the areas in which a SENSE-type reconstruction will work. A particularly interesting development in this regard is the class of autocalibrating techniques which acquire the coil map along with the image acquisition. The autocalibrating (AUTO-)SMASH technique proposed in 1998 by Jakob et al. (1998) also at Beth Israel Hospital in Boston was the first important technique in the area of autocalibrated parallel imaging. AUTO-SMASH uses the acquisition of several additional lines to obtain essentially the same reconstruction as in SMASH, without the need for a complete coil map. This is especially important in areas of the body near the heart, for example, where pure coil sensitivity information is difficult to obtain. In addition, it can be used in cases where patient motion and/or image artefacts limit the acquisition of the coil map. This method was further extended by Heidemann et al. (2001) using the Variable Density AUTO-SMASH (VD-AUTO-SMASH) technique. In this technique, the extra lines that are acquired for calibration are reused in the final image reconstruction. This provides a variable density sampling scheme, since the center of the k-space is fully sampled, while the outer parts are acquired with reduced encoding. Heidemann et al. (2001) demonstrated that this reduced image artefacts in a dramatic way. In addition, it was determined that in most cases, for the same number of acquired lines (i.e., for the same acquisition time), it is better to sample the center as fully as possible, while sampling the outer parts as sparsely as possible.

2.3.7 Improved Hybrid Methods

Both of these methods allowed for the quick and robust acquisition of coil sensitivity information but were in general inaccurate for many general coil array geometries, resulting in image artefacts. Around this time, several other investigators recognized that one could improve the quality of k-space reconstructions by using more generalized combinations compared with the original SMASH method to perform the reconstruction. This included the hybrid methods of SPACE-RIP (Kyriakos et al. 2000), and generalized encoding matrix formulation (Sodickson and McKenzie 2001), as well as the generalized SMASH (Bydder et al. 2002a) method. All of these methods result in higher image quality than the original SMASH method, due to the more accurate reconstructions. In particular, the generalized SMASH method has found great use in parallel imaging-based artefact and motion-correction strategies, which are discussed in Chap. 5 (e.g. Bydder et al. 2003).

2.3.8 Improved k-Space Reconstructions with GRAPPA

Another further improvement in image quality resulted from the combination of autocalibration and these general image reconstructions with a separate reconstruction for each coil in the array. This method, GeneRalized Autocalibrated Partially Parallel Acquisitions (GRAPPA), provided increased SNR compared with previous k-space reconstructions with the added robustness of an autocalibrated coil sensitivity estimation (Griswold et al. 2002a). As a result, GRAPPA is one of the current standard methods along with SENSE for routine parallel imaging.

2.3.9 Optimized Dynamic Parallel Imaging Using TSENSE and TGRAPPA

For dynamic imaging, where a single position in the subject is imaged repeatedly, such as cine imaging in cardiac studies, very few methods can come close to the adaptive sensitivity encoding incorporating temporal filtering (T-SENSE) strategy proposed by Kellman et al. (2001). This method uses the interleaved sampling scheme found in the UNFOLD method (Madore et al. 1999) to determine the coil sensitivities to be used in a normal SENSE reconstruction. By sampling in this way, the coil sensitivity information can be updated every few frames, resulting in a high-quality, robust image acquisition. This basic method has recently been extended by Breuer et al. (2005a) to include a GRAPPA reconstruction , also with high-quality results.

2.3.10 Controlling the Aliasing for Better Image Quality: CAIPIRINHA

Another interesting concept also proposed by Breuer et al. (2005b) is the idea that one can control how the aliasing appears in the image reconstruction by changing the way in which the data is acquired. This method, Controlled Aliasing In Parallel Imaging Results IN Higher Accelerations (CAIPIRINHA) (Breuer et al. 2005), provides another tool to optimize the SNR of the final image reconstruction by using all of the potential encoding power of an imaging array simultaneously. This is accomplished through the use of either a specially modulated RF pulse or a modified phase-encoding table for 3D imaging. CAIPIRINHA has already been shown to result in a significant SNR increase in many areas of MRI and should be even more relevant with the advent of coil arrays with 32 or more channels.

2.3.11 Methods for Non-Cartesian Imaging

The final significant development that we briefly review here is the development of parallel imaging methods for non-Cartesian acquisitions, such as spiral and radial acquisitions. The first significant progress in this regard was the development of the practical generalized SENSE reconstruction (Pruessmann 1999). Without any special care, such a reconstruction would require so much computing power, that it could take weeks or more to reconstruct a single non-Cartesian acquisition. Independently Pruessmann et al. (2001) and Kannengiesser et al. (2000) proposed using the conjugate gradient method for a rapid solution to this problem. This method results in a practical image reconstruction time and high-quality image reconstructions. Recently, a further improvement in image reconstruction has been obtained using a blockwise GRAPPA reconstruction for both 1D variable density (Heidemann et al. 2003), radial (Griswold et al. 2003), and spiral (Heberlein et al. 2004; Heidemann et al. 2004) acquisitions. As in the case of standard non-Cartesian acquisitions, time will tell what applications these accelerated non-Cartesian acquisitions will find in the clinical routine. One clear application will be in the area of fMRI data acquired using a spiral readout.

This short history summary should make it clear that the development of parallel imaging methods has not happened overnight; however, at this point, several methods have been clearly established on clinical platforms, in particular the SENSE and GRAPPA methods. In the following, more detailed descriptions of these methods are given, followed by some of the emerging parallel imaging concepts.

Unfortunately, much of the original literature describing these methods tends to be difficult to understand without a solid mathematical background. For this reason, the description given here will largely skip the mathematics and instead concentrate on a schematic description of the reconstructions. Those interested in the more mathematical aspects of the reconstructions should consult the original literature on these methods, or review articles such as (Blaimer et al. 2004), as well as recent workshop proceedings (Proc Second Int Workshop 2004).

2.4 Sensitivity Encoding in the Image Domain

SENSitivity Encoding (SENSE) is a general image-domain parallel imaging method which has been successfully implemented by many groups worldwide and is available on most modern clinical scanners. In contrast to other previous image domain reconstruction methods, SENSE includes a practical coil mapping procedure as well as an SNR-optimized reconstruction, and has now become the clinical standard for image domain parallel imaging reconstructions.

As in all parallel imaging methods, some fraction of the normally required lines is skipped in the acquisition of an image. This results in an aliased image; therefore, to understand the basic idea of how the SENSE reconstruction works, it is first critical to understand the basic process of aliasing, or folding, in the image domain. The SENSE reconstruction can then be seen simply as the reverse process, or an unfolding of aliased images.

As an example, the basic aliasing process for the first coil in the array is depicted in Fig. 2.4. Due to the reduced encoding, or undersampling, of the image, several pixels appear on top of each other in the aliased image; however, before addition of the two pixels, each individual pixel is weighted by the sensitivity of the coil at the respective pixel. Stated in simple mathematical terms, a single pixel in the folded image of coil 1 (I_1) is the coil sensitivity at the first aliased pixel (C_{11}) multiplied by the magnetization at pixel 1 (M_1) added to the coil sensitivity at the second pixel (C_{12}) times the magnetization of the second pixel (M_2).

$$I_1 = C_{11}M_1 + C_{12}M_2$$

What we need to know to generate an unfolded image is the underlying magnetizations, M_1 and M_2. This is essentially impossible with just this single folded coil image unless one of the C's is zero; however, if we have another coil with different coil sensitivities at the aliased pixels, we can write another equation for the second coil:

$$I_2 = C_{21}M_1 + C_{22}M_2$$

This then provides us with two equations in two unknowns, which is easily solvable with simple algebra for the desired magnetizations. With this solution we can reconstruct the unaliased full-FOV image. The mathematics given above is normally seen in the literature in a matrix form, where the various terms are grouped together:

$$\begin{bmatrix} I_1 \\ I_2 \end{bmatrix} = \begin{bmatrix} C_{11} & C_{12} \\ C_{21} & C_{22} \end{bmatrix} \begin{bmatrix} M_1 \\ M_2 \end{bmatrix}$$

or

$$I = CM$$

$$\text{with } I = \begin{bmatrix} I_1 \\ I_2 \end{bmatrix}, C = \begin{bmatrix} C_{11} & C_{12} \\ C_{21} & C_{22} \end{bmatrix}, \text{ and } M = \begin{bmatrix} M_1 \\ M_2 \end{bmatrix}$$

The solution to this problem can be found in general by calculating the inverse of the C matrix and by performing a matrix multiplication to solve for the unknown pixel intensities:

$$C^{-1}I = M$$

Pruessmann et al. (1999) extended this basic inversion to cases where one has more aliased images (i.e., more coil-array elements) than the number of pixels that need to be unaliased at any given location in the image. In this case, the C matrix is rectangular and a more generalized inverse needs to be used. In addition, the impact of correlated noise can be accommodated, thereby optimizing SNR as much as possible. A schematic diagram of this process is shown in Fig. 2.5.

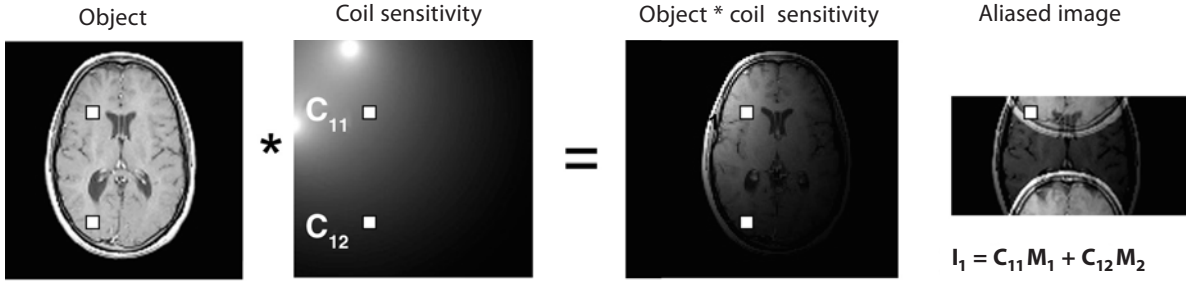

Fig. 2.4. The basic aliasing process. The underlying object is multiplied by the coil sensitivity, giving a normal-appearing surface coil image. When an image with reduced encoding is acquired, the aliased image on the right is obtained.

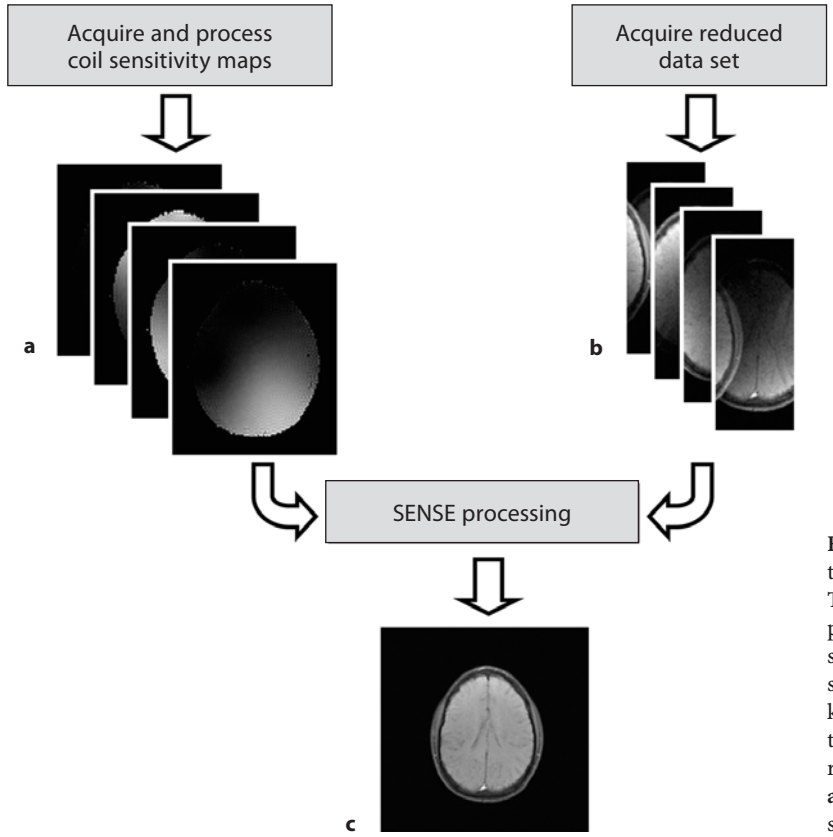

Fig. 2.5a–c. A flowchart depiction of the SENSE reconstruction process. **a** The first step is the acquisition and processing of images to determine coil sensitivity maps. **b** Data with reduced sampling are acquired and the reduced k-space data are Fourier transformed to yield aliased images. **c** The SENSE reconstruction is performed using **a** and **b** to yield the full FOV reconstructed image.

This modern SENSE implementation provides an SNR-optimized exact reconstruction. SENSE also provides an analytical description for the additional SNR losses that come about as part of the parallel imaging reconstruction process. While these properties are clearly advantageous, SENSE has the restriction that the coil sensitivities need to be known exactly in order for the reconstruction to be successful. In cases where noise, additional aliasing problems, or patient motion prohibit the exact knowledge of the coil sensitivities, severe image artefacts can result due to errors in the matrix inversion. For this reason, great care must be taken in the determination of the coil sensitivities.

2.4.1 Coil Sensitivity Mapping in the Image Domain

In their original paper, Pruessmann et al. (1999) proposed what has become the standard method to deal with noise in the coil sensitivity maps in the SENSE method. The method is based on a special acquisition designed for coil sensitivity calibration which collects information from both the array and a coil with homogeneous sensitivity, such as a standard body or head coil (see Fig. 2.6). Upon division of these two images, a pure map of coil sensitivity would be obtained in the absence of noise; however, the presence of noise (particularly in the homogeneous coil image) can severely corrupt this simple map. Since it can normally be assumed that the coil sensitivity profiles are relatively smooth, a local polynomial fit is used to smooth out the calculated sensitivity maps to remove contribution due to noise. Besides noise, there can be regions of the image with no sensitivity in either image, which leaves holes in the sensitivity map. This can lead to problems in later acquisitions if tissues move into these areas (e.g., the lungs in cardiac exams). For this reason, data is extrapolated a few pixels beyond the apparent borders of the object.

An easy and powerful method to eliminate the need for a body coil reference image is to use either a standard sum-of-squares image (Pruessmann et al. 1999) or the image from a single coil as a reference image (Bydder et al. 2002b). Either of these options are preferable whenever there is either not enough time to collect a body coil image, or in cases where

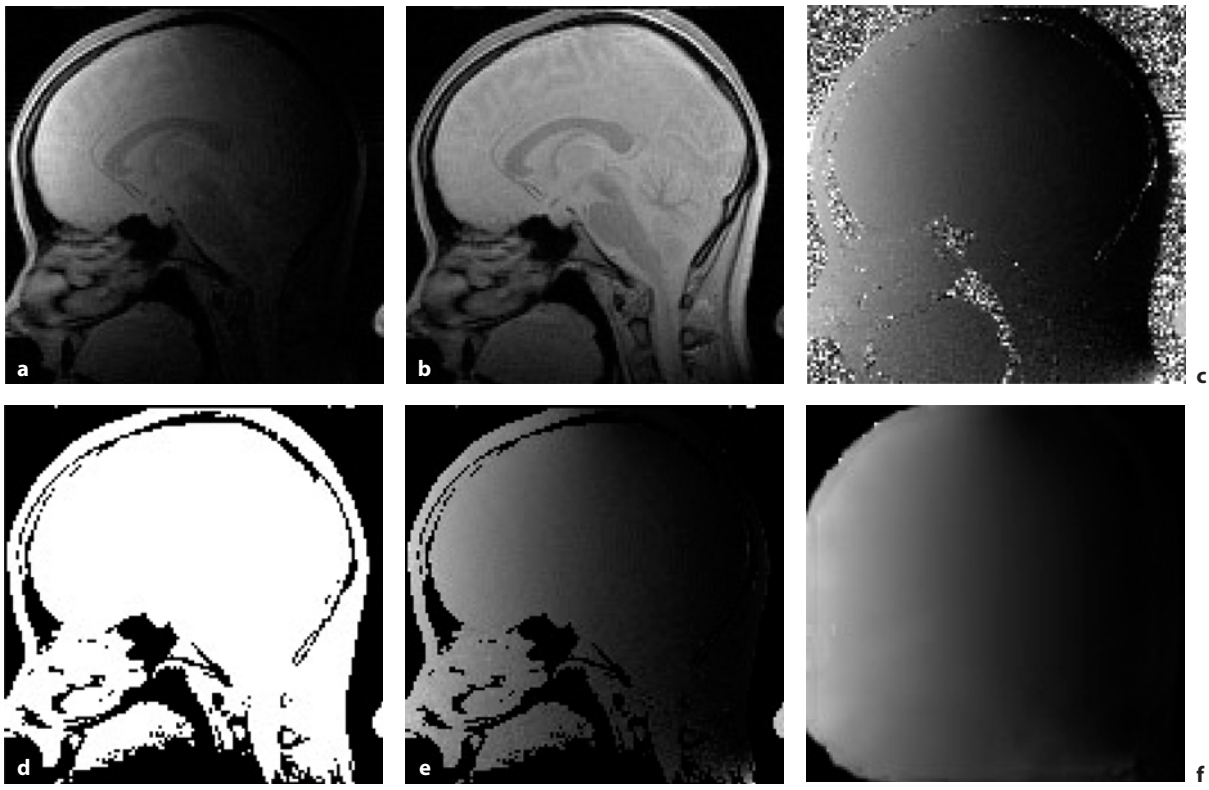

Fig. 2.6a–f. **a** Raw array coil image **b** Body coil image **c** Raw coil sensitivity map obtained by dividing **a** by **b**. **d** Intensity threshold. **e** Thresholded raw intensity map. **f** Final coil sensitivity map after polynomial fitting and extrapolation.

there is no body coil, such as in many high-field scanners (i.e., 4 T and above).

This class of methods works very well in situations where there is enough time to acquire coil sensitivity images of moderate resolution without patient motion, e.g., in head exams; however, these methods can be sensitive to patient motion, particularly in breathhold exams, and can produce serious errors whenever aliasing is present in the coil sensitivity maps, since the assumption of smoothness used in the polynomial fit is violated (see Fig. 2.7; Griswold et al. 2004; Goldfarb 2004). The final difficulty in this method is the potential requirement of an intensity threshold. Due to this threshold, all regions which fall below the threshold which are also distant from the object are set to zero intensity. This can lead to unexpected results, especially if tissues move into these regions at a later time point.

In recent years, several groups have also proposed other methods for the determination of the coil sensitivity maps. Walsh et al. (2000) initially proposed using an adaptive filter to optimize the suppression of background noise in normal array imaging. Since then, the method has also been used for calculation of coil sensitivity maps in parallel imaging (e.g., Kellman et al. 2001). The method is based on the calculation of the local signal and noise statistics at each pixel in the image. Walsh et al. (2000) showed that these local statistics can be used to provide a nearly optimal estimate of the coil sensitivity. The primary advantage of this method is that it works without a separate homogeneous coil image. The method can also be used in many cases to form an intensity normalization for the reconstructed image (Griswold et al. 2002b). Images are also produced with essentially normal background appearance. On the down side, the method is still rather sensitive to aliasing the coil images, and is computationally slow.

Another promising approach to coil mapping is wavelet smoothing and denoising (Liang et al. 2001; Lin et al. 2001). These methods are standard signal processing operations which can be performed quickly. It is potentially possible to use these techniques without an image from a homogeneous coil reference image, although the performance is much improved with such an image. The method can also

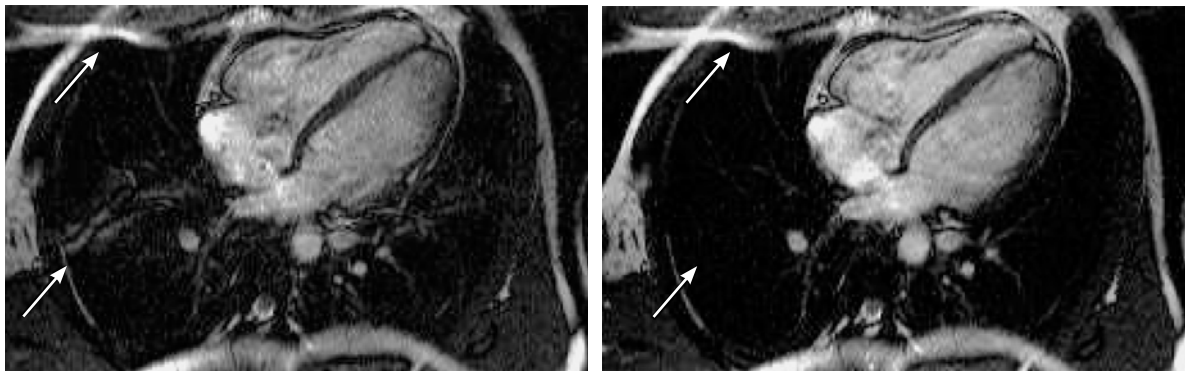

Fig. 2.7. The impact of aliasing in the full-FOV image in SENSE (*left*) and GRAPPA (*right*). The *arrows* show locations of artefacts and their corresponding sources, which are unresolved in the SENSE. These artefacts are properly reconstructed in the GRAPPA reconstruction.

work without an intensity threshold, so that the method is more user independent; however, edges can still remain in the final coil maps, which may require extrapolation, as in the polynomial fit method proposed by Pruessmann et al. (1999), in order to avoid motion-induced artefacts.

2.5 k-Space Domain Methods

In contrast to the SENSE method, which works entirely in the image domain, there are many methods which work entirely in k-space, although, at this time, the only k-space reconstruction method currently available on clinical scanners is the GRAPPA method; however, in order to understand the GRAPPA method, we first review the basics of the SMASH and AUTO-SMASH techniques to ease the understanding of the GRAPPA reconstruction process.

2.5.1 Basic Phase-Encoding Modulation

In order to understand the basics of any k-space method, one needs to understand the basic mechanism of phase encoding. The function of a simple phase-encoding gradient is to modulate the magnetization along the phase-encoding direction in a particular way. We then repeat the acquisition again with a different modulation and eventually build up enough information to reconstruct an image. Specifically, if we examine the first non-zero phase-encoding gradient, we see that the function of this gradient is to modulate the real part of the magnetization with one cycle of a cosine function over the FOV, while the imaginary part is modulated by one cycle of a sine function (see Fig. 2.8). The second non-zero gradient modulates the magnetization by two cycles, while the third creates a three-cycle modulation, and so on. In general, we can write the real and imaginary parts of the magnetization after the application of an arbitrary phase-encoding gradient in, for example, the y-direction as:

$$\text{Real}\{M\} = \cos(k_y y)$$

$$\text{Imag}\{M\} = \sin(k_y y),$$

where k_y is a normal row in k-space, as determined by the integral of phase-encoding gradient strength multiplied by the time that gradient was applied. This magnetization is typically written in the literature in a more compact form as a complex exponential:

$$M = e^{ik_y y}$$

Those with more math knowledge will recognize this as a term in the Fourier transform. One key feature of such a modulation is that if we repeat the same modulation again, we simply get double the modulation:

$$e^{ik_y y}\, e^{ik_y y} = e^{i2k_y y}$$

This simple fact forms one of the building blocks of the SMASH technique.

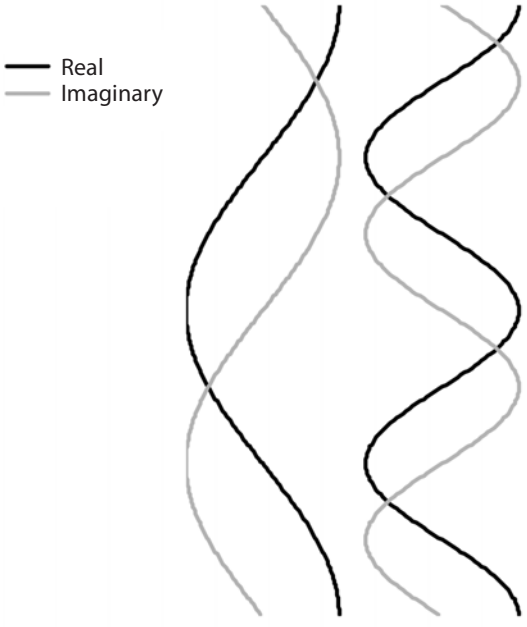

Fig. 2.8. Various examples of the spatial modulations produced by phase-encoding gradients are shown. The k_y-value corresponds to the number of cycles across the FOV.

2.5.2 Simultaneous Acquisition of Spatial Harmonics

The fundamental idea in SMASH and all k-space methods is that the modulation done normally only with phase-encoding gradients could be replaced by a modulation provided by the gradients and other modulations provided exclusively by the coil array. These two modulations work together as shown above to determine the final position of the line in k-space. The key insight that Sodickson and Manning (1997) had in the development of SMASH was that there are many possible modulations available for a given coil array. As long as more than one harmonic modulation can be formed from the coil array, a single line can be used to reconstruct multiple different lines of k-space, each using a different combination. In this way, one can acquire a set of data using just the normal phase-encoding gradients, and all other modulations, and hence all other sets of lines, could be reconstructed after the fact in a computer.

The SMASH reconstruction process is shown schematically in Fig. 2.9. We begin with a map of the coil sensitivities, as could be used in the SENSE method described above. These maps are then fit to modulations with different numbers of cycles – one for each of the lines that need to be reconstructed from each acquired line – so for a reduction factor of R, we need R separate combinations. Once these combinations are determined, they are applied to the acquired data. The first combination is applied to the acquired line and this reconstructed line is placed in the reconstructed k-space. The next combination is then applied to the same acquired line, but the reconstructed line is placed at the appropriately shifted location in the reconstructed k-space matrix. This continues until the entire k-space is filled. This final k-space matrix is then Fourier transformed to generate the final image.

2.5.3 Autocalibration in k-Space

Even though SMASH performs the reconstruction in k-space, it actually uses coil sensitivity maps in the image domain to determine the reconstruction parameters. For this reason, pure SMASH is limited by the coil mapping technique, which can be sensitive to errors such as noise and other gaps in the coil sensitivity maps, but is typically less flexible and results in lower-quality images compared with SENSE. The idea of autocalibration came from the need to obtain more robust coil sensitivity estimates specifically tailored for k-space reconstructions. The idea is actually a simple modification of the SMASH reconstruction (Fig. 2.10): Say we acquire the odd lines and want to use them to reconstruct both the odd and even lines. In normal SMASH, we would acquire data at line 1 and use this to reconstruct line 2 using a combination previously determined from coil sensitivity maps. The alternative way to do this found in autocalibrating methods is to actually acquire both lines 1 and 2 and to determine the correct combination by fitting these lines directly to each other in k-space. This combination can then be applied throughout the rest of k-space to reconstruct the rest of the missing lines.

Variable Density AUTO-SMASH (Heidemann et al. 2001) is a simple extension of this basic idea, wherein more than one reference line is acquired for determination of the reconstruction parameters. In this way, multiple fits can be used to determine the reconstruction parameters, resulting in a better fit. As shown by Heidemann et al. (2001), this results in a higher quality reconstruction. Additionally, the extra reference lines can be included in the final image reconstruction, resulting in fewer artefacts and higher SNR than a pure AUTO-SMASH reconstruction.

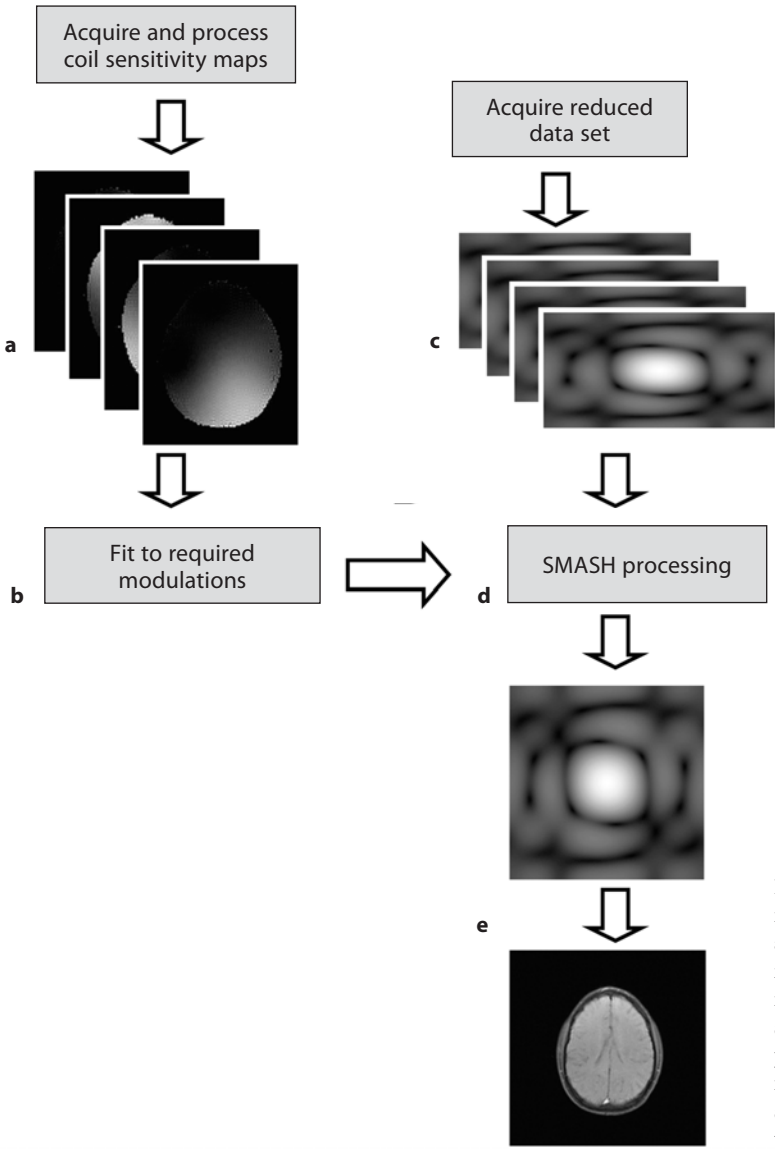

Fig. 2.9a–e. A flowchart depiction of the SMASH reconstruction process. **a** The first step is the acquisition and processing of images to determine coil sensitivity maps. **b** These coil sensitivity maps are fit to the desired modulations, as shown in Fig. 2.8. **c** Raw data with reduced sampling are acquired. **d** The SMASH reconstruction is performed using B and C to yield the full k-space data, which are then Fourier transformed **e** to yield the full-FOV reconstructed image.

This autocalibration process can result in a more robust estimation of the reconstruction parameters, since it requires such a short acquisition time that it can be acquired along with every scan. By fitting k-space line to k-space line, a pure coil sensitivity map is not needed – only the few lines of extra data. No body coil image and no intensity thresholds are needed, thereby generating normal-appearing images even in the background. Autocalibrating k-space methods are also insensitive to potential errors such as motion or gaps in the coil sensitivity maps. In addition, aliasing in the reconstructed images is not a problem, thereby allowing slightly folded images to be acquired without any problem with the reconstruction.

2.5.4 SNR in SMASH and AUTO-SMASH

One of the most significant limitations of both SMASH and AUTO-SMASH is their intrinsically lower SNR than other parallel imaging methods. Unlike conventional imaging or SENSE, SNR in SMASH or AUTO-SMASH is lower than ideal and essentially independent of the acceleration factor, so that SNR in a SMASH or AUTO-SMASH image acquired with low acceleration factors is substantially reduced compared with a more optimal image combination (Sodickson et al. 1999). This results from SMASH implicitly using a simple sum combination of the coil signals, compared with a more optimal pixel-by-pixel matched filter weighted recon-

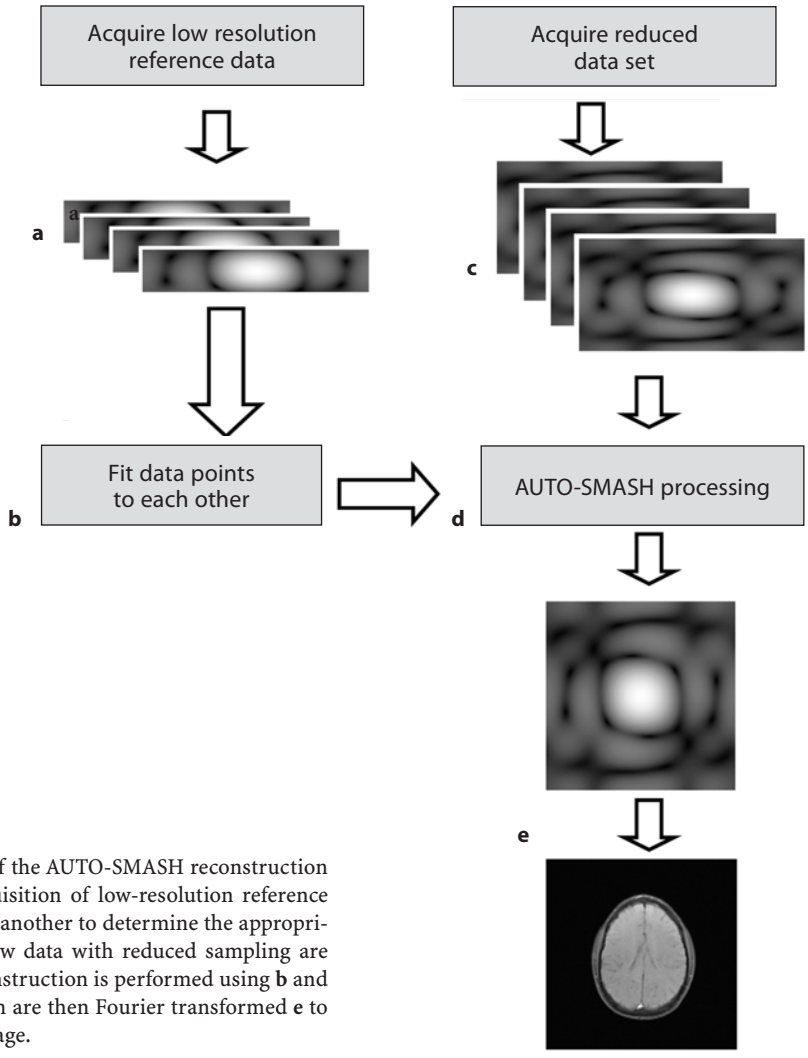

Fig. 2.10a–e. A flowchart depiction of the AUTO-SMASH reconstruction process. **a** The first step is the acquisition of low-resolution reference data. **b** These data are then fit to one another to determine the appropriate reconstruction parameters. **c** Raw data with reduced sampling are acquired. **d** The AUTO-SMASH reconstruction is performed using **b** and **c** to yield the full k-space data, which are then Fourier transformed **e** to yield the full-FOV reconstructed image.

struction, or sum-of-squares reconstruction which has previously been shown to maximize SNR (Roemer et al. 1990). SMASH an related methods are also sensitive to phase errors, resulting in complete loss of signal from some regions of the body (see Fig. 2.8 of Blaimer et al. (2004) for an example of this effect). For these reasons, these methods are rarely used today in favor of the GRAPPA method which is not sensitive to either of these issues.

2.5.5 Generalized Autocalibrating Partially Parallel Acquisitions

The GRAPPA method (Griswold et al. 2002a) was developed to address two primary limitations of previous k-space reconstruction methods: (a) SNR and phase sensitivity issues; and (b) poor image quality and residual artefacts due to inaccurate fits of the required harmonic functions. The reconstruction process is an extension of the basic VD-AUTO-SMASH reconstruction. As in VD-AUTO-SMASH, multiple reference lines are acquired in the center of k-space; however, instead of fitting one line to another line in order to reconstruct a point in a composite k-space data set, as one would do in VD-AUTO-SMASH, GRAPPA performs several reconstructions using multiple points on multiple lines to reconstruct each missing point in the k-space of each coil in the array (see Fig. 2.11). This results in a complete k-space data for each coil in the array, which can then be Fourier transformed and combined using a sum-of-squares reconstruction to obtain the final image.

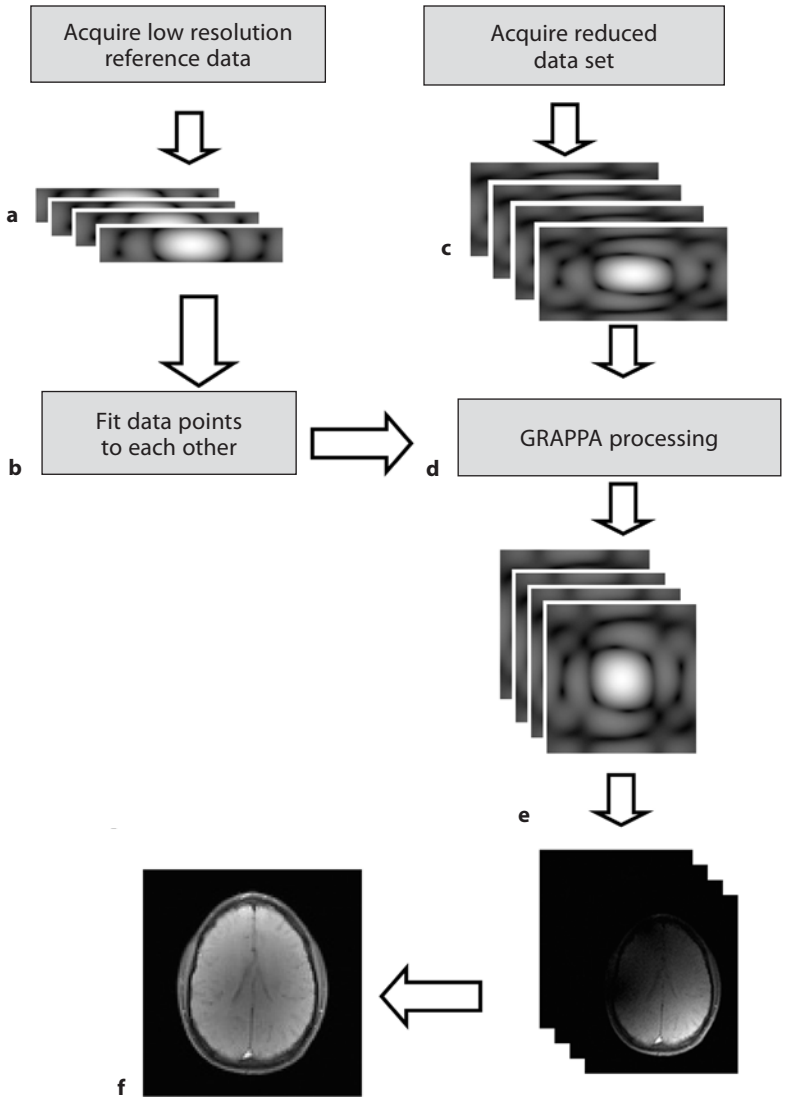

Fig. 2.11a–f. A flowchart depiction of the GRAPPA reconstruction process. **a** The first step is the acquisition of low resolution reference data. **b** These data are then fit to one another to determine the reconstruction parameters for reconstructing data in each coil of the array. **c** Data with reduced sampling are then acquired. **d** The GRAPPA reconstruction is performed using B and C to yield the full k-space data in each coil of the array, which are then Fourier transformed **e** to yield the full-FOV reconstructed images for each coil of the array. **f** These images are then combined using a normal combination method, such as a sum-of-squares reconstruction.

This process resolves many of the previous problems encountered with k-space parallel imaging methods. Firstly, by generating images in each coil which are then combined using the normal sum-of-squares method, the resulting SNR approaches the ideal SNR, especially at low accelerations where previous methods suffered the most serious problems. Secondly, by using more than one point to reconstruct each missing point, the fit to each missing data point is accurate regardless of the geometry of the coil array used for imaging. Finally, as in VD-AUTO-SMASH, one can reuse the extra reference lines in the final image acquisition to improve both SNR and artefact levels. As shown previously (Heidemann et al. 2001), in many cases it is advantageous to use the highest possible acceleration in the outer parts of k-space, thereby collecting as many lines as possible in the center of k-space, where most of the object information is found anyway.

GRAPPA is particularly useful in areas of the body where coil sensitivity information may be difficult to obtain, such as those which require breathhold exams. Here the autocalibrating acquisition is particularly advantageous since the reconstruction will not be dependent on breathhold position (Zech et al. 2004); however, this autocalibrating nature is also the most significant limitation of GRAPPA, namely that these extra reference lines need to be acquired, which can begin to dominate the acquisition time at the high accelerations being used for research pur-

poses today. In these cases, some alternative method of calibration is necessary. Another significant limitation of GRAPPA is the lack of a robust analytical description of the final image SNR. This feature, which would clearly be of interest for comparative studies, is currently under development by many groups and will surely become standardized in the coming years.

2.6 Extending Parallel Imaging to 3D and Multislice Applications

With the increased speed found on the present MR systems, increasingly more clinical applications are moving towards 3D acquisitions for potential increased SNR and volumetric visualization capability. Parallel imaging and 3D imaging both benefit from each other in a very synergistic way. The 3D imaging is slower per acquisition than a corresponding 2D scan, which limits the application of 3D imaging in areas of very rapid motion, or in high-resolution breathhold exams. Yet on the other side, 3D imaging typically has significantly higher SNR than a comparable 2D scan. This is already a perfect situation for acceleration by parallel imaging, but the combination is even better. Since there are two phase-encoding directions in 3D imaging, one can perform parallel imaging in both directions, as shown by Weiger et al. (2002). In cases where the coil array has sensitivity variations in both directions, an increased SNR or equivalently a higher total acceleration can be obtained. Weiger et al. (2002) demonstrated unequivocally that one can achieve a higher acceleration using parallel imaging in two directions, compared with accelerating only in one dimension, again, whenever the coil array has sensitivity variations in both directions. A similar idea was proposed by Larkman et al. (2001) for multislice imaging using multiband pulses. This method offers a similar gain in SNR performance as the straightforward 3D method, but it requires specialized RF pulses and potentially increased SAR compared with a normal 2D acquisition.

2.6.1 Controlled Aliasing in Parallel Imaging Results in Higher Accelerations

Controlled aliasing in parallel imaging results in higher accelerations (CAIPIRINHA) is an emerging parallel imaging method which aims to optimize parallel imaging performance in 3D and multislice imaging (Breuer et al. 2005b). CAIPIRINHA begins with observation that there are many possible ways to either undersample a 3D imaging experiment or to use different combinations of multiband pulses in a multislice experiment; however, the aliasing patterns of these different schemes will not necessarily be identical. For example, various different 3D sampling schemes and their respective aliasing patterns are shown in Fig. 2.12. Since these aliasing patterns are not the same, their SNR and encoding performance for parallel imaging will also not be identical. Unlike the normal straightforward undersampling scheme, different pixels which can be widely separated in both directions can be aliased together. The key point is that different sampling schemes (or multiband pulses) other than the normal straightforward ones could be optimal depending on the coil array used and the orientation and size of the imaging volume. CAIPIRINHA has already been shown to give more optimal results than the normal sampling schemes, especially for very thin 3D imaging slabs or closely spaced slices in a multislice experiment (Breuer et al. 2005b). Finally, CAIPIRINHA is also typically more robust against small changes in the position of the imaging volume than a normal 3D imaging scheme (Breuer et al. 2004). For these reasons, CAIPIRINHA should help make the application of parallel imaging in clinical 3D and multislice imaging more robust.

2.7 Conclusion

Many different parallel imaging reconstructions are possible. As described herein, the various methods all have differences in their theoretical and practical performances, especially in which kinds of coil sensitivity information is needed and how this information is acquired. A method should be selected based on the relative advantages or disadvantages for the specific application for which it is used. The following chapters of this book should give the reader a good

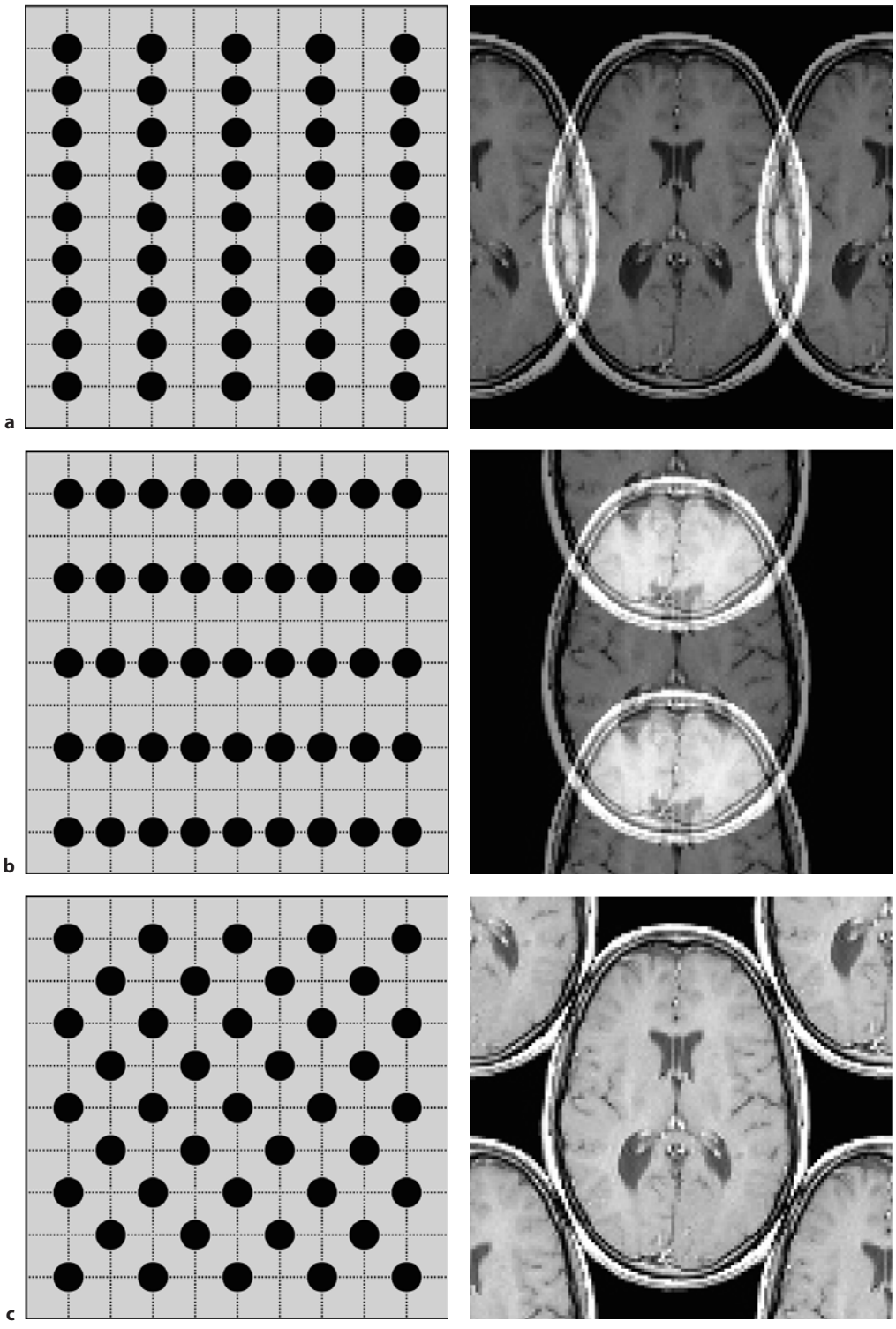

Fig. 2.12a–c. Various possible sampling schemes for a total acceleration factor of two. In this case, these images correspond to the two phase-encoding directions used in the 3D acquisition. The readout direction is into the page. The *first two rows* show typical 3D SENSE-type sampling patterns with reductions in either **a** the left–right direction or **b** the anterior–posterior direction. Both of these patterns show significant areas of overlap due to aliasing which roughly correspond to the areas of reduced signal-to-noise ratio (SNR). On the other hand, the CAIPIRINHA pattern (**c**) takes better advantage of the empty spaces in the FOV, resulting in fewer areas of overlap and therefore better SNR. Note that the acquisition time for all three patterns would be identical.

idea of which methods are currently used for some particular applications.

Acknowledgements. The author thanks J. Carlson and S. Wright for both their images and their insight into the early years of parallel imaging. P. Jakob, M. Blaimer, F. Breuer, M. Nittka, D. Balla, S. Kannengiesser, R. Heidemann, M. Mueller, J. Duerk, and J. Sunshine all provided assistance in the preparation of this chapter.

References

Blaimer M, Breuer F, Mueller M, Heidemann RM, Griswold MA, Jakob PM (2004) SMASH, SENSE, PILS, GRAPPA: how to choose the optimal method. Top Magn Reson Imaging 15:223–236

Breuer F, Blaimer M, Mueller M, Heidemann R, Griswold M, Jakob P (2004) Controlled aliasing in 3D parallel imaging (2D CAIPIRINHA). In: Proc 12th Annual Meeting of ISMRM, Kyoto, Japan, p 326

Breuer FA, Kellman P, Griswold MA, Jakob PM (2005a) Dynamic autocalibrated parallel imaging using temporal GRAPPA (TGRAPPA). Magn Reson Med 53:981–985

Breuer FA, Blaimer M, Heidemann RM, Mueller MF, Griswold MA, Jakob PM (2005b) Controlled aliasing in parallel imaging results in higher acceleration (CAIPIRINHA) for multi-slice imaging. Magn Reson Med 53:684–691

Bydder M, Larkman DJ, Hajnal JV (2002a) Generalized SMASH imaging. Magn Reson Med 47:160–170

Bydder M, Larkman DJ, Hajnal JV (2002b) Combination of signals from array coils using image-based estimation of coil sensitivity profiles. Magn Reson Med 47:539–348

Bydder M, Atkinson D, Larkman DJ, Hill DL, Hajnal JV (2003) SMASH navigators. Magn Reson Med 49:493–500

Carlson JW (1987) An algorithm for NMR imaging reconstruction based on multiple RF receiver coils. J Magn Reson 74:376–380

Carlson JW (2004) Historical perspectives on the development of a parallel MRI system for head imaging. In: Proc Second International Workshop on Parallel Imaging. Zurich, Switzerland

Carlson JW, Minemura T (1993) Imaging time reduction through multiple receiver coil data acquisition and image reconstruction. Magn Reson Med 29:681–688

Goldfarb JW (2004) The SENSE ghost: field-of-view restrictions for SENSE imaging. J Magn Reson Imaging 20:1046–1051

Griswold MA, Jakob PM, Nittka M, Goldfarb JW, Haase A (2000) Partiallay parallel imaging with localized sensitivities (PILS). Magn Reson Med 44:602–609

Griswold MA, Jakob PM, Heidemann RM, Nittka M, Jellus V, Wang J, Kiefer B, Haase A (2002a) Generalized autocalibrating partially parallel acquisitions (GRAPPA). Magn Reson Med 47:1202–1210

Griswold MA, Walsh DO, Heidemann RM, Haase A, Jakob PM (2002b) The use of an adaptive reconstruction for array coil sensitivity mapping and intensity normalization. In: Proc ISMRM, Honululu, Hawaii p 2410

Griswold MA, Heidemann RM, Jakob PM (2003) Direct parallel imaging reconstruction of radially sampled data using GRAPPA with relative shifts. Proc 11th Annual Meeting of the ISMRM, Toronto, p 2349

Griswold MA, Kannengiesser S, Heidemann RM, Wang J, Jakob PM (2004) Field-of-view limitations in parallel imaging. Magn Reson Med 52:1118–1126

Heberlein KA, Kadah Y, Hu X (2004) Segmented spiral parallel imaging using GRAPPA. Proc 12th Annual Meeting of the ISMRM, Kyoto, Japan, p 328

Heidemann RM, Griswold MA, Haase A, Jakob PM (2001) VD-AUTO-SMASH imaging. Magn Reson Med 45:1066–1074

Heidemann RM, Griswold MA, Jakob PM (2003) Fast parallel image reconstructions with non-cartesian trajectories. Proc 11th Annual Meeting of the ISMRM, Toronto, p 2347

Heidemann RM, Griswold MA, Krüger G, Kannengiesser SAR, Kiefer B, Jakob PM (2004) Fast parallel image reconstructions for spiral trajectories. In: Proc Second International Workshop on Parallel Imaging. Zurich, Switzerland

Hutchinson M, Raff U (1988) Fast MRI data acquisition using multiple detectors. Magn Reson Med 6:87–91

Jakob PM, Griswold MA, Edelman RR, Sodickson DK (1998) AUTO-SMASH, a self-calibrating technique for SMASH imaging. MAGMA 7:42–54

Jesmanowicz A, Froncisz W, Hyde JS (1987) A complication in prescan strategy when using surface coils. Magn Reson Med 5:318–322

Kannengiesser SAR, Brenner AR, Noll TG (2000) Accelerated image reconstruction for sensitivity encoded imaging with arbitrary k-space trajectories. Proc 8th Annual Meeting of the ISMRM, Denver, p 155

Kellman P, Epstein FH, McVeigh ER (2001) Adaptive sensitivity encoding incorporating temporal filtering (TSENSE). Magn Reson Med 45:846–852

Kelton JR, Magin RL, Wright SM (1989) An algorithm for rapid image acquisition using multiple receiver coils. In: Proc 8th Annual Meeting of SMRM, p 1172

Kwiat D, Einav S, Navon G (1991) A decoupled coil detector array for fast image acquisition in magnetic resonance imaging. Med Phys 18:251–265

Kyriakos WE, Panych LP, Kacher DF, Westin CF, Bao SM, Mulkern RV, Jolesz FA (2000) Sensitivity profiles from an array of coils for encoding and reconstruction in parallel (SPACE RIP). Magn Reson Med 44:301–308

Larkman DJ, Hajnal JV, Herlihy AH, Coutts GA, Young IR, Ehnholm G (2001) Use of multicoil arrays for separation of signal from multiple slices simultaneously excited. J Magn Reson Imaging 13:313–317

Liang ZP, Bammer R, Ji J, Pelc N, Glover G (2001) Making Better SENSE: wavelet denoising, Tikhonov regularization, and total least squares. In: Proc ISMRM, Glasgow, Scotland, p 2388

Lin FH, Kwong K, Chen Y, Belliveau J, Wald L (2001) Reconstruction of sensitivity encoded images using regularization and discrete time wavelet transform estimates of the coil maps. In: Proc ISMRM, p 2389

Madore B, Glover GH, Pelc NJ (1999) Unaliasing by Fourier-encoding the overlaps using the temporal dimension (UNFOLD), applied to cardiac imaging and fMRI. Magn Reson Med 42:813–828

Proc Second Int Workshop (2004) Proceedings of the Second

International Workshop on Parallel Imaging. Zurich, Switzerland. Available at http://www.mr.ethz.ch/parallelmri04/program.html

Pruessmann KP, Weiger M, Scheidegger MB, Boesiger P (1999) SENSE: sensitivity encoding for fast MRI. Magn Reson Med 42:952–962

Pruessmann KP, Weiger M, Bornert P, Boesiger P (2001) Advances in sensitivity encoding with arbitrary k-space trajectories. Magn Reson Med 46:638–651

Ra JB, Rim CY (1993) Fast imaging using subencoding data sets from multiple detectors. Magn Reson Med 30:142–145

Roemer PB, Edelstein WA, Hayes CE, Souza SP, Mueller OM (1990) The NMR phased array. Magn Reson Med 16:192–225

Sodickson A, Cory DG (1998) A generalized k-space formalism for treating the spatial aspects of NMR experiments. Progr Magn Reson 33:78–108

Sodickson DK, Manning WJ (1997) Simultaneous acquisition of spatial harmonics (SMASH): fast imaging with radiofrequency coil arrays. Magn Reson Med 38:591–603

Sodickson DK, McKenzie CA (2001) A generalized approach to parallel magnetic resonance imaging. Med Phys 28:1629–1643

Sodickson DK, Griswold MA, Jakob PM, Edelman RR, Manning WJ (1999) Signal-to-noise ratio and signal-to-noise efficiency in SMASH imaging. Magn Reson Med 41:1009–1022

Walsh DO, Gmitro AF, Marcellin MW (2000) Adaptive reconstruction and enhancement of phased array MR imagery. Magn Reson Med 43:682–690

Weiger M, Pruessmann KP, Boesiger P (2002) 2D SENSE for faster 3D MRI. MAGMA 14:10–19

Zech CJ, Herrmann KA, Huber A, Dietrich O, Stemmer A, Herzog P, Reiser MF, Schoenberg SO (2004) High-resolution MR-imaging of the liver with T2-weighted sequences using integrated parallel imaging: comparison of prospective motion correction and respiratory triggering. J Magn Reson Imaging 20:443–450

The g-Factor and Coil Design

3

David J. Larkman

CONTENTS

To help give this chapter a more intuitive feel most of the discussion surrounding g-factor and coil design issues are couched in terms of the well-known Cartesian SENSE reconstruction algorithm (cf. Chap. 2). This is justified as the conclusions and major observations are largely independent of the reconstruction algorithm used; however, it should be noted that there are differences between the levels of noise enhancement in SENSE and those methods which use fitting as an integral part of the reconstruction (e.g. GRAPPA) where some noise enhancement may be traded for systematic error. The main features of image degradation remain in all methods and the coil requirements are unchanged.

D. J. Larkman, PhD
Department of Imaging Sciences, Imperial College London, Hammersmith Hospital, London W12 0NN, UK

3.1 Array Coils Before Parallel Imaging

In the late 1980s array coils were developed for MRI. Initially, the motivation for this development was increase in signal-to-noise ratio (SNR), which can be achieved by using array coils to construct shaped regions of sensitivity. In general, the shape of the sensitivity of a single circular coil element is preserved as the coil size is increased, so if we make the coils bigger, the depth (penetration depth) and hence the volume of sensitivity increases. Both signal and the component of noise which comes from thermal effects within the subject can only be acquired from within a coil's sensitive volume. In an imaging experiment the sensitive volume of a coil extends over a limited region (before the sensitivity falls below the noise floor). We can localise signal in MRI, and indeed this is the strength of MRI, i.e. we can restrict the signal that is acquired in a coil to come from only a single slice in the volume (or slab or voxel depending on the localisation methods used); however, noise, because it is not generated by the RF we use to generate signal cannot be spatially localised, so we always collect noise from the whole volume of sensitivity of the coil. From this discussion it is clear that carefully tailoring the coils sensitivity to the volume of interest for imaging can increase SNR because noise is gathered from the smallest possible volume commensurate with the anatomy to be imaged.

The maximum SNR from an array coil is obtained only when the signals from each coil are combined in an appropriate way (see Fig. 3.1). If separate coil images are simply added, then distant coils with no significant sensitivity to the location of interest (contributing only noise) are combined with equal weight as those near the pixel of interest. Clearly this is not the right way to combine signals. A thorough treatment of how to optimally combine array coil signals for maximum SNR was presented by Roemer et al. (1990) and remained the standard reference for array

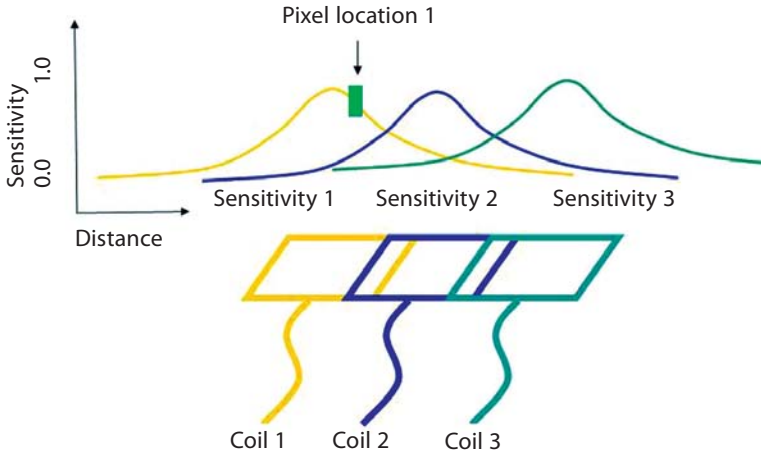

Fig. 3.1. The optimal combination of signals from array coils requires knowledge of the spatial variation of each element's coil sensitivity. Without knowledge of this sensitivity, only simple combinations of signals can be performed. In this example the signal at pixel location 1 has contributions from coils 1 and 2, but very little from coil 3. Coil 3 will contribute primarily noise leading to a sub-optimal combination at pixel 1. If the contribution is weighted by the sensitivity at this location, we can see that the contribution of coil 3will be weighted too close to zero, reducing the combined noise and hence increasing the signal-to-noise ratio.

coil signal combination since then. Roemer et al.'s (1990) key observation was that the optimal SNR in an image reconstructed from multiple coils is achieved by combining the signals on a pixel-by-pixel basis weighting each coil by the sensitivity of the coil at that location in space. In this way pixels close to a single coil element obtain the vast majority of their information (and noise) from only that coil, and pixels located between elements have shared information. This observation can be readily theoretically proved, and also feels intuitively correct; it has underpinned a lot of the thought processes which have developed in parallel imaging since then. Of course, what Roemer et al. (1990) also observed was that in general we do not know the spatial sensitivity of the coils, and that it varies throughout space, but they observed that for most SNRs the sum-of-squares combination approximated the sensitivity-combined result to within approximately 10%. This sidestepped the need to measure coil sensitivities and in doing so may well have inadvertently held up the development of parallel imaging as we know it (see also the history section in Chap. 2). If coil calibration had already been an integral part of array-coil imaging before parallel imaging, then some of the early parallel-imaging proposals (Hutchinson and Raff 1988; Carlson and Minemura 1993; Ra and Rim 1993) may well have been adopted more quickly. An interesting footnote to this general discussion of array coils not used for parallel imaging is that ultimately parallel imaging reached back and re-invented the optimal image combination. A SENSE reconstruction can be run with a "speed up" of 1 (i.e. "no acceleration"), and what will result is an optimally combined image weighted by the sensitivity of the coil elements. This has been extended to methods for doing such an optimal combination even in the absence of explicit separate coil sensitivity measurements (Bydder et al. 2002).

For array coils to produce maximum SNR they must be "independent", i.e. there is no crosstalk between coils (discussed later). This requirement imposes the need for multiple receiver chains on scanners, one for each receiver coil, which is expensive but, because of the requirement to combine coil data in the image domain, required. This means that the hardware for parallel imaging was well established and most commercial scanners already had four or more separate receiver channels by the mid-1990s. Parallel imaging was inevitable.

3.2 SNR in Parallel Imaging

Before we can consider in detail parallel-imaging coils, we need to look more closely at the implications of parallel imaging for the quality of the reconstructed image. We know in the context of decreasing acquisition time, parallel imaging has already made significant progress; however, empirically the community has found limits to acceleration with parallel imaging. Excessive noise in reconstructed images is widely acknowledged as the main limit, and Wiesinger et al.'s (2004) electrodynamics-based predictions of field-dependent limits in parallel imaging indicate that there is a fundamental upper acceleration limit for a given accepted level of noise enhancement independent of the detailed design of receive coils; however, for almost all exams we are yet to reach this limit in all desired imaging planes; thus, coil design is

still an important area of research in striving for this optimal performance. Typically, the practical speed-up limits for simple 2D multislice imaging lie at relatively modest accelerations of between 2.5 and 3.5 for imaging at 1.5 and 3 T, respectively. These limits, and those dictated by Wiesinger et al. (2004) are set by a somewhat arbitrary cut-off in SNR loss of 20% due to g-factor (i.e. g=1.2): if higher losses can be tolerated, then accelerations much higher have been demonstrated (Sodickson et al. 2005).

Considering the classic SNR equation for parallel imaging proposed by Pruessmann

$$\mathrm{SNR}_R = \frac{\mathrm{SNR}_0}{g\sqrt{R}}$$

We can see that the SNR in parallel imaging (SNR_R) is determined by three terms:

- The baseline SNR performance of the system, SNR_0, a function of many things including detector efficiency, TE, TR, sequence design, etc.
- A term $\sqrt{R}$ which relates to the parallel-imaging reduction (or acceleration) factor, R, and therefore the reduced number of data readouts.
- The g-factor, g, which is related to coil geometry but also (as we will see) the location of the imaging plane, the field of view, the speed-up factor, and the k-space sampling pattern.

Before looking at each term, it should be noted that the g-factor is not useful on its own for assessing a coils performance because there is no account taken of the baseline SNR. If SNR_0 is small, then the coil is not useful for normal or parallel imaging regardless of the value of g.

3.2.1 The Speed-up Term

The $\sqrt{R}$ term is inescapable for parallel-imaging methods which reduce the number of k-space lines measured. Because of the Fourier nature of the encoding in MRI, all readouts contribute to the final SNR of the image. Each point in the image domain is constructed from a weighted sum of all points in k-space (the Fourier transform), each point in k-space contains signal and noise, and so just as temporal averaging increases SNR by a factor proportional to the square root of the number of averages, so decreasing the number of measured points reduces the SNR by the same factor; however, there is a way that this term can be avoided, and that is to parallel image not by reduction of phase-encoded lines but by exciting multiple slices simultaneously (Larkman et al. 2004; Breuer et al. 2005). In these methods, because an increased number of spins are excited at the separate slice locations, the total signal sampled is increased and the $\sqrt{R}$ term no longer applies. These methods are not widely used because they require modification of the RF pulses in the sequence and therefore to some extent negate the beauty of parallel imaging, which requires no sequence modification; however, as we are required to squeeze increasingly more speed from our systems, these methods are likely to appear in the clinic.

For single-shot echo-planar imaging (EPI), if parallel imaging is used to reduce the length of the echo train, then the echo amplitude reduction due to T2*-decay from the first to the last echo is reduced as well. In combination with shorter achievable echo times, accessible now because of the shorter echo train, this makes it possible to produce an SNR gain using parallel imaging in EPI, and so EPI is often considered to be a case where the $\sqrt{R}$ term is avoided. Actually, it is still present but is offset by greater gains in SNR elsewhere (cf. Chap. 10).

3.2.2 The g-Factor Term

3.2.2.1 "Ill-Conditioned" Systems

The g-factor term arises as a result of the coil sensitivities being too similar. This ill-conditions the matrix inversion at the heart of parallel imaging (a phrase to which we will return). We have seen in the preceding chapter that exact parallel-imaging methods all boil down to assessing the solutions of a series of simultaneous equations; these are generally formulated into matrix algebra: small matrices in the case of image domain methods and larger ones for k-space methods or non-Cartesian reconstruction methods. Regardless of size, they all ultimately require a set of self-consistent simultaneous equations to be solved.

To solve simultaneous equations written in matrix form, the matrix is required to be inverted. Matrix inversion is a mathematical operation the details of which can be found in many accessible standard texts (Stroud 1990; Heath 2002) but are not relevant here. An important feature of matrix inversion is that if the simultaneous equations we are solving are sim-

ilar, then multiplying a vector by the inverse matrix produces solutions which are extremely sensitive to small changes in the vector, i.e. small changes (noise) in the vector are heavily amplified. In the extreme, if two equations are similar, i.e. two coils are similar (possibly very close together, or the field of view very small), and the difference between them is of the same order as the noise in the system, then to within noise the equations are the same and the correct solution cannot be found, because all solutions are dominated by the influence of noise. As the difference between the coil sensitivities increases approximate solutions can be found. It is worth emphasizing that if there is no noise (a situation achievable only theoretically) then g-factor noise will not arise. The g-factor noise originates in the aliased input data, not in the sensitivity measurement itself; however, the sensitivity data amplifies this noise.

In Fig. 3.2 the images also show the characteristic pattern of noise enhancement in parallel imaging. The regions of high noise have a particular shape which is a feature of the shape of the object to be imaged, they contain noise which varies within these regions and the main regions are modulated across the image in a way which relates to the speed-up factor.

Conceptually, "ill conditioning", which leads to the g-factor noise enhancement, is seen as a property of many systems unrelated to MRI. An ill-conditioned system is defined as one where disproportionately large changes occur at the output when small perturbations disturb the input. An everyday example of such a system is poorly installed shower where small adjustments to the temperature control produce large fluctuations in temperature, usually from dangerously hot to freezing cold. In the case of parallel imaging the small input perturbations are noise in the undersampled input data and the uncomfortable output is high levels of noise in the reconstructed image. The ideal g-factor is 1, where no enhancement of noise occurs; g-factors below 1.2 are typically tolerable depending on application and the statistical distribution of g-factors. The g-factor varies from pixel to pixel across the image domain, as the coil sensitivities vary in this way, so a g-factor *map* is required to describe the performance of a particular configuration. Often it is the mean g-factor that is quoted but it may be the peak g-factor that matters. The location of pathology is unpredictable and so may be obscured by noise anywhere in the image. Clearly the design of the coil is critical to achieving a g-factor close to 1 (the ideal).

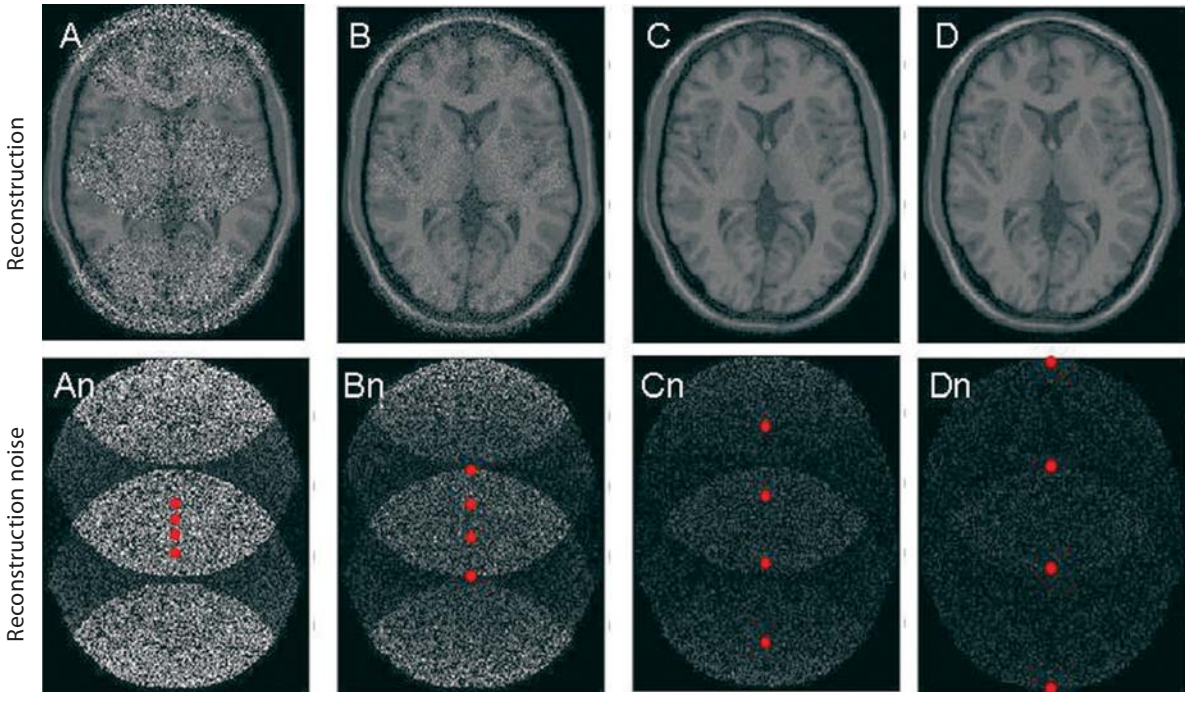

Fig. 3.2. Images from a simulated coil array. The array has four elements arranged linearly (in one dimension). The coils are designed such that their full width at half the maximum sensitivity is approximately 25% of the field of view. The reconstructions running from left to right show what happens if the coils are moved progressively further and further apart: the coils become less similar and the g-factor noise diminishes.

The location of the imaging plane is also critical as this affects the sensitivities seen by the coils. In general, parallel-imaging performance decreases with increasing distance from the coils, so that depth of the imaging plane is also an important factor.

3.2.2.2 Noise and k-Space Sampling

A further observation is that the g-factor is also dependent on the k-space sampling pattern. If we consider a simple uniformly undersampled Cartesian k-space then after reconstruction, if we look in k-space we can see that the noise generated by an ill-conditioned reconstruction "sits" on the newly generated k-space lines (Fig. 3.3A). This is intuitive. If the speed-up factor was 2, then in the image domain we would see the g-factor noise enhancement $N/2$ modulated (N number of lines of reconstructed image). This gives the familiar Cartesian SENSE g-factor noise distributions. The gap between sampled k-space lines is constant across k-space; thus, we expect that noise will also be distributed consistently.

If a radial acquisition is used (cf. Chap. 6), then the gap between sampled points is no longer constant (it increases towards the edges of k-space). This results in a non-uniform distribution of noise in k-space and so produces a very different image domain distribution of noise (Fig. 3.3B). So we can see that for identical coils and imaging plane, different sampling patterns will produce very different noise distributions in the image domain. In general, radial and spiral sampling patterns produce much more benign noise distributions than Cartesian sampling.

3.3 Coping With g-Factor Noise

We have seen that g-factor is the biggest single limit preventing us from accelerating indefinitely. In general, we wish to limit the g-factor to around 1.2; however, there may be circumstances where SNR is sufficiently high that greater losses can be toler-

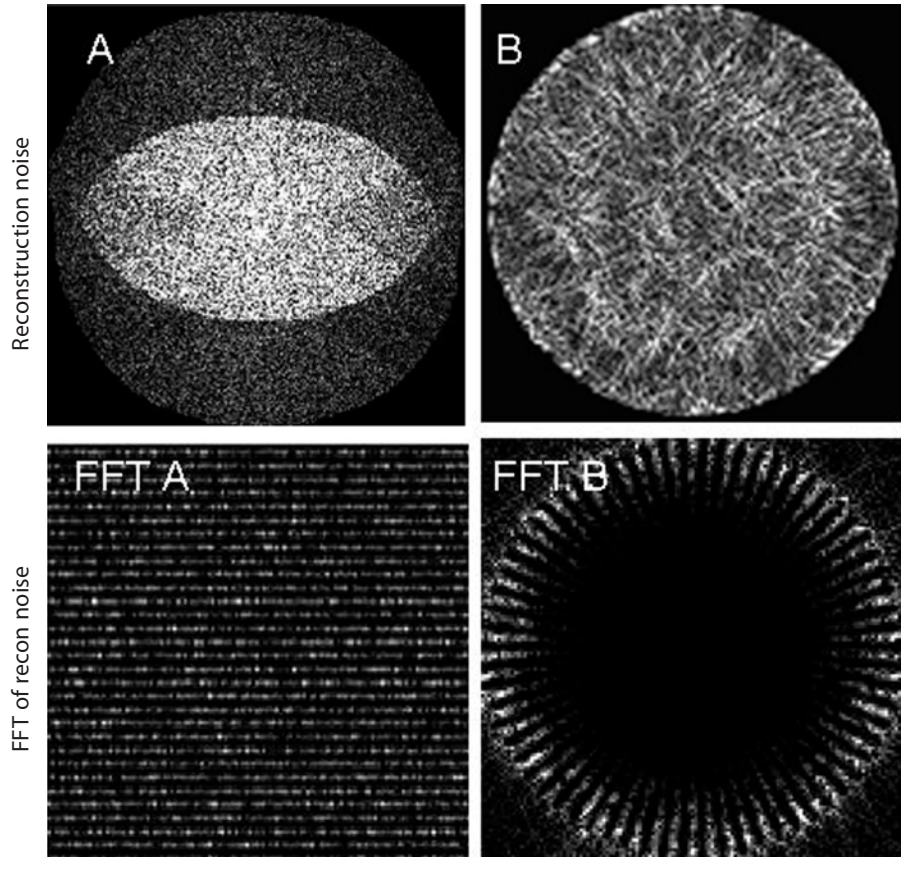

Fig. 3.3. A The image-domain noise distribution as a result of g-factor noise enhancement for a speed-up factor of 4. **FFT A** shows the equivalent k-space distribution of noise. The noise sits on the generated line in k-space giving a distinctive banded appearance to the noise. **B** Noise distribution for a radial acquisition in the image domain and (**FFT B**) shows the equivalent k-space where noise also sits on generated k-space points and its magnitude is related to the size of the gap in k-space that is being bridged (Courtesy of K. Pruessmann).

ated but only when the increase in speed provides a commensurate increase in diagnostic knowledge. We know that the g-factor noise comes from the ill-conditioning of a matrix inversion, and we know that this instability is produced by sensitivities that are too similar between the aliased pixels. The following sections describe strategies to reduce the g-factor.

3.3.1 Increasing the Distance Between Aliased Points

As is shown in Fig. 3.2, moving coils closer together reduces their difference and thereby increases g-factor. If we consider the (optimal) geometry described in Fig. 3.2D and 2Dn, then it is also true that the g-factor will increase if the field of view is reduced. This is because the pixels which become aliased onto each other when the acquisition is undersampled come closer together as the field of view is reduced; thus, the coils are less able to discriminate between them. As aliased pixel locations come increasingly closer together in Fig. 3.2d, the coil sensitivities of the aliased pixels become increasingly more similar, resulting in an increasingly higher g-factor. The same argument explains why high acceleration factors produce high g-factor noise: aliased pixels are closer together (there are also more of them). It also provides a qualitative explanation for the pattern of noise seen in the radial k-space image shown in Fig. 3.3B. In the center of k-space the points are close together. The field of view is inversely proportional to the sampling interval in k-space, so here we have a large field of view, a small speed-up factor, and therefore a low g-factor. As you move to the edges of k-space, the effective field of view decreases and thus the g-factor increases, producing increased g-factor noise. Of course, in the image domain the noise is distributed across the image.

Improvements in g-factor can be made by remembering the dependence on distance between aliased pixels particularly when considering 3D imaging. In a 3D volume acquisition there are two phase-encoding directions. This increases flexibility in the direction in which aliasing is induced. Where a volume acquisition is being sped up, acceleration can be in one of the two phase-encoding directions, or distributed between both. In general, it is advantageous to distribute between both, as is seen in Fig. 3.4; however, the aliased pixel spacing dictates the correct strategy: If relatively thin slabs are acquired by 3D methods, parallel imaging in the slab direction (partition or 3D direction) may be disadvantageous compared with acceleration in conventional (2D) phase-encoding direction.

If the speed-up is distributed between directions, then the distance between aliased pixels is not decreased when we move from twofold to fourfold speed-up, and this contribution to the g-factor remains largely unchanged provided that the coils have an equally favourable geometry in each direction. (The role the coils play in g-factor is discussed in the next section.) Matching the field of view to the field of view envisaged by the coil designer generally provides the best results for parallel imaging in terms of g-factor.

3.3.2 Coil Design

We know that there are speed-up limits independent of coil design, but there is still a gap between the theoretical speed-ups we should be able to achieve and that which we do actually achieve. Coil design is a rapidly evolving area with much of the established dogma being thrown into disarray (no pun intended) by the new design criteria imposed by parallel imaging; however, there are some basic design criteria that can be established. The problem of optimising a design subject to these criteria is not simple and is the unenviable task of the coil designer. It is beyond the scope of this chapter, but interesting to note, that approaches to coil design can differ depending on the reconstruction method being considered, e.g. one may choose to look at spatially localised coils, where tight localisation is required in the image domain or consider the extent of the k-space footprint where a broad range of spatial frequencies is best spreading over as large an area as possible in k-space. Both of these approaches (and others) ultimately result in similar coils design criteria, and it is these which we discuss.

When designing or choosing a coil for parallel imaging we need to consider the area of interest, e.g. if we are interested in looking at cortical grey matter only, then high-surface g-factors would be impossible to tolerate, but high g-factors in central parts of the brain may be acceptable. Alternatively, cardiac arrays need to have good sensitivity and g-factors at depth, but high g-factors near the surface in the chest wall and fat is not a problem. These factors deeply influence coil design. There are always tradeoffs, and designs optimised for one imaging plane or param-

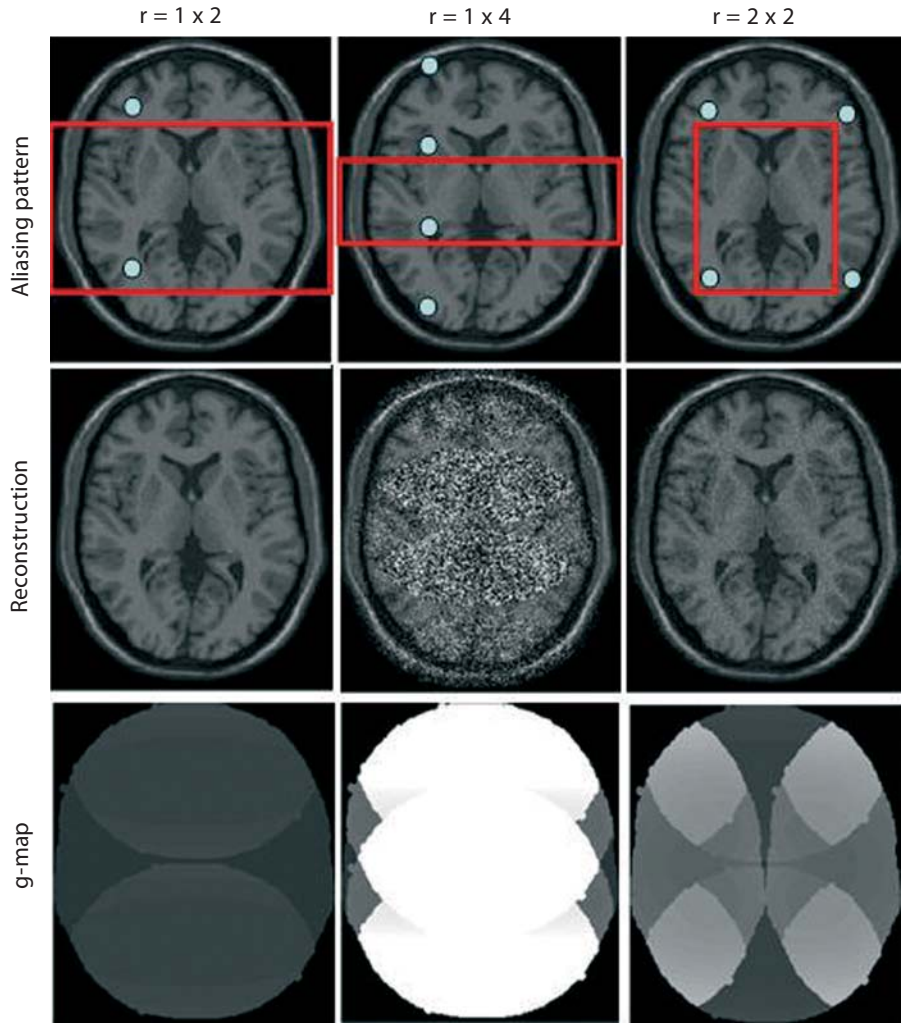

Fig. 3.4. A volume acquisition with the transverse plane containing the primary and secondary phase-encoding directions (frequency-encoding direction: head–foot). The *top row* shows the fully encoded image with the reduced field of view shown in *red*. An example pixel is chosen, and the location of pixels which will alias to this location shown for each speed-up strategy is shown in *blue*. It is instantly apparent that a 2D approach keeps these pixels furthest apart. The effect of this on the reconstructed images (*centre row*) and g-factor maps (*bottom row*) is obvious. Columns 2 and 3 both represent speed-up factors of 4, but the 2D case is by far the better reconstruction.

eter set can perform poorly for others, so the application is vital in designing the coil and correct use gives maximum benefit (cf. Chap. 14 about dedicated coil systems for different anatomical regions and Chap. 44 about future coil developments).

3.3.2.1 Number and Arrangement of Coils

In designing coils for maximum SNR, the coil size was generally dictated by the size of the anatomical region of interest. This meant that most targets could be adequately catered for with a relatively small number of coils leading to most coils (shoulder coils, pelvic coils, etc.) with relatively small numbers of elements. It was recognised that increased numbers of coil elements could improve SNR further, but the major gains could be made with these few elements and adding additional independent receiver channels to scanners is expensive and produced limited returns. As a rule of thumb, the optimal SNR is achieved in a single-loop element at approximately one diameter depth from the coil (Roemer et al. 1990), so if we are imaging the abdomen, then loops of approximately 20 cm diameter will perform well. Coils of this size can also be neatly packaged around the abdomen; thus, coil design is relatively simple.

These simple arguments for small numbers of receivers have been turned upside down by parallel imaging. It was very quickly realised that large numbers of channels can have significant benefits in providing the overdetermination of the matrix inversion at the heart of parallel imaging (overdetermination means that the speed-up factor is smaller than the number of available coils, which improves the condition of the inverse problem, making the reconstruc-

tions more stable and less prone to g-factor noise), allowing higher speed-up factors to be reached routinely and making the coils more flexible in terms of imaging plane and field of view. For true flexibility in imaging plane the g-factor needs to be as independent as possible of phase-encoding direction. This drives towards spherically symmetric coils with a large number of elements. Clearly this is not practical for real applications, but a head coil has been designed on this principle(Wiggins et al. 2005). For other applications 2D arrays are now recognised as being the next generation of coils. Two-dimensional grid-like structures provide the best compromise between anatomical suitability (they can be laid onto the patient) and directional independence of g-factor.

3.3.2.2 The Role of Phase in Coil Design

The role of receiver phase (manifest as phase information of the complex raw data) in the design of traditional array coils for optimal SNR is relatively limited. Because of Roemer et al.'s (1990) sum-of-squares approximation to optimal signal combination (for non-parallel-imaging applications), SNR is generally measured from magnitude images and so receiver phase is relatively unimportant. An exception to this are quadrature coils, of which detailed discussion is beyond the scope of this chapter; however, a simple description is that for SNR to be increased by using separate receivers, coils must "see" different volumes (measure different MR signals) to be considered independent, but this is not the full story. If the coils see the same volume but are sensitive to the MR signal with phase which is 90° shifted then again they can be considered as measuring different MR signal. In a single-loop element we are only sensitive, averaging over time, to half of the MR signal, as the rest of the signal is 90° out of phase. A quadrature head coil (often a birdcage design) is designed to be sensitive to both components of signal and hence receives twice the time averaged signal of a linear coil sensitive to the same volume (note this doubling in signal results in an increase in SNR of $\sqrt{2}$).

This independence brings with it the SNR gain associated with a two-element array coil but is of little use for parallel imaging, because although the views are "independent" in phase, they are not spatially varying (neither in magnitude nor in phase) and so do not provide any encoding information. The sensitivity of one quadrature component of the coil to two spatially separated pixel locations is the same. This hopelessly underdetermines the parallel-imaging problem and it cannot be solved. This points to one of the most dramatic changes to MR systems which arose as a result of parallel imaging: the introduction of the phased-array head coil. Prior to parallel imaging the birdcage was accepted as the gold-standard head coil and it performs very well with high and uniform SNR across the whole brain. Head-array-coil design has now been refined to the extent that SNR of bird cages can be matched in the centre of the brain with significant improvements at the periphery depending on exact coil geometry.

There are surface coil designs which aim to generate the SNR gain associated with quadrate reception but do have spatially varying phase. One such design is the butterfly loop coil shown in Fig. 3.5a.

In such a coil the symmetry of the magnitude receive field indicates that there are regions where the parallel-imaging performance of the coil will be poor; however, the spatially varying phase information breaks this symmetry restoring the parallel-imaging potential. This is an example where receiver phase plays a crucial role in conditioning the parallel-imaging problem. This demonstrates how powerful coil phase is in parallel imaging, and that if careful consideration is given to phase when designing coils for parallel imaging, performance can be significantly enhanced.

3.3.2.3 1D and 2D Arrays

When one-dimensional arrays are designed it is customary to overlap the individual elements. This overlap provides what is known as geometric decoupling, and the coils are kept independent because of this overlap (Roemer et al. 1990). The area of overlap is designed such that there is zero mutual inductance between the two coils. This prevents currents flowing in one coil due to currents being present in the other coil. When considering parallel imaging, such coil pairs can be demonstrated to be less than ideal for some applications, because when we consider the variation of sensitivity, as we move away from the coil the change in sensitivity may be small.

Looking at a simple example in Fig. 3.6 where the sensitivity of each coil to a pixel is now represented by a vector, shown as an arrow with magnitude (its length) and phase (its direction). If we look at the difference in sensitivity of a given coil to the two selected pixels for an overlapped pair (Fig. 3.6a), we

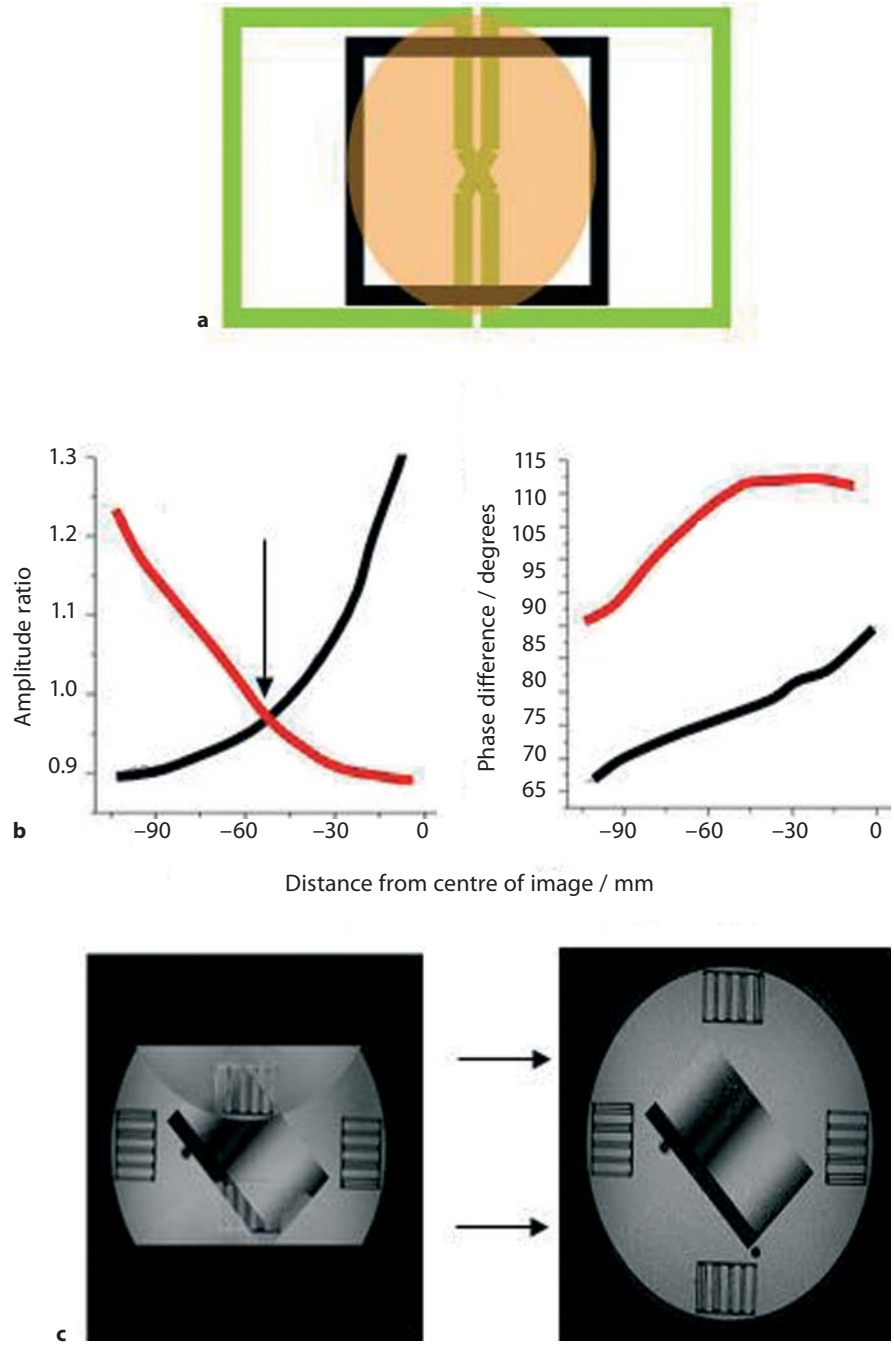

Fig. 3.5a–c. The butterfly-loop coil, an example of a coil pair where receiver phase plays an important role in parallel imaging. The coil itself has one element which is a single loop (*black*) and a second spatially coincident element which is a figure-of-eight shape (**a**, *green*, the butterfly coil). In this array the two receive fields are close to orthogonal above the centre of the array. If we inspect only the amplitude of the sensitivity, we see (**b**, *left*) that there are some locations where the amplitude sensitivity ratio between coils is the same for pixels in one half of the image (*red*) as the other half of the image, marked with an *arrow* (*black*) This would result in an ill-conditioned system and large noise amplification, however we do not see this in the reconstructed image (**c**, *right*). The reason is that the receiver phases are different in this locations indicated with *arrows* (**b**, *left*). This maintains the condition of the reconstruction and results in good reconstructions, even though the coils are not separated in space.

can see that the amplitude sensitivity varies in the same way, and for the two coils and the phase relationship between the two coils, it varies very little. If we consider the same two coils but now "underlapped" (Fig. 3.6b), we can see that the phase now varies rapidly as we move along this centreline making pixels close to the coils very different to pixels further away from the coil. This translates to a decrease in the g-factor for these pixels (Weiger et al. 2002).

Overlapped coils can have high g-factor close to the coils, whereas underlapped coils do not. A consequence of this underlapping is that the elements are no longer geometrically isolated, so other methods have to be employed to minimise current pick-up from one coil to another. The most common method

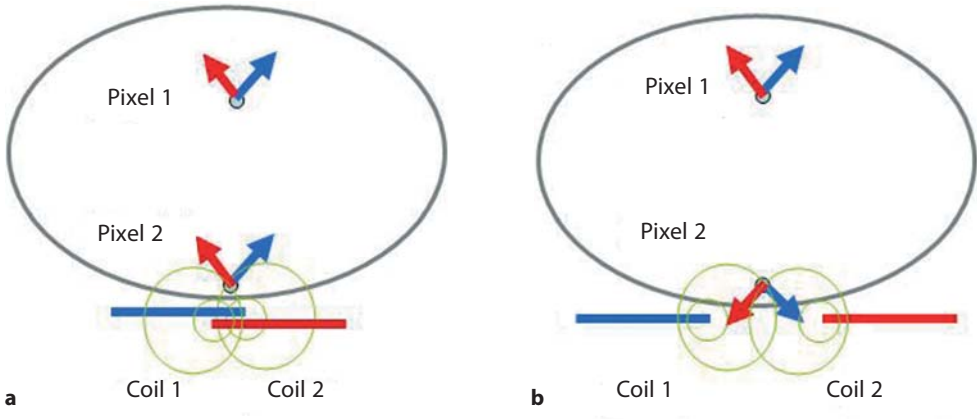

Fig. 3.6a,b. Two coils shown in *blue* and *red* are positioned **a** overlapped and **b** underlapped. The coil sensitivity is represented by the vectors shown as *arrows*. The direction of the arrows indicates phase. The receive field, resulting from an element of the coil conductor perpendicular to the page, is sketched in *green* for each coil. We can see that for pixel location 2 pulling the coils apart results in a large rotation of the phase of the receiver sensitivity. At pixel location 1 the field is largely unperturbed, as it is far from the coil. The result is that the sensitivity difference between these two pixels is increased for underlapped coils resulting in a lower g-factor and better parallel-imaging performance.

is the use of high-impedance pre-amps where a high impedance is presented to the coil. Impedance mismatch between coil and preamplifier blocks current (not signal voltage) and minimises the current flowing in the coil, thus reducing any coupling without adversely affecting SNR which is voltage dependent (Roemer et al. 1990). These high-impedance preamps not only allow underlapping but go some way to allowing freely positionable coil elements giving greater flexibility for improving g-factor on an exam-by-exam basis (i.e. making small movements to individual coil elements to reduce g-factor for a given imaging volume).

As a note about coil coupling, it is not intrinsically detrimental to parallel imaging provided that the coupling is well characterised and included in the reconstruction (Pruessmann et al. 2001); however, coupled coils can become inefficient and result in lower baseline SNR than uncoupled systems. For this reason it is best to design coils with the coupling as small as possible. This is a particular problem with freely positionable coil elements where the level of coupling changes with each position; thus, an optimal coil is difficult to design.

Increasing the number of elements is important to support desired speed-ups; typically a speed-up factor of 3 will require four or more coils to ensure that it is well conditioned. All these coils need to be preferentially arranged to optimise the difference in sensitivity along the direction of the acceleration. In general, we do not want the phase-encoding direction to be dictated by the coil design (which is implied above); instead, we want the choice of phase-encoding direction to be dictated by anatomical constraints. To achieve this flexibility but maintain achievable speed-ups, more coils are required to be able to encode in any direction. This quickly increases the number of elements desirable in a coil and gives an indication as to how they should be arranged. Two-dimensional arrays were developed to tackle exactly this problem, but they bring their own design problems. A simple 2D array might be a series of coils arranged as a rectangular grid. We have seen above that underlapping of coil elements can be advantageous for parallel imaging; however. one needs to be careful when moving to 2D arrays, because we now require array elements to be distributed in the B_0 direction as well as orthogonal to it, and here a second factor comes in to play: It is well known that if we consider a single loop laid in the coronal plane, then some (peripheral) part of its receive field will lie parallel to B_0 (Fig. 3.7). In MRI there is only sensitivity to magnetisation stored in the transverse plane perpendicular to B_0; thus, a B_0-directed receive field will not detect any signal. For a loop coil this results in dark regions in the coronal image and in a sagittal image dark bands which spread away from the coil, as illustrated in Fig. 3.7.

The consequence of this is that in the B_0 direction we may not want to underlap coil elements; otherwise, there will be areas where there is zero signal, which is not tolerable for parallel imaging or for normal imag-

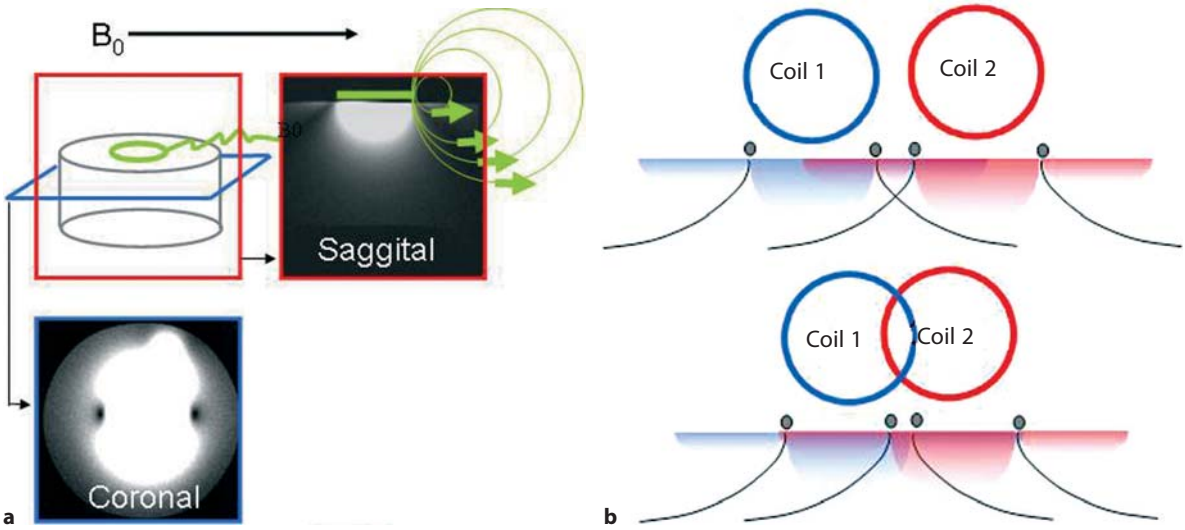

Fig. 3.7a,b. The two orthogonal images of a phantom shown in **a** demonstrate the loss of signal as the receive field (sketched in *green*) becomes parallel to B_0. In the sagittal image a line of zero signal following the *tangential arrows* is shown. In **b** this line of signal loss is represented as a *black line* emanating from the conductors of the coil. The magnitude sensitivity of each coil is shown in *red* and *blue* shading. If two coils are underlapped in this orientation, the *black lines* of zero signal intersect resulting in a region where neither coil has signal. If the coils are overlapped, then there is no region where both coils have zero signal, for this geometry relative to the main field is preferred.

ing, regardless of the g-factor. There are several array designs becoming available form the manufacturers that are simple 2D arrays of elements with underlapping in the left–right direction and overlapping in the B_0 direction.

It is evident that the design criteria for coils for parallel imaging are different to those for conventional imaging and designs which provide good sensitivity for conventional imaging are not always optimal for parallel-image acquisition.

3.3.3 Improving the Reconstruction Method

There is a third way to tackle g-factor noise enhancement, which is to use a mathematical technique known as regularisation (cf. also Chap. 46). This moderates the ill-conditioning of the matrix inversion previously mentioned by modifying the values of the sensitivities such that stable solutions can be found. Clearly this is a risky strategy to some extent, because although stability is increased, systematic errors or bias is generally introduced. Fortunately, the level of regularisation can be readily controlled, allowing "light" regularisation to be used. Regularisor terms can be simply numeric (not driven by the data) or they can be obtained from prior knowledge, e.g. knowledge of image noise or another MR image. It is always important to remember that when regularisation is being used, there is potential for information to appear in the image which comes from the regularisor, not from the original acquisition. Much progress is being made with these methods and much less biased approaches are being developed allowing increasingly higher speed-ups (Lin et al. 2004; Larkman et al. 2006).

3.4 Conclusion

Parallel imaging is fundamentally limited by g-factor. There are numerous strategies available to reduce the impact of the g-factor, much of which is beyond the operator's control in that it involves coil design. Coil design for parallel imaging is a very active area of research and development in both industry and academia; the coils produced are often very different to those formerly produced with maximum SNR as the design criteria. It is important to note that the lessons learned from coil design for optimal SNR

should not be forgotten. All coils designed for parallel imaging will be used for conventional imaging as well and should perform well under these conditions. It is also very important to note that in most applications the increased acquisition speed of parallel imaging comes at cost of lower sensitivity, and therefore maximising SNR is an even bigger imperative.

Beyond coil design, we have seen that coil positioning, choice of imaging plane and k-space trajectory can all influence the noise characteristics of the final reconstructed image; these are within the operator's control and coil placement in particular should be considered carefully with the acquisition in mind. Speed-up factors of 2–3 in one direction are readily accessible at 3 T, and it is expected that advances in the near future in both coil design and reconstruction methodology will make 1D speed-ups of 4–5 and even higher 2D speed-ups available. At these speed-ups it is the $\sqrt{R}$ term which will become limiting, and multislice excitations may allow these boundaries to be pushed further (Larkman et al. 2001).

References

Breuer FA et al. (2005) Controlled aliasing in parallel imaging results in higher acceleration (CAIPIRINHA) for multi-slice imaging. Magn Reson Med 53:684–691

Bydder M, Larkman DJ, Hajnal JV (2002) Combination of signals from array coils using image-based estimation of coil sensitivity profiles. Magn Reson Med 47:539–548

Carlson JW, Minemura T (1993) Imaging time reduction through multiple receiver coil data acquisition and image reconstruction. Magn Reson Med 29:681–687

Heath M (2002) Scientific computing: an introductory survey, 2nd edn. McGraw Hill, New York

Hutchinson M, Raff U (1988) Fast MRI data acquisition using multiple detectors. Magn Reson Med 6:87–91

Larkman DJ et al. (2001) Use of multicoil arrays for separation of signal from multiple slices simultaneously excited. J Magn Reson Imaging 13:313–317

Larkman DJ et al. (2006) Beyond the g-factor limit in sensitivity encoding using joint histogram entropy. Magn Reson Med 55:153–160

Lin FH et al. (2004) Parallel imaging reconstruction using automatic regularization. Magn Reson Med 51:559–567

Pruessmann KP et al. (2001) Advances in sensitivity encoding with arbitrary k-space trajectories. Magn Reson Med 46:638–651

Ra JB, Rim CY (1993) Fast imaging using subencoding data sets from multiple detectors. Magn Reson Med 30:142–145

Roemer PB et al. (1990) The NMR phased array. Magn Reson Med 16:192–225

Sodickson DK et al. (2005) Rapid volumetric MRI using parallel imaging with order-of-magnitude accelerations and a 32-element RF coil array: feasibility and implications. Acad Radiol 12:626–635

Stroud K (1990) Engineering mathematics, vol 1, 3rd edn. Macmillan, New York

Weiger M, Pruessmann KP, Boesiger P (2002) 2D SENSE for faster 3D MRI. MAGMA 14:10–19

Wiesinger F et al. (2004) Parallel imaging performance as a function of field strength: an experimental investigation using electrodynamic scaling. Magn Reson Med 52:953–964

Wiggins G et al. (2005) A 32 channel receive-only phased array head coil for 3T with novel geodesic tiling geometry. In: ISMRM 2005, Miami

Measurement of Signal-to-Noise Ratio and Parallel Imaging

4

Scott B. Reeder

CONTENTS

4.1 Introduction

The signal-to-noise ratio (SNR) of an image is a fundamental quantitative measure of MR image quality and system performance, and has enormous impact on the diagnostic quality of clinical studies. The SNR measurements provide a direct means for comparison of signal levels between different imaging method, patients, reconstruction methods, coils, and even different scanner systems. It is one of the essential measures of system performance and is used routinely in quality assurance protocols that monitor scanner performance (Price et al. 1990).

S. B. Reeder, MD, PhD
Departments of Radiology and Medical Physics, E3/311 CSC, University of Wisconsin, 600 Highland Avenue, Madison, WI 53792-3252, USA

The advent of parallel imaging with the development of SMASH (Sodickson and Manning 1997) and SENSE (Pruessmann et al. 1999), as well as other parallel imaging methods (Griswold et al. 2000, 2002; McKenzie et al. 2002; Kellman et al. 2001; cf. Chap. 2), has had tremendous impact on modern clinical scanning protocols. Parallel acceleration methods are commonly used to reduce acquisition time, with the trade-off that SNR of the resulting images will be reduced. For this reason, the ability to make accurate SNR measurements to measure the performance of parallel imaging applications is even more essential.

Unfortunately, routine methods commonly used to measure SNR with single coil imaging applications are no longer valid when using parallel imaging methods. Noise becomes distributed unevenly across the image (as discussed in Chap. 3) and application of routine measurement methods can lead to highly erroneous SNR measurements. Great caution must be used when measuring SNR with parallel-imaging applications.

In this chapter we review correct methods for the measurement of SNR in conventional single coil images, and review the underlying assumptions that are made. The concept of local noise amplification, characterized by the geometry, or "g-factor" is then discussed, and reasons why the application of conventional methods for SNR measurement will fail when applied to images acquired with parallel imaging. Finally, three methods for SNR measurement that are compatible with parallel-imaging applications are discussed.

4.2 SNR Measurement in MR Images

The signal-to-noise ratio, is exactly what the name implies, the signal in an image at a specific location, divided by the noise at that same location. "Signal" is commonly measured as the *average* signal in a small region of interest. "Noise" is typically quantified as the

root mean square (RMS) amplitude of the white noise that is superimposed on the signal. For MR systems, it has been shown that the noise has a Gaussian distribution with zero mean (McVeigh et al. 1985). Conveniently, the RMS amplitude of a Gaussian distribution equals its standard deviation, such that SNR of a *complex* image is measured as the ratio of the average signal (S) to the standard deviation of the noise (σ), i.e.,

$$\mathrm{SNR} = \frac{S}{\sigma} \tag{1}$$

After Fourier transformation into the spatial domain, noise is *evenly distributed* throughout the image. For this reason, SNR can be measured for single-coil acquisitions as the quotient of the average signal in a region of interest (ROI) within the object, and the standard deviation of the noise in a ROI outside the object, free from signal or artefact (i.e., "air"), as diagrammed in Fig. 4.1.

Most clinical MR images are presented as magnitude images, rather than complex images, and this greatly alters the behavior of the background noise, as shown in Fig. 4.2. After the magnitude operation, the noise distribution is skewed and no longer has a zero mean. In addition, the apparent standard deviation of the noise is *lower* than the true standard deviation, by a factor of 0.655, as described by Henkelman 1985).

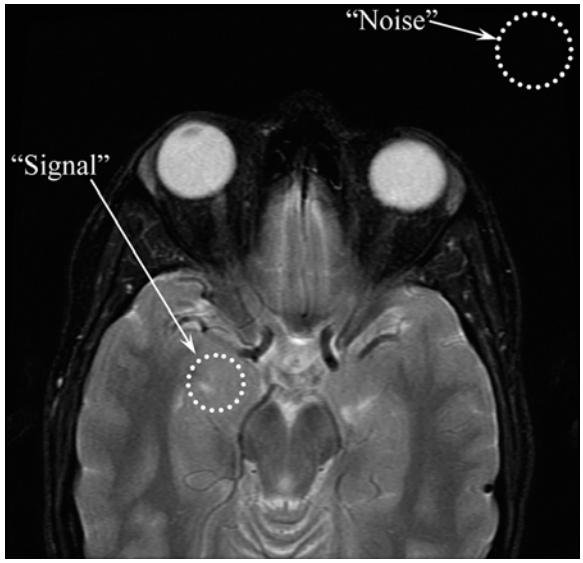

Fig. 4.1. Measurement of signal-to-noise ratio (SNR) from an image acquired with a single receive coil and *no* parallel imaging acceleration is determined from the ratio of the average signal in the "Signal" ROI and the standard deviation of the noise in the "Noise" ROI, placed outside the object. This approach assumes that noise is uniform across the image. In addition, a correction factor for the underestimation of noise must be made.

The noise in the magnitude image follows the statistics of a Rayleigh distribution (Edelstein et al. 1984), and measuring the standard deviation of the background noise from a magnitude image will overestimate SNR by approximately 53% (=1/0.655). In addition, as can be seen by the profile shown in Fig. 4.3, taking the magnitude of a complex image changes neither the signal nor the noise in object if the SNR is sufficiently high (≥5), even though the noise in the background region has been significantly altered, as was shown in Fig. 4.2; therefore, measurement of SNR from magnitude images acquired with single-coil acquisitions can be determined from the ratio of the average signal (S) in a "signal" ROI, and the apparent standard deviation (σ_{app}) within a "noise" ROI outside the object, and the appropriate correction factor, i.e.,

$$\mathrm{SNR}_{\mathrm{MAG}} = 0.655\frac{S}{\sigma_{\mathrm{app}}} \tag{2}$$

For multi-coil applications without parallel accelerations, images can be recombined in several different ways, although the "square root of sum of squares" method proposed by Roemer (et al. 1990) is a commonly used approach. Measurement of SNR from multi-coil images reconstructed using this approach can made in a similar manner as single coil acquisitions, except the correction factor changes slightly. For four or more coils, the correction factor is approximately 0.70 (Constantinides et al. 1997).

4.3 SNR and Parallel Imaging

The use of parallel imaging will degrade the SNR performance of the reconstructed image through two mechanisms (see also Chap. 3). First, SNR is reduced as a result of decreased data sampling, i.e.,

$$\mathrm{SNR}_R = \frac{\mathrm{SNR}_0}{\sqrt{R}}, \tag{3}$$

where R (≥1) is the "reduction" or acceleration factor used in the acquisition, and SNR_0 is the signal-to-noise ratio of the equivalent unaccelerated image.

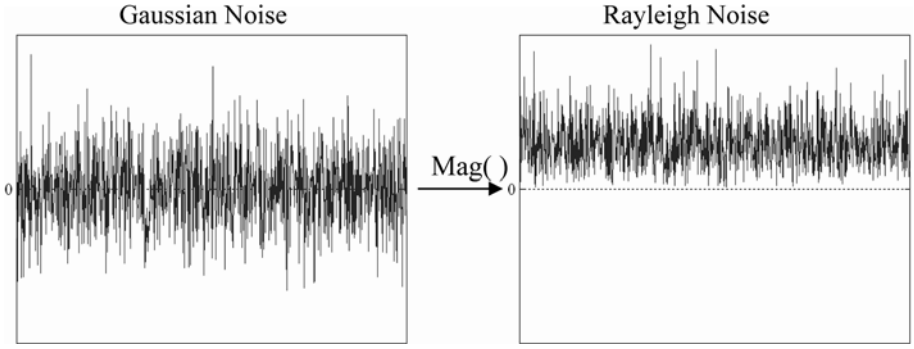

Fig. 4.2. The noise in a complex MR image has a Gaussian distribution with a zero mean and standard deviation,σ. With magnitude images, however, the noise has a Rayleigh distribution, with non-zero mean and an apparent standard deviation σ_{app}=0.655σ, an *under-estimation* of the true noise level.

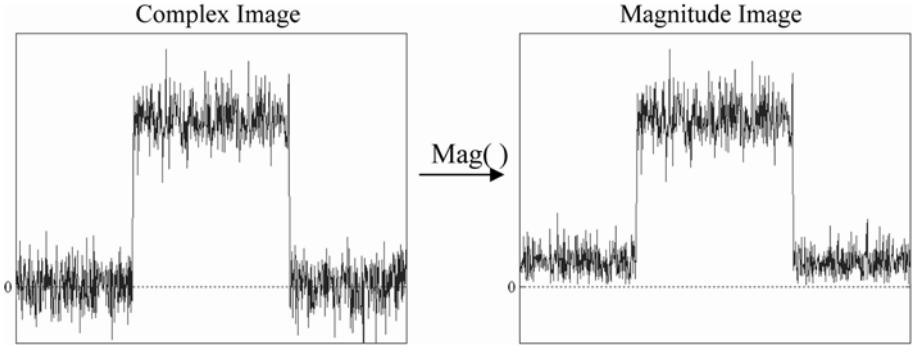

Fig. 4.3. The noise in a complex MR image has a Gaussian distribution with a zero mean and standard deviation, σ. With magnitude images, however, the noise in the background has a reduced apparent noise level, whereas noise in the region of signal remains unaffected if the SNR is sufficiently high.

This equation simply reflects that the image will be noisier when less data is acquired, directly analogous to signal averaging. This equation holds for low acceleration factors (R=2–3) with well designed coils, and the SNR performance of parallel imaging is simply related to the square root of the total scan time.

There is a second cause of SNR degradation that commonly occurs with parallel imaging. This degradation is a result of noise amplification that occurs with parallel imaging and reflects the ability of the parallel reconstruction algorithm to unwrap superimposed (aliased) pixels given a certain coil geometry (Pruessmann et al. 1999). This additional SNR degradation can be quantified with the so-called geometry or "g" factor (cf. Chap. 3), such that

$$\mathrm{SNR}_R = \frac{\mathrm{SNR}_0}{g\sqrt{R}}. \qquad (4)$$

Equation (4) can be rearranged as

$$g = \frac{\mathrm{SNR}_0}{\mathrm{SNR}_R\sqrt{R}}, \qquad (5)$$

which is the mathematical definition of the g-factor.

The g-factor always has a value of one or more and may be non-uniform across the image. It reflects an increase in local noise, not a decrease in signal, which is unchanged between the accelerated and unaccelerated images. It is also important to realize that the g-factor is highly dependent on the coil geometry and the resulting sensitivity profiles, the orientation of the phase-encoding direction, the acceleration factor (R), and the field of view (FOV). In addition, the object itself may have indirect but significant impact on the g-factor by the effective image masking on the sensi-

tivity profiles, due to the shape and size of the object. Typically, the g-factor is greatest in locations farthest from the coil elements, often near the center of the FOV in areas of critical clinical importance. Equation (5) can be further simplified by recalling that the signal from the accelerated and unaccelerated images, S_0 and S_R, respectively, are equal,

$$g = \frac{S_0/\sigma_0}{S_R/\sigma_R\sqrt{R}} = \frac{\sigma_R}{\sigma_0\sqrt{R}}, \quad (6)$$

demonstrating that only the noise from the accelerated and unaccelerated images must be measured in order to determine the g-factor.

4.4 Alternative Methods to Measure SNR

As characterized by the g-factor, noise is not evenly distributed in accelerated images reconstructed with parallel-imaging methods. Attempts to measure SNR using the approach described above may be incorrect if the noise level in the "noise" ROI is lower than in the area of interest where the signal is measured. For example, Fig. 4.4 shows a noisy one-dimensional magnitude image for the case where noise is uniformly distributed and a case where there is a higher level of noise at the center of the image. The true SNR at this location is very poor. Although measurement of the average signal at this location is unaffected, estimation of noise in an area outside the object (background noise) would be greatly underestimated, and *SNR would be erroneously overestimated.*

Figure 4.5 shows phantom images acquired with increasing acceleration factors. Although the average signal remains unchanged throughout the images, geographic regions of increased noise are very apparent, particularly at higher acceleration factors

Similar increases in noise can also be seen with clinical images, even with modest acceleration factors. Figure 4.6 shows an example of "in and out of phase" T1-weighted spoiled-gradient imaging in a patient with alcoholic steatohepatitis, acquired with an acceleration of two. Subtle increased noise at the center of the images is caused by local noise amplification that occurs with parallel imaging from a g-factor that is greater than one.

So how do we measure SNR in an accelerated image where the g-factor must be considered? A successful method for the measurement of SNR from images acquired with parallel-imaging accelerations must account for non-uniform noise throughout the image. In this chapter, three SNR measurement methods that account for non-uniform noise across the image are discussed. These methods include a "multiple acquisition" method, a "difference" method, and direct calculation of the g-factor using measured coil sensitivities.

4.4.1 Multiple Acquisition Method

A robust, although time-consuming method for measuring SNR, known as the "multiple acquisition" method, is performed by repeating an image acquisition many times. This method can be performed with magnitude images. Assuming that the scanner is stable and the signal does not vary from image to

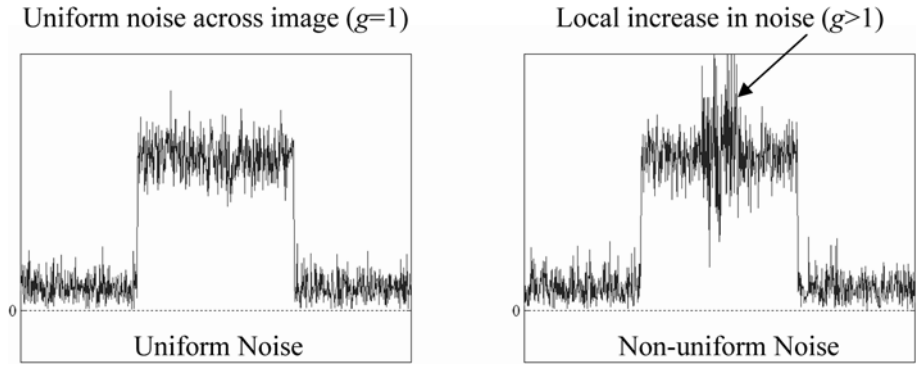

Fig. 4.4. Profile of image with noise with uniform noise across the image (left) compared to the profile of an image with non-uniform noise centrally (right). Even though the average signal is unchanged at this location, the noise is clearly higher at this location than elsewhere in the image. Accurate measurements of local SNR must take this local variation in noise into account.

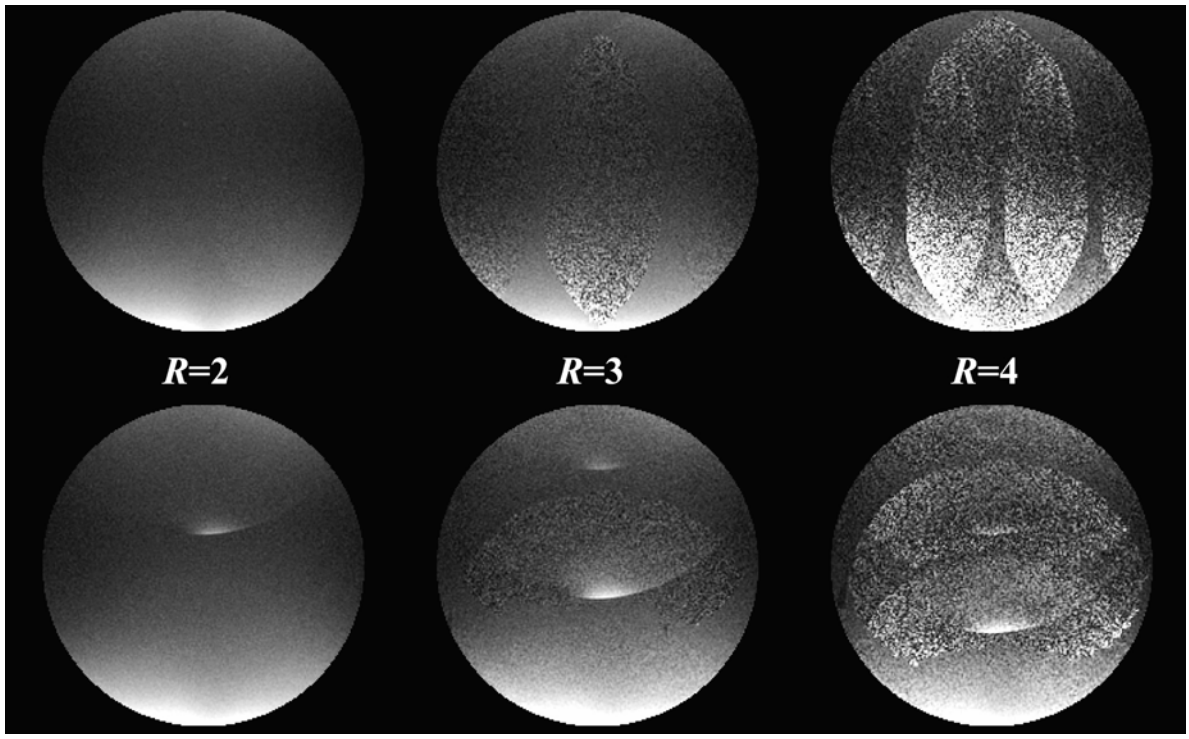

Fig. 4.5. Subjective increase in local noise of spoiled gradient-echo phantom images that worsens with increasing acceleration. Phase-encoding direction is left–right (*top row*) and up–down (*bottom row*), and the window/level is the same for all images. Although the average signal is similar between the images, there are areas of locally increased noise which severely degrade portions of the image, especially at higher acceleration factors.

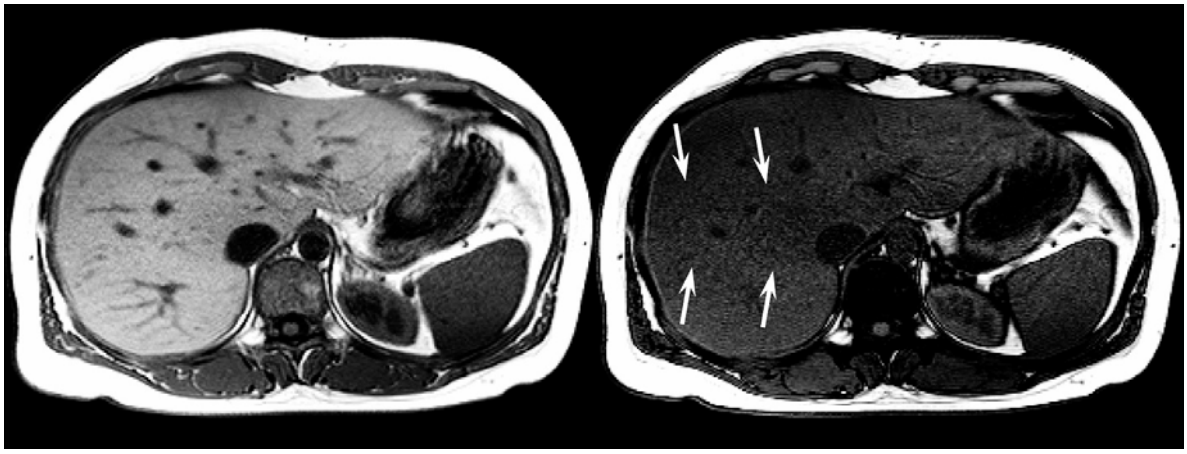

Fig. 4.6. In-phase (*left*) and out-of-phase (*right*) spoiled gradient-echo images of the liver in patient with alcoholic steatohepatitis. The drop in signal in the out-of-phase image reveals subtle increased local noise in the center of the liver (*arrows*), resulting from noise amplification characterized by $g>1$. The increase in noise near the center of the image is not caused by lower coil sensitivity, which would cause a decrease in signal, not an increase in noise.

image, the SNR can be determined on a *pixel-by-pixel basis*, providing a high-resolution "SNR image." The SNR at each pixel, determined using the multiple acquisition method is given by

$$\mathrm{SNR} = \frac{S_t}{\sigma_t}, \tag{7}$$

where S_t is the average signal and σ_t is the standard deviation of the signal measured from multiple images acquired over time for each pixel. This allows the measurement of SNR on a pixel-by-pixel basis, and permits accurate measurement of local SNR despite the presence of spatial variation in image noise. This method is shown schematically in Fig. 4.7 for a series of images with non-uniform noise throughout the image, demonstrating how SNR is measured for each pixel across the image.

With the multiple acquisition method, typically 30–300 images are acquired. The number of images will determine the uncertainty on the measurement of SNR itself. The more images that are acquired, the less uncertainty there is in the SNR measurement. Through standard propagation of error methods (Bevington and Robinson 1992), it can easily be shown that for an N image acquisition, the error on the SNR measurement itself is

$$\sigma_{\mathrm{SNR}} = \mathrm{SNR}\sqrt{\frac{2}{N}}. \tag{8}$$

For example, if the approximate SNR of an image was 20, and one desired an error of less than ±2 (i.e., 10%), one would need to acquire 200 or more images. An error of less than ±4 (i.e., 20%) would require 50 or more images.

It is important to discuss two important assumptions of the multiple acquisition approach. Firstly, it is imperative that there be no inherent signal fluctuations over time. Any signal fluctuations would be interpreted as noise and incorrectly decrease the apparent SNR measurement. The second major assumption is that the noise follows Gaussian statistics even when using magnitude images. As was shown and described in Fig. 4.3, the noise in a background region changes from Gaussian to Rayleigh statistics after the magnitude operation, causing an apparent (and erroneous) decrease in the standard deviation of the noise; however, the noise in an area of relatively high signal is unaffected and will maintain Gaussian statistics. Estimates of noise in this region are unaffected by the magnitude operation. In general, this assumption is true so long as SNR is approximately 5 or higher (Henkelman 1985). Above this SNR, noise is unaffected by the magnitude operation and SNR measurements made using the multiple acquisition method are valid. This also implies that SNR measurements made in background regions or areas of very low SNR are inherently incorrect. Masking of SNR values below 5 or a similar value can be performed to avoid display of these areas.

Finally, the multiple acquisition method can be extended to direct measurement of g-factor images. Two sets of images are required, one acquired without acceleration and the other with some acceleration factor, R. From Eqs. (5) or (6), a g-factor "image" can be easily calculated. Regions of SNR <5 can be

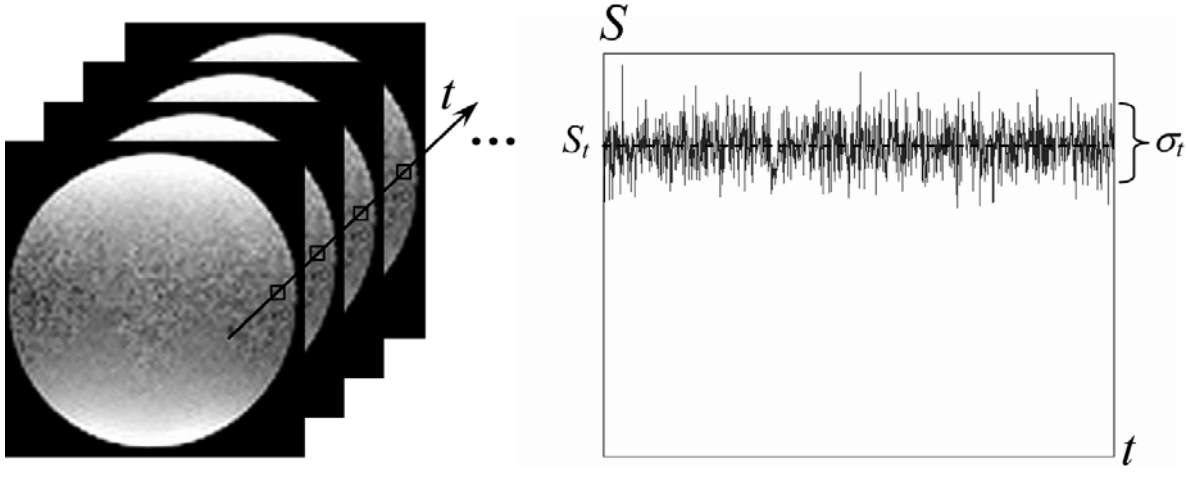

Fig. 4.7. The multiple acquisition method. Multiple identical images are acquired. For each pixel, the signal and standard deviation are measured over time, permitting direct calculation of the SNR for that pixel.

masked to zero. Examples of calculated g-factor images are shown in Fig. 4.8. From these images, it can be seen that the g-factor is highly dependent on position within the image, the acceleration factor, and the orientation of the phase-encoding direction.

Although the multiple acquisition approach is robust and accurate, it can be time-consuming and, in general, may be impractical for in vivo SNR measurements. It is best reserved for phantom experiments or specific in vivo cases where motion and physiological variations do not create signal fluctuations that would incorrectly be interpreted as noise.

4.4.2 Difference Method

A second method for measuring SNR can be performed through the acquisition of only two images, instead of large numbers (Price et al. 1990; Firbank et al. 1999). In this approach, an estimate of the mean signal is obtained from a small ROI from the sum of the images, and the standard deviation of the difference of the images is obtained from the same ROI. Because the noise is estimated from the difference of two magnitude images in a region with relatively high signal, the noise will maintain Gaussian statistics. The local SNR within the ROI from two images, $\mathbf{S}_1$ and $\mathbf{S}_2$, is then calculated as (Reeder et al. 2005)

$$\mathrm{SNR}_{\mathrm{ROI}} = \frac{S_{\mathrm{ROI}}}{\sigma_{\mathrm{ROI}}} = \frac{\mathrm{mean}(\mathbf{S}_1 + \mathbf{S}_2)|_{\mathrm{ROI}}}{\sqrt{2}\,\mathrm{std}(\mathbf{S}_1 - \mathbf{S}_2)|_{\mathrm{ROI}}}, \tag{9}$$

where the signal in the original image, S_{ROI} is half the average signal from the ROI in the sum image $(\mathbf{S}_1 + \mathbf{S}_2)$, i.e., $S_{\mathrm{ROI}} = \mathrm{mean}(\mathbf{S}_1 + \mathbf{S}_2)|_{\mathrm{ROI}}/2$, and the standard deviation of the noise in the original image is the standard deviation in the ROI of the difference image $(\mathbf{S}_1 - \mathbf{S}_2)$ divided by $\sqrt{2}$, i.e., $\sigma_{\mathrm{ROI}} = \mathrm{std}(\mathbf{S}_1 - \mathbf{S}_2)|_{\mathrm{ROI}}/\sqrt{2}$. The additional factor of $\sqrt{2}$ arises from the fact that when two images are added or subtracted, the variance of the new signal equals the sum of the variance of the noise of the two images, and the variance is simply the square of the standard deviation. If variations in noise across the region of interest are small, an accurate measurement of the local SNR is possible.

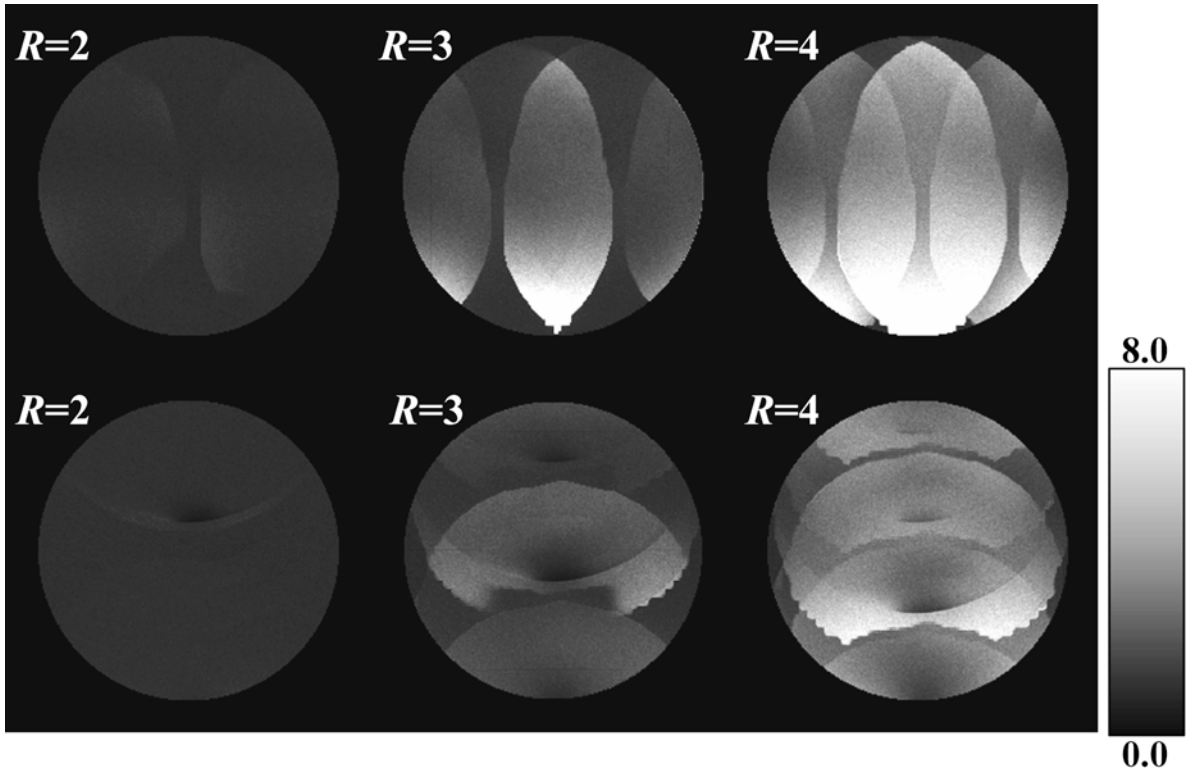

Fig. 4.8. Calculated g-factor images using Eq. (6) and the multiple acquisition method that acquired 200 consecutive spoiled gradient-echo images of a spherical phantom, such as those shown in Fig. 4.5. The phase-encoding direction is in the left–right direction (*top row*) and up–down direction (*bottom row*) for different acceleration factors (*R*).

This approach is known as the "difference method" and is shown schematically in Fig. 4.9.

The main advantage of the difference method is that only two images are required making in vivo measurements of SNR feasible. As with the multiple acquisition method, the signal must not fluctuate between the two images, or inaccurate SNR estimates will result. The main disadvantage of this method is that the effective spatial resolution of this method is lower and variations in SNR are "averaged" out over the ROI. For most clinical applications this is not a problem if small ROIs are used. In fact, this concept has been explored by Gizweski et al. (2005) by using a "sliding ROI" approach in conjunction with the difference method in order to generate a low-resolution SNR image.

The error on the estimates of the SNR in the region of interest is determined by the local SNR and the size of the ROI. It can be shown that the error on the estimate of SNR using the difference method is given by (Reeder et al. 2005)

$$\sigma_{SNR} \approx \mathrm{SNR}\sqrt{\frac{2}{N_{ROI}}}, \tag{10}$$

where N_{ROI} is the size of the ROI in pixels. For example, there will be an error of ±4 in the SNR measurement when the SNR is approximately 20 (i.e., a 20% error), when using an ROI of 50 pixels. Increasing the size of the ROI decreases this area but may average out variations in the local SNR.

Estimates of the g-factor can also be made with the difference method. This approach requires the acquisition of four images, two with an acceleration, R, and two with no acceleration. The difference of each pair of images can be used to estimate the standard deviation of the noise in the ROI of both accelerated and unaccelerated images. The g-factor is subsequently determined from Eq. (6), i.e.,

$$g = \frac{\mathrm{std}\left(S_1^R - S_2^R\right)}{\mathrm{std}\left(S_1^0 - S_2^0\right)\sqrt{R}}, \tag{11}$$

where $\mathrm{std}\left(S_1^R - S_2^R\right)$ is the standard deviation in the ROI of the difference of the accelerated images, and $\mathrm{std}\left(S_1^0 - S_2^0\right)$ is the standard deviation of the difference of the unaccelerated images. This approach has been shown to have very close agreement with the multiple acquisition method (Reeder et al. 2005). It

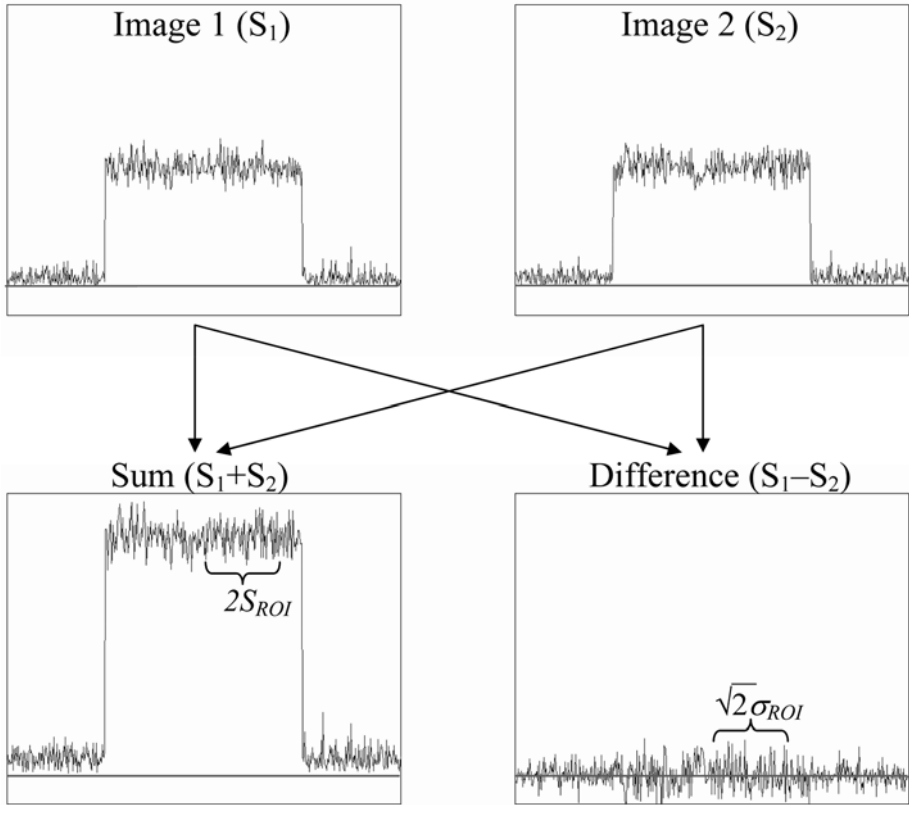

Fig. 4.9. The difference method. The average signal in the region of interest (ROI) of the sum image is twice the signal in the original images (S_{ROI}). The standard deviation in the ROI of the difference image equals $\sqrt{2}$ times the standard deviation of the noise in the original images (σ_{ROI}).

is important to use small ROIs with this approach, because an ROI that spans a sharp transition in the g-factor (e.g., Fig. 4.8) could lead to inaccurate estimation of the g-factor.

4.4.3 SNR Ratio Method

There are many situations where measurement of absolute SNR is not necessary, but the relative SNR may be sufficient. For example, flip-angle optimization may require acquisition of multiple images with identical imaging parameters except for the flip angle. The flip angle that generates the highest relative SNR or CNR in a particular tissue is then chosen.

For situations such as these where few parameters have changed, the SNR ratio method may be applicable; specifically, if parameters that affect the g-factor, such as field of view, matrix size, phase-encoding direction, coil sensitivities, the parallel-imaging acceleration factor or reconstruction algorithm, etc., *are unchanged between scans*. This means that the SNR ratio method cannot be used to analyze the SNR in comparisons of acquisitions with and without parallel imaging or with different acceleration factors as is often required in clinical studies.

To determine the SNR ratio, the average signal from one ROI in the area of interest (S_1, S_2), and the standard deviation of signal measured in a background "noise" ROI outside the body (σ_1, σ_2) are measured in both images, such that

$$\text{SNR Ratio} = \frac{\text{SNR}_1}{\text{SNR}_2} = \frac{S_1 \Big/ \left(\frac{g_{1,S}}{g_{1,\sigma}} \sigma_1 \right)}{S_2 \Big/ \left(\frac{g_{2,S}}{g_{2,\sigma}} \sigma_2 \right)} = \frac{S_1 \sigma_2}{S_2 \sigma_1} \qquad (12)$$

where $g_{i,S}$ is the g-factor at the ROI in the area of interest and $g_{i,\sigma}$ is the g-factor in the background "noise" ROI in images *i=1, 2*.

The SNR ratio method relies on the assumption that the g-factor is identical in the two images, i.e., $g_{1,S} = g_{2,S}$ and $g_{1,\sigma} = g_{2,\sigma}$. Accordingly, it is important to emphasize that the ROIs to determine signal and noise must be identical between the two images. In addition, the measurement of the signal and standard deviation cannot be used to measure the absolute SNR of that image for reasons discussed above. It is also noted that some reconstruction algorithms for parallel imaging set the background signal to 0. In this case the SNR ratio method cannot be applied since $\sigma_1 = \sigma_2 = 0$.

4.4.4 Direct Calculation of the g-Factor

As shown in the original description of the g-factor by Pruessmann et al. (1999), it is possible to calculate the g-factor directly if the coil sensitivities and noise correlation between separate coils is known. The coil sensitivities are complex (i.e., have magnitude and phase) which is information that is not typically available to most scanner operators. In addition, measurement of the noise correlation between the different coils requires additional measurements, and the calculation of g-factor images is complicated.

Recently, an elegant characterization of all noise contributions in an MR system has been performed by Kellman and McVeigh (2005) permitting the reconstruction of MR images with image intensity equal to SNR. In this work, noise contributions from coils, amplifiers, and filters, as well as additional noise amplification from parallel unwrapping, is calculated directly. Measurements of noise correlation between different coils are made during "pre-scan," and in combination with complex coil sensitivities, can be used to generate g-factor images directly. Examples of cardiac CINE images acquired with SSFP and TSENSE acceleration are shown in Fig. 4.10 along with their corresponding g-factor maps. Although this approach is more complicated and must be incorporated directly into the raw data reconstruction by the manufacturer of the imaging system, it provides robust and accurate estimates of SNR and the g-factor without additional image acquisition. The details of this work are beyond the scope of this chapter.

4.5 Special Considerations

4.5.1 TSENSE

The SNR performance of TSENSE (cf. Chap. 12) has the added benefit of temporal filtering. This SNR benefit is characterized by a simple modification of Eq. (4), specifically,

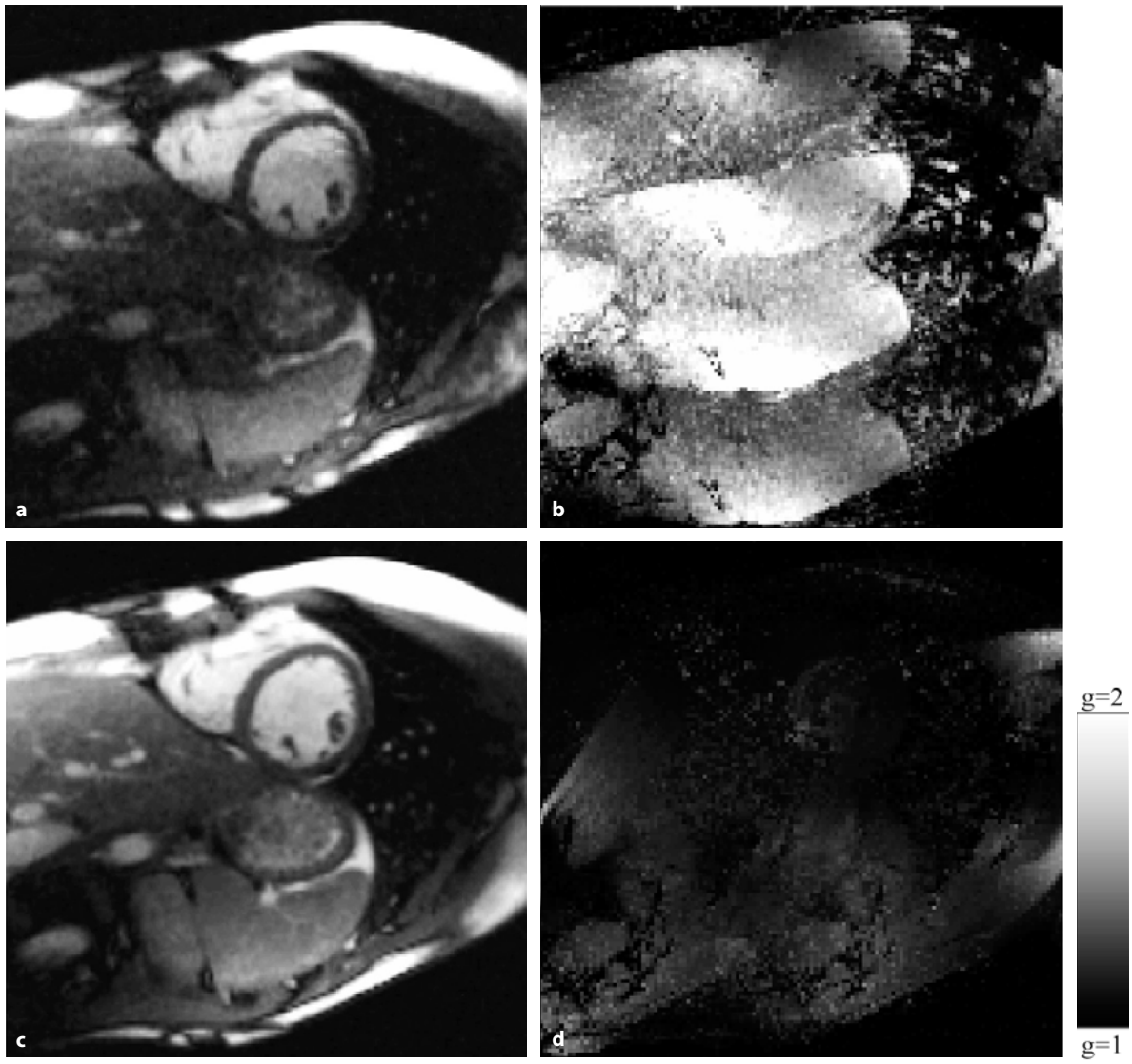

Fig. 4.10a–d. a,c Short-axis CINE SSFP images and **b,d** the corresponding g-factor images acquired using TSENSE (R=4) with the phase-encoding direction in the anterior–posterior direction (**a,b**) and in the left–right direction (**c,d**). The same scaling has been displayed for the g-factors. Note the strong dependence of the g-factor on phase-encoding orientation. (Courtesy of P. Kellman)

$$\mathrm{SNR} = \frac{\mathrm{SNR}_0}{g\sqrt{R}}\sqrt{\frac{\mathrm{BW}_{\mathrm{FULL}}}{\mathrm{BW}_{\mathrm{UNFOLD}}}}, \qquad (13)$$

where $\mathrm{BW}_{\mathrm{FULL}}$ and $\mathrm{BW}_{\mathrm{UNFOLD}}$ are the two-sided noise-equivalent temporal bandwidths for the full and reduced FOV acquisitions, respectively (Kellman et al. 2001). This filtering occurs in the time domain, by assuming relatively slow changes in the object between CINE image frames, allowing some temporal filtering to reduce image noise. Typically, $\mathrm{BW}_{\mathrm{FULL}}/\mathrm{BW}_{\mathrm{UNFOLD}} = 0.8$ improving SNR slightly. Knowledge of temporal filtering, if any, must be known before accurate estimates of the g-factor can be made using TSENSE.

4.5.2 Self-Calibrating Parallel-Acceleration Methods

As described in Chapter 2, parallel-imaging methods, such as generalized autocalibrating partial parallel acquisitions (GRAPPA), auto-SMASH (Jakob et al. 1998), and other variable density k-space sampling

methods (McKenzie et al. 2002), maintain full sampling at the center of k-space in order to obtain calibration information for unwrapping of undersampled outer regions of k-space. In many k-space-based reconstruction algorithms, these central calibration lines contribute to the reconstruction of the final image. This adds tremendous complexity to the SNR analysis of these images, because the central lines of k-space provide most of the contrast information in an image and carry most of the image *power* that primarily affects SNR. Higher spatial frequencies that carry important edge information are under-sampled and the noise distribution will be non-uniform across the image.

For these reasons, the measurement of SNR and g-factors should be applied very carefully to parallel imaging methods that use variable density k-space sampling. The multiple acquisition method remains valid because the noise distribution is still Gaussian in time. The difference method, however, will only be valid if the noise distribution is uniform across the ROI used. In general, this will not be true and caution should be exercised when using this method; however, *calculation of the g-factor may no longer be valid.* What is the effective acceleration factor that should be used in Eqs (4)–(6)? It is not simply the absolute time acceleration, because the undersampling of k-space is not uniform, and central k-space lines are weighted more heavily than higher spatial frequencies. Full characterization of SNR and the g-factor using variable-density k-space methods will prove very complex, and further work on this topic is required.

4.5.3 Measurement of SNR with Multi-Phase Contrast-Enhanced Imaging

Rapid, contrast-enhanced imaging, such as MR angiography or dynamic contrast-enhanced (DCE) imaging of solid organs (liver, brain, heart, etc.), are often combined with parallel-imaging applications in order to improve both temporal and spatial resolution of the acquisition. Measurement of SNR as well as contrast-to-noise ratio (CNR) between the background tissue and enhancing vessels/tissue is an important measure of the performance of these methods.

A variation in the difference method provides an opportunity to measure SNR in these circumstances. In this approach, at least two baseline non-contrast-enhanced images are required. As shown schematically in Fig. 4.11, estimates of the noise are made from the difference of two baseline images, $\mathbf{S}_1$ and $\mathbf{S}_2$. The local noise of $\mathbf{S}_1$ and $\mathbf{S}_2$ within an ROI is σ, which can be determined from the standard deviation of the difference image $(\mathbf{S}_1 - \mathbf{S}_2)$, i.e., . Signal enhancement is then determined from the difference of the enhanced image ($\mathbf{S}_3$) and a background image ($\mathbf{S}_1$ or $\mathbf{S}_2$), and is simply given by $\Delta S = \text{mean}(\mathbf{S}_3 - \mathbf{S}_2)|_{ROI}$; therefore,

$$\Delta\text{SNR} = \frac{\Delta S}{\sigma} = \frac{\sqrt{2}\,\text{mean}(\mathbf{S}_3 - \mathbf{S}_2)|_{\text{ROI}}}{\text{std}(\mathbf{S}_1 - \mathbf{S}_2)|_{\text{ROI}}}, \tag{14}$$

representing the SNR of the signal enhancement in the unsubstracted image, $\mathbf{S}_3$. More importantly, the SNR of the subtracted image $(\mathbf{S}_3 - \mathbf{S}_2)$, which is commonly used for visualization of angiographic images will have higher noise (by a factor of $\sqrt{2}$), such that

$$\Delta\text{SNR}_{\text{Diff}} = \frac{\Delta S}{\sigma} = \frac{\text{mean}(\mathbf{S}_3 - \mathbf{S}_2)|_{\text{ROI}}}{\text{std}(\mathbf{S}_1 - \mathbf{S}_2)|_{\text{ROI}}}. \tag{15}$$

Equations (14) and (15) provide a useful method of measuring the SNR of the signal enhancement that occurs with MRA or DCE imaging applications. It is valid with parallel imaging applications where the noise may be non-uniform across the image, and takes advantage of the multiple images acquired during the acquisition to determine noise and signal enhancement within the same ROI. It is important to note that these calculations must be performed with 2D planar images, and cannot be performed with maximum intensity projection (MIP) images that are commonly used to display angiographic images.

4.6 Summary and Conclusion

The measurement of SNR and CNR becomes increasingly important for parallel imaging applications where the overall amount of data is reduced, challenging the SNR performance of these techniques. Accurate evaluation of these methods is essential and an understanding of the limitations of conventional SNR measurement methods is crucial to avoid incorrect methods that can lead to erroneous estimates of SNR. The key concept is that from an SNR perspective, parallel imaging differs from conventional imaging by the fact that noise may have a non-uniform distribution across the image. Valid SNR measurement methods must determine both *the*

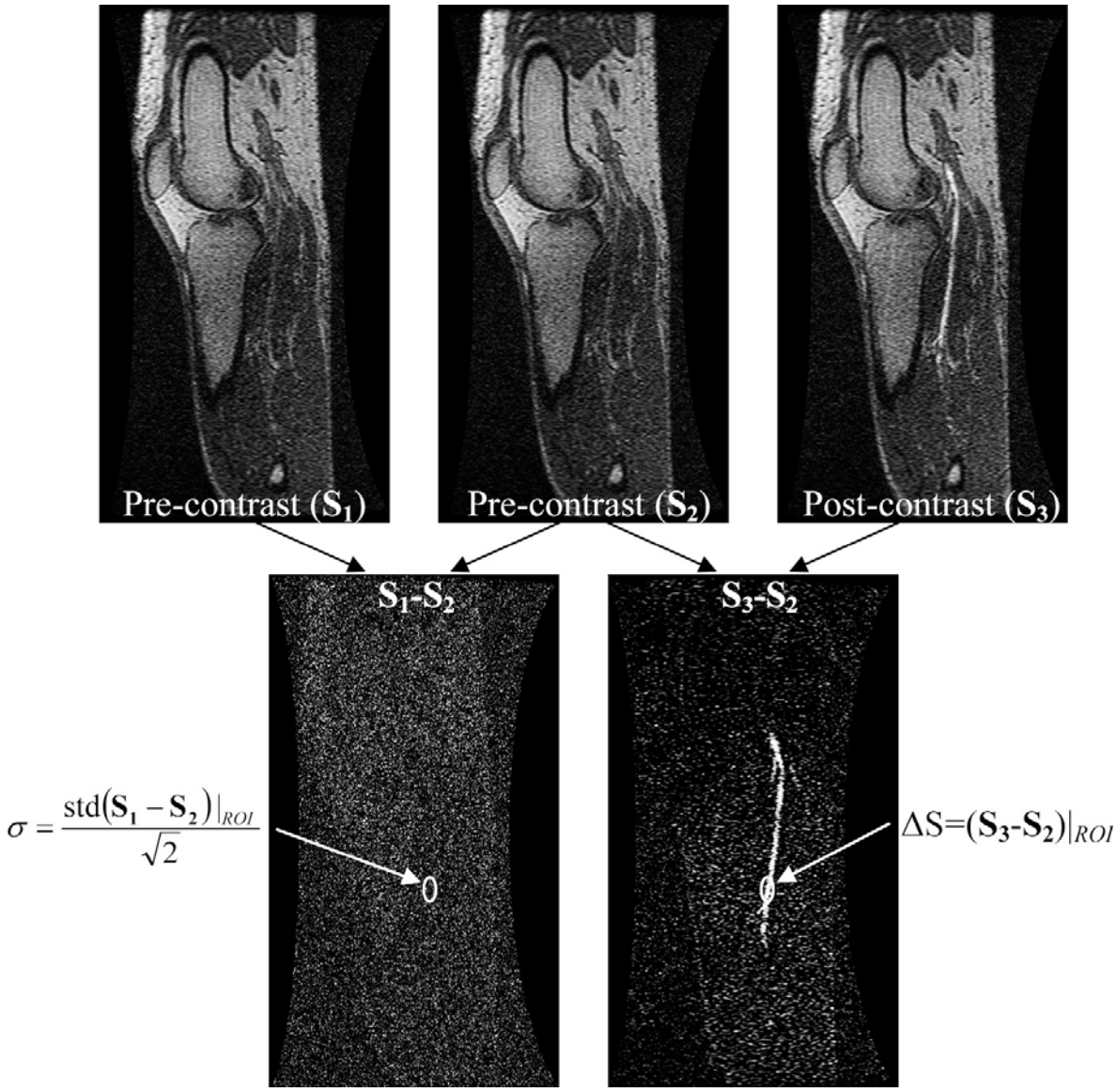

Fig. 4.11. The difference method applied to multi-phase contrast-enhanced angiography. The difference between two pre-contrast images is used to determine the noise, and the difference of the post-contrast and pre-contrast image is used to determine the signal enhancement, facilitating a quantitative SNR measurement of the contrast enhancement, even in the presence of non-uniform noise. Note that the ROI is larger than the vessel for illustrative purposes only, and should be chosen to "fit" the area of interest more accurately.

signal and noise within the same region of interest. In this chapter, we review the multiple acquisition and difference methods in detail in order to measure SNR and determine the g-factor. A variation in the difference method is described for measurement of SNR with dynamic contrast-enhanced and angiographic imaging. Finally, a new method that involves direct characterization of the system SNR permitting direct calculation of the g-factor is briefly discussed, although this approach may be complicated for most practitioners.

Acknowledgements. I thank A. Brau, PhD, for her assistance with the pulse sequence used to obtain the phantom images, as well as P. Kellman, PhD, and M. Griswold, PhD, for helpful discussions.

References

Bevington P, Robinson D (1992) Data reduction and error analysis for the physical sciences. McGraw-Hill, New York

Constantinides CD, Atalar E, McVeigh ER (1997) Signal-to-noise measurements in magnitude images from NMR phased arrays. Magn Reson Med 38:852–857

Edelstein W, Bottomley P, Pfeifer L (1984) A signal-to-noise calibration procedure for NMR imaging systems. Med Phys 11:180–185

Firbank MJ, Coulthard A, Harrison RM, Williams ED (1999) A comparison of two methods for measuring the signal to noise ratio on MR images. Phys Med Biol 44:N261–N264

Gizewski ER, Maderwald S, Wanke I, Goehde S, Forsting M, Ladd ME (2005) Comparison of volume, four- and eight-channel head coils using standard and parallel imaging. Eur Radiol 15:1555–1562

Griswold MA, Jakob PM, Nittka M, Goldfarb JW, Haase A (2000) Partially parallel imaging with localized sensitivities (PILS). Magn Reson Med 44:602–609

Griswold MA, Jakob PM, Heidemann RM et al. (2002) Generalized autocalibrating partially parallel acquisitions (GRAPPA). Magn Reson Med 47:1202–1210

Henkelman RM (1985) Measurement of signal intensities in the presence of noise in MR images. Med Phys 12:232–233

Jakob PM, Griswold MA, Edelman RR, Sodickson DK (1998) AUTO-SMASH: a self-calibrating technique for SMASH imaging. SiMultaneous Acquisition of Spatial Harmonics. Magma 7:42–54

Kellman P, McVeigh E (2005) Image reconstruction in SNR units, 2005. Proc Int Soc Mag Reson Med 13:2430

Kellman P, Epstein FH, McVeigh ER (2001) Adaptive sensitivity encoding incorporating temporal filtering (TSENSE). Magn Reson Med 45:846–852

McKenzie CA, Yeh EN, Ohliger MA, Price MD, Sodickson DK (2002) Self-calibrating parallel imaging with automatic coil sensitivity extraction. Magn Reson Med 47:529–538

McVeigh ER, Henkelman RM, Bronskill MJ (1985) Noise and filtration in magnetic resonance imaging. Med Phys 12:586–591

Price RR, Axel L, Morgan T et al. (1990) Quality assurance methods and phantoms for magnetic resonance imaging: report of AAPM Nuclear Magnetic Resonance Task Group No. 1. Med Phys17:287–295

Pruessmann KP, Weiger M, Scheidegger MB, Boesiger P (1999) SENSE: sensitivity encoding for fast MRI. Magn Reson Med 42:952–962

Reeder S, Wintersperger B, Dietrich O et al. (2005) Practical approaches to the evaluation of SNR performance with parallel imaging: application with cardiac imaging and a 32-channel cardiac coil. Magn Reson Med 54:748–754

Roemer PB, Edelstein WA, Hayes CE, Souza SP, Mueller OM (1990) The NMR phased array. Magn Reson Med 16:192–225

Sodickson DK, Manning WJ (1997) Simultaneous acquisition of spatial harmonics (SMASH): fast imaging with radiofrequency coil arrays. Magn Reson Med 38:591–603

Special Applications of Parallel Imaging

5

David Atkinson

CONTENTS

5.1 Introduction

As described in the previous chapters, the phrase "parallel imaging" refers to the simultaneous, or parallel, acquisition of data from multiple coils. These coils are located at different spatial positions and provide different, but connected, information about the patient. The most common use of parallel imaging is to enable image reconstruction following an acquisition that has been speeded up by skipping phase-encode lines. This chapter briefly highlights applications where a conventional speed-up can reduce artefacts and then examine applications where the extra information from multiple coils can be used in more novel ways to reduce artefacts.

D. Atkinson, PhD
Department of Medical Physics, University College London, London, WC1E 6BT, UK

5.2 Applications Enhanced by Parallel Imaging Speed-up

In general, the signal-to-noise ratio (SNR) of an image is improved by imaging for longer. Conversely, when parallel imaging is used to reduce acquisition times, there is an inherent reduction in image SNR as discussed in Chapters 3 and 4. This assumes that the signal is constant, but in some applications there is a rapid decay of signal and it is advantageous to acquire data quickly. Examples include hyperpolarized gas imaging where the signal decays rapidly once the gas comes into contact with tissue and the ultra-short TE imaging of very short-T2 musculoskeletal tissue. Another example is techniques using echo trains, such as echo-planar imaging (EPI), where the acquisition window is relatively long. In these cases, T2 effects cause a reduction of signal during the acquisition window leading to a loss of SNR and an image blurring. Parallel imaging shortens the echo-train length, reducing the signal-decay problem. There is a further benefit to shortening echo trains because k-space is now covered faster in the phase-encoded direction. When the magnetic field deviates from the ideal, such as in the presence of susceptibility effects, shortening the phase-encoded time gives less time for erroneous phase to build up. In the image, this is seen as reduced susceptibility artefacts and reduced distortions.

5.3 Parallel Imaging for Artefact Reduction

5.3.1 The Need for Artefact Correction

Shortened scan times can also help to reduce the chance of motion corrupting an image. In practice, the reduction in scan time is restricted to a factor

of about 2–3 in each phase-encoded direction. This limits the potential speed-up and scans may be longer than physiological effects such as respiration or cardiac motion. Furthermore, parallel imaging reduces image quality through the reduction in SNR and noise amplification due to g-factor effects (cf. Chap. 3); thus, there is a requirement to acquire data for periods longer than those over which dynamic changes might occur.

5.3.2 Artefact Causes

To form images, the raw MR data (k-space) is divided into blocks and each block is Fourier transformed to give an image. A block may correspond to a single slice in 2D multi-slice imaging or a whole volume in true 3D imaging. Separate averages and dynamic frames are composed of separate blocks. The Fourier transform process means that every single pixel in an image has a contribution from all points in the corresponding block of k-space (cf. chap. 1). A change in the patient (e.g. movement or blood in-flow effects) at anytime during k-space acquisition has the potential to affect every pixel in the image. Typically artefacts appear as a blurring of the image and ghosting in the phase-encoded direction(s).

There are essentially three strategies for reducing or eliminating these problems: acquiring and combining data in a more benign way; rejecting corrupted data; or correcting the data before forming the final image.

5.3.3 Phased-Array Combination

Prior to the emergence of speed-up techniques such as SMASH and SENSE, multiple coil phased-arrays were used to enhance image SNR (Roemer et al. 1990). A final image is formed from a combination of the individual coil images. In applications where ghosts have a periodicity which is both small and known, it has been shown that ghosts can be cancelled using images formed from certain coil combinations (Kellman and McVeigh 2001). An example application with low-periodicity ghosts is non-interleaved multi-shot EPI imaging.

When knowledge of the coil sensitivities is used in image reconstruction, ghosts that are widely separated from their source may be reduced in intensity. Kellman et al. (2004) demonstrated this in cardiac imaging where ghosts arising from the spinal fluid could overlay the myocardium of interest. Parallel imaging methods have similar benefits because they also use coil sensitivity information in the image reconstruction.

5.3.4 Averaging

In standard imaging, multiple averages are sometimes used to reduce the effect of motion ghosts. With parallel imaging, one fully sampled acquisition can be replaced by two scans each speeded-up by a factor of two. There is no increase in scan time, but now there are two images that can be averaged. The ghosts in the resultant image may be more benign than if just one fully sampled data set had been acquired (Larkman et al. 2004). Figure 5.1 demonstrates the potential benefits of averaging. A free-breathing subject was imaged with one fully sampled (R=1) scan, and then in the same total time, two speeded-up scans with reduction factors of 2 (R=2). The artefacts after averaging the two R=2 scans are more benign than in the single R=1 scan. This approach has the advantage that it can be applied on any MR imaging system that is capable of parallel imaging and does not require any additional reconstruction or post-processing software.

It is possible to process the two R=2 images separately. In theory they could be automatically assessed and one rejected if it was severely artefacted. An alternative is to manipulate the images before averaging to make the data consistent and in the following example, this is done by image registration.

Using parallel imaging, the time to acquire a single block of raw data may be shortened sufficiently to make breath-holding practical. Kellman et al. (2005) have recently demonstrated this in cardiac imaging and have used image registration to align images acquired in separate breath holds before they were combined. Figure 5.2 shows how the raw data block for a fully sampled acquisition might extend beyond a breath-hold, but with parallel imaging, it may be possible to fit acquisitions within breath-holds.

5.3.5 Detect–Reject

Parallel imaging can be used to detect short-lived data inconsistencies and to reconstruct the remain-

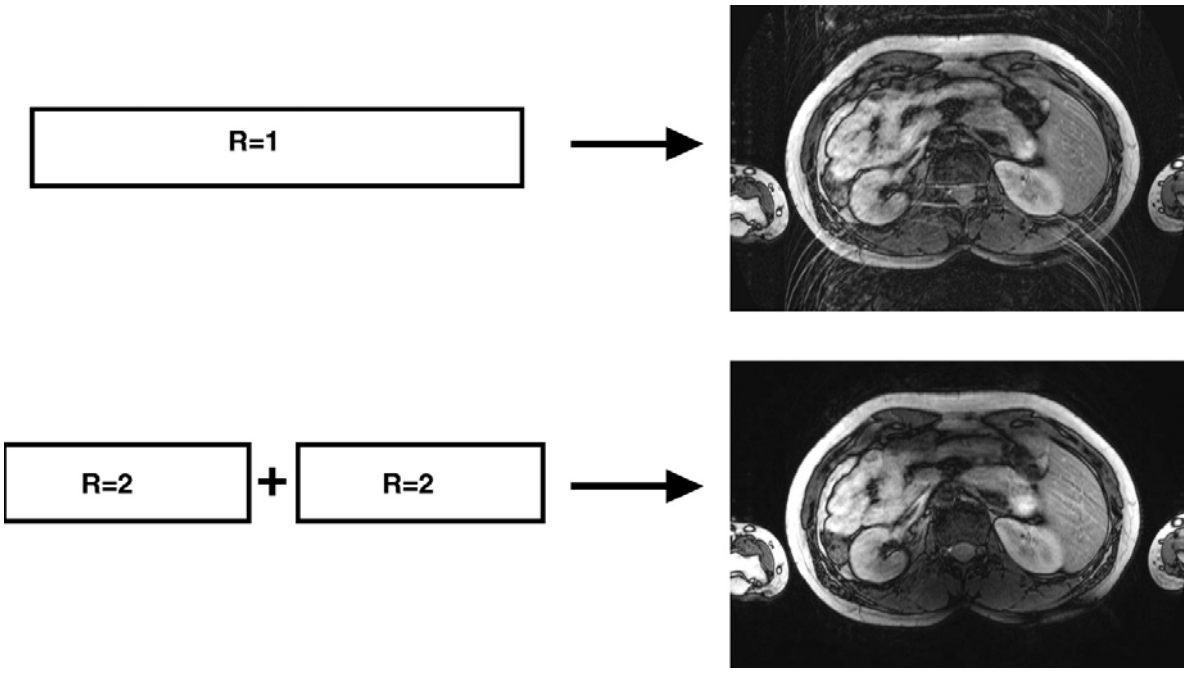

Fig. 5.1. Potential benefits from averaging two speeded-up scans compared with one fully sampled acquisition. *Rectangles* indicate blocks of raw data used to form images and their length represents the imaging time. Image examples were acquired on a free-breathing volunteer. *Top:* fully sampled; *bottom:* average of two faster scans reconstructed using parallel imaging. (Courtesy of D. Larkman, Hammersmith Hospital, Imperial College London)

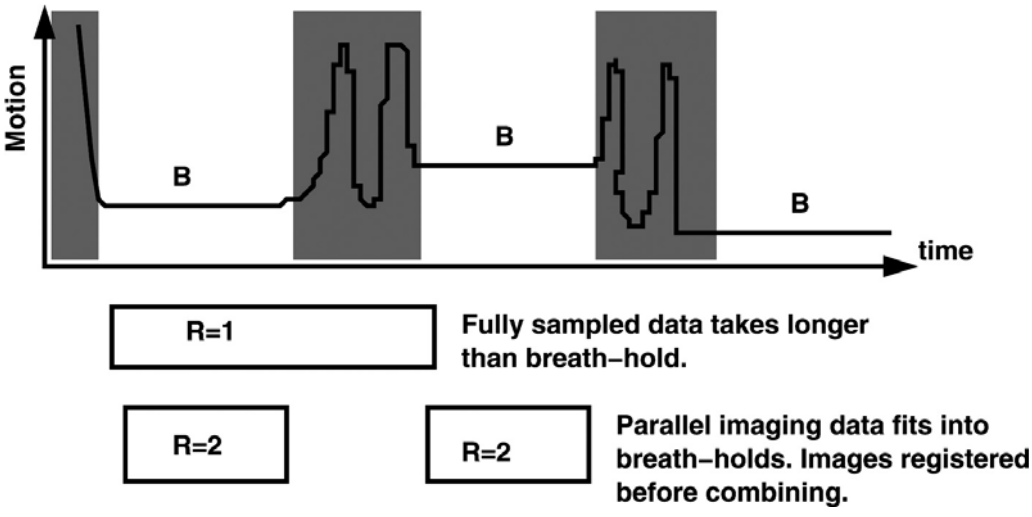

Fig. 5.2. *Upper graph* indicates respiratory motion with *B* denoting a breath-hold. Significant motion occurs at times shown *shaded*. Parallel imaging enables data acquisition time to fit into a breath-hold. Note that the breath-hold positions vary; hence, the need for image registration before image combination.

ing data once these have been removed. Bydder et al. (2002b) took a fully sampled acquisition and divided the k-space into two data sets as shown in Fig. 5.3. One data set was formed from only odd lines and the other from only even. Parallel imaging was then used to reconstruct two complete k-spaces. In the absence of artefacts, these should differ only by noise. In the presence of short-lived motions, such as a twitch or cough, isolated lines of k-space are damaged and these corrupted k-space lines can be identified when the two k-spaces are subtracted. The damaged lines were then excluded leaving a data set with an irregular sampling. Images were reconstructed from the irregular k-space by using the generalised SMASH approach (Bydder et al. 2002a).

5.3.6 Detect–Correct; SMASH Navigators

The previously described data rejection works well only if the artefact cause is localised in time. Furthermore, corrupt data is discarded, whereas potentially it could be fixed and included in the final reconstructed image. The SMASH navigator method (Bydder et al. 2003) was developed with the aim of stepping through k-space and correcting artefacts. In conventional SMASH parallel imaging, the coil sensitivities are used to predict k-space lines that have been skipped in the acquisition. Each missing line is estimated from its neighbouring acquired line. In the SMASH navigator method, the data is fully sampled (R=1) and SMASH is used to predict line 2, based on line 1. This prediction is compared with the actually measured line 2. Differences that are consistent with the effects of motion are extracted and used to correct the actually acquired data for line 2. The algorithm then uses the corrected line 2 to predict line 3 and so on until the whole of k-space has been analysed. This is depicted in Fig. 5.4.

This approach has the benefit that motion errors need not be localised in k-space and data is not thrown away; however, it requires a coil geometry that is favourable to SMASH reconstruction (typically a linear array coil), and, errors in the motion determination may propagate as successive lines are processed.

5.3.7 Coil-Based Artefact Reduction

Rather than stepping through k-space line by line, Atkinson et al. (2004) considered the whole k-space in one optimisation scheme. They also used the generalised SMASH method since this does not suffer the same restrictions on coil geometries as conventional SMASH. As outlined in Fig. 5.5, one image per coil was reconstructed from fully sampled data and an additional image 'F' computed using all the coil data simultaneously. In the absence of noise and artefacts, all these images should be identical and corrected for the different spatial coil sensitivities, which are known from a prior coil calibration scan. When in-

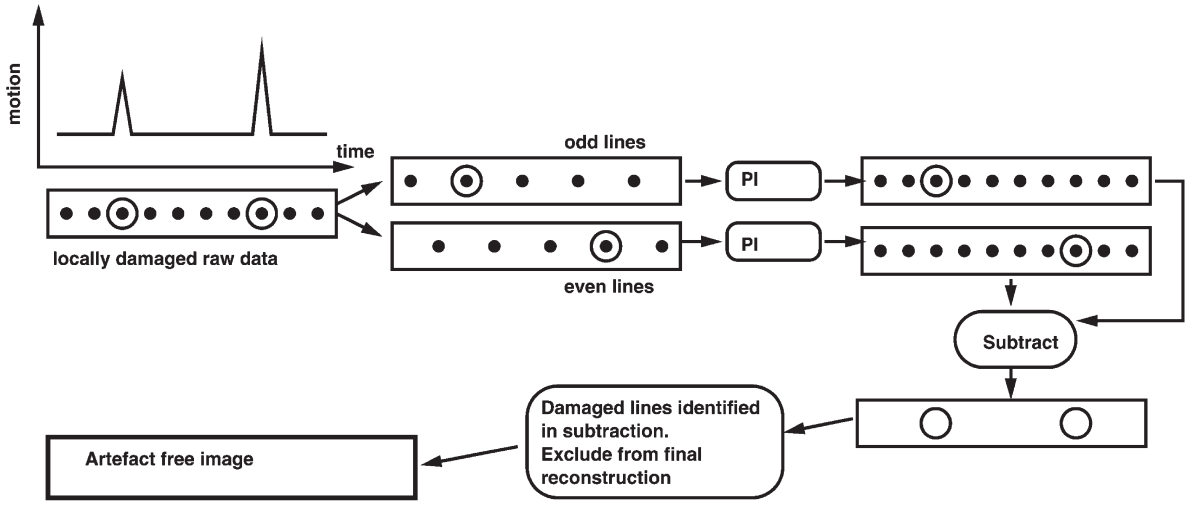

Fig. 5.3. The detect–reject method. K-space damaged by short motions is indicated with an *open circle*. *PI* parallel image reconstruction

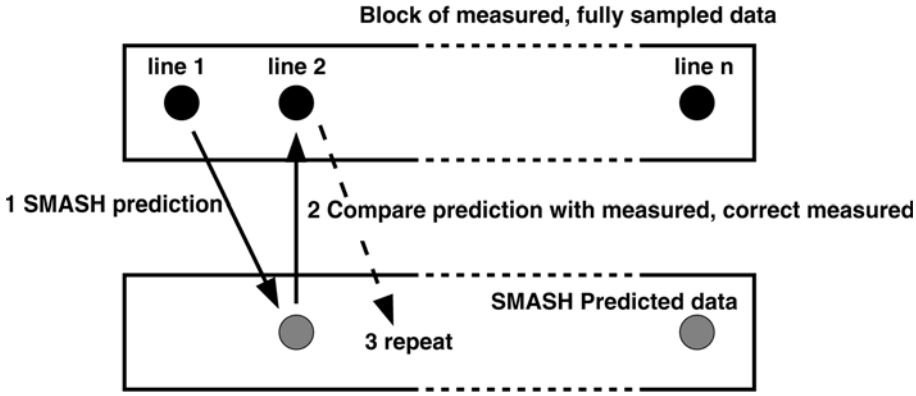

Fig. 5.4. The SMASH navigator method. *Line 1* of the measured data is used with SMASH to predict *line 2*. This is compared with the actually measured line 2. Differences consistent with motion are found and applied to the measured *line 2*. The sequence continues to the last line.

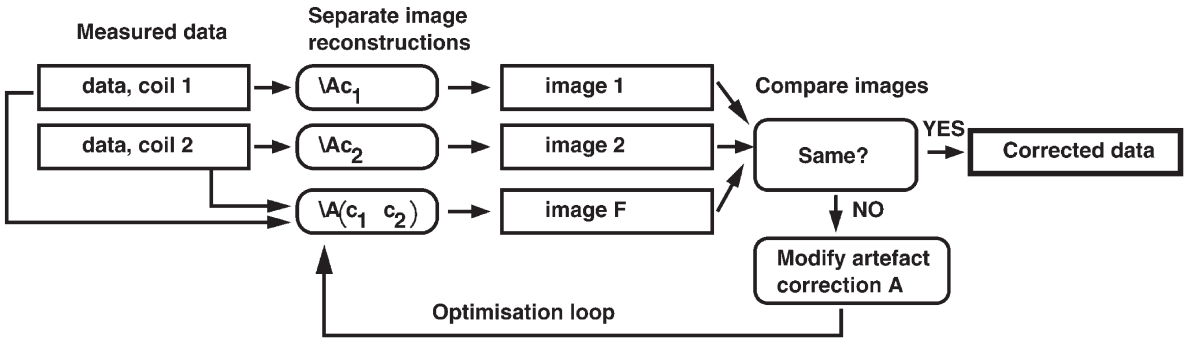

Fig. 5.5. The coil-based artefact reduction method of Atkinson et al. (2004). The algorithm starts with the measured data from each coil. The *\Ac* denotes generalised SMASH reconstruction with coil sensitivity data c modified by A, the current estimate of the artefact cause. *Image F* is formed using data from all coils. This illustration assumes non-accelerated scans, but in principle the method can also be applied to accelerated scans provided that the number of coils exceeds the speed-up factor.

flow or motion corrupts the data, these images differ and this can be detected by subtracting the images. Using a physical model of the artefact cause (e.g. rigid-body motion for imaging the head, or intensity changes in the aorta for axial abdominal imaging), the underlying data can be corrected. The artefact needs to be parameterised; for example, the effect of flowing blood was characterised by a complex multiplicative factor over the pixels containing the vessel. In order to find the values of these parameters, trial values are applied to the data and the images compared in an optimisation scheme. When the images are most similar, the artefact is at a minimum. One key step is that in the optimisation, the parameters are actually applied to the coil sensitivities and not to the object because the latter is unknown. This enables the multiple images (labelled 1,2,...F in Fig. 5.5) to be computed and then compared.

The method has the advantages that ghosts and artefacts do not need to be localised in the image, the artefact energy is put back in the correct place in the image (rather than data discarded) and there is no requirement for the artefact cause to be short-lived; however, a physical model of the artefact cause is required and in the case of flow, the user needs to specify the location of the artery causing the problem. Figure 5.6 presents results from this method on an abdominal image corrupted by flow artefacts from the aorta.

5.3.8 Consistency-Based Artefact Removal

Winkelmann et al. 2005 have recently proposed a scheme that can determine the location of ghosts and the source of flow-type artefacts. A standard SENSE

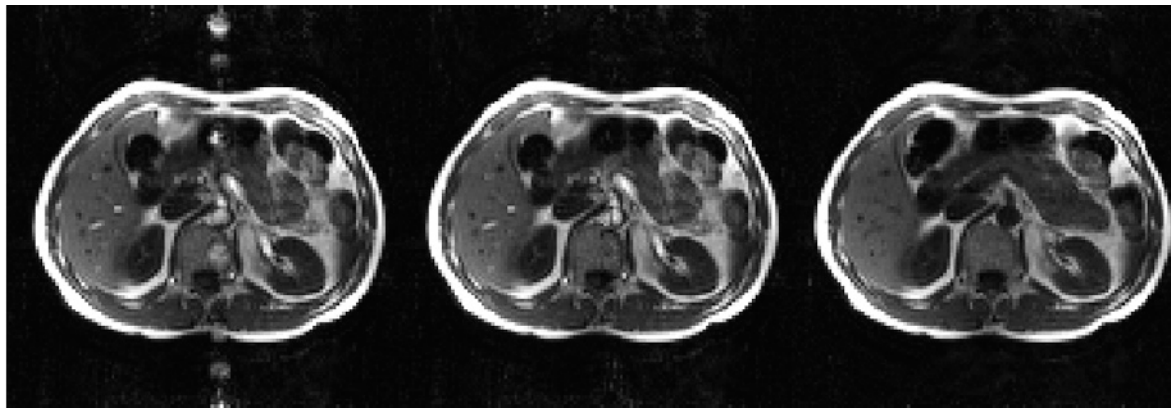

Fig. 5.6. Breath-hold image through the abdomen of a volunteer. *Left:* the original data shows a flow artefact arising from the aorta. *Middle:* the image corrected after using the method of Atkinson et al. (2004). *Right:* for comparison, the same slice imaged with saturation bands (not feasible in practice for multi-slice imaging)

reconstruction is performed to give one image. This is used with the coil sensitivities to predict the measured data. A consistency check between this prediction and the actually measured data reveals image locations that are overlaid by ghosts. An analysis of consistency enables the location of the artefact source to be determined. With this information, an extended SENSE reconstruction is performed in which both the underlying object and the overlying ghost are treated as unknowns. This is performed only in regions identified as being overlaid by ghosts. An outline of the technique is presented in Fig. 5.7 and an example of abdominal image correction presented in Fig. 5.8. The advantages of this method are that it automatically determines the location of the artefact source and no physical model of the cause is required. The disadvantages are that some data is discarded and the method is applicable only in situations where ghosts are spatially both localised and separated.

5.4 Discussion and Future

There now exist a number of schemes that use parallel imaging to reduce artefacts through the rejec-

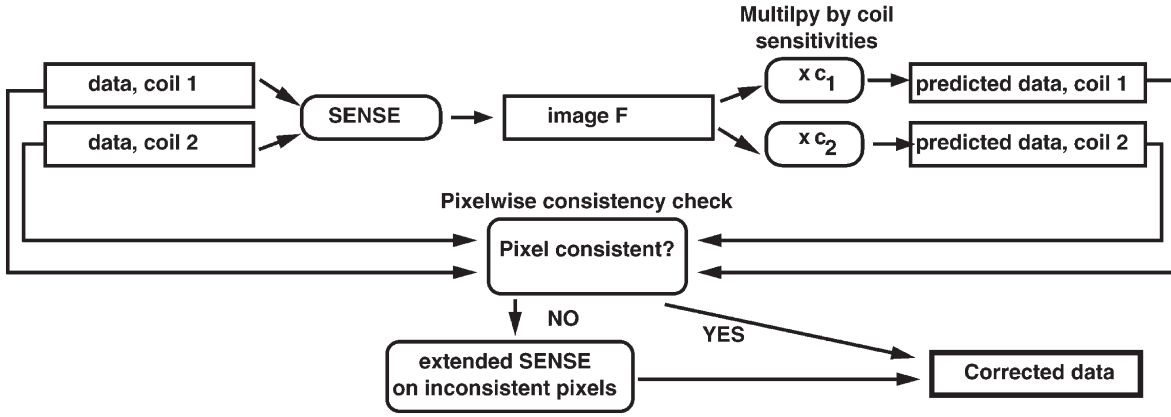

Fig. 5.7. The consistency-based artefact removal method of Winkelmann et al. (2005). The algorithm starts with the measured data from each coil. *Image F* is formed using a SENSE reconstruction and data from all coils. *Image F* is multiplied by the known coil sensitivities and the result is compared with the originally acquired coil data. Artefacts can then be removed using an extended SENSE reconstruction algorithm. A non-accelerated scan is shown for illustration and, in principle, the method can also be applied to accelerated scans provided the number of coils exceeds the speed-up factor.

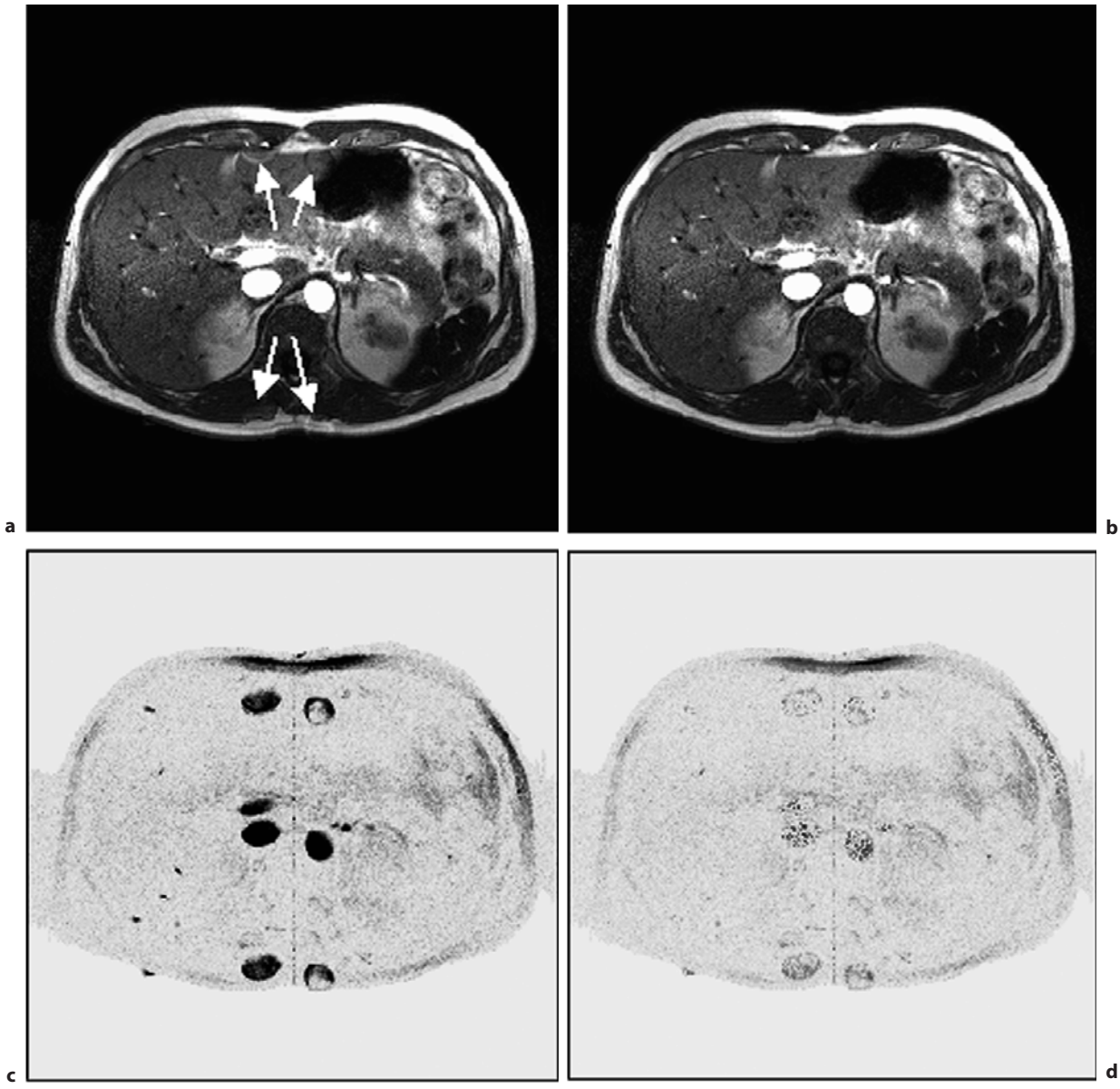

Fig. 5.8a–d. Ghost artefact removal using the extended SENSE reconstruction of Winkelmann et al. (2005). The conventional SENSE reconstruction shows **a** ghosting artefacts of a volunteer's aorta that are indicated by the *arrows*. **c** The consistency check of this SENSE reconstruction allows an identification of the ghosts and triggers an extended reconstruction to remove the artefacts (**b**). A final consistency check is shown in **d.** (Courtesy of R. Winkelmann, Philips Medical Systems)

tion or correction of data. The next stage will be for researchers to bring together their various advantages into a more unified scheme. As the underlying methods contain many similarities, hopefully this should be possible.

There is a current trend in MR scanner hardware towards greater numbers of receiver channels and coils (cf. Chapters 13 and 44). These are primarily intended for acquisition speed-up but the extra flexibility should allow for the inclusion of coils designed to make artefact correction most effective. We are likely to see the advantages of the different techniques described above brought together to provide a method that requires minimal user intervention and is applicable to a wide range of artefacts. In general motion is non-rigid and takes place in three dimensions. Recent work (Batchelor at al. 2005) has shown how to handle non-rigid motion and develop-

ments in 64-bit computer architectures should make the handling of large 3D data sets easier.

An alternative viewpoint might be to see physiological motion as part of the imaging process. An indication that this might be feasible was provided recently in moving table MRI where the table velocity is included in the parallel imaging reconstruction (Keupp et al. 2005).

5.5 Conclusion

In conclusion, the speed-up made possible by parallel imaging has added benefits when signal decay is a limitation, such as in the imaging of hyperpolarized gases or short-T2 tissues and when the decay over the acquisition window is significant. These applications can benefit from the vendors' implementations of parallel imaging without further modifications.

Research on the explicit use of multiple coils to detect artefacts and reject or correct the data has begun to appear in the literature. With the increasing number of numerical tools these bring, and the improvements in scanner and computer hardware, we can look forward to clinical applications of parallel imaging in the field of artefact correction.

References

Atkinson D, Larkman DJ, Batchelor PG et al. (2004) Coil-based artefact reduction. Magn Reson Med 52:825—830

Batchelor PG, Atkinson D, Irarrazaval P et al. (2005) A matrix description of general motion correction applied to multi-shot images. Magn Reson Med in press

Bydder M, Larkman DJ, Hajnal JV (2002a) Generalized SMASH imaging. Magn Reson Med 47:160–170

Bydder M, Larkman DJ, Hajnal JV (2002b) Detection and elimination of motion artefacts by regeneration of k-space. Magn Reson Med 47:677–686

Bydder M, Atkinson D, Larkman DJ, Hill DLG, Hajnal JV (2003) SMASH navigators. Magn Reson Med 49:493–500

Kellman P, McVeigh ER (2001) Ghost artefact cancellation using phased array processing. Magn Reson Med 46:335–343

Kellman P, Dyke CK, Aletras AH et al. (2004) Artefact suppression in imaging of myocardial infarction using B1-weighted phased-array combined phase-sensitive inversion recovery. Magn Reson Med 51:408–412

Kellman P, Larson AC, Hsu LY et al. (2005) Motion-corrected free-breathing delayed enhancement imaging of myocardial infarction. Magn Reson Med 53:194–200

Keupp J, Aldefeld B, Börnert P (2005) Continuously moving table SENSE imaging. Magn Reson Med 53:217–220

Larkman DJ, Atkinson D, Hajnal JV (2004) Artefact reduction using parallel imaging methods. Top Magn Reson Imaging 15:267–275

Roemer PB, Edelstein WA, Hayes CE et al. (1990) The NMR phased array. Magn Reson Med 16:192–225

Winkelmann R, Börnert P, Dössel O (2005) Ghost artefact removal using a parallel imaging approach. Magn Reson Med in press

Parallel-Imaging Reconstruction of Arbitrary-k-Space-Sampling Data

6

Roland Bammer, Chunlei Liu and Murat Aksoy

CONTENTS

6.1 Introduction

Understanding image reconstruction of arbitrary-k-space-sampling data is a crucial step towards achieving greater flexibility in sequence design for MR image acquisition. The Cartesian sampling method offers the easiest way to do image reconstruction because conventional MR data acquisition is typically done while the readout gradient is held constant. Using a constant readout gradient combined with equidistant sampling along the phase-encoding dimension results in a constant sampling of k-space in a rectilinear Cartesian fashion and allows image reconstruction by rapid 2D or 3D fast Fourier transform (FFT). However, several alternatives to conventional Cartesian MRI have been introduced in order to address problems such as diminished flow sensitivity as well as the need for greater navigator capabilities and faster speed. These alternatives include spiral and radial scanning as well as forms of echo-planar imaging (EPI). Whereas Cartesian sampling acquires data at regular positions, these trajectories acquire data at arbitrary positions in k-space, which makes image reconstruction considerably more difficult. This is because, although sampled at discrete time intervals, the data acquired during a variable gradient waveform are no longer located on an equidistant grid in k-space, thus preventing these data from being directly reconstructed via FFT. Therefore, it is essential to solve the problem of image reconstruction of arbitrary k-space sampling data in order to develop alternative image-acquisition methods that can overcome the limitations of conventional Cartesian sampling.

R. Bammer, PhD; C. Liu, PhD; M. Aksoy, MSc
Stanford University, Department of Radiology, Lucas Center, 1201 Welch Road, Stanford, CA, 94305-5488, USA

6.2 Generalized k-Space Characterization

Since data from non-Cartesian sampling cannot be reconstructed directly via FFT, it requires special reconstruction approaches. Initially, spiral waveforms were adapted so that either rectilinear sampling or projection reconstruction could be used to form an image. For example, the design of constant-angular-rate spirals allows the spiral samples in k-space to fall on radial spokes; they can then be reconstructed using the central slice theorem. However, two major

shortcomings of constant-angular-rate spirals are prolonged readouts and incomplete utilization of the system's gradient power. Furthermore, designing the acquisition waveform to satisfy a particular reconstruction algorithm significantly limits flexibility over a generalized k-space acquisition pattern. Therefore, efficient methods to reconstruct data acquired along arbitrary k-space trajectories have been proposed over the years.

In echo-planar imaging (similar to constant-angular-rate spiral imaging), data sampling only on the flat top of the EPI trapezoidals leads to overly prolonged readouts. On current-generation scanners, physiological and MR-hardware slew-rate limits in combination with the high maximum gradient amplitude significantly extend ramp times. To shorten readouts, data acquisition with EPI and short-TR steady-state-free-precession (SSFP) sequences also takes place during the ramp phase (a process also known as "ramp sampling"), yielding non-equidistantly sampled k-space data.

Spiral, EPI, radial, as well as vastly undersampled 3D radial acquisitions (VIPR) (Block et al. 2000) all rely on non-Cartesian sampling, either along one, two, or three dimensions, and require special reconstruction approaches. A generalized description of the acquired MR data over time is integral to the success of these methods and is the basis of our further considerations for a generalized parallel-imaging approach for data that are sampled on arbitrary k-space trajectories.

6.2.1 Generalized Signal Equation

Using discrete sampling in the time and spatial dimension, a particular MRI data sample point can be expressed as:

$$m(t_i) = \sum_{u=1}^{N\times N} \rho(\mathbf{r}_u)\exp(-\mathrm{j}\mathbf{k}(t_i)\cdot\mathbf{r}_u) \qquad [6.1]$$

$\rho(\mathbf{r}_u)$ is the original image information (e.g., proton-density-weighted signal) at spatial position $\mathbf{r}_u$; u is the index to the $N\times N$ image pixels.) Therefore, the entire acquisition of κ k-space points can be stored in a measurement vector $\mathbf{m} = [m(t_1)\ m(t_2)\ldots m(t_\kappa)]^T$ so that the signal formation in matrix form can be expressed as:

$$\mathbf{m} = \mathbf{E}\mathbf{v}, \qquad [6.2]$$

where $\mathbf{v} = [\rho(\mathbf{r}_1)\ \rho(\mathbf{r}_2)\ldots\rho(\mathbf{r}_{N^2})]^T$ is the spatial MR signal distribution in vector form and $\mathbf{E}$ is a matrix describing the process of signal formation. Notice that $\mathbf{k}(t_i)$ do not lie on Cartesian grid points, and therefore an image cannot be formed by direct inverse Fourier transform. The $N\times N$ image, $\mathbf{v}$, represented here in vectorized form, could theoretically be found via complex matrix inversion of the matrix $\mathbf{E}$. However, direct inversion of $\mathbf{E}$ is highly inefficient due to the enormous size of $\mathbf{E}$ (i.e., $\kappa \times N^2$ matrix elements). For N>128, the storage of the matrix $\mathbf{E}$ alone is several gigabytes and exceeds the capacity of current internal memory.

In the next sections of this overview, we will see that a more efficient way for image reconstruction is to resample the arbitrary k-space waveform data onto a 2D Cartesian grid first, and then to apply rapid FFT algorithms to reconstruct the image. Here, we will differentiate between "grid-driven" and "data-driven" resampling schemes. For the "grid-driven" approach, neighboring k-space points are used to estimate the value at the grid, whereas for the "data-driven" approach, the contribution from each acquired k-space sample is distributed to adjacent grid locations.

6.2.2 Grid-Driven Interpolation

Despite the overall tendency to employ the data-driven approach, the grid-driven method is an alternative worth consideration, particularly in the presence of significant sampling density variation where noise correlation might otherwise pose a problem. The basic concept of the grid-driven approach is to estimate the value at each grid location. This is determined from acquired k-space data in the vicinity of the particular node by bi-linear or tri-linear interpolation (Fig. 6.1). This "data pulling" approach generally does not need sampling density compensation and does not use all of the input data. The latter limits the signal-to-noise-ratio efficacy to some extent, but this drawback is offset by the fact that excessive data are normally acquired in the low spatial frequency range (see Sect. 6.2.6). To achieve acceptable reconstruction quality, this reconstruction normally requires resampling on a finer grid in k-space (at least 2×) or the use of more complex interpolators.

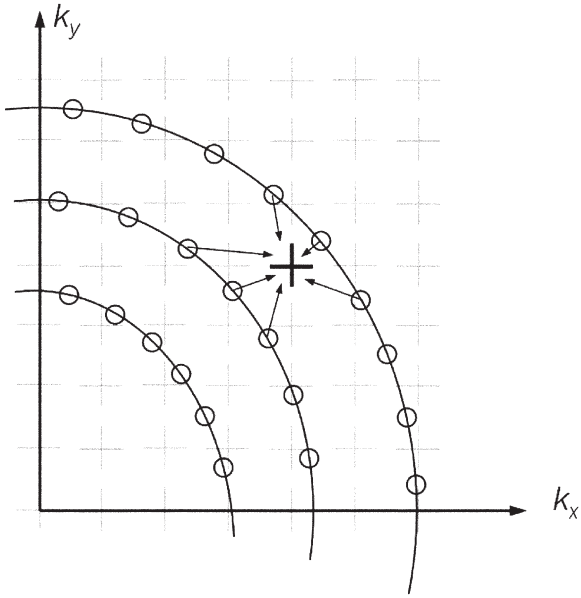

Fig. 6.1. Grid-driven interpolation for spiral data. The data in the vicinity (*arrows*) of a particular grid point (+) contribute to the grid point in question. These contributions can be determined by bilinear interpolation. The spiral sample point contributions are "pulled" to the grid location

6.2.3 Data-Driven Interpolation

The data-driven approach (Fig. 6.2) uses all sample points and therefore has a signal-to-noise-ratio advantage over the grid-driven method described in Sect. 6.2.2. The method is commonly referred to as "gridding" and has its origin in radio-astronomy. Data-driven resampling works by spreading the information of each k-space sample point to adjacent grid points. Here, the acquired data are weighted by a non-linear function, whose input argument is the distance between the sample point and the grid point. In other words, each k-space sample is convolved with a small kernel that is wide enough to include neighboring grid points. The contribution of each k-space sample is simply added so that the net signal will pile up in particular areas of k-space. Therefore, the variable sampling density may lead to non-uniform coverage of k-space that can ultimately alter the impulse response of the system. Density correction schemes need to be applied in order to achieve uniform sampling density (see Sect. 6.2.6). The ideal interpolator would be a sinc-kernel. However, to keep the number of multiplications and, hence, processing time down, the optimal interpolator is normally approximated by a much smaller, truncated kernel with a radius of a few k-space sample points.

6.2.4 Gridding Reconstruction

Gridding reconstruction is the most common method to reconstruct MR data that have been acquired with arbitrary-sampling trajectories. Under gridding reconstruction, in the broader sense, one understands a three-step approach of (1) interpolating arbitrary sampled data onto a Cartesian grid, (2) performing a sampling-density correction, and (3) correcting the effect of the interpolation kernel after FFT into the image domain.

To begin with, k-space samples are acquired on an arbitrary trajectory through k-space. As outlined in Sect. 6.2.3, each of these samples is convolved using a narrow convolution or gridding kernel, and its respective value at the grid location is computed (Fig. 6.3). While gridding each sampling point, also a k-space sampling-density correction is applied. Following the data-driven interpolation, an inverse 2D/3D FFT

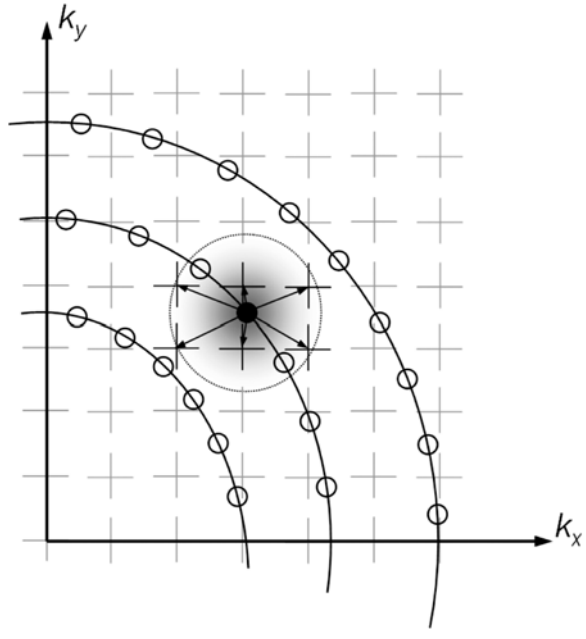

Fig. 6.2. Data-driven interpolation for spiral data. Every data sample that was acquired with the spiral waveform will contribute some fraction to the adjacent grid points in the vicinity of the spiral sampling point. The spiral sample points are "pushed" to the grid by convolving the sample data with a small kernel. The value of that convolution is added to the adjacent k-space grid points

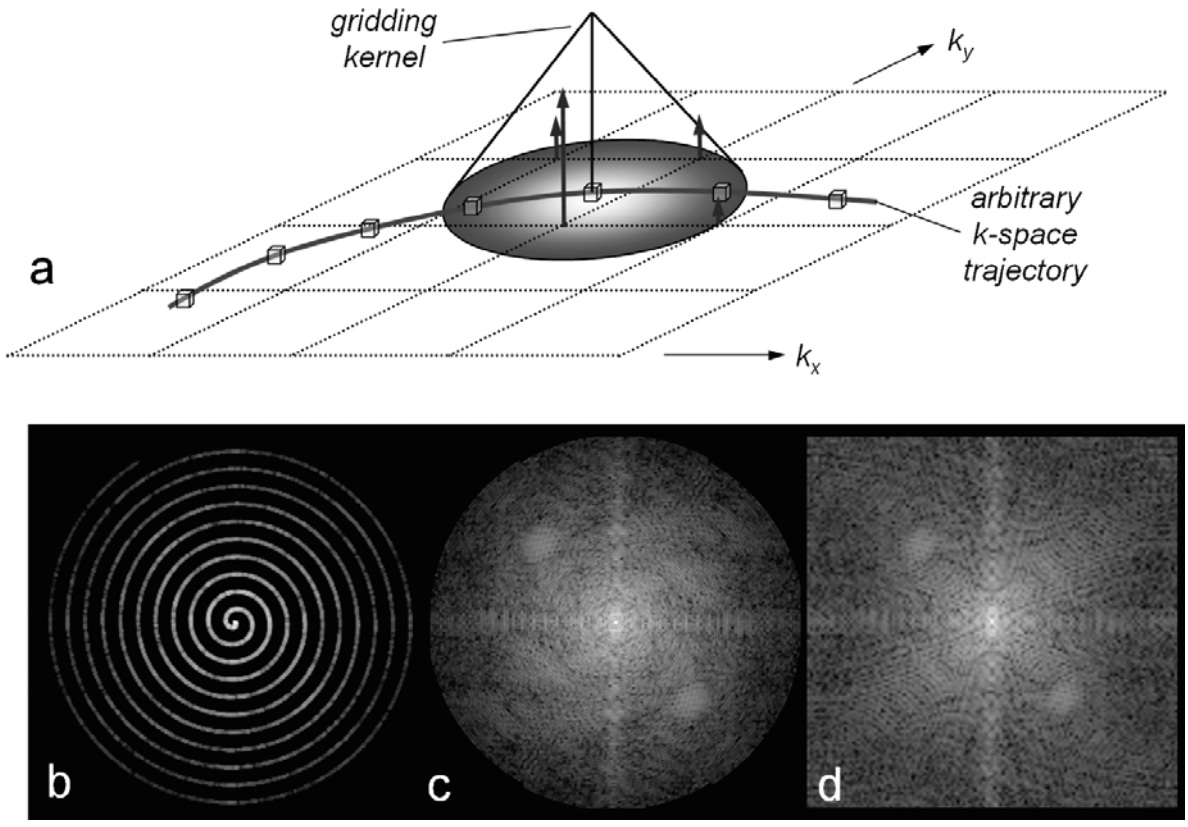

Fig. 6.3. a The k-space data samples (*small cubes*) are acquired using an arbitrary k-space trajectory (*blue line*) at the temporal sampling rate, t_s. Every sample point is convolved with a small kernel where the kernel argument is the distance between the true k-space position and the grid points. **b** One spiral interleaf out of six that has been gridded with a Kaiser-Bessel window (width =4 pixel). **c** Final k-space data after gridding all six interleaves. **d** Corresponding Cartesian k-space

generates images that are intensity modulated by the Fourier transform of the gridding kernel (Fig. 6.4). To avoid this intensity "roll-off" or apodization, the final image needs to be divided by this modulating function, which is the FFT of the gridding kernel.

Normally, image quality and reconstruction speed determine the choice of the gridding-kernel size as well as the size of the reconstruction grid. Although both the larger convolution kernel and the reconstruction grid (e.g., 2×) will improve image quality, they also require more computational effort. A wider kernel involves more grid points and, hence, more multiplications are needed; if computing power is limited, rapid reconstruction is required, or when numerous images are generated, the gridding kernel should be narrow. However, except for a sinc-interpolation, all truncated interpolators result in significant apodization. Here, the amount of intensity roll-off scales with the width of the kernel. One beneficial feature of the apodization is the suppression of artefacts at the edge of the field of view (FOV) resulting from the finite, rectilinear k-space sampling (causing replicas) and the convolution with the sampling function (causing side lobes) (Fig. 6.4); a complete roll-off correction is often avoided because this would exaggerate the aforementioned artefacts.

6.2.5 Reconstruction Grid Size

As mentioned above, side lobes from the first replica that is generated by the sampling pattern can overlap into the image and create considerable reconstruction artefacts at the edge of the FOV. Luckily, except increased FFT matrix size and an associated speed penalty, nothing precludes one to change the reconstruction grid from 1× to a higher-density grid, i.e., α×. If one elects to use a denser grid both the replica cross-talk (Fig. 6.5), and the required intensity roll-

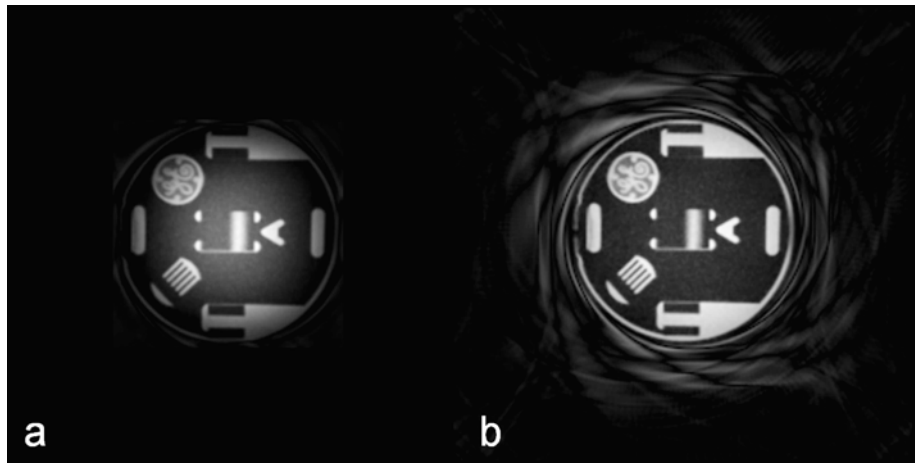

Fig. 6.4a,b. Apodization-correction at two different oversampling factors using a spiral acquisition with six interleaves. **a** Gridding data on a 1× grid leads to significant intensity roll-off across the field of view. Reconstruction artefacts at the edge of the field of view are no longer apparent. **b** On a 2× grid this roll-off is less pronounced, but still effective

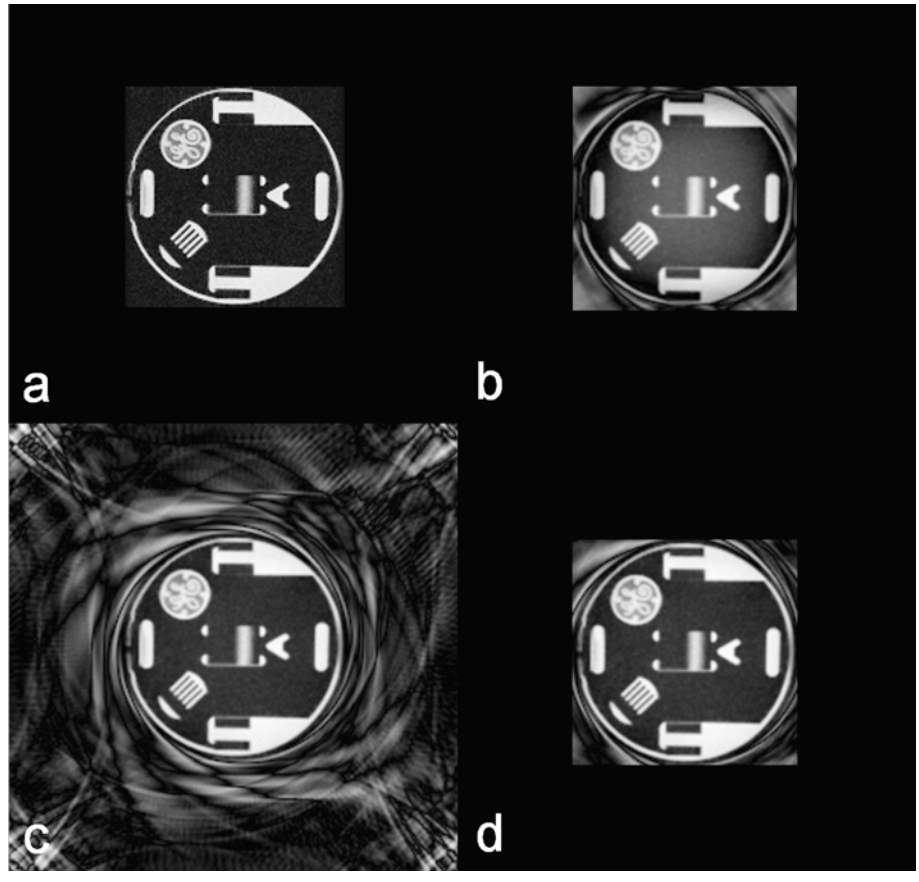

Fig. 6.5a–d. Gridding reconstruction with different oversampling factors in a quality phantom. **a** Cartesian phantom data. **b** Reconstruction of a six-interleaf spiral data set on a 1× grid; **c** the same data reconstructed on a 2× grid and **d** the cropped center part. The higher oversampling factor helps to diminish replica artefacts from the first side lobe

off (Fig. 6.4) can be diminished. Here, increasing the k-space grid density by a factor of α shifts the replicas of the reconstructed image apart by the same factor, producing less overlap (Fig. 6.5). A typical oversampling factor that is normally chosen is 2×, for which replica overlap is negligible (Fig. 6.5b). The central portion of the FOV is then cropped out to provide the target FOV (Fig. 6.5c). A recent study proposes the use of non-power-of-two oversampling factors that utilize new FFT algorithms (FFTW), which do not require power-of-two input matrices (Frigo and Johnson 1998). Increasing the oversampling factor, α, to a range $1<\alpha<2$ reduces both overlap from replicas as well as reconstruction time. The latter is of particular relevance for 3D reconstructions.

6.2.6 Sampling-Density Correction and Impulse-Response Function

Often the application of arbitrary k-space trajectories is accompanied by a non-uniform sampling density in k-space (e.g., around the origin of radial or spiral sampling data where signal values cover k-space more densely). The best way to see this effect is by gridding constant values along the arbitrary k-space trajectory (Fig. 6.6a). The non-uniform sampling degrades the impulse response of our image reconstruction system. Ideally one should get an impulse when the sampling density is uniform. The degradation of the impulse response can be corrected easily during gridding by normalizing each acquired k-space sample point with the corresponding sampling density at its targeted location (Fig. 6.6b). This approach is also known as pre-weighting or pre-compensation (Fig. 6.7c).

Alternatively, unity values can be gridded and the resulting k-space can be divided by the so-called density pattern (Fig. 6.7b). This approach is called post-weighting. While pre-weighting is applied to each sample point, post-weighting is applied on a grid-point basis. Post-weighting works well as long as the changes in sampling density do not vary too rapidly. Another advantage with post-weighting is that it does not require a priori sampling-density information, whereas for pre-weighting the density must be known up front. Both correction schemes can also be applied in concert (Fig. 6.7d). If there is rapid variation in the sampling density, the gridded density estimate can be incorrect due to the blurring by the gridding kernel.

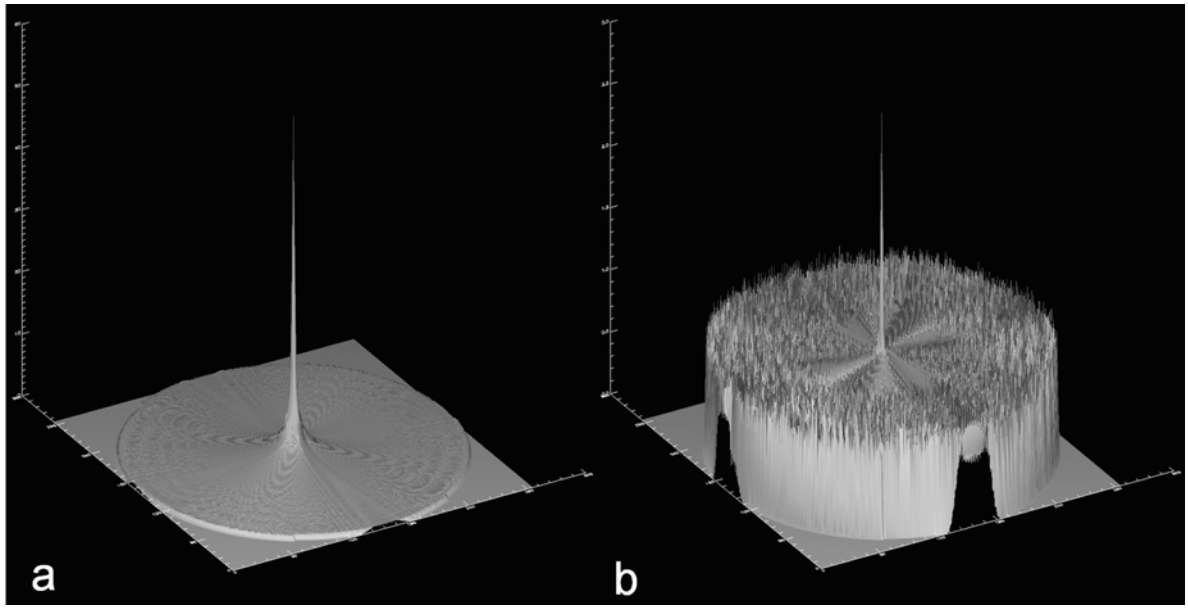

Fig. 6.6a,b. Sampling-density function for a spiral k-space trajectory observed by gridding unity in k-space. **a** Without sampling-density correction the central portion of k-space is overemphasized. This would lead to a significant degradation of the impulse response function resulting in strong image blurring (see Fig. 6.7). **b** If sampling density correction (i.e., pre-weighting) of the acquired k-space data is applied, the density distribution is much more uniform. To highlight the effect of residual non-uniformity, the sampling density correction was intentionally assumed slightly imperfect. This can be seen by the small residual center peak, which can be removed by dividing the gridded k-space by the function displayed in **b** (post-weighting). Note that the scaling of the ordinate is different in **a** and **b** for the purpose of better display

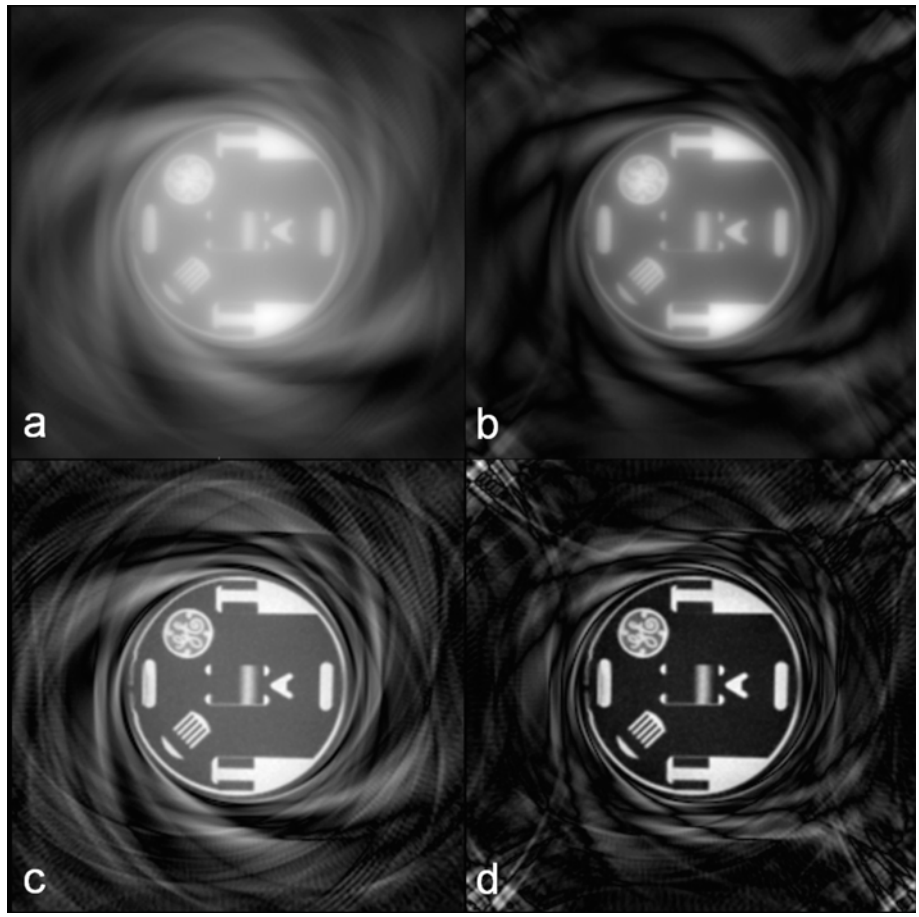

Fig. 6.7a–d. Effect of sampling density correction on the reconstructed data. **a** Without any correction the image appears overly blurred. The impulse response function, which is responsible for this blur, can be progressively improved by applying **b** post-weighting, **c** pre-weighting, or **d** a combined weighting of the k-space data. The post-weighting of the pre-weighted data was accomplished by dividing the gridded k-space data with the density function shown in Fig. 6.6b

6.2.7 Parallel Computing

The inherent localization of image and k-space data gives a high degree of available instruction-level parallelism (ILP) (Grama 2003). Methods exploiting such parallelism in the reconstruction process have thus far been targeted to specific applications rather than at attempts to develop the technology more generally. Modern computing platforms are nearing engineering limits in terms of operation speed. Current gains in hardware computation speed are mainly due to increased hardware parallelism. These CPUs already contain parallel-work constructs and are moving to directly parallel, multi-core technologies. Therefore, reconstruction methods designed for parallel computing will have almost directly linear increases in speed with each additional computation unit. Further speed benefits, in particular when multiple images are reconstructed at once, can be achieved by using pre-computed look-up tables for gridding kernels. It has been shown that there are significant benefits in reconstruction speed with few reconstruction errors (Beatty 2005).

6.2.8 Iterative Reconstruction and the Conjugate-Gradient Algorithm

In Sect. 6.2.1, we saw that the encoding matrix **E** with its $\kappa \times N^2$ entries produces excessively large matrices that pose feasibility limits in terms of invertibility and storage, even on state-of-the-art workstations. Therefore, a direct inversion of **E** to reconstruct an image is not practical. In Sect. 6.2.2 to 6.2.6, gridding reconstruction was introduced as a fast way to interpolate k-space data that were acquired with arbitrary k-space readouts onto a rectilinear grid and compute images. This is because FFT is much faster than a general discrete Fourier transform (i.e., $N^2 \log N$ vs. N^4 computational operations), but re-

quires data on an equidistant grid and power-of-two sample length.

The internal memory overload caused by oversized **E** created a problem that urgently needed to be resolved. Therefore, both Kannengiesser et al.(2000) and Pruessmann et al. (2001) independently proposed to use a conjugate-gradient (CG) algorithm (Golub and Van Loan 1983) to find an estimate of the final image in an iterative fashion. This approach has the advantage that the huge matrix never needs to be inverted directly. Nevertheless, the matrix product computation and the storage effort are still substantial.

Although the CG has been used for years to solve complex matrix problems, its application to MRI is relatively new. The combination of generalized SENSE and CG described below is an amazing and extremely powerful combination, which was certainly a great achievement in the field of medical image reconstruction.

6.3 Generalized SENSE Reconstruction

6.3.1 Parallel Imaging Using the CG Algorithm

In order to solve Eq. 6.2, at least N^2 linearly independent equations are needed. Normally, $\kappa \geq N^2$ samples are acquired so that Eq. 6.2 can be solved for the N^2 unknown pixel values. In parallel imaging, the k-space information acquired with regular gradient encoding is normally insufficient to fully reconstruct an image. However, similar to Cartesian SENSE (Pruessmann et al. 1999), a methodology exists to remove aliasing from undersampled k-space data that were acquired with arbitrary k-space trajectories. This generalized SENSE (GSENSE) approach solves Eq. 2 in the case of undersampled k-space data by using the spatially varying, complex coil sensitivity information of individual receiver coils:

where the matrix **E'** has elements $E'_{(l,q)p}=s_l(\mathbf{r}_p)\cdot\exp(-j\mathbf{k}_q\cdot\mathbf{r}_p)$ (similar to the exponential factor in Eq. 6.1), $s_l(\mathbf{r}_p)$ is the complex coil sensitivity of the l-th coil at position $\mathbf{r}_p$, and $\mathbf{m}_1 \ldots \mathbf{m}_{nc}$ are the k-space sampling data vectors for each of the nc coils. Alternatively, one could write $\mathbf{E'} = \mathbf{E}\cdot\mathbf{S}$, where **E** is the matrix from Eqs. 1 and 2, and $S_{(l,p),(l,p)}=s_l(\mathbf{r}_p)$ describes the coil sensitivities. In Eq. 3, the vectors $\mathbf{m'}=[\mathbf{m}_1\ \mathbf{m}_2 \ldots \mathbf{m}_{nc}]^T$ and **v** are of length $\kappa * nc$ and N^2, respectively, and consequently the new matrix **E'** must be of size $(\kappa * nc)\times N^2$. Figure 6.8 shows the progress of the iterated solution of the GSENSE approach (i.e., calculation of the image vector **v** that solves the matrix equation $\mathbf{m'}=\mathbf{E'v}$) when the CG algorithm is applied in conjunction with "preconditioners" to speed up convergence (Pruessmann et al. 2001) to the final solution.

6.3.2 Convergence and Termination

Our laboratory has had success using the CG method in combination with the transfer-function-based GSENSE approach (Lui et al. 2005; Wajer and Pruessmann 2001). The iterative approach is a robust method for solving the reconstruction problem of undersampled k-space data. Depending on the degree of undersampling, the number of iterations needed to converge to a solution can range from a few iterations to almost 100. The number of iterations is somewhat relative since the higher the reduction factor, the fewer samples are needed to be gridded during each iteration. Moreover, the convergence rate strongly depends on factors such as the coil configuration, FOV, trajectory type, and the sampling density. In the case of GSENSE the condition number is much larger than 1, which is indicative of an ill-conditioned problem. In this case, preconditioning is applied, improving the conditioning of the reconstruction problem and accelerating the convergence of the estimate to the targeted solution vector (Golub and O'Leary 1989). This is of particular interest for higher reduction factors. Initial work has introduced sampling-density and coil-inhomogeneity correction as precondi-

$$\mathbf{m'}=\mathbf{E'v}=\begin{pmatrix}\begin{pmatrix}m_1(t_1)\\ m_1(t_2)\\ \vdots\\ m_1(t_\kappa)\end{pmatrix}^T & \begin{pmatrix}m_2(t_1)\\ m_2(t_2)\\ \vdots\\ m_2(t_\kappa)\end{pmatrix}^T & \cdots & \begin{pmatrix}m_{nc}(t_1)\\ m_{nc}(t_2)\\ \vdots\\ m_{nc}(t_\kappa)\end{pmatrix}^T\end{pmatrix}^T=\mathbf{E'}\begin{pmatrix}\rho(\mathbf{r}_1)\\ \rho(\mathbf{r}_2)\\ \vdots\\ \rho(\mathbf{r}_{N^2})\end{pmatrix}, \qquad [6.3]$$

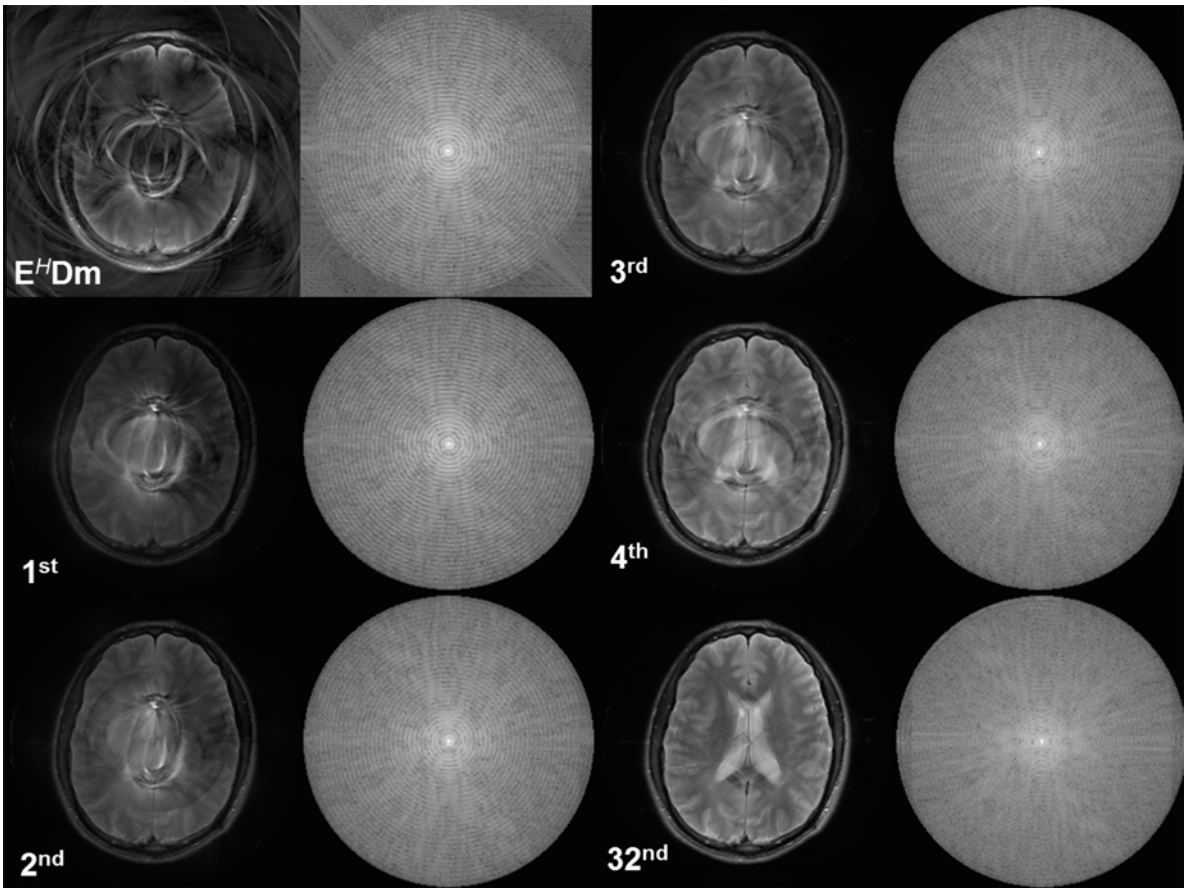

Fig. 6.8. The progress of the solution $\mathbf{v}^{(n)}$ and the corresponding k-space data during each iteration are shown for a spiral acquisition with an acceleration factor of R=4. The k-space intensity values are displayed on a logarithmic scale to improve visibility. If the acquired data undergo conventional gridding reconstruction (denoted **CE^{H}Dm),** the missing k-space data and the high degree of aliasing artefacts in the reconstructed image are clearly apparent. The convergence of the iterated solutions towards the final solution is shown for the 1st, 2nd, … 4th and the 32nd iteration, after which the algorithm has converged. With increasing iteration number, the residual aliasing artefacts diminish and the missing k-space information is synthesized by the GSENSE reconstruction

tioning methods. Figure 6.9 shows how the convergence towards the final solution depends on the preconditioning and parallel-imaging acceleration factor.

Terminating the CG iteration is still an unsolved and controversial topic. If the optimum solution is reached, further iteration only adds noise to the solution and should be avoided. Conversely, early termination will leave residual aliasing artefacts behind. This is analogous to the common problem of choosing the ideal regularization parameter: Too much regularization will lead to residual artefacts, whereas underregularization reduces the signal-to-noise ratio. If initialized with a zero image, the residual error norm rapidly decays and levels off after a certain number of iterations (Fig. 6.9). In this context, the corner of the L-shaped curve might represent the optimal iteration since at this point the residual artefacts and the signal-to-noise-ratio penalty might be well compromised (Qu et al. 2005). Frequently, this corner is hard to discern, and the optimal termination point is hard to select. Alternatively, using entropy measures in parallel imaging (Larkman et al. 2006) have the potential to control the amount of regularization or to find the endpoint of the CG iteration.

Regardless of whether generalized cross-validation (Golub and Van Loan 1983; Neumaier 1998), the L-curve criterion (Hansen and O'Leary 1993), or other methods are used to find the optimal regularization parameter, all will eventually lead to a different, optimal parameter. Our laboratory has begun to investigate the potential of psychophysical image quality measures to terminate the CG gradient iteration and

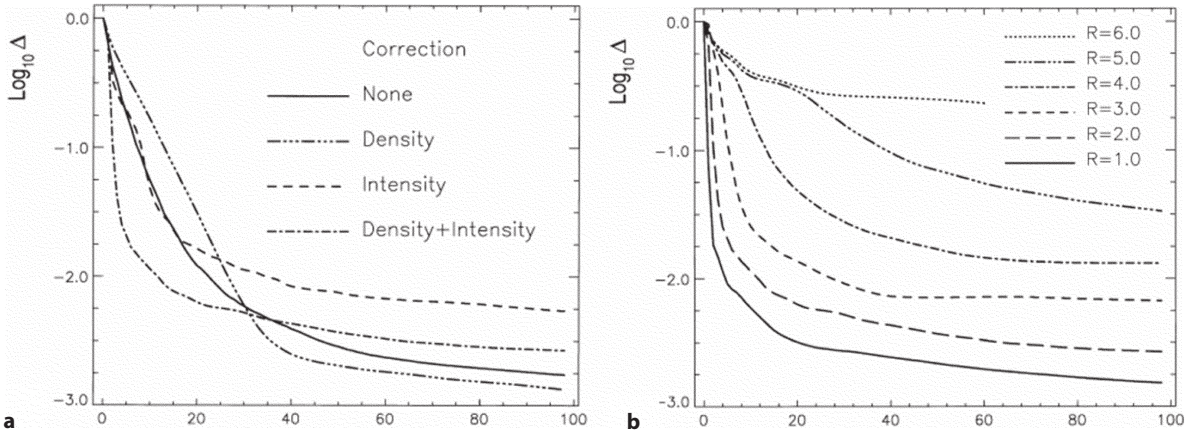

Fig. 6.9a,b. The CG GSENSE conversion rate measured by the relative norm of the difference between the true and estimated image. The *y*-axis is on a logarithmic scale. **a** The normalized image error decays rapidly during the first few iterations and levels-off thereafter. The convergence rate is heavily influenced by the type of preconditioning. **b** A similar decay of residual image error can be obtained across the range of reduction factors used, although convergence is at a much slower rate for higher reduction factors and overall final image error is higher for high reduction factors (images courtesy of Klaas Pruessmann, ETH Zurich)

for general regularization. One particularly appealing metric is the perceptual-difference model (PDM), which mimics the physiological response of a human observer to an image (Eckstein 2000). It is possible to use tools that have been developed under the umbrella of psychophysical science in order to perform an objective assessment of image quality, such as DCTune2.0 (Watson 2003). Originating from JPEG compression, this code is designed to mimic the human visual system and determines the visual difference between two images. Specifically, the PDM models aspects of the human visual pathway including grayscale nonlinearity of the retina, contrast-sensitivity function, spatial-frequency channels in the visual cortex, and a measure of the contrast and visual detection in an objective fashion. The model has two inputs: a reference, or gold standard, image and a processed test image (Wilson et al. 2003). The output is a spatial map showing the magnitude of image-perception differences expected with a human observer. Differences can be averaged either over the entire image or a region of interest in order to provide a scalar measure of degradation.

6.4 Off-Resonance Artefacts

Two of the major imperfections in MRI are the spatial inhomogeneity of the underlying magnetic field and local susceptibility, both of which typically cause distorted or blurred images. While global off-resonant effects can be demodulated prior to or during gridding by proper phasing of the data, local variations of magnet field strength can cause significant distortions in the final image since the linear relationship between spin phase and position is perturbed.

The most common approach to combat distortions from off-resonant spins is to apply multi-frequency reconstruction (MFR) (Man et al. 1997; Noll et al. 1991) or the frequency-segmented off-resonance correction (FSORC) method. Based on a frequency field map, k-space data are reconstructed at a slightly different carrier frequency. The carrier frequency typically varies by a few Hertz and is subdivided into *n* intervals resulting in *n* different images. The final image is generated by selecting pixels from those reconstructions that were reconstructed on the carrier frequency indicated by frequency field maps.

In order to accommodate the MFR/FSORC method into the GSENSE algorithm, the forward and backward gridding needs to be split into a number of similar reconstructions, each carried out at slightly different demodulation frequencies (Fig. 6.10). Similar to the original FSORC approach (as well as for GSENSE), the final reconstructed MFR image with off-resonance correction is created by combining all deblurred regions selected from the appropriate demodulated image. From Fig. 6.10, it is evident that the computational burden of FSORC is proportional to the number of demodulation frequencies used since the FFT is per-

formed on each demodulated k-space dataset. For that reason, MFR is often computationally intensive, particularly when a wide range of off-resonance frequencies exists across a scanned object.

Recently, a new fast off-resonance correction method, termed "block regional off-resonance correction" (BRORC) (Moriguchi et al. 2003), has been introduced. Our group has begun to explore its capacity for GSENSE reconstruction. In this method, the image is broken down into small submatrices that assume smoothly varying off-resonance across those submatrices. This method could potentially be 2×–4× faster than a ten-channel MFR reconstruction. Both FSORC and BRORC are well suited for parallel computing (Grama 2003).

Since the CG-based GSENSE reconstruction problem is already formulated as an iterative approach, iterative off-resonance correction methods considering off-resonance terms might be a viable alternative to explore. In particular, methods such as the method of Harshbarger et al. (1999) and the time-segmented method of Sutton et al. (2003) are known to provide better off-resonance correction performance, especially in areas where the field map smoothness is violated and MFR methods are known to perform poorly.

6.5 Motion and SENSE

6.5.1 Phase-navigated GSENSE

Researchers are often unaware of the complexity of the brain's physiologic motion, e.g., due to pulsatile CSF flow. In particular, phase errors that occur because of diffusion encoding are in general non-linear (Liu et al. 2004; Miller and Pauly 2002).

Subsequent investigations of this problem have combined a diffusion-weighted twice-refocused spin echo (TRSE) sequence with variable-density spiral (VDS) readout (Liu et al. 2004, 2005). Using a VDS waveform design (Kim et al. 2003), the *k*-space sampling density can be increased around the origin of *k*-space (Fig. 6.11a–b) and can be used to extract a low-resolution navigator image for each interleaf. Alternatively, a separate acquisition can provide a navigator image (Fig. 6.11c–d). These navigator images allow one to compute phase-error maps, and this phase information can then be subtracted from each interleaf. However, with the direct phase subtraction method, the background noise is relatively high. As a result, the contrast of the image can be relatively low. With the CG phase correction, the background noise is significantly reduced, and image contrast is restored (Fig. 6.12). Using VDS and full-phase correction, we were also able to generate DTI scans that are unmatched in resolution at this date (Fig. 6.13).

By treating the phase error as a modulating function that is superimposed on the conventional image encoding, we find that the phase-correction problem is very similar to the GSENSE reconstruction problem, and a combined reconstruction can therefore be found that unites both phase-perturbed and undersampled *k*-space data (Liu et al. 2005, 2005). Multi-coil, interleaved VDS DTI scans with R=1–3 are reconstructed using the combined GSENSE and phase-navigation approach (Fig. 6.14). As expected, the noise level rises with increasing R, but the overall acquisition time is reduced. If the readout length of each interleave is shortened by parallel imaging, then the geometric distortions would also be significantly reduced.

6.5.2 Motion-Corrected GSENSE

Involuntary patient motion is still one of the greatest challenges in MRI. Due to the sequential nature of the MR acquisition process, a significant amount of time can elapse between different samples in k-space, thus leaving many MRI sequences vulnerable to patient motion. The resulting increase in misregistration can

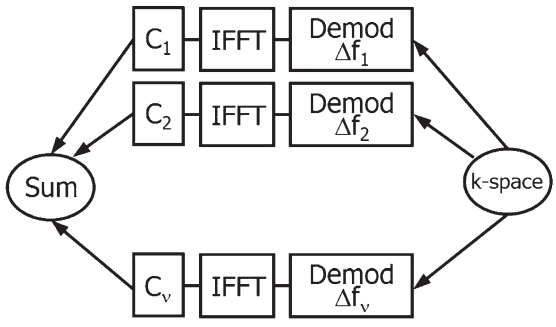

Fig. 6.10. Multi-frequency reconstruction (*MFR*) to address the off-resonance problem in image reconstruction. Instead of a simple backward-forward gridding procedure in CG GSENSE, the procedure has to be performed using demodulations with slightly off-resonant carriers. For each demodulation frequency, the image will be segmented based on the location corresponding to the carrier frequency range

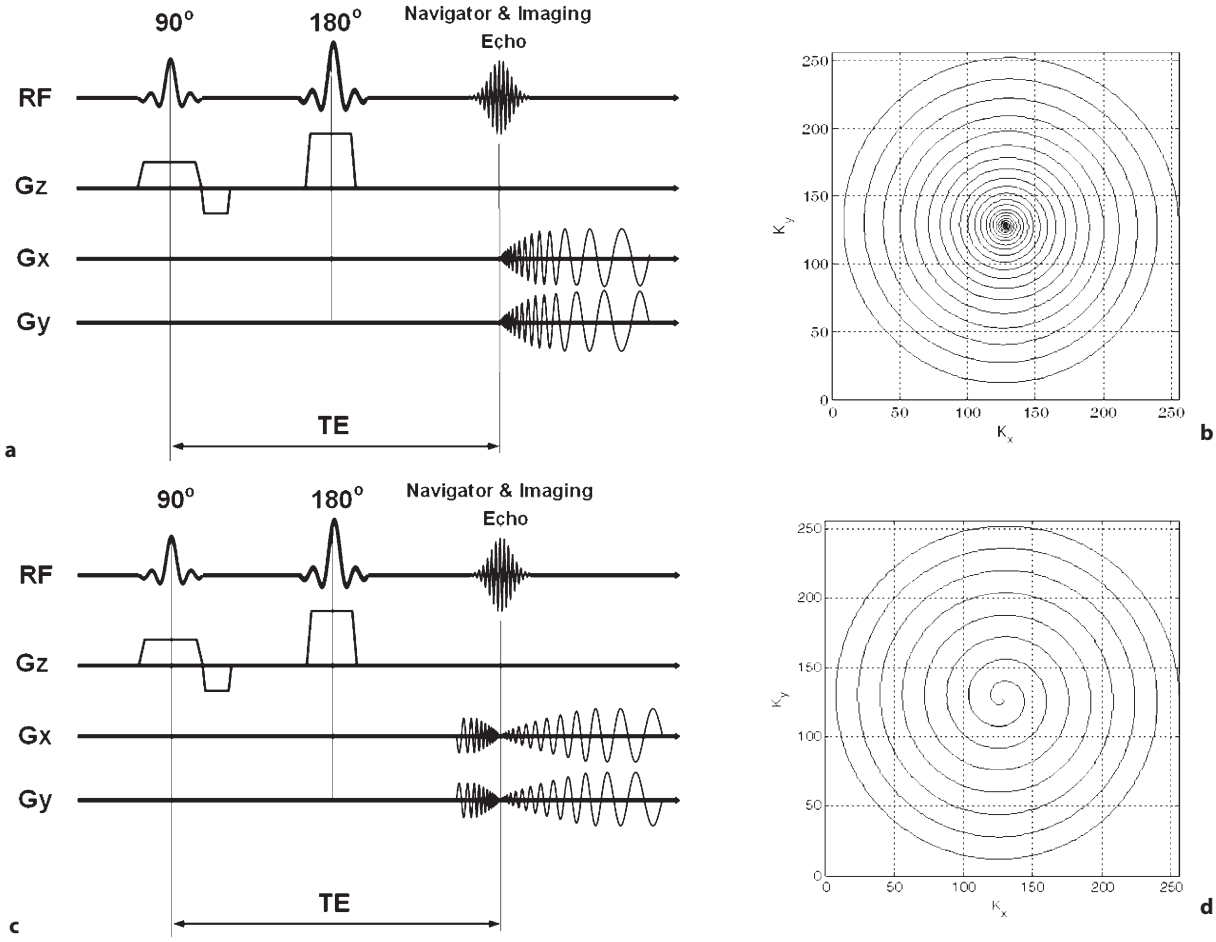

Fig. 6.11a–d. Spin-echo interleaved-spiral pulse sequence and k-space trajectories used to obtain navigator images. A variable-density spiral waveform **a,b** can be designed to cover enough information around the center of k-space so that a low resolution navigator image can be produced. Alternatively, a short (~3 ms–5 ms) single-shot spiral-in trajectory can be used during the initial spin-echo formation followed by a conventional interleaved spiral trajectory to form the desired image

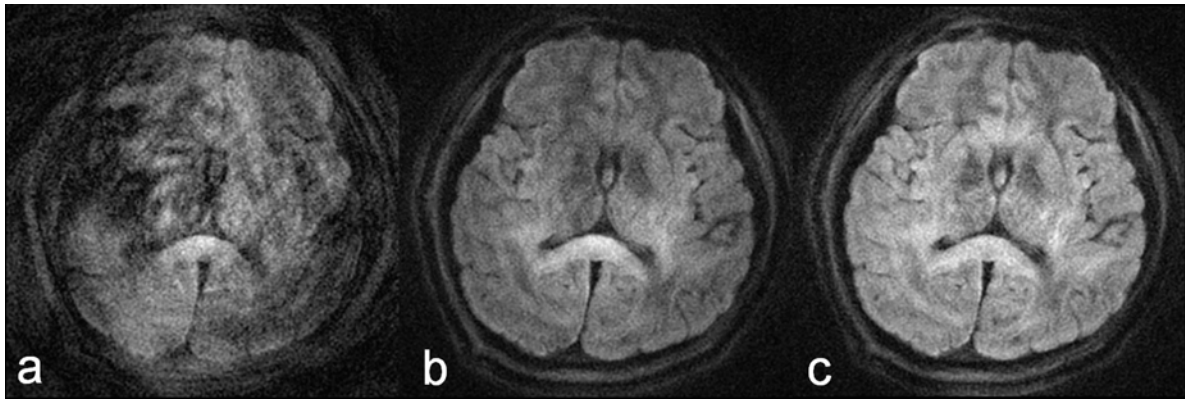

Fig. 6.12a–c. Diffusion-weighted image with 0.86×0.86 mm² resolution using **a** a conventional spiral readout, **b** a VDS readout with zeroth/first order motion correction, and **c** a VDS readout with non-linear phase subtraction. Conventional spiral suffers from significant ghosting artefacts that are greatly reduced with VDS. Additional signal can be recovered with non-linear phase correction by removing some of the destructive interference in the high-spatial-frequency range

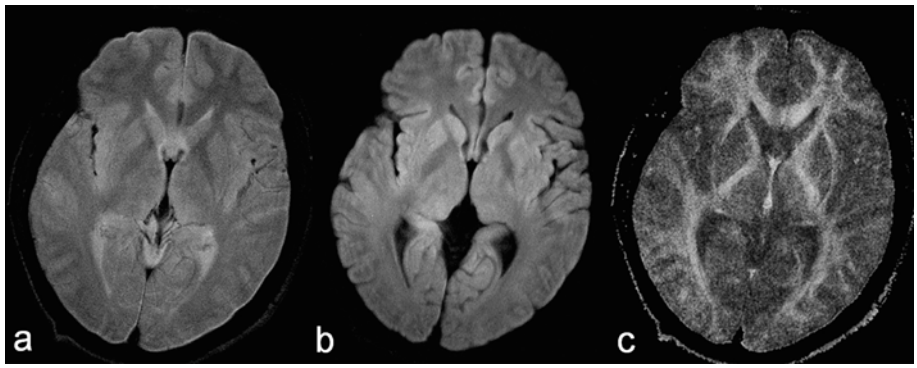

Fig. 6.13a–c. In vivo axial 512×512 DTI results acquired with 64-interleaf VD spiral. **a** b=0 image; **b** isotropic diffusion-weighted image, b=800 s/mm^2; **c** FA map

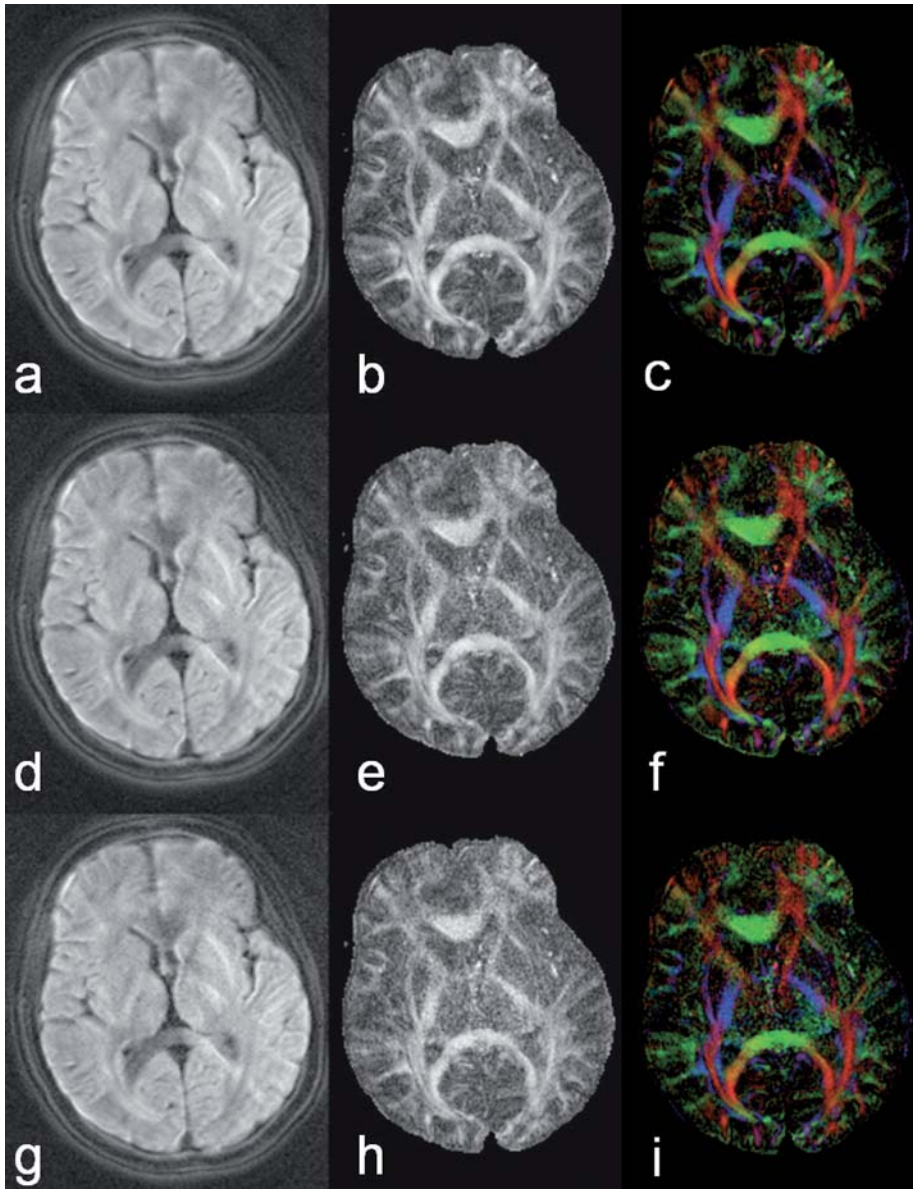

Fig. 6.14a–i. In vivo 256×256 multi-shot SENSE DTI using VDS, with reduction factors up to R=3, b=800 s/mm^2. **a-c** R=1; **d-f** R=2; **g-i** R=3; **a,d** and **g** typical final reconstructed diffusion-weighted image; **b,e** and **h** FA maps; **c,f** and **i** corresponding color-coded FA map

severely impair the diagnostic quality of an MR examination. The medical condition of a patient, such as tremor, pain, or mental status, often prevents even willing patients from holding still.

The way in which motion affects the final image depends upon the magnitude and direction of the motion as well as its temporal relation to the acquisition of k-space. Overall, the net effect of patient motion during MR imaging is k-space-data inconsistency, which produces distortions in the final image. If one can identify corrupted k-space data and has knowledge of the degree of motion, it is possible to correct, or at least reduce, image distortions in either a retrospective (Larkman et al. 2004; Atkinson and Hill 2003; Bydder et al. 2003) or prospective fashion (Thesen et al. 2000; Ward et al. 2000).

The simplest form of motion is rigid-body translation without elastic deformation. In k-space, translational motion is manifested by a linear phase shift along the direction of motion (Gonzales and Woods 1993). Rotational motion produces a slightly more complicated distortion pattern. For a given object, a rotation in image space produces the same rotation in k-space (Griswold et al. 2002). As a result, during sequential scanning the expected k-space information at a particular position will have been rotated away and will be partially missing or replaced by data that has already been acquired. These object rotations are often the source of significant image artefacts.

A novel approach for motion correction has recently been developed using a parallel-imaging-based synthesis of the missing k-space information. The method retrospectively corrects rigid body rotation and translation and compensates for the resulting variable-density sampling pattern. This method utilizes an augmented iterative parallel-imaging reconstruction approach to correct for motion regardless of the type of trajectory being used. In order to accomplish this, there are four specific modifications to the conventional GSENSE algorithm that need to be made.

- The correction for translational motion can be achieved by adding phase terms to the acquired data prior to gridding.
- Assuming the object rotation is known or can be derived from a navigator image, the corresponding k-space data need to be counter-rotated by the same angle.
- Even if the k-space samples are rotated back to their desired position and translation correction is applied, the rotated and shifted object has been exposed to different coil sensitivities relative to the original orientation. Therefore, the coil sensitivity map-in has to be modified for each profile/interleave accordingly. For an external coil-sensitivity scan in combination with a particular profile/interleave, this requires a 3D rotation and translation in the opposite direction.
- The rotation of k-space data will affect the sampling density in k-space. The altered sampling density needs to be corrected by one of the methods discussed in Sect. 6.2.6. Figure 6.15 shows the effects of rotational motion during an eight-interleave spiral acquisition. If the data are gridded along the desired spiral waveform without correction prior to gridding, significant distortions become apparent in the image (Fig. 6.15d). After correcting for rotational and translational motion, the image quality could be improved (Fig. 6.15g), but considerable variations in k-space sampling density and regional undersampling (Fig. 6.15h) still lead to noticeable artefacts. However, after ten iterations using the augmented GSENSE algorithm, the artefacts are barely noticeable in the final reconstruction (Fig. 6.15j).

The efficacy of this method for removing k-space inconsistencies can also be seen in the final k-space, which has a more homogeneous appearance overall (Fig. 6.15k). Figure 6.16 shows an in-vivo example using the spiral-in navigator sequence (Fig. 6.11c) in concert with the new parallel-imaging motion-correction approach. Due to the intentional head movements of the volunteer, considerable k-space fragmentation occurred, which led to significant artefacts in the conventional image reconstruction. These artefacts are predominantly visible around the frontal aspect of the brain because lying in the coil the axis of rotation is positioned at the back of the head. The amount of head rotation and translation was estimated from the navigator images. Correcting the k-space data only for rotational and translational effects clearly reduced image blurring, but the resulting k-space fragmentation led to considerable aliasing artefacts. With the application of the GSENSE-based correction scheme, these aliasing artefacts were suppressed quite well.

6.6 GRAPPA-Based Reconstructions

As a rule, parallel-imaging reconstruction techniques can be grouped into k-space- and image-space-based

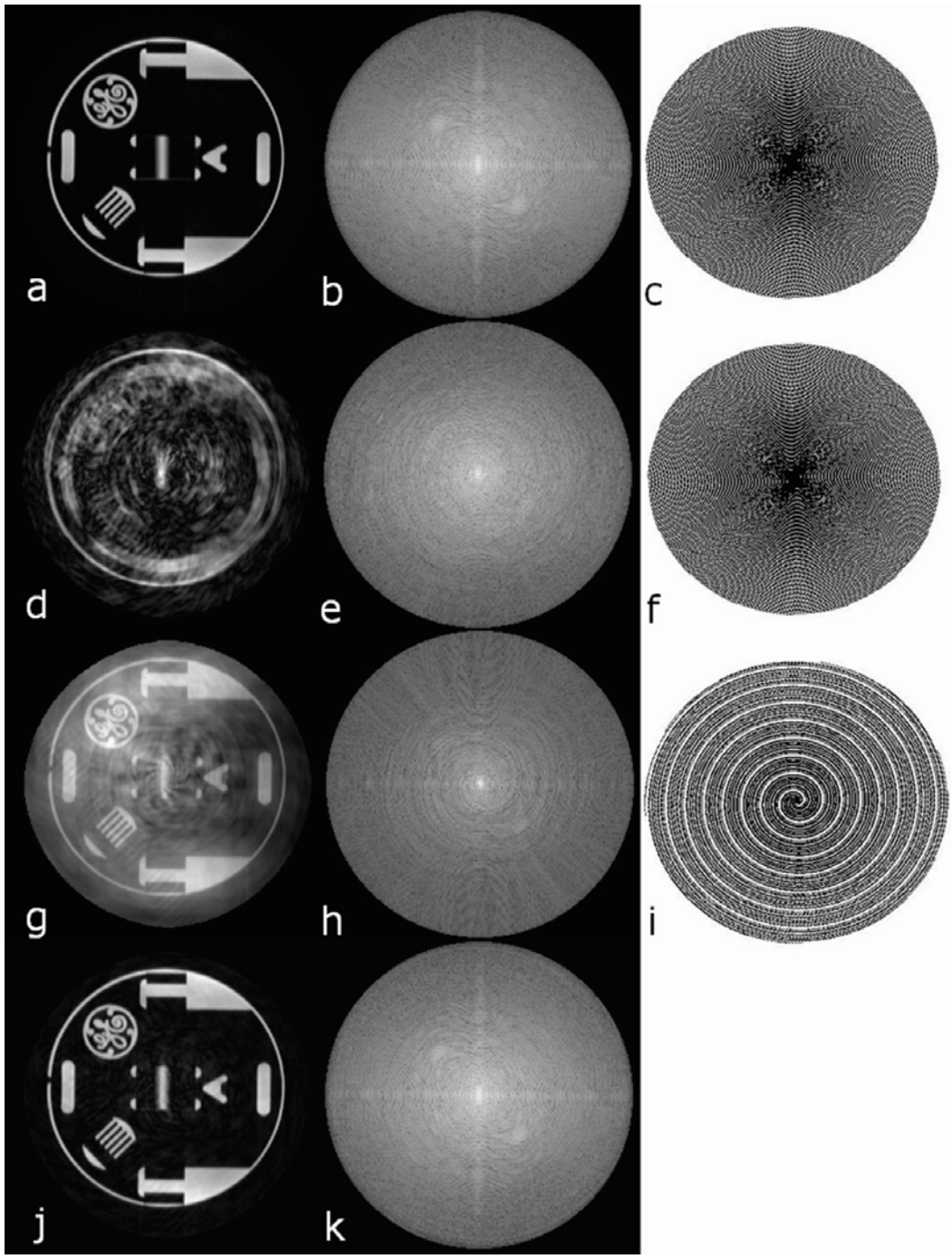

Fig. 6.15a–k. Assessment of the effect of object rotation during an interleaved spiral data acquisition (eight interleaves) simulated in a quality phantom. Six receiver coils are distributed equally around the circumference of the phantom. For each interleave, a random object rotation within the range of ±30° was introduced with the following results: **a** gridding reconstruction of a quality phantom without rotation; **b** gridded k-space data; **c** spiral sampling trajectory. If the acquired data are gridded according to the prescribed trajectory (**c** and **f**), inconsistencies in k-space **e** cause severe distortions in the reconstructed image **d**. Some of these distortions can be reduced **g** if one uses the object rotation to counter-rotate the k-space acquisition trajectory for that particular interleaf **i** and uses these corrected orientations for gridding **h**. Correction for altered sensitivity and an iterative SENSE reconstruction (ten iterations) can remove most of the residual k-space sampling errors **k** and provides an image almost free of artefacts **j**

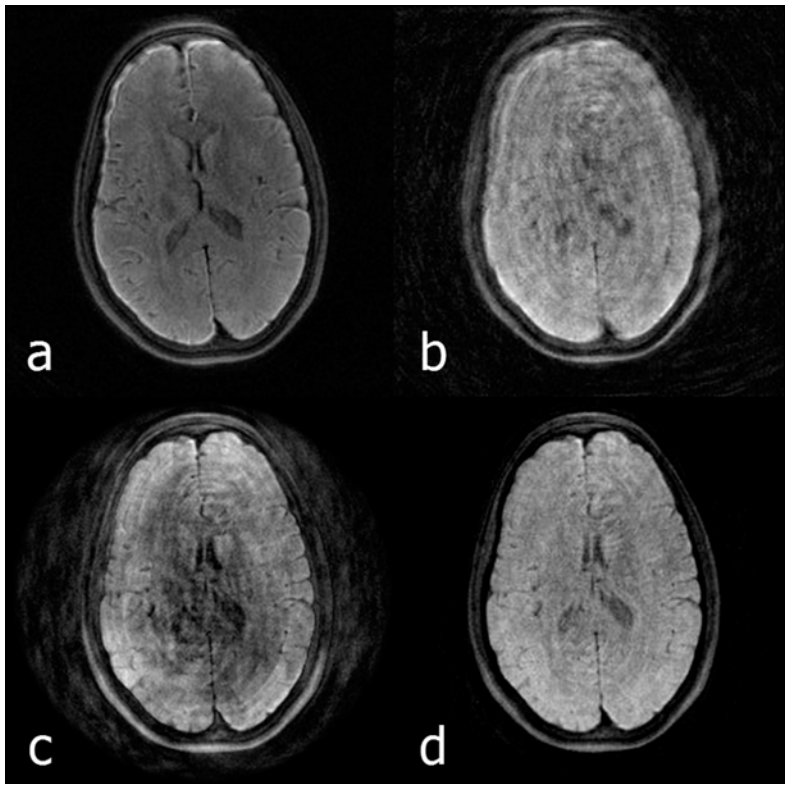

Fig. 6.16a–d. In vivo experiment conducted with a fully sampled low-resolution (32×32) single-shot spiral-in navigator preceding each conventional spiral interleave. **a** The reference sum-of-squares interleaved spiral image is acquired with no subject motion. **b** Significant artefacts are apparent if the volunteer performs moderate head motion during data acquisition and if no motion correction is applied. **c** Correction of k-space data for translational and rotation motion results in sharper object contours, but the image quality is still corrupted by residual ghosting from local undersampling and sampling density variations. **d** Improved image quality after the application of the augmented GSENSE reconstruction

methods, cf. Chapter 2. Generalized autocalibrating partially parallel acquisitions (GRAPPA) (Griswold et al. 2002) reconstruction is the most common k-space-based reconstruction algorithm. It synthesizes missing lines in k-space by using a weighting kernel, which is obtained after a training phase using additionally acquired auto-calibration lines (ACS). In addition, it does not require that accurate coil sensitivity maps be obtained. GRAPPA has proven to be a robust and reliable method, making it a popular choice for image reconstruction. Once the GRAPPA-weights have been determined, k-space synthesis can be performed very rapidly, especially when performed in hybrid space (Skare and Bammer 2005). Furthermore, a single set of weights can be applied to a time series of data such as from cine MRI, fMRI, or DTI scanning. However, a major drawback with GRAPPA reconstruction is that it is currently limited to Cartesian k-space data. As yet, only a few trajectories, such as spiral (Heberlein et al. 2004) and radial (Griswold et al. 2003) data, have been combined with GRAPPA reconstruction. The capacity of GRAPPA reconstruction for these arbitrary k-space waveforms is creating excitement in the community since it would provide much faster reconstructions than the time-consuming iterative GSENSE approach. While the basics of GRAPPA reconstruction are discussed elsewhere in this book, the remainder of this section will provide a brief overview of these non-Cartesian variants of GRAPPA.

In order to perform GRAPPA reconstructions on radial data, the k-space data need first to be transformed to an r-θ space (Fig. 6.17), where r and θ are the radial and azimuthal position in k-space, respectively. Thereafter, a modified Cartesian GRAPPA kernel estimation is applied to the data in the r-θ space. Unlike normal Cartesian GRAPPA, the determination of weights needs to be separated in segments along the r and θ coordinate; this is because the coil sensitivity varies with θ, and the radial spoke density varies with r so that the GRAPPA kernel also varies. In our example (Fig. 6.17), the r-θ space is segmented into 128 different regions (r×θ=8×16) so that the positioning of data points for each segment approximate a Cartesian tessellation. Figure 6.18 shows the results for radial GRAPPA reconstruction for outer reduction factors (ORF) of 2 and 4. It can be seen that the streak artefacts that are present in the sparse recon are removed. Since the radial trajectory is already oversampled at the center of k-space, the removal of

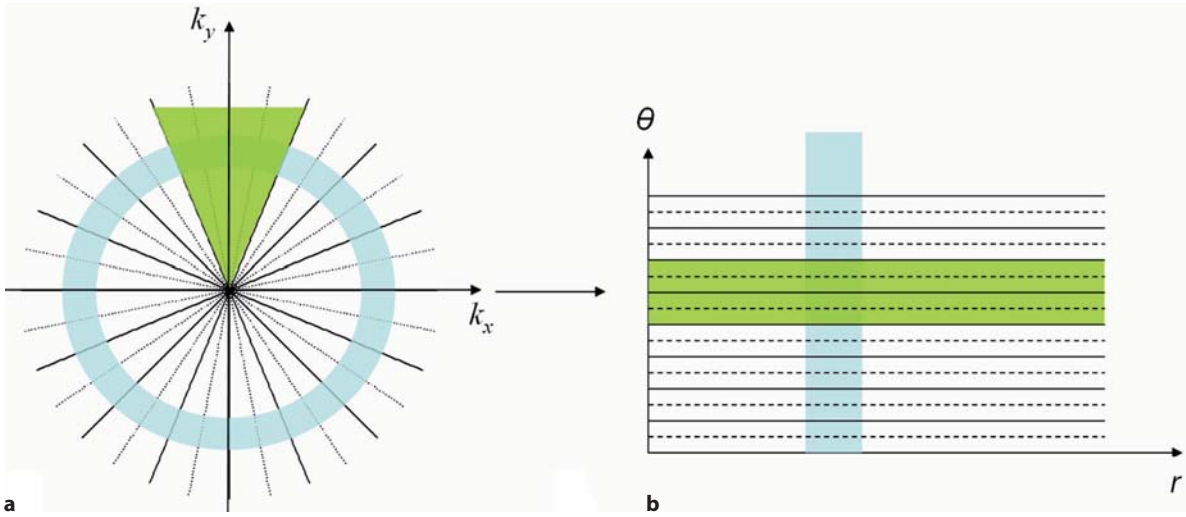

Fig. 6.17a,b. Radial GRAPPA reconstruction. **a** Radial k-space sampling pattern. **b** Radial k-space data after coordinate transformation into *r*-θ space. Undersampling occurs in the azimuthal dimension. *Solid lines* are acquired projections, whereas *dashed lines* are missing projections at critical sampling rate. The *r*-θ space is a rectilinear coordinate space where Cartesian GRAPPA can be applied with some restrictions. Unlike conventional Cartesian GRAPPA where the weights can be applied to the entire k-space, the radial GRAPPA approach must be divided in radial (*light blue*) and azimuthal (*light green*) segments. The radial segmentation is because of the strong sampling density variation along *r*, whereas the azimuthal segmentation is due to the relative coil sensitivity variation with θ

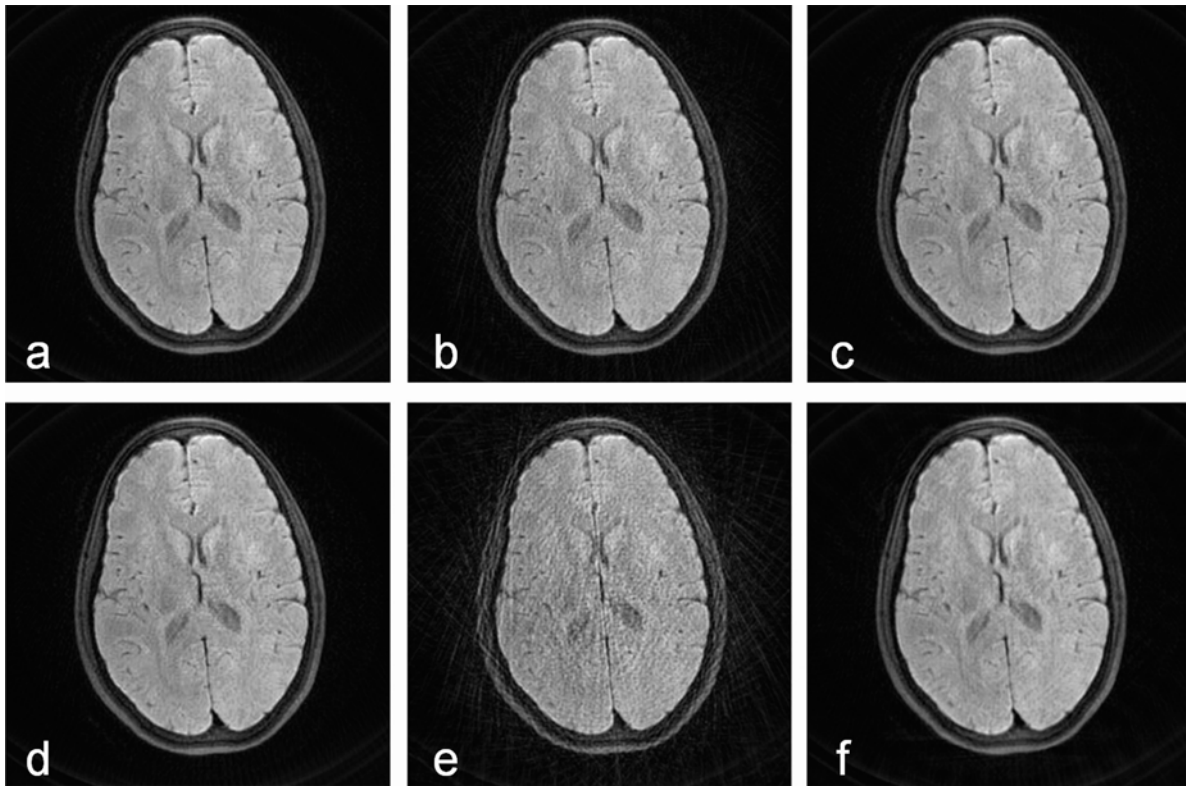

Fig. 6.18a–f. Example of a radial GRAPPA reconstruction. **a,d** Fully sampled radial acquisition; **b** two-times undersampled radial acquisition with conventional reconstruction shows moderate streak artefacts typical for this form of undersampled acquisition; **c** radial GRAPPA reconstruction without any noticeable artefacts; **e** four-times undersampled radial acquisition with conventional reconstruction demonstrates significant streak artefacts; **f** corresponding radial GRAPPA reconstruction shows reduced streak artefacts

the reconstructed lines from the center does not introduce any artefacts.

Similar to radial GRAPPA, also spiral k-space data must first be rearranged in order to be reconstructed by the Cartesian GRAPPA formalism. In our implementation, the data are first resampled from a constant linear velocity spiral onto a constant angular velocity spiral using linear interpolation of the acquired k-space data (Fig. 6.19a). With our MR system, k-space data are acquired every 4 μs so that interpolation results were proven to be reliable. The reason for switching to constant-angular-velocity spirals is that the sample points on the spiral trajectory line up along the radial dimension and represent a radial spoke. Therefore, after reorganization of the k-space data, it is possible to get samples on radial projections. Again, the data values on these radial projections are transformed into the θ-*r* space (Fig. 6.19b). In contrast to radial GRAPPA, where subsampling is along the azimuthal dimension, subsampling in spiral GRAPPA is along the radial dimension. The same methods described for radial GRAPPA can be used for spiral GRAPPA. Figure 6.20 shows the results for the spiral GRAPPA reconstruction for a reduction factor of $R=2$.

Both radial and spiral GRAPPA rely on a coordinate transformation so that Cartesian GRAPPA can be applied. This coordinate transformation also leads to a transformation of the GRAPPA kernel assumption, which can only be applied to restricted areas in k-space and hence restricts the versatility of this reconstruction approach. The limitation herein lies in the rigid approximation of the convolution of the coil sensitivities with the k-space data on a fixed grid. In order to provide greater flexibility to reconstruct k-space data that are not located on an equidistant grid, the GRAPPA kernel needs to be approximated sufficiently (similar to gridding) by interpolation functions.

6.7 Conclusion

The acquisition of MR data along k-space trajectories other then Cartesian is becoming increasingly attractive for a variety of MRI methods. While the reconstruction of Cartesian SENSE data is common practice now, speed and general complexity still pose a challenge to the reconstruction of undersampled MR data acquired with arbitrary k-space waveforms. However, once the reconstruction problem is formulated properly, it can be solved efficiently by the iterative conjugate-gradient algorithm. Moreover, generalizing the

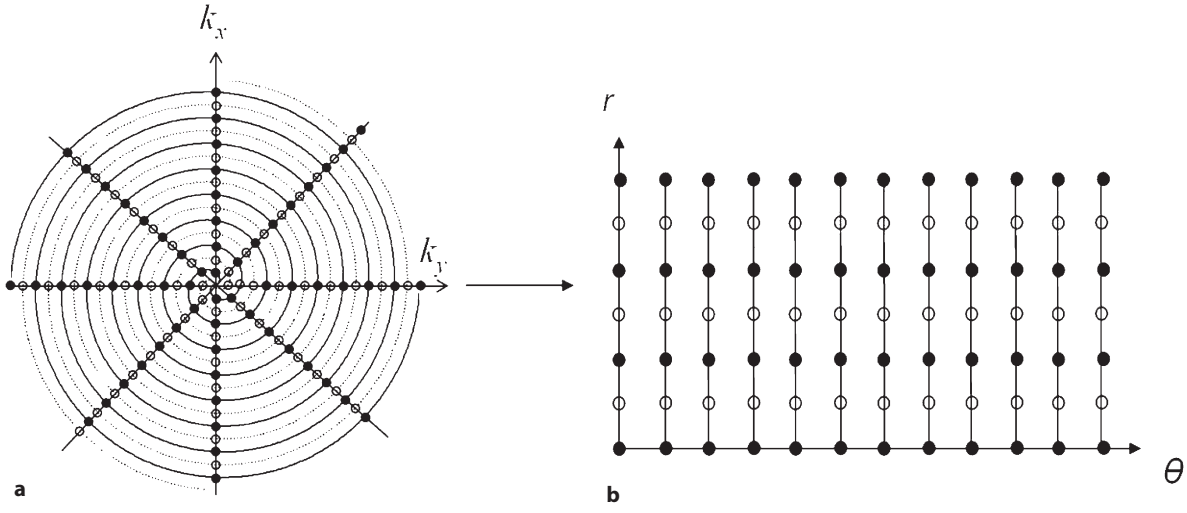

Fig. 6.19a,b. Spiral GRAPPA reconstruction. **a** Spiral k-space sampling pattern. The constant-linear-velocity spiral is first resampled onto a constant-angular-velocity spiral pattern using linear interpolation of the acquired k-space data. As a result the constant-angular-velocity spiral data line up in radial direction and can be warped into **b** an *r*-θ space. The *solid line points* are the actually acquired data, whereas *open points* are missing data samples. Undersampling occurs in the radial dimension. Again, the *r*-θ space is a rectilinear coordinate space where Cartesian GRAPPA can be applied. Restrictions similar to those for radial GRAPPA apply to spiral GRAPPA, particularly around the origin of k-space

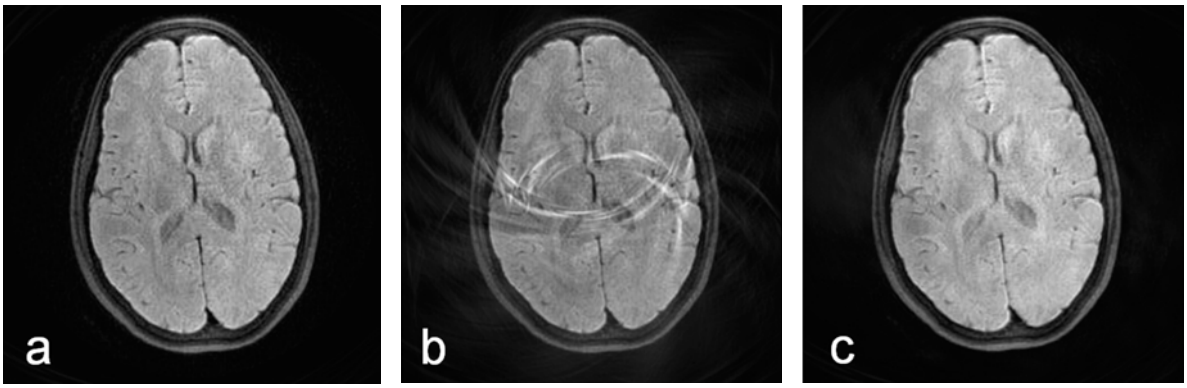

Fig. 6.20a–c. Example of a spiral GRAPPA reconstruction. **a** Fully sampled spiral acquisition; **b** two-times undersampled spiral acquisition with conventional gridding reconstruction demonstrates "swirl" artefacts typical for this form of undersampled acquisition; **c** spiral GRAPPA reconstruction without any noticeable artefacts

reconstruction problem and the extreme efficiency of the CG algorithm have opened possibilities for new variants of the GSENSE algorithm, such as navigator- and motion-correction schemes.

In summary, the reconstruction of non-Cartesian k-space data is a major contribution to the field of MR imaging. The work of researchers in this field has opened up many new avenues by removing many of the restrictions that are associated with rectilinear k-space sampling. This chapter demonstrates that the field of non-Cartesian sampling has accomplished a great deal and – even more importantly – promises exciting innovations in the near future.

Acknowledgements. This work was supported in part by the NIH (1R01EB002711, 1R01EB002711S1), the Center of Advanced MR Technology at Stanford (P41RR09784), Lucas Foundation, and Oak Foundation. The authors are grateful to Drs. Klaas Pruessmann, Marc Griswold, and John Pauly for many stimulating and insightful discussions during the last years. The authors would like to thank Dr. Susan Dunn for editing the manuscript.

References

Atkinson D, Hill DL (2003) Division of Radiological Sciences, Medical Engineering The Guy's King's, St Thomas' School of Medicine, Guy's Hospital London U. K. David Atkinson kcl ac uk. Reconstruction after rotational motion. Magn Reson Med 49:183–187

Beatty PJ, Nishimura DG, Pauly JM (2005) Rapid gridding reconstruction with a minimal oversampling ratio. IEEE Trans Med Imag 24:799–808

Block WF, Barger AV, Mistretta CA (1998) Vastly undersampled isotropic projection imaging. 8th Annual Meeting of the ISMRM:161

Bydder M, Atkinson D, Larkman DJ, Hill DL, Hajnal JV (2003) Robert Steiner MRI Unit Imaging Sciences Department, Clinical Sciences Centre Imperial College Hammersmith Hospital London UK. Smash navigators. Magn Reson Med 49:493–500

Eckstein MP, Abbey CK, Bochud FO (2000) A practical guide to model observers for visual detection in synthetic and natural noisy images. In: Beutel J, Kundel HL, Van Metter RL (eds) Handbook of medical imaging. SPIE, Billingham, WAp 593

Frigo M, Johnson SG (1998) Fftw: An adaptive software architecture for the fft. IEEE Int. Conf. Acoustics, Speech, and Signal Processing3:1381–1384

Golub GH, O'Leary DP (1989) Some history of the conjugate gradient and the lanczos algorithm:1948-1976. SIAM Review 31:50–102

Golub GH, Van Loan CF (1983) Matrix computations. Johns Hopkins University Press, Baltimore

Gonzales RC, Woods RE (1993) Digital image processing. Addison-Wesley, Reading, MA

Grama A, Gupta A, Karypis G, Kumar V (2003) Introduction to parallel computing. Addison Wesley, Reading, MA

Griswold MA, Heidemann RM, Jakob PM (2003) Direct parallel imaging reconstruction of radially sampled data using GRAPPA with relative shifts. 11th Annual Meeting of the ISMRM:2349

Griswold MA, Jakob PM, Heidemann RM, Nittka M, Jellus V, Wang J, Kiefer B, Haase A (2002) Generalized autocalibrating partially parallel acquisitions (GRAPPA). Magn Reson Med 47:1202–1210

Hansen PC, O'Leary DP (1993) The use of the l-curve in the regularization of discrete ill-posed problems. SIAM J Sci Comput 14:1487–1503

Harshbarger T, Twieg DB (1999) Iterative reconstruction of single-shot spiral MRI with off resonance. IEEE Trans Med Imag 18:196–205

Heberlein KA, Kadah Y, Hu X (2004) Segmented spiral parallel imaging using grappa. 12th Annual Meeting of the ISMRM:328

Kannengeisser SAR, Brenner AR, Noll TG (2000) Accelerated image reconstruction for sensitivity encoded imaging with arbitrary k-space trajectories. Annual Meeting of the ISMRM 1:155

Kim DH, Adalsteinsson E, Spielman DM (2003) Simple analytic variable density spiral design. Magn Reson Med 50:214–219

Larkman DJ, Atkinson D, Hajnal JV (2004) Imaging Sciences Department Hammersmith Hospital Imperial College London. London W. H. S. david larkman imperial ac uk. Artefact reduction using parallel imaging methods. Topics in magnetic resonance imaging: TMRI: 15:267–275

Larkman DJ, Batchelor PG, Atkinson D, Rueckert D, Hajnal JV (2006) Beyond the g-factor limit in sensitivity encoding using joint histogram entropy. Magn Reson Med 55:153–160

Liu C, Bammer R, Kim DH, Moseley ME, Lucas I (2004) Center Department of Radiology Stanford University California USA. Self-navigated interleaved spiral (snails): Application to high-resolution diffusion tensor imaging. Magn Reson Med 52:1388–1396

Liu C, Bammer R, Moseley ME (2005) High resolution multishot sense DTI using self-navigated interleaved spirals (snails). 13th Annual Meeting of the ISMRM:10

Liu C, Moseley ME, Bammer R (2001) Fast sense reconstruction using linear system transfer function. 13th Annual Meeting of the ISMRM, p 689

Liu C, Moseley ME, Bammer R (2005) Simultaneous phase correction and sense reconstruction for navigated multi-shot DWI with non-Cartesian k-space sampling. Magn Reson Med(in press)

Man LC, Pauly JM, Macovski A (1997) Department of Electrical Engineering, Stanford University California USA. Multifrequency interpolation for fast off-resonance correction. Magn Reson Med 37:785–792

Miller KL, Pauly JM (2002) Nonlinear navigated motion correction for diffusion imaging. 10th Annual Meeting of ISMRM:1110

Moriguchi H, Dale BM, Lewin JS, Duerk JL (2003) Department of Radiology University Hospitals of Cleveland, Case Western Reserve University Cleveland, Ohio USA. Block regional off-resonance correction (brorc): A fast and effective deblurring method for spiral imaging. Magnetic Resonance in medicine : official journal of the Society of Magn Reson Med 50:643–648

Neumaier A (1998) Solving ill-conditioned and singular linear systems: A tutorial on regularization. SIAM Rev 40:636–666

Noll DC, Meyer CH, Pauly JM, Nishimura DG, Macovski A (1991)A homogeneity correction for magnetic resonance imaging with time-varying gradients. IEEE Trans Med Imag 10:629–637

Pruessmann KP, Weiger M, Bornert P, Boesiger P (2001) Advances in sensitivity encoding with arbitrary k-space trajectories. Magn Reson Med 46:638–651

Pruessmann KP, Weiger M, Scheidegger MB, Boesiger P (1999) Sense: Sensitivity encoding for fast MRI. Magn Reson Med 42:952–962

Qu P, Zhong K, Zhang B, Wang J, Shen GX, (2005) Department of Electrical, Electronic Engineering the University of Hong Kong Pokfulam. Convergence behavior of iterative sense reconstruction with non-Cartesian trajectories. Magn Reson Med 54:1040–1045

Skare S, Bammer R (2005) Spatial modeling of the GRAPPA weights. 13th Annual Meeting of the ISMRM:2422

Sutton BP, Noll DC, Fessler JA (2003) Fast, iterative image reconstruction for MRI in the presence of field inhomogeneities. IEEE Trans Med Imag 22:178–188

Thesen S, Heid O, Mueller E, Schad LR (2000) Siemens Medical Systems M. R. Applications Development, Erlangen, Germany, stefan thesen med siemens de. Prospective acquisition correction for head motion with image-based tracking for real-time fmri. Magn Reson Med 44:457–465

Wajer FTA, Pruessmann KP (2001) Major speedup of reconstruction for sensitivity encoding with arbitrary trajectories. 9th Annual Meeting of ISMRM, p 767

Ward HA, Riederer SJ, Grimm RC, Ehman RL, Felmlee JP, Jack CR Jr (2000) Department of Radiology, Mayo Clinic, Rochester, Minnesota, USA. Prospective multiaxial motion correction for fMRI. Magn Reson Med 43:459–469

Watson AB (1993) A technique for visual optimization of dct quantization matrices for individual images. Society for Information Display Digest of Technical Papers, XXIV: 946–949

Wilson DL, Salem KA, Huo DL, Duerk JL (2003) Perception difference paradigm for analyzing image quality of fast MRI techniques. SPIE Medical Imaging on Image Perception, Observer Performance, and Technology, Billingham, WA

Complementary Techniques for Accelerated Imaging

7

Oliver Wieben

CONTENTS

7.1 Introduction

In many MR imaging applications, a short scan time is required to observe dynamic processes such as the beating heart, the passage of a contrast bolus, guidance of an interventional procedure, or to reduce artefacts from physiological motion. The previous chapters explored the design of rapid sequences, the use of alternative k-space trajectories, and parallel-imaging techniques to achieve faster acquisitions. This chapter discusses techniques that reduce imaging time for a desired spatial resolution by exploiting assumptions of redundancies in the sampling of static images or dynamic time series that allow minimal errors in the reconstruction. For all of these approaches, a single receiver coil is sufficient, and most of them can be combined with parallel imaging techniques when multi-channel receiver coils are used as described in Chap. 11.

O. Wieben, PhD
Department of Medical Physics and Radiology, University of Wisconsin-Madison, J5/150 CSC, 600 Highland Ave, Madison, WI, 53792-1590, USA

7.2 Partial Fourier Acquisitions

Partial Fourier imaging refers to MR acquisitions in which Fourier space is not sampled symmetrically around its origin. The missing data are either simply replaced by zeros, or they are calculated during the reconstruction process from the acquired data. Most commonly, data sampling in MR imaging occurs on a rectilinear grid in Fourier space, also referred to as k-space. Figure 7.1 illustrates strategies to save imaging time for a given field of view by purposefully leaving areas of the 2D Fourier space grid unsampled. The total imaging time is determined by the product of the number of phase-encoding steps and the repetition time, TR. The imaging time required to sample a 2D image (a) fully can be reduced by partial phase encoding, where some phase-encoding steps are not acquired (b). Alternatively, the minimum TR can be reduced by the acquisition of a partial echo (c), also referred to as an asymmetric or fractional echo, which also reduces flow-induced artefacts. It is possible to combine both partial phase encoding and partial echo acquisition to further minimize imaging time (d).

Even though most diagnostic images are shown as magnitude images, all MR images are completely characterized in a complex notation only. In other words, two matrices showing either the real and imaginary components or the magnitude and phase of the image data are required to represent uniquely such a data set. Figure 7.2 demonstrates the complex data sets of a head scan in k-space and in image space.

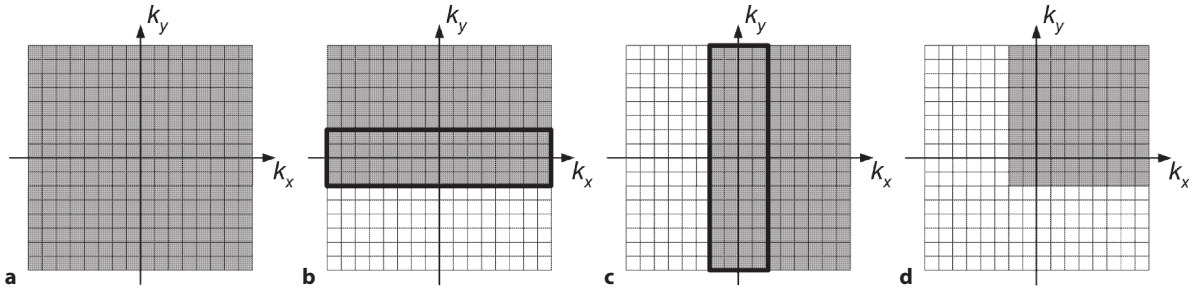

Fig. 7.1a–d. The Fourier space grid can be sampled more rapidly if areas are purposefully left out with a partial Fourier acquisition. In comparison to a fully sampled data set **a**, the imaging time can be shortened by reducing the number of phase-encoding steps for asymmetric coverage of k-space **b**. Alternatively, the echo time and repetition time can be reduced by the acquisition of a fractional echo along the readout direction **c**. These two techniques can be combined to further reduce total imaging time by sampling slightly more than one quadrant of k-space **d**. For proper image reconstruction, a certain region of k-space has to be sampled symmetrically around the origin to provide a reasonable low resolution phase estimate of the image (*solid rectangles* in **b** and **c**)

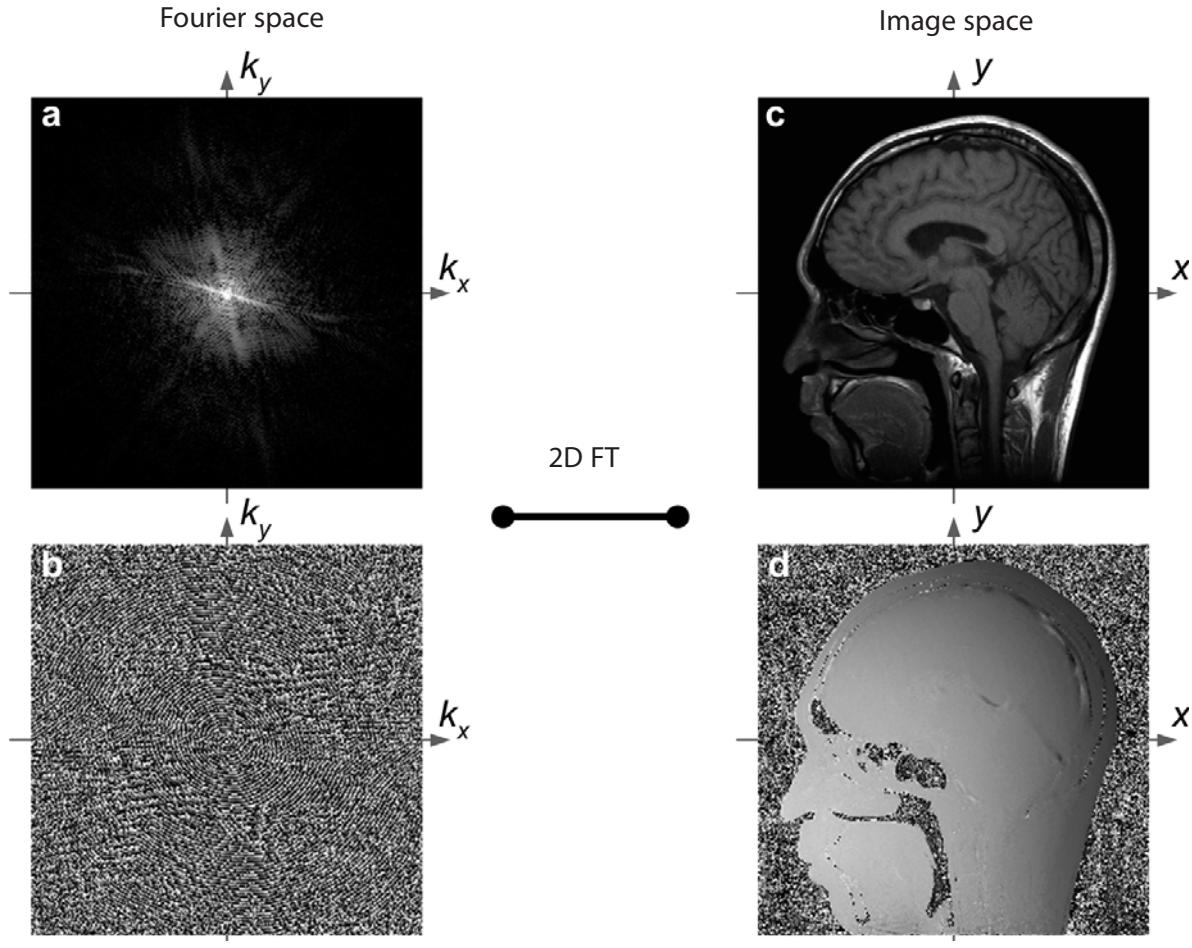

Fig. 7.2a–d. The magnitude **a** and phase **b** of the raw k-space signal acquired during a head scan. The magnitude **c** and phase **d** of the corresponding representation in image space is obtained by an inverse 2D Fourier transform. In this example, the image phase varies slowly in the diagonal of the sagittal slice, more rapidly at some tissue interfaces, and is random in the surrounding air

Some clinical applications require the preservation of the phase information throughout the reconstruction process, such as phase contrast imaging for velocity encoding, Dixon techniques for the separation of fat and water, and MR spectroscopy.

If an MR image would consist of real components only, then it could be represented by half of its Fourier components and, thus, the acquisition time could be cut in half. In this case, the image would have no phase terms, and one half of the Fourier coefficients could be synthesized by the complex conjugate of the other half of Fourier space. This property is also called Hermitian symmetry. However, in practice, MR images do have phase terms induced by susceptibility effects at tissue boundaries, inhomogeneities in the magnetic field, phase effects from flow and motion, eddy currents, data acquisition timing, and other sources as shown in Fig. 7.2. Therefore, the acquisition of only half the k-space data with a reconstruction by conjugate symmetry or other means fails in practice. Instead, several algorithms have been developed to sample slightly more than half of k-space for a better phase estimate from these low spatial frequencies (King 2004).

In the simplest approach, the missing k-space data are substituted by zeros prior to a standard image reconstruction. This zero-filling reduces the spatial resolution compared to a full acquisition and causes Gibbs ringing at sharp edges. However, the phase information of the image is preserved within the limits of the spatial resolution defined by the portion of k-space sampled on both sides of the origin.

More advanced algorithms, such as the Margosian (Margosian et al. 1986) and homodyne reconstructions (Noll et al. 1991), synthesize the missing data and incorporate phase corrections based on the symmetrically sampled low-resolution data strip around the origin. They also introduce merging filters for smoother transitions from unsampled to sampled data, thereby reducing ringing artefacts (McGibney et al. 1993). Within the limits of the accuracy of the phase estimate from the symmetrically sampled data portion, the Margosian and homodyne reconstructions provide a spatial resolution identical to the fully sampled data set. Compared to a full acquisition, the SNR is decreased because the total acquisition time has been reduced. This type of reconstruction leads to a loss of phase information and cannot be used for acquisitions that require a phase representation of the image data.

Figure 7.3 compares results from partial Fourier reconstruction techniques for various degrees of k-space coverage. When only slightly more than one half of k-space is sampled, the zero-filled reconstruction introduces severe ringing artefacts from the step-like transition in k-space (long arrows) and blurring due to the decreased spatial resolution. In comparison, the homodyne reconstruction restores most of the spatial resolution even if only slightly more than one half of k-space has been acquired and there are no truncation artefacts. However, there are also residual errors in the homodyne reconstruction in the regions where the phase estimate from the symmetrically sampled data does not sufficiently describe the actual phase of the phantom. Alternatively, iterative methods (Haacke et al. 1991) have been suggested, which potentially provide better phase estimates at regions with rapidly changing phase such as tissue boundaries with high susceptibilities.

Additional imaging time savings can be accomplished with partial Fourier acquisitions in more than one dimension, e.g., in both phase-encoding directions in 3D imaging or with a combined fractional echo acquisition and partial Fourier sampling in the phase-encoding direction. However, the missing data cannot be recreated with the 1D partial Fourier reconstruction methods discussed above, since only one quarter of k-space is properly sampled. Some imaging protocols offer double or even triple partial Fourier acquisitions combined with zero-filling of the missing data. While the large time savings of such acquisitions are tempting and the image quality is usually pleasing, important diagnostic information can be obscured when not properly acquiring or synthesizing k-space data. Xu and Haacke (2001) recently proposed an iterative solution that can properly synthesize data for such acquisition strategies, though these iterative solutions are not used on clinical scanners.

7.3 Zero-Filling for Image Interpolation

Zero-filling, also referred to as zero-padding, is commonly used for image interpolation in order to increase the apparent spatial resolution within a slice, in the slice-encoding direction, or both. With this technique, zeros are simply added to the outer regions of symmetrically sampled k-space so that the reconstructed images are represented on a larger grid. This is mathematically identical with a sinc-interpolation of the images. While zero-filling cannot increase the acquired spatial resolution, it can improve the representation of objects due to decreased partial volume

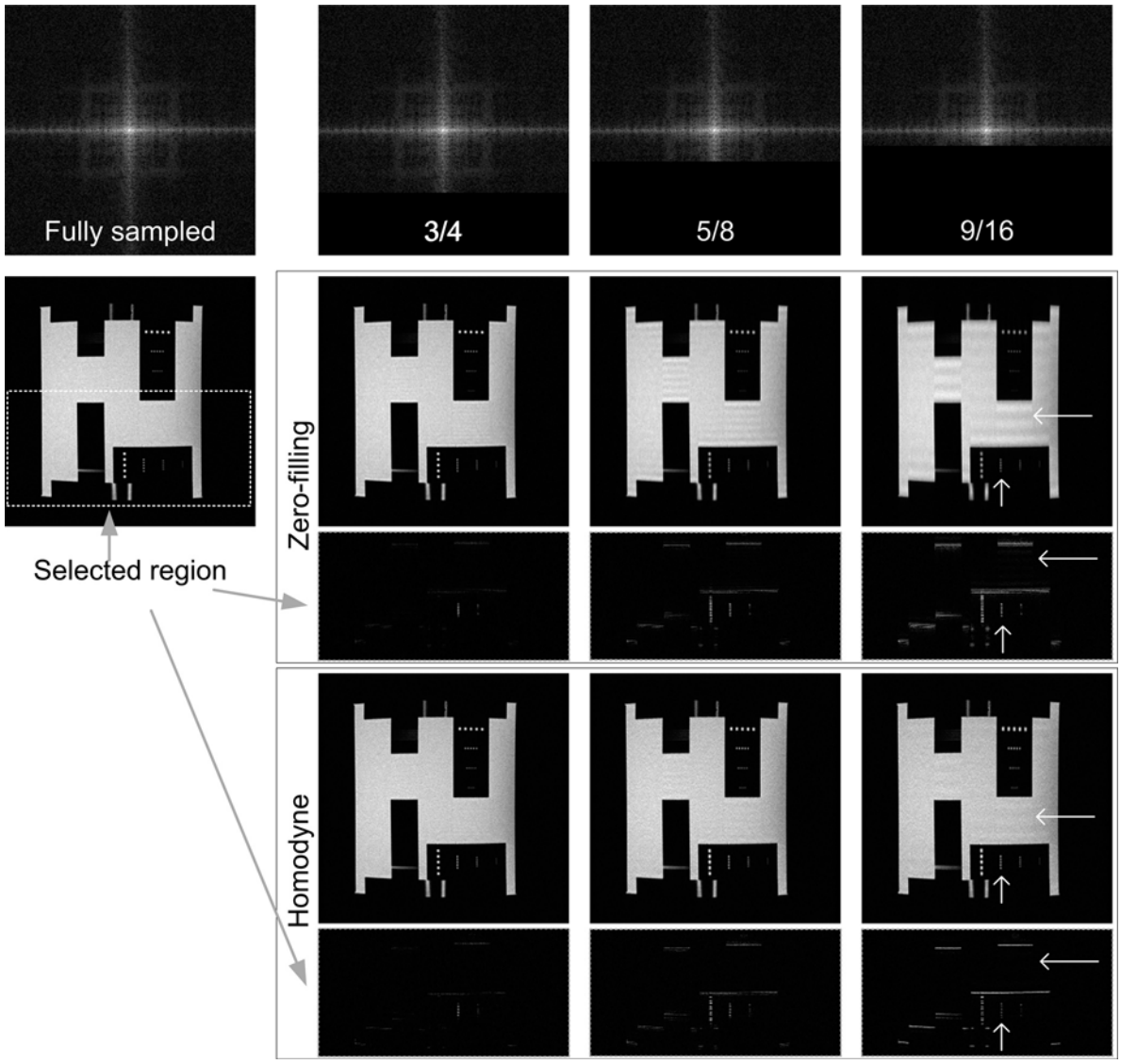

Fig. 7.3. Phantom results of partial Fourier reconstructions from various k-space subsets. The acquired k-space coverage is decreased from full sampling to an asymmetric coverage of 3/4, 5/8, and 9/16 (*left* to *right*). The corresponding images reconstructed by simple zero-filling and by homodyne reconstruction are displayed. A difference image of a selected region is also shown for comparison. The error increases as less data are actually acquired. The zero-filling reconstruction introduces ringing artefacts from the step function in k-space that are not present with the homodyne reconstruction (*long arrow*). Image blurring is also amplified for zero-filling (*short arrow*). The remaining errors in the homodyne reconstruction are caused by the insufficient spatial resolution for the phase estimate from the symmetrically sampled data. In clinical practice, sharp boundaries occur considerably less frequently than in the phantom. However, reconstruction errors can be introduced at high-contrast boundaries such as fat tissue-air interfaces

effects (Du et al. 1994) and the availability of a finer reconstruction grid for Fourier data in the corners of k-space (Bernstein et al. 2001). The former effect is helpful in visualizing vessels with a width less than one voxel and MIP renderings of angiography studies. The interpolation of diagonal edges through zero-filling also makes objects appear more natural.

Despite the additional burden on image reconstruction time as well as storage and archiving requirements, zero-filling by a factor of two is commonly used in clinical practice. Figure 7.4 illustrates the properties of zero-filling on a phantom. While it can be combined with partial Fourier acquisitions, it neither improves the actual spatial resolution nor reduces the scan time

for a given spatial resolution. It is important to note that the spatial resolution of relevance for any diagnostic scan is not the reconstructed, but the acquired resolution since the former can be arbitrarily increased by increasing the zero-padding factor.

7.4 View Sharing

View sharing is a method commonly used in dynamic processes such as cardiac or realtime imaging. As the name implies, some of the acquired data are shared among time frames in order to provide a faster frame rate than otherwise achievable. For this discussion, it is helpful to recall some of the properties of the acquired k-space data. For most imaging situations, the image contrast is mainly defined by the central region while finer image details such as edges are characterized by the outer k-space regions, which represent the higher spatial frequency regions; for a more detailed discussion, see Chapter 1.4.

With view-sharing techniques, images are generated at a faster rate than data can be acquired for completely new images. View-sharing techniques are typically based on a segmented k-space acquisition as shown for two examples in Fig. 7.5: a linear phase-encoding ordering with a traditional rectilin-

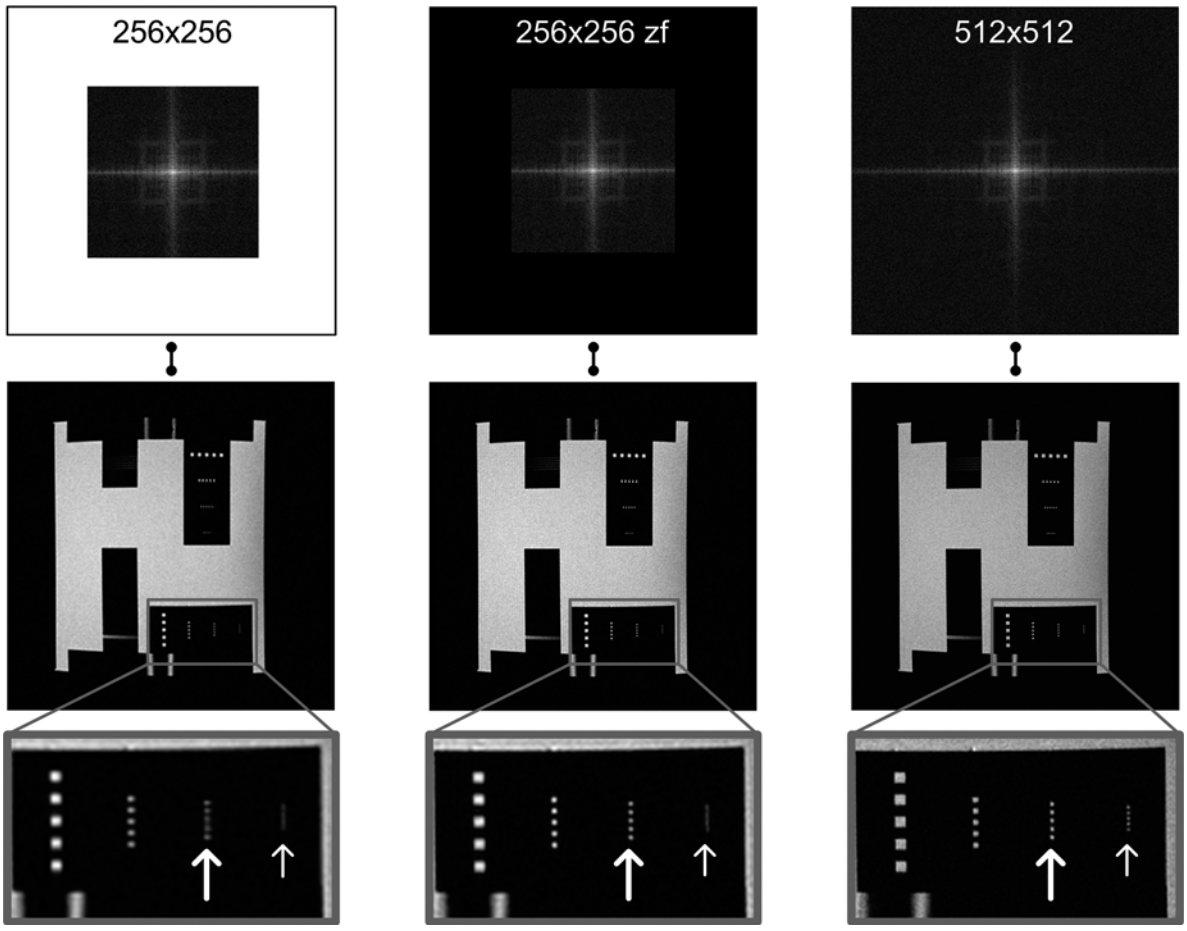

Fig. 7.4. The effects of zero-filling. This example from a phantom study shows the raw data matrix and the reconstructed image from a quality assurance phantom acquired with a 256×256 matrix (*left column*). If the raw data matrix is zero-padded to a 512×512 grid size prior to the reconstruction, then the image is interpolated to a larger grid (*center column*). For comparison, an image reconstructed from an acquired 512×512 matrix size is also shown (*right column*). Zero-filling reduces partial volume effects and can increase the apparent resolution as observed in the second smallest resolution pattern (*bold arrow*). However, it cannot improve the acquired spatial resolution as can be observed by the smallest pattern, which can only be resolved with a 512×512 acquired resolution (*thin arrow*)

ear Fourier trajectory (a) and an interleaved encoding scheme with a radial trajectory (b). For simplicity, k-space is divided into six segments with only four views per segment in both examples. Other trajectories such as spiral acquisitions and other view-ordering schemes can also be used.

A popular view-sharing technique commonly used in realtime imaging is the sliding window reconstruction as displayed in Fig. 7.6. In this example, Fourier space is divided into segments with a linear phase-encoding scheme. In a standard reconstruction, one image is reconstructed each time that all segments have been acquired. In addition, images can also be reconstructed at intermittent time frames, 'borrowing' the missing segments from the adjacent completely sampled image (Riederer et al. 1988). In this example, the sliding window reconstruction generates images at six times the rate of the traditional reconstruction.

If the imaging scene were static, all images would look identical, and no artefacts would occur. If motion occurs during the acquisition, then there can be inconsistencies in the k-space data, which in turn can lead to artefacts. It is important to note that this scheme does not increase the true temporal resolution, which

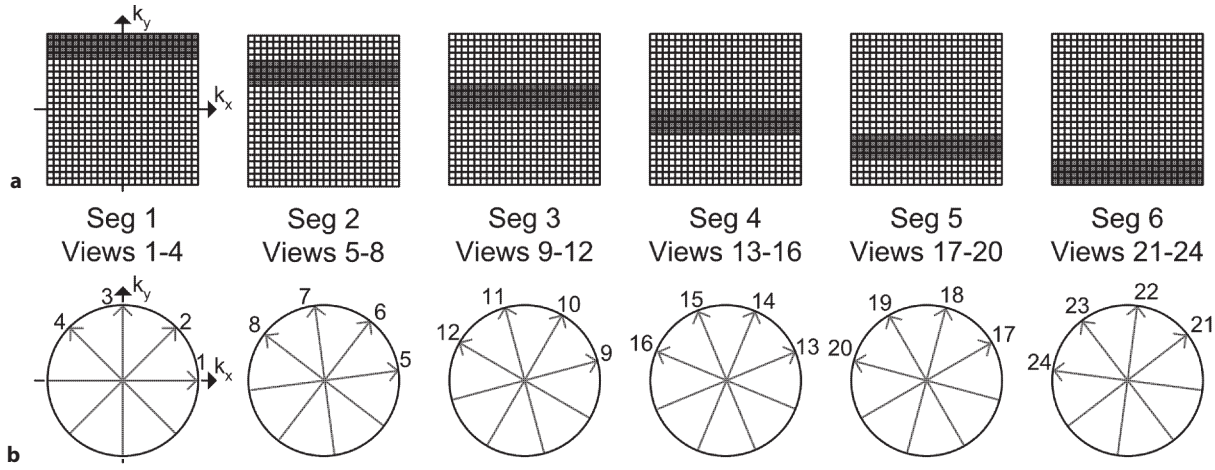

Fig. 7.5a,b. Examples for k-space segmentations: a linear phase-encoding scheme on a rectilinear grid, represented by six segments with four phase-encoding steps in each segment **a** and an interleaved radial acquisition scheme with an equal number of segments and views per segment **b**

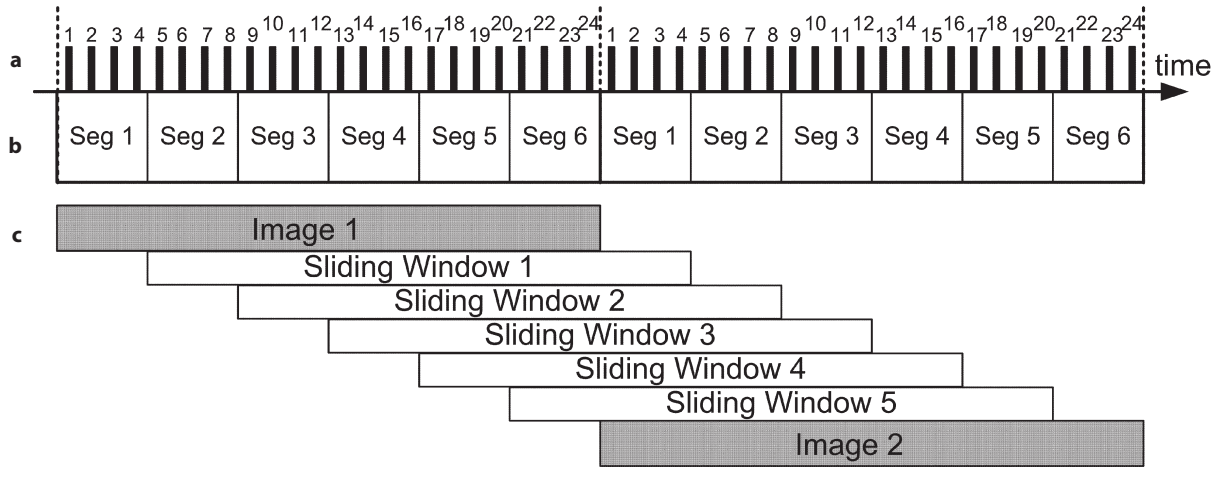

Fig. 7.6a–c. View sharing with a sliding window reconstruction. In this example, the phase-encoding steps are sequentially ordered in Fourier space and grouped in six segments **a**. The segments are repeatedly acquired **b** and complete images can be reconstructed after every six segments **c**. In addition, images can be generated for intermittent time frames by a sliding window reconstruction

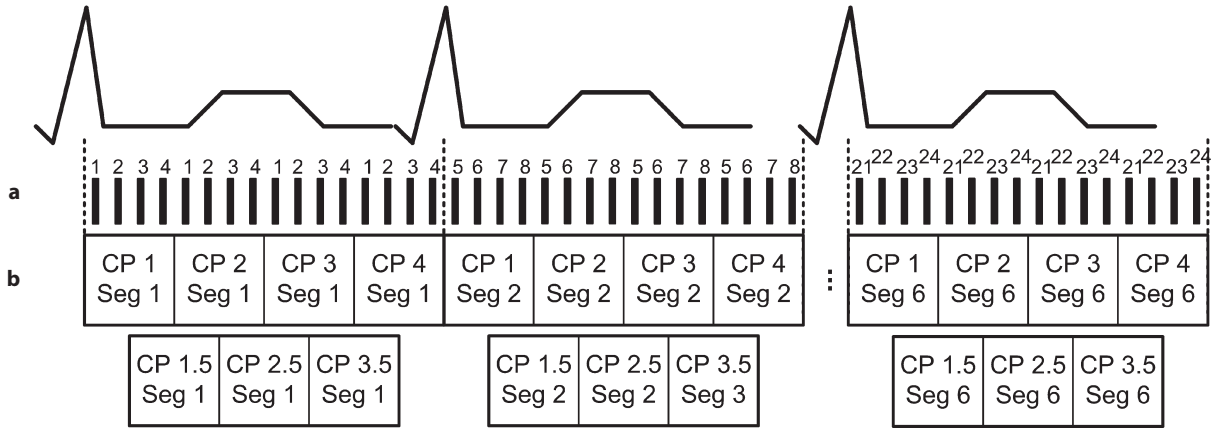

Fig. 7.7a,b. Example for a view-sharing acquisition in synchronization with the cardiac cycle. Within each RR cycle, segments of four views are repeatedly acquired until the next R-wave is detected **a**. Each segment characterizes a cardiac phase **b** and is subsequently combined with the segments of the identical cardiac phases in later RR intervals to generate images for each cardiac phase. Additional cardiac phases can be generated by view sharing among adjacent cardiac phases

is determined by the duration to acquire all segments to reconstruct one fully sampled image. However, the generation of intermittent images can generate a smoother display of the temporal evolution of the imaging scene. For most imaging scenes, the greatest visual change occurs when the contrast defining central k-space lines are acquired. Therefore, the sliding window reconstruction is often paired with an acquisition where central k-space views are acquired in each segment, such as interleaved Cartesian view-ordering schemes or a radial or spiral trajectory.

View-sharing techniques are adjusted to the cardiac cycle in multi-phase imaging, ECG gated acquisitions, such as the evaluation of cardiac function, or phase contrast imaging for the measurement of flow waveforms. One example of an interleaved acquisition paired with a radial k-space trajectory is demonstrated in Fig. 7.7. Here, the cardiac cycle is divided into successive acquisitions of the identical segment (a). Whenever a new R-wave is detected, the next segment is repeatedly acquired. For each cardiac phase, an image is reconstructed by grouping all segments for that particular phase together (b). Therefore, the true temporal resolution for this acquisition is given by the duration of each segment. If the number of views per segment is reduced, then the temporal resolution is increased, but so is the total scan time as more segments are required to cover an identical data matrix size in Fourier space. Similar to the sliding window reconstruction, intermittent phases of the cardiac cycle can be reconstructed by the sharing of views (c). Alternative view-sharing schemes for cardiac imaging share only high spatial frequencies among the cardiac phases, while every phase has its unique central region of k-space (Markl and Hennig 2001).

7.5 Keyhole Imaging

Keyhole imaging (Jones et al. 1993; van Vaals et al. 1993) was also developed to increase the temporal resolution for the imaging of dynamic processes such as the passage of a contrast bolus in MR angiography and perfusion imaging (Bishop et al. 1997; Chenevert et al. 1995; Jones et al. 1993; van Vaals et al. 1993), interventional procedures (Bakker et al. 1996; Duerk et al. 1996), and functional MRI studies (Gao et al. 1996), while maintaining high spatial resolution. The acquisition process is split into two phases: a dynamic phase in which only low resolution images are acquired with a high temporal resolution and a second phase where a reference image with high spatial resolution is acquired once either before or after the dynamic phase. These two acquisitions are then combined to generate a time series with high spatial and temporal resolution. Figure 7.8 shows how Fourier space is divided into a central region, representing the lower spatial frequencies, and an outer region, representing the higher spatial frequencies. For the generation of the dynamic series, the central region is updated for each image and combined with the higher spa-

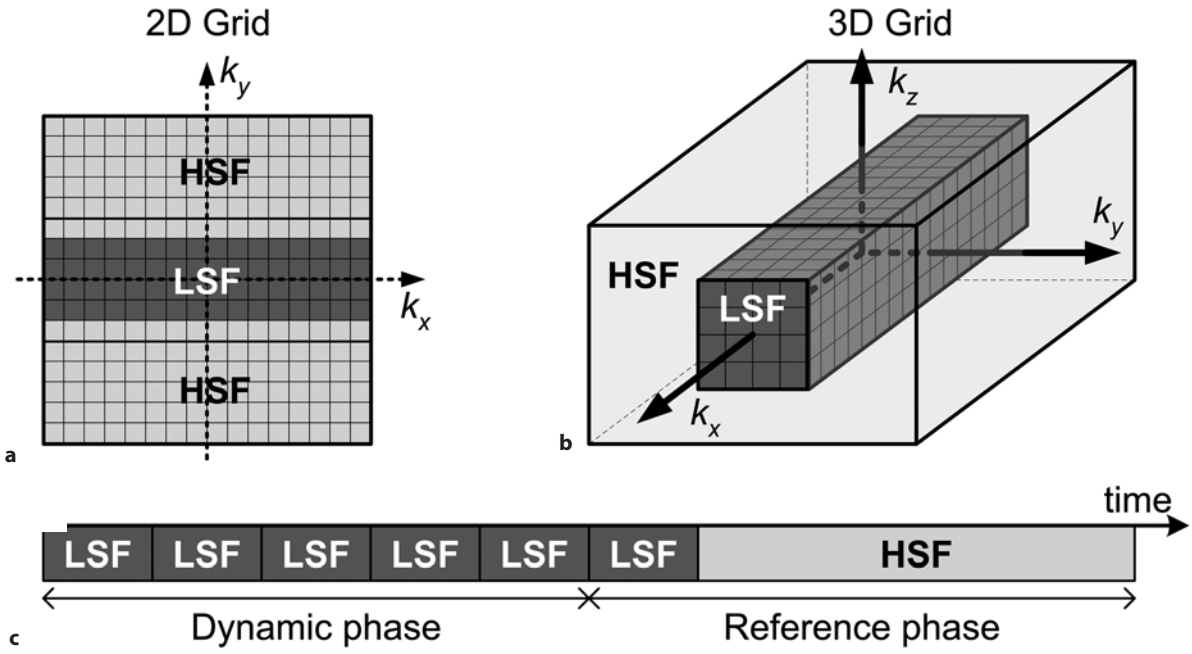

Fig. 7.8.a–c Keyhole imaging on a rectilinear 2D and 3D grid. The k-space is divided into a low spatial frequency region (*LSF*) around the k-space origin and the edge defining outer region of k-space (*HSF*). During the dynamic phase of the scan, the central region is repeatedly acquired with a high temporal and low spatial resolution. In a second phase of the acquisition, a reference data set with high spatial resolution is acquired. Subsequently, images are reconstructed from k-space data that share the identical high spatial frequencies with substituted dynamically acquired low spatial frequencies

tial frequencies, which have been acquired only once. The underlying assumption is that most of the signal changes are reflected in the central k-space region (see Fig. 7.8). In its most basic implementation, the central data are simply substituted for each time frame, but more complex algorithms also exist (Hu 1994).

In the 2D case, the keyhole region contains the data of echoes from central phase-encoding steps. In 3D spatial encoding, a column centered around the origin of k-space is acquired with full resolution in the readout direction and limited encoding steps in the phase-encoding direction, k_y, and the slice-encoding direction, k_z.

The drawback of the keyhole method is that the higher spatial frequencies are acquired only once. While dynamic low resolution images are captured, the image content corresponding to the high spatial frequencies is static. Therefore, the dynamic information is limited to objects exceeding a certain size, which is inversely proportional to the size of the central k-space region. If the relevant information under investigation contains changes in the outer portions of k-space, then keyhole imaging can produce images with an erroneous time course (Bishop et al. 1997; Oesterle et al. 2000).

7.6 TRICKS and TREAT

In contrast to keyhole imaging, 3D TRICKS (3D time-resolved imaging of contrast kinetics) (Frayne et al. 1996) also acquires the outer portions of k-space more than once. It is an acquisition scheme that combines various techniques including view sharing (Riederer et al. 1988), keyhole imaging (Jones et al. 1993; van Vaals et al. 1993), variable rate k-space sampling (Doyle et al. 1995), temporal interpolation (Polzin et al. 1996), and zero-filling (Du et al. 1994) for time-resolved CE-MRA and perfusion imaging.

High spatial and temporal resolution is achieved by sampling the data in k-space at different rates. Most of the energy of the MR signal is contained in the low spatial frequencies. Therefore, the acquisition time per image volume can be reduced by sampling the high frequencies less often than the low frequencies while still preserving the general flow patterns. The temporal undersampling of the edges of k-space leads to a complex relationship between temporal and spatial resolution.

In 3D TRICKS, k-space is divided into regions in k_y, k_z, or k_y and k_z based on their distance to the center of k-space. Figure 7.9a shows the original implementation where k-space is divided into three cuboids, labeled A, B, and C, based on the distance in the phase-encoding direction. The central region, A, contains the low spatial frequency information and is sampled every second time frame, while regions B and C are sampled every fourth time frame only (A,B,A,C,A,B,A,C,…). Frequently, an elliptical centric view-ordering scheme (Wilman and Riederer 1997) is used where the phase and slice-encode ordering is based on their distance in the k_y–k_z plane from the center of k-space. Figure 7.9b shows how the regions become a cylinder for the region containing lower spatial frequencies (label A) and cylindrical shells of equal volume for the regions representing higher spatial frequencies (labels B and C) in the k_y–k_z plane. In practice, most exams are acquired with a decreased spatial resolution in the slice-encoding direction, *z,* for a decreased imaging time and higher SNR. In this case, the higher spatial frequency regions become incomplete cylindrical shells. In addition, a slightly modified implementation of the TRICKS method, TREAT (time-resolved echo-shared angiographic technique), has been proposed, which spatially interleaves the higher spatial frequency regions (Fink et al. 2005).

Prior to the reconstruction, the acquired data are shared and interpolated as shown in Fig. 7.10. A complete 3D data volume is temporally interpolated by view sharing to reconstruct 3D data volumes for each time frame. Depending on the interpolation scheme, such as linear or nearest neighbor interpolation, the width of the interpolation window can vary. More advanced schemes incorporate the analysis of the contrast uptake curve into the interpolation. Some filtering effects are to be expected by using any interpolation scheme, which in turn may result in loss of contrast. In addition, ghosting artefacts may appear in the reconstructed images if the width of the interpolation window is longer than the passage time of the contrast agent (Maki et al. 1996).

3D TRICKS can acquire data sets continuously during the passage of the contrast agent and is relatively insensitive to variation in timing and the shape of the contrast bolus. An example for an examination of the lower legs is demonstrated in Fig. 7.11. The maximum intensity projection (MIP) images represent reformats of 3D volumes reconstructed for each time frame with a temporal resolution of 6.9 s. The data show snapshots prior to the arrival of the bolus, at peak arterial enhancement, and with venous contamination. No control volume or threshold has to be defined, and the sequence ensures the acquisition of the data during peak arterial enhancement. In addition, information on late filling vessels is obtained. However, some loss of spatial resolution has to be accepted for the gain in temporal resolution.

7.7 *k-t* Blast and *k-t* SENSE

In addition to techniques that take advantage of correlations either in k-space or in time as described above, the correlations in both can be explored to further accelerate image acquisition. Recently proposed examples of such approaches include unaliasing by Fourier-encoding the overlaps using the temporal dimension (UNFOLD) (Madore et al. 1999), sensitivity encoding incorporating temporal filtering (TSENSE) (Kellman et al. 2001), and highly constrained back projection (HYPR) processing

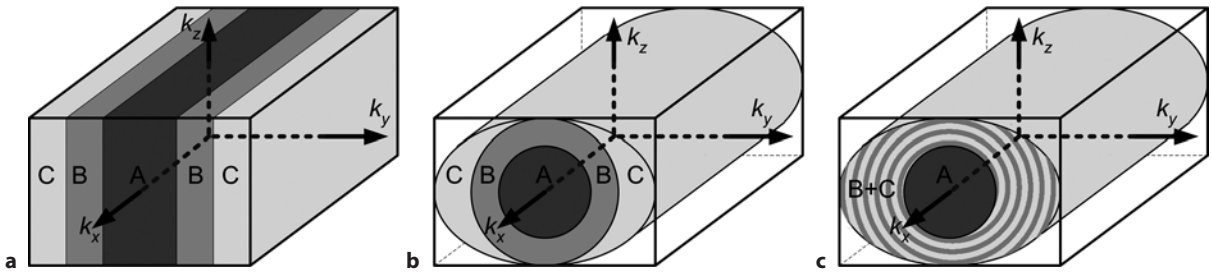

Fig. 7.9a–c. Different region encoding schemes for 3D TRICKS-like acquisitions with the readout direction in k_x and three regions, A, B, and C: linear centric encoding with cuboids **a**, elliptical centric view ordering **b**, and TREAT, an ordering scheme where the regions that define the higher spatial frequencies are interleaved in a spiral fashion **c**

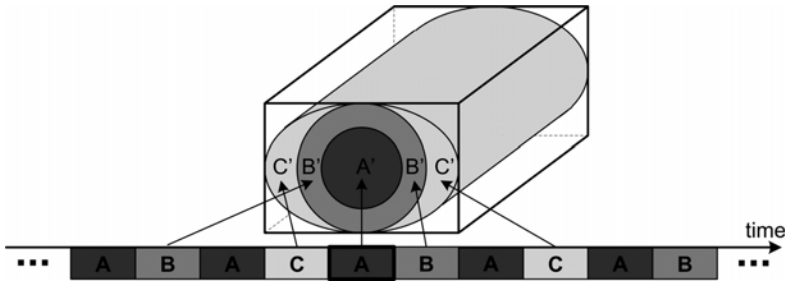

Fig. 7.10. The scheduling algorithm, view sharing, and temporal interpolation in 3D TRICKS. The regions are scheduled so that the central region, *A*, is acquired every other time frame, while the outer portions of k-space, *B* and *C*, are sampled less frequently. The acquired regions are shared between reconstructed images. In this example, the central region *A'* of the reconstructed time frame is the actually acquired region *A* while the regions *B'* and *C'* are linearly interpolated from adjacent regions. Image volumes are reconstructed for each interpolated k-space volume with an inverse 3D Fourier transform

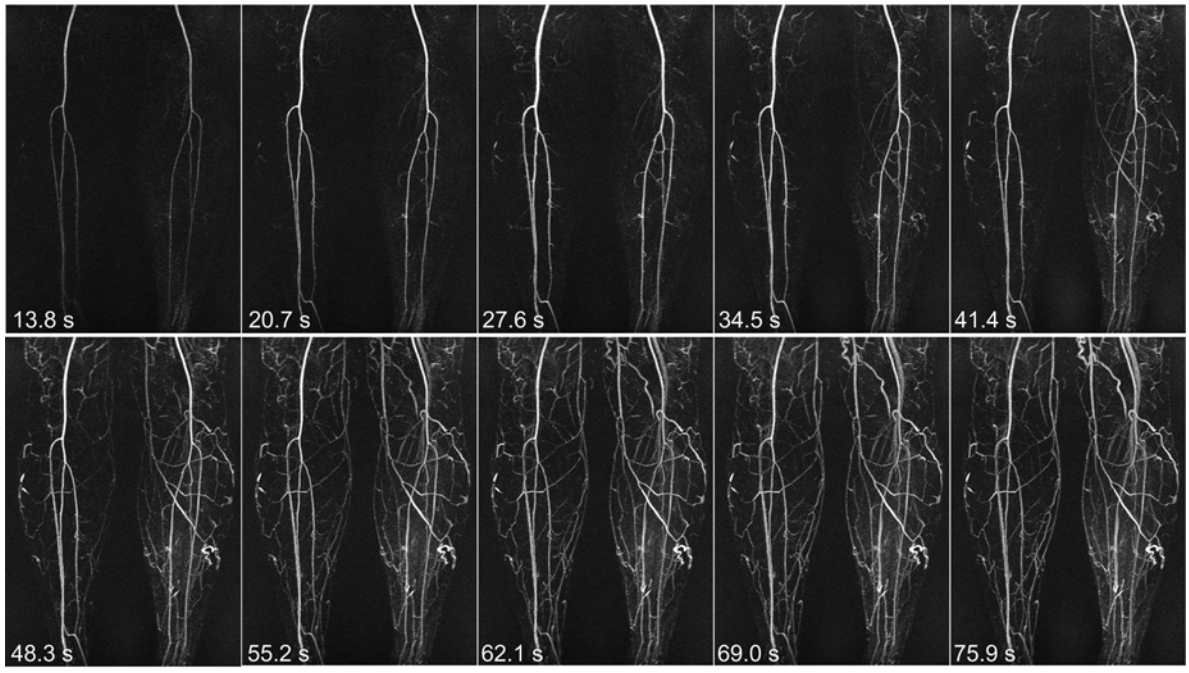

Fig. 7.11. 3D TRICKS examination in the lower legs of a patient. Shown are 10 consecutive coronal maximum intensity projection (MIP) images from a series of 20 time frames acquired during the passage of a gadolinium-based contrast agent. A new time frame is reconstructed every 6.9 s for a volume representing 72 slices. The subtraction of a pre-contrast mask suppressed stationary signal from the background. The first images show enhancement in the arteries without interference from veins and venous enhancement can be seen approximately 48.3 s after the start of the acquisition (courtesy of Frank R. Korosec, Ph.D., University of Wisconsin-Madison)

(Mistretta et al. 2006). In addition, the *k-t* BLAST (broad-use linear acquisition speed-up Technique) and *k-t* SENSE (sensitivity encoding) methods were proposed to facilitate rapid image acquisition for use with a single or multiple receiver coils, respectively (Tsao et al. 2003).

k-t BLAST and *k-t* SENSE are currently available on some commercial systems and use undersampling patterns in the spatiotemporal domain. The acquisition of dynamic data is viewed in a higher order space, the *k-t* space, where the time *t* spans an additional axis to the spatial coordinates. The exam-

ple of a cardiac cine acquisition in Fig. 7.12 illustrates some of the characteristics of this sampling pattern. The time series of images is represented by the spatial coordinates *x* and *y* and the time coordinate *t*. For each line along the *y*-direction, a new matrix is formed that represents the evolution of the signal along that line as a function of time. A Fourier transform is subsequently applied along the time axis to create a data representation in *y-f* space. Voxels on this line that experience no or little dynamic changes appear constant in the *y-t* matrix and are characterized by their low frequency components in the *y-f* matrix. Conversely, data points that change in signal intensity through the time series will be characterized by additional higher frequency components.

The acquisition of *k-t* BLAST images is divided in two stages: a training stage where data are rapidly acquired with a low spatial resolution in the phase-encoding direction and an acquisition stage where high resolution images are rapidly acquired by sparse sampling in k-space. This concept is illustrated in Fig. 7.13, where only the central 16 phase-encode lines are sampled for the first 40 time frames of a realtime cardiac application. In the acquisition stage, data sampling is accelerated by sparse sampling in *k-t* space, namely in the phase-encoding direction. In this example, only every fourth phase-encoding line is acquired for every time frame, thereby accelerating the acquisition by a factor of four. Sampling occurs on a sheared grid pattern where the acquired phase-encoding lines are shifted from one time frame to the next.

As a result of the undersampling, the data of the acquisition stage will produce images with foldover artefacts because the field of view was effectively reduced by the acceleration factor. This signal aliasing is resolved using a reconstruction filter derived from the expected signal distribution learned from the training stage. Tsao et al. (2003) discuss the details on the implementation of the multiple processing steps required for the image reconstruction.

The following acceleration factors have been reported for k-t BLAST and k-t SENSE, 4 for realtime cardiac imaging (Tsao et al. 2003), 3.8 and 5.3 for 2D cine phase contrast imaging (Baltes et al. 2005), and 4.3 for 3D cardiac cine acquisitions (Kozerke et al. 2004). While high acceleration factors are achieved at the expense of some noise amplifications, these studies showed that k-t BLAST processing generates images with small errors as compared to fully sampled data sets and is superior to a sliding window acceleration in terms of artefact power and signal error.

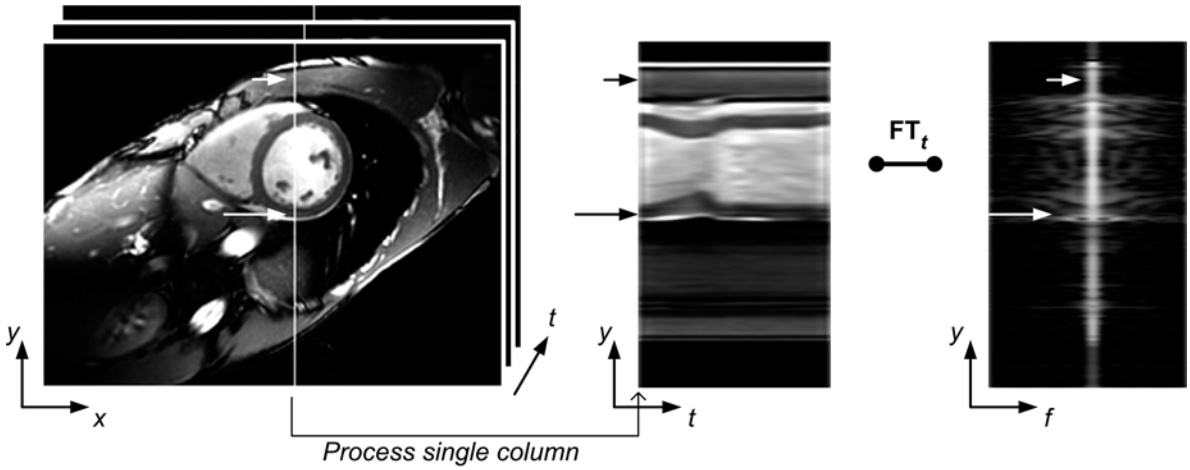

Fig. 7.12. Representation of a cardiac cine data set in *x-y* space (*left*). The processing of a single column through the left ventricle is shown in *y-t* (*center*), and *y-f* (*right*) space after a 1D Fourier transform in time. Areas with very little signal variation are represented by low frequency content as shown by the *short arrow*. Areas with high signal variations throughout the time series such as the voxels that partly represent fat and partly muscle throughout the cardiac motion are characterized by higher frequencies in the *y-f* space (*long arrow*)

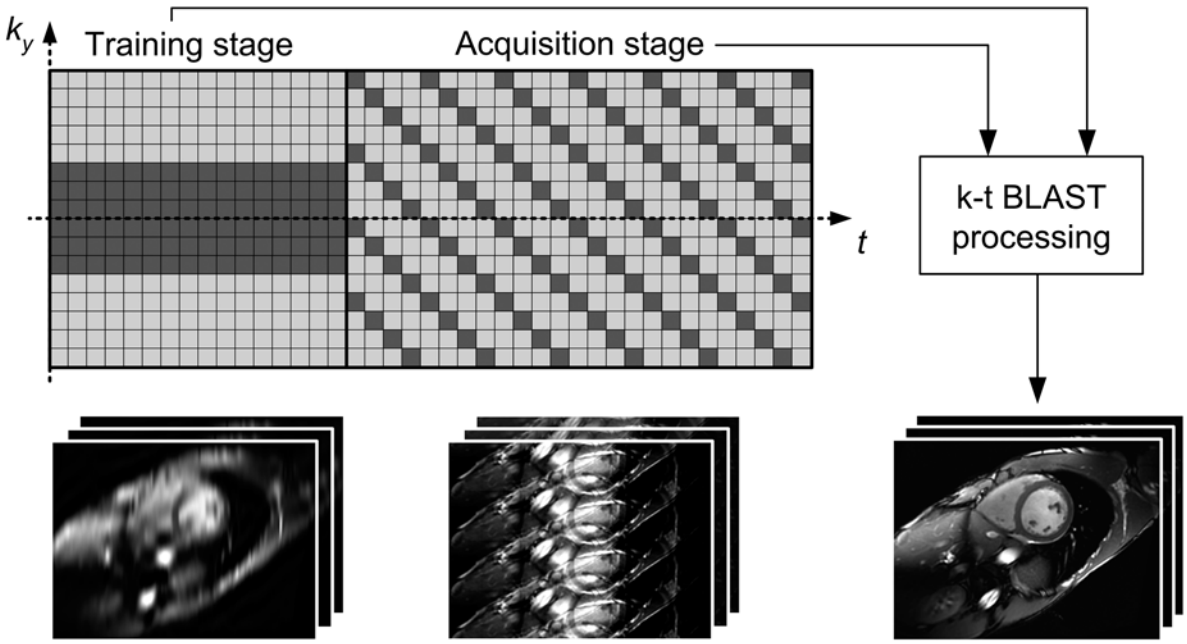

Fig. 7.13. Data sampling for *k-t* BLAST occurs in two stages: a training stage with fully sampled low resolution images and an acquisition stage with undersampled high spatial resolution images. In this diagram, only the central six phase-encoding lines are acquired during the training phase. Only every fourth phase encode is sampled in the acquisition stage and then shifted for the next time frame. With *k-t* BLAST processing, the data are analyzed and processed to reconstruct a fully sampled time series with a four-fold acceleration

References

Bakker CJ, Hoogeveen RM, Weber J, van Vaals JJ, Viergever MA, Mali WP (1996) Visualization of dedicated catheters using fast scanning techniques with potential for MR-guided vascular interventions. Magn Reson Med 36: 816–820

Baltes C, Kozerke S, Hansen MS, Pruessmann KP, Tsao J, Boesiger P (2005) Accelerating cine phase-contrast flow measurements using k-t BLAST and k-t SENSE. Magn Reson Med 54: 1430–1438

Bernstein MA, Fain SB, Riederer SJ (2001) Effect of windowing and zero-filled reconstruction of MRI data on spatial resolution and acquisition strategy. J Magn Reson Imaging 14: 270–280

Bishop JE, Santyr GE, Kelcz F, Plewes DB (1997) Limitations of the keyhole technique for quantitative dynamic contrast-enhanced breast MRI. J Magn Reson Imaging 7: 716–723

Chenevert TL, Helvie MA, Aisen AM, Francis IR, Adler DD, Roubidoux MA, Londy FJ (1995) Dynamic three-dimensional imaging with partial k-space sampling: initial application for gadolinium-enhanced rate characterization of breast lesions. Radiology 196: 135–142

Doyle M, Walsh EG, Blackwell GG, Pohost GM (1995) Block regional interpolation scheme for k-space (BRISK): a rapid cardiac imaging technique. Magn Reson Med 33: 163–170

Du YP, Parker DL, Davis WL, Cao G (1994) Reduction of partial-volume artefacts with zero-filled interpolation in three-dimensional MR angiography. J Magn Reson Imaging 4: 733–741

Duerk JL, Lewin JS, Wu DH (1996) Application of keyhole imaging to interventional MRI: a simulation study to predict sequence requirements. J Magn Reson Imaging 6: 918–924

Fink C, Ley S, Kroeker R, Requardt M, Kauczor HU, Bock M (2005) Time-resolved contrast-enhanced three-dimensional magnetic resonance angiography of the chest: combination of parallel imaging with view sharing (TREAT). Invest Radiol 40: 40–48

Frayne R, Grist TM, Korosec FR, Willig DS, Swan, JS, Turski PA, Mistretta CA (1996) MR angiography with three-dimensional MR digital subtraction angiography. TopMagn Reson Imaging 8: 366–388

Gao JH, Xiong J, Lai S, Haacke EM, Woldorff MG, Li J, Fox PT (1996) Improving the temporal resolution of functional MR imaging using keyhole techniques. Magn Reson Med 35: 854–860

Haacke EM, Lindskog ED, Lin W (1991) A fast, iterative, partial-Fourier technique capable of local phase recovery. J Magn Reson 92: 126–145

Hu X (1994) On the "keyhole" technique. J Magn Reson Imaging 4: 231

Jones RA, Haraldseth O, Muller TB, Rinck PA, Oksendal AN (1993) K-space substitution - a novel dynamic imaging technique. Magn Reson Med 29: 830–834

Kellman P, Epstein FH, McVeigh ER (2001) Adaptive sensitivity encoding incorporating temporal filtering (TSENSE). Magn Reson Med 45: 846–852

King KF (2004) Partial Fourier reconstruction. In: Bernstein MA, King KF, Zhou XJ (eds) Handbook of MRI sequences. Elsevier Academic Press, London, pp 546–557

Kozerke S, Tsao J, Razavi R, Boesiger P (2004) Accelerating cardiac cine 3D imaging using k-t BLAST. Magn Reson Med 52: 19–26

Madore B, Glover GH, Pelc NJ (1999) Unaliasing by Fourier-encoding the overlaps using the temporal dimension (UNFOLD), applied to cardiac imaging and fMRI. Magn Reson Med 42: 813–828

Maki JH, Prince MR, Londy FJ, Chenevert TL (1996) The effects of time varying intravascular signal intensity and k-space acquisition order on three-dimensional MR angiography image quality. J Magn Reson Imaging 6: 642–651

Margosian P, Schmitt F, Purdy D (1986) Faster MR imaging: Imaging with half the data. Health Care Instrumentation 1: 195–197

Markl M, Hennig J (2001) Phase contrast MRI with improved temporal resolution by view sharing: k-space related velocity mapping properties. Magn Reson Imaging 19: 669–676

McGibney G, Smith MR, Nichols ST, Crawley A (1993) Quantitative evaluation of several partial Fourier reconstruction algorithms used in MRI. Magn Reson Med 30: 51–59

Mistretta CA, Wieben O, Velikina J, Block W, Perry J, Wu Y, Johnson K, Wu Y (2006) Highly constrained backprojection for time-resolved MRI. Magn Reson Med 55: 30–40

Noll DC, Nishimura DG, Macovski A (1991) Homodyne detection in magnetic-resonance imaging. Ieee Trans Med Imaging 10: 154–163

Oesterle C, Strohschein R, Kohler M, Schnell M, Hennig J (2000) Benefits and pitfalls of keyhole imaging, especially in first-pass perfusion studies. J Magn Reson Imaging 11: 312–323

Polzin JA, Frayne R, Grist TM, Mistretta CA (1996) Frequency response of multi-phase segmented k-space phase-contrast. Magn Reson Med 35: 755–762

Riederer SJ, Tasciyan T, Farzaneh F, Lee JN, Wright RC, Herfkens RJ (1988) MR fluoroscopy: technical feasibility. Magn Reson Med 8: 1–15

Tsao J, Boesiger P, Pruessmann KP (2003) k-t BLAST and k-t SENSE: dynamic MRI with high frame rate exploiting spatiotemporal correlations. Magn Reson Med 50: 1031–1042

van Vaals JJ, Brummer ME, Dixon WT, Tuithof HH, Engels H, Nelson RC, Gerety BM, Chezmar JL, den Boer JA (1993) "Keyhole" method for accelerating imaging of contrast agent uptake. J Magn Reson Imaging 3: 671–675

Wilman AH, Riederer SJ (1997) Performance of an elliptical centric view order for signal enhancement and motion artefact suppression in breath-hold three-dimensional gradient echo imaging. Magn Reson Med 38: 793–802

Xu Y, Haacke EM (2001) Partial Fourier imaging in multi-dimensions: a means to save a full factor of two in time. J Magn Reson Imaging 14: 628–635

Part II:

Sequence Design for (Auto-Calibrated) Parallel Imaging

Measurement of Coil Sensitivity Profiles

8

Mathias Nittka

CONTENTS

8.1 Introduction

The concept of parallel imaging is based on local sensitivity variations of the receiving coil array (cf. chaps. 2 and 3). These so-called coil sensitivity profiles are incorporated into the spatial signal encoding. In turn, information about the sensitivity profile of each receiving coil element is a fundamental input parameter for image reconstruction.

The process of acquiring the coil sensitivity data is commonly called coil calibration. Precise coil calibration is a crucial step within parallel imaging and deviations can easily lead to a degradation in image quality. This chapter outlines the basic approaches and practical considerations of current calibration techniques.

M. Nittka, PhD
Siemens AG Medical Solutions, MREA, Karl-Schall-Str. 6, 91052 Erlangen, Germany

The most favourable coil calibration method would be to perform a single setup procedure once for each available receive coil array, e.g. by means of a phantom scan, and to apply this data set as a preset to any following parallel imaging scan.

There are two main reasons why such a "preset" calibration will not work in practice:

- The sensitivity profile of a coil is not static but is subject to changes induced by the interaction of the coils electromagnetic field and the dielectric properties of matter in its surrounding; thus, the coil profile varies when it gets close to a dielectric sample such as the human body. Even if the same coil is applied to the same body region, the variations from patient to patient may be not negligible.
- Many routinely used coils are flexible to adapt to different body shapes. If the coil bends, its receive characteristic will change, too.

Therefore, some kind of coil calibration has to be incorporated into every examination after patient and coils are positioned inside the scanner. For clinical routine use, the ideal calibration procedure should be fast, robust and reliable, ideally running unnoticed in the background without any need for user interaction. In practice, the most challenging task is to achieve a trade-off between additional calibration scan time and precision: high-precision calibration data, which might even be reacquired several times during an examination, may easily turn parallel imaging inefficient in terms of total scan time. Several different techniques for coil calibration found its way to clinical routine use. Each of them provides specific advantages and disadvantages for certain applications.

Before discussing some basic approaches, it should be noted that it is in general not required to determine absolute coil profiles for each coil. Most reconstruction methods applied with parallel imaging just require the relative sensitivity differences between the individual receive coils. This fact is significant, since of course the signal of any calibration scan performed on the patient

will consist of the superposition of the coils' sensitivity profiles with anatomical structures of different tissue types. One common method to calculate absolute sensitivity maps performs two interleaved acquisitions: the second acquisition uses the receive signal of the volume coil, which is usually only applied for RF transmission, instead that of the coil array. Taking the homogeneous receive profile of the volume coil as a reference, pure coil sensitivity maps can be determined by dividing out the underlying anatomy.

8.2 Two Basic Calibration Methods: Pre-scan vs Autocalibration

It is instructive to first look at two quite complementary calibration techniques, that both have found widespread use on commercial scanner software platforms: we refer to them here as the pre-scan method and the autocalibration method.

8.2.1 The Pre-scan Method

When faced with the problem of determining coil sensitivity profiles, one may consider this as the most straightforward approach: a coil calibration scan is performed right before the actual imaging scans are performed, i.e. when patient and coils are in position.

Typically, a 3D scan covering the maximum possible volume is performed. Any following parallel imaging scan may extract the coil calibration data from this data set by interpolation to the actual slice geometry (Fig. 8.1). In order to restrict the scan time, a fast gradient-echo sequence is applied with modest spatial resolution, resulting in a scan time well below a minute.

8.2.2 The Autocalibration Method

The autocalibration method integrates the acquisition of coil calibration data into the imaging scan instead of performing it as a separate calibration step. It was originally introduced as a SMASH variant (Jakob et al. 1998, Heidemann et al. 2001) but has meanwhile been applied with different reconstruction types (e.g. Griswold et al. 2002).

A few additional phase-encoding lines are added to the k-space sampling scheme of the accelerated sequence (Fig. 8.2). These additional calibration lines fill in the "gaps" in the central k-space region, which otherwise would be left out by the accelerated acquisition.

Thus, the central region of k-space is fully sampled to some extent and may supply the coil calibration data for the image reconstruction process. The k-space-based reconstructions make direct use of the additional lines to determine the reconstruction coefficients (upper row of Fig. 8.2). Image domain related methods Fourier-transform the fully sampled inner k-space region to a low-resolution image for each coil

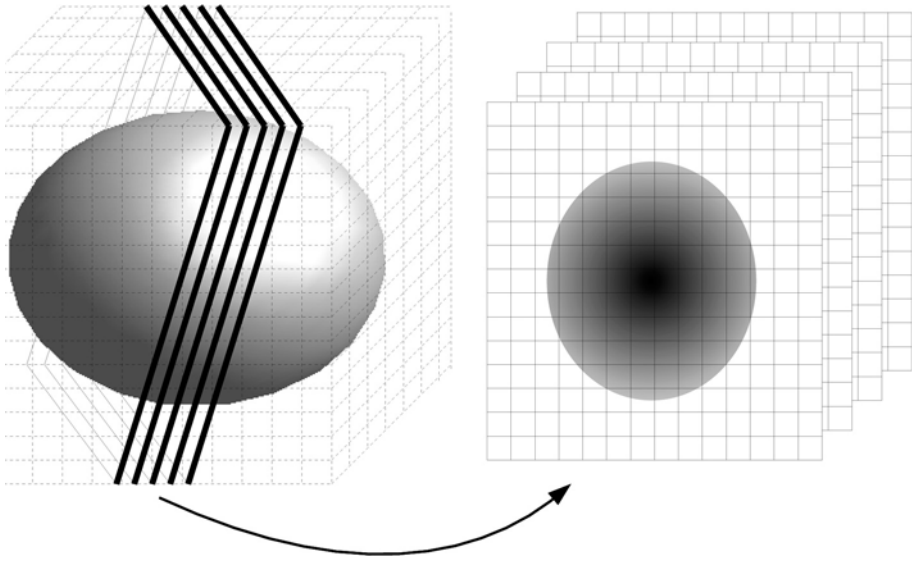

Fig. 8.1. A 3D pre-scan method. The whole imaging volume is covered by a 3D calibration scan. The coil profiles for any slice orientation may be extracted before image reconstruction.

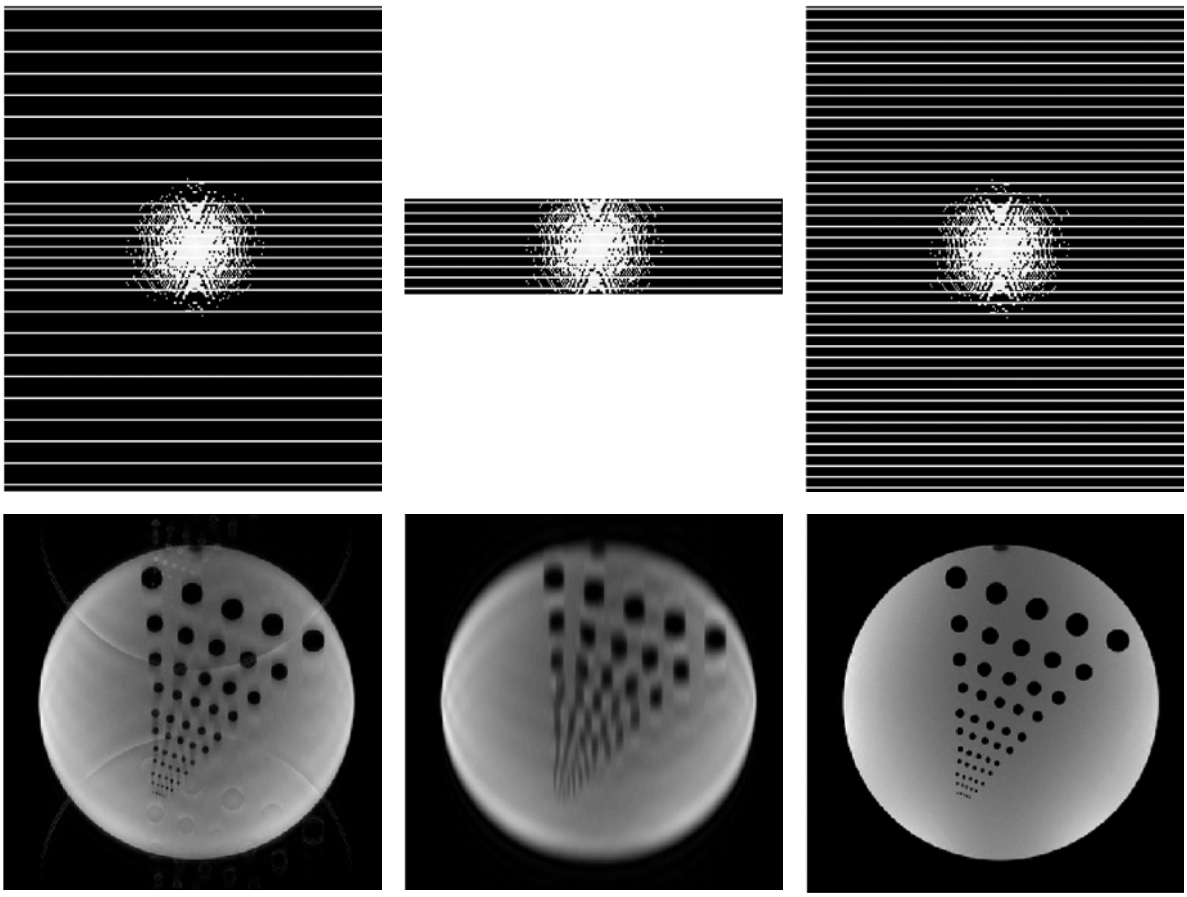

Fig. 8.2. Autocalibration method. Additional lines are added to the undersampled acquisition (*left*) resulting in a fully sampled, low-resolution image for each slice (*centre*), that may be used to reconstruct the final high-resolution image (*right*). *Upper row:* acquisition scheme in k-space. *Lower row:* corresponding data sets of upper row after Fourier transform.

element and extract the sensitivity information from them (lower row of Fig. 8.2).

In the ideal case, the pre-scan method offers the advantage that the calibration scan has to be performed only once for an examination. But there are cases that may turn this property into a disadvantage: any time that the coil profiles change, e.g. by an unwanted movement of the patient, the resulting mismatch between pre-scan and imaging scan may lead to artefacts. If the coil setup is changed intentionally, e.g. if the patient table is moved to another scan region position, the calibration pre-scan has to be repeated. The risk of unintended coil displacement is low for rigid, non-flexible coils. But even for rigid coils the problem might occur that parts of the patients body move to regions that did not contain any structures at the time the calibration took place: a priori, no coil sensitivity information is available within such regions. Such may occur, for example, for breath-hold exams, if a deep breath-hold moves the anterior body surface into regions that were not covered during the pre-scan. In such cases, an extrapolation of the pre-scan data is required, which may not be sufficiently accurate.

The intrinsic property of autocalibration that each slice carries its own calibration data is very appealing. Neither an interpolation to the scanned slice geometry is necessary, nor is there a problem if the coil position changes during the examination (due to patient movements or due to imaging protocols that scan at different table positions). Further on, the calibration lines may not only be used for the calibration but can also be incorporated into the final image, thus increasing the signal-to-noise ratio; however, autocalibration is also accompanied by a number of drawbacks.

Firstly, since the calibration data are part of the actual imaging scan, they do also carry the image contrast properties determined by the type and timing of the imaging sequence. This is not so much an issue for k-space based reconstruction algorithms (these benefit from the fact that the calibration lines are closely related to the image data). But this may cause complications for reconstructions that take place in the image domain: after the data set is Fourier transformed, the resulting calibration images may be superimposed by strong contrast or phase variations (e.g. gradient-echo sequences with opposed phase for water and fat) making it difficult to extract valid coil profiles from such images.

A more severe disadvantage may come along with the additional scan time required by the additional calibration lines. If the additional calibration lines make up for just a small fraction of the scanned matrix size, as it is the case for high-resolution protocols, the scan time is increased only by a few percent which can be regarded as well tolerable. If, however, the matrix size decreases and the acceleration factor increases, a high fraction of calibration lines may consume a considerable part of the acquisition time, turning the autocalibration approach ineffective.

Common to all imaging approaches that have to acquire coil calibration data is the question of which spatial resolution is required, since lower resolutions enable much faster calibration procedures. Fortunately, the resolution of the sensitivity map may be considerably lower than that of commonly used imaging protocols, since in general the sensitivity profiles of coils change smoothly; however, care has to be taken, if the coil wires are located close to the skin or if the diameter of the coil elements becomes very small: both effects result in high local field variations leading to reconstruction artefacts if not properly resolved by the calibration scan. Since many surface coil arrays are designed to be as close to the body surface as possible, some vendors suggest to locate additional distance pads between coil and patient, when these coils are used for parallel imaging.

8.3 Tailored Calibration Strategies

The broad range of applications that benefit from parallel imaging has led to a variety of sophisticated calibration approaches tailored for specific applications. The following two methods shall exemplify this for a number of practical aspects.

8.3.1 The Sequence-Based Pre-scan Method

The sequence-based pre-scan method combines the advantage of a fast, separately acquired calibration scan with that of an up-to-date calibration dataset of an autocalibration approach: a calibration scan is run directly prior (or after) each imaging scan (Fig. 8.3). Thus, each image is supplied with an up-to-date calibration data set.

This approach allows to tailor the calibration scan to the specific needs of different applications:

- Since the calibration scan is independent from the actual sequence, it may circumvent the problems of autocalibration discussed above (image contrast in calibration data), but keeping the advantage of constantly updated calibration data.
- Even though the calibration time has to be spent for each imaging sequence, it can be generally acquired much faster than a single 3D pre-scan, since the acquisition can be restricted to the current slice geometry instead of having to cover the whole volume.
- For certain pulse sequence types, the autocalibration approach might not be favourable. For example, single-shot sampling schemes, such as echo-planar imaging (EPI) or single-shot turbo spin echo sequences, strongly benefit from parallel imaging techniques, because the echo-train length is considerably reduced. Autocalibration would counteract this advantage by inserting additional echoes.
- The EPI provides a further example of how a dedicated calibration pre-scan may be adapted to sequence-specific calibration problems: EPI is often accompanied with strong susceptibility-induced distortions that might be difficult to reconstruct on the basis of a non-distorted calibration scan. The reconstruction may be facilitated, if an EPI sequence is employed for the calibration scan as well, thus intrinsically matching the geometric properties of the calibration data to the image data.

8.3.2 Self-calibration Methods

Some applications offer the advantageous situation that they do not require a separate calibration scan at all: the coil calibration data can directly be extracted from the imaging data. Two examples are radial sampling schemes and certain dynamic studies:

- If dynamic processes are scanned by succeeding image series, such as commonly performed for

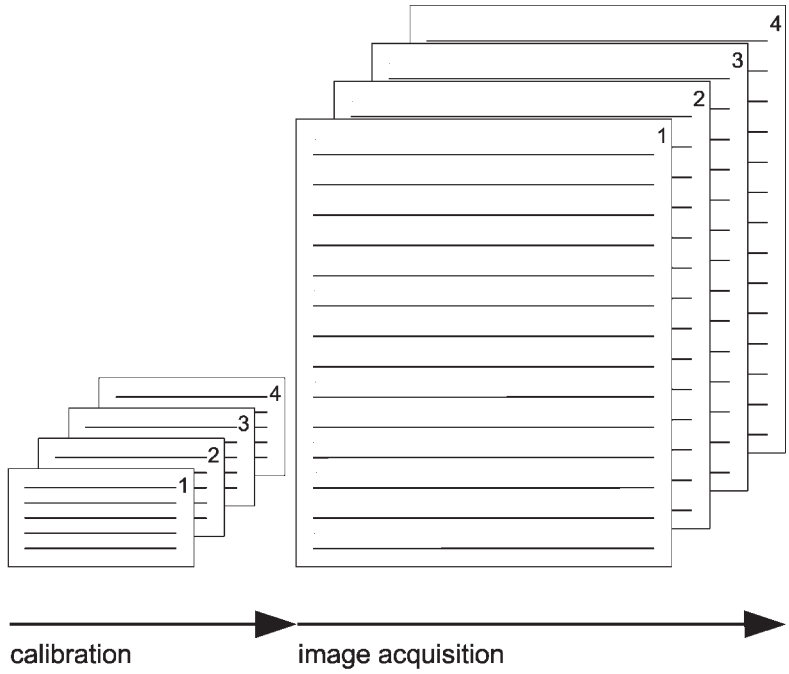

Fig. 8.3. "Sequence-based pre-scan" method. A calibration scan is performed immediately before (or after) each imaging sequence. In contrast to a single 3D (whole volume) pre-scan, the calibration scan only has to cover the slice geometry of the current sequence.

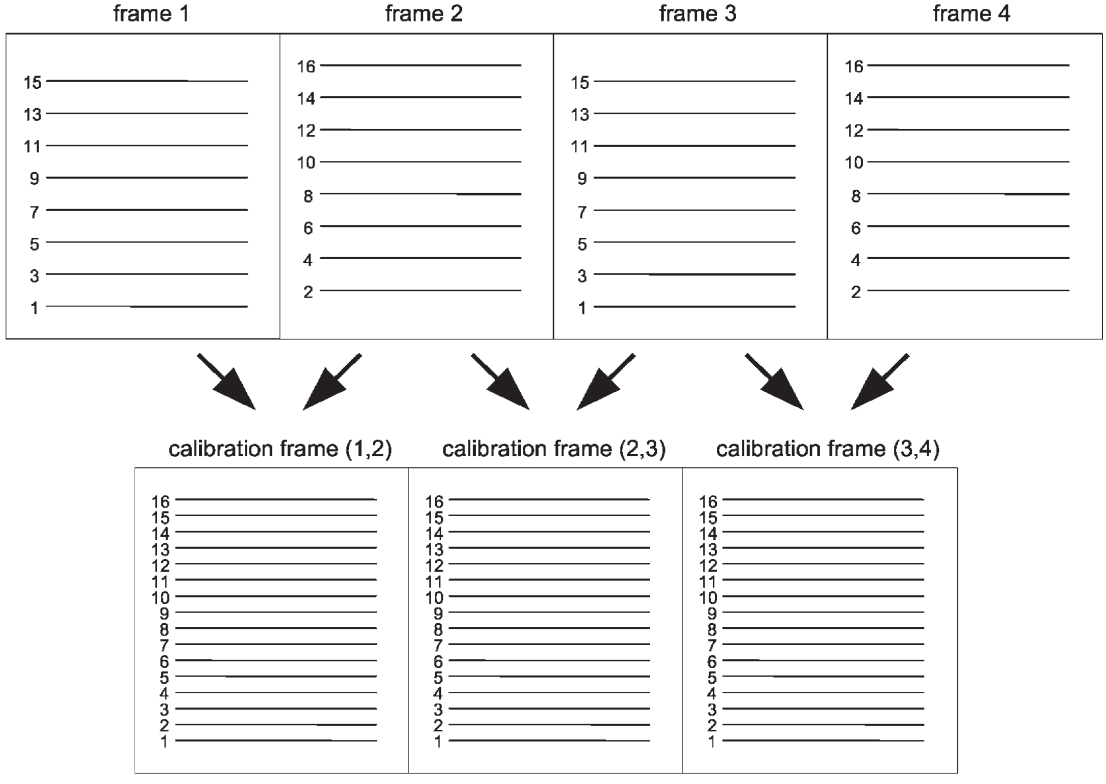

Fig. 8.4. Self-calibration scheme for time series. Succeeding undersampled frames of a time series are sampled in an interleaved fashion. The diagram shows a factor-2 accelerated acquisition scheme, where each frame either scans even or odd lines. An non-aliased calibration data set can be extracted for each pair of succeeding frames.

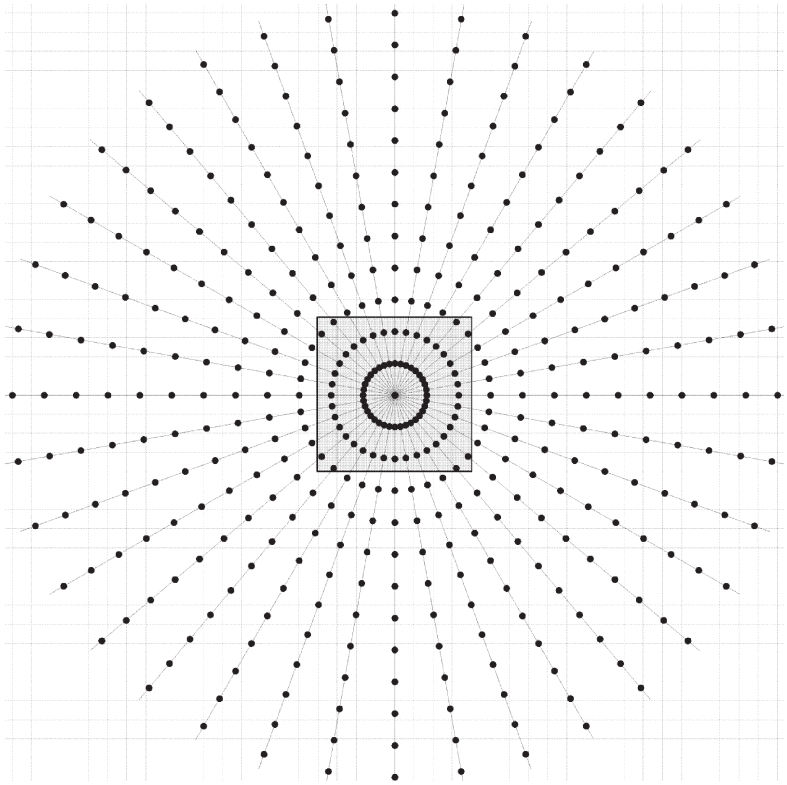

Fig. 8.5. Self-calibration method for radial scanning. The central k-space region of a radial acquisition is sampled with higher density than the outer region; thus, a non-undersampled region for coil calibration may be extracted (*grey region*).

cardiac cine imaging, self-calibrating parallel imaging can be easily achieved (cf. chap. 12; Kellman et al. 2001). A simple line-sharing scheme from succeeding time frames provides a non-undersampled image data for coil calibration, if the phase-encoding lines are sampled in an interleaved fashion (Fig. 8.4). The reduced temporal resolution of the calibration data subsets is not a problem, unless the coil profiles change considerably from frame to frame.

- It is the very nature of radial sampling schemes that the region towards k-space centre is sampled more densely than outer regions (Fig. 8.5); thus, an inner k-space region with dense sampling may provide the required calibration data to reconstruct missing k-space data in the subsampled outer k-space region.

8.4 Conclusion

The described methods for the measurement of coil sensitivity profiles have advantages and disadvantages in terms of time efficiency, user comfort, or robustness of reconstruction. Ideally, the optimum method should be selected depending on the application, pulse sequence, and anatomical region being imaged; however, in many cases, a certain method will be used because of the development history of the applied software or the general philosophy of the manufacturer who might prefer one of the described approaches. As a consequence of such differences, commercially available imaging systems still exhibit weaknesses and strengths in different areas of MRI examination.

References

Griswold MA, Jakob PM, Heidemann RM, Nittka M, Jellus V, Wang J, Kiefer B, Haase A (2002) Generalized autocalibrating partially parallel acquisitions (GRAPPA). Magn Reson Med 47:1202–1210

Heidemann RM, Griswold MA, Haase A, Jakob PM (2001) VD-AUTO-SMASH imaging. Magn Reson Med 45:1066–1074

Jakob PM, Griswold MA, Edelman RR, Sodickson DK (1998) AUTO-SMASH, a self-calibrating technique for SMASH imaging. MAGMA 7:42–54

Kellman P, Epstein FH, McVeigh ER (2001) Adaptive sensitivity encoding incorporating temporal filtering (TSENSE). Magn Reson Med 45: 846–852

Conventional Spin-Echo and Gradient-Echo Pulse Sequences

9

Olaf Dietrich

CONTENTS

9.1 Introduction

The basic idea of parallel imaging is to reduce the number of acquisition steps (i.e. phase-encoding steps) by decreasing the sampling density in k-space. Artefacts, in particular aliasing artefacts, that would result from the reduced sampling density are compensated by employing image data from several independent coil elements with different spatial sensitivity profiles for reconstruction. This basic concept of parallel imaging, i.e. reducing the sampling density and increasing the number of coil elements, can be combined with almost all types of MR pulse sequences. The only precondition with respect to the pulse-sequence design is that the phase-encoding sampling density in k-space can be varied, and this is true for virtually all pulse sequences that acquire at least two-dimensional k-space data, i.e. for all sequences apart from exotic techniques such as column-selective MRI or line scan imaging (Maudsley 1980; Gudbjartsson et al. 1996). The latter sequence types can, however, benefit from some more general parallel-imaging approaches, e.g. by acquiring data from two separate volumes at once. In this case more complex pulse-sequence modifications, such as the insertion of special RF pulses, are required (Larkman et al. 2001; Breuer et al. 2005).

Parallel imaging can be combined with conventional Cartesian k-space trajectories as well as with non-Cartesian sampling strategies such as radial or spiral trajectories; however, the complexity of the image reconstruction differs substantially depending on the k-space sampling strategy. Parallel imaging with non-Cartesian k-space trajectories requires very complex and time-consuming reconstruction algorithms and, thus, has not yet found general acceptance in clinical routine. More details about parallel imaging with non-Cartesian k-space techniques can be found in Chap. 6. The following sections discuss the application of parallel imaging in several basic pulse sequence types such as spin-echo or gradient-echo techniques. Generally, Cartesian k-space sampling is assumed, although many conclusions remain valid for other trajectories as well.

9.2 Spin-Echo and Gradient-Echo Sequences with Long Repetition Times

Spin-echo pulse sequences were historically the first sequences applied for MR imaging. They are still in general use in certain areas of MRI, in particular in T2- and T1-weighted imaging of the brain, because of their well-established contrast properties which are not fully reproduced by alternative techniques such as the faster turbo-spin-echo sequences (Henkelman et al. 1992; Stables et al. 1999). The main disadvan-

O. Dietrich, PhD
Department of Clinical Radiology, University Hospitals – Grosshadern, Ludwig Maximilian University of Munich, Marchioninistr. 15, 81377 Munich, Germany

tage of the spin-echo technique is the long acquisition duration of this sequence type: only a single line of k-space is acquired after each excitation, and excitations are separated by the repetition time, TR; thus, the total duration of acquisition is the product of the number of k-space lines and TR. The repetition times vary between about 600 ms for T1-weighting and 3000 ms for T2-weighting, resulting in acquisition durations between about 2:30 and 13 min for raw data with 256 lines of k-space. Fortunately, the long TR can be used to interleave the acquisition of several slices such that the acquisition of a complete multi-slice data set (and not only a single slice) is possible within the acquisition duration mentioned above.

To restrict the acquisition time of conventional spin-echo sequences, the number of phase-encoding steps is usually decreased by choosing a rectangular field of view. A further acceleration could be achieved by partial-Fourier techniques (MacFall et al. 1988; McGibney et al. 1993), however, at the cost of reduced image quality; thus, parallel imaging becomes highly attractive to either reduce the acquisition duration or to increase the maximum spatial resolution achievable within a given scan time. The main disadvantage of parallel imaging, the increased image noise, is often acceptable in spin-echo techniques because of the originally high signal-to-noise ratio of these techniques.

Parallel imaging always requires information about the spatial coil sensitivities that can be acquired either in a separate scan or integrated in the pulse sequence to be accelerated (cf. Chap. 8 about coil-sensitivity measurements). Whereas the choice when and how to acquire these data can be crucial in the design of fast sequences as discussed below, this question is relatively uncritical for conventional spin-echo techniques. In general, the acquisition of the actual image data takes much longer than the measurement of the coil sensitivity information, since the latter can be calculated from data with low spatial resolution; hence, the acceleration achieved by parallel imaging is almost not influenced by the acquisition of this reference data.

Consider, for example, the acquisition of 224 k-space lines with a TR of 3 s for T2-weighted spin-echo imaging. The acquisition duration of 224×3=672 s (11:12 min) can be reduced to 336 s (5:36 min) by applying parallel imaging with an acceleration factor of R=2 (Fig. 9.1). This acceleration is only slightly reduced by the additional acquisition of, for example, 16 auto-calibration or "reference" lines to determine the coil sensitivities. The reference lines prolong the total acquisition time to 384 s (6:24 min) which is still a substantial acceleration by more than 5 min (Fig. 9.1c).

Similarly, the matrix size in T1-weighted spin-echo imaging can be doubled without increase of scan time using parallel imaging. With a TR of 600 ms, the original acquisition with 224 phase-encoding steps takes 134 s. Parallel imaging with an acceleration factor of R=2 can be used to increase image resolution to 448 lines in phase-encoding direction in the same time. The additional acquisition of 16 reference lines increases the imaging duration by only 10s to a total of 144 s.

The integrated acquisition of auto-calibration lines is, on the one hand, relatively inefficient in theses cases because of the long TR while fast gradient-echo sequences could be employed much more efficiently to determine the coil sensitivities. This disadvantage does not, on the other hand, result in critical time penalties; thus, applying parallel imaging in conventional single-echo sequences with long TR provides substantial benefits because of the originally very long acquisition durations independent of the used implementation details.

Gradient-echo methods with large (90°) flip angles and long repetition times can provide T1-weighted or T2*-weighted images. With respect to parallel imaging, these sequences are very similar to conventional spin-echo techniques with comparable timing, and the arguments considered above apply as well.

9.3 Turbo-Spin-Echo Sequences

Turbo-spin-echo sequences, i.e. sequences that acquire a series of spin echoes after a single excitation, have become one of the most important techniques for reliable and high-quality morphological MRI. These sequences, which are also known as fast-spin-echo sequences, have properties similar to those of the original spin-echo sequences but are substantially faster, e.g. the acquisition time of a turbo-spin-echo sequence with an echo train length of five is only a fifth compared with a corresponding spin-echo sequence.

Most of the considerations about spin-echo techniques apply to turbo-spin-echo sequences as well. Typical acquisition times are still in the range between 1 and 4 min since a part of the reduced acquisition

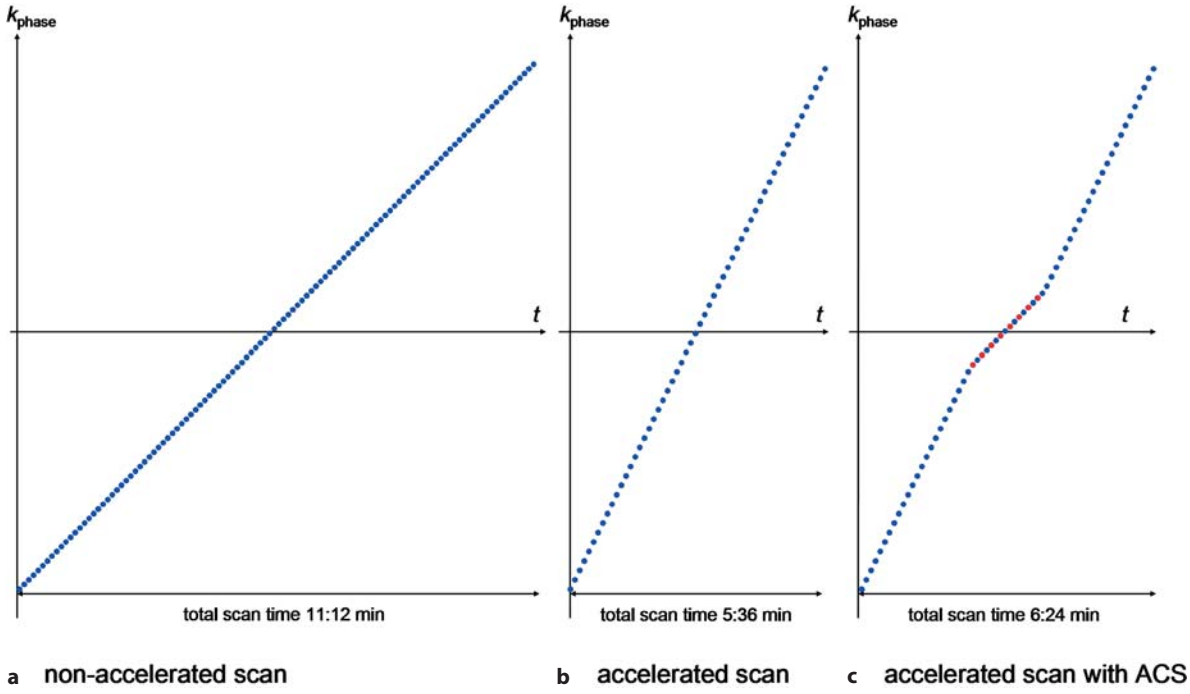

Fig 9.1a–c. Acceleration of conventional T2-weighted spin-echo imaging with TR of 3000 ms and 224 phase-encoding lines (each acquired line in k-space is illustrated as *filled circle*). **a** Non-accelerated acquisition with total scan time of 224×3s=672 s. **b** Scan with parallel-imaging acceleration factor R=2 and half scan time of 336 s. **c** Scan with acceleration factor R=2 and integrated acquisition of 16 additional auto-calibration signals (ACS) shown in *red*. The scan time is increased to 384 s; however, the acquisition is still about 5 min shorter than the original protocol without parallel imaging. (For better illustration, only every other k-space step is shown.)

duration is usually spent for higher spatial resolution; hence, combination with parallel imaging is still attractive to further accelerate the acquisition or to increase the matrix size.

A specific property of turbo-spin-echo sequences is that the echo train consists of spin echoes acquired after several different individual echo times. The effective echo time of a turbo-spin-echo sequence is defined by the echo time of the central k-space lines. A consequence of varying echo times for different parts of the k-space is that objects can appear slightly blurred in the image, i.e. the point-spread function has a larger width than in spin-echo sequences (Constable and Gore 1992; Chien and Mulkern 1992). Parallel imaging can be applied to reduce these effects by decreasing the echo-train length instead of shortening the total acquisition time. For example, the total scan time of a non-accelerated T2-weighting turbo-spin-echo sequences with an echo train length of 17, a TR of 5 s, and a resolution of 320 lines in phase-encoding direction is about 320/17×5 s=1:35 min. Applying parallel imaging with an acceleration factor of R=2, the acquisition time could be reduced by about 50%; however, it may be more beneficial in terms of image quality to combine parallel imaging with a reduction of the echo-train length from 17 to 9 echoes; thus, the scan time remains practically unchanged, but the turbo-spin-echo-related blurring will be reduced.

Since turbo-spin-echo sequences are considerably faster than spin-echo sequences, the averaging of several acquisitions becomes feasible as a means to increase the signal-to-noise ratio. In combination with parallel imaging, averaging can also be useful to reduce the sensitivity to motion artefacts. If the time saved by using parallel imaging is spent for averaging, the signal-to-noise ratio remains practically unchanged and the sensitivity to motion is reduced. In this case it is advantageous to acquire coil-sensitivity profiles only once and not repeatedly for each acquisition.

By increasing the length of the spin-echo train, the acquisition can be further accelerated to the point where all k-space lines are acquired after a single

excitation. These single-shot measurements and their special properties with respect to parallel imaging are discussed in Chapter. 10. Another technique becoming feasible with parallel imaging is three-dimensional turbo-spin-echo MRI. By combining strategies, such as variable flip angles, which allow very long echo trains (Mugler et al. 2000), and driven-equilibrium techniques to recover the longitudinal magnetization after the readout (Hargreaves et al. 1999; Melhem et al. 2001) with parallel imaging to reduce the acquisition duration, three-dimensional high-resolution turbo-spin-echo data sets with isotropic voxel size can be acquired in clinically acceptable scan times.

9.4 Fast Sequences for Dynamic MRI

Gradient-echo sequences are used for very different MRI applications. Apart from the gradient-echo sequences with long TR mentioned previously, there is a distinct group of gradient-echo sequences for fast data acquisition with small flip angles and short or very short repetition times. If these sequences are used for dynamic imaging, i.e. for repeated acquisitions of the same anatomical volume, their timing is usually carefully optimized to provide maximal temporal resolution. This can include the application of relatively low spatial resolution, e.g. 128×128 matrices, partial-Fourier techniques, or interpolation of slices in three-dimensional acquisitions. The purpose of all these approaches is to reduce the number of acquired k-space lines (i.e. phase-encoding steps) and, thus, to minimize the acquisition time for a single data set.

Obviously, parallel imaging is an additional important technique to accelerate these acquisitions. In contrast to the sequences discussed in the previous sections, now the strategy to acquire coil-sensitivity information becomes crucial, since the number of k-space lines acquired for imaging is relatively low and, thus, frequently of the same order of magnitude as the number of reference lines. Generally, integrated acquisition of reference lines, i.e. acquiring with a higher k-space sampling density in the centre of k-space than in the periphery, is relatively inefficient if data acquisition is either frequently repeated for dynamic MRI or if relatively small matrix sizes are acquired (Fig. 9.2).

Multi-slice perfusion imaging of the kidney or the myocardium, for instance, can be performed with a fast two-dimensional gradient-echo sequence. Assuming a 128×128 matrix and a 6/8 partial-Fourier acquisition, 96 k-space lines are acquired for each slice. With a repetition time of 5 ms, the acquisition of six slices requires 6×96×5 ms=2880 ms. Applying parallel imaging with an acceleration factor of 3, only 32 k-space lines are acquired for each slice; thus, six slices can be acquired in 6×32×5 ms=960 ms, i.e. the temporal resolution is substantially increased to slightly more than one data set per second. If 16 additional phase-encoding steps are performed to measure coil profile data (corresponding to a low resolution image consisting of 24 k-space lines), the acquisition time is increased to 1440 ms, i.e. an arterial bolus passage of 15 s is sampled by only 10 instead of 15 points. Thus, data describing the coil-sensitivity profiles should be acquired only once at the beginning of the measurement to obtain the highest possible temporal resolution. An alternative is fast auto-calibrating techniques such as the TSENSE acquisition (c.f. Chap. 12). It should be noted, however, that spoiled gradient-echo sequences are somewhat limited in their signal-to-noise ratio such that parallel imaging with acceleration factors >2 typically requires at least field strengths of 3 Tesla or above.

A considerably higher intrinsic signal-to-noise ratio is provided by steady-state free-precession (SSFP) sequences that are also frequently used for dynamic MRI with acquisition parameters similar to those of fast spoiled gradient-echo sequences. A typical application is imaging of the cardiac function. Due to their higher signal-to-noise ratio, they are generally much better suited for parallel-imaging applications with high acceleration factors, particularly at field strengths below 3 Tesla. Since the sequence timing is comparable to the one of gradient-echo sequences, all considerations discussed above apply and the integrated acquisition of reference lines should be avoided as well. More details about fast MR sequences for dynamic imaging are presented in Chapter11.

9.5 Conclusion

The main motivation for the application of parallel imaging in “conventional” pulse sequences is the

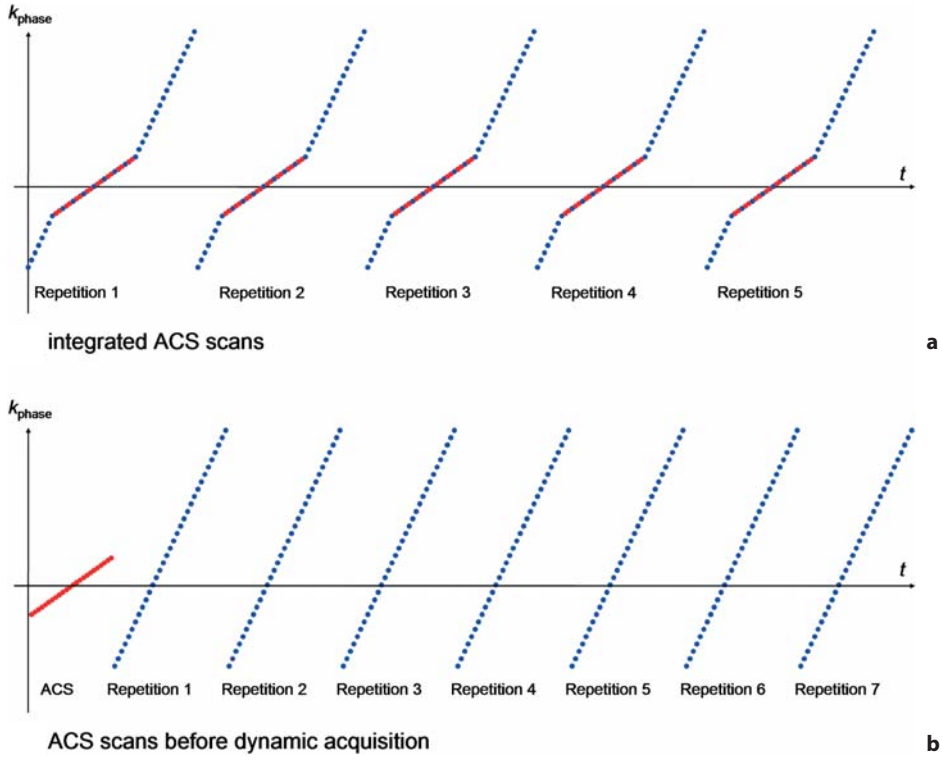

Fig 9.2a,b. Acquisition of auto-calibration signals (*ACS*) in fast pulse sequences for dynamic MRI. This example illustrates the repeated 6/8 partial-Fourier acquisition of a 128×128 matrix with a parallel-imaging acceleration factor of R=3. The ACS scans (shown in *red*) are either acquired integrated in each repeated measurement (**a**) or only once at the beginning of the dynamic imaging series (**b**). In the latter case, seven repetitions can be acquired in the same scan time required for five repetitions with integrated ACS scans.

acceleration of acquisition. This is relevant both for sequences with very long and for sequences with extremely short acquisition times. In the former case, the acquisition time can be easily reduced by several minutes, while in the latter, the temporal resolution for dynamic imaging can be substantially increased. The implementation of parallel imaging in these pulse sequences is relatively uncomplicated. In Cartesian k-space sampling, reducing the sampling density simply corresponds to choosing a smaller field of view. Only if the acquisition of coil-sensitivity profiles is to be integrated into the sequence, additional considerations are required to avoid inefficient sequence designs especially in dynamic MRI.

References

Breuer FA, Blaimer M, Heidemann RM, Mueller MF, Griswold MA, Jakob PM (2005) Controlled aliasing in parallel imaging results in higher acceleration (CAIPIRINHA) for multi-slice imaging. Magn Reson Med 53:684–691

Chien D, Mulkern RV (1992) Fast spin-echo studies of contrast and small-lesion definition in a liver-metastasis phantom. J Magn Reson Imaging 2:483–487

Constable RT, Gore JC (1992) The loss of small objects in variable TE imaging: implications for FSE, RARE, and EPI. Magn Reson Med 28:9–24

Gudbjartsson H, Maier SE, Mulkern RV, Morocz IA, Patz S, Jolesz FA (1996) Line scan diffusion imaging. Magn Reson Med 36:509–519

Hargreaves BA, Gold GE, Lang PK, Conolly SM, Pauly JM, Bergman G, Vandevenne J, Nishimura DG (1999) MR imaging of

articular cartilage using driven equilibrium. Magn Reson Med 42:695–703
Henkelman RM, Hardy PA, Bishop JE, Poon CS, Plewes DB (1992) Why fat is bright in RARE and fast spin-echo imaging. J Magn Reson Imaging 2:533–540
Larkman DJ, Hajnal JV, Herlihy AH, Coutts GA, Young IR, Ehnholm G (2001) Use of multicoil arrays for separation of signal from multiple slices simultaneously excited. J Magn Reson Imaging 13:313–317
MacFall JR, Pelc NJ, Vavrek RM (1988) Correction of spatially dependent phase shifts for partial Fourier imaging. Magn Reson Imaging 6:143–155
Maudsley AA (1980) Multiple-line-scanning spin density imaging. J Magn Reson 41:112–126
McGibney G, Smith MR, Nichols ST, Crawley A (1993) Quantitative evaluation of several partial Fourier reconstruction algorithms used in MRI. Magn Reson Med 30:51–59
Melhem ER, Itoh R, Folkers PJ (2001) Cervical spine: three-dimensional fast spin-echo MR imaging-improved recovery of longitudinal magnetization with driven equilibrium pulse. Radiology 218:283–288
Mugler JP III, Bao S, Mulkern RV, Guttmann CR, Robertson RL, Jolesz FA, Brookeman JR (2000) Optimized single-slab three-dimensional spin-echo MR imaging of the brain. Radiology 216:891–899
Stables LA, Kennan RP, Anderson AW, Gore JC (1999) Density matrix simulations of the effects of J coupling in spin echo and fast spin echo imaging. J Magn Reson 140:305–314

Single-Shot Pulse Sequences

10

Olaf Dietrich

CONTENTS

10.1 Introduction

Single-shot MRI pulse sequences acquire the complete k-space data required for image reconstruction after a single RF excitation. The most important single-shot techniques are single-shot gradient-echo techniques known as echo-planar imaging (EPI) and single-shot spin-echo techniques; the former were already suggested by Mansfield in 1977. In EPI a large number of gradient echoes are rapidly acquired either immediately following the excitation (called free-induction-decay EPI) or after one or several refocusing RF pulses (spin-echo EPI or stimulated-echo EPI). Single-shot spin-echo techniques are based on an echo train of multiply refocused spin echoes, i.e. the spins are refocused between successive echoes using, for example, 180° RF pulses. Spin-echo trains can be used in multi-shot and single-shot sequences. In both cases the generic technique is referred to as fast-spin-echo (FSE) or turbo-spin-echo (TSE) sequences. The single-shot spin-echo technique was first proposed by Hennig et al. (1986) under the acronym RARE (rapid acquisition with relaxation enhancement). Single-shot spin-echo sequences are frequently combined with half-Fourier techniques to reduce the length of the spin-echo train. This combination is sometimes called HASTE (half-Fourier-acquisition single-shot turbo-spin-echo) sequence.

The main difficulty of the single-shot techniques described above is the signal decay during the echo train due to transversal (T2 or T2*) relaxation. This signal decay limits the maximum duration of the echo train since, after a certain interval after excitation (e.g. 200 ms), no magnetization is left in the transversal plane (Fig. 10.1); thus, it does not make sense to use echo trains with an arbitrarily long duration, and the maximum number of echoes (i.e. the matrix size or image resolution) is restricted. A second problem arising from transversal relaxation is that echoes contributing to the same image are acquired with different signal intensities depending on their individual echo time. As a consequence, image artefacts arise, in particular blurring in phase-encoding direction is frequently observed. As discussed below, parallel imaging is a valuable method to overcome these disadvantages of single-shot sequences.

Most single-shot techniques acquire two-dimensional image data; however, three-dimensional techniques based on gradient echoes have also been proposed (Mansfield 1977; Song et al. 1994; Mansfield et al. 1995). Since the number of k-space lines required for a three-dimensional acquisition is typically substantially larger than for a two-dimensional image, echo trains tend to become very long resulting in very low signal of the majority of echoes because of transversal relaxation; however, with shortened echo trains due to parallel imaging, three-dimensional single-shot techniques might become much more attractive and applicable in the future.

O. Dietrich, PhD
Department of Clinical Radiology, University Hospitals – Grosshadern, Ludwig Maximilian University of Munich, Marchioninistr. 15, 81377 Munich, Germany

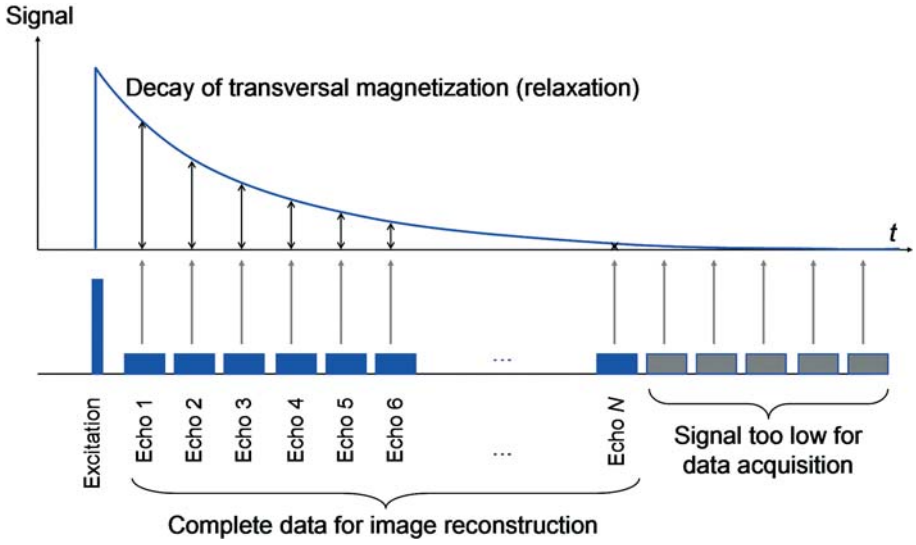

Fig 10.1. Single-shot sequences acquire the complete k-space data required for image reconstruction (echoes *1* to *N*) after a single RF excitation. The signal intensity decays during the acquisition of the echo train. This effect restricts the maximum length of the echo train and causes blurring of the resulting image.

10.2 Single-Shot Spin-Echo Techniques: RARE and HASTE

10.2.1 General Properties

In single-shot spin-echo techniques, the transversal magnetization decays exponentially with the time constant T2. After 3 × T2, the signal is decreased to about 5% of its initial intensity and, thus, becomes too low to acquire further spin echoes; hence, assuming typical T2 relaxation times between 35 and 130 ms depending on the examined tissue, the maximum duration of the echo train is restricted to 100 to 400 ms. Only special applications, such as MRI of liquids with very long T2 in MR cholangio-pancreaticography, is feasible with longer echo trains of several hundred milliseconds (cf. Chap. 22).

The maximum image resolution is restricted by the number of acquired echoes and therefore by the maximum echo-train duration, e.g. a typical echo spacing of 4 ms limits the number of echoes to about 100. These echoes can be used to fill, e.g. the k-space of a 256×96 acquisition (with 96 phase-encoding steps and anisotropic pixel size) or, using half-Fourier acquisition, of a 256×192 acquisition. The echo spacing can be reduced by increasing the receiver bandwidth or applying shorter RF pulses; however, this either decreases the signal-to-noise ratio of the acquisition or deteriorates slice profiles and increases the specific absorption rate (SAR).

A second point to consider is the image contrast, which is influenced by the effective echo time of the pulse sequence, i.e. the interval between excitation and the acquisition of the central k-space line. The effective echo time depends on the echo spacing and the selection and ordering of acquired k-space lines. The two most important k-space sampling schemes are centrically ordered and linearly ordered sampling (Fig. 10.2). Both schemes fulfil the condition that the time interval between the acquisitions of two adjacent k-space lines is constant for (almost) all lines; this condition prevents strong variations of signal intensity between neighbouring lines due to T2 relaxation. Obviously, with centrically ordered sampling, only very short echo times below 10 ms can be obtained, while with linearly ordered sampling of the full k-space, the echo time is half of the echo-train duration, e.g. about 200 ms. Using partial-Fourier or half-Fourier techniques, the echo time of linearly ordered sampling can be reduced down to a minimum of four to eight echo spacings, since a minimum of four to eight readouts before the k-space centre is required for phase correction.

Centrically ordered k-space sampling provides the shortest effective echo times as required, e.g. for proton-density-weighted or T1-weighted imaging. Nevertheless, linearly ordered k-space sampling is frequently preferred because of the shorter interval between the acquisitions of adjacent lines, which reduces image blurring; hence, reducing the minimal effective echo time of linearly ordered HASTE sequences is an important design issue for many imaging applications.

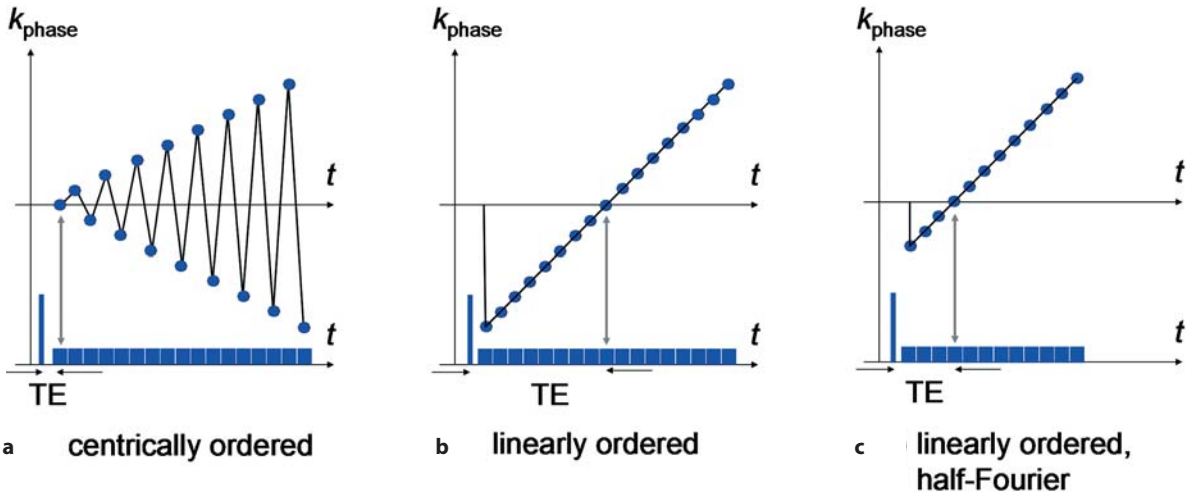

Fig 10.2a–c. Single-shot spin-echo sequences can acquire the lines in k-space (illustrated as *filled blue circles*) in different order; the most important schemes are **a** centrically ordered k-space sampling and **b** linearly ordered k-space sampling. **c** To reduce the minimal effective echo time, *TE*, (i.e. the interval from excitation to the readout of the central k-space line), linearly ordered k-space sampling is frequently combined with half-Fourier acquisition.

10.2.2 Parallel Imaging

Parallel imaging can be used to overcome several limitations of RARE or HASTE sequences: their maximum resolution can be increased, blurring can be decreased, and the minimal effective echo time can be reduced. Application of parallel imaging is relatively straightforward if the coil sensitivity information is acquired in a separate measurement independent of the single-shot application. In this case, the k-space distance, Δk, between adjacent lines is simply increased (by acquiring, for example, only every other line or every third or fourth line) as illustrated in Fig. 10.3). As a consequence, either the echo-train length can be reduced resulting in decreased T2 relaxation during readout and thus in decreased blurring (Fig. 10.4), or the sampled k-space range can be increased to acquire data of higher spatial resolution within the same total readout time as before. If image quality without parallel imaging is already substantially compromised by blurring, the former alternative is generally more attractive. An additional advantage is the reduced total duration of the acquisition enabling the acquisition of more slices, e.g. during one breath hold. It shouls be noted that the effective echo time is also substantially shortened due to parallel imaging, if the sequence samples the full k-space linearly ordered. The usually heavy T2 weighting is reduced, which might not be desired in all applications.

Alternatively, the usually low matrix size of single-shot spin-echo sequences can be increased, e.g. from 256×128 without parallel imaging to 256×256 with parallel imaging (Heidemann et al. 2003); thus, T2-weighted images with spatial resolution similar to much slower fast-spin-echo techniques (cf. Chap. 9) can be obtained by single-shot imaging.

A further important consequence of parallel imaging in single-shot applications in comparison with non-accelerated acquisitions with identical resolution is that fewer k-space lines with very low signal-to-noise ratio are acquired; thus, the average signal-to-noise ratio of all acquired k-space data is higher. This effect depends on the duration of the echo train and the T2 relaxation time of the imaged tissue and can partially compensate the intrinsically reduced signal-to-noise ratio of parallel imaging.

The described advantages of parallel imaging apply for centrically and linearly ordered k-space sampling as well as for full and partial-Fourier sampling; however, the reduction of effective echo time is a feature particularly interesting for half-Fourier sequences with linear k-space sampling. Since these sequences are frequently used for proton-density-weighted or T1-weighted MRI (using a magnetization preparation such as an inversion-recovery pulse), the shortest possible echo time is often desired. The effective echo time of these sequences is limited by the number of k-space lines acquired before the central line. These lines are required for phase correction. With k-space-based parallel-imaging techniques,

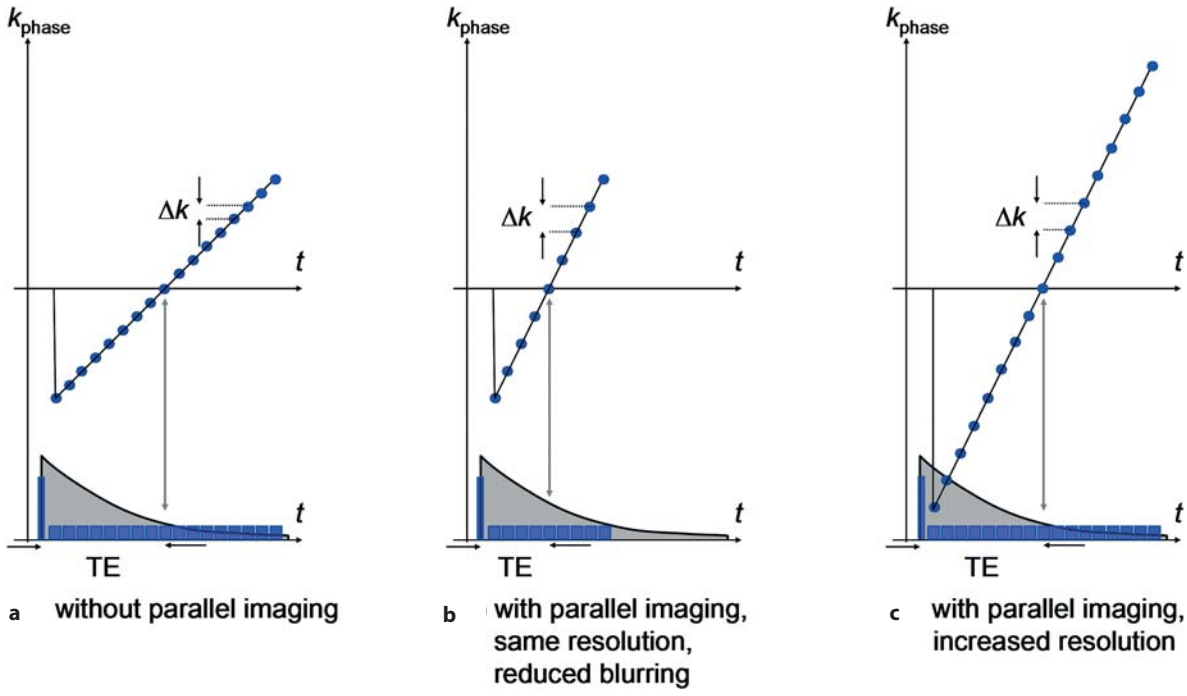

Fig 10.3a–c. Parallel imaging applied to a linearly ordered RARE sequence. **a** Acquisition without parallel imaging; all k-space lines (*filled circles*) are acquired. **b** Acquisition with parallel imaging (acceleration factor R=2) yielding the same spatial resolution as in **a;** only every other k-space line is acquired (i.e. the distance between lines in k-space, Δk, is doubled). The effective echo time (*TE*), the echo-train length, and, thus, image blurring, is reduced. **c** Acquisition with parallel imaging and the same echo-train length as in **a** in order to double the spatial resolution.

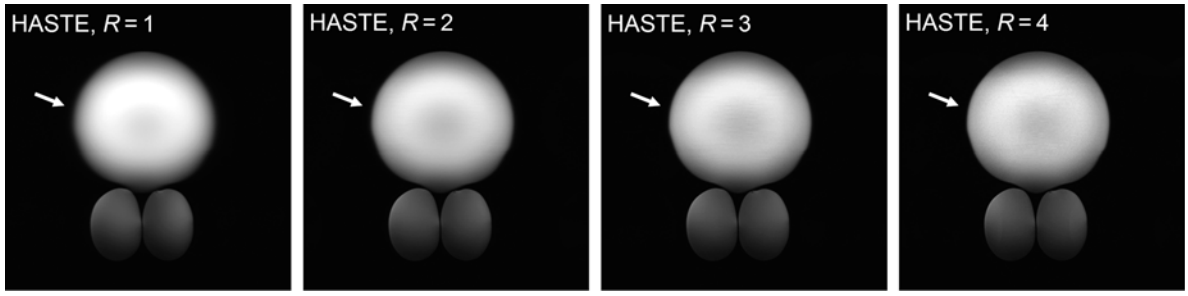

Fig 10.4. Phantom images demonstrate the reduction of blurring with increasing parallel-imaging acceleration factors, R, between 1 and 4. The images were acquired with a HASTE sequence at 3 T using a 12-element head coil, a 384×384 matrix, and phase encoding from left to right. The liquid in the large sphere has a shorter T2 relaxation time than the one in the small phantoms and, thus, exhibits more obvious blurring in phase-encoding direction (*arrows*).

such as GRAPPA, some of these lines can be generated synthetically, i.e. fewer lines have to be acquired before the central k-space line and the minimal effective echo time is reduced. The higher tissue signal at shorter effective echo times can also partially compensate the intrinsically reduced signal-to-noise ratio of parallel imaging (in addition to the effect described above which is caused by the reduced echo-train length).

10.2.3 Acquisition of Coil Sensitivity Information

In contrast to conventional spin-echo sequences (cf. Chap. 9), the integrated acquisition of auto-calibration signals containing coil sensitivity information may be disadvantageous in single-shot sequences. On the one hand, the echo train is prolonged by inserting

additional auto-calibration scans. This counteracts the attempt to shorten the echo train as much as possible in order to reduce blurring (and to compensate SNR losses). On the other hand, the minimal echo time of HASTE sequences cannot be reduced compared with non-accelerated imaging since the reference lines are acquired around the centre of k-space, i.e. at the very beginning of the echo train (Fig. 10.5); thus, the separate acquisition of either the spatial coil profiles or the auto-calibration signals required for k-space-based reconstruction techniques, such as GRAPPA, is frequently preferable for single-shot spin-echo sequences.

10.3 Single-Shot Gradient-Echo Techniques: EPI

10.3.1 General Properties

In single-shot gradient-echo techniques, the transversal magnetization decays rapidly with the time constant T2*. T2* is in general considerably shorter than T2 and in particular includes spin dephasing due to static magnetic field inhomogeneities. Typical T2* relaxation times range between 8 and 50 ms (Wielopolski et al. 1998; Barth et al. 1999) and depend on the shimming of the magnetic field as well as on the voxel dimensions. As a consequence of the short T2*, the total echo-train duration of single-shot gradient-echo sequences must be kept substantially shorter than of single-shot spin-echo techniques. Luckily, the echo spacing of gradient-echo techniques is also much smaller than that of spin-echo techniques, since no RF pulses and only short gradient pulses need to be applied between the readouts of successive lines; thus, a similar total number of echoes (about 100) can be acquired in single-shot gradient-echo MRI as in spin-echo MRI before the signal intensity has decreased too much for data acquisition.

The EPI sequences usually acquire the k-space lines linearly ordered, since, in this case, phase encoding during the echo train can be performed most efficiently by very small "blipped" gradients; thus, the minimal effective echo time depends (apart from matrix size and echo spacing) on the application of partial-Fourier techniques which allow reducing the number of phase-encoding steps before the acquisition of the central k-space line.

A major limitation of single-shot EPI sequences are severe image artefacts caused by chemical-shift and susceptibility effects. Spins with different Larmor frequencies are not rephased for each echo as in spin-echo techniques, but are allowed to evolve during the

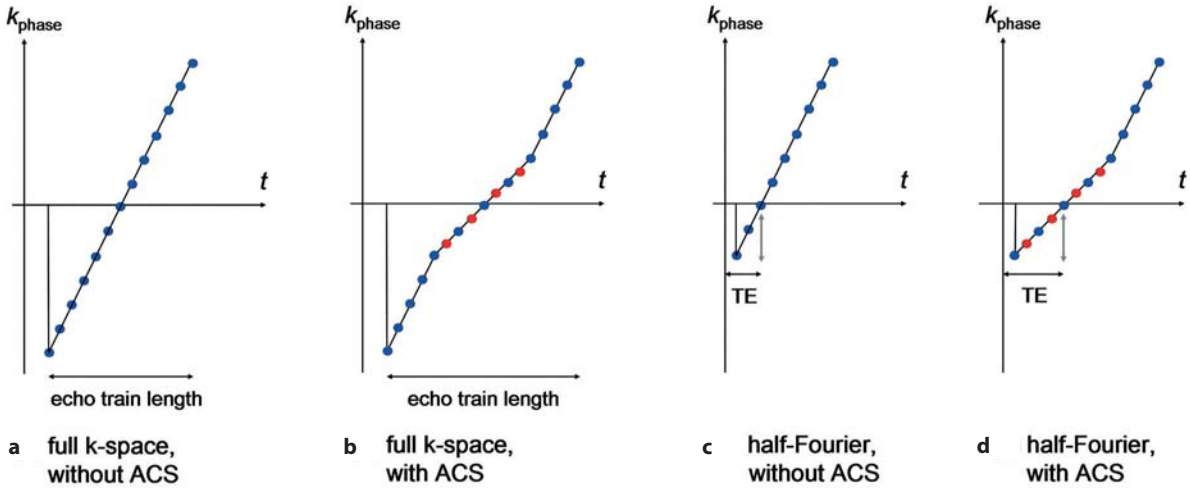

Fig 10.5a–d. Coil sensitivity information can be acquired either independent of the accelerated imaging scan or integrated in the actual acquisition as auto-calibration signals (*ACS*) shown in *red*. **a** Accelerated acquisition without ACS. **b** Accelerated acquisition with additional ACS. The total echo-train length is increased and the benefit of parallel imaging is reduced. **c** Accelerated half-Fourier acquisition without ACS. **d** Accelerated half-Fourier acquisition with additional ACS which increases the minimal effective echo time (*TE*).

echo train; thus, phase differences increase continuously during the acquisition. These additional phase differences in successive phase-encoding steps cause (frequently severe) image distortions whose extent depends on the ratio of the additional phase (proportional to the time interval between successive readouts Δt) and the phase difference induced by phase encoding itself, which is proportional to Δk; hence, two general strategies can be applied to reduce distortion artefacts caused by susceptibility effects: either Δk can be increased (i.e. the field of view is reduced in phase-encoding direction), or the interval between echoes, Δt, can be reduced (e.g. by increasing the receiver bandwidth).

10.3.2 Parallel Imaging

The benefits of parallel imaging for single-shot gradient-echo techniques include most of the advantages that are discussed for spin-echo-based techniques in section 10.2.1. In particular, either the echo-train length can be shortened or the spatial resolution (matrix size) can be increased with parallel imaging as illustrated in Fig. 10.3, e.g. T2*-induced blurring in the phase-encoding direction can be reduced with shorter echo trains. The implications for the minimum echo time and the signal-to-noise ratio are also analogous to the ones mentioned above: Shorter echo times can be achieved with parallel imaging and the inherent signal-to-noise loss of parallel imaging can be partially compensated by shorter echo trains with fewer echoes of low amplitude and by shorter effective echo times.

In addition to these effects, however, parallel imaging also reduces the image distortion caused by susceptibility effects. These distortion artefacts are proportional to the line distance in k-space, Δk, and this distance can be increased by a factor of 2 or higher using parallel imaging with an acceleration factor of R=2 or higher, respectively; thus, images with reduced distortions can be acquired as demonstrated in Fig. 10.6. Reducing image distortions is certainly one of the main motivations to apply parallel imaging to EPI sequences (Schmidt et al. 2005; Yang et al. 2004).

10.3.3 Acquisition of Coil Sensitivity Information

Integrated acquisition of coil sensitivity information is even less feasible for echo-planar techniques than for single-shot spin-echo sequences. The main

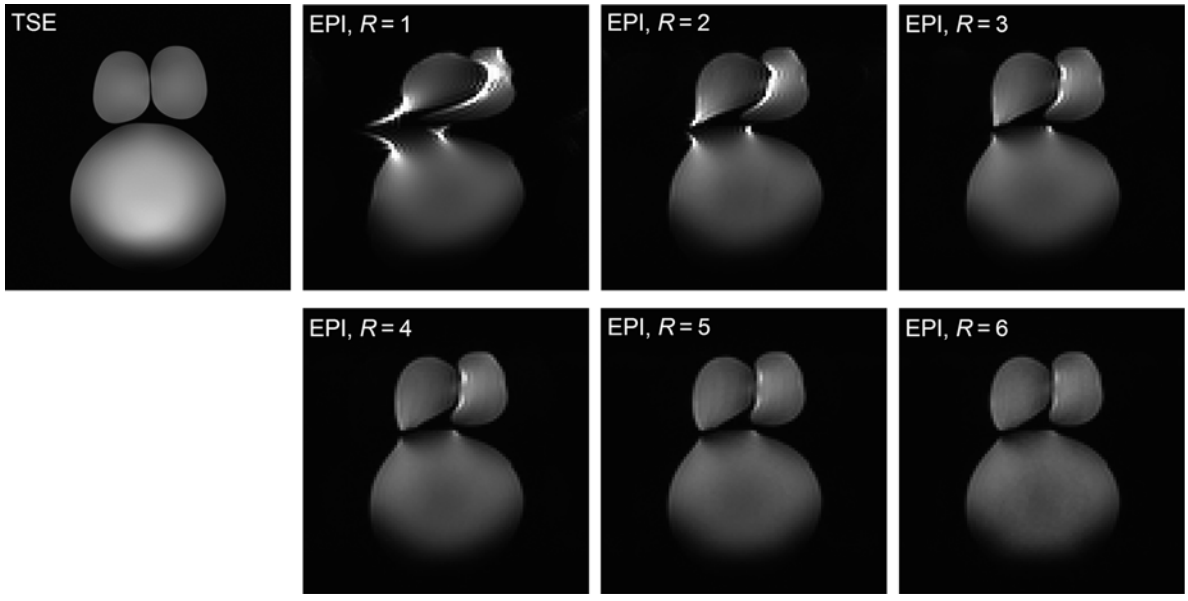

Fig 10.6. Phantom images demonstrate the effect of parallel imaging with different acceleration factors, *R*, between 1 and 6. In echo-planar imaging (*EPI*), severe distortion artefacts occur without parallel imaging and are reduced at increasing acceleration. The EPI acquisitions were performed at 3 T with a 12-element head coil, acquiring a 128×128 matrix with phase encoding from left to right. The non-distorted reference image was acquired with a turbo-spin-echo sequence with a 320×320 matrix and an echo-train length of 15.

problem is the irregular line spacing in k-space as illustrated above in Fig. 10.5. Since the line distance, Δk, is related to the extent of distortion artefacts, different levels of distortions will be "seen" by the low-resolution ACS acquisition with small Δk and by the under-sampled accelerated data set with large Δk; thus, the coil position information contained in the ACS is not consistent with the coil positions required for reconstruction of the under-sampled raw data resulting in reconstruction artefacts.

Similar problems can occur, however, when coil sensitivity information is taken from completely undistorted reference data such as obtained by short-TE gradient-echo scans. Care must be taken that the more or less distorted geometries of both the coil profiles and the parallel-imaging acquisition are consistent (Fig. 10.7). A possible way to acquire coil sensitivity profiles with the same distortion properties as the actual image acquisition is to acquire echo-planar interleaved k-space data that can be combined to a single full-field-of-view data set as illustrated in Fig. 10.7b. In this case, the line spacing, Δk, is the same for the ACS and the imaging data. An obvious disadvantage of this approach is the relatively long acquisition duration for ACS data; however, if the actual image acquisition is repeated several times, which is frequently the case in EPI applications such as cerebral-perfusion MRI or diffusion-tensor MRI, the additional duration of the auto-calibration scans is usually negligible in comparison with the total measurement duration.

10.4 Conclusion

In single-shot sequences, parallel imaging does not only reduce the number of required phase-encoding steps and, thus, accelerates the acquisition, but can also substantially improve the image quality: By shortening the echo train, image blurring caused by decaying transversal magnetization can be reduced, and in addition, EPI sequences show less distortion due to the increased step size in k-space. As a positive side effect, parallel-imaging-induced signal-to-noise losses are partially compensated by obtaining shorter effective echo times and by acquiring fewer echoes of very low amplitude; thus, single-shot sequences particularly benefit from the application of parallel-imaging methods.

Although only conventional Cartesian k-space techniques are discussed in this chapter, similar con-

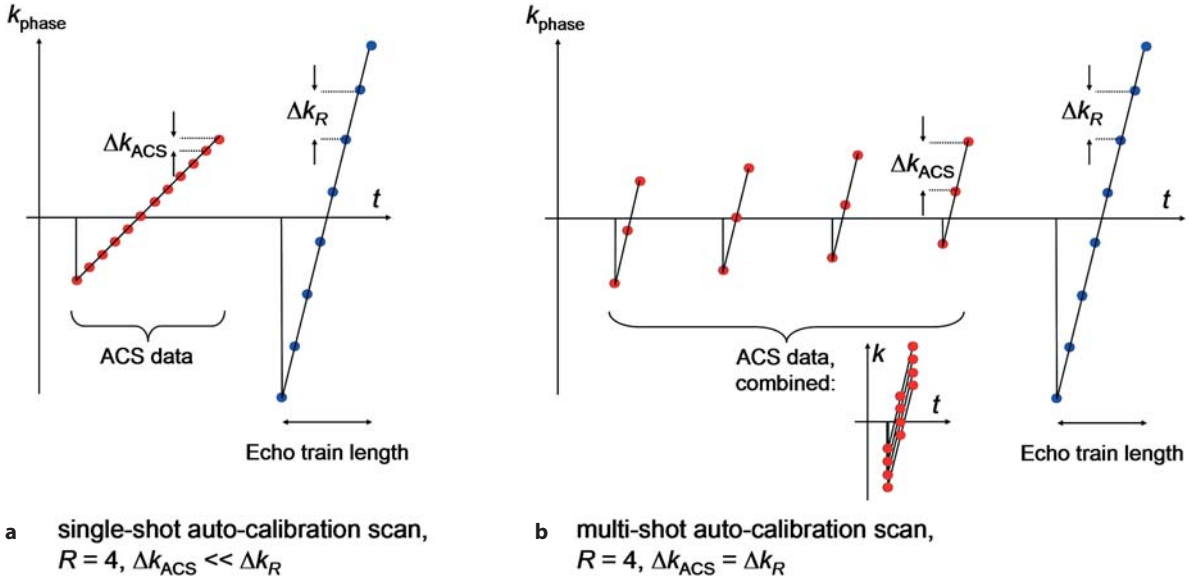

Fig 10.7a,b. Acquisition of auto-calibration signals (ACS) containing coil sensitivity information for parallel echo-planar imaging. **a** If all ACS lines are acquired in a single EPI scan, the line distance in k-space, Δk, is much smaller for the ACS scan than for the actual imaging scan with acceleration factor R, $\Delta k_{ACS} << \Delta k_R$. As a consequence, geometric distortions of the coil sensitivity data are not consistent with the distortions of the imaging data. **b** To obtain consistent line spacings in k-space and, thus, consistent distortion, ACS data can be acquired interleaved in multiple scans covering the same k-space range as in **a**.

clusions can be drawn for alternative techniques, in particular for single-shot spiral MRI (Weiger et al. 2002; Block and Frahm 2005). A further related technique is fast magnetization-prepared imaging, e.g. using snapshot-FLASH sequences (Haase et al. 1989). In this case the longitudinal magnetization is prepared and relaxes during the data acquisition analogous to the transversal magnetization in single-shot techniques. After an inversion-recovery pulse, for instance, data acquisition benefits from reduced acquisition times since T1-related signal variations during the data acquisition are decreased.

Important applications of single-shot sequences are echo-planar brain imaging (discussed in Chapters 18, 33, and 34), echo-planar abdominal imaging (Chap. 21), and single-shot spin-echo imaging such as MR cholangio-pancreaticography (Chap. 22) or MRI of the lung (Chaps. 20 and 38).

References

Barth M, Metzler A, Klarhofer M, Roll S, Moser E, Leibfritz D (1999) Functional MRI of the human motor cortex using single-shot, multiple gradient-echo spiral imaging. Magn Reson Imaging 17:1239–1343

Block KT, Frahm J (2005) Spiral imaging: a critical appraisal. J Magn Reson Imaging 21:657–668

Haase A, Matthaei D, Bartkowski R, Duhmke E, Leibfritz D (1989) Inversion recovery snapshot FLASH MR imaging. J Comput Assist Tomogr 13:1036–1040

Heidemann RM, Griswold MA, Kiefer B, Nittka M, Wang J, Jellus V, Jakob PM (2003) Resolution enhancement in lung 1H imaging using parallel imaging methods. Magn Reson Med 49:391–394

Hennig J, Nauerth A, Friedburg H (1986) RARE imaging: a fast imaging method for clinical MR. Magn Reson Med 3:823–833

Mansfield P (1977) Multi-planar image formation using NMR spin echoes. J Phys C: Solid State Phys 10:L55–L58

Mansfield P, Coxon R, Hykin J (1995) Echo-volumar imaging (EVI) of the brain at 3.0 T: first normal volunteer and functional imaging results. J Comput Assist Tomogr 19:847–852

Schmidt CF, Degonda N, Luechinger R, Henke K, Boesiger P (2005) Sensitivity-encoded (SENSE) echo planar fMRI at 3T in the medial temporal lobe. Neuroimage 25:625–641

Song AW, Wong EC, Hyde JS (1994) Echo-volume imaging. Magn Reson Med 32:668–671

Weiger M, Pruessmann KP, Osterbauer R, Bornert P, Boesiger P, Jezzard P (2002) Sensitivity-encoded single-shot spiral imaging for reduced susceptibility artefacts in BOLD fMRI. Magn Reson Med 48:860–866

Wielopolski PA, Schmitt F, Stehling MK (1998) Echo-planar imaging pulse sequences. In: Schmitt F, Stehling MK, Turner R (eds) Echo-planar imaging. Theory, technique and application. Springer, Berlin Heidelberg New York, pp 65–139

Yang QX, Wang J, Smith MB, Meadowcroft M, Sun X, Eslinger PJ, Golay X (2004) Reduction of magnetic field inhomogeneity artefacts in echo planar imaging with SENSE and GESEPI at high field. Magn Reson Med 52:1418–1423

Fast Sequences for Dynamic and Time-Resolved Imaging

11

Michael Bock

CONTENTS

11.1 Introduction

Time-resolved MR imaging is increasingly used in the clinical routine as it allows for monitoring dynamic changes of the morphology and the organ function. In general, the choice of the MR imaging technique is dictated by the time scale of the dynamic process to be imaged. If flexing of the knee is to be visualised, conventional spin echo techniques can be used, since the motion of the knee can take place in between 2-min-long image acquisitions. The breathing motion, if not forced, requires image acquisition times of the order of a second to capture the motility of the chest wall and the internal organs. The heart motion gives the most demanding time scale, where RR intervals of less than a second are found. In particular, the systolic motion of the heart and the blood in the adjacent vessels requires a temporal resolution of about 50 ms or less to suppress motion artefacts. All these given time scales are significantly shorter when small children or infants are studied. In contrast agent studies, the time scale is furthermore influenced by the injection rate and volume as well as the injection site, so that a second-long acquisition time might be sufficient to visualise contrast agent transit in the central arterial vasculature after injection through a peripheral vein, whereas sub-second time resolution is required for intra-arterial injection through a catheter.

A second, often conflicting requirement is given by the spatial dimensions of the target organ. To successfully diagnose a disease, the spatial resolution needs to be adapted to the geometry of the target organ. In the example of knee imaging, this might not be problematic, since long acquisition times can be utilised and even small tendons can be visualised. During the breathing and the heart cycle, however, the temporal restriction of a second or a sub-second exists, and the delineation of a coronary arterial tree becomes difficult. In this case, use has been made of the fact that most organ movements are periodic. The MR image acquisition was segmented and synchronised with the organ motion using a physiologic monitor (e.g., ECG, breathing belt, and pulse oximeter). Later, the different segments were combined to form an artefact-free MR image series at different time points during the periodic organ motion. Unfortunately, in contrast agent studies, signal changes are not periodic, and periodicity can also be destroyed by pathology (e.g., arrhythmia).

As has been explained in the previous sections, parallel imaging allows the significant reduction of the image acquisition time over conventional MRI without any loss in spatial resolution. Thus, sub-second temporal resolution can be achieved even

M. Bock, PhD
Deutsches Krebsforschungszentrum (dkfz), Abt. Medizinische Physik in der Radiologie (E020), Im Neuenheimer Feld 280, 69120 Heidelberg, Germany

with conventional fast gradient echo techniques. In this section, acquisition techniques will be presented that are typically used for dynamic MRI and that can be combined with parallel acquisition strategies. A more detailed description of fast imaging techniques and their implementation details can be found in textbooks (Vlaardingerbroek and den Boer 1996; Schmitt et al. 1998; Debatin and McKinnon 1998; Haacke et al. 1999; Bernstein et al. 2004).

11.2 Gradient-Echo Techniques

Today, fast MR imaging techniques predominantly use gradient echoes (GRE) for signal generation. In comparison to spin-echo (SE) techniques, GRE imaging offers several advantages for dynamic MRI with sub-second acquisition times:

- In a SE pulse sequence, a 90°–180° RF pulse combination is employed to create an echo, whereas a GRE requires only a single RF pulse, so that the effective time for the acquisition of a line in k-space is significantly shorter.
- The lack of 180°-refocusing pulses in GRE MRI reduces the RF energy transmitted per unit time. Thus, GRE techniques are less susceptible to limitations resulting from restrictions of the specific absorption rate (SAR).
- The use of 90°-excitation pulses in SE MRI leads to a saturation of the longitudinal magnetisation. After SE data acquisition, long signal recovery delays have to be introduced to establish sufficient magnetisation, which unnecessarily prolongs the total scan time. In GRE imaging typically lower flip angles are used, and pulse sequences with very short repetition times still yield sufficient signal.

In the following, two gradient echo pulse sequences are listed that are often used in dynamic studies. Since naming conventions and acronyms differ from one vendor to the next, a list of the different pulse sequence names is given in Table 11.1.

11.2.1 Spoiled Gradient Echo

In the year 1985, Haase and co-workers proposed a pulse sequence that sampled a gradient echo using low flip angle RF excitation (1986). They called this pulse sequence Fast Low Angle SHot (FLASH) to distinguish their approach from the SE techniques existing at that time.

Following a slice-selective RF excitation with a flip angle α, which is typically smaller than 90°, a frequency-encoded gradient echo is acquired (Fig. 11.1a). After data acquisition, the remaining transverse magnetisation is spoiled. Therefore, strong gradients are applied that create an intra-voxel dephasing before the next RF pulse. To increase the spoiling effect, the transmit phase of the RF pulses can also be varied in a pseudo-random fashion.

The repeated RF excitations at intervals TR lead to the establishment of a dynamic steady state of the longitudinal magnetisation. Assuming that the transverse magnetisation created by each RF excitation is no longer present at the end of each TR period (i.e., perfect spoiling), the signal equation for a FLASH pulse sequence can readily be computed:

$$S(\alpha, TR, TE; T1, T2^*) = \rho \cdot \sin(\alpha) \cdot \frac{1 - e^{-TR/T1}}{1 - \cos(\alpha) \cdot e^{-TR/T1}} \cdot e^{-TE/T2^*} \quad (11.1)$$

Here, ρ, T1 and T2* denote the object-specific spin density, longitudinal and apparent transverse relaxation times, respectively, whereas α, TE and TR are the

Table 11.1

General Electric	Philips	Siemens	Remarks
SPGR (spoiled GRASS)	FFE-T1	FLASH (fast low angle shot)	Spoiled gradient echo
GRASS (gradient-recalled acquisition in the steady state)	FFE (fast field echo)	FISP (fast imaging with steady precession)	Partially refocused gradient echo
FIESTA (fast imaging employing steady-state acquisition)	Balanced FFE	trueFISP	Fully refocused gradient echo
SSFP (steady-state free precession)	FFE-T2	PSIF (time-reversed FISP)	Refocusing of spin echo coherence path in subsequent TR

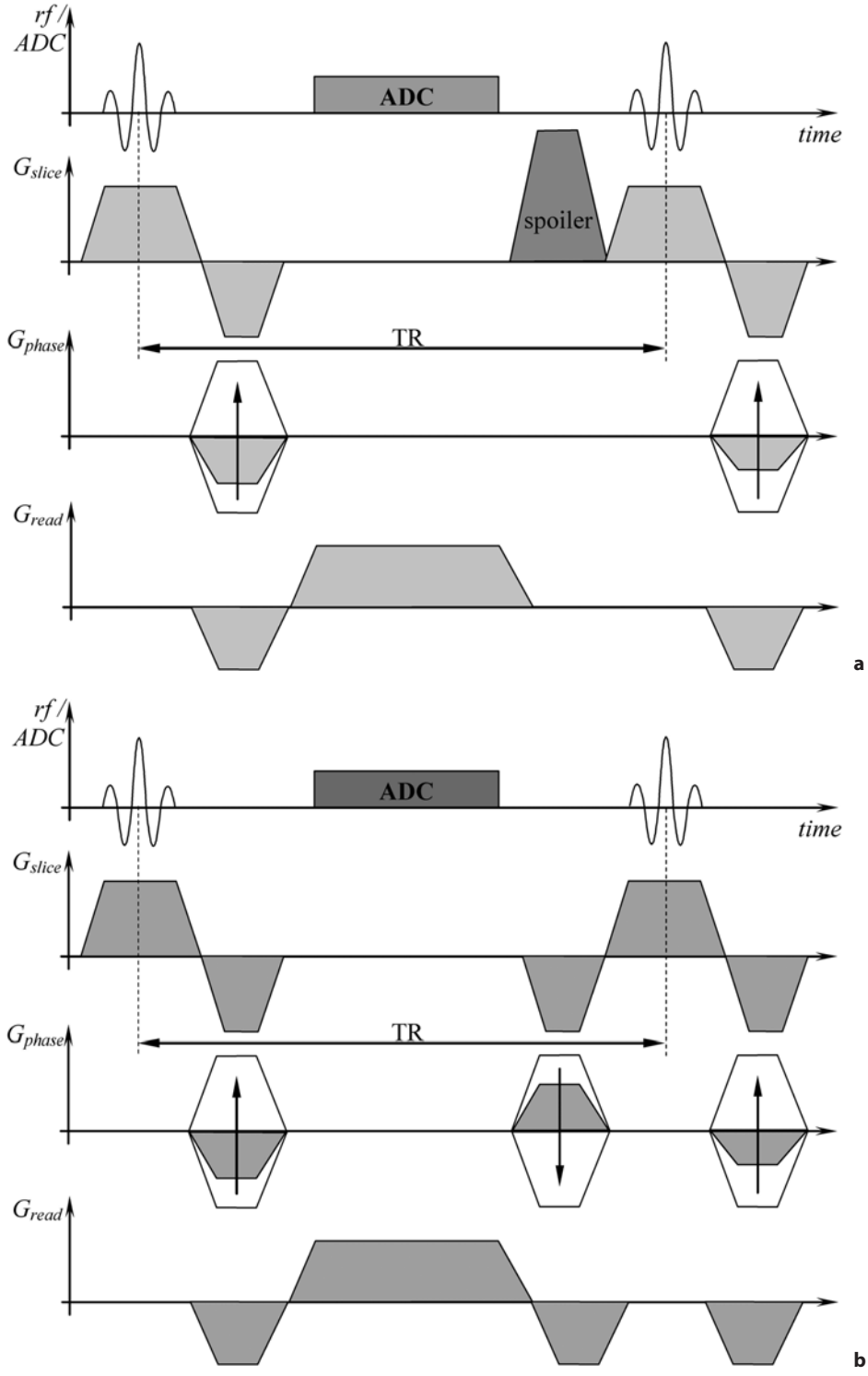

Fig. 11.1a,b. Timing diagrams of a FLASH **a** and a trueFISP **b** pulse sequence. In both gradient echo pulse sequences, the slice-selective RF excitation is followed by a conventional phase and frequency encoding. In the spoiled gradient echo sequence, coherences of the transverse magnetisation are reduced by the application of strong spoiler gradients. In the trueFISP pulse sequence, all gradient-induced phases are rewound (balanced) so that the transverse magnetisation fully contributes to the next RF excitation

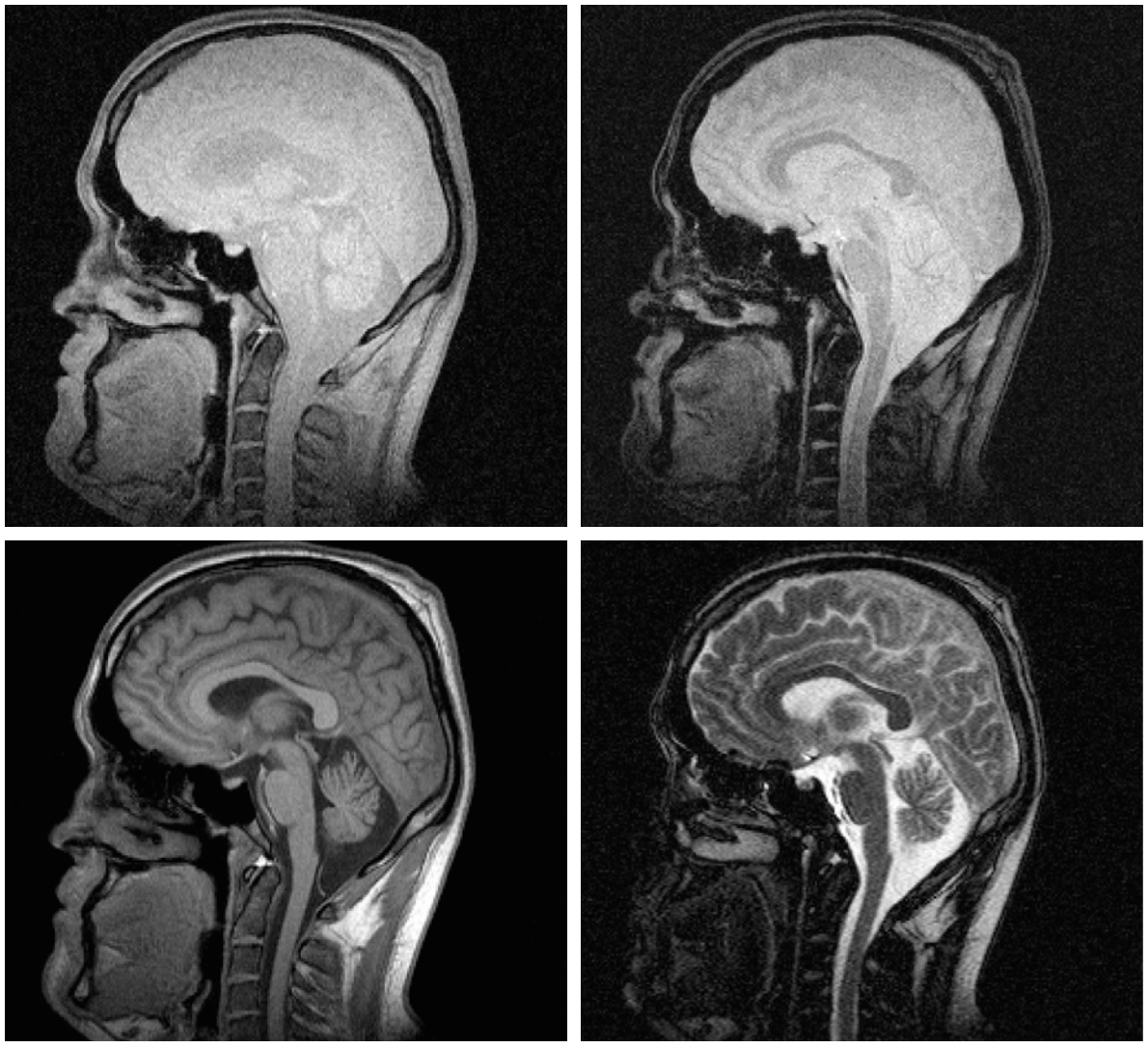

Fig. 11.2a–d. Spoiled **a-c** and balanced **d** gradient-echo images with different parameter settings. **a** For very low flip angles (here, α =10°), a short TE of 3.6 ms and a moderate TR of 74 ms, a nearly constant signal is seen in the FLASH image (spin density weighting). **b** At a longer echo time (TE=12 ms), the differences in the T2* values lead to a T2* weighted image. **c** A short TE and a longer TR of 150 ms in combination with higher flip angles (α=70°) result in a T1-weighted FLASH image. **d** With a fully balanced gradient-echo technique (trueFISP) also the transverse signal components contribute to the steady-state signal and a mixed contrast is established, which pronounces tissues with a high T2/T1 ratio (e.g., fluids). Here, the shortest possible TR and TE are chosen to avoid off-resonance artefacts

sequence-dependent parameters. In dynamic studies the parameters are often adjusted to create a specific contrast:

- For very low flip angles of 10° and less, cos(α) is close to 1 and *S* is nearly independent of T1. If also TE is shorter than T2*, only spin density changes lead to a contrast in the FLASH image. Since spin density does not vary significantly in many tissues (with the exception of lung tissue), images with low contrast are created (Fig. 11.2a).
- If TE is of the order of the object's T2*, a T2* contrast is established in the images, if flip angles are kept low to avoid an additional interfering T1 contrast. This contrast is advantageous in studies with a T2*-shortening contrast agent (e.g., ultra-small iron oxide particles, USPIO), where the arrival of the contrast in the target organ is seen as a signal reduction (Fig. 11.2b).
- A T1-contrast is achieved by adjusting both TR and α simultaneously. For high flip angles α>60°

and a TR that is short compared to the object's T1, a strong T1-contrast is established (Fig. 11.2c). To avoid signal saturation at very short TRs of 10 ms and less, the flip angle is typically reduced to α=10°…30°, which still provides a moderate T1 dependence of the signal.

11.2.2 Fully Balanced Gradient Echo

In recent years, another GRE sequence has been found to have multiple uses in dynamic MRI: the GRE sequence with fully balanced gradient timing (Oppelt et al. 1986). In the spoiled GRE sequence, the transverse magnetisation was suppressed after data acquisition and the steady state was solely dependent on the longitudinal relaxation.

In the fully balanced GRE sequence, all gradients are rewound at the end of TR so that the transverse magnetisation also contributes to the steady-state signal. The fully balanced GRE sequence is often used in combination with an alternation of the transmit RF phase for every other RF pulse (Fig. 11.1b).

Compared to the spoiled GRE sequence, the fully balanced GRE sequence yields a significantly higher signal since the transverse magnetisation is also utilised. Unfortunately, the image contrast is more difficult to compute and is dependent on the quotient of T2 and T1. Typically, this pronounces structures with a large T2/T1 ratio such as liquids (Fig. 11.2d). The fully balanced gradient timing refocuses the phase of the transverse magnetisation; however, so does every off-resonance. Therefore, these sequences are very sensitive to field inhomogeneities that produce dark artefact bands in the image. Since the value of the off-resonance phase is proportional to the repetition time, these artefacts are minimised by using the shortest possible TR.

11.3 Data Sampling

Gradient echo techniques provide a fast and efficient way to acquire image data; however, at a repetition time of 5 ms and 256 phase encoding steps, the total acquisition time per image still amounts to 1.3 s, which is by far too long to resolve the dynamics of the beating heart. Several modifications of the image acquisition have been proposed to accelerate the data acquisition process. Most of these techniques are independent of parallel imaging and can readily be combined with any parallel acquisition technique.

11.3.1 Partial-Fourier Techniques

In the ideal k-space representation of an MR image, a point symmetry relation (Hermitian symmetry) exists between data in the upper und the lower half of k-space (Fig. 11.3):

$$\tilde{S}(k_x, k_y) = \tilde{S}(-k_x, -k_y)^* \qquad (11.2)$$

Here, the asterisk denotes complex conjugation. Essentially, this relation reflects the fact that the phase of an ideal MR image should be constant everywhere in the image (i.e., without the loss of generality, it could be set to zero).

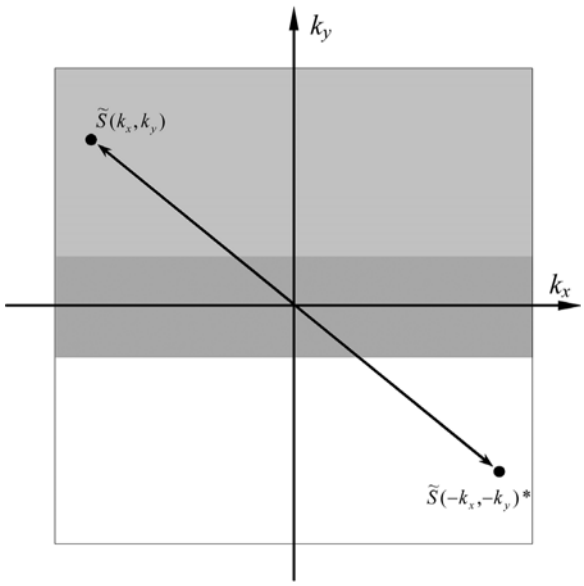

Fig. 11.3. In a partial Fourier k-space acquisition scheme, slightly more than half of k-space is acquired (*grey areas*), which results in an associated reduction in scan time. In the central region of k-space, a symmetric portion of the data is measured (*shaded area*) to estimate the low-order phase changes, which distort the Hermitian symmetry. When combined with parallel MRI, the original density of k-space lines is often maintained in this central section, because these data can also be used to calculate the weighting factors used for reconstruction of the unmeasured lines in the k-space periphery (e.g., in the GRAPPA algorithm)

Unfortunately, in a realistic MR experiment, this relation only holds approximately, since there are local off-resonances that lead to a non-zero phase distribution in the image. If one assumes that the phase varies only slowly over the image, a low-order phase estimate can be extracted from the central lines in k-space. This low-order phase estimate is then used to remove the phase variation and, subsequently, the lower half of k-space is reconstructed from data of the upper half. Techniques that sample only slightly more than one half of k-space are called partial-Fourier or half-Fourier techniques (Noll et al. 1991).

The assumption that the low-order phase estimate is sufficient to correct for asymmetries in k-space is not valid at tissue boundaries in gradient echo images. Here, susceptibility changes introduce local static field gradients, which do not influence spin echo images, but can lead to additional phase changes in gradient echo MRI. Since local phase changes are represented in the outer regions of k-space, partial-Fourier techniques often cannot recover the correct signal intensity at tissue boundaries.

Partial-Fourier imaging can favourably be combined with parallel imaging since both techniques require a central portion of k-space to be sampled at full k-space density (Bydder and Robson 2005). If, e.g., a 2/16th central section of k-space is acquired at full density and the remaining data in the upper half (7/16) at an acceleration factor of 2 (i.e., every other line is sampled), the total imaging time is reduced to (2/16)+(7/16)/2=11/32=34% of the original imaging time. During image reconstruction, the central k-space data are first used to synthesise the missing lines in the upper half (e.g., using an autocalibrated algorithm such as GRAPPA), and then the partial Fourier reconstruction algorithm is applied.

Since both techniques – partial-Fourier and parallel MRI – reduce the number of acquired k-space lines, an associated reduction in the SNR is observed. With partial-Fourier techniques, however, the SNR reduction is constant over the image, since no local information is used during image reconstruction.

11.3.2 View Sharing

Another way to increase the temporal resolution at least nominally is called view sharing. In view sharing, portions of k-space are shared between images and, thus, need not be reacquired. Several concepts of view sharing have been proposed:

- Keyhole MRI (van Vaals et al. 1993): In the most extreme version of view sharing, a full k-space data set is acquired only once (e.g., at the beginning of the dynamic series). Later, only the central portion of k-space is acquired and the missing outer k-space data are substituted using the lines from the full data set. Even though very high keyhole acceleration factors K (K=8 and more) can be achieved, the technique is not suitable in this form for clinical purposes, since the temporal variation in the high k-space regions (which is encoding the important edge features in the image) is not visualised at all (Fig. 11.4). In a variation of the keyhole technique, outer portions of k-space are sporadically re-acquired, which reduces the attainable acceleration factor K. Keyhole techniques can readily be combined with parallel imaging using the full density reference data set(s) for coil calibration. For a parallel acceleration factor of R, only every R-th k-space line is acquired in the dynamic phase. Depending on the frequency of repetition of the reference data set, an acceleration factor of nearly $K \times R$ can thus be achieved during the dynamic phase using parallel acquisition techniques. Sampling of the coil calibration data is preferably integrated in the acquisition of the reference data set(s) to achieve a maximum acceleration during the dynamic phase.
- TRICKS (Korosec et al. 1996): The time-resolved interpolated contrast kinetics or TRICKS technique is similar to keyhole imaging in design, though here k-space is not only divided into a central and an outer region, but several sections, A, B, C, etc., where the letters denote an increasing distance to the k-space centre. In TRICKS notation, the keyhole technique as described above acquires a full data set (A-B) followed by the repeated acquisition of the central section A: (A-B)-A-A-A-A-… With TRICKS, the central regions are acquired more often than the outer k-space regions; however, all regions of k-space are updated continuously (though not with the same frequency). For a segmentation of k-space into four regions A, B, C, and D, a TRICKS data acquisition could look like this: (A-B-C-D)-(A-B)-(A-C)-(A-B)-(A-D)-(A-B)-(A-C)-(A-B)-(A-D)-… A k-space data set would be synthesized from these data for each central section A using the nearest peripheral sections B, C, and D in time. All algorithms for parallel MRI can be used in combination with TRICKS; however, the highest acceleration is achieved when the coil sensitivity information is sampled first (e.g.,

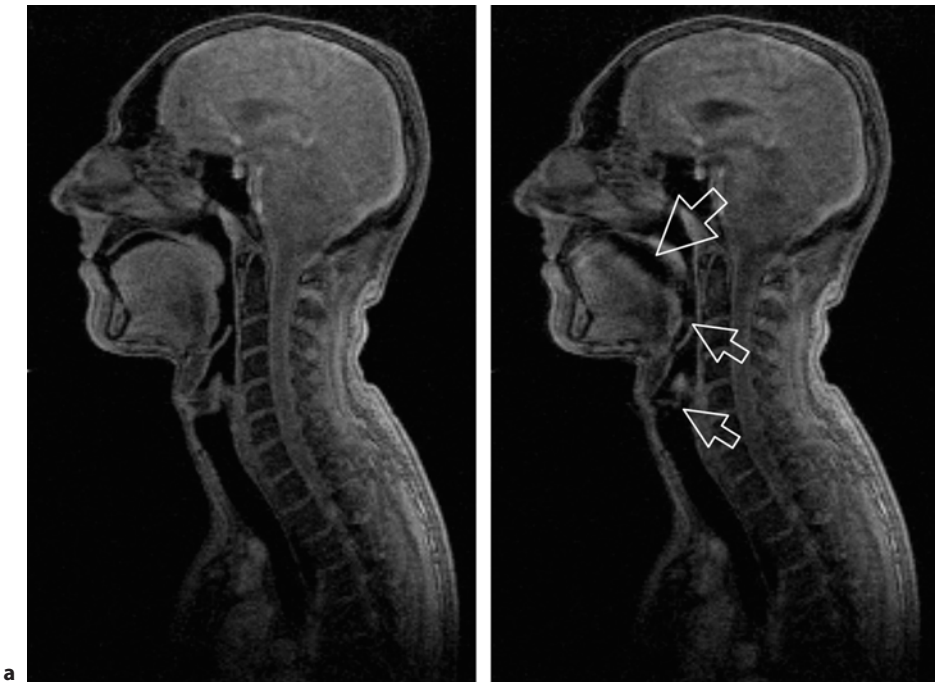

Fig. 11.4a–b. Initial full-resolution reference image **a** and subsequent keyhole image **b**, where only the central 1/8th of k-space was re-acquired and the k-space periphery was taken from **a**. In areas where motion has occurred such as the tongue and the larynx artefacts can be seen (*arrows*) and the precise location of the anatomical structures cannot be recovered

during the initial A-B-C-D part). In the dynamic phase, all data are acquired with full parallel acquisition acceleration and without any autocalibration data, thus increasing the temporal resolution. The combination of parallel imaging and TRICKS for fast angiographic MRI has also been referred to as the time-resolved echo-shared angiography technique, or TREAT.

- View sharing during ECG-gated scans (Foo et al. 1995): A special form of view sharing can be found in gated acquisition techniques (e.g., during ECG gating), where the total acquisition time is reduced by acquiring not only one but several k-space lines per synchronisation cycle and by sharing some of the data between successive (cardiac) phases. Compared to the previous techniques, ECG-synchronised view sharing is slightly different, since not all of k-space is acquired in one cardiac cycle and the acquisition is repeated several times. In the TRICKS notation ECG-gated view sharing with three k-space regions could, e.g., be realised in the following way: (ECG trigger)-A_i-B_i-A_i-C_i-A_i-B_i-A_i-C_i-…(ECG trigger) -A_{i+1}-B_{i+1}-A_{i+1}-C_{i+1}-A_{i+1}-B_{i+1}-A_{i+1}-C_{i+1}-… Here, the index *i* denotes the *i*th k-space line. View sharing in the cardiac cycle leads to temporal blurring, since the reconstructed temporal resolution is higher than the measured one: in the above example, in every second TR, an A-segment is sampled and the reconstructed time difference is 2·TR; however, 3·TR are required to fill k-space.

11.3.3 Echo-Planar Imaging

In conventional MRI pulse sequences, one line of k-space is acquired per RF excitation. This image acquisition technique is time-inefficient, since a constant fraction of the total scan time (50% and more) is spent on magnetisation preparation and is not used for data acquisition. In the year 1977, Sir Peter Mansfield proposed a method to acquire all k-space lines following a single RF excitation, which he called echo planar imaging Mansfield (1977). Essentially, the gradient echo in readout direction is refocused using gradients of alternating polarity, while a constant weak gradient or small blipped gradients are present in phase-encod-

ing direction (Fig. 11.5). The combination of these gradients leads to meandering k-space trajectory, and, if combined with an appropriate dephasing, allows to sample k-space in less than 100 ms.

Echo planar imaging (EPI) became clinically available in the early 1990s when powerful gradient systems (G_{max}>20 mT/m) with high slew rates [s_{max}>40 T/(m·s)] were introduced. The time-efficiency of an EPI pulse sequence can easily exceed 80%. Unfortunately, single-shot EPI pulse sequences suffer from several artefacts that limit their applicability in clinical MRI. During the long readout gradient echo trains, the signal decays with the apparent transverse relaxation time T2*, which creates a filter effect on the k-space data and limits the spatial resolution. Image distortions are often seen at tissue boundaries where the susceptibility changes lead to static field gradients that are of the same order of magnitude as the weak phase-encoding gradients. The long echo trains also make the data acquisition prone to off-resonance artefacts, which are often suppressed using water-selective excitation pulses. Single-shot echo planar images still suffer from artefacts in anatomical regions with heterogeneous tissues such as the abdomen.

A compromise between sampling efficiency and image quality is given by the segmented EPI technique, where only a certain number of k-space lines are acquired per RF excitation (McKinnon 1993). This k-space segmentation requires repeated RF excitations and a combination of k-space lines from different excitations, which makes segmented EPI more susceptible to motion artefacts. With segmented EPI the echo train length can be reduced to a level where distortion artefacts are tolerable and image acquisition times are still considerably shorter than conventional gradient warp techniques (Fig. 11.6). In general, the acquisition time per image TA can be written as:

$$TA = N_{lines} \cdot \left(\frac{t_{RF}}{n_{echoes}} + t_{ADC} \right) \qquad (11.3)$$

where t_{RF} denotes the time needed for RF excitation and initial phase encoding, t_{ADC} is the time required to sample a single line in k-space, and n_{echoes} is the number of gradient echoes per RF excitation. In Fig. 11.7, the acquisition time for N_{lines}=77 is shown as a function of n_{echoes}.

In echo planar imaging, additional reference scans are often performed to compensate for hardware imperfections and off-resonance effects. The combination of data acquired with positive and negative readout gradients often introduces small systematic differences between odd and even k-space lines, which manifest in ghost images shifted by half the field of view (N/2 ghosts or Nyquist ghosts). In the

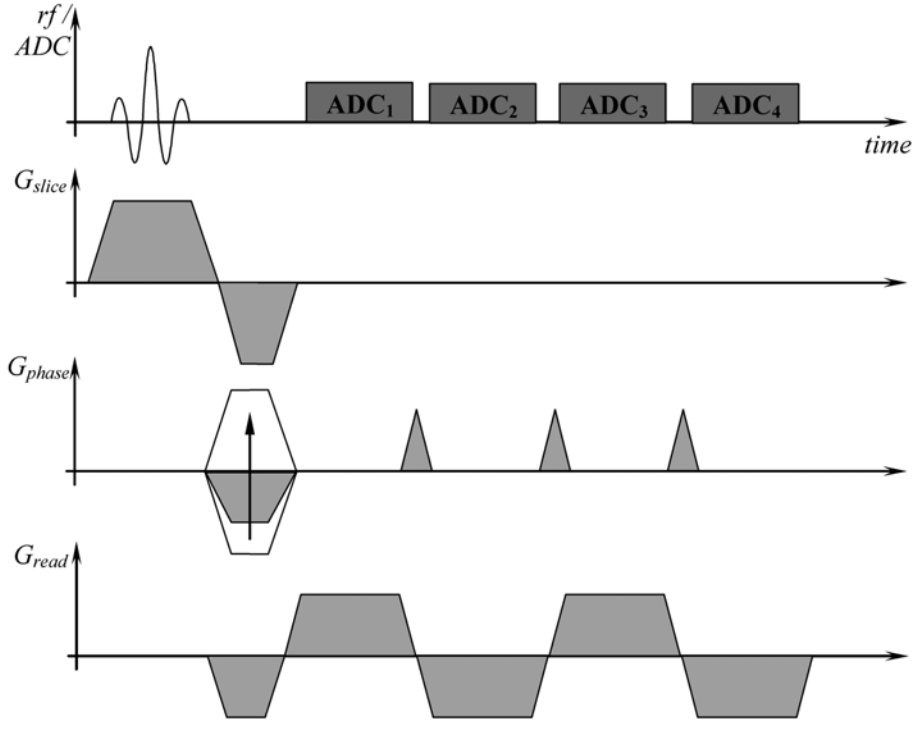

Fig. 11.5. Gradient timing of a segmented echo planar imaging pulse sequence. Following a conventional slice-selective RF excitation, a series of gradient echoes is acquired (here: four). In phase-encoding direction, a variable dephaser gradient table is used to shift the start of the k-space trajectory from the k-space centre to the periphery, and small trapezoidal gradients (so-called blips) are utilised for advancing to encode the different k-space segments. In the most extreme case, the number of echoes is equal to the matrix size, which results in the standard single-shot EPI pulse sequence

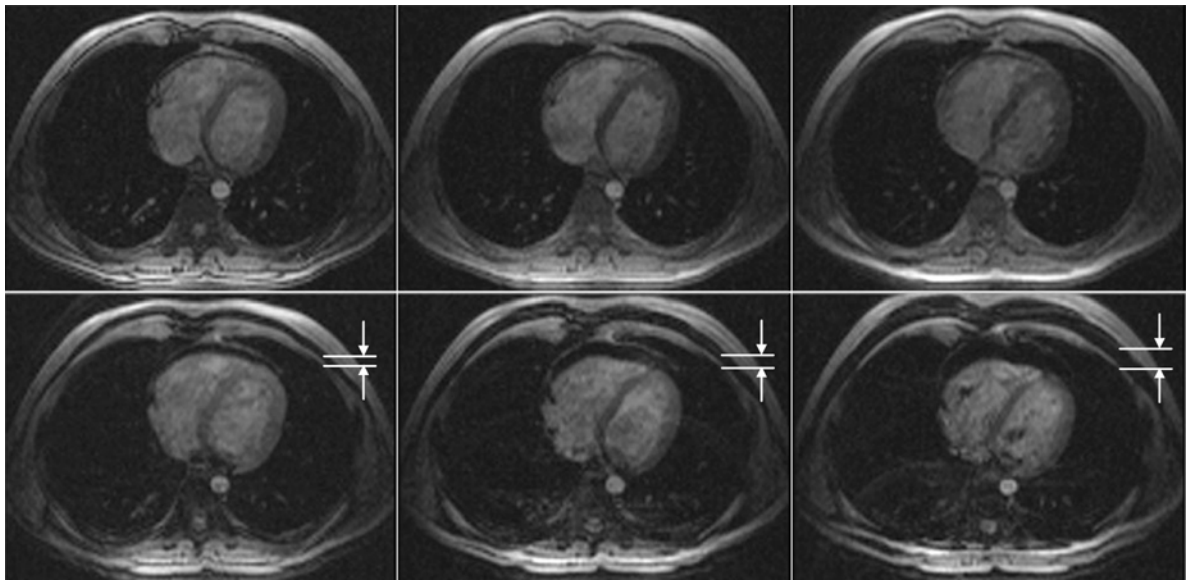

Fig. 11.6. Segmented EPI images of the heart with n_{echo}=3, 5, 7 (*top row*) and 15, 29, 45 (*bottom row*) lines per TR. Due to the linear k-space encoding, TE increases with the number of lines from 2.9 ms to 16 ms, which leads to an increased sensitivity to motion artefacts, e.g., in the heart chambers. With increasing n_{echo} also the fat-water shift increases (*arrows*) so that fat saturation techniques become necessary

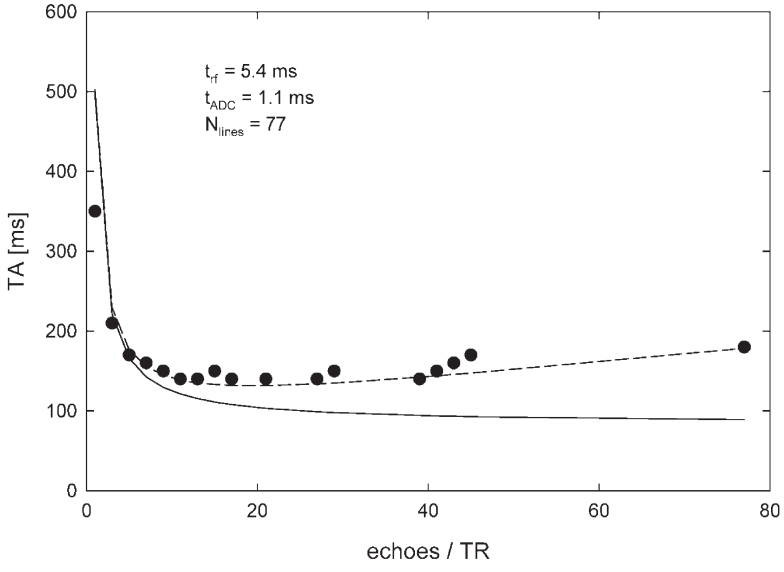

Fig. 11.7. Image acquisition time for a segmented EPI pulse sequence as a function of the number of echoes acquired per TR. The repetition time TR is minimized for each sequence and therefore increases with the number of echoes per TR. The *points* are values taken from a measurement, the *solid line* is the theoretical prediction and the *dotted line* takes an additional repetition for the measurement of reference lines into account. In a conventional data acquisition, only a single line is acquired per TR, whereas all lines (here: 77) are sampled in one TR a single-shot EPI. Segmented acquisition schemes allow trading acquisition time for echo train length so that both higher matrix sizes and lower artefact sizes are possible

reference scans, which are acquired without phase encoding, these shifts can be measured and used to correct the k-space lines before reconstruction. In segmented EPI acquisitions, larger portions of k-space are acquired with the same echo time, and phase discontinuities can occur between subsequent k-space segments. Here, the technique of echo time shifting (McKinnon 1993) can be employed to minimize phase discontinuities, however, at the expense of slightly prolonged repetition times.

With parallel imaging, fewer k-space lines need to be acquired, which allows reducing the echo train length and, accordingly, the blurring in phase-encoding direction. Additionally, the step width in k-space is increased by the use of stronger phase-encoding gradients, which helps to reduce the distortion arte-

facts. Even though the acquisition of coil sensitivity information can in principle be integrated into every EPI echo train, again the highest acceleration factors are achieved when extra reference scans with separate RF excitations are acquired prior to the dynamic phase of the acquisition. For acceleration factors of 3 and higher, these scans are typically segmented to achieve a similar timing as during dynamic data acquisition.

11.3.4 Non-Cartesian k-Space Sampling

As has been outlined in Chapter 6, MR raw data can be acquired on a non-Cartesian grid in k-space. In particular, radial (Lauterbur 1973) and spiral (Ahn et al. 1986) acquisition techniques have been used in the past for both 2D and 3D acquisitions. These special variants of non-Cartesian data sampling have several unique properties that render them well suited for fast MRI applications:

- Both imaging techniques start acquiring data at the centre of k-space. Since no additional spatial encoding is required between RF excitation and the beginning of the data acquisition, both methods can achieve very short echo times (TE<1 ms). At short echo times, motion artefacts are minimised, and tissues with very short T2* relaxation times (e.g., lung tissue with T2*<2 ms at 1.5 T) can be visualised.
- In particular during radial scanning, the centre of k-space is sampled more often than the periphery. During data reconstruction, this leads to an averaging of the low frequency components and additionally reduces motion artefacts (Fig. 11.8).

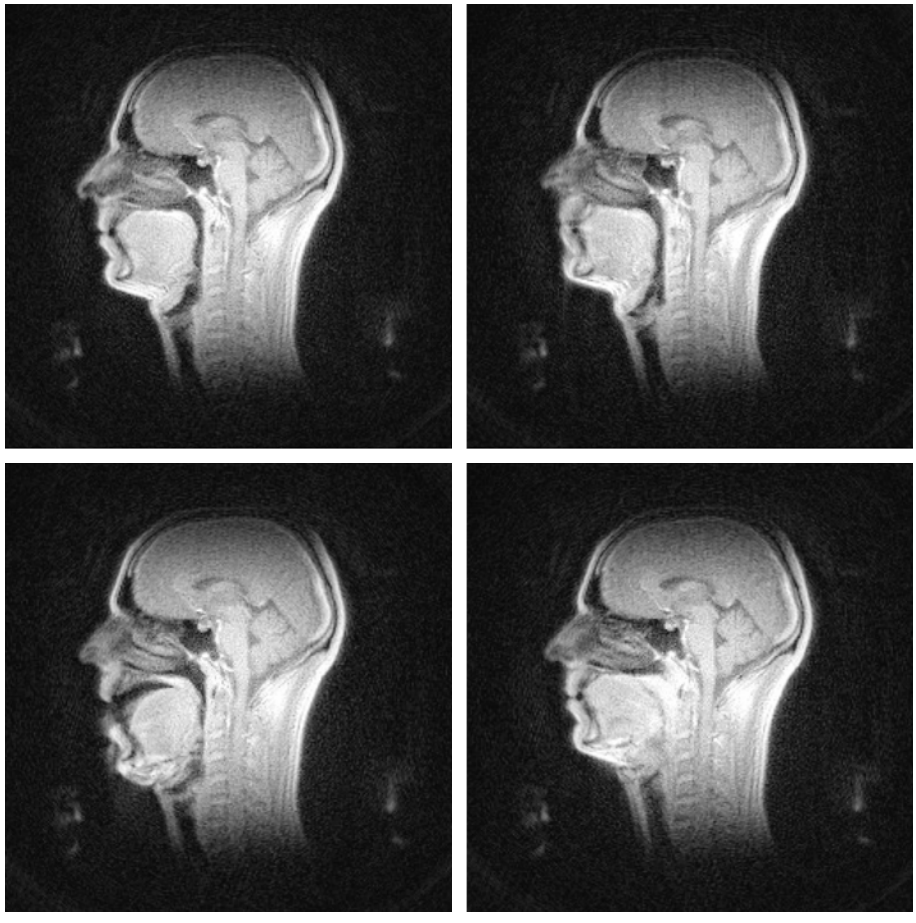

Fig. 11.8. Radial MR image time series showing the uncooperative author who is speaking and violently shaking his head. Due to the oversampling of the k-space centre motion artefacts are averaged, and no ghost images of the moving structures are seen. Also in this example view sharing was used to increase the temporal resolution

- To fulfil the Nyquist criterion, π-times more radial lines need to be sampled than rectilinear k-space lines. This number can be reduced to π/2, if the radial acquisition is not started at the k-space origin, but on one side of k-space, and the radial line is traversing the k-space centre. For fast MR applications, angular undersampling is employed and the number of radial lines is reduced significantly. Even though streak artefacts are thus induced in the MR images, a high spatial resolution (i.e., the resolution along the radial line) can be maintained in the reconstructed images.
- Both radial and spiral MRIs are often used in combination with view sharing. Therefore, a number n of the total number of lines (or spirals) N is reacquired after an initial full k-space data set, and the data are dynamically exchanged in k-space before image reconstruction.

Even though combining parallel imaging with radial or spiral MR techniques is not as straightforward as with conventional Cartesian k-space sampling, the concepts are essentially similar (Pruessmann et al. 2001). Using low-resolution coil sensitivity information, missing radial spokes or spiral arms are reconstructed as a weighted linear combination of the measured k-space data, where the weights are determined from the coil sensitivities.

Radial data sampling covers k-space more densely in the centre than in the periphery, which is not necessarily true for spiral MRI, where the distance between individual spiral arms can be much larger than the distance between data points along the spiral. The radial data oversampling near the k-space centre can be exploited during parallel imaging, because thus radial MRI automatically provides a low-resolution image of the coil sensitivities during image acquisition (Yeh et al. 2005).

11.4 How to Combine Fast Imaging Techniques

In the previous sections, several techniques to accelerate the MR image acquisition have been described. All of these techniques can be combined with parallel imaging, which results in an acceleration of the image acquisition. Furthermore, a mixture of techniques is possible, resulting in an even faster image acquisition scheme.

For a conventional trueFISP pulse sequence with TR=4 ms and 256 phase encoding steps, the acquisition time per image is about 1 s. Using a 6/8th partial Fourier technique, this acquisition time can be reduced to 768 ms, and the use of an acceleration factor of 3 in parallel imaging leads to an acquisition time of about 260 ms. A further reduction could be achieved with a segmented EPI acquisition, where, e.g., three lines are acquired per TR. Under typical conditions this could reduce the acquisition time by 40%, so that the final image acquisition time per image is 160 ms. Unfortunately, the prolonged TR would also lead to an increased susceptibility to off-resonance artefacts so that this technique might only be applicable in anatomical regions with a high B_0 field homogeneity such as the brain.

Another possible combination is the use of a spoiled gradient echo technique with a radial data acquisition to visualise the blood vessels after infusion of a T1-shortening contrast agent. Using angular undersampling, the number of radial spokes can be kept significantly shorter than the number of k-space lines required for a Cartesian data acquisition. At a TR of 4 ms, N_{radial}=100 radial spokes, the image data can be acquired in only 400 ms; however, streak artefacts from angular undersampling are to be expected in the final MR images. With a parallel imaging technique the acquisition time can easily be halved (TA=200 ms), and view sharing between subsequent radial data acquisitions could be used to further increase the (nominal) temporal resolution to 100 ms and less. Again, the high temporal resolution is traded against artefacts from temporal averaging and spatial undersampling.

11.5 Real-Time Image Reconstruction

In Cartesian MRI, image data are acquired on a rectilinear k-space grid and a simple Fourier transform (implemented with the fast Fourier transform algorithm, FFT) is sufficient to reconstruct the MR image. Even though the FFT needs to be performed separately for the data from each coil element, images can be reconstructed in (nearly) real-time using conventional computer hardware.

Already the introduction of a partial Fourier acquisition scheme increases the load on the computer system, because more images need to be recon-

structed in the same time. Furthermore, the reconstruction is more complicated and time-consuming, because the low-order phase estimate needs to be reconstructed and subtracted. View sharing additionally increases the computational burden, since even more images are reconstructed per unit time. Non-Cartesian image acquisition techniques are even more time-consuming during image reconstruction, because raw data are typically first interpolated to a Cartesian grid, and k-space density compensation needs to be performed.

The increased temporal resolution in the reconstructed images is thus often achieved through significantly prolonged image reconstruction times of several minutes. Even though ever-faster computer hard- and software are available, often image reconstruction cannot keep up with the high data rates during parallel imaging. Nevertheless, parallel acquisition techniques were successfully combined with real-time MRI to monitor interventional procedures. In Fig. 11.9, an active catheter tracking experiment is shown, where the slice position was automatically adjusted to the position of a small tracking coil at the tip of a catheter. With a trueFISP pulse sequence, a temporal resolution of 5 images/s is achieved using a GRAPPA factor of 2. Note that during interventional procedures the reconstruction factors for parallel imaging need to be re-acquired for each slice position. This limits the choice of parallel acquisition techniques to auto-correlation methods, where reference lines are continuously re-acquired for each new image position. To accelerate the reconstruction, all those imaging coils that were too far away from the imaging slice were dynamically excluded from the reconstruction (Müller et al. 2005).

11.6 Conclusion

Parallel-imaging techniques can readily be combined with nearly every existing fast MRI method. Coil sensitivity information is preferably acquired before the dynamic scan starts to increase the temporal resolution. When combined with partial-Fourier acquisition strategies, coil sensitivities can also

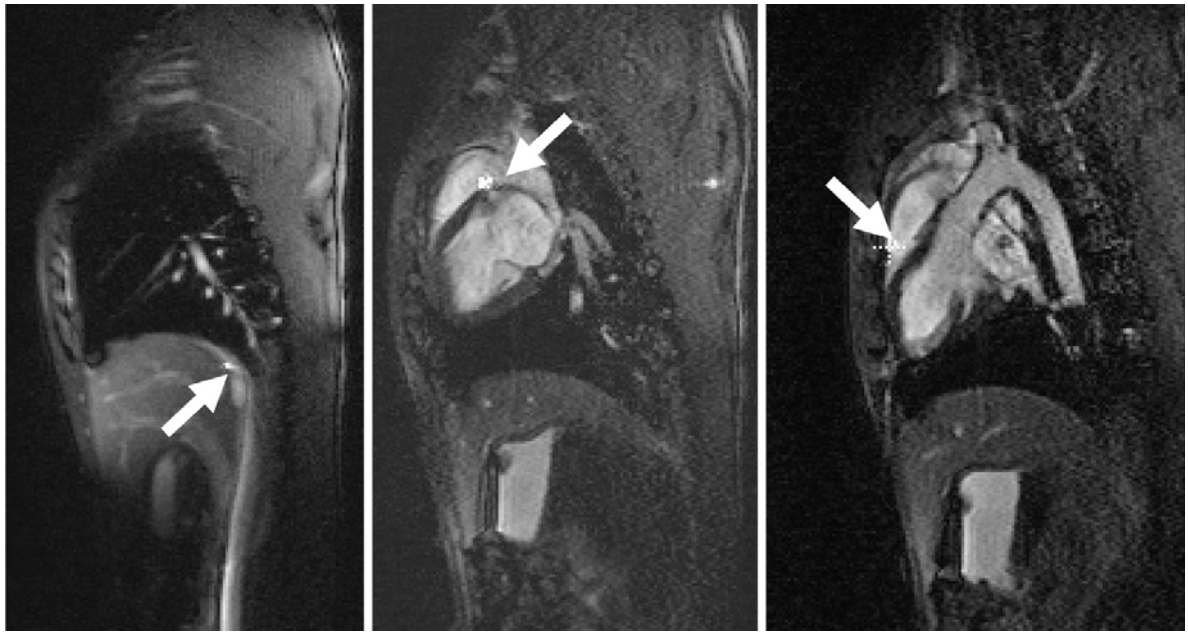

Fig. 11.9. Three images out of a real-time trueFISP time series acquired with active catheter tracking. In between the acquisition of two subsequent time frames, the position of a small tracking coil (*arrows*) was determined, and the imaging slice was automatically shifted to the current coil position. To accelerate the data acquisition, parallel imaging was employed (parallel imaging factor 2) so that the acquisition time per image could be reduced to 210 ms. At this high temporal resolution, motion artefacts of the beating heart of the animal were hardly visible. Since the image position was continuously changing, an algorithm with auto-calibration (GRAPPA) was chosen. With five imaging coils, a real-time image reconstruction was possible using an optimised reconstruction algorithm

be extracted from the same data as are required for low-order phase correction. Real-time parallel MRI is feasible, though challenging, because fast parallel-image reconstruction requires powerful computers and optimised reconstruction algorithms.

References

Ahn CB, Kim JH, Cho ZH (1986) High-speed spiral-scan echo planar NMR imaging. IEEE Trans Med Imag 5:2–7

Bernstein MA, King KF, Zhou XJ (2004) Handbook of MRI pulse sequences. Academic Press, San Diego

Bydder M, Robson MD (2005) Partial Fourier partially parallel imaging. Magn Reson Med 53:1393–1401

Debatin JF, McKinnon GC (eds) (1998) Ultrafast MRI: techniques and applications. Springer, Berlin Heidelberg New York

Feinberg DA, Oshio K (1992) Gradient-echo time shifting in fast MRI techniques for correction of field inhomogeneity errors and chemical shift. J Magn Reson 97:177–183

Foo TK, Bernstein MA, Aisen AM, Hernandez RJ, Collick BD, Bernstein T (1995) Improved ejection fraction and flow velocity estimates with use of view sharing and uniform repetition time excitation with fast cardiac techniques. Radiology 195:471–478

Haacke EM, Brown RW, Thompson MR, Venkatesan R (1999) Magnetic resonance imaging: physical principles and sequence design. Wiley and Sons, New York

Haase A, Frahm J, Matthaei D, Hanicke W, Merboldt KD (1986) FLASH imaging. Rapid NMR imaging using low flip-angle pulses. J Magn Reson 67:258–266

Korosec FR, Frayne R, Grist TM, Mistretta CA (1996) Time-resolved contrast-enhanced 3D MR angiography. Magn Reson Med 36:345–351

Lauterbur PC (1973) Image formation by induced local interactions: examples employing nuclear magnetic resonance. Nature 242:190–191

Mansfield P (1977) Multi-planar image formation using NMR spin echoes. J Phys C 10:L55–L58

McKinnon GC (1993) Ultrafast interleaved gradient-echo-planar imaging on a standard scanner. Magn Reson Med 30:609–616

Müller S, Bock M, Semmler W (2005) Why less can be more: a dynamic coil selection algorithm for real-time interactive MRI. Proc Intl Soc Mag Reson Med 13:2417

Noll DC, Nishimura GD, Macovski A (1991) Homodyne detection in magnetic resonance imaging. IEEE Trans Med Imag 10:154–163

Oppelt A, Graumann R, Barfuß H, Fischer H, Hartl W, Schajor W (1986) FISP: Eine neue schnelle Pulssequenz für die Kernspintomographie. Electromedica 54:15–18

Pruessmann KP, Weiger M, Bornert P, Boesiger P (2001) Advances in sensitivity encoding with arbitrary k-space trajectories. Magn Reson Med 46:638–651

Schmitt F, Stehling MK, Turner R (eds) (1998) Echo planar imaging: theory, technique and application. Springer, Berlin Heidelberg New York

van Vaals JJ, Brummer ME, Dixon WT, Tuithof HH, Engels H, Nelson RC, Gerety BM, Chezmar JL, den Boer JA (1993) "Keyhole" method for accelerating imaging of contrast agent uptake. J Magn Reson Imag 3:671–675

Vlaardingerbroeck MT, den Boer JA (1996) Magnetic resonance imaging: theory and practice. Springer, Berlin Heidelberg New York

Yeh EN, Stuber M, McKenzie CA, Botnar RM, Leiner T, Ohliger MA, Grant AK, Willig-Onwuachi JD, Sodickson DK (2005) Inherently self-calibrating non-Cartesian parallel imaging. Magn Reson Med 54:1–8

The Development of TSENSE

12

Peter Kellman

CONTENTS

12.1 TSENSE Method

12.1.1 Background

In dynamic imaging applications, temporal filtering and parallel imaging (spatial sensitivity encoding) may be combined to exploit the spatio-temporal correlation in the MR signals. In parallel imaging, the differences in spatial sensitivity of multiple receiver coils may be exploited using SENSE (Pruessmann et al. 1999) or SMASH (Sodickson and Manning 1997) techniques to eliminate the aliased component that results from undersampling k-space (for details see Chap. 2). In dynamic imaging, temporal correlations may be exploited by using temporal interpolation methods such as view sharing (Hu and Parrish 1994), sliding window reconstruction, (D'Arcy et al. 2002) or, more generally, UNFOLD filtering (Madore et al. 1999). These methods may be combined to achieve either higher acceleration factors (Kellman and McVeigh 2000) or to improve suppression of alias artefacts (Kellman et al. 2001). The incorporation of temporal processing with image domain parallel imaging is referred to as TSENSE. The combination may also be used to realize auto-calibrating parallel imaging for greater robustness since auto-calibrating methods are less sensitive to subject motion (Kellman et al. 2001). Auto-calibrating TSENSE produces full spatial resolution coil sensitivity estimates for computing unmixing coefficients and, furthermore, does not require additional central scan lines which reduce the effective acceleration factor.

A number of new parallel imaging methods have incorporated the TSENSE strategy to exploit spatio-temporal correlations, such as k-t SENSE (Tsao et al. 2003) and UNFOLD-SENSE (Madore 2004; Madore 2002), and Auto-SENSE (Kostler et al. 2003). A method for generalized phased-array ghost elimination (PAGE) (Kellman and McVeigh 2001; Kellman 2006) that uses parallel imaging to cancel ghosts arising from a variety of mechanisms uses the TSENSE method for auto-calibration. The TGRAPPA method is an extension of this technique to k-space domain parallel imaging (Breuer et al. 2005). The TSENSE methods may also be applied to non-Cartesian k-space acquisition such as radial or interleaved spiral (Nezafat et al. 2005).

12.1.2 Basic Concepts

A number of different methods have been demonstrated which increase the speed of MR acquisition by decreasing the number of sequential phase encodes

P. Kellman, PhD
Laboratory of Cardiac Energetics, National Institutes of Health/NHLBI, NIH Building 10/B1D-416, 10 Center Drive, msc-1061, Bethesda, MD 20892-1061, USA

through undersampling. Undersampling causes aliasing which results in a mixture of the desired image and wrap artefacts. Parallel imaging is one approach to undersampled image reconstruction. The mixture of desired image and alias artefacts may be separated using parallel imaging as shown in Fig. 12.1, in which the input images for individual coils have been reconstructed to a full FOV with wrap by zero-filling the undersampled k-space data. The individual coil images are then weighted and summed (pixelwise) with a phased-array combiner to cancel the wrap. The phased-array combiner coefficients are calculated based on in vivo estimates of the coil sensitivities by solving the inverse problem which maximizes the image SNR subject to a constraint of nulling the alias artefacts, the so-called SENSE method (see also Chapter 2; Pruessmann et al. 1999). In general, the noise level will vary across the FOV and may have hot spots due ill-conditioning of the parallel imaging solution. The noise amplification is also referred to as the g-factor and is discussed in detail in Chapter 3 (Pruessmann et al. 1999). Residual alias artefacts may also result due to errors in the sensitivity maps.

Another approach to undersampled image reconstruction for dynamic imaging uses temporal filtering (interpolation) to exploit inherent frame-to-frame correlation in dynamic imaging. The basic idea of interpolation is to compute additional time frames using a weighted sum of neighboring measurements to gain a higher temporal sampling rate. Interpolation may also be viewed as temporal filtering. There are a number of schemes for k-space sampling and interpolation. Consider the case for which the k-space lines in sequential images are varied in a time interleaved manner such that the full k-space is periodically acquired. This is shown in Fig. 12.2, in which there is a case of twofold undersampling, with odd lines and even lines acquired on alternate frames. Interpolation methods, such as view sharing, or more general filtering, such as UNFOLD, may be used to reconstruct images with suppressed alias artefacts. For example, a view-shared reconstruction uses two sequential frames in a sliding-window fashion. View sharing may be described as a filter that provides temporal smoothing (see Discussion). The image frame rate is increased, although the effective temporal resolution is not improved. Interpolation errors which result from rapid changes will cause ghosting artefacts. The ghosting artefacts will "flicker" at the frame rate due to the sign changes caused by the interleaved acquisition order. The desired pixel and the ghost artefact which is temporally modulated effectively share the temporal bandwidth. The UNFOLD method exploits the property that the outer portion of the field of view is relatively static and uses a temporal filter with greater bandwidth for dynamic regions, realizing improved temporal resolution. The concept of bandwidth sharing is illustrated by means of temporal spectra (i.e., FFT of images series along

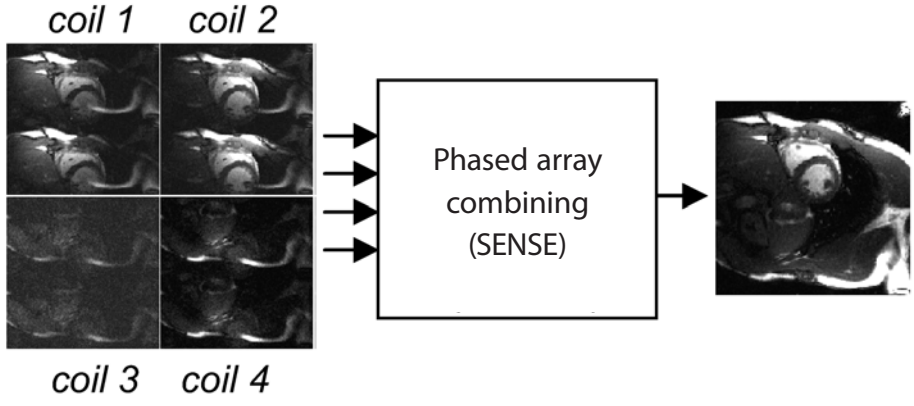

Fig. 12.1. Parallel imaging using SENSE method of phased-array combining

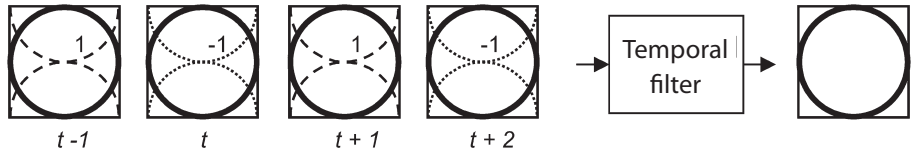

Fig. 12.2. Temporal filtering (interpolation) for suppression of reduced FOV alias artefacts

the time dimension) and is described more fully in the following paragraphs. Temporal filtering or interpolation may be equivalently implemented in the k-space domain providing the same effective bandwidth across the FOV, although this violates the strict bandwidth sharing formulation of the UNFOLD method.

12.1.3 Combined Spatial and Temporal Filtering

Parallel imaging and temporal filtering methods may be combined to achieve either higher acceleration factors or improved suppression of alias artefacts, and/or to realize auto-calibration of the parallel imaging combiner coefficients. The incorporation of temporal processing with image domain parallel imaging is referred to as TSENSE. Both parallel imaging and temporal filtering are linear operations and may be done in either order (commutative operations) as shown in Fig. 12.3. Figure 12.3a shows parallel imaging followed by temporal filtering, whereas Fig. 12.3b shows temporal filtering followed by parallel imaging; these are mathematically equivalent but will differ computationally. Figure 12.4 illustrates the case of auto-calibrating TSENSE, which may optionally include additional temporal filtering of the images. In the auto-calibrating scheme the temporal filter is typically a simple integration of multiple frames to provide a lower temporal resolution set of individual coil images with suppressed alias artefacts to compute the parallel-imaging coefficients.

Parallel imaging and temporal filtering may be combined to provide a higher acceleration factor, e.g., SENSE rate 2× UNFOLD rate 2, for a net TSENSE acceleration of rate 4 (Kellman and McVeigh 2000). In this case, coil sensitivities are estimated from separate reference data since the images may not be fully unfolded with a temporal filter for auto-calibration. Parallel imaging and temporal filtering may also be combined to provide a greater suppression of alias artefacts. For example, in the case of acceleration rate two aliased components are alternating phase; thus, the alias artefact is temporally frequency shifted to the band edge and may be suppressed by temporal low-pass filtering. The phase of the alias artefact does not alter the SENSE formulation; however, if the estimates of coil sensitivities are imperfect, there will be residual alias artefacts. Any residual artefact will be temporally frequency shifted to the band edge and thus may be further suppressed by temporal low-pass filtering. By combining both temporal and parallel imaging the resulting implementation achieves a high degree of alias artefact rejection with less stringent requirements on accuracy of coil sensitivity estimates and temporal low-pass filter selectivity than would be required using each method individually.

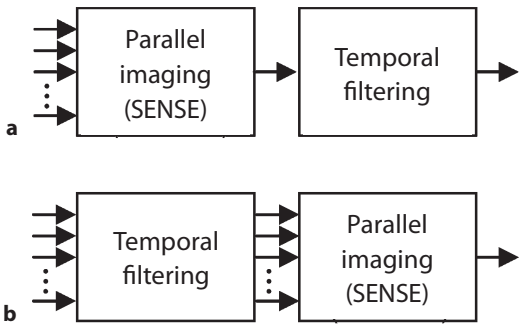

Fig. 12.3a,b. Combined parallel imaging with temporal filtering (TSENSE) implemented equivalently, as **a** parallel imaging then temporal filtering, or **b** temporal filtering then parallel imaging

12.1.4 k-space Undersampling and Temporal Spectra

A number of schemes may be used for undersampling the acquisition of phase encodes in a time series of images. A few schemes are depicted in Fig. 12.5 which illustrate the acquisition of k-space vs time for four consecutive frames, with the solid line indicating phase-encoded lines that are acquired and the dashed lines indicating phase encodes that are skipped. Figure 12.6 illustrates an image with alias artefacts and associated temporal spectra for the cases corresponding to Fig. 12.5, where the bold lined circle portrays the desired object and the alias ghost artefacts are normal solid (±FOV/4) and dashed lines (FOV/2). Figure 12.5a and b are for the case of R=2 undersampling, and Fig. 12.5c and d are for R=4.

Figure 12.5a shows the static case of (conventional) undersampling with a fixed pattern, i.e, odd lines acquired at each time frame. In this case, the temporal spectra of the desired image and aliased artefacts are overlapping and must be separated with parallel imaging. Figure 12.5b shows the case of undersampling by 2, acquiring even and odd lines on alternate time frames. In this case, the alias ghost artefact (separated by FOV/2) has alternating polarity (±1) and, therefore, is temporal frequency shifted to the band edge.

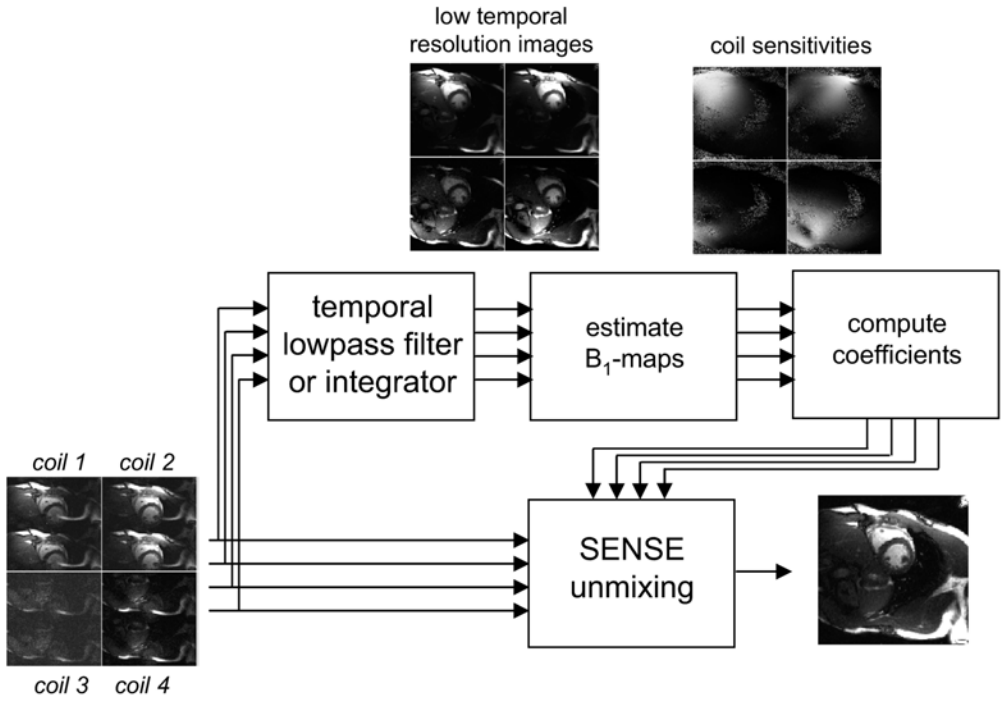

Fig. 12.4. TSENSE method for auto-calibrating parallel imaging

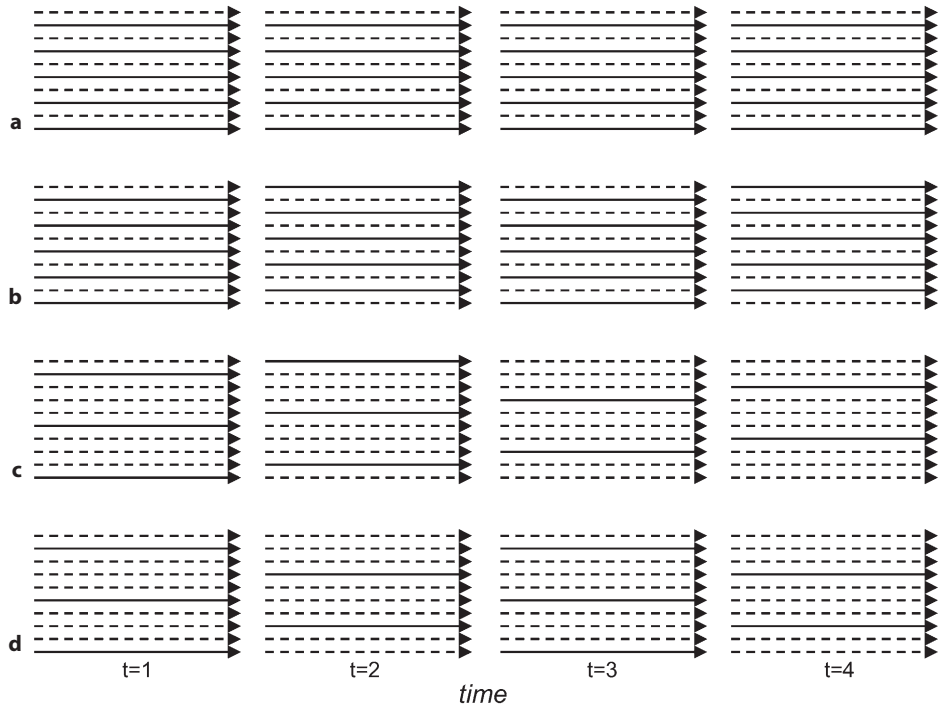

Fig. 12.5a–d. Various schemes for undersampled k-space acquisition. **a** Static phase encoding order (R=2); **b** odd–even phase encoding acquired on alternate time frames (R=2); **c** R=4 undersampled acquisition repeats every fourth frame (1,2,3,4, etc.); **d** R=4 undersampled acquisition repeats every other frame (1,3,1,3, etc.). *Solid lines* indicate phase-encoding lines that are acquired and *dashed lines* indicate phase encodes that are skipped.

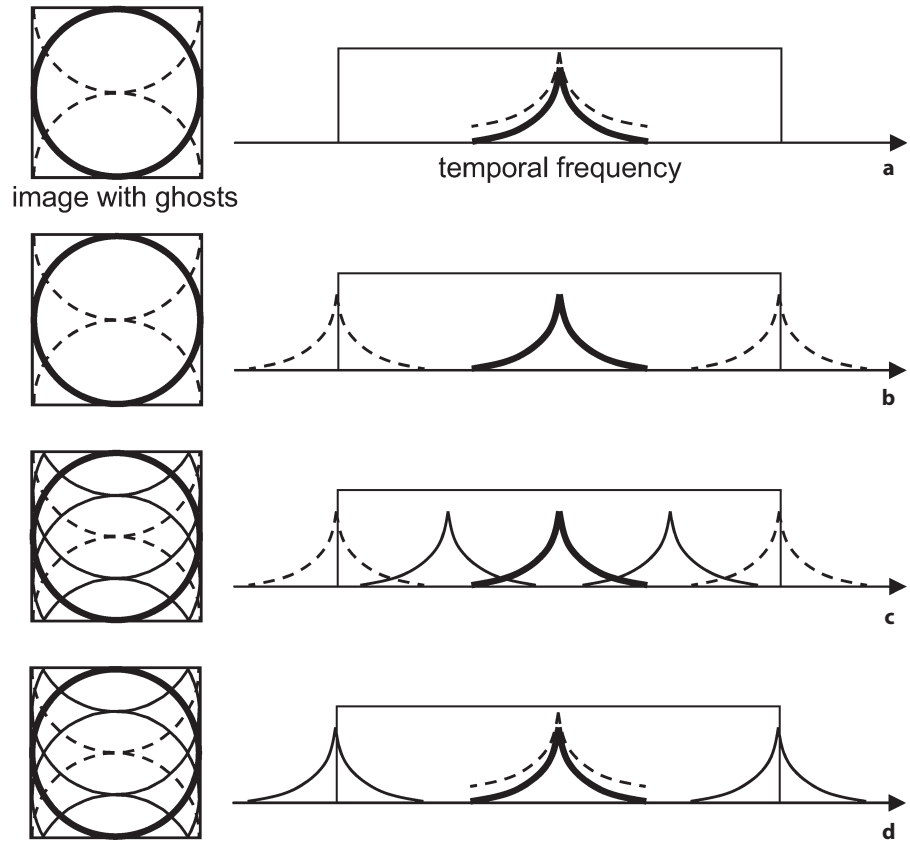

Fig. 12.6a–d. Temporal spectra and images with alias ghost artefacts illustrate the various undersampled k-space acquisition cases described in Fig. 12.5.

A real example of temporal spectra for the case of Fig. 12.6b is shown in Fig 12.7, illustrating several methods. The raw signal (normal solid line) has desired component (center) and aliased artefact (band edge). The UNFOLD method was applied using a temporal filter with magnitude frequency response shown with dashed line. The UNFOLD filter passband was 90% of the available bandwidth causing only a slight decrease of the effective temporal resolution. The spectra for the UNFOLD signal (solid gray line) shows that while the band edge is suppressed, the band edge artefact had a wider temporal bandwidth (i.e., was not completely stationary) resulting in residual artefact. The spectra for parallel imaging using SENSE (dotted line) resulted in fairly good artefact suppression independent of temporal frequency; however, some residual artefact is evident at the band edge. The combination of SENSE and UNFOLD (bold solid line), which may be implemented by either approach of Fig. 12.3, resulting in a high level of artefact suppression. (Note that in the sampling scheme of Fig. 12.5b, full k-space is acquired every R=2 frames, and the data may be integrated or low-pass filtered to derive a low temporal resolution set of individual coil images without artefacts, which may be used as an auto-calibrating reference as shown in Fig. 12.4.)

Figure 12.5c and d correspond to rate-4 acceleration using two different undersampling schemes which results in differences in the temporal spectra. In the case of Fig. 12.5c, the full k-space is acquired every R=4 frames (desired and alias spectra are distinct), and the data may also be used to derive an auto-calibrating references as previously described. The scheme of Fig. 12.5d does not acquire full k-space, and the spectrum for the FOV/2 alias artefact overlaps that of the desired image. This case does lend itself to the same auto-calibration method. Parallel imaging (R=2) may be used to suppress the FOV/2 artefact combined with temporal filtering (R=2) of the band edge to reconstruct images with net acceleration of rate R=4. This scheme uses parallel imaging to suppress the widely spaced ghost artefact (FOV/2) thereby improving the performance (SENSE g-factor). A number of other sampling

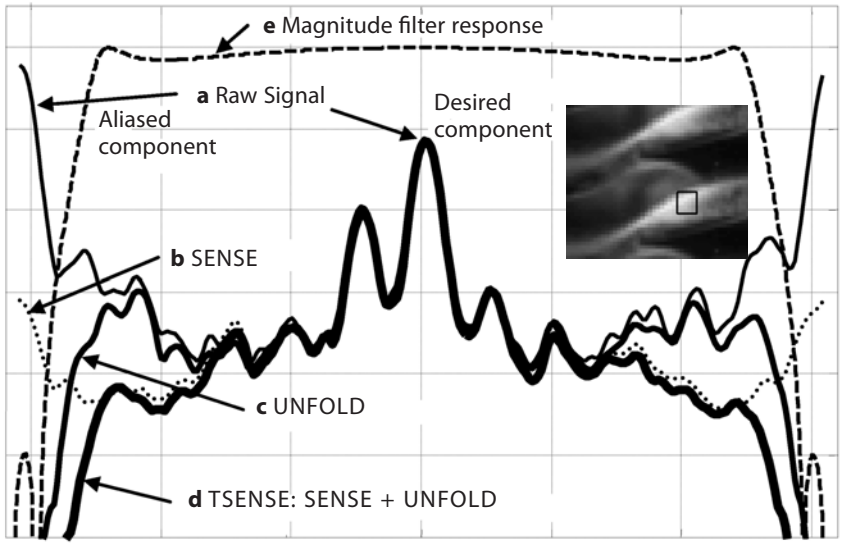

Fig. 12.7a–e. Average temporal spectrum of a region (*inset*) with both heart and aliased chest wall components. **a** Raw signal; **b** SENSE; **c** UNFOLD; **d** TSENSE; **e** temporal low-pass filter response

schemes are possible including variable density sampling (Madore 2004).

12.1.5 2D TSENSE

In volume imaging applications using two phase-encoding dimensions (or spectroscopic imaging), it may be preferable to perform accelerated imaging in each of the two phase-encoded directions as shown in Fig. 12.8, rather than a higher rate along a single direction. This has been referred to as 2D SENSE (Weiger et al. 2002). Depending on the specific coil sensitivity profiles and slice geometry, it may be possible to achieve a g-factor which is greatly reduced when compared with the same net acceleration along a single dimension. A sampling scheme for 2D TSENSE is shown in Fig. 12.9, corresponding to undersampling by rate 4 in the phase-encoding direction and by rate 3 in the partition-encoding direction.

12.2 Application Examples

The TSENSE may be used for a number of dynamic imaging applications. A few typical cardiac applications are presented as examples. The TENSE has also been applied in echo-planar imaging (EPI)-BOLD fMRI (de Zwart et al. 2002).

12.2.1 Cardiac Segmented Cine 2D Imaging

Cardiac MR imaging is challenging due to the simultaneous need for moderately high resolution, ability to image during cardiac and respiratory motion, and relatively low SNR of imaging in the heart at the center of the torso. Parallel imaging offers a means of decreasing acquisition time which offers the user more flexibility to meet these challenges.

The cardiac short-axis images shown in Fig. 12.10 were acquired using the 32-channel Siemens 1.5-T Avanto and a prototype 32-element cardiac array (Invivo Corp). The array consisted of two 16-element 2D arrays with overlapping hexagonal elements with one array positioned on the chest, and the second array positioned on the back of the

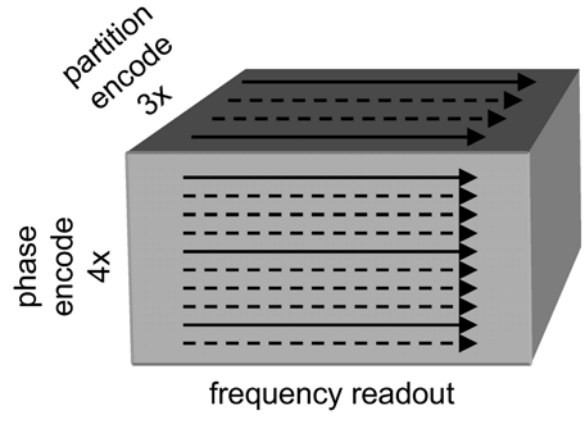

Fig. 12.8. k-space acquisition for 2D SENSE with under-sampling in both the phase and partition-encode directions.

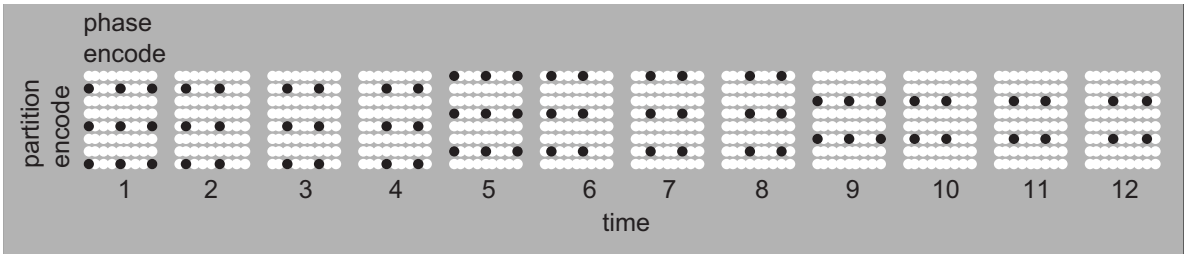

Fig. 12.9. k-space acquisition order for R=4×3=12 2D TSENSE example with under-sampling by four in the phase-encoding direction and undersampling by three in the partition-encoding direction. Complete k-space is acquired in R=12 phases.

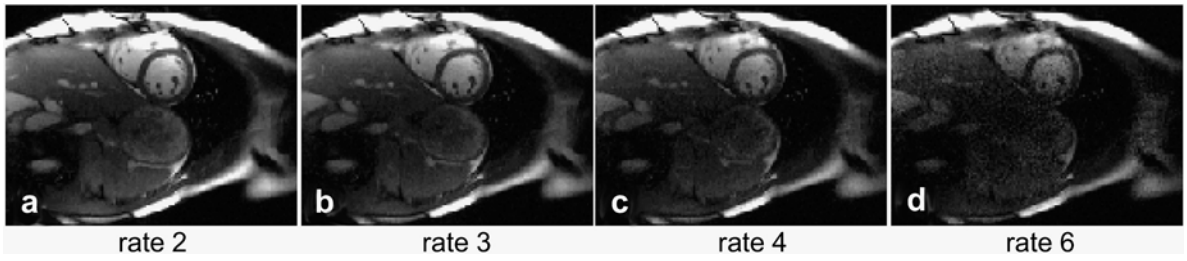

Fig. 12.10a–d. Short-axis cardiac cine images reconstructed using TSENSE at acceleration rates R=2, 3, 4, and 6

patient. The coverage of the array was approximately 35 cm in the left–right direction and 30 cm in the superior–inferior direction. Cardiac imaging was performed using a breath-held, segmented, ECG triggered, true-FISP cine sequence. B_1 maps were calculated using the auto-calibrating TSENSE method. A single, doubly oblique, short-axis slice was acquired with phase encoding performed along the anteroposterior direction. Imaging parameters were matrix size=192×108, FOV=320×240 mm^2, slice thickness=6 mm, readout flip angle=50°, TE/TR=1.41/2.82 ms, views per segment=9, in-plane spatial resolution=1.7×2.2 mm^2, and temporal resolution=25.4 ms. Breath-hold durations were 12, 6, 4, 3, and 2 heartbeats for acceleration at rates 1 (fully sampled), 2, 3, 4, and 6, respectively.

The quality of SENSE accelerated cardiac images at acceleration rates up to rate 4 was excellent using the 32-element array. Degradation was evident above rate 4 acceleration but may still be useful for some applications.

12.2.2 Real-Time Cardiac 2D Imaging

Patients with heart failure pose challenges for cardiac imaging due to increased difficulty with breathing and incidence of arrhythmias. Cardiac functional imaging using breath-held, gated, segmented acquisition will frequently have artefacts, as shown in Fig. 12.11a for a patient with arrhythmia. Real-time, non-breath-held, non-ECG triggered imaging is possible with accelerated parallel imaging. An example of a real-time image for the same patient acquired using rate-4 TSENSE is shown in Fig. 12.11b.

Imaging was performed on a 1.5-T Siemens Avanto using an 8-element cardiac array (Nova Medical, Wilmington, Mass.). A true-FISP sequence was used with the following typical parameters: TE/TR=1.4/2.8 ms; 50° readout flip angle; and 6-mm slice thickness. The acquisition matrix was 192×80 with FOV=300×250 mm^2 corresponding to an in-plane resolution of 1.6×3.1 mm^2, and a temporal resolution of 56 ms at rate R=4.

12.2.3 Contrast-Enhanced First-Pass Perfusion

Coverage of the entire heart during first-pass contrast-enhanced MRI with single-heartbeat temporal resolution is desirable for quantifying perfusion abnormalities. Multi-slice coverage may be achieved using saturation recovery with a relatively short preparation time (TI) and a gradient-echo (GRE) sequence with multi-shot EPI readout. Imaging quality may be improved at the expense of coverage by

increasing TI and readout flip angle. Parallel imaging may be applied to first-pass contrast-enhanced cardiac MR to yield greater spatial coverage for a fixed temporal resolution. Accelerated imaging also reduces the imaging duration per slice which reduces the possibility of motion blur. The saturation recovery time (TI) may be increased for improved contrast-to-noise ratio.

The TSENSE method (Kellman et al. 2001) was used to adaptively estimate B_1 maps using an interleaved phase-encoded acquisition order at acceleration rate R=2. The sequence timing is shown in Fig. 12.12 Odd and even phase-encoded lines were acquired on alternate heartbeats. The B_1 maps were calculated from a sliding window average of eight frames to reduce the sensitivity to breathing. No additional temporal filtering for further alias artefact suppression was applied to the TSENSE images.

Figure 12.13 shows example images of a single short-axis slice (of five acquired) during first-pass perfusion with dipyridamole induced stress and at rest for a patient with a stress perfusion deficit in the inferior and lateral wall. The perfusion deficit in the stress study is clearly evident in Fig. 12.13d.

Imaging was performed on a 1.5-T Siemens Avanto using an 8-element cardiac array (Nova Medical, Wilmington, Mass.). A GRE-EPI sequence was used with the following typical parameters: 90° saturation recovery; echo-train length=4; TR=6.2 ms; 25° readout flip angle; 1600 Hz/pixel BW; and 8-mm slice thickness. The acquisition matrix was 128×80 with FOV=360×270 mm^2 corresponding to an in-plane resolution of 2.8×3.4 mm^2. The TI was 110 ms, where TI is defined at the center of k-space acquisition. The imaging window was 62 ms (142 ms per slice SR preparation time and overhead). Single heartbeat temporal resolution was accomplished with spatial coverage of five slices at heart rates up to 80 bpm with consistently good contrast and overall image quality.

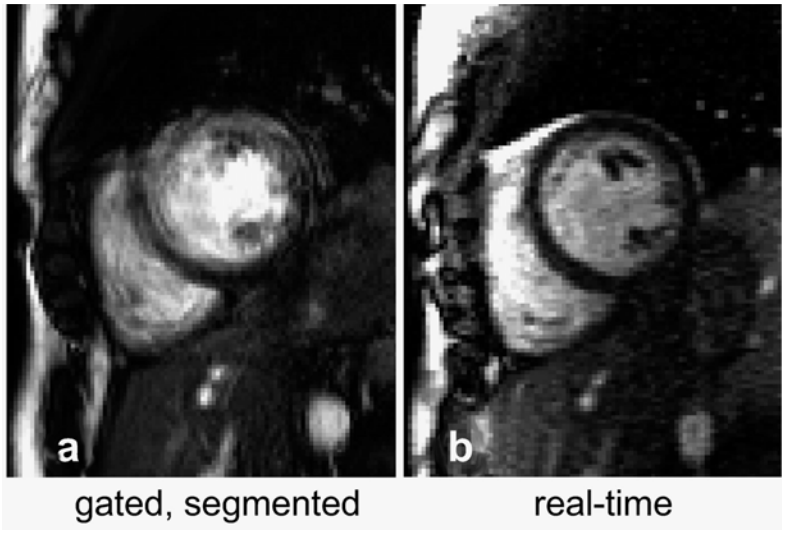

Fig. 12.11a,b. Short-axis cardiac cine image for a patient with arrhythmia for **a** conventional ECG-gated, segmented acquisition, and **b** real-time acquisition using TSENSE, non-ECG triggered

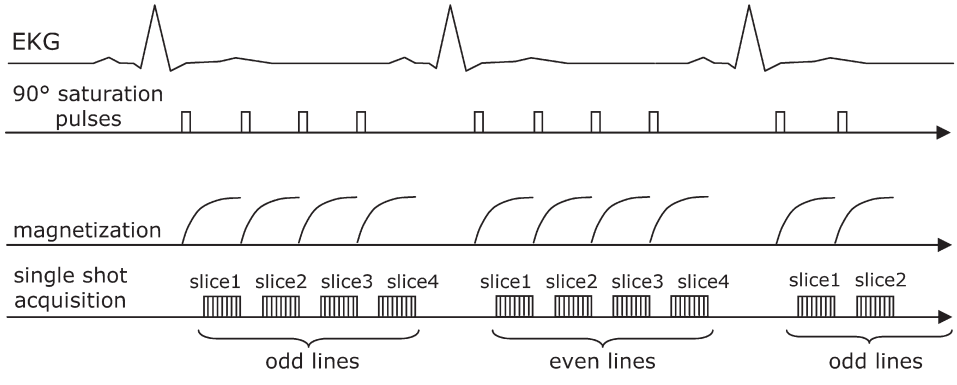

Fig. 12.12. Sequence timing for multislice first-pass contrast-enhanced perfusion with single-shot readout and single RR temporal resolution, acquiring even and odd phase-encoded lines on alternate heart beats for TSENSE reconstruction

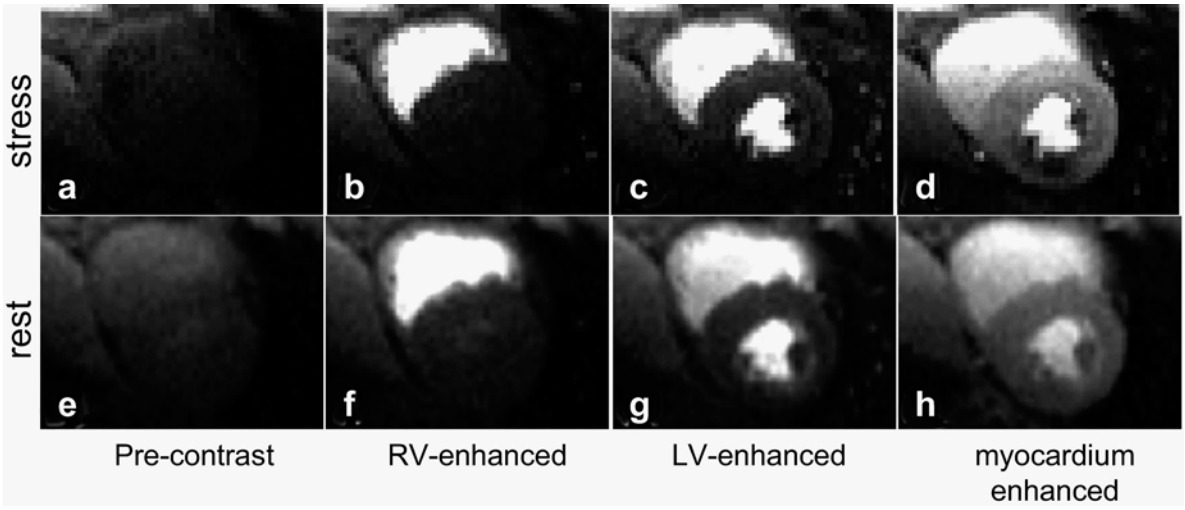

Fig. 12.13a–h. Example of first-pass contrast-enhanced perfusion images for patient with stress perfusion deficit in the inferior and lateral wall shown for single slice, acquired using GRE echo-planar sequence using rate-2 TSENSE. The *bottom row* is at rest and *top row* is with stress. **a,e** Pre-contrast; **b,f** RV enhanced; **c,g** LV enhanced; **d,h** myocardium enhanced

12.2.4 Cardiac Cine 3D Imaging

Cardiac cine 3D imaging offers the potential for full heart coverage in a single, segmented breath-held acquisition. A single acquisition eliminates breath-hold registration errors between slices that may occur in conventional 2D multislice imaging requiring multiple breath-holds. Parallel imaging using 2D SENSE (Weiger et al. 2002) was used to reduce the breath-hold duration. A gated, segmented trueFISP sequence at acceleration rate R=12 was used to achieve spatial resolution of 1.8×2.4×7 mm^3 and approximately 30-ms temporal resolution within a single 18-heartbeat breath-hold.

Doubly oblique imaging was used with the partition encoding along the long axis of the heart. The phase-encoded and frequency-readout directions were in the short-axis plane with the frequency readout along the longer dimension of the body after in-plane rotation was applied. Encoding directions are shown in Fig. 12.14. The acquisition used rate 4×3=12 undersampling, with rate-4 undersampling in the phase-encoded dimension and rate-3 undersampling in the partition-encoded direction. The B_1 maps were estimated using the auto-calibrating TSENSE method. The k-space undersampling varied cyclically with complete k-space acquired in R=12 phases. The complete data set was integrated to reconstruct B_1 maps for calculating SENSE unmixing coefficients. Since it is important to have artefact-free in vivo reference images for B_1 map estimates, approximately 25% slice oversampling was used in the partition-encoded dimension to reduce wrap. The acquisition matrix was 192×108×18 with four slices discarded after reconstruction. Example images for rate 4×3=12 are shown in Fig. 12.15 for a normal volunteer subject. The example shown used a FOV of 340×255×98 mm^3 providing a spatial resolution of 1.8×2.4×7 mm^3. At rate 4×3=12, the actual number of lines acquired were 108/4=27 phase encodes × 18/3=6 partition encodes. The sequence parameters were: bandwidth=1400 Hz/pixel; TR=3.08 ms; and 50° readout flip angle. There were nine views per segment providing 9×3.08=27.7 ms temporal resolution. The total breath-hold duration was (108/4) × (18/3) / 9=18 heart beats. Imaging was performed on a 32-channel Siemens Avanto 1.5 T scanner using a prototype 32-element cardiac phased array (Invivo Corp).

The measured g-factor values for which 95% of the pixels in the heart region fall below were 5.2 for rate 4×3=12 and 2.9 for rate 4×2=8. Despite a relatively high g-factor, the SNR and artefact suppression were quite good using 3D imaging.

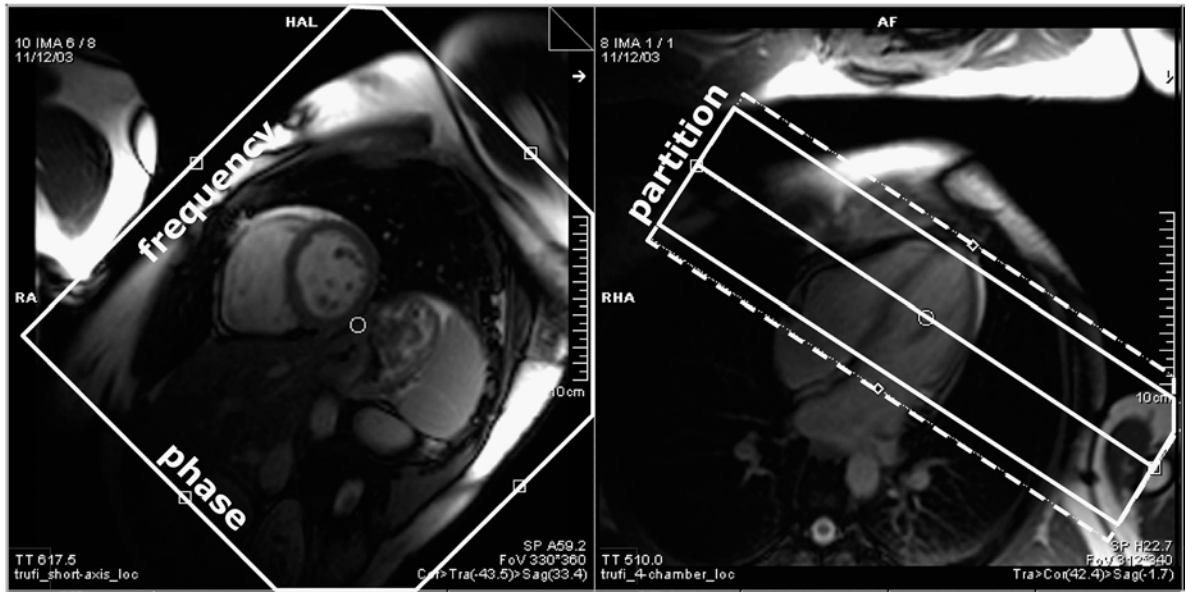

Fig. 12.14. Graphic prescription for cine 3D doubly oblique imaging. The partition encoding is along the long axis of the heart. The phase-encoded and frequency-readout directions were in the short-axis plane with the frequency readout along the longer dimension of the body after in-plane rotation was applied.

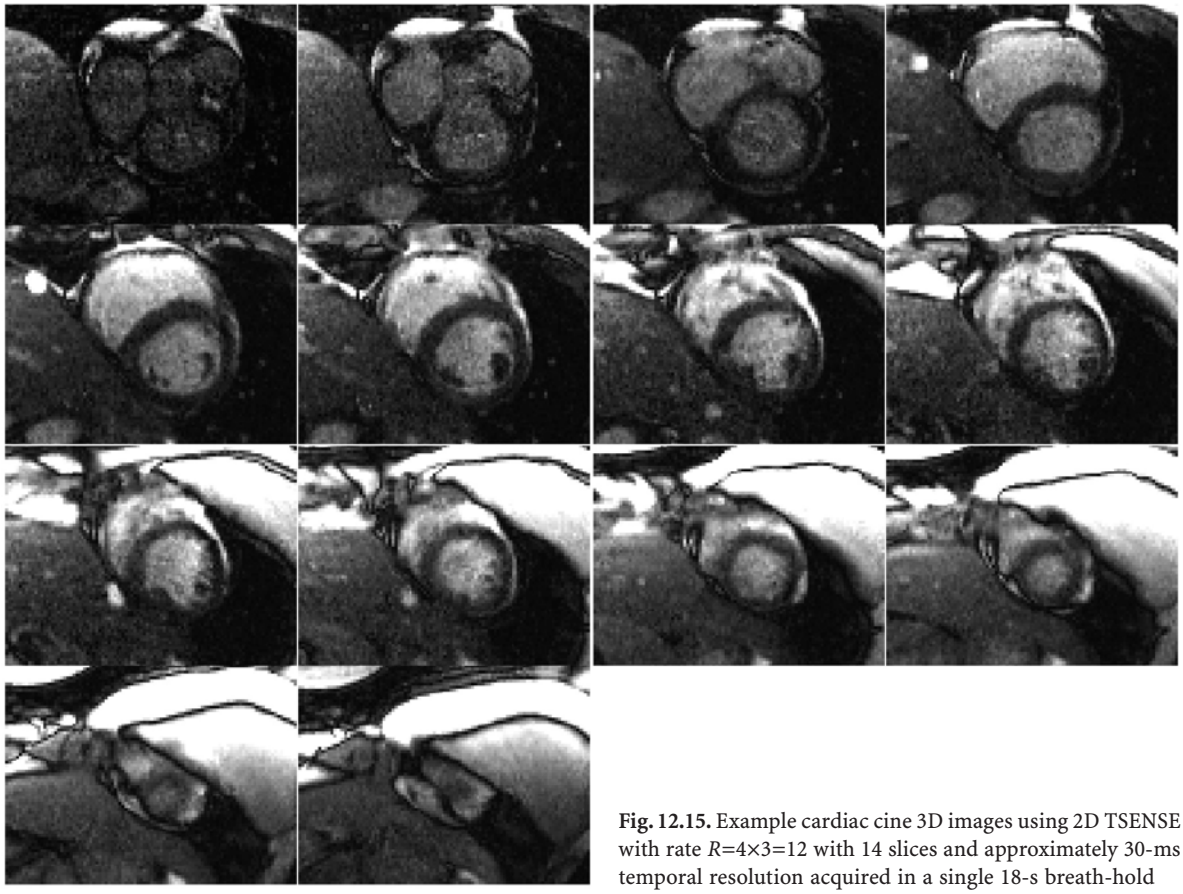

Fig. 12.15. Example cardiac cine 3D images using 2D TSENSE with rate R=4×3=12 with 14 slices and approximately 30-ms temporal resolution acquired in a single 18-s breath-hold

12.3 Discussion

Parallel imaging provides accelerated imaging with a wide temporal bandwidth. A number of methods, such as view sharing, produce temporally interpolated images at a higher frame rate; however, the effective temporal resolution is not improved. In order to place view sharing and more general temporal filtering (e.g., UNFOLD) in the same context, Fig. 12.16 illustrates the equivalence between k-space and image domain temporal filtering. In this diagram, the undersampled acquisition matrix has been zero-filled for missing data at each time frame. After temporal filtering, the missing k-space is filled with temporally interpolated values. In the case of simple view sharing which combines even and odd k-space data for each frame, the temporal filter is a sliding window filter which is applied to each k-space value after zero-filling (e.g., even, 0, even, 0, even .... or 0, odd, 0, odd,...). Equivalently, in the image domain, the FOV/2 artefacts are alternating sign (±1) and a sliding window filter at each pixel will cancel the alias artefact provided that it is stationary. The simple sliding window used in view-shared reconstruction is a crude low-pass filter which zeros the band edge with greatest artefact but does not improve the temporal resolution. Improved temporal filters which interpolate using additional time frames provide a flatter temporal frequency response, although they will have a correspondingly increased transient response which may cause intensity fluctuations (filter ringing). The filter may be implemented directly in the time domain as a weighted sum or equivalently using FFT-based filtering (at each pixel).

Temporal filtering (interpolation) methods rely on the tissue corresponding to aliased artefacts being sta-

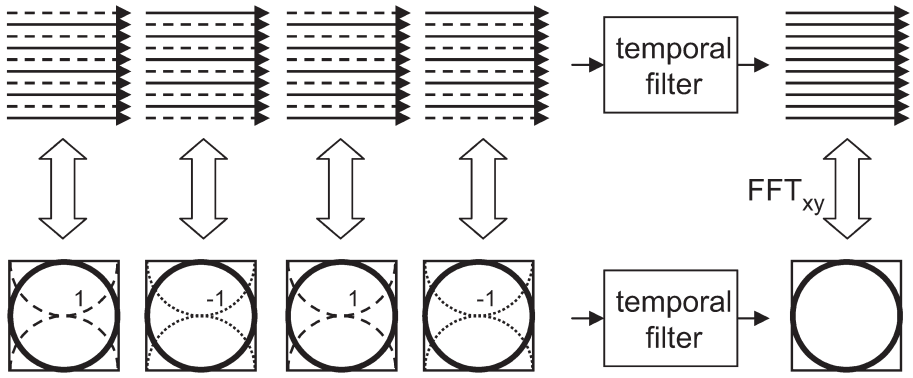

Fig. 12.16. Equivalence of k-space and image domain temporal filtering implementations

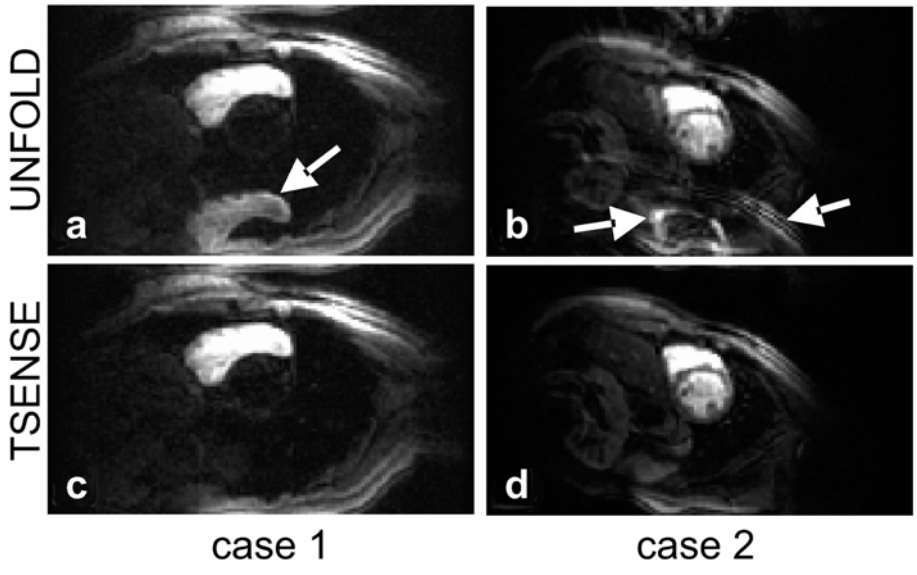

Fig. 12.17a–d. Residual artefacts in UNFOLD reconstruction due to dynamic signal fluctuation. *Arrows* in **a** indicate artefact due to rapid signal enhancement of RV blood pool and in **b** due to respiratory motion of chest wall

tionary with constant or slowly varying signal intensity. The extent that the tissue intensity is changing, there will be residual artefacts as illustrated in Fig. 12.17. In case 1 (left column), a first-pass contrast enhanced cardiac perfusion image is shown after UNFOLD filter reconstruction (Fig. 12.17a), for a time point where the right ventricle (RV) is enhancing. The rapid change in signal intensity due to contrast enhancement leads to a residual artefact of the RV displaced by FOV/2. The TSENSE reconstruction (Fig. 12.17c) of the same time frame using combined spatial and temporal filtering provides artefact suppression despite the rapid change. A second example in Fig. 12.17b and d shows a chest wall artefact due to respiratory motion in the UNFOLD reconstruction of Fig. 12.17b which is suppressed using TSENSE in Fig. 12.17d.

References

Breuer FA, Kellman P, Griswold MA et al. (2005) Dynamic autocalibrated parallel imaging using temporal GRAPPA (TGRAPPA). Magn Reson Med 53:981–985

d'Arcy JA, Collins DJ, Rowland IJ et al. (2002) Applications of sliding window reconstruction with cartesian sampling for dynamic contrast enhanced MRI. NMR Biomed 15:174–183

Hu X, Parrish T (1994) Reduction of field of view for dynamic imaging. Magn Reson Med 31:691–694

Kellman P, McVeigh ER (2000) Method for combining UNFOLD with SENSE or SMASH. Proc Eighth Scientific Meeting. Int Soc Magn Reson Med 1507

Kellman P, McVeigh ER (2001) Ghost artefact cancellation using phased array processing. Magn Reson Med 46:335–343

Kellman P, Epstein FH, McVeigh ER (2001) Adaptive sensitivity encoding incorporating temporal filtering (TSENSE). Magn Reson Med 45:846–852

Kellman P, McVeigh ER (2006) Phased array ghost elimination. NMR Biomed. 19:352–361

Kostler H, Sandstede JJ, Lipke C et al. (2003) Auto-SENSE perfusion imaging of the whole human heart. J Magn Reson Imaging 18:702–708

Madore B (2002) Using UNFOLD to remove artefacts in parallel imaging and in partial-Fourier imaging. Magn Reson Med 48:493–501

Madore B (2004) UNFOLD-SENSE: a parallel MRI method with self-calibration and artefact suppression. Magn Reson Med 52:310–320

Madore B, Glover GH, Pelc NJ (1999) Unaliasing by Fourier encoding the overlaps using the temporal dimension (UNFOLD), applied to cardiac imaging and fMRI. Magn Reson Med 42:813–828

Nezafat R, Kellman P, Derbyshire JA, McVeigh ER (2005) Real Time Blood Flow Imaging using Auto-Calibrated Spiral Sensitivity Encoding. Magn Reson Med. 54:1557–1561

Pruessmann KP, Weiger M, Scheidegger MB et al. (1999) SENSE: sensitivity encoding for fast MRI. Magn Reson Med 42:952–96.

Sodickson DK, Manning W (1997) Simultaneous acquisition of spatial harmonics (SMASH): fast imaging with radiofrequency coil arrays. Magn Reson Med 38:591–603

Tsao J, Boesiger P, Pruessmann KP (2003) k-t BLAST and k-t SENSE: dynamic MRI with high frame rate exploiting spatiotemporal correlations. Magn Reson Med 50:1031–1042

Weiger M, Pruessmann KP, Boesiger P (2002) 2D SENSE for faster 3D MRI. MAGMA 14:10–19

Zwart JA de, van Gelderen P, Kellman P et al. (2002) Application of sensitivity-encoded EPI for BOLD functional brain imaging. Magn Reson Med 48:1011–1020

Part III:
Technical Implementation in Clinical MRI

Design of Dedicated MRI Systems for Parallel Imaging

13

Arne Reykowski

CONTENTS

13.1 Introduction

This chapter discusses the requirements for modern MRI systems with parallel imaging capability. It explains the original motivation that led to the introduction of array coils and how this concept was later extended to parallel imaging. Data compression schemes, such as the Eigencoil or Matrix Coil (Mode Matrix) concepts, are introduced using a three-channel Mode Matrix as an example. Also, the differences between stationary and moving coil arrays are discussed. Finally, the necessary hardware and software components for a dedicated parallel imaging system are laid out in detail.

A. Reykowski, PhD
Invivo Corporation, 3545 SW 47th Ave, Gainesville, FL 32608, USA

13.2 Array Coils and Parallel Imaging

The use of multiple decoupled coil elements was first proposed by Roemer et al. in 1988 (Roemer et al. 1988; Roemer et al. 1990; Hayes and Roemer 1990). Although offering high signal-to-noise ratio (SNR), single surface coils are limited in their field of view (FOV). This limitation can be overcome by using several surface coil elements and arranging them in an array. The signals detected by the individual elements are not combined in hardware, e.g., linear polarized (LP) signals are combined to form circular polarized (CP) signals. Instead, each coil element in the array is independently fed into its own receiver channel and the final signal combination is done on a pixel-by-pixel basis in the image domain. This way, the high SNR of each individual coil element is preserved while the combined FOV of the array is much larger than the FOV of a single coil element (Fig. 13.1).

The first ideas to use the spatial information from coil arrays in order to accelerate image acquisition date back to 1988, as described in Chapter 2 (Hutchinson and Raff 1988; Kwiat and Einav 1991; Kelton et al. 1989; Ra and Rim 1993). It was, however, not before 1997 until feasibility was first demonstrated by experiments (Sodickson and Manning 1997; Pruessmann et al. 1999; Griswold et al. 2000; Griswold et al. 2002).

The use of spatial information for parallel imaging had a strong influence on array design and MRI system architecture. Typical arrays for non-parallel imaging consist of anterior and posterior groups of elements which are organized in head–feet direction. Most of these arrays have no independent elements in left–right direction. This is due mainly to the fact that arrays with independent elements in left–right direction do need a significant larger number of radio frequency (RF) channels but do not provide a major SNR improvement in the center region of the image.

In parallel imaging applications, however, maximizing the SNR in the image center is only one of sev-

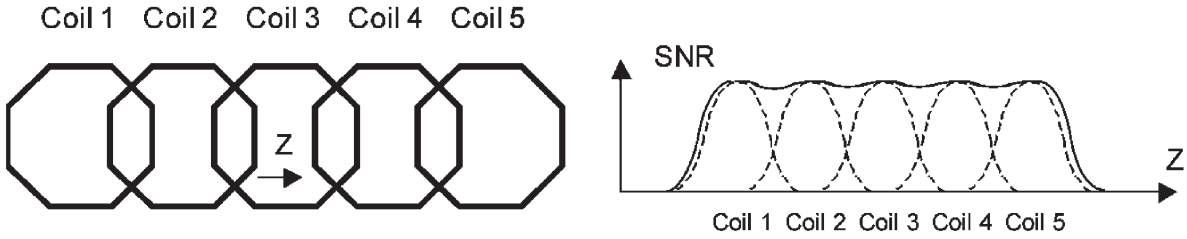

Fig. 13.1. Array technology allows maintaining the high signal-to-noise ratio of local coils while at the same time the field of view (FOV) of the array is much larger than the FOV of a single coil element.

eral design criteria. In addition to that, the elements of the array have to be organized along the phase-encoding direction in order to generate sufficient information for accelerated imaging. For a maximum degree of freedom, arrays for parallel imaging need to have elements in all three spatial directions, including left–right. This requirement leads to a significant larger number of array elements and RF channels for parallel imaging than for non-parallel imaging.

Before parallel imaging methods became a standard for clinical procedures, scanners were equipped with a maximum of eight RF channels. In contrast to that, recent MR systems which support parallel imaging in all spatial directions have up to four times as many RF channels.

13.3 Data-Reduction Concepts

The increase in the number of RF channels in combination with parallel imaging methods, such as SENSE or GRAPPA, leads to a more than proportional increase in reconstruction time. It is therefore prudent to keep the number of parallel RF channels to a necessary minimum. This can be accomplished by applying hardware- or software-based data compression schemes. Two hardware-based examples are the so-called Eigencoil and Matrix Coil concepts (King et al. 2003; Reykowski and Blasche 2004). Both concepts allow a scalable and efficient use of the number of receiver channels by transforming a given set of coil signals to an equal number of mode signals. While each of the original signals only covers a part of the FOV, each of the mode signals covers the entire FOV.

In the case of the Matrix Coil concept, the center piece is a signal combiner network which is called "Mode Matrix." A good analogy for this Mode Matrix combiner comes from broadcasting: firstly, radio transmissions used single-channel mono broadcast signals. Such a mono signal contains all necessary information to listen to a broadcast. It can be described as the sum of the signals for left and right audio or simply L+R (left plus right).

With the advent of stereo broadcasting, a transmission format had to be designed which ensured compatibility with existing mono radio receivers; therefore, stereo broadcast transmissions still transmit the mono L+R signal on a main channel. On a second channel, a differential signal L–R is transmitted. This is identical to transmitting L and R on two individual channels but at the same time ensures full compatibility with mono receivers (Fig. 13.2).

The Mode Matrix works in a similar fashion. All input signals are combined to a circular-polarized (CP) output signal on the main output channel. This CP Mode signal is the MR signal equivalent of the L+R

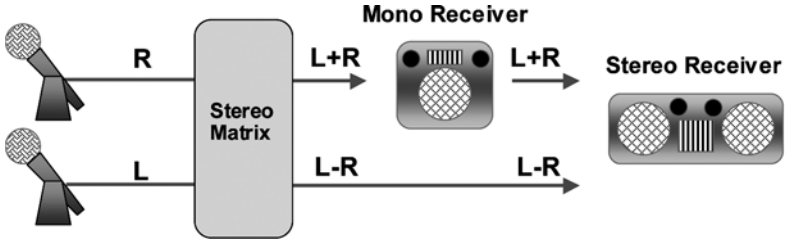

Fig. 13.2. Stereo broadcast consists of a mono broadcast signal plus a differential signal.

mono signal in broadcasting applications. It already provides close to optimum SNR in the important center region of the image. The higher-order output signals of the Mode Matrix contain differential information, designed to ensure RF channel scalability with respect to parallel imaging.

The sum of the three mode signals P, S, and T (for primary, secondary, and tertiary) contains the same information as the original signals R, M, and L (for right, middle, and left) from the coil elements (Fig. 13.3).

13.4 Stationary Coils and Moving Coils

Frequently, a discussion arises in the context of move-during-scan applications, whether it is more advantageous to use a stationary or a moving coil array for data acquisition. A stationary coil array is at a fixed position inside the magnet bore and does not move with the table. A moving coil array is attached to the table and thus moves with patient and table.

A stationary array has the advantage that it requires less coil elements, because it only has to cover a single FOV. Typically, the array is attached to the magnet bore and there is no need to place coils on top of the patient. The main disadvantage of such a stationary coil array is the reduced SNR, due to the fact that it is at a larger distance from the patient.

On the other hand, a moving coil array has the advantage of providing significantly higher SNR, especially in the periphery of the FOV. This SNR can be utilized to increase acceleration or resolution. In addition, dedicated surface coils with small FOVs can be easily added, for example, to provide high-resolution, high-SNR data of vessel walls or the bulbus. The disadvantage of a moving coil array is the higher number of array elements since it has to cover more than a single FOV.

In summary, a remote stationary array improves the work flow at the cost of imaging performance, whereas a local moving array increases performance in terms of acquisition speed and image quality but reduces work flow due to higher patient setup time.

13.5 Dedicated Parallel-Imaging Systems

A dedicated MRI system for parallel imaging has to contain all the necessary hardware and software to enable parallel data acquisition and processing in various regions of the human anatomy. Such a system should also support more recent trends such as high-resolution whole-body imaging with local coil arrays and move during scan techniques.

The parallel acquisition hardware should therefore consist of the following components:

- One or several arrays with multiple decoupled coil elements
- An RF switching matrix which allows selection of alternating subsets of coil array signals for acquisition to reduce the number of required receiver channels
- Means for array identification in order to determine which coil arrays are plugged into the system and where these arrays are located relative to the patient
- Static/dynamic detune signals for individual elements or array subsets
- Multiple independent receivers
- Fast image-processing system

For scanning more than a single FOV within one examination, the number of coil elements which can be connected to the system should ideally be substantially greater than the number of receiver channels.

The system has to support both, static and dynamic detuning:

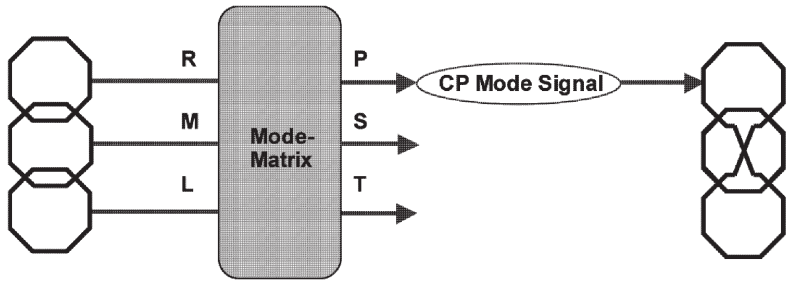

Fig. 13.3. In analogy to stereo broadcast, the Mode Matrix delivers a high SNR circular-polarized (CP) signal plus additional differential signals for iPAT applications.

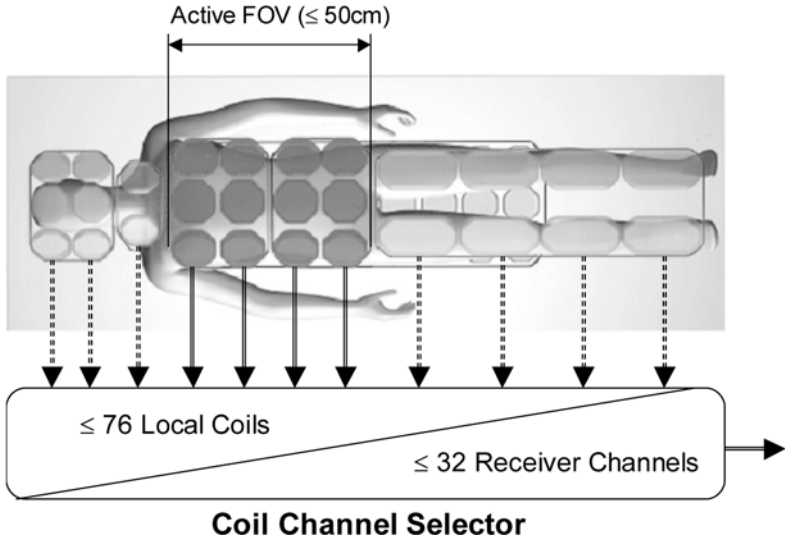

Fig. 13.4. Total imaging matrix for whole-body scans. In this example, a subgroup of up to 32 coil elements can be selected from a total of 76 coil elements.

- Non-active coil elements, i.e., those which are not within the active FOV, are statically detuned. This means that they are detuned during the transmit phase as well as receive phase of the experiment.
- Active coil elements, i.e., those which are in the active FOV, are dynamically detuned. This means that they are detuned during the transmit phase and tuned during the receive phase of the experiment.

The first versions of local coils were connected to the MRI system via a plug in the magnet covers; however, placing the coil plug in the covers has the disadvantage of relative movement between coil and coil plug. The connecting cable can create unwanted loops during patient table movement or can get caught between patient table and magnet covers. The operating personal has to be trained to observe cable movements and, if necessary, interact manually in order to prevent damage or injury; therefore, systems with such a configuration do not allow a 100% remote operation, especially not in case of move during scan applications with continuous table movement. For this reason, the majority of present-day MRI systems have the coil plugs designed so that they are moving with the patient table. The plugs can be either found distributed along the table or within a docking station on the magnet side of the table.

Figure 13.4 shows how matrix coils can be combined to form a "Total imaging matrix" (Tim) for whole-body coverage. In this specific example, up to 76 local coil elements can be connected to the system. From these 76 elements, a subset of up to 32 elements in the active FOV can be selected for image acquisition via a coil channel selector.

In the past, an exam was based on selecting elements of a single array of coils within a single FOV. Modern MRI systems, however, allow selection of a multitude of coil elements from a multitude of coil arrays, which extend over an area that is larger than a single FOV. The user interface of such a system should therefore aid in simplifying the exam setup procedure. The MRI system should be capable of detecting which coil elements are within the present FOV and choose the appropriate hardware settings based on easy-to-define protocol parameters such as FOV, acceleration factor, phase-encoding direction, and others.

References

Griswold MA, Jakob PM, Nittka M, Goldfarb JW, Haase A (2000) Partially parallel imaging with localized sensitivities (PILS). Magn Reson Med 44:602–609

Griswold MA, Jakob PM, Heidemann RM, Nittka M, Jellus V, Wang J, Kiefer B, Haase A (2002) Generalized autocalibrating partially parallel acquisitions (GRAPPA). Magn Reson Med 47:1202–1210

Hayes CE, Roemer PB (1990) Noise correlation in data simultaneously acquired from multiple surface coil arrays. Magn Reson Med 16:181–191

Hutchinson M, Raff U (1988) Fast MRI data acquisition using multiple detectors. Magn Reson Med 6:87–91

Kelton JR, Magin RL, Wright SM (1989) An algorithm for rapid image acquisition using multiple receiver coils. Proc SMRM 8th Annual Meeting, Amsterdam, p 1172

King SB, Varosi SM, Huang F, Duensing GR (2003) The MRI Eigencoil: 2N-Channel SNR with N-Receivers, Proc. ISMRM 11th Annual Meeting, Toronto, p 712

Kwiat D, Einav S (1991) A decoupled coil detector array for fast image acquisition in magnetic resonance imaging. Med Phys 18:251–265

Pruessmann KP, Weiger M, Scheidegger MB, Boesiger P (1999) SENSE: Sensitivity encoding for fast MRI. Magn Reson Med 42:952–962

Ra JB, Rim CY (1993) Fast imaging using subencoding data sets from multiple detectors. Magn Reson Med 30:142–145

Reykowski A, Blasche M (2004) Mode matrix: a generalized signal combiner for parallel imaging arrays. ISMRM 12th Annual Meeting, Kyoto, p 1587

Roemer PB, Edelstein WA (1987) Ultimate sensitivity limits of surface coils. Proc SMRM 6th Annual Meeting, New York, p 410

Roemer PB, Edelstein WA, Hayes CE, Souza SP, Mueller OM (1988) Simultaneous multiple surface coil NMR imaging. Proc SMRM 7th Annual Meeting, p 875

Roemer PB, Edelstein WA, Hayes CE, Souza SP, Mueller OM (1990) The NMR phased array. Magn Reson Med 16:192–225

Schnell W, Renz W, Vester M, Ermert H (2000) Ultimate signal-to-noise-ratio of surface and body antennas for magnetic resonance imaging. IEEE Trans Ant Prop 48:418–428

Sodickson DK, Manning WJ (1997) Simultaneous acquisition of spatial harmonics (SMASH): ultra-fast imaging with radiofrequency coil arrays. Magn Reson Med 38:591–603

Dedicated Coil Systems from Head to Toe

14

Randy Duensing

CONTENTS

R. Duensing, PhD
Department of Diagnostic Imaging, Invivo Corporation, 3545 SW 47th Avenue, Gainesville, FL 32608, USA

14.1 Introduction

Parallel-imaging algorithms have driven rapid changes to the RF sub-systems in clinical MRI scanners. The typical high-end scanner in use during 2003 had 4–8 RF receiver channels. These channels were used primarily for RF coil arrays designed to increase the signal-to-noise ratio (SNR) over a certain anatomical region. Because of the profound impact of parallel imaging on clinical practice, the state-of-the-art scanner in 2005 has 16, 18, or 32 receiver channels available for simultaneous acquisition. As is demonstrated in Chap. 3, while an asymptotic limit is reached, the more independent receiver coils employed, the higher the permissible reduction rates and the lower the resulting g-factors; therefore, the rapid demand for receiver channels has been matched by the demand for coil arrays that can be utilized on these systems. There are currently two disparate uses for arrays and parallel-imaging systems: the first utilizes specialized high-density coil arrays for optimizing the image quality in a given time for a specific anatomical or functional region; the second utilizes arrays with large or complete body coverage to allow rapid whole-body scans, including moving-table applications. These products are mostly available at 1.5 T on horizontal field systems, with growing availability at 3 T. The vertical field products for open low-field MRI systems lag behind horizontal field but are becoming available.

The state-of-the-art MRI system in 2006 comes with many array coils available. All of the major manufacturers have fielded systems with 32 receiver channels. Arrays with from 8 to 32 channels are either currently or soon will be available for orthopedic, body, head, breast, and vascular imaging. The "total imaging matrix" ("Tim") system introduced by Siemens Medical Solutions, Erlangen, Germany, utilizes 32 channels from 76 selectable array elements to cover most of the body, although specialty coils can also be employed for certain applications (cf. Chap. 13).

Table 14.1 presents URL list of some coil manufacturers and available coils.

Table 14.1. A URL list of some coil manufacturers and available coils

http://www.gehealthcare.com/usen/mr/mr_coils_allprod/index.html
http://www.medical.siemens.com/
http://www.medical.philips.com/main/products/mri/products/achieva15t/coils/
http://www.hitachimed.com/gallery.asp?ID=5
http://medical.toshiba.com/clinical/radiology/vantage-524-631-455.htm
http://www.invivomde.com/products/CoilProductsAll.aspx
http://www.medrad.com/products/mr/mr-coils/index.html
http://www.usainstruments.com/
http://scanmed.com/table.htm#table
http://www.novamedical.com/products.html
http://www.midwestrf.com/products.htm
http://www.temcoils.com/
http://www.rapidbiomed.de/humancoilsindex_27_26_0_f.htm
http://www.dotynmr.com/mri/mri_mainpg.htm
http://www.xlres.com/

A clinical RF coil array must be safe, ergonomically useable, reliable, and must provide high performance (SNR, uniformity, etc.). Parallel-imaging capability in arrays does not eliminate these requirements in traditional imaging procedures; instead, the additional requirements of parallel-imaging capability must be added without damaging performance. The RF coil sets the SNR for the study and no hardware can subsequently increase it. A drop of SNR of around 10–15% is visually noticeable, unless the SNR is extremely high at the start. This critical emphasis on SNR and parallel-imaging capability leads to new challenges discussed in this chapter.

14.2 Coil Sensitivities and Parallel Imaging

Parallel-imaging techniques, as have been described in previous chapters, rely upon the spatial distribution of coil elements to provide enough information to replace some of the standard acquisition points. Each phase-encoded step represents one coefficient of the Fourier series describing the image. If the coefficients of certain basis elements are not acquired, then these must be constructed from the other samples and the coil information. The coil sensitivity patterns, when described in the frequency domain, i.e. in k-space, generally have low spatial frequencies, and thus, multiplication by the sensitivity patterns (i.e., receiving with a given coil set) will produce components in the missing frequency locations. By acquiring with multiple coils with different sensitivity patterns, the missing Fourier coefficients can be approximated. This is simply solving a set of linear equations with enough equations to enable the unknowns to be calculated. The equations, in general, have complex coefficients. Images are usually observed in magnitude form, so it is easy to overlook the fact that two receiver channels may have similar amplitude patterns, but different phase behavior, thus enabling them to provide independent information (cf. Chap. 3).

Coil design for a give anatomy and application currently requires compatibility with parallel imaging. Virtually all new array coils built presently must include this capability. The reduction times, in a practical sense, are typically around a factor of 2–3. It is also common for certain studies to be performed with phase-encoding oriented in certain preferred directions generally due to motion of some kind (such as heart motion, respiration, and blood flow in vessels). In many cases, therefore, the ability to perform parallel imaging is only required in a particular plane. In such cases fewer channels are required than might otherwise be the case.

The g-factor equation is dependent upon field of view (FOV), location, reduction factor, and phase-encoded direction. This makes it extremely difficult to guide array design from g-factor analysis. From a practical standpoint, a design of array elements is proposed using the generic requirement that the magnetic field profiles are considerably different over the range of FOVs to be employed. The elements should be arranged such that composite image profile covers that FOV with adequate SNR. Generally, the accessible surface is covered with surface elements that cover all of the accessible surface area. The number of elements is often chosen on the basis of the number of channels utilized by the system to which the array will be attached. When a basic design can be described in software, then a g-factor analysis is carried out. A variety of reduction factors (R) should be tested to ensure that there are no aberrantly high g-factors for a range of, for example, R=1 to R=3. The results of this analysis may result in small changes to the layout of the array, or dismissal of the basic geometry. In some cases, it may be required to produce reduction-factor capability in two directions simultaneously. Although not equivalent to 2D, it may be acceptable to perform separate 1D analyses for coil design. As long as the total channel count "seeing" the

volume of interest is substantially higher than the total 2D reduction factor, then the separate reduction-factor analyses should provide the necessary information as to the acceptability of the array layout.

Several publications on the analysis of the g-factors of various coil layouts have been performed (Weiger et al. 2001; Zwart et al. 2002). These publications have demonstrated that two loops should be slightly separated instead of overlapped (for zero mutual inductance) to have the best g-factors and therefore the best parallel imaging capability (cf. Chap. 3); however, it has furthermore been shown (Griswold 2005) that the total SNR with moderate speed-up factors is similar between the two approaches. For large channel count arrays, the losses due to many coupling partners can significantly reduce the SNR; thus, it may be advantageous to design the coils for low coupling. Most existing clinical coil designs are made in this way.

14.3 SENSE vs GRAPPA

Generally, coils can be designed based on performance for either k-space-based techniques (such as GRAPPA) or image-space-based techniques. While there are differences in the spatial location of noise enhancement between the various techniques the overall performance is similar for a given array. This means that a coil that works well for SENSE works well for GRAPPA. (For detailed discussions of these issues see Chaps. 2 and 3.)

14.4 Reconstruction Time vs Number of Channels

High reduction factors in two dimensions, as sometimes employed for certain cardiac studies, result in a large numerical problem for the image reconstruction. The result is that reconstruction time can be quite long, e.g., a 3D volume with reduction factors of 3×3 acquired using a 32-channel array. If one compares this to a reduction factor of 2 for an 8-channel array, one would expect roughly a factor of 300 times longer reconstruction time; thus, a 2-s reconstruction turns into a 10-min reconstruction. Combiners (King et al. 2003; Reykowski and Blasche 2004) can be used to optimize the data density while still permitting the required field patterns in the speed-up directions (see Chap. 13). An N-fold reduction in the number of total channels results in at least a N^2 reduction in reconstruction time. Additionally, software algorithms can also be employed to reduce the effective channel count prior to reconstruction. These algorithms put as much energy into as few channels as possible and enable large improvements in speed while preserving nearly all of the SNR and parallel-imaging capability (Huang et al. 2005).

14.5 Uniformity Correction

Because parallel-imaging capability is driven by the relatively rapidly changing sensitivity patterns of many coils, the uncorrected uniformity of a standard phased-array image (root of sum of squares) may be poor. One method for correcting this intensity variation is to acquire a reference image with the body coil, so that the sensitivity maps are referenced to a constant sensitivity. Another method is to use filtering that seeks to remove low-frequency variation in the overall intensity without losing contrast in the image. Both of these have limitations and it appears that further advancements of software will be required to provide adequate uniformity for multi-channel arrays (Cheng and Huang 2005).

14.6 Very-High-Field Sensitivity Profiles

Considerable work has been performed to analyze the behavior of RF coils for very-high-frequency MRI (Wiesinger et al. 2004). This work has demonstrated that because of the rapid phase changes within the sample, higher reduction factors can be supported at higher frequencies (cf. Chap. 44). This is consistent with other technologies in which the wavelength is the limiting resolution factor. In conventional MRI, this wavelength shortening has no value and is unrelated to resolution. In a pure tomographic approach (i.e., no encoding), the resolution depends greatly upon wavelength. Reduction factors in the range of six or more (per dimension) appear to be plausible at 7 T and above.

14.7 Available Products

New coils are being developed rapidly for parallel-imaging capability in all application areas of the body. Generally, nearly all coils developed are or will be available for 1.5- and 3.0-T systems. In the following, each application area is related to the current state-of-the-art arrays and their capabilities.

14.7.1 Orthopedic Coils

Orthopedic arrays include specialized coils for the hand and/or wrist, the elbow, the shoulder, the knee, and the foot and/or ankle. Imaging of the hip is an emerging growth application as well. Currently, 8-channel arrays with parallel-imaging capability are available for the knee, wrist, and foot/ankle. Eight-channel prototypes, by several companies, have been demonstrated for the shoulder and hip. The wrist and knee coil permits transverse speed up directions, whereas the remainder can be used for any direction of acceleration. Figures 14.1–14.3 demonstrate available coils for foot-and-ankle MRI (Fig. 14.1), knee MRI (Fig. 14.2), and wrist MRI (Fig. 14.3).

14.7.2 Breast Coils

Breast imaging is a growing application area, and new coils are available with 7 and 8 channels. These arrays permit transverse acceleration directions. Prototypes with 12 and 16 channels have been fielded and it is anticipated that the next generation will permit accelerations in any direction. Figures 14.4 and 14.5 demonstrate available coils for breast-biopsy MRI applications.

14.7.3 Head Coils

State-of-the-art brain imaging is currently performed with either an 8-channel array or 12-channel array. The 8-channel array is designed for transverse speed-up factors, whereas the 12-channel version permits speed-up factors in any direction. Prototypes with 16–90 channels have been demonstrated (cf. Chap. 44),

Fig. 14.1. A GE 1.5-T 8-channel foot/ankle array

Fig. 14.2. A Philips 3-T 6- to 8-channel high-resolution knee array

Fig. 14.3. A GE 8-channel wrist coil

and it is likely that the next generation of head arrays will include at least 16 channels. Figures 14.6–14.9 demonstrate available coils for the head.

14.7.4 Cardiovascular and Torso Coils

Cardiovascular and torso arrays are currently available in configurations from 4 to 32 channels. The 32-channel versions permit very high two-direction speed-up capability, which may prove beneficial for permitting very fast cardiac imaging. Torso applications are particularly well suited to improvement from parallel imaging because of the rapid motion of both the lungs and heart. Figures 14.10–14.12 demonstrate available coils for cardiovascular and torso MRI.

Fig. 14.4. A GE 1.5-T 7-channel biopsy breast array

Fig. 14.5. A 16-channel prototype biopsy breast array

Fig. 14.6. In vivo 8-channel high-resolution head array

Fig. 14.7. A 16-channel prototype head coil

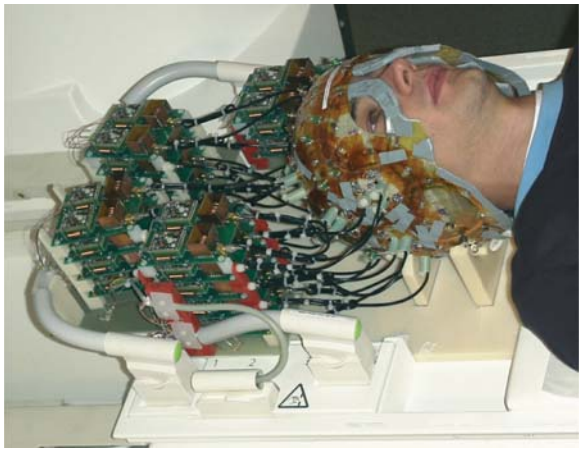

Fig. 14.8. A 32-channel MGH prototype head coil. (Courtesy of G. Wiggins, Massachusetts General Hospital)

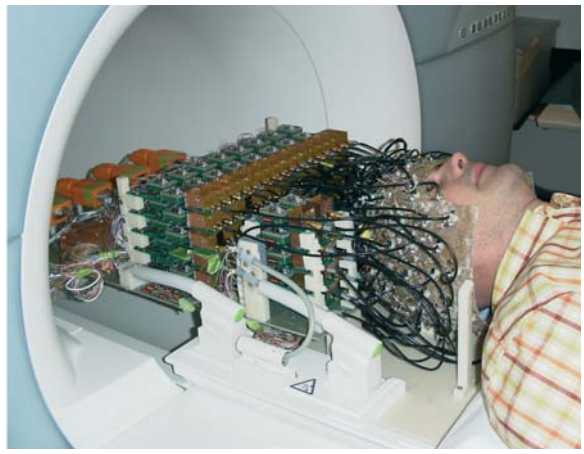

Fig. 14.9. A 90-channel MGH prototype head coil. (Courtesy of G. Wiggins, Massachusetts General Hospital)

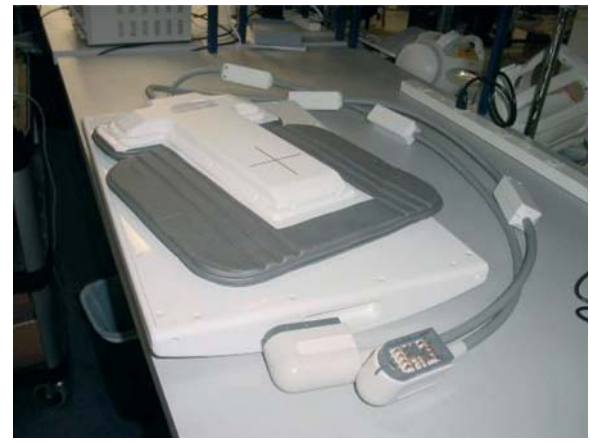

Fig. 14.10. In vivo 32-channel cardiac array

Fig. 14.11. Siemens "Panoramic" body arrays

Fig. 14.12. A GE 1.5-T 8-channel torso array

14.8 Limitations of Coil-Design Improvements

Without a change to a pulse sequence, parallel imaging always produces a loss of SNR that is at least related to the root of the time of the acquisition (see Chaps. 2–4); therefore, one requirement for parallel imaging that impacts the coil design is that the SNR must be such that a reduction by $\sqrt{R}$ still results in an image of adequate SNR to be diagnostically valuable. Generally, for structures deep within the body, new optimized array designs are not capable of producing SNR that has such relatively large gains over existing arrays. The SNR for shallower structures can be substantially improved by utilizing arrays with more, smaller elements, whereas the SNR in the center of the body remains comparable with the one achievable with optimized volume coils.

14.9 Transmit/Receive Arrays and Transmit SENSE

There are several transmit/receive (T/R) arrays currently in clinical use; these all employ a single transmit source with power splitters to direct the power to each element of the array. The goal for these coils has

been to create as uniform an excitation profile as possible, over a limited FOV. There are several reasons why one would want to employ a T/R array. The first reason would be to excite a local area because of wrap artefacts that occur when whole-body excitation is employed. Another reason is that very high peak B_1 fields may be difficult to achieve with the body coil, but are achievable with a local coil. Clinical T/R arrays may either use the same elements for transmit and receive, with power being distributed amongst the channels to produce the best uniform excitation, or separate elements may be used with the receive channels being essentially the same as a standard receive-only array. If transmit SENSE (Katscher et al. 2003) becomes clinically relevant (cf. Chap. 45), such coils will be relatively easily converted to multiport arrays.

14.10 Vertical Low-Field Parallel Imaging

Parallel-imaging techniques have recently been demonstrated on vertical low-field systems. (Warntjes et al. 2005) Generally, twofold or lower reduction factors are typically employed due to the coil design constraints placed upon vertical field receiving elements, and the intrinsically lower SNR available at lower field strengths.

14.11 Conclusion

In the current state of the art, coil arrays must be compatible with parallel-imaging methods. The speed-up factor and directions required are specific for the application. Dynamic studies have the greatest need for parallel imaging, as these studies can result in significantly improved results because of the shorter acquisition times. Virtually all manufacturers provide up to 32 channels on their high-end systems, and coil arrays to utilize these abilities are rapidly becoming available. These technological improvements are driven by the need for faster, better exams and improved patient throughput.

References

Cheng H, Huang F (2005) Proc 27th Annual International Conference of the IEEE EMBS, #642

Griswold M (2005) RF coils for parallel imaging. ISMRM 13th Scientific Meeting and Exhibition, Miami, Fla. (Morning categorical course "New Developments in MRI Hardware", 13 May 2005)

Huang F et al. (2005) Proc 27th Annual International Conference of the IEEE EMBS, # 651

Huang F et al. (2005) Proc 27th Annual International Conference of the IEEE EMBS, #1190

Katscher U, Bornert P, Leussler C, van den Brink JS (2003) Transmit SENSE. Magn Reson Med 49:144–150

King SB, Varosi SM, Huang F, Duensing GR (2003) The MRI eigencoil: 2N-channel SNR with N receivers. Proc Int Soc Magn Reson Med 11:712

Reykowski A, Blasche M (2004) Mode matrix: a generalized signal combiner for parallel-imaging arrays. Proc Int Soc Magn Reson Med 12:1587

Wiesinger F, Boesiger P, Pruessmann KP (2004) Electrodynamics and ultimate SNR in parallel MR imaging. Magn Reson Med 52:376–390

Warntjes M, Ylihautala M, Kuipers E, Bloemers K (2005) SENSE performance of the 1.0-T vertical-field MRI. Proc Int Soc Mag Reson Med 13:914

Weiger M, Pruessmann KP, Leussler C, Roschmann P, Boesiger P (2001) Specific coil design for SENSE: a six-element cardiac array. Magn Reson Med 45:495–504

Zwart JA de, Ledden PJ, Kellman P, van Gelderen P, Duyn JH (2002) Design of a SENSE-optimized high-sensitivity MRI receive coil for brain imaging. Magn Reson Med 47:1218–1227

Design of Parallel-Imaging Protocols

15

Stefan O. Schoenberg and Olaf Dietrich

CONTENTS

15.1 Introduction

Parallel-imaging techniques have only recently been introduced into clinical-routine MRI, but they have already gained wide clinical acceptance in numerous applications. Their substantial advantages in terms of higher spatial and temporal resolution and improved image quality in single-shot applications have influenced the design of imaging protocols for practically all applications ranging from MRI of the brain to imaging of the pedal arteries. In this chapter, general recommendations for the design of imaging protocols are listed (ordered by anatomic region) with the most important protocol requirements and their implications for parallel imaging.

More details to the specific protocols as well as technical background information and references to publications can almost always be found in the dedicated chapters which we also refer to in the "Anatomic region" column.

S. O. Schoenberg, MD; O. Dietrich, PhD
Department of Clinical Radiology, University Hospitals – Grosshadern, Ludwig Maximilian University of Munich, Marchioninistr. 15, 81377 Munich, Germany

15.2 Protocol Suggestions

All protocol suggestions are summarized in Table 15.1. The most frequently found motivation to apply parallel imaging in these examples is to increase the spatial resolution of the acquired data without prolongation of scan time. Other protocols in this list aim at increased temporal resolution in dynamic MRI, at improved image quality especially in single-shot applications, or at reduced scan times combined with decreased susceptibility to artefacts in moving structures.

The suggested parallel-imaging parameters of all considered protocols depend on the image geometry (i.e., slice orientation, phase-encoding direction, and 2D vs 3D acquisition, etc.) in combination with the available hardware, in particular the coil systems. Implementations on the various MR systems from different vendors may therefore vary. In several of the following examples we distinguish protocols for "standard" coil systems and dedicated "high-end" coil systems with improved parallel-imaging capabilities. The standard coil system typically consists of an 8-element head coil and of body surface-coil systems with three independent receiver channels in left–right direction (ideally positioned both anterior and posterior of the patient). If only coil systems with fewer elements are available, then the maximum acceleration factor, R, must be decreased, e.g., to R=2 in left–right direction. Newer coil systems with more independent elements (cf. Chaps. 14 and 44) often allow higher linear acceleration factors (e.g., R=4).

The listed protocol parameters, in particular the spatial resolution, are based on typical clinical imaging requirements. The suggested parallel-imaging parameters, such as the acceleration factor, R, are then selected as optimal compromise balancing short acquisition times, on the one hand, and sufficient image quality, particularly sufficient signal-to-noise ratio, on the other hand.

Table 15.1. Parallel-imaging protocol parameters

Anatomic regions and spectrum of disease	Protocol requirements	Requirements for parallel imaging
Brain:		
Stroke (Chaps. 18, 33, 34)	Reduction of distortion in diffusion-weighted and perfusion-weighted EPI images	Use routinely multi-element (≥8) head coils, R≥2
	Reduction of blurring in T2W TSE seq.	Improved results with ≥32 coil elements, R≥4
Tumors (Chap. 18)	Isotropic high spatial resolution	3D GRE and TSE seq. with 2D acceleration, R≥2×2; 3 T preferable
Congenital brain disease (Chap. 18)	Isotropic high spatial resolution	3D GRE and TSE seq. with 2D acceleration, R≥2×2; 3 T preferable
Arteriovenous malformations (Chaps. 18, 47)	Time-resolved 3D CE MRA	2D acceleration, R≥2×2
Skull base and larynx:		
Cranial nerves (Chap. 19)	High in-plane spatial resolution	Combine head coil with dedicated surface coils; use 1024 matrix with in-plane resolution ≤0.5×0.5 mm²; keep scan times <5 min
	Short scan times	
Inner ear (Chap. 19)	Isotropic high spatial resolution ≤0.7×0.7×0.7 mm³	T2W 3D TSE and GRE seq. with SENSE, R=2
Laryngeal tumors (Chap. 19)	Reduction of motion artefacts	Multiple averaging (NSA≥2), R=2
Lungs and heart:		
Infiltrates (Chap. 20)	Reduction of blurring and signal decay	SSTSE images (e.g., HASTE) with R=2; use external reference (ACS) scan for short echo times
Pulmonary arterial hypertension (Chaps. 37, 43)	Combine high-resolution and time-resolved 3D CE MRA	High acceleration factors R≥3 for high temporal and spatial resolution; 2D acceleration possible for high-resolution data sets with large anterior–posterior coverage; GRAPPA-based algorithms preferable
Congenital heart disease (Chaps. 28, 31)	Comprehensive assessment of cardiac and pulmonary vascular anatomy	Dedicated multi-element coils for small infants not yet available; multi-breath-hold multi-slice (≤3 slices per breath-hold) cardiac cine SSFP imaging with R=2
	Time-resolved MRA with scan times ≤8 s/frame and spatial resolution ≤1×1×1 mm³	Minimize FOV in left–right (phase-encoding) direction; thus, GRAPPA preferable due to aliasing, R=2
Cardiac function (Chap. 35)	Multi-slice cine MRI with high temporal resolution (≤50 ms)	Single-breath-hold multi-slice cardiac cine SSFP imaging with high acceleration factors R≥4 and TSENSE
Ischemic heart disease (Chap. 36)	Increase anatomic coverage (≥5 short-axis slices) and spatial resolution (≥192×192 matrix) for perfusion scans	Good results for saturation-recovery GRE (turbo-FLASH) with GRAPPA and R=2
	Reduce concentric rim-like susceptibility artefact	Segmented EPI techniques with TSENSE under clinical investigation
Liver:		
Hepatocellular carcinoma (Chap. 21)	Multi-breath-hold T2*W GRE seq. (SPIO-based CM)	Use GRAPPA (axial scans R=2, coronal R≥3) for large patients and small FOVs <35 cm
	Free-breathing T2W TSE seq.	R=2, scan time ≤4 min with navigator gating
	Dynamic volume-interpolated (e.g., VIBE) 3D GRE seq. with thin slices ≤3 mm and scan times ≤15 s for arterial, portal–venous, and equilibrium phase	R=2 for axial scans, R≥3 for coronal scans with isotropic spatial resolution ≤2×2×2 mm³, 3 T preferable
Metastasis (Chap. 21)	Isotropic spatial resolution <2×2×2 mm³ for 3D VIBE with positive liver-specific contrast agents (e.g., Gd-EOB-DTPA)	3 T preferable, coronal acquisition with R≥3
	Use diffusion-weighted black-blood EPI sequences for improved lesion detection	R=2, requires large FOV (50 cm) with homogeneous magnetic field

▷▷

Anatomic regions and spectrum of disease	Protocol requirements	Requirements for parallel imaging
MRCP (Chap. 22)	Combine RARE and HASTE seq. to account for uncooperative patients and detection of tumor morphology	R=2, higher acceleration factors problematic due to SNR constraints at 1.5 T
	Use 3D VFL-TSE for detection of small stones and evaluation of high-order branches (PSC) with isotropic spatial resolution <1×1×1 mm³	R≥3 feasible, 3 T preferable
	Use diffusion-weighted black-blood EPI sequences for assessment of cholestasis	R=2, requires large FOV (50 cm) with homogeneous magnetic field
Pancreas (Chap. 22)	Coronal acquisitions helpful for FS T1W and T2W HASTE	R=3 routinely feasible
	High diagnostic value of late arterial-phase in dynamic T1W 3D VIBE for detection of pancreatic tumors	R=2 for axial scans, R≥3 for coronal scans with isotropic spatial resolution ≤2×2×2 mm³
	3D VFL-TSE preferable for evaluation of pancreatic duct	R≥3 feasible
Musculoskeletal system:		
Knee (Chap. 24)	Reduce scan time <3 min per seq. particularly in patients with pain	R=2 for standard coil systems at 1.5 T; dedicated multi-element coils and 3 T preferable; R≥3 possible for 2D sequences, 2D acceleration with R=2×2 feasible for 3D sequences
Shoulder (Chap. 24)	Reduce scan time <3 min per sequence particularly in patients with pain	Avoid R>2, prone to severe aliasing artefacts in coronal scans with standard coils; dedicated multi-element coils and 3 T preferable
Angiography:		
Intracranial (Chaps. 18, 26)	Time-of-flight MRA: reduce scan time <5 min, isotropic resolution ≤0.7×0.7×0.7 mm³	R=2 or R=3, preferred phase-encoding direction is left–right since small volume coverage in slice direction limits the use parallel imaging in the cranio-caudal direction; 3 T preferable
	3D phase-contrast MRA for detection of sinus venous thrombosis in pregnant women: scan time <8 min, spatial resolution ≤1.5×1.5×1.5 mm³	2D acceleration in coronal and sagittal direction, R≥2×3; dedicated multi-elements with ≥8 elements required
	Dynamic 3D CE MRA for arteriovenous malformations, sinus venous thrombosis: temporal resolution ≤500 ms, spatial resolution ≤2×2×2 mm³	Use 2D acceleration with R≥3×2, combine with view sharing, keyhole techniques; dedicated multi-element coils with ≥8 elements required
Carotids (Chap. 27)	High-resolution 3D CE MRA for exact grading of carotid artery stenosis: ≤0.9×0.9×0.9 mm³, scan time ≤20 s	Standard coil systems: R=2 at 1.5 T; R=3 at 3 T
		Dedicated neurovascular coils: R=4
	Dynamic 3D CE MRA for delayed inflow with significant stenosis, flow reversal with subclavian steal syndrome: temporal resolution ≤2 s, spatial resolution ≤2×2×3 mm³	Standard coil systems: R=2 at 1.5 T; R=3 for 3 T
Renal arteries (Chap. 29, 39)	High-resolution 3D CE MRA for exact grading of renal artery stenosis on cross-sectional reformats: ≤0.9×0.9×0.9 mm³, scan time ≤20 s	R=3 in left–right direction, 2D acceleration difficult due to thin coronal slabs, limitations in coil design, and coil-sensitivity profiles
	Dynamic 3D CE MRA to detect increased CM transit time with significant stenosis, assessment of true and false lumen in aortic dissection: temporal resolution ≤2 s, spatial resolution ≤2×2×3 mm³	R=3 in left–right direction, combine with view-sharing techniques

▷▷

Anatomic regions and spectrum of disease	Protocol requirements	Requirements for parallel imaging
Peripheral arteries (Chaps. 30, 32)	Pelvic arteries: scan time <20 s, spatial resolution ≤1.5×1.5×2 mm³	*R*=3 in left–right direction
	Thighs: scan time <15 s, spatial resolution ≤1.5×1.5×2 mm³	*R*=3 in left–right direction
	Calves: scan time ≤30 s (elliptical–centric acquisition), spatial resolution ≤1.0×1.0×1.5 mm³	*R*=3 in left–right direction, *R*=4 possible with dedicated peripheral vascular coils
	Hybrid MRA for patients with rest pain or critical limb ischemia: time-resolved MRA (temporal resolution ≤4 s, spatial resolution ≤1.5×1.5×1.5 mm³) followed by standard three-station MRA	*R*=3 in left–right direction, *R*=4 possible with dedicated peripheral vascular coils, 3 T, and/or CM with higher relaxivity preferable

*3D CE MR*A 3D contrast-enhanced magnetic resonance angiography,
ACS auto-calibration signal,
CM contrast media,
EPI echo-planar imaging,
FOV field of view,
FS fat saturation,
GRE gradient echo,
HASTE half-Fourier-acquisition single-shot turbo spin echo,
MRCP magnetic resonance cholangio-pancreaticography,
NSA no. of signals averaged,
PSC primary sclerosing cholangitis,
R parallel-imaging acceleration factor,
RARE rapid acquisition with relaxation enhancement,
Seq. sequence,
SPIO superparamagnetic iron oxide,
SNR signal-to-noise ratio,
SSFP steady-state free precession,
SSTSE single-shot turbo spin echo,
T Tesla,
TSE turbo spin echo (fast spin echo),
VFL-TSE turbo spin echo with variable flip angle,
VIBE volume-interpolated breath-hold examination,
W weighted.

General Advantages of Parallel Imaging

16

Olaf Dietrich

CONTENTS

16.1 Introduction

As discussed in the previous chapters, the concept of parallel imaging is based on the reduction of the number of phase-encoding steps without compromising the spatial resolution or the field of view of an MR acquisition. Several, very different advantages arise from this idea that are summarized for various pulse-sequence types in Fig. 16.1. The most obvious of these advantages is the possibility of increasing the spatial resolution or of accelerating data acquisition. A supplementary beneficial consequence of a shorter scan time is a reduced susceptibility to motion artefacts. In addition, sequences with long echo trains and particularly single-shot pulse sequences benefit from improved image quality due to reduced geometric distortions and blurring. These advantages of parallel imaging are discussed in the following sections. Subsequently, the specific synergistic effects of parallel imaging at high field strengths, i.e. at 3 Tesla and above, will be elucidated at the end of this chapter.

O. Dietrich, PhD
Department of Clinical Radiology, University Hospitals – Grosshadern, Ludwig Maximilian University of Munich, Marchioninistr. 15, 81377 Munich, Germany

16.2 Spatial and Temporal Resolution

When applying parallel imaging with a reduction (or acceleration) factor of, for example, R=3, only a third of the k-space lines of a conventional, non-accelerated MR acquisition are required to reconstruct an image data set of the same spatial resolution and geometry as without acceleration. The two most important applications of this reduction of raw data are decreasing the total scan time (e.g. to a third of the original scan time for R=3) or increasing the spatial resolution.

The first of these approaches can be beneficial in acquisitions with comparatively long scan times (such as conventional T2-weighted high-resolution brain MRI or time-of-flight MR angiography of brain vessels that can take several minutes; cf. Chap. 26); however, reducing the acquisition time is even more important in dynamic MRI in order to increase the temporal resolution (e.g. for MRI of the cardiac function (cf. Chap. 35), or for multi-slice perfusion MRI; cf. Chaps. 33, 36, 37, and 39). Frequently, only a certain part of the time reduction obtained by parallel imaging is used to increase the temporal resolution, while at the same time the number of acquired slices or the spatial resolution is increased.

In many important MR applications, the total scan time is restricted by physiological constraints such as the maximal breath-hold duration of 20–25 s. These applications particularly profit from parallel-imaging techniques that increase the spatial resolution without exceeding the maximum possible scan time. Typical examples are abdominal MRI as described in Chaps. 21–23 or breath-hold MR angiography (cf. Chaps. 28 and 29). In both applications substantially higher spatial resolutions can be acquired with parallel imaging than with non-accelerated MRI. Often a compromise between increased in-plane resolution and reduced scan time per slice is chosen in order to increase the total number of acquired slices within one breath-hold; thus, either the covered volume can be extended or a better resolution (i.e. a smaller slice thickness) can be obtained in through-plane direction.

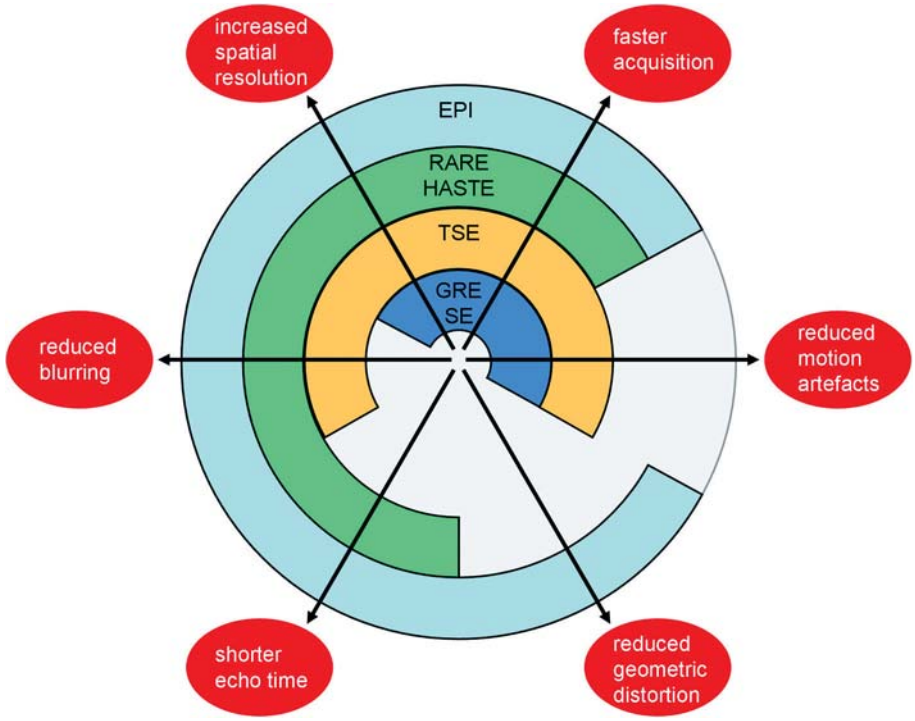

Fig. 16.1. Advantages of parallel-imaging techniques for some frequently used pulse-sequence types: echo-planar-imaging (*EPI*) sequences; single-shot turbo-spin-echo sequences (*HASTE*, *RARE*); turbo-spin-echo sequences (*TSE*); and spin-echo and gradient-echo sequences (*SE*, *GRE*).

16.3 Image Quality

An important positive side effect of shorter scan times is reduced susceptibility to motion artefacts. There are different kinds of involuntary motion arising, for example, from diaphragmatic contractions (cf. Chap. 29) or peristalsis (Froehlich et al. 2005) with typical time periods of 5–30 s; thus, MRI with relatively long scan times of 20 s or more will frequently be affected by motion artefacts, which can be reduced by applying parallel imaging to shorten the acquisition time. In order to maintain a certain signal-to-noise ratio (SNR) it can be advantageous to combine parallel imaging with data averaging of repeated acquisitions; thus, k-space data are more consistent before averaging because of the shorter acquisition duration (i.e. less motion during a single acquisition), and remaining motion artefacts will be attenuated due to the averaging process. More sophisticated data-correction schemes and advanced techniques for motion correction based on parallel imaging are described in Chap. 5.

In addition to reduced susceptibility to motion artefacts, particularly the image quality of single-shot pulse sequences as well as of multi-shot techniques with long echo trains benefits from parallel imaging as described in detail in Chaps. 9 and 10. A major source for image artefacts and especially for image blurring is transversal relaxation during the echo-train readout. By shortening the echo train of single-shot or conventional turbo-spin-echo sequences or of echo-planar sequences, the signal decay during the echo-train readout is reduced and the point-spread function of the sequence, i.e. the image quality, is improved. This effect has been proven to be especially useful for applications such as lung MRI with half-Fourier-acquisition single-shot turbo-spin-echo (HASTE) sequences (cf. Chap. 20) or MR cholangiopancreaticography (cf. Chap. 22).

Even more dramatic improvements due to parallel acquisition techniques are found in echo-planar imaging, which generally suffers from (often severe) geometric-distortion artefacts due to B_0 inhomogeneities and associated off-resonance effects. The extent of these artefacts depends the line distance in k-space (i.e. on the acquired field of view prior to parallel-imaging reconstruction) and on the echo spacing; hence, geometric distortions can be reduced by acquiring only every other or every third line in k-space with parallel-imaging techniques (cf. Chap. 10). Therefore, virtually all echo-planar-imaging applications benefit from parallel imaging, such as diffusion

and perfusion brain MRI (Chaps. 18, 33, and 34) or black-blood liver MRI (Chap. 21).

Finally, parallel imaging allows for reduced echo times in single-shot sequences with linear k-space sampling in phase-encoding direction (cf. Chap. 10); thus, higher signal intensities, i.e. improved SNRs, can be obtained, for example, in diffusion-weighted or diffusion-tensor MRI or in HASTE lung MRI (Chaps. 20 and 38).

16.4 High-Field MRI

In principle, the application of parallel-imaging techniques is completely independent of the static field strength, B_0, of an MRI system, although it may be limited by signal-to-noise-ratio constraints at very low field strengths (cf. Chap. 17); however, it turns out that parallel imaging provides several specific advantages when used at high field strengths, e.g. at 3 T or above. These specific advantages are associated with both the main motivation to proceed to higher field strengths, i.e. the increased signal-to-noise ratio, on the one hand, and with one of the main limitations of MRI at high field strengths, namely the substantial increase of required RF energy, on the other hand.

The SNR (cf. Chap. 1) of an MR acquisition increases approximately linearly with the static field strength, i.e. it is about twice as high at 3 than at 1.5 T. This effect can compensate an intrinsic disadvantage of parallel imaging, which is that the SNR decreases with the square root of the acceleration factor, R, if the geometry (voxel size and field of view) is held constant because of the shortened acquisition duration as illustrated in Fig. 16.2. Thus, the same SNR can be obtained at 3 T with an acceleration factor of R=4 as at 1.5 T without parallel-imaging acceleration, i.e. images of comparable quality can be acquired in only 25% of the original acquisition time. Comparing 1.5 and 7 T, substantially higher acceleration factors become theoretically feasible. The SNR increase by a factor of about 4.7 corresponds to an acceleration factor of approximately R=22, i.e. a reduction of scan time to <5% of its original value. In practice, smaller acceleration factors will be chosen because of limitations with respect to coil geometry and the g-factor; however, high two-dimensional acceleration of three-dimensional MR imaging has already been demonstrated, e.g. with R=3×4=12 (cf. Chap. 44), and appears particularly feasible at very high field strengths.

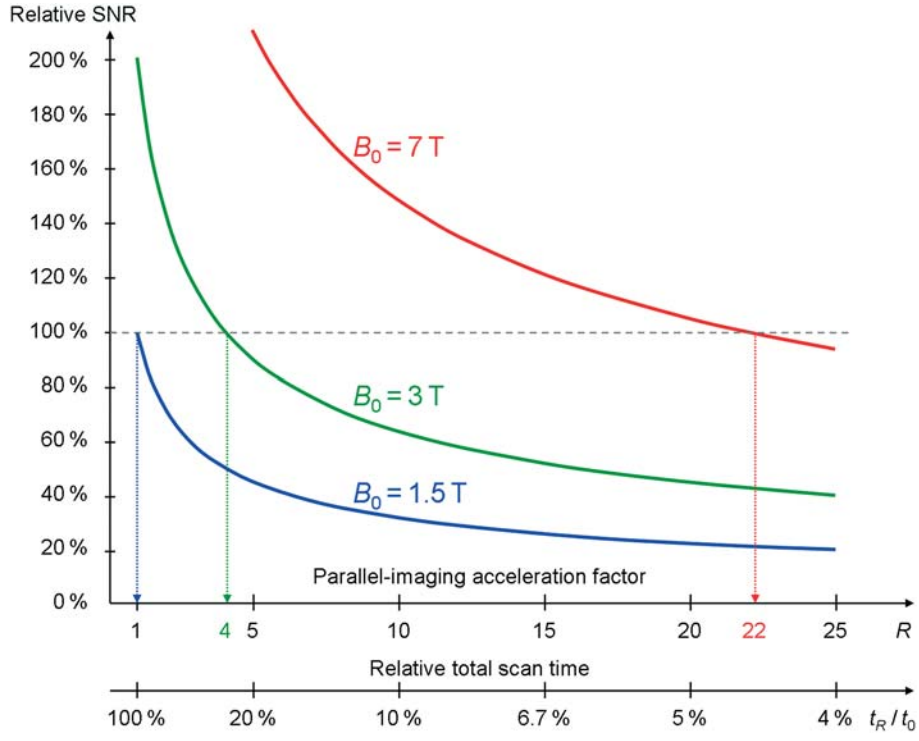

Fig. 16.2. Relative signal-to-noise ratios (SNR) for different parallel-imaging acceleration factors, R, and different static field strengths, B_0, of 1.5 T, 3 T, and 7 T. The resulting reduced acquisition time (ratio of acquisition time of accelerated acquisition, t_R, and non-accelerated acquisition, t_0) is shown below the acceleration factor. The SNR increases proportional to B_0 and decreases proportional to $1/\sqrt{R}$; effects of regional noise amplification due to the g-factor are neglected. For all three field strengths, acceleration factors resulting in the same relative SNR of 100 % are marked.

As mentioned above, the required RF energy increases substantially at high field strengths, since the energy of an RF pulse is proportional to the square of B_0; hence, the specific absorption rate (SAR) of two identical pulse sequences is about four times higher at 3 than at 1.5 T. This effect turns out to be a serious limitation for many protocols at 3 T, particularly if high-SAR sequences, such as turbo-spin-echo (TSE), HASTE, or steady-state free-precession (e.g. TrueFISP) sequences, are applied.

Fortunately, parallel imaging can help to reduce the average SAR of MR protocols under certain conditions. Consider, for example, a T2-weighted breath-hold multi-slice coronal TSE acquisition of the liver without parallel-imaging acceleration. While the SAR may be acceptable at 1.5 T, it is increased by a factor of 4 at 3 T and, thus, may exceed the allowed maximum. If parallel imaging with an acceleration factor of R=4 is applied, the number of refocusing RF pulse is decreased by 75%, and the field-strength-related SAR increase is completely compensated, i.e. the total RF energy of this sequence is reduced to the level of the non-accelerated sequence at 1.5 T. It is noteworthy, however, that the (long-term) averaged SAR of this protocol is only reduced, if no further RF pulses are applied during the total scan time of the non-accelerated sequence, i.e. the examination must be paused for the time difference between the non-accelerated and accelerated sequence. Similarly, the maximum possible flip angle of TrueFISP sequences may be higher with parallel-imaging acceleration than without (cf. Chap. 35). In all these cases, however, only the long-term average of the SAR can be decreased; thus, parallel-imaging reduction of SAR is particularly helpful for relatively short measurements such as breath-hold examinations with alternating intervals of RF-pulse application (measurement during breath-hold) and breaks between measurements.

Apart from the discussed compensatory effects with respect to SNR and SAR, there are several other synergistic implications of parallel-imaging techniques and high magnetic field strengths. Geometric distortions of echo-planar-imaging sequences, for example, increase at higher field strengths (Wang et al. 2002; Xu et al. 2004; Ardekani and Sinha 2005). This effect can ideally be compensated by parallel imaging as demonstrated in Chap. 10. Furthermore, it has been shown by Wiesinger et al. (2004) that lower g-factors at high linear acceleration factors can be obtained at high field strengths of more than about 4.5 T (cf. Chaps. 14 and 44). Finally, parallel-imaging techniques can be transferred to RF excitation; so-called parallel-excitation techniques can be used to compensate inhomogeneous signal distribution frequently observed at high and ultra-high field strengths. This approach is described in detail in Chap. 45.

16.5 Conclusion

Parallel imaging provides several essential advantages for a multitude of MRI applications. The primary motivation for parallel imaging was faster imaging and MRI with higher spatial resolution; however, it soon turned out that parallel-acquisition techniques offer several other advantages as well such as improved image quality of single-shot MRI due to decreased blurring and reduced geometric distortions. In addition, MRI at high and ultra-high field strengths specifically benefits from parallel imaging, which ideally complements the increased SNR and compensates the growing specific absorption rate and increasing geometric distortions. Consequently, parallel imaging has been introduced in an ever-growing number of MRI protocols for an immense variety of clinical and research applications.

References

Ardekani S, Sinha U (2005) Geometric distortion correction of high-resolution 3 T diffusion tensor brain images. Magn Reson Med 54:1163–1171

Froehlich JM, Patak MA, Weymarn C von, Juli CF, Zollikofer CL, Wentz KU (2005) Small bowel motility assessment with magnetic resonance imaging. J Magn Reson Imaging 21:370–375

Wang J, Alsop DC, Li L, Listerud J, Gonzalez-At JB, Schnall MD, Detre JA (2002) Comparison of quantitative perfusion imaging using arterial spin labeling at 1.5 and 4.0 Tesla. Magn Reson Med 48:242–254

Wiesinger F, Van de Moortele PF, Adriany G, De Zanche N, Ugurbil K, Pruessmann KP (2004) Parallel imaging performance as a function of field strength: an experimental investigation using electrodynamic scaling. Magn Reson Med 52:953–964

Xu D, Henry RG, Mukherjee P, Carvajal L, Miller SP, Barkovich AJ, Vigneron DB (2004) Single-shot fast spin-echo diffusion tensor imaging of the brain and spine with head and phased array coils at 1.5 T and 3.0 T. Magn Reson Imaging 22:751–759

Limitations of Parallel Imaging

17

Olaf Dietrich

CONTENTS

17.1 Introduction

Parallel imaging has been shown to be extremely valuable in a large number of MR applications and provides many substantial advantages summarized in the preceding chapter; however, there are also certain limitations associated with parallel-acquisition techniques, e.g. with respect to technical preconditions as well as image quality. Knowledge of these limitations is essential for the application of parallel imaging in general and for the design and optimization of parallel-imaging protocols in particular. Typical and important limitations associated with parallel-imaging techniques are discussed in the following sections.

O. Dietrich, PhD
Department of Clinical Radiology, University Hospitals – Grosshadern, Ludwig Maximilian University of Munich, Marchioninistr. 15, 81377 Munich, Germany

17.2 Technical Requirements

Parallel imaging is based on the combination of data acquisition with multi-element coil systems, on the one hand, and sophisticated reconstruction algorithms for undersampled multi-channel data, on the other hand. Consequently, an MRI system must fulfil certain specifications to be suited for parallel imaging.

17.2.1 Multi-Channel Receiver Hardware

The MRI system must allow for parallel data acquisition through several independent RF receiver channels. Although the minimum theoretical number of channels required for parallel imaging is two, generally at least 4–8 channels are recommended for parallel acquisition in clinical routine. For parallel imaging with more flexible imaging geometries or for whole-body applications, even more receiver channels and coil connectors are required (cf. Chaps. 13 and 44); thus, MRI systems for state-of-the-art parallel imaging should provide several (e.g. 8–32) RF receiver channels, i.e. in particular a correspondingly large number of independent RF amplifiers as well as extensive connective wiring, which considerably increase the complexity and costs of such MRI systems.

17.2.2 Multi-Element Coil Systems

In addition to the extended receiver capabilities of the MRI system, appropriate coil systems are needed for parallel MRI (cf. Chaps. 14 and 44). These coil systems should provide a large number of independent elements optimally arranged for parallel acquisition techniques. If the coil elements are distributed along a

single direction (e.g. from left to right), parallel imaging is restricted to applications with phase encoding in this direction (e.g. to MRI in axial or coronal orientation with phase encoding in left–right direction). As a rule of thumb, the highest possible acceleration factor, *R*, is given by the number of independent coil elements in phase-encoding direction.

To allow for a flexible choice of image orientation, phase-encoding direction, and acceleration factor, multi-element coils are required with a large number of elements distributed uniformly around the patient. With such coil systems, available, for example, for MRI of the head, high acceleration factors are feasible in all spatial directions. In body MRI, however, high acceleration factors are typical restricted to left–right and head–feet direction. In anterior–posterior direction, parallel imaging often remains limited to maximum acceleration factors of $R=2$ because of the typical coil configuration and the oblate–oval shape of the human abdomen and thorax (cf. Chap. 21). In general, the choice of several protocol parameters, such as image orientation, phase-encoding direction, or field of view, is more limited in parallel imaging than in conventional imaging and depends substantially on the coil systems used.

17.2.3 Image Reconstruction System

The separately acquired undersampled raw-data sets from all coil elements must be combined to a single resulting image data set without remaining aliasing artefacts. This is done with reconstruction algorithms that are generally much more complicated and computationally demanding than conventional image reconstruction, which is usually based on the (fast) Fourier transform of the acquired data. In particular, raw-data sets acquired for parallel imaging are typically very large because they consist of data from multiple separate coil elements; thus, large amounts of memory as well as very fast reconstruction systems are required in order to reconstruct these data sets within acceptable times. Consequently, many state-of-the-art parallel-imaging protocols depend on the newest generation of image reconstruction systems and will be prohibitively slow when transferred to older systems.

Several different reconstruction algorithms are provided by the vendors of MRI systems (cf. Chap. 2) with certain advantages and disadvantages with respect to image quality and reconstruction time. The optimization of parallel-imaging reconstruction is still a major subject of current research (cf. Chap. 46), and regular updates to the newest and most efficient algorithms are recommendable to constantly provide the best possible image quality.

17.3 Image Quality and Artefacts

Apart from the technical limitations mentioned above, the obtained image quality is the most important factor to be considered when applying parallel-acquisition techniques. Image quality in the context of parallel imaging is characterized by two aspects: the signal-to-noise ratio (SNR) and localized image artefacts.

17.3.1 Signal-to-Noise Ratio

The reduced SNR of parallel MRI is an intrinsic disadvantage common to all accelerated imaging techniques that acquire reduced data sets in order to shorten the scan time. As described in Chap. 1, the SNR is proportional to the square root of the total time spent for data acquisition (Edelstein et al. 1986; Haacke et al. 1999) and, thus, decreases with increasing acceleration. Consequently, MRI with a parallel-imaging acceleration factor of $R=4$ is associated with (at least) a 50% loss of SNR; therefore, parallel imaging is particularly suited for applications with originally high SNR. Typical examples are applications that are restricted by acquisition time rather than SNR such as abdominal breath-hold MRI, contrast-enhanced first-pass MR angiography, or time-resolved MRI. On the other hand, non-accelerated protocols with very low SNR and in particular MRI at low-field systems with field strengths, B_0, of less than 1 T, will frequently not benefit from parallel imaging. An exception to this general rule are certain low-SNR applications for that parallel imaging can be employed as a means to reduce motion sensitivity by averaging of multiply repeated accelerated acquisitions, i.e. without reduction of scan time (cf. Chap. 5).

It is also noteworthy that signal-to-noise losses become even more significant if parallel imaging is applied to increase the spatial resolution. A non-accel-

erated three-dimensional acquisition with isotropic spatial resolution of 1×1×1 mm³ may be converted to a protocol with acceleration factor R=4 and substantially improved isotropic resolution of 0.5×0.5×0.5 mm³ covering the same total volume of interest (i.e. the same three-dimensional field of view). If the echo (or readout) duration is kept constant by increasing the receiver bandwidth, the total scan time of both protocols will be identical, since the increased number of phase-encoding steps is compensated by the parallel-imaging acceleration; however, the voxel volume is reduced to an eighth of the original value and, thus, the SNR decreases as well by almost 90 %. For most protocols, this SNR loss will not be acceptable, which means that the theoretical potential of parallel imaging cannot always be completely exploited.

In addition to the SNR loss due to acceleration, image noise is also regionally amplified. This effect is quantitatively described by the g-factor (cf. Chap. 3; Pruessmann et al. 1999). Noise amplification depends on several parameters such as the coil geometry, the image orientation, and the acceleration factor, R, and typically appears as band-like structures over central image parts (cf. Fig. 2 of Chap. 3). Obvious disadvantages of such varying noise levels are that the SNR may be subjectively overestimated (based on lower noise levels outside the noise bands) resulting in unacceptably low SNR is some parts of the image. Furthermore, the objective determination of SNR and CNR is made much more difficult in parallel imaging than in conventional MRI as discussed in Chap. 4. To avoid degrading noise amplification, parallel-imaging acceleration, i.e. the acceleration factor, R, as well as the acceleration (or phase-encoding) direction, must be chosen appropriate with respect to the used coil system.

17.3.2 Localized Image Artefacts

Since parallel imaging is based on undersampling of k-space data in phase-encoding direction, aliasing (fold-over or wrap-around) artefacts may appear due to imperfect parallel-imaging reconstruction. These localized aliasing artefacts are complementary to noise amplification in parallel imaging; i.e., depending on the reconstruction algorithm, resulting images may contain either more stochastic noise and fewer remaining aliasing artefacts, or, vice versa, a lower noise level but more remaining aliasing. Further improvements of reconstruction techniques aim at optimally balancing both sources of artefacts (cf. Chap. 46).

A specific problem of parallel MRI with image-space-based reconstruction (e.g. with SENSE-related techniques) are residual aliasing artefacts in central parts of the field of view that arise if the reconstructed full field of view is smaller than the imaged object (Griswold et al. 2004; Goldfarb 2004); examples are shown in Fig. 7 of Chap. 1, and Fig. 1 of Chap. 21. The k-space-based reconstruction has been shown to be generally more robust for MRI with small fields of view.

17.4 Conclusion

There are two significant limitations to the application of parallel imaging: these are, on the one hand, relatively demanding hardware requirements including multi-channel RF receivers as well as multi-element coil systems combined with appropriate reconstruction systems and software. Most currently available new MRI systems fulfil all these requirements for parallel imaging or can be upgraded relatively easily, but older existing installations will often be too limited and not flexible enough for parallel imaging. On the other hand, not all protocols are equally suited for parallel imaging, and certain restrictions with respect to SNR, image geometry, or maximum achievable acceleration factors must be kept in mind. Nevertheless, parallel imaging has turned out to be one of the most important recent developments in MR imaging, impacting examination protocols in virtually all areas of research imaging and clinical MRI.

References

Edelstein WA, Glover GH, Hardy CJ, Redington RW (1986) The intrinsic signal-to-noise ratio in NMR imaging. Magn Reson Med 3:604–618

Griswold MA, Kannengiesser S, Heidemann RM, Wang J, Jakob PM (2004) Field-of-view limitations in parallel imaging. Magn Reson Med 52:1118–1126

Goldfarb JW (2004) The SENSE ghost: field-of-view restrictions for SENSE imaging. J Magn Reson Imaging 20:1046–1051

Haacke EM, Brown RW, Thompson MR, Venkatesan R (1999) Magnetic resonance imaging: physical principles and sequence design. Wiley-Liss, New York

Pruessmann KP, Weiger M, Scheidegger MB, Boesiger P (1999) SENSE: sensitivity encoding for fast MRI. Magn Reson Med 42:952–962

Part IV:
Clinical Applications: Imaging of Morphology

High-Resolution Imaging of the Brain

18

Roland Bammer and Scott Nagle

CONTENTS

18.1 Introduction

Resolution enhancement in MRI is of great potential for increased diagnostic accuracy in brain and spine imaging. With the advent of high-field systems increased signal-to-noise ratio (SNR) affords smaller voxel sizes, but overall scan time is still a limiting factor for high-resolution brain imaging in a clinical setting. Parallel imaging is of great benefit since it allows us to achieve high-resolution 2D and 3D acquisitions in clinically acceptable time frames. In addition, parallel imaging can also diminish the amount of image blurring and geometric distortions leading to obvious resolution and quality improvements without altering the acquisition matrix size.

R. Bammer, PhD; S. Nagle, MD, PhD
Department of Radiology, Stanford University, Lucas Center, 1201 Welch Road, Stanford, CA 94305-5488, USA

This chapter critically addresses the general advantages and limitations of high-resolution neuroimaging in concert with the additional capacity provided by parallel imaging. Specifically, the role of parallel imaging in high-resolution structural MRI, magnetic resonance angiography, and functional MRI in the broader sense (i.e., diffusion and perfusion MRI as well as classical functional MRI) are discussed.

The improved scanning efficiency of parallel imaging methods can be applied in a number of fruitful ways in the field of brain MR imaging. As described in the first part this book, these parallel-imaging strategies cleverly incorporate the spatially varying sensitivity profiles of multiple-channel receive coils in order to reduce the number of k-space measurements necessary to reconstruct an image (Hutchinson and Raff 1988; Kwiat et al. 1991; Sodickson and Manning 1977; Pruessmann et al. 1999). In conventional Cartesian k-space sampling schemes, this is typically realized by decreasing the number of phase-encoded steps. In cases of high SNR, the reduction of phase-encoded steps by a factor R (accompanied by its obligatory $\sqrt{R}$ decrease in SNR Pruessman et al. 1999) can be used to increase either spatial resolution or temporal resolution. These advantages are not mutually exclusive and it depends on the specific scan protocol whether one favors more rapid scanning or higher resolution. In addition, the artefact and blurring associated with several multiple-echo or long-readout sequences can be mitigated by parallel-imaging techniques (cf. Chap. 10).

Increasing the spatial resolution may allow the detection of smaller lesions, may better characterize the internal structure of larger lesions (e.g., calcification, blood products, demyelination, cystic components, etc.), and may better delineate the lesion boundaries with respect to normal anatomy, improving the accurate localization of a lesion (especially important in the prepontine, suprasellar, cerebellopontine angle, cavernous sinus, orbital, and Meckel's cave regions). The imaging of white matter disease, stroke, neoplasm, and vascular disease could all ben-

efit from these advantages. Pediatric and neonatal brain imaging also demands fast, high-resolution imaging because of the relatively small brain size and the difficulties in keeping a child still throughout the scan. Similar considerations apply also for imaging the spinal cord. Three-dimensional spoiled gradient-echo sequences, used in the evaluation of mesial temporal sclerosis in the work-up of seizures, tumor treatment planning, and voxel-based morphometry in neurodegenerative disorders, could benefit from the use of parallel imaging in both phase-encoded directions to further increase resolution without increasing scan time (Weiger et al. 2002a).

Conversely, shortened scan times alone can increase patient throughput, resulting in obvious operational and patient comfort improvements. Simply decreasing scan time reduces the risk of patient motion degrading a study. A number of other creative methods for further reducing motion artefacts through the use of parallel imaging have been proposed and demonstrated (Bammer et al. 2004; Kuhara and Ishihara 2000; Bydder et al. 2002, 2003; Atkinson et al. 2004).

Parallel imaging also yields advantages in other, less obvious ways. Conventional spin-echo T2-weighted imaging requires prohibitively long scan times due to the long TRs needed, resulting in the widespread adoption of fast spin-echo (FSE) or turbo spin echo (TSE) techniques. In order to increase their efficiency T2-weighted FSEs are usually carried out with relatively long echo trains. Unfortunately, such multi-echo sequences suffer from blurring and decreased SNR relative to conventional spin-echo sequences, due to the T2-decay occurring while the multiple echoes are being acquired (cf. Chap. 9). By using parallel-imaging methods to decrease the required number of phase-encoded measurements, the effective TE can be reduced by decreasing the echo-train length, simultaneously generating both improved SNR and decreased image blurring due to the fact that data in the periphery of k-space are being acquired earlier under the T2-decay curve (Fig. 18.1). Alternatively, for a given echo-train length the FSE scans can be made more efficient and fewer TR intervals are required to complete the acquisition of the required k-space information. Even there, the faster traversal through k-space can lead to reduced T2-blurring. Similarly, by reducing the read-out time, off-resonance artefacts can be reduced (Bammer et al. 2001a). In pulse sequences which are SAR-limited, such as FLAIR or single-shot FSE scans, parallel imaging offers the advantage of eliminating a large fraction of the RF excitation pulses and is particularly attractive at higher field strengths when other SAR-diminishing techniques, such as hyperechoes (Hennig and Scheffler 2001) or variable-rate selective excitation (VERSE, Conolly et al. 1988), are not an option.

The application of parallel imaging to intracranial MR angiography (MRA) offers many advantages and is discussed in detail in Chap. 26. Wilson et al. (2004) also provide an excellent review of the use of parallel imaging in MRA. Due to the small size of the vessels, and the presence of intravoxel dephasing on time-of-flight (TOF) images, high resolution is desired. Phase-contrast (PC) techniques must obtain fourfold more data than TOF if full 3D velocity measures are desired, leading to long scan times, especially if full brain coverage at high resolution is desired. Fortunately, MRA images (especially contrast-enhanced MRA images) often have a high baseline SNR and

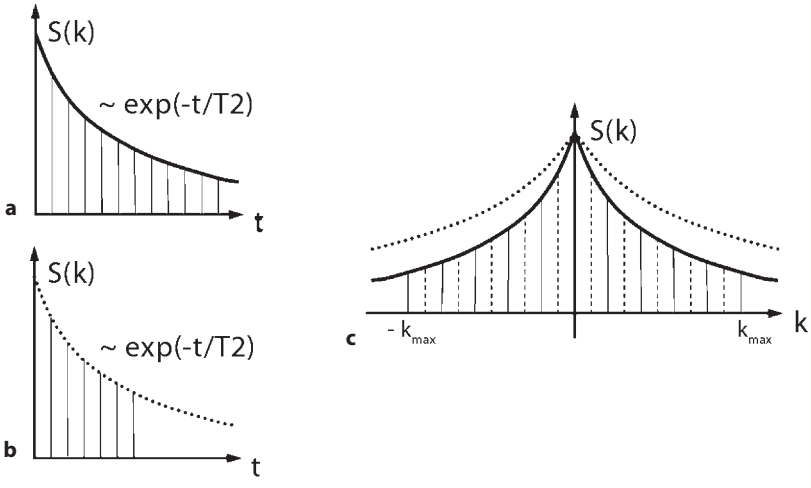

Fig. 18.1a–c. Example of k-space filter effect due to T2-decay in FSE. **a** During normal FSE readout the net magnetization decays with T2 (T2* in EPI) which in turn leads to a T2-dependent weighting of k-space that ultimately results in blurred images. **b** Using parallel imaging (R=2 in this example), the echo-train length can be shortened by 1/R. **c** As every other line in k-space (for the R=2 case) is skipped, the relevant k-space information is obtained much faster and the signal loss towards the edge of k-space is reduced (indicated by the *dotted line*). While the acquisition matrix remains the same, the apparent resolution is improved by blurring reduction.

could benefit from the application of parallel imaging to increase spatial resolution at the expense of a slight SNR loss, especially when moving to 3 T with its approximately doubled SNR (Weiger et al. 2000, 2002a) relative to 1.5 T.

Quantitative MR imaging methods, such as diffusion-weighted (DWI), diffusion tensor (DTI), perfusion-weighted imaging (PWI), and functional MRI (fMRI), rely for the most part on single-shot echo planar (EPI) pulse sequences (Mansfield 1977). The EPI pulse sequences offer especially attractive targets for the application of parallel imaging for much the same reasons as the multi-echo sequences described above. Due to their inherently long read-out times, EPI methods are prone to T2*-related signal decay and an extreme sensitivity to susceptibility effects (cf. Chap. 10). These effects manifest in blurred and geometrically distorted images (especially in regions of the brain near the skull base and paranasal sinuses). Often these regions of the brain are precisely the areas of interest in the clinical settings of stroke or when using fMRI to map cortical brain activity. In the setting of DTI for the purposes of white matter tractography, e.g., high spatial resolution, is critical for resolving regions where fiber tracks cross and to minimize partial-volume effects and geometric distortions of the tracts. Without parallel imaging it is difficult to acquire high-resolution DTI data in a reasonable amount of time. Fortunately, with EPI techniques the inherent $\sqrt{R}$ signal loss of using parallel imaging is mitigated by the fact that the signal is acquired earlier under the T2*-decay curve (at a shorter effective TE), resulting in a signal increase (cf. Chap. 10). The benefits of using parallel imaging in EPI applications have been successfully demonstrated in various studies (Bammer et al. 2001a, 2002; Griswold et al. 1999; Jaermann et al. 2004; Kuhl et al. 2005).

18.2 Structural MRI

Increasing the spatial resolution of MR scans, both in-plane and through-plane, offers the opportunity to better visualize structural changes and characterize individual lesions. Here, especially, MRI's diagnostic sensitivity to small lesions can be increased, and the conspicuity of small structural details in larger lesions (such as small calcifications or lipid deposits) may increase the diagnostic specificity. Although the exact role of higher-resolution in neuroradiology, especially in the context of varying levels of experience of individual readers, is thus far not known, it is reasonable to expect that the degree of confidence and the speed of interpretation increase with increasing spatial resolution.

In white matter diseases, such as multiple sclerosis (MS), appreciation of the internal complexity of these lesions can help to differentiate stages of inflammation, demyelination, and gliosis in the individual plaques, which is important in clinical management and the evaluation of response to therapy (Fig. 18.2). A recent study has shown that high-resolution structural MRI in MS patients promises to be more sensitive than conventional MRI (Erskine et al. 2005). This may be due to lesions being obfuscated by small vessels, confluent signal abnormalities, or partial-volume averaging. In some cases MS plaques can also be found in cortical and juxtacortical regions (Kidd et al. 1999; Kangarlu et al. 2004). Especially for cortical lesions, the lesion conspicuity is often impaired by different relaxation rates and significant partial-volume contamination; thus, high-resolution imaging can add to a higher diagnostic certainty.

Improved spatial resolution is also helpful for tumor imaging in regions of the brain where precise spatial localization is important: the cerebellopontine angle; the prepontine cistern; the suprasellar region; the cavernous sinus; the foramen of the ventricular system (Monroe, Magendie, and Lushke); and Meckel's Cave, in particular. The first step towards characterizing an intracranial lesion is the accurate localization into intraaxial or extraaxial compartments as the differential diagnoses for lesions in these compartments are distinct. These compartments are separated by the dura, and the higher the resolution, the easier it is to directly visualize the dural membranes and accurately localize the lesion. Even the differentiation of the most typical extraaxial lesions, such as meningioma and schwannoma, can be facilitated by an increased conspicuity of their diagnostic hallmarks (e.g., dural tail, calcification, lipid deposits). Furthermore, the internal structure of a neoplastic lesion has important implications in terms of differential diagnosis and is often best appreciated on higher-resolution images, with their greater anatomic detail and reduced partial-volume averaging. The presence of small flow voids, calcifications, lipid deposits, cystic lesions, and overall texture of a lesion may only be detectable at higher resolution and offer the possibility of increasing the specificity of the differential diagnosis reported by the radiologist (Fig. 18.3).

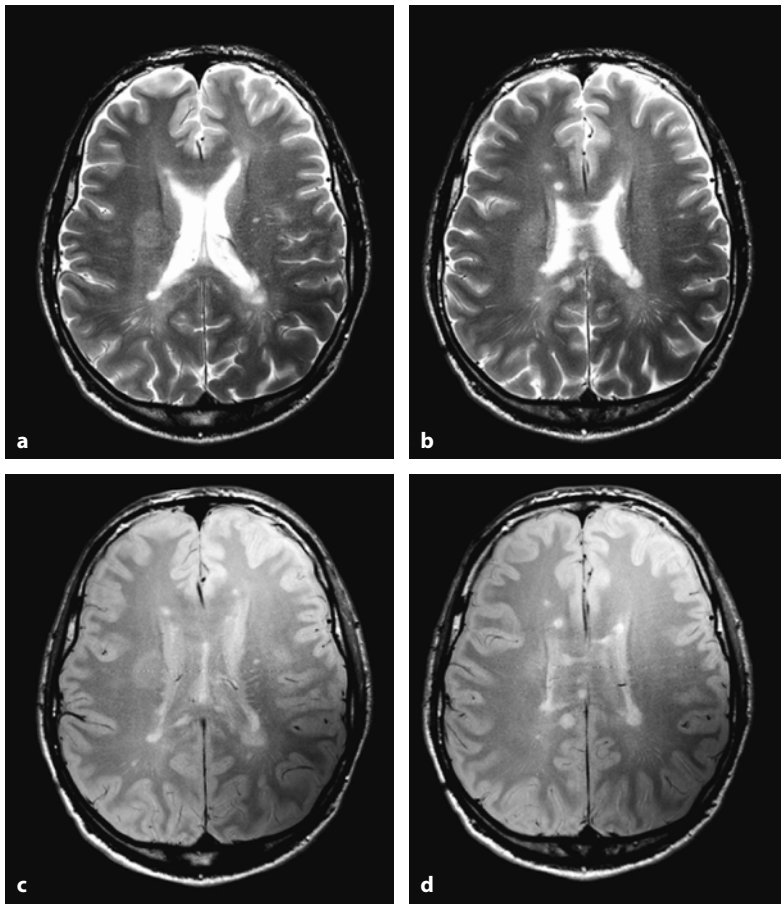

Fig. 18.2a–d. High-resolution (0.43×0.43-mm^2 in-plane resolution, 3 mm slice thickness) MRI at 1.5 T in a patient suffering from a relapsing/remitting form of multiple sclerosis with an enhancing lesion in the right periventricular area. **a,b** T2-weighted FSE scans. **c,d** Proton-density-weighted FSE scans. The improved appreciation of the internal complexity of these lesions might help to differentiate stages of inflammation, demyelination, and gliosis in the individual plaques. Enlarged perivenular spaces and associated focal lesions can be seen adjacent to the posterior horns of the lateral ventricles.

In cases in which the diagnosis is known and the purpose of the study is for preoperative planning (e.g., "cyber knife" stereotactic radiosurgery), precise definition of the lesion boundary is quite important in order to avoid damage to critical nearby structures. Even if the spatial resolution of most radiosurgery methods is beyond what conventional MRI provides, a clear demarcation between neoplastic tissue and adjacent non-neoplastic tissue is of great benefit both for treatment planning and for post-treatment follow-up for recurrent disease. For diffusely infiltrating tumors, such as glioblastoma multiforme, a higher spatial resolution might help differentiate between edematous and neoplastic tissue. Extracranially, the accurate diagnosis and preoperative planning for head and neck tumors relies on very accurate identification of the tissue planes transgressed by the tumor and would benefit from improved high-resolution imaging (cf. Chap. 19).

From an applications perspective, parallel imaging allows scanning with conventional resolution in less time or scanning with increased resolution without increasing scan time. These approaches are not mutually exclusive, as parallel imaging is best described as a tool to most efficiently acquire images using phased-array coils that are used for complementary image encoding. Due to the sequential image formation process in MRI, and the nature of Fourier encoding itself, the increase of spatial resolution is accompanied by a proportional increase in the number of phase-encoded steps. This in turn can increase the overall scan time quite dramatically, which is often forgotten in the excitement to move toward higher resolution. Aside from the scan time penalty, quadrupling the SNR loss when doubling the in-plane resolution must be affordable by the protocol, i.e., possible within reasonable scan times and supported by a considerable baseline SNR to begin with. Signal averaging can be used to compensate the SNR penalty to some extent but one has to keep in mind that, for example, compensating for a 4× loss in SNR it would require 16 averages to maintain equal SNR and thus excessively prolongs scan time.

Increasing resolution along the frequency-encoding direction (at a fixed gradient strength and band-

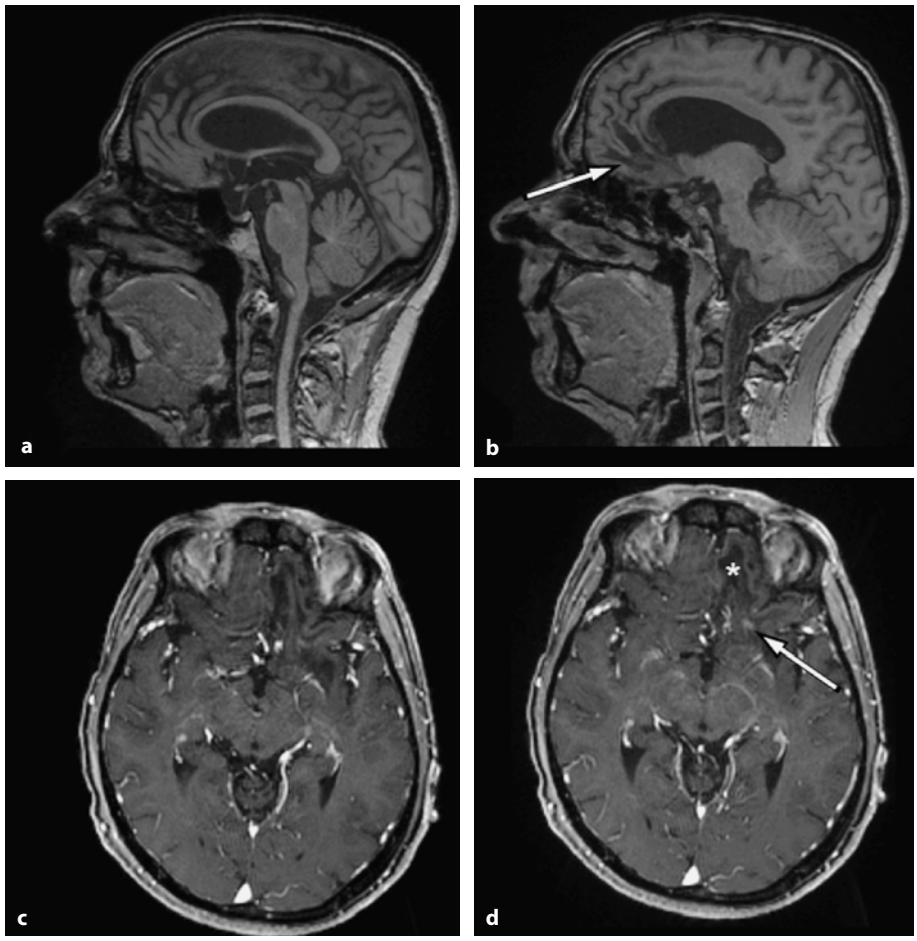

Fig. 18.3a–d. A 3D T1-weighted spoiled gradient-echo sequence (TR/TE=12/4.5 ms; α=20°; 0.86×0.86×1.5 mm^3) at 3 T with 2D-GRAPPA R=2×2 along both phase-encoding directions. Follow-up exam of a patient suffering from an anaplastic astrocytoma after partial resection, radiotherapy, and chemotherapy (*arrow*). High-resolution structural scanning was accomplished almost four times (plus time to acquire auto-calibration lines) faster than with conventional image encoding. **a** Mid-sagittal pre-contrast view. **b** Sagittal pre-contrast cut through the tumor. **c,d** Adjacent axial slices after contrast administration show edema (*asterisk*) and residual contrast enhancement (*arrow*). (Courtesy R. Stollberger and F. Payer, Medical University Graz, Austria)

width or water/fat shift per pixel) is accompanied by a proportional increase of the echo readout duration, which in turn prolongs the echo-train length of all FSE and EPI-based methods. For several sequences the consequences of larger echo spacings and overall echo train lengths are a reduced number of slices that can be interleaved per TR interval and a more significant k-space filtering effect due to the more pronounced T2-decay (Fig. 18.1). If possible, extended echo spacings are often remedied by increasing the readout gradient and bandwidth at the expense of a reduced SNR; however, with some methods the maximum gradient strength and slew rate are already at their limits (e.g., balanced-SSFP, EPI) and only fractional echoes or parallel imaging is a viable alternative. Increasing the resolution along the phase-encoding direction is very costly in terms of additional scan time.

With the introduction of new clinical 3 T systems and their higher baseline SNR, the use of larger acquisition matrices is becoming a viable option again. As the field strength increases from 1.5 to 3 T, the effective SNR gain doubles to what would otherwise be achieved only by a tedious averaging process at 1.5 T. As a rule of thumb one has to scan four times longer at 1.5 than at 3 T to achieve comparable SNR levels. Of course, relaxation and B_1 effects will mitigate this benefit slightly. Firstly, the prolonged tissue relaxation times require longer TR to provide adequate signal recovery. Secondly, B_1 inhomogeneities can lead to incomplete or partial excitation and refocusing as well as reduced receive sensitivity. Particularly for high field applications, parallel imaging is a very attractive option since it helps to keep high-resolution MRI within clinically acceptable time frames, and despite its inherent SNR loss still provides diagnostically adequate scans (Fig. 18.4).

The development of new RF coil designs has followed the introduction of parallel imaging (cf. Chap. 14). Specifically, multi-channel array coils, having between 8 and 16 independent receiver coils distributed around the subjects head, have been developed for brain imaging. In research studies,

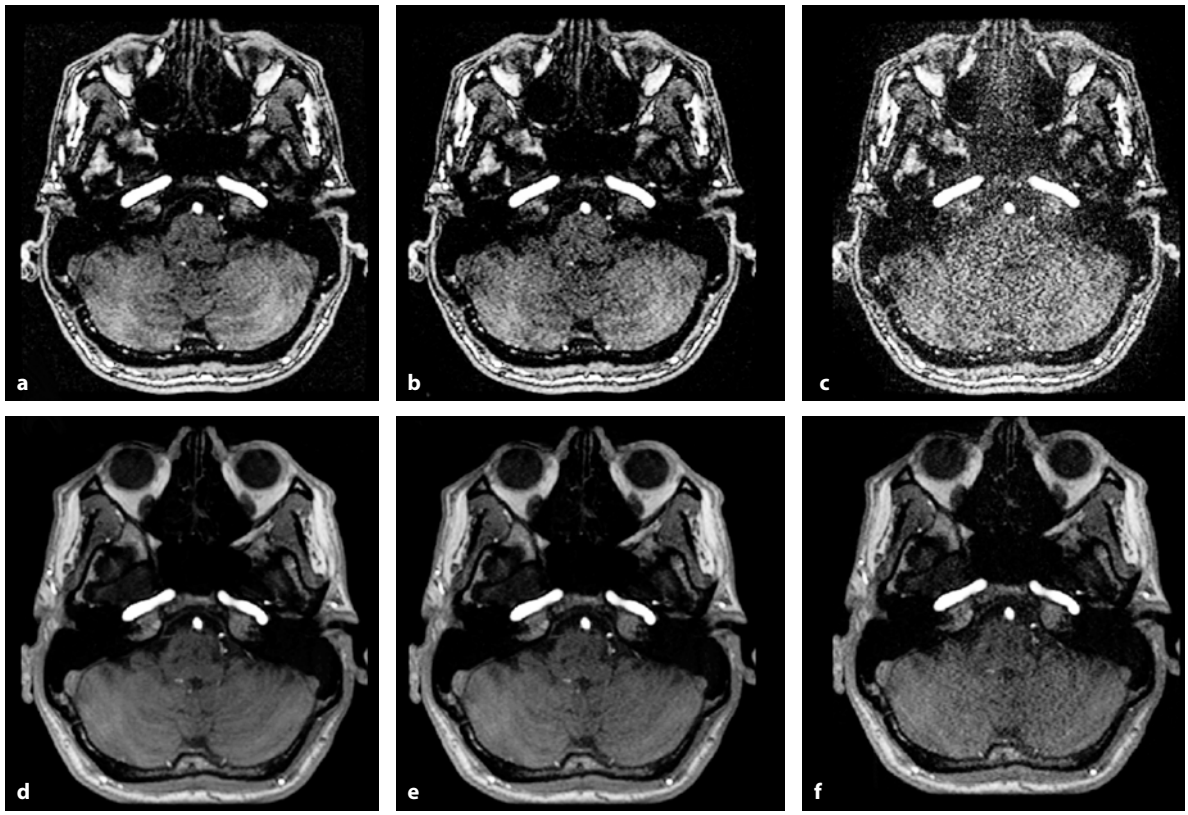

Fig. 18.4a–f High-resolution imaging of the brain and intracranial vessel at 1.5 T (*top row*) and 3.0 T (*bottom row*) in a normal volunteer using identical acquisition parameters. Comparison of GRAPPA-induced noise enhancement using reduction factors of R=1 (**a,d**), R=2 (**b,e**), and R=3 (**c,f**). Parallel imaging clearly benefits from the higher baseline SNR and the spatially more distinct RF characteristics at 3.0 T. The SNR measurements revealed comparable values for R=3 at 3.0 T and R=1 at 1.5 T.

scans have even been performed with prototype arrays containing more than 100 independent coils. In general, these array coils provide better SNR than comparable birdcage coils and boost regionally the SNR by factors up to two (Bammer et al. 2001b). At our institution we also made the observation that at 3 T the signal pile-up due the B_1-field focusing effect is less pronounced with these phased-array coils than with standard birdcage coils. Most likely, the higher coil sensitivity at the brain's periphery (i.e., these areas are closer to the coils) offsets the field focusing effect. Parallel imaging can be implemented in several ways to improve high-resolution structural brain imaging. The most important aspect is, of course, the reduction of overall scan time when other imaging options, such as partial k-space acquisition, fractional (i.e., rectangular) field of view (FOV), or reducing the number of signal acquisitions are already exhausted or are not an option. Given enough baseline SNR, parallel imaging allows one to acquire high-resolution scans within reasonable acquisition periods. Furthermore, parallel imaging's impact on image deblurring can also be considerable even without changing the acquisition matrix size. Here, the faster traversal through k-space leaves the signal less time to decay with T2 or T2*; thus, in addition to more rapid image formation, images will appear to have improved resolution because of the diminished blurring effects. An easily overlooked problem related to increasing in-plane resolution (especially in slice-selective MRI scans) is the frequent anisotropic voxel size. To prevent this voxel anisotropy from becoming even more exaggerated as in-plane resolution is increased it is paramount to reduce the slice thickness accordingly; however, this often reduces the available SNR even further and also requires an increased number of slices to cover a specific area.

For applications with a large number of slices and short repetition times (and when isotropic voxels and diminished partial-volume averaging are important) the use of 3D acquisitions with phase-encoding along two principal axes is advisable (see Fig. 18.3). Three-

dimensional imaging is frequently used for volumetric studies, stereotactic therapy planning, and angiographic studies. Typically, T1-weighted 3D spoiled gradient-echo sequences or MPRAGE sequences are used for image acquisition. Classically, 3D MRI is a very attractive method as it has increasing SNR benefits over 2D imaging with an increasing number of slices to cover the brain. While 2D acquisitions receive signal only from a thin slice, the signal in 3D acquisitions emanates from the entire slab.

In addition to the higher baseline SNR, 3D MRI provides the opportunity to perform parallel imaging along both phase-encoding directions independently. The overall scan acceleration will be the product of the accelerations achieved in each of the two phase-encoding directions. For the same overall acceleration factor it has been shown that acceleration in both dimensions provides a more benign g-factor-related noise enhancement than in only one dimension (cf. Chap. 3). This can be easily understood if one recalls the basic principle of SENSE. With increasing reduction factor, R, the distance between voxels that are aliased on top of each other will decrease. A reduced distance between aliased voxels also implies a less distinct coil sensitivity variation which makes it harder for the reconstruction to separate these voxels. An overall scan time reduction by a factor three or four can be achieved very easily with parallel imaging along both phase-encoded directions and has enormous consequences for sequences that run otherwise 15 min or more. In research settings, reduction factors of 8 and higher have been reported for 3D acquisitions; and some researchers presented results where the reduction factor even exceeded the theoretical limits of R (i.e., the number of independent receiver coils) by capitalizing on special mathematical regularization methods (Fig. 18.5; Katscher 2003). Although there is currently no strict convention in place, it is important to report the acceleration factor in both phase-encoded directions separately, i.e., $R_{3D}=3\times2$ for a twofold acceleration in the in-plane and a threefold acceleration in the through-plane phase-encoded direction. It is noteworthy that residual aliasing along the phase-encoding direction perpendicular to the slice is much harder to detect than the more obvious artefacts seen from in-plane reconstruction errors. If in doubt, a reformation of the data to an orthogonal plane might reveal the problem.

As already mentioned, imaging at higher resolution affords a better characterization of morphological abnormalities. Particular areas in which high resolution is of potential benefit is the hippocampus area, the pituitary region, the orbits, or the cranial nerves; however, the small FOVs that are generally used for these studies might pose a fundamental limit for parallel imaging and the currently available coils. In this context it is important to understand that a high degree of scan acceleration is only feasible if there is a significant variation in coil sensitivity across the FOV. If the spatial coil sensitivity variation becomes spatially less distinctive, it becomes more difficult to correctly separate the aliased voxels. The individual coil sizes as well as their size and orientation relative to the prescribed FOV are essential parameters and characterize the capacity of the parallel-imaging method to remove aliasing. This information is also matched by the spatially varying g-factor. In other words, with

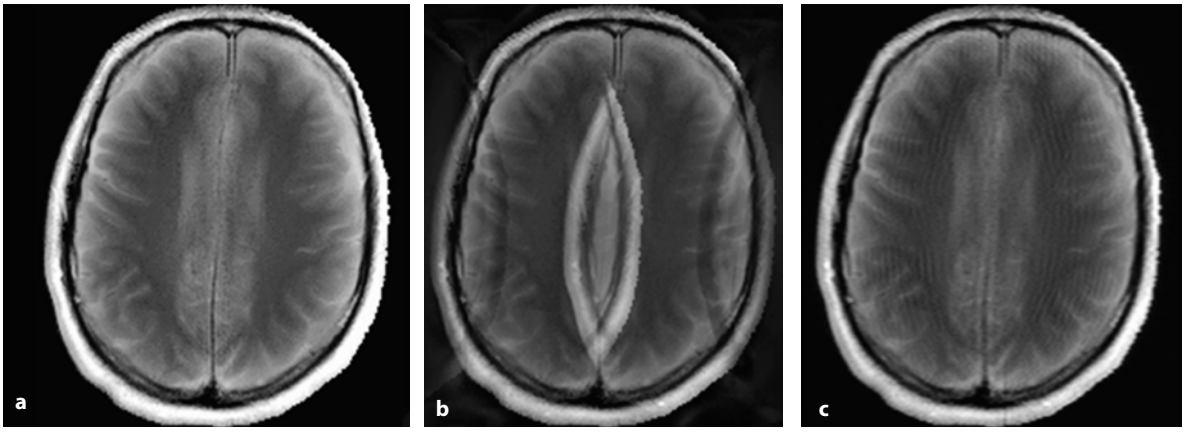

Fig. 18.5a–c. Example for a SENSE reconstruction with two surface coils and a reduction factor $R=3$. **a** Example image serving as input for the simulation (TSE/turbo factor 30, TE=100 ms, TR=2000 ms, pixel volume 0.9×0.9×8 mm³, $\alpha = 60°$, $B_0=1.5$T). **b** Reconstruction result for $R=3$ using a uniform k-space density. **c** Reconstruction result for the same parameters as for **b**, but using a Gaussian k-space density. (Courtesy of Dr. Katscher, Philips Research Labs, Hamburg, Germany)

diminishing FOVs and without adaptation of the individual coil element size, parallel imaging may no longer keep up in its ability to unfold aliased voxels. This might eventually become problematic for areas in the middle of the brain remote from all coil elements and at high acceleration factors.

18.3 MR Angiography

Angiographic sequences, in particular contrast-enhanced MRA, are generally not limited by SNR, and are therefore ideally suited for combining them with parallel imaging. As with conventional structural MRI, the ability to further reduce acquisition time can be beneficial not only in reducing patient motion but also in providing larger FOV or better spatial and temporal resolution; the latter enables the use of time-resolved MRA acquisitions that provide important functional information in addition to morphological details, representing a major advantage of MRI over advanced multi-detector CT angiography. Increased in-plane anatomic coverage in intracranial MRA afforded by parallel imaging allows one to display a larger part of the circle-of-Willis (COW), including ACA, MCA, and PCA and the distal portion of both the basilar artery and the ICAs. Increasing the coverage in cranio-caudal direction makes it also easier to prescribe the position of the image stack and to more accurately cover the targeted vessels. A shorter imaging time should also facilitate the use of this technique in restless and uncooperative patients, as in the setting of acute stroke or when imaging children.

Time-of-flight (TOF) MRA is based on flow effects and is one of the primary diagnostic tools for patients with suspected intracranial aneurysms and steno-occlusive disease. In particular, gradient-echo sequences are used for TOF MRAs, in which the inflow of fresh, unsaturated blood into RF-saturated tissue leads to increased signal intensity within vessels. Due to the small caliber of intracranial vessels and the presence of vessels throughout the brain, high-resolution imaging over larger FOVs is a prerequisite for an accurate diagnostic work-up. Specifically, high spatial definition is relevant for the imaging of both steno-occlusive disease and aneurysms where the visualization of fine anatomic details in the COW, such as small vessel branches and the neck of aneurysms, is needed. Likewise, the high spatial definition is advantageous in the characterization of AVMs (Fig.18.6). In this context, reducing the voxel size also diminishes the inherent sensitivity to intravoxel dephasing in TOF and further improves the quality of TOF MRA.

As with structural MRI, MRA also benefits from the SNR gain afforded by the migration to higher

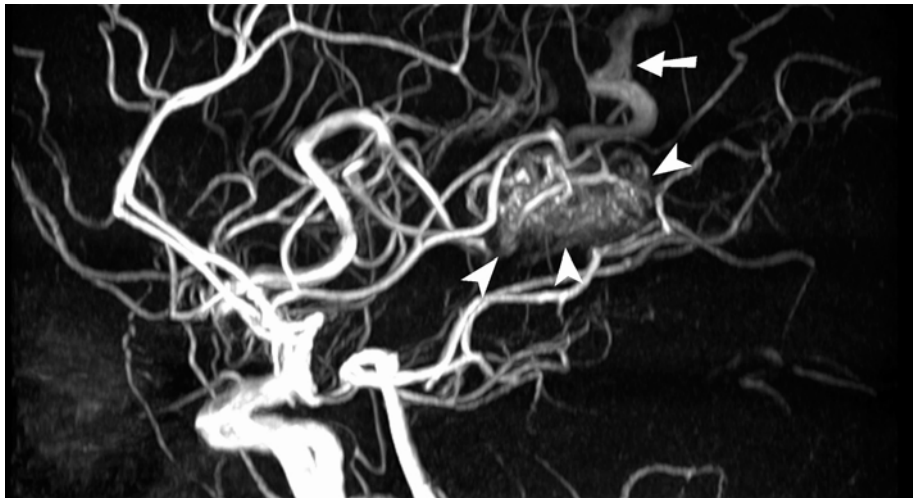

Fig. 18.6. Sagittal maximum intensity projection of a high-resolution axial T1-weighted 3D gradient-echo TOF MRA (acquisition matrix 832×1024; R=2.5) at 3 T in a patient suffering from an arteriovenous malformation (*arrowheads*) in the right insula region and a superficial venous drainage into the superior sagittal sinus (*arrow*). Increased baseline SNR at 3 T affords high-quality MRAs in this patient with great conspicuity of the ateriovenous malformation. The acquisition of 150 slices took 5:12 min. (Courtesy W. Willinek, Universiyt of Bonn, Bonn, Germany)

magnetic field strengths. In addition, the saturation effect of the surrounding parenchyma, and hence increased vessel-to-parenchyma CNR, is even more pronounced at 3 T due to the prolonged T1 relaxation times of semisolid tissues relative to essentially no change in T1 of blood. The extra SNR can be invested in high spatial resolution protocols, improving the depiction of small vessel segments (Willinek et al. 2003, 2004; Bernstein et al. 2001; Al-Kwifi et al. 2002; Thomas et al. 2002), and, in turn, improving image quality of intracranial aneurysms (Metens et al. 2000) and the diagnostic accuracy of detecting cerebrovascular disease. Since typical imaging times for high-resolution protocols are overly long, parallel imaging is ideally suited to reduce imaging time.

A recent study demonstrated the ability of parallel imaging to both reduce acquisition time and to improve the anatomic coverage for high spatial resolution TOF MRA at 3.0 T with comparable image quality. In this particular study, acquisition times were reduced from 7:57 to 5:12 min using reduction factors of 2.5, while the anatomic coverage was increased 1.5 times. In a series of 80 acute stroke patients we also observed that the overall quality of TOF MRA as well as the visualization of distal branches of the MCA, ACA, and PCA improved substantially after beginning to use multi-element head coils. This can most likely be attributed to the increased peripheral receive sensitivity of such coils.

Phase-contrast (PC) MRA (Dumolin et al. 1989) is another angiographic MR method and utilizes motion-probing gradients to provide flow-related contrast along the direction of the flow-encoding gradient. The PC MRA is important for evaluating lesions were blood deposition products appear hyperintense in TOF-MRAs (and therefore mimic inflow) or for abnormalities with slow flow where the TOF mechanism is lost by saturation effects (i.e., where not enough fresh blood replenishes saturated blood to provide sufficient vessel-to-parenchyma contrast). In addition, with PC-MRA, the velocity-encoding parameter can be used to better discriminate between fast-flowing arteries and the slow flow of blood in the veins. One application in which PC MRA is frequently used is MR venography. Unfortunately, PC MRA is a notoriously slow imaging technique. This is because at least two or up to four measurements are required to measure flow along one direction or three directions (plus a reference measurement). Parallel imaging can substantially speed up PC MRA. Here, the abundant SNR inherent in PCA supports the use high reduction factors. Furthermore, in 3D PC MRA, parallel imaging can be applied in both the phase and slice-encoding directions, allowing even higher reduction factors. Recently, it has been shown that reduction factors of up to 6–8 are possible in PC MRA of the brain with isotropic 1-mm^3 resolution. Without parallel-imaging scan-time reduction, such an examination would take about 40 min to complete, whereas with parallel imaging it is possible to reduce the overall acquisition time to 5–7 min (Fig. 18.7).

At our institution we have recently begun to perform 3D PC MRA to measure all three components of flow at several instances within the RR interval(R. Bammer et al., submitted). Such measurements provide us detailed information of blood flow within a 3D volume, temporally resolved across the cardiac cycle. The knowledge of magnitude and orientation of flow in space and its change over time throughout the RR interval allows us to provide streamline analysis and virtual particle tracing in intracranial vessels (Fig. 18.8). Due to this complex, multi-dimensional acquisition scheme, it is understandable that acquisition times are considerable. By means of GRAPPA we could cut down the acquisition time substantially. At 3 T a reduction factor of 3 was feasible without noticeable reconstruction artefacts or noise enhancement and without the use of contrast material (see Fig. 18.4).

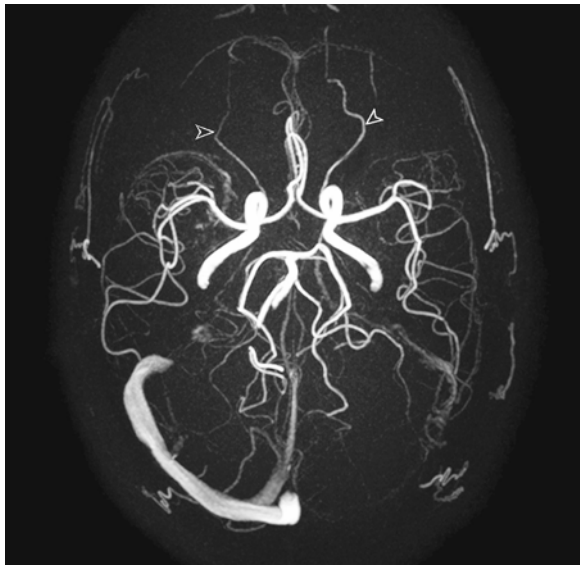

Fig. 18.7. Axial projection MIP of high-resolution whole-brain 3D MR venography at 3 T using phase-contrast MRA and SENSE in two directions. A SENSE reduction factor of 4 (2×2) was taken in slice and phase-encoding direction to acquire a true 512 matrix within 1:40 min. The high spatial resolution MRA allows for depiction of the ophthalmic arteries (*arrowheads*). (Courtesy of W. Willinek, Universiyt of Bonn, Bonn, Germany)

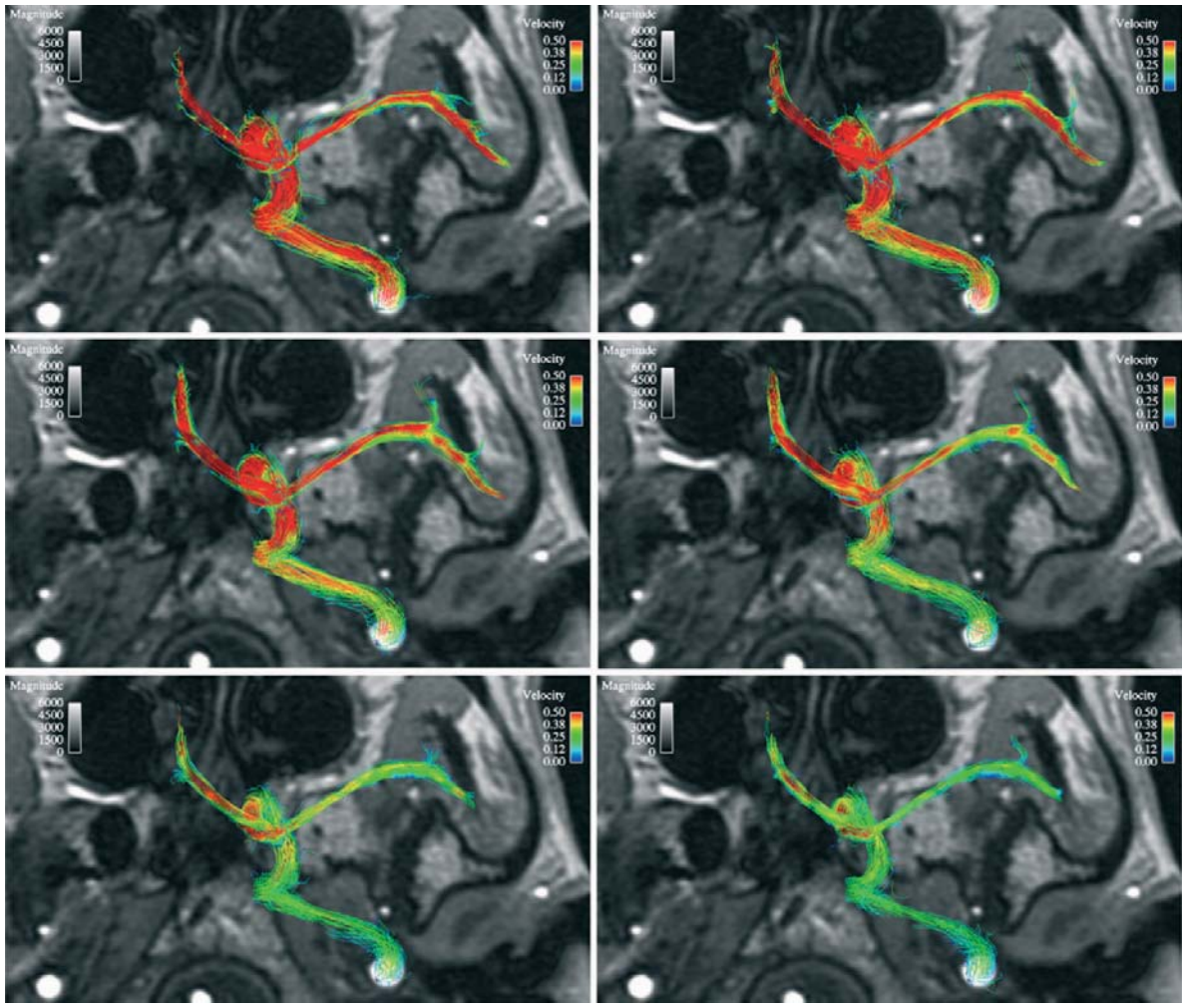

Fig. 18.8. Time-resolved (20 time points/RR interval) high-resolution streamline visualization of the left internal carotid artery, the middle cerebral artery, and the anterior cerebral artery. The time-resolved 3D velocity data were computed from high-resolution 3D phase-contrast MR scans with flow measurement along the principal axes. Streamline computation was performed by fourth-order Runge-Kutta numerical integration of the flow vector field. The streamlines are color coded [ranging from 50 cm/s (*red*) to 0 cm/s (*blue*)] based on the magnitude velocity. The images are arranged from top to bottom beginning with peak systole and ending with late diastole. The pulse wave traveling distally can be clearly appreciated.

The use of contrast material has clearly revolutionized the role of MRI in angiography. To perform contrast-enhanced (CE) MRA, a 3D spoiled gradient-echo sequence covering the anatomy of interest is synchronized to the arrival of a T1-shortening contrast-agent bolus. The use of CE MRA for neurovascular studies requires relatively short and exactly timed acquisitions to provide maximum arterial enhancement and avoid venous overlay. Capturing an arterial phase can either be accomplished by rapid acquisition of temporal dynamics (thus including at least one frame of pure arterial phase) or precisely timing a higher-resolution scan to the arrival of the bolus (using "fluoroscopic triggering" or other timing mechanisms; Fig. 18.9). A high temporal resolution is beneficial to CE MRA because it provides dynamic visualization of contrast kinetics that can include important information for diagnosis of certain vascular pathologies. Certainly, there is a trade-off between achievable temporal and spatial resolutions but parallel imaging can be used to improve temporal resolution without compromising resolution or artefact level. Recently, Golay et al. (2001) showed the utility of parallel imaging in time-resolved CE MRA of carotid arteries. Using R=2 they acquired a 270×65×50-mm^3 volume at a resolution

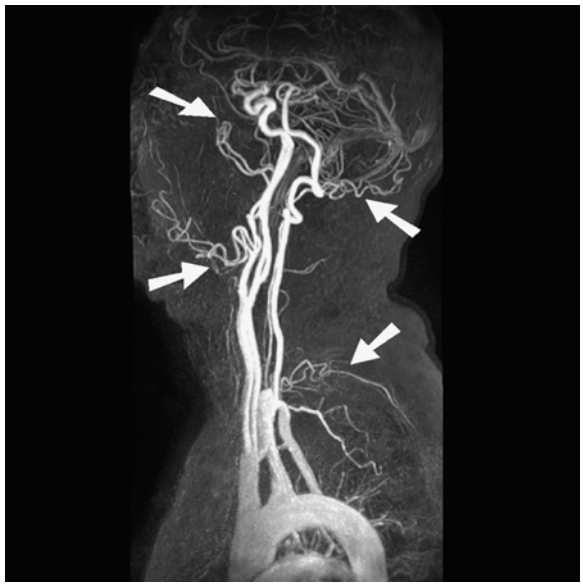

Fig. 18.9. Sagittal MIP of high-resolution coronal 3D contrast-enhanced MR angiography of the supra-aortic arteries using SENSE in two directions. A SENSE reduction factor of 4 (2×2) was taken in slice and phase-encoding direction to acquire 365 slices (matrix: 512×512 before zero-filling). Note that the entire supra-aortic arteries are displayed, including cervical, facial, and occipital branches (*arrows*). (Courtesy W. Willinek, University of Bonn, Bonn, Germany)

of 1.0×1.3×2.4 mm^3 in under 6 s. They found that this temporal resolution was sufficient to provide at least one dynamic acquisition with pure arterial phase without the need for timing the acquisition to peak arterial signal. Further improvements may be anticipated in this area, especially from combining parallel imaging with non-Cartesian trajectories, such as TRICKS (Turski et al. 2001) or VIPR (Du et al. 2004).

18.4 Quantitative/Functional MRI

Both quantitative and functional MRI methods usually require rapid imaging methods, such as EPI (Mansfield 1977) or spiral imaging (Meyer et al. 1992). Unfortunately, image quality and spatial resolution with EPI and spiral imaging is usually frustrated by geometric distortions, signal loss, and image blurring. These artefacts emanate from signal sources with off-resonant spin precession rates (relative to that of water), and the amount of phase offset that these spins accrue during the relatively long EPI and spiral readouts (cf. Chap. 10). A significant magnetic field inhomogeneity across a voxel can lead to incoherent phase accrual and leads to intravoxel dephasing and signal loss. Local susceptibility gradients, such as those around the auditory canals or the frontal sinuses, can also lead to signal pile-up artefacts. In EPI, these artefacts occur along the phase-encoding direction, whereas in other techniques, such as spiral or radial imaging, they can manifest as radial blurring. Despite the fact that EPI is an ultrafast MRI technique, the sampling of data along the phase-encoded direction is still slow (on the order of 1 ms/phase-encoded step) and gives rise to the aforementioned artefacts (Farzaneh et al. 1990). Signal T2* decay limits the possible achievable readout time and hence the ultimate resolution.

A strategy to reduce these susceptibility artefacts as well as those related to image blurring is to traverse k-space as fast as possible. In other words, the higher the k-space velocity (i.e., $\Delta k/\Delta t$), the lower are the artefacts. Interleaved trajectories in EPI and spiral imaging have been used to speed up the k-space traversal; however, the time to form an interleaved echo-planar image increases by the number of interleaves used times the respective repetition time. This fact limits the use of multi-shot methods for DWI and PWI since they normally require single-shot methods. Specifically, PWI methods that rely on the measurement of the bolus passage through the brain require high temporal resolution in order to follow contrast agent passage reliably through the brain. EPI is currently the only method that is capable of providing adequate temporal resolution.

In DWI, random bulk physiological motion during the diffusion-encoding phase leads to unpredictable phase accrual that may vary from shot to shot and is compounded with the intentional phase encoding. Using single-shot EPI guarantees an equal motion-induced phase error for each phase-encoding step that will vanish after magnitude calculation. Other than that, DWI theoretically does not require rapid image formation (if the phase perturbation can be corrected), although it is our experience that the likelihood of patient motion and blurring increases with prolonged scan times. Also, new advances in DTI require large numbers of individual DWI scans (Liu et al. 2004) and would lead to prohibitively long scan times if not carried out with fast imaging methods.

With parallel imaging, artefacts in EPI and spiral imaging can be reduced quite significantly. When

we first set out to use parallel imaging for our diffusion-weighted EPI methods (Bammer et al. 2001a) we aimed to accelerate k-space traversal – similar to interleaved EPI (Butts et al. 1994) acquisitions – to increase the bandwidth per pixel and hence diminish artefacts while maintaining a single-shot regime to provide high temporal resolution and avoid the need for phase navigation (Anderson and Gore 1994). The theoretical SNR loss in these sequences is mitigated by the shorter EPI readout, which leaves more time for the diffusion encoding (Bammer et al. 2001a). This in turn leads to shorter echo times and less T2 signal decay. In a standard Stejskal-Tanner DWI sequence, the effective time available for diffusion-encoding gradients to be played out is determined by the time between the 180° refocusing pulse and the begin of the EPI readout. Since the TE is determined by the time the center of k-space is traversed, the beginning of the EPI readout will significantly protrude into the second diffusion-encoding interval leaving only a significantly shortened interval open for diffusion encoding.

To improve the efficacy of DWI partial k-space acquisition (i.e., projection onto convex sets (POCS) or homodyne reconstruction) is normally used to reduce the number of gradient echoes required before the formation of the spin echo. The efficacy can be further improved by the use of parallel imaging since it essentially reduces the EPI train by the factor *R*. In addition, the shortened EPI readouts allow one to interleave more slices per TR or to reduce overall acquisition time, since often the EPI readout over all slices determines the minimum TR.

Using a GRAPPA-like approach at 1.5 T we were able to use reduction factors up to four to reduce distortions and simultaneously almost double the standard acquisition matrix to provide DWI scans at significantly improved spatial resolution (Fig. 18.10). Preliminary results from an NIH-funded study in 50 consecutive stroke patients showed that when SENSE and conventional single-shot EPI-based DWI were compared by rating the quality of scans from 1 (technically inadequate) to 5 (perfectly diagnostic scan). The mean score for conventional scans was 3.5 (±0.7), whereas the score for SENSE DWI was only slightly higher with 3.8 (±1.0); however, on a "winner-take-all" basis the SENSE DWI outperformed the conventional scan in 54%, performed equivalently in 16%, and underperformed in 30% of the cases. These results are slightly less optimistic than the study published recently by Kuhl et al. (2005) but still support the important trend towards improved image quality and diagnostic capacity with parallel imaging-enhanced DWI.

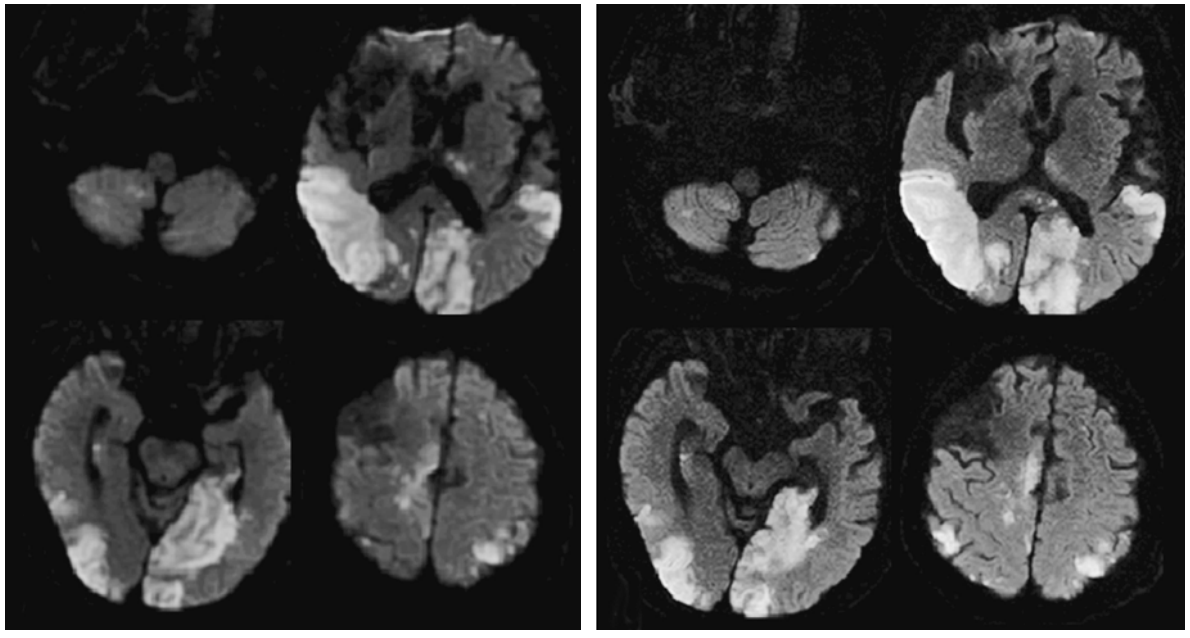

Fig. 18.10a,b. Diffusion-weighted imaging of a patient suffering from multiple ischemic lesions in different vascular territories. **a** Image quality on conventional single-shot EPI is frustrated by blurring and susceptibility artefacts. **b** Significantly better image quality is achieved by adding parallel imaging. In this case (*R*=3), the shortened readout afforded to increase the acquisition matrix from 128 to 192 with still reduced levels of geometric distortions. Small lesion conspicuity was considerably better due to the increased matrix size and the diminished T2*-related blurring.

In this context, we emphasize that SENSE DWI will change DWI's diagnostic sensitivity and specificity. The DWI is already a very sensitive methodology; however, the parallel-imaging-related resolution enhancement and the minimization of susceptibility artefacts will increase the confidence level of individual readers. Given the fact that most of the predilection sites for susceptibility distortions are known, it is rather unlikely to misclassify such hyperintense areas as stroke, although we have to admit that certain signal hyperintensities in the posterior fossa and the temporal lobe are sometimes quite challenging and require cross-referencing with other series and experience from other DWI scans to rule out ischemia. We instead expect that the hyperintensities from susceptibility distortions might mask truly existing ischemic changes and that these confounders can be minimized by applying parallel imaging to DWI. We also expect that the resolution enhancement will increase the diagnostic sensitivity to lacunar infarction and small embolic lesions; the latter are of great diagnostic relevance if they can be detected among larger pre-existing ischemic lesions and even more so in a different vascular territory/hemisphere; however, further study is needed in a much larger cohort in order to achieve enough statistical power to investigate how frequently diagnosis and treatment would be altered based on SENSE DWIs. This study is currently underway at our institution. Preliminary results show that parallel-imaging-enhanced DWI provides higher diagnostic sensitivity and confidence for small lesions, but in several embolic cases multiple, larger lesions have already provided enough evidence for the neuroradiologist to reach a diagnosis.

Both arterial spin labeling (ASL; Detre et al. 1994) and dynamic susceptibility contrast (DSC) (Rosen et al. 1989; Weiskoff and Rosen 1992) based perfusion-weighted MRI (PWI) will benefit similarly from parallel imaging if the data acquisition is performed with EPI or spiral MRI (which is normally the case; Reishofer et al. 2002; Bammer and Moseley 2004). In a recent study we were able to apply reduction factors of four to DSC-PWI scans without any apparent reconstruction artefacts other than the obligatory parallel-imaging-related noise enhancement (Fig. 18.11). Due to the significantly reduced EPI readout length, the overall brain coverage could be considerably increased. The improved resolution of the DSC-PWI scans led to an enhanced differentiation between cortical gray matter and juxta-cortical white matter in processed parameter maps [i.e., cerebral blood flow (CBF) or cerebral blood volume (CBV)]. Another artefact source in DSC-PWI that parallel imaging addresses very well is the magnetic susceptibility change that occurs during bolus passage. Because of the low bandwidth per pixel, the significant susceptibility changes can shift signal sources in large arteries by more than a pixel which makes the measurement of the arterial input function (AIF) extremely difficult (Rausch et al. 2000). Here, the increased bandwidth per pixel due to parallel imaging helps to reduce these shifts and allows for a more accurate measurement of the AIF.

The effects and consequences of applying parallel imaging to functional MRI are very similar to those

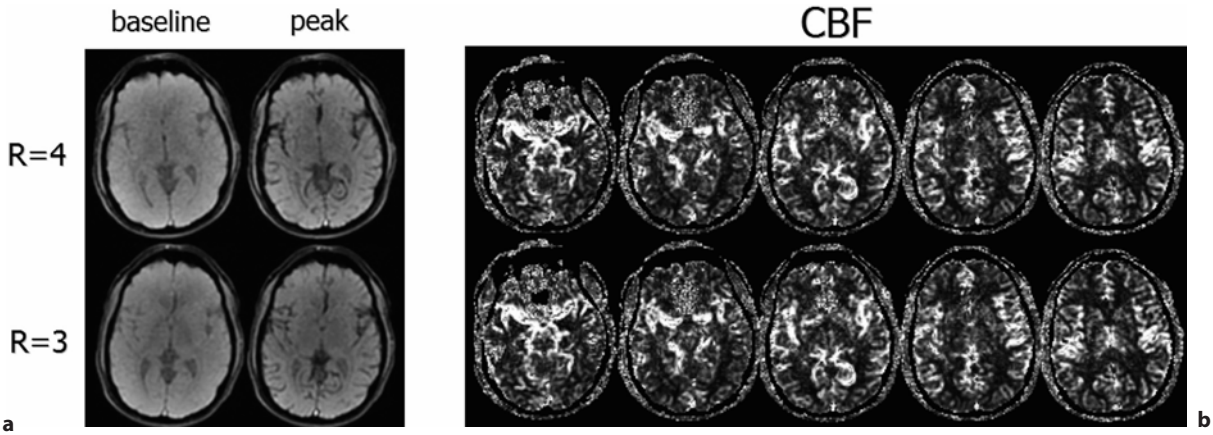

Fig. 18.11a,b. Dynamic-susceptibility contrast enhanced perfusion-weighted MRI. **a** T2*-weighted single-shot EPI with R=4 (*top*) and R=3 (*bottom*). The *first column* shows one of 15 baseline scans. The *second column* shows the maximum contrast change during the bolus passage. Despite the high acceleration, both data sets are of high quality without noticeable reconstruction artefacts. **b** Cerebral blood flow (CBF) maps calculated from R=3 (*top*) and 4 (*bottom*) scans using a deconvolution approach in combination with automatic AIF detection. The CBF maps obtained with R=4 are slightly noisier than R=3 maps.

of PWI (Golay et al. 2004). Within the past few years several studies have investigated the use of parallel imaging in fMRI, with reductions in distortion as their primary goal. Weiger et al. (2002b) implemented a spiral-SENSE technique and used it in visual, motor, and taste functional experiments. In their experiments, they found that the SNR and signal-to-fluctuation-noise ratio (SFNR) were generally diminished by 20 and 13%, respectively, when using a reduction factor R=2. It is important to note, however, that parallel imaging did not affect the detection power of the activation, and the number of activated voxels remained more or less constant over the experiments. Another important finding of Weiger et al.'s (2002b) study was the ability of parallel imaging to recover part of the signal loss present in the deep orbito-frontal areas. This is a very critical area to evaluate in several functional tasks. Its ability to be reliably scanned with fMRI is of great value.

In a similar study, Preibisch et al. (2003) examined the detection power using simple motor tasks relative to the reduction factor. They found that at intermediate reduction factors (R=2) they were able to increase the number of slices per unit of time at high spatial resolution, as well as decrease the distortions without significant loss in statistical power. At higher reduction factors, they experienced a rapid loss in SNR and loss in statistical power. Schmidt et al. (2003) and Morgan et al.(2004) found optimal reduction factors of 2–3 for SENSE EPI at 3.0 T, whereas Little et al. (2004) found no detrimental use in activation detection with R=3 using GRAPPA. In this context, it is important to point out that in fMRI the temporal stability ultimately determines the statistical significance of the fMRI activation. In general, this stability is determined by a sum of the physiological noise variance and image noise variance (Kruger and Glover 2001). In each parallel-imaging-enhanced scan the measured fMRI signal is certainly affected by the g-factor-related noise enhancement; however, if the physiological noise is the dominant noise source, especially with increasing field strength, the application of parallel imaging and hence the altered image noise will not much influence the sensitivity of the fMRI experiment.

18.5 Pediatric MRI

In general, the same considerations that apply to high-resolution structural MRI on the adult side apply also to the pediatric population; however, pediatric neuroimaging is further challenged by the smaller patient size as well as by the lack of cooperation that one can anticipate from these patients; the latter often requires the need for sedation or even anesthesia. Pediatric parallel imaging has therefore important benefits for pediatric patients. Capitalizing on the faster acquisition speed, patient studies can be performed much faster and children have to spend less time in the magnet. This will either shorten the sedation/anesthesia time or simply reduce patient anxiety. Of course, the gain in speed can be also invested in increasing the spatial resolution or to reduce geometric distortions. Like in adults the improved resolution might provide better lesion conspicuity or reveal hallmarks of disease otherwise unseen or equivocal.

So far, very little has been published on pediatric MRI in combination with parallel imaging. One limitation might be the limited availability of pediatric parallel imaging coils. Due to the wide range of head sizes seen in children and adolescents it is often difficult to provide size adequate head arrays. Currently, only a few vendors provide phased-array coils for pediatric imaging. A combined head and spine array coil is currently available for purchase from one coil manufacturer for only two size groups (group 1: up to 10 kg; group 2: 10–22.5 kg). All other patients have to be imaged with standard adult equipment. Compared with the adult hardware the pediatric head arrays have fewer coil elements, thus limiting the maximum reduction factor. Comprehensive neuroexams often also include spectroscopy, which requires special postprocessing for multi-coil acquisition. Unfortunately, some MR vendors do not fully support this function in their products and therefore some pediatric neuroradiologists are reluctant to use multi-element coils. Switching coils during the study might be an alternative but is more complicated in pediatric examinations because of the frequent need for anesthesia and the associated ramifications.

18.6 Conclusion

Neuroimaging is often challenged by the lack of detail in conventional structural and functional MRI scans as well as in MR angiography. The complexity of the brain's morphology and the need for early and accurate diagnosis motivates the push to higher resolution.

The sequential order of the MR acquisition procedures and the underlying biophysical MR properties that characterize tissue are significant speed-limiting factors in this otherwise very powerful modality. The introduction of parallel imaging has had a dramatic impact on the MRI community. Aside from accelerated image acquisition, it has been responsible for a remarkable overhaul of RF receiver technology (coils, electronic), which might have otherwise happened but probably not to such an extent.

Neuroimaging benefits from a deliberate and well-balanced application of parallel imaging in several ways. Firstly, parallel imaging provides enough speed benefits to acquire larger image matrices within a reasonable time. Secondly, it helps to diminishing blurring and geometric distortions. Thirdly, parallel imaging can be of utility to reduce motion artefacts and therefore improve the apparent resolution of neuroimaging studies. The true value of parallel imaging to high-resolution brain imaging can only be estimated. No conclusive studies are currently available and it also depends on the preferences of an individual radiologist whether or not resolution enhancement is truly relevant for the majority of examinations. It is a complex interplay between economic considerations, artefacts, and SNR that radiologists and institutions will have to balance as this technology continues to evolve.

Acknowledgements. This work was supported in part by the NIH (1R01EB002771, 1R01EB002771S3), the Center of Advanced MR Technology at Stanford (P41RR09784), Lucas Foundation, and Oak Foundation.

References

Al-Kwifi O et al. (2002) Vessel contrast at three Tesla in time-of-flight magnetic resonance angiography of the intracranial and carotid arteries. Magn Reson Imaging 20:181–187

Anderson AW, Gore JC (1994) Analysis and correction of motion artefacts in diffusion weighted imaging. Magn Reson Med 32:379–387

Atkinson D et al. (2004) Coil-based artefact reduction. Magn Reson Med 52:825–830

Bammer R et al. (2001a) Improved diffusion-weighted single-shot echo-planar imaging (EPI) in stroke using sensitivity encoding (SENSE). Magn Reson Med 46:548–554

Bammer R, Strasser-Fuchs S, Prokesch RW, Moseley ME, Fazekas F (2001b) Improved lesion conspicuity using radio-frequency array coils. Multiple Sclerosis 7 (Suppl 1):S88

Bammer R. et al. (2002) Diffusion tensor imaging using single-shot SENSE-EPI. Magn Reson Med 48:128–136

Bammer R, Schoenberg SO, Lucas I (2004) Current concepts and advances in clinical parallel magnetic resonance imaging. Top Magn Reson Imaging 15:129–158 Bammer R, Moseley ME (2004) In: 12th Annual Meeting of the ISMRM, 362, ISMRM, Kyoto, Japan

Bernstein MA et al. (2001) High-resolution intracranial and cervical MRA at 3.0 T: technical considerations and initial experience. Magn Reson Med 46:955–962

Butts K et al. (1994) Interleaved echo planar imaging on a standard MRI system. Magn Reson Med 31:67–72

Bydder M, Larkman DJ, Hajnal JV (2002a) Combination of signals from array coils using image-based estimation of coil sensitivity profiles. Magn Reson Med 47:539–548

Bydder M, Larkman DJ, Hajnal JV (2002b) Detection and elimination of motion artefacts by regeneration of k-space. Magn Reson Med 47:677–686

Bydder M et al. (2003) SMASH navigators. Magn Reson Med 49:493–500

Conolly SM, Nishimura DG, Macovski A (1988) Variable-rate selective excitation. J Magn Reson 78:440–458

Detre JA et al. (1994) Tissue specific perfusion imaging using arterial spin labeling. NMR Biomed 7:75–82

Du J et al. (2004) Contrast-enhanced peripheral magnetic resonance angiography using time-resolved vastly undersampled isotropic projection reconstruction. J Magn Reson Imaging 20:894–900

Dumoulin CL et al. (1989) Three-dimensional phase contrast angiography. Magn Reson Med 9:139–149

Erskine MK et al. (2005) Resolution-dependent estimates of multiple sclerosis lesion loads. Can J Neurol Sci 32:205–212

Farzaneh F, Riederer SJ, Pelc NJ (1990) Analysis of T2 limitations and off-resonance effects on spatial resolution and artefacts in echo-planar imaging. Magn Reson Med 14:123–139

Golay X et al. (2001) Time-resolved contrast-enhanced carotid MR angiography using sensitivity encoding (SENSE). Am J Neuroradio 22:1615–1619

Golay X, de Zwart JA, Ho YC, Sitoh YY (2004) Parallel imaging techniques in functional MRI. Topics in magnetic resonance imaging. Top Magn Reson Imaging 15:255–265

Griswold MA et al. (1999) Resolution enhancement in single-shot imaging using simultaneous acquisition of spatial harmonics (SMASH). Magn Reson Med 41:1236–1245

Hennig J, Scheffler K (2001) Hyperechoes. Magn Reson Med 46:6–12

Hutchinson M, Raff U (1988) Fast MRI data acquisition using multiple detectors. Magn Reson Med 6:87–91

Jaermann T et al. (2004) SENSE-DTI at 3 T. Magn Reson Med 51:230–236

Kangarlu A, Rammohan KW, Bourekas EC, RayChaudhry A (2004) In: 11th Annual Meeting of the ISMRM, Kyoto, Japan

Katscher U (2003) In: 11th Annual Meeting of the ISMRM 2342. Int Soc Magn Reson Med

Kidd D et al. (1999) Cortical lesions in multiple sclerosis. Brain 122:17–26

Kruger G, Glover GH (2001) Physiological noise in oxygenation-sensitive magnetic resonance imaging. Magn Reson Med 46:631–637

Kuhara S, Ishihara M (2000) In: 8th Annual Meeting of the ISMRM, Denver, Colorado

Kuhl CK et al. (2005) Sensitivity encoding for diffusion-weighted MR imaging at 3.0 T: intraindividual comparative study. Radiology 234:517–526

Kwiat D, Einav S, Navon G (1991) A decoupled coil detector array for fast image acquisition in magnetic resonance imaging. Med Phys 18:251–265

Little M, Papadakis A, McRobbie D (2004) In: 12th Annual Meeting of the ISMRM, 1025, Kyoto, Japan

Liu C, Bammer R, Acar B, Moseley ME (2004) Generalized diffusion tensor imaging (GDTI) using higher order tensor (HOT) statistics. Magn Reson Med

Mansfield P (1977) Multi-planar image formation using NMR spin echoes. J Phys C 10:L55–L58

Metens T et al. (2000) Intracranial aneurysms: detection with gadolinium-enhanced dynamic three-dimensional MR angiography: initial results. Radiology 216:39–46

Meyer CH, Hu BS, Nishimura DG, Macovski A (1992) Fast spiral coronary artery imaging. Magn Reson Med 28:202–213

Morgan P et al. (2004) In: 12th Annual Meeting of the ISMRM, 1030, Kyoto, Japan

Preibisch C et al. (2003) Functional MRI using sensitivity-encoded echo planar imaging (SENSE-EPI). NeuroImage 19:412–421

Pruessmann KP, Weiger M, Scheidegger MB, Boesiger P (1999) SENSE: sensitivity encoding for fast MRI. Magn Reson Med 42:952–962

Rausch M, Scheffler K, Rudin M, Radu EW (2000) Analysis of input functions from different arterial branches with gamma variate functions and cluster analysis for quantitative blood volume measurements. Magn Reson Imaging 18:1235–1243

Reishofer G et al. (2002) In: 10th Annual Meeting ISMRM, Honolulu

Rosen BR, Belliveau JW, Chien D (1989) Perfusion imaging by nuclear magnetic resonance. Magn Reson Q 5:263–281

Schmidt C, Degonda N, Henke K, Boesiger P (2003) In: 11th Annual Meeting of the ISMRM, 737, Toronto

Sodickson DK, Manning WJ (1997) Simultaneous acquisition of spatial harmonics (SMASH): fast imaging with radiofrequency coil arrays. Magn Reson Med 38:591–603

Turski PA et al. (2001) Contrast-enhanced magnetic resonance angiography of the carotid bifurcation using the time-resolved imaging of contrast kinetics (TRICKS) technique. Top Magn Reson Imaging 12:175–181

Weiger M et al. (2000) Contrast-enhanced 3D MRA using SENSE. J Magn Reson Imaging 12:671–677

Weiger M, Pruessmann KP, Boesiger P (2002a) 2D SENSE for faster 3D MRI. MAGMA 14:10–19

Weiger M et al. (2002b) Sensitivity-encoded single-shot spiral imaging for reduced susceptibility artefacts in BOLD fMRI. Magn Reson Med 48:860–866

Weisskoff RM, Rosen BR (1992) Noninvasive determination of regional cerebral blood flow in rats using dynamic imaging with Gd(DTPA). Magn Reson Med 25:211–212

Willinek WA et al. (2003) Time-of-flight MR angiography: comparison of 3.0-T imaging and 1.5-T imaging. Initial experience. Radiology 229:913–920

Willinek WA et al. (2004) Sensitivity encoding (SENSE) for high spatial resolution time-of-flight MR angiography of the intracranial arteries at 3.0 T. RoFo 176:21–26

Wilson GJ et al. (2004) Parallel imaging in MR angiography. Top Magn Reson Imaging 15:169–185

19 High-Resolution Imaging of the Skull Base and Larynx

Jan W. Casselman

CONTENTS

19.1 Dedicated Coils

There are only few regions in the body where so many anatomical structures are situated so close to one another as in the skull base or supra- and infra-hyoid neck; hence, the only way to visualise and distinguish all these structures is to acquire images with a resolution of 512×512 or even 1024×1024 matrix. However, the acquisition of images with such a high matrix is very time-consuming and often results in images with insufficient signal-to-noise ratio (SNR). These problems can be overcome by using phased-array surface coils or, using the Philips term, *synergy* surface coils. Surface coils can be placed close to the skin, or even on the skin, and will provide a much better SNR than routine head or neck coils. There must always be isolating material covering the coil so that the coil itself (metal) can never come in contact with a humid skin. Moreover, the use of phased-array or synergy coils also makes the use of "parallel imaging" possible. The use of a 2-element synergy coil, for instance, will enable us to reduce the imaging time by 50% (using a parallel imaging factor, *R*, of maximum 2). The maximum parallel imaging factor is equal to the number of coil elements; however, in practice the maximum parallel imaging factor used in the skull base and neck is *R*=2 when images with a very high matrix are used. Higher factors often result in an insufficient SNR.

Several synergy surface coils are available, but 8-cm-diameter surface coils are best suited for most of the skull base and head-and-neck structures. These surface coils will provide a good SNR in a circle of 8 cm around the centre of the coil, which means they provide good image quality up to a depth of 4 cm (Fig. 19.1). This also means that on the midline one often is confronted with reduced signal. In the neck the contrast between the signal intensity of different tissues is high, and this, together with the use of the "constant level appearance" (CLEAR) reconstruction method, which normalizes the surface-coil-induced signal variations over the field of view, results in images with good quality even for the midline structures and when a parallel-imaging technique is used. When this is attempted in the brain the images are still good when a larger "synergy head coil" is used and when CLEAR is applied; however, noise will often degrade the images severely on the midline when parallel imaging with a factor 2 or 3 is applied as well; hence, we hardly ever use small synergy surface coils to image the para-sellar or midline structures of the brain and skull base and even avoid using the larger synergy head coil in combination with parallel imaging in this region.

To assure image quality and to prevent coil heating, a small cushion is put between the two coil elements at the site where they could potentially touch each other (Fig. 19.2). The connection cables of the

J. W. Casselman, MD, PhD
Chairman, Department of Radiology, AZ St. Jan Brugge AV, Ruddershove 10, 8000 Brugge, Belgium

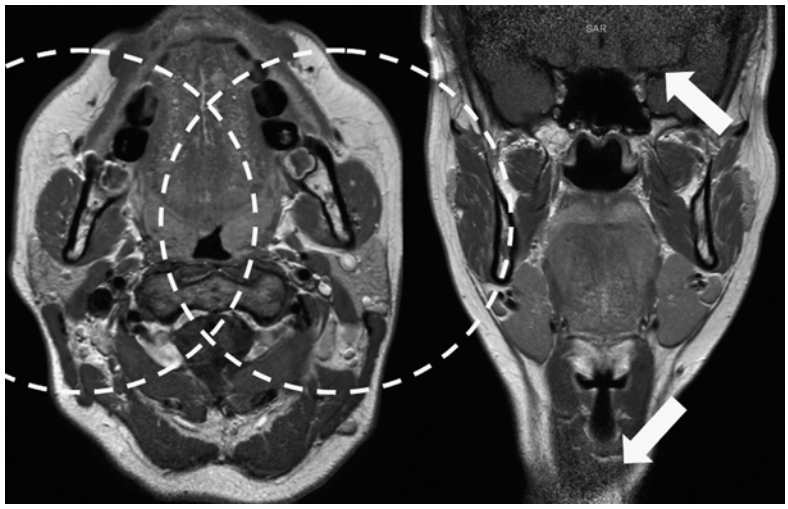

Fig. 19.1. Area in which synergy surface coils provide a good signal-to-noise ratio (SNR). Surface coils with a diameter of 8 cm will provide a good SNR until 4 cm depth (*dashed circles*). Note the noise visible anterior and posterior to the coil's 8-cm sensitivity area on the axial image. This loss of signal intensity outside the area in which the 8 cm coils provide good SNR is even more pronounced in the coronal plane (*arrows*).

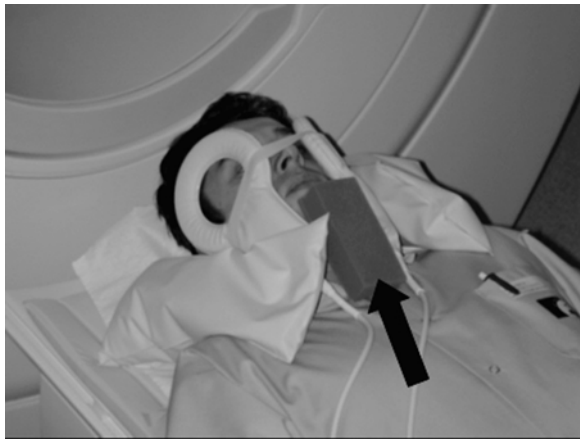

Fig. 19.2. Placement of synergy surface coils for orbit imaging. Synergy or phased-array "surface" coils can be placed closer to the area of interest than rigid larger neck or head coils; hence, they provide a better SNR and parallel imaging can also be applied. As a safety precaution a cushion has to be placed between the two surface coils so that they cannot touch each other (*arrow*). This assures image quality and prevents potential coil heating.

two coil elements must be placed parallel to the long axis of the tunnel and should certainly never cross one another.

Although the image quality of temporal bone or larynx images is better when surface coils are used, one cannot evaluate the whole brain or all the lymph nodes in the neck with these coils; therefore, the use of a "concentric synergy coil" system is recommended. For instance, a 2-element synergy surface coil is put inside an 8-element synergy head coil for temporal bone/brain imaging (Fig. 19.3), or a 2-element synergy surface coil is put inside a 3-element neck coil for oral cavity/neck (lymph node) imaging (Fig. 19.4). These same synergy coil sets can also be used in many other areas, e.g. orbit, olfactory bulbs, larynx, thyroid gland, etc. Simultaneous concentric placement of both synergy coils avoids time loss due to coil changing as the patients must no longer be removed from and put back into the tunnel. Moreover, the same localizers can be used for planning studies performed with the different synergy coil sets.

19.2 The 1024 Matrix

In head and neck studies visualisation of extremely small structures is often essential. Once coils are placed close to the skin and the SNR is optimised, one has two possibilities to achieve very high resolution.

The first solution is to use a very small field of view (FOV) of, for instance, 16 cm with a 512×512 matrix. The use of parallel imaging is then not recommended because the small FOV often results in a central aliasing artefact (Griswold et al. 2004); however, the combination of a small FOV and 512×512 matrix already provides high-resolution images (but faster imaging with less movement artefacts can be achieved when parallel imaging is used). With this technique the use of the CLEAR reconstruction method is required to assure homogeneous signal intensity throughout the image when multi-element synergy/phased-array coils are used. This technique can be applied in the larynx

where a FOV of 14 cm covers all necessary structures but is not possible at the level of the skull base, temporal bone (Fig. 19.5) and oropharynx (Fig. 19.6), because a larger FOV is needed to cover these structures.

In these latter areas a second solution, using a larger FOV of, for example, 24 cm in combination with a 1024×1024 matrix, is used. Such a large FOV allows one to use parallel imaging techniques without the danger of getting foldover artefacts. Moreover, parallel imaging is needed to reduce the long acquisition time caused by the high number of phase-encoding steps. When parallel imaging with sensitivity encoding (SENSE) is used, then CLEAR is automatically applied as well.

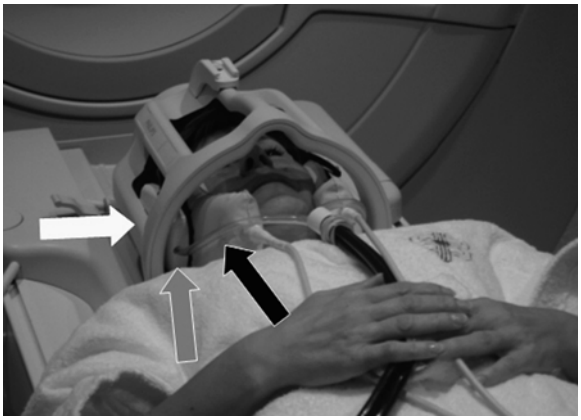

Fig. 19.3. Combined use of synergy head coil and synergy surface coils (concentric synergy coil technique) for temporal bone imaging. The best quality for local temporal bone imaging is provided by synergy surface coils (*black arrow*); however, one always has to evaluate the complete brain and auditory pathways and cortex as well and this is best achieved when the synergy head coil (*white arrow*) is used. The surface coils are kept in place and pushed closer to the skin and ears by placement of headphones (*grey arrow*) between the synergy head and surface coils.

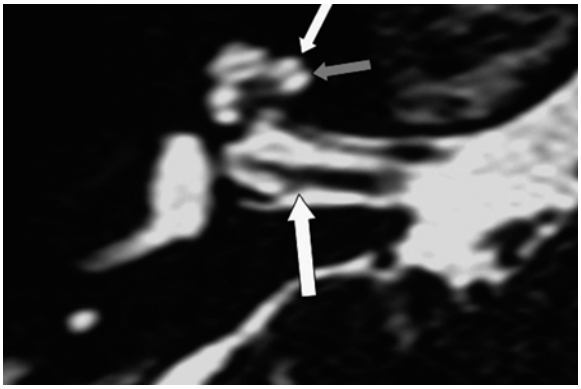

Fig. 19.5. The 1024-matrix driven-equilibrium RF reset pulse (DRIVE) sequence of the inner ear, using a two-element 8-cm synergy surface coil. Extremely high resolution can be achieved with this technique, showing the scala vestibuli (*small white arrow*) and scala tympani (*grey arrow*) separately in all turns of the cochlea and also showing the posterior ampullar nerve (*large white arrow*), leaving the inferior vestibular branch of the vestibulocochlear nerve in nearly all patients. The parameters of this sequence are given in Table 19.2.

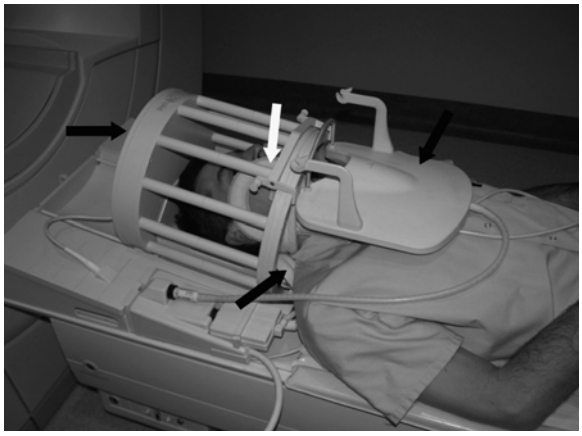

Fig. 19.4. Combined use of synergy head coil and synergy surface coils (concentric synergy coil technique) for oral cavity imaging. The synergy surface coils (*white arrow*) are placed inside the three-element neck coil (*black arrows*). The surface coils are used to look at the local situation in the oral cavity, and the synergy neck coil is used for lymph node staging.

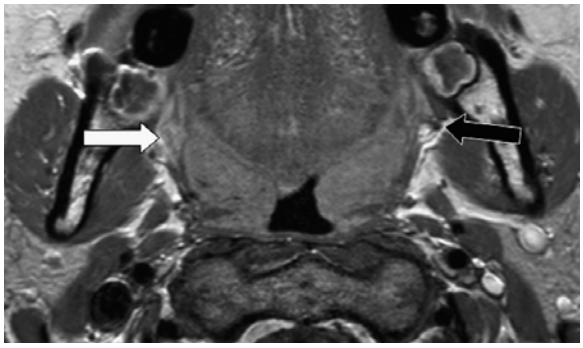

Fig. 19.6. The 1024-matrix gadolinium-enhanced T1-weighted image through the oral cavity using synergy surface coils. Patient with lingual nerve deficit following tooth extraction. The use of synergy surface coils allows one to get enough signal even when a 1024 matrix image is acquired. The use of sensitivity encoding (SENSE) made this possible in an acceptable acquisition time. (For the parameters of this sequence see Table 19.1.) Note the detailed visualisation of the normal left lingual nerve in its pterygomandibular fat pad (*black arrow*) and also note the damaged enhancing and thickened right lingual nerve with signal changes in the surrounding fat pad (*white arrow*), caused by extraction of tooth 48.

19.3 Imaging of Nerves in the Skull Base, Nerve-Exit Areas

19.3.1 The Anterior Skull Base

The olfactory nerve and optic nerve are the most important nerves in this region. For optimal visualisation 8-cm synergy/phased-array coils should be used, applying parallel-imaging techniques as well. For the olfactory nerves the coils are shifted towards the forehead, for the optic nerves the coils are placed on the lateral wall of the orbits. Both T1- and T2-weighted sequences can be used for both cranial nerves and the ideal plane is the coronal plane as it allows comparison of both nerves (Figs. 19.7, 19.8). Visualisation of the globe, lens and area of the optic disc are best seen in the transverse plane (Figs. 19.9, 19.10). The parameters of these sequences are listed in Table 19.1. The same coils and sequences can also be used for imaging of the oral cavity, sinuses and parotid glands. The only difference is the placement of the coils, which are always centred on the anatomical region to be visualised. The benefit of the parallel-imaging techniques is optimal when both coil elements are placed perfectly parallel to one another.

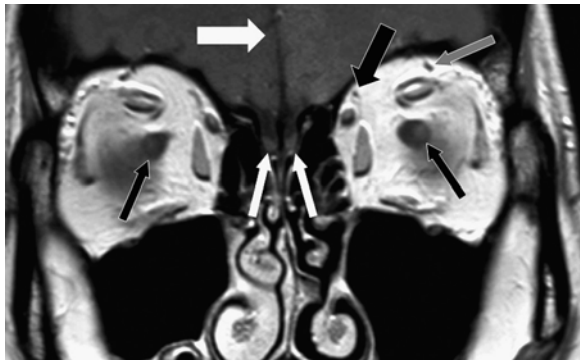

Fig. 19.7. Synergy surface coil coronal T1-weighted imaging of the olfactory bulbs. On this coronal 1024-matrix image the olfactory bulbs (*small white arrows*) and optic nerves (*small black arrows*) are seen in detail and can be compared. Also note the visualisation of the supraorbital branch (*grey arrow*) and supratrochlear branch (*large black arrow*) of the frontal nerve. The use of sensitivity encoding (SENSE) is not causing any noise in the area of the nasal septum and turbinates as these high signal structures contrast very well with the air in the nasal cavity and sinuses; however, noise becomes immediately obvious and disturbing in the brain structures near the midline (*large white arrow*).

The SNR is best when the coils are placed on the skin of the patient.

Small branches of the ophthalmic nerve and oculomotor nerves in the superior orbital fissure and orbita can also be visualised with this technique and are best seen in the coronal plane.

19.3.2 The Central Skull Base

As already mentioned, parallel imaging is less suited to study nerves located closer to the midline as signal drops in this area; however, once below the skull base parallel imaging enables the use of high spatial resolution with acceptable SNR even on the midline in an acceptable acquisition time. This is because the

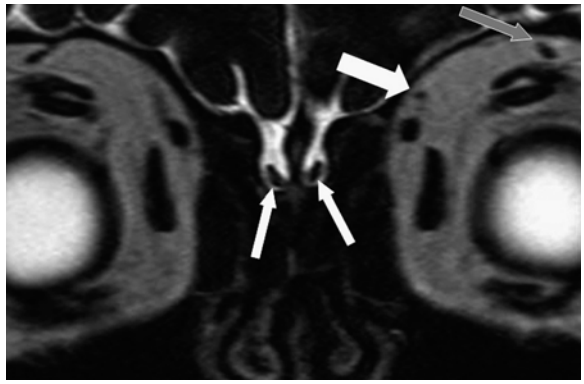

Fig. 19.8. Synergy surface coil coronal driven-equilibrium RF reset pulse (DRIVE) image of the olfactory bulbs. High-resolution imaging of the olfactory bulbs is again achieved using synergy surface coils, parallel imaging and a high matrix. Olfactory bulbs (*small white arrows*), supraorbital nerve (*grey arrow*), supratrochlear nerve (*large white arrow*) are seen.

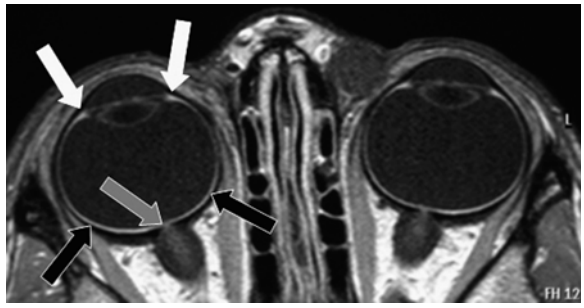

Fig. 19.9. Synergy surface coil contrast-enhanced T1-weighted image of the orbits. On this 1024-matrix image the enhancing ciliary bodies (*white arrows*) and choroid (*black arrows*), lens and optic disc (*grey arrow*) can be evaluated.

Table 19.1. Sequence parameters for imaging of the anterior skull base, orbits, oral cavity, oropharynx, salivary glands and sinuses

	FOV/RFOV	Matrix	Sense factor R	No. of slices/ thickness	Foldover direction/ syn. coil	Flip angle	TSE factor	TR/TE (ms)	NSA	Acq. time	Voxel size measured; voxel size reconstructed (mm)
T2 TSE	190 mm/80%	378×512	2	15/3 mm	RL/surface	90°	11	2750/80	8	4:29	0.52×0.55×3.0; 0.37×0.37×3.0
T1 TSE	190 mm/100%	400×1024	2	14/2 mm	RL/surface	90°	4	1130/15	6	5:09	0.47×0.54×2.0; 0.19×0.19×2.0

Acq. acquisition, *FOV* field of view, *L* left, *NSA* no. of acquisitions, *R* right, *RFOV* rectangular field of view, *Syn.* synergy, *TE* echo time, *TR* repetition time, *TSE* turbo spin echo.

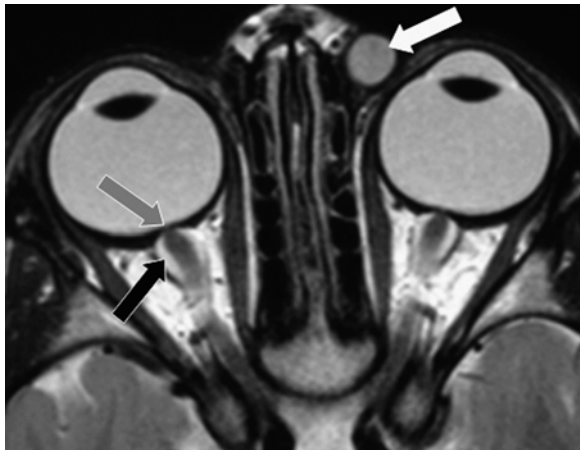

Fig. 19.10. Synergy surface coil T2-weighted image of the orbits. The optic disc (*grey arrow*) and the cerebrospinal fluid (*black arrow*) between the optic nerve and the meningeal sheath of the optic nerve are also depicted on this T2-weighted image. Also note the cystic lesion medial to the globe on the left side (*white arrow*).

contrast differences between tissues in this area are higher than in the brain. The whole skull base area can be studied using a synergy/phase-array head coil. More dedicated synergy surface coils can be used to achieve even higher resolution in more restricted anatomic regions as the oral cavity (Fig. 19.6) or parotid gland (Fig. 19.11) and facial nerve (Fig. 19.12) region.

In these regions both the axial and coronal plane are suited to study the nerves and skull base structures. The parameters of the T1- and T2-weighted turbo-spin-echo (TSE) sequences used to study the central skull base are similar to those used for the anterior skull base.

To visualise the nerves in the para-sellar area one has to use gadolinium-enhanced coronal T1-weighted images with very high resolution. CLEAR is applied to equalise the signal throughout the image (Fig. 19.13); parallel imaging can be used, but then the use of the synergy head coil (better SNR on the midline) is preferred over the use of synergy surface coils.

19.3.3 The Posterior Skull Base

The nerves in the cerebellopontine angle (CPA), internal auditory canal (IAC) and the membranous labyrinth are best visualised when T2-weighted 3D TSE sequences with an additional 90° RF reset pulse after the echo train (driven equilibrium (DRIVE) technique) and 3D steady-state free precession (SSFP) or balanced fast-field-echo (B-FFE) sequences are used. The value of parallel imaging in temporal bone imaging is twofold: firstly, it enables 1024-matrix imaging in an acceptable time; secondly it results in less T2* blurring, less susceptibility artefacts and less eddy-current distortion (Fig. 19.14). Again, as the inner ear structures are close to the surface, synergy/phased-array surface coils (Fig. 19.3) will provide better SNR than the synergy/phased-array head coil. The parameters of the DRIVE sequence are listed in Table 19.2. In this sequence the number of signals averaged is four (NSA=4) and the SENSE factor is nearly 2. Theoretically, a sequence without SENSE and NSA=2 should give the same results, but in practice the latter images are worse and lack sufficient signal, whereas the SENSE images have enough signal. This is only true when the SENSE technique is used in combination with more than one NSA and foldover suppression. This combination results in artefact reduction (van den Brink et al. 2003).

The lower cranial nerves inside the jugular foramen can only be visualised on high-resolution (512-matrix) gadolinium-enhanced MR angiography

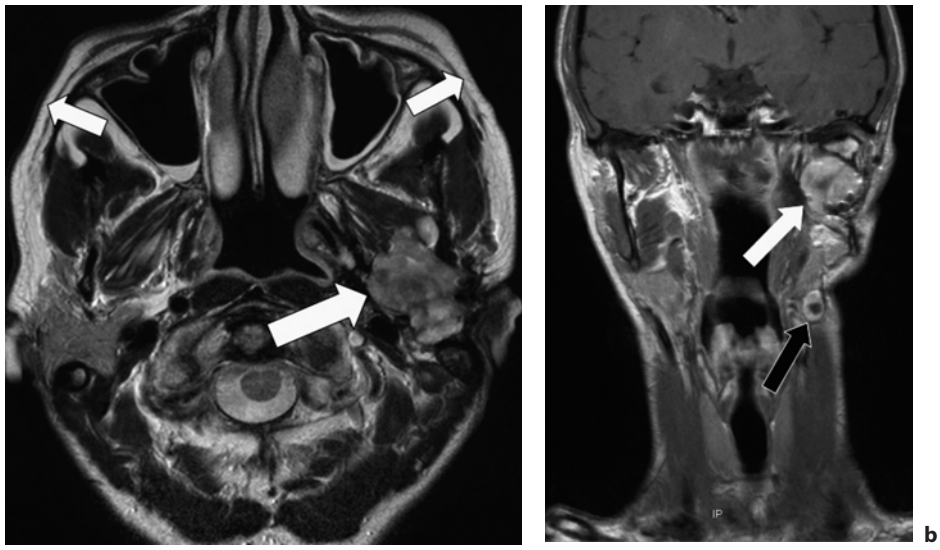

Fig. 19.11a,b. Synergy surface coil and synergy head-and-neck coil imaging of the parotid gland, using parallel imaging. **a** On the axial T2-weighted image a recurrent benign mixed tumor (*large white arrow*) is seen. The use of surface coils results in high-resolution imaging in an acceptable acquisition time. Impression of the surface coils on the skin (*small white arrows*). **b** The coronal gadolinium-enhanced T1-weighted image is made with the synergy head-and-neck coil. This enables visualisation of the complete neck and skull base which is needed to exclude seeding or lymph node involvement along the complete neck. Again sensitivity encoding (SENSE) was used to speed up the sequence. Recurrent benign mixed tumour (*white arrow*) is seen, as well as seeding of the tumour with recurrence along the previously made surgical line (*black arrow*).

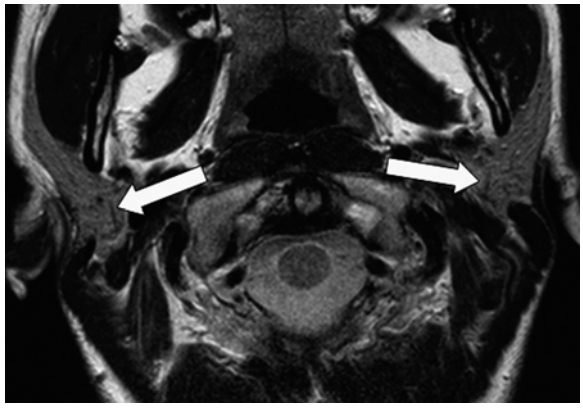

Fig. 19.12. High-resolution synergy surface coil imaging of the facial nerve. The combination of small synergy surface coils and parallel imaging results in images with an excellent signal-to-noise ratio and very high resolution in an acceptable acquisition time. On this T2-weighted turbo-spin-echo image the facial nerve can even be followed in the posterior part of both parotid glands (*white arrows*).

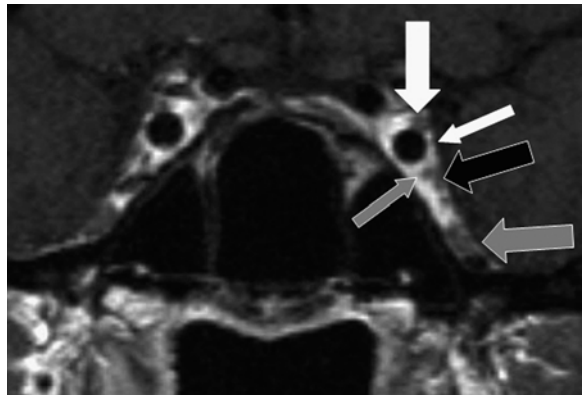

Fig. 19.13. Coronal contrast-enhanced T1-weighted image using the synergy head coil and applying "constant level appearance" (CLEAR). Parallel imaging was not used to avoid signal loss near the midline. CLEAR was used to achieve a homogeneous signal intensity throughout the image. The use of a high matrix and the intravenous injection of gadolinium allowed visualisation of cranial nerves III (*large white arrow*), IV (*small white arrow*), V_1 (*black arrow*), and V_2 (*large grey arrow*) in the wall of the cavernous sinus, and of cranial nerve VI (*small grey arrow*) deeper in the cavernous sinus.

Table 19.2. Sequence parameters for imaging of the temporal bone

	FOV/RFOV	Matrix	Sense factor R	No. of slices/ thickness	Foldover direction/ syn. coil	Flip angle	TSE factor	TR/TE (ms)	NSA	Acq. time	Voxel size measured; voxel size reconstructed (mm)
3D T2 DRIVE	240mm/ 75%	672×1024	1.7	48/0.7 every 0.35 mm	RL/surface	90°	11	1500/250	4	8:37	0.36×0.66×0.70; 0.23×0.23×0.35
3D FFE MRA	160mm/ 100%	304×512	2	192/1.0 every 0.5 mm	RL/head	20°	NA	23/6.9	1	8:35	0.53×0.53×1.0; 0.31×0.31×0.5

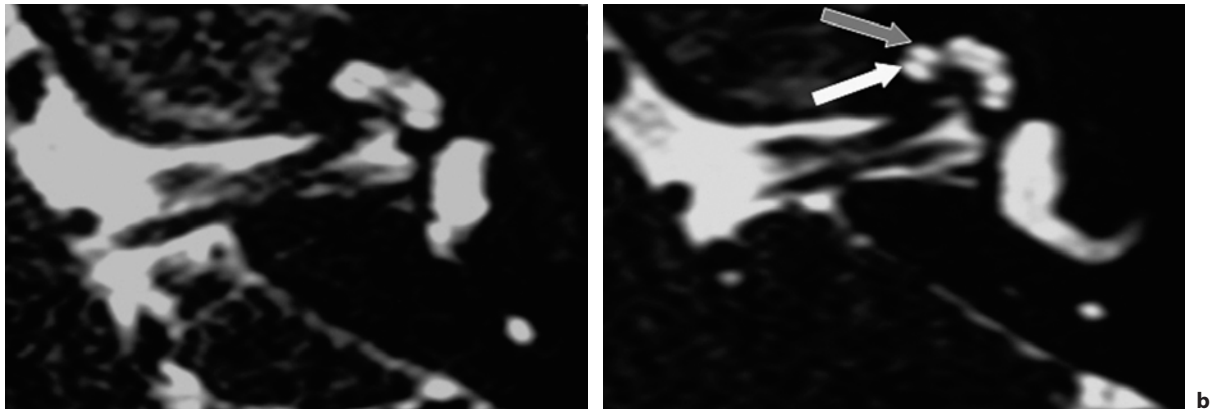

a b

Fig. 19.14a,b. Transverse driven-equilibrium RF reset pulse (DRIVE) image, achieved with synergy surface coils, and with a 1024 matrix. Image **a** is performed without sensitivity encoding (SENSE), image **b** (same patient, same sequence) is performed with SENSE. Note how the blurring and susceptibility artefacts disappear in **b**, and how the nerves, scala tympani (*white arrow*) and scala vestibuli (*grey arrow*) are better visualised once SENSE is used.

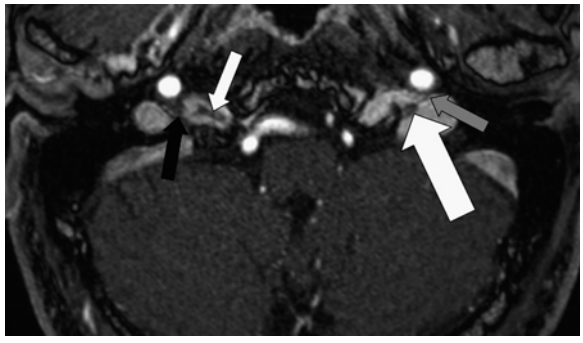

Fig. 19.15. Gadolinium-enhanced MR angiography (MRA) imaging of the jugular foramen achieved using parallel imaging, factor 2. Very thin gadolinium-enhanced high-resolution images can be achieved in an acceptable acquisition time because parallel imaging was used. This enables visualisation of all lower cranial nerves at the level of the jugular foramen and hypoglossal canal. Hypoglossal nerve (*small white arrow*), glossopharyngeal nerve located behind the carotid artery (*grey arrow*), vagus nerve and accessory nerve in their common sheath (*large white arrow*), with cranial nerves 9–11 packed together behind the carotid artery (*black arrow*). The nerves are hypointense and are visible because the surrounding venous structures enhance following intravenous contrast administration.

(MRA) time-of-flight images (Fig. 19.15). Again parallel imaging is required to achieve this resolution in an acceptable time; however, in this region the synergy/phased-array head coil is used so that global images of all arteries can be reconstructed. The parameters of this sequence can be found in Table 19.2.

Finally, it is challenging to visualise all cisternal segments of the 12 cranial nerves with one heavily T2-weighted sequence; therefore, high resolution must be achieved and a lot of thin slices (from olfactory nerve to cervical accessory nerve) must be made. It is obvious that such a large number of high-resolution slices can only be achieved when parallel-imaging techniques are used. The SENSE in combination with a balanced fast-field-echo (b-FFE) or true fast imaging with steady-state precession (true-FISP, FIESTA) sequence can provide these images (Fig. 19.16), and the parameters of this sequence are listed in Table 19.3. As many of the nerves are located close to the midline and can be found over a distance of >7 cm in cranial–caudal direction the use of a synergy/phased-array head coil is preferred.

Table 19.3. T2-weighted sequence covering all cranial nerves (cisternal segments)

	FOV/RFOV	Matrix	Sense factor R	No. of slices/ thickness	Foldover direction/ syn. coil	Flip angle	TSE factor	TR/TE (ms)	NSA	Acq. time	Voxel size measured; voxel size reconstructed (mm)
T2 B-FFE	220mm/75%	496×512	2	280/0.8 every 0.4 mm	RL/head	90°	11	800/250	1	6:19	0.44×1.03×0.80; 0.43×0.43×0.40

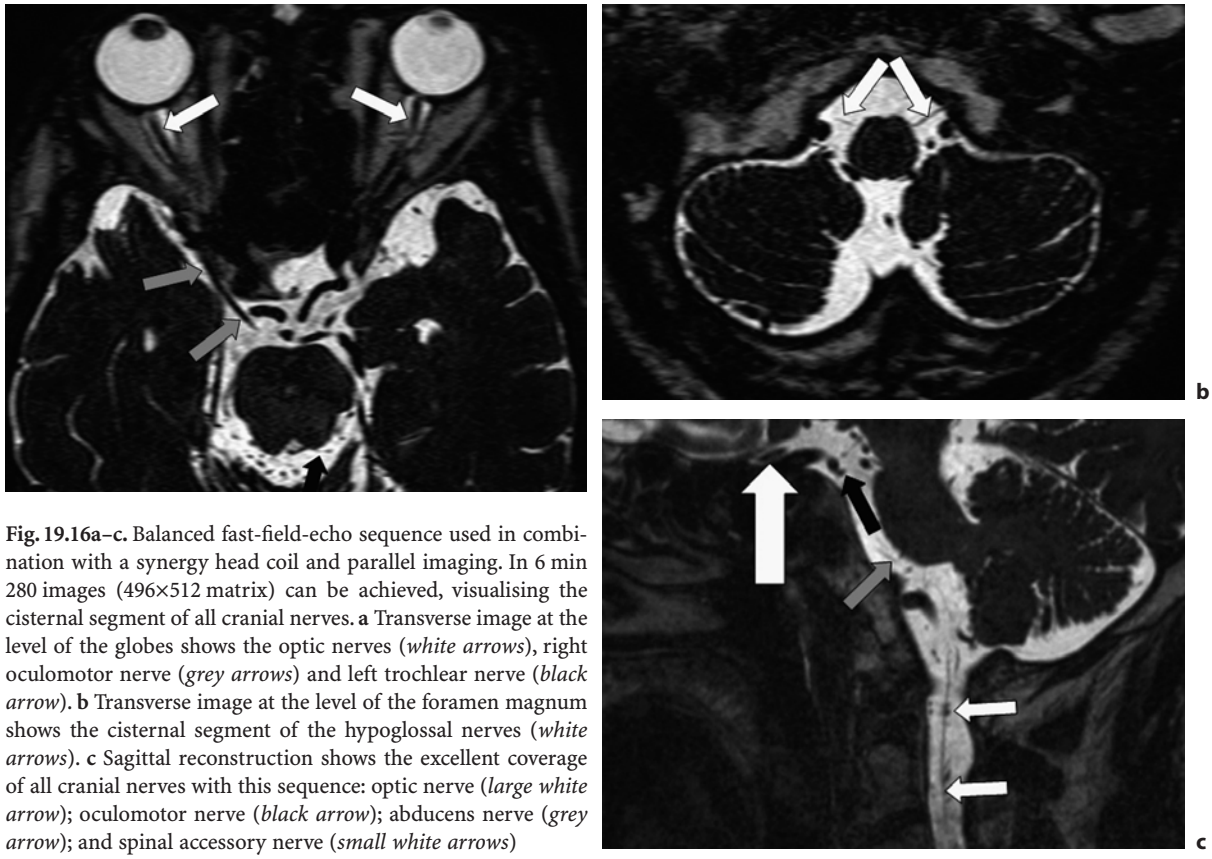

Fig. 19.16a–c. Balanced fast-field-echo sequence used in combination with a synergy head coil and parallel imaging. In 6 min 280 images (496×512 matrix) can be achieved, visualising the cisternal segment of all cranial nerves. **a** Transverse image at the level of the globes shows the optic nerves (*white arrows*), right oculomotor nerve (*grey arrows*) and left trochlear nerve (*black arrow*). **b** Transverse image at the level of the foramen magnum shows the cisternal segment of the hypoglossal nerves (*white arrows*). **c** Sagittal reconstruction shows the excellent coverage of all cranial nerves with this sequence: optic nerve (*large white arrow*); oculomotor nerve (*black arrow*); abducens nerve (*grey arrow*); and spinal accessory nerve (*small white arrows*)

19.4 High-Resolution Imaging of the Sinuses

The detailed anatomy of the sinuses and nasal cavity can again only be seen on high resolution images; hence, parallel imaging is used to reduce acquisition time or to image with a higher resolution in the same acquisition time. When the lesion is localised, then 8-cm diameter synergy/phased-array coils are preferred; however, when all sinuses have to be visualised or the lesion is more extensive, then the synergy/phased-array head coil is used. Transverse T2-weighted TSE images with a 512 or even 1024 matrix are used to cover all sinuses and localise the lesion. Then, depending on the location of the lesion, additional unenhanced and gadolinium-enhanced T1-weighted images are made in the axial or coronal plane. Anyway, the gadolinium-enhanced T1-weighted images are always made in two planes. Sagittal images are only used when the lesion is really a midline lesion.

19.5 High-Resolution Structural Imaging of the Larynx

The larynx is a complex structure that is moving all the time and which has small dimensions; therefore, it is obvious that high contrast resolution (high SNR

required) and high spatial resolution (512 matrix) are needed and this in a short acquisition time in order to avoid movement artefacts (Larkman et al. 2002). Moreover, lymph node staging must be performed as well; otherwise, an additional CT scan is needed. To combine larynx and lymph node imaging the "concentric synergy coil" technique is used, using 8-cm circular synergy coils to image the larynx and the 3-element synergy neck coil to image the lymph nodes (Fig. 19.17). Again both sets of synergy coils are positioned and plugged in at the same time; hence, the patient does not have to be removed from the tunnel to change coils and therefore a lot of time is gained.

Again the two 8-cm circular synergy coils are placed like a collar (bended) around the neck, touching the skin at the level of the larynx. They provide images with an excellent SNR when placed so close to the larynx (Fig. 19.18). This high SNR allows us to reduce the number of NSA to the minimum, even when a 512 matrix is used. Of course, this is only possible in a reasonable time when parallel imaging is used. The parameters of the T1- and T2-weighted sequences used to study the larynx are listed in Table 19.4. Finally, the synergy neck coil (consisting of the head coil and an anterior and posterior neck element) is used to study the whole neck and the lymph nodes. Again, parallel imaging is used to achieve gadolinium-enhanced coronal 512 matrix T1-weighted images in an acceptable time. The spatial resolution of these images will be lower as a larger FOV is used, and the SNR is worse as the synergy neck coils is further away from the skin (Fig. 19.11).

19.6 Conclusion

Parallel imaging is used presently in nearly all head-and-neck MR studies. When parallel imaging is used, one can produce images with the same resolution in a shorter time or images with a higher resolution in the same time. In the region of the skull base and the face the best choice is higher resolution, and in the moving parts of the neck (e.g. larynx) the best choice is the same resolution in a shorter time. Parallel imaging can also be used to produce a greater number of thin slices, covering a larger anatomical area, in the same time. Moreover, the use of parallel-imaging techniques also reduces T2* blurring, susceptibility artefacts and eddy-current distortion which is very helpful in these regions where both bone and air are present. Finally, the use of concentric sets of synergy coils enables both local high-resolution imaging and more global region imaging.

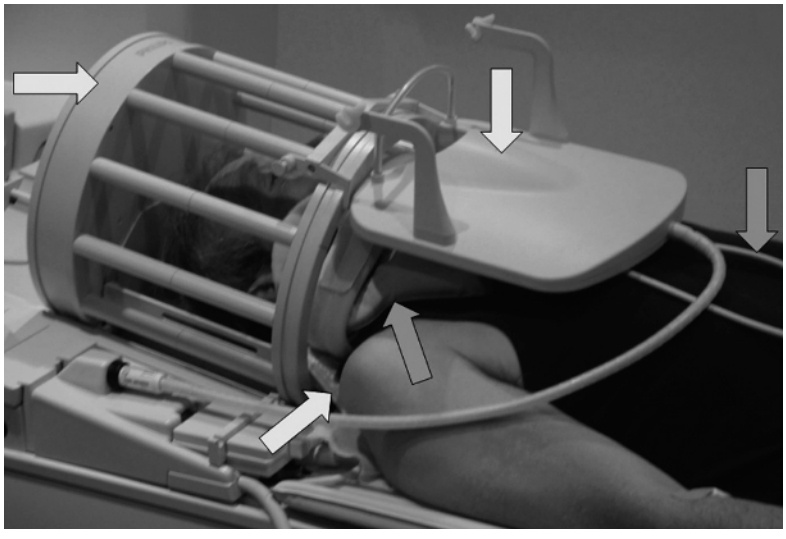

Fig. 19.17. Combined use of the synergy head coil and the synergy surface coils (concentric synergy coil technique) for temporal bone imaging. The synergy surface coils are placed around the neck at the level of the larynx and the cables of the two coil elements are placed parallel on the chest and belly of the patient (*grey arrows*). The three-element head-neck coil (*white arrows*) provides images with a larger field of view, needed for the staging of lymph nodes.

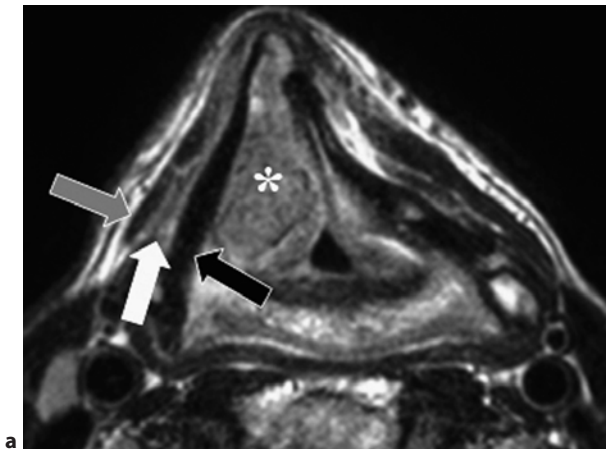

a

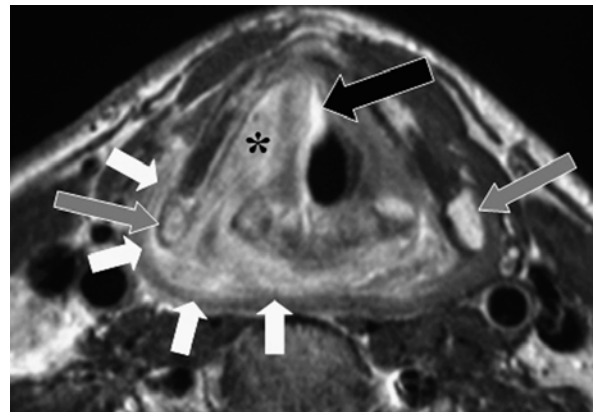

b

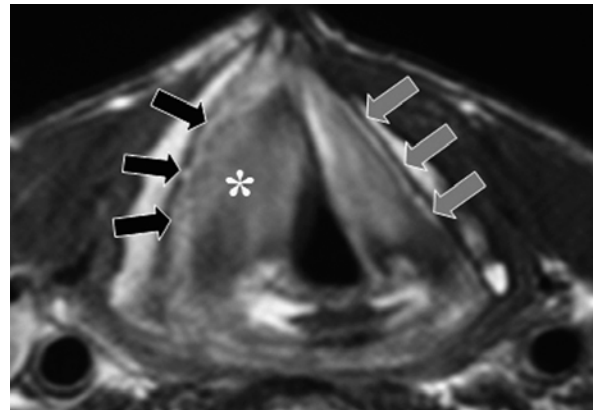

c

Fig. 19.18a–c. Magnetic resonance of the larynx using synergy surface coils, sensitivity encoding (SENSE) and a 512 matrix. The use of coils positioned close to the larynx results in images with a sufficient SNR, even when a 400×512 matrix is used and when slices are only 3 mm thick. The use of SENSE and constant level appearance (CLEAR), which is always combined with SENSE, reduces the acquisition time (and consequent motion artefacts) to 90 or 180 s, depending on the number of signals averaged used. **a** T2-weighted transverse image. Note the tumour in the right false vocal cord (*asterisk*) and the extralaryngeal extension (*white arrow*) between the non-ossified thyroid cartilage (*black arrow*) and the strap musculature (*grey arrow*). **b** T2-weighted image of a right pyriform sinus tumour with extension in the vocal cord (*asterisk*) and extension following the constrictor muscle (*white arrows*) towards its attachment on the oblique line on the external surface of the right thyroid cartilage. Note the Reinke oedema of the right vocal ligament (*black arrow*). The marrow in the posterior part of the right thyroid cartilage has the same signal intensity and same enhancement as the tumor, and hence the cartilage is invaded by tumour. Compare with the normal high signal intensity of fatty marrow inside the left thyroid cartilage (*grey arrows*). **c** Transverse T1-weighted image. Tumour of the right true vocal cord (*asterisk*) with irregular invasion of the paraglottic fat space (*black arrows*). Compare with the normal paraglottic fat space on the left side (*grey arrows*)

Table 19.4. Sequence parameters for imaging of the larynx

	FOV/RFOV	Matrix	Sense factor R	No. of slices/ thickness	Foldover direction/syn. coil	Flip angle	TSE factor	TR/TE (ms)	NSA	Acq. time	Voxel size measured; voxel size reconstructed (mm)
T2 TSE	210mm/80%	400×512	2	20/3 mm	AP/surface	90°	11	1704/80	2	3:21	0.52×0.53×3.00; 0.41×0.41×3.00
T1 TSE	200mm/80%	432×512	2	20/3 mm	AP/surface	90°	4	694/15	2	3:38	0.46×0.52×3.00; 0.39×0.39×3.00

References

Griswold MA, Kannengiesser S, Heidemann RM, Wang J, Jakob PM (2004) Field-of-view limitations in parallel imaging. Magn Reson Med 52:1118–1126

Larkman DJ, Bydder M, Callaghan MF, Melhem ER, Gilderdale DJ, Hajnal JV (2002) A feasibility study of detection and correction of motion artefacts in MR imaging of the larynx using parallel imaging. Proc Int Soc Mag Reson Med 10:75

van den Brink JS, Watanabe Y, Kuhl CK et al. (2003) Implications of SENSE MR in routine clinical practice. Eur J Radiol 46:3–27

Lung Imaging

20

Roger Eibel

CONTENTS

20.1 Introduction

Due to significant advantages of magnetic resonance imaging (MRI) over computed tomography (CT) in thoracic imaging, including its superb soft tissue contrast and the absence of radiation burden, MRI is traditionally considered a useful problem-solving technique with at least four indications in thoracic imaging:

R. Eibel, MD
Department of Clinical Radiologie, University Hospitals – Innenstadt, Klinikum der Ludwig-Maximilians-Universität München, Ziemssenstr. 1, 80336 München, Germany

- identification of mediastinal or chest wall invasion by tumor (Bergin et al. 1990; Brown and Aughenbaugh 1991; Heelan et al. 1989; Padovani et al. 1993)
- differentiation between solid and vascular hilar masses, without using contrast material (Glazer et al. 1985; Webb et al. 1984)
- demonstration of diaphragmatic abnormalities (Mirvis et al. 1988)
- assessment of mediastinal abnormalities in patients with treated lymphoma (Glazer et al. 1985; Nyman et al. 1987; Webb 1989)

However, it has to be taken into account that most of the studies that came to the above-mentioned results are from the 1980s or early 1990s. On the other hand, CT exceeds MRI in terms of spatial resolution, speed and superior display of air-containing structures. Especially with the advent of multidetector computed tomography (MDCT), nowadays most centers use CT for thoracic imaging, including the specific areas thought earlier to be the domain of "problem-solving" MRI (Hansell et al. 2005).

20.2 Special Problems in Lung Parenchymal MR Imaging

Some of the challenges for MR imaging of the lung are the cardiac and respiratory movement and the extremely low proton density of normal lung. In addition, the large tissue-air interface of the lung is responsible for susceptibility effects that lead to signal loss from intravoxel phase dispersion of spins in lung parenchyma, corresponding to a very low T2* relaxation time (Bergen et al. 1991). Therefore, the basic necessities are obviously a fast scan technique to overcome motion artefacts as well short echo times to minimize signal decay from T2* and T2 effects.

There is also a trade-off between resolution on the one hand and signal-to-noise ratio (SNR) and acquisition time on the other.

The relative SNR can be quickly derived from the following simple expression:

$$\mathrm{SNR} = \mathrm{K} \times \underbrace{\text{voxel volume}}_{=\Delta x \times \Delta y \times \Delta z} \times \frac{\sqrt{\text{number of measurements}}}{\sqrt{\text{receiver bandwidth}}} \quad (1)$$

K is constant and includes the coil filling factor, coil resistance, patient resistance, noise power spectrum, pulse sequence, and tissue parameters (Elster and Burdette 2001). It is easy to see that the bigger the voxel is, the bigger the signal. The term "number of measurements" represents the product of the number of averages and the total number of acquired signal components (data points in k-space) used in the Fourier reconstruction of the image. When the receiver bandwidth (BW) is low, less noise is encoded into the image. Conversely, large BWs span more frequencies and encode more noise.

Coming back to lung imaging, due to the extremely low proton density of normal lung, the voxel size in MRI needs to be larger than in CT to maintain a tolerable SNR. Or, in other words, nowadays it seems impossible to have the same scan thicknesses in MRI in lung parenchymal imaging that we are familiar with in CT and especially in MDCT, where 0.6 mm of the entire chest is possible within one breath hold. Slice thicknesses of less than 5 mm in MRI of the lung parenchyma usually results in an unacceptably low SNR (Hansell et al. 2005). A further reduction of resolution in the *z*-axis is the result of a necessary interspace between adjacent scans. Otherwise the "cross-talk" phenomenon further reduces the SNR (Naidich et al. 1999).

Additionally, the field of view is a factor that directly influences the SNR. Decreasing the field of view while keeping the matrix size constant results in a reduction of voxel volume. For example, reducing the field of view to half of its original size reduces the voxel volume fourfold and therefore the SNR by a factor of four as well (Hansell et al. 2005).

20.3 Technical Standards and Developments

These considerations bring us to technical standards and developments. To reduce motion artefacts from the heart, cardiac gating has been implemented in MR imaging. While it is perhaps not necessary for relative static lesions, for example, at the lung apex, it might be very helpful in the examination of especially the lingular segment and the left lower lobe. When dealing with cardiac gating, the TR time is equal to the R-R wave interval of the cardiac cycle. If the patient has a normal heart rate, the resulting TR is 800 to 1,000 ms, which is approximately equivalent to the TR of a T1-weighted spin-echo image. To acquire T2-weighted images in spin-echo technique, cardiac gating is adjusted to cover every third or fourth heartbeat (Hansell et al. 2005). The drawback of cardiac gating is that the scan time increases by approximately 15% (Mark et al. 1987).

Respiratory monitoring has become possible using an MR navigator echo, which tracks the diaphragm position in real time and uses this information to gate image data acquisition. Other techniques that had been implemented were averaging and reordering of phase encoding (Schmidt et al. 1997). All of these methods are not ideally suited for robust performance in clinical routine, and the best way to overcome the problem of cardiac, respiratory and otherwise patient movement is rapid breath-hold MRI with fast imaging techniques.

The three most popular methods are:

- Turbo-spin-echo (TSE) imaging;
- Gradient-echo (GRE) imaging;
- Steady-state free precession (SSFP) imaging.

The primary advantage of TSE is speed, without the usual concomitant loss of SNR. The essential difference between conventional spin-echo and TSE imaging is that in conventional spin-echo MRI typically only a single echo preceded by a single value of the phase-encoding gradient is acquired after each excitation. More than one echo may be acquired in multiecho spin-echo sequences in order to obtain several different contrasts within one acquisition. TSE uses a multiecho spin-echo sequence that changes the phase-encoding gradient for each of the echoes, which allows the acquisition of multiple lines of k-space after a single excitation (Westbrook 2002). A typical T2-weighted sequence as an example for the TSE is the half-Fourier acquired single-shot turbo-spin-echo sequence (HASTE). In a few studies, the value of T2-weighted TSE sequences has been documented to improve image quality and lesion detectability significantly (Haddad et al. 1995). The value of T2-weighted TSE sequences in detecting pulmonary pathologies, especially pneumonia in immunocompromised patients, in comparison with helical CT,

has been described in earlier studies (Leutner et al. 2000; Lutterby et al. 1996). However, the time of acquisition was between 9 and 19 min. In addition, on T2-weighted TSE images, the fat signal appears bright due to the J-coupling. To avoid this, fat saturation techniques like short TI inversion recovery (STIR) have been implemented with the disadvantage that some signal loss from other tissues occurs (Hansell et al. 2005).

Because no refocusing (180°) radiofrequency (RF) pulse is applied, the echo can be recorded much more quickly in GRE imaging than in spin-echo imaging. In GRE sequences, magnetic field gradients are used to dephase and then rephase the protons following an excitation pulse, and an echo is produced much more rapidly than by the spin-echo sequence. The echo time (TE) is generally shorter for GRE sequences than for spin-echo sequences. Reduced flip angles are used for the initial exciting pulse to avoid saturation. The combination of short TR and short TE values allows for very rapid signal acquisition (Frahm and Haenicke 1999). On the other hand, the gradient reversal refocuses only those spins that have been dephased by action of the gradient itself. Phase shifts resulting from magnetic field inhomogeneities and static tissue susceptibility gradients are not canceled at the center of the GRE as they are in spin-echo sequences (Elster and Burdette 2001). As mentioned previously in this chapter, the large tissue-air interface of the lung is responsible for a tremendous amount of susceptibility artefacts and short T2* relaxation times. In other words, GRE imaging has some drawbacks in pulmonary imaging because these artefacts cannot be significantly reduced or even avoided. As another aspect, GRE sequences do not demonstrate true T2 weighting, because the TE is never long enough and (without refocusing RF pulse) the signal is dominated by T2* effects.

A sequence design that overcomes those problems is the steady-state free precession (SSFP) sequence. The obtained images have sufficiently long TE and less T2* weighting. The steady state is maintained by using a flip angle between 30° and 45° in conjunction with a TR of less than 50 ms and without spoiling of the transversal magnetization after the echo readout. After applying an excitation pulse every TR, each RF pulse not only produces its own free induction decay, but also refocuses the signal produced in the previous excitations. The resulting images are T1-over-T2-weighted with the signal of fluids appearing bright (Elster and Burdette 2001; Westbrook 2002). On the other hand, with the advent of TSE, this sequence is no longer commonly used in pulmonary MR imaging.

In summary, lung parenchymal imaging with MR is challenging because of the susceptibility artefacts, low proton density and movement, and because the available sequences are in some instances inadequate (too sensitive for susceptibility or too slow).

An outstanding development in MR sequence design was the introduction of parallel imaging. With this technique, a further improvement of image quality became possible by shortening the echo times and the echo train length of single-shot sequences resulting in decreased blurring artefacts and less signal decay due to T2 effects (Heidemann et al. 2003) (cf. Chap. 10).

As a consequence, the HASTE technique has become very valuable for lung MRI. This sequence provides good image quality with short scan times and is inherently less sensitive for susceptibility artefacts than the GRE sequences (Leutner et al. 2000). To minimize artefacts from blurring and fast T2 decay, this sequence can now be combined with parallel acquisition techniques. In our examinations, parallel imaging is performed with the GRAPPA algorithm (cf. Chap. 2) (Griswold et al. 2002). This algorithm is less susceptible to artefacts from additional aliasing of tissue outside the field of view, which is especially important in coronal lung imaging where a sufficiently large field of view in the left-right direction is not always available. The GRAPPA parameters are set to a reduction factor of R=2 with 24 reference lines (i.e., 12 additionally acquired auto-calibration signal lines). For further reduction of the echo time, the reference lines were acquired prior to the HASTE read-out (external reference scan, cf. Chaps. 8 and 10). The hardware design used in our hospital for imaging of lung parenchyma is listed in Table 20.1. The particular parameters of our HASTE sequence used for pulmonary parenchymal imaging are listed in Table 20.2. Each 15-s breath-hold allowed covering

Table 20.1 Hardware aspects for parallel imaging

1.5-T MR
Maximum gradient strength 40 mT/m
Minimum rise time 120 μs
8 receiver channels
12 element array coil system was used consisting of one anterior and one posterior flexible coil, each with a set of 6 receiver elements
Outside elements on each side were combined to fit to the limit of eight receiver channels

Table 20.2 HASTE sequence for parallel imaging

TR 440 ms
TE 27 ms
Bandwidth 488 Hz/pixel
Echo spacing 3.76 ms
Slice gap 50%
FOV 256×256 (axial) or 320×256 (coronal, sagittal), respectively
The acquisitions to cover the lung parenchyma were interleaved

50% of the thorax diameter. Thus, the entire thorax could be imaged with a slice thickness of only 6 mm and an inplane spatial resolution of 0.8 mm, in the coronal, axial, and sagittal planes within six breath-holds.

20.4 Comparison of MRI with CT in the Detection of Parenchymal Abnormalities

To evaluate the image qualities of the HASTE sequence with parallel imaging in comparison to the standard of reference, thin-section helical high-resolution computed tomography (HRCT), we performed a study in which pulmonary abnormalities in 30 immunocompromised patients were analyzed (Eibel et al. 2005). All patients presented with fever of unknown origin or with clinical signs and symptoms of lung infection. The inclusion criterion for our study was a chest plain film (CXR) that was either normal or did not show consolidations or other abnormalities suggestive of pulmonary infection. Any suspicion of pneumonia on the CXR was an exclusion criterion for this study. Unenhanced HRCT was performed within 48 h after CXR with the patient in a supine position. A four-slice multi-detector CT (Somatom Sensation 4, Siemens Medical Solutions, Erlangen, Germany) was used with the following parameters: 4×1-mm collimation in the spiral technique; pitch 6; 120 mAs; 120 kV; about 35–50 s scan time. Scanning extended from the lung apices to below the costophrenic angles. Images were reconstructed with a high-spatial-frequency algorithm. To avoid divergent results from rapid changes of pulmonary infectious manifestations during therapy, the MR and CT examinations were done within 24 h. CT and MR findings were reviewed for the presence of nodules (number, margins, zonal distribution, halo sign of a surrounding area of ground-glass opacification, cavitation, and calcifications within the nodules), areas of consolidation (lobar distribution, size measured in centimeters in two directions, existence of cavitation, and calcifications), and areas of ground-glass attenuation. The extent of ground-glass opacities in each lung zone was scored using a four-point scale. Twenty-two patients had pulmonary abnormalities (ill-defined nodules, ground-glass attenuations, and consolidations) according to HRCT. In 21 patients (95%), the diagnosis of pneumonia was correctly established by evaluation of the MR images (Figs. 20.1 and 20.2). One false-negative finding occurred in a patient with only small ill-defined nodules, measuring less than 1 cm in CT. One false-positive finding in MRI was the result of blurring and respiratory artefacts (MRI sensitivity, 0.95; specificity, 0.88; positive predictive value, 0.95; negative predictive value, 0.88). There was no significant difference in the description of lesion location and distribution. To summarize this study, pulmonary MRI appears to be a reliable method for the detection and exclusion of pulmonary abnormalities suggestive of pneumonia in the immunocompromised patient. Therefore, it might be considered for the diagnostic work-up in young patients where radiation exposure from multiple CT examinations might be harmful. In the detection of ground-glass attenuation areas and consolidation, MRI seems to be equal to HRCT. Image degradation by motion artefacts is not only a problem in MRI, but also in CT. Nodules smaller than 10 mm are detected with higher sensitivity at HRCT images. Larger nodules were depicted equally well with both modalities. This lower sensitivity for small nodules is the result of the different slice thicknesses in HRCT with 1 mm and MRI with 6 mm. But as mentioned previously, it has to be proven in further studies if thinner slices are possible with regard to the consecutive lower SNR. On the other hand, in characterization of lung lesions, the MR images are sometimes problematic. It is not reliably possible to visualize calcifications in lung lesions, which can be an important sign of benignity. Also the crescent sign was difficult or impossible to delineate. As a consequence of this data, we can recommend MRI as a helpful follow-up tool to spare radiation, but CT remains in the primary position as the diagnostic method of choice in patients with infectious pulmonary abnormalities (Eibel et al. 2005).

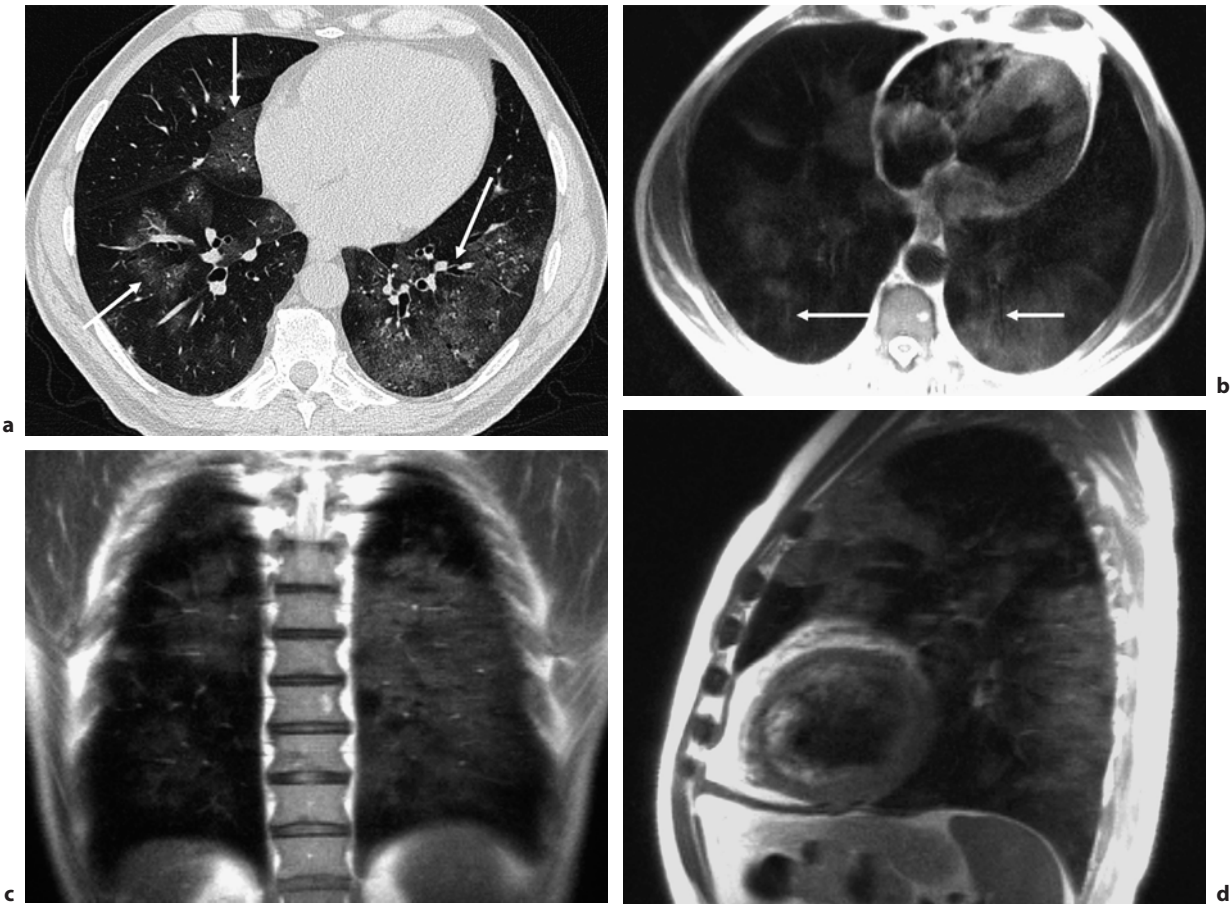

Fig. 20.1a–d. Images of a 76-year-old male (myelodysplasia) with *Pneumocystis jiroveci* pneumonia. **a** HRCT. Large ground-glass attenuation areas in both lower lobes and in the middle lobe adjacent to the pericardium were found. **b** Corresponding axial HASTE sequence with GRAPPA technique. The ground-glass areas are also visualized. The signal intensity is different from the consolidation area of Fig. 20.2; in addition some bronchi and vessels can be delineated in the ground-glass area (*arrows*). **c** Corresponding coronal HASTE with GRAPPA technique. **d** Corresponding sagittal HASTE with GRAPPA-technique

20.5 How Do Other Practitioners and Researchers Perform Lung Parenchymal MR Imaging?

This is a short review of the literature dealing with lung parenchymal imaging, except for lung functional MRI and MR angiography.

Bankier et al. (2004) performed a study in which he analyzed the impact of lung volume on MR signal intensity changes of the lung parenchyma. All MRI studies were performed on a 1.5-T machine, and they used a HASTE acquisition (echo spacing, 4.2 ms; TI_1, 800 ms; TI_2, 150 ms), the matrix size was 128×256, and the field of view was 450 mm. In conclusion he found that in healthy individuals, equal relative changes in lung volume cause equal relative changes in MR signal intensity of the lung parenchyma.

Eibel et al. gave a summary of different studies that deal with MR sequences for the detection and staging of malignant pleural mesothelioma. When looking at these studies comparing different breath-hold sequences such as T1-weighted 2D fast low-angle shot (FLASH) gradient-echo techniques with and without intravenous contrast, T2-weighted true fast imaging with steady precession (FISP) and T2-weighted HASTE, it can be said that most lesions can be detected with the contrast-enhanced 2D FLASH sequence. Pleural fluid was more accurately detected on T2-weighted fat-suppressed HASTE images than on contrast-enhanced T1-weighted fat-suppressed images. In patients who are surgical candidates and who have questionable areas of local tumor extension on CT, MRI may provide additional information to plan or avoid surgery. Surgical exploration can be

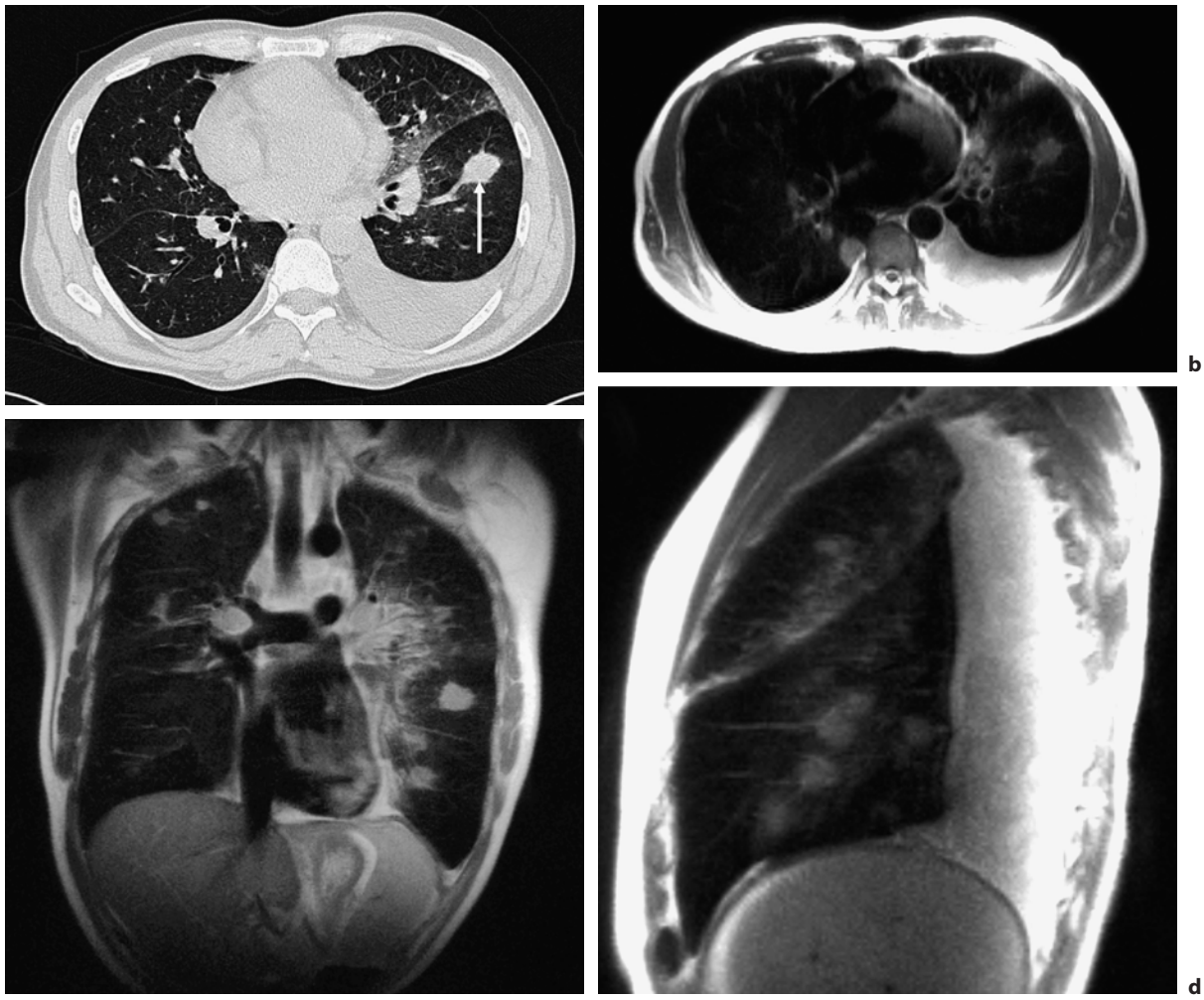

Fig. 20.2a–d. Patient with CLL and invasive pulmonary aspergillosis. **a** Thin-section CT delineates a large nodule in the left lower lobe (*arrow*) and some areas of ground-glass attenuation accentuated also in the left lung. Pleura effusion is present on the *left* more than on the *right*. **b** Corresponding HASTE sequence imaging in axial direction. **c** Corresponding HASTE sequence imaging in coronal direction. **d** Corresponding HASTE sequence imaging in sagittal direction

limited, and guidance of the surgeon to questionable areas is possible (Eibel et al. 2003; Knuuttila et al. 2001).

Rupprecht and coworkers (2002) described a steady-state free precession projection MRI as a potential alternative to the conventional chest X-ray in pediatric patients with suspected pneumonia. Thirty-five investigations were performed in 30 pediatric patients with suspected pneumonia. The MR investigations were performed in coronal slice orientation without cardiac or respiratory triggering in a low-field MR system. All pathological findings of the chest X-ray images were correctly identified by the MRI with good interobserver agreement (κ=0.82-0.85). Effusions as well as small pneumonic infiltrates were more precisely detected by the MRI studies (κ=0.82) as compared with X-ray. And due to these results, they conclude that low-field projection MRI is a promising alternative to pediatric chest X-ray. Due to its short examination time, it overcomes the physical limits of usual MRI methods and provides comparable diagnostic information.

Biederer et al. (2002) investigated the sensitivity of MRI in detecting alveolar infiltrates as an experimental study. The ten porcine lung explants were examined with MRI at 1.5 T before and after intratracheal instillation of either 100 or 200 ml gelatin-stabilized liquid to simulate alveolar infiltrates.

MR-examination comprised gradient echo (2D- and 3D-GRE) and turbo-spin-echo sequences (T2-TSE and T2-HASTE). The signal intensity of lung parenchyma was evaluated at representative cross sections using a standardized scheme. Control studies were acquired with helical CT. In conclusion, they found that MRI with T2-weighted sequences detects artificial alveolar infiltrates with high signal intensity and may be a highly sensitive tool to detect pneumonia in patients. With 2D- and 3D-GRE, the infiltrates were not visible, although the lung parenchyma signal increase was statistically significant.

Jung et al. (2000) performed a study in which they looked for MR characteristics of progressive massive fibrosis in 12 patients with coal workers' pneumoconiosis. The patients were evaluated using a 1.5-T MR unit with a T1-weighted FLASH applied before and after intravenous application of gadolinium diethylenetriamine penta-acetic acid (Gd-DTPA; 0.1 mmol/kg). Additional T2-weigthed sequences were performed. The characteristic MR findings of progressive massive fibrosis in coal workers' pneumoconiosis included high signal intensity in T1-weighted, low signal intensity in T2-weighted imaging and marked post infusion enhancement.

Semelka and co-workers (2000) evaluated the reproducibility and image quality of a three-dimensional gradient-echo sequence for imaging the lung parenchyma, with and without gadolinium administration, using a 2D spoiled gradient-echo sequence for comparison. Twenty patients without lung disease, three patients with pulmonary infiltrates, one patient with pulmonary metastasis, and one patient with primary lung cancer underwent paired 2D and 3D gradient-echo sequences without contrast (24 patients) and with contrast (18 patients). Infiltrates, lung cancer, and pulmonary metastasis were better shown on the gadolinium-enhanced 3D gradient-echo sequences than on the other sequences. Breath-hold 3D gradient-echo imaging resulted in good image quality and negligible image artefacts and was superior to 2D spoiled gradient-echo imaging.

Hatabu and colleagues (1999) evaluated the utility of a HASTE sequence at depicting lung parenchyma and lung pathology. Images were acquired with ECG-triggering and breath-holding. In three volunteers, signal intensity measurements from lung parenchyma were performed using four sequences: (1) HASTE; (2) conventional spin echo; (3) fast spin echo; (4) gradient echo. The scan time for HASTE was 302 ms for each slice. The HASTE sequence clearly demonstrated various pulmonary disorders, including lung cancer, hilar lymphadenopathy, and metastatic pulmonary nodules as small as 3 mm, pulmonary hemorrhage, pulmonary edema, and bronchial wall thickening in bronchiectases. They concluded that their preliminary results indicate that the HASTE sequence provides a practical means for breath-hold MR imaging of lung parenchyma.

Already in 1995, Moody et al. (1995) analyzed a rapid gradient-echo technique optimized to allow breath-held imaging of the lung parenchyma. The ability of this Turbo-FLASH gradient echo sequence (TR 4.7 ms, echo time TE 2 ms) to detect interstitial lung disease was then compared with high resolution computed tomography. Comparison of the optimized magnetic resonance imaging technique with high resolution computed tomography showed no significant difference (P=0.17) when assessing the proportion of diseased to normal lung.

Yankelevitz and coauthors (1994) used MRI to evaluate the treatment response of ten consecutive lung cancer patients while they were receiving radiation therapy. Patients were scanned before treatment, during treatment, at completion of treatment, and if possible, at 3-month intervals thereafter. The initial tumor response to radiation was increasing signal intensity and increasing heterogeneity, best seen on T2-weighted images. Small tumors virtually disappeared, whereas larger masses remained as complex cystic structures or developed cavities. The adjacent irradiated lung parenchyma revealed an increased signal on both the T1- and T2-weighted images as early as 17 days after the start of treatment. The signal intensity continued to increase for several months after treatment, but subsequently decreased.

20.6 Conclusion

Lung parenchymal imaging with MR is challenging because of some substantial drawbacks. But every lung pathology that comes along with increased attenuation values in CT will have positive effects on these above-mentioned drawbacks: (1) the extremely low proton density of normal lung is increased and (2) the large tissue-air interface of the lung, responsible for susceptibility artefacts, is reduced in the cases of pneumonia, pneumonitis, edema, and carcinoma, respectively. On the other hand, most lung diseases

will make the patient unable to hold his/her breath for more than a few seconds. For this reason, fast imaging techniques are necessary with high resolution to detect even smaller lesions. From a technical point of view, perhaps it will never be possible with MR to scan as thinly as with CT. This means that the special resolution in the *z*-axis is not comparable in the evaluation of lung parenchyma, and very tiny lung lesions, especially small lung nodules (smaller than 1 cm in diameter), cannot be reliably detected. On the other hand, the multiplanar capabilities of MRI allow performing imaging in perpendicular slice orientations making use of the high in-plane spatial resolution in different directions. Calcium in nodules is not, or is not reliably detectable, and because a small air crescent sign in consolidations can be overlooked on MR images, it is, at least at the moment, not the method of choice to evaluate pneumonia and nodules primarily. For these instances, thin-section CT will remain the standard of reference.

With parallel imaging on the other hand, it is now possible to scan the lung in breath-holds with subcentimeter resolution in the *z*-axis so that the long examination times from earlier sequences have now become a thing of the past. Especially for follow-up examinations in immunocompromised patients and in some instances for the staging of malignant diseases (malignant pleural mesothelioma, and lung cancer, respectively), MR can add important information or can help to avoid radiation burden.

20.7 Recommendations

1. To evaluate malignant pleural or lung parenchymal disease (if CT is not possible or not conclusive with therapeutic consequences):
   a. Contrast-enhanced 2D FLASH sequence (parallel imaging), with and without fat-saturation
   b. Fast single-shot HASTE with parallel imaging
2. To evaluate pneumonia, pneumonitis, lung nodules, interstitial disease, and pleural effusion (for follow-up to avoid repetitive radiation burden, not for primary imaging of these diseases):
   a. Fast single-shot HASTE with parallel imaging
   b. As an option, additional contrast-enhanced 2D FLASH (parallel imaging)
   c. As an option, additional imaging with steady-state free precession (true FISP)

References

Bankier AA, O'Donnell CR, Mai VM, Storey P, De Maertelaer V, Edelman RR, Chen Q (2004) Impact of lung volume on MR signal intensity changes of the lung parenchyma. J Magn Reson Imaging 20:961–966

Bergin CJ, Glover GH, Pauly JM (1991) Lung parenchyma: magnetic susceptibility in MR imaging. Radiology 180:845–848

Bergin CJ, Healy MV, Zincone GE, Castellino RA (1990) MR evaluation of chest wall involvement in malignant lymphoma. J Comput Assist Tomogr 14:928–932

Biederer J, Busse I, Grimm J, Reuter M, Muhle C, Freitag S, Heller M (2002) Sensitivity of MRI in detecting alveolar Infiltrates: Experimental studies. Rofo174:1033–1039

Brown LR, Aughenbaugh GL (1991) Masses of the anterior mediastinum: CT and MR imaging. AJR Am J Roentgenol 157:1171–1180

Eibel R, Herzog P, Dietrich O, Rieger C, Ostermann H, Reiser MF, Schoenberg SO (2005) Detection of pulmonary abnormalities in immunocompromised patients: Fast single-shot MRI with parallel imaging in comparison to thin-section helical CT. Radiology, accepted in 2005

Eibel R, Tuengerthal S, Schoenberg SO (2003) The role of new imaging techniques in diagnosis and staging of malignant pleural mesothelioma. Curr Opin Oncol 15:131–138

Elster AD, Burdette JH (2001) Questions and answers in magnetic resonance imaging, 2nd edn. Mosby, St Louis

Frahm J, Häenicke W (1999) Rapid scan techniques. In: Magnetic resonance imaging, 3rd edn. Mosby, St Louis, pp 87–124

Glazer GM, Gross BH, Aisen AM, Quint LE, Francis IR, Orringer MB (1985) Imaging of the pulmonary hilum: a prospective comparative study in patients with lung cancer. AJR Am J Roentgenol 145:245–248

Glazer HS, Lee JK, Levitt RG, Heiken JP, Ling D, Totty WG, Balfe DM, Emani B, Wasserman TH, Murphy WA (1985) Radiation fibrosis: differentiation from recurrent tumor by MR imaging. Radiology 156:721–726

Griswold MA, Jakob PM, Heidemann RM, et al (2002) Generalized autocalibrating partially parallel acquisitions (GRAPPA). Magn Reson Med 47:1202–1210

Haddad JL, Rofsky NM, Ambrosino MM, Naidich DP, Weinreb JC (1995) T2-weighted MR imaging of the chest: comparison of electrocardiograph-triggered conventional and turbo spin-echo and nontriggered turbo spin-echo sequences. J Magn Reson Imaging 5:325–329

Hansell DM, Armstrong P, Lynch DA, Page McAdams H (2005) Imaging of the diseases of the chest. Technical considerations, 4th edn. Elsevier Mosby, Philadelphia: pp 1–26

Hatabu H, Gaa J, Tadamura E, Edinburgh KJ, Stock KW, Garpestad E, Edelman RR (1999) MR imaging of pulmonary parenchyma with a half-Fourier single-shot turbo spin-echo (HASTE) sequence. Eur J Radiol 29:152–159

Heelan RT, Demas BE, Caravelli JF, Martini N, Bains MS, McCormack PM, Burt M, Panicek DM, Mitzner A (1989) Superior sulcus tumors: CT and MR imaging. Radiology 170:637–641

Heidemann RM, Ozsarlak O, Parizel PM, et al (2003) A brief review of parallel magnetic resonance imaging. Eur Radiol 13:2323–2337

Jung JI, Park SH, Lee JM, Hahn ST, Kim KA (2000) MR characteristics of progressive massive fibrosis. J Thorac Imaging 15:144–150

Knuuttila A, Kivisaari L, Kivisaari A, et al (2001) Evaluation of pleural disease using MR and CT. With special reference to malignant pleural mesothelioma. Acta Radiol 42:502–507

Leutner CC, Gieseke J, Lutterbey G, et al (2000) MR imaging of pneumonia in immunocompromised patients: comparison with helical CT. AJR Am J Roentgenol 175:391–397

Lutterbey G, Gieseke J, Sommer T, Keller E, Kuhl C, Schild H (1996) A new application of MR tomography of the lung using ultra-short turbo spin echo sequences. ROFO 164:388–393

Mark AS, Winkler ML, Peltzer M, Kaufmann L, Higgins CB (1987) Gated acquisition of MR images of the thorax: advantages for the study of the hila and mediastinum. Magn Reson Imaging 5:57–63

Mirvis SE, Keramati B, Buckman R, Rodriguez A (1988) MR imaging of traumatic diaphragmatic rupture. J Comput Assist Tomogr 12:147–149

Moody AR, Bolton SC, Horsfield MA (1995) Optimization of a breath-hold magnetic resonance gradient echo technique for the detection of interstitial lung disease. Invest Radiol 30:730–737

Naidich DP, Webb WR, Müller NL, et al (1999) Principles and techniques of thoracic CT and MR. Computed tomography and magnetic resonance of the thorax, 3rd edn.Lippincott-Raven, Philadelphia, pp 14–15

Nyman R, Rehn S, Glimelius B, Hagberg H, Hemmingsson A, Jung B (1987) Magnetic resonance imaging for assessment of treatment effects in mediastinal Hodgkin's disease. Acta Radiol 28:145–151

Padovani B, Mouroux J, Seksik L, Chanalet S, Sedat J, Rotomondo C, Richelme H, Serres JJ (1993) Chest wall invasion by bronchogenic carcinoma: evaluation with MR imaging. Radiology 187:33–38

Rupprecht T, Bowing B, Kuth R, Deimling M, Rascher W, Wagner M (2002) Steady-state free precession projection MRI as a potential alternative to the conventional chest X-ray in pediatric patients with suspected pneumonia. Eur Radiol 12:2752-2756. Epub 2002 Apr 30

Schmidt MA, Yang GZ, Keegan J, Jhooti P, Gatehouse PD, Carr DH, Hansell DM, Firmin DN (1997) Non-breath-hold lung magnetic resonance imaging with real-time navigation. MAGMA 5:123–128

Semelka RC, Cem Balci N, Wilber KP, Fisher LL, Brown MA, Gomez-Caminero A, Molina PL (2000) Breath-hold 3D gradient-echo MR imaging of the lung parenchyma: evaluation of reproducibility of image quality in normals and preliminary observations in patients with disease. J Magn Reson Imaging 11:195–200

Webb WR (1989) MR imaging of treated mediastinal Hodgkin's disease. Radiology 170:315–316

Webb WR, Gamsu G, Stark DD, Moore EH (1984) Magnetic resonance imaging of the normal and abnormal pulmonary hila. Radiology 152:89–94

Westbrook C (2002) MRI at a glance, 1st edn. Blackwell Science, Oxford

Yankelevitz DF, Henschke CI, Batata M, Kim YS, Chu F (1994) Lung cancer: evaluation with MR imaging during and after irradiation. J Thorac Imaging 9:41–46

Liver Imaging

21

Christoph J. Zech

CONTENTS

21.1 Introduction

Magnetic resonance imaging has been used since the early 1990s as a standard procedure in abdominal imaging. Since then, various technical developments have taken place that have helped to further increase the diagnostic value of the method and to further establish image quality. Important milestones towards a fast and robust utilization of MRI in abdominal imaging have been the development of gradient-echo (GRE) sequences, single-shot techniques and phased-array coils. However, it is only now that abdominal imaging has reached a quality in which respiratory or motion artefacts are negligible and spatial resolution is considered sufficient. Among many other influences, the development of 3D sequences, navigator triggering and parallel-imaging strategies has had important influence in that field. The introduction of high-field systems might allow an additional increase in spatial resolution and image quality. This chapter provides an overview about the above-mentioned important technical developments for MRI of the liver. It gives background knowledge about these techniques and discusses the clinical value of each innovation derived from the recent literature as well as from our own experience.

C. J. Zech, MD
Department of Clinical Radiology, University Hospitals – Grosshadern, Ludwig Maximilian University of Munich, Marchioninistr. 15, 81377 Munich, Germany

21.2 3D Sequences

The evolution from 2D to 3D sequences has been of special value for typical applications requiring a very high spatial resolution and dedicated post-processing as, for example, MR angiography. However, it has also gained importance in liver imaging (Lee et al. 2000). The two basic applications of 3D sequences in abdominal imaging are dynamic studies after bolus injection of contrast agents with T1-weighted 3D gradient-echo sequences and depiction of the biliary tree with MR cholangiography (MRC) with T2-weighted 3D turbo-spin-echo (TSE) sequences, which will be discussed in Chap. 22. The advantage of all 3D techniques is that an isotropic 3D dataset can be acquired, for which various means of post-processing are possible (Lee et al. 2000; Schaible et al. 2001; Hennig et al. 2005). With 3D sequences a high spatial resolution can be acquired. The resulting loss of signal-to-noise ratio (SNR) can be compensated with the substantial shortening of the T1 relaxation time by gadolinium chelates for dynamic examinations on the one hand and the long T2 relaxation time

of fluids for MRC on the other. Moreover, the inherent higher SNR of 3D sequences versus 2D sequences allows increasing spatial resolution in 3D sequences without a relevant loss of SNR in comparison to an equivalent 2D sequence (Rofsky et al. 1999).

The basic principle of 3D sequences is the excitation of not only a single slice, but rather the whole examination volume, the so-called slab. Therefore, an additional, second phase-encoding gradient in the slice direction (*z*-axis in axial acquisitions) is added to the usual frequency-encoding and phase-encoding gradients in the *x*- and *y*-axis. The slab is divided into partitions (in contrast to the single slices in 2D techniques). 3D techniques have the capacity to examine the liver with high spatial resolution in-plane and along the *z*-axis, without gaps and with fat saturation within one breath-hold (Rofsky et al. 1999). Although more phase-encoding steps are needed, in contrast to 2D techniques, the overall acquisition time is shortened in 3D sequences by applying low flip angles of only 15° to 20° and a repetition time of less than 5 ms (Nitz et al. 2003).

A dedicated 3D sequence for abdominal imaging is the so-called VIBE sequence (volumetric interpolated breath-hold examination), which is further accelerated by zero-filling of the k-space in the slice direction (Rofsky et al. 1999). With this sequence, a slab of about 20-cm thickness can be acquired at 1.5-T in 15 to 20 s with 4-mm slice thickness and a matrix size of 256×192. The VIBE sequence has to be considered superior to a T1-weighted 2D GRE sequence in the early dynamic phases after the injection of gadolinium contrast agents due to a high contrast between gadolinium-enhancing lesions and fat-saturated liver parenchyma in combination with high spatial resolution (Rofsky et al. 1999; Dobritz et al. 2002).

21.3 Navigator Triggering

Artefacts from respiratory motion are one of the most important phenomena disturbing imaging quality in MR examinations of the liver. A breath-hold time of 20 s or less is crucial, therefore, for an acceptable image quality even in patients with a good general state of health. However, this restriction makes an increase in spatial resolution almost impossible, since other sequence parameters with influence on the acquisition time like the repetition time or the flip angle have to be kept in certain ranges to assure an appropriate T1 and T2 weighting.

The development of very robust 3D GRE sequences has at least in part solved these problems for T1-weighted sequences, since ultra-short repetition times and low flip angles ensure a short acquisition time with evenly increased spatial resolution, as mentioned in Sect. 21.2.

The introduction of T2-weighted TSE and single-shot sequences in the 1990s has made breath-hold examinations of the liver feasible in more or less acceptable image quality. Apart from the breath-hold strategy, respiratory-triggered T2-weighted sequences have been the focus of various studies (Katayama et al. 2001; Augui et al. 2002; Zech et al. 2004). According to Katayama et al. (2001), one advantage of respiratory triggering is a better T2 contrast with an improved signal-to-noise ratio of the liver parenchyma and improved liver-to-lesion contrast in comparison to breath-hold T2-weighted TSE and single-shot sequences. Our own experience shows also superiority of respiratory triggering over breath-hold strategies.

Respiratory triggering can be realized with a respiratory belt or with a navigator sequence. For triggering with the belt, a flexible, air-filled tube is used, which is extended when the patient breathes in and the circumference of the abdomen is enlarged. The extension of the air-filled tube causes a negative pressure in the tube, which is transmitted to the MR system by a connecting system. The variation of air pressure in the tube represents the movement of the abdominal wall and can be used as an indicator of the respiratory position of the patient. Instead of the belt, also an air-filled cushion can be used, which is squeezed during inspiration resulting in a positive pressure. Triggering with navigator sequences has been developed mainly for cardiac imaging. The basic principle of the navigator-based technique is the direct visualization of the diaphragm movement with sequences that have typically a low spatial, but high temporal resolution. This can be achieved by means of a gradient-echo sequence with a very low flip angle (<10°), with a small field of view (and accordingly only a few phase-encoding steps) and with a low matrix size. Moreover, the low flip angle ensures that magnetization is not saturated and dark lines in the anatomical images therefore are avoided.

For both ways of triggering, the acquisition of the image data typically takes place in the longer expiration phase. The acquisition begins when the respiratory level is below a predefined point (usually around

20% of the maximal level of inspiration). This point is called the triggering threshold. Acquisition is triggered when the respiratory curve falls below this value. Since during the inspiration phase the tissue has time to rebuild longitudinal magnetization, the effective repetition time is always longer than the minimal repetition time and is equal to the respiratory cycle time. The time of a single respiratory cycle usually is between 3 and 5 s; therefore, the effective repetition time is ideal for a good T2 weighting. This makes all free-breathing techniques interesting, especially for T2-weighted sequences, whereas the development of robust and effective T1-weighted gradient-echo sequences with respiratory triggering is still in progress.

One of the most important drawbacks of all free-breathing techniques has been their long time of acquisition, which led sometimes to sequences lasting around 10 min with gross movement artefacts. This problem has been addressed successfully with the help of parallel imaging strategies, as will be pointed out in Sect. 21.4.1.

21.4 Parallel Imaging

The balance between spatial resolution, signal-to-noise ratio and acquisition time is crucial for liver MRI. Parallel imaging as a universal tool for accelerated acquisition is therefore of high interest for liver imaging.

21.4.1 Current Value of Parallel Imaging for Liver MRI

With the introduction of parallel-imaging techniques, the image acquisition can be accelerated. In a recently published evaluation, the acquisition time for high-resolution (5-mm slice thickness, full 320 matrix) T2-weighted TSE sequences with fat-saturation was markedly reduced for breath-hold sequences from 19 to 13 s per nine slices and for respiratory-triggered sequences from a mean of 7:02 min to 4:00 min when parallel imaging with an acceleration factor of R=2 and the GRAPPA algorithm (see Chap. 2) were utilized (Zech et al. 2004). This study also showed that this reduction in acquisition time is possible without negative impact on image quality. Neither the breath-hold nor the respiratory-triggered sequences with parallel imaging were rated inferior in comparison to the corresponding non-accelerated sequences. Similar results were also found for a T1-weighted 3D GRE sequence, which can be used as a dynamic sequence after injection of gadolinium (McKenzie et al. 2004). Although image quality in this evaluation was rated inferior for some categories, the authors concluded that overall utilization of parallel imaging is beneficial also in T1-weighted 3D GRE sequences, especially in patients with limited breath-hold capacity (McKenzie et al. 2004). With the use of parallel imaging in T2-weighted single-shot sequences, as for example half-Fourier acquired single-shot turbo spin echo (HASTE) sequences, the decreased number of phase-encoding steps enables shortened echo trains. This leads to an improved clarity of edges and reduces blurring; cf. Chap. 10.

One problem of parallel acquisition methods is the inferior SNR of these sequences (Griswold et al. 2002). However, a high SNR and contrast-to-noise ratio (CNR) are crucial in liver imaging due to intrinsic low contrast between certain liver lesions and adjacent liver parenchyma. The GRAPPA algorithm shows an improved SNR ratio in comparison to previous AUTO-SMASH techniques (Griswold et al. 2002). Compared with mSENSE, aliasing artefacts in the central parts of the field of view are reduced with GRAPPA; however, image noise is increased in the central parts of the field of view, which is less disturbing compared to real aliasing in our experience (Fig. 21.1). Therefore, it might be favorable to use this algorithm for liver MRI, although comparative studies for image quality or lesion detection are not present.

With the GRAPPA algorithm, image noise is concentrated in the center of the image. This has some drawbacks. Firstly, in the center of a transversal plane of the upper abdomen, there are always important anatomical structure and liver parenchyma, which might be obscured by these artefacts, although increased image noise is less disturbing than central aliasing, as discussed above. Secondly, as mentioned beforehand in Chap. 4, the calculation of SNR and CNR is not correct with the standard method (using the standard deviation of the background noise). This can cause problems not only for scientific evaluations, but might also be problematic in the daily routine since, e.g., it might affect the accurate measurement of signal loss or increase after contrast agent injection for the characterization of focal liver lesions when liver-specific contrast agents are used. However,

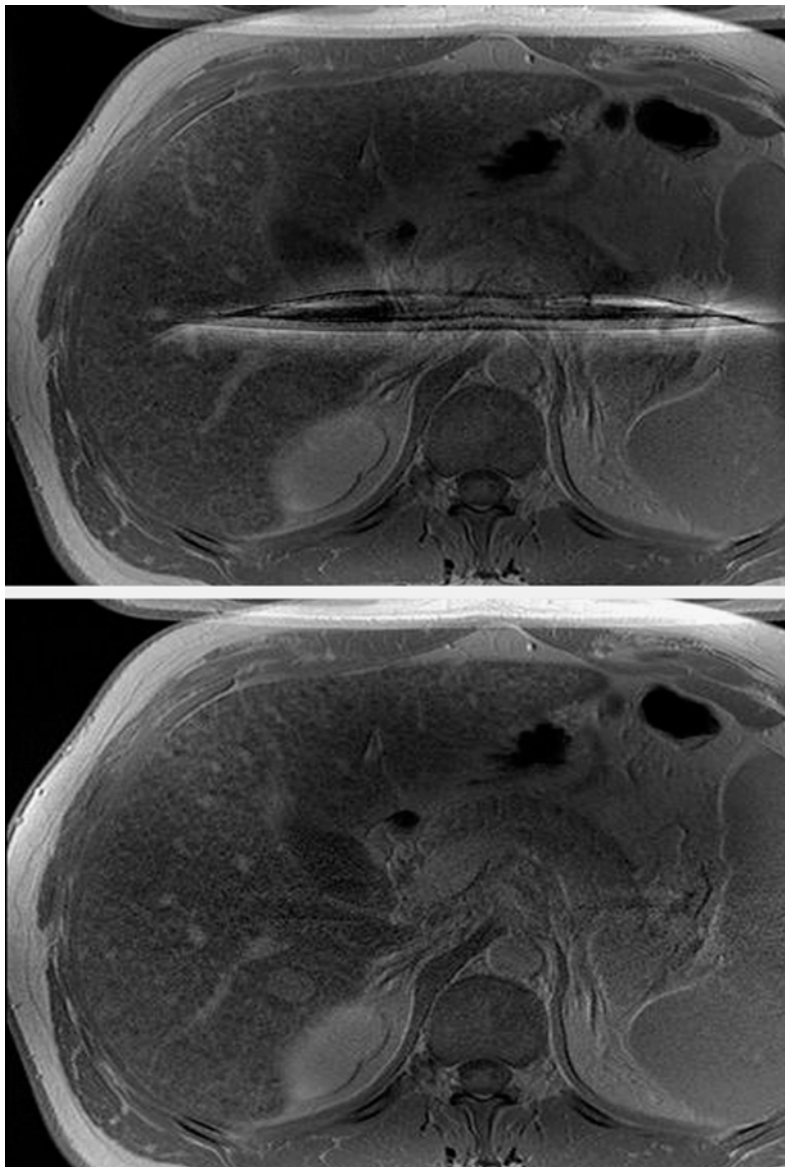

Fig. 21.1. Appearance and spatial distribution of artefacts arising from the different parallel-imaging algorithms. For both sequences a too-small field of view was chosen to generate superaliasing. With the mSENSE algorithm (*upper row*) this results in severe central aliasing, which obscures central parts of the section shown. With the GRAPPA algorithm image quality is also slightly reduced by centralized image noise; however, in direct comparison to the mSENSE image there are fewer artefacts

if the signal intensity is measured at the same position pre- and post-contrast and if the parameter settings (especially the acceleration factor) and the coil geometry are not changed, this systematic mistake can be negligible. Altogether the overall image quality in an intra-individual comparison was not rated inferior for the parallel-imaging sequences despite these drawbacks (Zech et al. 2004). This indicates that the SNR loss for parallel imaging is within a limit that does not visually disturb the images (Fig. 21.2).

In our experience, we can fully recommend the use of parallel imaging with an acceleration factor of R=2 in liver MRI. For breath-hold techniques, the saved time with parallel imaging is on the one hand important to minimize respiratory artefacts, and on the other hand the saved time can be used for, e.g., T2-contrast optimization employing a longer TR and a shorter echo train length or to increase the spatial resolution. For respiratory-triggered sequences the work-flow and patient acceptance can be increased by shorter times of acquisition. Moreover, the spatial resolution can be optimized for the combination of respiratory triggering with parallel imaging even up to a full 384 matrices without running into gross artefacts from patient movement, which becomes problematic in respiratory triggered sequences exceeding 5 min time of acquisition (Fig. 21.3).

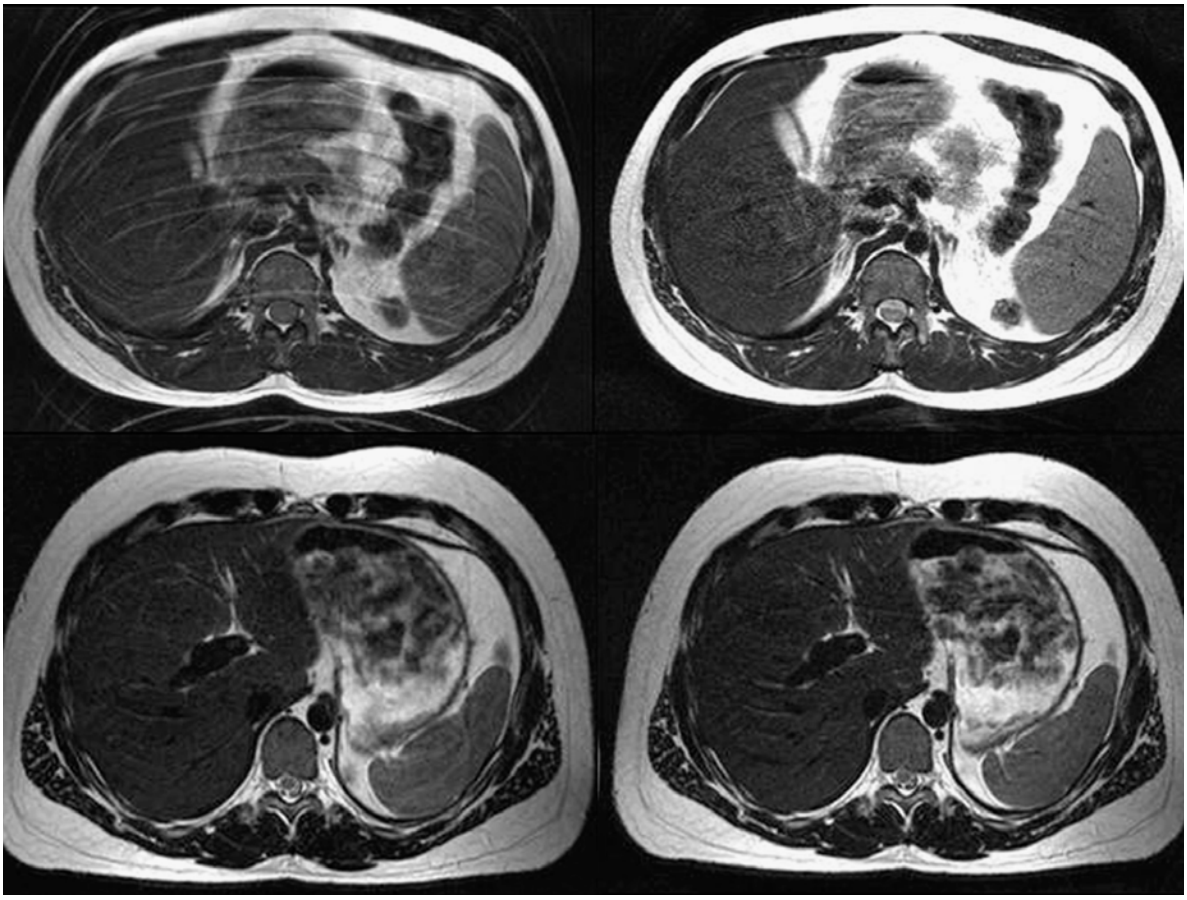

Fig. 21.2. Differences in image quality for breath-hold sequences without (*upper left*) and with parallel imaging (GRAPPA algorithm, acceleration factor *R*=2) (*upper right*) as well as for respiratory-triggered sequences without (*lower left*) and with parallel imaging (GRAPPA algorithm, acceleration factor *R*=2) (*lower right*) in a T2-weighted TSE sequence in a healthy volunteer. Note the significantly improved image quality with parallel imaging in the breath-hold examination (*upper row*) due to the reduced breathing artefacts. The image quality in the respiratory-triggered sequences shows no significant difference (*lower row*); however, with utilization of parallel imaging, it was possible to reduce the time of acquisition from 6:24 min to 3:01 min in this volunteer

21.4.2 Higher Acceleration Factors with Multi-Channel Systems

The introduction of higher acceleration factors is still problematic. One major problem is the loss of the signal-to-noise ratio, which reaches a critical level with acceleration factors of *R=4* (Fig. 21.4). The second difficult point is that the phase-encoding direction in most clinically applied abdominal sequences is anterior-posterior for the transversal orientation, which is still the most important orientation in the abdomen. The anterior-posterior phase-encoding direction is chosen due to the rectangular field of view, which helps to save acquisition time by a reduced number of phase-encoding steps.

To achieve optimally differing coil sensitivity profiles in the phase-encoding direction, the elements of a phased-array coil have to be arranged parallel to the direction of the phase-encoding steps. This is anatomically difficult for more than two coil elements in transversal slices with phase encoding in the anterior-posterior direction because of the typically larger left-right diameter of the abdomen compared to its anterior-posterior diameter. Thus, optimal coil geometry for parallel imaging with higher acceleration factors in a transversal orientation is not pro-

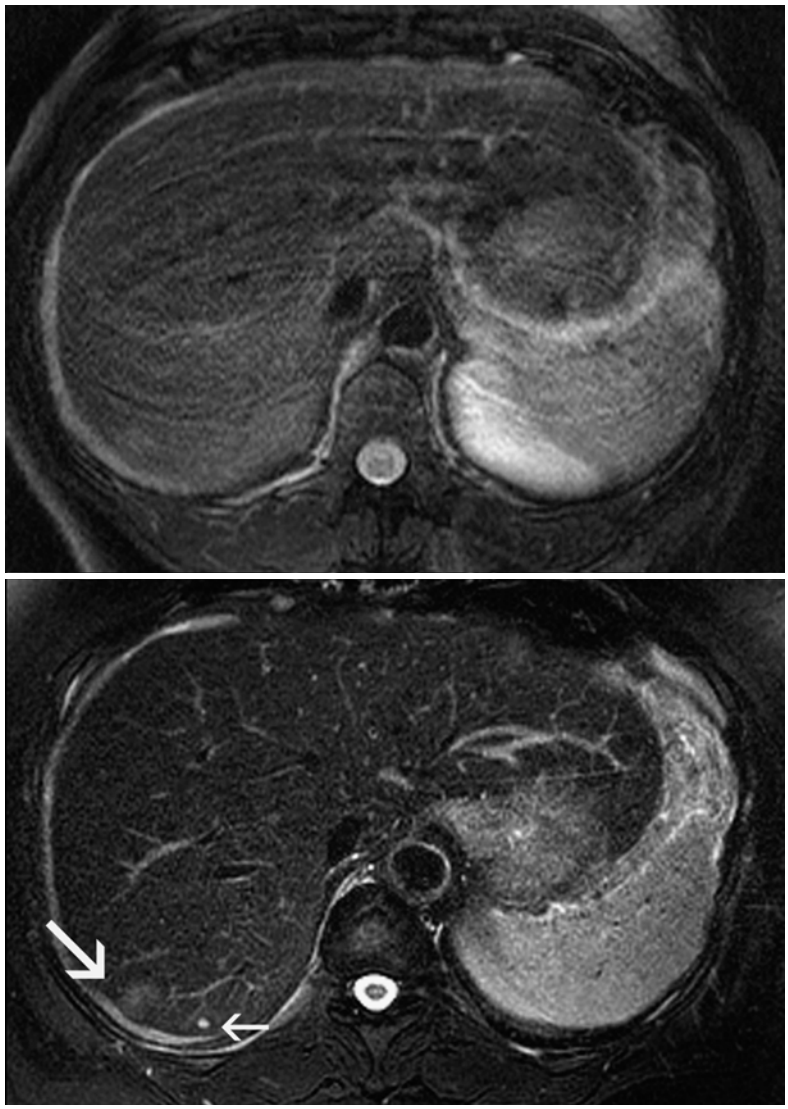

Fig. 21.3. Female patient suffering from breast cancer; MRI to rule out liver metastases. Although the patient has been in a good general state of health, she was not able to hold her breath properly, which is indicated by severe breathing artefacts in the T2-weighted TSE sequence with fat saturation. These artefacts also obscure the focal liver lesion in segment 7. In the corresponding slice of the respiratory-triggered T2-weighted TSE sequence, the focal lesion with only slight hyperintensity (*arrow*), suspicious of a metastasis, is excellently depicted. Note also the tiny liver cyst adjacent to the metastasis (*small arrow*). The time of acquisition was three times a 16-s breath-hold (effective time of acquisition with intervals between the individual breath-holds was around 2 min) versus 2:51 min for the respiratory-triggered sequence. Both sequences are acquired with parallel imaging (acceleration factor R=2)

vided by typically used coil systems, in contrast to the coronal orientation with phase encoding in the left-right direction. However, with dedicated coil arrangements, imaging artefacts in axial slices can be decreased. In case of multi-channel MR systems, more than one conventional phased-array coil (with, e.g., six coil elements each) can be wrapped around the abdomen as shown in Fig. 21.5. Therefore, higher factors of acceleration are theoretically feasible in the anterior-posterior direction; however, they still suffer from increased artefacts.

For the coronal orientation, the multi-channel phased-array coils placed on the abdomen have an ideal position to acquire higher acceleration factors in the left-right direction. This is helpful for the acquisition of MRCP examinations, as discussed in Chap. 22.

Innovative coil designs may enable higher accelerations in the future; however, meanwhile acceleration factors of usually up to R=2 are feasible for the transversal orientation, whereas factors up to R=4 are feasible for the coronal orientation.

21.4.3 Combination of Specific Sequence Types with Parallel Imaging

The utilization of parallel imaging offers advantageous effects in several sequence types, especially in the different single-shot techniques. Single-shot fast spin echo pulse sequences, such as the HASTE sequence, often suffer from image artefacts related

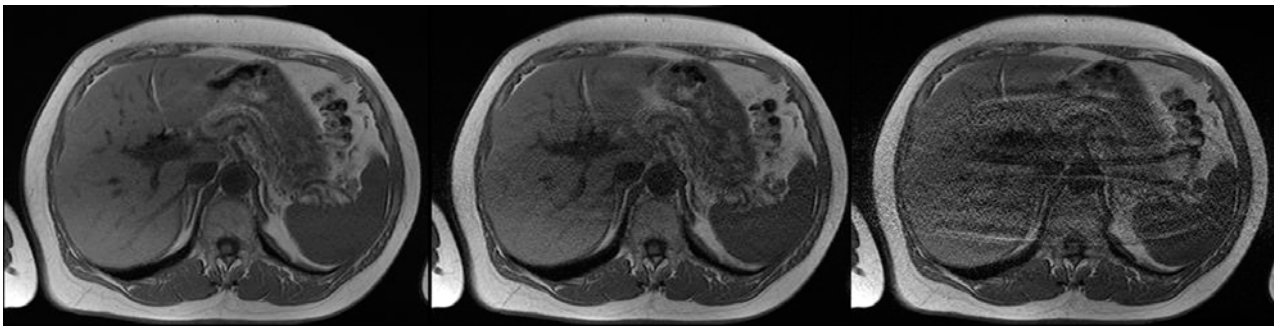

Fig. 21.4. Limitations for the utilization of higher acceleration factors in transversal studies of the upper abdomen. The same T1-weighted gradient-echo sequence with an acceleration factor of R=2 (*left*), R=3 (*middle*) and R=4 (*right*) is presented. Imaging artefacts due to parallel imaging cannot be delineated with an acceleration factor of R=2, whereas with a factor of R=3 substantial and a factor of R=4 severe artefacts in the center of the field of view can be delineated. These artefacts are also present with multi-channel MRI systems due to the coil geometry for the transversal orientation with the typical coil sensitivity profiles (explanation in the text)

to their long echo trains with apparent blurring due to the T2 signal decay during the readout of the echo train (cf. Chap. 10). This problem can be reduced by applying parallel imaging. With an acceleration factor of 2, approximately only half of the phase-encoding steps have to be measured. The thereby shortened length of the echo train results in more signal, since late echoes with low signal are no longer acquired. This leads to an increased image quality with reduced blurring artefacts without the loss of spatial resolution (Fig. 21.6).

The shortened echo train is of particular value for echo-planar imaging (EPI) sequences since they suffer from severe distortions due to eddy-current and off-resonance phenomena. Because of their high sensitivity for inhomogeneities in the magnetic field, these sequences at present do not play a major role in daily clinical practice for abdominal imaging. Parallel imaging together with optimized gradient systems can help to establish a robust image quality for abdominal EPI sequences. The black-blood effect, which can be achieved by utilizing a slight diffusion gradient (e.g., with a b-value of 50 s/mm^2), helps to establish a contrast situation which is optimal for the detection of focal liver lesions: since the liver as well as the hepatic vasculature is dark, focal lesions are depicted as bright spots within a dark background. Especially the problem of small peripheral liver veins mimicking or masking small focal liver lesions is markedly reduced (Fig. 21.7).

Preliminary results in comparison to a standard T2-weighted TSE sequence have shown promising results with regard to image quality, robustness, and liver lesion detection (Zech et al. 2005). However, susceptibility artefacts, especially at the liver margins, are still present, which can cause false-positive findings. Therefore, the value of these sequences might be the fast perception of lesions, which has to be validated on the additionally performed contrast-enhanced examination.

21.4.4 Application of Parallel Imaging at High-Field Systems

With 1.5-T state-of-the-art scanners, a very high image quality can be reached with parallel imaging in combination with navigator triggering, as mentioned earlier. However, signal-to-noise constraints still exist at 1.5 T: with parallel imaging the SNR is at least reduced by the square root of the acceleration factor R. Thus, with higher acceleration factors, e.g, of three, the SNR is reduced to at least 58% of the original value. This causes a visible increase of image noise in the images at 1.5 T. Moreover, an increase in spatial resolution in breath-hold examinations at 1.5 T is nearly impossible, since a breath-hold time of about 20 s cannot be exceeded.

Due to the higher SNR at 3 T, image noise at comparable acceleration factors is barely visible in the images, even when a very high spatial resolution is acquired (see also Fig. 21.6). Especially T1-weighted gradient-echo sequences, which are unsuitable for respiratory triggering, can be acquired in a very high spatial resolution with excellent image quality within

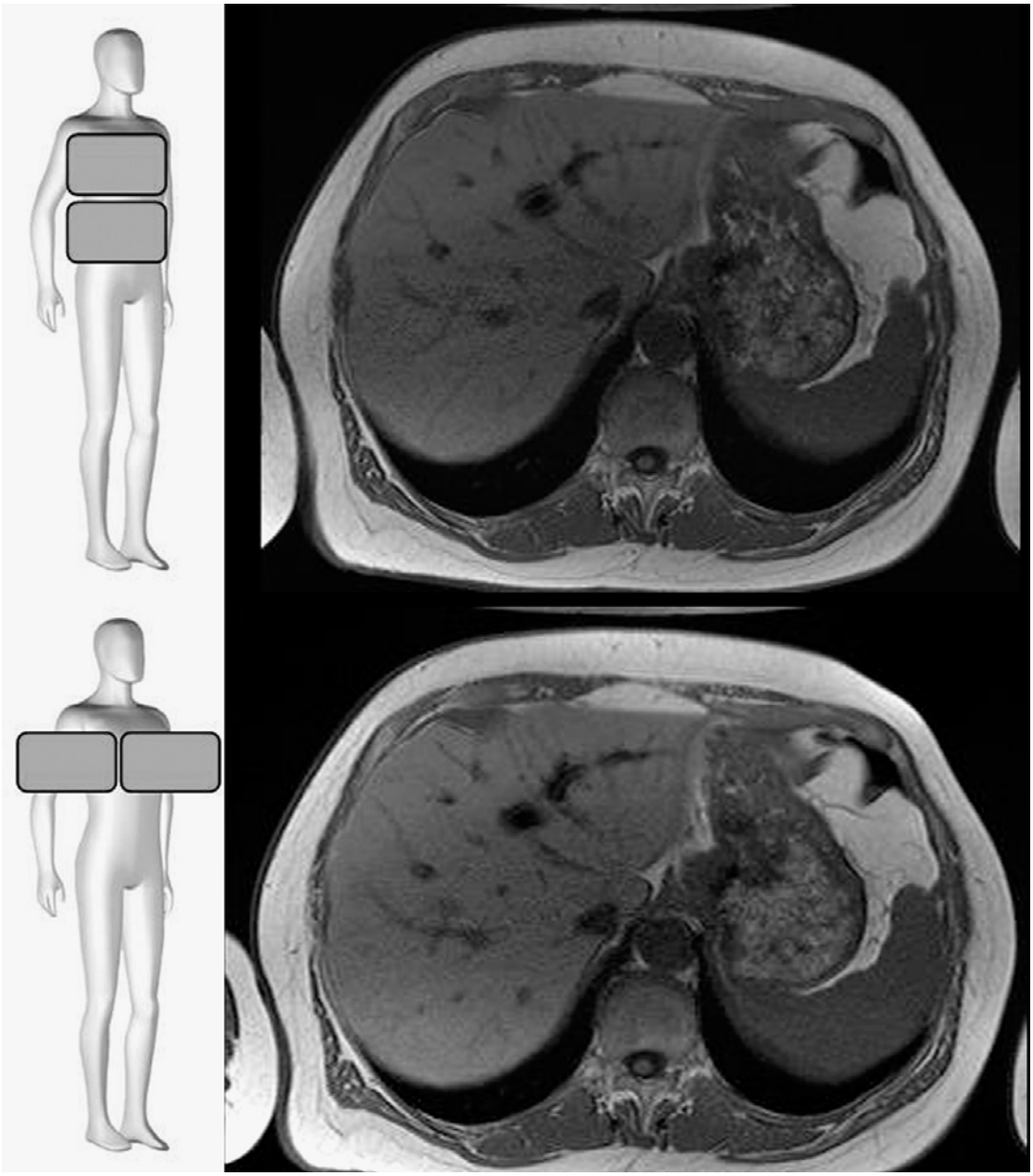

Fig. 21.5. Two different coil arrangements for a T1-weighted 2D gradient-echo sequence. With multi-channel systems, as shown here with the Total Imaging Matrix (TIM) system (Siemens Medical Solutions, Erlangen, Germany), more than one phased-array coil can be positioned on the patient. The phased-array coils consist of two clusters with up to three matrix coil elements each, which can be used as separate receivers in the so-called triple mode (see Chap. 13). The *upper row* shows a conventional arrangement, which enables covering the whole abdomen without patient movement or coil repositioning. Together with the three spine elements integrated into the patient table, six coil elements are available for signal reception at each anatomic level. The lower row shows a coil arrangement for dedicated MR examinations of the upper abdomen (e.g., dedicated MRI of the liver), where two flexible coil arrays are wrapped around the patient. With the help of this arrangement, more sensitivity profiles from a total of 18 different coil elements (2×2×3 elements in the phased-array coils + 1×2×3 elements in the spine matrix) help to decrease the typical parallel imaging artefacts (centralized increase in noise), which can be delineated in the images of the *upper row*. Both sequences have the same imaging parameters and use parallel imaging (GRAPPA algorithm) with an acceleration factor of R=2.

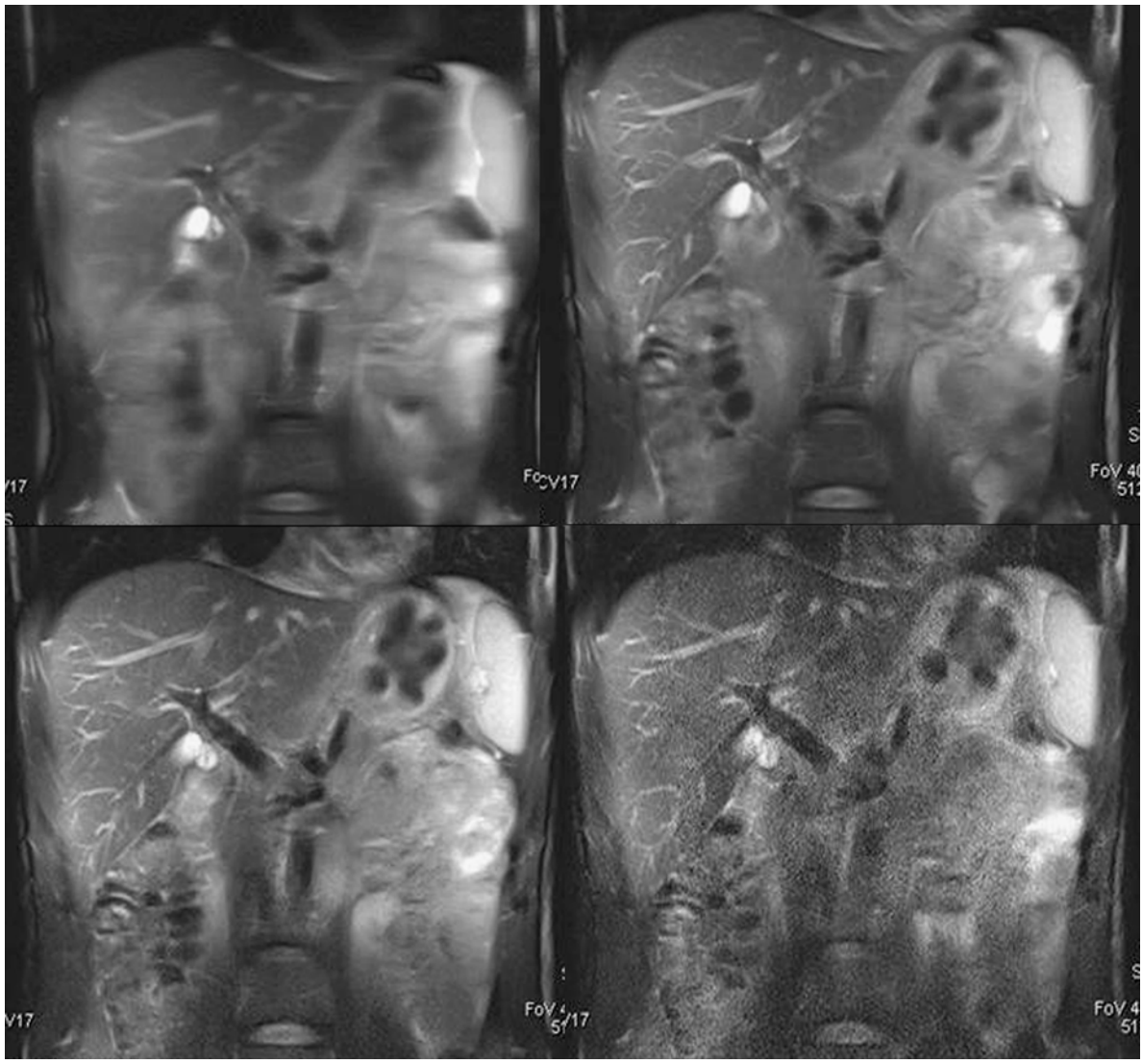

Fig. 21.6. Influence of parallel imaging on blurring artefacts in single-shot sequences for the example of a coronal HASTE sequence of the liver. The sequences were acquired with a dedicated 32-channel coil (Rapid Biomedical, Rimpar, Germany). Without parallel imaging severe blurring artefacts obscure the margins of the liver (*upper left*), with increasing acceleration factors of *R*=4 (*upper right*), *R*=6 (*lower left*) and *R*=8 (*lower right*) these blurring artefacts disappear, because the echo train length can be reduced effectively from 1,756 ms without parallel imaging to 220 ms with an acceleration factor of *R*=8. However, due to increased image noise in the center of the field of view – which is a typical artefact from parallel imaging – the optimal image quality is reached at a factor of *R*=6. The high image quality despite such a high acceleration factor is due to the field strength of 3 Tesla in this example (courtesy of Mark Griswold PhD, RAPID Biomedical, Rimpar, Germany and University of Wuerzburg)

an acceptable time of acquisition, which is not possible with 1.5 T systems (Figs. 21.8 and 21.9).

However, the application of abdominal studies to high-field systems is still considered problematic due to arising new problems. One of these problems is the specific absorption rate (SAR), which increases quadratically with the field strength, resulting in a major limitation, particularly for turbo-spin-echo sequences (Kangarlu et al. 1999). Among other innovative techniques, such as, for example, the hyperecho technique (Scheffler et al. 2003), which cannot be explained in detail here, parallel imaging helps to decrease the number of phase-encoding steps, thereby reducing the SAR effectively by 1/*R* with respect to the long-term averaging of SAR contributions. Other problems like dielectric resonance effects can be addressed by

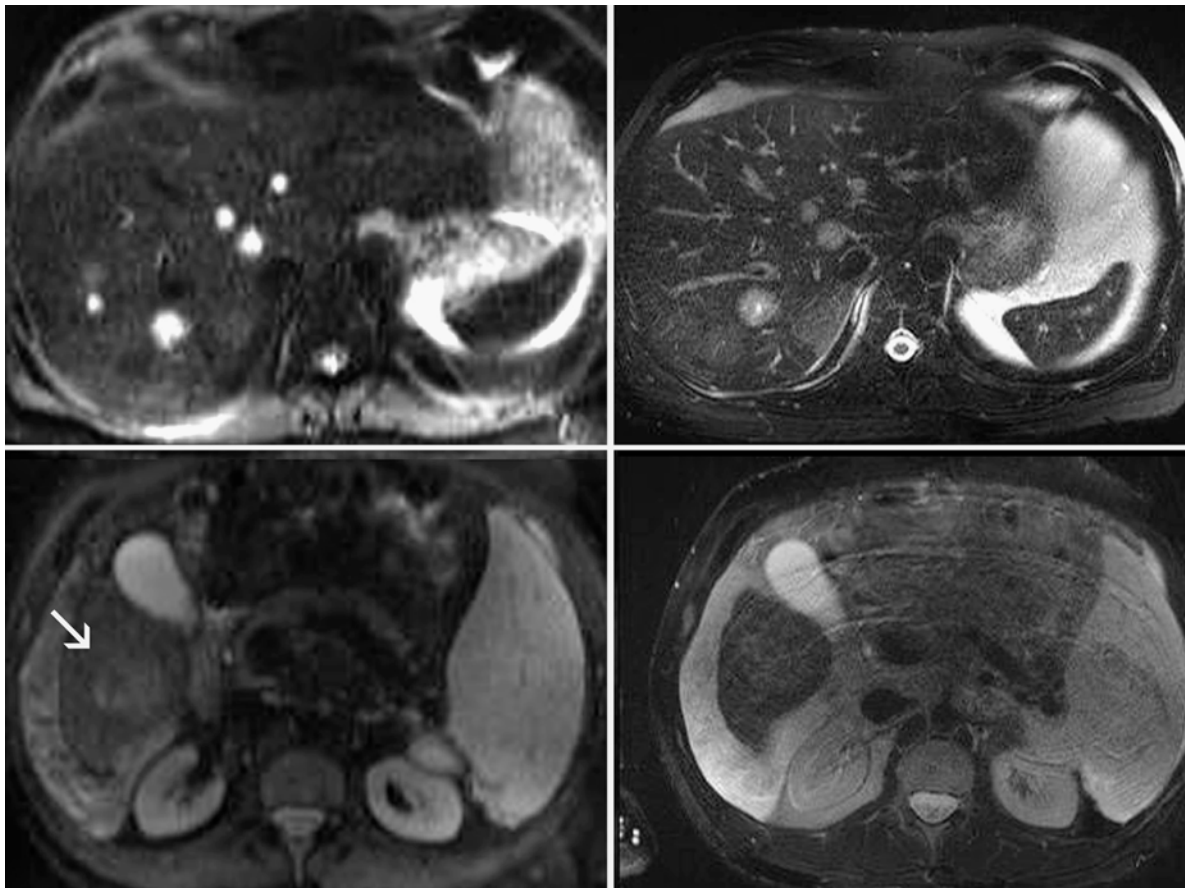

Fig. 21.7. Comparison of a diffusion-weighted EPI sequence (*left*) with a standard T2-weigthed TSE sequence (*right*). Due to the black-blood effect of the diffusion-weighted sequence, multiple liver metastases in this patient suffering from colorectal carcinoma can be delineated easily in contrast to the T2-weighted sequence, where high signal from liver vessels makes the evaluation more difficult in the *upper row*. The *lower row* shows a patient with liver cirrhosis and ascites suffering from a hepatocellular carcinoma, which can be delineated only in the diffusion-weighted sequence (*arrow*) due to fewer artefacts and superior tumor-to-liver contrast

external dielectric gel pads, placed on the anterior body surface, which increase the resistance for focal eddy currents. Overall, the combination of higher field strength with parallel imaging might offer new horizons for abdominal MRI.

21.5 Summary

In summary, the above-mentioned innovations help to establish a very high quality in MRI examinations of the liver. Each innovation alone, but particularly their combination, is of great value. Whereas the application of 3D sequences and navigator triggering is still confined to some sequences, parallel imaging is a universal technique to speed up the acquisition in all sequence types used for liver imaging at present. Moreover, the utilization of parallel imaging also allows increasing the spectrum of suitable sequences, as shown above with the example of diffusion-weighted EPI sequences. This outstanding and universal role of parallel imaging holds also true for the combination of parallel imaging with high-field MR systems.

Future developments have to aim at new coil geometries and more refined algorithms, which might allow even higher acceleration factors also for transversally orientated acquisitions without the loss of image quality. This is of importance as this will remain the orientation of choice for liver imaging.

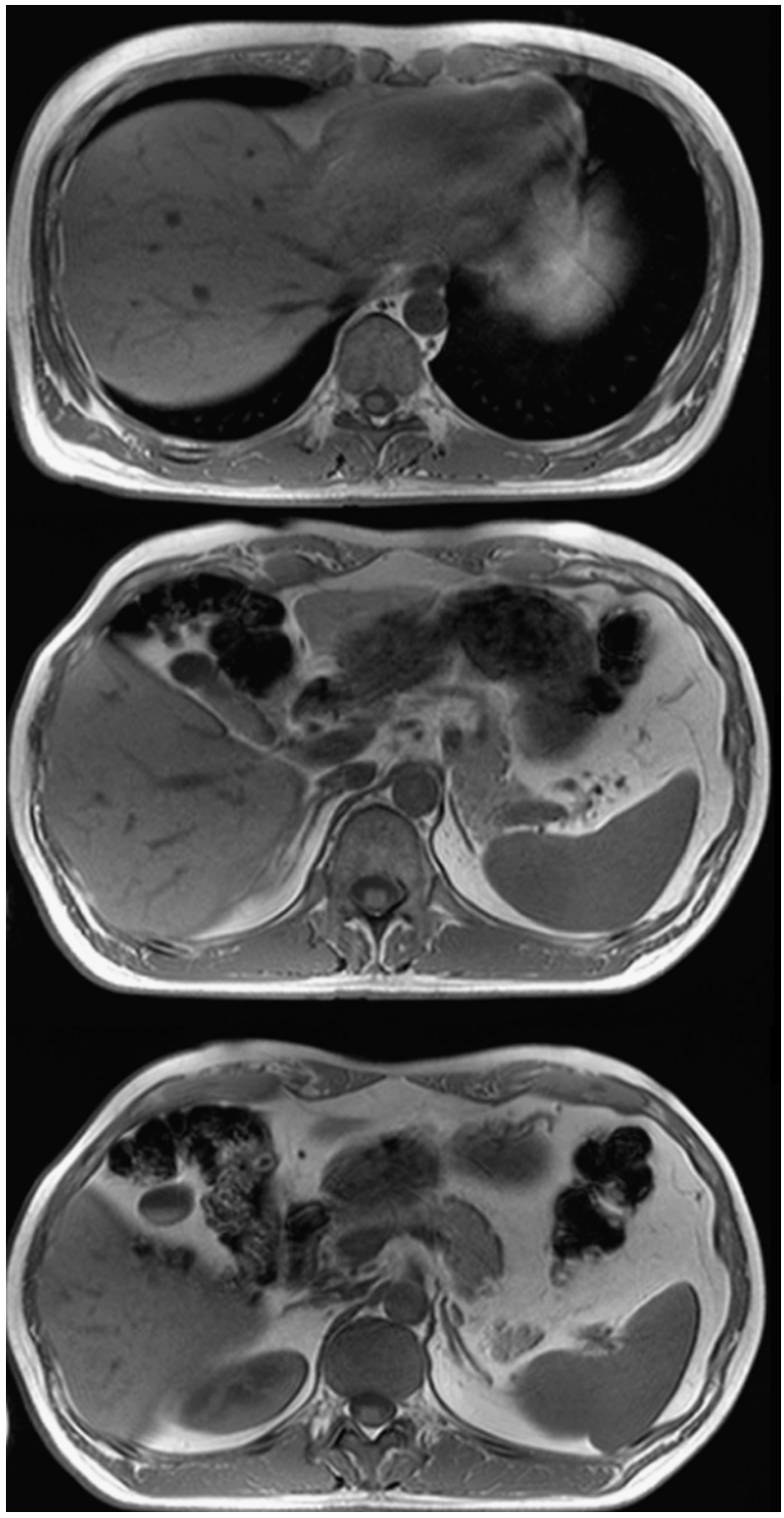

Fig. 21.8. T1-weighted 2D gradient-echo sequence from a 3-T MRI system (Magnetom Tim Trio, Siemens Medical Solutions, Erlangen) at three different levels. Throughout the whole liver, an excellent image quality can be seen. Note also the brilliant delineation of the right (*middle*) and left (*lower*) adrenal gland. This sequence with a 384 matrix and 5-mm slice thickness can be acquired at 3 T using a parallel imaging acceleration of R=2 within 3×17-s breath-hold (with a total of 39 slices the whole liver can be imaged without limitations in anatomic coverage)

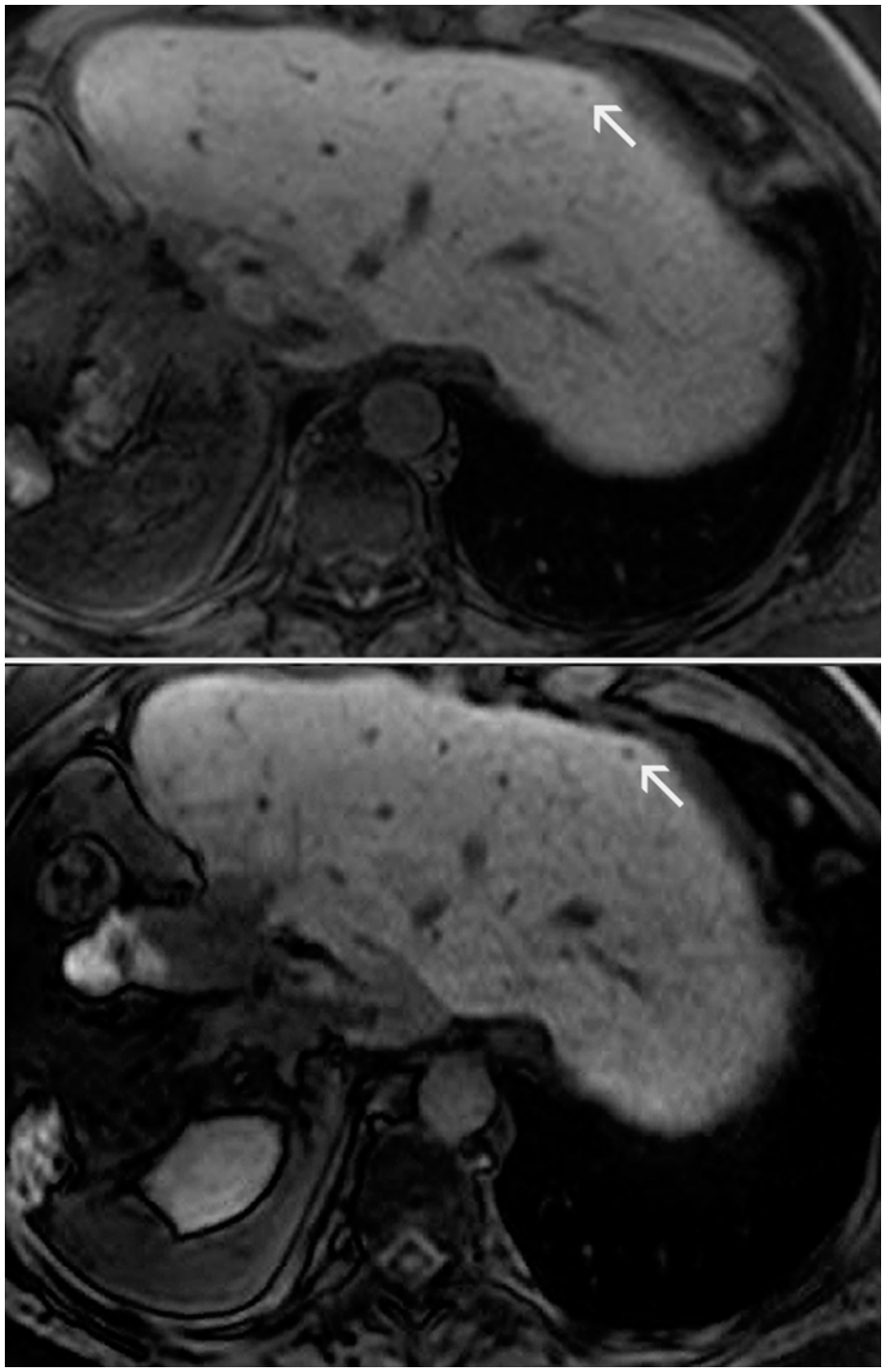

Fig. 21.9. MR examination of a 49-year-old female suffering from a Klatskin tumor with status post right-sided hemihepatectomy. T1-weighted 3D gradient-echo sequence (VIBE) in the liver-specific phase after injection of Gadolinium-EOB-DTPA (Primovist, Schering Deutschland GmbH, Berlin) at a 1.5-T MRI system (Magnetom Avanto, Siemens Medical Solutions, Erlangen) in the *upper row* and a 3-T MRI system (Magnetom Tim Trio, Siemens Medical Solutions, Erlangen) in the *lower* row. Note the excellent visualization of only 2 mm measuring tiny metastasis in the periphery of liver segment 2, which is enlarged after the hemihepatectomy; the depiction of the subtle finding is sharper in the sequence acquired on the 3-T MRI system due to the increased spatial resolution (3-mm slices; 256×180 in-plane matrix at 1.5 T; 2-mm slices; 320×160 in-plane matrix at 3 T; parallel imaging acceleration of R=2 in both acquisitions)

References

Augui J, Vignaux O, Argaud C et al (2002) Liver: T2-weighted MR imaging with breath-hold fast-recovery optimized fast spin-echo compared with breath-hold half-Fourier and non-breath-hold respiratory-triggered fast spin-echo pulse sequences. Radiology 223:853–859

Dobritz M, Radkow T, Nittka M, Bautz W, Fellner FA (2002) VIBE with parallel acquisition technique - a novel approach to dynamic contrast-enhanced MR imaging of the liver. Röfo Fortschr Geb Rontgenstr Neuen Bildgeb Verfahr 174:738–741

Griswold MA, Jakob PM, Heidemann RM et al (2002) Generalized auto-calibrating partially parallel acquisitions (GRAPPA). Magn Reson Med 47:1202–1210

Hennig J, Weigel M, Scheffler K (2003) Multiecho sequences with variable refocusing flip angles: optimization of signal behavior using smooth transitions between pseudo steady states (TRAPS). Magn Reson Med 49:527–535

Kangarlu A, Baertlein BA, Lee R, et al (1999) Dielectric resonance phenomena in ultra high field MRI. J Comput Assist Tomogr 23:821–831

Katayama M, Masui T, Kobayashi S et al (2001) Fat-suppressed T2-weighted MRI of the liver: comparison of respiratory-triggered fast spin-echo, breath-hold single-shot fast spin-echo, and breath-hold fast-recovery fast spin-echo sequences. J Magn Reson Imaging 14:439–449

McKenzie CA, Lim D, Ransil BJ et al (2004) Shortening MR image acquisition time for volumetric interpolated breath-hold examination with a recently developed parallel imaging reconstruction technique: clinical feasibility. Radiology 230:589–594

Lee VS, Lavelle MT, Rofsky NM et al (2000) Hepatic MR imaging with a dynamic contrast-enhanced isotropic volumetric interpolated breath-hold examination: feasibility, reproducibility, and technical quality. Radiology 215:365–372

Nitz WR (2003) Magnetic resonance imaging. Sequence acronyms and other abbreviations in MR imaging. Radiologe 43:745–763

Rofsky NM, Lee VS, Laub G et al. (1999) Abdominal MR imaging with a volumetric interpolated breath-hold examination. Radiology 212:876–884

Schaible R, Textor J, Kreft B, Neubrand M, Schild H (2001) Value of selective MIP reconstructions in respiratory triggered 3D TSE MR-cholangiography on a workstation in comparison with MIP standard projections and single-shot MRCP. Röfo Fortschr Geb Rontgenstr Neuen Bildgeb Verfahr 173:416–423

Zech CJ, Herrmann KA, Huber A, Dietrich O, Stemmer A, Herzog P, Reiser MF, Schoenberg SO (2004) High-resolution MR-imaging of the liver with T2-weighted sequences using integrated parallel imaging: Comparison of prospective motion correction and respiratory triggering. J Magn Reson Imaging 20:443-450

Zech CJ, Schoenberg SO, Menzel MI, Herrmann KA, Dietrich O, Reiser MF (2005) Black-blood-EPI sequences with parallel imaging for detection of focal liver lesions - comparison to a standard T2-weighted sequence. Proc Intl Soc Mag Reson Med 13:2070

22 High-Resolution Imaging of the Biliary Tree and the Pancreas

Astrid M. Wallnoefer, Christoph J. Zech and Karin A. Herrmann

CONTENTS

22.1 Introduction

Endoscopic retrograde cholangio-pancreaticography (ERCP) is still referred to as the gold standard in the diagnosis of pancreatico-biliary pathology. It was introduced as a diagnostic modality in 1968. As an invasive procedure it is associated with a morbidity of 7% and a mortality of 0.2% to 1.0%. With the introduction of pulse sequences for the non-invasive magnetic resonance cholangio-pancreaticography (MRCP) in 1986 by Hennig et al. (1986), a competitive diagnostic modality has become available that meanwhile is well accepted as a less intricate alternative to the invasive retrograde endoscopic cholangio-pancreaticography. Since MRCP has experienced tremendous technical improvement over the years, the method has evolved into a quick, simple, low-risk non-invasive imaging modality with the potential to replace ERCP in many respects. In certain aspects, it can also be considered superior to percutaneous ultrasound, computed tomography and percutaneous transhepatic cholangiography (PTC).

The following outline is designed to first give an overview on the current technical standards of MRCP imaging and the traditional and conventional state-of-the-art MRCP sequences and secondly to focus on the distinct technical advances and improvements with parallel imaging techniques with respect to the image acquisition and image quality of MRCP in diagnosing pancreatico-biliary pathologies.

22.2 Clinical Applications of MRCP

Numerous indications can be cited for MRCP as a non-invasive technique to assess the entire pancreatico-biliary system. The most frequent indication is to

A. M. Wallnoefer, MD; C. J. Zech, MD; K. A. Herrmann, MD
Department of Clinical Radiology, University Hospitals – Grosshadern, Ludwig Maximilian University of Munich, Marchioninistr. 15, 81377 Munich, Germany

rule out or confirm intra- or extrahepatic cholestasis, cholelithiasis and cholecystolithiasis.

22.2.1 Biliary Stones

Compared to ERCP, cholelithiasis can be diagnosed on standard MRCP with a sensitivity and specificity of 92% (80%-97%) and 97% (90%-99%), respectively (Guibaud et al. 1995; Holzknecht et al. 1998; Kim et al. 2002; Soto et al. 2000). The sensitivity in detecting biliary stones strongly correlates to the size of the stone and varies from 64% to 100% with a cut-off criterion of either greater or lesser than 3 mm (Mendler et al. 1998).

22.2.2 Biliary Stenosis

MRCP is also very sensitive in the detection and precise localization of stenoses within the pancreaticobiliary system. Sensitivities ranging from 91%–99% (mean 97%), and specificities around 84% have been reported with typical sequences currently proposed for this purpose (Holzknecht et al. 1998; Magnuson et al. 1999; Rosch et al. 2002). The underlying cause of the stenosis can be identified as benign or malignant with a sensitivity of 88% (70%-99%) (Holzknecht et al. 1998; Rosch et al. 2002; Urban et al. 2002). The sensitivity in the detection of stenosis depends on the degree of the luminal narrowing and the degree of the resulting cholestasis. High-grade and intermedium-grade stenoses are generally easily detected. Difficulties may be encountered in detecting low-grade stenoses in cases of minor or absent cholestasis as it is often the case in primary sclerosing cholangitis (PSC).

With conventional MRCP imaging, pathologic changes of the intra- and extrahepatic bile ducts in primary sclerosing cholangitis (PSC) can be identified with a sensitivity of 88% and a specificity of 97% (Fulcher et al. 2000). However, MRCP is still limited in the depiction of early pathologic changes in PSC presenting as discrete lumen irregularities in the second and higher-order branches. Owing to the availability of simultaneous cholangioscopy and endosonography and the option of direct injection and active dilatation of the biliary system with contrast medium, ERCP is still superior to MRCP for the assessment of low-grade stenoses without prestenotic dilatation. With ERCP, the volume charge and increased intraluminal pressure created by the injection of the contrast medium will induce active dilatation of the duct system and enlarge the lumen to its maximum diameter. Subtle parietal irregularities and low-grade stenoses are more easily displayed.

However, forced injection of contrast medium may result in iatrogenically induced pancreatitis or cholangitis (Loperfido et al. 1998). In a large trial including 2,769 patients with diagnostic and therapeutic ERCPs, the rate of major complications was 1.38% in the diagnostic investigations (n=942) with a mortality rate of 0.21% (Loperfido et al. 1998). Major complications were moderate and severe pancreatitis, cholangitis, hemorrhage and duodenal perforation.

22.2.3 Benign and Malignant Stenosing Disease

Differentiating between benign and malignant underlying pathology is successful with MRCP with a reasonably high sensitivity of 88% (70–99%) (Rosch et al. 2002; Urban et al. 2002). In contrast to ERCP, MRCP can be combined with further morphologic imaging sequences such as spin-echo and gradient-echo sequences in the same examination so as to complete the diagnostic work-up and include information on the hepatic parenchyma. By depicting also the tissue adjacent to the biliary system, potential mass effects, tumors or inflammatory reactions can be identified with an extended MRCP protocol, which significantly supports the differentiation between benign and malignant processes.

22.2.4 Post-Operative Assessment of the Biliary System

Further strengths of MRCP as a non-invasive procedure lie in the imaging of postoperative conditions when the access to the biliary system is limited for ERCP or PTC. MRCP is the modality of choice in the primary workup of postoperative complications to evaluate postoperative biliary leakage, stenoses or strictures of the bilio-digestive anastomosis, ischemic strictures as an early complication after liver transplantation and post-inflammatory or post-interventional fibrostenosis after cholecystectomy. These pathologies are well identified and distinguished with MRCP due to its high soft tissue contrast and the capability for imaging of the iuxta-luminal structures.

22.2.5 Normal Variants of the Biliary System

A non-invasive assessment of the biliary system is also warranted to rule out normal variants prior to biliary surgery or liver transplantation in order to prevent potential anatomy-related intra-operative complications. MRCP is ideal in this context, and normal anatomy, anatomic variants and congenital abnormalities of the biliary system and the pancreatic duct system such as a pancreas divisum have been shown to be easily identified with MRCP.

22.2.6 Pancreatic Duct System

In addition to the imaging of the biliary system, MRCP plays a major role in the non-invasive assessment of recurrent and chronic pancreatitis in ruling out or confirming potential underlying causes such as strictures of the biliary duct or pancreatic duct system, choledocholithiasis and tumors. The non-invasiveness of MRCP is again particularly advantageous in these cases, since with ERCP, imaging of the pancreatic duct can be difficult and prone to complications in the presence of chronic pancreatitis and strictures. ERCP implies a certain risk to induce pancreatitis as an iatrogenic complication in these cases.

22.3 Standard MRCP Sequences

Wallner et al. (1991) were the first to describe the value of T2-weighted sequences in the depiction of the biliary system with MRI. Thanks to the long T2 relaxation times of static or low-flow fluid, bile can be easily depicted on T2-weighted images, while fluid with shorter T2 relaxation times is less well appreciated due to lower signal on T2-weighted images. With ongoing improvements of the gradient systems, increased spatial resolution and shorter acquisition times have been achieved. State-of-the-art MRCP imaging currently uses ultra-fast turbo-spin-echo sequences. Two typical MRCP sequences are pivotal representatives of those:

- the (single-slice) thick-slab RARE-sequence (rapid acquisition with relaxation enhancement) (Nitz et al. 1999) and
- the (multi-slice) two-dimensional (2D) fast-spin-echo/turbo-spin-echo sequence with half-Fourier acquired k-space (single-shot FSE/TSE).

The RARE-sequence represents the so-called "projection technique." This type of MRCP is based on a 2D single-shot technique using one single slice with a high slice thickness of 30 mm to 100 mm (Laubenberger et al. 1995; Obenauer et al. 1999). The resulting T2-weighted image is similar to projection radiography. 2D-TSE sequences are used for the multi-slice approach. The most frequently employed sequence type of the multi-slice technique is the T2-weighted 2D half-Fourier-acquired single-shot turbo-spin-echo (HASTE) sequences. This acronym is subsequently used as a synonym for all thin-slice 2D-TSE sequences.

22.4 Technical Developments and Value of Parallel Imaging for MRCP

The major issues addressed with parallel-imaging techniques are the reduction of acquisition time, reduction of image blurring and simultaneous increase in spatial resolution. For MRCP, the use of 12-channel phased-array coils will allow acceleration factors (R) of, e.g., 6; however, signal-to-noise constraints favor the use of a maximum acceleration factor of 3. With 32-channel phased-array coils and higher field strengths, an acceleration factor of 6 is feasible without major limitations in image quality. In addition, high-resolution three-dimensional (3D) imaging of the biliary system with an isotropic voxel size of 1×1×1 mm³ or less has become feasible with parallel imaging using a T2-weighted 3D-TSE sequence with ultra-long echo trains, variable flip angles and restore pulses. This sequence opens new horizons for 3D post-processing and 3D image display and can be expected to revolutionize the diagnostic capabilities of MRCP in imaging the pancreatico-biliary system.

The benefits of parallel imaging for the quality and performance of MRCP are manifold. In the following sections, the distinct effects of parallel imaging on standard MRCP sequences will be described in detail. Furthermore, newly developed parallel-imaging sequences for MRCP will be presented and discussed as to their additional diagnostic value in current MR pancreatico-biliary imaging.

22.4.1 Thick-Slab Single-Shot RARE Sequences

The RARE sequence is a single-shot TSE technique. It was first established by Hennig et al. (1986) and introduced into clinical practice by Laubenberger et al. (1995) as an MRCP sequence in 1995. The RARE sequence is characterized by one 90° RF pulse followed by a single, particularly long echo train comprising, e.g., 256 or more spin echoes. All data are acquired after one single RF excitation pulse within one single echo train; every single spin echo will be separately phase-encoded. The echo time usually exceeds 635 ms and, thus, practically all signal from tissue apart from the bile is suppressed. The acquisition time of one single measurement is in the order of 1 s. In order to include the pancreatico-biliary system in its entire extent within one single planar projection, the measurement slab has a thickness of 30 mm to 100 mm (Laubenberger et al. 1995; Obenauer et al. 1999). Three different projections are acquired, which are angulated along the relevant anatomic structures of the biliary system such as the intra-hepatic bile ducts, the bile duct bifurcation, the choledochal duct and the pancreatic duct. These projections can be planned on standard T1- or T2-weighted sequences of the liver and the pancreas in transverse orientation.

The large slice thickness of RARE-sequences usually results in a certain impairment of the overall image quality. Subtle pathologic changes of the pancreatico-biliary system and small intra-ductal concrements may be missed on these projections, especially when surrounded with fluid. Furthermore, the detailed diagnostic analysis of the of the biliary system may suffer from projection effects of overlaying structures with high T2-weighted signal intensities such as ascites or other pathologic fluid collections that occur in exudative pancreatitis, pancreatic rupture or postoperative exudates. The diagnostic value of this projection technique is significantly limited in those cases.

The immanent advantage of RARE sequences is the ultra-fast image acquisition in the order of 1 s. Hence, for severely ill patients with limited respiratory capacities, the RARE sequence may be the only imaging technique to obtain sufficient image quality with the least artefacts. For RARE imaging, parallel-imaging techniques shorten the echo train length and thus reduce the blurring of the image (Fig. 22.1).

22.4.2 Two-Dimensional Multi-Slice Acquisitions – HASTE Sequence

The HASTE sequence is a single-shot TSE sequence allowing for sequential acquisition of high-resolution T2-weighted images. If used in the context of MRCP, this sequence is applied in transverse and coronal orientations and typically in conjunction with spectral fat saturation. Due to its high echo train length, this sequence type is particularly appropriate to imaging fluid. The entire 2D image data are acquired in a single echo train employing half-Fourier acquisition, which relies on the symmetry of the k-space.

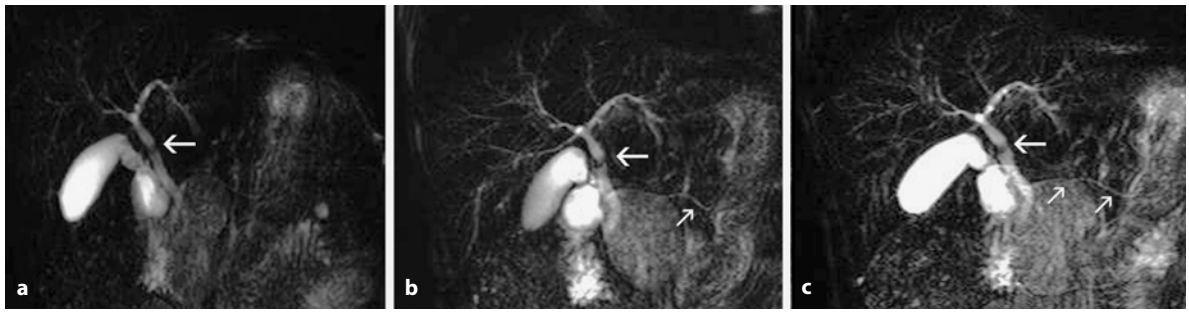

Fig. 22.1a–c. Influence of parallel imaging techniques on blurring artefacts and visualization of peripheral biliary ducts in a T2-weighted RARE sequence as used for MRC with a standard phased-array coil on a 32-channel 1.5-T system (Magnetom Avanto, Siemens Medical Solutions). Without parallel imaging **a** only the common bile duct and the biliary tree up to the first order are visualized in this 47-year-old female patient without a pathological finding. The signal extinction in the common bile duct (*arrow*) is caused by a flow artefact arising from the hepatic artery. Note the blurry depiction of the biliary structures; the pancreatic duct cannot be visualized. With increasing acceleration factors of **b** R=3 and **c** R=4 these blurring artefacts disappear because of the reduced echo train length. Note the depiction of the biliary tree up to the second to third order and faint visualization of the pancreatic duct (*small arrows*) in the images with parallel imaging

The acquired data fill half of the k-space while the remaining k-space data are reconstructed exploiting k-space symmetry. Usually, slightly more than half of the k-space is filled with primary data to perform a phase correction of the mirrored data. Since only half of the k-space is actively measured, this technique is very time effective. As a single-shot technique, HASTE is less susceptive to motion artefacts.

If used in the context of MRCP, HASTE images can be acquired using respiratory gating. To implement respiratory gating, a navigator is positioned at the dome of the diaphragm. The diaphragmatic movements are monitored with 2D gradient echo sequences using low spatial resolution and high temporal resolution with an image acquired every 150 ms (Zech et al. 2004). Navigator-based respiratory motion correction allows for both a free-breathing mode (respiratory gating) or a breath-hold mode for multi-stack breath-hold examinations, the latter being less frequently employed for MRCP imaging. Application of respiratory gating in multi-breath-hold examinations guarantees the correct display of the positions of the sequentially acquired slices within one slice stack without slice gaps or overlay. Without respiratory gating in this context so-called "serious misregistration artefacts" may occur. These artefacts represent gaps in the image information between subsequent image slices due to a different position of the diaphragm in different breath-holds. Respiratory gating for multi-breath-hold examinations helps to reduce these artefacts to a certain degree (Zech et al. 2004) since the patient's respiratory cycles may vary in depth and differ in the positioning of the diaphragm at each single breath hold, which may impair the diagnostic analysis.

HASTE sequences are distinctly robust against susceptibility artefacts, which is particularly advantageous in postoperative imaging of the biliary system if metallic clips have been used after cholecystectomy, liver resection or liver transplantation. As compared to the RARE and the subsequently mentioned 3D-TSE sequences, HASTE is characterized by a relatively short echo time of, e.g., 100 to 150 ms and a good depiction of soft tissue structures. The detailed evaluation of anatomic background allows for the differentiation of benign and malignant stenosis. HASTE is superior to other above-mentioned MRCP sequences in distinguishing structures adjacent to the biliary system. Periductal edema as an early indicator of initial cholangitis may be particularly appreciated in HASTE imaging with fat saturation (Fig. 22.2).

The major drawbacks of HASTE imaging are flow artefacts, which are likely to occur in the transverse slice orientation. To date, their origin remains unclear. One primary hypothesis is that they could be the consequence of arterial pulsation of adjacent vascular structure such as the hepatic artery or the portal vein (Holzknecht et al. 1998). Furthermore, the typically applied slice thickness of 3 mm in the *z*-axis may be considered a limitation in the detection of very small intra-ductal concrements.

Apart from this, HASTE imaging suffers from the presence of image blurring. With increasing duration of the echo train, the relevant signal in the tissue continuously decreases because of T2 relaxation, while image blurring increases. This effect is increased if tissue with relatively short T2 relaxation times (compared to the long T2 of fluids) is imaged, which is the case in HASTE sequences, while the thick-slab RARE techniques suppress virtually all signal from non-fluids. The essential benefit of parallel imaging in HASTE imaging lies in the reduction of these blurring artefacts, cf. Chap. 10. With parallel imaging, the echo train length can be significantly shortened, which results in a reduction of the image blurring. With higher acceleration factors, however, the gain in image quality is counterbalanced by the disproportionately increasing inherent noise created by parallel imaging at higher acceleration factors, since the distinct reconstruction algorithms additionally contribute to the lowering of the signal-to-noise as compared to non-accelerated imaging techniques (Heidemann et al. 2003). Currently, acceleration factors up to 3 are recommended and considered appropriate with a 32-channel acquisition system at 1.5 T. These parameters seem to represent an acceptable compromise between reducing image acquisition time and blurring artefacts on the one hand and decreasing signal-to-noise ratios on the other hand. With acceleration factors of 4 and more, the image noise increases to an unacceptable degree, mainly in the central portions of the resulting MR image. Higher acceleration factors of $R=6$ are possible when increasing the field strength from 1.5 to 3 T. An example of typical blurring artefacts with HASTE and the positive effect of parallel imaging in reducing the blurring are shown in Fig. 22.3 for a 3-T system.

22.4.3 Three-Dimensional Turbo-Spin-Echo Sequences – 3D-TSE

With the availability of parallel imaging, 3D imaging of the pancreatico-biliary system became both

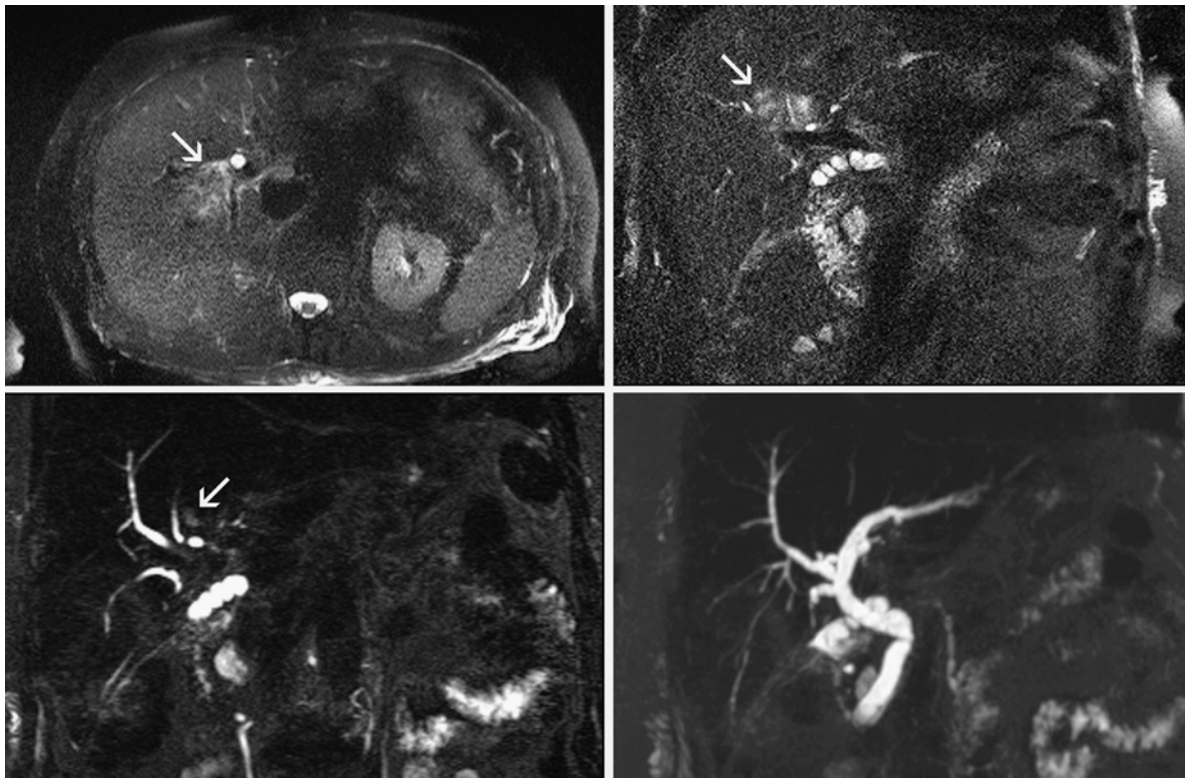

Fig. 22.2a–d. A 50-year-old female patient presenting with laboratory signs of inflammation after cholecystectomy is shown. HASTE sequence (slice thickness 3 mm; parallel-imaging acceleration factor *R*=2) discloses diffusely increased signal intensity in the central portion of the porta hepatis paralleling the vascular structures corresponding to a periductal edema and thus suggesting cholangitis **a.** The identical finding is shown in the coronal plane **b** of the HASTE-sequence (slice thickness 3 mm; acceleration factor *R* = 3). The corresponding slice in 3D-TSE imaging (slice thickness 1.5 mm; acceleration factor *R*=2) does not depict the periductal edema in single slice **c** or MIP display **d**. The intra-hepatic bile ducts show no irregularities

reachable and a future challenge. A T2-weighted 3D-TSE sequence has been proposed for the purpose of MRCP imaging (Barish et al. 1995; Soto et al. 1995). In 3D imaging, one single volume is acquired with contiguous slices and no gaps. 3D imaging requires an additional phase-encoding gradient along the slice-selection *z*-axis in addition to the frequency-encoding and phase-encoding gradients in the *x*-*y* plane. The spatial resolution of 3D-TSE sequences is significantly higher in the *z*-axis as compared to 2D imaging. On modern multi-channel MR-scanners with the option for parallel imaging, high-resolution imaging with isotropic voxel size and a spatial resolution of 1×1×1 mm³ are feasible.

By convention, the 3D slab for the MRCP imaging is oriented in the coronal plane, since the most distal portions of the pancreatic duct and the biliary ducts have orthogonal positions. Due to a longer time of acquisition, the application of navigator-based respiratory triggering is mandatory. The 3D properties of this T2-weighted TSE sequence and the isotropic voxel size allow for the 3D-post-processing of all data sets with multi-planar reformats (MPR), maximum intensity projections (MIP) and volume-rendering techniques and other 3D functions (Fig. 22.4). These functions provide new facilities in displaying the pancreaticobiliary system that have not been accessible up to now. Volume-rendering techniques seem distinctly helpful to improve the display of variations in the caliber of the intra-hepatic biliary ducts more conspicuously (Fig. 22.5). This improvement is particularly obvious in the second and higher order branches, which are not adequately displayed on 2D sequences.

High-resolution imaging requires longer acquisition times. The overall acquisition time of 3D-TSE sequences is generally substantially higher than with all previously mentioned sequence types and reduces to only 3-5 min with parallel imaging. This comparably long acquisition time of 3D-TSE sequences will result in severe motion artefacts, which is why respi-

ratory triggering is mandatory. For an efficient image acquisition and good image quality, a deep and regular respiration cycle is favorable to accelerate the data acquisition, since irregular breathing may increase the acquisition time to over 5 min. Without parallel imaging, the acquisition time with this sequence type usually exceeds 8 min.

In conventional imaging, motion artefacts are reduced by increasing the number of averages. This approach can also be employed with parallel-imaging techniques. Doubling the averaging and using parallel imaging at an acceleration factor of 2 will still allow keeping the acquisition time constant, e.g., at 5 min. The resulting diagnostic image will be less disturbed with motion artefacts. With an acceleration factor of 4 and an 8-channel coil system at 3 T, the overall acquisition time for a 3D-TSE can be further diminished to values of 2 to 3 min. Nonetheless, motion artefacts cannot be entirely eliminated with these techniques.

According to initial preliminary results, 3D-TSE sequences with parallel imaging and respiratory triggering yield significantly better image quality compared to RARE and 2D HASTE imaging in breath-hold technique (Miller et al. 2004). Our own experience supports these results according to which the 3D-TSE with parallel imaging yields better results in image quality and the detection of small details such as the smallest intra-ductal concrements (Wallnoefer et al. 2005). Isotropic spatial resolution allows for multi-planar reconstruction and reformats of projection images in any virtual plane. In this same preliminary study, the conspicuity of all structures except the duodenum and the gallbladder was significantly better with respiratory-triggered 3D-MRCP (Miller et al. 2004).

3D-TSE with the free-breathing mode was superior to the breath-hold 3D-TSE and thick-slab 2D-RARE breath-hold technique regarding signal-to-noise and contrast-to-noise ratios (Zang et al. 2004). However,

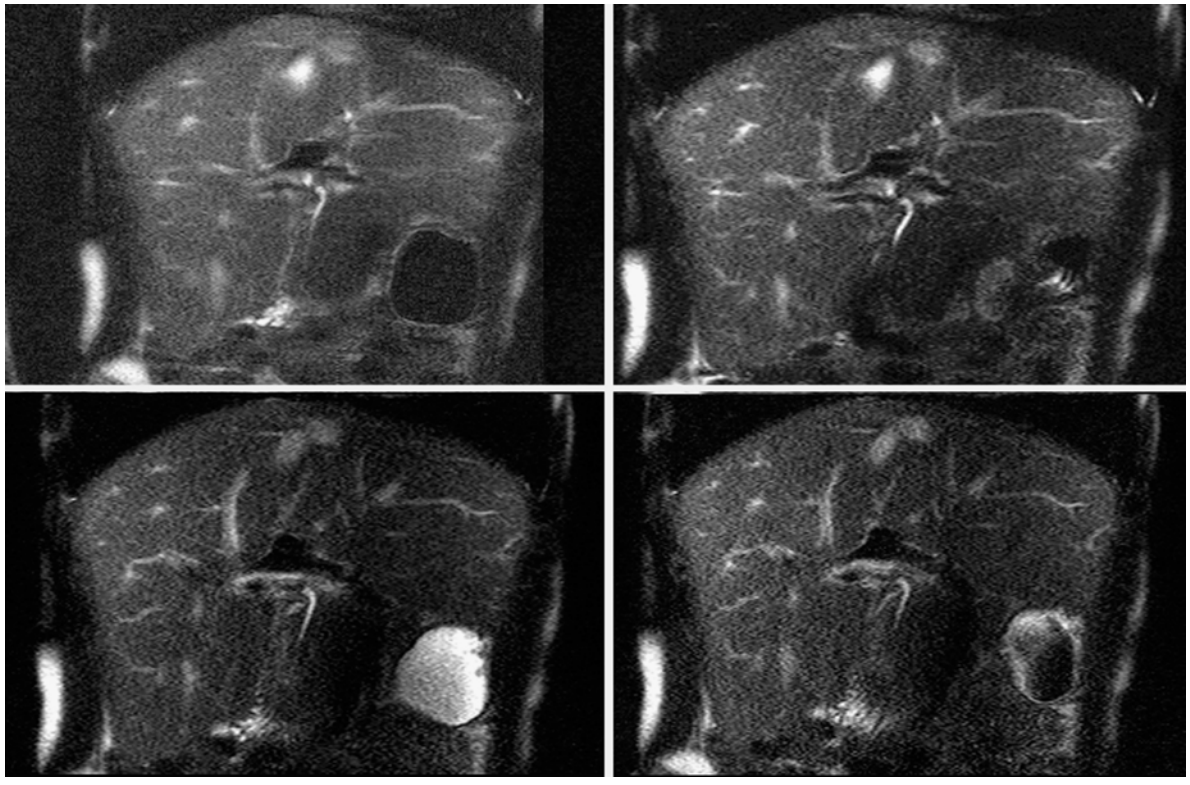

Fig. 22.3a–d. Influence of parallel imaging techniques on blurring artefacts in a T2-weighted HASTE sequence as used for MRC with a standard phased-array coil on a 32-channel 3-T system (Magnetom Tim Trio, Siemens Medical Solutions). Without parallel imaging severe blurring artefacts obscure the margins of the liver **a**, with increasing acceleration factors of **b** *R*=4, **c** *R*=6 and **d** *R*=8 these blurring artefacts disappear, because the echo train length can be reduced effectively from 1,756 ms without parallel imaging to 220 ms with an acceleration factor of *R*=8; however, due to increased image noise in the center of the field of view – which is a typical artefact from parallel imaging – the optimal image quality is reached at a factor of *R*=6. The high image quality despite such a high acceleration factor is owing to the field strength of 3 T in this example

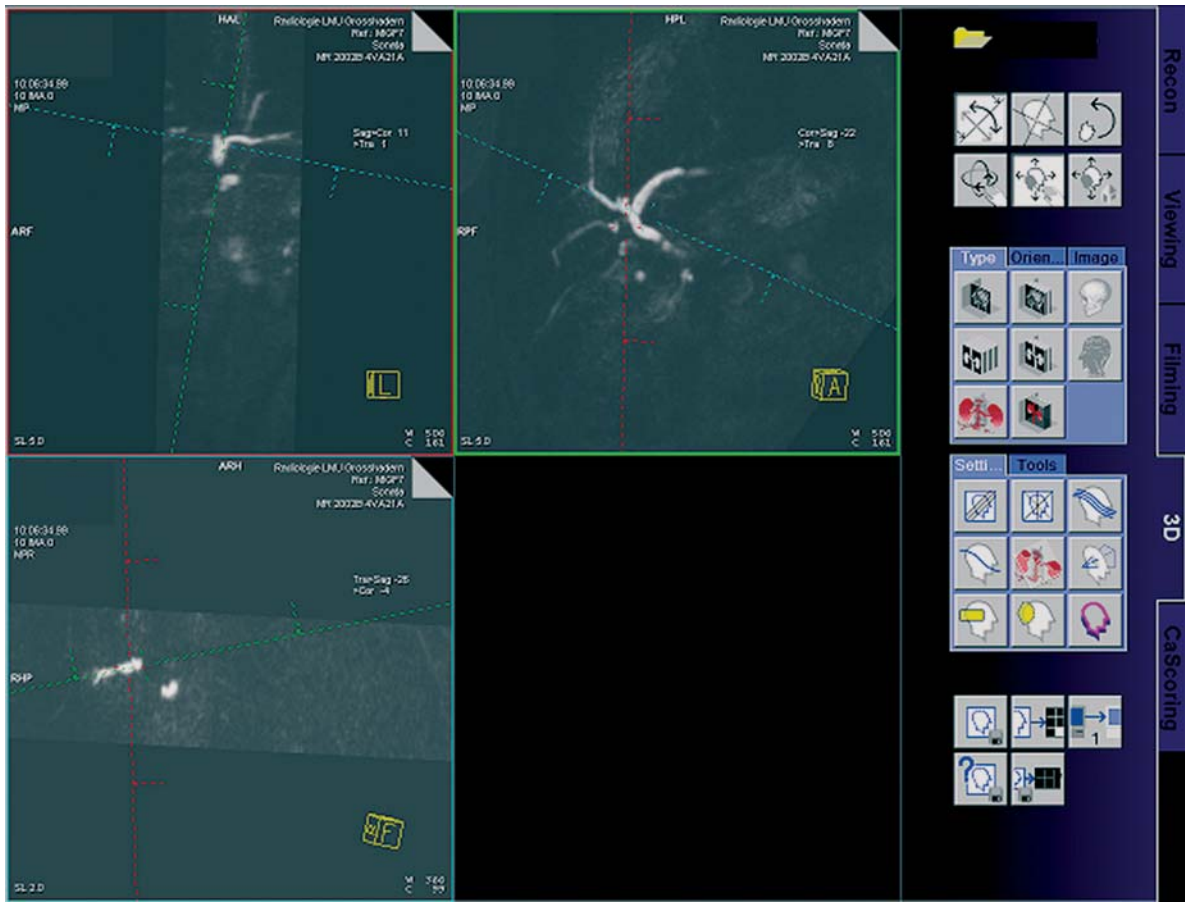

Fig. 22.4. 3D post-processing options for 3D-TSE sequences on a standard 3D Workstation (Leonardo, Siemens Medical Erlangen): MPR, MIP and volume-rendering techniques

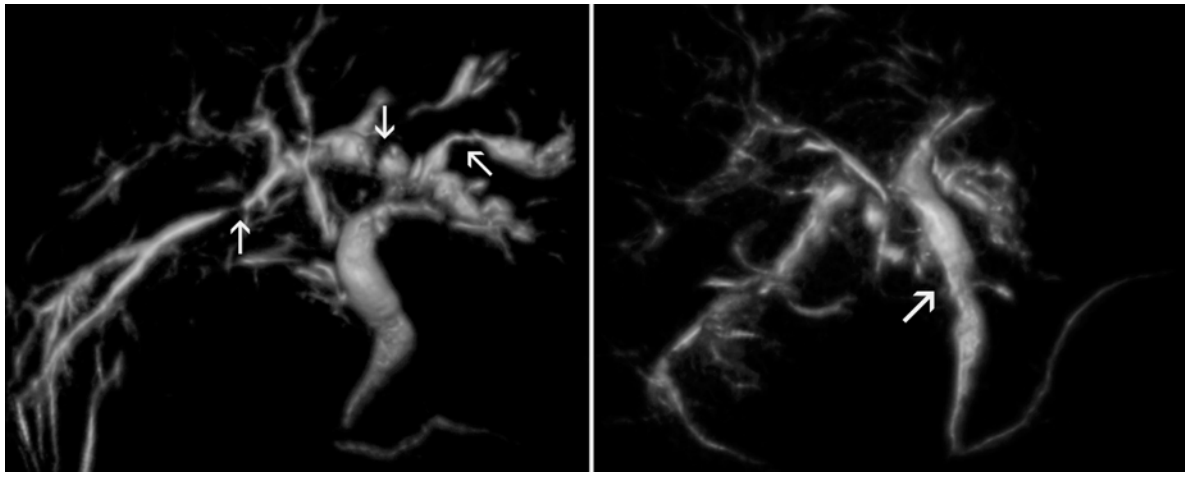

Fig. 22.5. A 42-year-old male patient with primary sclerosing cholangitis (PSC). Volume rendering of a submillimeter 3D dataset with 0.9×0.9×0.9 mm^3 voxel size acquired on a 3-T MR system (Magnetom Trio, Siemens Medical Solutions, Erlangen). On the *left side* a view from the anterior and on the *right side* a view from the oblique anterior-lateral is shown. The anterior view shows the severe intra-hepatic biliary duct stenoses (*arrows*) with pre-stenotic dilatation in both liver lobes. The anterior-lateral view shows the stenosis in the common bile duct (*larger arrow*), suspicious of a cholangiocarcinoma, which was confirmed by surgery

in case of an unstable respiration, drop-outs in image quality can occur with the free-breathing technique (Masui et al. 2004).

Preliminary results have shown 3D-TSE sequences to provide a higher sensitivity in the detection of small gall stones when compared to the HASTE and RARE sequences. Especially prepapillary concrements are more reliably detected on 0.6-1.2-mm slices and represent a significant increase in diagnostic performance. Multi-planar reformations are particularly helpful in doubtable cases of pathologic findings identified in one plane. In these cases multi-planar reconstructions help to specify the diagnosis without additional data acquisition. When compared to the HASTE sequence, 3D-TSE images are less susceptible to intra-luminal flow artefacts according to our own experience, which supports the high performance in diagnosing small stones. Figure 22.6 shows an example of a 68-year-old patient presenting with a small prepapillary concrement.

Owing to higher spatial resolution and options of 3D post-processing, the assessment of low-grade peripheral stenoses that do not reveal cholestasis is facilitated especially in patients with primary sclerosing cholangitis (PSC). These patients profit from 3D-TSE and parallel imaging. The combination of parallel imaging techniques and higher field strength will most probably enhance this diagnostic benefit and increase the diagnostic quality as has been shown in Fig. 22.5 (a 42-year-old patient with PSC and cholangio-cellular carcinoma). Further studies have to clarify if MRI at its latest state-of-the-art imaging with the newest technological advances can challenge the standard of ERCP.

One major disadvantage of the 3D-TSE sequence is its relatively long acquisition time and therefore its potential susceptibility to motion artefacts. Strong T2-weighting and long echo time result in excellent depiction of fluid-filled structures, but suppress

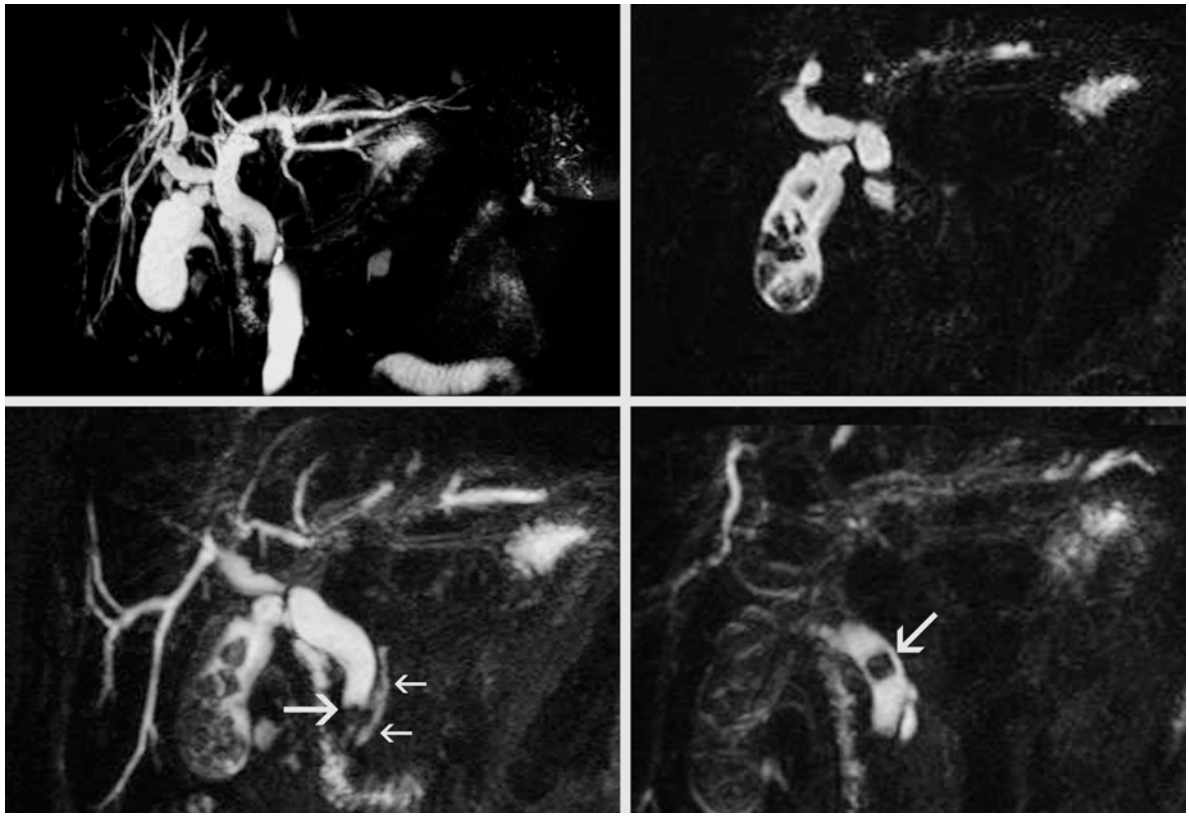

Fig. 22.6a–d. 3D-TSE MRCP of a 68-year-old female patient with acute onset of jaundice is shown. All images (thick MIP, thin MIPs and MPRs) are derived from one single dataset, which was acquired in 4 min 15 s. The thick MIP clearly shows the intra- and extrahepatic cholestasis **b**; however, only the morphology of the common bile duct disruption raises suspicion of a pre-papillary concrement, which cannot be appreciated in this image. An MPR shows multiple concrements in the gallbladder **a**. The thin MIP reconstructions **d, c** can clearly visualize this pre-papillary concrement (*arrow*) and a further concrement in the common bile duct along with multiple biliary concrements in the gall-bladder; note also the slight dilatation of the proximal pancreatic duct (*small arrows*)

clear delineation of surrounding organic and soft tissue structures. Anatomic relationships, parenchymal structures and the characterization of the tissue adjacent to the biliary system are more conspicuous on HASTE sequences than on RARE or 3D-TSE imaging.

22.4.4 Diffusion Weighted Imaging of the Liver with Black-Blood Echo-Planar Imaging

The advent of parallel imaging techniques opens the access to new sequence types. Diffusion-weighted black-blood echo-planar imaging (BB-EPI) sequences were introduced for liver imaging to determine their potential diagnostic purposes in pancreatico-biliary pathologies. The use of parallel imaging allows implementing this type of sequences without major image distortion, cf. Chap. 10. Apparently, BB-EPI sequences present as favorable in the imaging of the biliary system and open new horizons of diagnostic information.

According to our own preliminary experience in ten healthy volunteers, BB-EPI sequences are capable of distinguishing dilated and cholestatic segments of the bile system from non-dilated bile ducts. Intrahepatic cholestasis and limited and reduced bile flow result in an increase in signal intensity within the corresponding bile ducts. The underlying cause of cholestasis does not have any influence on this effect and does not affect the presence of this finding. In our study design, ten healthy volunteers underwent MRCP with standard sequences and BB-EPI after fasting for >6 h before and after a high-caloric meal. In all situations, the bile ducts were depicted with low signal intensity on BB-EPI. When compared to patients with cholestasis proven at ERCP, dilated and cholestatic bile ducts exhibited high signal intensities within the corresponding depending segments (Fig. 22.7). Hence, BB-EPI seems to be capable of differentiating between cholestatic and non-cholestatic segments, independently of the diameter of the respective bile duct.

22.5 Future Developments for MRCP

Breath-hold sequences are indispensable in abdominal MR imaging. With parallel imaging, the total acquisition time for those sequence types can be significantly reduced. Typical acquisition times are in the range of 20 to 25 s per breath-hold. In patients with respiratory impairment and in severely ill patients, this may exceed their limits of compliance. Parallel imaging is very helpful to compensate for these inabilities.

A major motivation of parallel imaging is to increase spatial and temporal resolution simultaneously. Signal-to-noise is limited with short acquisition times. High-field scanners at 3 T will provide a higher

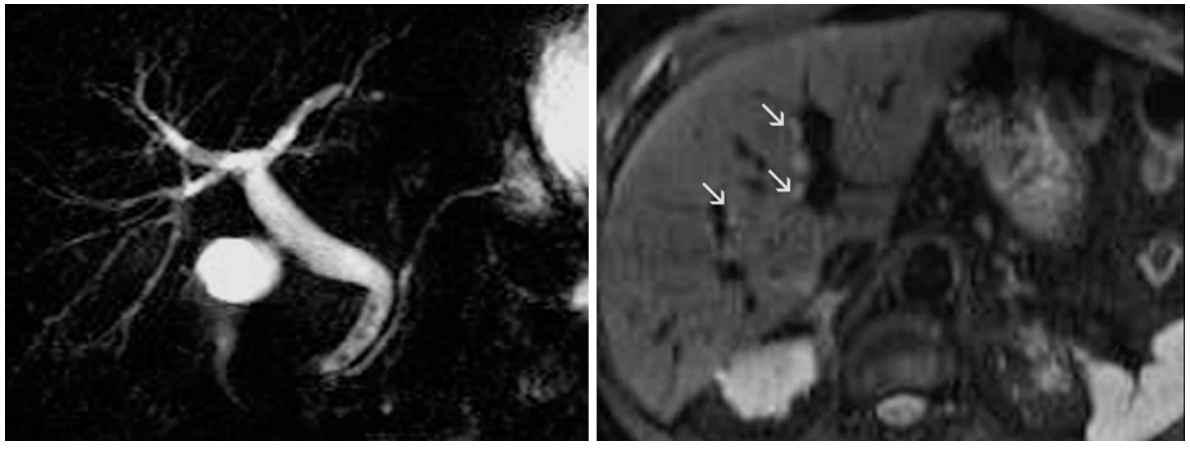

a b

Fig. 22.7a,b. 3D-TSE sequence (acceleration factor R=2) with MIP projection **a** in a 40-year-old female patient with small intraductal concrements in the prepapillary section of the choledochal duct associated with intra- and extra-hepatic cholestasis. **b** Black-blood echo planar imaging (EPI; b-value: 50 s/mm²; acceleration factor R=2) in the same patient shows increased signal within the dilated biliary system indicating limited free motion and reduced bile flow, therefore supporting the diagnosis of cholestasis

signal-to-noise ratio. Besides the advantageous effects on image quality and image acquisition time, high-field imaging is linked to higher specific absorption rates (SAR), which may rise in critical regions.

With respect to MRCP imaging with HASTE sequences, this is particularly of concern since this type of sequence requires multiple refocusing 180° pulses and thus causes high SAR. Lowering the flip angles of these refocusing pulses, e.g., with an optimized series of refocusing pulses <180° (hyperecho technique, Hennig and Scheffler 2001) could contribute to solving this problem. The increase in the signal-to-noise ratio at 3 T in conjunction with the hyperecho technique and higher acceleration factors would allow HASTE imaging to be improved and more advanced in spatial and temporal resolution. 3D-TSE imaging will profit from 3 T in that higher spatial resolution will improve the depiction of fourth and fifth level intrahepatic bile ducts so that a higher sensitivity and diagnostic reliability may be achieved in the early stages of PSC and other benign or malignant pathologies in their early stages. However, one drawback is the occurrence of signal loss from dielectric artefacts in the abdomen at 3 T (Table 22.1).

22.6 Pancreatic Imaging

Magnetic resonance imaging is an established diagnostic procedure in the assessment of pancreatic disease. With the help of a gadolinium-enhanced MRI, pathological conditions such as ductal adenocarcinoma, chronic pancreatitis, neuroendocrine tumors, cystic neoplasms and intraductal papillary mucinous tumors can be detected and differentiated with high confidence (Pamuklar et al. 2005; Pilleul et al. 2005). Due to the small extension of the pancreas and of pancreatic lesions, a high spatial resolution is mandatory for the exact evaluation of pancreatic pathologies. This fact makes modern multidetector-CT (MDCT) scanners a strong competitor for pancreatic MRI, since excellent image quality and the highest spatial resolution can be provided by MDCT robustly (Prokesch et al. 2003). Therefore, all techniques that can increase the spatial resolution, that can overcome the problem of respiratory motion and that can decrease the time of acquisition are of high interest for pancreatic MRI (Fig. 22.8). Along with the innovations described in Chap. 21, parallel imaging helps to achieve that goal. If image quality and spatial resolution can be kept at a high level, MRI has several advantages over CT. On the one hand tissue characterization and differentiation are made easier by the intrinsic high signal intensity differences of pancreatic tissue, fluid, fat or tumor tissue. This capability can be increased by using extracellular contrast agents or even tissue-specific contrast agents such as, for example, mangafodipir trisodium (Teslascan, GE Healthcare, Norway) (Schima et al. 2002) (Fig. 22.9). On the other hand, imaging of the pancreatic duct structures is non-invasively possible without differences in image quality in comparison to the invasive procedure of ERCP (Calvo et al. 2002).

As pointed out for the liver in Chap. 21, parallel imaging can be recommended as a standard with an acceleration factor of R=2 for the transversal as well as the coronal orientation. Aliasing artefacts have to

Table 22.1 Sequence parameters for MRCP with parallel acquisition techniques

Sequence parameters	RARE sequence	T2-HASTE	3D TSE
TR	4,500 ms	1,040 ms	2,000 ms*
TE	635 ms	114 ms	889 ms
FOV	320 mm	380 mm	400 mm
Slice thickness	50 mm	3 mm	1.5 mm
Number of slices	1	36	40
Resolution	1.1×0.9×50 mm³	1.4×1.4×3.0 mm³	1.2×1.1×1.5 mm³
Matrix	384	320	384
Time of acquisition	0.5 s	2-3×18-15 s	3-5 min
Respiratory acquisition mode	Breath-hold	Breath-hold or respiratory gating	Respiratory gating

*Effective time of repetition with respiratory gating depends on the length of the individual respiratory cycle of the patient and ranges between 4 and 5 s

be avoided by applying GRAPPA or choosing a sufficiently large field of view, because any artefacts in the center of the field of view will obscure the region of the pancreatic head and might result in an insufficient study. The background of these phenomena has already been displayed in Chap. 21.4.1. In contrast to MRI of the liver, the coronal orientation is very helpful in pancreatic imaging; therefore, the application of higher acceleration factors, as is possible for coronal acquired sequences or the combination of parallel imaging in two orientations in 3D sequences, is of relevance in the daily practice. This holds true both for T1-weighted 3D gradient-echo sequences, which are required for the detection of pancreatic adenocarcinoma and which allow an excellent depiction of the pancreatic parenchyma, as well as for T2-weighted 3D TSE sequences for the depiction of the pancreatic duct.

References

Barish MA, Yucel EK, Soto JA et al (1995) MR cholangiopancreatography: efficacy of three-dimensional turbo spin-echo technique. AJR 165:295–300

Calvo MM, Bujanda L, Calderon A, et al (2002) Comparison between magnetic resonance cholangiopancreatography and ERCP for evaluation of the pancreatic duct. Am J Gastroenterol 97:347–353

Fulcher AS, Turner MA, Franklin KJ et al (2000) Primary sclerosing cholangitis: evaluation with MR cholangiography - a case-control study. Radiology 215:71–80

Guibaud L, Bret PM, Reinhold C et al (1995) Bile duct obstruction and choledocholithiasis: diagnosis with MR cholangiography. Radiology 197:109–115

Heidemann RM, Oszarlak O, Parizel PM et al (2003) A brief review of parallel magnetic resonance imaging. Eur Radiol 13:2323–2337

Hennig J, Nauerth A, Friedburg H (1986) RARE imaging: a fast imaging method for clinical MR. Magn Reson Med 3:823–833

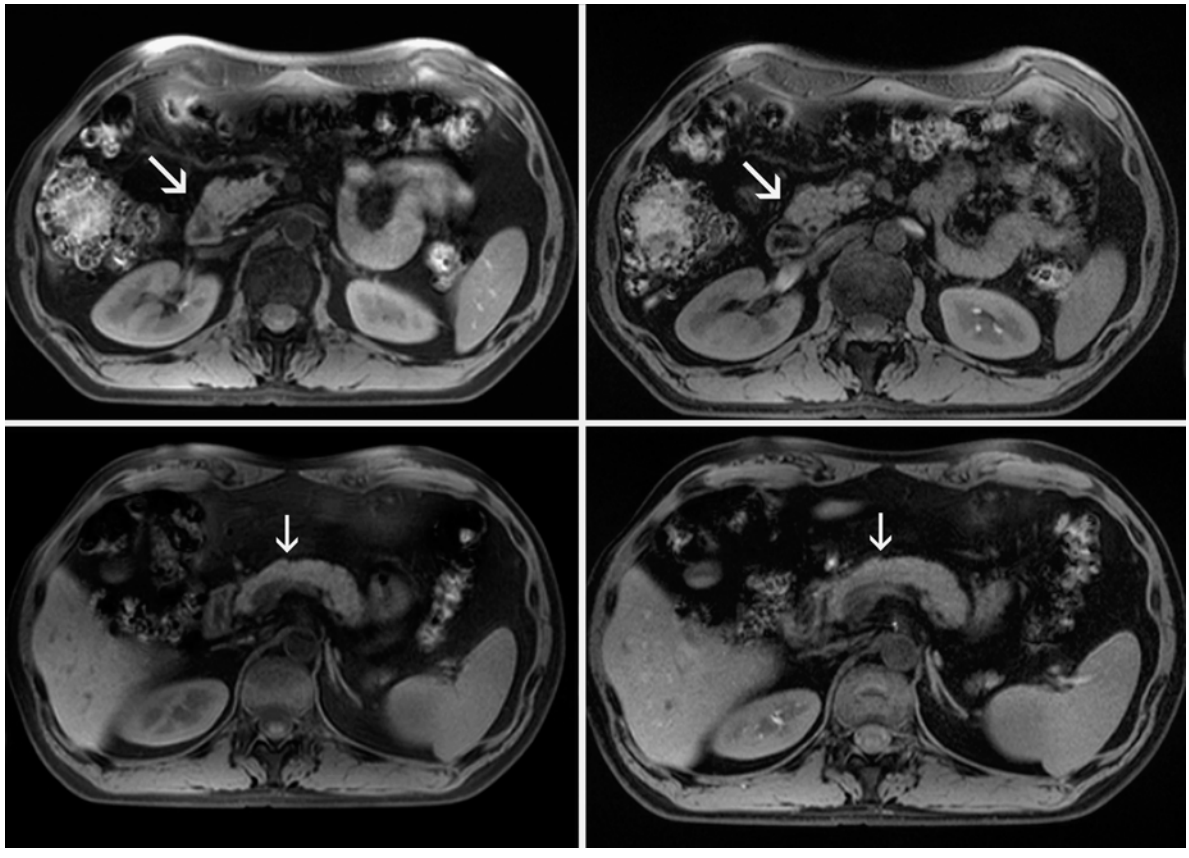

Fig. 22.8. Depiction of the pancreas with a T1-weighted 2D FLASH sequence with fat saturation on a 3-T system (Magnetom Trio, Siemens Medical Solutions) in a healthy volunteer. The sequence with 5-mm slice thickness and a 320×256 matrix (*left*) shows already a very good visualization of the anatomical area of the pancreatic head and the pancreatic tail (*arrows*). However, on the 3-T system a substantial increase in spatial resolution with 3-mm slice thickness and a 384×320 matrix is still possible without a visible loss of signal (*right*). Note the superior visualization of the pancreas on the *right side*. Both sequences are acquired with parallel imaging (GRAPPA; acceleration factor of R=2)

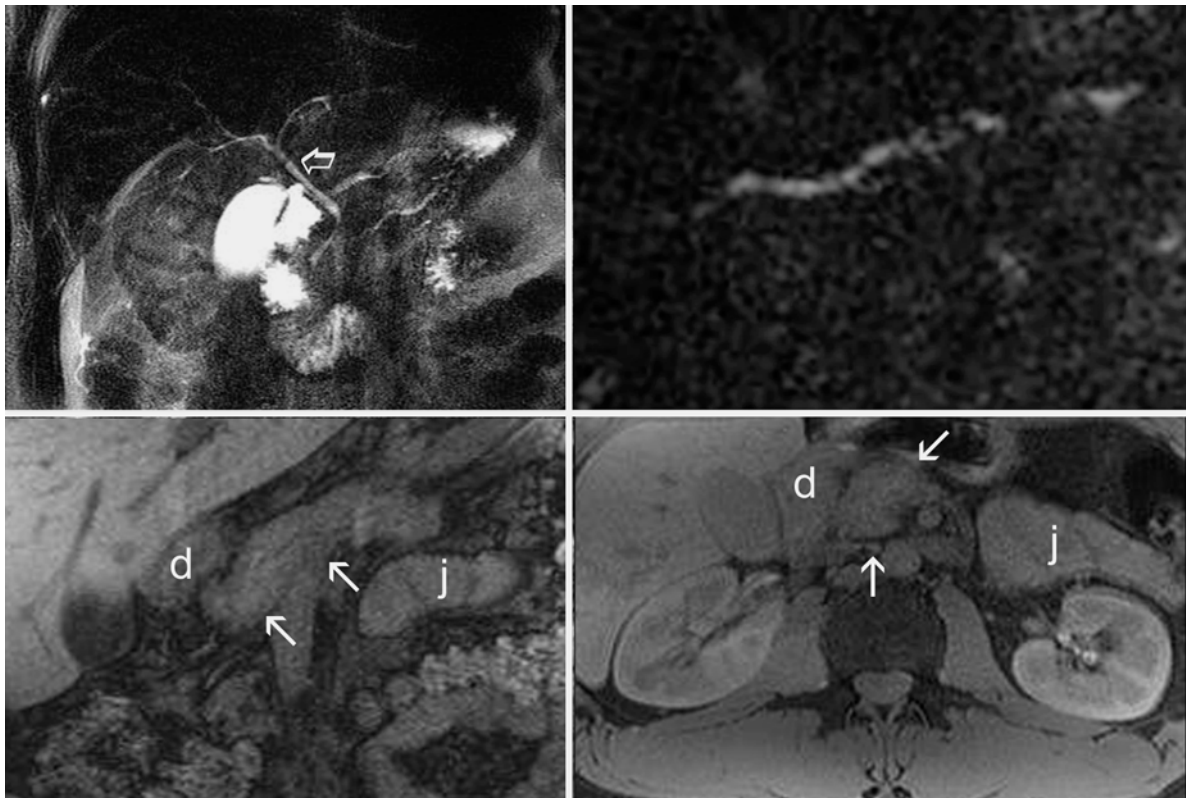

Fig. 22.9a–d. A 27-year-old male patient with a history of recurrent pancreatitis. MRCP and MRI of the pancreas after slow infusion of mangafodipir trisodium (Teslascan, GE Healthcare, Norway) on a 3-T system. Thick-slab RARE sequence demonstrates a normal finding of the biliary system **a**. Note the signal extinction in the common bile duct (*broad arrow*) due to pulsation of the hepatic artery. A dedicated examination of the pancreatic duct with help of a T2-weighted 3D-TSE fat-saturated sequence (displayed a thick MIP orientated along the axis of the pancreatic duct in coronal orientation) shows severe changes with duct irregularities, compatible with a status post recurrent pancreatitis; there is no evidence of a malignant stenosis with pre-stenotic duct dilatation **b**. The mangafodipir-enhanced images **c, d** show absence of a tumor in the pancreas (*arrows*), duodenum (*d*) and jejunal loops (*j*)

Hennig J, Scheffler K (2001) Hyperechos. Magn Reson Med 46:6–12

Holzknecht N, Gauger J, Sackmann M et al (1998) Breath-hold MR cholangiography with snapshot techniques: prospective comparison with endoscopic retrograde cholangiography. Radiology 206:657–664

Kim JH, Kim MJ, Park SI et al (2002) MR cholangiography in symptomatic gallstones: diagnostic accuracy according to clinical risk group. Radiology 224:410–416

Laubenberger J, Büchert M, Schneider B et al (1995) Breath-hold projection magnetic resonance-cholangio-pancreaticography (MRCP): a new method for the examination of the bile and pancreatic ducts. Magn Res Med 33:18–23

Loperfido S, Angelini G, Benedetti G et al (1998) Major early complications from diagnostic and therapeutic ERCP: a prospective multicenter study. Gastrointest Endosc 48:1–10

Magnuson TH, Bender JS, Duncan MD et al (1999) Utility of magnetic resonance cholangiography in the evaluation of biliary obstruction. J Am Coll Surg 189:63–72

Masui T, Katayama M, Yhamasita S (2004) Comparison of respiratory triggered and breath hold MRCP using 3D FR TSE with an 8 channel phased array coil in combined use of ASSET ISMRM, Kyoto, Japan. Proc Int Soc Magn Reson Med 12:907

Mendler MH, Bouillet P, Sautereau D et al (1998) Value of MR cholangiography in the diagnosis of obstructive diseases of the biliary tree: a study of 58 cases. Am J Gastroenterol 93:2482–2490

Miller FH, Fasanati N, Hammond P et al. (2004) MRCP with the use of navigator-echo triggering TSE: a comparison with single shot techniques ISMRM, Kyoto, Japan. Proc Int Soc Magn Reson Med 12:432

Nitz WR (1999) MR imaging acronyms and clinical applications. Eur Radiol 9:979–997

Nitz WR (2003) Magnetic resonance imaging. Sequence acronyms and other abbreviations in MR imaging. Radiologe 43:745–763

Obenauer S, Fischer U, Heuser M et al (1999) Optimierung der MR-Cholangiopankreatikographie. Fortschr Röntgenstr 171:450–454

Pamuklar E, Semelka RC (2005) MR imaging of the pancreas. Magn Reson Imaging Clin N Am 13:313–330

Pilleul F, Rochette A, Partensky C, Scoazec JY, Bernard P, Valette PJ (2005) Preoperative evaluation of intraductal papillary

mucinous tumors performed by pancreatic magnetic resonance imaging and correlated with surgical and histopathologic findings. J Magn Reson Imaging 21:237–244

Prokesch RW, Schima W, Chow LC, Jeffrey RB (2003) Multidetector CT of pancreatic adenocarcinoma: diagnostic advances and therapeutic relevance. Eur Radiol 13:2147–2154.

Rosch T, Meining A, Fruhmorgen S et al (2002) A prospective comparison of the diagnostic accuracy of ERCP, MRCP, CT and EUS in biliary strictures. Gastrointest Endosc 55:870–876

Schima W, Fugger R, Schober E, Oettl C, Wamser P, Grabenwoger F, Ryan JM, Novacek G (2002) Diagnosis and staging of pancreatic cancer: comparison of mangafodipir trisodium-enhanced MR imaging and contrast-enhanced helical hydro-CT. Am J Roentgenol 179:717–724

Soto JA, Barish MA, Yucel EK et al (1995) Pancreatic duct: MR cholangiopancreatography with a three-dimensional fast-spin-echo technique. Radiology 196:459–464

Soto JA, Barish MA, Alvarez O et al (2000) Detection of choledocholithiasis with MR cholangiography: comparison of three-dimensional fast spin-echo and single- and multisection half-Fourier rapid acquisition with relaxation enhancement sequences. Radiology 215:737–745

Urban M, Holzer B, Sebesta C et al (2002) Efficacy of diagnosis of mechanical cholestasis by magnetic resonance cholangiography. World J Surg 26:353–358

Wallner BK, Schumacher KA, Weidenmaier W, Friedrich JM (1991) Dilated biliary tract: evaluation with MR-cholongiography with a heavily T2-weighted contrast enhanced fast-sequence. Radiology 181:805–808

Wallnoefer AM, Herrmann KA, Beuers U, Zech CJ, Gourtsoyianni S, Reiser MF, Schoenberg SO (2005) Comparison of 2D and 3D sequences for MRCP: Clinical value of the different techniques. Radiologe 45:993–1003

Zang J, Krinsky A, Lee VS (2004) Volumetric MR cholangiopancreatography with 3D turbo spin echo and parallel acquisition technique ISMRM, Kyoto, Japan. Proc Int Soc Magn Reson Med 12:431

Zech CJ, Herrmann KA, Huber A et al (2004) High resolution MR-imaging of the liver with T2-weighted sequences using integrated parallel imaging: comparison of prospective motion correction and respiratory triggering. J Magn Reson Imaging 20:443–450

Zech CJ, Schoenberg SO, Herrmann KA et al (2004) Modern visualization of the liver with MRT. Current trends and future perspectives. Radiologe 44:1160–1169

Parallel Imaging in Inflammatory Bowel Disease

23

Karin A. Herrmann

CONTENTS

23.1 Introduction

Small-bowel (SB) imaging, thus far, has been the domain of radiological and fluoroscopic imaging techniques such as small-bowel follow-through and barium-sulfate double-contrast enteroclysis, both representing the gold standard for SB imaging (Maglinte et al. 1992; Maglinte et al. 1996). They provide dynamic information on SB motility and morphologic information on the intra-luminal mucosal surface and the SB lumen. Yet, these techniques require the exposure to ionizing radiation and, as they are pure "luminograms," they are restricted to imaging the lumen and the mucosal surface. Overlay of structures due to the projection technique may limit the diagnostic quality of the examination, and mural and extramural processes are not depicted with this imaging modality.

MRI is suitable for overcoming most of these problems of conventional projection radiography and provides additional advantages: representing a multi-planar cross-sectional imaging modality, MRI readily depicts both intra-luminal mucosal as well as submucosal, mural and extramural pathology. In this quality, MRI currently competes with upcoming multi-planar multi-detector computed tomography of the bowel (Maglinte et al. 2003; Furukawa et al. 2004), yet, MRI is not related to radiation exposure. Furthermore, it offers additional tissue characterization due to its high soft-tissue contrast properties.

Over the past 5 years, considerable progress has been made in the technical development of ultra-fast imaging sequences in MRI, providing short acquisition times and breath-hold examination for abdominal imaging in general and for bowel imaging in particular. This may be why MRI of the small and large bowel has been fostered with increasing attention and great success, first and foremost in the imaging of Crohn's disease (Maglinte et al. 2003; Gourtsoyiannis et al. 2002).

23.2 Technical Considerations of Small-Bowel Imaging with MRI

Formerly, MRI of the small and large bowel has suffered from significant technical limitations related to respiratory movements, bowel motility and the tortuous course of this tubular organ within the abdominal cavity. The break-through for MRI of the intestinal tract was linked to the advent of fast and ultra-fast imaging sequences in the early 1990s (Nitz 2002; Papanikolaou et al. 2002;

K. A. Herrmann, MD
Department of Clinical Radiology, University Hospitals – Grosshadern, Ludwig Maximilian University of Munich, Marchioninistr. 15, 81377 Munich, Germany

Gourtsoyiannis and Papanikolaou 2005), comprising single-shot turbo-spin-echo sequences (e.g., SSFSE, HASTE or FIESTA), steady-state free-precession sequences (e.g., FISP, True FISP, FFE, GRASS) and gradient-echo sequences with low flip angles (GRE, FLASH) as well as fast-spin-echo or turbo-spin-echo sequences (FSE and TSE) (Nitz 2002; Papanikolaou et al. 2002; Gourtsoyiannis and Papanikolaou 2005; Nitz 1999). Mainly due to their robustness against motility artefacts, these ultra-fast sequences helped to realize high-quality imaging of the abdominal organs and the bowel, and can, by now, be considered state-of-the-art sequences for this purpose.

When performing MRI of the SB, further distinct challenges will be encountered. As is known from well-established conventional radiological techniques (Maglinte et al. 2003), the SB lumen and wall is more reliably assessed in full bowel distension. Therefore, intra-luminal contrast media have to be administered in order to distend the bowel and to render mucosal, submucosal and mural abnormalities more conspicuous. A number of different intra-luminal contrast media are available for MRI of the SB. According to their signal characteristics in conjunction with typical imaging sequences, intra-luminal contrast media are classified in positive, biphasic and negative. Positive intra-luminal contrast agents exhibit high signal intensity in both T1-weighted and T2-weighted imaging. Biphasic contrast media have high signal intensity on T2-weighted images and low signal on T1-weighted images. Typical representatives of the latter group are polyethylene glycol (PEG) (Gourtsoyiannis et al. 2002; Laghi et al. 2003; Prasopoulos et al. 2001), methylcellulose aqueous solution, locust bean gum solution and water (Gourtsoyiannis et al. 2000). Negative intra-luminal contrast with both T1-weighted and T2-weighted sequences is basically achieved with substances containing iron-oxide particles (Boraschi et al. 2004; Herrmann et al. 2005; Maccioni et al. 2004; Holzknecht et al. 2003). To date, there is no common sense in the literature as to which contrast medium to prefer for adequate SB imaging.

Further controversy exists in the literature as to whether to apply these substances orally or to perform nasojejunal intubation and direct intra-luminal infusion. Oral application is favoured in children (Laghi et al. 2003). Yet in general, MRI of the SB after oral ingestion of the contrast medium may suffer from incomplete and inhomogeneous distension or even collapse of segments of bowel in up to 23% of the cases, mainly concerning the jejunum or the terminal ileum (Born et al. 2003; Schreyer et al. 2004). With nasojejunal intubation and automatic infusion of the contrast medium, the administration of the contrast medium is constantly supervised using MR-fluoroscopy with the patient already inside the magnet. At the instant of appropriate and homogeneous distension of all SB segments, standard imaging sequences are acquired while full dilatation of the bowel is maintained using antispasmotic drugs such as butylscopolamine or glucagon. This procedure is called MR-enteroclysis (MRE) and is recommended by many authors (Laghi et al. 2003; Papanikolaou et al. 2002; Prasopoulos et al. 2001; Gourtsoyiannis et al. 2000; Herrmann et al. 2005; Herrmann et al. 2006a; Gourtsoyiannis et al. 2001) since it provides homogeneous dilatation of the entire small bowel at the instant of investigation.

Homogeneous SB distension as provided with MRE is warranted in almost all issues of SB assessment, especially if high-resolution imaging of the small bowel is attempted. In the absence of adequate active SB distension, SB may remain collapsed and appropriate diagnostic interpretation is hampered. Collapsed SB wall may be misinterpreted as thickened from inflammatory or neoplastic processes, and subtle abnormalities of the fold pattern or mucosa may be obscured. This is one major argument why MRE should be preferred to MRI after oral contrast media. Initial experiences have shown that MRE is the preferable technique to profit from the advantages of parallel imaging in SB imaging (Herrmann et al. 2006b).

23.3 Clinical Applications of MRE

Crohn's disease (CD) of the SB is one major indication for SB imaging with MRI and MRE. Its purpose is to determine the presence, extent and severity of this disease. Facing the young age of patients affected with this chronic disease, MRI seems to be preferable to CT and CT enteroclysis in this respect. Further indications for MRE, though currently less well established, are the search for benign or malignant neoplasms and the identification of the underlying pathology in mechanical SB obstruction (Papanikolaou et al. 2002; Prassopoulos et al. 2001). In the diagnostic management of postoperative adhesions and intestinal hemorrhage or small bowel ischemia, the usefulness of MRE has not been explored so far.

23.4 MRE in Crohn's Disease

Crohn's disease (CD) in its initial stages is characterized by small superficial lesions of the mucosal surface, mucosal fissures and ulcera. In order to establish the diagnosis of early CD and to depict these subtle mucosal lesions in imaging, high spatial resolution is required. Up to now, MRE was clearly limited in this respect, and inferior to conventional radiographic imaging techniques, the latter offering a spatial resolution of far less than 1 mm^3.

In contrast, MRE has proven to be a very reliable in disclosing transmural and extramural disease. Appropriate dilatation of the SB provided, the disruption of the mucosal fold pattern, deep mucosal ulcera, inflammatory stenosis, prestenotic dilatation, internal enteric fistulae and abscesses can easily be visualized in MRE (Prasopoulos et al. 2001; Herrmann et al. 2005; Herrmann et al. 2006a; Maccioni et al. 2000; Rieber et al. 2000; Rieber et al. 2002). Since different stages of inflammation in CD may be encountered in one patient, distinguishing acute inflammatory from chronic inflammatory and fibrotic disease is pivotal to decide subsequently for an appropriate therapy, whether surgical or medical. MRE provides this information due to its capacity of tissue characterization. Thickening of the SB wall and submucosal edema with hyperintense signal on T2-weighted imaging, increased contrast medium uptake of the thickened SB wall and the depiction of enlarged, contrast-enhancing mesenteric lymphadenopathies are typical signs of active inflammatory CD in MRE (Prasopoulos et al. 2001; Gourtsoyiannis et al. 2004). In contrast, fibrotic strictures of the SB wall are slightly hypointense on T2-weighted and SSFP images, show less contrast uptake, yield marked prestenotic dilatation, but are generally not associated with wall thickening. Since their appearance and signal characteristics are close to normal bowel wall, active SB distension with MRE is required to unveil these lesions as strictures (Umshcaden and Gasser 2003; Umschaden et al. 2000).

Both inflammatory stenosis and fibrotic stricture in CD result in SB obstruction. Acute and chronic transmural inflammation with stenosis and post-inflammatory scar formation impair SB motility. Subtle, sub-occlusive disease may only be revealed with an increased volume charge as is provided in MRE. To disclose disturbances of SB motility and sub-occlusive disease, time-resolved dynamic information is obtained from MR-fluoroscopy which is implemented in MRE using rapid repetition of ultra-fast sequences [e.g., single-shot turbo-spin-echo (HASTE) or rapid acquisition with relaxation enhancement (RARE) sequences]. This technique permits to observe the propagation of the intra-luminal contrast medium and the subsequent dilatation of the SB. To date, the named sequences are both used as a projection technique and are clearly limited in spatial resolution.

23.5 Parallel Imaging Techniques and MRE

Numerous advantages can be anticipated from parallel imaging techniques in SB-MRE. Improving spatial resolution while reducing acquisition time creates options for 3D imaging, including 3D post-processing of the bowel, and may enable and foster the assessment of mucosal lesions – still a major limitation of MRE. Respiratory and motion artefacts may be reduced at shorter acquisition time, and overall examination time can be shortened, limiting the period of patients' discomfort due to SB filling to a minimum.

To implement SB-MRE with parallel imaging, ideally a 32-channel whole-body MRI system is required. The typical setting for SB-MRE with parallel imaging includes two 6-element phased-array body coils to cover the entire abdomen anteriorly and a 12-element spine array coil posteriorly (Fig. 23.1a). Providing this coil setting, parallel acquisition can be performed in two dimensions by applying a parallel imaging acceleration factor of R=3 in the left-right direction (phase-encoding direction) and an acceleration factor of R=2 in the anterior-posterior direction (partition direction) (Fig. 23.1b), which results in a total nominal 2D acceleration factor of 6.

The image reconstruction in phase-encoding direction is based on the generalized partially parallel acquisition technique (GRAPPA) (Griswold et al. 2002). This reconstruction algorithm requires the measurement of a total of 24 reference lines to determine the coil profiles. In the anterior-posterior direction, the image reconstruction is performed in the image domain using a SENSE-like algorithm and a total of 64 reference lines. The integrated acquisition of the reference lines reduces the effective acceleration of parallel imaging in both the phase-encoding and the partition direction. Thus, the effective acceleration factor in phase-encoding direction is 2.53 (nominal acceleration factor R=3); in partition

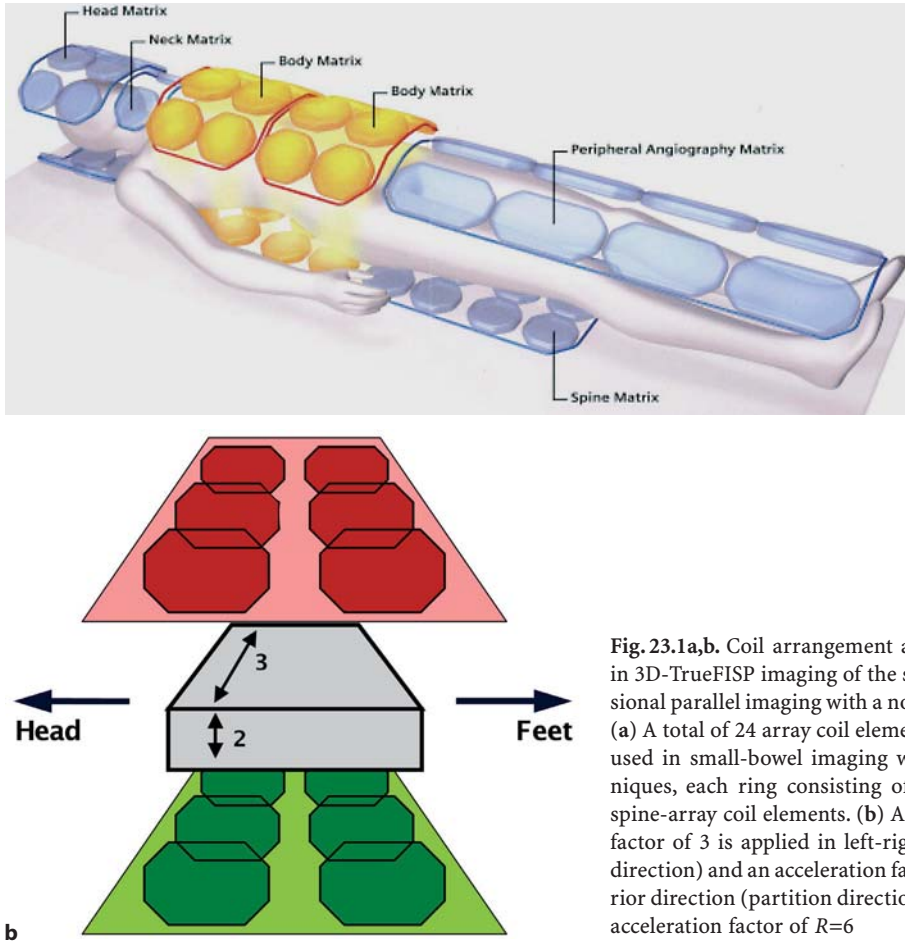

Fig. 23.1a,b. Coil arrangement and parallel-acquisition setup in 3D-TrueFISP imaging of the small bowel using two-dimensional parallel imaging with a nominal acceleration factor of 6: (**a**) A total of 24 array coil elements arranged in four rings are used in small-bowel imaging with parallel acquisition techniques, each ring consisting of three body-array and three spine-array coil elements. (**b**) A parallel-imaging acceleration factor of 3 is applied in left-right direction (phase-encoding direction) and an acceleration factor of 2 in the anterior-posterior direction (partition direction) resulting in a total nominal acceleration factor of R=6

direction it is 1.24 (nominal acceleration factor R=2). Hence, under these conditions with 2D parallel imaging, a total effective acceleration factor of R_{eff}=3.13 can be achieved. One of the first sequences for abdominal MRI that employs parallel imaging in two dimensions with acceleration factors greater than 3 is the recently introduced 3D-TrueFISP sequence.

23.6 3D-TrueFISP with 2D Parallel Imaging

Steady-state free-precession sequences such as TrueFISP are particularly valuable and have been recommended for SB imaging with MRE (Gourtsoyiannis et al. 2002; Prasopoulos et al. 2001; Gourtsoyiannis et al. 2000), since they have a very distinct signal behavior with both T1 and T2 signal properties and an individual intrinsic chemical-shift effect (also called "ink artefacts"), resulting in an excellent soft tissue contrast (Prasopoulos et al. 2001). Therefore, the introduction of a 3D-TrueFISP sequence with parallel imaging is of particular importance for SB imaging and MRE, opening promising options of image quality improvement.

High-resolution 3D-TrueFISP imaging with 2D parallel imaging at a nominal acceleration factor of 6 can be performed within one single breath-hold of 18 s, covering the entire abdomen and providing an isotropic spatial resolution of 1.8×1.8×1.8 mm^3 (Fig. 23.2). Due to the isotropic properties of this 3D-TrueFISP sequence, 3D post-processing tools can be applied to create maximum-intensity projections (MIP), multi-planar reformations (MPR) in any arbitrary plane and so-called curved reformats (CR) (Fig. 23.3a,b). Curved reformats allow transforming curvilinear, tortuous structures into virtually linear structures on two-dimensional presentations. For 3D post-processing, the 3D source images are transferred to a commercially available dedicated post-processing workstation (e.g., Leonardo, Siemens Medical systems, Erlangen, Germany).

23.7 Clinical Impact of High-Resolution 3D-True-FISP and 3D Post-Processing

3D post-processing in 3D-TrueFISP imaging is distinctly helpful in many issues of SB disease. According to a recent preliminary study, 3D post-processing yields additional diagnostic information in up to 77% of all patients (Herrmann et al. 2006b). This additional information has relevant diagnostic impact in therapeutic decision making in more than 54% of the cases. Both CR and MRP contribute to this result; the combination of both is the most effective.

In the assessment of CD on standard coronal or transverse images, the exact length of stenosis may be difficult to determine if a long segment of SB is affected and has a tortuous course within the abdominal cavity. In these cases, 3D post-processing with CRs is most helpful. An interactive tool is used to trace the course of the bowel loop manually within the 3D data set (Fig. 23.3a). The curvilinear course of the bowel segment is then virtually "straightened" and "unfolded" and displayed as a linear structure (Fig. 23.3B) The planar presentation of the affected bowel segment facilitates the exact measurement of the length of a stenosis (Fig. 23.3b), which may be relevant in the decision making for a potential surgical intervention. Likewise, CRs support the assessment of mucosal fissures and ulcera in rendering them more conspicuous on linear planar images (Fig. 23.3b) (Herrmann et al. 2006b). Especially in the terminal ileum, applying CRs has major impact on diagnosing the presence of CD while improving the evaluation of the mucosa.

In a complex arrangement of bowel loops affected with CD, also known as "inflammatory pseudo-tumors" or "conglomerate tumors" in CD, CRs and MPRs are particularly useful and capable of adding relevant information in better depicting the local extent and involvement of adjacent structures and providing a better orientation within the abdominal cavity.

In the presence of complex internal entero-enteric fistula, MPR can be adjusted to the course of the fistulous tract and show the origin and the site where the fistulous tract abuts the distal target organ. Likewise, the point of departure of complications such as abscesses may be clarified more easily with appropriate orientation of MPR planes (Fig. 23.4b).

In neoplastic disease of the bowel, MPRs have proven to be useful in the assessment of the tumor extent and infiltration into adjacent structures (Herrmann et al. 2006b). Extra-luminal infiltration into the mesentery or other structures is best disclosed on MPRs strictly orthogonal to the bowel lumen.

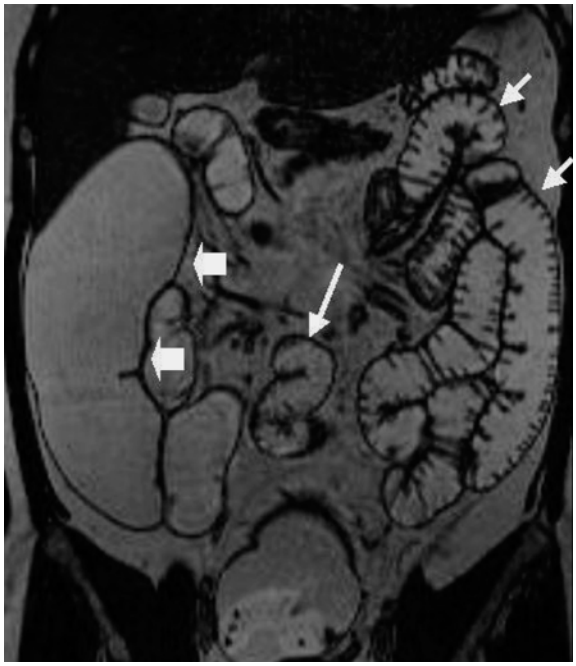

Fig. 23.2. High-resolution 3D-TrueFISP imaging with 2D parallel imaging and an acceleration factor of R=6: Coronal view of an MR-enteroclysis with biphasic intra-luminal contrast (0.5% methyl-cellulose solution) in the small (*small short arrows*) and large bowel (*large short arrows*). The jejunal fold pattern (*small short arrows*) and the less pronounced ileal folds (*small long arrow*) are very well depicted due to the high spatial resolution of 1.8×1.8×1.8 mm³ with isotropic voxel size

To successfully apply 3D post-processing tools and obtain these results, the bowel has to be fully distended. This is why the authors emphasize the importance of SB distension as an indispensable prerequisite for high-resolution imaging with 3D-TrueFISP including these options for 3D post-processing.

23.8 Future Improvement and Perspectives of SB Imaging with MRE and Parallel MRI

Parallel-imaging techniques and a higher field strength of 3 T are generally considered ideal mutual adjuncts since higher signal at 3 T compensates for the noise induced in parallel imaging techniques. Yet, TrueFISP imaging at 3 T suffers from distinct

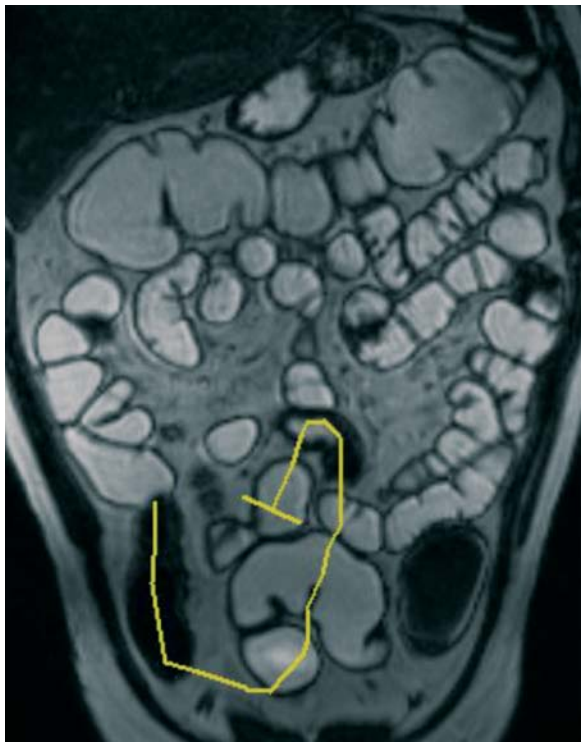

a

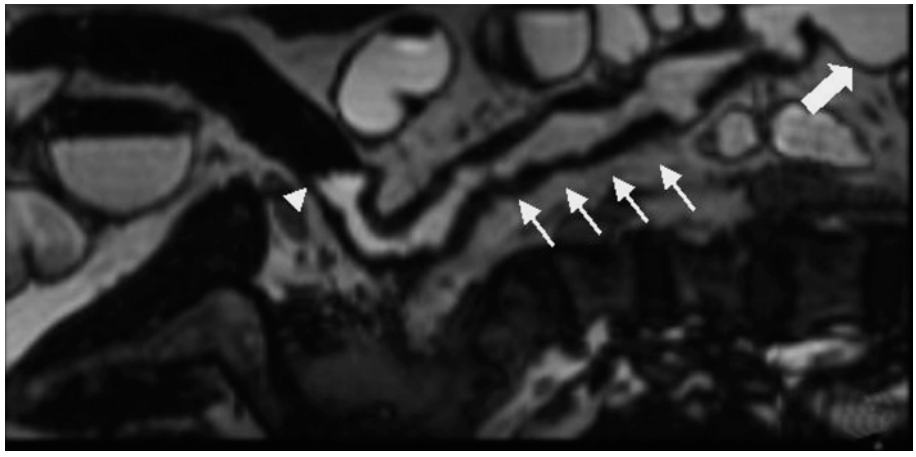

b

Fig. 23.3a,b. Curved reformat (CR): The tortuous and convoluted course of a long-segment inflamed and stenosed small-bowel loop is manually traced within the 3D data set (**a**, *yellow line*) to create the CR. Most of the course of the traced small-bowel loop is outside the shown image plane but is indicated by the *yellow line*. The long-segment stenosis is presented in a linear planar fashion (**b**, proximal to distal from *right* to *left*) depicting more clearly the mucosal ulcera and cobblestone pattern (**b**, *small white arrows*) as compared to normal mucosa. The linear planar presentation facilitates the exact measurement of the length of stenosis and of the prestenotic dilatation in the middle ileum (**b**, *large white arrow*). The *small white arrowhead* **b** indicates the air-fluid level in the terminal ileum which, at that time, was filled with air.

artefacts due to more pronounced sensitivity to susceptibility effects. Therefore, the issue of TrueFISP imaging at 3 T has to be addressed before integrating SB imaging into a 3 T clinical setting.

In contrast, parallel imaging at 3 T now offers further refinement of other imaging sequences such as T1-weighted fat-saturated gradient-echo images (e.g., VIBE sequence and volume-interpolated breath-hold examination sequences), generally used for contrast-enhanced SB imaging after intravenous application of gadolinium. These sequences can now be acquired with isotropic voxel size, so that 3D post-processing is also applicable to these sequences. To date, 3D GRE sequences have proven their usefulness in MR-colonoscopy (Debatin and Lauenstein 2003). According to some preliminary experience, better signal-to-noise ratios and higher spatial resolution can be achieved with parallel imaging and 3 T for this application. In the future, increased spatial resolution and further improvements in terms of image quality of TrueFISP imaging holds great promise of improving the assessment of mucosal lesions in CD. MRE would then evolve to be a comprehensive diagnostic tool in the diagnostic workup of CD, covering its entire spectrum of macroscopic clinical presentation.

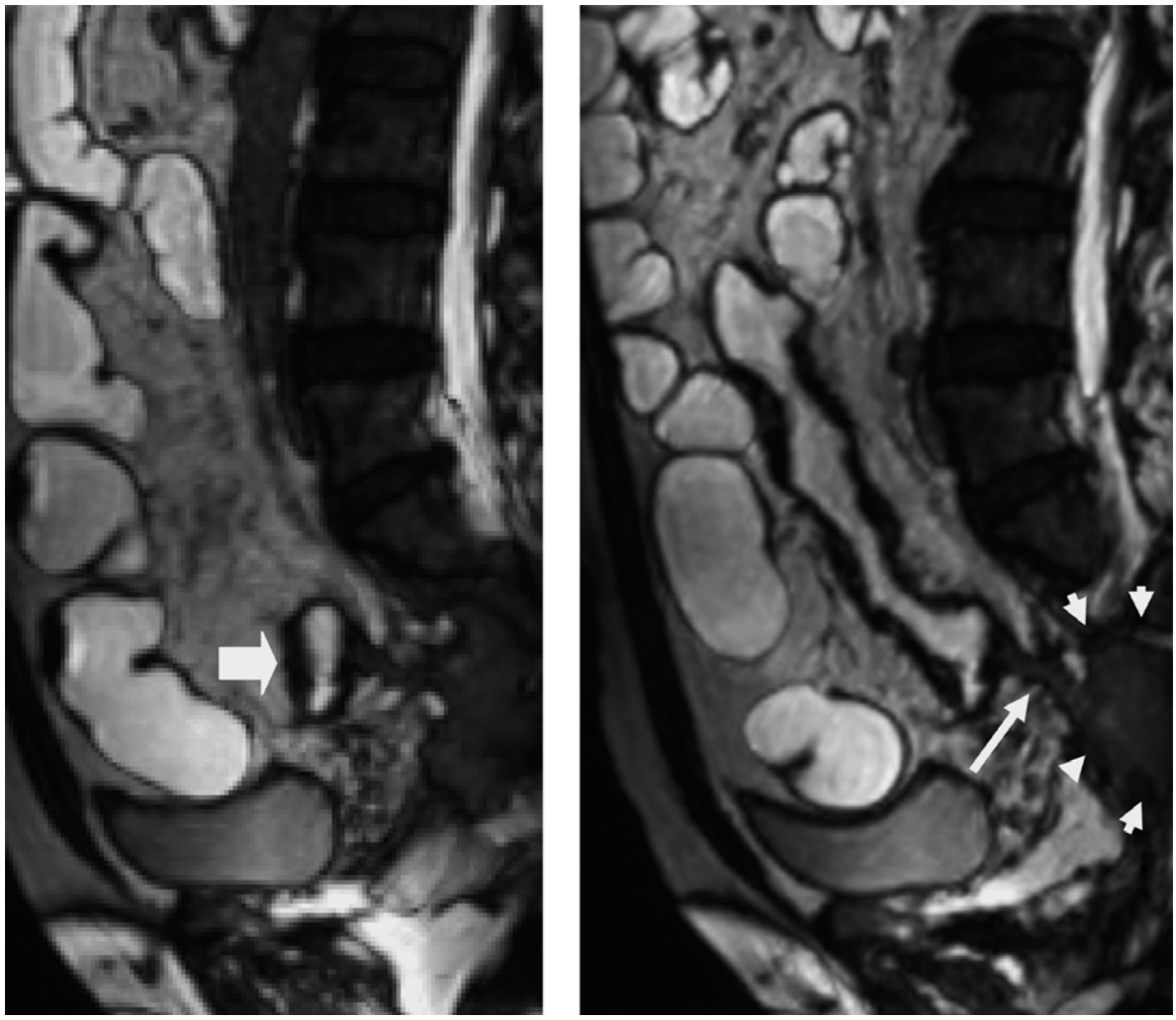

Fig. 23.4a,b. Standard sagittal slice orientation (**a**) and para-sagittal multi-planar reformation (MPR) from 3D-TrueFISP sequence (**b**) in a 36-year-old patient with CD: On the sagittal plane, a small portion of a long-segment inflammatory stenosis of CD is shown (**a**, *large arrow*) adjacent to an indeterminate irregular mass in the pre-sacral region (**a**). The distinct MPR oriented along the course of the inflamed bowel segment elucidates the presence of a fistula (**b**, *small long arrow*) arising from the backside of the inflamed bowel loop (**a**, *large arrow*) and giving origin to a pre-sacral abscess (**b**, *small short arrows*)

References

Boraschi P, Braccini G, Gigoni R, Cartei F et al (2004) MR enteroclysis using iron oxide particles (ferristene) as an endoluminal contrast agent: an open phase III trial. Magn Reson Imaging 22:1085–1095

Born C, Nagel B, Leinsinger G, Reiser M (2003) [MRI with oral filling in patients with chronic inflammatory bowel diseases]. Radiologe 43:34–42

Debatin JF, Lauenstein TC (2003) Virtual magnetic resonance colonography. Gut 52 [Suppl] 4:iv17–22

Furukawa A, Saotome T, Yamasaki M, Maeda K et al (2004) Cross-sectional imaging in Crohn disease. Radiographics 24:689–702

Gourtsoyiannis N, Papanikolaou N, Grammatikakis J, Maris T et al (2000) MR imaging of the small bowel with a true-FISP sequence after enteroclysis with water solution. Invest Radiol 35:707–711

Gourtsoyiannis N, Papanikolaou N, Grammatikakis J, Maris T et al (2001) MR enteroclysis protocol optimization: comparison between 3D FLASH with fat saturation after intravenous gadolinium injection and true FISP sequences. Eur Radiol 11:908–913

Gourtsoyiannis N, Papanikolaou N, Grammatikakis J, Papamastorakis G, et al (2004) Assessment of Crohn's disease activity in the small bowel with MR and conventional enteroclysis: preliminary results. Eur Radiol 14:1017–1024

Gourtsoyiannis N, Papanikolaou N, Grammatikakis J, Prasso-

poulos P (2002) MR enteroclysis: technical considerations and clinical applications. Eur Radiol 12:2651–2658
Gourtsoyiannis NC, Papanikolaou N (2005) Magnetic resonance enteroclysis. Semin Ultrasound CT MR 26:237–246
Griswold MA, Jakob PM, Heidemann RM, Nittka M et al (2002) Generalized autocalibrating partially parallel acquisitions (GRAPPA). Magn Reson Med 47:1202–1210
Herrmann KA, Dietrich O, Kuehn B, Seiderer J, Ochsenkuehn T, Crispin A, Struwe A, Reiser MF (2006b) Magnetic resonance enteroclysis of small bowel disease: Value of single-breath-hold high resolution 3D TrueFISP imaging using two-dimensional parallel acquisition techniques. J Magn Reson Imaging (accepted)
Herrmann KA, Michaely HJ, Zech CJ, Seiderer J et al (2006a) Internal fistulas in Crohn disease: magnetic resonance enteroclysis. Abdom Imaging (in press)
Herrmann KA, Zech CJ, Michaely HJ, Seiderer J et al (2005) Comprehensive magnetic resonance imaging of the small and large bowel using intraluminal dual contrast technique with iron oxide solution and water in magnetic resonance enteroclysis. Invest Radiol 40:621–629
Holzknecht N, Helmberger T, Herrmann K, Ochsenkuhn T, et al (2003) [MRI in Crohn's disease after transduodenal contrast administration using negative oral MRI contrast media]. Radiologe 43:43–50
Laghi A, Paolantonio P, Catalano C, Dito L et al (2003) MR imaging of the small bowel using polyethylene glycol solution as an oral contrast agent in adults and children with celiac disease: preliminary observations. AJR Am J Roentgenol 180:191–194
Maccioni F, Viscido A, Broglia L, Marrollo M et al (2000) Evaluation of Crohn disease activity with magnetic resonance imaging. Abdom Imaging 25:219–228
Maccioni F, Viscido A, Marini M, Caprilli R (2002) MRI evaluation of Crohn's disease of the small and large bowel with the use of negative superparamagnetic oral contrast agents. Abdom Imaging 27:384–393
Maglinte DD, Bender, GN, Heitkamp, DE, Lappas, JC et al (2003) Multidetector-row helical CT enteroclysis. Radiol Clin North Am 41:249–262
Maglinte DD, Chernish, SM, Kelvin, FM, O'Connor, KW et al (1992) Crohn disease of the small intestine: accuracy and relevance of enteroclysis. Radiology 184:541–545
Maglinte DD, Kelvin, FM, O'Connor, K, Lappas, JC et al (1996) Current status of small bowel radiography. Abdom Imaging 21:247
Maglinte DD, Lappas JC, Heitkamp DE, Bender GN et al (2003) Technical refinements in enteroclysis. Radiol Clin North Am 41:213–229
Maglinte DD, Siegelman ES Kelvin FM (2000) MR enteroclysis: the future of small-bowel imaging? Radiology 215:639–641
Nitz WR (1999) MR imaging: acronyms and clinical applications. Eur Radiol 9:979–997
Nitz WR (2002) Fast and ultrafast non-echo-planar MR imaging techniques. Eur Radiol 12:2866–2882
Papanikolaou N, Prassopoulos P, Grammatikakis I, Maris T et al (2002) Technical challenges and clinical applications of magnetic resonance enteroclysis. Top Magn Reson Imaging 13:397–408
Prassopoulos P, Papanikolaou N, Grammatikakis J, Rousomoustakaki M et al (2001) MR enteroclysis imaging of Crohn disease. Radiographics 21 Spec No:S161–172
Rieber A, Aschoff A, Nussle K, Wruk D et al (2000) MRI in the diagnosis of small bowel disease: use of positive and negative oral contrast media in combination with enteroclysis. Eur Radiol 10:1377–1382
Rieber A, Nussle K, Reinshagen M, Brambs HJ et al (2002) MRI of the abdomen with positive oral contrast agents for the diagnosis of inflammatory small bowel disease. Abdom Imaging 27:394–399
Schreyer AG, Geissler A, Albrich H, Scholmerich J et al (2004) Abdominal MRI after enteroclysis or with oral contrast in patients with suspected or proven Crohn's disease. Clin Gastroenterol Hepatol 2:491–497
Umschaden HW, Gasser J (2003) MR enteroclysis. Radiol Clin North Am 41:231–248
Umschaden HW, Szolar D, Gasser J, Umschaden M et al (2000) Small-bowel disease: comparison of MR enteroclysis images with conventional enteroclysis and surgical findings. Radiology 215:717–725

Musculoskeletal Imaging: Knee and Shoulder

24

Bernd Romaneehsen and Karl-Friedrich Kreitner

CONTENTS

24.1 Introduction

The knee and the shoulder are the most frequently examined joints of the body with a variety of types of traumatic and degenerative conditions affecting them. Magnetic resonance imaging is regarded as the noninvasive investigation technique of choice for the detection of internal derangements of the knee and shoulder. To distinguish small anatomic details, high-standard MR investigations have to be performed. Parallel imaging is one of the most promising recent advances in MR technology. Within the last years, parallel-imaging methods have become commercially available. The basic feature of parallel imaging, using multi-element coils, is a scan time reduction without violating image quality. Another application of parallel imaging especially important for musculoskeletal MRI is to translate the speedup to enhance resolution in an attempt to increase the diagnostic accuracy. To date most parallel imaging applications are still dealing with cardiovascular and breath-hold examinations (Dietrich et al. 2002, Griswold et al. 2002; van den Brink et al. 2003). However, fast parallel imaging has also been shown to be an accurate and economic tool in MR imaging of several musculoskeletal regions (Romaneehsen et al. 2003).

To obtain optimized MR investigations of the musculoskeletal system, two fundamental prerequisites have to be respected: high spatial resolution and high sensitivity for the visualization of free water-bound protons, because almost all pathologic conditions of the musculoskeletal system exhibit an increase of free water (Stäbler et al. 2000). To increase spatial resolution, the image matrix has to be maximized with a field of view as small as possible to decrease pixel size, and slice thickness has to be low. These conditions are limited by the signal-to-noise ratio (SNR). An increase in the number of acquisitions to improve SNR consequently results in longer examination times. Generally, the SNR in images that were acquired with parallel imaging is decreased relative to acquisitions with conventional, full k-space acquisition by at least the square root of the reduction factor R (Bammer and Schoenberg 2004) as discussed in the first part of this book. On the other hand, parallel imaging approaches may as well be used to increase the SNR efficiency. The basic idea is to use parallel imaging for reducing the number of phase-encoding steps, while counter-balancing the resulting scan time savings by increasing the repetition time (Weiger et al. 2005). Besides SNR limitations, current musculoskeletal MR imaging also suffers from long acquisition times with the risk of motion artefacts due to patient discomfort; these artefacts can also be reduced by applying correction

B. Romaneehsen, MD; K.-F. Kreitner, MD
Department of Diagnostic and Interventional Radiology, Johannes-Gutenberg-University of Mainz, Langenbeckstr. 1, 55131 Mainz, Germany

schemes based on parallel imaging as described in Chap. 5. In addition, the increasing pressure in clinical practice to increase patient throughput prompted the development of faster imaging techniques. Parallel imaging holds promise to solve these problems in musculoskeletal imaging.

At present, the only commercially available techniques for daily clinical routine are GRAPPA and SENSE (cf. Chap. 2). In comparison to SENSE, parallel imaging with GRAPPA is particularly beneficial in areas where accurate coil sensitivity maps may be difficult to obtain (Dietrich et al. 2002). Such inhomogeneous regions with low spin density are for example the lung and the abdomen (Oberholzer et al. 2004). However, whenever an accurate homogeneous coil sensitivity map can be acquired, SENSE provides the best possible reconstruction, especially in highly accelerated applications (Blaimer et al. 2004; Griswold et al. 2002). To date, the parallel MR imaging technique with the most widespread use is SENSE, which is offered by many companies (van den Brink et al. 2003).

In the subsequent sections, examples of the use of SENSE in clinical routine imaging of the knee and shoulder are provided.

24.2 Technical Considerations

All examinations presented here have been performed on a 1.5-T whole-body scanner (MAGNETOM Sonata, Siemens Medical Solutions, Erlangen, Germany) with a maximum gradient strength of 40 mT/m and maximum slew rate of 200 T/m/s. The scanner is equipped with a whole-body array interface (Maestro) that enables signal detection with multiple array-coil elements. For parallel imaging, an implemented modified SENSitivity Encoding (mSENSE) algorithm with a reduction factor of 2 is generally used. Accurate coil sensitivity estimation is a crucial step for SENSE reconstruction. In order to assess the coil sensitivity profile for the integrated parallel acquisition technique (iPAT, Siemens Medical Solutions, Erlangen, Germany), 24 k-space lines were sampled as additional reference lines during imaging. For mSENSE, no threshold has to be used to determine if the reference image intensity is sufficient for coil map calculation, and the calibration runs automatically. The phased-array coil used in the examples presented here is a commercially available flexible six-channel body array coil that is intended for cardiac imaging. Due to the flexible nature of the coil, it could be used as a wrap-around coil for knee imaging covering a volume of about 25 cm in a proximal-to-distal direction or as a surface coil.

24.3 Imaging of the Knee

24.3.1 Basic Principles

The knee is one of the most commonly involved joints in sports injuries and degenerative disorders related to our bipedal nature. The reported high accuracy of magnetic resonance imaging for the detection of internal derangement of the knee has resulted in MRI being preferred over diagnostic arthroscopy by most leading orthopedic surgeons (Helms 2002a). MRI is useful in the early diagnosis and initiation of appropriate therapy.

The examined knee should be placed in a comfortable position; we propose to do it in mild flexion. Slight external rotation may facilitate imaging the anterior cruciate ligament. For imaging the knee, a variety of imaging concepts with different sequences obtained are available. This can include conventional spin-echo T1-weighted, proton-density (PD)-weighted, or gradient-echo sequences (Cheung et al. 1997; Helms 2002, b). In addition, cartilage-sensitive sequences such as dual echo in the steady state (DESS), steady-state free precision (SSFP) or three-dimensional spoiled gradient-echo (SPGR) and fast low-angle shot (FLASH) have been shown to be accurate and reliable in case of suspected cartilage lesions (Hargreaves et al. 2003). Many radiologists apply fat suppression to rid the image of the diverting high signal emanating from the fat in the soft tissues and fatty marrow in the bones and to distinguish fat from fluid, both of which are of high signal in fast-spin-echo (FSE) sequences. Frequency-selective fat-signal elimination requires high-field systems; relaxation-time-dependent methods (short-tau inversion recovery: STIR) are also available on low-field systems. A routine MR protocol should include images in axial, oblique coronal, and oblique sagittal planes. Typical section thickness is 3 mm to 5 mm, with a field of view limited to 160×160 mm² and a minimum matrix-size

of 256×256. Our standard examination protocol for the traumatic knee consists of proton-density and T2-weighted FSE sequences in all orientations with additional fat-suppression in the axial and coronal planes (TR=3,240 ms; TE=14/85 ms) using only one excitation. We use a section thickness of 4 mm, a 256×256 matrix size, and a 150×150 mm field of view to obtain high quality images accompanied by short scanning times. The resulting in-plane resolution is 0.6×0.6 mm².

The use of parallel imaging implies specific artefacts. An artefact particular to SENSE imaging occurs when the reconstructed FOV is smaller than the object being imaged. In contrast to conventional imaging, this intrinsic aliasing artefact not only contaminates the edges of the FOV, but also the central portion, and can disturb clinical interpretation (Goldfarb 2004). For this reason, we set the knee on a dedicated brace, which elevates the examined knee to the contralateral knee and avoids aliasing in coronal and axial sections. As mild folding artefacts still could persist (Fig. 24.1), we use moreover a 100% phase oversampling, as we do in our routine standard examination protocol without parallel imaging, too. However, in a study consisting of 90 patients, the influence of these quite rare artefacts was without any negative effects on image evaluation (Romaneehsen et al. 2004).

Performing with a parallel imaging acceleration factor of R=2, the scanning time could be reduced from 5:09 min (without parallel imaging) to 2:42 min with SENSE for each sequence, resulting in a total imaging time of 8:06 min for our routine knee examination. SENSE leads to a 48% reduction of scan time.

There are only a limited number of publications dealing with parallel imaging applications in MRI of the knee joint. Niitsu et al. (2003) used a pair of SENSE-compatible flexible coils with two elliptical coil elements and an overall reduction factor of 2. In this study, images of intermediate-weighted FSE and fast field echo (FFE) using parallel imaging were obtained. Time savings were partly utilized to double the number of acquired slices in adding two high-resolution 3D sequences to the standard protocol. Compared with conventional imaging, they found identical accuracies for ligament and meniscus pathologies. Two other studies (Kwok et al. 2003; Magee et al. 2004) used the SMASH technique (cf. Chap. 2). As with SENSE, SMASH imaging results in a significant decrease in imaging time without any effect on MRI interpretation or patient clinical outcome. Magee et al. (2004) report on potentially fewer artefacts from patient motion on SMASH T2-weighted images. We could confirm this observation in a larger performance study using parallel imaging with mSENSE (Romaneehsen et al. 2004). High-quality MRI suffers from long acquisition times with the risk of motion artefacts due to patient discomfort. Particularly MR examinations in patients fol-

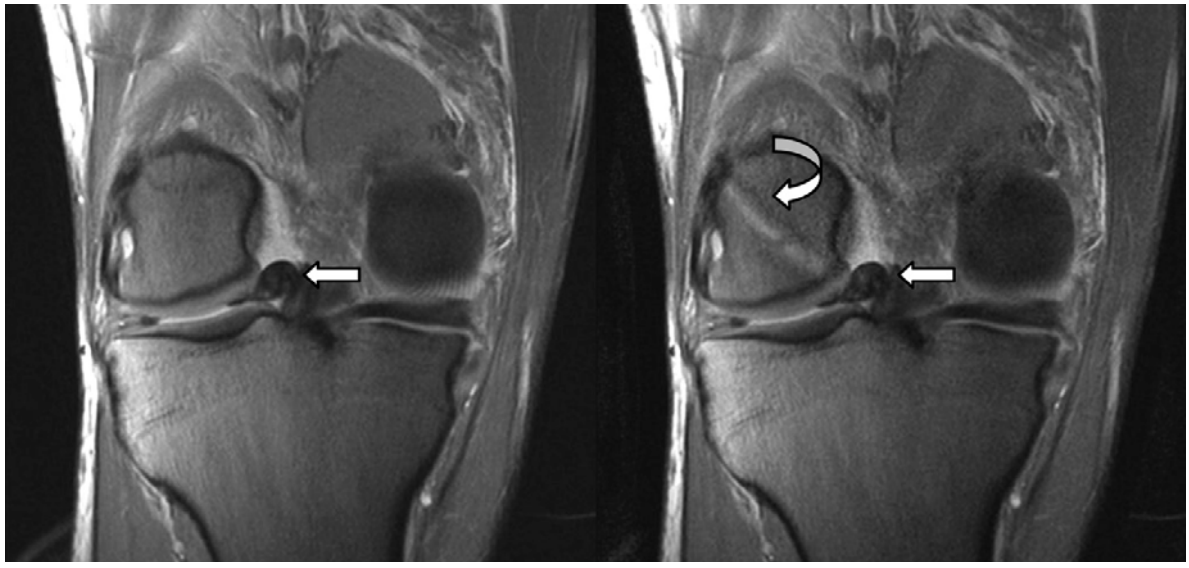

a b

Fig. 24.1a,b. A 28-year-old man with bucket-handle tear of the lateral meniscus. The image reveals a truncated meniscus with a displaced fragment seen in the intercondylar notch (*straight arrow*). The tear was confirmed at arthroscopy. Coronal fat-suppressed proton-density FSE images without **a** and with parallel imaging **b.** Slight SENSE-typical backfolding artefact (*curved arrow*) in **b** without any effect on MRI interpretation or diagnosis

lowing an acute injury may be influenced by severe motion artefacts due to pain during scanning. Our study reflects this phenomenon. Regarding motion artefacts, conventional imaging resulted in a lesser number of good and excellent images as compared with parallel imaging using SENSE (Fig. 24.2).

In the following, examples of typical traumatic disorders of the knee joint obtained with the SENSE technique are introduced.

24.3.2 Meniscal Tears

The menisci are very important for knee function and contribute to distributing compressive and torsional forces. The role of MR imaging in the diagnosis of meniscal tears is considerably well established. Current sensitivity and specificity for meniscal tears range from 90% to 95% in most reports (Helms 2002a). The posterior horn of the medial meniscus is the most common location to have a tear. There are two major criteria routinely applied for the diagnosis of meniscal tears: (1) abnormal signal intensity; (2) abnormal morphology. Increased T2-weighted signal is considered to be a tear when it unequivocally extends to the articular surface. Apart from this, in the elderly there is often severe degeneration with extensive high-signal intensity within the menisci. Increased signal in the periphery of the meniscus could be observed in meniscal contusion, which occurs when the meniscus gets trapped between the femur and the tibia during a traumatic event. An indistinct and amorphous pattern as well as an adjacent bone contusion should alert one to the possible presence of this finding. In peripheral sagittal sections, both menisci commonly have a "bow-tie" configuration. Morphological abnormalities include an abnormal meniscal size and truncation of both horns with blunt and irregular margins. Meniscal tear configurations are described as horizontal, vertical, radial, displaced flap, bucked-handle or meniscocapsular separation (Fig. 24.3). Generally speaking, vertical tears are traumatic and horizontal tears are of a degenerative nature (Osterle 2003). A key consideration is the recognition of unstable – clinically significant – meniscal tears. Unstable menisci and displaced meniscal fragments cause mechanical problems possibly resulting in a locked knee and require surgery for removal or reattachment. Criteria for unstable lesions include the presence of a displaced meniscal fragment (Fig. 24.4) and a complex tear or a tear having T2 hyperintensity, indicating intramenisical fluid (Carrino and Schweitzer 2002).

A bucket-handle tear is a specific type of displaced meniscus. It is a large circumferential vertical tear through the pars intermedia that predominately involves the medial meniscus. Confirmation will almost always be found in the form of a displaced meniscal fragment that is visualized elsewhere in

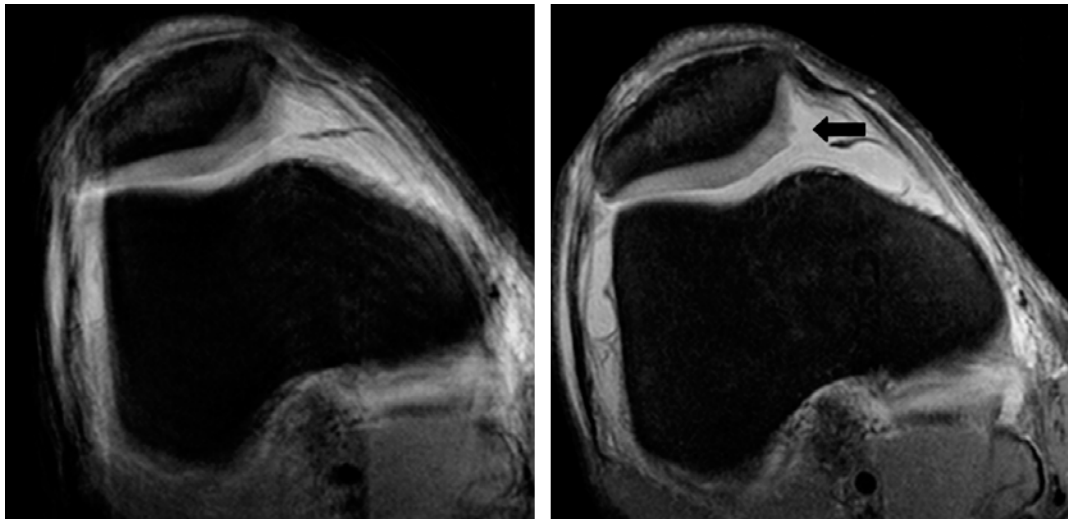

Fig. 24.2a,b. Comparison of conventional **a** and parallel imaging **b** by using identical coil and scan parameters. The acquisition time was 5:09 min without SENSE and 2:42 min with SENSE. The axial PD-weighted FS image shows a focal cartilage defect after traumatic luxation of the patella in **b** (*arrow*) that could not be depicted in **a**

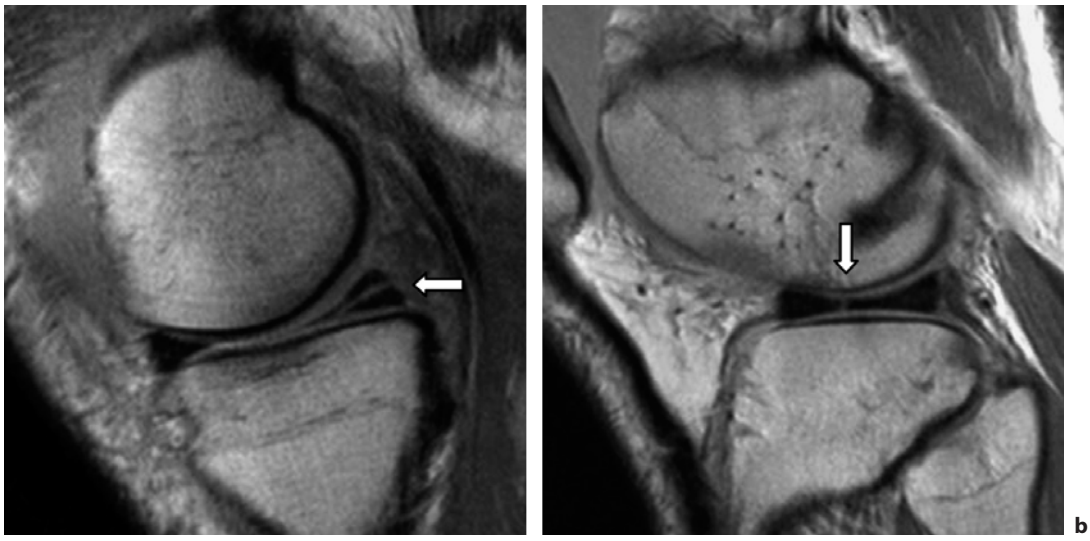

Fig. 24.3. a Typical degenerative oblique tear of the posterior horn extending to the inferior and posterior meniscal surface (*arrow*). **b** Traumatic radial tear after acute injury. Sagittal PD-weighted image through the body of the meniscus with a radial tear shows a small gap in the normal "bow-tie" configuration of the mid portion of the meniscus (*arrow*)

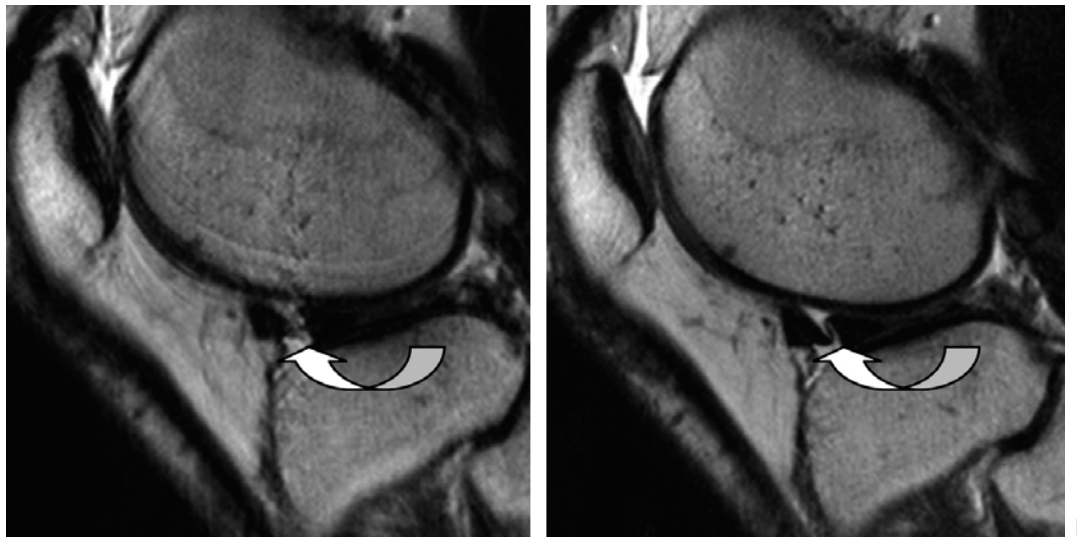

Fig. 24.4a,b. A 32-year-old-handball player after acute trauma of the left knee. Dislocated rupture of the posterior horn of the lateral meniscus, which is flipped anteriorly. **a,b** Proton-density- and T2-weighted sagittal FSE images show a diminutive posterior horn. The posterior third of the meniscus has been dislocated anteriorly (*arrow*). Using SENSE in **b** (scan time 2:42 min) shows diagnostic findings more clearly than **a** (scan time 5:09 min) because of suppression of pain-induced motion artefacts

the data set. A group of MR imaging signs for securing the diagnosis have been reported. Of these, the double posterior cruciate ligament (PCL) sign, fragments in the intercondylar notch, absent "bow-tie", flipped meniscus and double anterior horn signs are well known and widely used (Aydingöz et al. 2003) (Fig. 24.5). Often the inner meniscal fragment displaces away from the meniscus medially into the intercondylar notch (Fig. 24.1). The double PCL sign is more common in bucket-handle tears of the medial meniscus than in the lateral meniscus because the anterior cruciate ligament (ACL) serves as a barrier; however a torn ACL would not prevent the fragment from displacement.

The radiologist has to be familiar with several frequent pitfalls encountered with MRI of the menisci. Normal anatomic structures, such as the transverse ligament, the popliteus tendon or the menisco-femoral ligaments, may be confused with displaced fragments. Chondrocalcinosis within the meniscus or acute injuries with meniscal contusion may produce increased signal and mimic fluid from a meniscal tear (Carrino and Schweitzer 2002).

24.3.3 The Ligaments

Acute ligamentous injuries in the knee are relatively common. On MRI the most prominent feature of an acute tear is an increased T1 and T2 signal representing focal hemorrhage and edema replacing the normal low signal linear ligament.

The anterior cruciate ligament (ACL) tears most commonly occur in the mid-portion or in the proximal femoral attachment. Primary and secondary signs are described for diagnosing ACL tears (Barry et al. 1996). The most important primary sign of an ACL tear is an absent or discontinuous ACL. An abnormal condition is present when the fibers show an irregular, wavy contour with focal or diffuse increased signal intensity (Fig. 24.6). Indirect signs of a torn ACL include a buckled PCL, anterior translation of the tibia (>5 mm), a bone contusion or impression fracture in a characteristic location (subarticular lateral femoral condyle and posterolateral tibia), and injury of medial collateral ligament, caused by anterior subluxation of the tibia and valgus force at the time of injury.

Typical MR imaging signs are less obvious when the ligament is avulsed at its femoral end as the ACL may retain a fairly normal alignment. Axial and coronal sections may be useful to distinguish discontinuity between the proximal ligament and the femoral condyle as well as secondary signs. An important associated condition with ACL tears is an avulsion fracture at the insertion of the meniscotibial aspect of the joint capsule (segond fracture), which is readily detected on radiography.

PCL tears are less common than ACL tears and often associated with other injuries, especially an ACL or posterolateral corner lesion (Carrino and Schweitzer 2002). The common mechanism is a hyperextension injury, an external rotation or a so-called "dashboard injury." Acute tears mostly occur as mid-substance interstitial lesions manifesting diffuse widening with increased T1 and T2 signal intensity. There may also be complete disruption or an avulsion involving the tibial attachment (Fig. 24.7).

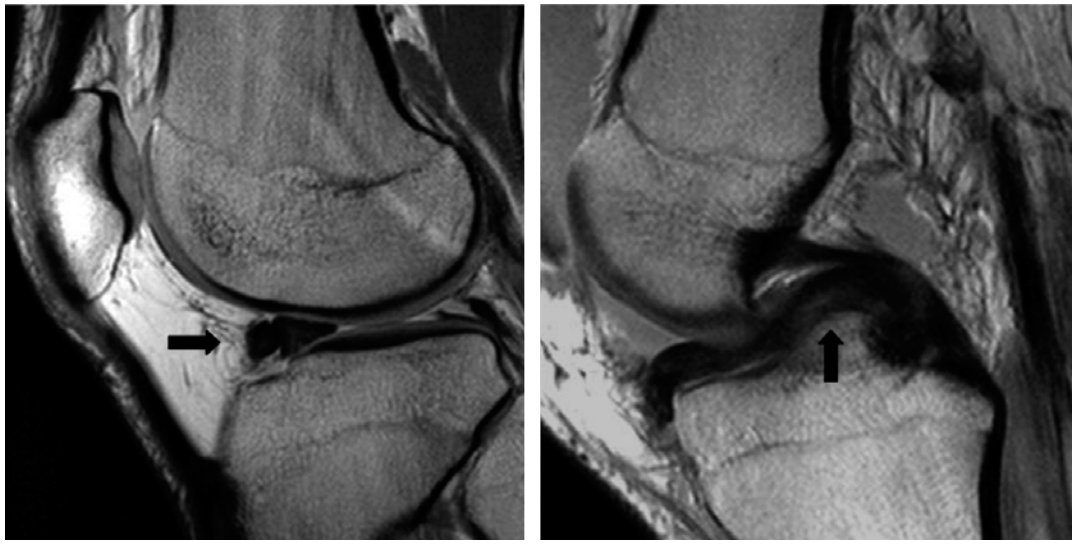

Fig. 24.5a,b. Bucket-handle tears. **a** Doubled anterior horn sign. The posterior fragment is adjacent to the anterior horn, creating the appearance of an abnormally large anterior horn (*arrow*). **b** Double PCL sign, which is characterized by the presence of a meniscal fragment parallel and anterior to the PCL (*arrow*)

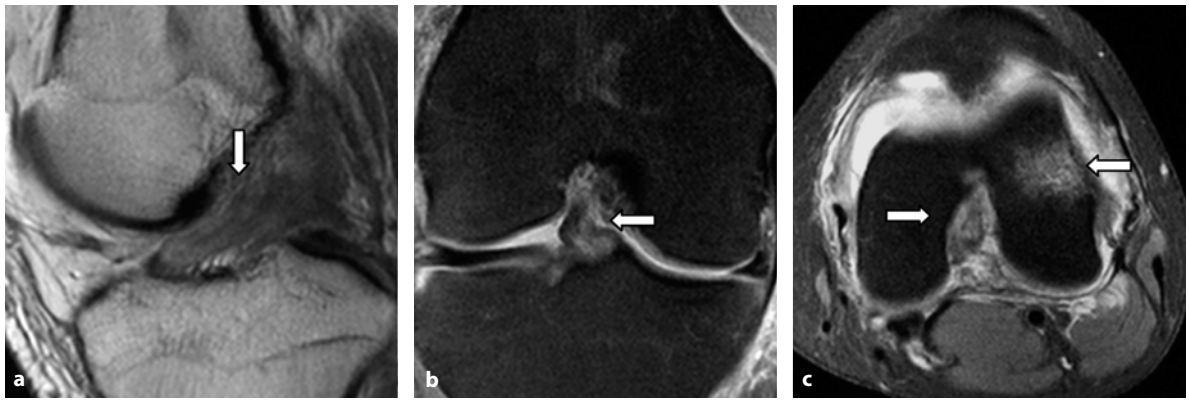

Fig. 24.6a–c. Acute anterior cruciate ligament (ACL) tear. **a** Ill-defined mass representing focal hemorrhage replacing the normal low signal linear ligament (*arrow*). Coronal **b** and axial **c** PD T2-weighted images with fat-saturation in a 36-year-old man after a skiing accident. Avulsion of ACL with increase in signal intensity. Typical associated edema in the lateral femoral condyle (*arrows*)

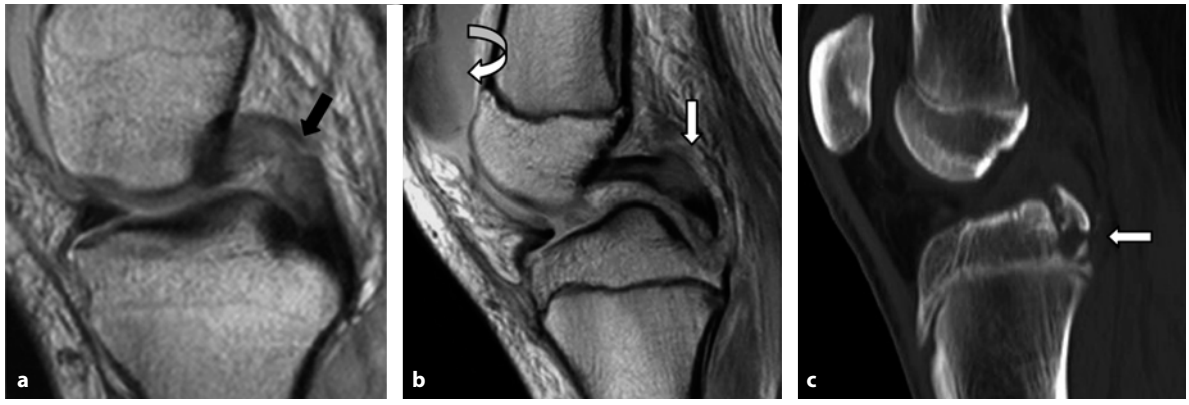

Fig. 24.7a–c. Acute posterior cruciate ligament (PCL) tear. **a** Diffuse pathologically increased signal and widening of the PCL (*black arrow*). **b**,**c** Focal disruption in the mid portion of the ligament. Additional bony fragment avulsed off at its tibial attachment (*white arrows*) and hemarthros (*curved arrow*) in a 16-year-old-woman after sports-related injury of the left knee. **c** Computed tomography, sagittal multiplanar reconstruction (MPR)

Medial collateral ligament (MCL) injuries are common and usually partial. They are often seen as part of a more complex injury, which is also true for the more rare tears of the lateral collateral ligament. Isolated tears are treated conservatively. Minor edema may be seen in the adjacent tissue or bony structure.

24.3.4 Osteochondral Pathologies

Much interest in MR imaging of the knee has focused on cartilage. Investigators have reported favorable results with optimized sequences (Kornaat et al. 2004). A wide variety of pulse sequences dedicated to cartilage imaging demonstrate, that, to date, there is no general consensus about MRI assessment of articular cartilage (McCauley and Disler 1998). Routine protocols are generally designed for assessment of the menisci, ligaments and bone. Although the commonly used proton-density weighted sequence with fat suppression is less sensitive in identifying defects, it is able to discern the frequent accompanying subchondral edema in the adjacent bone. Specialized sequences can be used in case optimum visualization of cartilage is required (Hargreaves et al. 2003; Kornaat et al. 2004). Cartilage lesions are diagnosed as alterations of the cartilage surface with

areas of increased signal intensity corresponding to the synovial fluid extending down into the cartilage. This is facilitated by the arthrogram-like effect of T2-weighted sequences. Diagnostic criteria are the assessment of cartilage thickness, e.g., the reduction by less or more than 50%, the detection of focal cartilage lesions, exposure of the subchondral bone and the evaluation of signal alterations within articular cartilage (Fig. 24.8a).

Dislocation of the patella often causes defects in the retropatellar cartilage surface (Fig. 24.2). MRI will show a characteristic pattern with subcortical edema at the anterolateral aspect of the femoral condyle. There may be a corresponding edema of the medial aspect of the patella or a cartilage fragment from a medial patellar osteochondral fracture (Fig. 24.8b). Because of strong lateral forces, the medial retinaculum is usually torn.

24.4 Imaging the Shoulder

24.4.1 Basic Principles

Due to its excellent soft-tissue contrast and multiplanar acquisition, MR imaging provides an optimal noninvasive assessment of both intraarticular and extraarticular shoulder joint pathologies. The most common indications for MRI of the shoulder are impingement syndrome, rotator cuff tear, glenohumeral instability, and posttraumatic disorders (Vahlensieck 2000). The discussion whether direct MR arthrography or unenhanced imaging should be used for shoulder imaging is still ongoing. MR arthrography extends the capabilities of conventional MR imaging and has been proven to increase accuracy in partial-thickness tears and evaluation of labral-ligamentous abnormalities because contrast solution distends the joint capsule, outlines intraarticular structures, and leaks into abnormalities (Elentuck and Palmer 2004; Steinbach et al. 2002).

The patients should be positioned supine with the arms along their side, the affected arm in neutral to slight external rotation. Three well-defined planes have been established for standard examination. The series begins with an axial plane that serves as a localizer for the subsequent two planes. The additional planes are an oblique-coronal (parallel to the course of the supraspinatus muscle) and an oblique-sagittal plane, located perpendicular to the supraspinatus muscle. For the question of an anteroinferior glenohumeral instability and delineation of subtle undersurface or partial-thickness rotator cuff tears, diagnostic confidence may be further increased when the shoulder is imaged with additional sections in abduction and external rotation (ABER position)

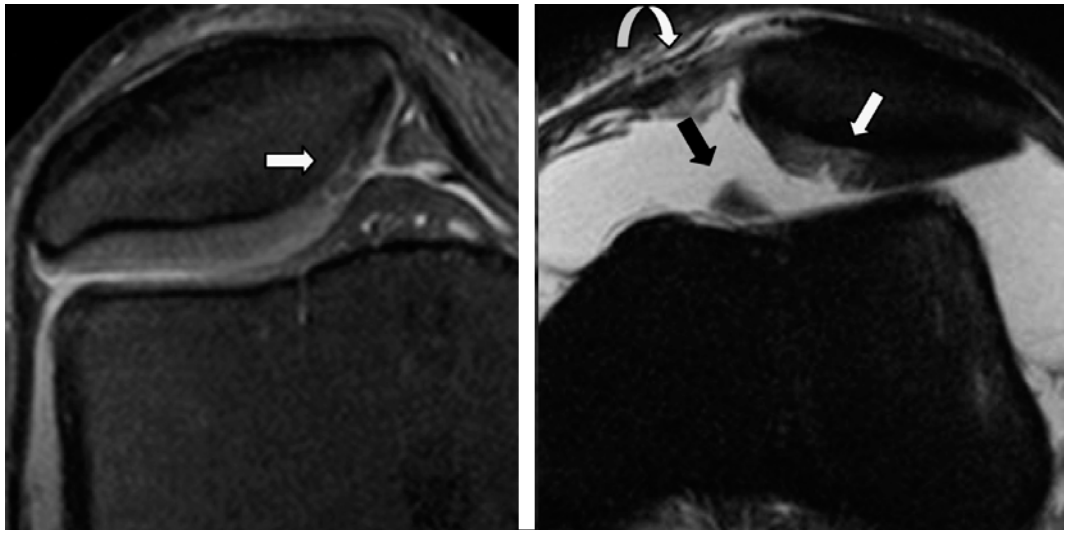

Fig. 24.8a,b. Articular cartilage defects. **a** Subtle full-thickness defect involving the medial facet of the patella (*arrow*). **b** Patellar dislocation. Cartilage defect in the retropatellar surface (*white arrow*). The corresponding chondral flake (*black arrow*) is embedded in front of the femoral condyle. There is partial tear of the medial retinaculum (*curved arrow*). **a,b** Imaging time 2:42 min with SENSE (acceleration factor *R*=2)

(Grainger et al. 2000; Kwak et al. 1998). This position is achieved by flexing the elbow and placing the patient's hand behind the head or neck. Oblique-axial T1-weighted images are then acquired, parallel to the long axis of the humeral shaft.

For signal detection, the employment of surface coils around the shoulder is mandatory. To achieve high-signal resolution, a section thickness of 3-4 mm is usually used in combination with an imaging matrix of 256×192 or more and a maximum 160 mm FOV. A variety of different scanning protocols are known. Using a high-field MR scanner, an example of a routine pulse sequence protocol include (1) axial fast-spin-echo proton-density and fat-suppressed T2-weighted sequence; (2) oblique-coronal PD FS T2-weighted FSE; (3) oblique-coronal T1-weighted SE; (4) oblique-sagittal T2-weighted SE. T1-weighted SE sequences, with or without fat-saturation, should be obtained following MR arthrography. In this case an additional T2-weighted sequence is helpful in the identification of extraarticular fluid collections, such as paralabral cysts (Steinbach et al. 2002). To the authors' knowledge only one study using parallel imaging in MRI of the shoulder has been published in *medline* so far (Magee et al. 2003). T2-weighted SMASH acquisitions as opposed to fat-saturated T2-weighted images result in a significant decrease in scan time (>5 min) and yield fewer motion artefacts, while no negative effect on diagnostic quality could be observed.

We can confirm these results from our own initial experience in shoulder MR imaging using parallel imaging. In the author's institution, different modified examination protocols exist depending on the clinical question. An example of a MR arthrography protocol consists of (1) a T1-weighted TIRM (Turbo Inversion Recovery Magnitude) sequence in the oblique coronal plane (TR=4,000 ms, TE=27 ms, TI=130 ms, 160×160 mm² FOV, 394×512 matrix, and 4-mm section thickness); (2) a fat-saturated PD-weighted FSE sequence in the axial plane (160×160 mm² FOV, 512×512 matrix, and 3-mm section thickness); (3) a two-dimensional T2*-weighted gradient-echo sequence (fast low-angle shot; FLASH) in the oblique sagittal orientation (160×160 mm² FOV, 307×384 matrix size, and 4-mm section thickness). The used sequences result in an in-plane resolution between 0.6×0.3 mm^2 and 0.6×0.6 mm^2. To avoid folding artefacts, the authors use 100% phase oversampling. Performing this protocol with parallel imaging using an acceleration factor of 2 results in a total imaging time of 6:36 min compared to 12:24 min by using a conventional imaging technique; thus, a scan time reduction of 47% is achieved. Our implemented Siemens scanner software (Maestro) enables both the mSENSE and GRAPPA techniques. In the authors' opinion, both parallel acquisition techniques produce images of consistent and good quality. Generally speaking, images obtained with the GRAPPA technique appear slightly more noisy due to an inaccurate calculation of missing lines in k-space, and mSENSE images seems to suffer from slight aliasing artefacts outside the FOV in some cases (Fig. 24.9) (Blaimer et al. 2004).

24.4.2 The Rotator Cuff

The rotator cuff is composed of the musculotendineous parts of the subscapularis, supraspinatus, infraspinatus and teres minor muscles, which predominantly stabilize the shoulder joint. These muscles can be affected by degeneration or trauma. Defects of the rotator cuff can be classified into partial-thickness and full-thickness tears irrespective of the etiology. Most of them are the result of attritional change and tendon degeneration due to impingement syndrome or overuse. The condition primarily affects the supraspinatus tendon and overlying subacromial bursa. It is presumed that 95% of rotator cuff tears are caused by impingement mechanisms within the restricted subacromial space (Vahlensiek 2000). Degeneration of the tendon is very common, particularly in the elderly in whom it can be regarded as a normal aging process. The differential diagnosis of acute vs. chronic tendonitis, degeneration and partial thickness tears of the rotator cuff is difficult. While the signal intensity of normal tendons is low on all sequences, in acute tendonitis MR images show diffuse or patchy high signal within the tendon on T1- and T2-weighted images. Chronic tendonitis is thought to cause abnormally increased signal on T1 without a signal increase on T2-weighted images. In partial thickness tears, MR imaging findings exhibit focal areas of mildly increased signal intensity on T1-weighted images, high signal intensity on T2-weighted images, and contour irregularities (Lee and Lang 2000). In conventional MR imaging of the shoulder, minute partial tears tend to be mistaken for tendinopathy, and high-grade partial tears can be misinterpreted for complete full-thickness tears. In addition, the "magic angle" artefact may lead to a mild increased signal within the tendon on T1-

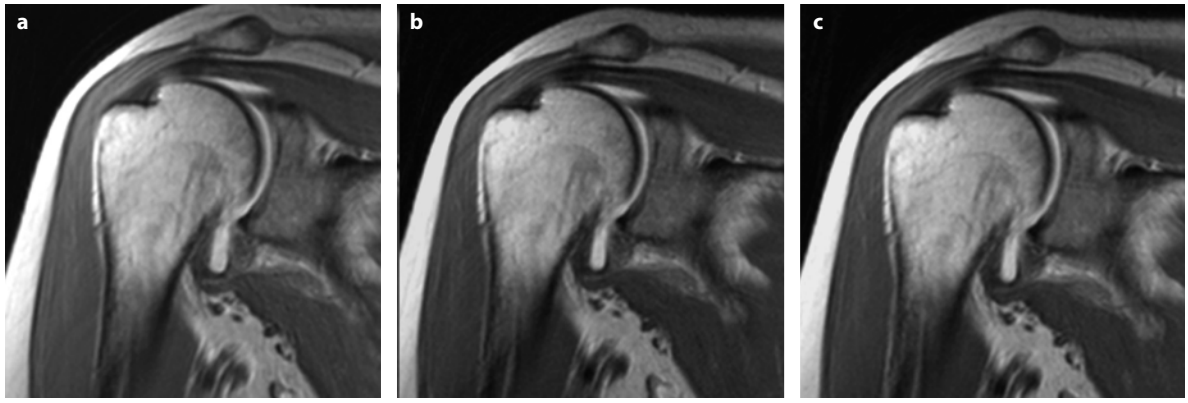

Fig. 24.9a–c. Oblique coronal T1-weighted MR arthrography images in a patient after tuberculum majus fracture. All images obtained with identical scan parameters **a** conventional, **b** GRAPPA, **c** mSENSE acquisition technique. Imaging time **a** 5:14 min; **b** and **c** 2:46 min using an acceleration factor *R*=2. Notice no discernible difference in image quality

weighted images and could be responsible for a false diagnosis (Erickson et al. 1993). These diagnostic difficulties can be resolved using MR arthrography, which is shown to be superior to conventional imaging (Flannigan 1990). The decision to perform MR arthrography is primarily based on the patient's age and the clinical need to differentiate between partial-thickness and small complete tears.

Partial tears involve the articular surface more often than the bursal surface and are seen as focal high signal, irregularities and fraying. In this location, high-signal intensity contrast solution can fill these focal cuff defects without leaking into the subacromial-subdeltoid space. The criterion for the diagnosis of a full-thickness rotator cuff tear is filling of the subacromial-subdeltoid bursa with contrast media that has extravasated into the bursa through the cuff defect (Fig. 24.10). Diagnostic accuracy of MR arthrography is increased when fat-suppressed images are acquired. On standard T1-weighted images, bursal fat and gadolinium have similar signal intensities, so it may be difficult to distinguish an extravasation. Other signs of a complete tear are a gap within the tendon, retraction of the musculotendinous junction, and fatty atrophy of the muscle. The accuracy of MR arthrography in the diagnosis of tears of the rotator cuff approaches 100% (Elentuck and Palmer 2004; Kreitner et al. 2003).

24.4.3 The Glenohumeral Unit

Anteroinferior instability is the most common type to involve the glenohumeral joint, occurring in 95% of all patients (McCarthy 2003). Generally, glenohumeral instability is present when symptoms occur due to the translation of the humeral head out of the glenoid fossa. Fractures of the osseous glenoid and humeral head as well as tears of the labroligamentous complex are frequently associated features. From a clinical point of view, there are two main categories to be differentiated, which require different forms of treatment: (1) TUBS, which is characterized by a history of trauma resulting in unidirectional anterioinferior instability, commonly linked with a fibrous or osseous Bankart lesion that requires surgical repair; (2) AMBRI: this category describes an atraumatic instability that is multidirectional and bilateral. This pattern is believed to be the result of atraumatic ligamentous and capsular laxity. It usually responds to a rehabilitation program followed by inferior capsular shift if indicated.

Evaluation of shoulder instability and diagnosis of anterior labral lesions routinely entails a MR arthrogram. The major limiting factors of conventional MR imaging include normal variability in labral morphology and difficulty distinguishing pseudotears from true labral tears. Signs of labral tears are a detached and displaced or absent labrum, a blunted edge and labral fragmentation. However, conventional MR imaging has been used with inconsistent success to evaluate shoulder instability. The reported

accuracy for the diagnosis of anterior labral lesions has been reported with sensitivities ranging from 44 to 95% and specificities ranging from 67 to 86% (Palmer 1997). One of the major advantages of MR arthrography lies in the full distention of the capsule, improving dramatically the visualization of the labral-ligamentous complex, which consists of the glenoid labrum in combination with the superior, middle, and inferior glenohumeral ligaments (IGHL) (Fig. 24.11). The reported accuracy of arthrographic MR images for the diagnosis of labral anormalities has been demonstrated as greater than 90% (Elentuck and Palmer 2004; Kreitner et al. 2003). The anterior band of the IGHL is the main passive stabilizer of the shoulder and functions as a unit with the glenoid labrum. The origin of the IGHL creates a stress point on the glenoid labrum. During anteroinferior shoulder dislocation, subluxation or excessive abduction-external rotation, commonly the anteroinferior aspect of the glenoid labrum tears. Avulsion of

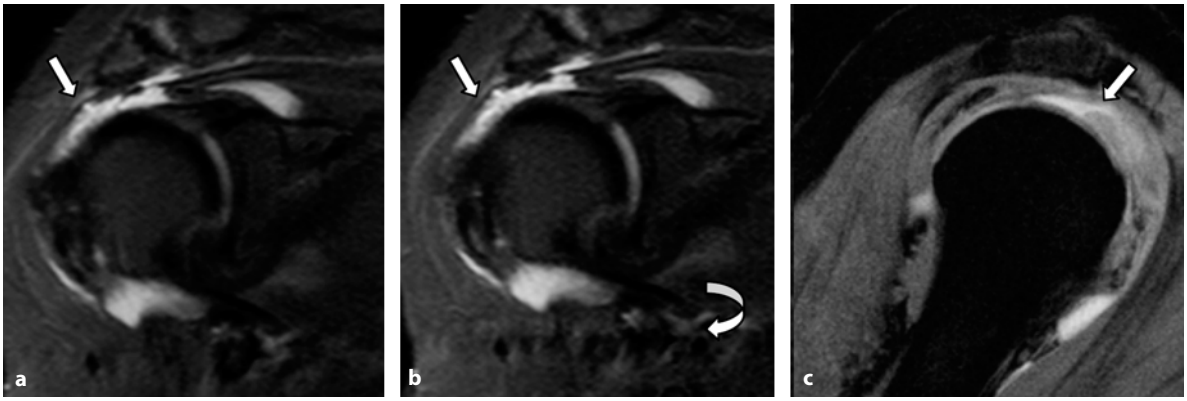

Fig. 24.10a–c. Full-thickness rotator cuff tear of the supraspinatus tendon. **a,b** Following intra-articular injection, T1-TIRM oblique coronal images demonstrate a gap and retraction of the supraspinatus tendon (*arrow*) and high-signal contrast material passing from the joint into the subdeltoid-subacromial space. Notice slight artefacts appearing in **b** obtained with SENSE (*curved arrow*) compared with conventional technique in **a**. **c** Fat saturated PD-FSE oblique sagittal image demonstrates the anteroposterior dimension of the defect (*arrow*)

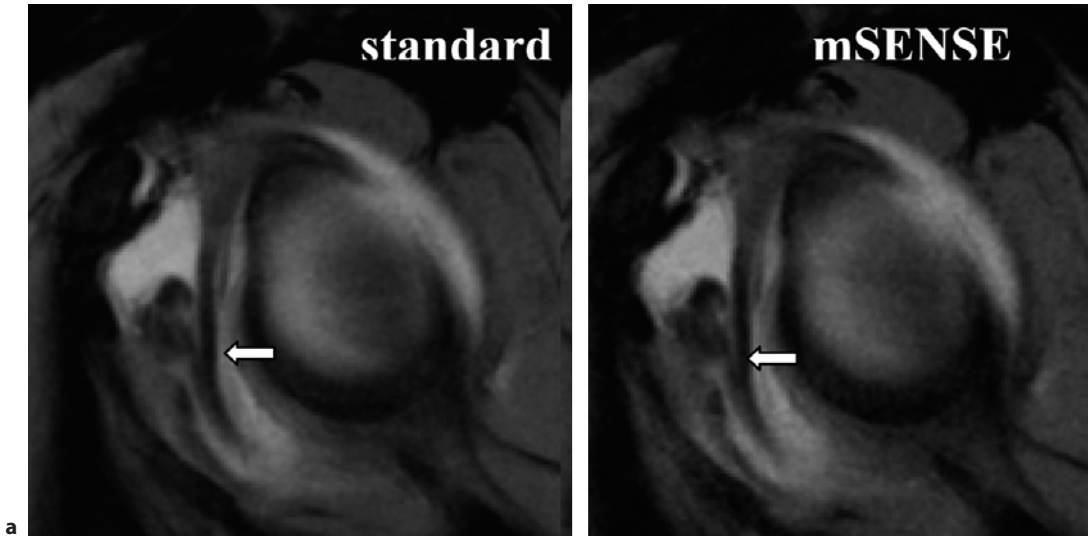

Fig 24.11a,b. Normal anatomy as depicted on sagittal oblique T1-weighted 2D FLASH MR arthrographic images obtained with fat suppression; **a** conventional and **b** mSENSE technique. Lateral view on the labrum glenoidale with glenohumeral ligaments (*arrow*). All details are clearly portrayed with both techniques. Imaging time **a** 4:54 min, **b** 2:35 min

the labroligamentous complex with complete disruption of the scapular periosteum is termed a fibrous Bankart lesion. The presence of an associated adjacent glenoid rim fracture is referred to as an osseous Bankart lesion.

MR arthrography can help to differentiate between Bankart variations, where the periosteum remains intact, such as Perthes lesion, anterior labroligamentous periostal sleeve avulsion (ALPSA), glenolabral articular disruption (GLAD) and humeral avulsion of the glenohumeral ligament (HAGL). Although MR arthrography has demonstrated high accuracy in the detection of anteroinferior glenoid labral tears, diagnostic confidence may be further increased when the shoulder is imaged in the ABER position (Grainger et al. 2000; Kwak et al. 1998). SLAP (superior labral, anterior and posterior to the biceps tendon tear) lesions are frequent and clinically important abnormalities that most commonly result from repetitive traction to the biceps tendon as seen in throwing athletes. The original classification described four types of SLAP lesions ranging from degeneration and fraying to a bucket-handle tear (Kreitner et al. 1998). Labral tears and instability can be accompanied by the development of paralabral cysts or ganglia. Such cysts may extend into the surascapular or spinoglenoid notch and produce an entrapment neuropathy of the suprascapular nerve. Denervation of this nerve results in weakness of the supraspinatus and infraspinatus muscles and pain simulating impingement syndrome.

24.5 Conclusion

In the last years, parallel imaging strategies have seen increasing acceptance of clinical MR. Research and implementation were focused on cardiovascular, brain and breath-hold MR examinations (Bammer and Schoenberg 2004; Oberholzer et al. 2003; van den Brink et al. 2003). Until now, only a limited number of studies have been related to musculoskeletal imaging (Kwok et al. 2003; Magee et al. 2003; Magee et al. 2004; Niitsu and Ikeda 2003; Romaneehsen et al. 2003, 2004).

In this chapter, the clinical applications of parallel MR imaging of the knee and shoulder joint have been demonstrated. In addition, a brief overview of typical pathologies and their appearance on MRI studies obtained with the SENSE technique was provided. Shortening examination time is one main advantage of parallel imaging, especially in patients who suffered from an acute traumatic injury. Because of subtle anatomic details high spatial resolution is a crucial parameter in musculoskeletal MR imaging. In practice, both commercially available parallel imaging techniques (SENSE, GRAPPA) as well as the SMASH technique have been proven to produce images with comparable quality. With the advent of parallel imaging, the authors expect an increase in diagnostic accuracy as the result of possible higher resolution acquired at the same time as with conventional technique. At 3 T already extremely high, isotropic spatial resolution can be obtained in a moderate examination time (Schick 2005). Recently, MR systems with up to 32 channels as well as high-field 3-T scanners have become available, but not yet widely introduced in the clinical routine. During the next few years, new concepts of image acquisition and reconstruction techniques, e.g., Transmit SENSE (Katscher et al. 2003) (cf. Chap. 45), higher acceleration factors, as well as the development of adapted coil systems (cf. Chap. 44), will broaden the wide acceptance in musculoskeletal parallel imaging.

References

Aydingöz Ü, Firat AK, Atay ÖA, et al (2003) MR imaging of meniscal bucket-handle tears: a review of signs and their relation to arthroscopic classification. Eur Radiol 13: 618–625

Bammer R, Schoenberg SO (2004) Current concepts and advances in clinical parallel magnetic resonance imaging. Top Magn Reson Imaging 15: 129–158

Barry KP, Mesgarzadeh M, Triolo J, et al (1996) Accuracy of MRI patterns in evaluating anterior cruciate ligament tears. Skeletal Radiol 25: 365–370

Blaimer M, Breuer F, Mueller M, et al (2004) SMASH, SENSE, PILS, GRAPPA: how to choose the optimal method. Top Magn Reson Imaging 15: 223–236

Bredella MA, Tirmann PF, Peterfy CG, et al (1999) Accuracy of T2-weighted fast spin-echo MR imaging with fat saturation in detecting cartilage defects in the knee: comparison with arthroscopy in 130 patients. Am J Roentgenol 172:1073–1080

Carrino JA, Schweitzer ME (2002) Imaging of sports-related knee injuries. Radiol Clin North Am 40: 181–202

Cheung L, Li K, Hollett M, et al (1997) Mensical tears of the knee: value of fast spin-echo vs. conventional spin-echo pulse sequences. Radiology 203: 508–512

Dietrich O, Nikolaou K, Wintersberger BJ, et al (2002) iPAT: Applikationen für schnelle und kardiovaskuläre MRT. Electromedia 70: 149–162

Elentuck D, Palmer WE (2004) Direct magnetic resonance arthrography. Eur Radiol 14: 1956–1967
Erickson J, Prost RW, Timins ME (1993) "Magic angle" effect: background physics and clinical relevance. Radiology 188: 23–25
Flannigan B, Kursunoglu-Brahme S, Schnyder S, et al (1990) MR arthrography of the shoulder: comparison with conventional MR imaging. Am J Roentgenol 155: 829–832
Goldfarb JW (2004) The SENSE ghost: field-of-view restrictions for SENSE imaging. J Magn Reson Imaging 20: 1046–1051
Grainger AJ, Elliott JM, Campbell RSD, et al (2000) Direct MR arthrography: a review of current use. Clin Radiol 55: 163–176
Griswold MA, Jakob PM, Heidemann RM, et al (2002) Generalized autocalibrating partially parallel acquisitions (GRAPPA). Magn Reson Med 47: 1202–1210
Hargreaves BA, Gold GE, Beaulieu CF, et al (2003) Comparison of new sequences for high-resolution cartilage imaging. Magn Reson Med 49: 700–709
Helms CA (2002) The impact of MR imaging in sports medicine. Radiology 224:631–635
Helms CA (2002) The meniscus: recent advances in MR imaging of the knee. Am J Roentgenol 179: 1115–1122
Katscher U, Börnert P, Leussler C, et al (2003) Transmit SENSE. Magn Reson Med 49: 144–150
Kornaat PR, Doornbos J, van der Molen AJ, et al (2004) Magnetic resonance imaging of knee cartilage using a water selective balanced steady-state free precession sequence. J Magn Reson Imaging 20: 850–856
Kreitner KF, Botchen K, Rude J, et al (1998) Superior labrum and labral-bicipital complex: MR imaging with pathologic-anatomic and histologic correlation. Am J Roentgenol 170: 599–605
Kreitner KF, Loew R, Runkel M, et al (2003) Low-field MR arthrography of the shoulder joint: technique, indications, and clinical results. Eur Radiol 13: 320–329
Kwak SM, Brown RR, Trudell D, et al (1998) Glenohumeral joint: comparison of shoulder positions at MR arthrography. Radiology 208: 375–380
Kwok WE, Zhong J, You Z, et al (2003) A four-element phased array coil for high resolution and parallel MR imaging of the knee. Magn Reson Imaging 21: 961–967
Lee SU, Lang P (2000) MR and MR arthrography to identify degenerative and posttraumatic diseases in shoulder joint. Eur J Radiol 35: 126–135
Magee T, Shapiro M, Williams D, et al (2003) Usefulness of the simultaneous acquisition of spatial harmonics technique during MRI of the shoulder. Am J Roentgenol 181: 961–964
Magee T, Shapiro M, Williams D (2004) Usefulness of the simultaneous acquisition of spatial harmonics technique for MRI of the knee. Am J Roentgenol 182: 1411–1414
McCarthy C (2003) Glenohumeral instability. Imaging 15: 174–179
McCauley T, Disler D (1998) MR imaging of articular cartilage. Radiology 209: 629–640
Niitsu M, Ikeda K (2003) Routine MR examination of the knee using parallel imaging. Clin Radiol 58:801–807
Oberholzer K, Romaneehsen B, Kunz P, et al (2004) Contrast-enhanced 3D MR angiography of the pulmonary arteries with integrated parallel acquisition technique (iPAT) in patients with chronic-thromboembolic pulmonary hypertension CTEPH - sagittal or coronal acquisition? Fortschr Roentgenstr 176: 605–609
Osterle S (2003) Imaging the knee. Imaging 15: 217–241
Palmer WE (1997) MR arthrography of the rotator cuff and labral-ligamentous complex. Semin Ultrasound CT MRI 18: 278–290
Pruessmann KP, Weiger M, Scheidegger MB (1999) SENSE: Sensitivity encoding for fast MRI. Magn Reson Med 42: 952–962
Romaneehsen B, Oberholzer K, Mueller LP, et al (2003) Rapid musculoskeletal magnetic resonance imaging using integrated parallel acquisition techniques (iPAT) –initial experiences. Fortschr Roentgenstr 175:1193–1197
Romaneehsen B, Oberholzer K, Mueller LP, et al (2004) Fast MRI of the knee using a parallel acquisition technique (SENSE): a prospective performance study. Proceedings of the 90th scientific assembly and annual meeting of the RSNA, Chicago
Schick F (2005) Whole-body MRI at high field: technical limits and clinical potential. Eur Radiol 15: 946–959
Stäbler A, Glaser C, Reiser M (2000) Musculoskeletal MR: knee. Eur Radiol 10: 230–241
Steinbach LS, Palmer WE, Schweitzer ME (2002) Special focus session: MR arthrography. RadioGraphics 22: 1223–1246
Vahlensieck M (2000) MRI of the shoulder. Eur Radiol 10: 242–249
Van den Brink JS, Watanabe Y, Kuhl CK, et al (2003) Implications of SENSE in routine clinical practice. Eur J Rad 46: 3–27
Weiger M, Boesiger P, Hilfiker PR, et al (2005) Sensitivity encoding as a means of enhancing the SNR efficiency in steady-state MRI. Magn Reson Med 53: 177–185

Advanced Methods of Fat Suppression and Parallel Imaging

25

Scott B. Reeder and Charles A. McKenzie

CONTENTS

25.1 Introduction

Uniform and reliable suppression of fat is essential for accurate diagnoses in many areas of MR imaging. This is particularly true for sequences such as T1-weighted spoiled gradient echo sequences (SPGR), steady-state free precession (SSFP), and fast spin-echo (FSE) imaging where fat is bright and may obscure underlying pathology. Conventional fat-saturation is often adequate for areas of the body with relatively homogeneous main (B_0) magnetic field; however, there are many applications where fat-saturation commonly fails. Off-isocenter imaging, extremity imaging, large field of view (FOV) imaging, and areas such as the skull base and brachial plexus, as well as many others, are all examples of imaging applications where B_0 is rarely homogenous. Conventional fat-saturation pulses are also sensitive to RF (B_1) inhomogeneities, which may be problematic for transmit surface coil applications.

Short-TI inversion recovery (STIR) imaging provides very uniform fat-suppression, but has mixed contrast that is highly dependent on T1, and has reduced the signal-to-noise ratio (SNR) (Bydder et al. 1985). In addition, the possibility of suppressing contrast-enhanced tissue limits STIR to proton density or T2-weighted applications, and most clinical T1-weighted applications rely solely on conventional fat-saturation methods. STIR also has reduced sequence efficiency because of the need to play an inversion pulse followed by a relatively long inversion time (TI) (approximately 200 ms at 1.5 T). Other fat-suppression techniques include water-selective "spectral-spatial" pulses, and although these water-selective methods are insensitive to B_1 inhomogeneities, they remain sensitive to B_0 inhomogeneities (Meyer et al. 1990; Block et al. 1997).

First described in 1984 by Dixon (1984), "in and out of phase" imaging exploits the difference in chemical shifts between water and fat in order to separate water and fat into separate images. This approach was further refined by Glover using a "three-point" method that acquired three separate images at different echo times to compensate for B_0 field inhomogeneities (Glover 1991; Glover and Schneider 1991). Three-point water-fat separation methods have been successfully applied to other sequences including fast spin-echo (FSE) (Hardy et al. 1995), gradient echo (GRE) imaging (Wang et al. 1998), steady-state free precession (SSFP) (Reeder et al. 2003) and spiral methods (Moriguchi et al. 2003). Chemical-shift-based water-fat separation methods that measure field inhomogeneities, and subsequently compensate for them, provide robust water-fat separation in areas that are challenging for conventional fat-saturation methods.

S. B. Reeder, MD, PhD
Department of Radiology, E3/311 CSC, 600 Highland Avenue, Madison, WI 53792-3252, USA
C. A. McKenzie, PhD
Department of Radiology, Beth Israel-Deaconess Medical Center, Boston, MA

In addition, water-fat separation methods are insensitive to B_1 inhomogeneities and are well suited for transmit surface coil applications. A final advantage of water-fat separation methods compared with fat suppression methods is the availability of the fat image, which improves tissue characterization through direct visualization of fat in addition to water.

A recently described method, IDEAL (Iterative Decomposition of water and fat with Echo Asymmetry and Least-squares estimation), has been applied to FSE (Reeder, Pineda, Wen et al. 2005) and gradient echo imaging (Reeder, Pineda, Yu et al. 2005). This method uses an iterative method to determine the field inhomogeneity map, allowing the algorithm to remove phase shifts in the source images caused by field inhomogeneities, and subsequently calculates separate water and fat images in the least squares sense. This method allows for arbitrary and unequally spaced echoes, allowing the optimal combination of echo shifts to be used to maximize the SNR performance of the water-fat decomposition (see below). In this chapter, examples of water-fat decompositions will be shown using the IDEAL method, although other chemical shift-based water-fat methods can also be combined with parallel imaging.

25.2 Chemical-Shift-Based Water-Fat Separation

For most clinical MR applications an image will contain both water and fat. The signal from a voxel will have a complex dependence on the amount of water and fat in that voxel, as well as the echo time and the local field inhomogeneity. Mathematically, the signal from such a voxel can be written,

$$s(t_n) = \left(W + Fe^{i2\pi\Delta f_{fw} t_n}\right) e^{i2\pi\psi t_n} \quad (1)$$

where t_n is the echo shift from the spin-echo or TE=0 for gradient echo imaging, W and F are signal intensities from water and fat, Δf_{fw} is the chemical shift between water and fat, approximately –210 Hz at 1.5 T or –420 Hz at 3.0 T, and ψ is the off-resonance frequency shift (Hz) resulting from local B_0 inhomogeneities. Figure 25.1 shows a vector diagram of the signal contributions from water (*red*) and fat (*blue*) to the observed signal (*purple*) when water and fat are in-phase (t=0) and at some time t chosen to achieve a phase θ between water and fat. The angle $\varphi = 2\pi\psi t$ is the phase resulting from local field inhomogeneity, ψ, acting on both the water and fat vectors.

By sampling $s(t_n)$ at three or more different echo times t_n, there is sufficient information to decompose water from fat. The specific choice of echo times greatly influences the best possible SNR performance of the water-fat decomposition. For example, conventional three-point methods, first described by Glover (Glover 1991; Glover and Schneider 1991), acquired echoes with a relative water-fat phase shift ($\theta = 2\pi\Delta f_{fw} t_n$) of -π, 0, π, i.e.: out of phase, in-phase, and out of phase. With this echo combination, the effective number of signal averages (NSA) can be shown to be approximately 2.7, about 10% less SNR than the maximum possible NSA of 3.0, which would be achieved if all the information from the three source images was

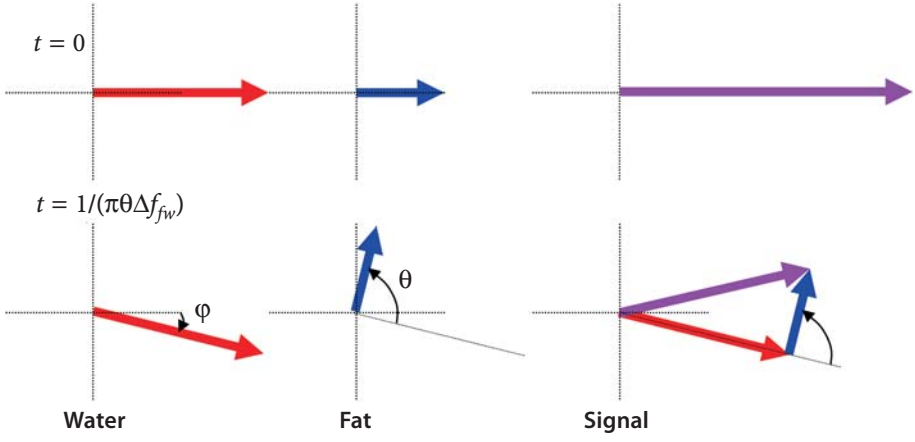

Fig. 25.1. Water (*red*) and fat (*blue*) signal add to form the observed signal (*purple*), shown at two different echo times, t=0 (in-phase) and $t = 1/2\pi\theta\Delta f_{fw}$

used efficiently to separate water from fat. Recently, it has been shown that the SNR of the water and fat image is maximized when the relative phase of water and fat is perpendicular (i.e.: $\theta = 2\pi\Delta f_{fw} t_n = \pi/2, 3\pi/2$, etc.), for one of the echoes, and the other two echoes are acquired with a relative phase shift $2\pi/3$ before and after the perpendicular echo (Pineda et al. 2005). This would correspond to echo shifts of -0.4ms, 1.2 ms and 2.8 ms for FSE imaging at 1.5 T. For this combination of echoes, the SNR performance reaches the maximum possible with NSA=3.0. This work has also shown that in general, there is a strong dependence of the SNR behavior on the proportion of water and fat in a voxel, except for the above combination of echo shifts when the NSA is 3.0 for all ratios of water and fat. Figure 25.2 summarizes one possible water-fat separation approach using IDEAL. It is important to note that although it is possible to acquire all three echoes within a single TR using an echo-planar readout, multi-echo approaches are restrictive, and it is difficult to achieve the optimal echo shifts while maintaining flexibility in the acquisition paramters such as bandwidth and matrix size.

Figure 25.3 shows an example of a calculated water T2-weighted FSE image of the brachial plexus of a normal volunteer acquired with a neurovascular coil, compared with a conventional T2-weighted fat-saturated FSE image. Large areas of failed fat-suppression seen in the fat-saturated image, caused by severe susceptibility commonly seen in the head and neck region, show uniform separation of water from fat in the IDEAL image.

Extremities such as the ankle and foot are also challenging areas where conventional fat-saturation commonly fails as a result of unfavorable geometry that exacerbates susceptibility differences. Figure 25.4 is an example of IDEAL-FSE imaging in an ankle with a metallic fixation plate, demonstrating improved suppression of fat compared to conventional fat-saturation, despite the presence of metallic hardware.

Characterization of tissues through direct visualization of fatty tissue is a distinct advantage of water-fat separation methods. For example, Fig. 25.5 shows separated T2-weighted-FSE water and fat images, as well as recombined images from the pelvis of a woman with an adnexal mass. A large component of this bright mass separates into the fat-only image, confirming the diagnosis of ovarian dermoid with high confidence.

As a companion case to the images shown in Fig. 25.5, Fig. 25.6 shows T1-weighted IDEAL-FSE images through the pelvis of a woman with endometriosis. A small hyperintense mass along the right pelvic side-wall separates into the water-only image, indicating that this is not a fatty mass as may have been initially suspected on a non-fat suppressed image.

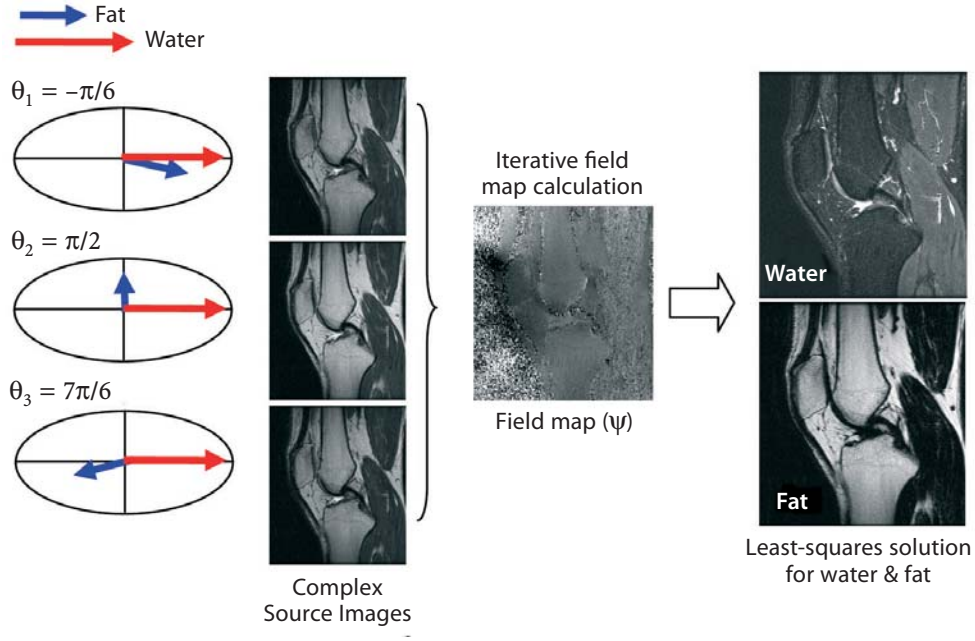

Fig. 25.2. Schematic of the IDEAL water-fat separation method. Three complex images acquired at optimized echo shifts (θ_1, θ_2, and θ_3) are used by an iterative field map calculation to determine the field map (ψ). The effects of the field map are removed from the source images and water and fat images are subsequently calculated using a least-squares solution

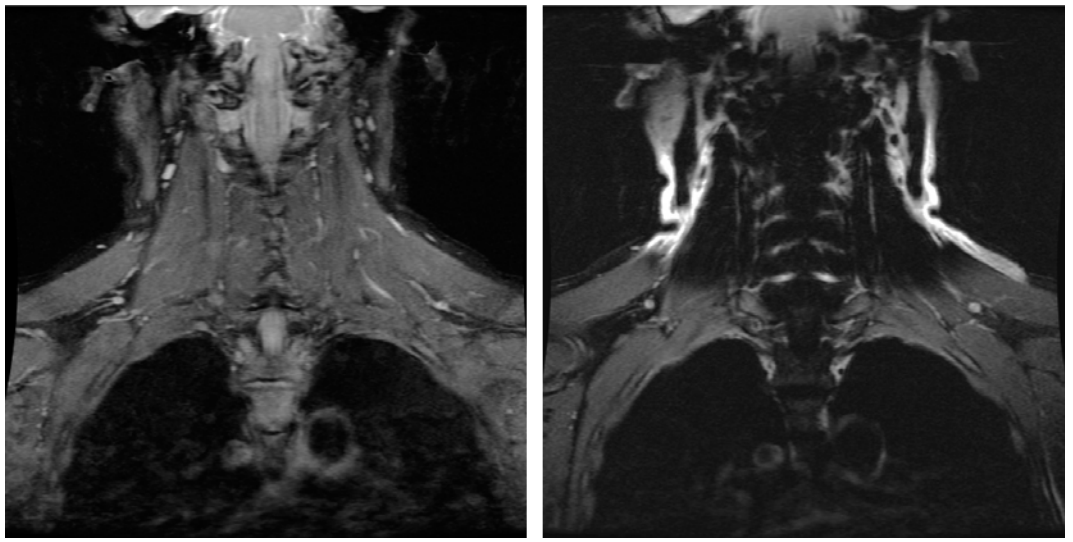

Fig. 25.3a,b. a Coronal water T2-weighted IDEAL-FSE image of the brachial plexus and cervical spine shows tremendously improved fat suppression in comparison to **b** conventional fat-saturated FSE imaging, which shows large areas of failed fat saturation and inadvertent water suppression leading to a non-diagnostic image

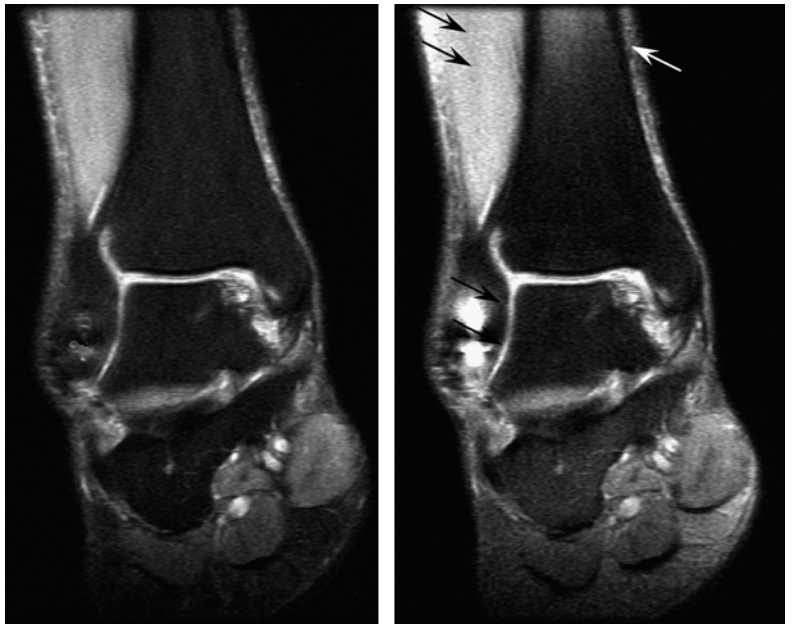

Fig. 25.4a,b. Coronal T2-weighted images of an ankle with a metallic fibular screw acquired with **a** IDEAL-FSE and **b** conventional fat-saturated FSE. Areas of failed fat-saturation near the screw as well as elsewhere are seen in the fat-saturated image (*arrows*)

An interesting variation of chemical shift-based imaging is the separation of water and silicone. Silicone and water have a relative chemical shift of approximately –315 Hz at 1.5 T (Schneider and Chan 1993). This opens the potential for water-silicone separation, an application particularly important for evaluation of silicone breast implant rupture. An effective approach using a STIR inversion pulse to suppress signal from fat within the breast has been described by Ma et al. (2004). In this approach, the separation of water and silicone is performed by adjusting the echo shifts slightly to achieve the same phase shifts normally used between water and fat. Because water and silicone have a relative chemical shift larger than that between water and fat, the echo shifts are smaller than those used for water-fat sepa-

ration. Figure 25.7 shows an example of T2-weighted IDEAL-STIR imaging of a breast containing a composite saline-silicone implant demonstrating uniform separation of silicone and water with uniform suppression of fat. The silicone component has ruptured and is clearly visualized in the silicone-only image.

25.2.1 Noise Performance of Water-Fat Separation Methods

As mentioned above, the noise performance of an estimation technique such as water-fat decomposition used in chemical shift-based separation methods can be described with the effective number of signal averages (NSA), which is equivalent to signal averaging commonly used to describe MR acquisitions. With conventional three-point methods, NSA is 2.7, and with IDEAL, NSA is 3.0, the maximum possible for any three-point method, utilizing all available signal in an efficient manner. An effective average of three implies that the SNR of the decomposed water and fat images will increase by $\sqrt{3}$ (≈1.73) compared to the SNR of a single source image.

25.3 Parallel Imaging and Water-Fat Separation: Complementary Methods

Accelerating a water-fat separation acquisition with parallel imaging will help alleviate the three-fold increase in scan time compared with conventional fat-saturated methods. However, from Chaps. 2 and

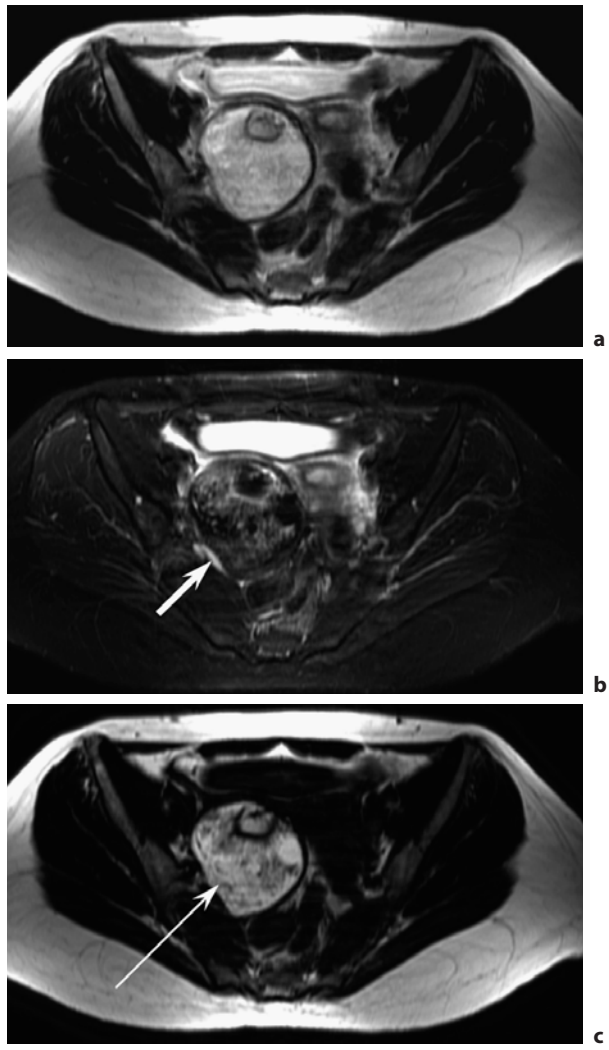

Fig. 25.5a–c. T1-weighted IDEAL-FSE **a** recombined, **b** water and **c** fat images in a woman with a right adnexal mass. A large component of this mass separates into the fat image (*thin arrow*) confirming the diagnosis of ovarian dermoid with high confidence. Note the small amount of free pelvic fluid (*thick arrow*) in the water image

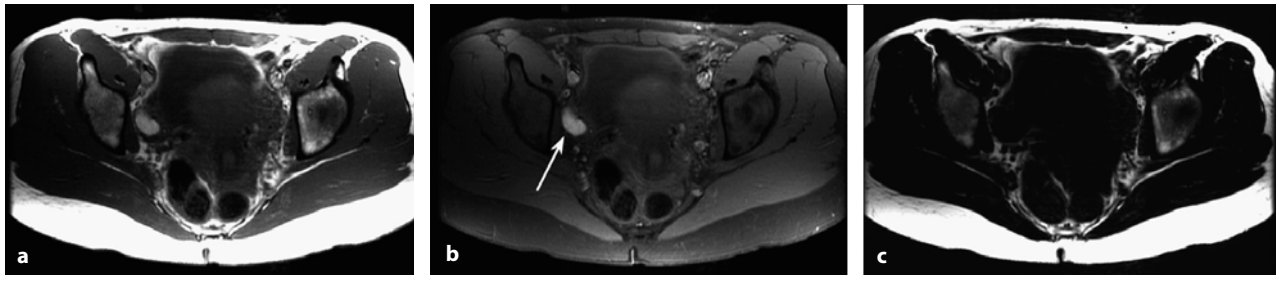

Fig. 25.6a–c. T1-weighted IDEAL-FSE **a** recombined, **b** water and **c** fat images in a woman with endometriosis showing a small hyperintense mass along the right pelvic sidewall, representing a small endometrioma. It is not a fatty mass as was initially suspected on non-fat suppressed imaging

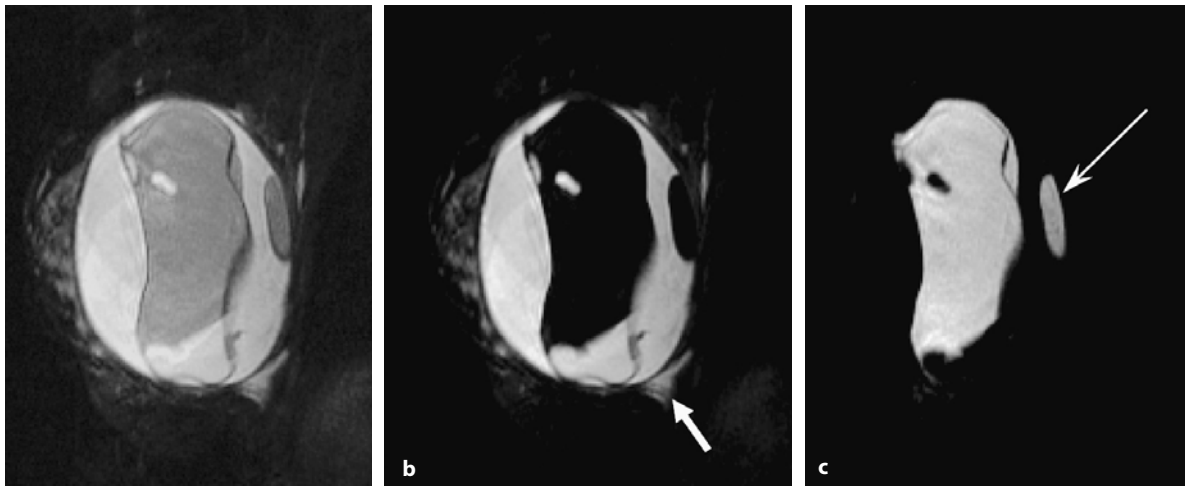

Fig. 25.7a–c. Sagittal T2-weighted IDEAL-STIR **a** recombined, **b** water, and **c** silicone images of a breast containing a composite water-silicone implant with rupture of the silicone component (*long arrow*) and a small amount of pericapsular fluid (*short arrow*). The STIR pulse is used to suppress fat, while IDEAL exploits the chemical shift between water and silicone to separate these components

3, we know that there is an inherent SNR penalty that occurs when we use parallel imaging to accelerate an acquisition. As described in those chapters, the local SNR at a pixel within an accelerated image is given by,

$$\mathrm{SNR}_R = \frac{\mathrm{SNR}_0}{g\sqrt{R}} \tag{2}$$

where SNR_0 is the SNR of the pixel in an unaccelerated image, R is the "reduction" or acceleration factor, and g is the "geometry" or g-factor that reflects additional noise amplification due to ill-conditioning of the unwrapping process. Although the g-factor always has a value of 1.0 or higher, it is close to 1.0 for well-designed coil arrays and low acceleration factors. The g-factor depends on a wide variety of parameters including orientation of the phase encoding direction, the acceleration factor used, field of view, the object being imaged, and the design of the coil elements in the array used for data reception.

For a water-fat separation acquisition, the SNR is given by

$$\mathrm{SNR}_R = \frac{\mathrm{SNR}_0\sqrt{\mathrm{NSA}}}{g\sqrt{R}} \tag{3}$$

From this equation, we see that the decrease in SNR from accelerating an acquisition ($1/\sqrt{R}$) is offset by the effective averaging that occurs from decomposing water and fat from multiple images A($\sqrt{\mathrm{NSA}}$). The maximum possible NSA is 3.0, just as if the three images had been averaged together. If our water-fat decomposition has been optimized, as is the case with IDEAL (i.e., NSA=3.0), and if we assume that the g-factor is low (i.e.: g,1.0), we see that SNR_R=SNR_0 when R=3, i.e., there is no SNR penalty. Therefore, when R=3, we effectively achieve water-fat separation for "free."

As we can see, parallel imaging and water-fat separation methods are complementary methods: parallel imaging alleviates the scan time penalty inherent to multi-point water-fat separation methods, while the high SNR behavior of water-fat separation compensates for the SNR penalty of parallel imaging.

25.3.1 Combining Parallel Imaging and Water-Fat Separation Methods

Figure 25.8a shows a schematic of the three k-space data matrices acquired for a fully sampled data set required for a three-point water-fat separation. If the three data sets are under-sampled in the phase encoding direction (Fig. 25.8b, R=2 in this example), we can unwrap the subsequent aliasing with a parallel imaging reconstruction algorithm of our choice and accelerate the acquisition. Separate calibration images containing coil sensitivities would be required to reconstruct the data set acquired in Fig. 25.8b.

Alternatively, only the edges of k-space can be undersampled, leaving full sampling at the center of k-space (Fig. 25.8c). The higher sampling density at the

center of k-space provides the necessary coil sensitivity information needed to unwrap the undersampled portions of k-space. This additional information provides a "self" or "auto"-calibration, eliminating the need for an external calibration (cf. chapters 2 and 8). Because the three images acquired at the different echo times must be at the same location, they will have the same coil sensitivities, and therefore can use the same coil sensitivity information, either from a separate calibration scan, or from central k-space lines. This scheme is shown in Fig. 25.8c where fully sampled central k-space lines are acquired for echo 1. It is important to realize that these additional self-calibration lines can be acquired for any of the three echoes and can be applied for all three images, making this an efficient use of the self-calibration. This approach is described in more detail elsewhere (McKenzie et al. 2004). In this work, we apply both image domain unwrapping (SENSE) (Pruessmann et al. 1999) as well as a generalized k-space based algorithm (generalized encoding matrix (GEM), Sodickson and McKenzie 2001) for reconstruction of undersampled data.

The major disadvantage of self-calibration methods in parallel imaging is the penalty required to acquire the additional central k-space lines. However, since this information can be used for all three images in the multi-point acquisition, the overall time penalty is relatively small. For this reason, we prefer the modified self-calibration approach, which uses calibration data from one of the three images, because we achieve the same benefits of self-calibration, most notably the decreased motion sensitivity from misregistration of calibration data and under-sampled data, while paying a relatively minor penalty for the acquisition of a few additional self-calibrating lines.

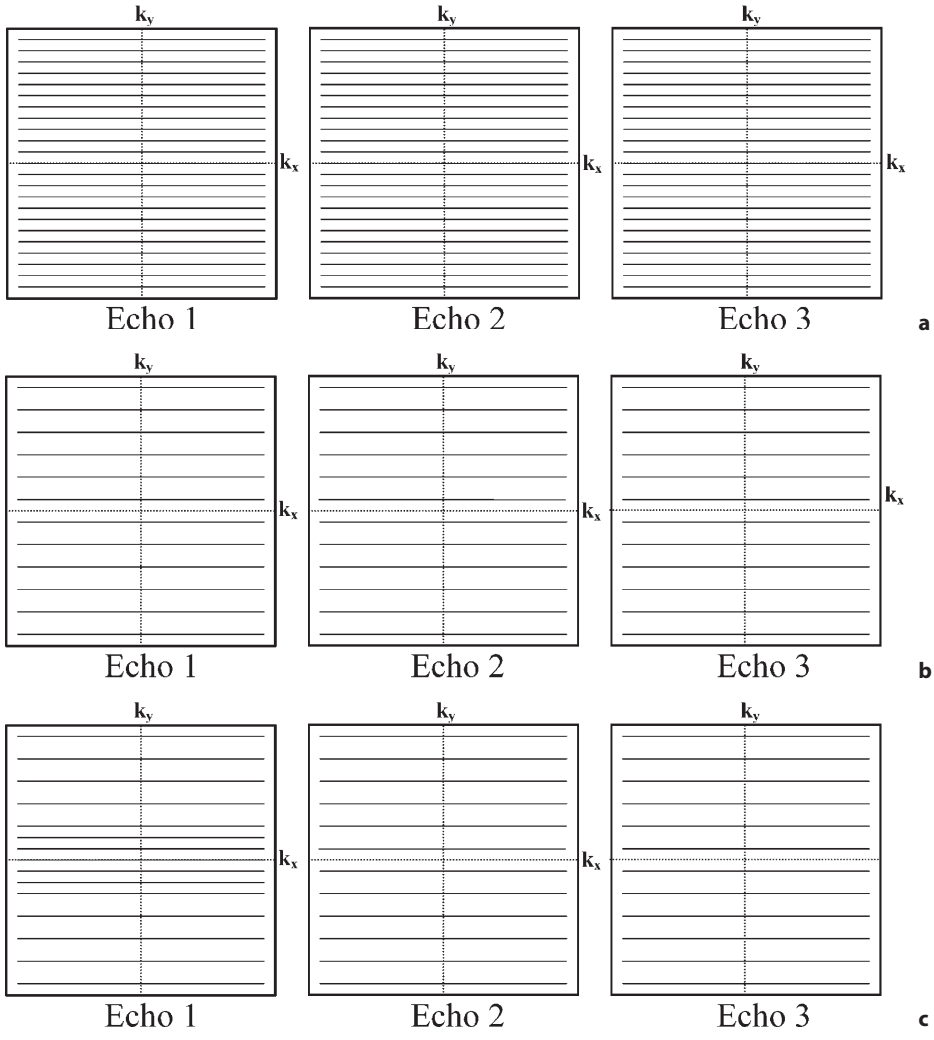

Fig. 25.8. a Fully sampled k-space for the three echoes acquired at different echo times. **b** Undersampling of echoes will accelerate the acquisition, although a separate calibration image would be required. **c** Full sampling of central k-space is performed for one of the three images (echo 1 in this example), providing a "self-calibration" used to unwrap aliasing for all three images

Further reductions in sampling can be made through the use of reduced sampling strategies. In general, field inhomogeneities vary slowly over the image, and can be well characterized with low-resolution images, which require little time to acquire. Once the field map is known, only two full-resolution images acquired at different echoes times are required to decompose water from fat (Reeder, Wen et al. 2004; Brau et al. 2005). For single coil applications, this offers an approximately 30% decrease in minimum scan time. When used with multi-coil and parallel imaging applications, substantial decreases in scan time can be achieved even with small parallel reduction factors (R=2–3) (Brau et al. 2005). This under-sampled two-point approach is illustrated in Fig. 25.9. The image acquired at echo 1 is a low-resolution full-field-of-view (FOV) image used as a calibration scan to unwrap the under-sampled full-resolution reduced-FOV images acquired at echo times 2 and 3. The unwrapped images at echo times 2 and 3 (Fig. 25.9b) are then low-pass filtered (Fig. 25.9c) to obtain three low-resolution images that are then used to measure the field map, ψ. Finally, the field map is demodulated from images acquired at echo times 2 and 3, which are then used to decompose water and fat. Note that the data from the low-resolution image is used for both field map calculation and for parallel imaging calibration, further enhancing the efficiency of this approach. Details of this approach are described elsewhere (Brau et al. 2005). Using a parallel reduction factor of 2, scan time reductions of 63% compared with a non-accelerated three-point scan can be achieved, while a reduction factor of 3 provides 75% scan time reduction, providing scan times faster than conventional fat-saturated imaging.

A final approach that has also shown early initial success is one-point water-fat separation (Yu et al. 2004;

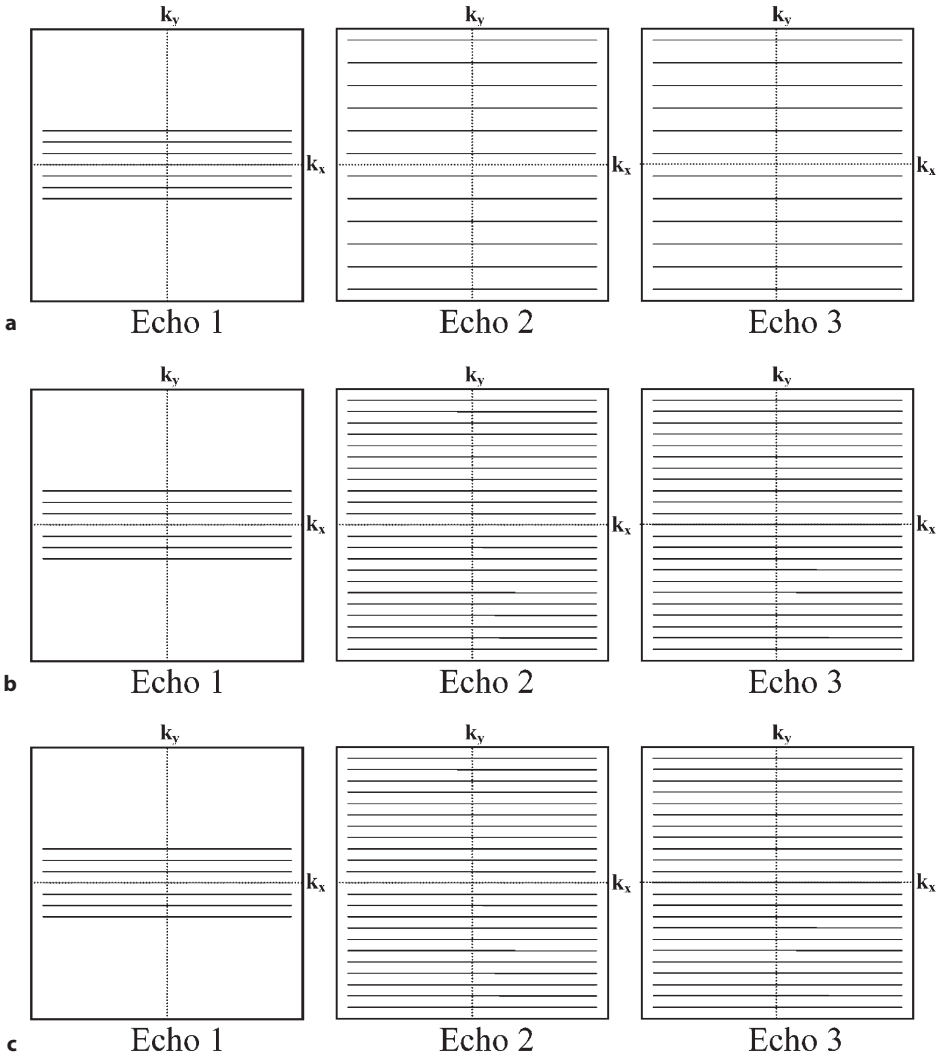

Fig. 25.9a–c. Under-sampled two-point sampling strategy. **a** Image acquired at echo time 1 is a low-resolution, full-FOV image used as a calibration scan to unwrap the under-sampled full-resolution, reduced-FOV images acquired at echo times 2 and 3. The central lines of k-space from unwrapped images **b** at echoes 2 and 3 are used to obtain three low-resolution data sets **c** that are then used to determine the field map, ψ. Finally, the field map is demodulated from images acquired at echo times 2 and 3, which are then used to decompose water and fat

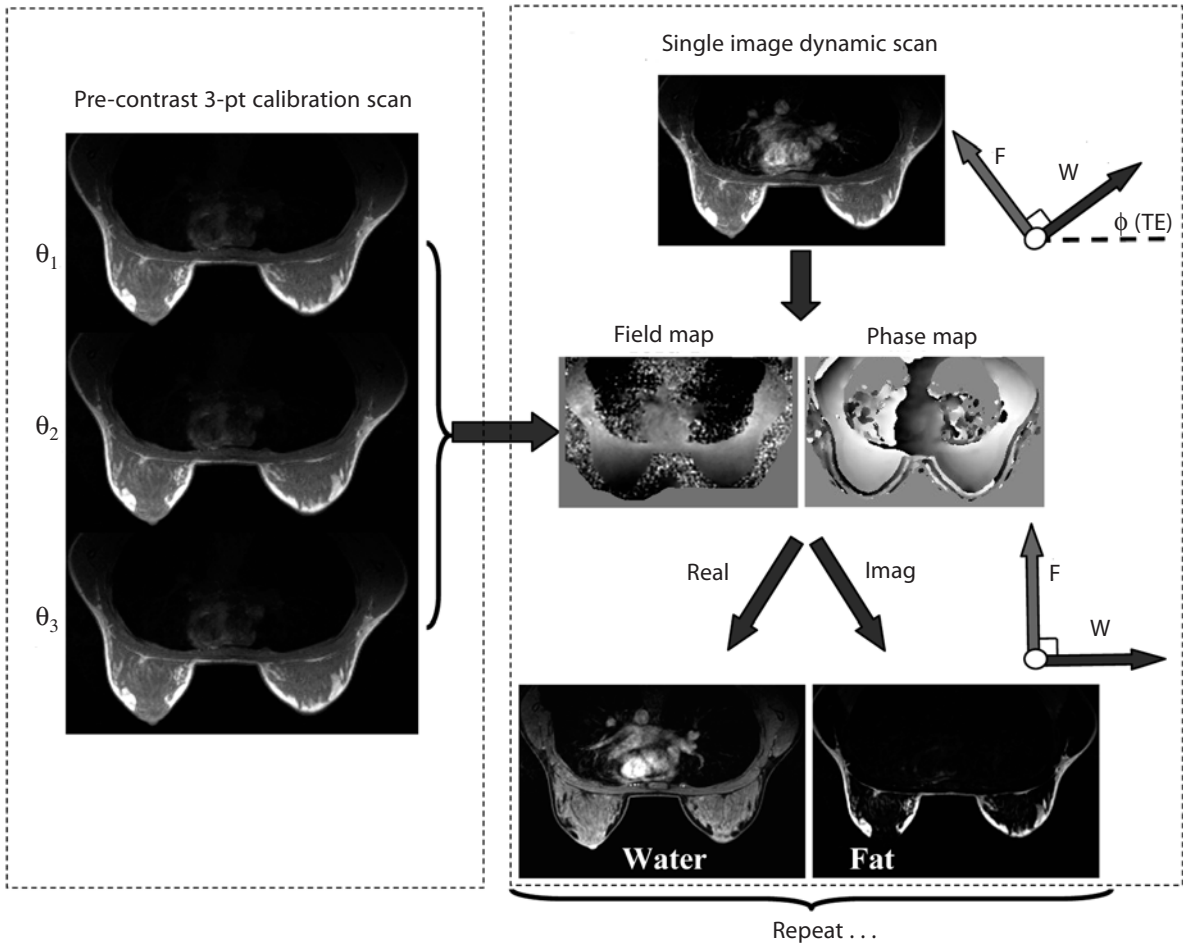

Fig. 25.10. Dynamic scanning with single-image water-fat separation. A three-image pre-contrast calibration scan is used to the local field map and additional constant phase shifts that will result in a combined phase shift, ϕ. The effects of ϕ are removed from single images acquired with $\theta=\pi/2$, during the injection of contrast, leaving the resulting water and fat signal in the real and imaginary components of the signal, respectively

Hoory et al. 2005; Son et al. 2005; Yu et al. 2005). This approach is particularly useful for dynamic contrast-enhanced imaging and CINE cardiac imaging where repeated high spatial and temporal resolution imaging at the same location is desired (Yu et al. 2004; Hoory et al. 2005; Son et al. 2005; Yu et al. 2005). Repetitive same location imaging permits the acquisition of a pre-contrast calibration scan of the site to be imaged to measure the field map and constant phase shifts from coils, dielectric effects, etc. This three-image calibration is used to remove the local phase shift, ϕ, that results from a combination of constant phase shifts and field inhomogeneity. This approach differs from two- and three-point water-fat separation methods where only the effect of the field inhomogeneity needs to be removed and the resulting water and fat images are complex images that contain the additional constant phase shifts, which are removed through the magnitude operation. With the one-point technique, images are then acquired during dynamic imaging with the TE adjusted so that water and fat are perpendicular ($\theta=\pi/2$) (Fig. 25.10). The calibration phase and field map images are used to remove the local phase shift, ϕ, leaving the water and fat signal in the real and imaginary components of the signal, respectively. Changes in the field map from the presence of gadolinium in dynamic contrast-enhanced imaging have been shown to be negligible for concentrations of gadolinium expected in vivo (Hoory et al. 2005).

The acquisition time of the calibration image can be reduced using parallel imaging and/or the low-resolution field map approaches described above. More importantly, the images acquired during dynamic contrast bolus injection can also be accelerated, using

the initial calibration images as coil sensitivity maps to unwrap the single image dynamic acquisitions. This approach permits the acquisition of separate water and fat images with scan times that are half (R=2), one third (R=3) or less (R>3) than conventional non-accelerated fat-saturated imaging (Yu et al. 2005).

25.3.2 Applications of Parallel Imaging and Water-Fat Separation

Although the three-fold increase in scan time of water-fat separation methods can be used efficiently from an SNR perspective, long minimum scan times are unacceptable for many applications. These include cardiac and abdominal imaging that requires rapid imaging to acquire high-resolution images within a breath-hold. For example, a recently described three-point water-fat separation approach in the heart acquires three complete sets of SSFP CINE images at different echo shifts in order to decompose separate water and fat CINE images of the heart (Reeder, Markl et al. 2005; Reeder, McKenzie et al. 2004). The three-fold increase in scan time limits acquisitions to single slices with reduced spatial and temporal resolution. Figure 25.11 shows an example of water-only CINE SSFP images from a normal volunteer acquired during a 26-s breath-hold compared with images acquired with a parallel acceleration of 2, using the three-point self-calibration method described above (Fig. 25.8c). Comparable image quality has been achieved in nearly half the scan time.

Figure 25.12 shows T2-weighted IDEAL-FSE and T1-weighted IDEAL-SPGR images of the ankle acquired using the two-point method without parallel acceleration, compared with conventional fat-saturated methods. Without parallel imaging, the two-point approach offers a modest, but important 30% scan time reduction.

Contrast-enhanced breast imaging with MRI has become a gold standard for the diagnosis of inva-

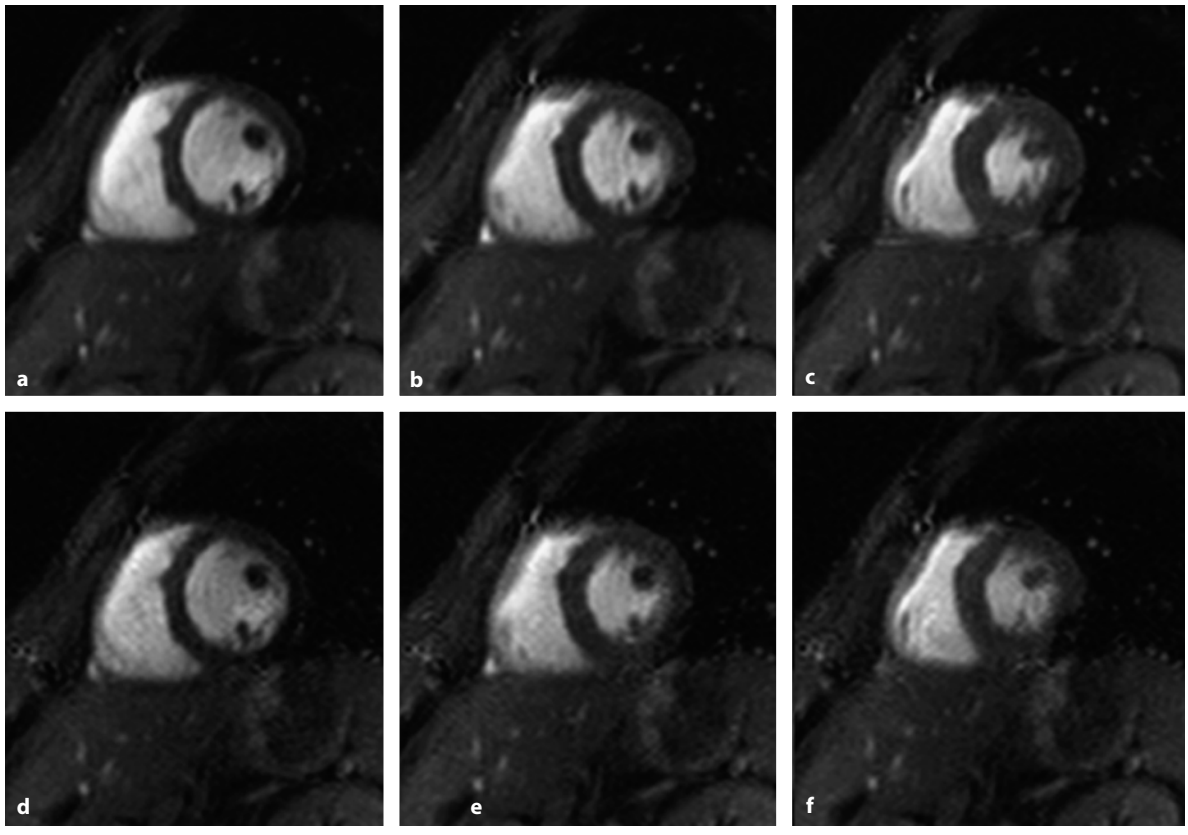

Fig. 25.11a–f. CINE SSFP water-only images shown at end-diastole **a,d**, mid-systole **b,e** and end-diastole **c,f** acquired without **a–c** and with **d–f** parallel acceleration (R=2) using the self-calibrated three-point method. Although image quality is comparable, the scan time is nearly half using the accelerated method

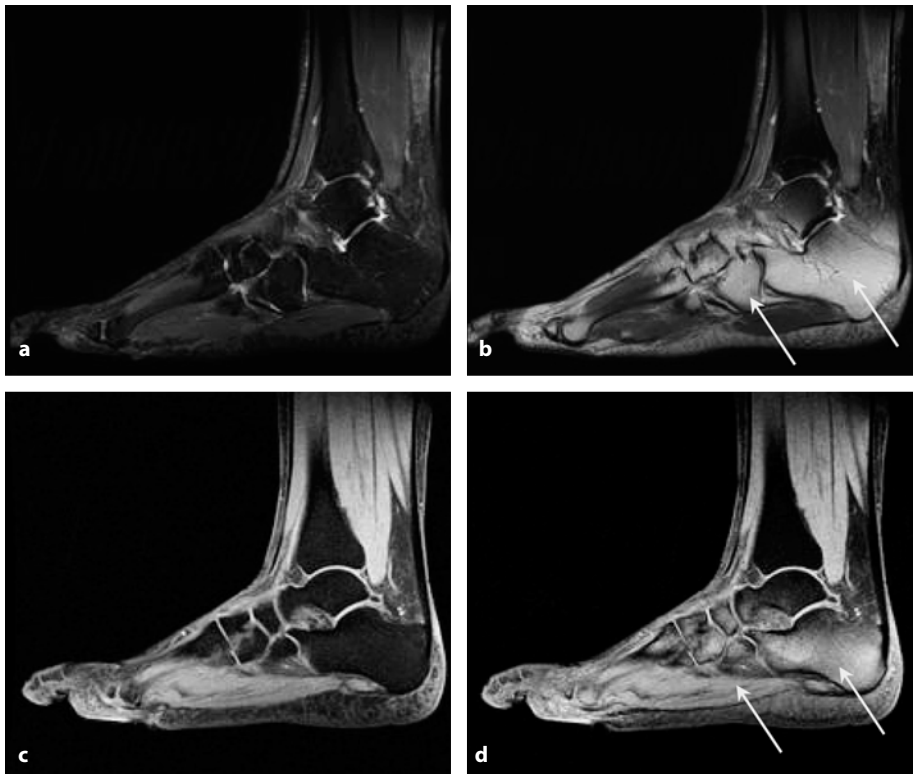

Fig. 25.12a–d. Sagittal imaging of the foot with **a** two-point T2-weighted IDEAL-FSE and **c** two-point IDEAL-SPGR. Conventional fat-saturated T2-weighted FSE **b** and SPGR **d** imaging is shown for comparison and reveals large areas of failed fat suppression (*arrows*). Images courtesy of Anja CS. Brau, PhD, GE Healthcare

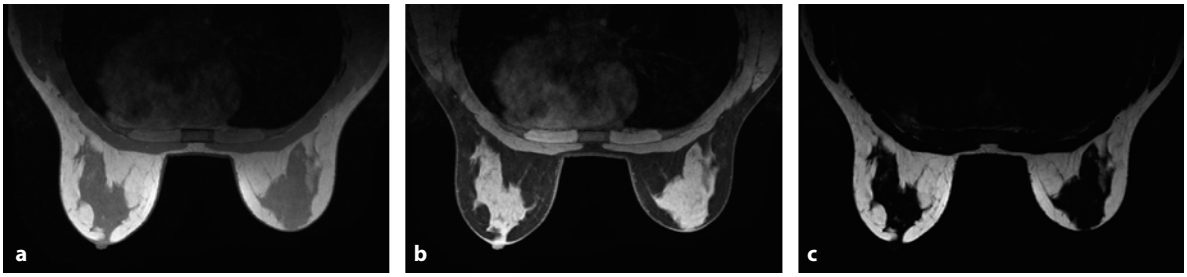

Fig. 25.13a–c. Axial three-point 3D-IDEAL-SPGR recombined **a**, water **b** and fat **c** breast images acquired in a normal volunteer using a reduction factor of three (R=3). SNR performance and scan time of this acquisition are comparable to conventional fat-saturated imaging, but with uniform separation of water and fat across both breasts. Scan time was 2:10 min for 48 slices covering both breasts with 512×256 matrix size and 0.6×1.2×4 mm^3 resolution. TR/TE=10.6/4.0 ms

sive breast cancers, with sensitivity and specificity exceeding 90% (Agostan et al. 2001). Robust fat suppression is of paramount importance when imaging the breast, which is largely comprised of fatty tissue that can obscure enhancing lesions. Imaging of both breasts simultaneously is highly desirable to avoid two separate exams with repeated contrast injections. Although conventional fat saturation works relatively well for imaging one breast, which is relatively easy to shim for magnetic field inhomogeneities, uniform suppression of fat for bilateral breast imaging is very challenging because it is very difficult to achieve uniform field homogeneity over both breasts. For this reason, water-fat separation methods that compensate for field inhomogeneities are well suited for bilateral breast imaging application.

The increased scan time of three-point water-fat separation methods may be prohibitive, however, and reduction of scan times with parallel imaging would reduce or eliminate the scan time penalty and provide uniform fat-suppression. Figure 25.13 shows an example from a pre-contrast three-point 3D-IDEAL-SPGR acquisition in the breast of a normal volunteer, using an acceleration of three (R=3). Excellent separation of

water and fat is seen across the entire image in images that were acquired in approximately the same scan time as a conventional fat-saturated image.

Although high-resolution morphological imaging of breast lesions is very important in the characterization of breast malignancies, dynamic contrast-enhanced (DCE) imaging of the breast has been shown to improve the specificity greatly in the detection of invasive breast cancers (Agostan et al. 2001). However, DCE imaging is a highly challenging application: the optimal approach provides complete coverage of both breasts with high spatial and high temporal resolution with uniform fat-suppression. The use of single-point water-fat separation methods in combination with parallel imaging may be able to satisfy these requirements. For example, the images shown in Fig. 25.14 (the same volunteer as shown in Fig. 25.13) were acquired during dynamic contrast injection. Both breasts were imaged at 1.5 T with a single-point 3D-IDEAL-SPGR approach combined with a parallel acceleration of three (R=3). Images with 0.6×1.2×4.0 mm^3 resolution were acquired through the entire breast every 43 s using a 512×256×48 matrix. The scan time is approximately one third of a conventional non-accelerated fat-saturated scan.

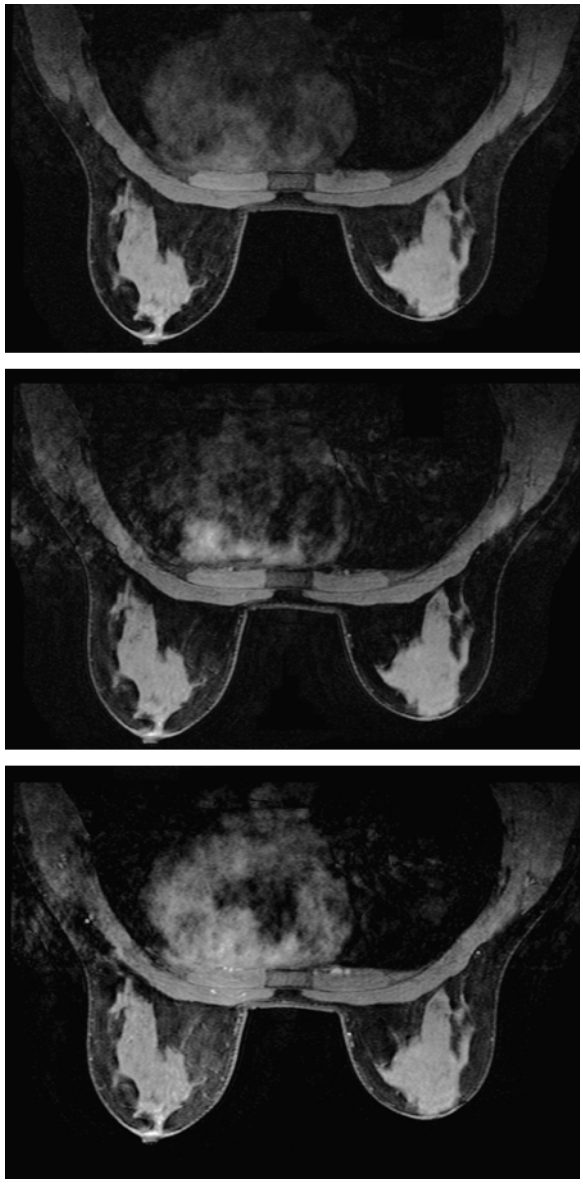

Fig. 25.14a–c. Dynamic contrast-enhanced 3D-IDEAL-SPGR water-only single-point images obtained with an acceleration of three (R=3), before **a** and after **b,c** contrast injection. Scan time of each phase was 43 s for 48 slices covering both breasts with 512×256 matrix size and 0.6×1.2×4 mm^3 resolution. TR/TE=10.6/4.0 ms

Dynamic contrast-enhanced imaging of the liver is also essential for the characterization of liver lesions such as hepatocellular carcinomas and metastatic disease. Rapid, high-resolution breath-hold imaging of the abdomen with uniform suppression of fat is essential. Figure 25.15 shows breath-held 3D-IDEAL-SPGR water and fat images acquired with an acceleration of two (R=2) in two different patients. One patient is normal and the second patient has diffuse fatty infiltration of the liver (steatohepatitis). Separate water and fat images indicate uniform separation of water and fat. These images can be recombined into calculated "in-phase" and "out-of-phase" images, analogous to conventional in-phase and out-of-phase imaging usually acquired as a separate acquisition. Although the fatty infiltration of the second patient can be seen in the fat image (Fig. 25.15f), it is more apparent in the recombined out-of-phase image (Fig. 25.15h).

Dynamic contrast-enhanced imaging of the liver can also be performed with the accelerated one-point methods described in this chapter. Figure 25.16 shows breath-held 3D-IDEAL-SPGR images of the liver acquired at 3.0 T using the single-image approach. Images acquired with an accelerated three-point method are shown for comparison. Both approaches used a parallel acceleration of two (R=2).

25.4 Conclusion

Chemical-shift-based water-fat separation methods such as conventional three-point "Dixon" methods and IDEAL are capable of providing high-quality

images with uniform and robust fat suppression despite the presence of field inhomogeneities, even in challenging areas of the body. Although these methods are SNR efficient, their main drawback is the three-fold increase in the minimum scan time. Applications that require short minimum scan times, such as cardiac and abdominal breath-held imaging, as well as dynamic contrast-enhanced imaging of the liver or breast, would benefit from water-fat separation methods if the scan times could be reduced.

Fortunately, parallel imaging can be exploited to reduce the amount of data required to reconstruct an image. Importantly, these parallel imaging methods preserve the phase content of the complex source images, permitting the combination of parallel imaging with water-fat separation methods. These methods

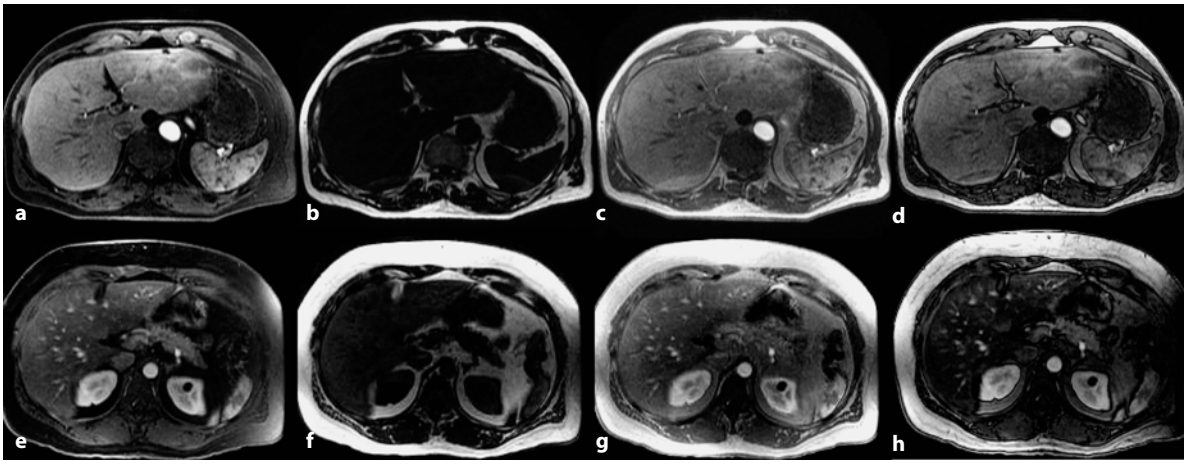

Fig. 25.15a–h. Breath-held contrast-enhanced 3D-IDEAL-SPGR water **a,e**, fat **b,f**, recombined in-phase **c,g** and recombined out of phase **d,h** images acquired at 1.5 T with an acceleration of two (R=2). The patient shown in the *top row* is normal; however, the patient in the bottom row has diffuse fatty infiltration of the liver seen as low-level signal in the fat image **f**, but most apparent as signal drop in the calculated out-of-phase image **h**

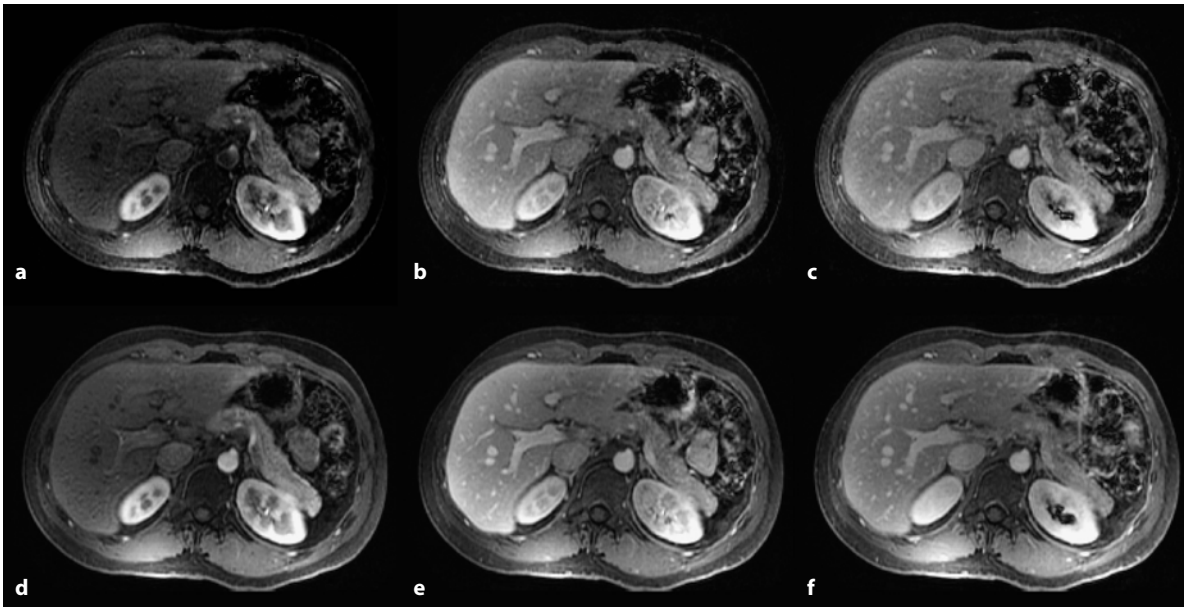

Fig. 25.16a–f. Dynamic contrast-enhanced image of the liver acquired at 3.0 T with 3D-IDEAL-SPGR using the one-point method **a-c** during the arterial **a**, portal venous **b** and delayed **c** phases after the injection of contrast. Three-point images **d–f** show comparable image quality, but with three times the scan time. Both methods used a parallel acceleration of two (R=2)

are highly complementary: parallel imaging alleviates the scan time penalty of the separation method, while the SNR penalty of parallel imaging is offset by the high SNR performance of the water-fat decomposition. In this work we reviewed the combination of parallel imaging with self-calibrating three-point and two-point methods, as well as with a one-point method well suited for dynamic contrast-enhanced imaging.

Acknowledgments. The authors wish to thank Chris Beaulieu, Anja Brau, Jean Brittain, Garry Gold, Jane Johnson, Norbert Pelc, Angel Pineda, Neil Rofsky, Ann Shimakawa and Huanzhou Yu for their generous assistance.

References

Agoston AT, Daniel BL, Herfkens RJ, et al (2001) Intensity-modulated parametric mapping for simultaneous display of rapid dynamic and high-spatial-resolution breast MR imaging data. Radiographics 21:217–226

Block W, Pauly J, Kerr A, Nishimura D (1997) Consistent fat suppression with compensated spectral-spatial pulses. Magn Reson Med 38:198–206

Brau AC, McKenzie CA, Shimakawa A, et al (2005) Accelerated IDEAL water-fat separation techniques for single- and multi-coil applications. ISMRM, Miami Beach, p 491

Bydder GM, Pennock JM, Steiner RE, Khenia S, Payne JA, Young IR (1985) The short TI inversion recovery sequence - an approach to MR imaging of the abdomen. Magn Reson Imaging 3:251–254

Dixon W (1984) Simple proton spectroscopic imaging. Radiology 153:189–194

Glover G (1991) Multipoint Dixon technique for water and fat proton and susceptibility imaging. J Magn Reson Imaging 1:521–530

Glover GH, Schneider E (1991) Three-point Dixon technique for true water/fat decomposition with B0 inhomogeneity correction. Magn Reson Med 18:371–383

Hardy PA, Hinks RS, Tkach JA (1995) Separation of fat and water in fast spin-echo MR imaging with the three-point Dixon technique. J Magn Reson Imaging 5:181–185

Hoory T, Ramsay E, Plewes D (2005) Fast Bo insensitive Dixon fat suppression for dynamic breast MRI. ISMRM, Miami Beach, p 898

Ma J, Choi H, Stafford RJ, Miller MJ (2004) Silicone-specific imaging using an inversion-recovery-prepared fast three-point Dixon technique. J Magn Reson Imaging 19:298–302

McKenzie CA, Reeder SB, Shimakawa A, Pelc NJ, Brittain JH (2004) Abdominal three-point Dixon imaging with self-calibrating parallel MRI. ISMRM, Kyoto, p 917

Meyer CH, Pauly JM, Macovski A, Nishimura DG (1990) Simultaneous spatial and spectral selective excitation. Magn Reson Med 15:287–304

Moriguchi H, Lewin JS, Duerk JL (2003) Dixon techniques in spiral trajectories with off-resonance correction: a new approach for fat signal suppression without spatial-spectral RF pulses. Magn Reson Med 50:915–924

Pineda AR, Reeder SB, Wen Z, Yu H, Pelc NJ (2005) Cramer-Rao bounds for three-point decomposition of water and fat. Magn Reson Med 54:625–635

Pruessmann KP, Weiger M, Scheidegger MB, Boesiger P (1999) SENSE: sensitivity encoding for fast MRI. Magn Reson Med 42:952–962

Reeder SB, Markl M, Yu H, Hellinger JC, Herfkens RJ, Pelc NJ (2005) Cardiac CINE imaging with IDEAL water-fat separation and steady-state free precession. J Magn Reson Imaging 22:44–52

Reeder SB, McKenzie CA, Markl M, Yu H, Pelc NJ, Brittain JH (2004) Parallel cardiac CINE imaging: application to Dixon water-fat separation and steady-state free precession. Int Soc Magn Reson Med 12th Meeting, p 267

Reeder SB, Pelc NJ, Alley MT, Gold GE (2003) Rapid MR imaging of articular cartilage with steady-state free precession and multipoint fat-water separation. AJR Am J Roentgenol 180:357–362

Reeder SB, Pineda AR, Wen Z, et al (2005) Iterative decomposition of water and fat with echo asymmetry and least squares estimation (IDEAL): application with fast spin-echo imaging. Magn Reson Med 54:636–644

Reeder SB, Pineda AR, Yu H, et al (2005) Water-fat separation with IDEAL-SPGR. ISMRM, Miami Beach, p 105

Reeder SB, Wen Z, Yu H, et al (2004) Multicoil Dixon chemical species separation with an iterative least-squares estimation method. Magn Reson Med 51:35–45

Schneider E, Chan TW (1993) Selective MR imaging of silicone with the three-point Dixon technique. Radiology 187:89–93

Sodickson DK, McKenzie CA (2001) A generalized approach to parallel magnetic resonance imaging. Med Phys 28:1629–1643

Son J, Ji J, Ma J (2005) Three-dimensional T1-weighted MR imaging using a one-point Dixon technique with arbitrary echo time. ISMRM, Miami Beach, p 893

Wang Y, Li D, Haacke EM, Brown JJ (1998) A three-point Dixon method for water and fat separation using 2D and 3D gradient-echo techniques. J Magn Reson Imaging 8:703–710

Yu H, McKenzie CA, Shimakawa A, et al (2005) Parallel imaging accelerated single acquisition water-fat separation for dynamic imaging. ISMRM, Miami Beach

Yu H, Reeder SB, Markl M, Pelc NJ (2004) Single acquisition water fat separation for SSFP cardiac CINE imaging: feasibility study. ISMRM, Kyoto, p 263

Part V:
Clinical Applications: Angiography

MRA of Brain Vessels

26

Romhild M. Hoogeveen

CONTENTS

26.1 Introduction

The brain is an excellent area for parallel imaging. One reason for this is that the head is almost cylindrical in shape, allowing coil elements around the brain to "see" an equal share of the brain. This allows the possibility of reaching high acceleration factors. Another reason is that the head is a relatively small object and that the number of elements in commercially available coils (e.g., eight) is getting close to optimal for parallel imaging. Finally, the sizes of the head do not vary as much as other body parts, thus allowing a more optimal design of the head coil.

Because of the many coil elements circularly positioned around the brain, the two main directions for parallel imaging are left-right and antero-posterior. In many 3D sequences, both directions can be used, e.g., in 2D SENSE (Weigert et al. 2002), and high speedup factors can be reached up to the number of coil elements. This is particularly useful in large volume scans, such as 3D phase-contrast or 3D contrast-enhanced (CE) MRA of the brain.

The reasons for using parallel imaging for MRA are manifold: (1) lengthy sequences, such as 3D time-of-flight MRA, can be shortened, (2) spatial resolution can be increased, particularly in CE-MRA sequences with abundant SNR, (3) the number of slices can be increased to gain more volume coverage, (4) higher temporal resolution can be obtained in dynamic sequences and (5) venous contamination in first-pass CE-MRA can be further reduced as k-space is traversed with more speed.

In most MRA methods at 1.5 T there is abundant SNR available to justify the use of parallel imaging, e.g., to decrease scan time or to increase resolution. It may be clear that with the doubling of SNR in the head at 3 T, the use of parallel imaging is almost indispensable. Using parallel imaging at 3 T has the additional benefit of reducing the SAR values.

In the next sections we will address the use of SENSE parallel imaging (Pruessmann et al. 1999) for various MRA methods.

26.2 Time-of-Flight MRA Using SENSE

Currently, the most frequently used MRA technique in the brain is 3D time-of-flight (TOF) MRA to image the intracranial arteries without the use of a contrast agent. TOF-MRA needs to be planned perpendicular to the arterial inflow, and axial slices are acquired. Consequently, the choice of the slice-encoding direction is fixed: feet-head. The small volume coverage in slice-direction limits the use of SENSE in this direction. The preferred phase-encoding SENSE direction is therefore the left-right phase-encoding direction. In this setup, typically a SENSE speedup factor of two to three can be obtained, which is used for shortening the sequence and improving the spatial

R. M. Hoogeveen, PhD
Philips Medical Systems, Clinical Scientist, QR0113 – PO Box 10000, 5680 DA Best, The Netherlands

resolution at the same time. A TOF example can be found in Fig. 26.1 using a SENSE factor of R=2.5. This protocol took less than 5 min (in the past, without SENSE this would have been 12 min) for a resolution of 0.4×0.7×0.5 mm³, 512 scan matrix and 150 slices. Images were acquired on a Philips Achieva 3.0-T system equipped with an eight-element head coil.

SENSE in TOF-MRA enables the possibility to further increase the acquisition matrix. Traditionally, 512 matrices were used, but now routinely matrices between 512 and 1,024 can be applied (both on 1.5 T and 3 T). The extra gain in SNR at 3 T even permits to go beyond 1,024-matrix scanning. In all these cases, SENSE or other strategies for parallel imaging are crucial to keep the imaging time within clinically acceptable limits.

26.3 Phase-Contrast MRA Using SENSE

In the early 1990s, there was a debate about whether TOF-MRA was preferred above phase-contrast MRA (PCA) in the brain. PCA has a number of advantages over TOF-MRA: better suppression of the background, no severe in-plane saturation and no limits in the choice of the positioning of the imaging volume. The inherently longer scan times of PCA, however, prevented the technique to become used routinely. The only main application where PCA is still used in the brain is venography, e.g., for evaluating the sagittal sinus and its branches to exclude sinus venous thrombosis in pregnant women.

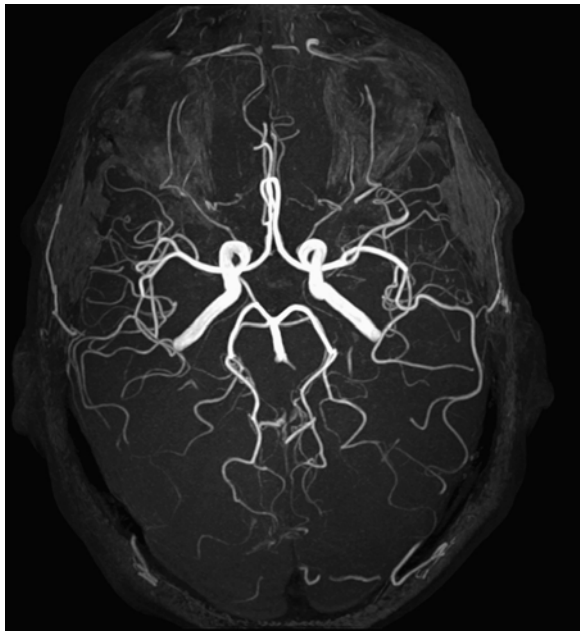

Fig. 26.1. Inflow time-of-flight MRA at 3.0 T using SENSE and an 8-channel head-coil. Protocol parameters: 3D T1-weighted gradient-echo sequence with TR/TE/flip =25/3.45/20°; matrix 512; reconstruction matrix 1,024; resolution: 0.4×0.7×0.9 mm³; interpolated to 0.2×0.35×0.45 mm³; 150 slices in four chunks/subvolumes; SENSE acceleration R=2.5; scan time 4:48 min–12 min without SENSE.

With the availability of parallel imaging techniques, the main disadvantage of PCA can now be overcome, and this might cause a renaissance for PCA. Since PCA can be planned in any direction, the favorable choice of the phase/slice-encoding directions is left-right and anterio-posterior (see Sect. 26.1). With coronal and sagittal imaging, SENSE can be applied in these two directions together, and much higher speedup factors can be obtained than in TOF imaging. In contrast to TOF-MRA, with PCA whole-brain angiography or whole-brain venography can be performed. With SENSE acceleration factors of 6-8 (combination of, e.g., 2×3 and 2×4), a whole-brain PCA acquisition with a spatial resolution of about 1×1×1 mm³ can be obtained in 4-7 min (Hoogeveen et al. 2003); see Fig. 26.2. Without SENSE, the acquisition time would have been clinically unacceptable (roughly 40 min). The availability of high acceleration factors opens doors to sequences that would just take too long to be practical.

SENSE and PCA are a perfect match, not only because PCA exhibits inherently long scan times that could never be significantly shortened by stronger gradients, but also because PCA has a very high SNR and CNR. The future will tell whether PCA will revive again.

26.4 Contrast-Enhanced MRA Using SENSE

Although contrast-enhanced (CE) MRA has replaced TOF-MRA in many parts of the body, this is not the case for the brain. The arterio-venous circulation time in the brain is so fast (3–4 s) that a venous-free contrast-enhanced image of the brain arteries cannot be acquired with a sufficiently high spatial resolution. The contrast-enhanced timing-robust angiography (CENTRA) technique (Philips Medi-

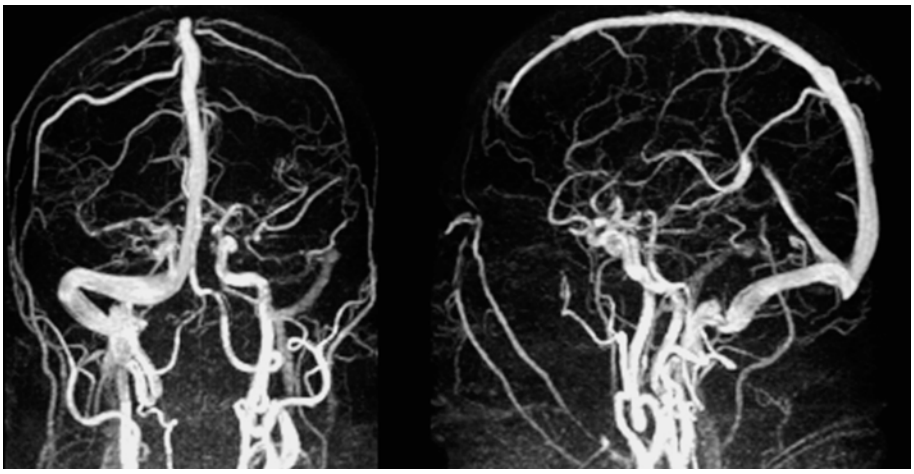

Fig. 26.2. Whole-brain phase-contrast venography at 1.5 T using an 8-element SENSE head coil. A SENSE reduction factor of R=8 was used, thereby reducing the scan time from impractical 40 min to about 5 min. Parameters: 3D T1-weighted PCA; three flow directions; V_{enc}=10 cm/s; TR/TE/flip: 15 ms/4 ms/15°; FOV 256×192 mm²; matrix 256; 365 coronal slices; acquisition resolution: 1.0×1.0×1.2 mm³; reconstructed to 0.5×0.5×0.6 mm³

cal Systems) (Willinek et al. 2002) – a version of elliptical centric imaging (Wilman et al. 1997) with improved robustness – can be used in CE-MRA to extend the imaging time beyond the arterio-venous window to prevent venous opacification. The addition of SENSE to the CENTRA technique for CE-MRA in the brain has two main advantages: the spatial resolution can be further improved and at the same time, k-space is traversed much faster outwards from the center of k-space, thereby improving venous suppression. With the availability of CENTRA with parallel imaging, CE-MRA of the brain is starting to be used routinely for anatomical imaging.

26.4.1 Anatomical Imaging: CENTRA and SENSE

The main reason to use CE-MRA instead of TOF-MRA in the brain is to image regions where TOF-MRA fails: in areas with complex flow, around stenoses and in aneurysms, and in areas where TOF-MRA suffers from saturation artefacts, such as in AVMs. Also patients with coiled aneurysms are eligible for CE-MRA rather than the more artefact-prone TOF-MRA technique. Typically, a coronal or transverse volume is planned around the circle of Willis, and SENSE is applied in a left-right direction with acceleration factors of 2–3. An example is found in Fig. 26.3. For timing of the contrast agent, either a test-bolus can be used or fluoroscopic triggering (e.g., BolusTrak) can be applied.

Similar to the PCA technique (Sect. 26.3), higher acceleration factors can be used when the volume is larger and two phase-encoding directions are used. Recently, this has led to a 40-s high-resolution arterial whole-brain protocol with SENSE acceleration factor R=8 (2×4); see Fig. 26.4. By extending this scan with a second acquisition, a steady-state volume can be obtained with detailed high-resolution venous information (Fig. 26.4, right image). Without the high acceleration of parallel imaging, this protocol would not have been possible.

In summary, parallel imaging in the brain in combination with CENTRA or similar techniques is an essential ingredient for contrast-enhanced high-resolution MRA of the brain.

26.4.2 Functional, Time-Resolved Imaging: CENTRA Keyhole and SENSE

Dynamic imaging of a contrast bolus injection is clinically relevant in patients with AVMs or highly vascularized tumors such as glomus tumors or juvenile nasoangiofibromas. In both cases, information about the feeding and draining vessels and enhancement of the AVM or tumor is needed. So far, DSA is the gold standard for these applications because the temporal resolution of MR does not

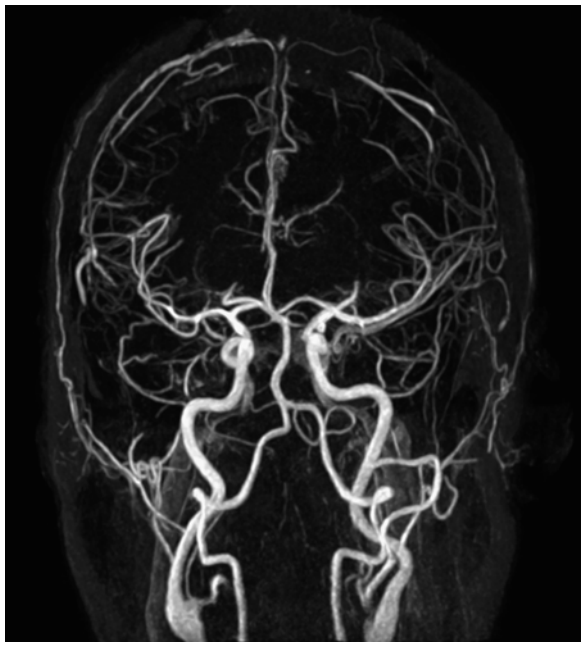

Fig. 26.3. High-resolution arterial 3D CE-MRA of the circle of Willis using CENTRA and SENSE. Imaging was performed using an 8-channel head coil at 3.0 T. CENTRA was used to obtain high-resolution images with excellent suppression of venous signal. For timing of the contrast arrival, BolusTrak fluoroscopic triggering was used. Spatial resolution: 0.52×0.69×0.45 mm³ (oc); 130 slices. Protocol parameters: TR/TE/flip =6.5 ms/1.92 ms/30°; FOV 210×180 mm²; matrix 400/512r. SENSE with acceleration factor *R*=2.5 was used. Scan time was 45 s, and no venous enhancement was seen. Courtesy: University Medical Center Utrecht, The Netherlands

meet the required speed: roughly 1 s/volume or better. To meet this requirement, first, spatial resolution can be somewhat lowered (1–2 mm) and high acceleration SENSE factors should be used. With this, frame rates in the order of 5 s/volume can be obtained. Additionally, CENTRA keyhole imaging (Hoogeveen et al. 2004; Willinek et al. 2005) can be used to further speed up the acquisition. The combination of SENSE and CENTRA with keyhole imaging has now routinely led to the following 4D protocol: SENSE acceleration: 6–8, CENTRA keyhole acceleration: 6×, whole-brain coverage with 140 slices of 1.1 mm (in-plane resolution 1.1×1.4 mm²) and 29 volumes in 20–30 s.

An example is shown in Fig. 26.5: a complete high-resolution 3D volume can be dynamically scanned with a temporal resolution of less than 1 s (0.66 s/volume). Zooming in on a few dynamic frames, the arterial feeders and venous drainage of an AVM can be recognized (Fig. 26.6).

Specifically, in dynamic imaging, it is important to acquire calibration data for the sensitivity of the coils before the actual acquisition. Most SENSE implementations usually do this. Techniques with autocalibration of the coil systems (e.g., GRAPPA with calibration during the scan) will provide lower frame rates in these applications because time is lost for the calibration during the scan (cf. Chaps. 8 to 10). This limitation could be overcome with the implementation of more recent algorithms for dynamic imaging

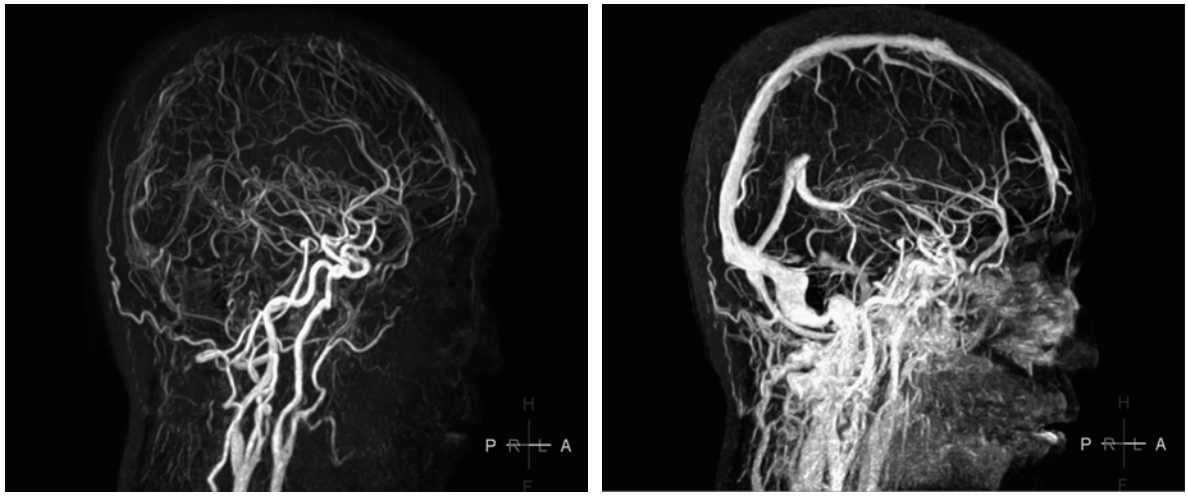

Fig. 26.4. MIP projections of a dynamic 3D arterial and venous high-resolution whole brain CE-MRA acquisition using an 8-channel head coil at 3.0 T. Spatial resolution: 0.63×0.63×0.5 mm³ (oc). The volumes of each phase (arterial/venous) contained 365 slices and were acquired in just 40 s using a SENSE acceleration of *R*=8. Further protocol parameters: TR/TE/flip =5.0 ms/1.5 ms/30°. FOV 250×212; matrix 400/512r. Fluoroscopic triggering was obtained using BolusTrak and a CENTRA profile order of the 3D acquisition to suppress veins in the arterial phase. Courtesy: ASAN Medical Center, Seoul, Korea

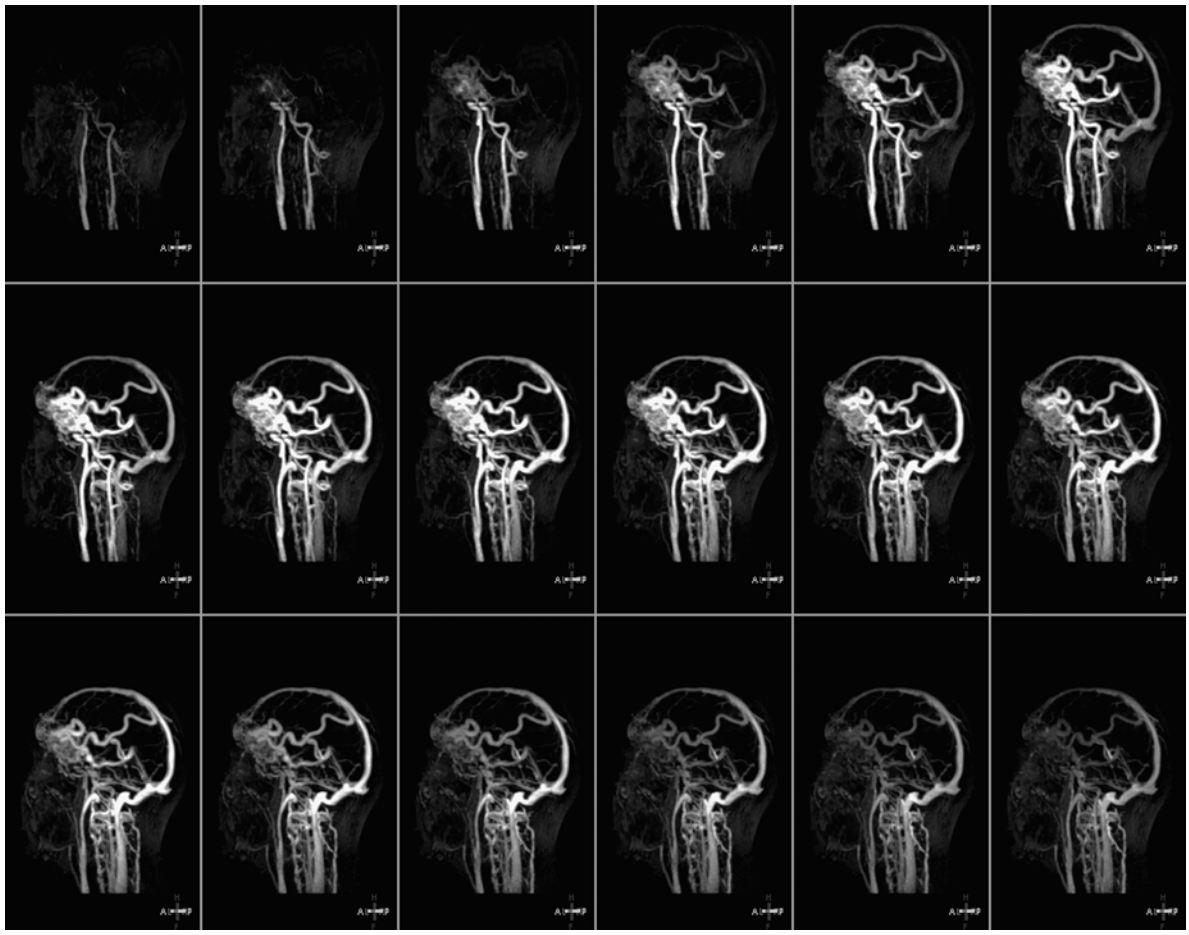

Fig. 26.5. MIP projections of a 4D CE-MRA brain protocol using CENTRA keyhole and SENSE. An 8-channel head-coil was used on an Achieva 3.0-T MR system. Protocol parameters: 29 consecutive 3D volumes with 140 slices. Spatial resolution of 1.1×1.4×1.1 mm³ (oc). SENSE acceleration R=6; CENTRA keyhole acceleration factor: 6; total acceleration factor: 36. Temporal resolution: 0.66–1.1 s/volume. Courtesy: Bonn University Hospital, Bonn, Germany

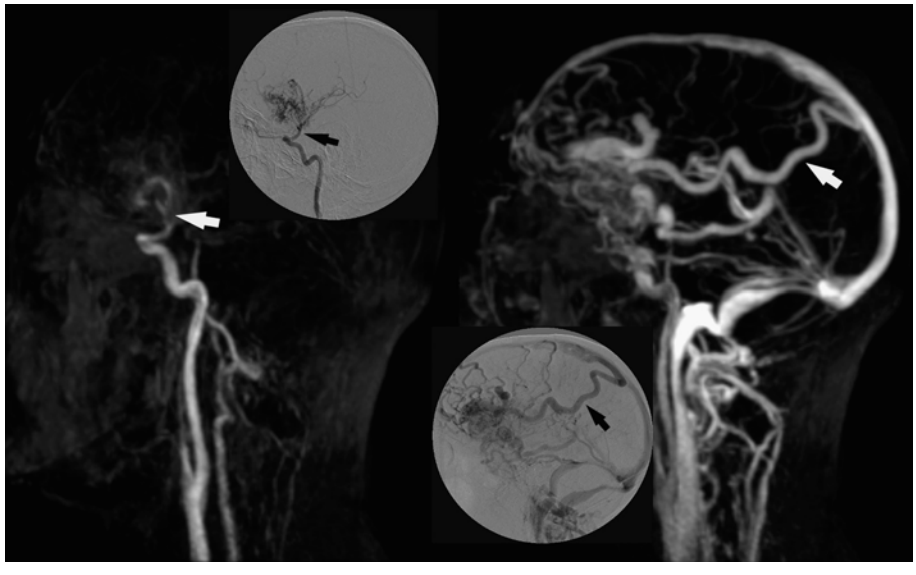

Fig. 26.6. Comparison of a few projections of the 4D CE-MRA dataset from Fig. 26.5 with DSA. *Left* MR image shows the arterial feeder of an AVM, *right* MR image shows the venous drainage of the same AVM. The MR images show a very good correlation with DSA (see *insets*). Courtesy: Bonn University Hospital, Bonn, Germany

like TSENSE (Kellman et al. 2001) or *k-t* BLAST/*k-t* SENSE (Tsao et al. 2003) (cf. Chaps. 7 and 12).

In conclusion, the combination of parallel imaging with other speedup techniques (viz. SENSE with CENTRA keyhole) can lead to acceleration factors up to 50×, and this opens new possibilities for dynamic MR imaging.

References

Hoogeveen RM et al (2004) Fast dynamic, high resolution contrast-enhanced MR angiography with CENTRA keyhole and SENSE [abstract]. Proc Int Soc Mag Reson Med 12:9

Hoogeveen RM, Visser F, van den Brink J (2003) High-resolution isotropic whole-brain angiography at 1.5 T and 3.0 T with PCA using highly accelerated SENSE imaging [abstract]. Proc Int Soc Mag Reson Med 11:329

Kellman P, Epstein FH, McVeigh ER (2001) Adaptive sensitivity encoding incorporating temporal filtering (TSENSE). Magn Reson Med 45:846–852

Pruessmann KP, Weiger M, Scheidegger MB, Boesiger P (1999) SENSE: sensitivity encoding for fast MRI. Magn Reson Med 42:952–962

Tsao J, Boesiger P, Pruessmann KP (2003) k-t BLAST and k-t SENSE: dynamic MRI with high frame rate exploiting spatiotemporal correlations. Magn Reson Med 50:1031–1042

Weiger M, Pruessmann K, Boesiger P (2002) 2D SENSE for faster 3D MRI. MAGMA 14:10–19

Willinek W, Gieseke J, Conrad R, Strunk H, Hoogeveen R, von Falkenhausen M, Urbach H, Kuhl CK, Schild HH (2002) Randomly segmented central k-space ordering in high-spatial-resolution contrast-enhanced MR angiography of the supraaortic arteries: initial experience. Radiology 225:583–588

Willinek WA, von Falkenhausen M, Gieseke J, Blömer R, Urbach H, Hoogeveen R, Schild HH (2005) High temporal and high spatial resolution contrast-enhanced MR angiography with CENTRA keyhole and SENSE at 3.0 T. Fortschr Röntgenstr 177:587–588

Wilman A et al (1997) Fluoroscopically triggered contrast-enhanced three dimensional MR angiography with elliptical centric view order: application to the renal arteries. Radiology 205:137–146

MRA of the Carotid Arteries

27

Henrik J. Michaely and Kambiz Nael

CONTENTS

27.1 Introduction

The common carotid arteries arising in most cases from the aortic arch on the left side and the innominate artery on the right side provide the main blood supply to the brain. The common carotid arteries divide at the carotid bulbus into the external carotid artery, which supplies the neck and the soft tissues of the head with blood. In contrast, the internal carotid artery (ICA) runs into the cranium without giving rise to any branches other than the internal ophthalmic artery and exclusively supplies the brain with blood. Pathologies of the external carotid arteries only rarely become symptomatic and are only rarely treated. However, diseases of the ICAs can be life threatening and have therefore been intensively investigated.

The most common disease of the ICA is atherosclerotic plaque formation and stenosis at the bifurcation at the level of the carotid bulbus. These alterations of the ICA have been identified as a main risk factor and were found an etiologic factor for 80% of all ischemic brain insults in patients. Since stroke related to ischemia from carotid emboli is one of the leading causes of death in western countries with a rising incidence in developing countries, extensive studies have been conducted on which patients benefit from therapy. Two independent studies, the North American Symptomatic Carotid Endarterectomy Trial (NASCET) (1991) and the European Carotid Surgery Trial (ESCT) (Barer 1998) could prove that patients with a high-grade stenosis of the ICA benefit from surgery. The studies' threshold for a high-grade significant stenosis was set at 70% diameter lumen narrowing measured on digital subtraction X-ray angiography (DSA) images as the standard of reference. These findings underline the need for reliable imaging of the ICA. The DSA is still considered as the gold standard. However, it is expensive (U-King-Im, Hollingworth et al. 2004), bears a non-negligible risk of 1-2% for complications such as embolism, stroke (Willinsky et al. 2003) and even death (Waugh and Sacharias 1992), may lead to impaired renal function (Niendorf et al. 1991; Heyman and Rosen 2003) and exposes the patient to ionizing radiation (Fig. 27.1).

Because of these drawbacks of DSA, magnetic resonance angiography (MRA) and Doppler ultrasound (DUS) have become the diagnostic imaging modalities of choice for ICA stenoses (U-King-Im, Trivedi et al. 2004). The application of DSA is nowadays limited to cases with ambivalent findings in MRA and DUS or for therapeutic purposes.

H. J. Michaely, MD
Department of Clinical Radiology, University Hospitals – Grosshadern, Ludwig Maximilian University of Munich, Marchioninistr. 15, 81377 Munich, Germany
K. Nael, MD
Department of Radiological Sciences, David Geffen School of Medicine at UCLA, 10945 LeConte Ave, Suite 3371, Los Angeles, CA 90095, USA

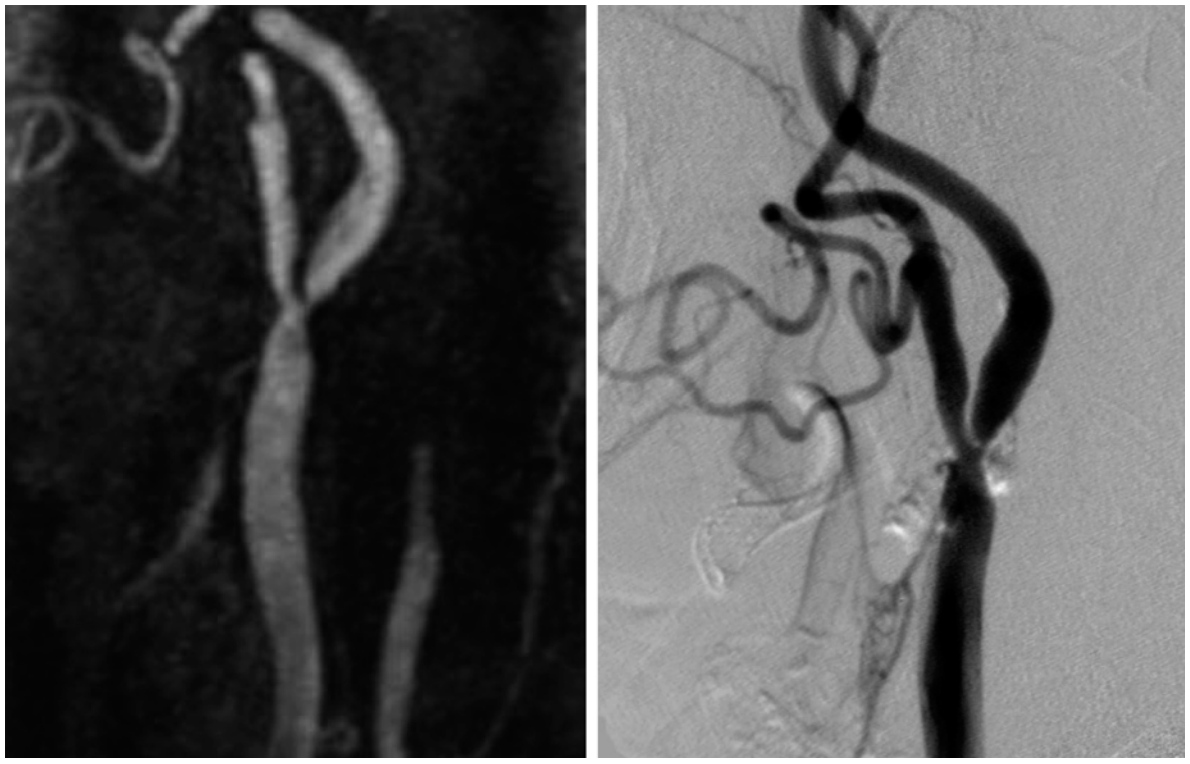

a b

Fig. 27.1a,b. High-grade left CAS at the bifurcation in 68-year-old patient. The lateral view of the CE-MRA **a** correlates excellently with that of the intra-arterial conventional digital subtraction angiography **b**. Figure reprinted with permission from: Michaely HJ, Herrmann KA, Kramer H, Laub G, Reiser MF, Schoenberg SO "The significance of MR angiography for the diagnosis of carotid stenoses" Radiologe, 2004 Oct 44(10): 975-984

27.2 MRA Techniques

27.2.1 Phase-Contrast and Time-of-Flight Techniques

MRA techniques have undergone a remarkable evolution since the first description of an angiographic magnetic resonance technique roughly 20 years ago (Wedeen et al. 1985). The initial techniques used for carotid MRA were time-of-flight (TOF) and phase-contrast (PC) MRA. Both require neither the administration of MR contrast agents nor high-performance gradient systems to detect the vessels. However, their drawbacks are the relatively long acquisition times that are in the order of several minutes and that make them more susceptible to motion artefacts such as breathing artefacts and artefacts from swallowing (Patel et al. 1995; Saloner 1998), which cannot be suppressed throughout a 4-min scan. TOF techniques are in addition susceptible to slow blood flow and tend to show signal loss (Prince et al. 1997) in case of stenotic vessel lesions due to turbulent flow and subsequent intravoxel dephasing. While this seemed like a disadvantage of this technique at first, the dephasing effect was then specifically used to detect high-grade stenoses, which lead to spin dephasing (Nederkoorn et al. 2002). However, TOF techniques still perform relatively well in the detection of atherosclerotic vessel disease with sensitivities and specificities only 5-13% lower than with contrast-enhanced techniques (Anzalone et al. 2005). For the intracranial MRA, TOF techniques remain the gold standard and seem to profit strongly from the combination of parallel imaging and 3-T systems (Willinek et al. 2004; Willinek et al. 2003). No reports on the application of parallel imaging for carotid MRA have been published yet. Similarly, PC techniques – even though not widely used outside the head any more – seem to gain some support again for the depiction of intracranial vessels and in particular of the intracranial veins as shown in Chap. 26.

27.2.2 High-Spatial-Resolution MRA

The NASCET trial drastically demonstrated the positive effects of surgical therapy in patients with at least 70% diameter stenosis of the internal carotid artery (NASCET 1991). From these results arises the strong clinical need for an exact depiction and hence exact grading of carotid artery stenoses (CAS). The mean diameter of the internal carotid artery (ICA) is estimated to be 5-6 mm. In case of an at least 70% CAS, the remaining lumen would be 1.8 mm in the best case. To exactly assess these CAS and to avoid partial volume effects and hence wrong grading of these CAS, the pixel size has to be smaller than the remaining lumen. The literature states that a value of three pixels within the vessel of interest is required for exact grading stenoses (Hoogeveen et al. 1998; Westenberg et al. 2000). This implies that the optimal spatial resolution for depiction of 70% CAS is at the order of 0.6×0.6 mm^2 in-plane or even better. This knowledge fueled the evolution of MRA techniques to obtain the best possible spatial resolution. This has been greatly fostered by the advent of high-performance MR scanners, which facilitated the application of contrast-enhanced (CE) MRA techniques. CE-MRA is independent of pulsatility and flow artefacts and can acquire one entire 3D data set in a single breathhold, thereby also eliminating motion artefacts from breathing and swallowing (Prince 1994). An initial technique for improved spatial resolution was the elliptical centric reordered k-space (Riederer et al. 2000) readout, which enables longer scan times without venous overlay (Huston et al. 1999). With this technique the k-space is filled from the center to the periphery. Therefore, the contrast agent bolus has to reach the vessel area of interest exactly at the start of the sequence. There are two main advantages to this approach. Since the contrast-determining parts of k-space are filled at the start of the scan when the contrast agent bolus passes through the arteries, this approach leads to a very weak venous signal and hence almost no venous overlay even with prolonged scan times. Using automatic or semiautomatic fluoroscopic techniques, the test bolus can be omitted and the scan time decreased (Butz et al. 2004). However, this approach requires more profound operator experience since it is more difficult to initiate the scan correctly during real-time visualization of the rapidly passing contrast media bolus.

Parallel imaging represented the next technical evolution leading to a better spatial resolution of CE MRA. The application of parallel acquisition techniques (Griswold et al. 2002; Pruessmann et al. 1999) to high-resolution MRA of the carotid arteries was used by most groups to decrease the scan time and improve spatial resolution. Since sufficient signal-to-noise ratio (SNR) or contrast-to-noise ratio (CNR) is available, no major adoptions to non-parallel-imaging techniques have to be done. A spatial resolution of roughly 1.0×1.0×1.0 mm^3 can be acquired in 20 s or less on most current 1.5-T scanners with multi-channel technique and a parallel-imaging acceleration factor of R=2. Using parallel imaging a carotid artery scan with slightly decreased – yet diagnostic – spatial resolution can be incorporated into a whole-body protocol (Kramer et al. 2005). The rationale for a slightly decreased spatial resolution is derived from the faster scan times needed to catch the same bolus of contrast agent at the calves. Exemplary sequence parameters for a dedicated high-resolution MRA of the carotid vessels can be found in Table 27.1. However, since only every second line (acceleration factor R=2) or even every third line (acceleration factor R=3) of k-space is acquired, the center of k-space is traversed much faster compared to non-accelerated acquisitions. This may hamper fluoroscopically triggered elliptical-centric MRA acquisitions since a slightly delayed start of the acquisition can lead to a substantially decreased image contrast and quality. Therefore, Cartesian acquisition seems preferential with parallel imaging since it is less sensitive to slightly mistimed initiation of the scan. On the other hand, a

Table 27.1 Imaging parameters for carotid CE-MRA at 1.5 T (Siemens Magnetom Avanto)

	Time-resolved MRA	High-resolution MRA
Repetition time (ms)	2.37	3.69
Echo time (ms)	0.82	1.23
Flip angle	20°	30°
Bandwidth (Hz/pixel)	750	360
Field of view (mm^2)	320×200	330×212
Matrix size	256×218	448×349
Voxel size (mm^3)	1.5×1.5×3.0	0.9×0.7×0.9
Parallel imaging	GRAPPA, R=2	GRAPPA, R=2
Partial Fourier	6/8 (phase-enc. direction)	Off
Acquisition time	1.6 s/3D data set	0:23 min
Slice thickness (mm)	3.0	0.9
Contrast	10 ml at 4 ml/s	20 ml at 1.5 ml/s
k-space trajectories	Cartesian	Cartesian

recent publication found beneficial effects of SENSE in combination with elliptic centric k-space sampling in terms of increased venous suppression (Hu et al. 2004). Most groups used "conventional" phased-array coils for parallel imaging. For cardiac applications, a 32-channel coil that enables acceleration factors of 4-5 is already available (Reeder et al. 2005). When dedicated neurovascular coils become available, higher acceleration factors will also be employed for the carotid arteries. As explained later, the inherently higher signal at 3 T represents an ideal compensatory complement of parallel imaging (Michaely et al. 2005a).

To compensate for the loss of SNR and CNR with parallel imaging at 1.5 T already, the application of either 1-molar contrast agents (gadobutrol, Gadovist, Schering, Berlin, Germany) (Goyen at al. 2001), or agents with higher relaxivity due to weak protein binding like Gd-BOPTA (Mulithance, Bracco, Milan, Italy) (Goyen and Debatin 2003) or strong protein binding like the intravascular MS-325 is recommended (EPIXpharmaceuticals, Boston, MA, and Vasovist, Schering AG, Berlin, Gemany). For the latter, approval by the European Agency for the Evaluation of Medicinal Products (EMEA) and the FDA is expected soon. The latter also allows imaging of the carotid arteries in the steady state. Theoretically, these longer scan times should translate into a higher spatial resolution (Fig. 27.2).

In summary, for high-resolution CE-MRA of the carotid arteries parallel imaging successfully lead to an increased performance in terms of imaging speed as well as spatial resolution. It is up to the individual user whether a higher spatial resolution and accelerated acquisition or a combination of both, which is preferred at our institution, is chosen as benefiting from parallel imaging. Apart from the well-known signal loss, which can be compensated with the appropriate contrast agent, there is no disadvantage associated with the application of parallel acquisitions techniques in CE-MRA of the carotid arteries. No reports on major aliasing or third arm artefacts are known either. Recent studies even report that the signal loss – though it can be objectively measured – is diagnostically not impairing (Michaely et al. 2005; Summer et al. 2004).

27.2.3 High-Temporal-Resolution MRA

As high-spatial-resolution MRA is always at risk for venous overlay and does not display dynamic flow

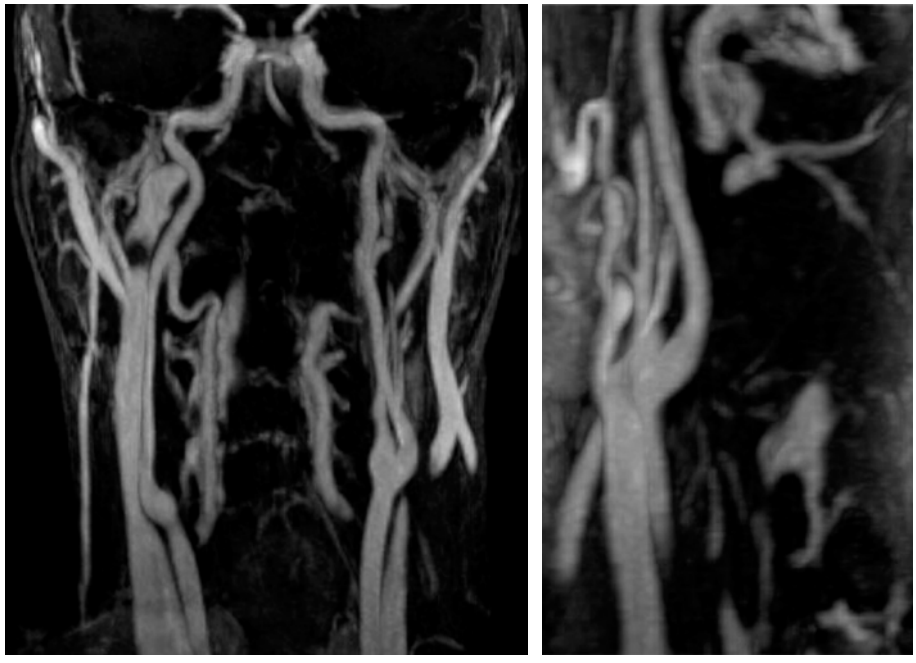

Fig. 27.2. a Coronal and **b** sagittal thin-MIP views of a 30-year-old healthy volunteer who underwent carotid MRA at 1.5 T (sequence parameters in Table 27.1) with intravascular contrast agent (Gadofosveset). In these steady-state images 15 min after the initial administration of the contrast agent the carotid arteries can be clearly followed. Due to the intravascular character of the contrast agent there is also strong venous contrast

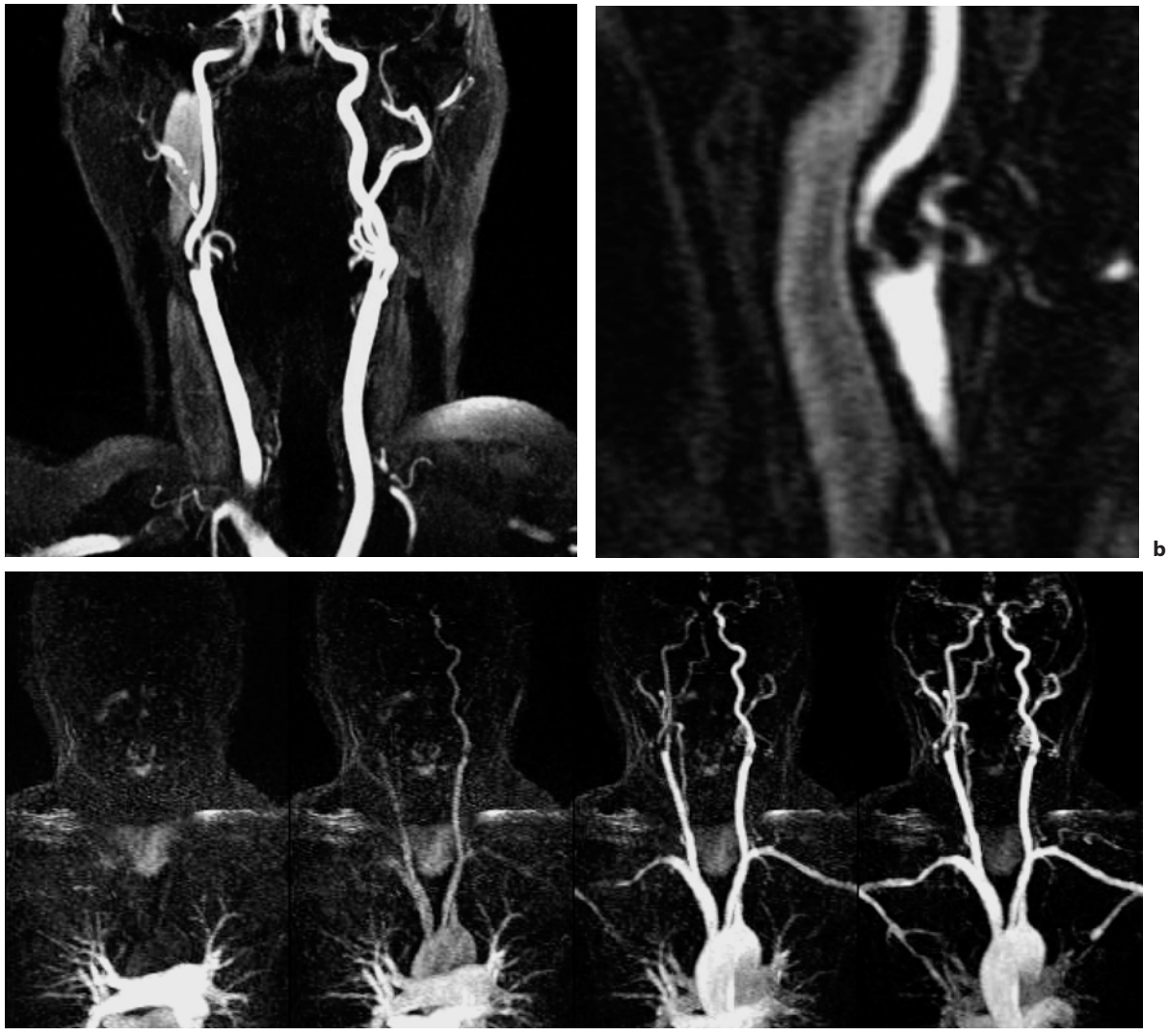

Fig. 27.3. a Coronal MIP view of a right-sided, short, high-grade CAS at the bulbus, which can also be clearly demonstrated in the sagittal view **b**. In the time-resolved MRA **c** using TREAT with a temporal resolution of 2 s/3D frame a markedly delayed flow in the affected right ICA can be appreciated. Figure reprinted with permission from: Michaely HJ, Herrmann KA, Kramer H, Laub G, Reiser MF, Schoenberg SO "The significance of MR angiography for the diagnosis of carotid stenoses" Radiologe, 2004 Oct 44(10): 975-984

information due to its static nature, time-resolved MRA techniques have been presented by various groups (Willig et al. 1998; Klisch et al. 2000; Golay et al. 2001; Fellner et al. 2005; Warmuth et al. 2005; Lenhart et al. 2002). The overall approach is to trade spatial resolution for temporal resolution and hereby to acquire several 3D data sets in the same time as a single data set of the high-spatial resolution MRA. Initially, multiphasic 2D time-resolved techniques have been used that can be used as a test-bolus sequence additionally providing information about vascular hemodynamics (Wikstrom et al. 2003).

Time-resolved 3D data sets combine the information about blood flow hemodynamics with that of vessel morphology (Fig. 27.3). Initially, multi-phasic 3D gradient-echo sequences were used that yielded a 3D dataset every 10 s (Lenhart et al. 2002; Naganawa et al. 2001) with, however, markedly reduced spatial resolution. Therefore, it is not surprising that the overall sensitivity and specificity of these sequences for the detection of CAS is significantly lower than those of high-resolution MRA (Lenhart et al. 2002). The introduction of parallel imaging led to a considerable decrease in scan time to 4 to 6 s per 3D data

set allowing the visualization of more than one frame free of venous overlay (Golay et al. 2001). A different approach, the so-called view-sharing technique, was also reported to allow time-resolved MRA with a high temporal resolution; this technique has been called TRICKS (time-resolved imaging of contrast kinetics) (Naganawa et al. 2001; Korosec et al. 1996; Mistretta et al. 1998). The combination of these two techniques, view-sharing and parallel imaging, is sometimes referred to as TREAT (time-resolved echo-shared angiography technique) and enables high-spatial-resolution and high-temporal-resolution data acquisition in a single exam, cf. Chaps. 7 and 11 (Saloner 1998). By this means, spatial resolutions in the order of acquired 1.5×1.5×3.0 mm^3 voxel size can be obtained with a temporal resolution of 1.6 s/3D frame (Staikov et al. 2000). This technique will be valuable in the detection of delayed flow in case of CAS or reversed flow as in the case of subclavian steal syndrome (Figs. 27.4, 27.5). Further progress of this technique can be achieved at 3 T as laid out in the following paragraph.

27.3 Measurement of Carotid Artery Stenosis

Atherosclerotic changes and hence carotid artery stenoses are the most common pathologic changes of the carotid arteries. From the NASCET and ESCT results, it becomes obvious that an exact determination of the degree of CAS is pivotal for further management of the patient as a higher degree of stenosis may warrant an operative therapy. Typically, CAS was measured as the reduction of the diameter as done on a lateral DSA projection view. The NASCET measures carotid artery diameter at the site of stenosis and relates this diameter to the distal non-stenotic vessels segment (NASCET 1991), while the ECST measures stenosis of the remaining lumen at the carotid bifurcation in rela-

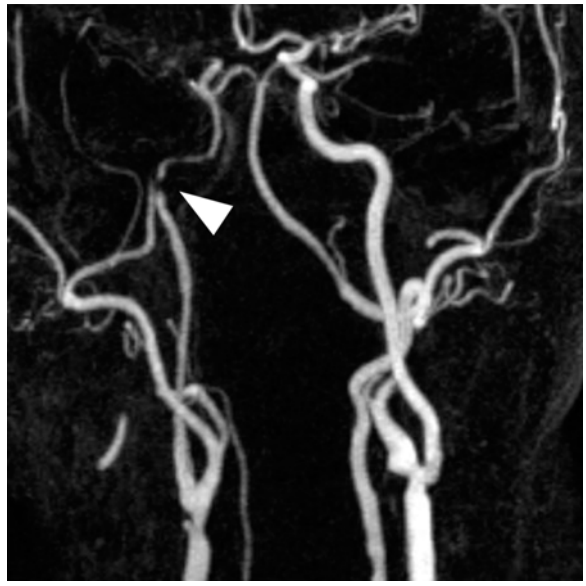

a

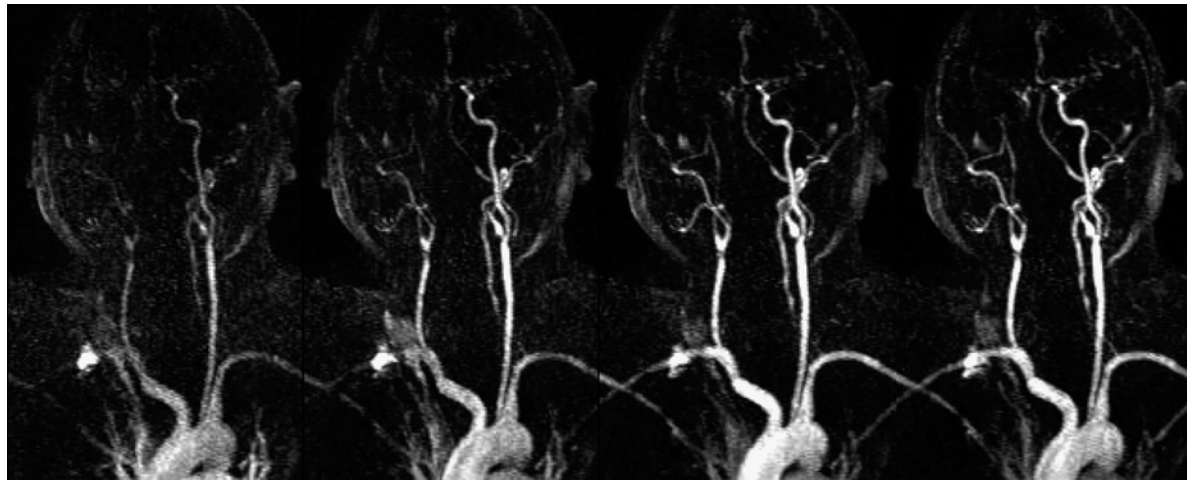

b

Fig. 27.4. a Coronal MIP view of a distal CAS that leads to a significantly delayed flow **b** in the affected vessel and that is therefore deemed hemodynamically significant. Distal internal carotid artery stenoses in the petrous part of the ICA can be easily demonstrated in the MRA while CTA and DUS often are not able to depict these lesions due to the bony surroundings of the ICA. Figure reprinted with permission from: Michaely HJ, Herrmann KA, Kramer H, Laub G, Reiser MF, Schoenberg SO "The significance of MR angiography for the diagnosis of carotid stenoses" Radiologe, 2004 Oct 44(10): 975-984

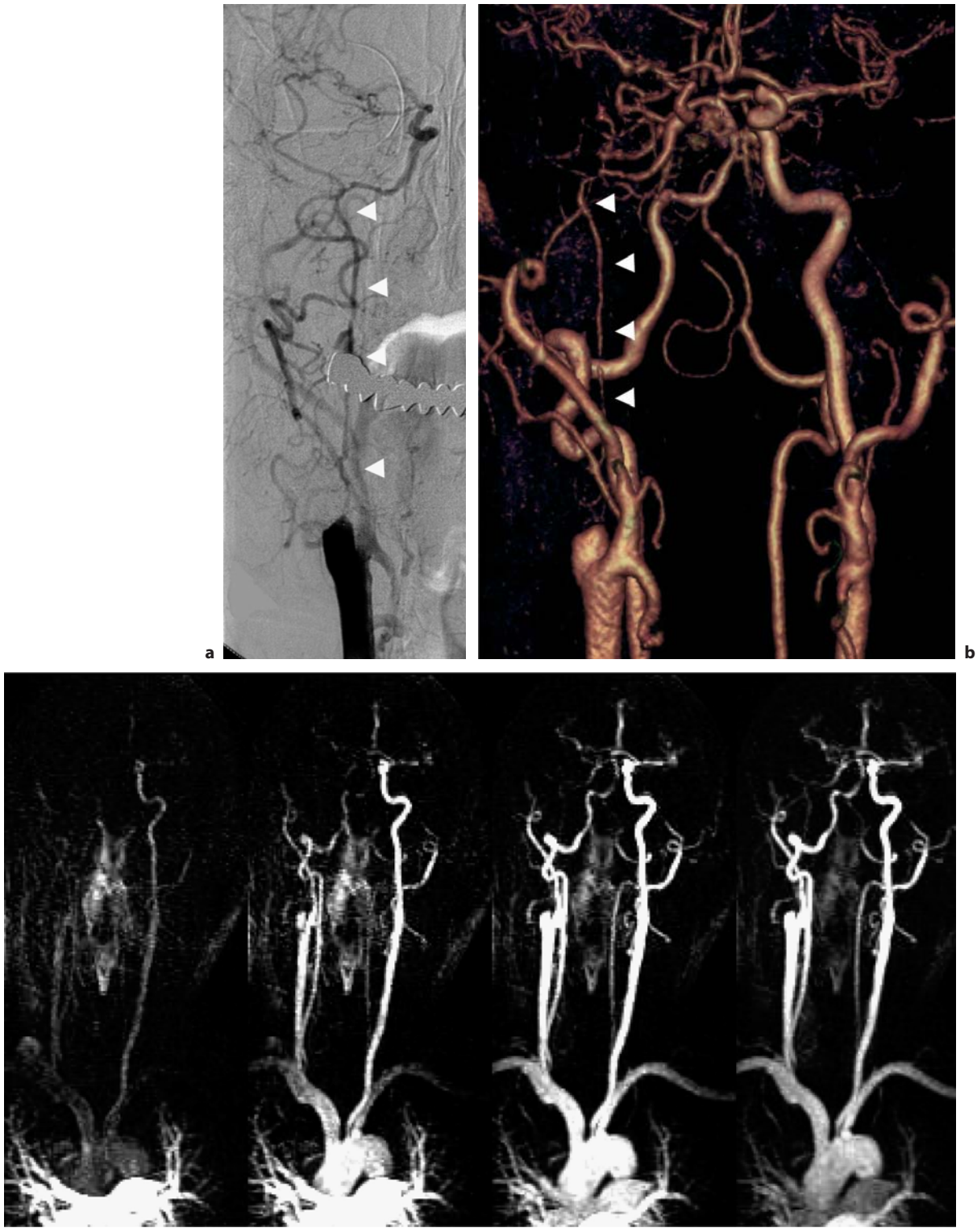

Fig. 27.5. a Long-segment, high-grade pseudoocclusion (*small arrows*) of the ICA seen in the DSA projection. Note the artefacts caused by the patient's teeth. **b** The remaining lumen can be easily seen (*small arrows*) in the 3D reconstruction of the high-resolution MRA. **c** In the time-resolved TREAT-MRA the stenotic vessel can again be clearly depicted with delayed inflow. Figure reprinted with permission from: Michaely HJ, Herrmann KA, Kramer H, Laub G, Reiser MF, Schoenberg SO "The significance of MR angiography for the diagnosis of carotid stenoses" Radiologe, 2004 Oct 44(10): 975-984

tion to the initial, non-stenotic lumen (Staikov et al. 2000). A recent study comparing the results of CAS measured with CE-MRA according to the NASCET and the ECST method in comparison the conventional angiography as the gold standard found a significant higher sensitivity with the use of the NASCET criteria (U-King Im et al. 2004). It seems therefore appropriate to use the NASCET criteria when measuring the degree of stenosis on CE-MRA data. In a meta-analysis, the sensitivity and specificity of the MRA for the grading of relevant CAS were found to be 95% and 90% (Nederkoorn et al. 2003), which was higher than the corresponding results for DUS or computed tomography angiography (CTA). However, the included studies used maximum intensity projections of the MRA that do not benefit from the three-dimensional character of the MRA. This may be one explanation for the often-cited fact that MRA tends to overestimate the degree of stenosis. It seems more accurate to use the area of the stenosis instead of the diameter of the stenosis, a technique that proved extremely useful and precise for the renal arteries already (Michaely et al. 2005b). Measuring the stenosis in the cross-sectional view also takes the excentric nature of atherosclerotic changes better into account than looking at the diameter of the stenosis only (Fig. 27.6). Simply using the source images or DSA-like projections (Nederkoorn et al. 2002) is already advantageous in terms of diagnostic accuracy (Anderson et al. 1994). In cases of complicated vascular anatomy, curved reformats are another possible solution for exact vessel diameter assessment (Gonschior et al. 2001).

Fibromuscular dysplasia (FMD) occurring in the supraaortic vessels in 30% of all patients with FMD poses a further diagnostic challenge to MRA (Slovut and Olin 2004). Particularly in patients

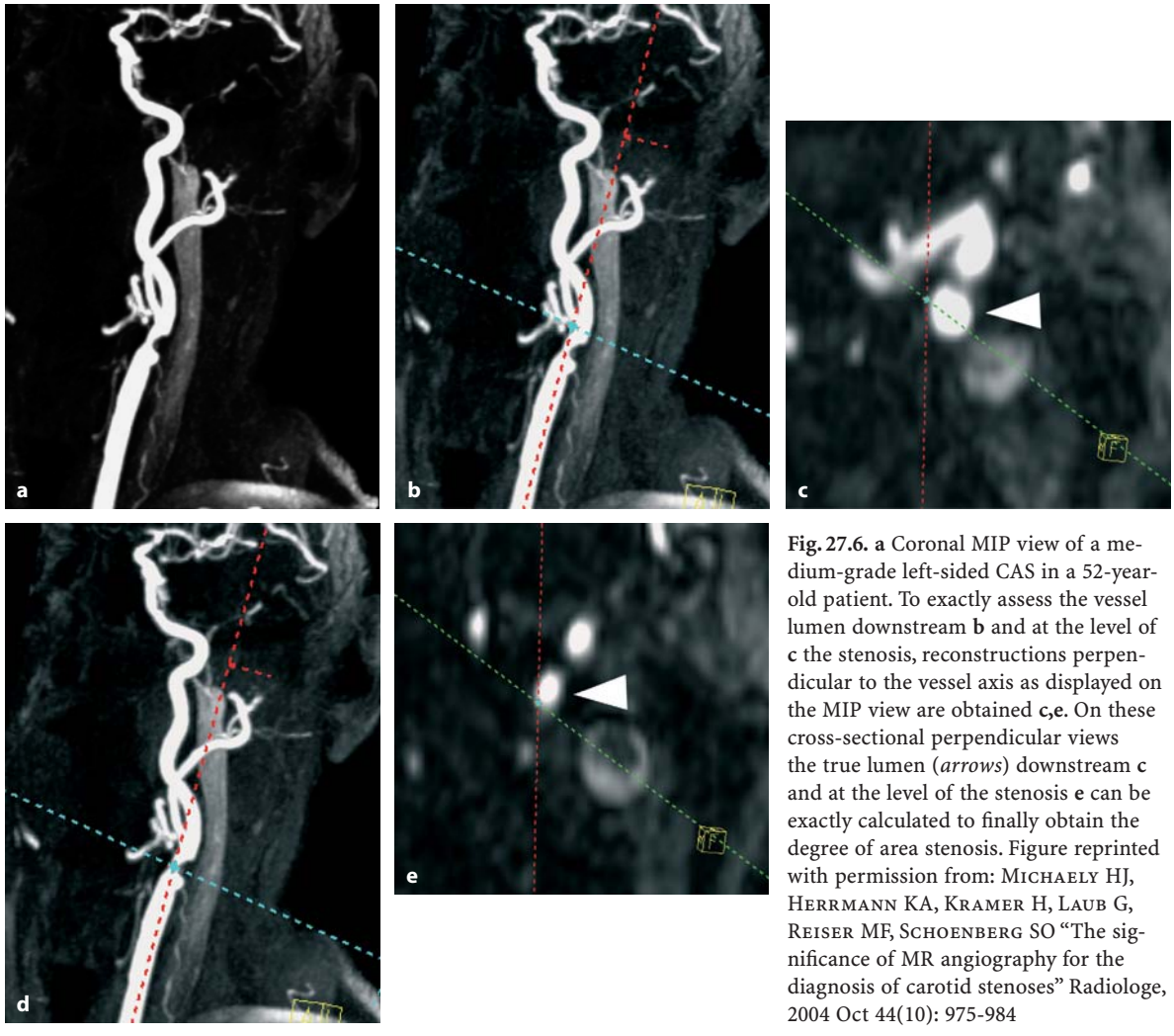

Fig. 27.6. a Coronal MIP view of a medium-grade left-sided CAS in a 52-year-old patient. To exactly assess the vessel lumen downstream **b** and at the level of **c** the stenosis, reconstructions perpendicular to the vessel axis as displayed on the MIP view are obtained **c,e**. On these cross-sectional perpendicular views the true lumen (*arrows*) downstream **c** and at the level of the stenosis **e** can be exactly calculated to finally obtain the degree of area stenosis. Figure reprinted with permission from: Michaely HJ, Herrmann KA, Kramer H, Laub G, Reiser MF, Schoenberg SO "The significance of MR angiography for the diagnosis of carotid stenoses" Radiologe, 2004 Oct 44(10): 975-984

with FMD, the higher spatial resolution associated with the application of parallel imaging will prove highly advantageous since the typical string-of-beads changes of the vessel wall are difficult to discern on standard resolution MRA images. However, there are no published data on the performance of CE-MRA with parallel acquisition techniques available at this point (Fig. 27.7-27.9).

27.4 Functional Characterization of Carotid Artery Disease

By adding just a few sequences the MRA of the carotid vessels can be enhanced by functional data. Primarily, MR phase-contrast flow measurements yield valuable extra information about the hemodynamic impact of a CAS (van Everdingen et al. 1997). In a study on 86 patients, the mean flow in the ICA was 206 ml/min with a maximal flow velocity of 37 cm/s, which was on average reduced to 143 ml/min and 23 cm/s in case of CAS. Even the entire flow pattern of all supraaortic vessels changes and can be used as an additional functional parameter in the comprehensive assessment of CAS (Cosottini et al. 2005). Applying parallel imaging alone or in combination with other acceleration algorithms such as k-t-BLAST (Tsao et al. 2003) to PC-MR flow measurements, acquisition time can be decreased by a factor of up to 3.5 (Beerbaum et al. 2003). Another – yet still experimental way – to characterize the flow in a stenotic ICA is the application of MRA sequences with a high temporal resolution. This approach does not allow measuring the flow volumes and velocities; however, it may allow detecting delayed flow in the stenosed vessel or even collateral vessels.

Adding T1-weighted spin-echo sequences post contrast, particularly in combination with custom-

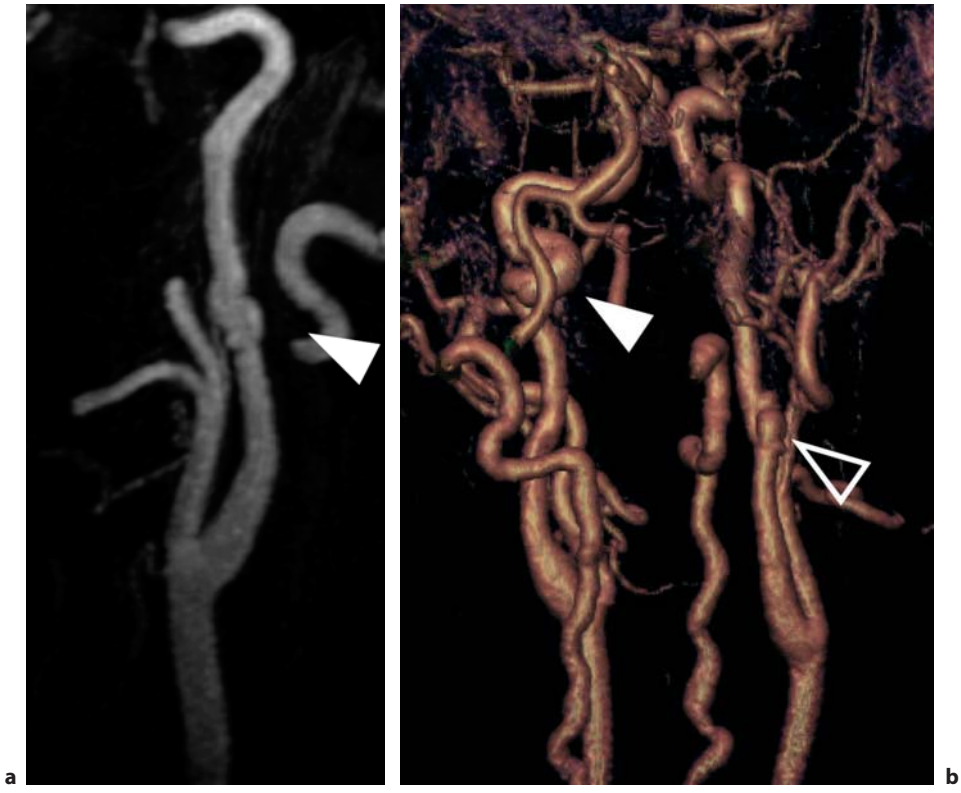

Fig. 27.7. a Sagittal MIP view of the ICA of 43-year-old female patient with FMD: The characteristic string of beads appearance of the ICA can be well appreciated. **b** The volume-rendered reconstruction of the MRA data of the same patient shows the above-mentioned alterations (*open arrow*) but also an affection of the contralateral side (*solid arrow*). Figure reprinted with permission from: Michaely HJ, Herrmann KA, Kramer H, Laub G, Reiser MF, Schoenberg SO "The significance of MR angiography for the diagnosis of carotid stenoses" Radiologe, 2004 Oct 44(10): 975-984

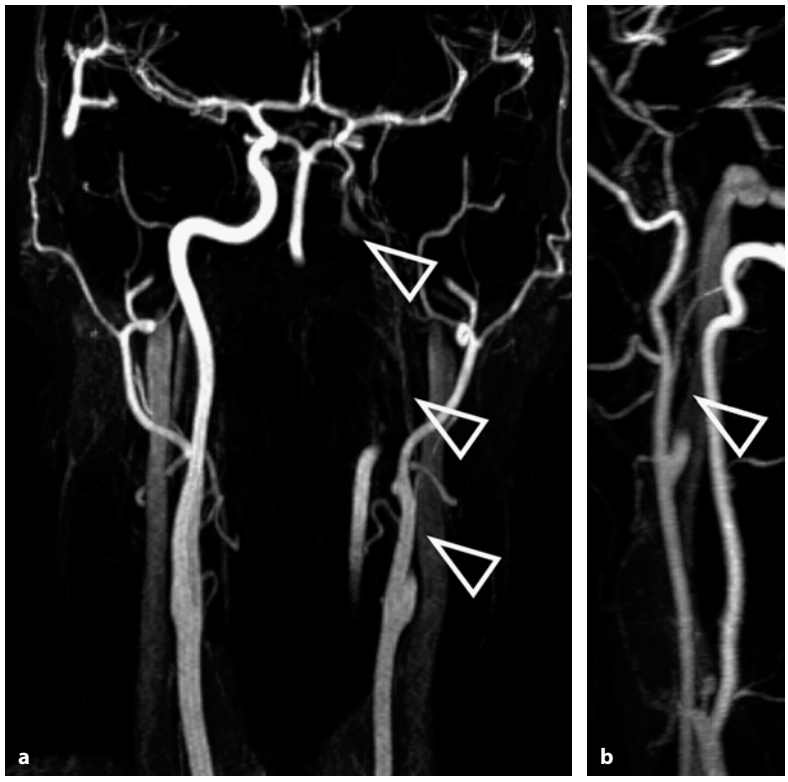

Fig. 27.8. a 30-mm thick coronal MIP view of the MRA in a 19-year-old patient after motor vehicle accident. On the left side the ICA cannot be depicted any more correlating to a traumatic occlusion of the vessel (*open arrows*) **b** Equally, in the sagittal thick-MIP view the ICA cannot be depicted and reveals a sudden stop of enhancement at the bulbus (sequence parameters in Table 27.1)

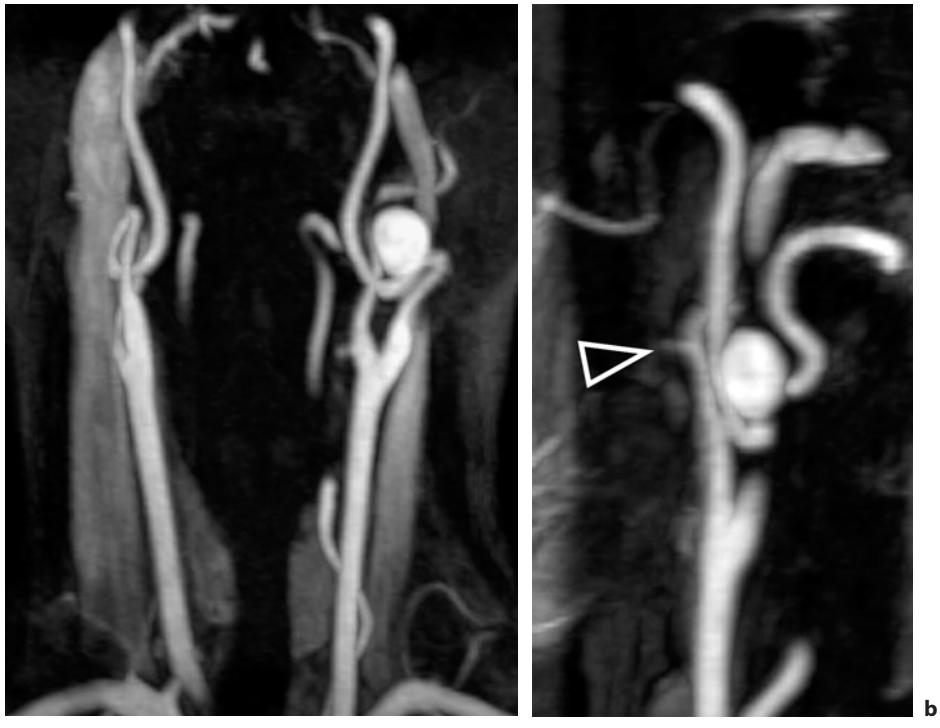

Fig. 27.9. a 30-mm-thick coronal MIP view of a 43-year-old male patient with the incidental finding of an ICA aneurysm. Due to the tortuous course of the ICA as seen also on the contralateral side in the coronal view the allocation of the aneurysm to the ICA or ECA is demanding. **b** In the sagittal view a branch coming off the ECA can be seen (*arrow*), thereby allowing to allocate the aneurysm to the ICA (sequence parameters in Table 27.1).

ized coils, enables plaque or vessel wall imaging. This field of ongoing research has not reached clinical routine so far, mainly because the local, customized coils are not readily available yet. However, improved coil technology will foster the characterization of plaques by means of MRI in the near future (Hofmann et al. 2003; Yu et al. 2003; U-King-Im 2004). With the currently available hardware solely the plaque surface can be safely assessed. A correlation between the irregularity of the plaque surface with neurological symptoms was proven (Troyer et al. 2002).

27.5 Comparison to Ultrasound and Intravascular Ultrasound

Apart from MRA, ultrasound and particularly DUS have evolved into the main tool for the detection and grading of CAS. While there is little doubt that DUS is cheaper and readily available, there is an ongoing debate about the value of DUS. DUS is a powerful tool in the hands of an experienced examiner, yet the reproducibility of the DUS results is often poor compared to MRA (Bucek et al. 2002; Mathiesen et al. 2000; Mikkonen et al. 1996). Studies comparing the diagnostic accuracy of MRA and DUS found MRA to be more accurate, but also suggested using DUS and MRA in combination for an even higher reliability (U-King-Im, Trivedi et al. 2004). This is particularly due to the fact that DUS is more sensitive for long stenoses, the so-called pseudo-occlusions (Nederkoorn et al. 2003; Wardlaw et al. 2001). New technologies such as intravascular ultrasound (IVUS), which is already widely used in cardiac and abdominal intervention, could improve the diagnostic accuracy and reliability of ultrasound examinations; however, these techniques are too invasive and bear the risk of plaque rupture with the spread of emboli. As of now, there are no published data for the application of IVUS at the carotid arteries available.

27.6 Carotid MRA at 3 Tesla

The introduction of whole-body, 3-T MR imaging systems with the potential to generate higher signal-to-noise ratio (SNR) opened up new horizons to improve image quality in MR imaging. The theoretical SNR advantage at 3 T is especially relevant for MR angiographic applications, where a boost in SNR can significantly improve the image quality (Fig. 27.10–27.12).

The main advantage of MR imaging at 3 T is the SNR gain, which scales approximately linearly with the field strength B_0 from 1.5 T to 3.0 T imaging (Willinek et al. 2003; Campeau et al. 2001). Also, since the longitudinal relaxation time (T1) of unenhanced blood increases with field strength, sensitivity to injected gadolinium agents for CE-MRA is relatively increased. The higher SNR can be used to reduce acquisition time, improve spatial resolution, or a combination of both (Willinek et al. 2003; Campeau et al. 2001; Thulborn 1999). For CE-MRA

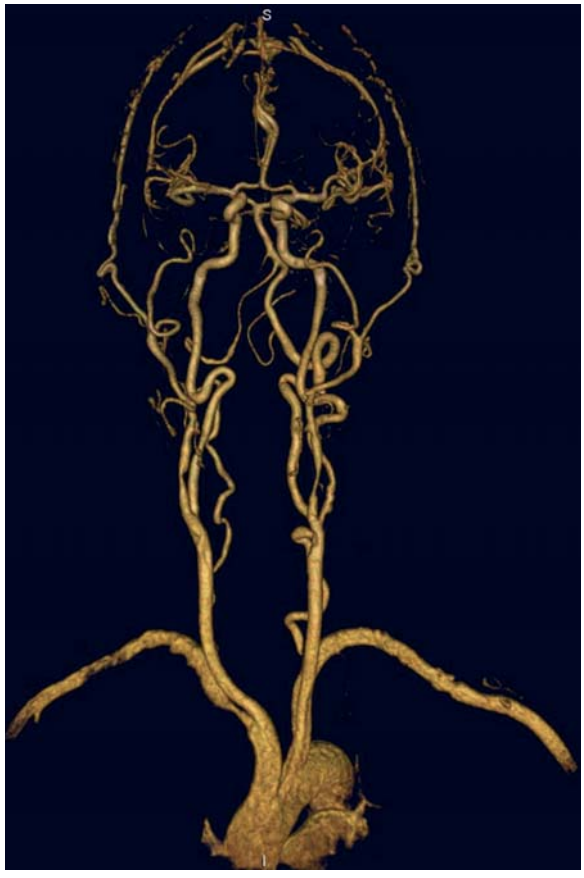

Fig. 27.10. 3D CE-MRA at 3.0 T in a normal subject. The whole 3D data set from aortic arch to intracranial vasculatures was acquired in a 20-s breath hold with a voxel dimension of 0.8×0.7×0.8 mm^3, using parallel imaging with the GRAPPA algorithm and a high acceleration factor of R=4 (sequence parameters in Table 27.2)

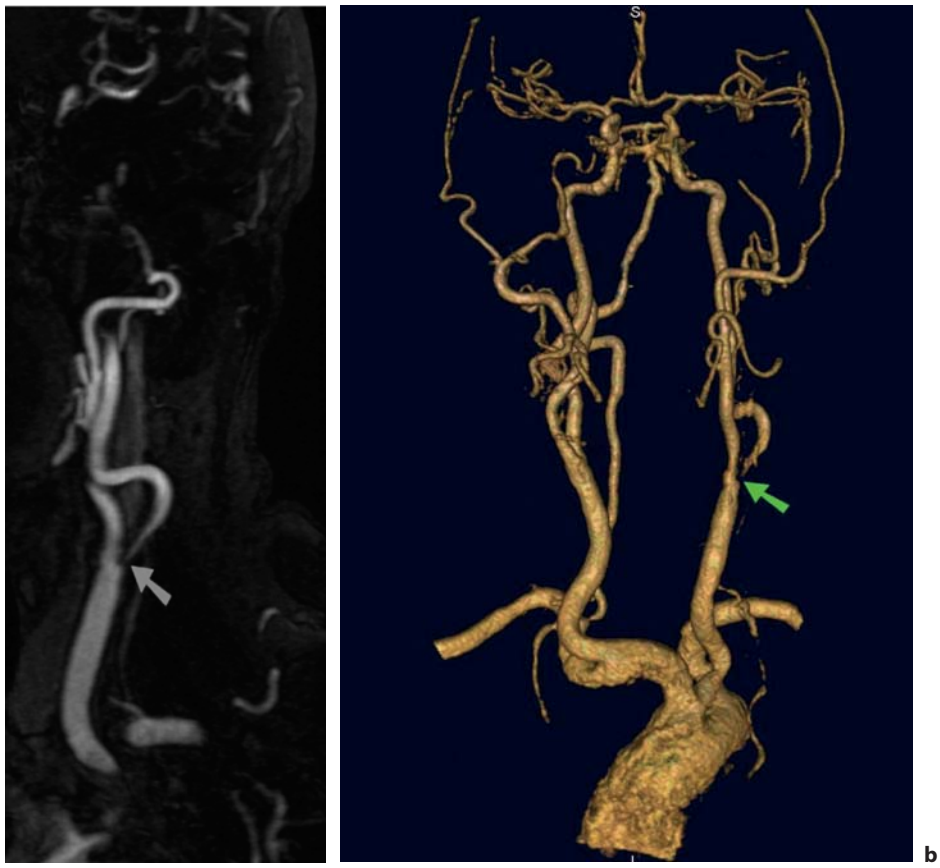

Fig. 27.11a,b. 3D CE-MRA at 3.0 T. Atherosclerosis in a 58-year-old patient seen **a** on the sagittal oblique thin MIP (10 mm) and **b** coronal volume rendering with severe stenosis of the left internal carotid artery (sequence parameters in Table 27.2)

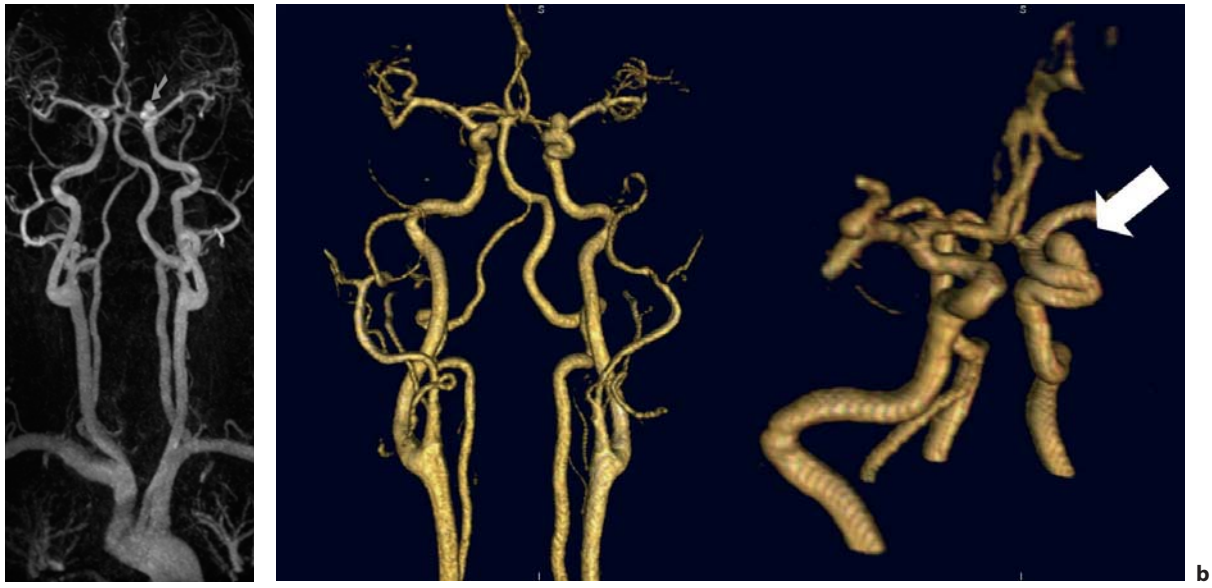

Fig. 27.12a,b. Standardized coronal MIP **a** and coronal as well as oblique VR images **b** from high-spatial-resolution 3D CE-MRA at 3.0 T, showing an aneurysm at the supraclinoid portion of the left internal carotid artery (*arrow*) (sequence parameters in Table 27.2)

with short acquisition times and high spatial resolution, the inter-relation between SNR and the acquisition parameters has to be thoroughly regarded. Because SNR is proportional to the voxel size and the square root of the imaging time, rapid acquisition of a high-spatial-resolution image causes loss of SNR in two ways. For implementations of fast imaging techniques such as time-resolved MRA with segmented k-space and parallel acquisition techniques, SNR can fall below the lower limit at 1.5 T while being still acceptable at 3.0 T.

However, other factors, particularly related to the increased specific absorption rate (SAR) at higher fields, need to be considered as well. To avoid SAR limitations, parallel imaging seems to be a suitable way. As the SAR scales with the square of the field strength, the SAR at 3.0 T is four times the SAR at 1.5 T. Application of parallel imaging with an acceleration factor of R reduces the SAR to $1/R$ of its original value (at least with respect to long-term averaging of SAR), implying that parallel imaging can significantly reduced the SAR limitations. In practice this simplified approach has to be adapted as the sampling density (and thus the short-term average of SAR during acquisition) and is not reduced with parallel imaging. Another approach to lower the SAR is to apply lower flip angles. Due to the longer T1 times at 3 T, even lower flip angles than conventionally used still succeed in sufficient background suppression.

There are several studies evaluating carotid and intracranial 3D TOF-MRA at 3.0 T that have revealed significant improvement in image quality and diagnostic accuracy compared to the results of 3D TOF-MRA at 1.5 T (Willinek et al. 2003; Al-Kwifi et al. 2002; Bernstein et al. 2001; Gibbs et al. 2004). Published data on the application of 3D CE-MRA at 3.0 T are however very limited. Bernstein et al. have shown that TOF-MRA and CE-MRA of carotid and intracranial circulation at 3.0 T are feasible, and image quality was superior to that of a well-established 1.5 T protocol. At our institution, we are using a 3-T MR system to acquire CE-MRAs in different parts of body, including the carotids (Table 27.2), and the results are highly satisfactory to the point that the CE-MRA has been integrated into the clinical routine examinations. It seems likely that the introduction of more sensitive multi-element coil systems at 3.0 T will permit further improvement in imaging quality and performance, as it has at 1.5 T (Bodurka et al. 2004; de Zwart et al. 2004; King et al. 2001).

Table 27.2. Imaging parameters for carotid CE-MRA at 3.0 T (Siemens Magnetom TRIO)

	Time-resolved MRA	High-resolution MRA
Repetition time (ms)	2.16	3.07
Echo time (ms)	0.95	1.28
Flip angle	16°	19°
Bandwidth (Hz/pixel)	1090	790
Field of view (mm^2)	390×340	390×305
Matrix size	384×260	576×432
Pixel size (mm^3)	1.3×1.0×3.0	0.7×0.9×0.8
Parallel imaging	GRAPPA, R=3	GRAPPA, R=4
Partial Fourier	6/8 (phase-enc. direction)	6/8 (phase-enc. direction)
Acquisition time	2 s/3D data set, total 20 s	21 s
Slice thickness (mm)	3.0	0.8
Contrast	6 ml at 3 ml/s	25 ml at 1.2 ml/s
k-space trajectories	Cartesian	Cartesian

References

Al-Kwifi O, Emery DJ, Wilman AH (2002) Vessel contrast at three Tesla in time-of-flight magnetic resonance angiography of the intracranial and carotid arteries. Magn Reson Imaging 20:181–187

Anderson CM, Lee RE, Levin DL, de la Torre Alonso S, Saloner D (1994) Measurement of internal carotid artery stenosis from source MR angiograms. Radiology 193:219–226

Anzalone N, Scomazzoni F, Castellano R et al (2005) Carotid artery stenosis: intraindividual correlations of 3D time-of-flight MR angiography, contrast-enhanced MR angiography, conventional DSA, and rotational angiography for detection and grading. Radiology 236:204–213

Barer D (1998) Endarterectomy for recently symptomatic carotid stenosis. Lancet 352:143–144

Beerbaum P, Korperich H, Gieseke J et al (2003) Rapid left-to-right shunt quantification in children by phase-contrast magnetic resonance imaging combined with sensitivity encoding (SENSE). Circulation 108:1355–1361

Bernstein MA, Huston J, 3rd, Lin C, Gibbs GF, Felmlee JP (2001) High-resolution intracranial and cervical MRA at 3.0 T: technical considerations and initial experience. Magn Reson Med 46:955–962

Bodurka J, Ledden PJ, van Gelderen P et al (2004) Scalable multichannel MRI data acquisition system. Magn Reson Med 51:165–171

Bucek RA, Reiter M, Koppensteiner I et al (2002) B-flow evaluation of carotid arterial stenosis: initial experience. Radiology 225:295–299

Butz B, Dorenbeck U, Borisch I et al (2004) High-resolution contrast-enhanced magnetic resonance angiography of the carotid arteries using fluoroscopic monitoring of contrast

arrival: diagnostic accuracy and interobserver variability. Acta Radiol 45:164–170
Campeau NG, Huston J, 3rd, Bernstein MA, Lin C, Gibbs GF (2001) Magnetic resonance angiography at 3.0 Tesla: initial clinical experience. Top Magn Reson Imaging 12:183–204
Cosottini M, Pingitore A, Michelassi MC et al (2005) Redistribution of cerebropetal blood flow in patients with carotid artery stenosis measured non-invasively with fast cine phase contrast MR angiography. Eur Radiol 15:34–40
de Zwart JA, Ledden PJ, van Gelderen P et al (2004) Signal-to-noise ratio and parallel imaging performance of a 16-channel receive-only brain coil array at 3.0 Tesla. Magn Reson Med 51:22–26
Fellner C, Lang W, Janka R et al (2005) Magnetic resonance angiography of the carotid arteries using three different techniques: accuracy compared with intraarterial x-ray angiography and endarterectomy specimens. J Magn Reson Imaging 21:424–431
Gibbs GF, Huston J, 3rd, Bernstein MA, Riederer SJ, Brown RD Jr (2004) Improved image quality of intracranial aneurysms: 3.0-T versus 1.5-T time-of-flight MR angiography. AJNR Am J Neuroradiol 25:84–87
Golay X, Brown SJ, Itoh R, Melhem ER (2001) Time-resolved contrast-enhanced carotid MR angiography using sensitivity encoding (SENSE). AJNR Am J Neuroradiol 22:1615–1619
Gonschior P, Pragst I, Valassis G, Vogel-Wiens C, Huber A (2001) High-resolution MR angiography: results in diseased arteries. J Invasive Cardiol 13:151-157; discussion 158–170
Goyen M, Debatin JF (2003) Gadobenate dimeglumine (MultiHance) for magnetic resonance angiography: review of the literature. Eur Radiol 13 Suppl 3:N19–27
Goyen M, Lauenstein TC, Herborn CU et al (2001) 0.5 M Gd chelate (Magnevist) versus 1.0 M Gd chelate (Gadovist): dose-independent effect on image quality of pelvic three-dimensional MR-angiography. J Magn Reson Imaging 14:602–607
Griswold MA, Jakob PM, Heidemann RM et al (2002) Generalized autocalibrating partially parallel acquisitions (GRAPPA). Magn Reson Med 47:1202–1210
Heyman SN, Rosen S (2003) Dye-induced nephropathy. Semin Nephrol 23:477–485
Hofmann LV, Liddell RP, Arepally A et al (2003) In vivo intravascular MR imaging: transvenous technique for arterial wall imaging. J Vasc Interv Radiol 14:1317–1327
Hoogeveen RM, Bakker CJ, Viergever MA (1998) Limits to the accuracy of vessel diameter measurement in MR angiography. J Magn Reson Imaging 8:1228–1235
Hu HH, Madhuranthakam AJ, Kruger DG, Huston J, 3rd, Riederer SJ (2004) Improved venous suppression and spatial resolution with SENSE in elliptical centric 3D contrast-enhanced MR angiography. Magn Reson Med 52:761–765
Huston J, 3rd, Fain SB, Riederer SJ et al (1999) Carotid arteries: maximizing arterial to venous contrast in fluoroscopically triggered contrast-enhanced MR angiography with elliptic centric view ordering. Radiology 211:265–273
King SB DG, Peterson D, Varosi S, Molyneaux DA. (2001) A comparison of 1, 4, and 8 channel phased array head coils at 1.5 T. 9th Annual Meeting of ISMRM, Glasgow, Scotland
Klisch J, Strecker R, Hennig J, Schumacher M (2000) Time-resolved projection MRA: clinical application in intracranial vascular malformations. Neuroradiology 42:104–107
Korosec FR, Frayne R, Grist TM, Mistretta CA (1996) Time-resolved contrast-enhanced 3D MR angiography. Magn Reson Med 36:345–351
Kramer H, Schoenberg SO, Nikolaou K et al (2005) Cardiovascular screening with parallel imaging techniques and a whole-body MR imager. Radiology 236:300–310
Lenhart M, Framme N, Volk M et al (2002) Time-resolved contrast-enhanced magnetic resonance angiography of the carotid arteries: diagnostic accuracy and inter-observer variability compared with selective catheter angiography. Invest Radiol 37:535–541
Mathiesen EB, Joakimsen O, Bonaa KH (2000) Intersonographer reproducibility and intermethod variability of ultrasound measurements of carotid artery stenosis: The Tromso Study. Cerebrovasc Dis 10:207–213
Michaely HJ, Herrmann KA, Kramer H et al (2004) The significance of MR angiography for the diagnosis of carotid stenoses. Radiologe 44:975–984
Michaely HJ, Nael K, Schoenberg SO et al (2005a) High spatial resolution magnetic resonance angiography of the renal arteries at 3.0 Tesla - Feasibility. Rofo in press
Michaely HJ, Schoenberg SO, Oesingmann N et al (2005b) Functional assessment of renal artery stenosis using dynamic MR perfusion measurements - feasibility. Radiology in press
Mikkonen RH, Kreula JM, Virkkunen PJ (1996) Reproducibility of Doppler ultrasound measurements. Acta Radiol 37:545–550
Mistretta CA, Grist TM, Korosec FR et al (1998) 3D time-resolved contrast-enhanced MR DSA: advantages and tradeoffs. Magn Reson Med 40:571–581
Naganawa S, Koshikawa T, Fukatsu H et al (2001) Contrast-enhanced MR angiography of the carotid artery using 3D time-resolved imaging of contrast kinetics: comparison with real-time fluoroscopic triggered 3D-elliptical centric view ordering. Radiat Med 19:185–192
NASCET (1991) Clinical alert: benefit of carotid endarterectomy for patients with high-grade stenosis of the internal carotid artery. National Institute of Neurological Disorders and Stroke Stroke and Trauma Division. North American Symptomatic Carotid Endarterectomy Trial (NASCET) investigators. Stroke 22:816–817
Nederkoorn PJ, Elgersma OE, Mali WP et al (2002) Overestimation of carotid artery stenosis with magnetic resonance angiography compared with digital subtraction angiography. J Vasc Surg 36:806–813
Nederkoorn PJ, van der Graaf Y, Eikelboom BC et al (2002) Time-of-flight MR angiography of carotid artery stenosis: does a flow void represent severe stenosis? AJNR Am J Neuroradiol 23:1779–1784
Nederkoorn PJ, van der Graaf Y, Hunink MG (2003) Duplex ultrasound and magnetic resonance angiography compared with digital subtraction angiography in carotid artery stenosis: a systematic review. Stroke 34:1324–1332
Niendorf HP, Haustein J, Cornelius I, Alhassan A, Clauss W (1991) Safety of gadolinium-DTPA: extended clinical experience. Magn Reson Med 22:222-228; discussion 229–232
Patel MR, Kuntz KM, Klufas RA et al (1995) Preoperative assessment of the carotid bifurcation. Can magnetic resonance angiography and duplex ultrasonography replace contrast arteriography? Stroke 26:1753–1758
Prince MR (1994) Gadolinium-enhanced MR aortography. Radiology 191:155–164

Prince MR, Schoenberg SO, Ward JS et al (1997) Hemodynamically significant atherosclerotic renal artery stenosis: MR angiographic features. Radiology 205:128–136

Pruessmann KP, Weiger M, Scheidegger MB, Boesiger P (1999) SENSE: sensitivity encoding for fast MRI. Magn Reson Med 42:952–962

Reeder SB, Wintersperger BJ, Dietrich O et al (2005) Practical approaches to the evaluation of signal-to-noise ratio performance with parallel imaging: Application with cardiac imaging and a 32-channel cardiac coil. Magn Reson Med

Riederer SJ, Bernstein MA, Breen JF et al (2000) Three-dimensional contrast-enhanced MR angiography with real-time fluoroscopic triggering: design specifications and technical reliability in 330 patient studies. Radiology 215:584–593

Saloner D (1998) Determinants of image appearance in contrast-enhanced magnetic resonance angiography. A review. Invest Radiol 33:488–495

Slovut DP, Olin JW (2004) Fibromuscular dysplasia. N Engl J Med 350:1862–1871

Staikov IN, Arnold M, Mattle HP et al (2000) Comparison of the ECST, CC, and NASCET grading methods and ultrasound for assessing carotid stenosis. European Carotid Surgery Trial. North American Symptomatic Carotid Endarterectomy Trial. J Neurol 247:681–686

Summers PE, Kollias SS, Valavanis A (2004) Resolution improvement in thick-slab magnetic resonance digital subtraction angiography using SENSE at 3T. J Magn Reson Imaging 20:662–673

Thulborn KR (1999) Clinical rationale for very-high-field (3.0 Tesla) functional magnetic resonance imaging. Top Magn Reson Imaging 10:37–50

Troyer A, Saloner D, Pan XM, Velez P, Rapp JH (2002) Major carotid plaque surface irregularities correlate with neurologic symptoms. J Vasc Surg 35:741–747

Tsao J, Boesiger P, Pruessmann KP (2003) k-t BLAST and k-t SENSE: dynamic MRI with high frame rate exploiting spatiotemporal correlations. Magn Reson Med 50:1031–1042

U-King-Im JM, Hollingworth W, Trivedi RA et al (2004) Contrast-enhanced MR angiography vs intra-arterial digital subtraction angiography for carotid imaging: activity-based cost analysis. Eur Radiol 14:730–735

U-King-Im JM, Trivedi RA, Cross JJ et al (2004) Measuring carotid stenosis on contrast-enhanced magnetic resonance angiography: diagnostic performance and reproducibility of 3 different methods. Stroke 35:2083–2088

U-King-Im JM, Trivedi RA, Graves MJ et al (2004) Contrast-enhanced MR angiography for carotid disease: diagnostic and potential clinical impact. Neurology 62:1282–1290

U-King-Im JM, Trivedi RA, Sala E et al (2004) Evaluation of carotid stenosis with axial high-resolution black-blood MR imaging. Eur Radiol 14:1154–1161

van Everdingen KJ, Klijn CJ, Kappelle LJ, Mali WP, van der Grond J (1997) MRA flow quantification in patients with a symptomatic internal carotid artery occlusion. The Dutch EC-IC Bypass Study Group. Stroke 28:1595–1600

Wardlaw JM, Lewis SC, Humphrey P et al (2001) How does the degree of carotid stenosis affect the accuracy and inter-observer variability of magnetic resonance angiography? J Neurol Neurosurg Psychiatry 71:155–160

Warmuth C, Ruping M, Forschler A et al (2005) Dynamic spin labeling angiography in extracranial carotid artery stenosis. AJNR Am J Neuroradiol 26:1035–1043

Waugh JR, Sacharias N (1992) Arteriographic complications in the DSA era. Radiology 182:243–246

Wedeen VJ, Meuli RA, Edelman RR et al (1985) Projective imaging of pulsatile flow with magnetic resonance. Science 230:946–948

Westenberg JJ, van der Geest RJ, Wasser MN et al (2000) Vessel diameter measurements in gadolinium contrast-enhanced three-dimensional MRA of peripheral arteries. Magn Reson Imaging 18:13–22

Wikstrom J, Johansson L, Karacagil S, Ahlstrom H (2003) The importance of adjusting for differences in proximal and distal contrast bolus arrival times in contrast-enhanced iliac artery magnetic resonance angiography. Eur Radiol 13:957–963

Willig DS, Turski PA, Frayne R et al (1998) Contrast-enhanced 3D MR DSA of the carotid artery bifurcation: preliminary study of comparison with unenhanced 2D and 3D time-of-flight MR angiography. Radiology 208:447–451

Willinek WA, Born M, Simon B et al (2003) Time-of-flight MR angiography: comparison of 3.0-T imaging and 1.5-T imaging – initial experience. Radiology 229:913–920

Willinek WA, Gieseke J, von Falkenhausen M et al (2004) Sensitivity encoding (SENSE) for high spatial resolution time-of-flight MR angiography of the intracranial arteries at 3.0 T. Rofo 176:21–26

Willinsky RA, Taylor SM, TerBrugge K et al (2003) Neurologic complications of cerebral angiography: prospective analysis of 2,899 procedures and review of the literature. Radiology 227:522–528

Yu B, Mang Pan X, Saloner D, Troyer A, Rapp JH (2003) Double-lumen carotid plaque: a morbid configuration. J Vasc Surg 37:1314–1317

MRA of the Pulmonary Circulation

28

Kambiz Nael and J. Paul Finn

CONTENTS

28.1 Introduction

Computed-tomography angiography (CTA) is widely regarded as the technique of choice for non-invasive workup of acute and chronic pulmonary vascular disease. The success of CTA in the thorax is due in part to the high spatial resolution of CT, and advances in multi-slice technology have dramatically increased the speed and simplicity of CTA. However, lack of exposure to ionizing radiation and using a safe, non-nephrotoxic contrast agent, in addition to its capability of multiplanar imaging over a large field of view, make 3D contrast-enhanced MR angiography (CE-MRA) a compelling alternative diagnostic modality for workup of pulmonary circulation.

K. Nael, MD; J. P. Finn, MD
David Geffen School of Medicine, UCLA Radiol Sci, BOX 957206, 3371, VUB, Los Angeles, CA 90095-7206, USA

Over the past decade thanks to numerous advances in pulse sequences and scanner hardware and software, the image quality and reliability of 3D CE-MRA has gained wide acceptance, moving from the experimental field into clinical practice. This chapter describes existing state-of-the-art 3D CE-MRA techniques for the assessment of the pulmonary circulation. Developing tools that are likely to enhance the future impact of pulmonary CE-MRA are highlighted. Finally, current clinical experience and clinical applications of CE-MRA in the pulmonary vasculature are summarized.

28.2 CE-MRA Techniques

CE-MRA relies on the T1-shortening effect of paramagnetic contrast agents in the vascular bed during the image acquisition (Prince et al. 1993) and is typically performed using a T1-weighted fast spoiled 3D gradient-recalled-echo (GRE) pulse sequence.

Recent advances in hardware and software technology have played an important role in the evolution of CE-MRA in terms of temporal and spatial resolution. With the newest generation of MR gradients, including a slew rate of up to 200 mT/m/ms and gradient strengths up to 45 mT/m, a 3D GRE sequence with TR of about 2 ms and TE of about 1 ms is now achievable, allowing the acquisition of an entire high-resolution 3D data set in less than 20 s breath-hold. Refinements such as asymmetrical echo and different k-space sampling schemes have also improved the performance of CE-MRA.

Controlled contrast administration is an essential component of CE-MRA. To ensure image quality, it is well recognized that the low-spatial-frequency k-space data, which are principally responsible for image contrast, should be aligned with the peak vascular enhancement during a gadolinium-enhanced

3D MRA (Earls et al. 1996; Kreitner et al. 2001). Reliable timing can be achieved by use of a test bolus scan prior to the administration of the full contrast-media volume. Alternatively, some workers use real-time bolus monitoring, with or without centric k-space reordering (Foo et al. 1997; Ho and Foo 1998). Both approaches can be used successfully, and the choice of which to use depends on user preference and, to some extent, vendor platform.

Besides the conventional way of performing CE-MRA, integration of ultrafast MR techniques can now generate temporally resolved 3D MRA, which depict the transit of the paramagnetic contrast agent through the vascular system (Finn et al. 2002; Korosec et al. 1996). This allows a real-time visualization of the first pass of a contrast bolus that previously has been a unique feature of conventional X-ray angiography.

Ultra-short TR sequences, in combination with sparse k-space sampling, can result in acquisition of 3D data sets in time frames ranging from a few seconds to a fraction of a second (Finn et al. 2002). Higher frame rates can be achieved by reducing the size of k-space, which is regularly updated. Specific examples using this approach include "keyhole" imaging (van Vaals et al. 1993) and other "data sharing" techniques such as time-resolved imaging of contrast kinetics (TRICKS) (Korosec et al. 1996), or time-resolved echo-shared angiographic technique (TREAT) (Fink et al. 2005); cf. Chaps. 7 and 11. The advantage to these approaches is that the major contribution to image contrast lies in the data, which are updated frequently, and interpolating the high-spatial-frequency data yields full 3D k-space datasets, i.e., high spatial resolution. A general limitation of time-resolved MRA techniques is that the spatial resolution of the individual 3D data set is limited when compared to single-phase MRA acquisitions and, with data sharing, only the low-spatial-frequency data have the prescribed temporal resolution. This latter limitation can be addressed by applying parallel-imaging techniques, using arrays of surface coils and receiver channels to reduce the number of phase-encoding steps to be measured (De Zwart et al. 2004; King et al. 2001; Bodurka et al. 2004; Hayes and Roemer 1990), improving both temporal and spatial resolution (Fink et al. 2003). It seems likely that imaging at higher magnetic fields, such as 3 T, may be helpful in overcoming the signal-to-noise-ratio (SNR) limitations accompanying fast imaging techniques (Nael et al. 2006a).

28.3 Recent Advances

Parallel imaging (Sodickson et al. 2000; Weiger et al. 2000; Pruessmann et al. 1999; Griswold et al. 2002) represents one of the most significant recent advances in MR imaging and offers improved performance over a range of MRA applications. Traditionally, spatial encoding with MRI has been accomplished by the use of imaging gradients and spatially selective RF pulses. With parallel imaging, component coil signals in an RF coil array are used to partially encode spatial information by substituting for phase-encoding gradient steps that have been omitted. Therefore, only a fraction of k-space, defined by the acceleration factor, is sampled, and then the whole dataset is reconstructed afterward. In theory, the acquisition can be accelerated by a factor equal to the number of coil elements in the array (Sodickson et al. 1997). However, in practice SNR represents a fundamental challenge and is increasingly limiting as acceleration advances. As the acceleration factor increases, the noise is also amplified. Independently, decreased acquisition time leads to deterioration of image SNR.

The major strategies to counteract the SNR deterioration of parallel-imaging techniques are employing higher magnetic fields, minimizing noise amplification through improvement and adjustment in array coil geometry and sensitivity, or use of a contrast agent with greater T1 relaxation (Weiger et al. 2001; de Zwart et al. 2002). To offset acquisition- and reconstruction-related SNR losses associated with parallel imaging, practical parallel imaging should include the use of many-element arrays and an MR system with a large number of receiver channels. The suitability of the coil array geometry for certain protocol parameters such as slab dimension and orientation can be quantified by the so-called g-factor (Pruessmann et al. 1999) (cf. Chap. 3), and generally improves with the number of coil elements used. Coils with an improved (closer to 1) g-factor allow parallel imaging with higher acceleration rates while minimizing noise amplification. As a result, appropriately designed array coils with better sensitivity profiles and more channels will improve the overall SNR, the efficiency of parallel imaging and result in higher spatial resolution (De Zwart et al. 2004; King et al. 2001; Hayes and Roemer 1990).

Today, surface-coil arrays with up to 32 channels and MR systems with up to 32 independent wide-

band receiver channels have become available commercially (Hardy et al. 2004; Zhu et al. 2004). The introduction of multi-element RF receiver coils and the associated multi-channel RF receiver electronics, combined with more effective implementation of parallel imaging, has introduced "multi-channel parallel data acquisition" as the latest addition to the fast-imaging toolbox. Increasing the number of receiver channels and/or phased-array coil elements can potentially improve the SNR and provide larger fields of view, with good temporal and spatial resolution (Fig. 28.1). This offers the promise of highly accelerated imaging.

Three-Tesla whole-body MR systems are also now commercially available. The promise of higher SNR in comparison to 1.5 T (Willinek et al. 2003; Campeau et al. 2001) can be used to reduce acquisition time, improve spatial resolution, or a combination of both (Campeau et al. 2001; Robitaille et al. 2000; Thulborn 1999). Implementation of fast-imaging tools such as time-resolved MRA sequences and parallel acquisition at 3.0 T provides new options for more efficient use of fast image acquisition (Fig. 28.2). Also, since the longitudinal relaxation time, T1, of unenhanced blood increases with field strength, sensitivity to injected gadolinium agents for CE-MRA is heightened, adding the advantage of using less contrast material. The SNR advantage at 3 T is especially noticeable for MRA applications.

There is growing evidence that high-magnetic-field CE-MRA may substantially enhance the performance of CE-MRA in clinical applications. At our institution, we use CE-MRA at 3 T for evaluation of multiple vascular territories, including the pulmonary (Nael et al. 2005a; Nael et al. 2005b; Nael et al. 2006), the carotid (Nael et al. 2006a), abdominal (Michaely et al. 2005) and lower extremity (Nael et al. 2006a) circulations. Based on very satisfactory results, we have incorporated 3-T CE-MRA into our routine clinical practice.

28.4 The Role of Pulmonary CE-MRA in Clinical Applications

As CTA continues to be widely regarded as the technique of choice for the workup of acute and chronic pulmonary vascular disease, there will remain a subset of patients who, due to renal impairment,

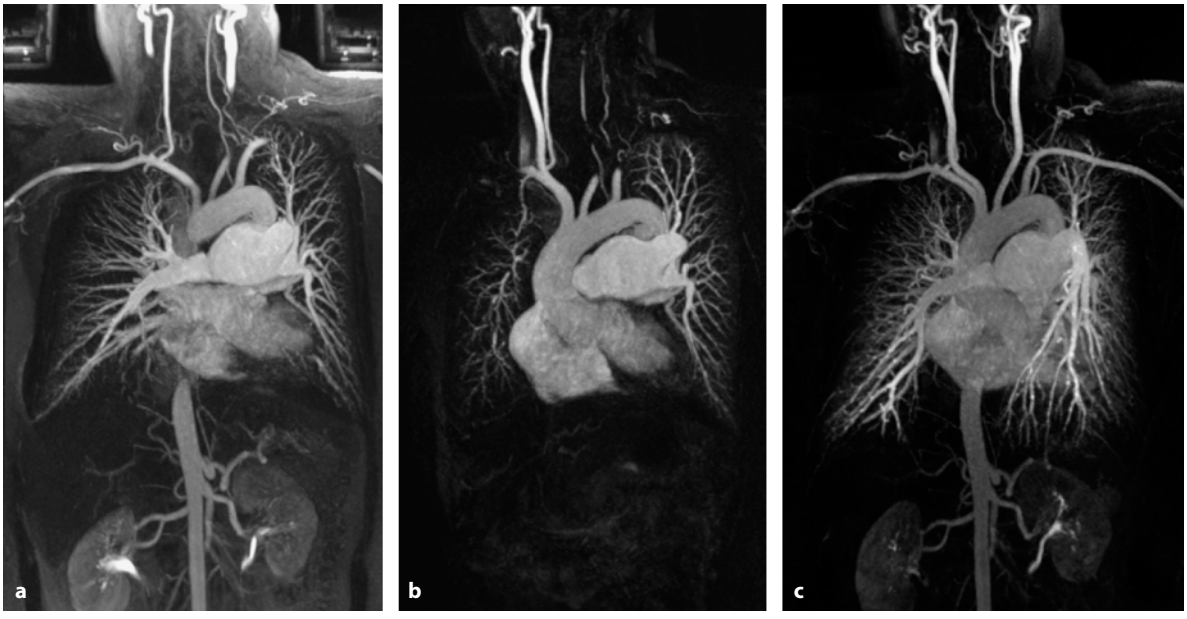

Fig. 28.1a–c. Coronal **a** and sagittal-oblique **b** thin MIP and coronal-oblique full-thickness MIPs **c** from a high-spatial-resolution CE-MRA in a subject with severe pulmonary stenosis, show post-stenotic dilatation of the left pulmonary artery. The data was acquired on a 32-channel 1.5-T MR scanner, using 26 phased-array coil elements. By integration of parallel acquisition (GRAPPA algorithm, acceleration factor R=2), the entire 3D data set was acquired in a 19-s breath-hold with voxel dimension of 1×1×1 mm^3, over a 500-mm field of view

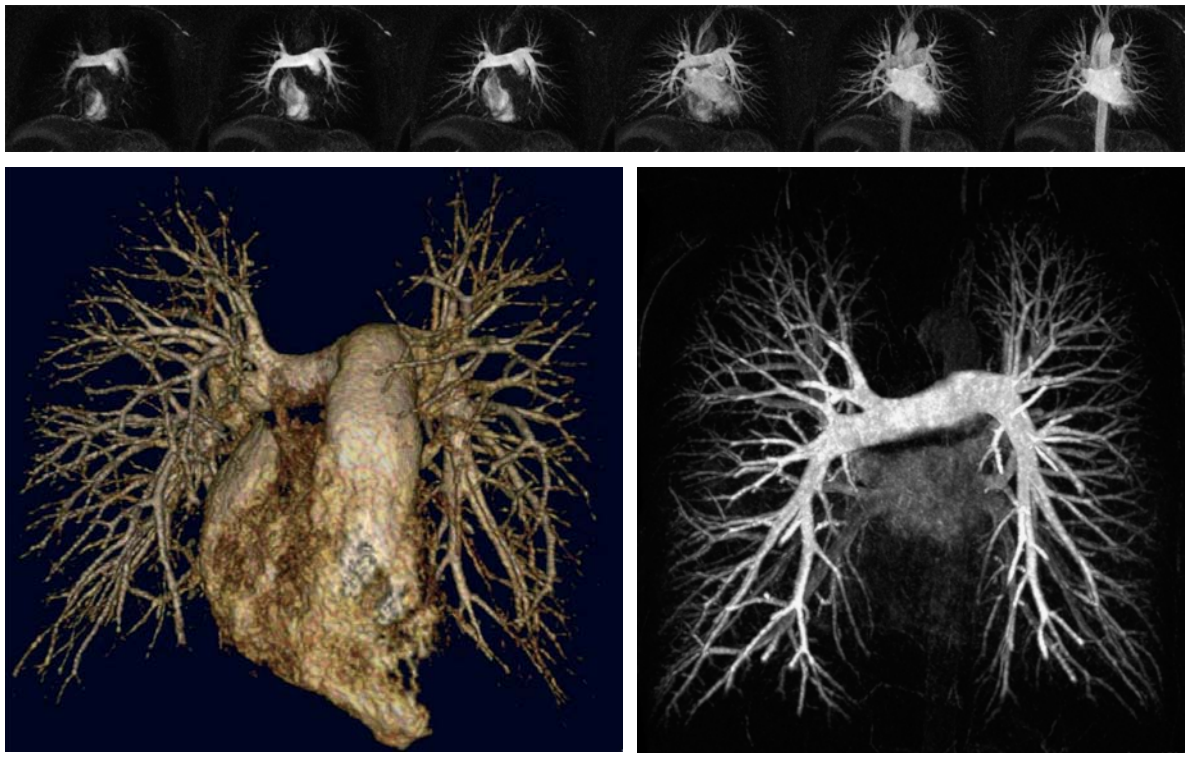

Fig. 28.2a–c. Coronal MIP series from time-resolved MRA **a** shows sequential filling of the pulmonary and systemic vasculatures. By using a four-segmented echo-shared sequence and aggressive parallel acquisition (GRAPPA, *R*=4) at 3.0 T a high-temporal (1 s) and high-spatial-resolution (1×1.2×3 mm^3) 3D time-resolved MRA was obtained. Coronal volume-rendered **b** and full-thickness MIPs **c** from high-spatial-resolution CE-MRA show the pulmonary arterial tree with extreme details up to the fifth order branches. By implementing aggressive parallel acquisition (GRAPPA, *R*=4) and use of a 32-channel body array coil at 3 T, the entire 3D data set was acquired during an 18-s breath-hold and with voxel dimension of 0.7×0.7×0.8 mm^3

contrast-media sensitivity, or radiation burden, are not good candidates for CTA. There is, therefore, a role for magnetic resonance angiography (MRA) in the lungs. MR imaging of the pulmonary vasculature has been challenging for a variety of reasons, including respiratory motion and susceptibility artefacts at air-tissue interfaces.

With current hardware, MRA can now resolve up to fifth-order pulmonary branches in a single short breath hold (Nael et al. 2005a). Time-resolved MRA is helpful for lung imaging and can reveal the dynamic information in vascular beds with rapid circulation such as the pulmonary vasculature (Finn et al. 2002; Goyen et al. 2001; Hatabu et al. 1999; Nicolaou et al. 2004). Time-resolved MRA can provide insight into cardiopulmonary hemodynamics (Figs. 28.3 and 28.4). Enhancement of lung parenchyma and filling patterns in arterivenous fistulae, shunts, and congenital heart anomalies may be best appreciated by highly temporally resolved imaging.

28.4.1 Pulmonary Embolism

There are several studies that have described the use of pulmonary MRA for pulmonary embolism (PE) with high sensitivity and specificity in large lobar and segmental vessels (Meaney et al. 1997; Steiner et al. 1997; van Beek et al. 2003; Gupta et al. 1999). The sensitivity decreased for emboli in the subsegmental vessels (Gupta et al. 1999; Meaney et al. 1999). Dynamic MRA may provide supplemental functional and perfusion information, which can help in the diagnosis of pulmonary embolism (Fink et al. 2004; Kluge et al. 2004) (Fig. 28.5a,b).

Currently, the role of MRA in PE is mostly for follow-up of stable patients and chronic pulmonary embolism. Another advantage of MRA over alternative diagnostic strategies for work-up of patients with suspected PE relates to the fact that it can be complemented by MR venography of the pelvic and femoral

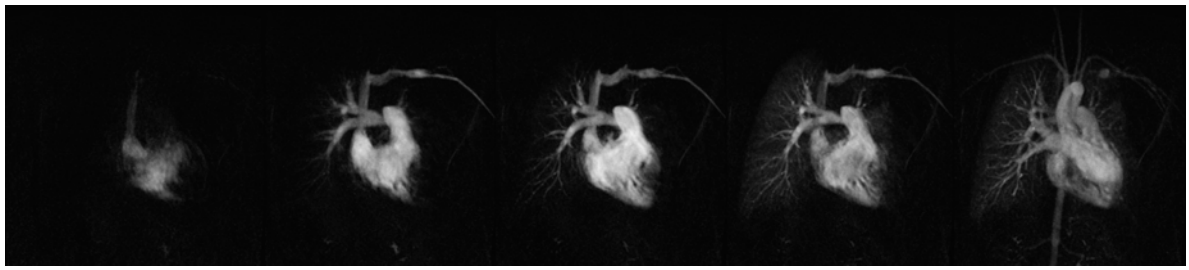

a

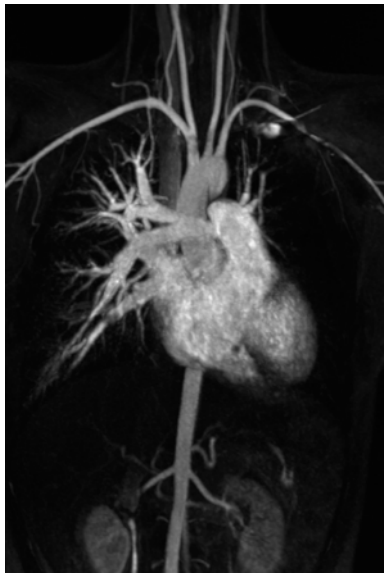

b

Fig. 28.3a,b. Coronal MIPs from time-resolved MRA **a** (GRAPPA, *R*=2, temporal resolution 1.5 s) and coronal MIP image from high-spatial-resolution CE-MRA **b** (voxel dimension of 1×1×1.5 mm^3 over a 500-mm field of view in a 19-s breath-hold, using GRAPPA with an acceleration factor of *R*=2 at 1.5 T) show stenotic and hypoplastic left pulmonary artery. In the perfusion phase of the time-resolved MRA, note the delayed enhancement of left parenchyma and decreased perfusion, indicating the significance of the left pulmonary artery stenosis

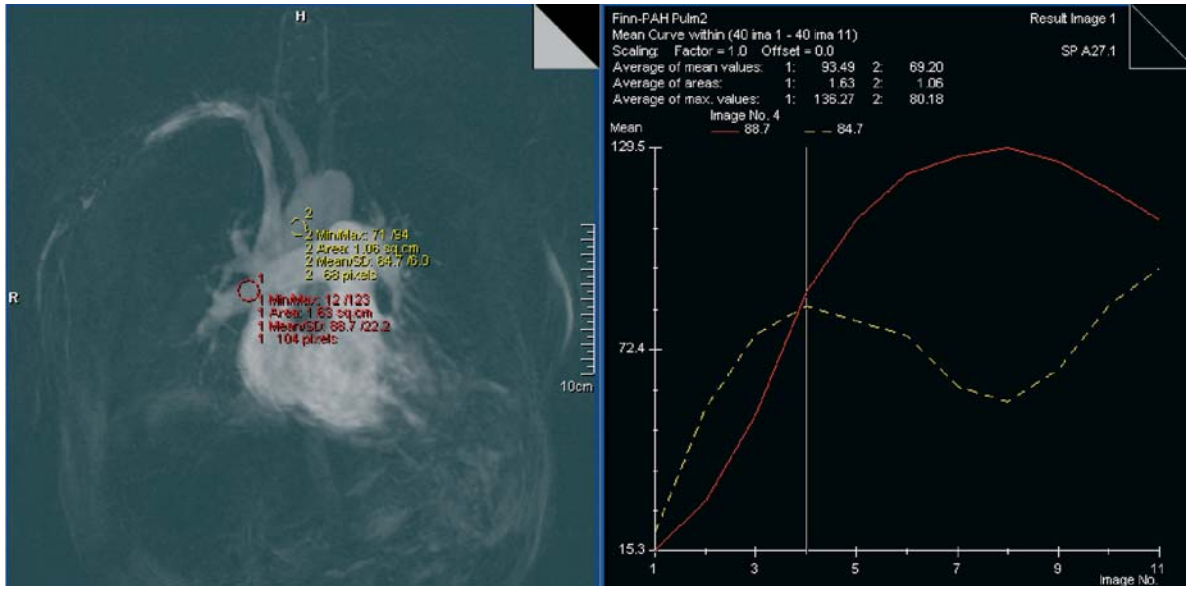

Fig. 28.4. Evaluation of the signal intensity versus time from a time-resolved MRA shows early enhancement of the aorta (*yellow line*) before the peak enhancement of the pulmonary artery (*red line*). This indicates the presence of a right-to-left shunt and Eisenmenger pathophysiology in this subject with severe pulmonary hypertension and right-sided heart failure

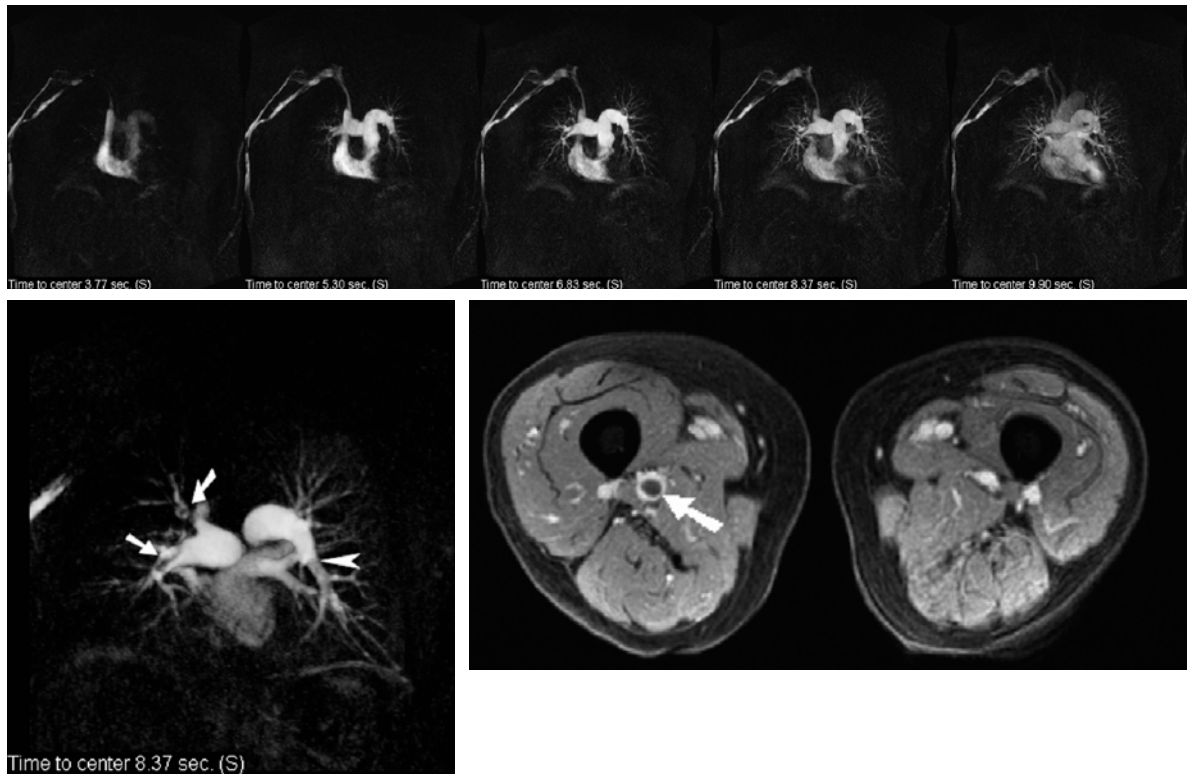

Fig. 28.5a–c. Coronal MIP images **a** and coronal thin-MIP from the arterial phase **b** of a time-resolved MRA show the sequential filling of pulmonary arteries and parenchymal enhancement. Several regions of filling defects in right and left pulmonary arteries (*arrows*) indicate the presence of extensive thrombo-embolism. The decreased parenchymal enhancement in the right upper and lower lobe indicates the perfusion defect as a result of pulmonary embolism. The 3D data sets were acquired with in-plane resolution of 1.5×1.2 mm^2 and temporal resolution of 1.5 s, using GRAPPA with an acceleration factor of R=2 at 1.5 T. Axial T1-weighted fat-saturated image of the thighs **c** shows presence of extensive thrombosis in the right femoral vein

veins (Fig. 28.5c). The signs of chronic pulmonary embolism on MRA include vascular webs and bands, wall thickening, distal arterial tapering and multiple distal perfusion defects (Ley et al. 2003).

Although pulmonary MRA may still not be practical in acutely ill patients with severe shortness of breath, its role is likely to increase as advanced techniques make their way into routine clinical practice.

28.4.2 Pulmonary Arterial Hypertension

Pulmonary arterial hypertension (PAH) is diagnosed when pulmonary arterial pressure is greater than 30 mmHg by cardiac catheterization and can be either primary or secondary to congenital heart disease, chronic lung disease, or chronic thromboembolism.

CE-MRA is a very useful non-invasive test to identify PAH, where a decrease in the number of segmental or subsegmental pulmonary arteries and abnormal tapering of segmental vessels (pruning) are characteristic findings (Ley et al. 2003; Laffon et al. 2001; Kreitner et al. 2004; Nikolaou et al. 2005) (Fig. 28.6). Time-resolved MRA permits direct visualization of shunts and concomitant velocity-encoded cine MRI and phase-contrast MRA can provide valuable information regarding cardiac function and chamber size, as well as quantitative measurements of blood velocity and flow in the pulmonary arteries (Hoeper et al. 2001; Saba et al. 2002); cf. Chap. 43.

28.4.3 Complex Congenital Heart Disease

Since most congenital heart abnormalities tend to present early in life, CE-MRA is gaining interest as a non-invasive diagnostic measure for both primary diagnosis and follow-up imaging. Congenital-heart-

disease patients are patients for life and require continuous follow-up into adult life. In many ways, MRI is the clear front runner for evaluation of patients with congenital heart disease. Complex cardiac and vascular anatomy can be depicted by cine MRI and 3D CE-MRA, and the ability to rotate the 3D data is a very useful feature (Fig. 28.7). Congenital vascular shunts can be intracardiac, such as atrial or ventricular septal defects, or extra-cardiac, such as patent ductus arteriosus, aorto-pulmonary window or intra-pulmonary shunt. Time-resolved MRA can be extremely useful in detecting shunts and in characterizing their flow direction. The postoperative follow-up of congenital heart disease is a powerful and exciting application for pulmonary CE-MRA (Fig. 28.8); cf. Chap. 31.

Cardiac cine and velocity-encoded cine imaging can provide additional diagnostic information about cardiac function, flow and velocity quantification across the cardiac valves and shunt fraction in a single non-invasive examination session.

28.4.4 Tumors

Pulmonary CE-MRA may play an important role as a part of pre-surgical evaluation for mediastinal or

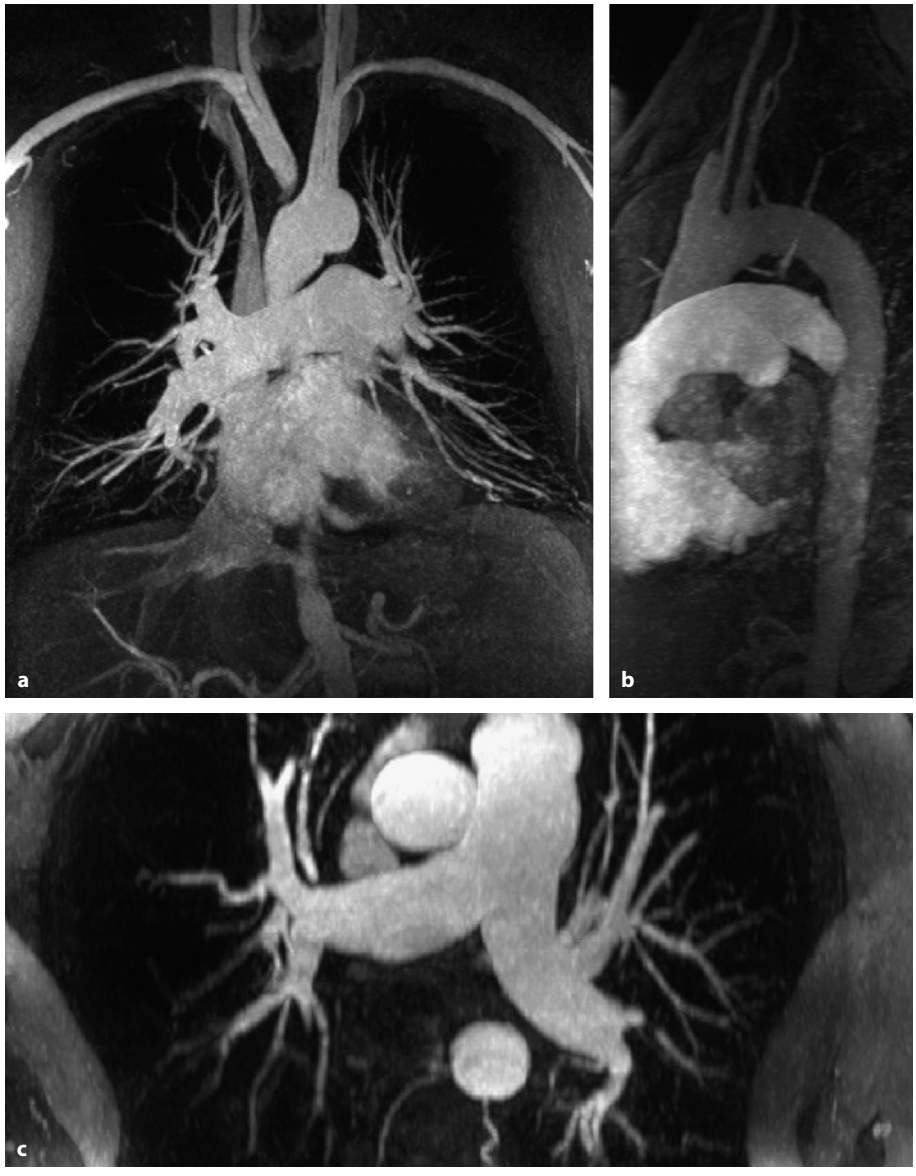

Fig. 28.6a–c. Coronal **a**, sagittal **b** and axial **c** thin-MIP (20 mm) image **a** of CE-MRA at 3 T shows significant dilatation of central pulmonary arteries and abnormal proximal-to-distal tapering (pruning) of the pulmonary arteries in a subject with pulmonary arterial hypertension. The 3D data set was acquired during an 18-s breath-hold with a voxel dimension of 0.7×0.9×1 mm^3, using GRAPPA with an acceleration factor of R=3 at 3 T

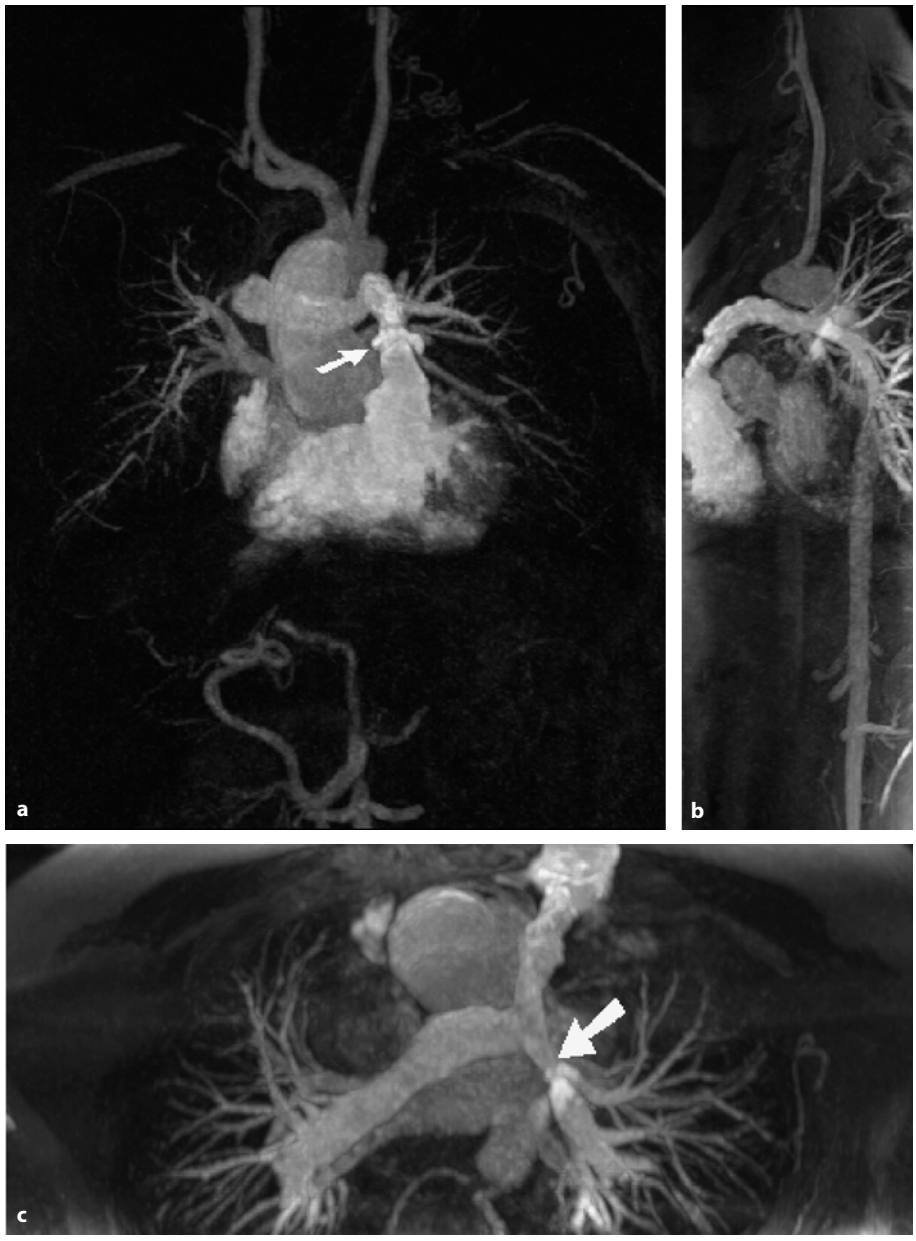

Fig. 28.7a–c Coronal **a**, sagittal **b** and axial **c** thin-MIP images from a high-spatial-resolution CE-MRA in a 21-year-old subject with repair of tetralogy of Fallot, revealing a pulmonary-artery conduit with valve (**a**, *arrow*), coursing from the right ventricular outflow tract to the main pulmonary trunk. The conduit shows narrowing after the valve toward the left main pulmonary artery (**c**, *arrow*). (voxel dimension of 1×1×1.5 mm^3, over a 500-mm field of view in 19-s breath-hold, using GRAPPA with R=2 at 1.5 T)

lung tumors (Kauczor et al. 1992). Acquisition of the second or thrid run should be performed as a major complication of thoracic tumors is the obstruction of thoracic central veins due to the compressive effect or secondary infiltration. The combination of CE-MRA and a T1-weighted pre- and post-contrast imaging for assessment of the tumor in coronal and axial planes is extremely useful in visualizing tumor extension, involvement of the vasculature and evaluation of surrounding soft tissue, and can be used for presurgical planning.

28.4.5 Venography

Typically, there are two superior and two inferior pulmonary veins. Altered development of the pulmonary venous system typically results from persistent communication with the systemic system, manifesting as anomalous pulmonary venous drainage (Fig. 28.9a). These abnormalities can be either complete or partial and are often associated with intracardiac congenital heart diseases such as a sinus-venosus-type atrial

septal defect (Fig. 28.9b). Several studies have shown the feasibility and accuracy of 3D CE-MRA in the depiction of anomalous pulmonary venous return and the location of drainage (Prasad et al. 2004).

Pulmonary venous mapping is another indication for pulmonary venography. In patients with atrial fibrillation, RF ablation has emerged as a treatment of choice in many patients with curative potential. CE-MRA has been shown as a powerful tool for pulmonary venous mapping in preparation for catheter-guided RF ablation therapy of ectopic arrhythmogenic foci in these patients (Fig. 28.10). CE-MRA can be used as an accurate diagnostic tool to define pulmonary venous anatomy, improve pre-procedural planning and decrease fluoroscopic procedural time as well as post-procedural follow-up (Tsao and Chen 2002; Collins et al. 2002).

28.5 Conclusion

In the appropriate patient population, all relevant disease entities of the pulmonary vasculature can be evaluated using 3D CE-MRA, sometimes more comprehensively than with any other single modality. The addition of time-resolved MRA is appropriate for assessing high-flow vascular lesions, shunts and congenital heart anomalies. Parallel imaging and multi-element coil technology can further improve the performance of 3D CE-MRA in order to achieve higher temporal and spatial resolution and the role of 3-T imaging remains to be fully defined.

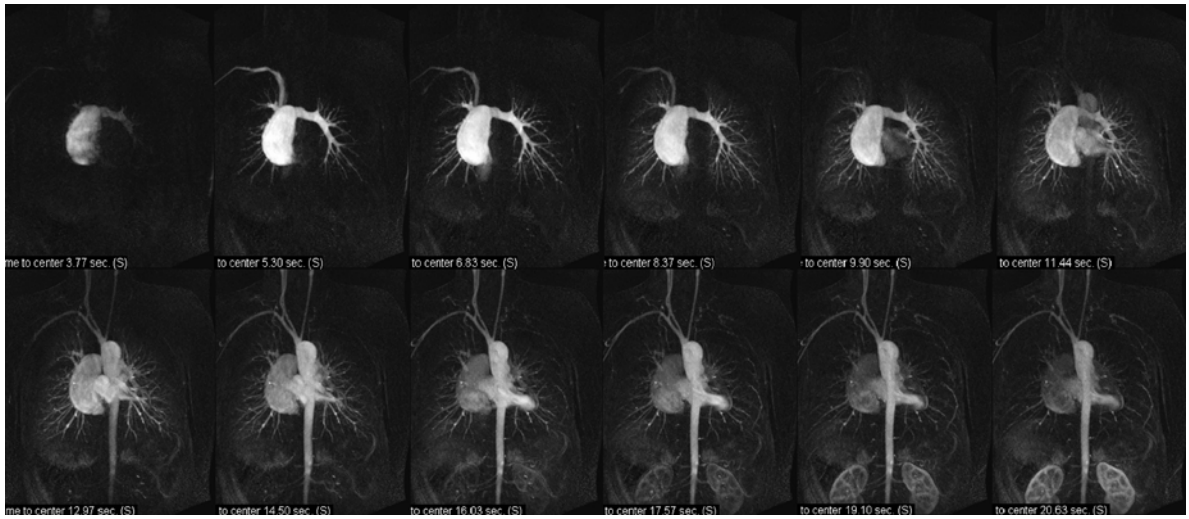

a

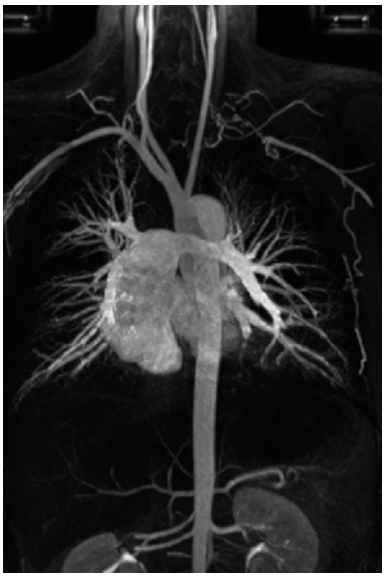

b

Fig. 28.8a,b. Coronal MIP from a time-resolved MRA **a** (in-plane resolution 1.6×1.3 mm^2, temporal resolution 1.2 s, GRAPPA, R=2) and coronal full-thickness MIP from high-spatial-resolution CE-MRA **b** (1×1×1.5 mm^3 voxels, over a 500-mm field of view in 20-s breath-hold, using GRAPPA with R=2 at 1.5 T) in a 21-year-old subject with single ventricle and transposition of great arteries (*TGA*), repaired with Fontan operation. Fontan shunt is widely patent, providing the pulmonary artery flow and perfusing both lungs symmetrically. There is no evidence of right-to-left or left-to-right shunting. The proximal part of the left subclavian artery is occluded, as a result of a previous Blalock-Tausig shunt

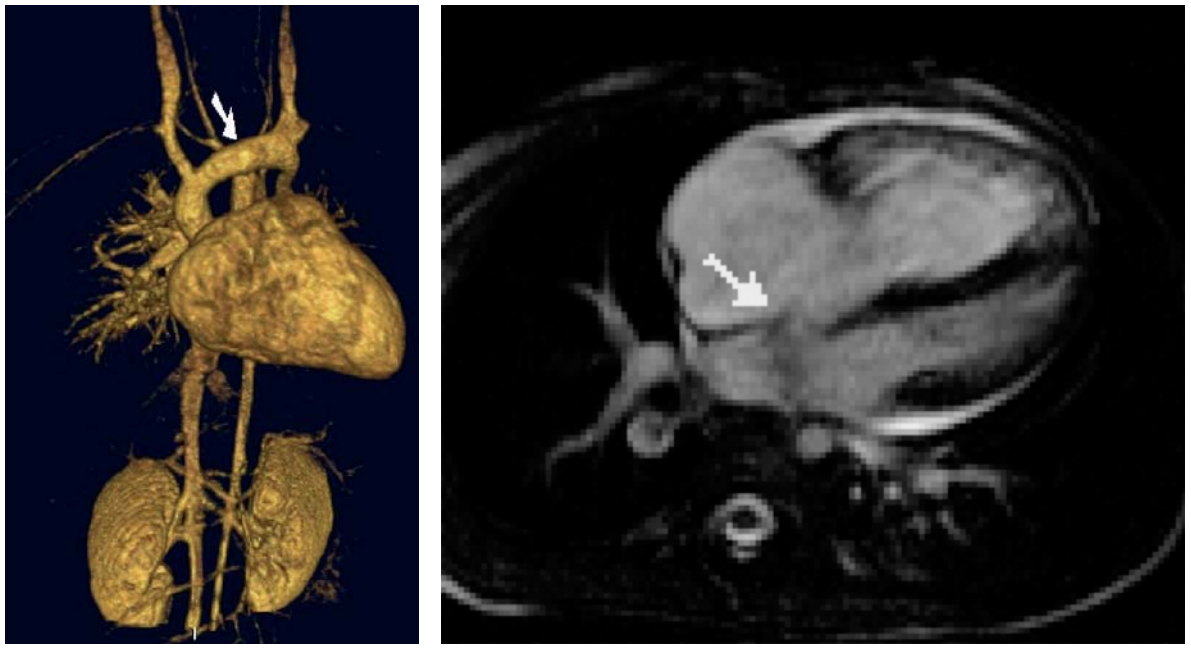

Fig. 28.9a,b. Coronal volume-rendered image **a** from a high-spatial-resolution CE-MRA (voxel dimension of 1×1×1 mm^3, over a 450-mm field of view in 18-s breath-hold, using GRAPPA with *R*=2 at 1.5 T) showing partial anomalous pulmonary venous return with a prominent left vertical vein (*arrow*), draining into the left brachiocephalic vein. Four-chamber-view cardiac SSFP cine MRI **b** shows the presence of sinus-venosus-type ASD, as a common association with this anomaly

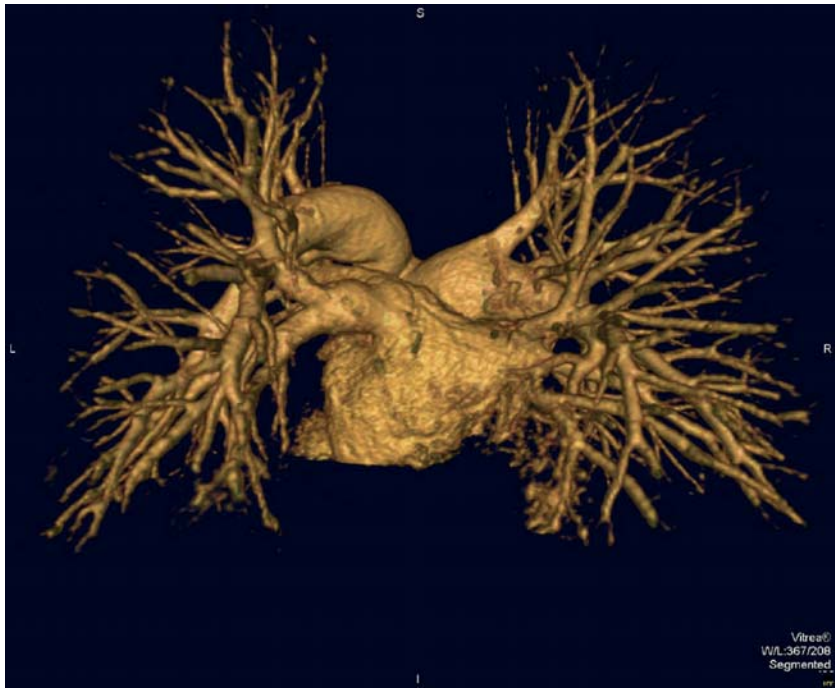

Fig. 28.10. 3D volume-rendered image from a CE-MRA defines pulmonary venous anatomy, which can improve pre-procedural planning and decrease fluoroscopic procedural time during the ablation treatment of ectopic arrhythmogenic foci in patients with atrial fibrillation. By implementing fast parallel imaging (GRAPPA, *R*=3) at 3 T, the entire 3D data set was acquired during an 18-s breath-hold with voxel dimension of 0.8×0.8×1 mm^3

References

Balci NC, Yalcin Y, Tunaci A, Balci Y (2003) Assessment of the anomalous pulmonary circulation by dynamic contrast-enhanced MR angiography in under 4 seconds. Magn Reson Imaging 21:1–7

Bodurka J, Ledden PJ, van Gelderen P, et al (2004) Scalable multichannel MRI data acquisition system. Magn Reson Med 51:165–171

Campeau NG, Huston J, 3rd, Bernstein MA, Lin C, Gibbs GF (2001) Magnetic resonance angiography at 3.0 Tesla: initial clinical experience. Top Magn Reson Imaging 12:183–204

Collins JD PF, Song GK, Bello D, Betts D, Finn JP (2002) Preablative pulmonary venous mapping by high-resolution MR angiography facilitates electrophysiologic pulmonary vein ablation and reduces fuoroscopic time in patients with paroxysmal atrial fbrillation [abstract]. In: Presented at the North American Society for Cardiac Imaging 30th Annual Meeting and Scientifc Session in conjunction with the Third International Workshop on Coronary MR and CT Angiography, Dallas, TX

de Zwart JA, Ledden PJ, Kellman P, van Gelderen P, Duyn JH (2002) Design of a SENSE-optimized high-sensitivity MRI receive coil for brain imaging. Magn Reson Med 47:1218–1227

de Zwart JA, Ledden PJ, van Gelderen P, Bodurka J, Chu R, Duyn JH (2004) Signal-to-noise ratio and parallel imaging performance of a 16-channel receive-only brain coil array at 3.0 Tesla. Magn Reson Med 51:22–26

Earls JP, Rofsky NM, DeCorato DR, Krinsky GA, Weinreb JC (1996) Breath-hold single-dose gadolinium-enhanced three-dimensional MR aortography: usefulness of a timing examination and MR power injector. Radiology 201:705–710

Fink C, Bock M, Puderbach M, Schmahl A, Delorme S (2003) Partially parallel three-dimensional magnetic resonance imaging for the assessment of lung perfusion--initial results. Invest Radiol 38:482–488

Fink C, Ley S, Kroeker R, Requardt M, Kauczor HU, Bock M (2005) Time-resolved contrast-enhanced three-dimensional magnetic resonance angiography of the chest: combination of parallel imaging with view sharing (TREAT). Invest Radiol 40:40–48

Fink C, Risse F, Buhmann R et al (2004) Quantitative analysis of pulmonary perfusion using time-resolved parallel 3D MRI - initial results. Rofo Fortschr Geb Rontgenstr Neuen Bildgeb Verfahr 176:170–174

Finn JP, Baskaran V, Carr JC, et al (2002) Thorax: low-dose contrast-enhanced three-dimensional MR angiography with subsecond temporal resolution--initial results. Radiology 224:896–904

Foo TK, Saranathan M, Prince MR, Chenevert TL (1997) Automated detection of bolus arrival and initiation of data acquisition in fast, three-dimensional, gadolinium-enhanced MR angiography. Radiology 203:275–280

Goyen M, Laub G, Ladd ME et al (2001) Dynamic 3D MR angiography of the pulmonary arteries in under 4 s. J Magn Reson Imaging 13:372–377

Griswold MA, Jakob PM, Heidemann RM et al (2002) Generalized autocalibrating partially parallel acquisitions (GRAPPA). Magn Reson Med 47:1202–1210

Gupta A, Frazer CK, Ferguson JM et al (1999) Acute pulmonary embolism: diagnosis with MR angiography. Radiology 210:353–359

Hardy CJ, Darrow RD, Saranathan M et al (2004)Large field-of-view real-time MRI with a 32-channel system. Magn Reson Med 52:878–884

Hatabu H, Tadamura E, Levin DL et al (1999) Quantitative assessment of pulmonary perfusion with dynamic contrast-enhanced MRI. Magn Reson Med 42:1033–1038

Hayes CE, Roemer PB (1990) Noise correlations in data simultaneously acquired from multiple surface coil arrays. Magn Reson Med 16:181–191

Ho VB, Foo TK (1998) Optimization of gadolinium-enhanced magnetic resonance angiography using an automated bolus-detection algorithm (MR SmartPrep). Original investigation. Invest Radiol 33:515–523

Hoeper MM, Tongers J, Leppert A, Baus S, Maier R, Lotz J (2001) Evaluation of right ventricular performance with a right ventricular ejection fraction thermodilution catheter and MRI in patients with pulmonary hypertension. Chest 120:502–507

Kauczor HU, Gamroth AH, Tuengerthal SJ et al (1992) [MR angiography. Its use in pulmonary and mediastinal space-occupying lesions]. Rofo 157:15–20

King SB DG, Peterson D, Varosi S, Molyneaux DA (2001) A comparison of 1, 4, and 8 channel phased array head coils at 1.5 T. In: 9th Annual Meeting of ISMRM, Glasgow, Scotland, p 1090

Kluge A, Dill T, Ekinci O et al (2004) Decreased pulmonary perfusion in pulmonary vein stenosis after radiofrequency ablation: assessment with dynamic magnetic resonance perfusion imaging. Chest 126:428–437

Korosec FR, Frayne R, Grist TM, Mistretta CA (1996) Time-resolved contrast-enhanced 3D MR angiography. Magn Reson Med 36:345–351

Kreitner KF, Kunz RP, Kalden P, et al (2001) Contrast-enhanced three-dimensional MR angiography of the thoracic aorta: experiences after 118 examinations with a standard dose contrast administration and different injection protocols. Eur Radiol 11:1355–1363

Kreitner KF, Ley S, Kauczor HU et al (2004) Chronic thromboembolic pulmonary hypertension: pre- and postoperative assessment with breath-hold MR imaging techniques. Radiology 232:535–543

Laffon E, Laurent F, Bernard V, De Boucaud L, Ducassou D, Marthan R (2001) Noninvasive assessment of pulmonary arterial hypertension by MR phase-mapping method. J Appl Physiol 90:2197–2202

Ley S, Kauczor HU, Heussel CP et al (2003) Value of contrast-enhanced MR angiography and helical CT angiography in chronic thromboembolic pulmonary hypertension. Eur Radiol 13:2365–2371

Meaney JF, Ridgway JP, Chakraverty S et al (1999) Stepping-table gadolinium-enhanced digital subtraction MR angiography of the aorta and lower extremity arteries: preliminary experience. Radiology 211:59–67

Meaney JF, Weg JG, Chenevert TL, Stafford-Johnson D, Hamilton BH, Prince MR (1997) Diagnosis of pulmonary embolism with magnetic resonance angiography. N Engl J Med 336:1422–1427

Michaely HJ, Nael K, Schoenberg SO et al (2005) The feasibility of spatial high-resolution magnetic resonance

angiography (MRA) of the renal arteries at 3.0 T. Rofo 177:800–804
Nael K GS, Saleh R, Lee M, Ruehm S Laub G, Finn JP (2006c) Lower extremity MRA with extended field of view: using a 32 channel MR scanner. J Cardiovasc Magn Reson 8:55–56
Nael K KU, Lee M, Goldin J, Laub G, Finn JP (2005a) High spatial resolution contrast-enhanced MRA (CEMRA) of the pulmonary circulation at 3.0 Tesla: Initial results. In: Proceeding of 91st Scientific Assembly & Annual Meeting, RSNA, Chicago, p 242
Nael K MH, Lee M, Krammer U, Goldin J, Oesingmann N, Laub G, Finn JP (2000b) Time-resolved pulmonary MR angiography and perfusion imaging at 3.0 T: Initial results with echo-sharing and parallel acquisition. In: Proceeding of the 13th annual ISMRM meeting, Miami Beach, Florida, p 2777
Nael K SR, Michaely HJ, Goldin J, Lee M, Laub G, Finn JP (2006b) Contrast-enhanced MRA at 3.0 T for evaluation of the pulmonary arterial hypertension. J Cardiovasc Magn Reson 8:57–58
Nael K, Michaely HJ, Villablanca P, Salamon N, Laub G, Finn JP (2006a) Time-resolved contrast enhanced magnetic resonance angiography of the head and neck at 3.0 Tesla: Initial results. Invest Radiol 41:116–124
Nikolaou K, Schoenberg SO, Attenberger U et al (2005) Pulmonary arterial hypertension: diagnosis with fast perfusion MR imaging and high-spatial-resolution MR angiography – preliminary experience. Radiology 236:694–703
Nikolaou K, Schoenberg SO, Brix G et al (2004) Quantification of pulmonary blood flow and volume in healthy volunteers by dynamic contrast-enhanced magnetic resonance imaging using a parallel imaging technique. Invest Radiol 39:537–545
Prasad SK, Soukias N, Hornung T et al (2004) Role of magnetic resonance angiography in the diagnosis of major aortopulmonary collateral arteries and partial anomalous pulmonary venous drainage. Circulation 109:207–214
Prince MR, Yucel EK, Kaufman JA, Harrison DC, Geller SC (1993) Dynamic gadolinium-enhanced three-dimensional abdominal MR arteriography. J Magn Reson Imaging 3:877–881
Pruessmann KP, Weiger M, Scheidegger MB, Boesiger P (1999) SENSE: sensitivity encoding for fast MRI. Magn Reson Med 42:952–962
Puvaneswary M, Leitch J, Chard RB (2003) MRI of partial anomalous pulmonary venous return (scimitar syndrome). Australas Radiol 47:92–93
Robitaille PM, Abduljalil AM, Kangarlu A (2000) Ultra high resolution imaging of the human head at 8 Tesla: 2K×2K for Y2K. J Comput Assist Tomogr 24:2–8
Saba TS, Foster J, Cockburn M, Cowan M, Peacock AJ (2002) Ventricular mass index using magnetic resonance imaging accurately estimates pulmonary artery pressure. Eur Respir J 20:1519–1524
Sodickson DK, Manning WJ (1997) Simultaneous acquisition of spatial harmonics (SMASH): fast imaging with radiofrequency coil arrays. Magn Reson Med 38:591–603
Sodickson DK, McKenzie CA, Li W, Wolff S, Manning WJ, Edelman RR (2000) Contrast-enhanced 3D MR angiography with simultaneous acquisition of spatial harmonics: A pilot study. Radiology 217:284–289
Steiner P, McKinnon GC, Romanowski B, Goehde SC, Hany T, Debatin JF (1997) Contrast-enhanced, ultrafast 3D pulmonary MR angiography in a single breath-hold: initial assessment of imaging performance. J Magn Reson Imaging 7:177–182
Thulborn KR (1999) Clinical rationale for very-high-field (3.0 Tesla) functional magnetic resonance imaging. Top Magn Reson Imaging 10:37–50
Tsao HM, Chen SA (2002) Evaluation of pulmonary vein stenosis after catheter ablation of atrial fibrillation. Card Electrophysiol Rev 6:397–400
van Beek EJ, Wild JM, Fink C, Moody AR, Kauczor HU, Oudkerk M (2003) MRI for the diagnosis of pulmonary embolism. J Magn Reson Imaging 18:627–640
van Vaals JJ, Brummer ME, Dixon WT, et al (1993) "Keyhole" method for accelerating imaging of contrast agent uptake. J Magn Reson Imaging 3:671–675
Weiger M, Pruessmann KP, Kassner A et al (2000) Contrast-enhanced 3D MRA using SENSE. J Magn Reson Imaging 12:671–677
Weiger M, Pruessmann KP, Leussler C, Roschmann P, Boesiger P (2001) Specific coil design for SENSE: a six-element cardiac array. Magn Reson Med 45:495–504
Willinek WA, Born M, Simon B et al (2003) Time-of-flight MR angiography: comparison of 3.0-T imaging and 1.5-T imaging--initial experience. Radiology 229:913–920
Zhu Y, Hardy CJ, Sodickson DK et al (2004) Highly parallel volumetric imaging with a 32-element RF coil array. Magn Reson Med 52:869–877

MRA of the Renal Arteries

29

Stefan O. Schoenberg and Johannes Rieger

CONTENTS

29.1 Controversies in Grading of Renal-Artery Stenosis

Due to the lack of ionizing radiation, nephrotoxic contrast agents and invasiveness, 3D contrast-enhanced magnetic-resonance angiography (3D-CE-MRA) has become the technique of choice for angiographic imaging of the renal arteries (Vasbinder et al. 2001). These advantages are further enhanced by the possible addition of a range of functional techniques for assessment of the hemodynamic significance of renal artery stenosis, staging of parenchymal disease and functional evaluation of the urinary outflow tract (Michaely et al. 2006a, 2006b; Schoenberg et al. 2006). These techniques, including ECG-gated flow measurements in the renal artery, time-resolved contrast-enhanced perfusion measurements and dynamic MR urography, can be easily combined with 3D-CE-MRA, thereby offering a comprehensive morphologic and functional evaluation of the renal vascular system within a single magnetic-resonance imaging exam. Two recent large meta-analyses have clearly demonstrated the superior accuracy of 3D-CE-MRA compared to all other imaging techniques of the renal artery for grading of renal artery stenosis, including data of publications from almost 1 decade (Vasbinder et al. 2001; Tan et al. 2002). Therefore, 3D-CE-MRA is currently considered the technique of choice for most referring clinicians to detect and grade renal artery stenosis.

One large Dutch multi-center trial (the RADISH study), however, recently reported completely contradictory results in terms of the accuracy of both MRI and computed-tomography angiography (CTA) for grading of renal artery stenosis, thereby questioning the established role of 3D-CE-MRA for clinical routine use (Vasbinder et al. 2004). In this study, substantially worse sensitivities and specificities were found for both MRA and CTA, ranging below 80% for the entire study population of 365 patients. The results were even worse when the results of the relatively large number of fibromuscular-dysplasia (FMD) patients were assessed alone with a sensitivity of less than 30%. However, even when only the subgroup of atherosclerotic stenoses exceeding 70% was selectively evaluated, the overall accuracy did not exceed 85%.

Although the overall results were somewhat discouraging for the use of 3D-CE-MRA, they can be explained to a large degree by several causes that have been analyzed in various studies. These underlying causes include the lack of sufficient spatial resolution, random motion of the renal arteries, eccentricity of atherosclerotic disease, evaluation of the diameter stenosis instead of the area stenosis as well as inter-

S. O. Schoenberg, MD
Department of Clinical Radiology, University Hospitals – Grosshadern, Ludwig Maximilian University of Munich, Marchioninistr. 15, 81377 Munich, Germany
J. Rieger, MD
Department of Clinical Radiology, University Hospitals – Innenstadt, Ludwig Maximilian University of Munich, Pettenkoferstr. 8a, 80336 Munich, Germany

observer variability and incomplete accuracy of the standard of reference, i.e., digital subtraction angiography. In the RADISH study, typical voxel volumes of 4 to 7 mm³ were used, and only the diameter stenosis was reported for numerical grading of the renal artery stenosis. On the other hand, a recent study has shown that isotropic voxel volumes of less than 0.8 mm³ are feasible using 3D-CE-MRA acquisition accelerated by parallel-imaging techniques (Schoenberg et al. 2005). For the first time, not only the reduction of the vessel diameter at the site of a renal artery stenosis was measured, but also the resulting decrease in vessel area in comparison to the normal renal artery downstream. This measurement of area stenosis has been well established within invasive techniques such as intravascular ultrasounds for exact grading of coronary artery stenosis (Hanekamp et al. 1999). Pathology studies have shown that atherosclerosis does not occur concentrically in the wall of the vessel, but is a non-uniform eccentric process leaving an irregularly shaped residual lumen of the remaining artery (Jeremias et al. 2000). Therefore, the only exact measure of the true reduction of vessel lumen is by cross sections perpendicular to the long axis of the vessel.

Due to its three-dimensional acquisition, 3D-CE-MRA in principle holds the potential to perform reconstructions along any desired imaging plane, thus allowing assessment of area stenosis (Fig. 29.1). However, it is well known that due to the short imaging time required to perform the entire 3D-CE-MRA scan within a single breath hold of less than 25 s, spatial resolution is usually not equal along all three scan orientations. Typically, spatial resolution is the highest in the frequency-encoding head-feet direction followed by the phase-encoding left-right direction, while the lowest resolution is acquired in the second phase-encoding (or partition-encoding) anterior-posterior direction. For coronal display of the image in maximum-intensity projection, the relatively poor resolution in partition-encoding direction is not visualized; however, it becomes immediately evident when sagittal or oblique reconstructions are performed. In this case geometric distortions from non-isotropic voxel sizes result in a decreased accuracy of the vessel-area measurements. The use of isotropic voxel sizes, as shown in one study, enables a distortion-free reconstruction of the vessel area in any desired three-dimensional orientation. Good results could be demonstrated in correlation to invasive reference measurements by intravascular ultrasounds of the renal artery (Schoenberg et al. 2005).

The assessment of area stenosis instead of diameter stenosis creates another positive effect on the reliability of renal artery stenosis grading by 3D-CE-MRA, namely the reduction of interobserver variability. A number of studies have shown that

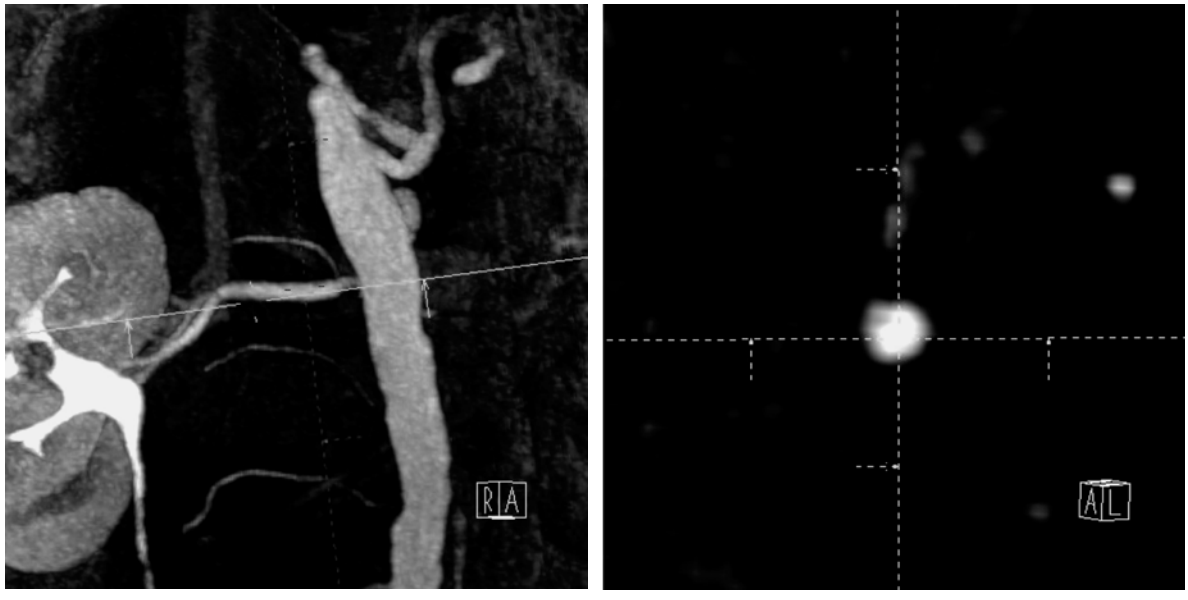

Fig. 29.1. Assessment of area stenosis on 3D-CE-MRA with isotropic sub-millimeter spatial resolution. On the coronal MIP view (*left side*) the renal artery stenosis appears to be 50–75%. On the cross-section reformats (*right side*) perpendicular to the vessel orientation at the site of the stenosis and downstream the stenosis it becomes evident that this stenosis is only of low grade with a measured lumen reduction of 30%. This was confirmed by intravascular ultrasound

interobserver variability is at least as important for a reliable grading of renal artery stenosis as the accuracy of the technique itself (Schoenberg et al. 2002; van Jaarsveld et al. 1999). Two large studies have reported kappa values (κ) as a measure of interobserver agreement of less than 0.6, which highlights the problem of the variability of results among different readers. It could be shown in one study that measurement of diameter stenosis is subject to a much higher interobserver variability than assessment of area stenosis (Schoenberg et al. 2005). This is particularly true for stenoses in the range of 30%–70%, for which a tremendous variation of the results could be shown among two observers. These variations are reduced to less than 20% when using the assessment of area stenosis.

One of the most difficult problems to solve in 3D-CE-MRA is random motion of the distal renal arteries induced by involuntary contractions of the diaphragm, which cannot be suppressed by breathing suspension or ECG gating. One study therefore concluded that the accuracy for grading of distal renal artery stenosis is inherently limited (Vasbinder et al. 2002). Since these contractions occur somewhat periodically in the order of several seconds, one possibility would be to reduce the acquisition to less than 10 s for a 3D data set and to use a time-resolved approach. This time-resolved approach has also proven in another study to be superior in terms of vessel visibility in the distal main renal artery, the anterior and posterior divisions as well as the proximal segmental intrarenal arteries due to the absence of overlaying enhancing renal parenchyma (Schoenberg et al. 1999). The down side of this approach, however, is that in current acquisitions scan times in the order of 20 s are at least required to obtain the mandatory isotropic spatial resolution of 1 mm^3 or less. One study has demonstrated the use of spiral echo-planar imaging (EPI) for accelerating the acquisitions in the *x-y* plane for time-resolved 3D-CE-MRA of the renal arteries; nevertheless, the spatial resolution could not be increased to voxel lengths of less than 1.5 mm (Amann et al. 2002).

In summary, the requirements for state-of-the-art 3D-CE-MRA of the renal arteries raise the need for a substantial acceleration of the acquisition, which ideally can be delivered by use of parallel-imaging techniques. In the following part, the application of parallel imaging is described for standard MRI systems, multi-channel MRI scanners, dedicated multi-element coils as well as at higher field strengths beyond 1.5 T.

29.2 Implementation of 3D-CE-MRA with Parallel Imaging on Standard MRI Systems

Today standard MRI systems are equipped with at least eight independent receiver channels, which allow the use of eight-element phased-array coils for abdominal imaging. Typically, parallel-imaging acceleration factors of $R=2$ have been used together with this type of coils, thereby accelerating the acquisition twofold. Initial data have been presented by a few centers using the SENSE algorithm already a few years ago (Weiger et al. 2000; Walter et al. 2003). These preliminary studies could demonstrate advantages in terms of either faster acquisitions or higher resolution within the same scan time compared to non-accelerated imaging. Shorter acquisition times resulted in a lesser number of artefacts from respiratory motion. However, none of these early studies could show a gain in diagnostic accuracy in comparison to the standard of reference: digital subtraction angiography (DSA). The overall acceptance of parallel imaging was initially limited by the presence of folding artefacts from signal of tissue outside the field of view (FOV) propagated into the center of the image, often referred to as super-aliasing. Therefore, many researchers still used non-accelerated acquisitions and spent the additional signal-to-noise on higher bandwidths, shorter repetition times, fractional echo and smaller fields of view to also accelerate acquisition unrelated to the use of parallel imaging. One study, however, showed that the GRAPPA algorithm, recently introduced into clinical applications, is substantially more robust to super-aliasing as compared to the mSENSE algorithm (Schoenberg et al. 2005; Griswold et al. 2002). Thus, smaller FOVs tailored to the dimensions of the renovascular tree could be used even without disturbing central aliasing artefacts. Therefore, the gain in acquisition speed by parallel-imaging acceleration could be fully exploited without the need for larger number of phase-encoding steps in the left-right direction for encoding of a larger FOV. The use of GRAPPA with an acceleration factor of 2 resulted in isotropic voxel lengths of 0.9 mm and a scan time of 23 s. Using multiplanar reconstructions, the largest cross-sectional diameter at the site of the stenosis was used for comparison with DSA, which resulted in a significantly improved accuracy as compared with conventional in-plane diameter measurements of renal artery stenosis. The maximum variation between 3D-CE-MRA and DSA was reduced from 40% to less than 20% (Schoenberg et al. 2005).

One drawback for the use of parallel imaging is the loss of signal-to-noise ratio (SNR), which decreases in the range of 30% for an acceleration factor of 2. This effect can be effectively counterbalanced to a certain degree by the use of contrast agents with higher relaxivities such as 1-molar agents like gadobutrol (Gadovist, Schering AG, Berlin, Germany) or weakly protein-binding contrast agents such as gadolinium-BOPTA (MultiHance, BRACCO SpA, Milan, Italy) or strongly protein-binding agents (Vasovist, Schering AG, Berlin, Germany). Both Vasovist and Gadovist are now approved for the use of 3D-CE-MRA of the renal arteries, and the approval for MultiHance is expected in the near future.

29.3 The Use of Multi-Channel MRI Scanners

The recent introduction of MRI systems with up to 32 independent receiver channels has further advanced the possibilities for parallel-imaging acceleration of 3D-CE-MRA. Usually 12 to 18 different coil elements are used for acquisition of a 3D-CE-MRA data set, thereby improving the g-factor of the coil set-up. Thus, acceleration factors of 3 can be routinely used with no visible loss of image quality despite a numerically higher noise level (Michaely et al. 2006c) (Figs. 29.2a, 29.2b and 29.3). Typically, the acquisition is accelerated in the left-right direction since the coil sensitivity profiles differ the most in this direction. Acquisition time can be reduced to 16 s for a 3D-CE-MRA scan with a spatial resolution of 1 mm³. One recent study has found better image quality for scans with a threefold acceleration compared to standard twofold acceleration in terms of vessel visibility in particular in the distal segments of the renal vascular bed (Michaely et al. 2006c). Although the calculated noise level was higher by 30%, this did not visually affect image quality. Therefore, these acquisition parameters can be currently recommended as a reliable approach to high-resolution renal MRA with relatively short acquisition times.

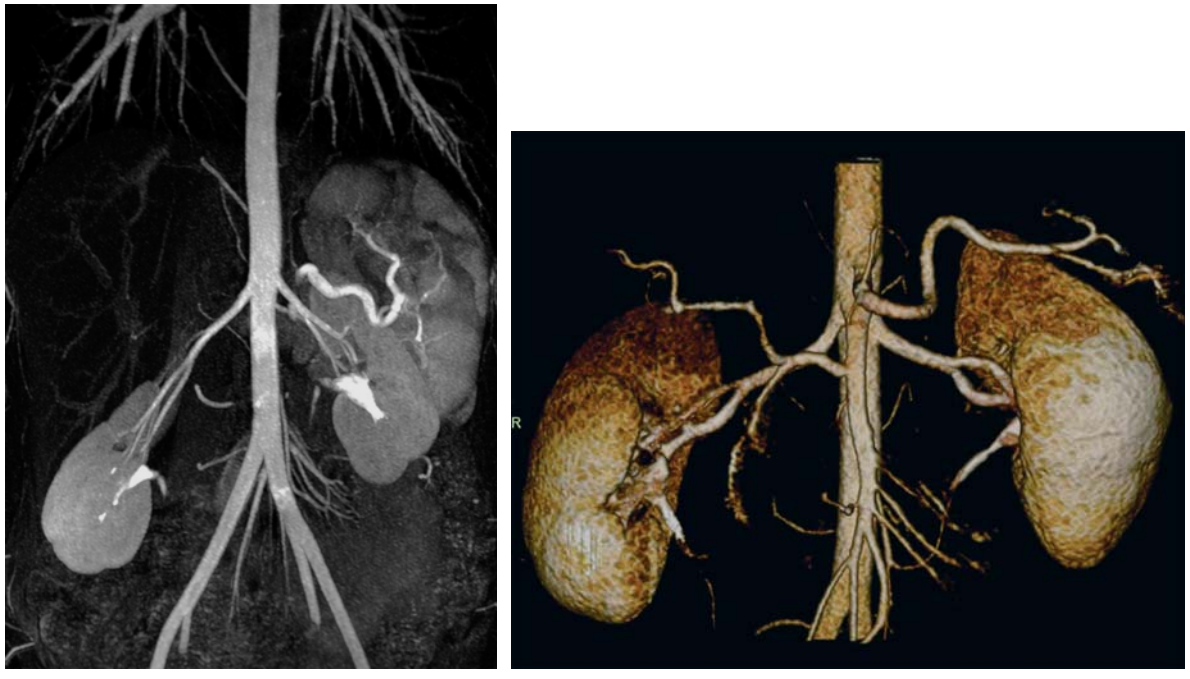

Fig. 29.2. a High-resolution renal MRA at 3 T with a spatial resolution of 0.9×0.8×0.9 mm³ acquired in just 16 s with GRAPPA and acceleration factor *R*=3 (40 reference lines, phase encoding and acceleration in left-right direction). The entire slab thickness is 72 mm. **b** High-resolution MRA at 3 T acquired with GRAPPA and acceleration factor *R*=3 (24 reference lines, phase encoding and acceleration in left-right direction) in 18 s with a spatial resolution of 0.9×0.8×0.9 mm³. In contrast to the above shown MRA, this protocol used phase oversampling and a slab thickness of 87 mm to cover a larger volume of the abdominal vessels and to increase the SNR

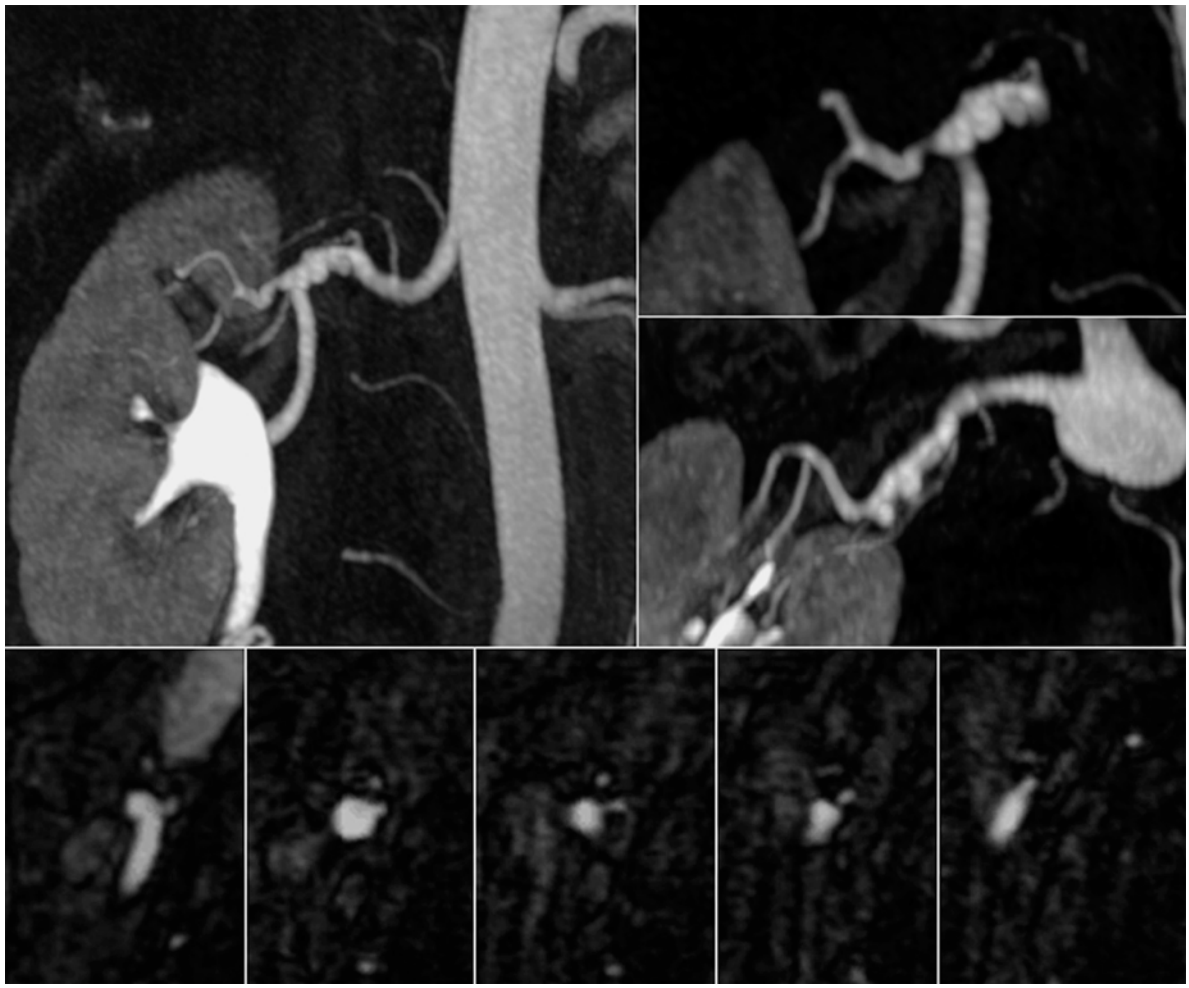

Fig. 29.3. FMD at 3 T; typical string-of-bead appearance of fibromuscular dysplasia (*FMD*) in a 72-year-old patient with moderate hypertension. The high spatial resolution (0.9×0.8×0.9 mm³) of this MRA allows a clear depiction of these characteristic changes on multiplanar reformats in the cross-sectional view (*lower row*). Courtesy of Dr. Paul Finn, UCLA

29.4 3D-CE-MRA with Parallel Imaging at 3 Tesla

Parallel-acquisition techniques reduce the signal-to-noise ratio by approximately the square root of the acceleration factor, if the g-factor is not taken into account. Since SNR increases linearly with the field strength, 3D-CE-MRA could be theoretically performed with an acceleration factor of 4 at 3 T while maintaining the same SNR as compared to 1.5 T without parallel-imaging acceleration. Thus, acceleration factors of 3 to 4 can be routinely performed with excellent image quality. One preliminary study has shown the feasibility of a high-resolution 3D-CE-MRA scan with isotropic voxel sizes of 0.9×0.9×0.9 mm³ in 16 s scan time (Michaely et al. 2005) (Fig. 29.2a). The authors could demonstrate an excellent vessel visibility up to the level of the segmental arteries with almost no artefacts from respiratory motion. The use of higher acceleration factors is thereby not limited by the signal-to-noise ratio, but by the geometry of the coils. Although 32-channel 3-T MRI systems are now available, the maximum number of different receiver coil elements in the left-right direction does not exceed 4, thus allowing a maximum of fourfold acceleration in the phase-encoding direction (Fig. 29.4). Higher acceleration factors are theoretically possible when using parallel imaging with acceleration in two dimensions, i.e., an acceleration factor of 4 in phase-encoding direction and an acceleration factor of 2 in partition-encoding (3D) direction totalling to an overall acceleration of R=8. The problem of this 2D

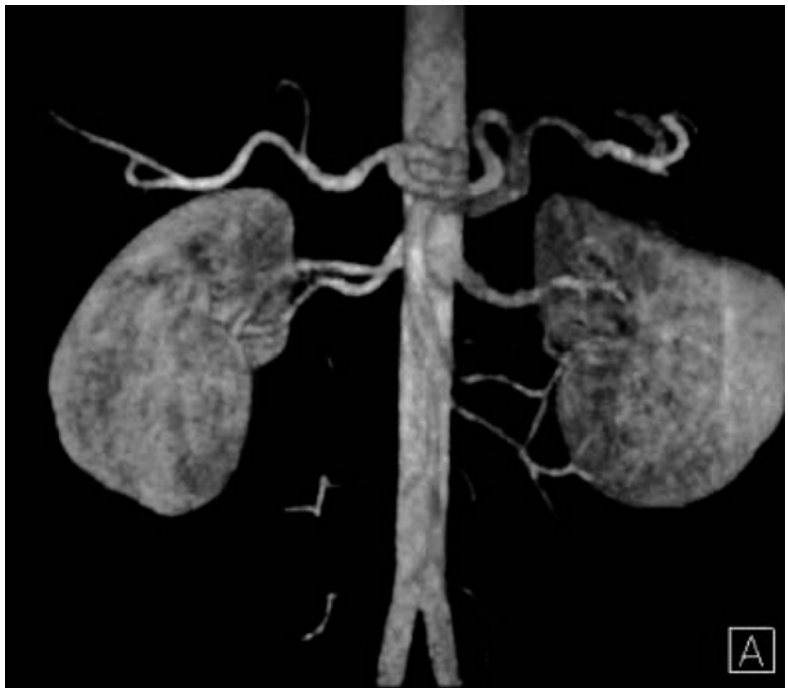

Fig. 29.4. "Prototype MRA" acquired with parallel-imaging acceleration factor R=4 (GRAPPA, phase encoding and acceleration in left-right direction) on a 32-channel 3-T system with a 32-element coil. The scan time for this sequence was 14 s with a spatial resolution of 1.0×0.8×1.0 mm³ and a 3D slab thickness of 104 mm. Even though 1.0-molar contrast agent (Gd-BOPTA) was used to compensate for the SNR penalty with parallel imaging, there is a perceivable amount of image noise. Improved reconstruction algorithms may overcome this problem in the future

parallel-imaging acceleration for coronal 3D-CE-MRA is that due to the relatively thin slab (in partition/3D direction) positioned in the core of the human body the sensitivity profiles of the different coil elements located anterior and posterior are not distinct enough to allow reliable parallel imaging in the partition-encoding direction (Fig. 29.5). Thus, the use of parallel imaging in two dimensions is still limited despite the excess of signal-to-noise ratio at 3 T. Nevertheless, other techniques already benefit from 2D parallel-imaging acceleration even at 1.5 T such as 3D steady-state-free-precession (SSFP) imaging of the small and large bowel (Herrmann et al. 2006). However, the fundamental difference of this technique is that first, the SNR is substantially higher for SSFP sequences compared to gradient-echo sequences used for 3D-CE-MRA, and second, this approach requires complete anatomic coverage of the entire anterior-posterior dimension of the human body to provide images free of aliasing. Therefore, images with three- to fourfold acceleration at 3 T using voxel lengths of 0.8 or less and acquisition times of 15 s are currently considered state of the art.

No data from systematic studies exist for the overall gain in accuracy using these highly accelerated acquisitions. However, it can be expected that the increase in acquisition speed and resolution is particularly beneficial to diseases of the renal artery with subtle irregularities of the vascular wall such as fibromuscular dysplasia (Fig. 29.3). Accurate detection of stenosis in fibromuscular dysplasia is challenging for several reasons. First, the dysplastic changes of the vessel wall with the typical string-of-beads appearance often cause multiple stenoses of varying grade. Second, the changes can appear very subtle when looking on the vessel in a coronal view, thereby underestimating the true reduction of lumen diameter. Therefore, it is very important to reconstruct the images perpendicular to the long axes of the vessel to truly see the multiple reductions of the vessel lumen and correctly identify the target site of the maximum degree of stenosis. Third, FMD typically involves the distal main artery as well as the intrarenal segments, which are not only smaller, and thus require higher spatial resolution to accurately assess stenosis changes, but also require shorter scan times to reduce the amount of overlaying enhancing renal parenchyma and random motion from diaphragmatic contractions.

29.5 Multi-Element Coils

Although 32-channel MR systems are now used in clinical routine, dedicated multi-element coils with

more than 30 elements targeted to a single field of view are not provided by the large manufacturers at this point. However, prototypes are available now from independent companies or research units that can be used together with these 32-channel MR systems, cf. Chaps. 14 and 44. One research group has already demonstrated the possibilities of massively accelerated 3D imaging with acceleration factors of up to 16 using a prototype 32-element coil (Zhu et al. 2004). In our own experience, using a dedicated 32-element flexible phased-array coil on a 32-channel 3-T MR system, acquisition time for a 3D-CE-MRA scan could be reduced to only 13 s at an isotropic spatial resolution of 1×1×1 mm³ (Fig. 29.4). Although all these results have to be considered preliminary and experimental at this point, they clearly show the way towards improvement of the accuracy of contrast-enhanced MRA particularly for the assessment of distal renal artery stenosis.

29.6 Time-Resolved 3D-CE-MRA with Parallel-Acquisition Techniques

Time-resolved 3D-CE-MRA of the renal artery has a number of theoretical advantages for the diagnostic work up of renal-artery disease. First, vascular structures with substantially different enhancement kinetics such as the true and false lumen in aortic dissections involving also the renal arteries, primary renal-artery dissection as well as renal-artery aneurysms with delayed filling can be separately visualized on the individual time frames (Schoenberg et al. 1999; Schoenberg et al. 2001) (Fig. 29.6). Second, the short acquisition times reduce the amount of overlay from enhanced renal parenchyma, thus allowing a better visualization of the intrarenal branches, which is still a limitation of current 3D-CE-MRA as compared to DSA with a high frame rate. This is also the reason that the assessment of vascular disease primarily involving the intrarenal branches is still a domain of DSA, including vasculitis such as polyarteritis nodosa. Third, involuntary motion from diaphragmatic contractions can be reduced when a high frame rate is used for the time-resolved 3D-CE-MRA acquisition.

Despite these clear advantages, time-resolved 3D-CE-MRA has not been widely used due to constraints in spatial resolution (Fig. 29.6). One study has already shown a clear advantage of multi-phase time-resolved acquisitions compared to static single-phase scans in terms of visibility of distal vessel segments (Schoenberg et al. 1999). In this study, a frame rate of 6 s per MRI scan with a reconstructed spatial resolution of 1.8×1.8×1.5 mm³ was used. Overall accuracy compared to DSA was good with sensitivities and specificities exceeding 90%; however, only a small number of distal renal artery stenosis were present while most of these stenoses were located in

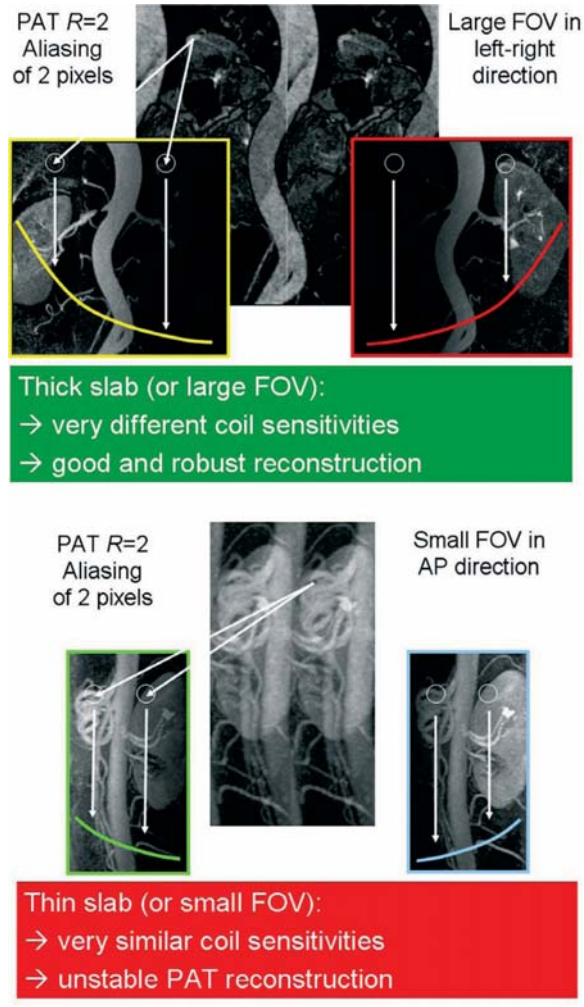

Fig. 29.5. Limitations of parallel acquisition techniques (*PAT*) for renal 3D-CE-MRA. With big volumes acquired in phase-encode direction (most often left-right direction as shown on *top*), the coil sensitivities differ enough to reconstruct the image correctly. With small volumes as in the case of parallel imaging in anterior-posterior direction in a thin slab (*bottom illustration*), the coil sensitivities are not different enough for a robust reconstruction. The results are partially aliased images with increased folding artefacts in the center

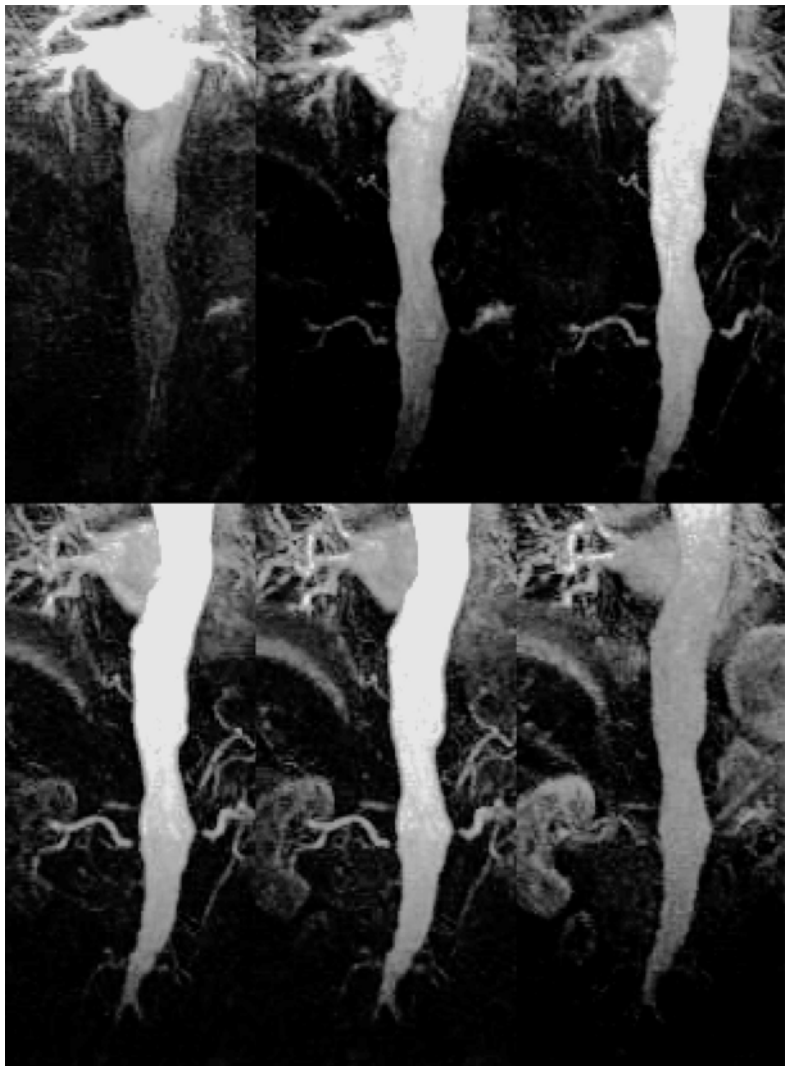

Fig. 29.6. Time-resolved renal MRA in a patient with bilateral renal artery stenoses acquired at 1.5 T. This sequence used view sharing with parallel imaging (GRAPPA, R=2) to achieve a spatial resolution of 2×2×3 mm³ with a temporal resolution of 1.9 s/3D volume. The kidneys show symmetric enhancement, the proximal stenosed part of the renal arteries cannot be seen due to the narrow lumen. This fast imaging technique allows following the course of the contrast agent bolus through the abdominal vessels

the proximal segment of the main renal artery. Due to the increasing demands in spatial and temporal resolution, this approach has not been investigated further until recently despite the number of advantages. With the introduction of a combined use of view-sharing techniques together with parallel imaging known as "time-resolved echo-shared angiographic technique" (TREAT) frame rates in the order of 1.8 s are feasible while maintaining a spatial resolution of 1.3×1.0×4.3 mm^3 (Nael et al. 2006). However, no systematic studies have been published on the overall value of this technique for assessment of renal artery stenosis. Nevertheless, a major shift of paradigm for renal 3D-CE-MRA can be expected integrating the demands for spatial and temporal resolution as well as short acquisition times.

References

Amann M, Bock M, Floemer F, Schoenberg SO, Schad LR (2002) Three-dimensional spiral MR imaging: Application to renal multiphase contrast-enhanced angiography. Magn Reson Med 48:290–296

Griswold MA, Jakob PM, Heidemann RM et al (2002) Generalized autocalibrating partially parallel acquisitions (GRAPPA). Magn Reson Med 47:1202–1210

Hanekamp CE, Koolen JJ, Pijls NH, Michels HR, Bonnier HJ (1999) Comparison of quantitative coronary angiography, intravascular ultrasound, and coronary pressure measurement to assess optimum stent deployment. Circulation 99:1015–1021

Herrmann KA, Dietrich O, Michaely HJ, Seiderer J, Reiser MF, Schoenberg SO (2006) Magnetic resonance enteroclysis of small bowel disease: value of single-breath-hold high resolution 3D TrueFISP imaging using two-dimensional parallel acquisition techniques. J Magn Reson Imaging (accepted)

Jeremias A, Huegel H, Lee DP et al (2000) Spatial orientation of atherosclerotic plaque in non-branching coronary artery segments. Atherosclerosis 152:209–215

Michaely HJ, Herrmann KA, Kramer H, Dietrich O, Reiser MF, Schoenberg SO (2006c) High-resolution renal MRA: comparison of image quality and vessel depiction with different parallel imaging acceleration factors. J Magn Reson Imaging (accepted)

Michaely HJ, Herrmann KA, Nael K, Oesingmann N, Reiser MF, Schoenberg SO (2006b) Functional renal imaging: nonvascular renal disease. Abdom Imaging , epub:Jan 30

Michaely HJ, Nael K, Schoenberg SO et al (2005) The feasibility of spatial high-resolution magnetic resonance angiography (MRA) of the renal arteries at 3.0 T. Rofo 177:800–804

Michaely HJ, Schoenberg SO, Oesingmann N et al (2006a) Renal arteary stenosis: functional assessment with dynamic MR perfusion measurements--feasibility study. Radiology 238:586–596

Nael K, Michaely HJ, Villablanca P, Salamon N, Laub G, Finn JP (2006) Time-resolved contrast enhanced magnetic resonance angiography of the head and neck at 3.0 T: initial results. Invest Radiol 41:116–124

Schoenberg SO, Bock M, Knopp MV et al (1999) Renal arteries: optimization of three-dimensional gadolinium-enhanced MR angiography with bolus-timing-independent fast multiphase acquisition in a single breath hold. Radiology 211:667–679

Schoenberg SO, Knopp MV, Londy F et al (2002) Morphologic and functional magnetic resonance imaging of renal artery stenosis: a multireader tricenter study. J Am Soc Nephrol 13:158–169

Schoenberg SO, Londy FJ, Licato P, Williams DM, Wakefield T, Chenevert TL (2001) Multiphase-multistep gadolinium-enhanced MR angiography of the abdominal aorta and runoff vessels. Invest Radiol 36:283–291

Schoenberg SO, Rieger J, Weber CH et al (2005) High-spatial-resolution MR angiography of renal arteries with integrated parallel acquisitions: comparison with digital subtraction angiography and US. Radiology 235:687–698

Schoenberg SO, Rieger JR, Michaely HJ, Rupprecht H, Samtleben W, Reiser MF (2006) Functional magnetic resonance imaging in renal artery stenosis. Abdom Imaging 31:200–212

Tan KT, van Beek EJ, Brown PW, van Delden OM, Tijssen J, Ramsay LE (2002) Magnetic resonance angiography for the diagnosis of renal artery stenosis: a meta-analysis. Clin Radiol 57:617–624

van Jaarsveld BC, Pieterman H, van Dijk LC et al (1999) Inter-observer variability in the angiographic assessment of renal artery stenosis. DRASTIC study group. Dutch Renal Artery Stenosis Intervention Cooperative. J Hypertens 17:1731–1736

Vasbinder GB, Nelemans PJ, Kessels AG et al (2004) Accuracy of computed tomographic angiography and magnetic resonance angiography for diagnosing renal artery stenosis. Ann Intern Med 141:674–682

Vasbinder GB, Nelemans PJ, Kessels AG, Kroon AA, de Leeuw PW, van Engelshoven JM (2001) Diagnostic tests for renal artery stenosis in patients suspected of having renovascular hypertension: a meta-analysis. Ann Intern Med 135:401–411

Vasbinder GBC, Maki JH, Nijenhuis RJ et al (2002) Motion of the distal renal artery during three-dimensional contrast-enhanced breath-hold MRA. J Magn Reson Imaging 16:685–696

Walter C, Philippi G, Westerhausen R, Kooijman H, Hoffmann HG, Busch HP (2003) [High resolution contrast-enhanced 3D MR-angiography of renal arteries using parallel imaging (SENSE)]. Rofo Fortschr Geb Rontgenstr Neuen Bildgeb Verfahr 175:1244–1250

Weiger M, Pruessmann KP, Kassner A et al (2000) Contrast-enhanced 3D MRA using SENSE. J Magn Reson Imaging 12:671–677

Zhu Y, Hardy CJ, Sodickson DK et al (2004) Highly parallel volumetric imaging with a 32-element RF coil array. Magn Reson Med 52:869–877

Peripheral MR Angiography

30

Tim Leiner

CONTENTS

30.1 Introduction

Dynamic three-dimensional (3D) contrast-enhanced magnetic resonance angiography (CE-MRA) has evolved over the past decade from an experimental imaging modality to a highly accurate technique that is now routinely used in clinical practice. CE-MRA is the current standard-of-reference MRA technique for non-invasive evaluation of the upper and lower extremity vasculature (Yucel et al. 1999; Ho et al. 1999, 1999). The recent clinical introduction of parallel imaging has significantly advanced the field of peripheral CE-MRA because it can be used in concert with and amplifies other recent improvements such as centric k-space encoding and view-sharing techniques (Pruessmann et al. 1999; Sodickson et al. 1997; Weiger et al. 2000). The high signal-to-noise ratio available in CE-MRA techniques can be used to increase scan efficiency through parallel imaging by acquisition of higher-spatial-resolution volumetric datasets free from disturbing venous overlay in shorter imaging times. This chapter provides considerations on how parallel imaging can be applied to optimize image quality of upper and lower extremity 3D CE-MRA.

30.2 Theoretical Background

30.2.1 General MR Angiographic and Physiological Considerations

In general, the choice of imaging parameters for 3D CE-MRA acquisitions is governed by the following antithetical constraints: (1) the desire for high vessel-to-background contrast, (2) the desire for time-resolved imaging, and (3) the desire for high reso-

T. Leiner, MD, PhD
Department of Radiology, Peter Debijelaan 25, NL-6229HX, Maastricht, The Netherlands

lution images in three dimensions. In conventional X-ray angiography, the first two of these constraints are easily reconciled because of the very high spatial and temporal resolution of the technique. The typical acquisition duration for an image with a 1,024×1,024 matrix is about 50 ms. Although high vessel-to-background contrast is easily achieved by injecting MR contrast media, the MR imaging process is, however, inherently slow. This is in contrast to X-ray angiography where image acquisition is virtually instantaneous. In MR imaging, acquisition duration is directly proportional to the desired spatial resolution, volumetric coverage and hardware performance. This is the result of the fact that MR data acquisition occurs in a sequential order, i.e., point by point or line by line. For example, acquisition of a single image using a Cartesian readout with 256×256 matrix and TR of 5 ms takes 1.28 s. A volumetric acquisition covering 20 slices would take over 25 s when using the same imaging parameters. Consequently, MR imaging acquisition speed is fundamentally limited by the maximum switching rates of gradients and pulses, and in the current era of ultra-fast hardware, physiological constraints resulting from the need to avoid neuromuscular stimulation and excessive deposition of RF power in biological tissues.

Since the maximum field of view (FOV) of commercially available MR imagers is typically around 40-45 cm, an additional constraint is the fact that two or three consecutive acquisitions are needed to image the entire upper or lower extremity peripheral vascular tree. Because of the inherently slow MR imaging process, one of the major limitations of 3D CE-MRA is simultaneous depiction of arteries and veins, which often hampers image interpretation, especially of small distal arteries.

Another limitation of conventional CE-MRA is the limited spatial resolution. In order to accurately describe degree and length of arterial stenoses it is paramount that the resolution of the 3D CE-MRA dataset needs to meet minimal standards. It is known from the work by Hoogeveen et al. (1998) and Westenberg et al. (2000) that at least three pixels are needed across the lumen of an artery to quantify the degree of stenosis with an error of less than 10%. When this constraint is kept in mind, it is obvious that higher resolution is needed to accurately characterize stenoses in small forearm or lower-leg arteries as opposed to the subclavian or iliac arteries. In general, voxel dimensions should be kept as close to isotropic (equal length in all dimensions) as possible to avoid blurring when viewing vessels in projections with lower spatial resolution. In addition, non-isotropic voxels are suboptimal for the detection and characterization of eccentric stenoses.

Given the considerations above, it is clear that the attractiveness of parallel imaging lies in the fact that it is a versatile tool that can be applied not only to reduce scan time, but also to increase acquired spatial resolution within the conventional scan duration, or to increase volume coverage per unit time.

30.2.2 Parallel Imaging in CE-MRA

Parallel imaging uses the spatial variation in coil sensitivities of multi-element phased-array surface coils to increase phase-encoding step size and consequently the number of phase encodings required to reconstruct a set of images. In conventional Cartesian Fourier encoding, reducing the density of phase-encoding steps decreases the reconstructed FOV. If the imaged object is larger than the reconstructed FOV, aliasing results. However, parallel imaging removes the potential aliasing and reconstructs the full FOV, thus delivering full-FOV images with fewer phase encodings in a shorter scan time (Wilson et al. 2004). The reconstruction process required to make up for k-space undersampling can either occur in k-space (Sodickson et al. 1997; Jakob et al. 1998; Kyriakos et al. 2000; Heidemann et al. 2001; Griswold et al. 2002), or in image space (Pruessmann et al. 1999), cf. Chap. 2. All major MR hardware manufacturers currently market coils capable of parallel imaging for neurovascular, thoracic, abdominal and upper and lower extremity applications, cf. Chap. 14. For further details and in-depth discussion of the physical and mathematical principles of parallel imaging, the reader is referred to the first three chapters of this volume.

In clinical practice parallel imaging is a versatile tool that can be used to amplify other strategies aimed at decreasing disturbing venous enhancement and increasing spatial and temporal resolution. The most important of these tools are centric k-space encoding and partial k-space updating strategies, cf. Chaps. 7 and 11. A basic understanding of these techniques is needed to understand how parallel imaging can be used to improve image quality.

Centric k-space encoding is based on the principle of acquiring views close to the origin of the k_y-k_z plane first. In other words, contrast-determining central k-space views are acquired first, followed by

the resolution determining peripheral views. In CE-MRA, the major advantage of this strategy is that the center of k-space can be acquired after arterial, but before venous enhancement, providing a high degree of venous suppression (Wilman and Riederer 1997; Willinek et al. 2002). When parallel imaging is applied, either the same number of central views can be acquired in less time, or the k-space radius that is traversed in the same time can be increased, thus even further suppressing venous signal.

There are two well-known partial k-space updating strategies that are used in clinical practice: (1) keyhole and (2) time-resolved imaging of contrast kinetics (TRICKS). In the keyhole method a small number (about 25%) of central k-space views are repeatedly sampled to monitor contrast bolus passage. Subsequently, a reference dataset that covers all the views is collected. After the acquisition is completed, the high spatial frequencies of the reference dataset are combined with each set of central k-space data to generate a series of images with full spatial resolution (van Vaals et al. 1993). TRICKS is a variation of the keyhole principle whereby the k_y-k_z plane is divided into multiple equal areas that are each updated with a different frequency, with the center being updated most often. The difference with the keyhole technique is that the peripheral parts of k-space are also updated multiple times, but at a much lower rate compared to the center. In addition, instead of reconstructing a full spatial resolution dataset based on a single sampling of the outer parts of k-space, TRICKS uses a sliding-window reconstruction by combining the center of k-space with the nearest acquired peripheral parts of k-space (Korosec et al. 1996). Parallel imaging can be combined with keyhole or TRICKS to further increase temporal resolution with a factor equal to the undersampling factor. In this way a synergistic reduction in scan time is achieved relative to a series of conventional scans with sequential full sampling of each k-space.

Recent improvements in MR gradient speed add additional significant opportunities to optimize imaging protocols by allowing ultrashort TR values of down to 1 ms. A major advantage of parallel imaging, however, is that image contrast is not directly affected because acquisition parameters such as TR and TE and bandwidth can be kept the same if so desired. Conversely, parallel imaging can also be applied to increase TR (thereby increasing T1 relaxation and allowing decreased read-out bandwidth) to improve the signal-to-noise ratio without changing acquisition time (Wilson et al. 2004).

30.3 Upper-Extremity CE-MRA

30.3.1 Anatomical and Physiological Considerations

With the elbow extended, the upper extremity of a 170-cm-tall adult is about 75 cm long. This implies that at least two FOVs of about 40 cm in the craniocaudal direction are needed to depict all the relevant arteries. A FOV of 20-25 cm suffices if the main area of interest is the distal forearm and hand. The diameter of the subclavian artery is about 1.0-1.3 cm, and the diameter of the axillary artery is about 6-8 mm. Distally, the arteries progressively taper to a diameter of about 1-2 mm at the level of the palmar arch in the hand.

The mean time of selective arterial opacification in the upper extremity is relatively short. Winterer et al. (2000) found a mean bolus arrival time of 27 s measured at the level of the terminal radial and ulnar arteries, and a mean time window of selective arterial enhancement of 11-14 s. However, large inter-individual differences in contrast medium circulation times were found. The period between arterial and venous enhancement can be substantially lengthened by applying supra- (>200 mmHg) or sub-systolic (>60 mmHg) compression just proximal to the wrist with an MR compatible blood pressure cuff. This effectively increases the period of selective arterial enhancement and hence the imaging window needed to achieve the ultra-high spatial resolution needed to evaluate arterial occlusive disease optimally in the small hand vessels (Wentz et al. 2003; Bilecen et al. 2004).

30.3.2 Imaging Protocol and Parameters

High-quality upper-extremity CE-MRA demands large FOV imaging with high spatial resolution, short imaging times and dedicated multi-element surface coils capable of parallel imaging. Because synchronization of peak arterial contrast enhancement with acquisition of the center of k-space is essential to obtain the best image quality, it is advisable to assess individual circulation times with a test bolus of 1-2 ml of gadolinium followed by 25 ml of saline flush. Alternatively, real time bolus visualization software [e.g. BolusTrak (Philips Medical Systems); SmartPrep

Table 30.1. Recommended imaging parameters for upper extremity CE-MRA

Description	Sequence	Orientation	Coverage	Coil	TR/TE (ms)	FA (degrees)	FOV (mm)	Matrix	Slice thickness* (mm)	No. of partitions	NSA	Duration (s)	Parallel imaging acceleration factor	Comments
Localizer	2D bSSFP	Coronal, sagittal and transverse	Thorax, upper arm, forearm/hand	Body surface PA	<5/<2	60-90	430×430	256	≤10 mm	Tailor to anatomy	1	<30 s per orientation	None	Acquire in multiple stations if necessary
Bolus timing	2D CE-T1w GRE	Coronal	Thorax and upper arm or forearm and hand	Body	<5/<2	30-40	430×430	256	80-100	Single thick slice, tailor to anatomy	0.67	1 s per phase	None	Acquire during breath-hold for thorax
3D HR CE Aortic arch and proximal upper extremity	3D CE-T1w GRE	Coronal	Thorax and upper arm	Body surface PA	<5/<2	30-40	430×350-400	430-512	<2.0	Tailor to anatomy	0.67	<20-25 s	2-3	Acquire during breath-hold
3D HR CE distal upper extremity	3D CE-T1w GRE	Coronal or sagittal	Forearm and hand	Rectangular-FOV extremity coil	<5/<2	30-40	400-430×100-120	430-512	<1.5	Tailor to anatomy	0.67	<15 s per phase	2-3	Acquire multi-phase acquisition
3D HR CE hand	3D CE-T1w GRE	Coronal	Wrist and hand	Small-FOV extremity coil	<5/<2	20-40	250×120-150	256-512	<1.0	Tailor to anatomy	0.67	<20 s per phase (longer under compression)	2-3	Acquire multi-phase acquisition, use supra-systolic compression for best results

TR: repetition time; TE: echo time; FA: flip angle; FOV: field-of-view (frequency × phase); NSA: number of signals averaged (number below 1 indicates partial or fractional echo); *non-interpolated, truly acquired slice thickness; PA: phased array

(GE Health) or CareBolus (Siemens Medical Solutions)] can be used (Wikstrom et al. 2003; Foo et al. 1997; Luccichenti et al. 2003). In Table 30.1, recommended sequence parameters are listed for localizer and timing scans as well as high spatial resolution 3D CE-MRA of the upper extremity arteries. In Table 30.2, recommended contrast medium injection parameters are listed. A simple rule of thumb is that the contrast medium should be injected for no more than 40-60% of the duration of the acquisition (or a single dynamic phase when multiphase imaging is performed) (Prince 1998).

When information is needed about both the proximal and distal upper-extremity arteries, two FOVs need to be imaged. This can either be done with a single injection of contrast medium in combination with table movement in between acquisitions or by performing two separate acquisitions with separate injections of half each of the total amount of contrast medium. Because of the short circulation times in the upper extremity, the latter approach is recommended because it usually leads to better results, especially when the forearm and hand are imaged first. Another important caveat of upper extremity CE-MRA is to inject contrast medium on the asymptomatic side in order to avoid susceptibility-induced intra-arterial signal loss (Siegelman et al. 2000). When both upper extremities need to be imaged, it is advisable to inject contrast medium on the right because of the greater distance of the right brachiocephalic vein and the superior vena cava to the large arteries.

30.3.3 Clinical Applications

CE-MRA is a powerful technique for the diagnosis of pre-interventional treatment planning and post-interventional follow-up of a broad spectrum of congenital and acquired upper extremity occlusive disease. It is important to keep in mind that sub-millimeter isotropic resolutions are necessary to depict distal upper extremity arterial disease reliably.

30.3.3.1 Atherosclerotic occlusive disease

Although atherosclerosis is the most common cause of upper extremity arterial stenosis in the large arteries down to the wrist, its incidence is much lower when compared to the lower extremities. The most frequent site of occlusion is the brachiocephalic trunk or the proximal subclavian artery (Fig. 30.1). In case of occlusion, collateral blood supply is established via the side branches of the subclavian artery and the axillary artery (Fig. 30.2). Subclavian artery stenosis or occlusion is not infrequently accompanied by retrograde collateral blood flow in the ipsilateral vertebral artery. This is also known as subclavian steal. Retrograde flow can be depicted on the 2D time-resolved test-bolus scan or with non-enhanced time-of-flight or phase-contrast MRA acquisitions (Tay et al. 2005; Wu et al. 2005; Bitar et al. 2004).

Table 30.2. Suggested injection protocols for upper extremity CE-MRA using commercially available 0.5 M gadolinium chelates

Indication (approach)	Contrast volume/ injection rate	Saline flush volume/ injection rate	Comments
Timing (2D time-	1-2 ml at 2-3 ml/s	25 ml at same rate*	Choose largest FOV to obtain information about all relevant arteries. Can provide resolved test bolus approach) information on direction of flow in cases of suspected subclavian steal.
Distal or proximal upper extremity (as part of two-station upper extremity examination)	20 ml at 3.0 ml/s	25 ml at 3.0 ml/s*	Two separate single-phase injections (two-station approach for depiction of entire upper extremity)
Distal or proximal upper Extremity (single station examination)	35 ml at 3.0 ml/s	25 ml at 3.0 ml/s*	Single-phase injection for depiction of either proximal or distal upper extremity.

The maximum contrast dose that may be given for all injections together is 0.3 mmol/kg. In this table a patient body weight of 75 kg was assumed. LL, lower leg station; Ao/UL, aortoiliac and upper leg stations; *saline is always injected at the same rate as the last phase of the contrast injection

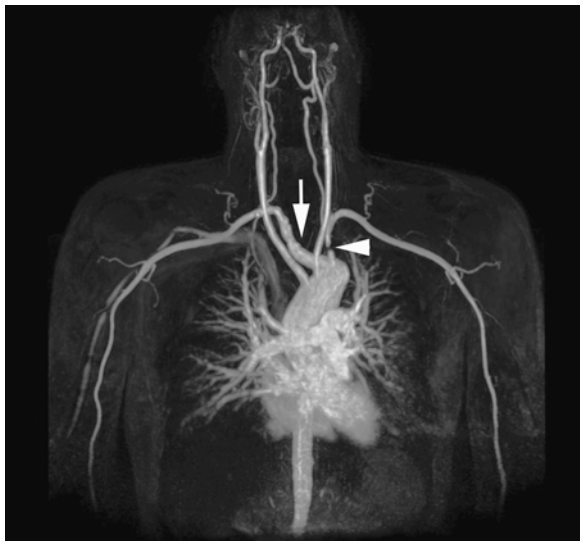

a

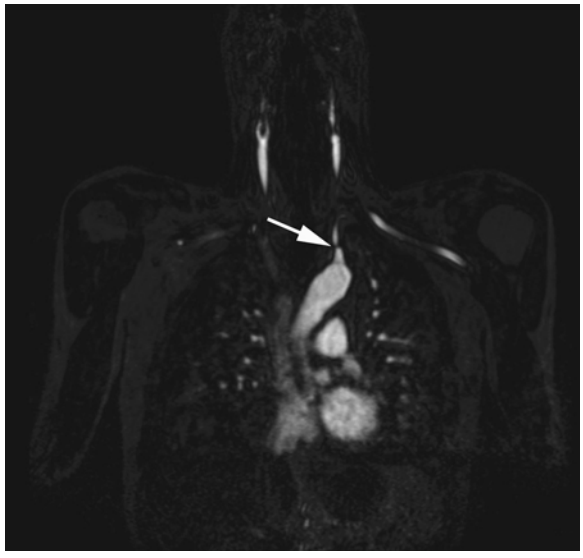

b

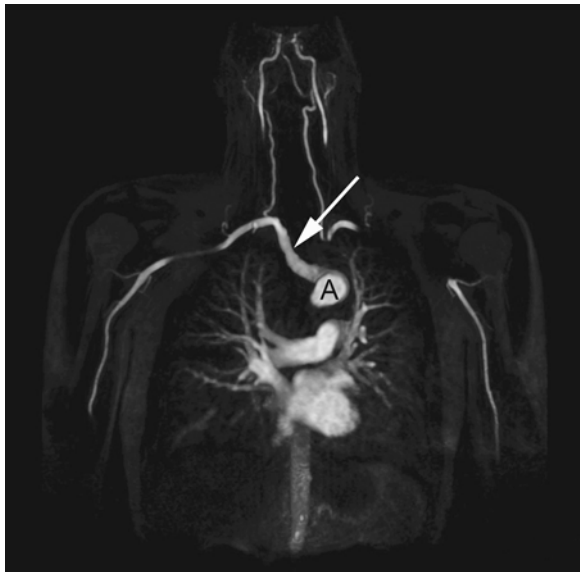

c

30.3.3.2 Vasculitis

Different entities of vasculitis regularly affect upper extremity arteries. Wall thickening and enhancement on post-contrast T1-weighted imaging as well as central aneurysms without a history of trauma or infection suggest a vasculitis (Bley et al. 2004; Bley et al. 2005). Vasculitides affecting the subclavian artery are Takayashu's and Behçet's disease. The axillary artery is involved in giant cell arteritis and systemic lupus erythematosis (SLE). Thromboangiitis obliterans (TAO; Buerger's disease) often specifically affects the forearm arteries in patients with this disease. The angiographic hallmark of TAO is widespread arterial occlusion with numerous corkscrew collaterals (Olin et al. 1990). Arteries of the hand are discussed below.

30.3.3.3 Aneurismal disease

Aneurysms of upper extremity arteries are frequently secondary to iatrogenic arterial trauma or as the result of blunt or penetrating trauma to the chest. Less frequent causes include vasculitis and hematogeneous infection (mycotic aneurysm). Because the contrast-enhanced portion of the exam only provides a luminogram, a standard T1-weighted acquisition should always be performed to assess the true size of the aneurysm including any mural thrombus. Alternatively, this information can also be obtained from high quality balanced steady-state free precession (bSSFP) localizer images.

30.3.3.4 CE-MRA of Hand Arteries

Contrast-enhanced MR angiography of peripheral arterial disease in palmar and digital arteries is challenging, but possible. Best results are achieved with a dedicated small-FOV coil, the application of supra- or

Fig. 30.1a–c. A 45-year-old male patient with complaints of numbness in the left hand. The full-volume maximum intensity projection reveals a high-grade stenosis in the left subclavian artery (**a**, *arrowhead*) and an aberrant right subclavian artery (**a**, *arrow*). Review of the original partitions reveals a residual pinpoint-shaped lumen of the left subclavian artery **b**. A sub-volume rendering shows the arteria lusoria as the last main branch of the aortic arch **c**. *A*: aortic arch (TR/TE: 4.0 ms/1.5 ms, SENSE acceleration factor *R*=2)

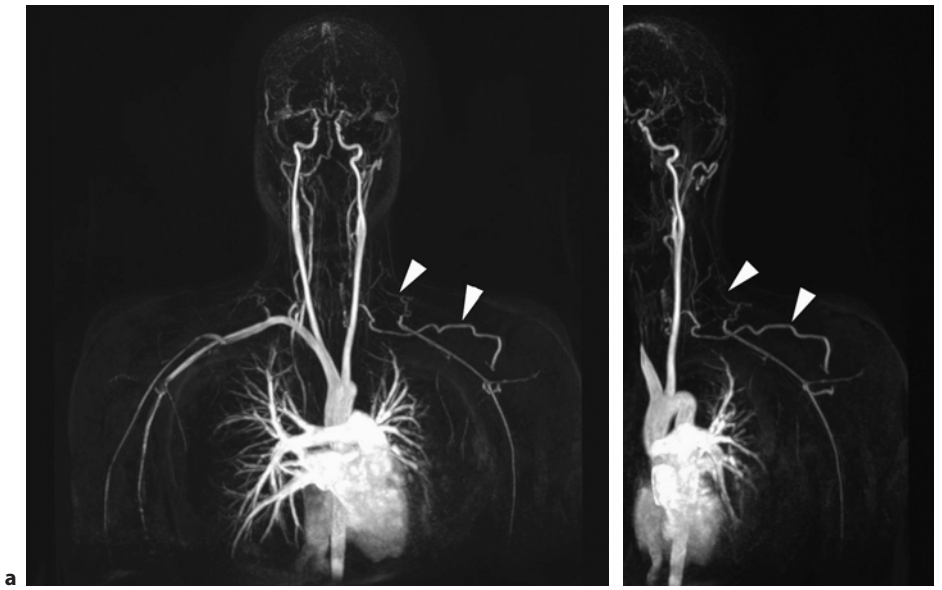

Fig. 30.2a,b. A 17-year-old female patient who complained of weakness in the left arm. The patient underwent surgical repair for an aortic coarctation at the age of 7 years. High-resolution MRA shows occlusion of the left subclavian artery **a** because it was used as a patch to repair the coarctation. Collateral branches arising from the costocervical trunk (*medial arrowhead*) and the thyrocervical trunk (*lateral arrowhead*) reconstitute the axillary artery. A *left anterior oblique view* **b** better shows the origin of the collaterals (TR/TE: 4.0 ms/1.5 ms, SENSE acceleration factor *R*=2)

sub-systolic compression at the time of selective arterial enhancement (Winterer et al. 2000; Wentz et al. 2003; Bilecen et al. 2004), and the use of high parallel-imaging acceleration factors (Table 30.1). This approach basically creates a longer 'arteriovenous window' that allows for ultra-high spatial-resolution imaging with sub-millimeter isotropic voxels.

Indications for imaging of the hand are suspected emboli in patients with atrial fibrillation or atherosclerotic disease in proximal upper-extremity arteries, preoperative imaging in patients undergoing plastic surgery of the hand, vibration tool users with symptoms of arterial occlusion in the hand, hypothenar hammer syndrome (Fig. 30.3) and patients with suspected vasculitis. Connective tissue disorders such as scleroderma, rheumatoid arthritis, and SLE are associated with multiple occlusions of the small arteries of the hand, palm and digits. Small distal aneurysms are associated with polyarteritis nodosa.

30.3.3.5 Dialysis access fistulae

Arteriovenous fistulae for (AVF) for hemodialysis vascular access have a high risk of thrombosis due to stenoses that jeopardize flow and patency, and early detection and treatment of these stenoses can prevent thrombosis (Murphy et al. 2000; NKF-DOQI 1997). In current clinical practice, stenosis detection and grading in AVF and the venous outflow segments are performed using digital subtraction angiography (DSA). The arterial part of the AVF is visualized according to the method of Staple (1973), using a proximal cuff to interrupt flow in order to achieve retrograde filling of the arterial part of the AVF. Analysis of DSA images acquired with this method can be difficult due to vessel overlay, especially at the level of the anastomoses. Due to the temporary flow interruption, the hemodynamic situation is altered, which potentially limits the value of DSA. Furthermore, because of incomplete retrograde filling, the feeding artery and arterial part of the AVF are not always depicted in their entirety (Bos et al. 2001; Waldman et al. 1996).

Because of the reasons outlined above, the preinterventional workup in patients with hemodialysis access failure requires imaging from the aortic valve and superior vena cava down to the distal arteriovenous anastomosis in the elbow or forearm region. The demands of a large FOV combined with the extremely high flow rates in these shunts make parallel imaging particularly useful for imaging dialysis

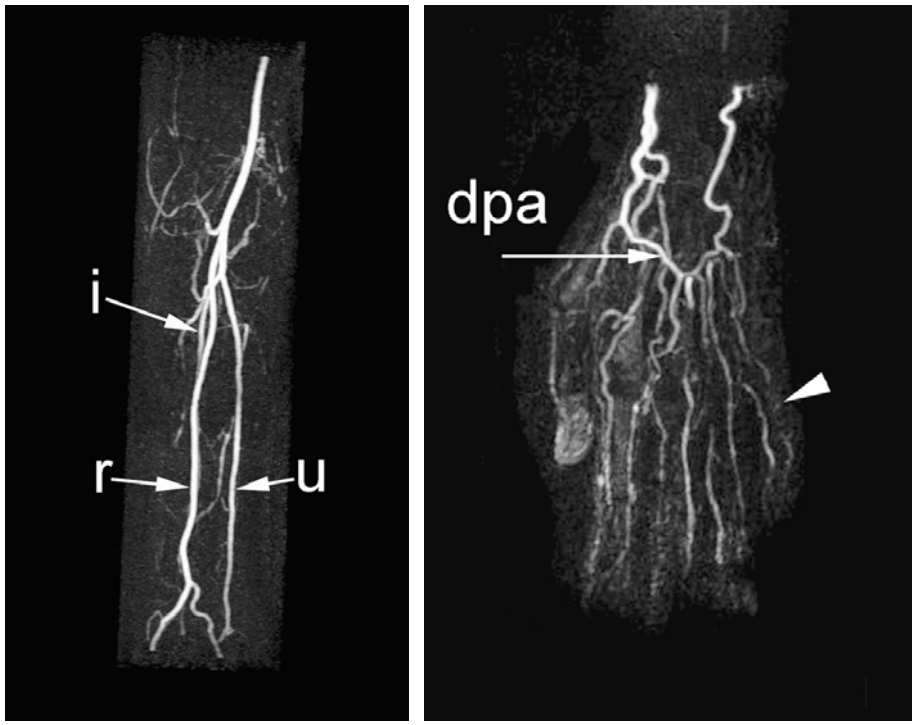

Fig. 30.3a,b. A 37-year-old construction worker suspected of having hypothenar hammer syndrome. Contrast-enhanced MRA of the forearm **a** reveals normal radial (*r*), ulnar (*u*) and interosseous artery (*i*). Dedicated imaging of the hand **b** reveals an occluded superficial palmar arch, but patent deep palmar arch (*dpa*). There is scarce vascular supply to the fourth and fifth fingers (*arrowhead*) (TR/TE: 5.0 ms/1.7 ms, SENSE acceleration factor *R*=2)

access fistulae and supplying arteries and draining veins (Fig. 30.4). Furthermore, 3D CE-MRA provides unlimited viewing angles, which are very helpful in planning the proper intervention. For instance, Planken et al. (2003) demonstrated that multiphase 3D CE-MRA detected flow-limiting stenoses in two patients (13%) with failing hemodialysis access fistulae that were not seen with conventional DSA. Only after these stenoses were removed did flow improve.

30.4 Lower-Extremity CE-MRA

30.4.1 Anatomical and Physiological Considerations

The lower extremity peripheral arterial tree extends from the infrarenal aorta down to the feet and has a total length of about 90-120 cm. To depict all relevant arteries, at least three separate acquisitions are needed: one acquisition to cover the aortoiliac arteries, one to cover the superficial femoral and proximal popliteal arteries, and an additional acquisition to cover the distal popliteal, lower leg and pedal arteries. As outlined in the section on upper extremity CE-MRA above, best results are obtained when the acquisition is tailored to the arterial dimensions in the specific FOV (Leiner et al. 2000). The diameter of the infrarenal aorta is usually around 2.0-2.5 cm, the diameter of the superficial femoral artery is about 7-10 mm, and the arteries at the level of the ankle and foot have diameters of around 1.0-2.0 mm. In most patients, peripheral arteries are slightly curved in the anteroposterior direction, and the coverage needed is usually less than 10 cm. In the presence of an aortic aneurysm, iliac arterial elongation, collaterals bridging iliac or superficial femoral arterial obstructions or a femorofemoral crossover bypass graft, the AP coverage needed to depict these vessels may be markedly increased (up to 15-20 cm). Review of the transverse localizer images ensures that these structures are not excluded from

the 3D CE-MRA imaging volume. This is particularly important if a patient has a femorofemoral cross-over bypass graft because these grafts are usually not seen on TOF MIPs due to in-plane saturation artefacts (Ho et al. 1999). Other patients that demand special attention are those with (thoraco-) abdominal aortic aneurysms where flow may be markedly slower compared to patients without aneurysms (Nijenhuis et al. 2004). If insufficient delay time is observed between the injection of contrast and imaging, this will result in incomplete opacification of the aneurysm at the time of imaging. To avoid this problem, either a longer delay between injection and start of acquisition, or a multiphasic acquisition should be used (Schoenberg et al. 2001).

The mean time of selective arterial opacification at different levels in the lower extremity varies widely. Patients with a history of heart failure usually exhibit slower venous return, while patients with ulcers often have an extremely short arteriovenous window. Prince et al. (2002) demonstrated that after arrival in the common femoral artery (CFA), intravenously injected contrast material travels down the peripheral arteries at about 6 s per station. In 87 patients undergoing time-resolved 2D CE-MRA, the mean travel time of contrast material to the CFA was 24 s, with an additional 5 s to reach the popliteal artery and 7 s to reach the ankle arteries. In the same study, they found that the mean time window of arterial enhancement was 49 s in the pelvis, 45 s in the thigh, and 35 s in the calf.

Similar to the upper extremity, the period between arterial and venous enhancement can be substantially lengthened by applying venous compression. In contrast to the upper extremity, however, suppression of venous enhancement in the distal lower extremity is already achieved at with a blood pressure cuff inflated to 50-60 mmHg either just proximal to or just distal to the knee joint (Herborn et al. 2004; Bilecen et al. 2004).

30.4.2 Imaging Protocol and Parameters

Because of the lower injection rate and hence the lower vessel-to-background contrast, non-enhanced 'mask' acquisitions are usually acquired prior to the

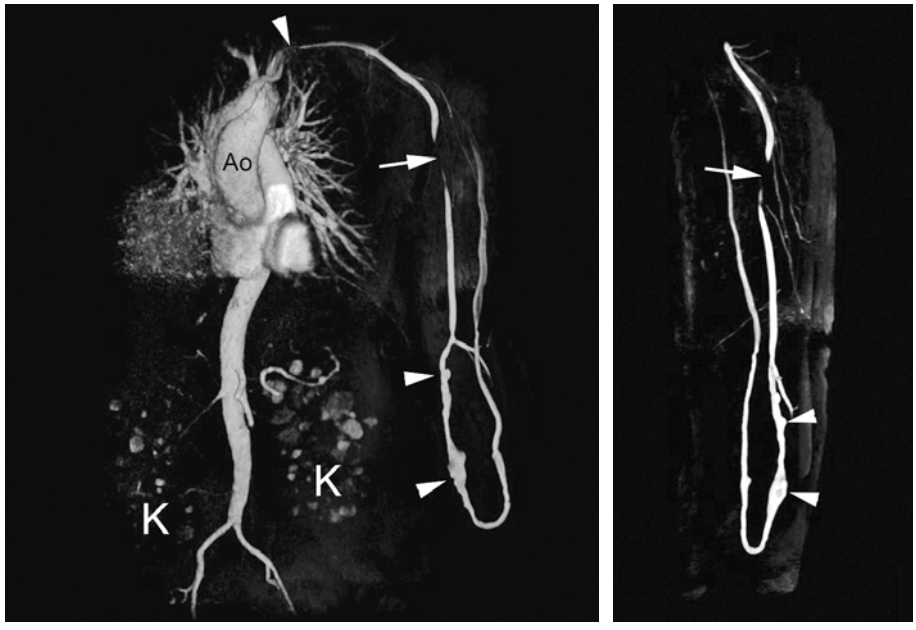

Fig. 30.4a,b. A 67-year-old patient with polycystic kidney disease and flow-declined hemodialysis access fistula in the left forearm **a**. There are high-grade stenoses in the subclavian (*top arrowhead*) and brachial artery supplying the shunt (*arrow*). In addition, there are multiple aneurismal dilations in the loop graft (**a**, *lower arrowheads*). Note enhancement of residual kidney parenchyma. Zoomed subvolume maximum intensity projection of the left forearm and antecubital region more clearly shows high-grade stenosis (*arrow*) and aneurysms (*arrowheads*). *K*: kidney (TR/TE: 4.0 ms/1.5 ms, SENSE acceleration factor *R*=2)

contrast-enhanced acquisitions in patients undergoing lower extremity MRA. After the acquisition has ended, the non-enhanced images are subtracted from the enhanced images to suppress non-vascular background signal.

Currently, the most commonly used and easiest approach to lower-extremity CE-MRA is acquisition of three consecutive, identical imaging volumes during injection of a fixed dose (0.2-0.3 mmol/kg) or volume (30-45 ml) of 0.5 M gadolinium chelate (Ho et al. 1998; Meaney et al. 1999). Although this approach is fast, it cannot be used in every patient. This is because image quality of the distal arteries tends to be worse compared to aortoiliac arteries due to low spatial resolution (which is usually sufficient for characterizing atherosclerotic aortoiliac lesions) and the presence of disturbing venous enhancement in the lower leg station in a substantial number of patients (Reid et al. 2001). Despite these drawbacks, this technique is well suited for the diagnostic imaging workup of the vast majority of patients with intermittent claudication. However, it is paramount that inferior image quality due to the problems as described above becomes clinically relevant in patients with severely diseased lower leg arteries. Specific groups in which the three-consecutive-station approach does not work well are patients with diabetes mellitus, who are known to have primarily very distal disease (Menzoian et al. 1989), and patients with chronic critical ischemia who have severe stenoses and occlusions from the aorta down to the feet ('multi-level' disease). To overcome these difficulties, the previously described approach with fixed imaging parameters in each location has been refined to optimize imaging parameters for each station, i.e., lower resolution for aortoiliac arteries, and higher resolution and more anatomical coverage (to include the pedal arch) for the lower leg arteries (Leiner et al. 2000) (Fig. 30.5).

Despite the introduction of station-optimized imaging, the most important problem standing in the way of universal acceptance of peripheral CE-MRA as an alternative for intraarterial digital subtraction angiography (IA-DSA) still remains venous enhancement in the lower-leg station. This problem is particularly prevalent in patients with cellulitis (Wang et al. 2002) and arteriovenous malformations in the context of diabetes mellitus (who also comprise a large subgroup of the patients with chronic critical ischemia). Furthermore, it is these patients in which adequate depiction of the lower-leg arteries is mandatory because they are often candidates for peripheral bypass surgery.

There are several general acquisition strategies that can be used to decrease the chance for disturbing venous enhancement. These are: (1) lowering TR and TE; (2) the use of a separate acquisition for the lower leg station; (3) the use of centric k-space filling; (4) the use of a time-resolved acquisition strategy (keyhole or TRICKS); (5) the use of infra-systolic venous compression, (6) use of parallel imaging to amplify the other strategies. The most straightforward way of preventing venous enhancement is by shortening acquisition duration. This should be done, first of all, by lowering TR and TE to the shortest possible value, without excessively increasing bandwidth. In addition, partial or fractional echo should be used. When the three-consecutive-station approach is used, it is particularly important to image the first two stations (i.e., aortoiliac and upper legs) as fast as possible. Once the acquisition of the lower legs is started, this will allow a relatively long (and thus high-resolution) scan given that none or minimal venous enhancement is already present, and centric k-space filling is used in this station. With the introduction of multi-element (peripheral) surface coils and parallel imaging, acquisition speed can be increased further (Maki et al. 2002; Bezooijen et al. 2004; de Vries et al. 2005). Another way to obtain images of the lower legs free of venous enhancement is to switch from a 3D high-resolution acquisition to a 2D projection acquisition, analogous to IA-DSA (Wang et al. 2001). A disadvantage of this latter method is that additional views demand separate injections of contrast medium.

To avoid the limitations of imaging three consecutive stations, an alternative approach is to use a dual-injection protocol in which the lower legs are imaged first, and the aortoiliac arteries and upper legs are imaged afterwards in a separate acquisition. The rationale for this 'hybrid' approach (Morasch et al. 2003) is that it is easier in this way to obtain high-resolution 3D images of the lower leg station free of disturbing venous enhancement. The initial acquisition of the lower legs is typically done using up to 15-20 ml 0.5 M Gd-DTPA and can be either mono- or multiphasic. Because synchronization of central k-space lines is optimized with regards to contrast enhancement in the lower leg arteries, venous enhancement is virtually eliminated. After imaging the lower legs is completed, a moving table acquisition is performed to image the aortoiliac and upper-leg arteries using the remaining volume of contrast agent (Fig. 30.6). The greatest benefit of using the hybrid approach can obviously be expected in patients with chronic critical ischemia, patients with arteriovenous fistulae (such as in diabetes mellitus), and patients with cellulitis (Wang et al. 2001).

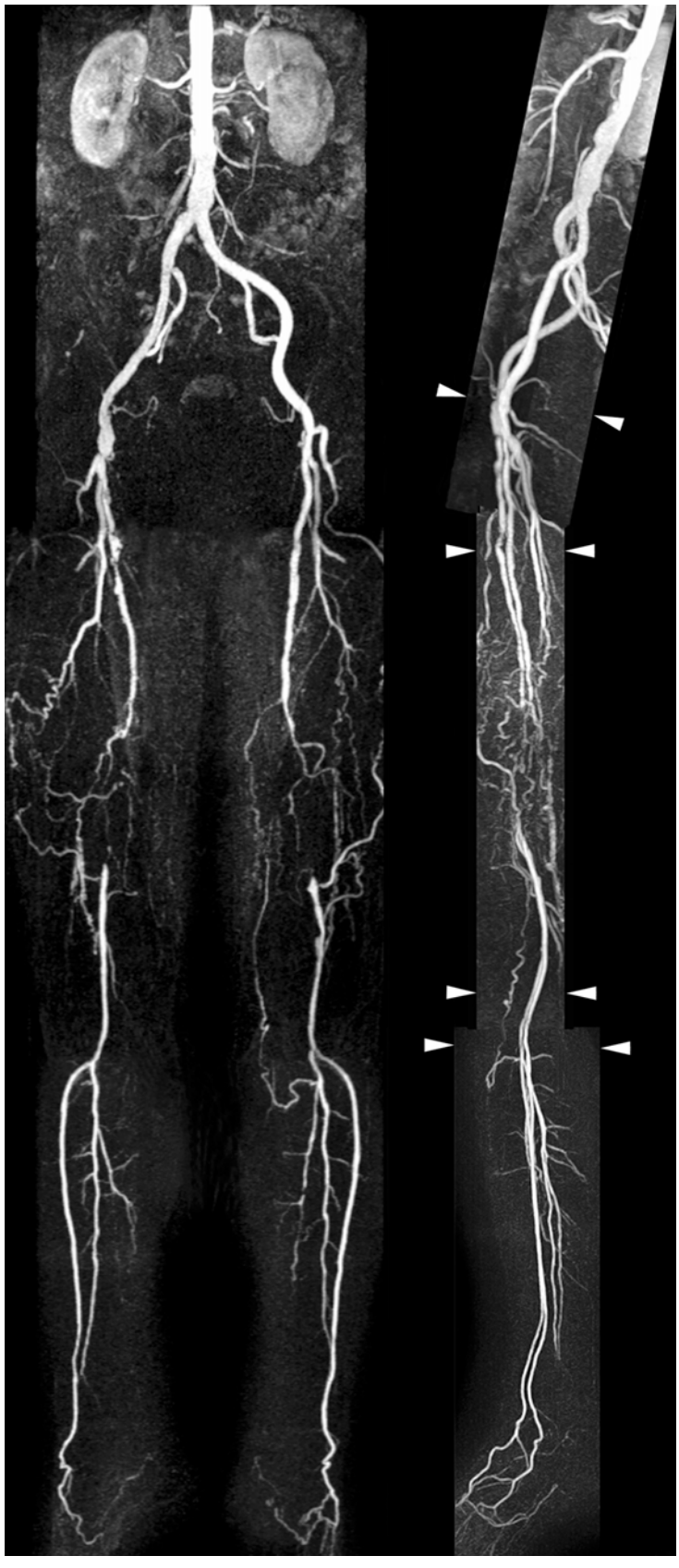

Fig. 30.5. Flexible imaging parameter peripheral CE-MR angiogram in 70-year-old patient suffering from intermittent claudication. Coronal three-station maximum intensity projection shows bilateral occlusion of the superficial femoral arteries (*left panel*). Use of station optimized volumes of different thickness can clearly be appreciated in *right panel* (*arrowheads*) (iliac and upper-leg stations: TR/TE: 4.0 ms/1.5 ms, SENSE acceleration factor *R*=2; lower-leg station: TR/TE: 4.0 ms/1.6 ms, *R*=3)

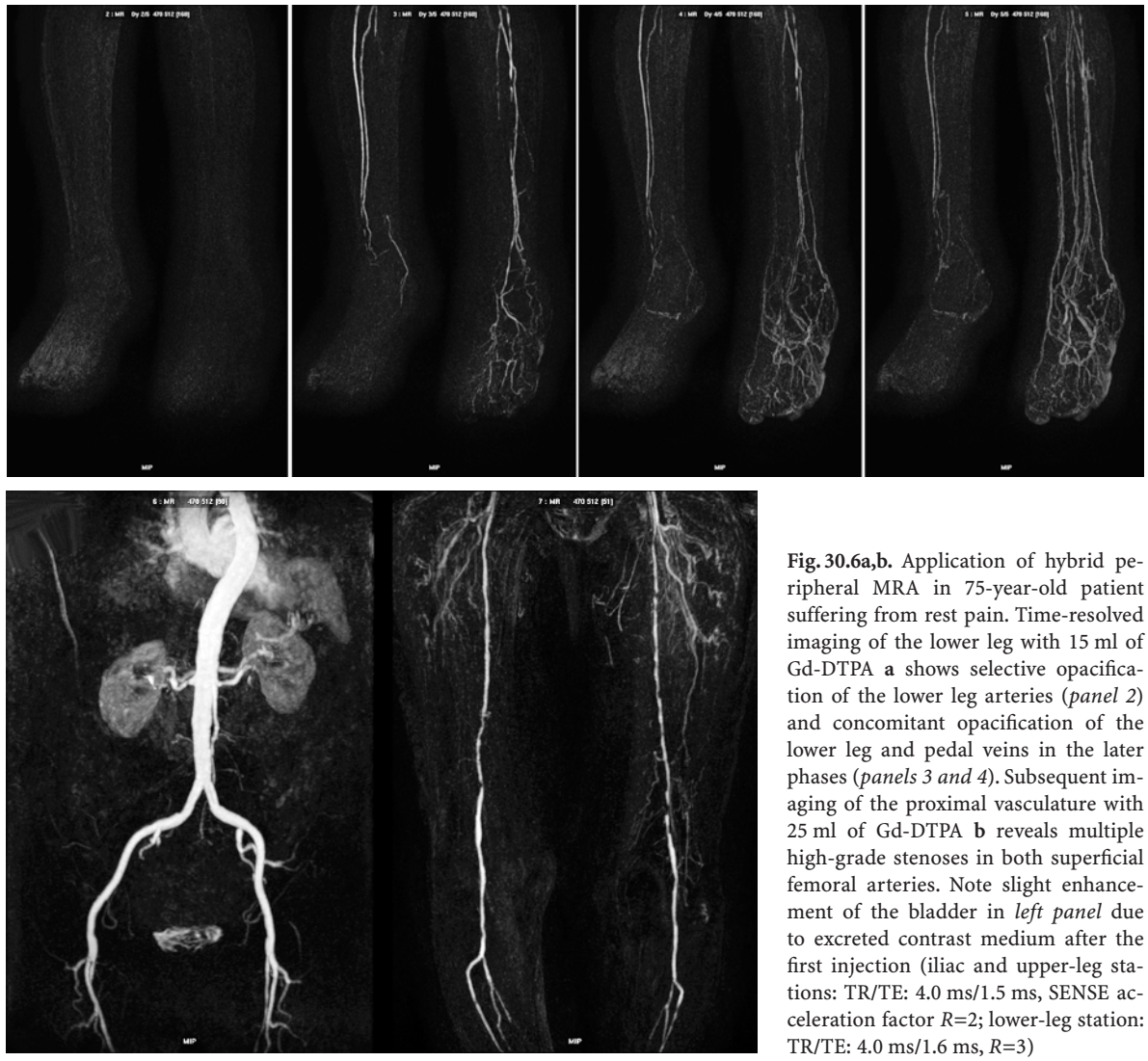

Fig. 30.6a,b. Application of hybrid peripheral MRA in 75-year-old patient suffering from rest pain. Time-resolved imaging of the lower leg with 15 ml of Gd-DTPA **a** shows selective opacification of the lower leg arteries (*panel 2*) and concomitant opacification of the lower leg and pedal veins in the later phases (*panels 3 and 4*). Subsequent imaging of the proximal vasculature with 25 ml of Gd-DTPA **b** reveals multiple high-grade stenoses in both superficial femoral arteries. Note slight enhancement of the bladder in *left panel* due to excreted contrast medium after the first injection (iliac and upper-leg stations: TR/TE: 4.0 ms/1.5 ms, SENSE acceleration factor R=2; lower-leg station: TR/TE: 4.0 ms/1.6 ms, R=3)

Independent of which approach one chooses to peripheral MRA, an absolute requirement is the use of surface coils, at least for the lower legs. The use of such surface coils increases the signal-to-noise ratio, which allows for an increase in spatial resolution, which in turn increases arterial conspicuity and improves disease characterization in small, distal, diseased arteries. Conversely, the increase in the signal-to-noise ratio can be used to increase acquisition speed in order to avoid venous enhancement. Almost all vendors have phased-array surface body- or torso-coils that can be used to image the lower leg. In addition, all major MRI vendors are now selling dedicated multi-station peripheral vascular coils capable of parallel imaging with coverage exceeding 100 cm (Fig. 30.7). Several authors have shown that the use of such coils is beneficial in terms of both increased signal-to-noise ratio as well as increased anatomical coverage (55-57).

Recommended sequence parameters for three-consecutive-station high-spatial-resolution 3D CE-MRA of the lower extremity are listed in Table 30.3. In Table 30.4, recommended parameters are listed for lower leg and pedal CE-MRA. In Table 30.5, contrast medium injection parameters are listed.

30.4.3 Clinical Applications

As is true for the upper extremity, CE-MRA is a powerful technique for diagnostic and preinterventional workup of congenital and acquired lower extremity

occlusive disease. It is again important to stress that sub-millimeter isotropic resolutions are necessary to reliably depict lower-leg and pedal arterial disease.

30.4.3.1 Atherosclerotic Occlusive Disease

The vast majority (>80%) of lower extremity arterial disease is due to atherosclerotic peripheral arterial occlusive disease (APAOD). APAOD is a major healthcare problem in Western society with an estimated prevalence in the general population of 2.5% in the age group over 50 years of age. In the age group over 70 years old, the prevalence is estimated at about 7% (Dormandy et al. 2000). Patients who have complaints of APAOD usually present with a history of intermittent claudication. Intermittent claudication is caused when blood flow to exercising leg and calf muscles is insufficient compared to metabolic demands. Upon cessation of exercise, complaints usually disappear rapidly. The clinical course of intermittent claudication in terms of progression of disease in the symptomatic limb is usually benign since only about a quarter of patients will ever significantly deteriorate (Dormandy et al. 2000). With an intervention rate of approximately 5%, only 1-3% of all patients with intermittent claudication will ever undergo a major amputation (Society for Vascular Surgery 1986). Angiographically, intermittent claudication is characterized by either a short, isolated aortoiliac or superficial femoral lesion or a longer iliac or superficial femoral occlusion. In more severe cases, combined lesions are seen (Fig. 30.8).

About 5% of patients with intermittent claudication progress to chronic critical ischemia, that is, the oxygen and nutrient supply of the distal lower extremity fall below the level for maintenance of normal cellular processes in resting conditions. Clinically, this is manifested by rest pain and tissue loss (i.e., non healing ulcers and gangrene). The incidence of chronic critical ischemia is estimated to be between 300-1,000 per million per year in the general population (Dormandy et al. 2000). Because of the severity of complaints, an invasive intervention is attempted in all but the worst cases. Despite advances in endovascular and vascular surgical therapy, however, the rate of major amputation in the general population remains in excess of 0.03% in industrialized countries (Dormandy and Ray 1996). In contrast to patients with intermittent claudication, imaging outflow arteries is an essential part of the imaging workup and is potentially limb-saving in patients with chronic critical ischemia, particularly when it is taken into account that IA-DSA is known to fail in visualizing patent crural and foot arteries, which are demonstrated with other modalities (Beard et al. 1988; Owens et al. 1992). In order to achieve the best possible image quality, it is recommended to use the hybrid approach as described above when dealing with patients with chronic critical ischemia.

The angiographic hallmark of chronic critical ischemia is bilateral, multiple severe stenoses and occlusions at different levels in the peripheral arterial tree (Fig. 30.9). Patients with diabetes are a well-recognized subgroup with primarily distal atherosclerotic occlusive disease and preservation of normal inflow (Fig. 30.10).

Fig. 30.7. Dedicated multi-station parallel imaging capable peripheral vascular coil (Philips Medical Systems, Best, The Netherlands). Note how feet can be included in the distal station. In each station there are two elements anterior to the patient and two elements posterior to the patient

Table 30.3. Recommended 3D CE-MRA sequence parameters for three-station peripheral CE-MRA

Description	Sequence	Orientation	Coverage	Coil	TR/TE (ms)	FA (degrees)	FOV (mm)	Matrix	Slice thickness* (mm)	No. of partitions	NSA	Duration (s)	Parallel imaging acceleration factor	Comments
Proximal station	T1w GRE	Coronal	Abd aorta to prox. SFA	Surface PA/peripheral vascular	5/2.5	30-40	430×300	400×200	≤2.5	Tailor to anatomy	0.67	10-15	2-3	Acquire during breath hold
Middle station	T1w GRE	Coronal	CF to trifurcation	Surface PA/peripheral vascular	4/1	30-40	430×350	400×256	2.0-2.5	Tailor to anatomy	0.67	7-12	2-3	
Lower station	T1w GRE	Coronal	P3 to pedal arch	Surface PA/peripheral vascular	<4/<2	30-40	430×300	430×300	<1.0-1.5	Tailor to anatomy	0.67	30-60	3-4	Use supragenual venous compression

CAPTION: For localizer and bolus timing parameters see table 1. T1w: T1-weighted; GRE: gradient-recalled echo; SE: spin echo; TR: repetition time; TE: echo time; FA: flip angle; FOV: field of view (frequency × phase); NSA: number of signals averaged (number below 1 indicates partial or fractional echo); * non-interpolated, truly acquired slice thickness; Abd: abdominal; prox: proximal; SFA: superficial femoral artery; CF: common femoral artery; P3: popliteal artery below knee joint; PA: phased array.

Table 30.4. Recommended imaging parameters for lower leg and pedal MRA

Description	Sequence	Orientation	Coverage	Coil	TR/TE (ms)	FA (degrees)	FOV (mm)	Matrix	Slice thickness* (mm)	No. of partitions	NSA	Duration (s)	Parallel imaging acceleration factor	Comments
3D entire lower leg	3D CE-T1w GRE	Coronal or sagittal	P3 to pedal arch	Body/surface PA	<5/<2	30-40	430×300	Same value as FOV	≤1.0-1.5	Tailor to anatomy	0.67	<10, MP <30† <45‡	3-4	Use in combination with keyhole or TRICKS
3D foot and ankle only	3D CE-T1w GRE	Sagittal	Ankle to pedal arch (single foot only)	Head/knee	<5/<2	30-40	430×300	Same value as FOV	≤1.0	Tailor to anatomy	0.67	<10, MP	2-8	Use in combination with keyhole or TRICKS
2D time resolved	2D CE-T1w GRE	Sagittal	P3 to pedal arch (single foot only)	Body/surface PA	<10/<2	60-80	Tailor to anatomy	256	Up to 100	Single thick slice, tailor to anatomy	0.67	3-5 (per phase)	2 or less	To preserve SNR the acceleration factor should not be chosen too high

CAPTION: 3D: three-dimensional; 2D: two-dimensional; CE: contrast-enhanced; T1w: T1-weighted; TR: repetition time; TE: echo time; FA: flip angle; FOV: field-of-view (frequency × phase); NSA: number of signals averaged (number below 1 indicates partial or fractional echo); * non-interpolated, truly acquired slice thickness; P3: popliteal artery below knee joint; PA: phased array; MP: multiphasic acquisition. † When acquired as last station in three-station runoff protocol; ‡ when acquired as dedicated lower leg examination with infrasystolic venous compression

Table 30.5. Suggested injection protocols for lower extremity CE-MRA using commercially available 0.5 M gadolinium chelates

Indication (approach)	Contrast volume/injection rate	Saline flush volume/ injection rate	Comments
Intermittent claudication (3-consecutive station bolus-chase protocol)	15-20 ml at 1.0-2.0 ml/s	25 ml at 0.5-1.0 ml/s*	dual-phase injection
	20-25 ml at 0.5-1.0 ml/s		
Chronic critical ischemia (hybrid approach)	LL: 15–20 ml at 2.0–3.0 ml/s	25 ml at 1.5–3.0 ml/s*	Two separate single-phase injections
	Ao/UL: 20 ml at 2.0–3.0 ml/s	25 ml at 1.5–3.0 ml/s*	
Intermittent claudication/Chronic critical ischemia (2D time-resolved test bolus approach)	6 ml at 2 ml/s	30 ml at 1.5-2.0 ml/s	Lower leg only

CAPTION: The maximum contrast dose that may be given for all injections together is 0.3 mmol/kg. In this table, a patient body weight of 75 kg was assumed. LL, lower leg station; Ao/UL, aortoiliac and upper leg stations; *saline is always injected at the same rate as the last phase of the contrast injection

Obtaining a high-quality full anatomic study from the infrarenal aorta down to the lower-leg and pedal arteries is essential in the preinterventional workup of distal peripheral arterial disease. The hybrid approach as described above is best suited to achieve this aim.

30.4.3.2 Aneurismal Disease

An aneurysm is defined as a focal enlargement of an artery to more than 1.5 times its normal diameter. For the aorta, the general cutoff value is 3 cm, and for the iliac arteries 1.8 cm. Aneurysms are either 'true' when intima, media and adventitia are involved or 'false' if less than three layers are involved. False aneurysms are frequently associated with confined rupture of arterial vessel wall, either spontaneous or due to trauma.

Patients with gross aneurismal dilatation of the thoracic and abdominal aorta need be imaged with a multiphase protocol to ensure optimal opacification of all the arteries in the FOV. Parallel imaging is very helpful in achieving high spatial and high temporal resolution in such patients. In patients with aortic or peripheral arterial aneurysms, transverse post-contrast T1-weighted images through the aneurysm should always be obtained to assess the presence of any mural thrombus and hence the true diameter of the artery in question.

30.4.3.3 Non-Atherosclerotic Causes of Peripheral Arterial Disease

Approximately 20% of chronic arterial occlusions are based on diseases other than atherosclerosis that cause luminal narrowing and/or occlusion. The presence, location and progression of arterial stenoses and occlusions may reflect an underlying systemic disease or may be an expression of regional inflammatory or degenerative processes. Lower extremity arterial diseases other than APAOD are aneurysmal disease, popliteal entrapment syndrome, cystic adventitial disease, arterial fibrodysplasia, non-specific aortoarteritis (Takayasu's disease), and a host of uncommon vasculitides, the most important of which is thromboangiitis obliterans (Buerger's disease) (Rudofsky 2003). In addition, congenital connective tissue diseases such as Marfan's syndrome, Ehlers-Danlos syndrome, pseudoxanthoma elasticum, homocystinurea, and neurofibromatosis are well known for their peripheral arterial involvement (Rooke and Joyce 2000). Congenital and acquired clotting disorders may also manifest themselves with symptoms of peripheral arterial disease. Rare causes of peripheral arterial disease are primary tumors, radiation therapy, and the iliac syndrome in cyclists. An acute arterial occlusion always necessitates a prompt search for atrial fibrillation, ulcerative endocarditis, and mural thrombi overlying the site of myocardial infarction.

Acknowledgement. R. Nils Planken, MD, of Maastricht University Hospital, Department of Radiology, is kindly acknowledged for contributing Fig. 30.4.

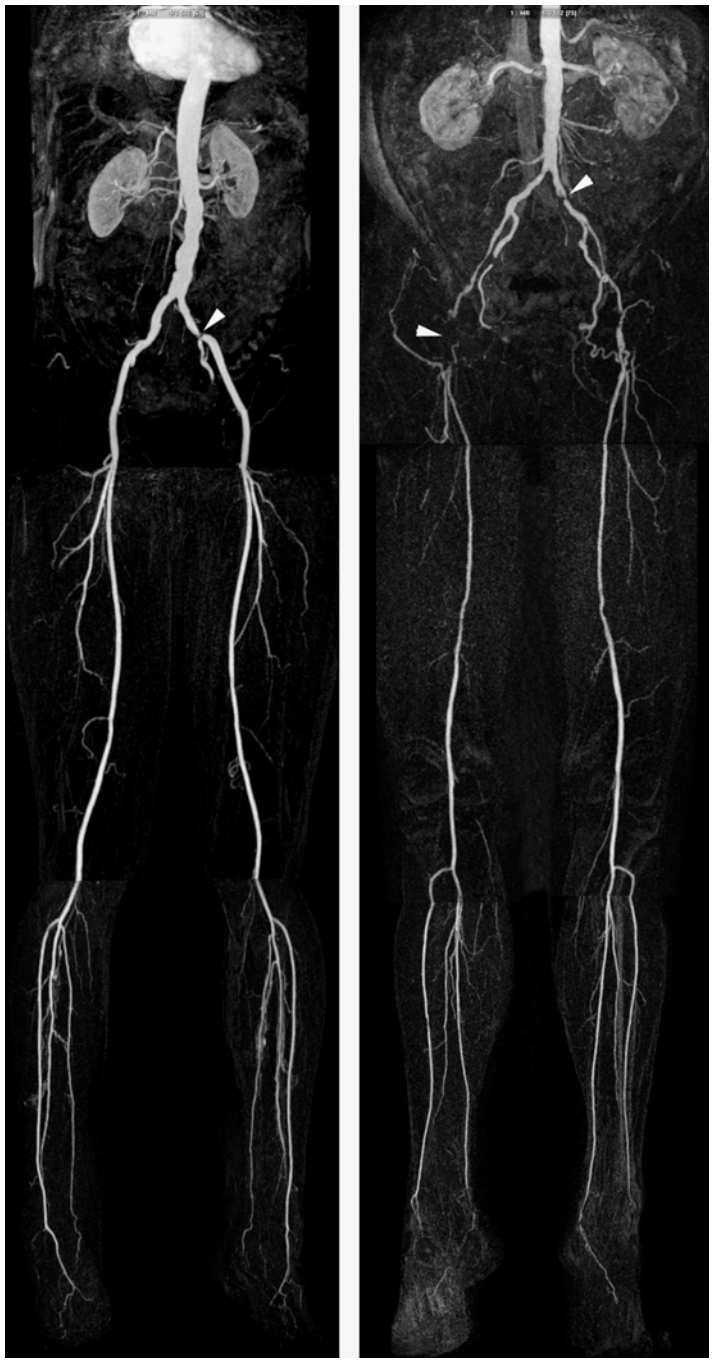

a b

Fig. 30.8a,b. CE-MRA examples of patients with intermittent claudication. **a** 51-year-old male with moderate intermittent claudication. There is an isolated high-grade stenosis in the left distal common iliac artery (*arrowhead*). **b** A 63-year-old male patient with severe intermittent claudication. There is an occlusion of the right external iliac and common femoral artery (*left arrowhead*), as well as a high-grade stenosis in the distal left common iliac artery (*right arrowhead*) (iliac and upper-leg stations: TR/TE: 4.0 ms/1.5 ms, SENSE acceleration factor *R*=2; lower-leg station: TR/TE: 4.0 ms/1.6 ms, *R*=3)

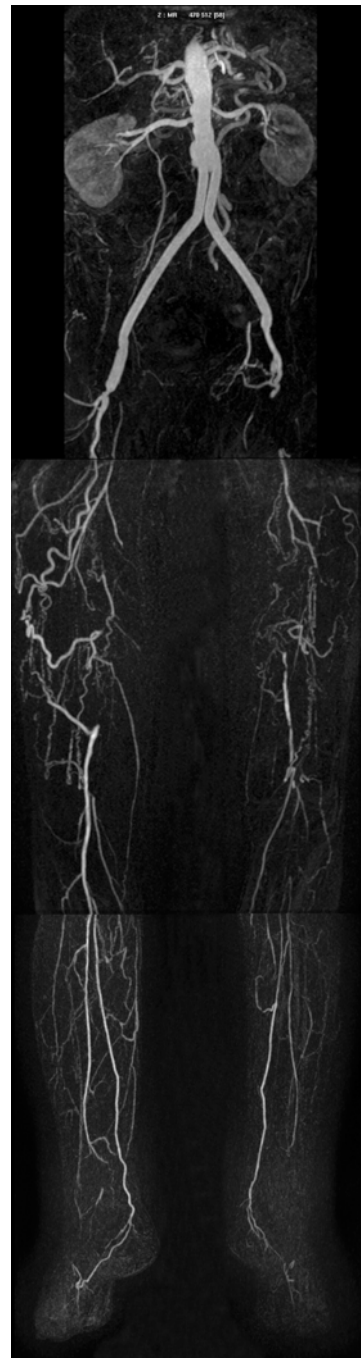

Fig. 30.9. A 57-year-old male patient with chronic critical ischemia of the left leg. The patient had undergone aortobifemoral bypass grafting for abdominal aortic aneurysm 3 years earlier. In the left leg there is an isolated popliteal artery segment that was used as a target vessel for an iliacofemoral bypass graft (iliac and upper-leg stations: TR/TE: 4.0 ms/1.5 ms, SENSE acceleration factor *R*=2; lower-leg station: TR/TE: 4.0 ms/1.6 ms, *R*=3)

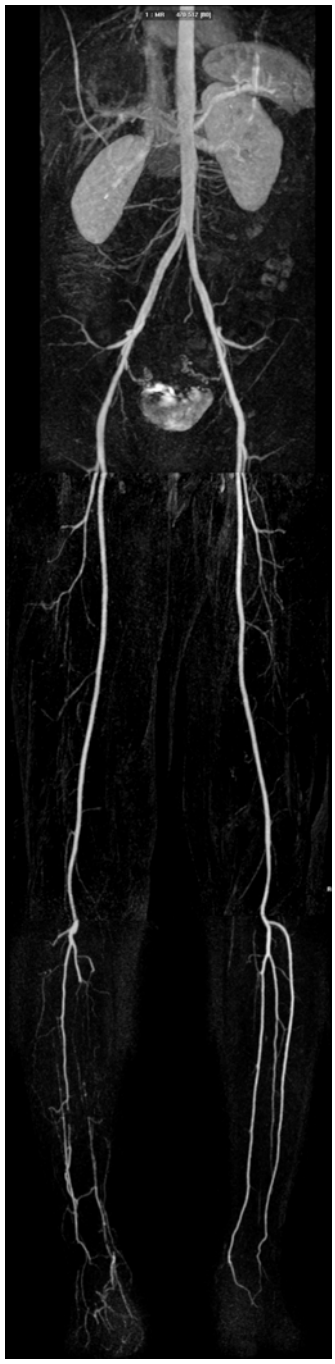

Fig. 30.10. A 45-year-old female patient with diabetes mellitus type 2. There is extensive occlusive disease in the right lower leg arteries. The proximal arteries are spared (iliac and upper-leg stations: TR/TE: 4.0 ms/1.5 ms, SENSE acceleration factor *R*=2; lower-leg station: TR/TE: 4.0 ms/1.6 ms, *R*=3)

References

Beard JD, Scott DJ, Evans JM, Skidmore R, Horrocks M (1988) Pulse-generated runoff: a new method of determining calf vessel patency. Br J Surg 75:361–363

Bezooijen R, van den Bosch HC, Tielbeek AV et al (2004) Peripheral arterial disease: sensitivity-encoded multiposition MR angiography compared with intraarterial angiography and conventional multiposition MR angiography. Radiology 231:263–271

Bilecen D, Aschwanden M, Heidecker HG, Bongartz G (2004) Optimized assessment of hand vascularization on contrast-enhanced MR angiography with a subsystolic continuous compression technique. AJR Am J Roentgenol 182:180–182

Bilecen D, Jager KA, Aschwanden M, Heidecker HG, Schulte AC, Bongartz G (2004) Cuff-compression of the proximal calf to reduce venous contamination in contrast-enhanced stepping-table magnetic Resonance angiography. Acta Radiol 45:510–515

Bitar R, Gladstone D, Sahlas D, Moody A (2004) MR angiography of subclavian steal syndrome: pitfalls and solutions. AJR Am J Roentgenol 183:1840–1841

Bley TA, Wieben O, Uhl M, Thiel J, Schmidt D, Langer M (2005) High-resolution MRI in giant cell arteritis: imaging of the wall of the superficial temporal artery. AJR Am J Roentgenol 184:283–287

Bley TA, Wieben O, Vaith P, Schmidt D, Ghanem NA, Langer M (2004) Magnetic resonance imaging depicts mural inflammation of the temporal artery in giant cell arteritis. Arthritis Rheum 51:1062–1063; author reply 1064

Bos C, Smits JH, Zijlstra JJ et al (2001) MRA of hemodialysis access grafts and fistulae using selective contrast injection and flow interruption. Magn Reson Med 45:557–561

de Vries M, Nijenhuis RJ, Hoogeveen RM, de Haan MW, van Engelshoven JM, Leiner T (2005) Contrast-enhanced peripheral MR angiography using SENSE in multiple stations: feasibility study. J Magn Reson Imaging 21:37–45

Dormandy JA, Ray S (1996) The natural history of peripheral arterial disease. In: Tooke JE, Lowe GD (eds) A textbook of vascular medicine. Arnold, London, 162–175

Dormandy JA, Rutherford RB (2000) Management of peripheral arterial disease (PAD). TASC Working Group. TransAtlantic Inter-Society Concensus (TASC). J Vasc Surg 31: S1–S296

Fellner FA, Requardt M, Lang W, Fellner C, Bautz W, Cavallaro A (2003) Peripheral vessels: MR angiography with dedicated phased-array coil with large-field-of-view adapter feasibility study. Radiology 228:284–289

Foo TK, Saranathan M, Prince MR, Chenevert TL (1997) Automated detection of bolus arrival and initiation of data acquisition in fast, three-dimensional, gadolinium-enhanced MR angiography. Radiology 203:275–280

Goyen M, Ruehm SG, Barkhausen J et al (2001) Improved multi-station peripheral MR angiography with a dedicated vascular coil. J Magn Reson Imaging 13:475–480

Griswold MA, Jakob PM, Heidemann RM et al (2002) Generalized autocalibrating partially parallel acquisitions (GRAPPA). Magn Reson Med 47:1202–1210

Heidemann RM, Griswold MA, Haase A, Jakob PM (2001) VD-AUTO-SMASH imaging. Magn Reson Med 45:1066–1074

Herborn CU, Ajaj W, Goyen M, Massing S, Ruehm SG, Debatin JF (2004) Peripheral vasculature: whole-body MR angiography with midfemoral venous compression – initial experience. Radiology 230:872–878

Ho KY, Leiner T, de Haan MW, Kessels AG, Kitslaar PJ, van Engelshoven JM (1998) Peripheral vascular tree stenoses: evaluation with moving-bed infusion-tracking MR angiography. Radiology 206:683–692

Ho KY, Leiner T, de Haan MW, van Engelshoven JM (1999) Peripheral MR angiography. Eur Radiol 9:1765–1774

Ho KY, Leiner T, van Engelshoven JM (1999) MR angiography of run-off vessels. Eur Radiol 1999; 9:1285–1289

Hoogeveen RM, Bakker CJ, Viergever MA (1998) Limits to the accuracy of vessel diameter measurement in MR angiography. J Magn Reson Imaging 8:1228–1235

Jakob PM, Griswold MA, Edelman RR, Sodickson DK (1998) AUTO-SMASH: a self-calibrating technique for SMASH imaging. SiMultaneous Acquisition of Spatial Harmonics. Magma 7:42–54

Korosec FR, Frayne R, Grist TM, Mistretta CA (1996) Time-resolved contrast-enhanced 3D MR angiography. Magn Reson Med 36:345–351

Kyriakos WE, Panych LP, Kacher DF et al (2000) Sensitivity profiles from an array of coils for encoding and reconstruction in parallel (SPACE RIP). Magn Reson Med 44:301–308

Leiner T, Ho KY, Nelemans PJ, de Haan MW, van Engelshoven JM (2000) Three-dimensional contrast-enhanced moving-bed infusion-tracking (MoBI-track) peripheral MR angiography with flexible choice of imaging parameters for each field of view. J Magn Reson Imaging 11:368–377

Leiner T, Nijenhuis RJ, Maki JH, Lemaire E, Hoogeveen R, van Engelshoven JM (2004) Use of a three-station phased array coil to improve peripheral contrast-enhanced magnetic resonance angiography. J Magn Reson Imaging 20:417–425

Luccichenti G, Cademartiri F, Ugolotti U, Marchesi G, Pavone P (2003) Magnetic resonance angiography with elliptical ordering and fluoroscopic triggering of the renal arteries. Radiol Med (Torino) 105:42–47

Maki JH, Wilson GJ, Eubank WB, Hoogeveen RM (2002) Utilizing SENSE to achieve lower station sub-millimeter isotropic resolution and minimal venous enhancement in peripheral MR angiography. J Magn Reson Imaging 15:484–491

Meaney JF, Ridgway JP, Chakraverty S et al (1999) Stepping-table gadolinium-enhanced digital subtraction MR angiography of the aorta and lower extremity arteries: preliminary experience. Radiology 211:59–67

Menzoian JO, LaMorte WW, Paniszyn CC et al (1989) Symptomatology and anatomic patterns of peripheral vascular disease: differing impact of smoking and diabetes. Ann Vasc Surg 3:224–228

Morasch MD, Collins J, Pereles FS et al (2003) Lower extremity stepping-table magnetic resonance angiography with multilevel contrast timing and segmented contrast infusion. J Vasc Surg 37:62–71

Murphy GJ, White SA, Nicholson ML (2000) Vascular access for haemodialysis. Br J Surg 2000; 87:1300–1315

Nijenhuis RJ, Leiner T, Cornips EM et al (2004) Spinal cord feeding arteries at MR angiography for thoracoscopic spinal surgery: feasibility study and implications for surgical approach. Radiology 233:541–547

NKF-DOQI (1997) Clinical practice guidelines for the treatment of anemia of chronic renal failure. National Kidney Foundation-Dialysis Outcomes Quality Initiative. Am J Kidney Dis 30:S192–240

Olin JW, Young JR, Graor RA, Ruschhaupt WF, Bartholomew JR (1990) The changing clinical spectrum of thromboangiitis obliterans (Buerger's disease). Circulation 82:IV3–8

Owen RS, Carpenter JP, Baum RA, Perloff LJ, Cope C (1992) Magnetic resonance imaging of angiographically occult runoff vessels in peripheral arterial occlusive disease. N Engl J Med 326:1577–1581

Planken RN, Tordoir JH, Dammers R et al (2003) Stenosis detection in forearm hemodialysis arteriovenous fistulae by multiphase contrast-enhanced magnetic resonance angiography: preliminary experience. J Magn Reson Imaging 17:54–64

Prince MR (1998) Contrast-enhanced MR angiography: theory and optimization. Magn Reson Imaging Clin N Am 6:257–267

Prince MR, Chabra SG, Watts R et al (2002) Contrast material travel times in patients undergoing peripheral MR angiography. Radiology 224:55–61

Pruessmann KP, Weiger M, Scheidegger MB, Boesiger P (1999) SENSE: sensitivity encoding for fast MRI. Magn Reson.Med 42:952–962

Reid SK, Pagan-Marin HR, Menzoian JO, Woodson J, Yucel EK (2001) Contrast-enhanced moving-table MR angiography: prospective comparison to catheter arteriography for treatment planning in peripheral arterial occlusive disease. J Vasc Interv Radiol 12:45–53

Rooke TW, Joyce JW (2000) Uncommon arteriopathies. In: Rutherford RB (ed) Vascular surgery. W.B. Saunders, Philadelphia, pp 418–434

Rudofsky G (2003) Peripheral arterial disease: chronic ischemic syndromes. In: Lanzer P, Topol EJ (eds) PanVascular medicine. Springer, Berlin Heidelberg New York, pp 1363–1422

Ruehm SG, Hany TF, Pfammatter T, Schneider E, Ladd M, Debatin JF (2000) Pelvic and lower extremity arterial imaging: diagnostic performance of three-dimensional contrast-enhanced MR angiography. AJR Am J Roentgenol 174:1127–1135

Schoenberg SO, Londy FJ, Licato P, Williams DM, Wakefield T, Chenevert TL (2001) Multiphase-multistep gadolinium-enhanced MR angiography of the abdominal aorta and runoff vessels. Invest Radiol 36:283–291

Siegelman ES, Charafeddine R, Stolpen AH, Axel L (2000) Suppression of intravascular signal on fat-saturated contrast-enhanced thoracic MR arteriograms. Radiology 217:115–118

Society for Vascular Surgery/North American Chapter (1986) Suggested standards for reports dealing with lower extremity ischemia. Prepared by the Ad Hoc Committee on Reporting Standards, International Society for Cardiovascular Surgery. J Vasc Surg 4:80–94

Sodickson DK, Manning WJ (1997) Simultaneous acquisition of spatial harmonics (SMASH): fast imaging with radiofrequency coil arrays. Magn Reson Med 38:591–603

Staple TW (1973) Retrograde venography of subcutaneous arteriovenous fistulas created surgically for hemodialysis. Radiology 106:223–224

Tay KY, JM UK-I, Trivedi RA et al (2005) Imaging the vertebral artery. Eur Radiol 15:1329–1343

van Vaals JJ, Brummer ME, Dixon WT et al (1993) "Keyhole" method for accelerating imaging of contrast agent uptake. J Magn Reson Imaging 3:671–675

Waldman GJ, Pattynama PM, Chang PC, Verburgh C, Reiber JH, de Roos A (1996) Magnetic resonance angiography of dialysis access shunts: initial results. Magn Reson Imaging 14:197–200

Wang Y, Chen CZ, Chabra SG et al (2002) Bolus arterial-venous transit in the lower extremity and venous contamination in bolus chase three-dimensional magnetic resonance angiography. Invest Radiol 37:458–463

Wang Y, Winchester PA, Khilnani NM et al (2001) Contrast-enhanced peripheral MR angiography from the abdominal aorta to the pedal arteries: combined dynamic two-dimensional and bolus-chase three-dimensional acquisitions. Invest Radiol 36:170–177

Weiger M, Pruessmann KP, Kassner A et al (2000) Contrast-enhanced 3D MRA using SENSE. J Magn Reson.Imaging 12:671–677

Wentz KU, Frohlich JM, von Weymarn C, Patak MA, Jenelten R, Zollikofer CL (2003) High-resolution magnetic resonance angiography of hands with timed arterial compression (tac-MRA). Lancet 361:49–50

Westenberg JJ, van der Geest RJ, Wasser MN et al (2000) Vessel diameter measurements in gadolinium contrast-enhanced three-dimensional MRA of peripheral arteries. Magn Reson.Imaging 18:13–22

Wikstrom J, Johansson L, Karacagil S, Ahlstrom H (2003) The importance of adjusting for differences in proximal and distal contrast bolus arrival times in contrast-enhanced iliac artery magnetic resonance angiography. Eur Radiol 13:957–963

Willinek WA, Gieseke J, Conrad R et al (2002) Randomly segmented central k-space ordering in high-spatial-resolution contrast-enhanced MR angiography of the supraaortic arteries: initial experience. Radiology 225:583–588

Wilman AH, Riederer SJ (1997) Performance of an elliptical centric view order for signal enhancement and motion artefact suppression in breath-hold three-dimensional gradient echo imaging. Magn Reson Med 38:793–802

Wilson GJ, Hoogeveen RM, Willinek WA, Muthupillai R, Maki JH (2004) Parallel imaging in MR angiography. Top Magn Reson Imaging 15:169–185

Wilson YG, George JK, Wilkins DC, Ashley S (1997) Duplex assessment of run-off before femorocrural reconstruction. Br J Surg 84:1360–1363

Winterer JT, Scheffler K, Paul G et al (2000) Optimization of contrast-enhanced MR angiography of the hands with a timing bolus and elliptically reordered 3D pulse sequence. J Comput Assist Tomogr 24:903–908

Wu C, Zhang J, Ladner CJ, Babb JS, Lamparello PJ, Krinsky GA (2005) Subclavian steal syndrome: diagnosis with perfusion metrics from contrast-enhanced MR angiographic bolus-timing examination – initial experience. Radiology 235:927–933

Yucel EK, Anderson CM, Edelman RR et al (1999) Magnetic resonance angiography: update on applications for extracranial arteries. Circulation 1999; 100:2284–2301

Pediatric Congenital Cardiovascular Disease

31

Stefan O. Schoenberg and Christian Fink

CONTENTS

31.1 Role of Angiography in Pediatric Congenital Cardiovascular Disease

Several pediatric congenital cardiovascular diseases result in life-threatening consequences for the infant and thus require urgent surgery. Often these congenital abnormalities involve both the heart and the large vessels, which require a stepwise approach for an ultimately curative surgical correction. The role for three-dimensional contrast-enhanced MR angiography (3D-CE-MRA) is to identify the enhancement kinetics in the lung and systemic circulation, the presence of aberrant arteries and veins as well as the three-dimensional relationship of the heart and large vessels including associated pathologies (Fig. 31.1). Common indications for pre-surgical MR imaging with contrast-enhanced 3D MR angiography include pulmonary atresia, tetralogy of Fallot and partial anomalous pulmonary venous return (PAPVR).

Pulmonary atresia or stenosis can be isolated or associated with other anomalies, such as in tetralogy of Fallot. Tetralogy of Fallot is among the most common cyanotic heart diseases in children and accounts for approximately 4% to 8% of all congenital cardiac lesions (Boechat et al. 2005). The role of 3D-CE-MRA is to identify various degrees of pulmonary artery stenosis ranging from focal narrowing of the main pulmonary trunk to complete absence of the main pulmonary artery or the non-confluence of the left and right pulmonary artery or its branches (Fig. 31.2). In the latter cases, enlarged major aorto-pulmonary collateral arteries (MAPCA) are present to sustain arterial blood flow to the lungs. For surgical reconstruction of the pulmonary arteries, it is of high importance that the intrapulmonary vascular bed is normal and only the mediastinal segment is stenosed or absent. In this case, complete reconstruction of the native pulmonary artery is feasible by various techniques, whereas otherwise pulmonary perfusion can only be maintained by the persistence of MAPCAs.

In addition, 3D-CE-MRA plays a major role for the assessment of post-surgical changes. One of the historically frequently performed initial operations is a Blalock-Taussig shunt in which blood flow to the lung is established by a surgical shunt between the subclavian artery and the ipsilateral pulmonary artery. This surgical technique is a palliative procedure aiming to maintain pulmonary perfusion until the pulmonary artery branches reach an age and size that permit complete repair. 3D-CE-MRA needs to evaluate the patency of the shunt, its caliber and any stenoses of the intrapulmonary vascular bed distally from the site of the shunt anastomosis. Since the late 1950s, a shunt anastomosis between the superior vena cava (SVC) and the right pulmonary artery has been performed, called the Glenn shunt, to improve pulmonary blood flow (Fig. 31.1). Compared to systemic-pulmonary artery shortcuts such as the Blalock-Taussig shunt,

S. O. Schoenberg, MD; C. Fink, MD
Department of Clinical Radiology, University Hospitals – Grosshadern, Ludwig Maximilian University of Munich, Marchioninistr. 15, 81377 Munich, Germany

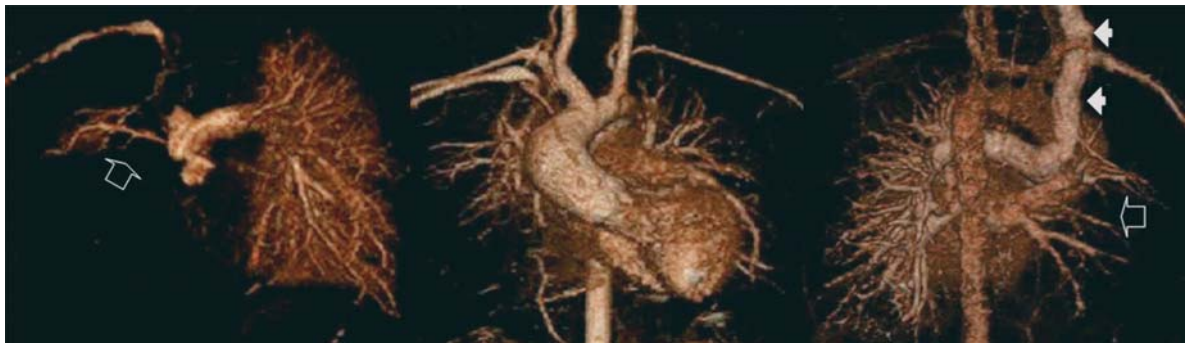

Fig. 31.1. A 5-year-old male infant with a high-grade stenosis of the main pulmonary artery. In the first frame (*left*) of the time-resolved 3D-CE-MRA complete enhancement of the left lung is present with a normal caliber of the left pulmonary artery while the right pulmonary artery is atretic with only small residual branches filling just a few areas of the right upper lung lobe (*open arrow*). In the second frame (*middle*) there is a persistent perfusion defect of the right middle and lower lung lobe present. Only in the third phase (image seen from a posterior reverse view), the venous inflow into the lungs is visualized demonstrating the presence of a Glenn shunt with anastomosis of the superior vena cava and the pulmonary artery (*solid arrowheads*). This example highlights the importance of a time-resolved MRA with parallel imaging in order to display all relevant vascular anatomy as well as functional parameters of pulmonary perfusion

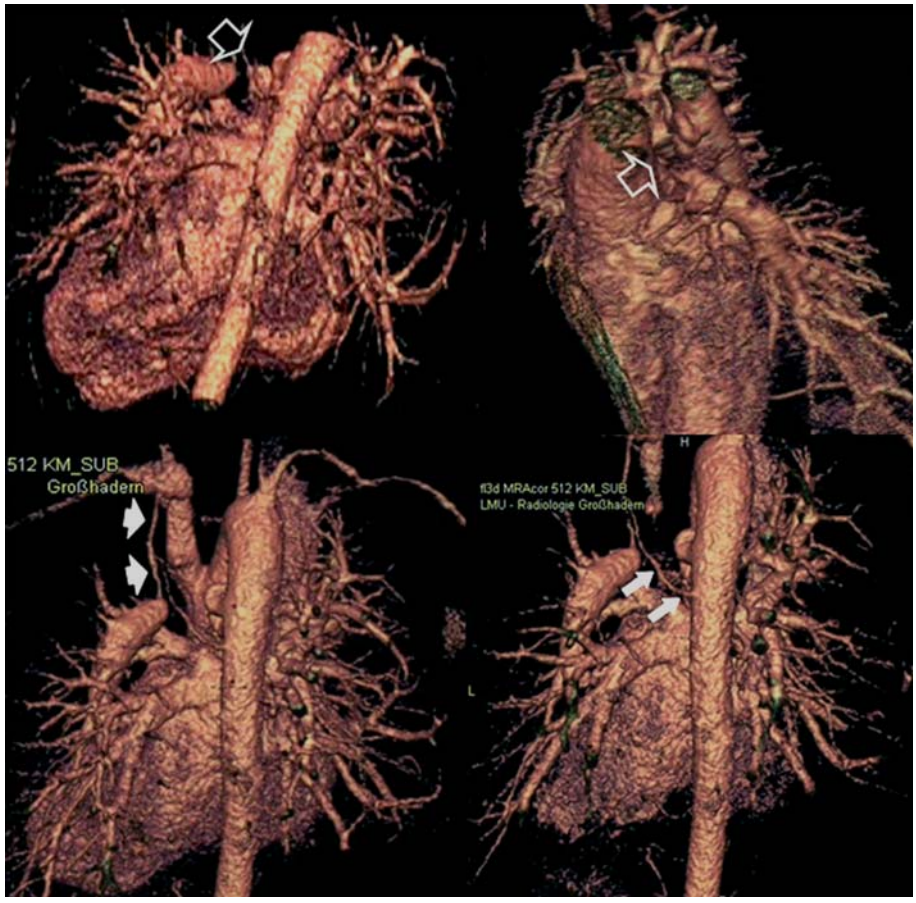

Fig. 31.2. A 4-year-old female infant with complete atresia of the main pulmonary artery (*open arrows* on *upper left* and *right images*). The patient presented with signs of poor oxygenation. The systemic phase of the time-resolved 3D-CE-MRA scan (*lower left image*, seen from a posterior reverse view) shows a Blalock-Taussig shunt with a too-small caliber to ensure adequate perfusion of the left lung (*solid arrowheads*). In addition, aortic-to-pulmonary collateral arteries are visualized in this phase of contrast-media transit (*lower right image*, seen from a posterior reverse view), also sustaining pulmonary perfusion (*solid arrows*)

the Glenn shunt does not create volume or pressure overload of the right ventricle. It provides venous flow to the lung fields for oxygenation rather than an arterio-venous mixture. The venous return is under relatively low pressure, unlike systemic-pulmonary artery shunts, and the risk for pulmonary artery distortion and late pulmonary vascular obstructive disease is substantially less. Unlike the classic Glenn shunt, the bidirectional Glenn shunt (BDG or hemi-Fontan) allows for flow to both lungs by dividing the superior vena cava and connecting it to the pulmonary artery. Any other existing connection from the heart or from a previous palliative shunt that is connected to the pulmonary artery is closed. Since this procedure leaves the pulmonary artery tree intact, it facilitates the subsequent Fontan operation in order to establish a total cavo-pulmonary connection (TCPC) without remaining cyanosis. Since this operation requires a low resistance of the pulmonary vascular bed, it is often preceded by the BDG procedure below the age of 6 months.

Another important anomaly that can be effectively imaged with 3D-CE-MRA is partial anomalous pulmonary venous return (PAPVR). In this congenital vascular anomaly, pulmonary veins are draining into the vena cava or right atrium instead of the left atrium, thus creating a left-to-right shunt. Most frequently, the right superior pulmonary artery drains into the superior vena cava, but virtually any abnormal drainage of pulmonary veins into any systemic venous vessel is possible (Fig. 31.3). A re-entering of the abnormal pulmonary vein into the vena cava below the diaphragm is termed "scimitar syndrome." Usually this anomalous venous return is to the inferior vena cava, but it may also be to the portal vein, a hepatic vein, or the right atrium. Any extent of anomalous pulmonary venous return can occur, ranging from a single abnormally draining pulmonary vein to a total anomalous pulmonary venous drainage of all four veins into the right atrium (Fig. 31.4). The role of 3D-CE-MRA prior to surgery is to identify the number and location of normally and abnormally draining veins as well as the anatomic relationship of the right and left atrium. In addition, the presence of a common conduit for the abnormally draining veins needs to be identified and its location relative to the atria in order to redirect blood flow to the left atrium. PAPVR is present in 10% to 15% of patients with atrial septal defects of the septum secundum and in nearly 100% of patients with defects involving the sinus venosus, which occurs at the level of the superior vena cava and the left atrium (Wang et al. 2003). This defect can be reliably detected if axial ECG-gated SSFP sequences are prescribed along the superior vena cava. In one study of 20 consecutively enrolled patients, a combined protocol of fast cine MRI and 3D-CE-MRA correctly diagnosed anomalous pul-

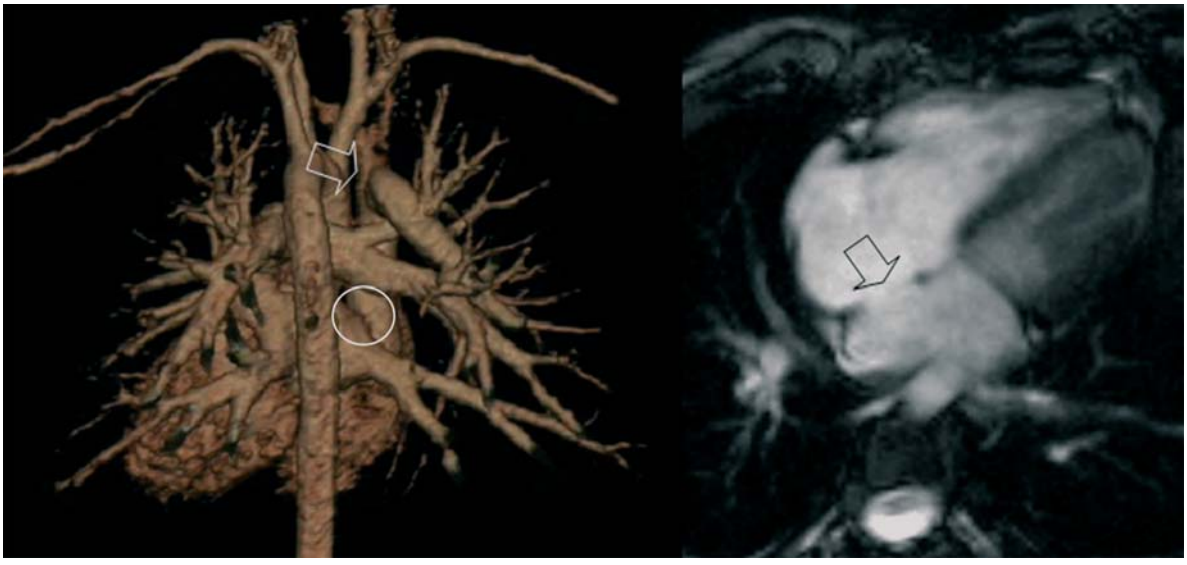

Fig. 31.3. A 6-year-old infant with partial anomalous pulmonary venous return (PAPVR). 3D-CE-MRA (seen from a posterior reverse view) demonstrates the right upper pulmonary vein emptying into the superior vena cava. Note that the other three pulmonary veins are regularly emptying into the left atrium, while the orifice of the right upper pulmonary vein is absent (*circle*). ECG-gated cardiac MRI with a steady-state free-precession sequence demonstrates a large ostium secundum atrio-septal defect (*open arrow*) associated with the PAPVR

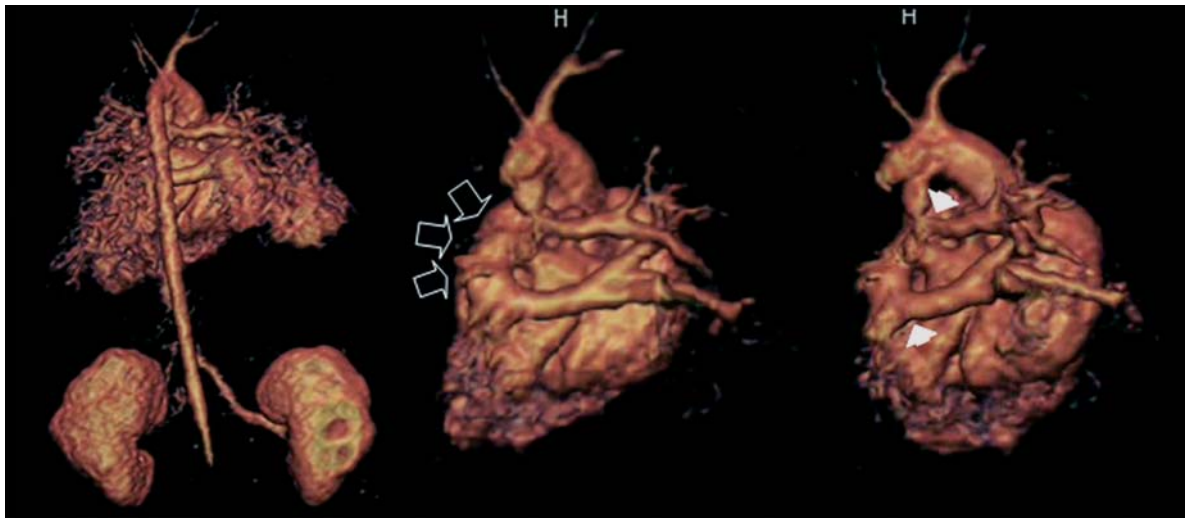

Fig. 31.4. A 2-week-old premature infant with total anomalous pulmonary venous return. Images are all seen from a posterior reverse view. The left upper and lower pulmonary veins are both emptying into a large collecting vessel behind the right heart (*open arrows*) draining into the right atrium. The right pulmonary veins are also draining into the right atrium (not displayed). This type of congenital cardiovascular anomaly requires associated septal defects to ensure mixing of oxygenated venous and deoxygenated systemic arterial blood for survival of the infant

monary veins and atrial septal defects in all patients who underwent surgery (Ferrari et al. 2001). For the assessment of abnormal pulmonary veins, the authors reported an agreement between MRI and catheterization results in 74% of patients and between MRI and transesophageal echocardiography in 75% of patients. For atrial septal defects, their MRI protocol agreed with catheterization and TEE in 53% and 83% of patients, respectively (Ferrari et al. 2001).

The complex post-surgical anatomy underlines the challenges for the implementation of 3D-CE-MRA. Since the patients are frequently below 6 months of age, high spatial resolution with isotropic voxel sizes of at least 1 mm^3 are mandatory in order to identify the individual vascular structures. In addition, the relevant vascular anatomy in the systemic venous and arterial circulation as well as the pulmonary arterial and venous tree may display substantially different enhancement kinetics, therefore requiring a temporally resolved MRA scan (Fig. 31.1).

31.2 Limitations to the Use of Parallel Imaging in the Pediatric Population

Since strict requirements for 3D-CE-MRA exist in terms of temporal and spatial resolution for the assessment of congenital cardiovascular disease, acceleration of the acquisition by parallel acquisition techniques is essential for a comprehensive diagnostic work-up. However, implementation of parallel imaging techniques in newborns or small infants is highly challenging for several reasons. First, dedicated multi-element coils for thoracic imaging that offer the possibility for highly accelerated parallel imaging within a small field of view are not commercially available from the large vendors. Second, existing multi-element receive-only head or knee coils for adults, which could be used for imaging of small infants, do not permit sufficient access for ventilation hoses and intravenous lines to connect to these critically ill intubated patients. Third, due to the small anatomy, high spatial resolution and small fields of view are mandatory, which result in a poor signal-to-noise ratio (SNR). Thus, further reduction of SNR by parallel imaging can only be tolerated to some extent, thereby limiting the use of higher acceleration factors.

31.3 Implementation of 3D-CE-MRA with Parallel Imaging on Standard MRI Systems

Despite the described limitations, parallel imaging can be successfully implemented in the clinical routine for angiographic assessment of congenital car-

diovascular disease. On a standard 8-channel MRI scanner, standard coils for adults with 8 to 12 elements (4 to 6 anterior and posterior) allow the acceleration of the 3D-CE-MRA scan with acceleration factors between R=2 and R=3. Since these coils have to be placed over the entire infant, a rectangular field of view of 19×38 cm² with a 384 matrix should be applied to minimize scan time, while preserving a spatial resolution of 1 mm both in the phase- and frequency-encoding direction. With a standard repetition time of 2.5 to 3 ms, 180 to 190 phase-encoding steps and 40 to 50 partitions, the scan time would add up to approximately 20 to 25 s. Using acceleration factors between 2 and 3, the entire acquisition can be reduced to approximately 8 s, thus allowing a multiphasic 3D-CE-MRA approach of four consecutive phases within a single breath-hold (Schoenberg et al. 2004).

Due to the rectangular field of view, extensive aliasing of the infant's arm into the region of interest occurs. In non-accelerated acquisitions, these aliasing artefacts can be eliminated by acquiring one unenhanced mask data set, either as a separate breath-hold scan or within the time-resolved acquisition. With the use of parallel imaging, additional artefacts from aliasing propagated into the center of the field of view can potentially occur, further affecting the image quality. However, it has been shown that the GRAPPA algorithm is relatively insensitive to these artefacts and thus can be considered the technique of choice for coronal 3D-CE-MRA acquisitions when small fields of view have to be chosen in the phase-encoding direction (Griswold et al. 2004).

In addition to the selection of scan parameters, a number of other factors have to be considered for successful imaging with 3D-CE-MRA in small infants. The amount and type of contrast media have to be carefully selected. Gadopentetate dimeglumine (Magnevist, Schering AG, Berlin, Germany) is approved for children under the age of 6 months to a maximum dose of 0.2 mmol/kg b.w., which equals 0.4 ml/kg b.w. Thus, the maximum volume of contrast media in a 2-kg premature newborn amounts to 0.8 ml (Fig. 31.4). Gadodiamide (Omniscan, GE Healthcare) has been reported as safe at 0.1 mmol/kg for MRI in infants younger than 6 months of age by a phase-III open-multicenter study (Marti-Bonmati et al. 2000). With such small doses and due to the short circulation times of the contrast media, it is important to realize which type of venous access the infant has. In case of a central intravenous line, injection rates of 0.5 ml/s are recommended, and the scan has to be initiated approximately 2 s prior to the injection in order to synchronize the central parts of k-space with the first pass of the contrast media bolus through the cardiopulmonary system. If the patient has a peripheral intravenous access in place, a temporal delay of 3 s between the start of the injection of the contrast media at a recommended rate of 1 ml/s and the subsequent initiation of the MRI scan is advised in order to ensure the arrival of the contrast media during the first time frame of the acquisition.

Special care needs to be taken to ensure good breath-hold acquisitions without respiratory motion through all four phases of the multiphasic 3D-CE-MRA scan. Usually, these infants are under general anesthesia and directly monitored by a team of anesthesiologists and nurses. Thus, a clear strategy between the latter and the radiologist and technician has to be elaborated concerning when to initiate the breath-hold period, the MRI scan and the contrast-media injection. This can be well realized if the anesthesia team is present in the scanner room; however, it needs to be ensured that all equipment for ventilation, anesthesia and monitoring of the infant is fully MR compatible.

31.4 Post-Processing of Time-Resolved 3D-CE-MRA Scans

For image analysis, all individual time frames of the multiphasic scan need to be subtracted from the unenhanced mask images in order to eliminate aliasing artefacts. It is important to review all consecutive data sets, since with congenital cardiovascular abnormalities or after surgical correction fundamentally different enhancement kinetics of vascular structures might occur compared with a normal vascular anatomy, i.e., vessels or surgical prostheses that are expected to enhance on the first time frame might not be visualized before the fourth time frame and vice versa.

Unlike in imaging of adults, it is recommended for post-processing of 3D-CE-MRA of infants to start with a volume-rendering algorithm in order to achieve a three-dimensional display of the data set. This helps to get an impression of the overall anatomic relationship of the different vascular structures of interest. In the next step, it is then advised to verify

a presumed diagnosis by detailed multiplanar reformats of the individual structures of interest.

In summary, time-resolved 3D-CE-MRA is a valuable tool for the assessment of congenital cardiovascular disease in infants. Due to the small size of these patients, special attention has to be paid to the selection of acquisition and injection parameters. Despite the fact that optimized multi-element coils for this clientele are still not widely available, a reasonable gain in speed can be realized with parallel acquisition techniques on standard MRI scanners.

References

Boechat MI, Ratib O, Williams PL, Gomes AS, Child JS, Allada V (2005) Cardiac MR imaging and MR angiography for assessment of complex tetralogy of Fallot and pulmonary atresia. Radiographics 25:1535–1546

Ferrari VA, Scott CH, Holland GA, Axel L, Sutton MS (2001) Ultrafast three-dimensional contrast-enhanced magnetic resonance angiography and imaging in the diagnosis of partial anomalous pulmonary venous drainage. J Am Coll Cardiol 37:1120–1128

Griswold MA, Kannengiesser S, Heidemann RM, Wang J, Jakob PM (2004) Field-of-view limitations in parallel imaging. Magn Reson Med 52:1118–1126

Marti-Bonmati L, Vega T, Benito C, Munoz A, Niewel M, Menor F, Meurer K, Encina JL (2000) Safety and efficacy of Omniscan (gadodiamide injection) at 0.1 mmol/kg for MRI in infants younger than 6 months of age: phase III open multicenter study. Invest Radiol 35:141–147

Schoenberg S, Kozlik-Feldmann R, Michaely HJ, Huber A, Netz H, Reiser MF (2004) Lungenvenenfehlmündungen bei Neugeborenen: Stellenwert der hochauflösenden mehrphasischen 3D MR-Angiographie mit paralleler Bildgebung. Fortschr Röntgenstr 176:S183

Wang ZJ, Reddy GP, Gotway MB, Yeh BM, Higgins CB (2003) Cardiovascular shunts: MR imaging evaluation. Radiographics 23:S181–194

High-Resolution Whole-Body MRA

32

Konstantin Nikolaou

CONTENTS

32.1 Clinical Background

Today, contrast-enhanced magnetic resonance angiography (CE-MRA) allows the reliable detection of regional stenotic vascular lesions with high diagnostic quality and accuracy, e.g., in the carotid arteries (Remondo et al. 2002), renal arteries (Schoenberg et al. 2003), abdominal and pelvic arteries (Schoenberg et al. 2002), and peripheral vessels (Huber et al. 2003); cf. the preceding chapters. In this regard, it has already become the diagnostic method of choice for certain indications, replacing invasive catheter-based X-ray angiography. However, a number of pathologic entities, e.g., atherosclerosis, diabetic vasculopathy, or inflammatory vessel changes like Takayasu arteritis, must be interpreted as systemic diseases, simultaneously affecting several regions of the body. Recently, a number of studies have investigated the feasibility of whole-body MRA (Ruehm et al. 2001; Herborn et al. 2004). In order to assess vascular pathologies in more than one vascular region, several of these previous studies shared dedicated rolling platforms that are combined with fast imaging in order to cover the entire body within a short scan time (Ruehm et al. 2000). First results have been promising, but come along with reduced image quality and spatial resolution, because of the necessity of fast imaging and coverage of a large field of view.

Parallel imaging is a recently introduced technique that is based on the spatial differences of the MR signal received by the elements of multi-channel RF coil systems. In essence, this technique holds the potential to increase spatial or temporal resolution at low cost in scan time. While this method has already gained acceptance in the clinical routine for the dedicated evaluation of certain organ systems, its use in a whole-body imaging protocol has so far been difficult (Weiger et al. 2000). This is predominantly because parallel imaging requires a well-defined position of various receiver coils, which used to be difficult for imaging of the entire body during table movement. Integrated parallel acquisition techniques with autocalibration of coils within each scan (see Chap. 8) allow using almost every combination of different receiver coils and permit repositioning of the table during the various steps of image acquisition (Griswold et al. 2002). Recently, it could be shown that by integrating auto-calibrating parallel-imaging techniques into a comprehensive whole-body cardiovascular screening protocol, all relevant vascular sys-

K. Nikolaou, MD
Department of Clinical Radiology, University Hospitals – Grosshadern, Ludwig Maximilian University of Munich, Marchioninistr. 15, 81377 Munich, Germany

tems can be examined without compromising spatial or temporal resolution (Kramer et al. 2004).

In addition to continuing improvements in software (i.e., MR sequences and acquisition strategies) and hardware (e.g., dedicated 32-channel whole-body MRI scanner), the development of new and refined MR contrast agents will further improve and change imaging strategies in whole-body MRA. Alternative paramagnetic contrast agents for enhancing MR angiographic images, known as blood-pool agents, are currently being studied. One such compound is gadofosveset trisodium (MS 325, EPIX Medical, Cambridge, Mass; Vasovist, Schering AG, Berlin, Germany). This compound is a small-molecule contrast agent that binds noncovalently to serum albumin. This reversible albumin binding of gadofosveset enhances the paramagnetic effectiveness of gadolinium and allows lower contrast agent doses than are needed with conventional MR agents (Lauffer et al. 1998). In addition, the albumin-binding characteristic extends the vascular lifetime of the agent, and thus gadofosveset allows longer vascular imaging time, potentially higher spatial resolution, and larger anatomic coverage. By combining new 32-channel MR systems with matrix coils and intravascular contrast agents, whole-body MRA can be performed with only a single injection of contrast agent, scanning the complete vasculature without compromises in spatial resolution or anatomic coverage, and without repositioning the patient.

32.2 Whole-Body MRA: Technical Developments

Below, consecutive technical advances over recent years will be described in detail, consequently improving whole-body MRA by a combination of technical innovations, new MR sequences and acquisition techniques, as well as optimized MR scanner designs. In detail, the following applications of whole-body MRA will be described and discussed:

- Whole-body MRA without parallel imaging
- Whole-body MRA implementing parallel imaging on a standard MR scanner
- Whole-body MRA implementing parallel imaging on a 32-channel MR scanner
- Whole-body MRA using a 32-channel scanner and intravascular contrast agent
- Whole-body MRA with moving-table continuous data acquisition

32.2.1 Whole-Body MRA Without Parallel Imaging: Compromises in Temporal and Spatial Resolution

Without parallel imaging, dedicated whole-body MR angiography is subject to several limitations concerning volume coverage, acquisition time, and spatial resolution, and requires several contrast injections. Limitations in the applicable dosage of contrast agent had initially restricted MRA to the display of the arterial region exceeding a single field of view greater 40 to 50 cm. Imaging of consecutive vascular regions with separate injections of contrast agent was therefore not possible. To enable a fast coverage of the whole body within an acceptable time and with acceptable doses of contrast agents, dedicated acquisition techniques have been developed. The implementation of bolus-chase techniques extended the imaging field of view to two to three regions (Meaney et al. 1999). To achieve complete coverage of the full body vasculature, dedicated rolling platforms have been implemented, scanning the different regions of the body subsequently by moving the receiver coil over the body on a dedicated rolling table (Herborn et al. 2004). A more recent design uses a pair of multi-channel phased-array surface coils that remain stationary at the iso-center of the scanner. The patient, lying on a moving-table bed, is slid between the coils to as many as five to six different positions for whole-body coverage (Quick et al. 2004).

The latest whole-body MR angiography protocol using a rolling-table-platform technique is based on the acquisition of five slightly overlapping 3D data sets in immediate succession, as described by Goyen et al. (2003). This way, 176 cm in the cranio-caudal direction are acquired in five stations, overlapped by 3 cm. On a state-of-the-art 1.5-T MR scanner (e.g., Siemens Sonata, Siemens Medical Solutions, Erlangen, Germany), the following parameters can be implemented for each of the five stations: TR/TE 2.4 ms/1.0 ms; flip angle 24°, field of view 390×390 mm²; matrix 256×220; slice thickness 1.9-2.9 mm, acquisition time per station 12 s, amounting to 72 s. The contrast injection protocol uses a biphasic injection with a dose of 0.2 mmol per kg body weight, diluted with saline to a total volume of 60 ml. The first 30 ml are administered at a rate of 1.2 ml/s, while the second 30 ml are administered at a rate of 0.7 ml/s, flushed with 30 ml of saline at 0.7 ml/s.

Initial results in the detection and characterization of vascular disease using the acquisition tech-

niques described above have been encouraging. However, despite employing fast imaging sequences, this approach still suffers from distinct limitations in spatial and temporal resolution. The reconstructed voxel volumes using such a protocol range from 1.8 mm^3 to 2.7 mm^3 on average using a zero-interpolation technique (ZIP), and from 5.1 mm^3 to 7.8 mm^3 without ZIP. While this spatial resolution may be acceptable for the detection of a severe arterial stenosis, accurate grading is not possible. Current state-of-the-art protocols for carotid and renal artery 3D CE-MRA require voxel volumes in the range of 1.0 mm^3 to identify the cut-off value of a 75% diameter reduction for hemodynamically significant stenosis (Schoenberg et al. 2005). Thus, whole-body MRA using rolling-table techniques without implementation of parallel imaging would require an additional high-resolution 3D MRA if a questionable stenosis is identified. This option is especially relevant for accurate assessment of carotid and renal artery disease.

32.2.2 Whole-Body MRA with Implementation of Parallel Imaging

Parallel-imaging techniques use the spatially distributed information provided by multi-channel phased-array surface coils in order to increase imaging speed in selected applications. In applications where sufficient signal-to-noise ratio (SNR) is available, the employment of these techniques often results in various possible improvements of the acquisition protocol, e.g., faster acquisition speed can be converted into increased spatial resolution. In this regard, parallel acquisition techniques have been successfully applied to MRA studies (Schoenberg et al. 2005). Concerning whole-body MRA, the implementation of parallel-imaging strategies results in a more flexible choice of imaging parameters. Determining the best balance between SNR, voxel size, contrast profile and acquisition time at each vascular bed is a challenging, and patient-specific, task.

Below, a possible contrast injection and data-acquisition protocol using parallel-acquisition strategies for whole-body MRA is being given. These protocol parameters have been implemented on a state-of-the art 1.5-T MR system with eight receiver channels (Magnetom Sonata, Siemens Medical Solutions, Erlangen, Germany). In contrast to dedicated whole-body MRI hardware such as the rolling table or platform technique described above, this protocol can be adjusted with the standard phased-array receiver coils provided by the manufacturer. Three contrast injections are needed to cover the whole body vasculature. The patient is lying on the scanner table in a supine position. For the first contrast injection (carotid arteries, patient positioning: supine, head first), a dedicated head-and-neck coil is used. This scan of the carotid arteries is performed using a test bolus scan prior to acquisition. A dose of 0.1 mmol/kg body weight of a standard gadolinium chelate (Magnevist, Schering AG, Berlin, Germany) is injected at a rate of 1.5 ml/s. For the second, biphasic injection, the patient has to be repositioned (supine, feet first), and the phased-array body coil covering the patient's abdomen, as well as a peripheral coil system covering the patient's legs, are applied. Then, for MR angiography of the abdomen and peripheral arteries, a biphasic injection protocol is used starting with 10 ml at an injection rate of 1 ml/s followed by an injection of 15 ml at an injection rate of 0.5 ml/s. In total, five stations are acquired: carotid arteries, abdominal aorta, thigh, calf and feet. All stations are acquired with a parallel-imaging acceleration factor of two using GRAPPA reconstruction (Griswold et al. 2002); this permits a spatial resolution ranging from 1.2 to 1.9 mm^3 for each station (Table 32.1).

It could be shown that parallel imaging offers the possibility to substantially increase temporal and spatial resolution for whole-body MRA (Quick et al. 2004). In a recent study by Kramer et al. (2004), in more than 85% of the cases, no venous overlay occurred and the image quality was rated as good or better. These results

Table 32.1. Protocol parameters for whole-body MRA on a standard MR scanner using parallel imaging and multiple contrast injections

	CA volume (ml)	Flow rate (ml/s)	Scan time (s)	Spatial resolution (mm^3)	Voxel volume (mm^3)
Injection 1					
Carotid arteries	15	1.5	19	0.9×1.7×1.3	1.9
Injection 2					
Abdominal aorta	10	1.5	21	1.6×0.8×1.5	1.9
Thigh			10	1.4×1.0×1.5	2.1
Injection 3					
Calf	15	0.7	10	1.3×0.9×1.3	1.5
Feet			21	1.2×1.1×0.9	1.2

(CA = contrast agent)

were only possible using a special set up of different surface receiver coils that allowed parallel imaging in all vascular regions. Due to the inbuilt auto-calibration scan, table movement in between the different scans is not a problem for parallel imaging (Jakob et al. 1999). However, two major limitations remain using a standard MRI system: the necessity of three injections of contrast agent, as well as having to reposition the patient after imaging the upper body. Therefore, whole-body MRA cannot be accomplished in one step, and is still rather time-consuming.

32.2.3 Optimized Whole-Body MRA Using Parallel Acquisition Techniques and a 32-Channel MR System

With implementation of dedicated 32-channel whole-body MR systems, a new approach for high-resolution whole-body 3D MRA becomes feasible: firstly, the availability of 32 channels with up to 76 connected matrix coil elements (cf. Chap. 13) offers the possibility to use higher parallel-imaging acceleration factors for 3D contrast-enhanced MRA, thus reducing the scan time significantly, without compromises in spatial resolution. Secondly, the improved geometry of the matrix coil system increases the SNR of the acquisition, which is important for parallel-imaging applications since parallel imaging by itself reduces SNR. Thirdly, the range of over 2 m of table movement allows the scanning of different vessel territories in a deliberate order. Now, a biphasic high-resolution scan of the lower legs can be performed directly after imaging the carotids, after only a single injection of contrast, i.e., the table movement is faster than the passage time of the contrast bolus passing from the carotid arteries to the lower legs; this allows a sufficient time window to ensure pure arterial contrast of the lower legs. This overcame the limitations of the earlier whole-body MRA protocols, where venous overlay was still present in a certain percentage of the cases, even with implementation of parallel imaging. Additional injections for a separate scan of the lower leg can hereby be completely avoided. Thus, the total dose of contrast media can be kept to a minimum. With the second injection of contrast, the abdominal aorta and thighs are scanned (Fig. 32.1). Details on an exemplary examination protocol for whole-body MRA using a 32-channel scanner and applying parallel imaging is given in Table 32.2 and 32.3. These protocol parameters have been implemented on a 1.5-T MR scanner (Magnetom Avanto, Siemens Medical Solutions, Erlangen, Germany) providing a gradient strength of 40 mT/m and maximum slew rate of 200 mT/m/ms. Surface coils are used for signal reception in all body regions. The surface coils, which cover the complete body, consist of up to 76 coil elements that can be assigned to 32 independent

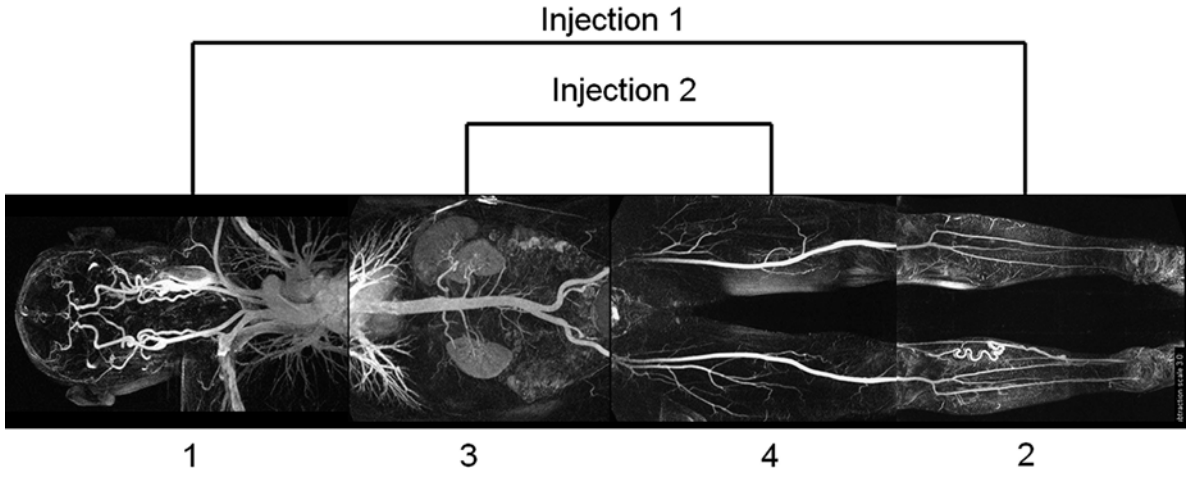

Fig. 32.1. High-spatial-resolution whole-body MRA acquired with parallel-imaging techniques on a whole-body scanner, enabling coverage of the whole body vasculature in four acquisition steps and with two injections of contrast agent, without the need of repositioning the patient. A biphasic high-resolution scan of the lower legs can be performed directly after imaging the carotids, after only a single injection of contrast, i.e., the table movement is faster than the passage time of the contrast bolus passing from the carotid arteries to the lower legs; this allows a sufficient time window to ensure pure arterial contrast of the lower legs (*1* and *2*). With the second injection of contrast, the abdominal aorta and thighs are scanned (*3* and *4*). All vascular beds (*1* to *4*) are acquired with a high spatial resolution

Table 32.2. Improved MRA parameters on a 32-channel whole-body scanner using parallel imaging and two contrast injections

Injection 1 (contrast: 0.1 mmol/kg body weight; flow rate: 1.5 ml/s)			
Vascular territory	Scan time (s)	Spatial resolution (mm^3)	Voxel volume (mm^3)
Carotid arteries	12	1.0×1.0×1.0	1.0
Lower leg	29	1.0×1.0×1.0	1.0
Injection 2 (contrast: 0.1 mmol/kg body weight; flow rate: 1.5 ml/s)			
Vascular territory	Scan time (s)	Spatial resolution (mm^3)	Voxel volume (mm^3)
Abdominal aorta	26	1.0×0.8×1.0	0.8
Upper leg	15	1.5×1.0×1.5	2.3

Table 32.3. Whole-body MRA using intravascular contrast agents: first-pass and steady-state imaging: Spatial resolution vs. acquisition time

First-pass imaging			
Vascular territory	Spatial resolution (mm^3)	Voxel volume (mm^3)	Acquisition time
Carotid arteries	1.0×1.0×1.0	1.000	0:12 min
Lower leg	1.0×1.0×1.0	1.000	0:29 min
Steady-state imaging			
Carotid arteries	0.8×0.8×0.8	0.512	0:40 min
Thorax	1.0×1.0×1.0	1.000	0:37 min
Abdomen	1.0×1.0×1.0	1.000	0:35 min
Upper leg	0.5×0.5×0.5	0.125	5:46 min
Knee	0.5×0.5×0.5	0.125	3:40 min
Lower leg	0.42×0.42×0.42	0.074	6:16 min

receiver channels, i.e., up to 32 coil elements may be used simultaneously in the field of view.

The consistent use of parallel imaging on a dedicated 32-channel whole-body scanner enables visualization of the vasculature with a true voxel volume of about 1.0 mm^3 for all vascular territories. Now, performing whole-body MRA in a screening scenario, the results of the whole-body exam can be expected to be as reliable as any dedicated single MRA exam of a certain vascular bed or any comparable reference modality. This is of special importance, as in a typical screening scenario, a low prevalence of pathological findings is expected; and additional reference studies are only acceptable if suspicion is based on MRI. The higher the diagnostic accuracy of whole-body MRA as the screening modality, the fewer additional studies will become necessary.

Concluding, with the implementation of parallel-imaging techniques on a dedicated whole body MR scanner, the total scan time can be significantly reduced, and superior image quality can be achieved. This is possible due to higher acceleration factors and the large range of table movement that obviates the necessity for repositioning of the patient. A second contributing factor is the coil design using matrix coil systems. Because of this whole-body matrix coil system with complete anatomic coverage, no patient or coil repositioning is necessary. Earlier, MRA was considered to typically overestimate the degree of stenosis rather than underestimating it, which was supposed to be regarded as a known limitation of MRA (Chiowanich et al. 2000). However, increased spatial resolution and SNR, as achieved with the newest MRA techniques described above, appear to be promising to enhance further the diagnostic accuracy of whole-body MRA examinations, even in small supra-aortal and lower-leg arteries.

32.2.4 Whole-Body MRA with Intravascular Contrast Agents

While the sufficient and optimized SNR achieved by the methods described above supports the spatial resolution required for detailed analysis of small branch arteries, time constraints induced by the short intra-arterial presence of any extracellular contrast agent limit data acquisition times and hence do not permit full exploitation of the spatial resolution potential. With the introduction of blood-pool contrast agents, these limitations might be overcome (Perrault et al. 2003).

Below, experience of an ongoing study combining state-of-the-art MRI techniques with a new intravascular contrast compound are reported. In this initial study, ten healthy volunteers and ten patients with proven atherosclerotic disease underwent whole-body MRA on a 32-channel 1.5-T MRI scanner with matrix coils and parallel imaging (Magnetom Avanto, Siemens Medical Solutions, Erlangen, Germany), using a similar coil setup as described above. For contrast-enhanced MRA, a strongly albumin-binding gadolinium chelate (gadofosveset trisodium, MS-325, EPIX Pharmaceuticals, Cambridge, MA and Schering AG, Berlin, Germany) with a half-life time of about 15 h, was injected with a flow rate of 1 ml/s. After injection of such a contrast

compound, two acquisition phases can be discerned. In the first pass, so-called "dynamic" phase, typical pure arterial angiograms can be obtained, similar to any arterial angiogram acquired with conventional extracellular contrast agents. In this "dynamic phase" after contrast injection, angiograms of the carotid arteries and calves were obtained during first pass of MS-325, with 1×1×1 mm^3 isotropic spatial resolution. Again, as described above, the carotid and lower-leg arteries can be acquired after a single contrast injection, as with the new whole-body scanner generations, table movement is faster than the passage of the contrast bolus, and purely arterial angiograms of the lower legs can be acquired, even in several phases. Following this dynamic phase, the contrast compound distributes in the complete body vasculature, arterial and venous system, and reaches an equilibrium phase after a few minutes. In this so-called "steady state," very high spatial resolutions can be achieved, as certain vascular beds such as the lower extremity can be scanned for several minutes, while vascular territories affected by respiratory and cardiac motion are still subject to limitations in acquisition time. Scanning the peripheral vasculature after injection of MS-325 in the steady-state, a voxel volume of 0.074 mm^3 (i.e., 0.45×0.45×0.45 mm^3 isotropic spatial resolution) was realized (Table 32.1). In the ten patients included, all results of whole-body MS-325 MR angiograms were compared to state-of-the-art MRA protocols using conventional gadolinium chelates as the reference standard.

First results of this ongoing study are very encouraging. In the dynamic phase, MR angiograms of both the carotid and the lower-leg arteries with pure arterial contrast were consistently obtained without venous overlay (Fig. 32.2). For the thorax and abdomen, MR angiograms were obtained with 1 mm^3 isotropic spatial resolution within a single breath-hold during the steady-state phase of MS-325. In the thigh, knee and calf station of the lower extremity, the ultra-high-resolution MRA datasets with voxel volumes between 0.075 and 0.130 mm^3 revealed excellent vessel contrast and high signal-to-noise ratio (Fig. 32.3). In patients, MRA data obtained with this protocol showed excellent agreement with the conventional reference MR angiograms.

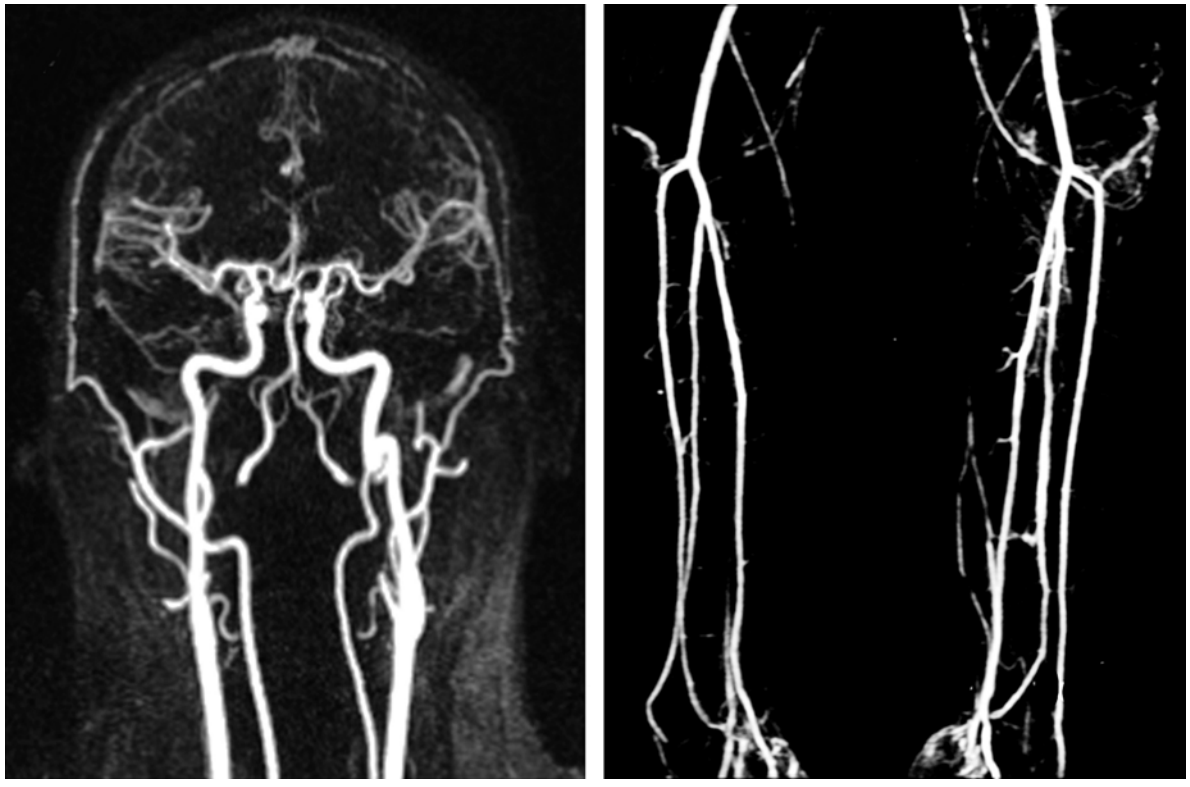

a b

Fig. 32.2a,b. Intravascular contrast agents in whole-body MRA. The contrast agent used is a strongly albumin-binding gadolinium chelate (gadofosveset trisodium, MS-325, EPIX Pharmaceuticals, Cambridge, MA, and Vasovist, Schering AG, Berlin, Germany) with a half-life time of about 15 h that is injected with a flow rate of 1 ml/s. In the dynamic phase (first pass of the contrast), angiograms of the carotid arteries **a** and calves **b** are obtained with 1×1×1 mm^3 isotropic spatial resolution

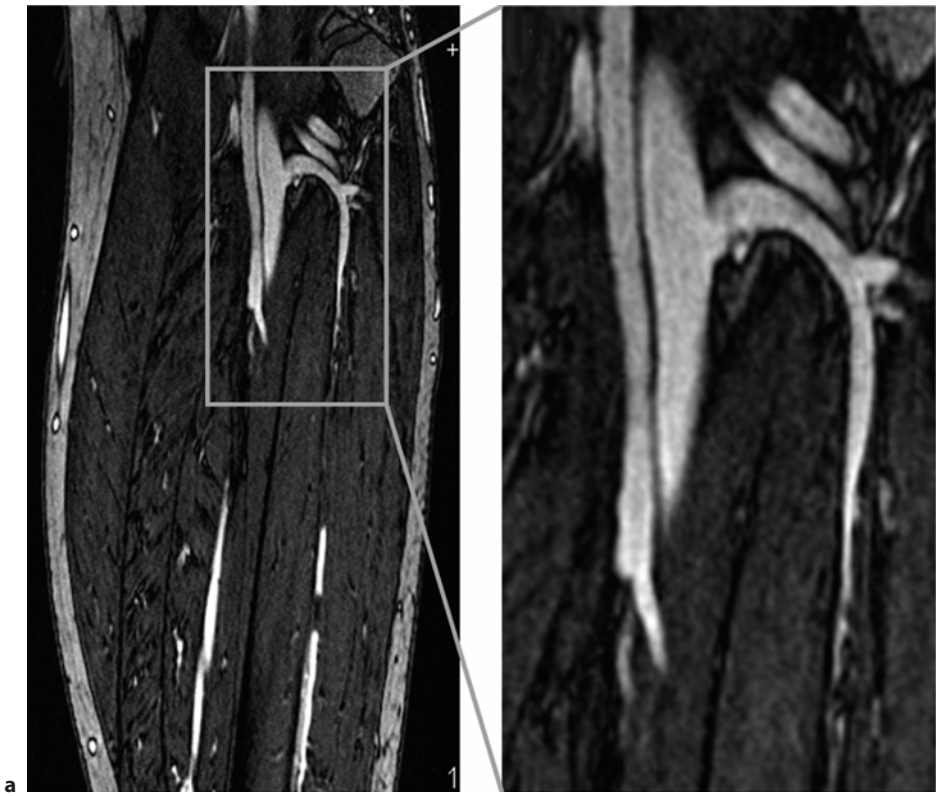

Fig. 32.3a,b. Steady-state imaging (equilibrium phase): After injection of an intravascular contrast compound (gadofosveset trisodium, MS-325, EPIX Pharmaceuticals, Cambridge, MA, and Vasovist, Schering AG, Berlin, Germany), a homogenous and high signal of the complete vasculature (arteries and veins) is maintained for a prolonged time period. During this "steady-state imaging," repeated measurements of selected vascular beds can be performed. In the example given, the calf is being examined after a single injection of the contrast, with increasing spatial resolutions of up to 0.42 mm voxel length (**a**, **b** = magnified view), i.e., a voxel volume of 0.074 mm^3. These high-resolution datasets display smallest vessels of the calf in great detail, maintaining a very high signal-to-noise ratio

Concluding, the combination of a whole-body MRI scanner and a blood-pool imaging agent allows acquisition of a whole-body MR angiogram without compromises in spatial resolution or anatomic coverage. First-pass imaging is feasible and delivers purely arterial angiograms comparable to state-of-the-art first-pass angiograms of any given vascular bed using standard, extracellular contrast agents. During steady-state, very high spatial resolutions can be achieved that have not been reported for three-dimensional MR angiograms so far.

32.2.5 Whole-Body MRA with Moving-Table Continuous Data Acquisition

As described above, the combination of a whole-body MR scanner with the application of intravascular contrast agents is one suitable approach to overcome the constraints in timing and in spatial resolution of conventional multi-station, first-pass MRA techniques. Recently, other new methods are being introduced to overcome the restrictions of whole-body MR imaging with multi-station techniques. This is done with continuous MR data acquisition while the scanner table is being moved, a technique referred to as "continuously moving table" (CMT) MRI. Upon measurement, each MR signal is mapped into data space according to the specific longitudinal table position at which it was acquired, creating a dataset with one arbitrarily long, net field of view in the longitudinal direction. These methods utilize continuous acquisition of either 2D or 3D data sets. While 2D moving-table acquisitions with the slice selection along *z*-direction are promising (Barkhausen et al. 2001; Shankaranarayanan et al. 2003), this approach is

substantially constrained in *z*-direction resolution, in SNR due to the restriction to 2D imaging, and/or by scan time. On the other side, a 3D axial approach can be limited by the RF slab profile. Other techniques combine the resolution and SNR benefits of 3D acquisition with no apparent boundary artefacts (Kruger et al. 2002). This way, the motion can be accounted for exactly with sub-pixel accuracy. Also, phase (Dietrich and Hajnal 1999) or frequency (Zhu and Dumoulin 2003) encoding along the *z*-direction may overcome the limitations described above, but these algorithms tend to be demanding on field homogeneity and excitation profiles. Such techniques also inherently require knowledge of the actual table position during data acquisition. Zenge et al. (2005) have combined a data reconstruction method recently introduced by Kruger et al. (2002) for the frequency encoding along z-direction, with a manually positioned moving-table platform with integrated surface phased-array RF coils and high-precision positional feedback provided by a laser sensor that is triggered by the MR scanner (Zenge et al. 2004). The positional data are used to compensate for nonlinear manual table translation in order to enable continuous 2D and 3D whole-body data acquisition during table movement. In general, methods used to generate extended-field-of-view images fall into three distinct types: (1) methods in which the echo readout is orthogonal to the table motion direction (Liu and Rutt. 1998), (2) methods in which the echo readout is along the direction of table motion (Kruger et al. 2002), and (3) methods that use projection reconstruction to distribute the echo readout in all directions (Fain et al. 2004). The integration of parallel imaging using both SENSE or GRAPPA techniques with continuously moving-table MRI have recently been demonstrated (Keupp et al. 2005; Zenge et al. 2005). The implementation of parallel-imaging CMT is not trivial and must address specific issues including coils, sensitivity-map calibration, and image reconstruction. Another technical consideration is gradient warp or non-linearity. Specifically, the gradient-warp phenomenon imposes constraints on the manner and order in which calibration for parallel imaging, unfolding, and gradient-warp correction must occur in CMT reconstruction. Future work will have to focus on these issues to further elaborate on this fascinating new acquisition technique. Figure 32.4 shows examples of CMT-MRA of the peripheral run-off in healthy volunteers, both without and with implementation of parallel-imaging techniques.

32.3 Whole-Body MRA: Clinical Examples for Applications

Below, selected and exemplary disease entities are discussed. In these pathologies, whole-body MRA techniques could be in particular preferable to the extensive standard work-up using a whole array of diagnostic tests and imaging modalities. Here, whole-body MRA could enable a fast, reliable, and cost-effective comprehensive diagnostic work-up.

32.3.1 Whole-Body MRA in Systemic Atherosclerosis

Treatment strategies of atherosclerotic vessel wall lesions, including surgical and percutaneous catheter-based interventions as well as pharmacological treatment, depend on the accurate classification of the disease with respect to the location, extent, and severity of arterial involvement. For this purpose several imaging techniques, including conventional catheter angiography, duplex ultrasound, as well as computed-tomography angiography and magnetic-resonance angiography, are in clinical use. Despite the recognition that atherosclerotic disease is systemic, affecting the entire arterial system, the diagnostic approach to atherosclerosis has remained segmental. Largely, this approach has been a reflection of limitations inherent to the imaging techniques used. Risks associated with invasiveness, contrast, and radiation-dose limitations as well as cost and time constraints have meant that diagnostic analysis has focused on one arterial region. In recent years, first reports have shown the ability of whole-body MRA techniques to depict and quantify vascular lesions accurately in several anatomic regions within a single MRA examination (Ruehm et al. 2001). More elaboration on the technique of whole-body MRA for the systemic detection of atherosclerosis has brought improvements in diagnostic accuracy, patient management, and acquisition strategies (Herborn et al. 2004). Still, the clinical utility and socio-economic value of this diagnostic approach in the setting of preventive imaging or screening will require further validation in larger patient cohorts (Goyen et al. 2005) (see chapter 40 for more details on the potential of whole-body MRA in screening for systemic atherosclerosis).

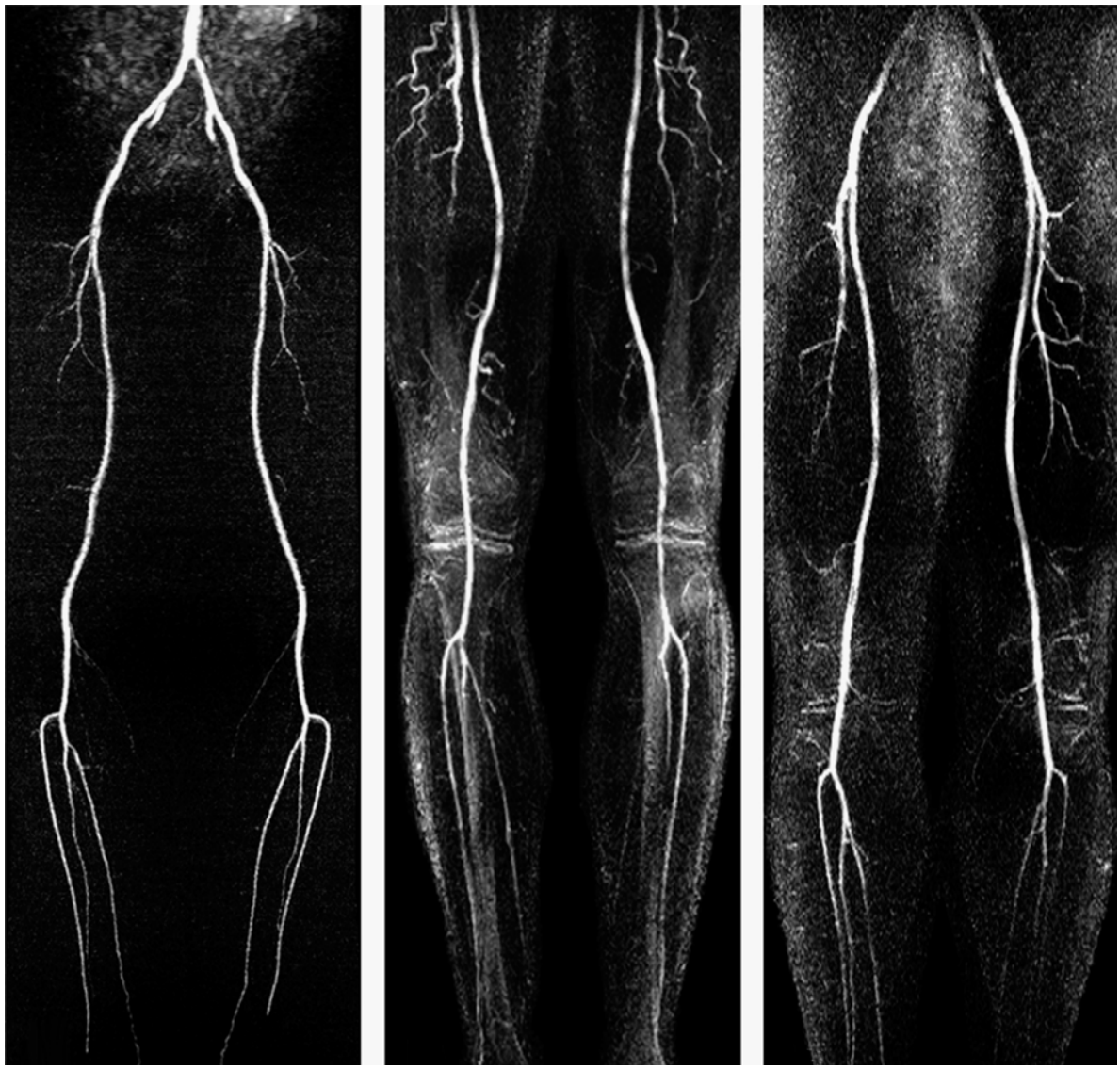

Fig. 32.4a–c. Peripheral run-off MRA using a continuously-moving-table (*CMT*) technique: **a** shows the MRA of a healthy volunteer using a standard 3D CMT method, and **b** and **c** show two MRA datasets of healthy volunteers acquired with parallel-imaging techniques (SENSE). Courtesy of Dr. Kruger and Dr. Riederer, Department of Radiology, Mayo Clinic College of Medicine, Rochester, Minnesota, USA

32.3.2 Takayasu Arteritis

Takayasu arteritis is a form of large vessel vasculitis with a possible autoimmune origin that may cause stenosis of the aorta and its major branches. Six types of Takayasu arteritides are recognized; the type depends on whether the ascending aorta, descending thoracic aorta, abdominal aorta, aortic cervicobrachial branches, or renal arteries are affected. The coronary and pulmonary arteries are also sometimes involved. Clinical features of the disease include diminished or absent pulses, claudication, hypertension, and mesenteric angina. Conventional angiography has been the standard imaging tool for the diagnosis and evaluation of Takayasu arteritis, although it demonstrates only the lumen of the vessel and has a higher risk for complications such as dissection in these patients. Less invasive cross-sectional methods like three-dimensional MRA can effectively demonstrate thickening of the vessel wall, which may be the earliest manifestation of the disease, occurring

before stenosis and dilatation. Additional high-resolution T1- and T2-weighted MR imaging in particular allows better soft-tissue differentiation and can show other signs of inflammation, including mural edema and increased mural vascularity. Other advantages of MR imaging are the lack of iodinated contrast material or ionizing radiation. When compared to conventional angiography, MR angiography can effectively provide additional anatomic information, including vessel wall thickness; it is also capable of demonstrating mural inflammatory signs, which sometimes represent the only clue to diagnosis in the early phases (Nastri et al. 2004). Consequently, MR angiography is a reliable alternative tool for the diagnosis, assessment of severity, and follow-up of large vessel vasculitides such as Takayasu arteritis, with the advantages of not using nephrotoxic contrast media or ionizing radiation. In Fig. 32.5, an example of a whole-body MR angiogram in a patient suffering from Takayashu arteritis is given.

32.3.3 Diabetes

In patients with diabetes, assessment of the vascular system is essential, due to generalized macro- and microangiopathy, typically associated with diffuse medial vascular calcifications. Additionally, detailed information on the vascular supply can help deline-

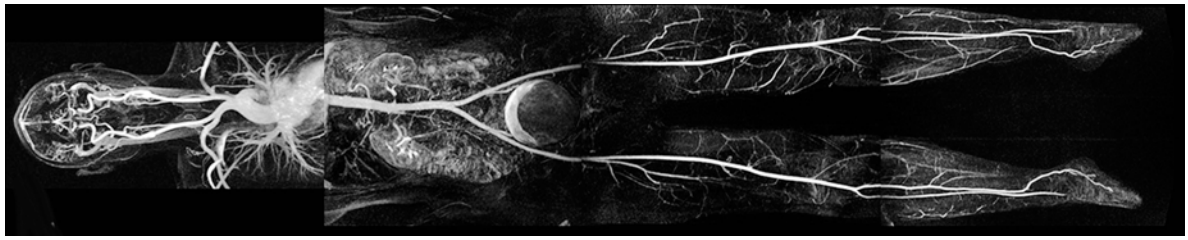

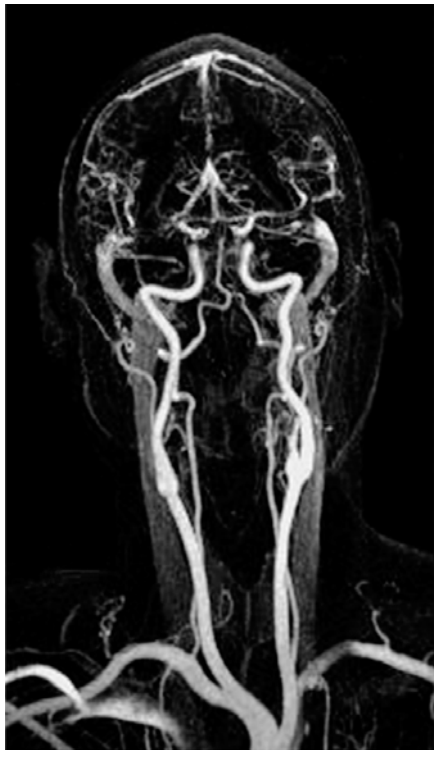

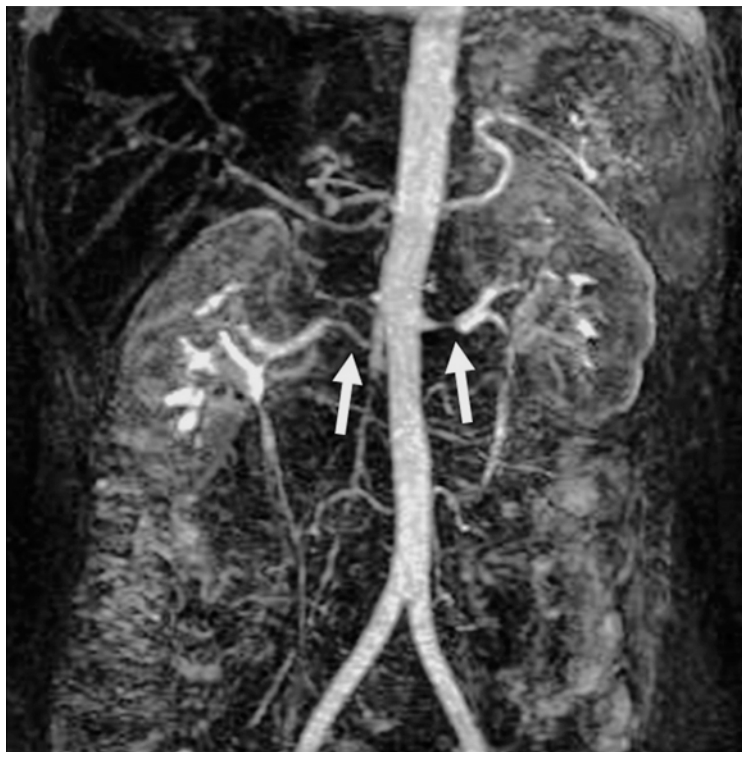

Fig. 32.5a–c. In a 38-year-old woman with suspected Takayasu arteritis, whole-body MRA was performed on a 32-channel whole-body MR scanner with parallel imaging. The complete vasculature was examined **a.** Taken from this whole-body MRA dataset, the high-resolution MR angiograms of the carotid arteries and the supraaortic vessels **b** did not show any pathologic findings. At the height of the renal arteries, however, high-grade bilateral renal artery stenoses could be proven as a result of the inflammatory involvement of these vascular territories in Takayashu arteritis **c**

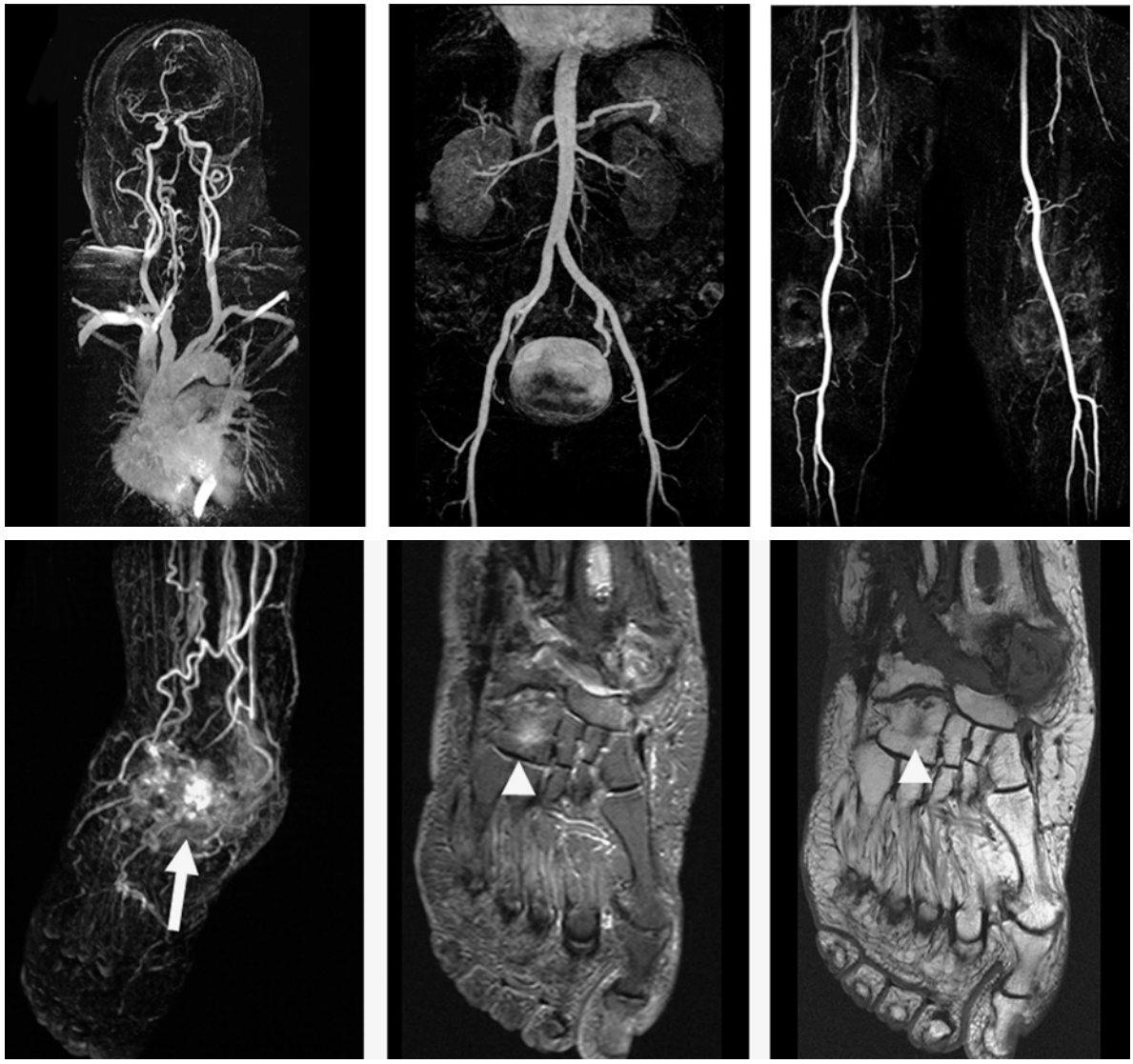

Fig. 32.6a,b. A 66-year-old male patient with a long history of diabetes, suffering from a soft-tissue lesion at his right foot. A whole-body MRA was performed on a 32-channel MR system using parallel-imaging techniques. Severe vascular pathologies could be excluded in the carotid arteries, the abdominal aorta, and the upper leg **a**. However, in the patient's right foot, a severe soft-tissue hyperperfusion was demonstrated due to a diabetic Charcot's foot, as seen on the lower station of the whole-body MR angiogram (**b**, *arrow*). In the additional STIR and T1-weighted sequences, inflammatory involvement of the cuboid bone can be seen (**b**, *arrowheads*)

ate the relative contribution of neurologic and vascular abnormalities causing a given lesion, e.g., in the diabetic foot. In diabetic pedal vascular disease, extensive and multisegmental involvement of the normal collateral circulation is common (Chomel et al. 2004). Surgical revascularization remains the most important therapeutic option for limb salvage in patients with severe arterial occlusive disease, particularly those with diabetes. Digital subtraction angiography has traditionally been used for the precise preoperative imaging that is required when a surgical revascularization technique is indicated. However, 3D contrast-enhanced MR angiography is rapidly gaining acceptance as a versatile non-invasive alternative to conventional angiography. With the implementation of whole-body MRA techniques, indications for 3D contrast-enhanced MR angiography in diabetic patients will be likely to increase. Figure 32.6 gives an example the whole-body MR angiogram of a patient with diabetes, enabling a complete and detailed diagnostic workup of the body vasculature and of a diabetic foot.

32.4 Conclusion

Up to now, long acquisition times and limitations in temporal and spatial resolution were limiting factors for using MRI as a tool for whole-body angiography. New acquisition techniques such as parallel imaging and multi-slice sequences together with new developed hardware can solve these problems. It is now possible to achieve a comprehensive exam including whole-body MRA, without compromising temporal or spatial resolution within a reasonable scan time. In the future, the application of intravascular contrast agents will further enhance image quality, protocol flexibility, and diagnostic accuracy.

References

Barkhausen J, Quick HH, Lauenstein T, Goyen M, Ruehm SG, Laub G, Debatin JF, Ladd ME (2001) Whole-body MR imaging in 30 s with real-time true FISP and a continuously rolling table platform: feasibility study. Radiology 220:252–256

Chiowanich P, Mitchell DG, Ortega HV, Mohamed F (2000) Arterial pseudostenosis on first-pass gadolinium-enhanced three-dimensional MR angiography: new observation of a potential pitfall. AJR Am J Roentgenol 175:523–527

Chomel S, Douek P, Moulin P, Vaudoux M, Marchand B (2004) Contrast-enhanced MR angiography of the foot: anatomy and clinical application in patients with diabetes. AJR Am J Roentgenol 182:1435–1442

Dietrich O, Hajnal JV (1999) Extending the coverage of true volume scans by continuous movement of the subject. In: Proceedings of the 7th Annual Meeting of ISMRM, Philadelphia, p 1653

Fain SB, Browning FJ, Polzin JA, Du J, Zhou Y, Block WF, Grist TM, Mistretta CA (2004) Floating table isotropic projection (FLIPR) acquisition: a time-resolved 3D method for extended field-of-view MRI during continuous table motion. Magn Reson Med 52:1093–1102

Fain SB, King BF, Breen JF, Kruger DG, Riederer SJ (2001) High-spatial-resolution contrast-enhanced MR angiography of the renal arteries: a prospective comparison with digital subtraction angiography. Radiology 218:481–490

Goyen M, Herborn CU, Kroger K, Lauenstein TC, Debatin JF, Ruehm SG (2003) Detection of atherosclerosis: systemic imaging for systemic disease with whole-body three-dimensional MR angiography--initial experience. Radiology 227:277–282

Goyen M, Herborn CU, Kroger K, Ruehm SG, Debatin JF (2005) Total-body 3D magnetic resonance angiography influences the management of patients with peripheral arterial occlusive disease. Eur Radiol 1-7

Griswold MA, Jakob PM, Heidemann RM, Nittka M, Jellus V, Wang J, Kiefer B, Haase A (2002) Generalized autocalibrating partially parallel acquisitions (GRAPPA). Magn Reson Med 47:1202–1210

Herborn CU, Goyen M, Quick HH, Bosk S, Massing S, Kroeger K, Stoesser D, Ruehm SG, Debatin JF (2004) Whole-body 3D MR angiography of patients with peripheral arterial occlusive disease. AJR Am J Roentgenol 182:1427–1434

Ho KY, Leiner T, de Haan MW, Kessels AG, Kitslaar PJ, van Engelshoven JM (1998) Peripheral vascular tree stenoses: evaluation with moving-bed infusion-tracking MR angiography. Radiology 206:683–692

Huber A, Scheidler J, Wintersperger B, Baur A, Schmidt M, Requardt M, Holzknecht N, Helmberger T, Billing A, Reiser M (2003) Moving-table MR angiography of the peripheral runoff vessels: comparison of body coil and dedicated phased array coil systems. AJR Am J Roentgenol 180:1365–1373

Huston J, Fain SB, Wald JT, Luetmer PH, Rydberg CH, Covarrubias DJ, Riederer SJ, Bernstein MA, Brown RD, Meyer FB, Bower TC, Schleck CD (2001) Carotid artery: elliptic centric contrast-enhanced MR angiography compared with conventional angiography. Radiology 218:138–143

Jakob PM, Griswold MA, Edelman RR, Manning WJ, Sodickson DK (1999) Accelerated cardiac imaging using the SMASH technique. J Cardiovasc Magn Reson 1:153–157

Keupp J, Aldefeld B, Bornert P (2005) Continuously moving table SENSE imaging. Magn Reson Med 53:217–220

Kramer H, Schoenberg SO, Nikolaou K, Huber A, Struwe A, Winnik E, Wintersperger B, Dietrich O, Kiefer B, Reiser MF (2004) [Cardiovascular whole body MRI with parallel imaging]. Radiologe 44:835–843

Kruger DG, Riederer SJ, Grimm RC, Rossman PJ (2002) Continuously moving table data acquisition method for long FOV contrast-enhanced MRA and whole-body MRI. Magn Reson Med 47:224–231

Lauffer RB, Parmelee DJ, Dunham SU, Ouellet HS, Dolan RP, Witte S, McMurry TJ, Walovitch RC (1998) MS-325: albumin-targeted contrast agent for MR angiography. Radiology 207:529–538

Liu K, Rutt BK (1998) Sliding interleaved kY (SLINKY) acquisition: a novel 3D MRA technique with suppressed slab boundary artefact. J Magn Reson Imaging 8:903–911

Meaney JF, Ridgway JP, Chakraverty S, Robertson I, Kessel D, Radjenovic A, Kouwenhoven M, Kassner A, Smith MA (1999) Stepping-table gadolinium-enhanced digital subtraction MR angiography of the aorta and lower extremity arteries: preliminary experience. Radiology 211:59–67

Nastri MV, Baptista LP, Baroni RH, Blasbalg R, de Avila LF, Leite CC, de Castro CC, Cerri GG (2004) Gadolinium-enhanced three-dimensional MR angiography of Takayasu arteritis. Radiographics 24:773–786

Perrault LP, Edelman RR, Baum RA, Yucel EK, Weisskoff RM, Shamsi K, Mohler ER (2003) MR angiography with gadofosveset trisodium for peripheral vascular disease: phase II trial. Radiology 229:811–820

Quick HH, Vogt FM, Maderwald S, Herborn CU, Bosk S, Gohde S, Debatin JF, Ladd ME (2004) High spatial resolution whole-body MR angiography featuring parallel imaging: initial experience. Rofo 176:163–169

Remonda L, Senn P, Barth A, Arnold M, Lovblad KO, Schroth G (2002) Contrast-enhanced 3D MR angiography of the carotid artery: comparison with conventional digital subtraction angiography. AJNR Am J Neuroradiol 23:213–219

Ruehm SG, Goyen M, Barkhausen J, Kroger K, Bosk S, Ladd ME, Debatin JF (2001) Rapid magnetic resonance angiography for detection of atherosclerosis. Lancet 357:1086–1091

Ruehm SG, Goyen M, Quick HH, Schleputz M, Schleputz H, Bosk S, Barkhausen J, Ladd ME, Debatin JF (2000) [Whole-body MRA on a rolling table platform (AngioSURF)]. Rofo 172:670–674

Schoenberg SO, Essig M, Hallscheidt P, Sharafuddin MJ, Stolpen AH, Knopp MV, Yuh WT (2002) Multiphase magnetic resonance angiography of the abdominal and pelvic arteries: results of a bicenter multireader analysis. Invest Radiol 37:20–28

Schoenberg SO, Rieger J, Johannson LO, Dietrich O, Bock M, Prince MR, Reiser MF (2003) Diagnosis of renal artery stenosis with magnetic resonance angiography: update 2003. Nephrol Dial Transplant 18:1252–1256

Schoenberg SO, Rieger J, Weber CH, Michaely HJ, Waggershauser T, Ittrich C, Dietrich O, Reiser MF (2005) High-spatial-resolution MR angiography of renal arteries with integrated parallel acquisitions: comparison with digital subtraction angiography and US. Radiology 235:687–698

Shankaranarayanan A, Herfkens R, Hargreaves BM, Polzin JA, Santos JM, Brittain JH (2003) Helical MR: continuously moving table axial imaging with radial acquisitions. Magn Reson Med 50:1053–1060

Weiger M, Pruessmann KP, Kassner A, Roditi G, Lawton T, Reid A, Boesiger P (2000) Contrast-enhanced 3D MRA using SENSE. J Magn Reson Imaging 12:671–677

Zenge MO, Ladd M, Vogt FM, Brauck K, Joekel M, Barkhausen J, Kannengiesser S, Quick HH (2005) High-resolution continuously acquired peripheral MRA featuring self-calibrated parallel imaging. In: Proceedings of the 13th Annual Meeting of ISMRM, Miami

Zenge MO, Ladd ME, Vogt FM, Brauck K, Barkhausen J, Quick HH (2005) Whole-body magnetic resonance imaging featuring moving table continuous data acquisition with high-precision position feedback. Magn Reson Med 54:707–711

Zenge MO, Quick HH, Vogt F, Ladd M (2004) MR imaging with a continuously rolling table platform and high-precision position feedback. In: Proceedings of the 12th Annual Meeting of ISMRM, Kyoto, Japan, p 444

Zhu Y, Dumoulin CL (2003) Extended field-of-view imaging with table translation and frequency sweeping. Magn Reson Med 49:1106–1112

Part VI:
Clinical Applications: Function

Imaging of CNS Diffusion and Perfusion

33

Marco Essig, Bram Stieltjes, and Wolfgang Reith

CONTENTS

33.1 Introduction

The assessment of cerebral functions has long been the domain of positron-emission tomography (PET) and single-photon-emission computed tomography (SPECT). With the use of fast imaging sequences and the availability of contrast agents the assessment and monitoring of physiological and pathophysiological cerebral processes using magnetic resonance imaging (MRI) has become possible. Presently, T1-weighted, as well as T2*-weighted contrast-enhanced fast-imaging sequences, can be used for the assessment of tissue perfusion, vascularity and microcirculation. Diffusion MRI allows the functional assessment of white matter viability and structure. To obtain physiological information from MRI the measurements have to be performed with a high temporal resolution in combination with sufficient MR signal.

M. Essig, MD; B. Stieltjes, MD
Abt. Radiologische Diagnostik und Therapie, Deutsches Krebsforschungszentrum Heidelberg, Im Neuenheimer Feld 280, 69120 Heidelberg, Germany
W. Reith, MD
Radiologische Universitätsklinik, Abt. für Neuroradiologie, Kirrbergerstr. 1, 66421 Homburg/Saar, Germany

Most functional MR imaging methods are based on an echo-planar imaging (EPI) acquisition with the limitation of low signal-to-noise ratio (SNR) and a limited spatial resolution. Especially diffusion-weighted MRI and diffusion tensor imaging (DTI) with intrinsic low signal intensities due to the diffusion weighting are limited because of their strong link between voxel size and SNR; therefore, any improvement of the SNR will enable a better spatial resolution which is possible by use of higher magnetic fields (e.g. 3 T).

Herein the application of parallel imaging in diffusion and perfusion MRI of the brain is described. For single-shot acquisitions, such as echo-planar imaging, parallel imaging is particularly advantageous since the reduction of the SNR is counterbalanced by the shortening of the echo-train length. Since advantages of parallel imaging are more obvious on high-field systems, most reports are from 3-T systems or higher. Owing to largely independent physics, the two approaches can be readily combined. Considering the specific advantages and disadvantages of high field strength and parallel imaging, it is found that the combination is particularly synergistic. In the joint approach, the two concepts play different roles. Higher field strength acts as a source of higher baseline SNR, whereas parallel imaging acts as a means of converting added SNR into a variety of alternative benefits. This interplay holds promise for a broad range of clinical applications, as recently illustrated by several imaging studies at 3 T. As a consequence, clinical MRI at 3 T and higher is expected to rely more on parallel imaging than at lower field strength.

33.2 Diffusion MRI

Diffusion-weighted imaging (DWI) has become one of the most important tools in the MR assessment of

ischaemic changes of the brain (Warach 1995) and in the differential diagnosis of cystic brain lesions (Bukte 2005). Diffusion-tensor imaging (DTI) is a promising non-invasive method for studying white-matter structure of the human brain in vivo (Conturo 1999; Stieltjes 2001). So far, the majority of DWI and DTI studies have been performed at a field strength of 1.5 T and with standard gradient and coil systems (Hunsche 2001; Bammer 2001). Due to the EPI-based acquisition DWI and DTI suffer also from the typical artefacts at the scull base and at tissue borders (Fig. 33.1). In addition, the measurements are time-consuming, which may limit the results in restless and uncooperative patients. Also, to ensure acceptable acquisition times, the spatial resolution used for DWI is low; typically a 128×128 matrix and a minimum of 6-mm slice thickness are used to keep the SNR and the acquisition time within clinically acceptable limits.

To overcome these limitations, there are two major approaches: the combination of high-field (≥3 T) systems is ideally suited to improve DWI; and DTI, because of the double SNR compared with 1.5 T (Hunsche 2001). The high magnetic field strength, however, will degrade the image quality because of the exponential increase of susceptibility artefacts, increased image distortion and blurring; these, however, are strongly reduced by parallel-imaging techniques (Fig. 33.2). Moreover, at higher field strength the geometry factor remains close to 1 at higher reduction rates (Wiesinger 2004), thus increasing the potential of parallel imaging as a method to reduce EPI-induced blurring and increase effective SNR.

In recent years there have been a variety of reports on the use of parallel imaging for DWI and DTI both in brain and the spinal cord (Kuhl 2005; Jaermann 2004; Tsuchiya et al. 2005; Schwartz 2005). To prospectively evaluate whether diffusion-weighted MRI with sensitivity encoding (SENSE) at 3 T can help to improve image quality and confidence in and accuracy of diagnosis of ischaemic lesions, Kuhl et al. (2005) compared parallel-imaging DWI with conventional DWI in patients with ischaemia. Using an eight-element SENSE-compatible receive-only surface coil they compared image quality, SNR, relative signal intensity and lesion contrast for diagnostic accuracy of and confidence in detection of apparent-diffusion-coefficient (ADC) lesions. The authors found no major SENSE-related reconstruction artefacts. Using DWI/DTI in combination with SENSE, consistently and significantly ($p<0.001$) higher image quality scores were achieved because of substantial reduction of image distortions and blurring especially in areas close to the base and the vertex of the scull where conventional DWI suffers from substantial geometric distortions. Lesion contrast was equivalent with both techniques; however, the diagnostic confidence for demonstration and exclusion of lesions was significantly ($p<0.001$) higher at MRI with SENSE. In 3 patients, small microembolic lesions were only prospectively diagnosed at MR imaging with SENSE, whereas they were masked by adjacent susceptibility

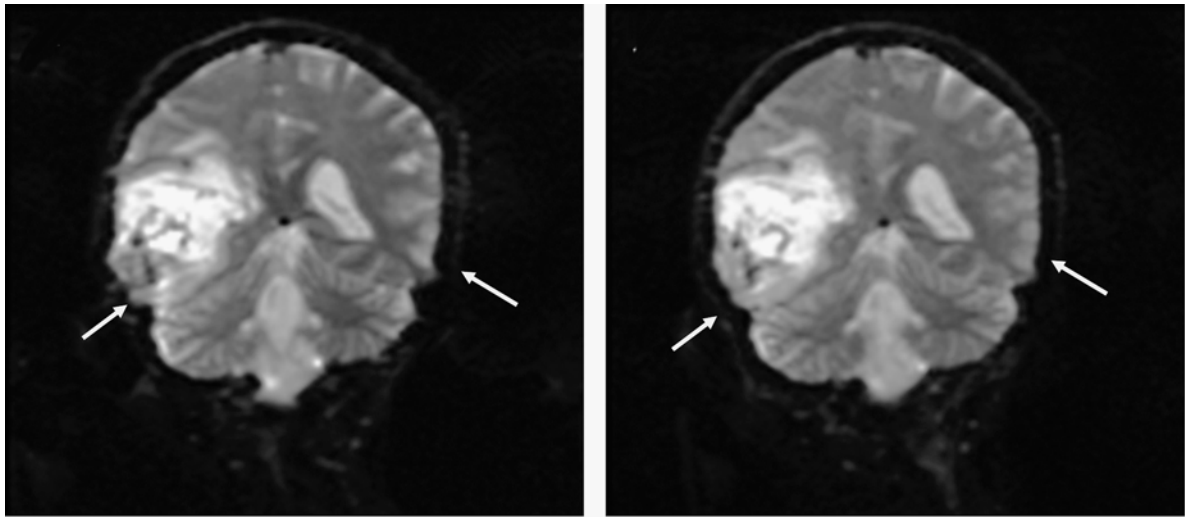

Fig. 33.1a,b. A 55-year-old patient with right temporoparietal glioblastoma. Diffusion-weighted imaging performed at 1.5 T without parallel imaging **a** and with parallel imaging **b**. Parallel imaging resulted in substantial better image quality. N/2 artefacts are reduced as well as distortion artefacts at the scull base (*arrows*).

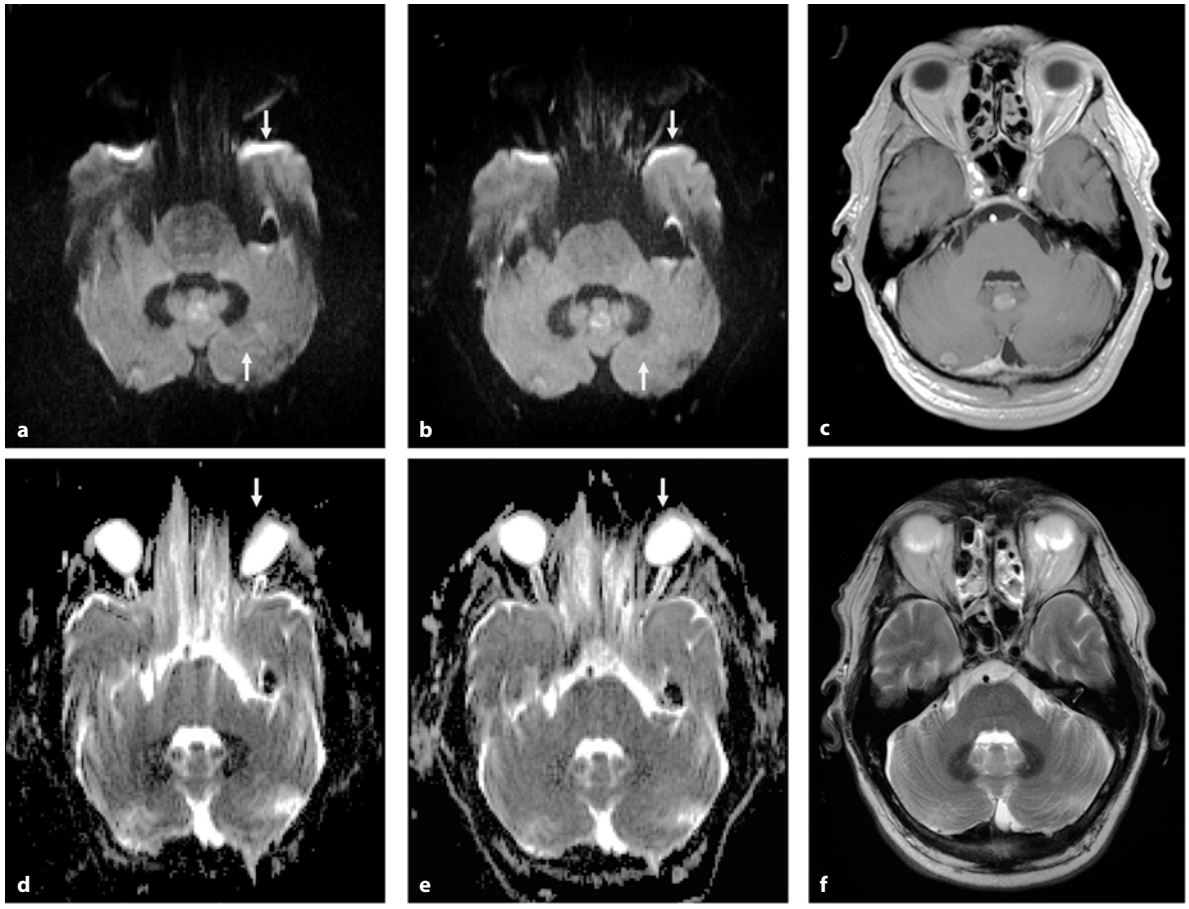

Fig. 33.2a–f. A 59-year-old man with brain metastases: diffusion-weighted MRI with b-value 1000 s/mm² **a,c** ADC maps. **b,d** Contrast-enhanced T1-weighted and **e** T2-weighted acquisition. All images were acquired at 3 T. Acquisitions **a,b** without and **c,d** with parallel imaging were compared. Parallel imaging reduces distortion and aliasing artefacts, partially obscuring the small metastasis in the non-accelerated image (*arrows*). Imaging parameters were: matrix 192×192; field of view 230×230 mm²; slice thickness 5 mm. Timing without parallel imaging: TR/TE=4500/127 ms; with parallel imaging: TR/TE=3000/95 ms

effects and therefore overlooked at MR imaging with conventional (full) phase encoding.

Jaermann et al. (2004) evaluated SENSE DTI at 3 T in a recent publication in nine healthy volunteers. Susceptibility-related artefacts, most pronounced close to the skull base, frontal cavity and inner ear, could be effectively compensated by the use of parallel imaging with shortening of the EPI readout. They observed the same substantial artefact suppression at 3 T as previously described at a field strength of 1.5 T (Bammer 2001, 2002). Another advantage of parallel imaging is the effect it has on actual resolution. Reducing signal decay during the readout effectively broadens the associated k-space filter, leading to a narrower point spread function and higher actual resolution than with conventional DTI (cf. Chap. 10; Jaermann 2004). This can be noted when comparing images of the same matrix size and field of view. Here images recorded using SENSE show sharper borders.

Although distortions are most pronounced at tissue–air borders, all field inhomogeneities lead to slight disruption in observed fiber orientation. This may lead to alterations in overall fiber direction and thus hamper the results, especially when using fiber tracking. This effect again would be most pronounced in areas where two fiber systems cross. In Fig. 33.3a fibertracking of the corona radiata was performed. Note that the fibers do not reach the motorcortex and are bent backwards, due to mixing of other fiber systems. In the data set using parallel imaging with acceleration factor R=2 the fibers do reach up to the cortex (Fig. 33.3b). This shows the effect of relatively small distortions on overall fiber orientation. (For further details about application of parallel imaging in DTI see Chap. 34).

a

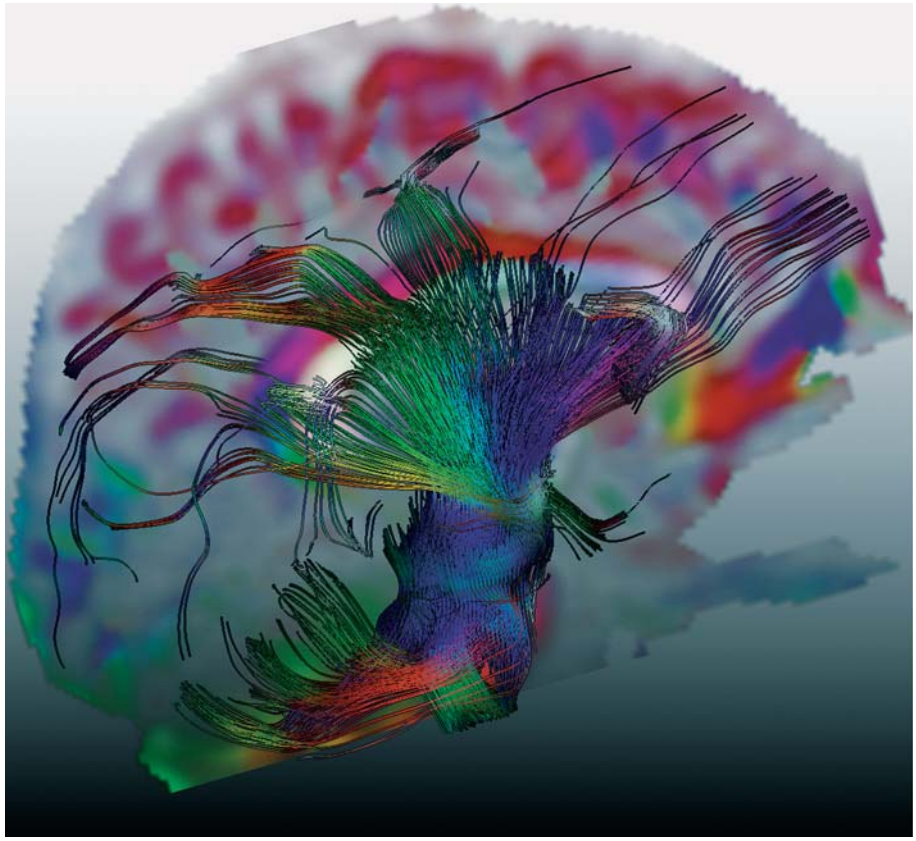

b

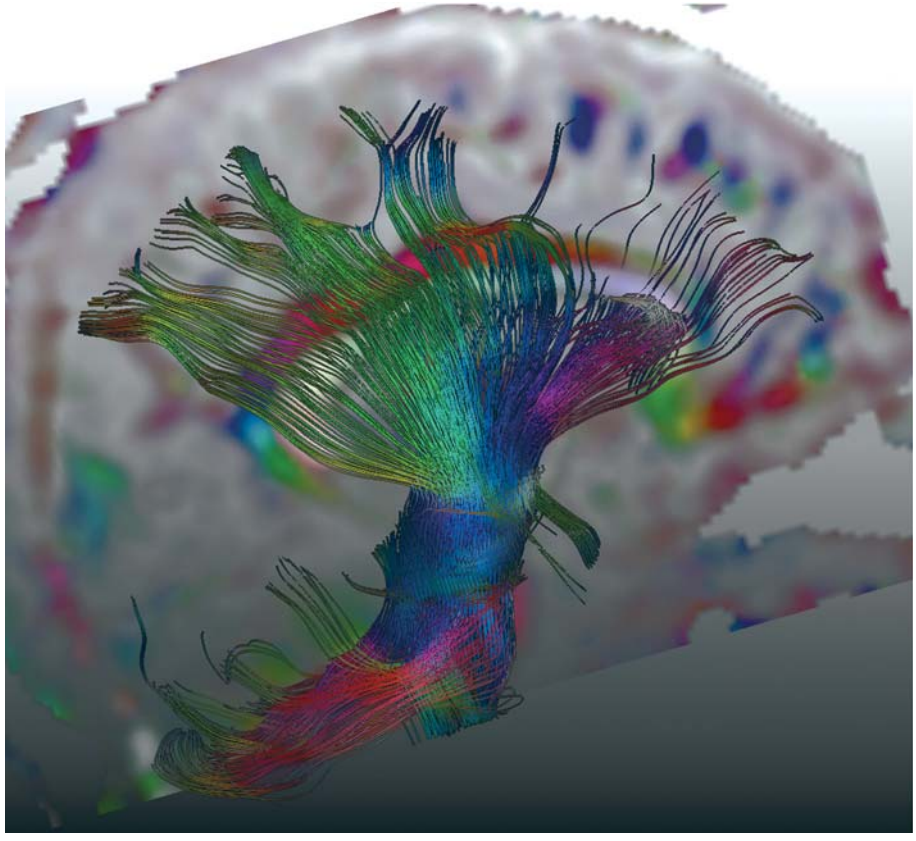

Fig. 33.3a,b. Reconstruction of the internal capsule **a** without and **b** with parallel imaging. Stream tubes were obtained using a FACT-based fiber-tracking algorithm (Mori 1999). Fibers are overlaid on sagittal color-coded fractional-anisotropy map.

In conclusion, the combination of EPI and parallel imaging for DWI/DTI is extremely favourable, reducing EPI-induced artefacts and small distortions. Furthermore, due to the strong reduction in readout echo-train length, the inherent reduction of SNR in SENSE imaging is counteracted increasing the effective SNR and resolution. Combination of parallel imaging and higher field strengths will even enhance these positive effects.

33.3 Perfusion MRI

Perfusion is physiologically defined as the steady-state delivery of blood to an element of tissue. The term "perfusion" is also used to emphasize contact with the tissue, or in other words, capillary blood flow. Because perfusion and blood volume is disturbed in many disease processes, monitoring of this key physiological parameter can often provide insight into disease. Consequently, the measurement of perfusion for medical purposes has been performed in almost all organs using many techniques.

During the past decade several methods have been described to non-invasively measure perfusion with MRI. Most effort in this context has been made in the perfusion imaging of the brain with two major approaches: contrast-enhanced techniques based on tracer-kinetic models and non-enhanced techniques based on arterial spin labeling. Whereas the contrast-enhanced techniques are well established, the non-enhanced techniques are of increasing interest with the use of high-field MR systems; especially in the latter the limited anatomic coverage and common EPI artefacts have been limitations in the past. With the use of parallel-imaging techniques the method might be improved substantially.

At a field strength of 1.5 T the main approaches to assess brain tissue perfusion are dynamic contrast-enhanced techniques (DCE MRI): T2*-based perfusion MRI and tracer-kinetic MRI.

T2*-based perfusion MRI is based on a rapid contrast-media injection and the evaluation of the signal-intensity–time curve with spin-echo or gradient-echo EPI sequences. Compared with the previously used gradient-echo sequences, the EPI-based sequences have the advantage of a better anatomic coverage but the disadvantage of the EPI technique, namely a reduced spatial resolution and more artefacts, e.g. at the scull base and close to bone/air interfaces. This is a major drawback, especially in the assessment of small structures at the temporal lobes which are of importance in the assessment of neurodegenerative diseases and in lesions (e.g. ischaemic or tumorous) close to areas with a high potential for artefacts. Theoretically the use of parallel imaging might reduce these artefacts and allows to measure at a higher spatial resolution. The encoding time reduction with the use of parallel imaging can be used to achieve a higher temporal resolution of a conventional dynamic scan or to increase the spatial resolution of the typically low resolution of dynamic scans. For EPI acquisitions the echo-train length could be reduced with reduction of image distortion and blurring. Disadvantages of parallel imaging are the reduction of the SNR and some restrictions in scan prescriptions as well as additional and new artefacts induced by parallel imaging (Madore and Pelc 2001).

Stollberger and Fazekas (2004) evaluated the influence of parallel imaging on DCE MRI. In their review article they discuss both the T2*-based perfusion MRI and the tracer-kinetic MRI in different clinical applications. With the currently used slice thickness of 5–7 mm it seems not to be possible with non-accelerated acquisitions to cover the whole brain as desired especially for perfusion stroke imaging. Another problem is the determination of the arterial input function which suffers from partial-volume effects, arterial voxel shift, saturation effects of the arterial input function and blurring.

The application of parallel imaging seems to be an almost ideal method to reduce the above-mentioned problems. Firstly, the possible shorter echo-train length reduces image distortion and blurring. In brain-tumor imaging the authors describe an advantage especially for lesions close to the scull base and in the postoperative assessment. Images can be interpreted even in the close vicinity of an artefact due to surgical material at the site of craniotomy. With their proposed protocol, it was possible to cover the whole brain at a very high temporal resolution of <1.5 s per repetition. The reduction of artefacts (Fig. 33.4), reduced blurring and the shortening of the echo time enabled better determination of the arterial input function. A further reduction of the echo time is possible with the implementation of interleaved EPI sequences. The combination of such sequences with parallel imaging allows the acquisition of a double-echo sequence in which the first echo can be measured with an echo time well below 10 ms, whereas the second echo can be optimized for an ideal weight-

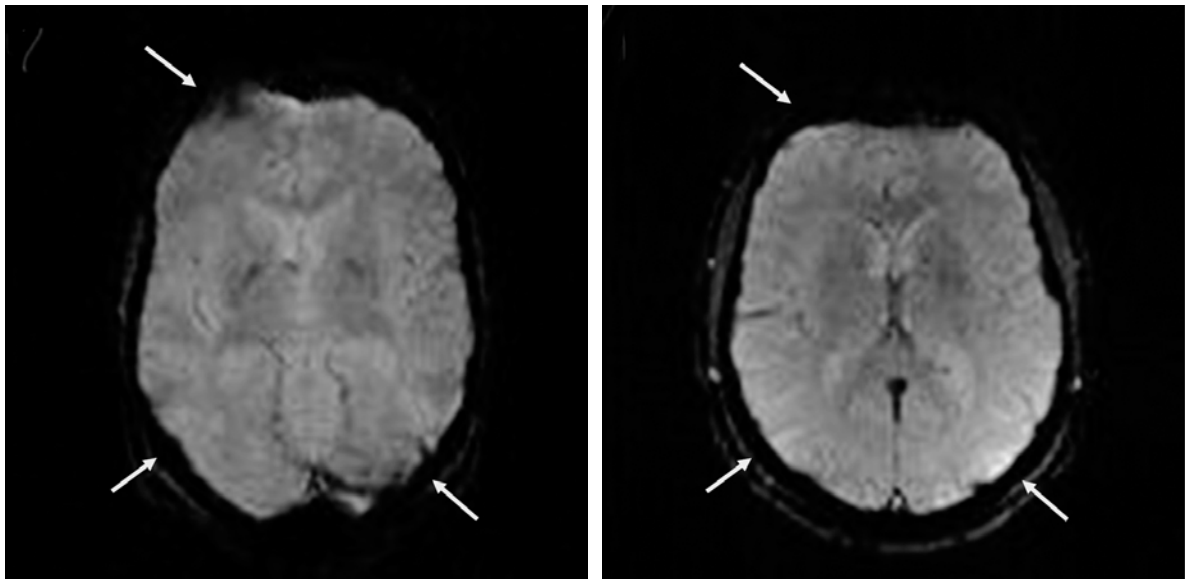

Fig. 33.4a,b. a Echo-planar imaging T2*-based perfusion MRI source image without parallel imaging. Note the pronounced frontal and occipital image distortion, especially at the bone/air/tissue interfaces (*arrows*) . **b** With the use of parallel imaging (acceleration factor *R*=2) the artefacts could be substantially reduced. The image is less blurred and less image distortion is seen (*arrows*).

ing of the parenchyma. The double-echo sequence is an elegant method for suppressing T1-enhancement in cases of leaky microvessels and contrast agent extravasation (Vonken et al. 2000; Uematsu et al. 2000).

In tracer-kinetic MRI, parallel MRI can be used to reduce the scan time or to increase the scan resolution at the same scanning time or to achieve an optimal compromise of both (Stollberger 2004). The advantage of parallel imaging for tracer-kinetic MRI has been shown for imaging of the breast and liver (Kuhl 2002; McKenzie 2004); however, for CNS indications, e.g. brain-tumor characterization, there are no data available.

For non-enhanced perfusion MRI, a variety of continuous and pulsed arterial-spin-labeling (ASL) MRI techniques have been demonstrated in recent years and the influence of parallel imaging on these techniques have been evaluated mainly on 3-T MRI systems.

Talagala and colleagues (2004) from the NIH presented a first study on whole-brain 3D perfusion MRI at 3 T using continuous arterial spin labeling with a separate labeling coil. This approach provided an increased SNR in perfusion images because there are no magnetization transfer effects. In their work, they also demonstrated the ability to acquire perfusion images in all brain regions with good sensitivity. Furthermore, they showed that the method can be performed safely on humans without exceeding the current RF-power-deposition limits because it uses a local labeling coil. The current method can be extended to even higher fields, and further improved by the use of multiple receiver coils and parallel-imaging techniques to reduce scan time or provide increased resolution.

In a recent study Wang et al. (2005) evaluated the feasibility and efficacy of using an array coil and parallel imaging in continuous-arterial-spin-labeling (CASL) perfusion MRI. An 8-channel receive-only physed-array head coil was used in conjunction with a surrounding detunable volume transmit coil. The SNR, temporal stability, cerebral blood flow (CBF) and perfusion-image coverage were measured from steady-state CASL scans using a standard volume coil, an array coil and a phased-array coil with two- and threefold accelerated parallel imaging. They describe that compared with the standard volume coil, the array coil provided three times the average SNR and higher temporal stability for the perfusion-weighted images, even with threefold acceleration. Although perfusion images of the array coil were affected by the inhomogeneous coil sensitivities, this effect was invisible in the quantitative CBF images,

which showed highly reproducible perfusion values compared with the standard volume coil. The unfolding distortions of parallel imaging were suppressed in the perfusion images by pairwise subtraction, although they sharply degraded the raw EPI images. Moreover, parallel imaging provided the potential of acquiring more slices due to the shortened acquisition time and improved coverage in brain regions with high static field inhomogeneity.

33.4 Conclusion

The assessment of tissue function is one of the most challenging goals in neuroimaging. Presently, structural MRI allows not only for the evaluation of the tissue characteristics, but also the assessment of tissue integrity. Diffusion-weighted MRI and diffusion-tensor imaging have enabled to visualize neuronal pathways and structural details. Functional MRI allows to gather non- or minimally invasively information about the tissue perfusion, vascularity and metabolism.

Recent investigations have shown that most of the advanced structural and functional MR sequences benefit substantially from the application of parallel-imaging techniques. Methodological and first clinical studies describe a significant artefact reduction, the possibility of faster acquisition and a more robust assessment of the structural and functional parameters with the use of parallel imaging. Further developments can be expected with new and optimized coil arrays in the near future.

References

Bammer R, Keeling SL, Augustin M, Pruessmann KP, Wolf R, Stollberger R, Hartung HP, Fazekas F (2001) Improved diffusion-weighted single echo-planar imaging (EPI) in stroke using sensitivity enconding (SENSE). Magn Reson Med 46:548–554

Bammer R, Auer M, Keeling SL et al. (2002) Diffusion tensor imaging using single-shot SENSE-EPI. Magn Reson Med 48:128–136

Bukte Y, Paksoy Y, Genc E, Uca AU (2005) Role of diffusion-weighted MR in differential diagnosis of intracranial cystic lesions. Clin Radiol 60:375–383

Conturo TE, Lori NF, Cull TS et al. (1999) Tracking neuronal fiber pathways in the living human brain. Proc Natl Acad Sci USA 96:10422–10427

Hunsche S, Mosely M, Stoeter P, Hedehus M (2001) Diffusion-tensor MR imaging at 1.5 and 3.0 T: initial observations. Radiology 221:550–556

Jaermann T, Crelier G, Pruessmann KP et al. (2004) SENSE-DTI at 3 T. Magn Reson Med 51:230–236

Kuhl CK, Morakkabati N, Sondermann E et al. (2002) Dynamic breast MR imaging using sensitivity encoding (SENSE). Proc Int Soc Mag Reson Med 10:1410

Kuhl CK, Gieseke J, Falkenhausen M von et al. (2005) Sensitivity encoding for diffusion-weighted MR imaging at 3.0 T: intraindividual comparative study. Radiology 234:517–526

Madore B, Pelc NJ (2001) SMASH and SENSE: experimental and numerical comparisons. Magn Reson Med 45:1103–1111

McKenzie CA, Lim D, Ransil BJ et al. (2004) Shortening MR image acquisition time for volumetric interpolated breath-hold examination with a recently developed parallel imaging reconstruction technique: clinical feasibility. Radiology 230:589–594

Mori S, Crain BJ, Chacko VP et al. (1999) Three-dimensional tracking of axonal projections in the brain by magnetic resonance imaging. Ann Neurol 45:265–269

Stieltjes B, Kaufmann WE, van Zijl PC et al. (2001) Diffusion tensor imaging and axonal tracking in the human brainstem. Neuroimage 14:723–735

Stollberger R, Fazekas F (2004) Improved perfusion and tracer kinetic imaging using parallel imaging. Top Magn Reson Imaging 15:245–254

Talagala SL, Ye FQ, Ledden PJ, Chesnick S (2004) Whole-brain 3D perfusion MRI at 3.0 T using CASL with a separate labeling coil. Magn Reson Med 52:131–140

Tsuchiya K, Fujikawa A, Suzuki Y (2005) Diffusion tractography of the cervical spinal cord using parallel imaging. Am J Neuroradiol 26:398–400

Uematsu H, Maeda M, Sadato N et al. (2000) Vascular permeability: quantitative measurements with double-echo dynamic MR imaging. Theory and clinical application. Radiology 214:912–917

Vonken EP, van Osch MJ, Bakker CJ et al. (2000) Simultaneous quantitative cerebral perfusion and Gd-DTPA extravasation measurement with dual-echo dynamic susceptibility contrast MRI. Magn Reson Med 43:820–827

Wang Z, Wang J, Connick TJ, Wetmore GS, Detre JA (2005) Continuous ASL (CASL) perfusion MRI with an array coil and parallel imaging at 3 T. Magn Reson Med 54:732–737

Warach S, Gaa J, Siewert B, Wielopolski P, Edelman RR (1995) Acute human stroke studied by whole brain echo planar diffusion-weighted magnetic resonance imaging. Ann Neurol 37: 231–241

Wiesinger F, Van de Moortele P-F, Adriany G, de Zanche N, Ugurbil K, Pruessmann KP (2004) Parallel imaging performance as a function of field strength: an experimental investigation using electrodynamic scaling. Magn Reson Med 52: 953–964

Diffusion Tensor Imaging of the Brain

34

Thomas Benner, Ruopeng Wang and Van J. Wedeen

CONTENTS

34.1 Introduction

The basic principles of simple, i.e., non-tensor diffusion imaging (Wesbey et al. 1984; Le Bihan 1991; Basser 1995) have been known for many years and since then have been used most frequently in the field of acute cerebral ischemia (Le Bihan et al. 1988; Moseley et al. 1990); cf. Chap. 33. Diffusion-anisotropy and diffusion-tensor imaging (DTI) were introduced only years later (Basser et al. 1994; Pierpaoli and Basser 1996; Mattiello et al. 1997). Diffusion imaging – non-tensor and tensor – and mapping of apparent diffusion coefficient (ADC) and fractional anisotropy (FA) has become a widespread tool in many research fields such as neurodevelopment (Neil et al. 2002; Beaulieu et al. 2005; Snook et al. 2005), aging (Nusbaum et al. 2001; Moseley 2002; Salat et al. 2005), degenerative diseases (Shiga et al. 2004; Choi et al. 2005; Fellgiebel et al. 2005), tumors (Cruz and Sorensen 2005; Nguyen et al. 2005; Nimsky et al. 2005) and stroke (Warach et al. 1992; Hossmann and Hoehn-Berlage 1995; Baird and Warach 1998; Sotak 2002). With the availability of diffusion-tensor imaging, fiber tracking or tractography of white-matter fiber tracts was made possible (Wedeen et al. 1996; Conturo et al. 1999; Mori et al. 1999). More recently, advanced diffusion-imaging techniques such as high-angular-resolution diffusion imaging (HARDI), q-ball imaging, q-space imaging and diffusion-spectrum imaging have gained popularity, but are not yet widespread, mostly because of the high hardware-performance requirements and the long scan times required (Wedeen et al. 2000; Frank 2001; Basser 2002; Tournier et al. 2004; Tuch 2004; Wedeen et al. 2005).

Especially for fiber tracking, image quality is a major concern. One of the main problems is image distortion caused by eddy currents induced by the diffusion gradients. Minimization of these eddy-current artefacts at the time of acquisition is important and can be done on the hardware level, e.g., by using specifically optimized gradient coils and on the software level, e.g., by using a twice-refocused spin-echo sequence (Reese et al. 2003). Further post-processing might be required to correct for remaining eddy-current artefacts as well as subject motion. Software tools are available for this purpose, e.g., the Oxford Centre for Functional Magnetic Resonance Imaging of the Brain (FMRIB) Software Library (FSL) (Jenkinson and Smith 2001) or Automated Image Registration (AIR) (Woods et al. 1998). However, such tools are not yet integrated into the clinical workflow. Dependent on the area of interest and the spatial resolution, pulsatile motion of the brain has to be taken into account (Norris 2001). Use of cardiac triggering might therefore be necessary for some applications at the cost of increased scan time.

T. Benner, PhD; R. Wang, MS; V. J. Wedeen, MD
MGH/MIT/HMS Athinoula A. Martinos Center for Functional and Structural Biomedical Imaging, Building 149 13th Street (2301), Charlestown, MA 02129, USA

34.2 Benefits of Parallel Imaging

With the availability of multi-channel receive coils, new parallel-imaging methods such as GRAPPA and SENSE were introduced (Pruessmann et al. 1999; Griswold et al. 2002), cf. Chap. 2. These methods provide a number of benefits for their use in DTI with echo-planar-imaging (EPI) techniques: reduction of susceptibility artefacts, faster imaging, and the feasibility of acquisitions with high spatial resolution.

34.2.1 Reduced Distortions

One major benefit of parallel imaging is the reduction of distortions caused by susceptibility artefacts as shown in Figs. 34.1, 34.2 and 34.3; cf. Chap. 10. The data for these figures was acquired on a 1.5-T Siemens Avanto whole-body MR scanner (Siemens Medical Solutions, Erlangen, Germany) using a custom-built head coil with 23 receive elements (Wiggins et al. 2005). This coil provides a significantly better signal-to-noise ratio (SNR) at the cortex and still improved SNR for deep brain structures. The study was done on a normal subject using auto-align for slice positioning (van der Kouwe et al. 2005). As a result of the different echo times and repetition times for non-accelerated and accelerated scans, the number of non-diffusion-weighted images and diffusion-weighted images was adjusted for the three scans to result in approximately the same scan time for all three scans (see Table 34.1 for a complete list of imaging parameters).

Figure 34.1 shows two slices of mean non-diffusion-weighted images and color-coded FA maps for scans done without acceleration and with acceleration factors R=2 and R=3, respectively. Severe distortions can be seen in the non-accelerated images (left column) in areas of air-tissue interfaces, i.e., near the brain stem, the ear canals and the frontal sinus. An increase of the acceleration factor decreases the distortions (middle and right column). This can also be observed in the color-coded FA maps as well as in the boxoid representation (Fig. 34.2), which are calculated from the whole data set and therefore exhibit the same distortion artefacts. Note also, that due to the comparable scan times SNR is similar for non-accelerated scans and accelerated scans. Although the effect of reduced distortions is not visible in fiber tracking as shown in Fig. 34.3, the same image distortions shown in Figs. 34.1 and 34.2 affect the location and direction of the fiber tracts.

Table 34.1. Protocol parameters for DTI scans shown in Figs. 34.1, 34.2, 34.3 and 34.7

Acceleration factor (R)	1	2	3
Parallel-imaging algorithm	-	GRAPPA	GRAPPA
Number of reference lines	-	30	60
TR (s)	9.2	7.2	6.6
TE (ms)	89	77	74
Number of slices	60	60	60
FOV (mm)	256	256	256
Slice thickness (mm)	2.0	2.0	2.0
Gap (%)	0.0	0.0	0.0
Matrix size	128	128	128
b-value (s/mm^2)	700	700	700
Bandwidth (Hz/Px)	1628	1628	1628
Echo spacing (ms)	0.69	0.7	0.72
Non-diff.-weighted images	8	10	11
Diff.-weighted images	48	60	66
Number of averages	1	1	1
Acquisition time (min:s)	8:44	8:31	8:55

34.2.2 Faster Imaging

Another advantage of using parallel imaging in EPI is the resulting shorter echo times, which in turn result in higher signal and shorter repetition times. Without acceleration, scan times would be about 15% to 60% longer as compared to an acceleration factor R=2 (Table 34.2). For DTI, this translates into either shorter scan times, e.g., to achieve ultra-fast imaging, or into more coverage at the same scan duration, or into more acquisition volumes, i.e., a higher number of non-diffusion-weighted and diffusion-weighted images. The latter has been shown beneficial for the robust estimation of anisotropy, tensor orientation, and mean diffusivity (Jones 2004).

Figure 34.4 shows the images from an ultra-fast DTI scan with whole-brain coverage acquired in only 20 s (see Table 34.2 for imaging parameters). This full tensor acquisition allows the calculation of FA maps as well as fiber tracking. However, given the very anisotropic voxel size and low number of diffusion-gradient directions, any fiber-tracking result would be sub-optimal. Without acceleration, the scan time for a similar tensor acquisition would increase

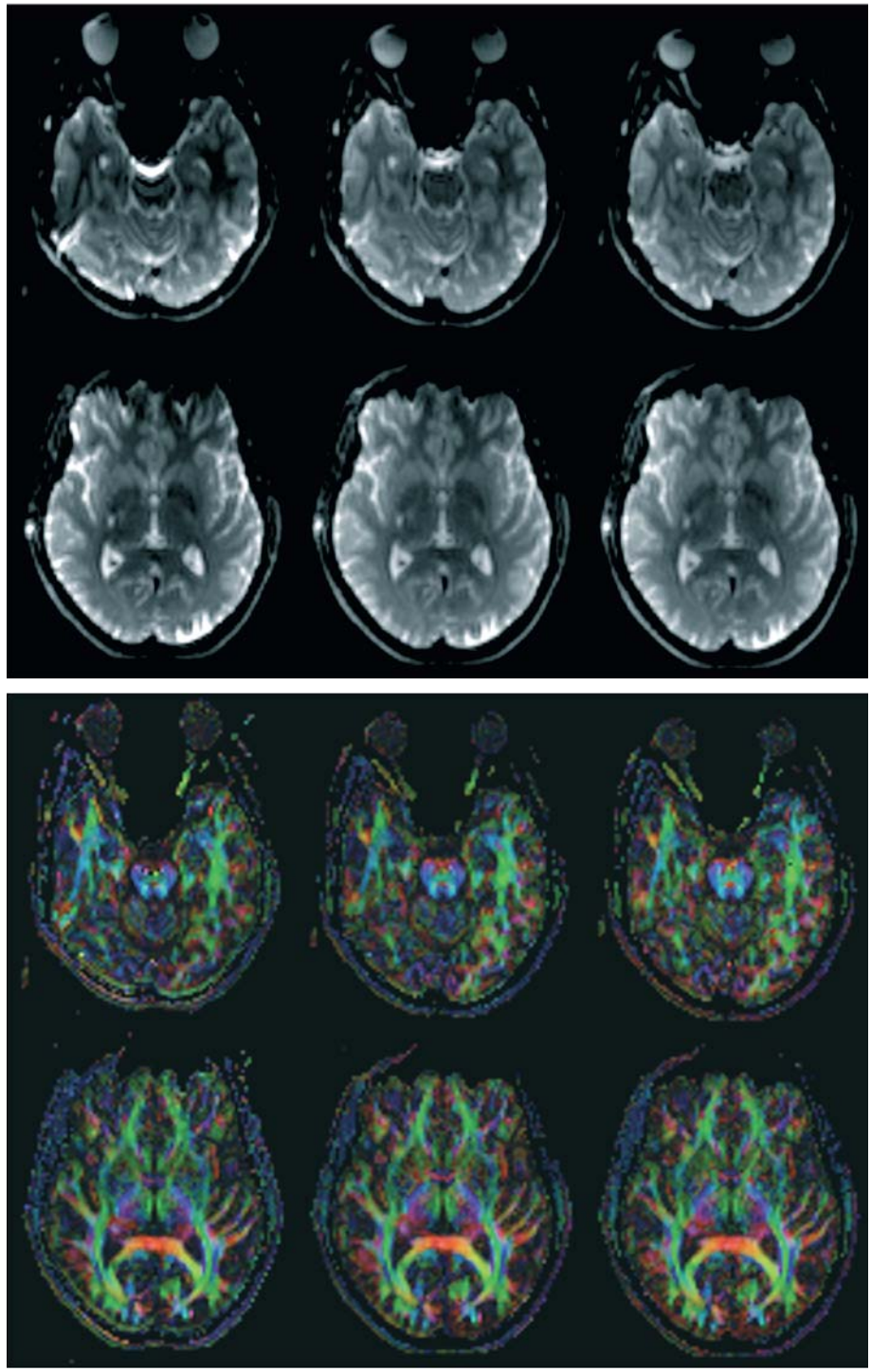

Fig. 34.1. Two slices of mean non-diffusion-weighted images (*top panel*) and color-coded fractional anisotropy (FA) maps (*bottom panel*) for non-accelerated (*left column*) and accelerated scans with factor R=2 (*middle column*) and R=3 (*right column*). Notice the effect of parallel-imaging acceleration in typical areas of susceptibility distortions near the brain stem, ear canals, and frontal sinus. Distortion artefacts decrease with increasing acceleration factor. Also notice decrease in signal-to-noise ratio with increasing acceleration factor

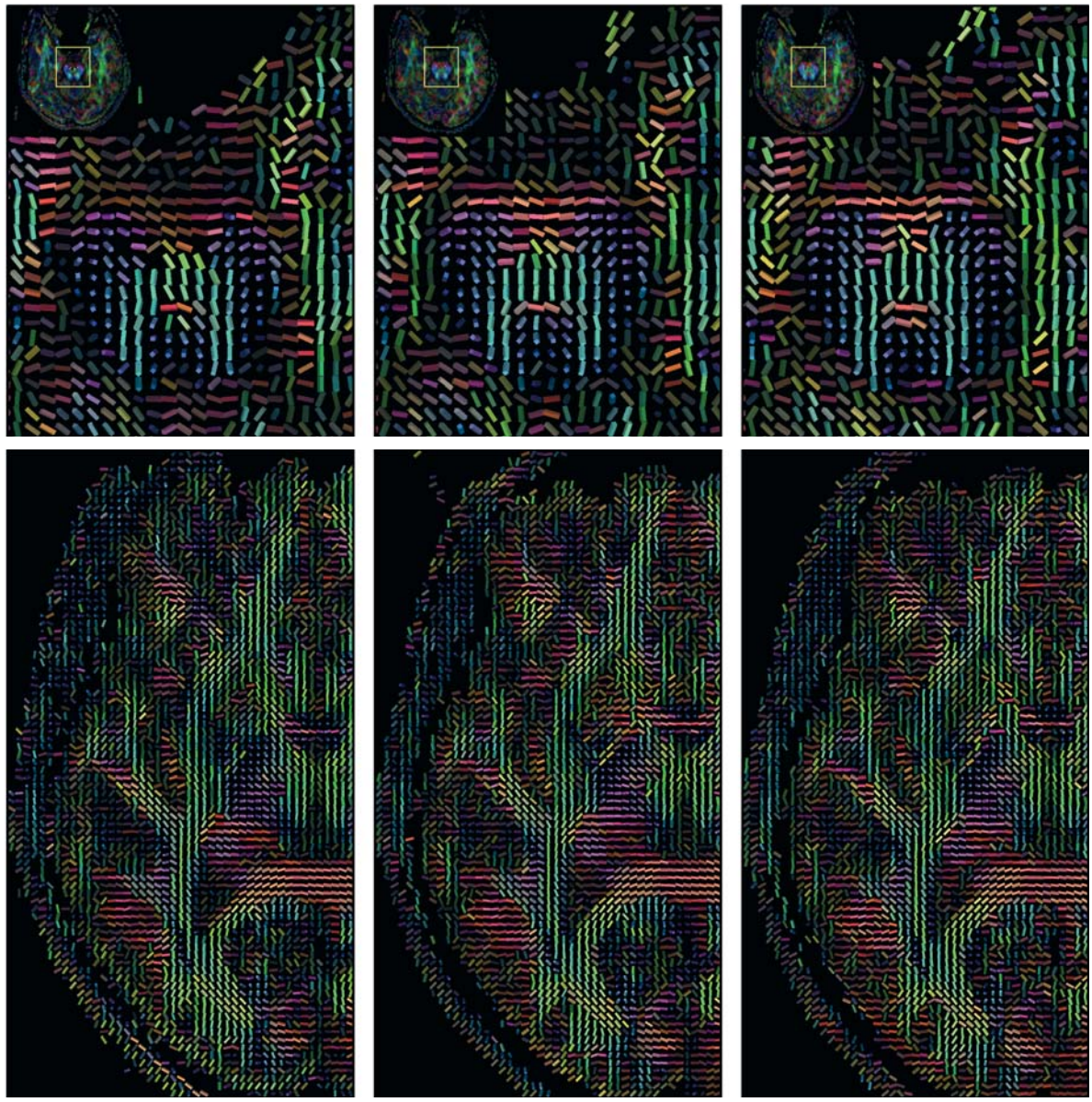

Fig. 34.2. Detailed view of images shown in Fig. 34.1 in boxoid representation. Non-accelerated scan is shown in *left column*; accelerated scans using factor R=2 and R=3 are shown in the *middle* and *right* column, respectively. Each boxoid per voxel represents the major eigenvector in direction as well as color coding. Notice effect of susceptibility artefacts on boxoid orientation in the anterior part of the brain stem (*top row*) as well as slight change in shape (*bottom row*). Overall, tensor orientation in all images looks comparable

by 30%. This difference in duration can be important in a clinical setting where shorter scan durations allow higher patient throughput and better image quality for patients who are likely to move during a long acquisition. While SNR is somewhat lower in the images from the accelerated scan, the overall image quality is comparable to the data without acceleration. Additionally, the accelerated data benefit from reduced distortion artefacts as described before.

34.2.3 Higher Resolution

Because of the long readout times for large matrix sizes, single-shot EPI is usually limited to maximum matrix sizes of around 128×128 and to maximum isotropic spatial resolutions of 2×2×2 mm³. Parallel imaging allows pushing this limit to larger matrix sizes and therefore to higher spatial resolutions. Figure 34.5

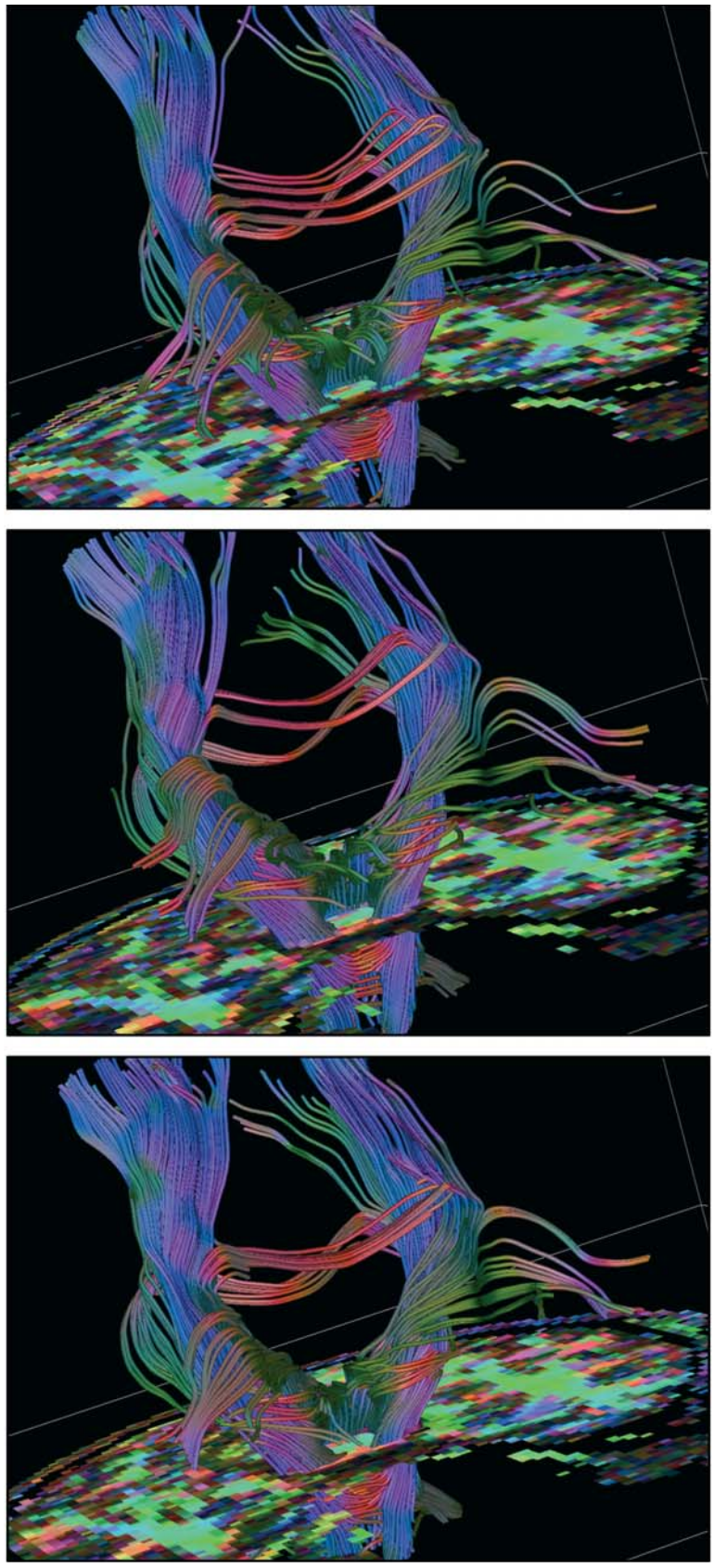

Fig. 34.3a–c. Region-of-interest-based fiber tracking for non-accelerated scan **a** and accelerated scans using factor R=2 **b** and R=3 **c**, respectively. View is from anterior-right-superior. Identical regions were positioned in the brain stem. Images show good visual agreement of fiber tracks for all three scans

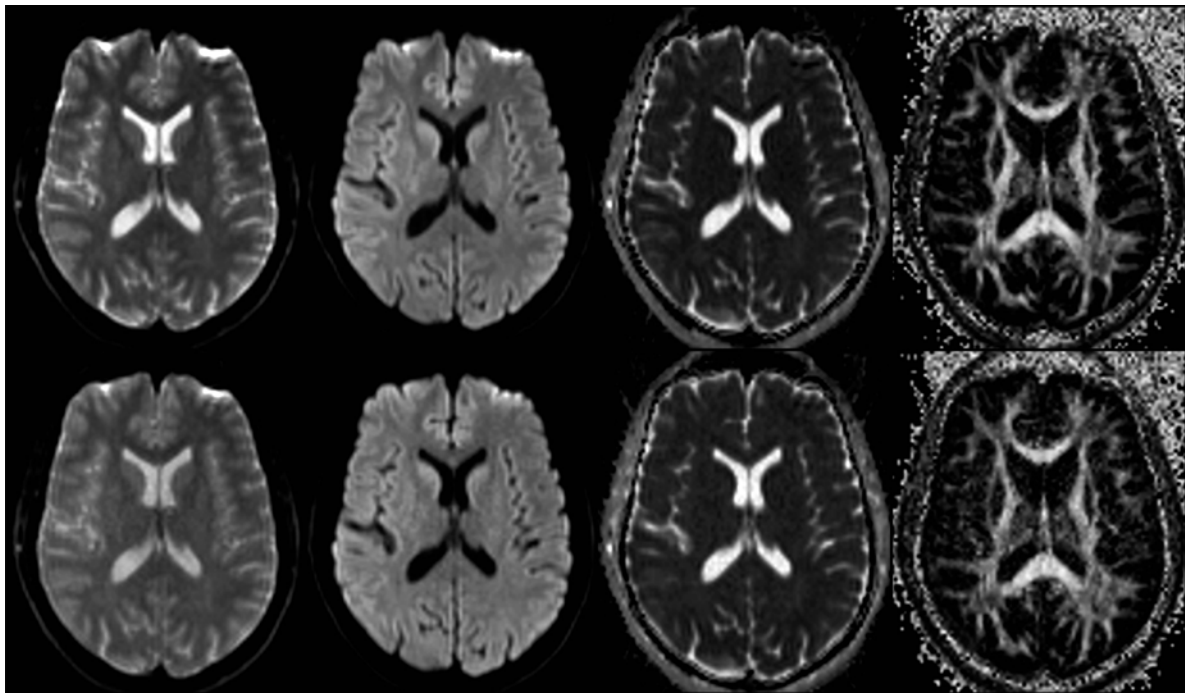

Fig. 34.4. Mean non-diffusion-weighted image, mean diffusion-weighted image, apparent-diffusion-coefficient (ADC) map and fractional-anisotropy (FA) map (from *left* to *right*) using no acceleration (*top row*) and using an acceleration factor R=2 (*bottom row*). The scan times for a full tensor scan were 26 s and 20 s, respectively. Notice slight loss in signal-to-noise ratio for the accelerated scan, but otherwise comparable image quality. Background noise in FA maps is caused by automatic threshold and using intensity normalization. See Table 34.2 for complete acquisition parameters

Table 34.2. Protocol parameters for DTI scans, some of which are shown in the figures. Scan time increase for acceleration factor R=1 compared to R=2

	Ultra-fast		Clinical		Very high res.		HARDI		DSI	
Acceleration factor (R)	1	2	1	2	1	2	1	2	1	2
Parallel imaging algorithm	-	GRAPPA	-	GRAPPA	-	GRAPPA	-	GRAPPA	-	GRAPPA
Number of reference lines	-	30	-	30	-	48	-	42	-	44
TR (s)	3.3	2.5	3.7	2.9	17.5	11.1	10.9	8.9	5.3	4.7
TE (ms)	86	73	94	82	145	97	129	111	159	148
Number of slices	21	21	23	23	64	64	60	60	25	25
FOV (mm)	230	230	220	220	208	208	211	211	192	192
Slice thickness (mm)	5.0	5.0	5.0	5.0	1.0	1.0	2.2	2.2	2.0	2.0
Gap (%)	30.0	30.0	20.0	20.0	0.0	0.0	0.0	0.0	0.0	0.0
Matrix size	128	128	128	128	208	208	96	96	96	96
b-value (s/mm^2)	1,000	1,000	1,000	1,000	700	700	3,000	3,000	8,500	8,500
Bandwidth (Hz/Px)	1,446	1,446	1,628	1,628	1,046	1,046	1,628	1,628	1,628	1,628
Echo spacing (ms)	0.76	0.78	0.69	0.7	1.03	1.04	0.69	0.7	0.69	0.7
Non-diff.-weighted images	1	1	5	5	10	10	1	1	1	1
Diff.-weighted images	6	6	30	30	60	60	122	122	514	514
Number of averages	1	1	1	1	1	1	1	1	1	1
Acquisition time (min:s)	0:26	0:20	2:13	1:44	20:43	13:08	22:33	18:25	45:35	40:25
Scan-time increase at R=1 compared to R=2 (%)	30		28		58		22		13	

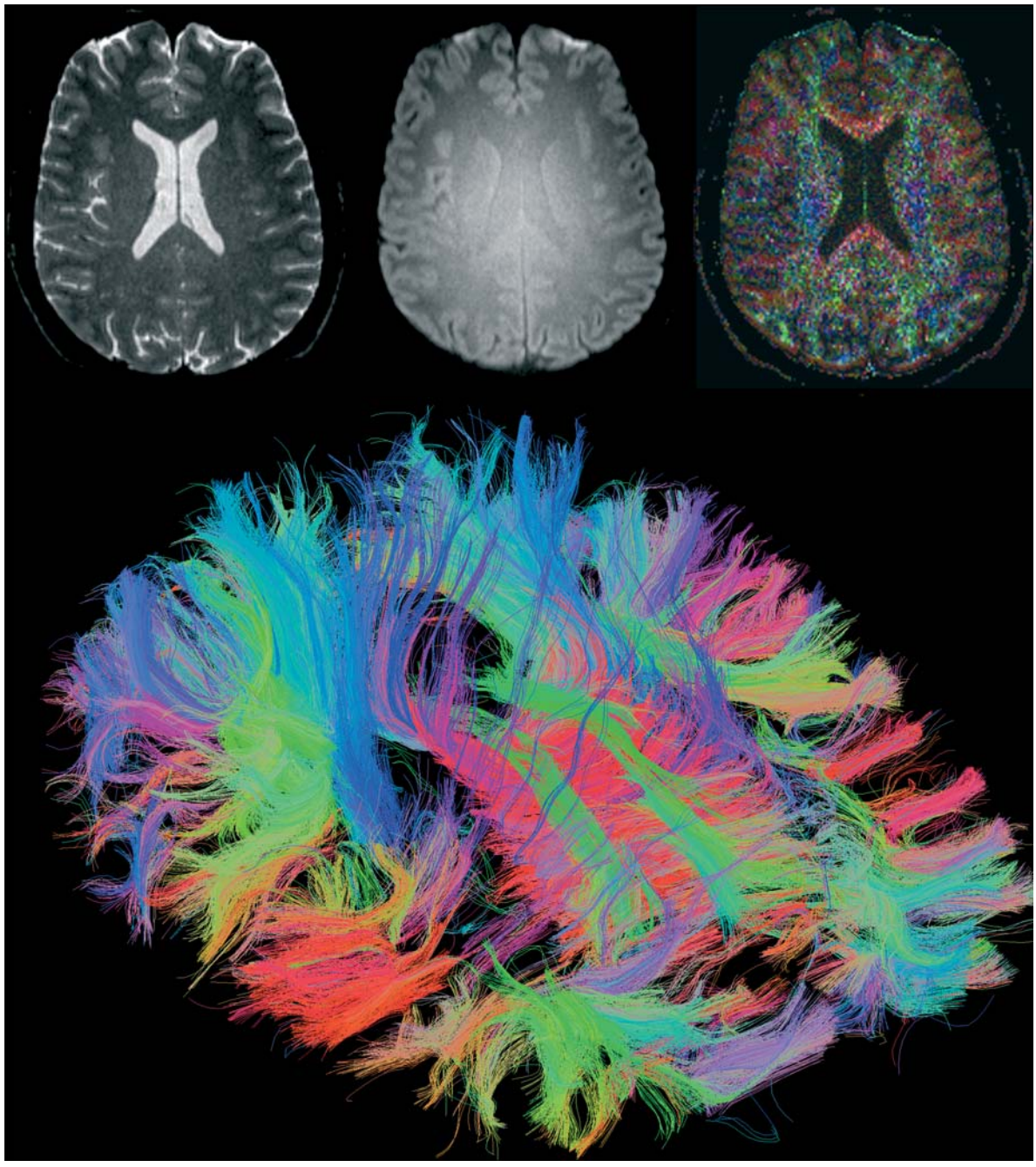

Fig. 34.5. Mean non-diffusion-weighted images, mean diffusion-weighted images and color-coded fractional anisotropy (FA) map (*top row*, *left* to *right*) from one slice of a high-resolution scan with 1×1×1-mm³ isotropic resolution as well as whole-brain fiber tracking. Only fibers intersecting two transverse slices are shown for clarity. View is from anterior-right-superior. Note detail in mean non-diffusion-weighted image and clear delineation between gray and white matter. Increased signal intensity in the middle of the brain most prominently in the mean diffusion-weighted image is due to intensity normalization. Noisy FA map can be attributed to low signal-to-noise ratio given the high spatial resolution. See Table 34.2 for complete acquisition parameters

shows the results of a 1-mm³ isotropic DTI scan using an acceleration factor R=2 acquired within 13 min (see Table 34.2 for imaging parameters). Without acceleration, the acquisition time would increase by nearly 60% to over 20 min due to an increase of TE from 97 ms to 145 ms and a resulting increase of TR from 11.1 s to 17.5 s. At these spatial resolutions and the given scan time, the coverage in this example is limited to a thin slab of only 64 mm. While the SNR is low – as can be appreciated most easily in the FA map – the mean non-diffusion-weighted and mean diffusion-weighted images show fine detail and good contrast, e.g., between grey and white matter. Fiber tracking – while limited to a thin slab – resolves more detail and takes advantage of reduced partial-volume effects. Of course, such experiments would strongly benefit from higher SNR, which could be gained by using MR scanners at higher field strength without an increase in scan time.

34.3 DTI Protocols

Tables 34.1 and 34.2 list the protocol parameters for a number of DTI scans, ranging from ultra-fast 20-s acquisitions over clinical-style protocols to research protocols used for high-resolution imaging, FA mapping and fiber tracking. An ultra-fast acquisition with an acquisition time of less than 30 s is ideally suited for emergency-room patients or uncooperative patients where a routine DTI scan over 2 to 3 min would not be feasible or would result in unusable images. A clinical-style scan can be done with acceleration in 1:44 min compared to 2:13 min without acceleration – an increase of nearly 30%.

Accurate estimation of FA and tensor at isotropic resolution (here 2.0×2.0×2.0 mm³) with whole-brain coverage requires scan times in the order of 10 min. Data from these scans are better suited for co-registration to other scan types, e.g., MPRAGE scans, because of sufficient SNR and the isotropic spatial resolution. Co-registration is necessitated in most studies that investigate changes in FA over time or differences in FA over patient groups. Furthermore, these data allow more accurate tensor-based fiber tracking because of the larger number of diffusion-weighted volumes.

More sophisticated techniques like high-angular-resolution diffusion imaging (HARDI), q-space imaging, q-ball imaging and diffusion-spectrum imaging (DSI) allow estimation of more than one fiber orientation per voxel as they are typically found in the sampled voxels at currently used voxel sizes (Wedeen et al. 2000; Frank 2001; Basser 2002; Tournier et al. 2004; Tuch 2004; Wedeen et al. 2005). Figure 34.6 shows an example of the same anatomical region represented as diffusion tensor boxoids and DSI probability-density functions (PDFs). While the tensor representation only resolves one major diffusion direction as the average of the fiber populations in that voxel, the PDF representation resolves multiple fiber orientations per voxel. Crossings of fibers can therefore not be resolved using a simple tensor model, but require more sophisticated imaging techniques like DSI and the corresponding processing methods. Since fiber crossings are abundant in the human brain, only a fraction of all fibers can be found using the tensor model, i.e., mostly major fiber tracts with a very dominant fiber orientation per voxel. Furthermore, a higher number of anatomically incorrect fibers are found due to the restrictions of the tensor model.

The duration of q-ball or DSI scans is in the range of 20 min to 1 h due to the high b-values (>3,000 s/mm²) and the large number of diffusion-gradient directions that are required. Full brain coverage can often not be achieved in reasonable scan times at a spatial resolution that still provides sufficient anatomical detail. MR-scanner gradient performance is the major limiting factor for these types of scans. To make these scans possible in a clinically acceptable time, MR gradient performance has to increase significantly. A typical whole-body clinical MR scanner today offers a gradient strength of about 40 mT/m and a slew rate of about 200 T/m/s. To minimize the diffusion encoding time and therefore scan time, gradient coils with twice or more the currently available gradient strength are required. This performance can be achieved with switchable body gradient coils or special head-only gradient coils.

34.4 Fiber Tracking

34.4.1 Methodical Considerations

Tensor-model-based fiber tracking relies on the assumption that the principal eigenvector per voxel represents the orientation of the dominant axonal

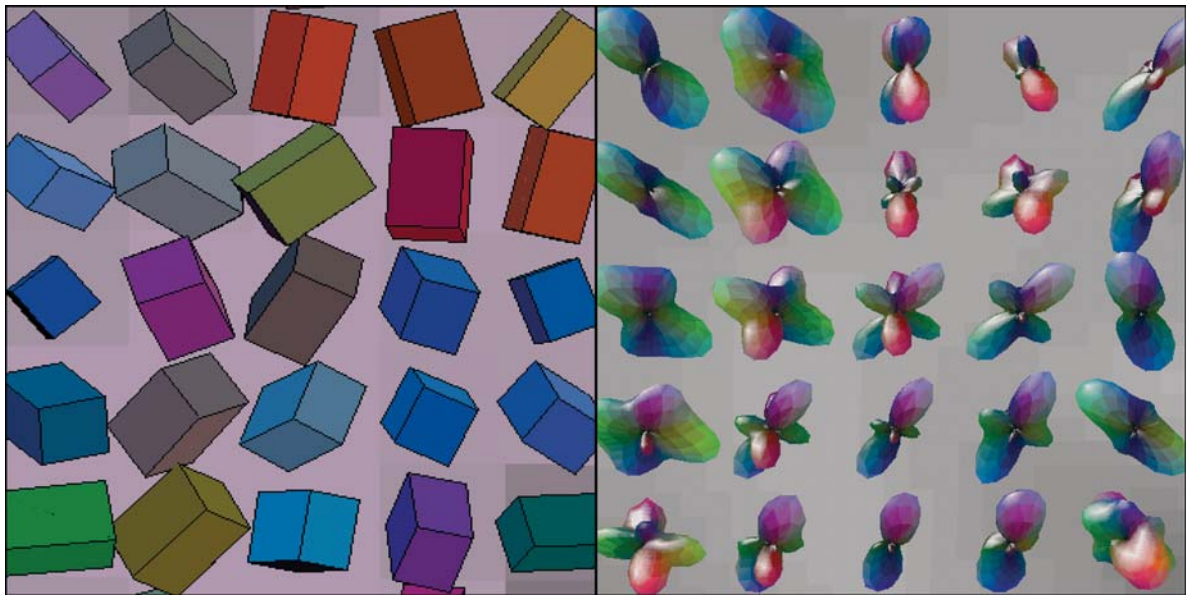

Fig. 34.6a,b. Detailed view of diffusion tensor boxoid representation **a** compared to diffusion spectrum imaging probability density function (PDF) representation **b** of the same anatomical region. Note the multiple separate peaks of the PDFs while the boxoids only show the average diffusion direction of the fiber population found in that voxel

fibers in that voxel. Once the tensors are calculated from the diffusion data, fiber tracking (or tractography) can be performed. The most frequently used technique for fiber tracking uses line propagation to create fiber tracts like that used in FACT (fiber assignment by continuous tracking) (Mori et al. 1999; Xue et al. 1999). Starting from a seed point, a line is propagated by following the local principal-eigenvector direction. A sub-voxel step size is required for successful fiber tracking. Line propagation is usually terminated based on local criteria like the anisotropy or the angle between adjacent fiber segments. Voxels with low anisotropy are found in CSF and gray matter where no or little coherent axonal fiber orientation is found. An appropriate angle threshold depends on the region of interest and the spatial resolution.

Fiber tracking can benefit from parallel imaging in a number of ways: reduced distortions result in fiber tracts that more closely match true anatomy as well as other, less distorted images; faster imaging allows more diffusion directions to be sampled resulting in a more robust tensor estimation and enables advanced imaging techniques like HARDI, q-ball imaging, and DSI; higher spatial resolution reduces partial-volume effects and results in a more detailed depiction of the anatomy.

To visualize fiber-tracking results, the large number of calculated fiber tracts has to be reduced (Fig. 34.7). This can be done by either limiting the seed points to only a region of interest or by retrospective selection of fibers from the whole-brain fiber-tracking results according to certain criteria. These criteria might require that fibers cross a certain slice or a number of slices or that fibers have a certain length or orientation or correlate to each other (Wedeen et al. 2005). A further help is the color coding of fibers, which can either be done on a segment-by-segment basis or using the same color for all segments of a fiber to allow natural grouping of fiber bundles. Colors can be assigned according to a local measure like FA, ADC, or curvature or according to a global measure like overall orientation or curvature. Figures 34.5, 34.7 and 34.8 show applications of some of these criteria.

Currently, most fiber-tracking algorithms and visualization tools do not provide features to assess the uncertainty of fiber orientation. However, uncertainty can be large in areas of, e.g., low SNR, eddy-current artefacts, motion artefacts or pulsatile motion. Therefore, measures of fiber-orientation uncertainty are important. One approach uses the bootstrap method to assign confidence values to results obtained with deterministic tracking algorithms (Jones and Pierpaoli 2005).

While fiber tracking can provide insight into individual normal or diseased anatomy – mostly by visual

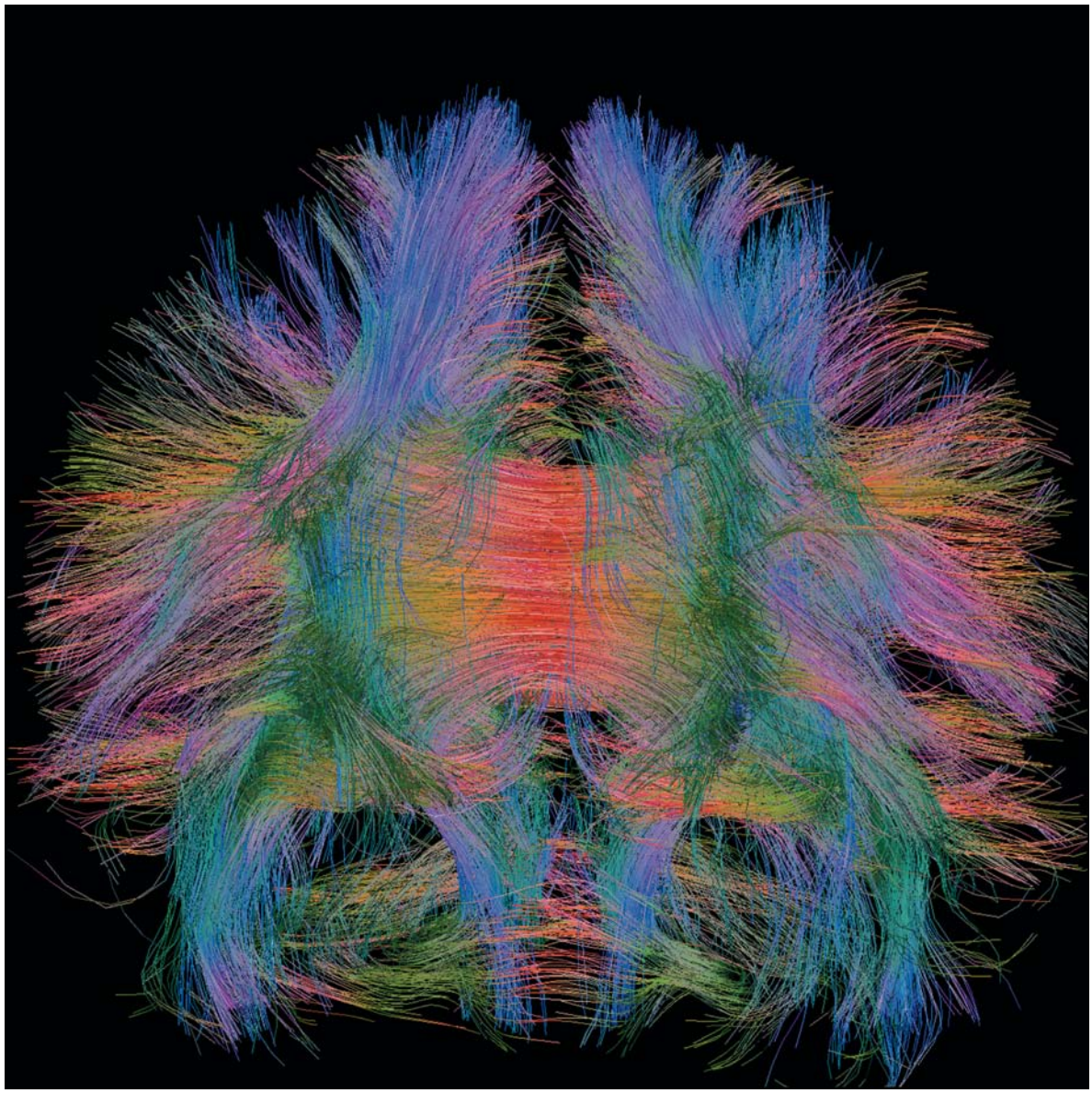

Fig. 34.7. Frontal view of whole-brain fiber tracking for accelerated scans using acceleration factor of R=2. Only every forth of all fibers with a length of more than 40 mm are shown for readability. Color coding is according to local fiber segment orientation

comparison of tracks in the affected hemisphere to the tracks of the contralateral hemisphere – serial studies looking at multiple time points of the same subject and comparative studies trying to find similarities and differences between subjects are currently limited due to the non-scalar nature of the tractography data. To allow straightforward comparison and evaluation, the fiber-tracking data would have to be turned into one or more scalar values similar to an FA map or new methods would have to be developed to allow direct comparison of fiber-tracking results.

34.4.2 Clinical Applications

Figure 34.8 shows images of a patient 5 days after a stroke in the left centrum semiovale, which is clearly identifiable in mean non-diffusion-weighted and mean diffusion-weighted images. While the color-coded FA map hints at a disturbance of anisotropy in the area of the lesion, whole-brain fiber tracking shows no clear evidence of affected fibers in the area of the lesion in comparison with the contralateral

hemisphere. While mean non-diffusion-weighted and mean diffusion-weighted images are easy to interpret, maps of FA or color-coded FA are harder to read due to the strong contrast between gray and white matter and the higher level of noise. Fiber-tracking results are even harder to interpret since in most cases the only reference for visual comparison is the contralateral hemisphere. However, right-left symmetry is not perfect, making any comparison uncertain. Furthermore, while typical MR images can be adjusted in a fairly limited number of ways (e.g., window level and center for display), visualization of fiber tracking results offers a nearly endless range of adjustable parameters, making a close inspection very time consuming.

Fiber tracking can be more straightforward to interpret if the changes are more pronounced as can be the case in tumors. Figure 34.9 shows the results of fiber tracking in a number of stages during and 3 months after surgery of an oligoastrocytoma (Nimsky et al.

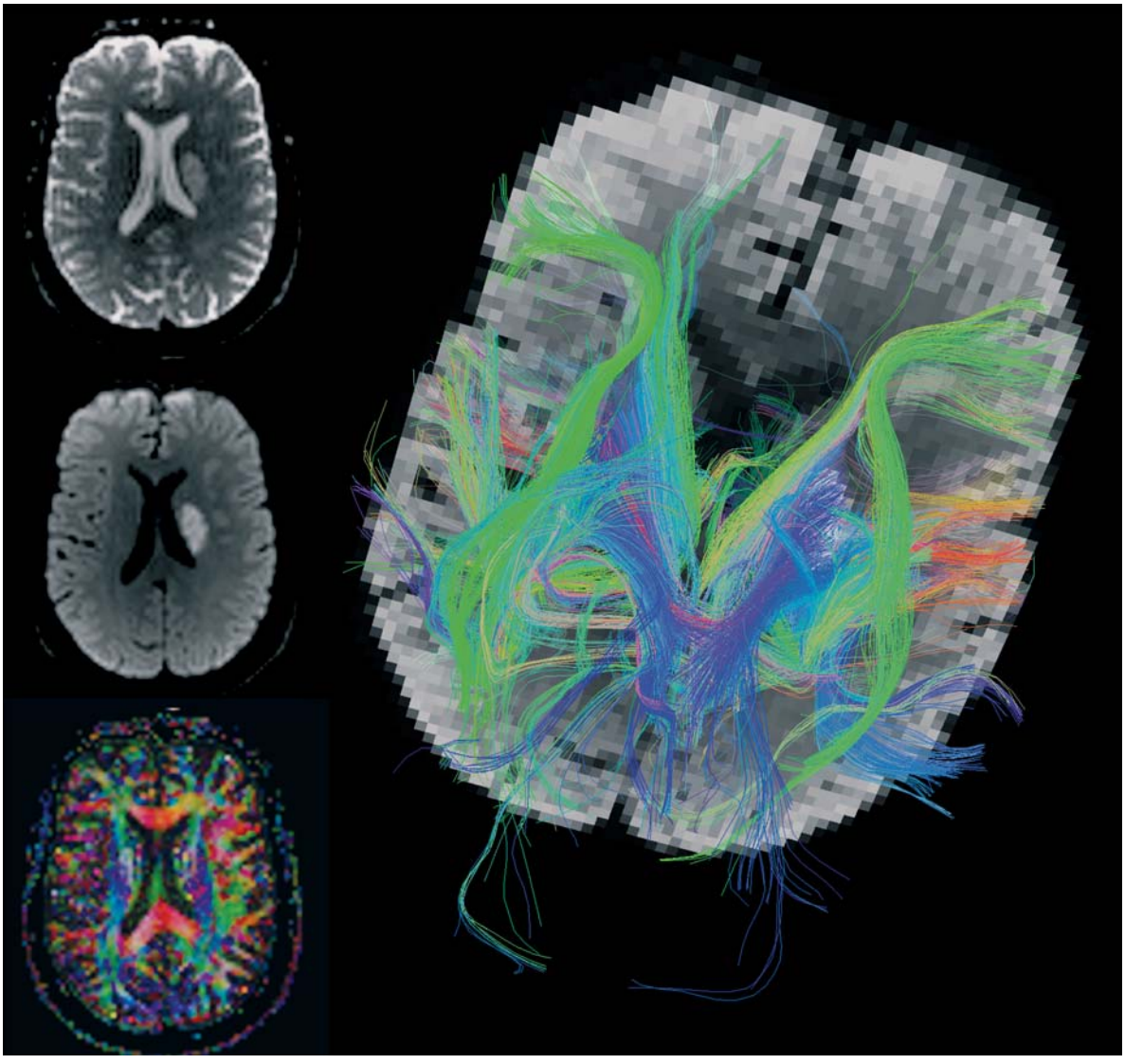

Fig. 34.8. Mean non-diffusion-weighted image, mean diffusion-weighted image and color-coded fractional anisotropy (FA) map (*left column*, *top* to *bottom*) from one slice of a patient with infarct in the left centrum semiovale as well as whole-brain fiber tracking. Only fibers intersecting a few transverse and coronal slices through the lesion are shown for clarity. View is from anterior-right-inferior. The infarcted area is clearly visible on mean non-diffusion-weighted and mean diffusion-weighted images and can also be seen in the background plane of the whole-brain fiber tracking image. No obvious differences between infarcted area and contralateral side are visible in fiber tracking

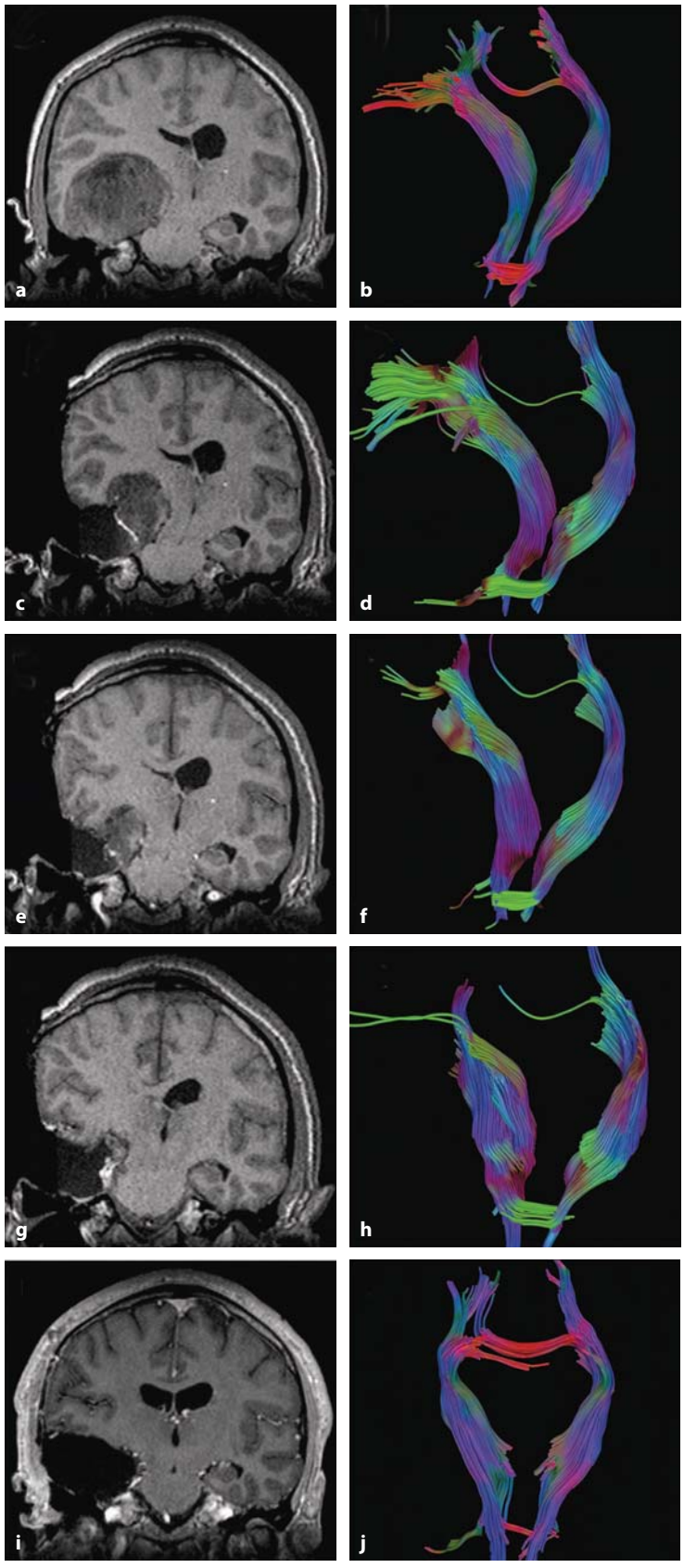

Fig. 34.9a–j. Intraoperative tractography visualizes a marked outward shifting of the right pyramidal tract during resection of a right temporoparietal oligoas-trocytoma WHO Grade III in a 29-year-old male patient (**a,c,e,g,i**) T1-weighted coronal MRI scans; (**b,d,f,h,j**) tractography of the pyramidal tracts; **a** and **b**, preoperative; **c,d–g,h**, during tumor resection with *G* and *H* after completed tumor removal; *I* and *J*, 3 months after surgery. Note that the color coding of the anteroposterior direction is exchanged with the left/right direction because of the horizontal placement of the head for surgery during imaging in **d,f,h** [reprinted with permission from (Nimsky et al. 2005)]

2005). During the course of the surgery, multiple DTI data sets were acquired within 5 min, each covering the whole brain at a isotropic spatial resolution of 1.9×1.9×1.9 mm³. In this study, comparison of preoperative and intra-operative fiber tracking visualized shift and deformation of major white matter tracts caused by the tumor resection. The position of white matter tracts relative to the resection cavity margin is important to minimize the risk of injury to these essential motor fibers. This study also demonstrates the need for an intra-operative update of navigation systems during such procedures.

34.5 Conclusion

Diffusion-tensor imaging requires the acquisition of a large number of mostly diffusion-weighted volumes, and echo-planar imaging is the method of choice for the imaging of the brain. Parallel-imaging techniques provide a number of major benefits for this application: (1) decreased distortion in EPI scans, i.e., better match with true anatomy and other images and therefore easier co-registration; (2) shorter echo times and resulting shorter repetition times that make otherwise prohibitively long scans feasible and allow ultra-fast imaging or more coverage or additional measurements at the same scan time; (3) feasibility of high-spatial-resolution imaging, providing anatomical details that would be hard to achieve otherwise. With reduction in signal-to-noise ratio being the major disadvantage, parallel imaging has become a standard tool for diffusion-tensor imaging of the brain given the widespread availability of phased-array head coils.

Acknowledgements. The authors would like to thank Cristina Granziera, Chris Melinosky, A. Gregory Sorensen, André J. W. van der Kouwe, Larry L. Wald and Graham C. Wiggins.

References

Baird AE, Warach S (1998) Magnetic resonance imaging of acute stroke. J Cereb Blood Flow Metab 18: 583–609

Basser PJ, Mattiello J, LeBihan D (1994) MR diffusion tensor spectroscopy and imaging. Biophys J 66: 259–67

Basser PJ (1995) Inferring microstructural features and the physiological state of tissues from diffusion-weighted images. NMR Biomed 8: 333–344

Basser PJ (2002) Relationships between diffusion tensor and q-space MRI. Magn Reson Med 47: 392–397

Beaulieu C et al (2005) Imaging brain connectivity in children with diverse reading ability. Neuroimage 25: 1266–1271

Choi SJ et al (2005) Diffusion tensor imaging of frontal white matter microstructure in early Alzheimer's disease: a preliminary study. J Geriatr Psychiatry Neurol 18: 12–19

Conturo TE et al (1999) Tracking neuronal fiber pathways in the living human brain. Proc Natl Acad Sci USA 96: 10422–10427

Cruz Junior LC, Sorensen AG (2005) Diffusion tensor magnetic resonance imaging of brain tumors. Neurosurg Clin N Am 16: 115–134

Fellgiebel A et al (2005) Color-coded diffusion-tensor-imaging of posterior cingulate fiber tracts in mild cognitive impairment. Neurobiol Aging 26: 1193–1198

Frank LR (2001) Anisotropy in high angular resolution diffusion-weighted MRI. Magn Reson Med 45: 935–939

Griswold MA et al (2002). Generalized autocalibrating partially parallel acquisitions (GRAPPA). Magn Reson Med 47:1202–1210

Hossmann KA, Hoehn-Berlage M (1995) Diffusion and perfusion MR imaging of cerebral ischemia. Cerebrovasc Brain Metab Rev 7: 187–217

Jenkinson M, Smith S (2001) A global optimisation method for robust affine registration of brain images. Med Image Anal 5: 143–156

Jones DK (2004) The effect of gradient sampling schemes on measures derived from diffusion tensor MRI: a Monte Carlo study. Magn Reson Med 51: 807–815

Jones DK, Pierpaoli C (2005) Confidence mapping in diffusion tensor magnetic resonance imaging tractography using a bootstrap approach. Magn Reson Med 53: 1143–1149

Le Bihan D et al (1988) Separation of diffusion and perfusion in intravoxel incoherent motion MR imaging. Radiology 168: 497–505

Le Bihan D (1991) Molecular diffusion nuclear magnetic resonance imaging. Magn Reson Q 7: 1–30

Mattiello J, Basser PJ, Le Bihan D (1997) The b matrix in diffusion tensor echo-planar imaging. Magn Reson Med 37: 292–300

Mori S et al (1999) Three-dimensional tracking of axonal projections in the brain by magnetic resonance imaging. Ann Neurol 45: 265–269

Moseley M (2002) Diffusion tensor imaging and aging - a review. NMR Biomed 15: 553–560

Moseley ME et al (1990) Diffusion-weighted MR imaging of acute stroke: correlation with T2-weighted and magnetic susceptibility-enhanced MR imaging in cats. AJNR Am J Neuroradiol 11: 423–429

Neil J et al (2002) Diffusion tensor imaging of normal and injured developing human brain - a technical review. NMR Biomed 15: 543–552

Nguyen TH et al (2005) MR tractography with diffusion tensor imaging in clinical routine. Neuroradiology 47: 334–343

Nimsky C et al (2005) Preoperative and intraoperative diffusion tensor imaging-based fiber tracking in glioma surgery. Neurosurgery 56: 130–137; discussion 138

Norris DG (2001) Implications of bulk motion for diffusion-weighted imaging experiments: effects, mechanisms, and solutions. J Magn Reson Imaging 13: 486–495

Nusbaum AO et al (2001) Regional and global changes in cerebral diffusion with normal aging. AJNR Am J Neuroradiol 22: 136–142

Pierpaoli C, Basser PJ (1996) Toward a quantitative assessment of diffusion anisotropy. Magn Reson Med 36: 893–906

Pruessmann KP et al (1999) SENSE: sensitivity encoding for fast MRI. Magn Reson Med 42: 952–962

Reese TG et al (2003) Reduction of eddy-current-induced distortion in diffusion MRI using a twice-refocused spin echo. Magn Reson Med 49: 177–182

Salat DH et al (2005) Age-related alterations in white matter microstructure measured by diffusion tensor imaging. Neurobiol Aging 26: 1215–1227

Shiga Y et al (2004) Diffusion-weighted MRI abnormalities as an early diagnostic marker for Creutzfeldt-Jakob disease. Neurology 63: 443–439

Snook L et al (2005) Diffusion tensor imaging of neurodevelopment in children and young adults. Neuroimage 26: 1164–1173

Sotak CH (2002) The role of diffusion tensor imaging in the evaluation of ischemic brain injury - a review. NMR Biomed 15: 561–569

Tournier JD et al (2004) Direct estimation of the fiber orientation density function from diffusion-weighted MRI data using spherical deconvolution. Neuroimage 23: 1176–1185

Tuch DS (2004) Q-ball imaging. Magn Reson Med 52: 1358–1372

van der Kouwe AJ et al (2005) On-line automatic slice positioning for brain MR imaging. Neuroimage 27: 222–230

Warach S et al (1992) Fast magnetic resonance diffusion-weighted imaging of acute human stroke. Neurology 42: 1717–1723

Wedeen VJ et al (1996) Diffusion aniostropy and white matter tracts. Second International Conference on Functional Mapping of the Human Brain, Boston, MA, USA

Wedeen VJ et al (2000) Mapping fiber orientation spectra in cerebral white matter with Fourier transform diffusion MRI. Int Soc Magn Reson Med, California

Wedeen VJ et al (2005) DSI tractography of CNS fiber architecture and cortical architectonics. Int Soc Magn Reson Med, Miami

Wesbey GE, Moseley ME, Ehman RL (1984) Translational molecular self-diffusion in magnetic resonance imaging. II. Measurement of the self-diffusion coefficient. Invest Radiol 19: 491–498

Wiggins GC et al (2005) A 96-channel MRI system with 23- and 90-channel phased array head coils at 1.5 Tesla. Int Soc Magn Reson Med, Miami

Woods RP et al (1998) Automated image registration: I. General methods and intrasubject, intramodality validation. J Comput Assist Tomogr 22: 139–152

Xue R et al (1999) In vivo three-dimensional reconstruction of rat brain axonal projections by diffusion tensor imaging. Magn Reson Med 42: 1123–1127

Imaging of Cardiac Function

35

Bernd J. Wintersperger

CONTENTS

35.1 Basics of Cardiac Functional Analyses with MRI

Cardiac magnetic resonance imaging (MRI) is extensively and routinely used in the assessment of global cardiac-function and regional wall-motion analysis. It has been validated and established as the standard of reference because of its high accuracy, its low intra- and interobserver variability and its high interstudy reproducibility. Therefore, it is well suited not only for initial diagnosis and disease workup, but also for sequential follow-up and therapy monitoring. This is best reflected by the fact that by far most studies on the influence of drugs on the cardiac function demand sequential MRI cardiac functional analysis.

General basic cardiac functional analysis using MRI methods consists of imaging the heart along its different axes that are well known from other imaging modalities such as echocardiography. Cine imaging using modern MR scanners is based on the use of steady-state free precession (SSFP) techniques commonly referred to as balanced FFE, FIESTA or TrueFISP on different vendors' scanners. It has been shown that the contrast-to-noise ratios (CNR) markedly exceed those of gradient-recalled echo (GRE) techniques (Barkhausen et al. 2001; Carr et al. 2001; Thiele et al. 2001; Moon et al. 2002) (Fig. 35.1). This improved CNR facilitates a better delineation of epi- and endocardial borders and therefore improves the efficiency and accuracy of semi-automated contour detection algorithms. Volumetric assessment of the ventricles is most commonly based on stacks of double-oblique short-axis slices. This allows the application of Simpsons' rule for volumetric assessment. In addition, regional wall-motion analysis can be based on the same data since in short-axis orientation the myocardium is usually uniformly cut in a perpendicular fashion. Therefore, qualitative and quantitative assessment of wall thickening can be best accomplished by this approach. For acquisition of cine data sets, segmented single-slice SSFP techniques are used. The combination of all required axes covered with a single-slice each breath-hold therefore takes considerable time (about 15 to 20 min).

Since cardiac cine MRI is limited to breath-hold imaging, any technique that allows for the reduction of the data acquisition time while maintaining the high standards of cine MRI is most welcome. One of the primary aims of cardiac cine imaging is to further increase acquisition speed. This chapter gives guidance for the use of parallel-imaging algorithms in conjunction with cardiac cine MRI, and proposals for sequence parameters for various applications are illustrated.

B. J. Wintersperger, MD
Department of Clinical Radiology, University Hospitals – Grosshadern, Ludwig Maximilian University of Munich, Marchioninistr. 15, 81377 Munich, Germany

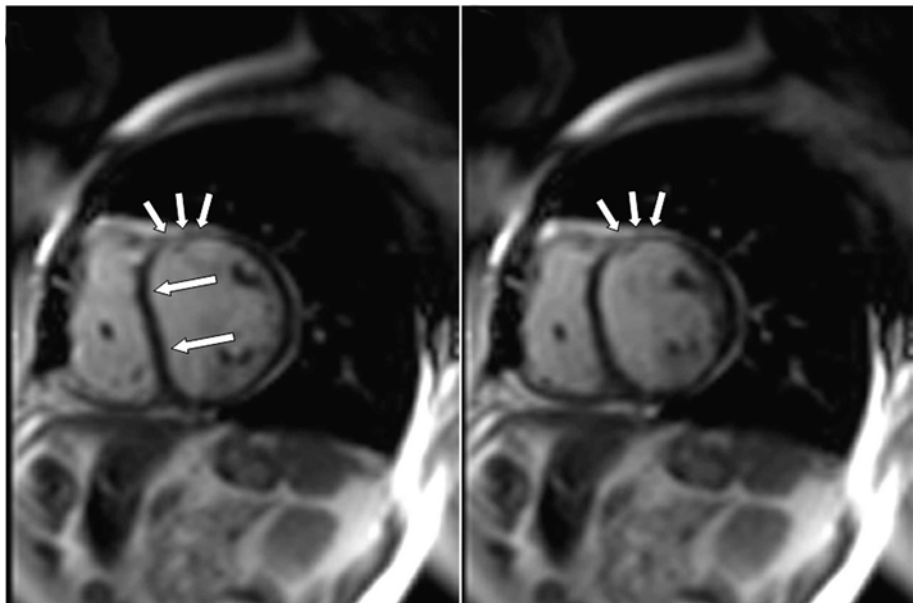

Fig. 35.1a,b. Real-time cine SSFP images in a patient with myocardial infarction, ischemic cardiomyopathy and pulmonary hypertension acquired with 128 matrix and 50 ms temporal resolution (GRAPPA *R*=2) in breath-hold. Frames in **a** early systole and **b** diastole do show a dyskinetic septum slightly bulging into the left ventricle (*large arrows*), a marked thinning of the anterior wall due to scarring and an overall severely impaired left-ventricular function (ejection fraction 24%)

35.2 Real-Time Cine Techniques

Real-time cine imaging is a fast imaging technique that needs to be capable of freezing cardiac and respiratory motion. The technique can basically be used either without or with ECG gating and breath-holding.

Real-time techniques sample data for each frame in a continuous fashion within a single cardiac cycle. This allows real-time cine imaging to be used also in patients that are not capable of breath-holding as the technique virtually freezes cardiac and respiratory motion. Conventionally, this aim has been pursued by the use of more efficient data acquisition schemes such as echo-planar or spiral MR imaging. The availability of parallel-imaging strategies now also allows for a considerable gain in acceleration. It has been shown that real-time techniques are capable of analyzing global cardiac function within a single breath-hold (Barkhausen et al. 2002; Lee et al. 2002). A major factor influencing volumetric accuracy, however, is temporal resolution as shown by Miller et al. in a volunteer study (Miller et al. 2002). To avoid offsets of end-systolic volume (ESV), the temporal resolution needs to be in the range of about 50 ms or less. This requirement can hardly be met by full k-space coverage using non-EPI techniques (Barkhausen et al. 2002; Kramer et al. 2003). Parallel imaging allows overcoming these limitations without further reduction in spatial resolution. It has already been shown that real-time cine SSFP techniques using parallel imaging allow for accurate evaluation of global left-ventricular function (Wintersperger et al. 2003). Within a reasonable breath-hold length of about 20 heart beats, 10 short-axis slices can be acquired. However, spatial resolution still suffers as a result of the real-time approach and the restrictions of the temporal resolution. Hence, accuracy of quantitative wall thickness assessment might be limited while qualitative wall motion analysis in dobutamine stress imaging seems to be possible (Kramer et al. 2003).

The real benefit of real-time cine MR, however, is the ability to scan without the need for breath-holding and ECG gating. While non-cooperative patients may only be one possible indication, insights into cardiac motion under physiologic conditions (regular respiratory cycles) is likely to be the more inter-

esting perspective of this technique. Francone et al. (2005) demonstrated the ability of real-time cine imaging to allow for differentiation of cardiac diseases such as constrictive pericarditis and restrictive cardiomyopathy. They focused on septal wall motion abnormalities and found significant differences that are most likely based on different filling and pressure patterns. It is obvious that breath-holding does have an impact on cardiac filling as the intra-thoracic pressure affects venous return, which can be nicely shown during Valsalva maneuvers. But there is a need for further investigations in respect to physiologic cardiac motion and function using real-time cine MRI to give new insights into various diseases.

Currently used parallel-imaging acceleration factors in real-time cine MRI are in the range of R=2-3 depending on the available coil systems and reconstruction algorithms. The number of spatially distributed coil elements determines the theoretically possible maximal acceleration, thus further speed-up is limited to multi-channel (>16 independent RF channels) systems only. In real-time cine MRI, a strong focus has to be put on the selection of the field of view (FOV). In order to maximize spatial resolution, the FOV is usually kept at a minimum, thus potentially raising the need for a larger rectangular FOV, which directly affects the number of phase-encoding steps and also the temporal resolution of the real-time cine scan. Previously used workarounds like switching off posterior coil elements to avoid aliasing do not work anymore as the spatial distribution of signal is needed for image reconstruction. Restrictions regarding FOV may occur in combination with parallel imaging as some of the available reconstruction algorithms such as SENSE are not able to handle pre-aliased image data robustly and therefore artefacts arise (Griswold et al. 2004). GRAPPA has been shown to allow for less artefact-affected images than SENSE or mSENSE in cardiac cine imaging (Hunold et al. 2004). TSENSE is an alternative algorithm that is dedicated to the use in dynamic MR techniques. Based on a high-resolution sensitivity profile and other implementations, TSENSE does not show major artefacts in cases of a limited FOV. In addition it allows getting to higher acceleration factors based on its data sampling scheme, which is highlighted in other chapters of this book (Chaps. 8 and 12). In real-time cine imaging, however, TSENSE may be of limited use in patients with exaggerated breathing and thus major variation of cardiac position during the respiratory cycle. As sensitivity profile information

Table 35.1. Proposals for real-time and segmented cine SSFP protocols; protocols are based on a 45 mT/m gradient system (Siemens Magnetom Avanto); changes may apply depending on scanners and detailed scan parameters (e.g. bandwidth) needed for clinical purpose

Purpose	Matrix	Phase-enc. lines	Lines/segment	Algorithm	Parallel-imaging acceleration R	Spatial resolution (mm²)	Temp. resolution (ms)	Remarks
Real-time cine MRI (higher spatial resolution)	192	80	n.a.	TSENSE	3	2.0×3.6^{+}	~64	TSENSE algorithm may show artefacts in exaggerated breathing; GRAPPA algorithm less sensitive to exaggerated breathing
Real-time cine MRI (higher temporal resolution)	128	60	n.a	TSENSE	3	3.0×4.7^{+}	~48	TSENSE algorithm may show artefacts in exaggerated breathing; GRAPPA algorithm less sensitive to exaggerated breathing
Real-time cine MRI (higher temporal resolution)	128	60	n.a	GRAPPA	2	3.0×4.7^{+}	~47	About 12 reference lines; protocol is using shared-phases technique
Segmented cine MRI (standard spatial resolution)	192	117	17	TSENSE	2-4	1.9×2.5$^{\&}$	~48	Increasing noise with higher acceleration; R=4 allows for about five slices/breath-hold
Segmented cine MRI (higher spatial resolution)	256	156	17	TSENSE	2-3	1.4×1.9$^{\&}$	~48	R=4 may not be recommended with the lower SNR in higher spatial resolution

+ Based on a 380×285 mm² FOV (75% rectangular in phase-enc. direction) and based on a 360×292 mm² FOV (81% rectangular in phase-enc. direction)

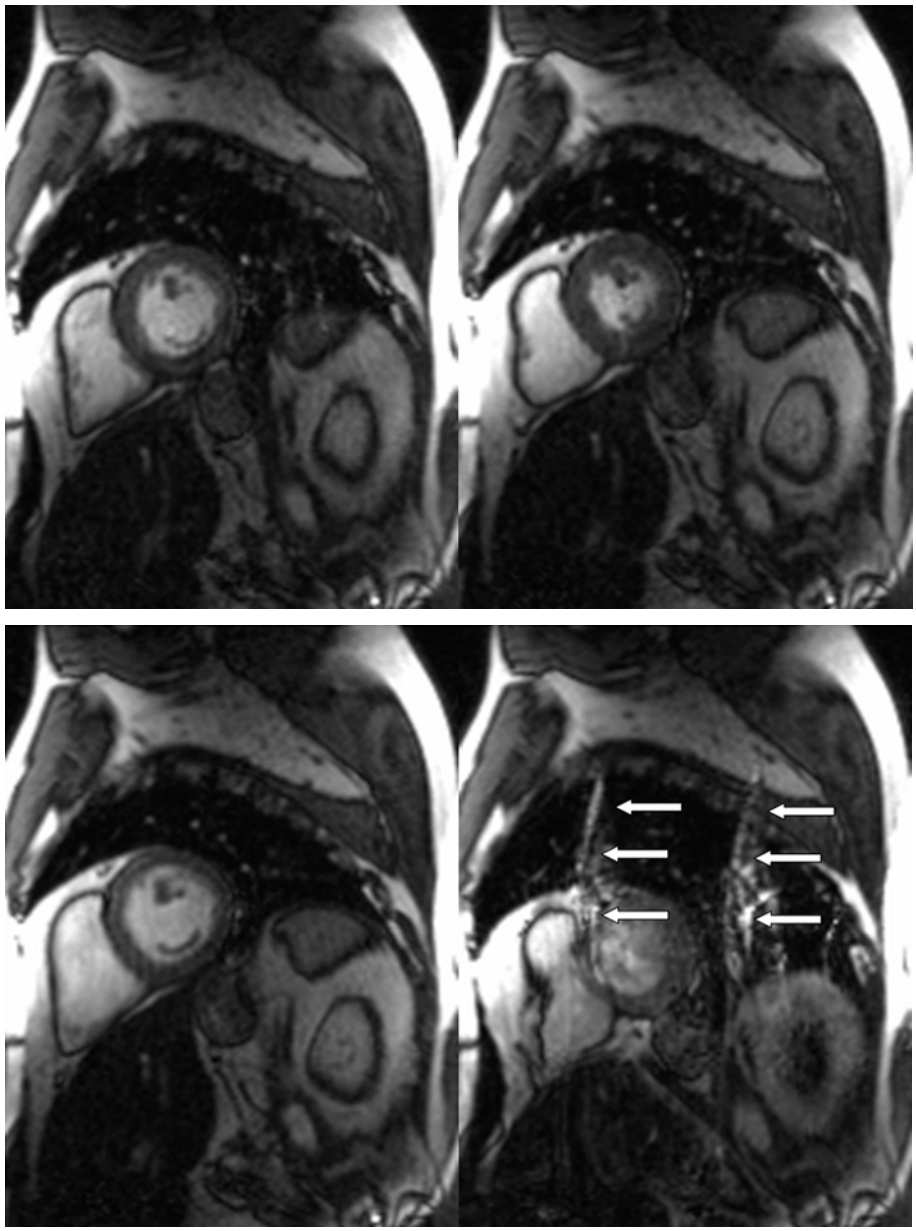

Fig. 35.2. a Image frames of a TSENSE (*R*=3) real-time cine SSFP acquisition in a volunteer with normal respiration. Only minor changes in the diaphragm and chest wall are noted. **b** Same volunteer and imaging technique as in **a** now with exaggerated breathing and thus major differences in the position of the heart and the chest wall. These major offsets lead to reconstruction artefacts (*arrows*) using TSENSE (*R*=3) as the sensitivity map is averaged over multiple frames

in TSENSE is averaged over multiple phases, major changes in the gross anatomy appearance will lead to major artefacts in reconstruction (Guttman et al. 2003) (Fig. 35.2). Hence, TSENSE might not be considered as the algorithm of choice for real-time cine MRI in patients with exaggerated breathing, although it provides excellent quality in patients with shallow to normal breathing. An overview of protocol proposals in different applications is given in Table 35.1.

35.3 Segmented Cine Techniques

Segmented cine imaging is considered to be the most common technique used in the daily routine of clinical cardiac MRI. Basically, the technique of acquiring multiple phase-encoding steps differs from real-time cine MRI in that data sampling is accomplished over multiple cardiac cycles (Fig. 35.3). Thus, this tech-

nique does raise the need for an adequate breath-holding. Change of either temporal or spatial resolution does have an implication on the number of heart beats needed for scanning, but they are not directly linked as in real-time cine imaging. The acquisition of high resolution (spatial, temporal or both) restricts this technique to single-slice acquisitions only. Hence, further speed-up of data acquisition is desirable. Any reduction in the data acquisition time comes along with a loss regarding the signal-to-noise ratio (SNR). SSFP cine techniques, however, do offer a high intrinsic SNR and CNR, thus allowing for sacrifices.

However, there are certainly limits to the acceptable loss in the signal-to-noise ratio. In addition, artefacts may also arise in segmented cine MRI with the use of parallel-imaging techniques. k-space-based algorithms have been shown to allow for a better image quality regarding artefacts at an acceleration of R=2 (Hunold et al. 2004). This study compared mSENSE and GRAPPA reconstructions and also showed a superior SNR level for the GRAPPA algorithm. Changes in SNR, CNR and overall image appearance also depend on the coil geometry used (see below). On standard coil arrays and scanner systems, the acceptable acceleration factor will be in the range of R=2-3, which already allows a considerable speed-up in data acquisition. Using multi-channel MR systems, the acceptable acceleration rate may even be up to R=4 without a change in volumetric accuracy.

The speed-up of data acquisition resulting in shorter breath-hold periods allows for one of the following changes:

- Use of segmented cine MRI in patients with severe dyspnea
- Improvement of spatial or temporal resolution
- Data acquisitions with multi-slice approaches

Dyspneic patients may not be able to hold their breath for an adequate period to maintain acceptable results with segmented cine imaging. Real-time cine MRI with its restrictions to either spatial or temporal resolution might be the only option for these patients. The shortening of breath-hold periods to only about three to six heart beats may allow the use of segmented cine techniques, thus enabling a better volumetric accuracy and a higher confidence level for wall motion assessment.

Spatial resolution in segmented cine MRI does not represent a common problem. Techniques are anyway designed to use matrices in the range of 192-256, thus enabling pixel sizes of 1-2 mm^2. Further improvement of spatial resolution may be desirable in some instances; however, the further reduction is at the additional sacrifice of SNR (Fig. 35.4).

Temporal resolution should not be worse than 45-50 ms as shown by different studies. The isovolumetric relaxation at end-systole represents a very short

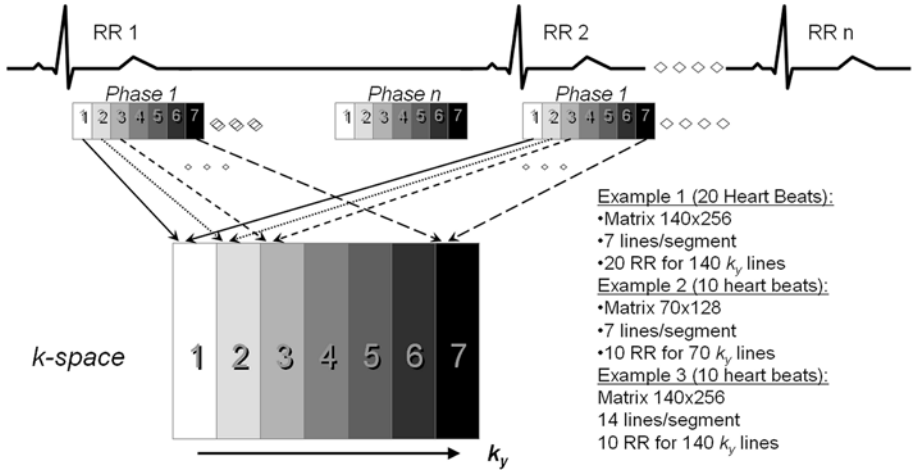

Fig. 35.3. Schematics of segmented data sampling in cine imaging; the phase-encoding steps (k_y lines) for each frame are acquired over multiple cycles and not consecutively in a single cycle as done in real-time cine MRI. In the shown example, seven lines are acquired for each frame in each cardiac cycle. In addition, examples to calculate the data acquisition length for a given number of phase-encoding steps and number of lines per segment are given. Spatial resolution is improved with increasing number of phase-encoding steps, while temporal resolution can be improved by reducing the number of lines per segment. Both strategies influence the number of heart beats required for data acquisition

time period between aortic valve closure and mitral valve opening. This period is flanked by rapid cardiac output in systole and the rapid filling in early diastole. The length of the isovolumetric end-systolic period has been reported to be as short as ~40 ms (Weissler et al. 1968). Focusing on this problem, Setser and coworkers (2000) suggested a sampling frequency of 20–25 Hz based on theoretically necessary data sampling frequencies (based on Nyquist criteria) and volunteer studies. The proposed frequency corresponds to a temporal resolution of 50-40 ms at a heart rate of 60 bpm (Setser et al. 2000). These results were confirmed by another volunteer study using various temporal resolutions (Miller et al. 2002).

Improvement of temporal resolution allows for a more detailed visualization of wall and valve motions. Improvement of temporal resolution beyond 25-30 ms is unlikely to allow further improvement for clinical indications and is only at the cost of additional scan time.

As stated above, regular non-accelerated cine SSFP imaging is performed with single-slice techniques only. The ability to acquire multiple slices within a reasonable breath-hold without the loss of spatial or temporal resolution has to be considered as the major benefit of parallel imaging in combination with cine MRI. Shortening of breath-hold periods would allow for the acquisition of more than one slice at the same time. In patients with normal breath-hold capabilities, multi-slice data acquisitions are now feasible, thus allowing for a considerable shorting of overall functional evaluation of the heart. Short axis coverage is now possible with as many as two breath-holds (five slices each) only without any change in the parameters of spatial or temporal resolution. However, this requires acceleration factors as high as R=4 and thus leads to considerable loss in SNR and CNR (Fig. 35.5, TSENSE at 1.5 T: R=1 to R=4). Volumetric accuracy regarding global ventricular function is maintained while regional wall motion and/or visualization of subtle structures may be limited based on increased image noise and artefacts (Wintersperger et al. 2006). These high acceleration factors demand not only multi-element coil arrays and multi-channel MR systems, but also dedicated algorithms for parallel-imaging reconstructions. Sensitivity maps in parallel imaging are either provided by separate scans (e.g., SENSE and SMASH) or by integrated acquisition of

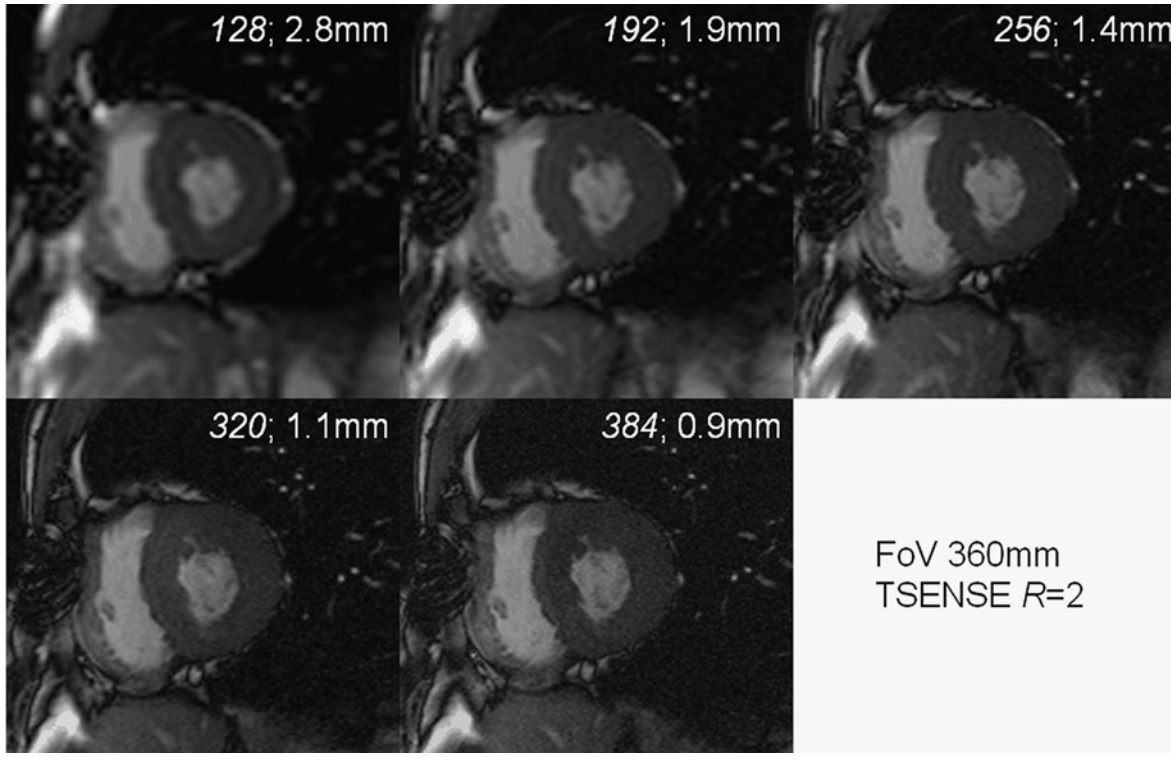

Fig. 35.4. Illustration of the influence of spatial resolution on image appearance, image details and noise; with improved spatial resolution more details are shown, but at the cost of SNR as the noise increases with smaller image voxels. A 256 matrix is a good trade-off in terms of spatial resolution and noise. All data shown here are acquired with TSENSE (R=2)

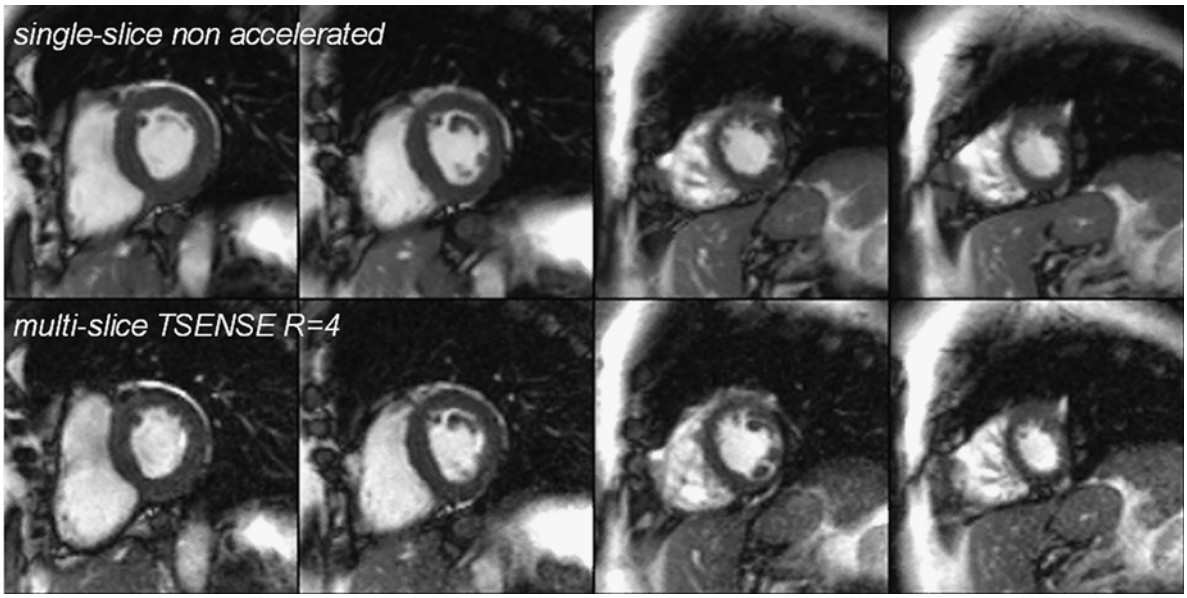

Fig. 35.5. Comparison of cine SSFP data acquired without and with TSENSE acceleration. *Upper-row* images show part of a short-axis data set in early diastole acquired in a single-slice non-accelerated technique. *Lower row* shows the matching locations of a multi-slice TSENSE acquisition (five slices/breath-hold) using a four-fold acceleration (R=4). Acceleration comes along with increased noise and thus reduced SNR, but data acquisition does require only two breath-holds

this additional data during the diagnostic scan (e.g., mSENSE and GRAPPA). As explained in detail in the technical parts of this book (Chaps. 2, 8, and 12), the effective acceleration factor R is less than the nominal acceleration as additional phase encodings are performed for sensitivity-profile measurements. In cine imaging, these "reference lines" or "auto-calibration signal" (ACS) lines are acquired during every single phase. Depending on the acceleration factor R, these lines represent an increasing percentage of all lines to be acquired. To avoid these problems of limited acceleration, dedicated algorithms for dynamic imaging techniques are to be preferred. TSENSE has been shown to allow for higher acceleration in cine MRI than GRAPPA based on its interleaved acquisition of even and odd phase-encoded lines that automatically incorporate a high-resolution sensitivity-profile map of the coil array (Reeder et al. 2005; Wintersperger et al. 2006) (Fig. 35.6). Unlike basic SENSE techniques without additional improvement (e.g., UNFOLD), TSENSE is less susceptible to artefacts arising from pre-aliased images. In any patient, however, the field of view should be optimized in terms of size and rotation (if possible on a scanner) to avoid any additional wrapping and thus artefacts. Regardless of the algorithm used for accelerated cine imaging, multi-slice imaging also faces the need for multiple dummy cardiac cycles that are used for steady-state preparation rather than for data sampling. Each 2D slice is preceded by a magnetization preparation cycle (for steady-state), thus acquiring five slices/breath-hold already includes five preparation cycles. With increasing acceleration, these preparation cycles may cover as much as 25% to 40% of the breath-hold period (Wintersperger et al. 2006).

Useful and possible protocols and accelerations are actually dependent on scanner and coil arrays being used for cine imaging on the scanner. In addition, the clinical background of a patient and the reason for MR referral should also be included in the decision-making process. Once assessment of global left-ventricular functional parameters is the only reason for cine MRI, high acceleration factors may be used to allow for multi-slice segmented SSFP cine imaging, thus shortening the examination time. Regarding subtle wall motion abnormalities and changes, no data have yet been published on the influence of different acceleration factors. It has been shown, however, that noise and artefacts show a steady incline with increasing acceleration that may limit the diagnostic quality of the scans (Wintersperger et al. 2006). Various scan setting proposals for the use of segmented cine SSFP sequences are shown in Table 35.1.

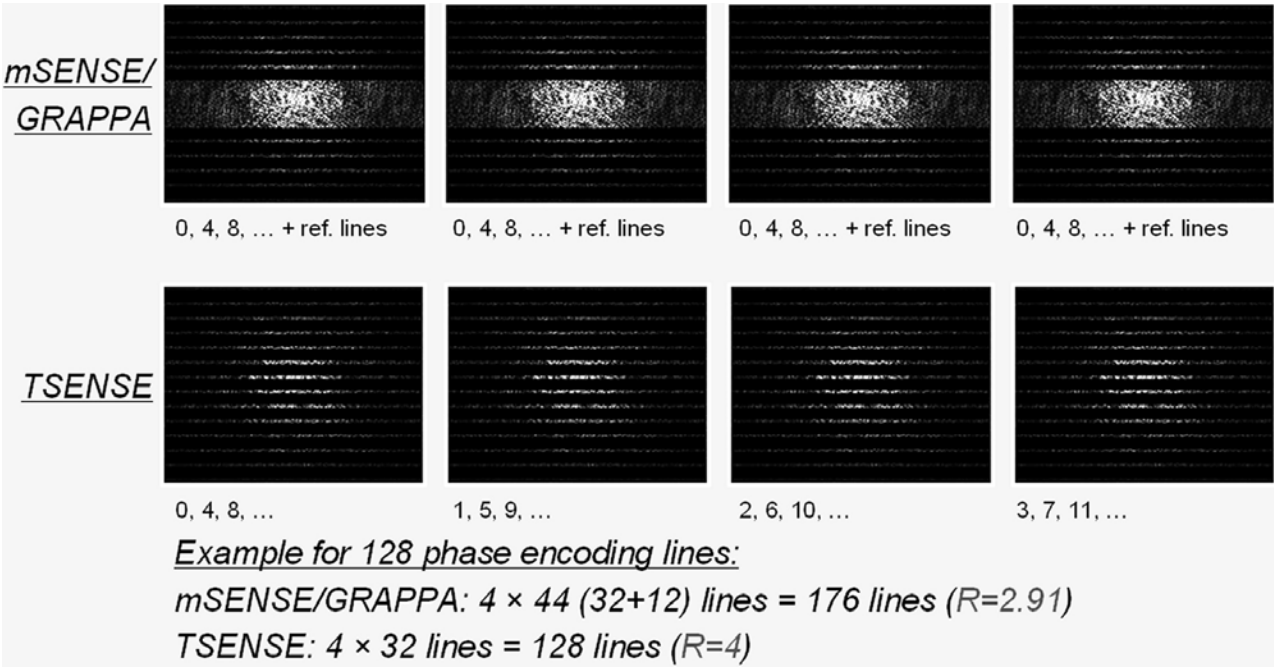

Fig. 35.6. Schematic comparison of different parallel-imaging algorithms in cine imaging that shows the amount of k-space that needs to be acquired at a standard acceleration of R=4: while mSENSE/GRAPPA needs to cover more data within the center of k-space at each frame (reference lines) than in the periphery, TSENSE allows only to acquire every fourth line through k-space. Comparative calculations show that the effective acceleration is higher with TSENSE

35.4 Parallel Cine Imaging at 3 Tesla

With the ongoing introduction of whole body MR systems operating at 3 T, significant efforts have been made to also establish cardiac MR imaging at this field strength (Noeske et al. 2000; Stuber et al. 2002; McGee et al. 2004; Schar et al. 2004). The intrinsic gain of SNR coming along with higher magnetic field strength has been considered a favorable chance to allow parallel imaging with even higher acceleration factors. Theoretically, a two-fold increase of SNR at 3 T can be expected compared to 1.5 T. In practice, an 80% to 90% SNR gain in vivo has already been shown for segmented cine GRE techniques (Wen et al. 1997; McGee et al. 2004). Cine SSFP techniques at 3 T, however, are considered to be challenging based on their intrinsic properties. At 1.5 T, cine SSFP techniques have been shown to be favorable compared to GRE techniques as they allow for a higher constant CNR ratio and thus better contour delineation (Barkhausen et al. 2001). SSFP techniques, however, are based on longitudinal and transversal steady-state magnetization requiring continuous ongoing RF pulsing with relatively large excitation angles (about 45° to 65°). Thus, these sequences are considered techniques with a high specific absorption rate (SAR). In addition, the change from 1.5 T to 3 T markedly increases RF deposition by a factor of 4, thus leading to potential limitations in the use of SSFP techniques at this field strength. Reduced excitation angles are the consequence of these SAR limitations and may sacrifice the excellent CNR for which SSFP techniques are well known. Theoretical considerations and simulations showed optimal CNRs at flip angles of 54° and 42° for 1.5 T and 3 T, respectively (Schar et al. 2004). There are many influencing factors, however, that in the end may lead to different results among which flow might be the most principal and variable one. All current published data on cine imaging at 3 T is based on either GRE techniques or adapted excitation angles that are considerably lower than typically used at 1.5 T. Gutberlet and coworkers showed an approximately 100% gain in SNR at 3 T while CNR did increase by only 19% (!) at 3 T compared to 1.5 T. A much worse contrast of the

left-ventricular blood pool and the myocardium may have contributed to these findings.

Parallel imaging at 3 T, therefore, may have complimentary advantages: compensation for the loss of SNR imposed by accelerated imaging and the reduction of total energy deposition because of the reduced scan times. The latter advantage allows for improved excitation angles at 3 T, thus leading to improved or even optimized CNR of the blood pool and the myocardium. A marked reduction in energy deposition by the use of parallel imaging techniques has been demonstrated for a twofold acceleration (R=2) using GRE cine techniques (McGee et al. 2004). In addition, Wintersperger and co-workers (2006) demonstrated that possible limitations on excitation angles may be overcome with parallel imaging, thus leading to a higher gain in CNR (Fig. 35.7). The sacrifice in SNR by parallel imaging at 3 T is actually less than predicted by physics, as without these algorithms cine SSFP imaging would struggle with low flip angles and non-optimized SNR and CNR (Wintersperger et al. 2006).

As stated above, the natural gain in SNR at 3 T is perfectly suited for being sacrificed to faster acquisitions by means of parallel imaging. The lower SNR induced by the use of these algorithms that decrease the SNR by at least a factor of $1/\sqrt{R}$ is compensated by the higher SNR at 3 T. Looking at the performance of parallel imaging at 3 T compared to 1.5 T, it is easy to see that the loss of SNR introduced by a parallel-imaging acceleration factor of R=4 is approximately compensated by the SNR increase of a factor of 2 from 1.5 T to 3.0 T. Therefore, a four-fold gain in acquisition speed is feasible at 3 T with virtually no penalty in SNR compared to 1.5 T if the g-factor of the coil system is not taken into account. With the gain in SNR in vivo being little less than 100%, a four-fold acceleration may result in a minor inferior SNR compared to non-accelerated cine SSFP at 1.5 T (Wen et al. 1997; Wintersperger et al. 2006). However, within this range of acceleration, the g-factor (geometry factor of the coil array, cf. Chap. 3) does play an incremental role in regard to aggravated SNR losses (Wintersperger et al. 2006). As already stated above, the major benefit of data acquisition shortening is the ability to acquire multiple slices within a single breath-hold. In fact at R=4 up to five slices can be acquired in a breath-hold, thus enabling a dual breath-hold approach to short axis ventricular coverage of cine MRI (Fig. 35.8). The data acquisition time needed once compared with a standard single-slice cine imaging can be reduced by a factor of about 4 to 5 (Wintersperger et al. 2006).

The four-fold increase of SAR at 3 T compared to 1.5 T can be partially counteracted by using slightly longer RF pulses for excitation. However, this will

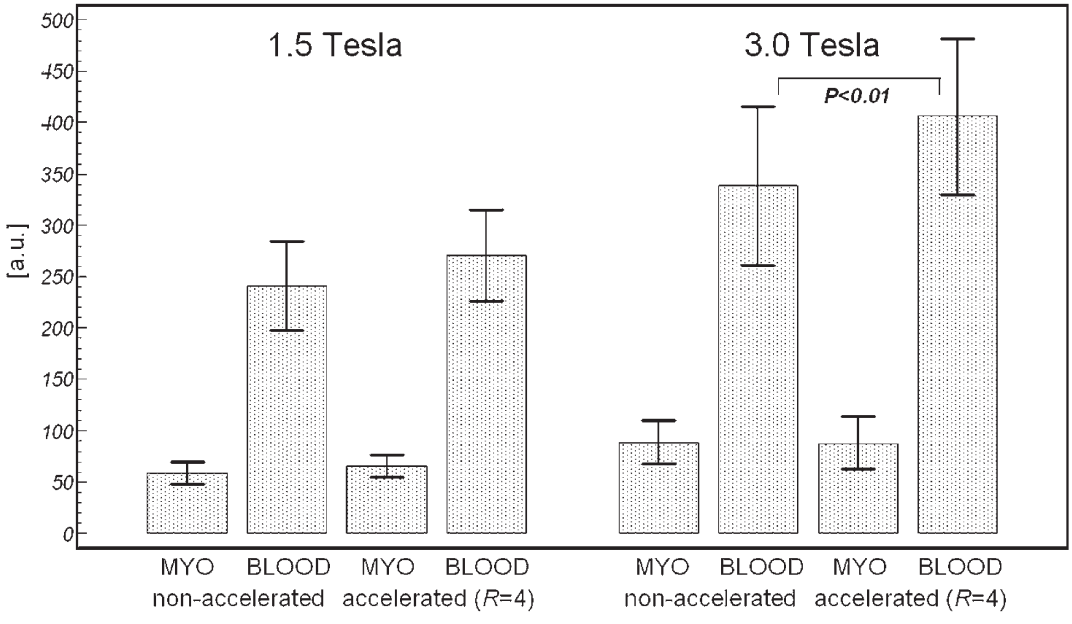

Fig. 35.7. Comparative data of cine SSFP imaging performed at 1.5 and 3 T. While at 1.5 T the acceleration (R=4) did not show an impact on the blood-pool signal, at 3 T TSENSE acceleration allowed higher flip angles, thus leading to higher blood-pool signal. SNR of course is considerably reduced with four-fold acceleration based on increased image noise that is inhomogeneously distributed

result in minor prolonging of TR (by about 200 μs), und thus temporal resolution is somewhat worse compared to 1.5 T. If necessary, this could be overcome by re-adjusting (reducing) the number of lines per segment acquired each heart beat. Otherwise, proposed protocols for 1.5-T cine SSFP imaging can be used as a reference for 3-T cine SSFP MRI.

Apart from the benefits of 3 T in cine SSFP imaging in combination with reduced k-space sampling, artefacts still coming along with SSFP at the higher field strength need to be considered. Frequency fine tuning is especially of interest to locate possible off-resonance artefacts outside the volume of interest (Deshpande et al. 2003; Schar et al. 2004) (Fig. 35.9). In addition new shimming techniques with high-order shimming may further improve and stabilize image quality (Schar et al. 2004).

35.5 Dedicated Multi-Channel Coils for Cine Imaging

To optimize MR imaging of the body and the extremities, arrays of surface coils have been used for improved SNR in recent years. Standard coil arrays for cardiac MRI mostly consist of four to eight single coil elements arranged in the array including an anterior and posterior part. A typical eight-element array consists of four anterior elements and four posterior elements, with both groups arranged in a 2-by-2 fashion. With the advent of parallel imaging, the spatially distributed signal detection became even more relevant as the paramount precondition for parallel-imaging reconstruction of undersampled k-space data and consequently marked reductions in acquisition time. Using an eight-element coil array with the above-mentioned coil arrangement, the maximum factor of acceleration would actually be limited to R=2 in all orthogonal planes. Thus, for the use of higher acceleration factors more coil elements within an array would actually be needed, also necessitating multiple receiver channels. In addition to the number of elements within a coil array, also the number of receiver channels is a concern for spatial differentiation of single coil elements because these elements need to be connected to separate receiver channels. It basically makes no sense in regard to higher acceleration factors to use a 16-element coil array plugged into an 8-receiver-channel MR system as the elements will be paired to a single receiver channel.

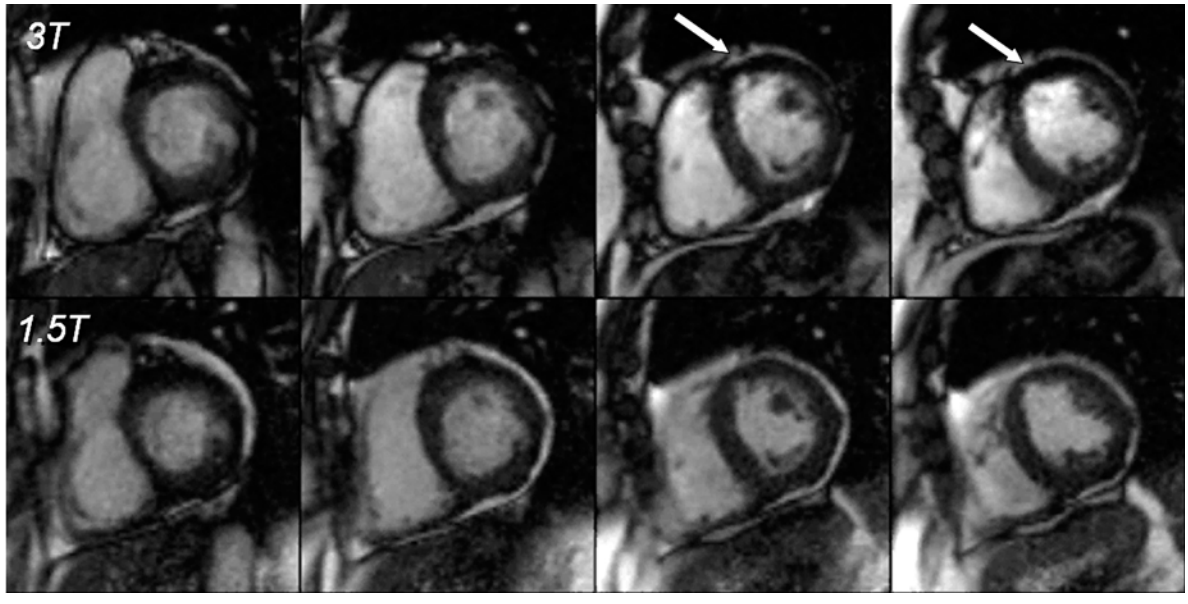

Fig. 35.8. Illustration of TSENSE accelerated cine SSFP imaging performed in a patient with chronic myocardial infarction at (*upper row*) 3 T and (*lower row*) 1.5 T; 3-T images show less image noise and higher blood-pool signal though minor off-resonance artefacts (*arrows*) are noted

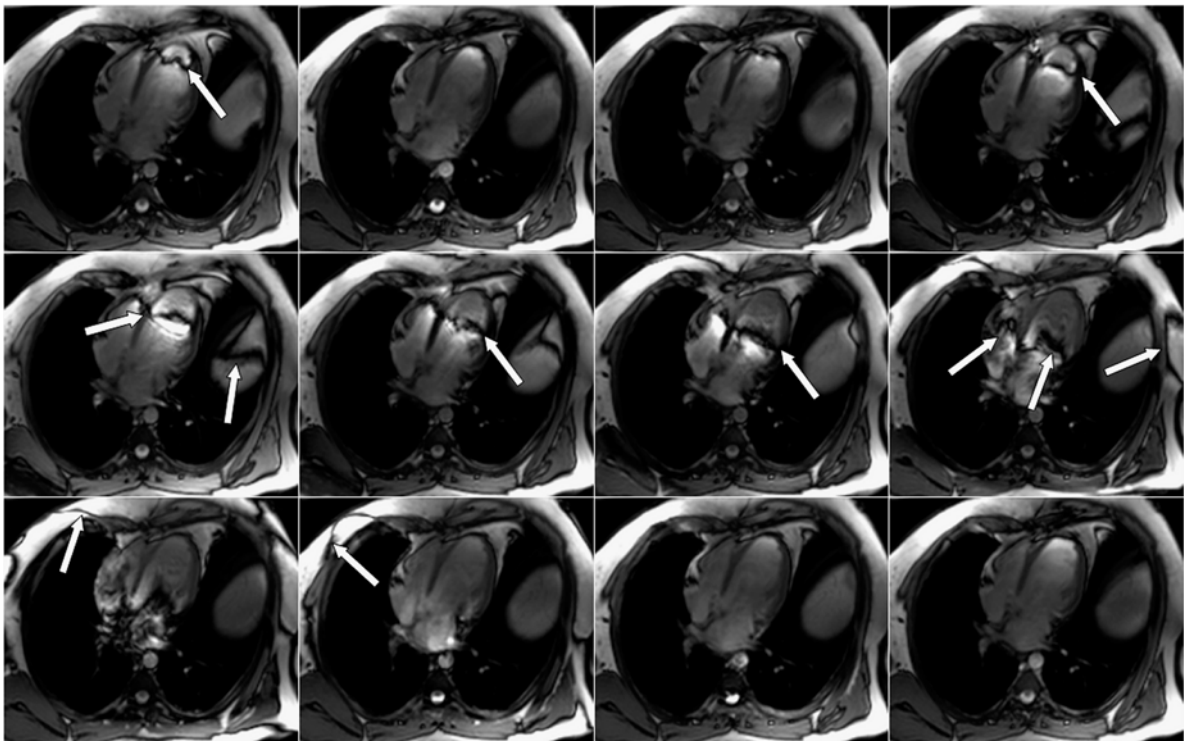

Fig. 35.9. SSFP frequency scouting performed at 3 T (Siemens Magnetom Trio Tim) with consecutive images from *left upper corner* to *right lower corner*. These images demonstrate a frequency shift from –240 Hz to +200 Hz. Bands of off-resonance artefacts are shown in different areas of the FOV within and outside the heart. For diagnostic cine imaging, the proper frequency shift should be applied. Note: When imaging is performed in other planes than the frequency scouting, new offsets might be necessary to optimize image quality

These restrictions to acceleration by parallel imaging have been overcome by the development of multi-channel MR systems of 1.5 T and 3 T with up to 32 independent receiver channels. These allow for the use of coil arrays with more than eight elements for cardiac imaging (Wintersperger et al. 2006). Having these many receiver channels in place, even dedicated coils have been developed for different applications such as MR angiography and cardiac imaging (Zhu et al. 2004; Reeder et al. 2005). Early results using these coils at 1.5 T do show good g-factor behavior close to optimized simulations with a g-factor close to 1 for R=1-4 (Ohliger et al. 2003; Reeder et al. 2005). Based on the steady decline of SNR with increasing acceleration and the increasing g-factor, acceptable accelerations in the range of R=4 (in 2D MRI) maintained diagnostic accuracy while acceleration factors up to R=7 have been tested with cine TSENSE imaging (Wintersperger et al. 2006). With the development of these dedicated coils to be used at 3 T, further gains in acquisition speed seem to be possible. Early investigational tests of such coil designs in combination with high accelerations have shown promise for acquisitions of a whole ventricular coverage in a single breath-hold (Fig. 35.10). Alternatively, spatial resolution may be increased as better SNR behavior can be estimated with the increasing number of small local coil elements. New approaches to cardiac cine MRI, however, may be developed, such as high-resolution cine imaging without the need for breath-holding.

However, the concept of cine SSFP imaging including its magnetization preparation (to prepare the steady state) needs to be thought over as it requires dummy cycle preparation for each individual slice. Thus, in fast multi-slice cine imaging at high acceleration rates that necessitate only a single heart beat for data sampling of each individual slice, preparation would cover as much as 50% of the total scan time. Thus, new imaging strategies have to be developed to allow k-space undersampling in not only one but two dimensions. This would lead into the direction of 3D cine MRI with the possibility of volumetric preparation of the steady state.

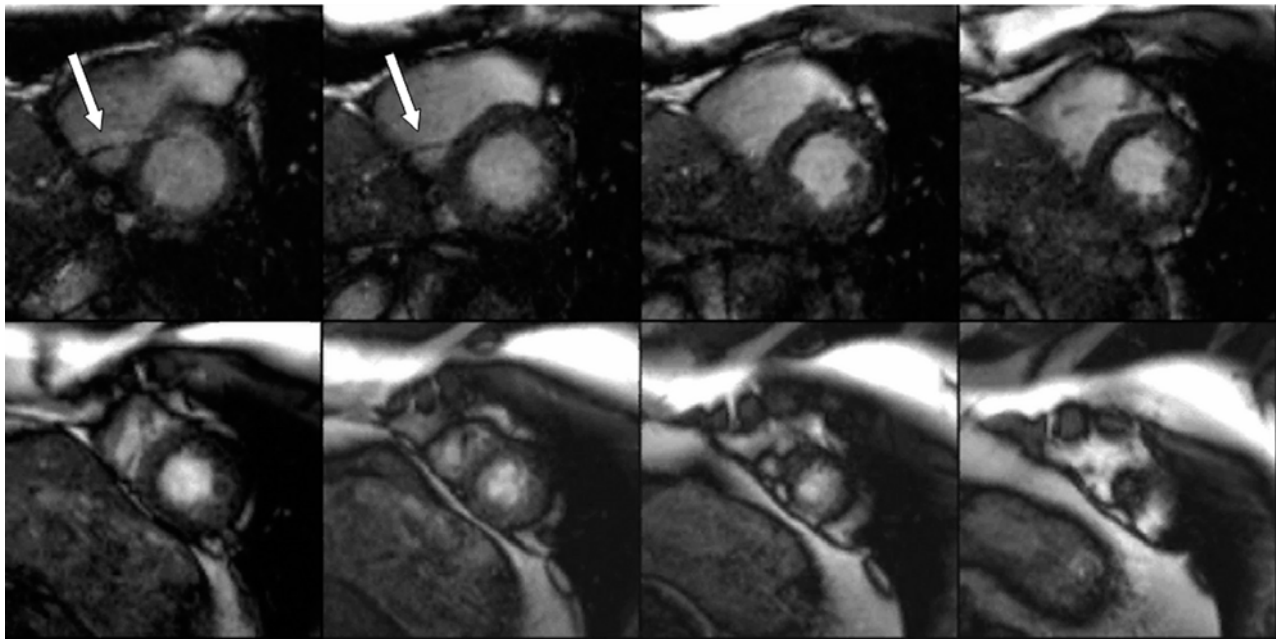

Fig. 35.10. Single breath-hold coverage of a left ventricle at 3 T (TRIO Tim) using a 32-element cardiac coil (RAPID Biomedical) and TSENSE with six-fold acceleration (R=6). Images are acquired with 192 matrix size and a temporal resolution of 50 ms. Few TSENSE artefacts are noted near the base of the heart, not affecting the diagnostic quality of the data set

35.6 4D Cine Assessment of Cardiac Function

As shown above, the ability of parallel imaging to allow for a reduction in scan time in fact opens many new options. Instead of just cutting down breath-hold periods for single-slice cine MRI, multi-slice approaches seem to be a more straight forward change of paradigms for imaging of cardiac function.

The benefit of cross-sectional imaging techniques such as MRI in respect to functional analysis is their ability to create a 3-dimensional data set for volumetric analysis. It has been shown that this ability of cine MRI secures its status as the reference standard in volumetric analysis of the heart. Other methods implemented either in echocardiography or ventriculography face the problem of geometric assumptions, which can be quite accurate in normally shaped ventricles (Dulce et al. 1993). In cases encountering any disturbances of regional wall motion, these techniques are likely to fail or to show inadequate results as the criteria of the geometric assumptions are not met anymore. In addition to global functional parameters, acquiring data along the short axis of the heart also enables regional wall motion analysis according to the proposed segmental model of the American Heart Association (AHA) (Cerqueira et al. 2002). Although the use of Simpson's rule with contiguous coverage along the entire short axis from the apex to the atrioventricular-valve plane has major benefits in terms of accuracy based on its 3D modeling, the valve plane itself can be much better identified in 2- and 4-chamber views. New, semi-automated software algorithms allow for the combination of both the short-axis information as well as the long-axis definition of the apex and valve planes. These models also incorporate a computerized left-ventricular model, thereby reducing the number of required short-axis views. This ideally combines with the ability of accelerated cine MRI to acquire multiple slices within a single breath-hold. These slices do not have to be positioned in parallel along the short axis of the heart as shown earlier (Figs. 35.5, 35.8, 35.10), but can be acquired along multiple planes to fulfill the data requirements for 4D post-processing software

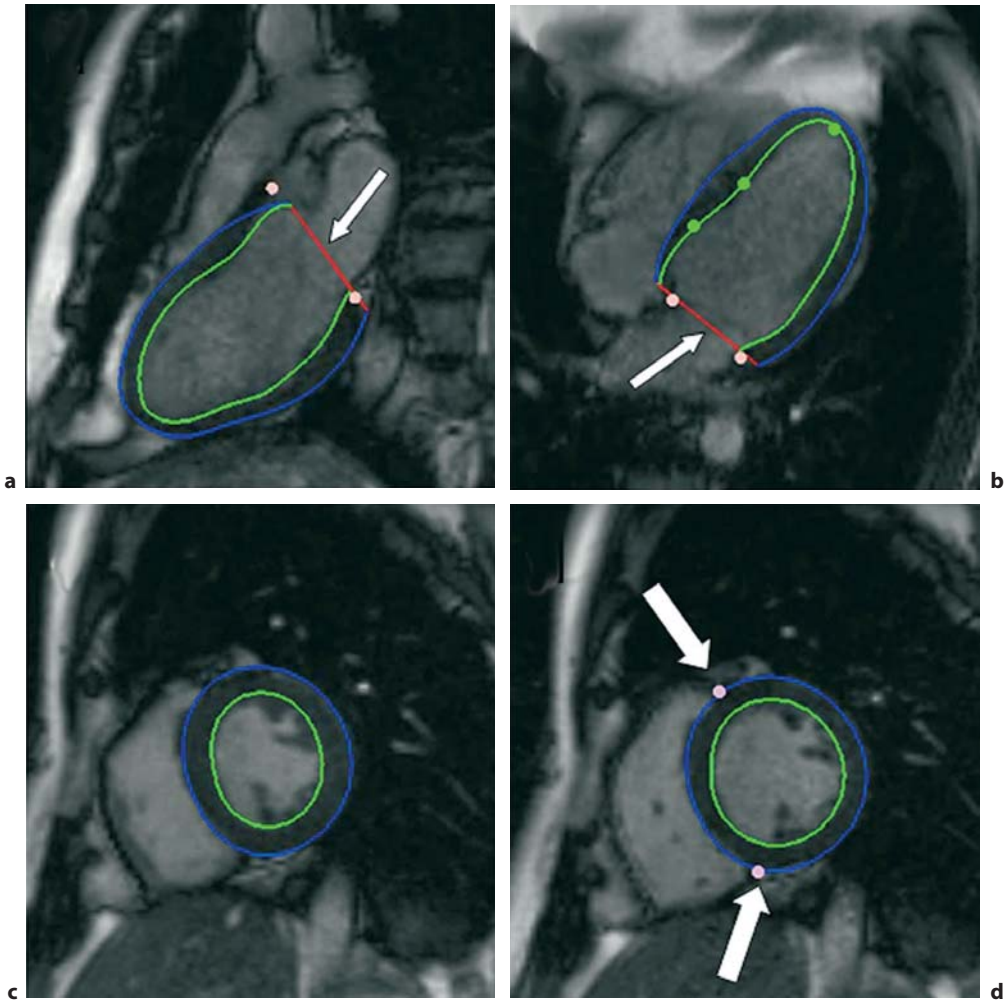

Fig. 35.11a–d. Multi-planar data set acquired in a single breath-hold for analysis with a 4D post-processing tool (CIM; University of Auckland). No adjustment of **a,b** long axis planes and **c,d** short axis images is necessary as they were acquired at the same diaphragm position. The software incorporates a model of the left ventricle. In addition, several markers to define the right-ventricular attachments (*large arrows*) and the plane of the mitral valve (*small arrows*) are set

options (Fig. 35.11). With the use of single-slice cine acquisitions, data acquired along different cardiac axes are needed to adjust for matching within chosen landmarks of the cardiac anatomy such as the cardiac apex (Young et al. 2000). The inherent limited accuracy of geometry-based techniques can be eliminated by the acquisition and incorporation of additional short axis data. Fast accelerated cine imaging with the acquisition of two long-axis planes (vertical long axis + four-chamber views) allows for an additional three to four short-axis slices distributed over the length of the ventricles. The further improvement of SNR behavior at 3 T and possibly also multi-element coil arrays may change the approach to functional evaluation and cut down acquisition time from a multi breath-hold single-slice approach to a multi-planar multi-slice approach within a single breath-hold. This change in paradigm would allow for a marked reduction in the scan time needed for functional analysis of the heart.

References

Barkhausen J et al. (2002) Assessment of ventricular function with single breath-hold real-time steady-state free precession cine MR imaging. AJR Am J Roentgenol 178: 731–735

Barkhausen J et al (2001) MR evaluation of ventricular function: true fast imaging with steady-state precession versus fast low-angle shot cine MR imaging: feasibility study. Radiology 219: 264–269

Carr JC et al. (2001) Cine MR angiography of the heart with segmented true fast imaging with steady-state precession. Radiology 219: 828–834

Cerqueira MD et al (2002) Standardized myocardial segmentation and nomenclature for tomographic imaging of the heart: a statement for healthcare professionals from the Cardiac Imaging Committee of the Council on Clinical Cardiology of the American Heart Association. Circulation 105: 539–542

Deshpande VS et al (2003) Artefact reduction in true-FISP imaging of the coronary arteries by adjusting imaging frequency. Magn Reson Med 49: 803–809

Dulce MC et al (1993) Quantification of the left ventricular volumes and function with cine MR imaging: comparison of geometric models with three-dimensional data. Radiology 188: 371–376

Francone M et al (2005) Real-time cine MRI of ventricular septal motion: a novel approach to assess ventricular coupling. J Magn Reson Imaging 21: 305–309

Griswold MA et al (2004) Field-of-view limitations in parallel imaging. Magn Reson Med 52: 1118–1126

Guttman MA et al (2003) Real-time accelerated interactive MRI with adaptive TSENSE and UNFOLD. Magn Reson Med 50: 315–321

Hunold P et al (2004) Parallel acquisition techniques in cardiac cine magnetic resonance imaging using TrueFISP sequences: comparison of image quality and artefacts. J Magn Reson Imaging 20: 506–511

Kramer U et al (2003) Multislice TrueFISP-MR-Bildgebung zur Erkennung stressinduzierter myokardialer Funktionsstörungen bei koronarer Herzerkrankung. Fortschr Röntgenstr 175: 1355–1362

Lee VS et al (2002) Cardiac function: MR evaluation in one breath hold with real-time true fast imaging with steady-state precession. Radiology 222: 835–842

McGee KP et al (2004) Cardiac magnetic resonance parallel imaging at 3.0 Tesla: technical feasibility and advantages. J Magn Reson Imaging 19: 291–297

Miller S et al (2002) MR Imaging of the heart with cine true fast imaging with steady-state precession: influence of spatial and temporal resolutions on left ventricular functional parameters. Radiology 223: 263–269

Moon JC et al (2002) Breath-hold FLASH and FISP cardiovascular MR imaging: left ventricular volume differences and reproducibility. Radiology 223: 789–797

Noeske R et al (2000) Human cardiac imaging at 3 T using phased array coils. Magn Reson Med 44: 978–982

Ohliger MA et al (2003) Ultimate intrinsic signal-to-noise ratio for parallel MRI: electromagnetic field considerations. Magn Reson Med 50: 1018–1030

Reeder SB et al (2005) Practical approaches to the evaluation of signal-to-noise ratio performance with parallel imaging: Application with cardiac imaging and a 32-channel cardiac coil. Magn Reson Med 54: 748–754

Schar M et al (2004) Cardiac SSFP imaging at 3 Tesla. Magn Reson Med 51: 799–806

Setser RM et al (2000) Quantification of left ventricular function with magnetic resonance images acquired in real time. J Magn Reson Imaging 12: 430–438

Stuber M et al (2002) Preliminary report on in vivo coronary MRA at 3 Tesla in humans. Magn Reson Med 48: 425–429

Thiele H et al (2001) Functional cardiac MR imaging with steady-state free precession (SSFP) significantly improves endocardial border delineation without contrast agents. J Magn Reson Imaging 14: 362–367.

Weissler AM et al (1968) Systolic time intervals in heart failure in man. Circulation 37: 149–159

Wen H et al (1997) The intrinsic signal-to-noise ratio in human cardiac imaging at 1.5, 3, and 4 T. J Magn Reson 125: 65–71

Wintersperger BJ et al (2006) Cardiac SSFP CINE MR imaging at 3T: impact of parallel imaging acceleration on volumetric accuracy and signal parameters. Invest Radiol 41: 141–147

Wintersperger BJ et al (2003) Single breath-hold real-time cine MR imaging: improved temporal resolution using generalized autocalibrating partially parallel acquisition (GRAPPA) algorithm. Eur Radiol 13: 1931–1936

Wintersperger BJ et al (2006) Cardiac CINE MR Imaging with a 32-channel cardiac coil and parallel imaging: impact of acceleration factors on image quality and volumetric accuracy. J Magn Reson Imaging 23: 222–227

Young AA et al (2000) Left ventricular mass and volume: fast calculation with guide-point modeling on MR images. Radiology 216: 597–602

Zhu Y et al (2004) Highly parallel volumetric imaging with a 32-element RF coil array. Magn Reson Med 52: 869–877

Imaging of Cardiac Perfusion

36

Armin Huber

CONTENTS

36.1 Background

A decrease in myocardial perfusion represents the first effect of occluding coronary artery disease (CAD). It can be detected before clinical symptoms or left ventricular dysfunction become obvious (Nesto and Kowalchuk 1987). Therefore, the assessment of myocardial perfusion representing the functional relevance of coronary stenoses appears the most promising concept for a noninvasive test to detect early CAD. Imaging of myocardial perfusion is currently dominated by nuclear-medicine techniques. Single-photon-emission computed tomography (SPECT) using Thallium-201 or TC-99m sestamibi accounts for the majority of clinical studies, whereas positron emission tomography (PET), which must be considered the standard of reference for perfusion imaging, is available only at specialized centers. For the detection of significant CAD, these techniques provide sensitivity and specificity values ranging between 83% and 95%, and 53% and 95%, respectively (Hannoush et al. 2003; Schwaiger and Melin 1999; Schwaigwer et al. 1994; Muzik et al. 1998; Demmer et al. 1989). Furthermore, a wide range of clinical studies has documented an important prognostic significance for perfusion deficits detected by nuclear techniques (Iskander and Iskanderian 1998; Mansoor and Heller 1997). SPECT and PET do, however, have important limitations. These include attenuation artefacts, exposure to ionizing radiation, and poor spatial resolution, which do not allow the reliable detection of subendocardial perfusion defects (Wagner et al. 2003).

With recent hardware and software improvements, magnetic resonance imaging is emerging as an attractive alternative to nuclear medicine techniques for imaging of myocardial perfusion. First-pass myocardial perfusion imaging is based on fast T1-weighted image sets collected during injection of an intravenously administered contrast bolus resulting in enhancement of healthy myocardial tissue compared to the precontrast images. Although both MRI and nuclear medicine techniques can measure myocardial perfusion, important differences between both methods have to be considered. With Thallium-201 or TC-99m sestamibi SPECT, the signal intensity in the myocardium depends on the myocardial blood flow and the amount of viable cells extracting the tracer into the intracellular space. Therefore, areas with decreased myocardial perfusion as well as areas with a reduced number of viable cells result in reduced tracer uptake (Mansoor and Heller 1997; Ragosta and Beller 1993). In contrast, the myocardial signal intensity on MR images during first-pass perfusion of a paramagnetic contrast agent depends on myocardial blood flow, vascular permeability, and the size of the extracellular space. The viability of myocardial cells does not affect signal characteristics. Thus, reperfused

A. Huber, MD
Department of Clinical Radiology, University Hospitals – Grosshadern, Ludwig Maximilian University of Munich, Marchioninistr. 15, 81377 Munich, Germany

but infarcted myocardium appears dark on SPECT images, whereas it may be hypointense or hyperintense to normal myocardium on first-pass MRI at rest. Accurate analysis of first-pass perfusion studies requires profound knowledge of the MR hardware and software potential, the characteristics of paramagnetic contrast agents, and the pathophysiology of myocardial perfusion. In addition, it is necessary to keep in mind differences, advantages, and limitations of MR perfusion measurements with respect to other clinically available methods. This chapter explores the pathophysiologic background, recent technical developments, and current clinical status of first-pass MRI of myocardial perfusion.

36.2 Pathophysiology of Myocardial Perfusion

Stenoses of an epicardial coronary artery lead to reduced perfusion and correspondingly diminished myocardial oxygen delivery. However, at rest, the equilibrium between perfusion, metabolism, and contractile function can be normal even in cases of moderate to severe stenoses. Therefore, these stenoses are clinically occult in perfusion studies at rest. At stress, induced pharmacologically or by physical exercise, there is a three- to fourfold increase in contractile function accompanied by a fourfold increase in oxygen demand and perfusion (Bourdarias 1995; Wilke et al. 1997). Whereas the flow in normal coronary arteries can be increased by vasodilation, moderate and severe stenoses become flow limiting, resulting in perfusion deficits, wall motion abnormalities, and symptomatic angina. Therefore, different stress tests are clinically used to detect myocardial ischemia (Iliceto 1995). In the progression of ischemia, successive myocardial events occur. These are known as the cascade of ischemia (Nesto and Kowalchuk 1987) (Fig. 36.1). Initially, hypoperfusion can only be detected in the subendocardial layer of the myocardium (Bache and Schwartz 1982). Further reduction of the blood flow due to more severe stenoses leads to transmural perfusion deficits. Progression of ischemia leads to diastolic, followed by systolic, wall motion abnormalities, which can be detected by stress echocardiography or dobutamine stress MRI (Nagel et al. 1999). Finally, electrocardiographic changes can be detected and typical symptomatic angina may occur. As perfusion abnormalities are the first step in this cascade of ischemia, direct visualization of these perfusion deficits seems to be the diagnostic test of first choice in patients with suspected CAD.

36.3 Pulse-Sequence Techniques

Since 1991, imaging of first-pass wash-in effects by the application of a bolus of extravascular contrast agents is possible using gradient-refocused-echo sequences (Schaefer et al. 1992; van Rugge et al. 1991). For successful examinations a magnetic field strength of 1.5 T is necessary to achieve sufficient signal-to-noise ratio (SNR) and contrast-to-noise ratios (CNR) as well as high-performance gradients to enable fast data acquisition with high spatial resolution. For first-pass MR perfusion imaging of the myocardium contradictory requirements have to be fulfilled to some degree: Sufficient temporal resolution to image several slices in each, or at least every second, heartbeat in order to sample the first pass of the contrast bolus is necessary. A temporal resolution with imaging of one slice position every heart beat allows for postprocessing with a semiquantitative or quantitative evaluation (Al-Saadi et al. 2000; Jerosch-Herold et al. 1998). A temporal resolution with imaging of one slice every second heart beat allows for a visual evaluation (Ishida et al. 2003), not for semiquantitative or quantitative postprocessing.

High spatial resolution including an in-plane resolution of 3 mm is necessary to distinguish the sub-

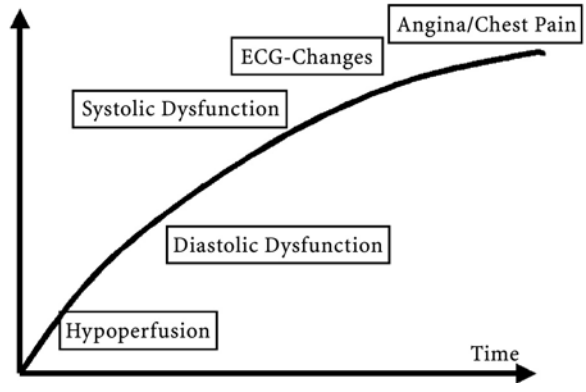

Fig. 36.1. Ischemic cascade. Hypoperfusion is the first pathological change in the myocardium during development of coronary artery disease

endocardial and subepicardial layers of the myocardium. A slice thickness of 8-10 mm is adequate for discrimination of different perfusion areas in relation to the long axis of the heart. In order to cover the ventricular myocardium as completely as possible, at least four to six slices should be acquired. A nearly linear relationship between contrast dose and signal intensity is mandatory to image normal and ischemic regions of the myocardium with high contrast. To meet these goals, myocardial first-pass perfusion sequences make use of various magnetization preparation techniques. These include inversion recovery, saturation recovery, and partial or notch pulse saturation. The preparation pulses support the T1-contrast of the consecutive perfusion images, acquired with different, fast data readout methods like gradient echo imaging, echo-planar imaging (EPI), or steady-state free precession (SSFP) techniques (Fig. 36.2) (Fenchel et al. 2004; Schreiber 2002; Hunold et al. 2004; Koestler et al. 2004).

Figure 36.3 shows the diagram of a first-pass perfusion sequence using a nonselective saturation-recovery preparation. The combination of magnetization preparation and data readout is repeated as often as it fits into the RR interval. To cover a maximum number of slices, the inversion time (TI) between the magnetization preparation and the data readout segment needs to be kept as short as possible. However, TI plays an important role in determining SNR and CNR (Bertschinger et al. 2001). A short TI permits the collection of more slices per cardiac cycle, whereas a long TI improves SNR and CNR. A possible solution is presented by a notch pulse saturation technique that combines a long TI with fast multislice data acquisition (Slavin et al. 2001; Bertschinger et al. 2001) (Fig. 36.4). For data readout, different types of techniques can be used. Following a magnetization preparation pulse, a series of gradient-recalled echoes is generated. Using, for example, 100 phase-encoding steps, the data acquisition per slice requires 100×TR. In contrast to standard gradient-echo techniques, which generate only one echo per excitation, segmented EPI sequences collect several echoes per excitation (Sakuma et al. 1999). The advantage of this sequence is related to acquisition time, because the data acquisition time per slice amounts to only 25×TR for 100 phase-encoding steps and an EPI factor of 4.

The use of parallel imaging allows for reduction of the acquisition time required for the readout segment. However, the inversion time remains the same. Without parallel imaging, the time for the inversion preparation is similar to the acquisition time for the readout segment. Therefore, an acceleration factor of 2 reduces the time frame per slice only by 25%. In addition to the shorter scan time per slice, artefacts are reduced by the reduction of the acquisition time for the readout segment.

36.4 Parallel-Imaging Techniques

36.4.1 GeneRalized Autocalibrating Partially Parallel Acquisitions (GRAPPA)

In GRAPPA (Griswold et al. 2002), uncombined images without aliasing artefacts are reconstructed for each coil element in the array by generating the missing k-space lines for each coil element (cf. Chap. 2). A Fourier transform can then be used to reconstruct the uncombined image for each coil. The set of uncombined images can be combined using a normal sum-of-squares reconstruction. Advantages of the GRAPPA algorithm for cardiac perfusion MRI are the integrated acquisition of the reference lines (auto-calibration signals) in the undersampled acquisition of k-space lines during the readout segment, which allows for reduction of the influence of motion artefacts and for an update of the coil sensitivity profile for each time frame. Thus, there is an SNR loss within one frame as known for the use of parallel imaging; however, no additional SNR or CNR loss need to be expected for the signal change over time, which is important for accurate assessment and analysis of the signal-time curves during first-pass for each myocardial segment (Fig. 36.5). A disadvantage compared to the TSENSE and auto-SENSE techniques discussed below is the additional need of acquisition time for the reference lines (Fig. 36.6). The real (or effective) acceleration factor is reduced by the ratio of the number of additional reference lines and of totally acquired k-space lines (including the reference lines).

36.4.2 TSENSE

TSENSE is a fast imaging technique that can be used for a dynamic acquisition of images in the same slice posi-

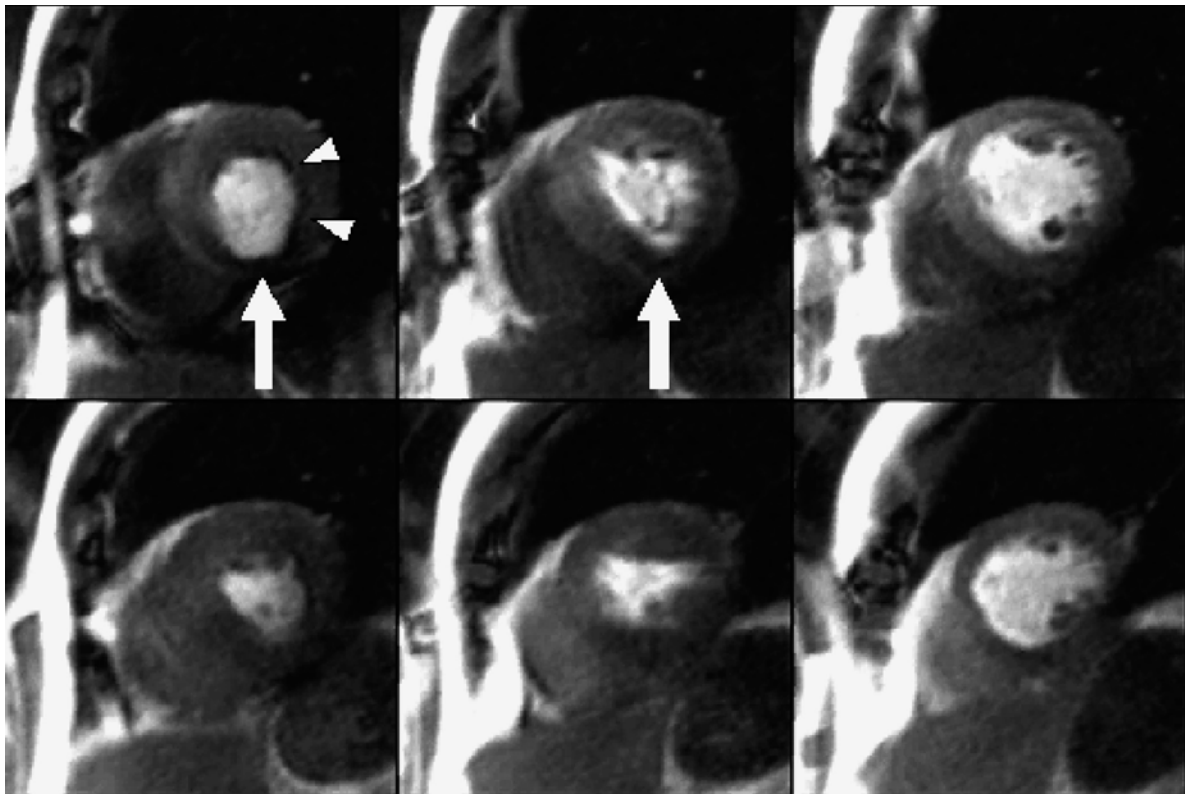

a

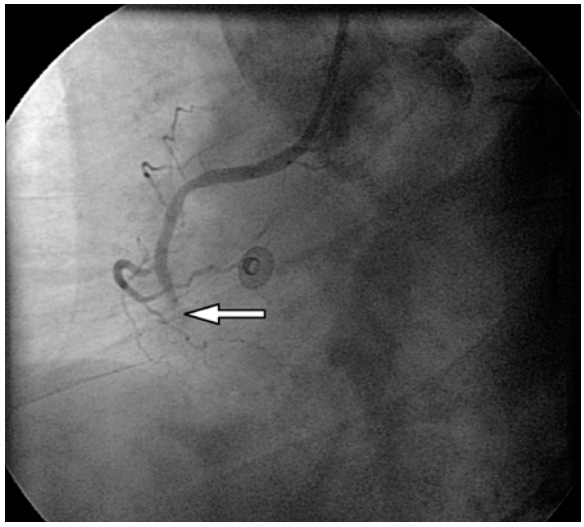

b

Fig. 36.2a,b. A 59-year-old woman with high-grade stenosis in the right coronary artery. Perfusion images acquired with a saturation-recovery TrueFISP sequence. The basal and mid-papillary slices show a perfusion defect in the inferior segments under adenosine stress (*arrow*, first line). In addition, a subendocardial susceptibility artefact can be identified (*arrowheads*). Invasive coronary angiography reveals an occlusion of the right coronary artery (*arrow*)

tion (Kellman et al. 2001); a detailed description can be found in Chap. 12. In contrast to techniques such as GRAPPA or auto-SMASH and similar to auto-SENSE, no additional reference lines have to be acquired for reconstruction of full images after acquisition of only an undersampled part of the k-space lines per frame, e.g., of every other k-space line for an acceleration factor of R=2. Thus, a nominal acceleration factor of 2 results in a true shortening of the acquisition time per frame by a factor of 0.5 (Fig. 36.7).

36.4.3 Auto-SENSE

Auto-SENSE uses coil sensitivity information acquired during a series of dynamic scans for a SENSE reconstruction (Koestler et al. 2003). By interleaving the acquisition of different undersampled parts of the k-space from a subset of the dynamic series where no changes occur, a full k-space data set can be generated to extract coil sensitivity information. When the

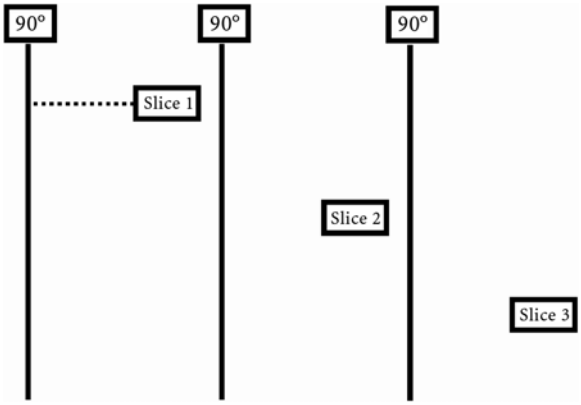

Fig. 36.3. Non-selective saturation-recovery preparation. An inversion time (*dotted line*) of about 100 ms is necessary for adequate preparation of the T1 contrast. No data acquisition is possible during the inversion time. The number of slices is limited by the length of the RR interval and the length of the inversion time and the read-out segment

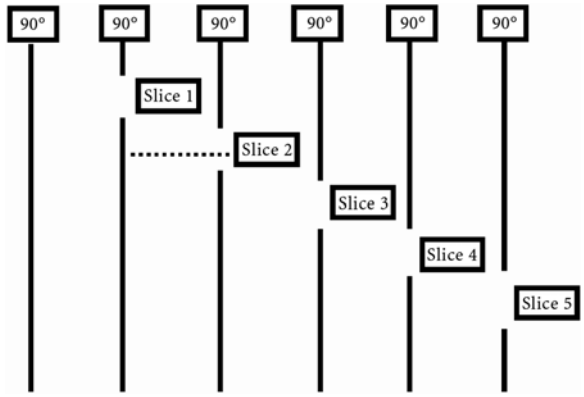

Fig. 36.4. Notch pulse saturation with a slice-selective saturation pulse allows for acquisition of one slice during preparation of another slice. A higher number of slices can be acquired during one RR interval with an identical inversion time (*dotted line*) compared to a non-selective preparation

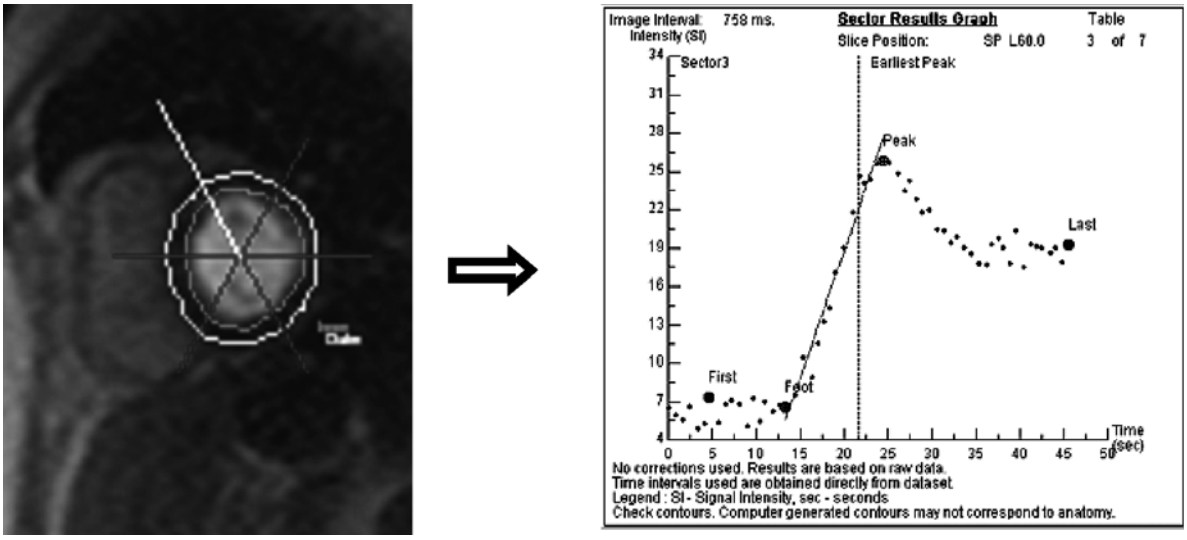

Fig. 36.5. One image of a dynamic series of 60 images acquired during first pass of the contrast agent is shown. The endocardial and epicardial contours allow defining the left-ventricular myocardium. In each of six segments a signal-time curve is calculated by plotting the signal intensity values over the time-point of acquisition. The signal-time curves allow determining semiquantitative perfusion parameters like upslope, maximum signal and area-under-curve

patient can hold the breath for the dynamic acquisition of the perfusion images, the whole series can be used to determine the coil sensitivities. Since no additionally acquired lines in k-space are necessary in auto-SENSE, the full maximum acceleration factor of SENSE can be reached. In contrast to conventional SENSE imaging, a separate prescan to determine the coil sensitivity profiles is not needed with auto-SENSE. Thus, auto-SENSE combines the advantages of the self-calibrating and traditional calibration methods: the elimination of motion-related miscalibration and achievement of the full maximum acceleration factor.

Auto-SENSE has been reported to be more robust for heart perfusion imaging than alternative approaches such as UNFOLD or TSENSE. Image artefacts such as those presented by Madore (1999) or Kellman et al. (2001) for SENSE reconstruction were not noticed in the study of Koestler et al. (2003),

possibly because of the improved determination of coil sensitivity information particularly in the lungs. Due to the accelerated image acquisition compared to commonly used turbo-FLASH sequences (Wilke et al. 1997; Jerosch-Herold et al. 1998) without parallel imaging, auto-SENSE heart perfusion imaging allows a complete coverage of the human heart with a single contrast-agent administration.

36.5 Parallel Imaging in the Clinical Assessment of Myocardial Perfusion

Reports in the literature for evidence of superiority of parallel imaging concerning the diagnostic accuracy for detection of coronary artery stenoses or occlusions or for the assessment of the hemodynamic relevance of intermediate lesions are still limited, especially in larger patient populations with correlation of MR perfusion results with coronary angiography, scintigraphy or PET. The GRAPPA technique seems to be most promising in preserving the contrast change from frame to frame, which is important for the detection and accurate assessment of the short upslope segment of the signal-time curve from the foot-point to the signal maximum. The introduction of the GRAPPA technique may improve the diagnostic accuracy for a visual assessment of the images as the number of myocardial segments with susceptibility artefacts is reduced from 15% to 5% by this technique (Figs. 36.8-10) (Hubert et al. 2006). The most important disadvantage of the GRAPPA technique is that the additional acquisition of reference lines is time consuming. Usually 12 to 24 reference lines have to be acquired.

In contrast to the GRAPPA technique, both auto-SENSE and TSENSE do not require acquisition of additional k-space lines. Thus, the theoretical acceleration factor of, e.g., 2 can be used. However, there may be a loss of contrast sharpness for image contrast change from frame to frame by temporal smearing (Fig. 36.11). This may be a problem for the auto-SENSE (Madore et al. 1999) and the TSENSE technique (Kellman et al. 2001).

The readout technique of choice for the use of parallel imaging is probably the gradient-echo readout. The gradient-echo EPI hybrid technique causes more noise and in the combination with parallel imaging, which causes an additional SNR loss, the gradient-echo EPI-readout technique can be expected to be inferior. The SSFP technique allows for achieving a higher SNR and CNR per frame (Fenchel et al. 2004; Schreiber 2002; Hunold et al. 2004), however, the linearity of contrast agent concentration and signal intensity in the myocardium (Koestler et al. 2004) is inferior compared to gradient-echo techniques. Therefore, hypoperfused areas can appear bright in spite of a low contrast agent concentration in the myocardium. Thus, an evaluation by eye-ball may underestimate pathological findings when an SSFP readout technique is used.

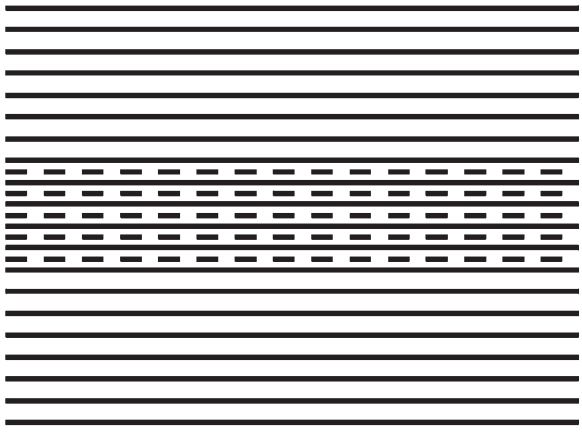

Fig. 36.6. Parallel imaging with an acceleration factor R=2 and integrated acquisition of reference lines. Every second k-space line is acquired. In addition reference lines (*dashed lines*) are acquired to estimate the coil sensitivity profiles

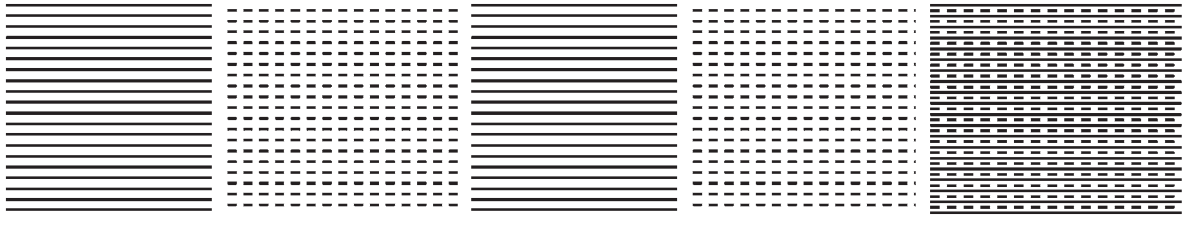

Fig. 36.7. The even k-space lines are acquired during the 1st, 3rd and n-th RR interval. The *odd lines* are acquired during the 2nd, 4th and (n+1)-th RR interval. From two frames, a full k-space information can be obtained

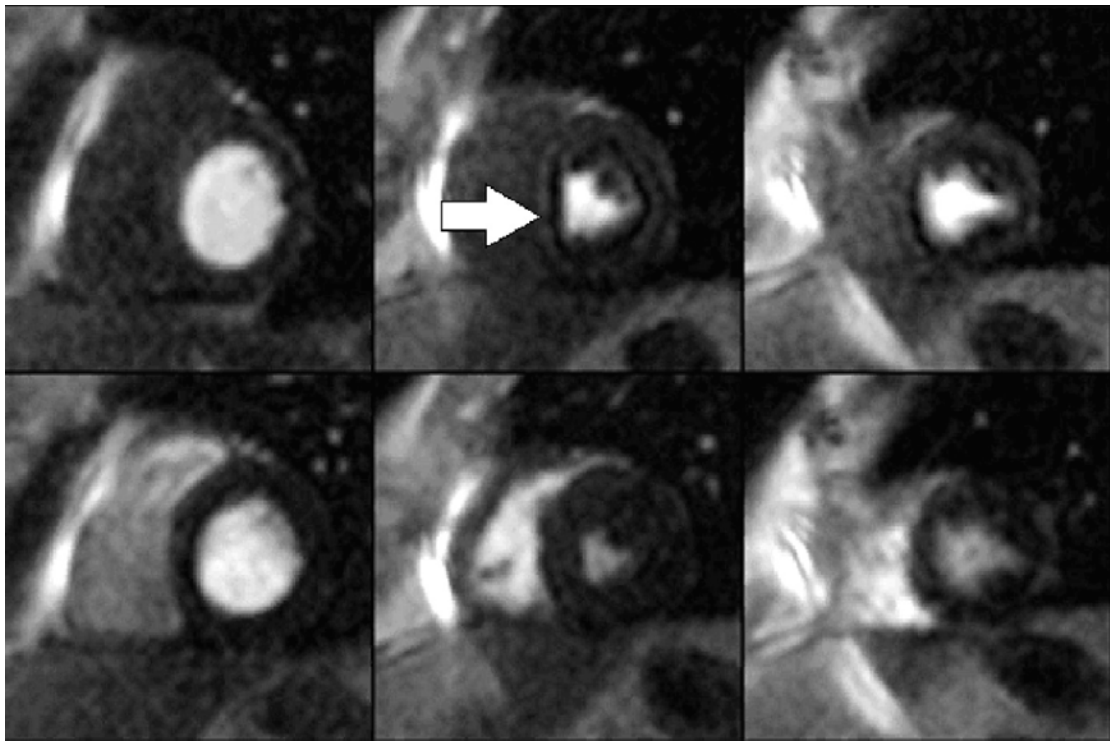

Fig. 36.8. A 62-year-old man with suspicion of coronary artery disease. Three short-axis images were acquired with a saturation-recovery turboFLASH pulse sequence without parallel imaging. The *first line* shows images that were acquired during adenosine infusion. The images in the *second line* were acquired at rest. The dark subendocardial rim (*arrow*) is a typical susceptibility artefact. No perfusion defect can be identified

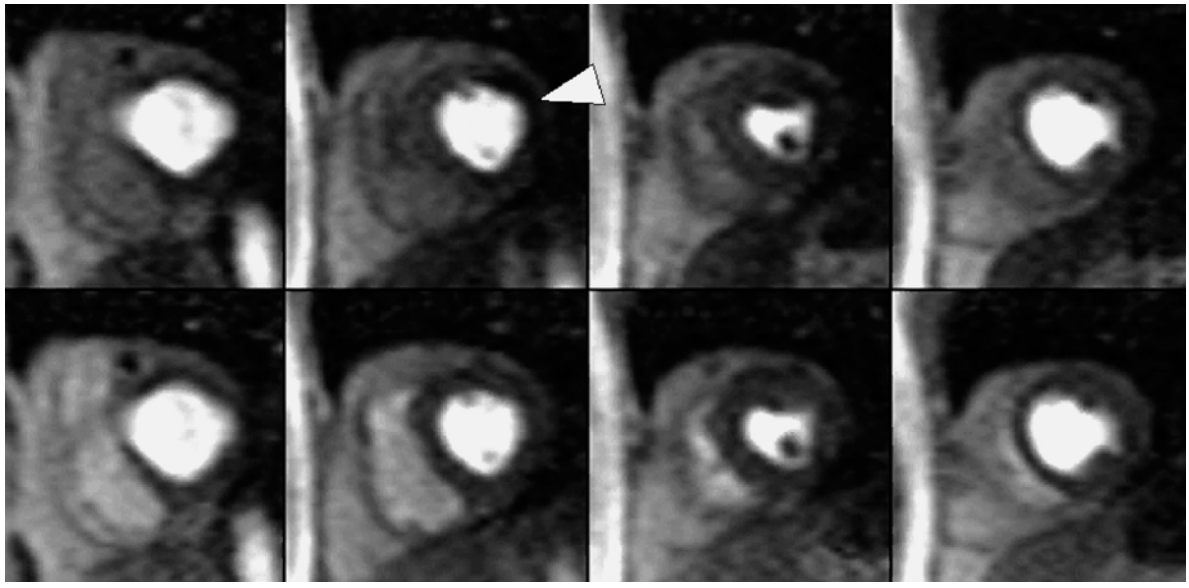

Fig. 36.9. A 71-year-old man with suspicion of coronary artery disease. Four short-axis images were acquired with a saturation-recovery turboFLASH pulse sequence with parallel imaging (acceleration factor R=2). The *first line* shows images which were acquired during adenosine infusion. The images in the *second line* were acquired at rest. The *dark area* in the anterolateral and inferolateral segment (*arrowhead*) is caused by a perfusion defect, which is visible during adenosine stress, not at rest. A susceptibility artefact cannot be identified

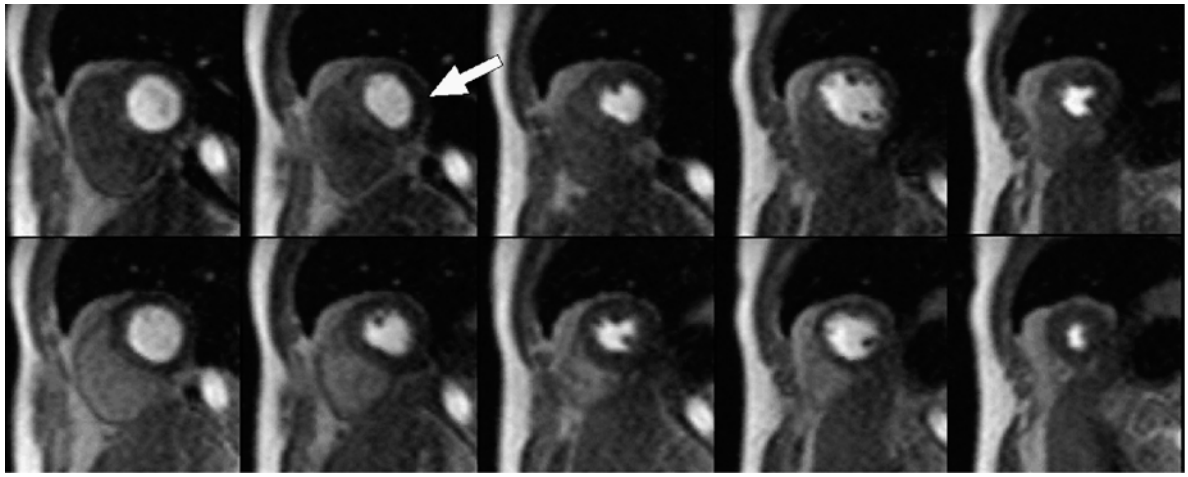

Fig. 36.10. A 58-year-old man with a stenosis (>75%) in the circumflex artery: five slices in short-axis orientation, acquired with a saturation-recovery turboFLASH pulse sequence with parallel imaging. The shorter acquisition window per slice allows for acquisition of five slices instead of three slices which can be acquired with a conventional technique without parallel imaging. A perfusion defect is visible in the anterolateral and inferolateral segments (*arrow*)

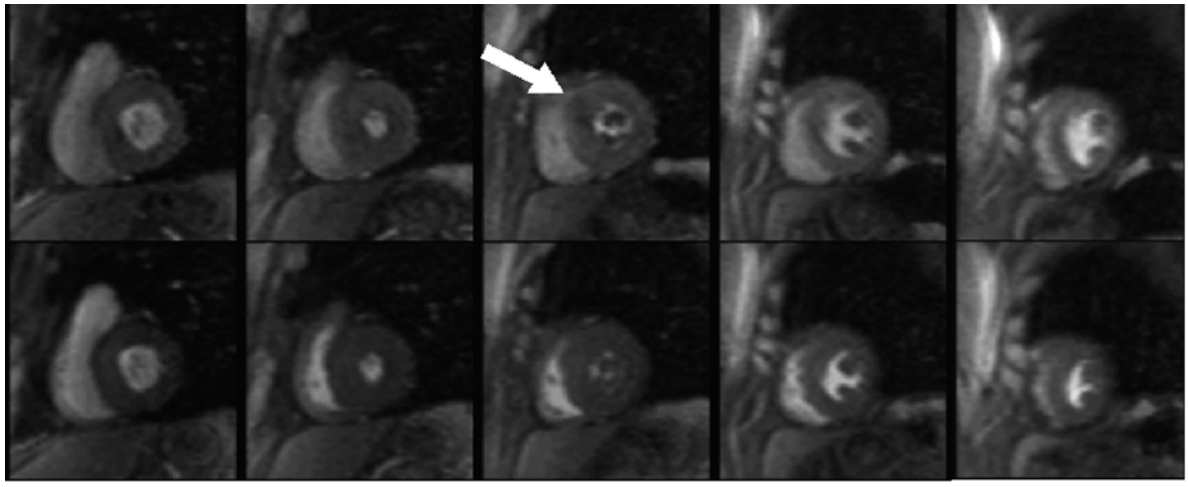

Fig. 36.11. A 79-year-old patient: five slices in short axis orientation, acquired with an EPI TSENSE gradient-echo pulse sequence. The *first line* shows images which were acquired during adenosine infusion. The images in the second line were acquired at rest. The perfusion defect, caused by a high-grade stenosis of the LAD (>75%), is visible, but shows a weak contrast

References

Al-Saadi N, Nagel E, Gross M, Bornstedt A, Schnackenburg B, Klein C, Klimek W, Oswald H, Fleck E (2000) Noninvasive detection of myocardial ischemia from perfusion reserve based on cardiovascular magnetic resonance. Circulation 101:1379–1383

Bache RJ, Schwartz JS (1982) Effect of perfusion pressure distal to a coronary stenosis on transmural myocardial blood flow. Circulation 65:928–935

Bertschinger KM, Nanz D, Buechi M et al (2001) Magnetic resonance myocardial first-pass perfusion imaging: parameter optimization for signal response and and cardiac coverage. J Magn Reson Imaging 14:556–562

Bourdarias JP (1995) Coronary reserve: concept and physiological variations. Eur Heart J 16 [Suppl I]:2–6

Demer LL, Gould KL, Goldstein RA et al (1989) Assessment of coronary artery disease severity by positron emission tomography. Comparison with quantitative arteriography in 193 patients. Circulation 79:825–835

Epstein FH, London JF, Peters DC et al (2002) Multislice first-pass cardiac perfusion MRI: validation in a model of myocardial infarction. Magn Reson Med 47:482–491

Fenchel M, Helber U, Simonetti OP, Stauder NI, Kramer U,

Nguyen CN, Finn JP, Claussen CD, Miller S (2004) Multislice first-pass myocardial perfusion imaging: Comparison of saturation recovery (SR)-TrueFISP-two-dimensional (2D) and SR-TurboFLASH-2D pulse sequences. J Magn Reson Imaging 19:553-563

Griswold MA, Jakob PM, Heidemann RM, Nittka M, Jellus V, Wang J, Kiefer B, Haase A (2002) Generalized autocalibrating partially parallel acquisitions (GRAPPA). Magn Reson Med 47:1202-1210

Hannoush H, Shaar K, Alam S, Nasrallah A, Sawaya J, Dakik HA (2003) Analysis of referral patterns, predictive accuracy, and impact on patient management of myocardial perfusion imaging in a new nuclear cardiology laboratory. J Nucl Cardiol 10:148–153

Huber A, Schweyer M, Schönberg S, Mühling O, Nähbauer M, Reiser (2006) Impact of parallel imaging (iPAT) on image quality and visual vs. semiquantitative evaluation of MR perfusion of the myocardium. Eur Radiol 16 [Suppl 1]:223

Hunold P, Maderwald S, Eggebrecht H, Vogt FM, Barkhausen J (2004) Steady-state free precession sequences in myocardial first-pass perfusion MR imaging: comparison with TurboFLASH imaging. Eur Radiol 14:409-416

Iliceto S (1995) Pharmacological agents for stress testing in the diagnosis of coronary artery disease. Eur Heart J 16 [Suppl M]:1–2

Ishida N, Sakuma H, Motoyasu M, Okinaka T, Isaka N, Nakano T, Takeda K (2003) Noninfarcted myocardium: correlation between dynamic first-pass contrast-enhanced myocardial MR imaging and quantitative coronary angiography. Radiology 229:209-216

Iskander S, Iskandrian AE (1998) Risk assessment using single-photon emission computed tomographic technetium-99m sestamibi imaging. J Am Coll Cardiol 32:57–62

Jerosch-Herold M, Wilke NM, Stillman AE (1998) Magnetic resonance quantification of the myocardial perfusion reserve with a Fermi function model for constrained deconvolution. Med Phys 25:73–84

Kellman P, Epstein FH, McVeigh E (2001) Adaptive sensitivity encoding incorporating temporal filtering (TSENSE). Magn Reson Med 45:846–852

Koestler H, Ritter C, Lipp M, Beer M, Hahn D, Sandstede J (2004) Prebolus quantitative MR heart perfusion imaging. Magn Reson Med 52:296-299

Koestler H, Sandstede J, Lipke C, Landschuetz W, Beer M, Hahn D (2003) Auto-SENSE perfusion imaging of the whole human heart. J Magn Reson Imaging 18:702–708

Madore B, Glover GH, Pelc NJ (1999) Unaliasing by Fourier-encoding the overlaps using the temporal dimension (UNFOLD), applied to cardiac imaging and fMRI. Magn Reson Med 42:813–828

Mansoor MR, Heller GV (1997) Recent developments in the prognostic use of myocardial perfusion imaging. Curr Opin Cardiol 12:571–580

Muzik O, Duvernoy C, Beanlands RS et al (1998) Assessment of diagnostic performance of quantitative flow measurements in normal subjects and patients with angiographically documented coronary artery disease by means of nitrogen-13 ammonia and positron emission tomography. J Am Coll Cardiol 31:534–540

Nagel E, Lehmkuhl HB, Bocksch W et al (1999) Noninvasive diagnosis of ischemia-induced wall motion abnormalities with the use of high-dose dobutamine stress MRI: comparison with dobutamine stress echocardiography. Circulation 99:763–770

Nesto RW, Kowalchuk GJ (1987) The ischemic cascade: temporal sequence of hemodynamic, electrocardiographic and symptomatic expressions of ischemia. Am J Cardiol 59:23C–30C

Ragosta M, Beller GA (1993) The noninvasive assessment of myocardial viability. Clin Cardiol 16:531–538

Sakuma H, Takeda K, Higgins CB (1999) Fast magnetic resonance imaging of the heart. Eur J Radiol 29:101–113

Schaefer S, van Tyen R, Saloner D (1992) Evaluation of myocardial perfusion abnormalities with gadolinium-enhanced snapshot MR imaging in humans. Work in progress. Radiology 185:795–801

Schreiber WG, Schmitt M, Kalden P, Mohrs OK, Kreitner KF, Thelen M (2002) Dynamic contrast-enhanced myocardial perfusion imaging using saturation-prepared TrueFISP. J Magn Reson Imaging 16:641-652

Schwaiger M (1994) Myocardial perfusion imaging with PET. J Nucl Med 35:693–698

Schwaiger M, Melin J (1999) Cardiological applications of nuclear medicine. Lancet 354:661–666

Slavin GS, Wolff SD, Gupta SN, Foo TK (2001) First-pass myocardial perfusion MR imaging with interleaved notched saturation: feasibility study. Radiology 219:258–263

van Rugge FP, Boreel JJ, van der Wall EE et al (1991) Cardiac first-pass and myocardial perfusion in normal subjects assessed by subsecond Gd-DTPA-enhanced MR imaging. J Comput Assist Tomogr 15:959–965

Wagner A, Mahrholdt H, Holly TA et al (2003) Contrast-enhanced MRI and routine single photon emission computed tomography (SPECT) perfusion imaging for detection of subendocardial myocardial infarcts: an imaging study. Lancet 361:374–379

Wilke N, Jerosch-Herold M, Wang Y et al (1997) Myocardial perfusion reserve: assessment with multisection, quantitative, first-pass MR imaging. Radiology 204:373–384

Imaging of Pulmonary Perfusion

37

Christian Fink

CONTENTS

37.1 Introduction

Pulmonary blood flow (perfusion) is essential for an efficient gas exchange in the lungs. The balance between ventilation and perfusion is pathologically altered in a variety of lung diseases. In pulmonary vascular diseases pulmonary perfusion is changed by a reduction of blood flow either in the pulmonary arterial system [e.g., pulmonary embolism (PE), pulmonary hypertension (PH) or venous system (e.g., venoocclusive disease)] (Bailey et al. 2000; Fazio and Wollmer 1981). Apart from pulmonary vascular disease, pulmonary perfusion can also be reduced in a regional destruction or displacement of the capillary bed in parenchymal lung disease (e.g., tumor; fibrosis). Finally, pulmonary perfusion can be reduced in a regulatory way by the mechanism of hypoxic vasoconstriction. Pulmonary hypoxic vasoconstriction, which was initially described by Euler and Liljestrand (1946), leads to a reduction of perfusion in non-ventilated lung and is therefore frequently observed in airway diseases such as chronic obstructive pulmonary disease (COPD).

There are several motivations for a better knowledge of the regional lung perfusion in all of these disease entities: First of all, perfusion imaging may be used to establish the diagnosis by the demonstration of a characteristic perfusion pattern. One example is pulmonary embolism, in which peripheral wedge-shaped perfusion defects are a characteristic finding (Fazio and Wollmer 1981).

Furthermore, knowledge of pulmonary perfusion may be essential for the planning of lung surgery. In patients with non-small-cell lung cancer, perfusion imaging is frequently used to estimate the postoperative lung function (Bollinger et al. 2002). Perfusion imaging is also used in patients with emphysema to determine the extent of volume-reduction surgery of the lung (Hunsacker et al. 2002).

In clinical medicine, pulmonary perfusion has traditionally been assessed by radionuclide lung scintigraphy after intravenous administration of radioactively labeled macroaggregates (^{99m}Tc-MAA) (Fazio and Wollmer 1981). Using conventional planar scintigraphy, the method is limited by a poor spatial resolution and the disadvantages of a projection method. A certain improvement is achieved with single-photon-emission computed tomography (SPECT) imaging; however, other disadvantages of the method such as a lack of anatomical and temporal information remain. For a quantitative approach to perfusion imaging of the lung, $H_2{}^{15}O$ positron-emission tomography (PET) has been proposed (Schuster et al. 1995; Serizawa et al. 1994). However, the method is technically complex and requires a cyclotron production of the tracer with an extremely short half-life. Consequently, this method has been limited to a research setting.

C. Fink, MD
Department of Clinical Radiology, University Hospitals – Grosshadern, Ludwig Maximilian University of Munich, Marchioninistr. 15, 81377 Munich, Germany

37.2 Imaging Technique and Feasibility Studies

Similar to other body regions such as the heart or brain, contrast-enhanced perfusion MRI has also been attempted in the lungs. Technically, pulmonary perfusion MRI is realized by rapid T1-weighted MR imaging of the first pass of a contrast agent bolus through the lungs following peripheral intravenous injection. Due to the requirement of very rapid imaging to visualize the pulmonary transit of the contrast agent bolus, the majority of the initial studies of pulmonary perfusion MRI have been limited to two-dimensional single-slice or multi-slice MRI (Uematsu et al. 2004). For a potential clinical use, however, 2D MRI provides only a poor through-plane spatial resolution and anatomic coverage and therefore may not allow for the detection of minor perfusion abnormalities, such as segmental or subsegmental perfusion defects in PE. With the availability of high-performance gradient systems, time-resolved 3D MRI of the lungs has become feasible (Goyen et al. 2001; Schoenberg et al. 1999). Consequently, this technique has also been proposed for the assessment of lung perfusion by several groups. However, spatial and temporal resolution of pulmonary perfusion MRI in these studies was still insufficient to be clinically acceptable. Typically, the partition thickness ranged between 10 and 30 mm, while a temporal resolution between 5 and 7 s was achieved (Iwasawa et al. 2002; Matsuoka et al. 2001; Makagawa et al. 2001).

With the application of parallel-imaging techniques in combination with improved high-performance gradient systems, the spatial and temporal resolution of MRI can be significantly improved. Consequently, this technical improvement has also been utilized for qualitative and semi-quantitative perfusion MRI of the lungs. In one feasibility study, 2 volunteers and 14 patients with different lung diseases (mainly COPD) were examined with a contrast-enhanced pulmonary perfusion MRI technique using the generalized autocalibrating partially parallel acquisitions (GRAPPA) technique (Griswold et al. 2002). In general, the GRAPPA algorithm can be expected to be advantageous compared to a SENSE approach for imaging lung tissue, because of the low intrinsic signal intensity of the lung parenchyma. In the lung tissue, coil sensitivity profiles in image space as required for the SENSE reconstruction may be affected by substantial errors, cf. Chap. 2. Using a parallel imaging acceleration factor of $R=2$ and a short repetition time (TR=1.9 ms), a 3D volume with 32 coronal partitions (spatial resolution of $3.6\times2.0\times5.0\ mm^3$) covering the entire lungs could be acquired in 1.5 s. For 10 of the 14 patients of this study, conventional perfusion scintigraphy was available for comparison. Perfusion MRI with parallel imaging allowed the acquisition of perfusion data with a spatial resolution that was sufficient to differentiate perfusion abnormalities from normally perfused lung (Figs. 37.1 and 37.2). When the results of the perfusion-weighted MRI data were compared to scintigraphy, a good inter-modality agreement was observed ($\kappa=0.74$) (Fink et al. 2003).

To assess the reproducibility of these findings, another study with identical imaging technique was performed in 7 healthy volunteers and 20 consecutive patients with suspected lung cancer or metastasis. All patients had previously been examined with perfusion scintigraphy. In this study, pulmonary perfusion MRI allowed for the detection of perfusion defects with a high accuracy (sensitivity 88% to 94%, specificity 100%) compared to the gold-standard perfusion scintigraphy. In all volunteers and three patients without perfusion defects at perfusion scintigraphy, MRI also showed no perfusion abnormalities. A very good interobserver agreement ($\kappa=0.86$) of pulmonary perfusion MRI for the detection of perfusion defects was found (Fink et al. 2004c).

Although the temporal and spatial resolution of pulmonary perfusion MRI has been substantially improved by parallel imaging, some applications (e.g., absolute quantification, pediatric imaging) might even require a higher spatial or temporal resolution. This can be achieved by combining parallel imaging with other k-space sampling methods that result in a reduction of the imaging time of MRI.

One example of these alternative k-space sampling methods is view sharing, which has already been used to improve the temporal resolution of time-resolved 3D MRA (Korosec et al. 1996); cf. Chaps. 7 and 11. By sampling center parts of k-space more frequently than k-space periphery, the total acquisition time of MRI is reduced with view sharing. In detail, the low-frequency k-space data that contribute most significantly to the image contrast are sampled more frequently than the high-frequency k-space data, which are interpolated between consecutive time frames. Recently, a 3D FLASH imaging sequence combining view sharing with parallel imaging has become available under the acronym TREAT (time-resolved echo-shared angiographic technique) (Fink et al. 2005a). In a feasibility study, the potential benefit of the combination of parallel imaging with view sharing for contrast-enhanced MRA and perfusion MRI

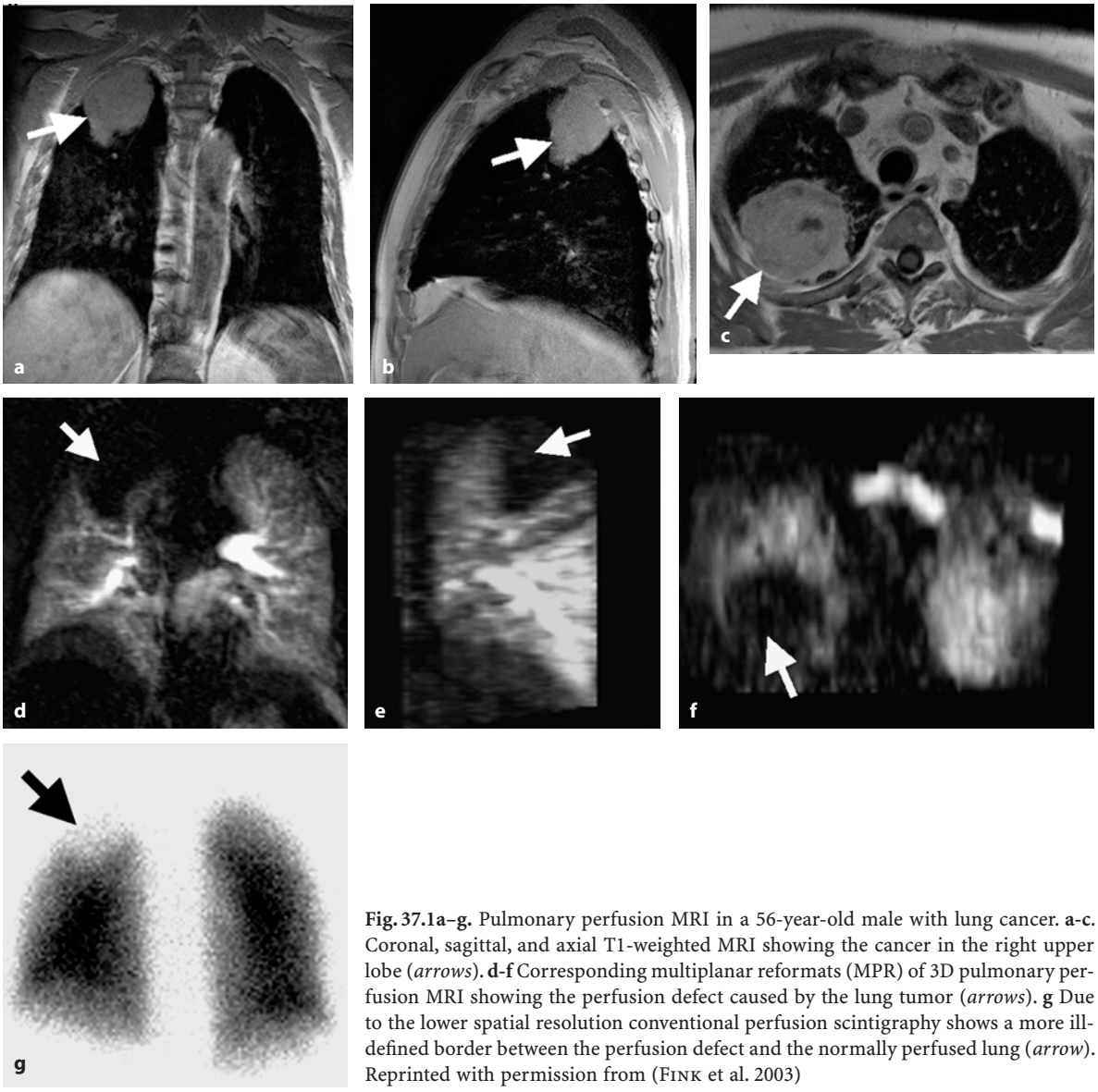

Fig. 37.1a–g. Pulmonary perfusion MRI in a 56-year-old male with lung cancer. **a-c.** Coronal, sagittal, and axial T1-weighted MRI showing the cancer in the right upper lobe (*arrows*). **d-f** Corresponding multiplanar reformats (MPR) of 3D pulmonary perfusion MRI showing the perfusion defect caused by the lung tumor (*arrows*). **g** Due to the lower spatial resolution conventional perfusion scintigraphy shows a more ill-defined border between the perfusion defect and the normally perfused lung (*arrow*). Reprinted with permission from (Fink et al. 2003)

was evaluated. Since depending on the reduction rate of acquired high-frequency k-space data, blurring artefacts of enhancing structures can occur with view sharing, the initial step was a simulation of the effect of different k-space segmentation factors (n=3-6) on the image quality of the TREAT acquisition. It was shown that a view-sharing factor of n=3, corresponding to an increase of the temporal resolution by a factor of 1.5, achieves a satisfactory image quality without an increased rate of blurring artefacts.

In a clinical study in 36 patients with different cardiovascular or pulmonary disease, the image data of TREAT were compared to image data acquired in a patient group with a similar distribution of age and disease state using time-resolved MRI with parallel imaging, but without view sharing. Both sequences used the same imaging parameters, except that the spatial resolution was improved with TREAT by 33%. In this comparison, the image quality of TREAT was rated significantly higher than that of the parallel MR sequence without view sharing (Fink et al. 2005a). These results of the initial report were recently also confirmed in an interindividual comparison of view-shared and non-view-shared time-resolved MRA (Fink et al. 2005c). In practice, a combination of parallel imaging and view sharing might allow for a spatial

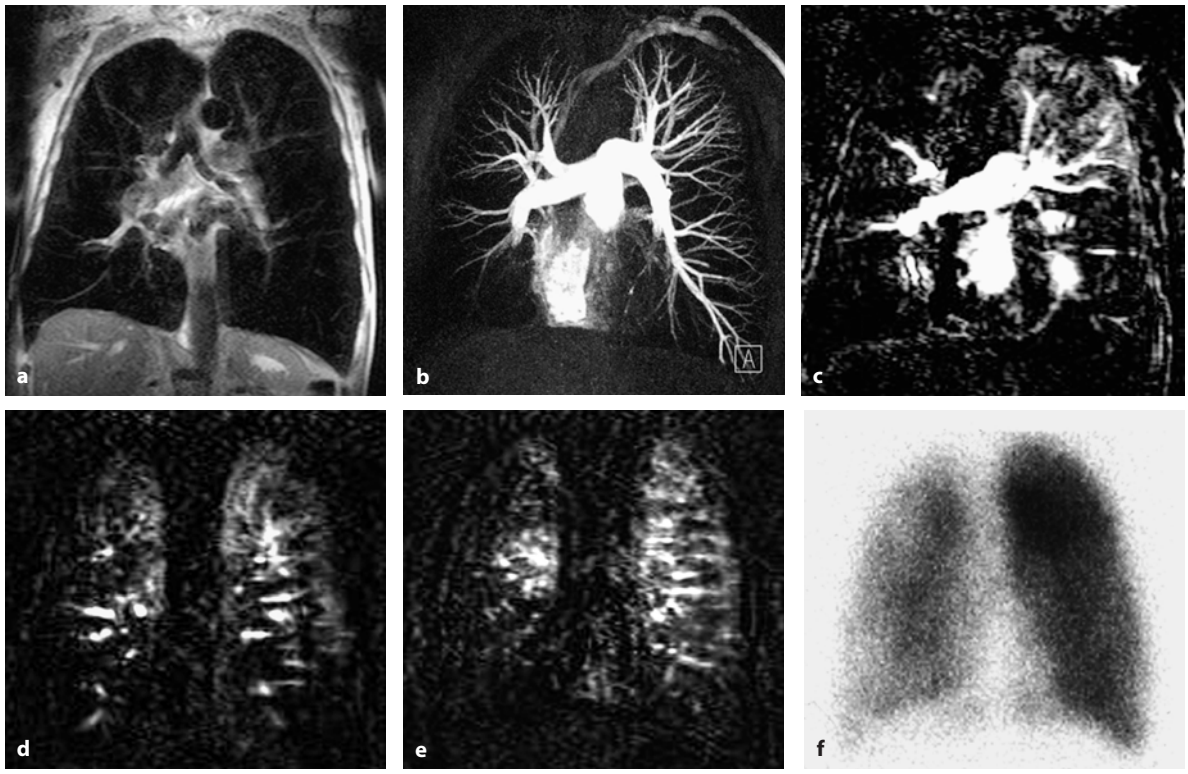

Fig. 37.2a–f. MRI of lung perfusion in a 63-year-old male with emphysema. **a** Coronal HASTE MRI shows emphysematous "barrel chest" aspect of the thorax. **b** High-resolution 3D MRA demonstrates tapering of right lower lobe artery and hypovascularity of right lung due to emphysema. **c-e** Pulmonary perfusion MRI shows bilateral perfusion defects most likely caused by parenchymal distortion and hypoxic vasoconstriction. **f** As a projection method, planar perfusion scintigraphy falsely demonstrates a more homogenous perfusion pattern. Reprinted with permission from (Fink et al. 2003)

resolution sufficient to detect even subtle perfusion defects that might be undetectable at conventional perfusion scintigraphy. In addition, view sharing may be used to further decrease the scan time for special applications such as quantitative perfusion MRI.

A major drawback of parallel imaging is the increase of image noise. For the visualization of lung perfusion, the time-resolved image data are usually post-processed by subtraction of a pre-contrast data set from the data set with the peak enhancement of the lung parenchyma. Unfortunately, this results in an additional increase of the noise in the image data. Correlation analysis has previously been proposed for time-resolved MRA to improve image background suppression and arteriovenous separation (Bock et al. 2000; Strecker et al. 2000). In these studies, it has also been demonstrated that the SNR of time-resolved MRI processed with correlation analysis is superior compared to image data processed with subtraction. Therefore, correlation analysis has recently also been evaluated for the post-processing of pulmonary perfusion MRI. Compared to subtraction an approximately 1.8 higher SNR of perfused lung parenchyma was achieved with correlation analysis in comparison to subtraction (Fink et al. 2004b). In addition, it has been shown that correlation analysis might also be used for the suppression of the signal of intrapulmonary blood vessels, which is not only useful for the assessment of qualitative pulmonary perfusion MRI, but also for quantification of perfusion from MRI (Risse et al. 2004).

37.3 Quantification of Pulmonary Perfusion

Apart from a qualitative assessment of lung perfusion, also a quantification of perfusion on the basis of indicator-dilution theory has been proposed for pulmonary perfusion MRI. Assuming no

relevant extravasation of the contrast agent during the first-pass through the lungs, pulmonary blood flow (PBF) can be quantified from the knowledge of the arterial input function (AIF) and tissue concentration-time curve $C(t)$ using deconvolution analysis (Ostergaard et al. 1996; Weisskoff et al. 1993):

$$C(t) = PBF \cdot AIF \otimes R(t) = PBF \int AIF(\tau) \times R(t - \tau) d\tau$$

Neglecting differences in arterial and capillary hematocrit and tissue density, the pulmonary blood volume (PBV) can be calculated as the area under the concentration-time curve $C(t)$ normalized to the area under the AIF:

$$PBV = \frac{\int C(\tau)\, d\tau}{\int AIF(\tau)\, d\tau}$$

According to the central volume theorem, the mean transit time (MTT) can be calculated from PBF and PBV:

$$MTT = \frac{PBV}{PBF}$$

In a pig model, Hatabu et al. (1999) demonstrated a very good correlation between perfusion parameters obtained from perfusion MRI and microsphere perfusion measurements. Initial experiments with this technique in human volunteers have shown the feasibility of MRI to demonstrate regional differences of lung perfusion parameters in different lung regions (e.g., gravity-dependent vs. non-gravity-dependent lung) (Levin et al. 2001). However, to achieve a temporal resolution sufficient for perfusion quantification, both of these initial studies were limited to 2D MRI with a moderate in-plane and through-plane spatial resolution.

In a more clinically orientated approach, Ohno et al. (2004) have recently also proposed perfusion quantification of the entire lung in patients with pulmonary hypertension or lung cancer using time-resolved 3D MRI. However, without the availability of parallel-imaging techniques, the spatial resolution in these studies had to be reduced (i.e., the lungs were covered with only ten coronal partitions with a thickness of 10 mm to 20 mm) to allow for a sufficient temporal resolution for perfusion quantification.

More recently, two groups have evaluated the use of parallel imaging to improve the temporal and spatial resolution for quantitative pulmonary perfusion MRI. In a pilot study, we evaluated the feasibility of 3D quantitative perfusion MRI in eight patients with PE or PH (Fink et al. 2004d). In patients with PE or chronic thromboembolic PH (CTEPH) characteristic wedge-shaped perfusion defects with decreased PBF and PBV and increased MTT were observed (Fig. 37.3). Patients with primary PH (PPH) or Eisenmenger syndrome showed a more homogeneous perfusion pattern. Although showing a quite large inter-individual variation, the mean PBF and PBV found in this pilot study (PBF: 104–322 ml/100 ml/min; PBV: 8–21 ml/100 ml) were comparable to values previously obtained by $H_2{}^{15}O$ PET (Schuster et al. 1995; Serizawa et al. 1994).

In another study, the effect of breath-holding on pulmonary perfusion was investigated (Fink et al. 2005b). Therefore, nine healthy volunteers were examined with pulmonary perfusion MRI with parallel imaging during end-inspiratory and end-expiratory breath-holds. It was shown that perfusion was significantly increased at expiratory breath-hold when compared to inspiratory measurements. This was also confirmed by phase-contrast MR measurements of the macroscopic blood flow in the pulmonary arteries. The findings of this study can be explained by the well-known effect that lung inflation causes a compression of the alveolar blood vessels. As a consequence, pulmonary vascular resistance is increased and pulmonary perfusion is reduced during inspiratory breath-hold (Brower et al. 1985; Hakim et al. 1982; Raj et al. 1987).

The aim of a study by Nikolaou et al. (2004) was to determine the optimum contrast agent dose for quantitative pulmonary perfusion MRI. The rationale behind this study was that a potential source of error of quantitative perfusion MRI results from a missing linearity between the local MR contrast-agent concentration and observed signal-intensity changes. Especially for the determination of the arterial-input function, there may be a non-linear relation between the contrast-agent concentration and signal-intensity changes. On the other hand, the contrast-agent dose may not be arbitrarily reduced, since pulmonary perfusion MRI, especially if combined with parallel imaging, suffers from a poor SNR. In a phantom experiment with a 3D FLASH pulse sequence (TR=1.7 ms; TE=0.6 ms; α=25°) with GRAPPA (acceleration factor R=2), Nikolaou et al. could demonstrate a linear relation between relative signal increase and contrast agent concentration up to 5.0 mmol/l. In a subsequent volunteer study, three different contrast agent doses (2, 4, and 8 ml Gadodiamide equivalent to a dose of 0.014, 0.029, and 0.057 mmol/kg body weight in a 70 kg volunteer) were compared. It was shown that the doses of 0.029 and 0.057 mmol/kg

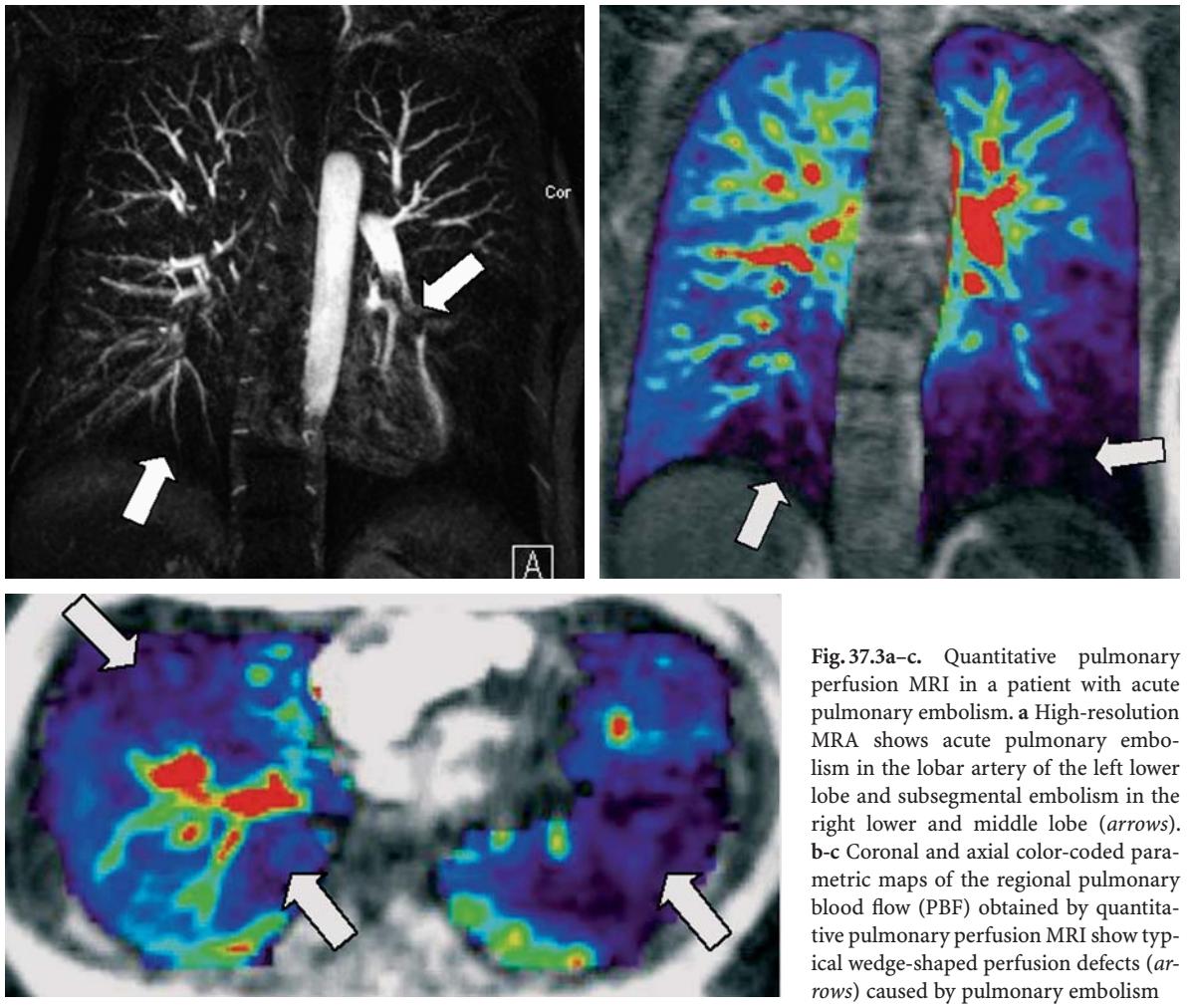

Fig. 37.3a–c. Quantitative pulmonary perfusion MRI in a patient with acute pulmonary embolism. **a** High-resolution MRA shows acute pulmonary embolism in the lobar artery of the left lower lobe and subsegmental embolism in the right lower and middle lobe (*arrows*). **b-c** Coronal and axial color-coded parametric maps of the regional pulmonary blood flow (PBF) obtained by quantitative pulmonary perfusion MRI show typical wedge-shaped perfusion defects (*arrows*) caused by pulmonary embolism

body weight yielded the best agreement with the reference value from the literature. Finally, using a dose of 0.057 mmol/kg body weight, quantification of pulmonary perfusion was reproducible in 16 volunteers, indicating a potential for a clinical use.

37.4 Clinical Applications

37.4.1 Pulmonary Embolism and Pulmonary Hypertension

In a study in 48 patients with suspected PE, Ohno et al. (2004) compared the diagnostic accuracy of time-resolved 3D MRA using SENSE parallel imaging with multi-detector CT (MDCT) and ventilation-perfusion scintigraphy (VQ scan). Conventional pulmonary angiography served as the gold standard. PE was diagnosed when an area of decreased perfusion in the lung parenchyma with or without a corresponding filling defect in the pulmonary artery was observed. In this study it was shown that time-resolved MRA had a higher diagnostic accuracy for the detection of PE when compared to MDCT and VQ scan. In detail, the sensitivity of time-resolved MRA was 92% compared to 83% (MDCT) and 67% (VQ scan). Similarly, the specificity of time-resolved MRA was 94% compared to 94% (MDCT) and 78% (VQ scan). Both the positive and negative predictive value (PPV and NPV) of time-resolved MRA was superior to MDCT and scintigraphy [PPV: 85% (MRA), 83% (MDCT), and 50% (VQ scan); NPV: 97% (MRA), 94% (MDCT), and 88% (VQ scan)]. Based on these results, a comprehensive imaging of PE by MRI using parallel imaging might be

considered more frequently in the future. This includes the group of patients with low clinical probability for PE, especially if of young age, which in clinical practice is frequently exposed to the substantial radiation dose of MDCT of up to 4 mSv to 8 mSv, despite an overall prevalence of PE of only 3.4% (Wells et al. 1998). In addition, pulmonary perfusion MRI as a radiation-free method might be used to assess the resolution of thromboembolism during anticoagulative therapy.

Apart from PE, pulmonary perfusion MRI might be used for the differentiation of primary or secondary (i.e., chronic thromboembolic) PH (Ley et al. 2004; Nicolaou et al. 2004). Whereas chronic thromboembolic PH features segmental perfusion defects, primary PH (PPH) often shows a more diffuse and patchy perfusion pattern (Fink et al. 2005b; Nicolaou et al. 2005; Ley et al. 2004) (Fig. 37.4). The differentiation of PPH and CTEPH is of clini-

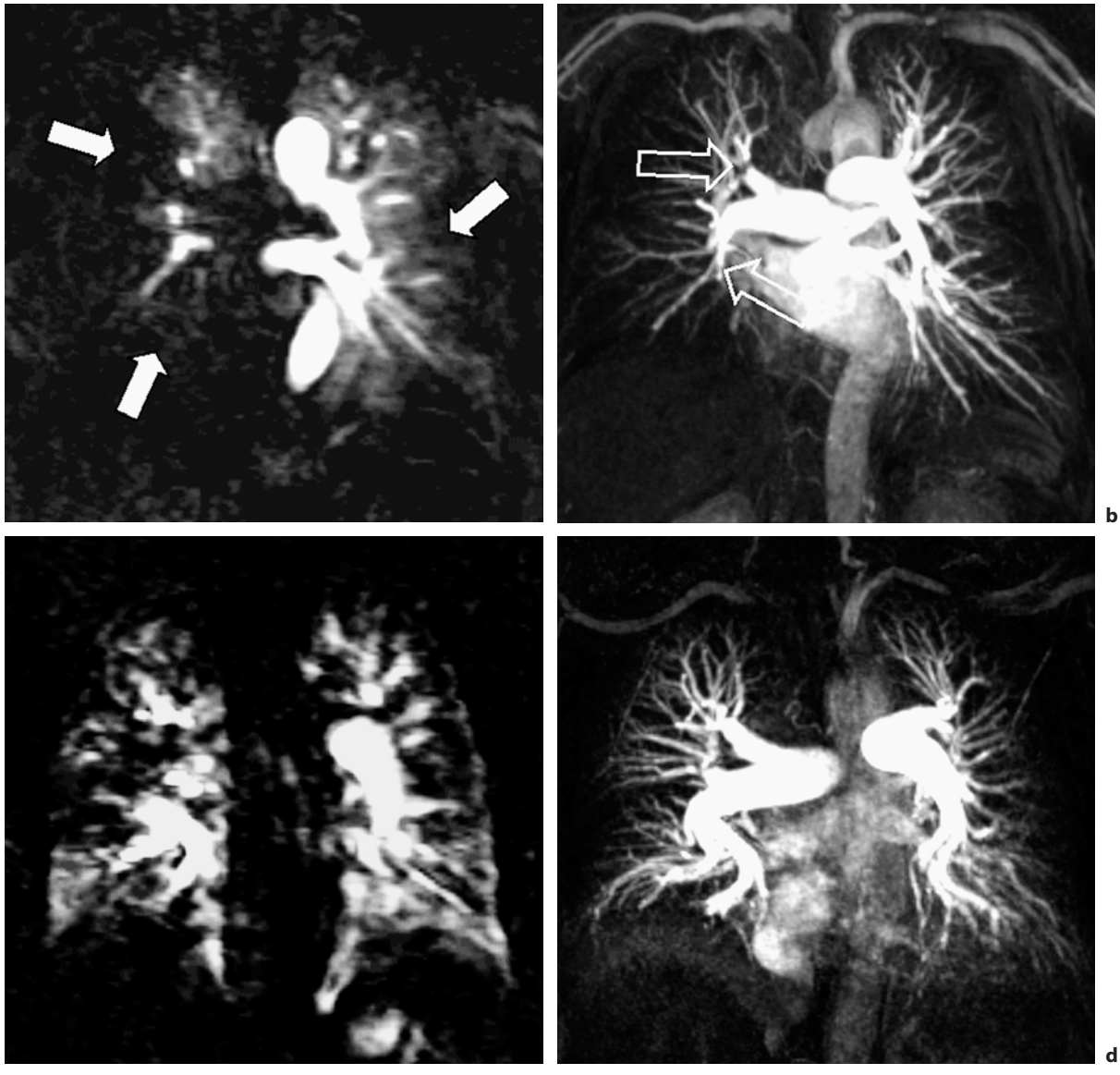

Fig. 37.4a–c. Pulmonary perfusion MRI for the differentiation of different entities of pulmonary hypertension. Pulmonary perfusion MRI **a** and high-resolution MRA **b** of a patient with chronic thromboembolic pulmonary hypertension shows typical segmental perfusion defects of the lung (*arrows*) caused by chronic thromboembolism. The MRA shows typical features of CTEPH such as central arterial dilatation and peripheral webs and bands (*open arrow*). In contrast, pulmonary perfusion MRI **c** of a patient with PPH shows a more homogeneous perfusion pattern without segmental distribution of the perfusion defects. MRA in this patient also reveals dilatated central pulmonary arteries as a typical feature of PH

cal relevance since effective but diverse therapeutic options (i.e., medical vs. surgical) are available for both disease entities.

In a study by Nikolaou et al. (2005) in 29 patients with PH, the accuracy of a combined MR protocol of pulmonary perfusion MRI and high-spatial-resolution MRA with parallel imaging for the differentiation of different forms of PH was assessed. For comparison perfusion scintigraphy was available in the majority of patients. It was shown that, using the comprehensive MR imaging protocol, a correct differentiation of PPH and CTEPH could be made in 90% of the patients. MR perfusion imaging showed an agreement (i.e., identical diagnosis on a per patient basis) of 79% to perfusion scintigraphy. The interobserver agreement was good (κ=0.63). Further studies are required to evaluate the potential of pulmonary perfusion MRI for the assessment of patients with PH. Apart from the differentiation between different entities of PH, pulmonary perfusion MRI might be used for the functional staging of PH and might be integrated into comprehensive imaging protocols of PH (Kreitner et al. 2004; Ley et al. 2004; Nikolaou et al. 2005).

37.4.2 Cystic Fibrosis

Even more than in adults, the radiation dose is a critical factor in pediatric imaging. Therefore, radiation-free imaging techniques, such as MRI, are a desirable alternative to conventional imaging methods. This holds especially true for patients with chronic diseases in which frequent follow-up exams are usually required in the course of the disease. One typical example is patients with cystic fibrosis (CF), in which the life expectancy is mainly determined by the course of pulmonary complications.

In a pilot study, the correlation of lung perfusion changes with structural abnormalities of the lung was assessed in 11 children with CF. In addition to morphologic imaging, the regional lung perfusion changes were assessed with a time-resolved 3D-FLASH sequence with GRAPPA (acceleration factor R=2). In total 198 lung segments were analyzed by two radiologists in consensus and scored for changes of the lung morphology (1= normal; 2= mild; 3= severe) as well as for perfusion changes (0=normal; 1=defect). Segmental perfusion defects were observed in all patients and were predominantly located in the upper lobes (80%). Normal lung parenchyma showed a homogenous perfusion in 86% of analyzed lung segments, while in 97% of the cases severe morphological changes (e.g., severe bronchiectasis and fibrotic changes) led to perfusion defects (P<0.0001) (Fig. 37.5). Segments with mild morphological changes showed either normal (53%) or impaired perfusion (47%). Although more studies are required to further assess the potential of pulmonary perfusion MRI in CF, the results of this pilot study indicate that perfusion MRI might help to identify patients in which intensified therapy might improve the lung function and possibly prevent irreversible loss of tissue structure and lung function (Eichinger et al. 2004).

37.5 Future Developments

The relevance of higher magnetic field strengths (B_0≥3 T) for pulmonary MRI has not yet been clinically evaluated. On the one hand, an increased field strength should result in a proportionally better SNR, which is especially desirable in the lung parenchyma with intrinsic low signal. On the other hand, the increased signal might be canceled due to the higher susceptibility effects in the heterogeneous lung tissue resulting in reduced T2* relaxation times at 3 T. Especially the combination of high field strength with higher parallel imaging acceleration factors should lead to synergistic effects and requires further research. Due to the coronal orientation of the acquired 3D slabs in lung perfusion imaging, acceleration factors greater than 2 should be feasible with typical phased-array surface coil systems that are positioned on top of the patient's chest and provide several coil elements with distinct coil sensitivity profiles in left-right direction.

Moreover, new parallel-imaging reconstruction algorithms, which do not require repeated measurements of the coil sensitivity profiles (e.g. TSENSE), are another promising development for pulmonary perfusion MRI with increased temporal resolution. Apart from MR hardware and software developments, further improvement of pulmonary perfusion MRI might be achieved with intravascular gadolinium-based MR contrast agents, which will become clinically available in the near future. In addition to the higher T1 relaxivity that will improve the signal characteristics of perfused lung, comprehensive

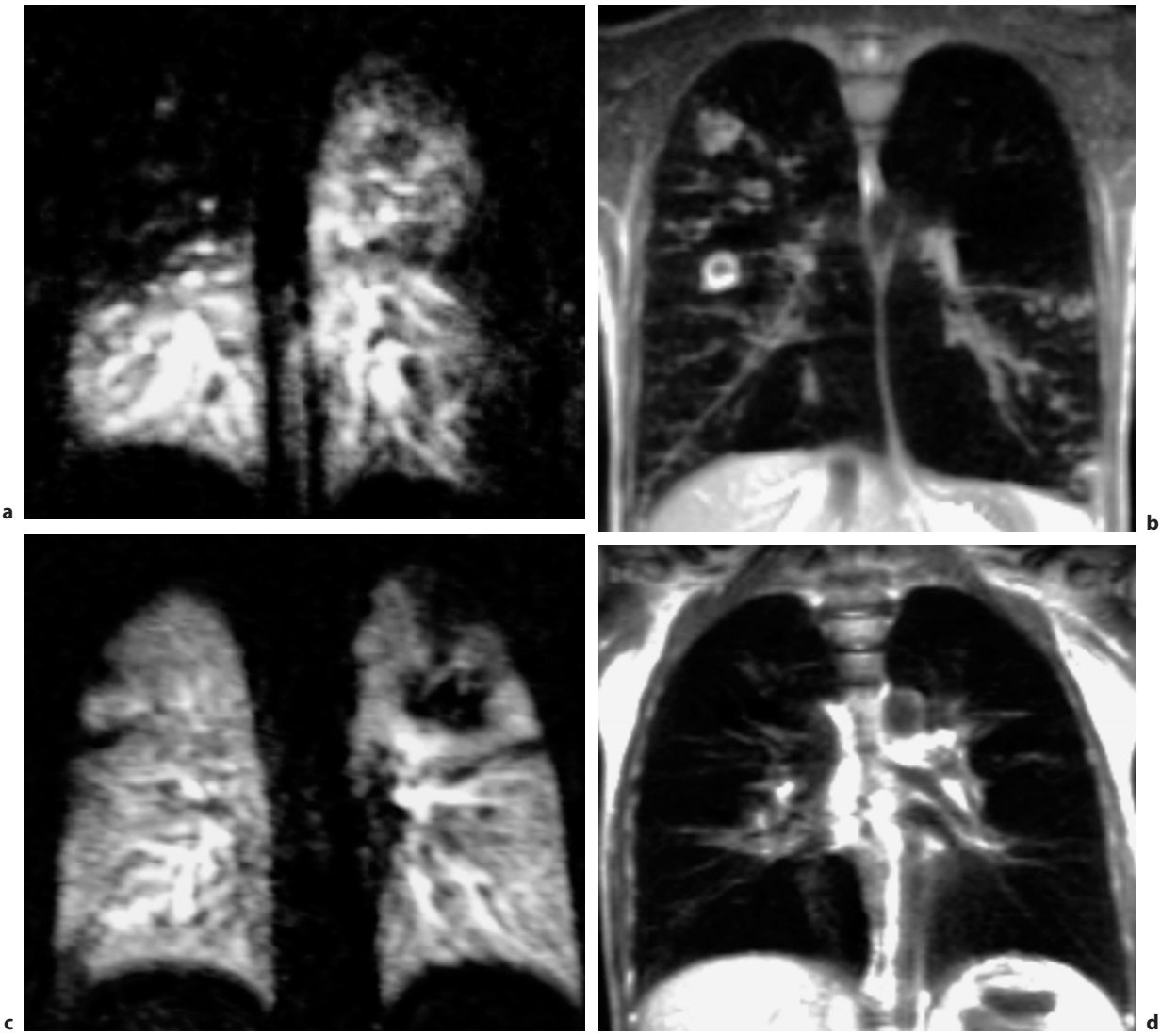

Fig. 37.5a–d. Pulmonary perfusion MRI in children with cystic fibrosis. Excellent correlation of severe perfusion changes demonstrated by pulmonary perfusion MRI **a** and severe morphologic (e.g., bronchiectatic) changes as revealed by HASTE-MRI **b** in a child with severe cystic fibrosis. Similarly minor perfusion changes in the upper lobes **c** correlate well with minor morphologic tissue changes in another child with CF **d**

imaging protocols comprising first-pass perfusion MRI and steady-state high-spatial-resolution MRA may be realized (Fink et al. 2004b).

In conclusion, parallel imaging has significantly improved the potential of non-invasive imaging of pulmonary perfusion using MRI. Despite the promising results of initial pilot studies in various pulmonary diseases, further studies evaluating pulmonary perfusion MRI for the clinical assessment of pulmonary disease are required.

References

Bailey CL, Channick RN, Auger WR, et al (2000) "High probability" perfusion lung scans in pulmonary venoocclusive disease. Am J Respir Crit Care Med 162: 1974–1978

Bock M, Schoenberg SO, Floemer F, Schad LR (2000) Separation of arteries and veins in 3D MR angiography using correlation analysis. Magn Reson Med 43: 481–487

Bolliger CT, Guckel C, Engel H et al (2002) Prediction of functional reserves after lung resection: comparison between quantitative computed tomography, scintigraphy, and anatomy. Respiration 69: 482–489

Brower R, Wise RA, Hassapoyannes C, Bromberger-Barnea B, Permutt S (1985) Effect of lung inflation on lung blood volume and pulmonary venous flow. J Appl Physiol 58: 954–963

Eichinger M, Fink C, Puderbach M et al (2004) Contrast-enhanced 3D MRI of lung perfusion in children with cystic fibrosis. J Cyst Fibros 3: 54

Euler US, Liljestrand G (1946) Observations on the pulmonary arterial blood pressure in the cat. Acta Physiol Scand 12: 301–320

Fazio F, Wollmer P (1981) Clinical ventilation-perfusion scintigraphy. Clin Physiol 1: 323–337

Fink C, Bock M, Ley S, Buhmann R, Puderbach M, Kauczor HU (2004a) Time-resolved parallel 3D MRA of the lung: application of correlation analysis. RSNA

Fink C, Bock M, Puderbach M, Schmahl A, Delorme S (2003) Partially parallel three-dimensional magnetic resonance imaging for the assessment of lung perfusion – initial results. Invest Radiol 38: 482–488

Fink C, Ley S, Kroeker R, Requardt M, Kauczor HU, Bock M (2005a) Time-resolved contrast-enhanced three-dimensional magnetic resonance angiography of the chest: combination of parallel imaging With view sharing (TREAT). Invest Radiol 40: 40–48

Fink C, Ley S, Puderbach M, Plathow C, Bock M, Kauczor HU (2004b) 3D pulmonary perfusion MRI and MR angiography of pulmonary embolism in pigs after a single injection of a blood pool MR contrast agent. Eur Radiol 14: 1291–1296

Fink C, Ley S, Risse F et al (2005b) Effect of inspiratory and expiratory breathhold on pulmonary perfusion: assessment by pulmonary perfusion magnetic resonance imaging. Invest Radiol 40: 72–79

Fink C, Puderbach M, Bock M et al (2004c) Regional lung perfusion: assessment with partially parallel three-dimensional MR imaging. Radiology 231: 175–184

Fink C, Puderbach M, Ley S, Zaporozhan J, Plathow C, Kauczor HU (2005c) Time-resolved echo-shared parallel MRA of the lung: observer preference study of image quality in comparison with non-echo-shared sequences. Eur Radiol 15: 2070–2074

Fink C, Risse F, Buhmann R et al (2004d) Quantitative analysis of pulmonary perfusion using time-resolved parallel 3D MRI - initial results. Rofo Fortschr Geb Rontgenstr Neuen Bildgeb Verfahr 176: 170–174

Goyen M, Laub G, Ladd ME et al (2001) Dynamic 3D MR angiography of the pulmonary arteries in under 4 seconds. J Magn Reson Imaging 13: 372–377

Griswold MA, Jakob PM, Heidemann RM et al (2002). Generalized autocalibrating partially parallel acquisitions (GRAPPA). Magn Reson Med 47: 1202–1210

Hakim TS, Michel RP, Chang HK (1982) Effect of lung inflation on pulmonary vascular resistance by arterial and venous occlusion. J Appl Physiol 53: 1110–1115

Hatabu H, Tadamura E, Levin DL et al (1999) Quantitative assessment of pulmonary perfusion with dynamic contrast-enhanced MRI. Magn Reson Med 42: 1033–1038

Hunsaker AR, Ingenito EP, Reilly JJ, Costello P (2002) Lung volume reduction surgery for emphysema: correlation of CT and V/Q imaging with physiologic mechanisms of improvement in lung function. Radiology 222: 491–498

Iwasawa T, Saito K, Ogawa N, Ishiwa N, Kurihara H (2002) Prediction of postoperative pulmonary function using perfusion magnetic resonance imaging of the lung. J Magn Reson Imaging 15: 685–692

Korosec FR, Frayne R, Grist TM, Mistretta CA (1996) Time-resolved contrast-enhanced 3D MR angiography. Magn Reson Med 36: 345–351

Kreitner KF, Ley S, Kauczor HU et al (2004) Chronic thromboembolic pulmonary hypertension: pre- and postoperative assessment with breath-hold MR imaging techniques. Radiology 232: 535–543

Levin DL, Chen Q, Zhang M, Edelman RR, Hatabu H (2001) Evaluation of regional pulmonary perfusion using ultrafast magnetic resonance imaging. Magn Reson Med 46: 166–171

Ley S, Kreitner KF, Fink C, Heussel CP, Borst MM, Kauczor HU (2004) Assessment of pulmonary hypertension by CT and MR imaging. Eur Radiol 14: 359–368

Matsuoka S, Uchiyama K, Shima H et al (2001) Detectability of pulmonary perfusion defect and influence of breath holding on contrast-enhanced thick-slice 2D and on 3D MR pulmonary perfusion images. J Magn Reson Imaging 14: 580–585

Nakagawa T, Sakuma H, Murashima S, Ishida N, Matsumura K, Takeda K (2001) Pulmonary ventilation-perfusion MR imaging in clinical patients. J Magn Reson Imaging 14: 419–424

Nikolaou K, Schoenberg SO, Attenberger U et al (2005) Pulmonary arterial hypertension: diagnosis with fast perfusion MR imaging and high-spatial-resolution MR angiography--preliminary experience. Radiology 236: 694–703

Nikolaou K, Schoenberg SO, Brix G et al (2004) Quantification of pulmonary blood flow and volume in healthy volunteers by dynamic contrast-enhanced magnetic resonance imaging using a parallel imaging technique. Invest Radiol 39: 537–545

Ohno Y, Hatabu H, Higashino T et al (2004). Dynamic perfusion MRI versus perfusion scintigraphy: prediction of postoperative lung function in patients with lung cancer. AJR Am J Roentgenol 182: 73–78

Ohno Y, Hatabu H, Murase K, et al (2004) Quantitative assessment of regional pulmonary perfusion in the entire lung using three-dimensional ultrafast dynamic contrast-enhanced magnetic resonance imaging: Preliminary experience in 40 subjects. J Magn Reson Imaging 20: 353–365

Ohno Y, Higashino T, Takenaka D et al (2004) MR angiography with sensitivity encoding (SENSE) for suspected pulmonary embolism: comparison with MDCT and ventilation-perfusion scintigraphy. AJR Am J Roentgenol 183: 91–98

Ostergaard L, Weisskoff RM, Chesler DA, Gyldensted C, Rosen BR (1996) High resolution measurement of cerebral blood flow using intravascular tracer bolus passages. Part I: Mathematical approach and statistical analysis. Magn Reson Med 36: 715–725

Raj JU, Chen P, Navazo L (1987) Effect of inflation on microvascular pressures in lungs of young rabbits. Am J Physiol 252: H80–84

Risse F, Fink C, Kuder TA, Buhmann R, Kauczor HU, Schad LR (2004) Suppression of the pulmonary vasculature in quantitative lung perfusion MRI. Magma 17: 208

Schoenberg SO, Bock M, Floemer F et al (1999) High-resolution pulmonary arterio- and venography using multiple-bolus multiphase 3D-Gd-mRA. J Magn Reson Imaging 10: 339–346

Schuster DP, Kaplan JD, Gauvain K, Welch MJ, Markham J (1995) Measurement of regional pulmonary blood flow with PET. J Nucl Med 36: 371–377

Serizawa S, Suzuki T, Niino H, Arai T, Hara T (1994) Using H2(15)O and C15O in noninvasive pulmonary measurements. Chest 106: 1145–1151

Strecker R, Scheffler K, Klisch J et al (2000) Fast functional MRA using time-resolved projection MR angiography with correlation analysis. Magn Reson Med 43: 303–309

Uematsu H, Hatabu H, Fink C, Kauczor HU (2004) MR pulmonary perfusion. In: Kauczor HU (ed) Functional imaging of the chest. Springer, Berlin Heidelberg New York, pp 189–199

Weisskoff RM, Chesler D, Boxerman JL, Rosen BR (1993) Pitfalls in MR measurement of tissue blood flow with intravascular tracers: which mean transit time? Magn Reson Med 29: 553–558

Wells PS, Ginsberg JS, Anderson DR et al (1998) Use of a clinical model for safe management of patients with suspected pulmonary embolism. Ann Intern Med 129: 997–1005

Oxygen-Enhanced Imaging of the Lung

38

Olaf Dietrich

CONTENTS

38.1 Introduction

Magnetic resonance imaging of the lung is considerably more difficult than MRI of most other organs due to the very low signal intensity of the lung tissue caused by its low average proton density and short T2* relaxation time. Both properties are a consequence of the heterogeneous microstructure of the lung parenchyma, which consists mainly of microscopic air-filled alveoli with a large interface between air spaces and tissue or blood. Hence, large local variations of susceptibility occur within small spatial scales influencing the static magnetic field and thus the Larmor frequencies of the protons. A direct visual assessment of the lung parenchyma or of the ventilation as well as diagnostics of pathologically changed lung tissue is therefore often not possible with conventional proton MRI.

Several techniques have been proposed to overcome these limitations such as MRI of hyperpolarized noble gases (Middleton et al. 1995; Altes and Salerno 2004; van Beek et al. 2004; Ishii et al. 2005) or signal enhancement with aerosols of gadolinium-based contrast agents (Berthezene et al. 1992; Suga et al. 2002; Haage et al. 2005). These techniques, however, involve complex and expensive hardware devices to prepare the contrast-agent aerosol or the hyperpolarized gases. In addition, the acquisition of MR signals from hyperpolarized gases requires specifically adapted RF equipment such as RF coils tuned to the Larmor frequency of helium or xenon. A further disadvantage of MRI with gadolinium aerosols is that the inhalation of gadolinium-based contrast agents is still controversial and not yet thoroughly evaluated in humans. Against this background, oxygen-enhanced lung MRI must be seen as an approach to visualize the lung that is technically much less demanding than the methods mentioned above: oxygen is generally available in every clinical environment and the administration of oxygen is relatively safe.

In the following sections of this chapter, the physiological and technical basis of oxygen-enhanced MRI of the lung will be described. Some details of implementation such as multi-slice-acquisition techniques and triggering schemes are elucidated before the chapter concludes with a discussion of the specific advantages and applications of parallel imaging for oxygen-enhanced MRI of the lung.

O. Dietrich, PhD
Department of Clinical Radiology, University Hospitals – Grosshadern, Ludwig Maximilian University of Munich, Marchioninistr. 15, 81377 Munich, Germany

38.2 Oxygen-Enhanced Lung MRI

38.2.1 Contrast Mechanism and Physiology

Inhaled molecular oxygen (O_2) was first suggested by Edelman et al. (1996) as a paramagnetic contrast agent for proton MRI of the lung. The contrast mechanism of molecular oxygen is similar to the one of gadolinium-based contrast agents (although of a substantially smaller extent): the longitudinal relaxation (T1) of the protons of the blood is shortened depending on the O_2 concentration. Averaging over all tissue compartments within a single voxel, an effective oxygen-induced T1 reduction of about 10% to 15% is observed in the lung parenchyma after inhalation of pure oxygen (Edelman et al. 1996; Chen et al. 1998; Loffler et al. 2000). This reduction results from differently changed T1 values of all protons that contribute to the voxel signal, i.e., averaged over all kinds of tissue such as blood, blood vessels, alveolar cells, and connective tissue. The most important contribution, however, is caused by the increased concentration of solved oxygen in the capillary blood of the lung. Hence, oxygen-based lung imaging provides combined information about three physiological parameters (Edelman et al. 1996; Loffler et al. 2000):

- the inhaled oxygen must reach the lung area under consideration; thus, sufficient ventilation of the area is a necessary precondition for oxygen-enhanced lung MRI;
- in addition, fresh capillary blood must be supplied in which the oxygen can be solved; lung perfusion therefore is a second requirement for the observation of reduced T1 values;
- finally, the transition of the oxygen from the alveoli into the capillaries of the lung, i.e., oxygen diffusion, is required for signal enhancement.

Thus, oxygen-enhanced lung MRI can be regarded as imaging of "lung function" understood as the combination of these three parameters.

A recently described alternative contrast mechanism for oxygen-enhanced lung imaging is based on the reduction of transversal T2* relaxation by about 10% after inhalation of oxygen (Pracht et al. 2005). Although the measurement of this effect is difficult and prone to systematic errors because of the extremely short T2* times of lung tissue between 1.6 ms and 1.9 ms, this approach might be useful to determine ventilation properties with reduced influence of perfusion and diffusion effects.

38.2.2 MRI Pulse Sequences

Several pulse sequences can be employed for oxygen-enhanced T1-weighted lung MRI provided the following prerequisites are fulfilled:

- The pulse sequences must provide sufficient T1 weighting to be sensitive to the oxygen-induced T1 shortening. This is usually achieved by a magnetization preparation with an inversion pulse (180° pulse, inversion-recovery technique). Typical inversion times are either about 700 ms (Edelman et al. 1996; Stock et al. 1999; Ohno et al. 2001; Vaninbroukx et al. 2003; Naish et al. 2005) or about 1,300 ms (Loffler et al. 2000; Muller et al. 2002; Mai et al. 2003; Dietrich et al. 2005).
- Fast data acquisition is recommendable to reduce motion artefacts caused by cardiac motion, blood flow, and respiration. Single-shot sequences (with complete data acquisition after a single excitation) have successfully been employed in order to avoid motion-related effects.
- The pulse sequences should be insensitive to variations of susceptibility and to short T2* relaxation times; this requirement excludes echo-planar techniques or gradient-echo sequences with non-ultra-short echo times.

Sequences with the listed properties that have been employed for oxygen-enhanced lung MRI are, e.g., single-shot turbo-spin-echo sequences with centrically reordered k-space sampling that are also known as RARE (rapid acquisition with relaxation enhancement) sequences (Chen et al. 1998; Stock et al. 1999; Loffler et al. 2000; Muller et al. 2002; Vaninbroukx et al. 2003). A similar sequence with even shorter acquisition time is the half-Fourier-acquired single-shot turbo-spin-echo (HASTE) sequence (Edelman et al. 1996; Ohno et al. 2001; Nakagawa et al. 2001; Mai et al. 2003; Dietrich et al. 2005). Oxygen MRI of the lung at low fields below 0.5 T has been performed with steady-state free-precession (SSFP) techniques such as the TrueFISP sequence (Muller et al. 2001). Finally, snapshot-FLASH sequences with ultra-short echo times below 2 ms have been used for oxygen-enhanced lung MRI; these sequences are particularly suited for the measurement of quantitative T1 maps (Jakob et al. 2001). All listed pulse sequences are

combined with an inversion-recovery preparation to achieve sufficient T1 weighting.

38.2.3 Acquisition Paradigms and Data Evaluation

The change of longitudinal relaxation after O_2 inhalation can be used to visualize the ventilated lung tissue. A difference map of T1-weighted images acquired during the inhalation of oxygen on the one hand and of room air on the other hand shows the lung parenchyma hyperintense relative to the surrounding tissue. Typically a block paradigm is used for data acquisition consisting of alternating blocks with inhalation of room air and oxygen as illustrated in Fig. 38.1. The acquisition of several repetitions is required since both the expected signal difference and the signal-to-noise ratio of the lung tissue are relatively small. Thus, averaging of, e.g., 20 to 40 repetitions breathing oxygen and of a similar number of repetitions breathing room air is used to increase the signal-to-noise ratio of the resulting difference maps.

The signal difference can be either visualized directly (Chen et al. 1998; Stock et al. 1999; Mai et al. 2000; Nakagawa et al. 2001) or as relative difference after pixel-wise normalization to the room-air signal (Edelman et al. 1996; Muller et al. 2002; Ohno et al. 2002; Dietrich et al. 2005). Calculating absolute or relative difference maps is a relatively simple way to visualize lung function and can be performed on most MRI systems without additional post-processing software. However, it must be taken into consideration that a certain time interval is required after switching the gas supply from air to oxygen (and vice versa) until T1 (and, hence, the signal intensity) reaches a steady-state value as demonstrated in Fig. 38.1. This process is described by an exponential change with time constants between 23 s and 83 s in healthy volunteers (Arnold et al. 2004; Naish et al. 2005).

The interval between the steady states could be avoided by waiting a few minutes after switching the gas supply before the data acquisition is continued (Mai et al. 2003). However, Muller et al. (2002) demonstrated that the slope of the signal increase correlates well with other clinical parameters. Hence, it appears useful to acquire data continuously in order to cover the intermediate signal dynamics as well and, thus, to be able to determine

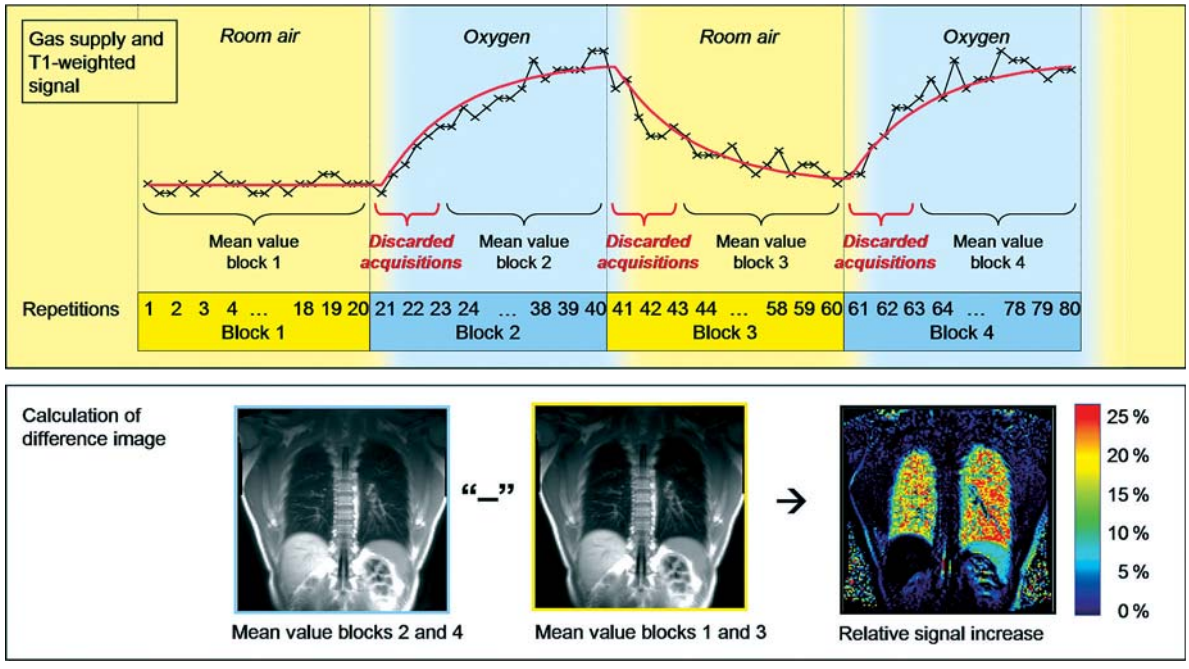

Fig. 38.1a,b. Block paradigm for oxygen-enhanced lung MRI. **a** Data acquisition: T1-weighted images are continuously acquired in four blocks with 4×20 repetitions; in blocks 1 and 3 room air is supplied, in blocks 2 and 4 pure oxygen. The T1-weighted signal varies relatively slowly after switching the gas supply and reaches exponentially its new steady state. Thus, several repetitions are discarded before calculating the pixel-by-pixel mean value of each block. **b** The relative signal increase is calculated as the difference of the averaged images in blocks 2 and 4 on the one hand and 1 and 3 on the other hand, normalized to the averaged room air image. The lung parenchyma and the spleen appear hyperintense in the difference map.

both difference images and time constants of the signal change. When calculating relative or absolute difference maps, a certain number of repetitions within each block of the paradigm should be discarded after switching the gas supply to avoid systematically decreased differences. For example, in a paradigm of 4×20 respiratory-triggered repetitions an optimized ratio of signal difference and statistical error was found if about five to eight repetitions were discarded (Dietrich et al. 2006).

38.2.4 Clinical Applications

Oxygen-enhanced lung imaging has been evaluated in several studies demonstrating a good correlation between MRI parameters and conventional methods of lung diagnostics such as evaluation of the diffusion capacity of carbon monoxide (DLCO), the forced expiratory volume in 1 s (FEV1), or results of ventilation scintigraphy. Ohno et al. (2001, 2002) examined patients with lung cancer and with lung emphysema and demonstrated good correlation of maximum signal enhancement in oxygen-enhanced MRI on the one hand and FEV1 and DLCO on the other hand. The same group described that oxygen-enhanced MRI could be used to successfully predict the postoperative FEV1 in patients with bronchial carcinoma (Ohno et al. 2005). Nakagawa et al. (2001) demonstrated in patients with pulmonary embolism that oxygen-enhanced MRI did not show any ventilation defects in agreement with ventilation scintigraphy; in these patients ventilation contrast appears to dominate the perfusion- and diffusion-based contributions. A study by Muller et al. (2002) in patients with various pulmonary diseases showed a good correlation between the signal slope after switching the gas supply to pure oxygen and the DLCO. Jakob et al. (2004) found in patients with cystic fibrosis that the dependence of T1 on different O_2 concentration correlates well with affected lung areas characterized by perfusion defects.

38.3 Advanced Techniques

38.3.1 Multi-Slice Techniques

Oxygen-enhanced MRI of the lung is based on T1-weighting sequences such as single-shot turbo-spin-echo techniques or ultrafast gradient-echo techniques. Both sequence types require an additional T1-sensitizing magnetization preparation that is usually realized as an inversion pulse. This 180° RF pulse (as well as the refocusing RF pulses of the turbo-spin-echo sequence) can be implemented either as slice-selective pulses that influence only the spins in a two-dimensional section or as non-selective pulses that invert all spins within the RF coil. Multi-slice acquisitions can be performed only with slice-selective inversion and refocusing pulses.

Most oxygen-enhanced imaging studies have been performed with non-selective inversion or refocusing pulses (Mai et al. 2003; Jakob et al. 2001; Nakagawa et al. 2001) such that an interleaved inversion and acquisition of multiple slices is not possible. Hence, either single-slice imaging was used or the total duration of acquisition was considerably prolonged in order to acquire up to four slices in successive imaging experiments.

The acquisition time of multiple slices can be decreased by employing slice-selective RF pulses and interleaving inversion preparation and image data readout, i.e., the inversion time, TI, between inversion and readout of a single slice is used to invert one or several more slices as demonstrated in Fig. 38.2. A potential disadvantage of using slice-selective inversion can be an increased sensitivity to perfusion effects: the signal within the slice will be influenced by inflowing non-inverted spins from outside the slice. To minimize this effect, the thickness of the inverted slice can be chosen larger, e.g., by a factor of 2, than the thickness of the image slice.

It has been demonstrated in a comparison of non-selective inversion and slice-selective inversion with doubled inversion slice thickness that similar results can be obtained with both techniques (Dietrich et al. 2005). The T1-weighted images and calculated maps of relative signal increase showed some differences with respect to the signal within the pulmonary vessels. However, the signal increase in the large pulmonary vessels is less important for evaluation of the lung function than the signal distribution in the lung parenchyma, which was similar for both techniques.

A fast multi-slice acquisition for oxygen-enhanced lung imaging is particularly valuable in clinical studies that require an assessment of the complete lung and, at the same time, are to be combined with several other MRI acquisitions of the lung such as pulmonary MR angiography or perfusion imaging. Single-slice techniques are often not acceptable in these studies because of their limited anatomic coverage or their long acquisition times.

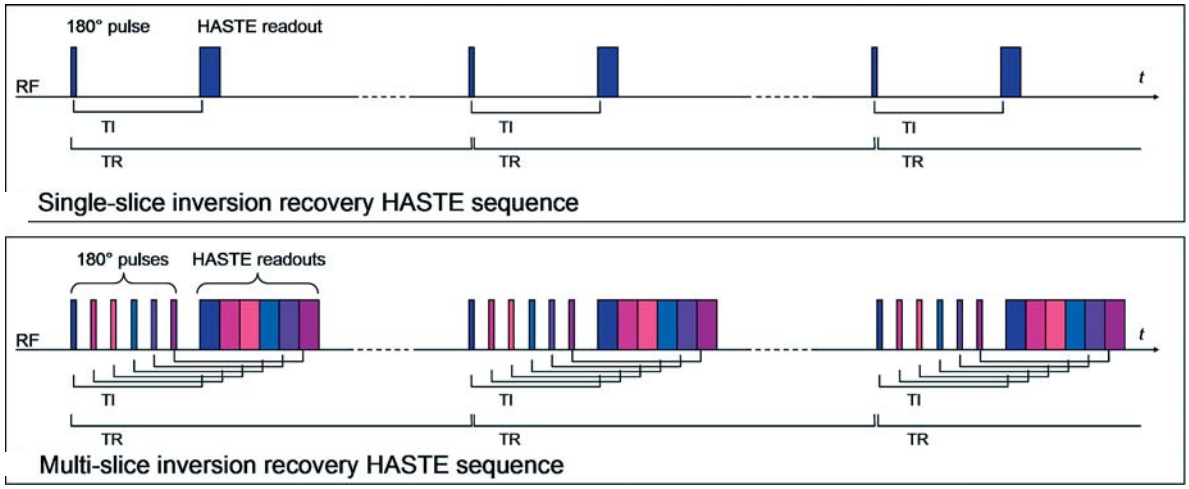

Fig. 38.2a,b. a Three repetitions of a single-slice inversion-recovery HASTE sequence. Only a single slice is acquired; the inversion (180°) pulse as well as the refocusing pulses may be non-selective. **b** Three repetitions of a multi-slice inversion-recovery HASTE sequence. Six slices (shown in *different colors*) are acquired; inversion (180°) pulses and readouts are interleaved. All 180° RF pulses must be slice-selective.

38.3.2 ECG and Respiratory Triggering

Reliable triggering is particularly important for MRI of the lung because of the high level of motion in the thorax due to pulsatile blood flow, cardiac motion, and respiration. Vaninbroukx et al. (2003) demonstrated that oxygen-enhanced MRI of the lung benefits from both ECG triggering and respiratory triggering in comparison to MRI without triggering. ECG triggering helps to acquire all repetitions in identical cardiac phases and to avoid motion artefacts due to acquisition during the systolic phase. Even more important is respiratory triggering to acquire all repetitions with identical positions of the diaphragm, since the signal intensity of the lung parenchyma depends substantially on the respiratory phase (Mai et al. 2000). The signal intensity typically varies by at least 50% due to the change of proton density during respiration, and this signal variation is superimposed on the oxygen-induced signal increase. It appears advantageous to choose end-expiration for image acquisition to obtain the maximal lung signal and a more uniform diaphragm position than after repeated inspirations (Losert et al. 2002).

Thus, a combined application of ECG and respiratory triggering should be incorporated in a fast T1-weighting pulse sequence to facilitate robust oxygen-enhanced MRI of the lung in clinical routine. If combined with a multi-slice inversion-recovery single-shot turbo-spin-echo sequence, a complex trigger scheme is required to move the data readout into the diastolic phase. A possible trigger and sequence scheme, which has been evaluated by Dietrich et al. (2005), is shown in Fig. 38.3; the acquisition is respiratory-triggered to start in end-expiration and an additional short delay, T_D, is calculated from the ECG signal such that the actual data readout takes place in the diastolic cardiac phase. Since the acquisition of all slices cannot be fitted into a single RR interval, the readout is divided into two parts with three HASTE readouts.

38.4 Parallel Imaging

Parallel imaging has been demonstrated to provide several advantages for single-shot lung MRI in general (Heidemann et al. 2003) and in particular for oxygen-enhanced MRI of the lung using a triggered single-shot pulse sequence as described in the preceding section (Dietrich et al. 2005). The general advantages of parallel imaging for single-shot sequences such as shorter echo trains, reduced blurring, or shorter echo times are already elucidated in Chaps. 10 “Single-shot pulse sequences” and 20 “Lung imaging.”

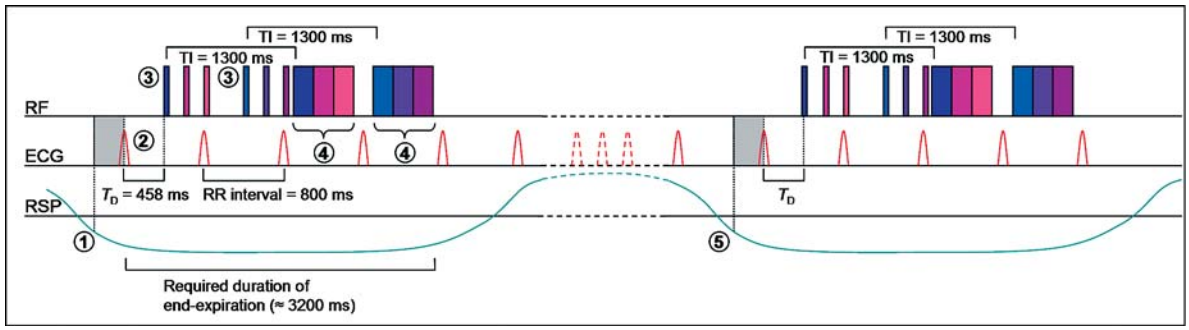

Fig. 38.3. Inversion-recovery HASTE sequence with respiratory (RSP) and ECG triggering. (*1*) Sequence start in end-expiration. (*2*) After the next R wave, the delay T_D is inserted and (*3*) the slice-selective inversion pulses for 2×3 slices are applied. (*4*) The delay T_D has been calculated from the current heart rate such that all six HASTE readouts lie in the diastole. (*5*) The sequence is repeated in the next respiratory cycle.

38.4.1 Sequence Timing

In combination with the ECG- and respiratory-triggered multi-slice sequence for oxygen-enhanced MRI of the lung shown in Fig. 38.3, parallel imaging exhibits specific advantages as a consequence of the reduced duration of the echo train, i.e., the shorter turbo-spin-echo readout. Using parallel imaging with an acceleration factor of R=2, the number of echoes required for the acquisition of a 128×128 matrix with a HASTE sequence can be reduced from 72 to 36; thus, the total readout time can be decreased from 214 ms/slice to 115 ms/slice (echo spacing 2.7 ms) including the time for signal excitation and spoiler gradients. In addition, a minimal echo time of 11 ms instead of 19 ms without parallel imaging can be achieved.

When applying parallel imaging, it is important to note that the coil-sensitivity information should not be acquired as integrated auto-calibration signals (ACS, cf. Chap. 8) since this increases the number of echoes required for each image. Instead, the ACS (or reference) lines can be acquired in a separate scan immediately before the first repetition of the oxygen-enhanced MR examination. This reference scan should be triggered to the same respiratory phase as the subsequent image acquisitions as shown in Fig. 38.4. Since the image acquisition is repeated, e.g., 80 times with identical coil configuration, it is much more efficient to acquire the coil-sensitivity information only once instead of doing so in each repetition.

As illustrated in Fig. 38.3, the timing of this sequence (in particular the delay T_D) is adapted online during the scan in order to place the HASTE readouts within the diastole. However, this is only possible, if the duration of the (e.g., three) subsequent HASTE readouts is sufficiently short such that:

- they fit into a single RR interval;
- they do not overlap the readouts of the other block, cf. Fig. 38.5b;
- they do not overlap the inversion pulses of the other block, cf. Fig. 38.5c.

The first issue is achieved by dividing the data acquisition in two parts with, e.g., three HASTE readouts. The second and third of these problems can be avoided by not fully interleaving acquisitions as illustrated in Fig. 38.5d. However, the total duration of the data acquisition, i.e., the required duration of end-expiration, is substantially prolonged in this case. As a consequence, more motion artefacts occur, since the end-expiration duration of volunteers and patients is frequently too short for this non-interleaved acquisition. As a rule of thumb, even if patients are asked to breathe slowly and regularly, the required duration of end-expiration should remain below about 3 s to avoid artefacts caused by respiration during a free-breathing acquisition.

Due to the complex combination of respiratory triggering, ECG triggering, and the split acquisition consisting of two blocks, the required duration of end-expiration depends substantially on the heart rate. This dependence is plotted in Fig. 38.6 for the described HASTE sequence with and without parallel imaging. The longer end-expiration durations without parallel imaging are explained by the switching from the fully interleaved scheme (Fig. 38.5a) to the non-interleaved scheme (Fig. 38.5d). For four slices (corresponding to two readouts in each RR interval) the interleaved acquisition without parallel imaging works for heart rates between 57/min and 140/min

(red area in Fig. 38.6a), but this range is considerably reduced for six slices (three readouts in each diastole). In this case, heart rates between 71/min and 93/min are required for an interleaved acquisition without parallel imaging (red area in Fig. 38.6b), whereas with parallel imaging this range is considerably larger with heart rates between 57/min and 170/min (blue area). Interleaved acquisitions of eight slices are possible with parallel imaging only (Fig. 38.6c). The computations show that in particular for three and four slices per RR interval, the end-expiration duration is decreased from about 5 s without to less than 3 s with parallel imaging for the typical range of heart rates in patients and volunteers. For example, the acquisition of six slices with three slices per diastole at a heart rate of 70/min requires an end-expiration duration of 5,130 ms without parallel imaging and is shortened to 2,565 ms with parallel imaging. Averaged over the range of typical heart rates between 60/min and 100/min, the mean end-expiration duration is 4,112 ms (standard deviation 1,045 ms) without parallel imaging and is significantly reduced to 2,727 ms (257 ms) with parallel imaging ($P<0.001$, Wilcoxon two-sample test) (Dietrich et al. 2005).

38.4.2 Image Examples

Images acquired with a respiratory- and ECG-triggered inversion-recovery HASTE sequence based on the considerations described above are shown in Fig. 38.7. The sequence was implemented on a 1.5-T whole-body MR system (Magnetom Sonata, Siemens Medical Solutions, Erlangen, Germany) with a high-performance gradient system providing a maximum gradient strength of 40 mT/m and a maximum gradient slope of 200 mT/(m ms). A dedicated parallel-imaging surface-coil system consisting of 12 coil elements (6 posterior and 6 anterior) was used; 8 of these 12 elements are combined in pairs of 2 such that together with the remaining 4 elements the coil system matches the 8 receiver channels of the MR system. T1 weighting of the HASTE sequence was achieved with an optimized inversion time (Loffler et al. 2000) of 1,300 ms and a repeat time of one respiratory cycle (thus ranging between about 5 s and 10 s). To minimize artefacts, a linear k-space readout in phase-encoding direction with an echo spacing of 2.7 ms was used resulting in a (minimum) echo time

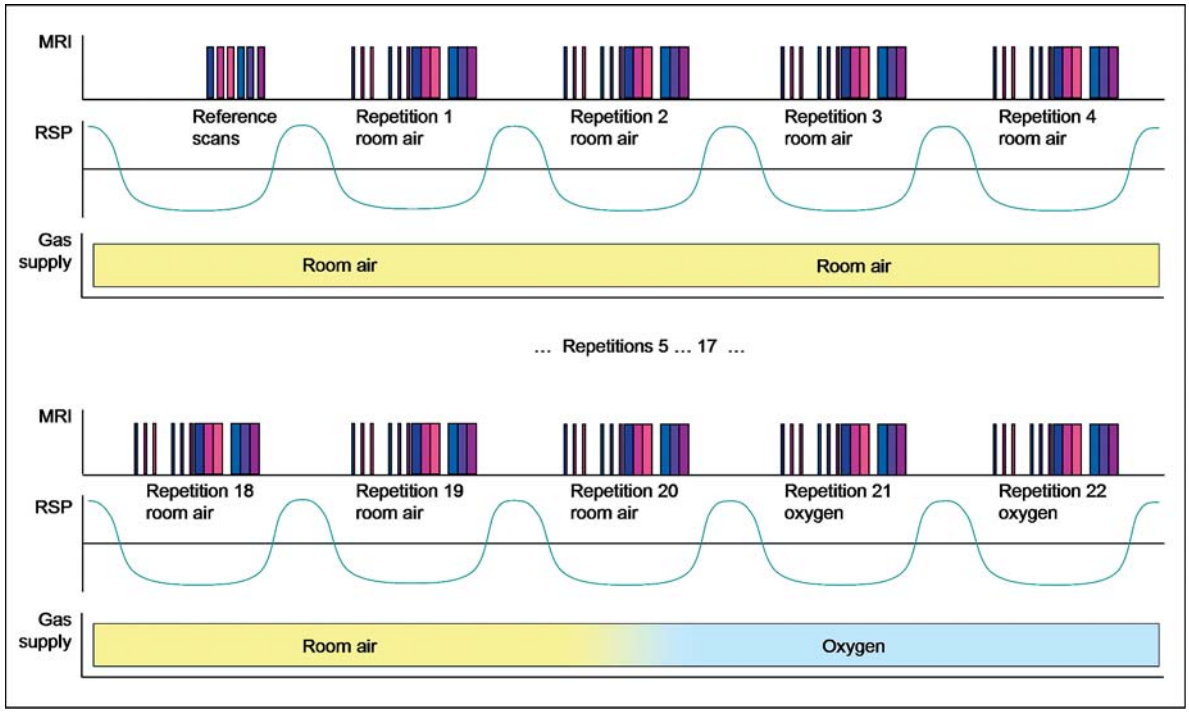

Fig. 38.4. Overview of oxygen-enhanced lung MRI examination with parallel imaging. Auto-calibration signals (*reference scan*) are acquired at the beginning of the sequence in the same respiratory (RSP) phase (end-expiration) as the following image acquisitions. The gas supply is switched after 20 repetitions from room air to oxygen. The examination consists of a total of 80 repetitions (4 blocks of 20 repetitions, blocks 1 and 3: room air; block 2 and 4: oxygen).

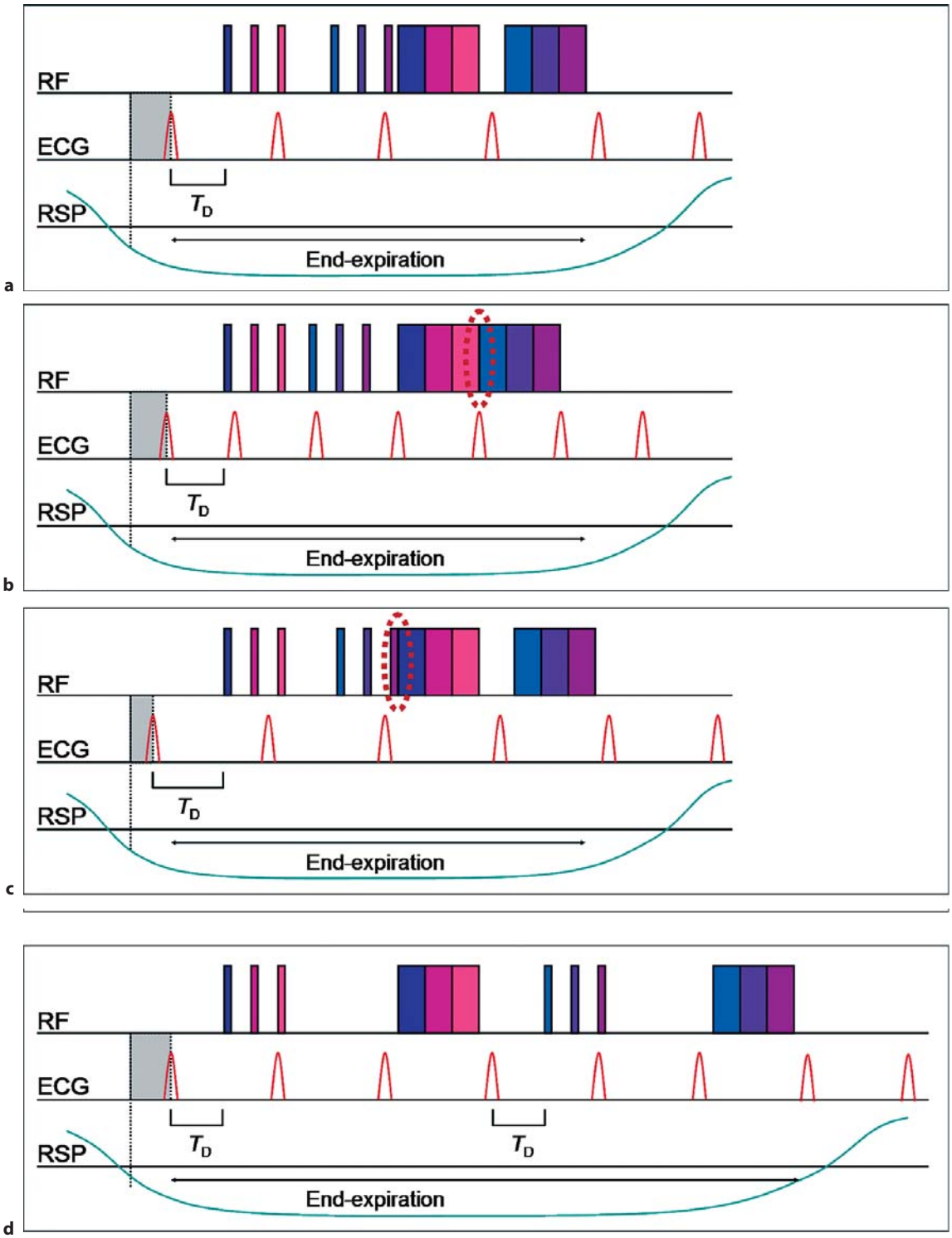

Fig. 38.5. **a** Ideal respiratory- and ECG-triggered acquisition of six slices. **b** If the duration of the RR interval is decreased by a certain amount, the HASTE readouts would overlap, which is technically impossible. **c** If the duration of the RR interval is increased by a certain amount, the first HASTE readout would overlap with the last inversion pulse, which is also impossible. **d** To avoid the timing problems shown in **b** and **c,** an alternative multi-slice acquisition scheme is chosen depending on the current heart rate. A disadvantage of this alternative scheme is the considerably prolonged acquisition (i.e., required end-expiration) time.

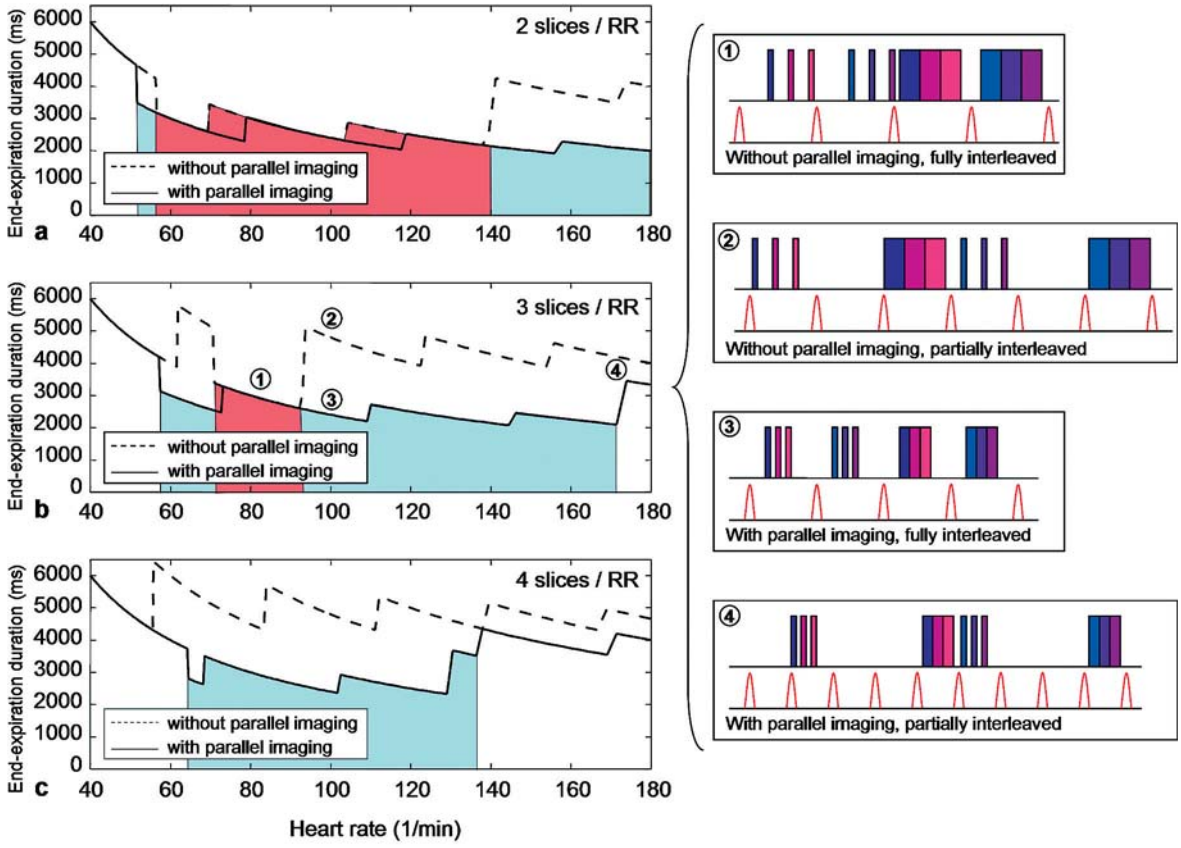

Fig. 38.6a–c. Simulation of duration of data acquisition (i.e., required duration of end-expiration) with (*solid line*) and without (*dashed line*) parallel imaging depending on the heart rate: **a** acquisition of four slices, **b** acquisition of six slices, **c** acquisition of eight slices. The duration of data acquisition is substantially reduced when using parallel imaging. The *colored area* indicates heart rates that allow the fully interleaved acquisition without (*red*) and with parallel imaging (*blue*). The diagrams on the right hand side elucidate fully (*1*, *3*) and partially (*2*, *4*) interleaved acquisitions with (*3*, *4*) and without (*1*, *2*) parallel imaging in the case of six acquired slices **b**.

of 19 ms without and of 11 ms with parallel imaging. Up to six coronal slices were acquired with a field of view of 400×400 mm^2, a 128×128 matrix, a slice thickness of 8 mm, and a gap between the slices of 16 mm. The thickness of the slice-selective inversion pulses was set to 16 mm, i.e., to twice the thickness of the imaging slice to reduce perfusion effects and signal alterations due to the inflow of non-inverted spins. The image acquisition was repeated 80 times in total, divided into 4 blocks with 20 repetitions each. The subjects were administered room air in the first and third block, and oxygen in the second and fourth block.

The sequence was used to compare images with and without parallel imaging. Without parallel imaging, only four coronal slices were acquired to facilitate a robust triggering. With parallel imaging, acquisitions with either four or six coronal slices were performed. The GRAPPA algorithm (Griswold et al. 2002) was used for parallel-imaging reconstruction and the 24 central k-space lines were used for auto-calibration. The T1-weighted images in Fig. 38.7 demonstrate the reduced blurring with parallel imaging. No degrading loss of signal-to-noise ratio is visible in the T1-weighted images acquired with parallel imaging in comparison to the non-accelerated acquisitions.

Maps of the relative signal difference due to inhalation of oxygen acquired in healthy volunteers with and without parallel imaging are shown in Fig. 38.8. Although the signal enhancement appears to be larger with parallel imaging than without in several volunteers, no significant difference was observed comparing all acquisitions with four slices (Dietrich et al. 2005). Examples of oxygen-enhanced lung MRI acquiring six coronal slices are shown in Fig. 38.9. All data sets are based on the acquisition of 80 repetitions and thus

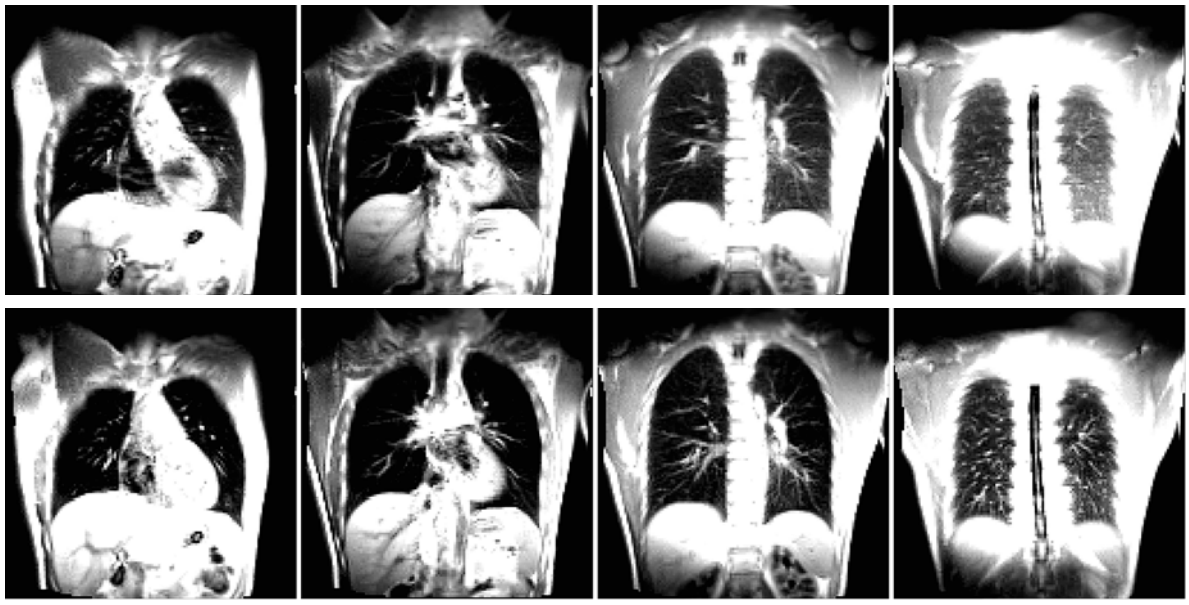

Fig. 38.7a,b. T1-weighted images acquired with a respiratory- and ECG-triggered inversion-recovery HASTE sequence **a** without and **b** with parallel imaging. Note the sharper delineation of pulmonary vessels with parallel imaging.

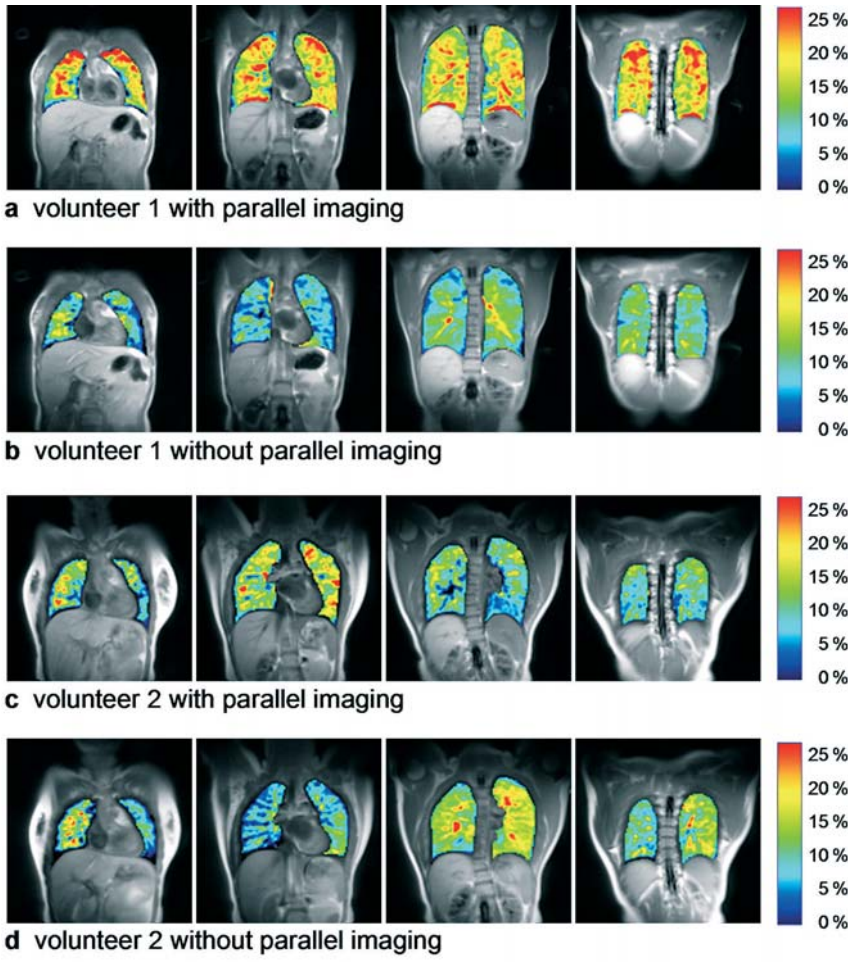

Fig. 38.8a–d. Parameter maps displaying the oxygen-induced relative signal increase in the lung in two healthy volunteers with parallel imaging **a,c** and without **b,d.**

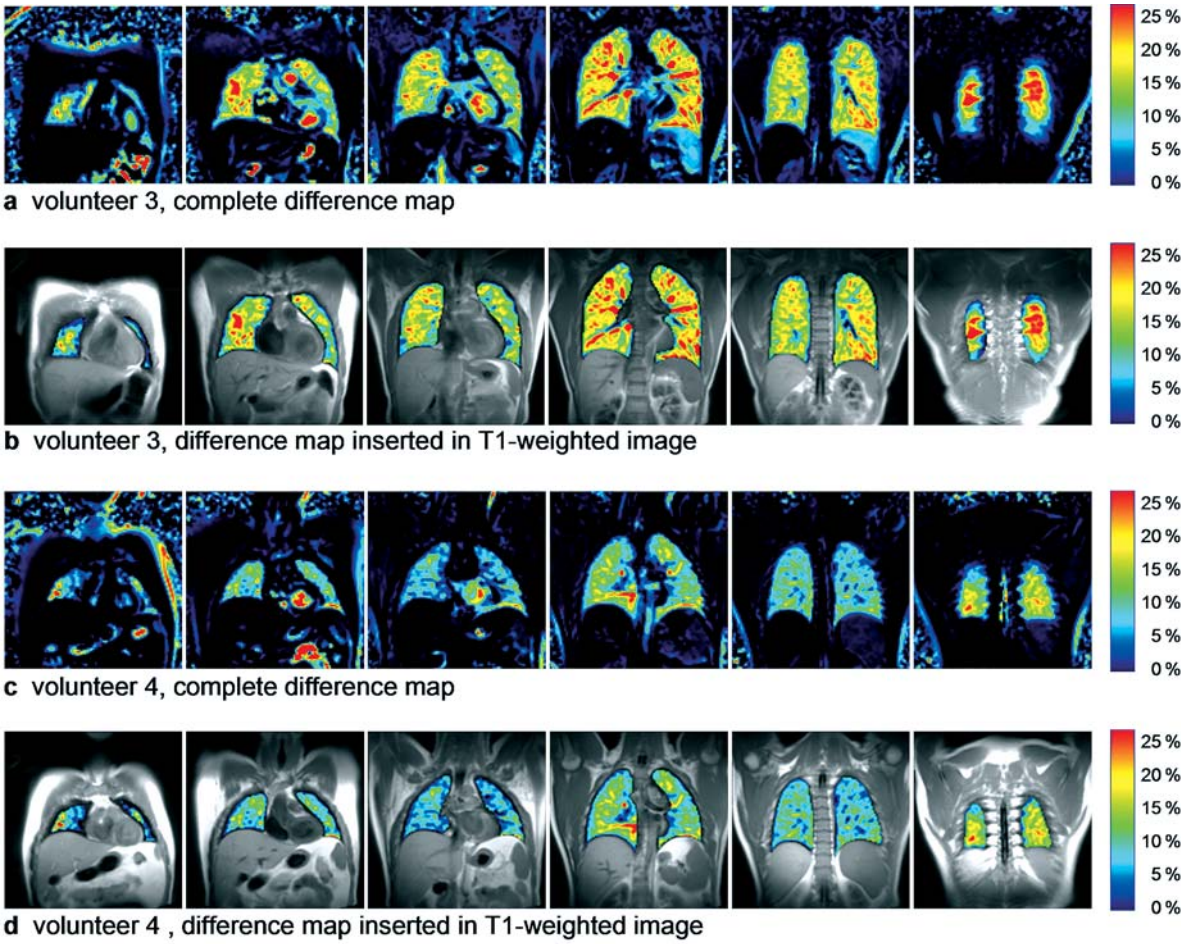

Fig. 38.9a–d. Parameter maps displaying the oxygen-induced relative signal increase in two healthy volunteers acquired with parallel imaging. The complete parameter maps **a,c** demonstrate that oxygen-induced signal enhancement is observed predominantly in the lung, in the large cardiopulmonary vessels, and in the ventricles. The same data are shown inserted in the T1-weighted acquisition **b,d** after manual segmentation of the lungs.

the total time of acquisition was always 80 respiratory cycles (plus 1 additional cycle for the acquisition of reference scans when using parallel imaging). Since the respiration frequency varied inter-individually between about 6/min and 10/min, the total acquisition time varied as well between 8 and 13 min.

38.5 Conclusion

Using slice-selective RF pulses, parallel imaging, and combined respiratory and ECG triggering, oxygen-enhanced lung MRI with the acquisition of six slices and 80 repetitions can be performed in 8 to 13 min depending on the respiratory frequency of the examined subject. Parallel imaging provides the substantial advantage that the actual acquisition time, i.e., the required end-expiration time, becomes significantly shorter. Thus, acquisition of up to six slices is feasible in a free-breathing oxygen-enhanced lung examination. In conclusion, oxygen-enhanced lung imaging becomes sufficiently robust and fast to be included into a clinical routine MRI examination of the lung consisting of other morphologic and functional methods such as pulmonary MR angiography and lung perfusion MRI.

References

Altes TA, Salerno M (2004) Hyperpolarized gas MR imaging of the lung. J Thorac Imaging 19:250–258

Arnold JF, Fidler F, Wang T, Pracht ED, Schmidt M, Jakob PM (2004) Imaging lung function using rapid dynamic acquisition of T1-maps during oxygen enhancement. MAGMA 16:246–253

Berthezene Y, Vexler V, Clement O, Muhler A, Moseley ME, Brasch RC (1992) Contrast-enhanced MR imaging of the lung: assessments of ventilation and perfusion. Radiology 183:667–672

Chen Q, Jakob PM, Griswold MA, Levin DL, Hatabu H, Edelman RR (1998) Oxygen enhanced MR ventilation imaging of the lung. MAGMA 7:153–161

Dietrich O, Losert C, Attenberger U, Fasol U, Peller M, Nikolaou K, Reiser MF, Schoenberg SO (2005) Fast oxygen-enhanced multislice imaging of the lung using parallel acquisition techniques. Magn Reson Med 53:1317–1325

Dietrich O, Losert C, Attenberger U, Reuter C, Fasol U, Peller M, Nikolaou K, Reiser MF, Schoenberg SO (2006) Oxygen-enhanced MRI of the lung: optimized calculation of difference images. Radiologe 46:300-308

Edelman RR, Hatabu H, Tadamura E, Li W, Prasad PV (1996) Noninvasive assessment of regional ventilation in the human lung using oxygen-enhanced magnetic resonance imaging. Nat Med 2:1236–1239

Griswold MA, Jakob PM, Heidemann RM, Nittka M, Jellus V, Wang J, Kiefer B, Haase A (2002) Generalized autocalibrating partially parallel acquisitions (GRAPPA). Magn Reson Med 47:1202–1210

Haage P, Karaagac S, Spuntrup E, Truong HT, Schmidt T, Gunther RW (2005) Feasibility of pulmonary ventilation visualization with aerosolized magnetic resonance contrast media. Invest Radiol 40:85–88

Heidemann RM, Griswold MA, Kiefer B, Nittka M, Wang J, Jellus V, Jakob PM (2003) Resolution enhancement in lung 1H imaging using parallel imaging methods. Magn Reson Med 49:391–394

Ishii M, Fischer MC, Emami K, Alavi A, Spector ZZ, Yu J, Baumgardner JE, Itkin M, Kadlecek SJ, Zhu J, Bono M, Gefter WB, Lipson DA, Shrager JB, Rizi RR (2005) Hyperpolarized helium-3 MR imaging of pulmonary function. Radiol Clin North Am 43:235–246

Jakob PM, Hillenbrand CM, Wang T, Schultz G, Hahn D, Haase A (2001) Rapid quantitative lung 1H T1 mapping. J Magn Reson Imaging 14: 795–799

Jakob PM, Wang T, Schultz G, Hebestreit H, Hebestreit A, Hahn D (2004) Assessment of human pulmonary function using oxygen-enhanced T(1) imaging in patients with cystic fibrosis. Magn Reson Med 51:1009–1016

Loffler R, Muller CJ, Peller M, Penzkofer H, Deimling M, Schwaiblmair M, Scheidler J, Reiser M (2000) Optimization and evaluation of the signal intensity change in multisection oxygen-enhanced MR lung imaging. Magn Reson Med 43:860–866

Losert C, Nikolaou K, Scheidler J, Mueller CJ, Schwaiblmair M, Reiser MF (2002) Optimized respiratory and ECG gating in oxygen-enhanced MR ventilation imaging of the lung. Proc Intl Soc Mag Reson Med 10:1971

Mai VM, Chen Q, Li W, Hatabu H, Edelman RR (2000) Effect of respiratory phases on MR lung signal intensity and lung conspicuity using segmented multiple inversion recovery turbo spin echo (MIR-TSE). Magn Reson Med 43:760–763

Mai VM, Tutton S, Prasad PV, Chen Q, Li W, Chen C, Liu B, Polzin J, Kurucay S, Edelman RR (2003) Computing oxygen-enhanced ventilation maps using correlation analysis. Magn Reson Med 49:591–594

Middleton H, Black RD, Saam B, Cates GD, Cofer GP, Guenther R, Happer W, Hedlund LW, Johnson GA, Juvan K, Swartz J (1995) MR imaging with hyperpolarized 3He gas. Magn Reson Med 33:271–275

Muller CJ, Loffler R, Deimling M, Peller M, Reiser M (2001) MR lung imaging at 0.2 T with T1-weighted true FISP: native and oxygen-enhanced. J Magn Reson Imaging 14:164–168

Muller CJ, Schwaiblmair M, Scheidler J, Deimling M, Weber J, Loffler RB, Reiser MF (2002) Pulmonary diffusing capacity: assessment with oxygen-enhanced lung MR imaging preliminary findings. Radiology 222:499–506

Naish JH, Parker GJ, Beatty PC, Jackson A, Young SS, Waterton JC, Taylor CJ (2005) Improved quantitative dynamic regional oxygen-enhanced pulmonary imaging using image registration. Magn Reson Med 54:464–469

Nakagawa T, Sakuma H, Murashima S, Ishida N, Matsumura K, Takeda K (2001) Pulmonary ventilation-perfusion MR imaging in clinical patients. J Magn Reson Imaging 14:419–424

Ohno Y, Hatabu H, Takenaka D, Adachi S, Van Cauteren M, Sugimura K (2001) Oxygen-enhanced MR ventilation imaging of the lung: preliminary clinical experience in 25 subjects. AJR Am J Roentgenol 177:185–194

Ohno Y, Hatabu H, Takenaka D, Van Cauteren M, Fujii M, Sugimura K (2002) Dynamic oxygen-enhanced MRI reflects diffusing capacity of the lung. Magn Reson Med 47:1139–1144

Ohno Y, Hatabu H, Higashino T, Nogami M, Takenaka D, Watanabe H, Van Cauteren M, Yoshimura M, Satouchi M, Nishimura Y, Sugimura K (2005) Oxygen-enhanced MR imaging: correlation with postsurgical lung function in patients with lung cancer. Radiology 236:704–711

Pracht ED, Arnold JF, Wang T, Jakob PM (2005) Oxygen-enhanced proton imaging of the human lung using T2*. Magn Reson Med 53:1193–1196

Stock KW, Chen Q, Morrin M, Hatabu H, Edelman RR (1999) Oxygen-enhanced magnetic resonance ventilation imaging of the human lung at 0.2 and 1.5 T. J Magn Reson Imaging 9:838–841

Suga K, Ogasawara N, Okada M, Matsunaga N, Arai M (2002) Regional lung functional impairment in acute airway obstruction and pulmonary embolic dog models assessed with gadolinium-based aerosol ventilation and perfusion magnetic resonance imaging. Invest Radiol 37:281–291

van Beek EJ, Wild JM, Kauczor HU, Schreiber W, Mugler JP 3rd, de Lange EE (2004) Functional MRI of the lung using hyperpolarized 3-helium gas. J Magn Reson Imaging 20:540–554

Vaninbroukx J, Bosmans H, Sunaert S, Demedts M, Delcroix M, Marchal G, Verschakelen J (2003) The use of ECG and respiratory triggering to improve the sensitivity of oxygen-enhanced proton MRI of lung ventilation. Eur Radiol 13:1260–1265

Imaging of Renal Perfusion

39

Henrik J. Michaely and Niels Oesingmann

CONTENTS

39.1 Introduction

In the past years, the focus of MR imaging of the kidneys has changed from pure visualization of renal (vessel) morphology and the grading of renal-artery stenosis (RAS) by MR angiography (MRA) (Schoenberg et al. 2003; Shetty et al. 2000; Tan et al. 2002; Prince 1998) to more comprehensive approaches. These include MR flow measurements to evaluate the hemodynamic significance of a RAS (de Haan et al. 2000; de Haan et al. 2003; Schoenberg et al. 2000) and more recently also renal perfusion measurements (Michaely et al. 2006a; Lee et al. 2001; Gandy et al. 2003; Montet et al. 2003; Lee et al. 2003; Karger et al. 2000; Michaely et al. 2004; Michaely et al. 2005a). While the MRA and MR flow measurements can characterize the renal macrovasculature, perfusion is intended to display the renal microvasculature. Hence, perfusion measurements aim at demonstrating the capillary blood flow in the renal parenchyma, and especially in the highly vascularized renal cortex. The literature presents multiple concepts for renal perfusion imaging (Michaely et al. 2006a; Lee et al. 2001; Gandy et al. 2003; Lee et al. 2003; Karger et al. 2000; Michaely et al. 2004; Aumann et al. 2003; Berr et al. 1999; Bjornerud et al. 2002; Ichikawa et al. 1997; Laissy et al. 1994; Prasad et al. 1999; Roberts et al. 1995; Schoenberg et al. 2003; Trillaud et al. 1993; Vallee et al. 2000; Williams et al. 1994; Michaely et al. 2005b). In general, three different methods for MR perfusion imaging of the kidney have been described for renal artery stenosis, namely qualitative assessment of renal perfusion with arterial spin-labeling (ASL) techniques without contrast agents, semi-quantitative perfusion measurements with extracellular gadolinium chelates, and quantitative assessment of renal perfusion with intravascular contrast agents with absolute parameters of regional renal perfusion (Michaely et al. 2006a; Aumann et al. 2003; Prasad et al. 1999). Even though they are all subsumed under renal perfusion, they use different techniques and thus have different aims. Contrast-enhanced (CE) first-pass perfusion studies mainly aim at assessing the impact of renal artery stenosis or renal parenchymal disease on the parenchymal perfusion or aim at assessing the patency of a renal artery stent (Gandy et al. 2003; Michaely et al. 2005a; Vallee et al. 2000).

An approach completely different from the CE techniques is arterial spin labeling where blood is used as endogenous contrast agent (Karger et al. 2000; Michaely et al. 2004; De Bazelaire et al. 2005; Gunther et al. 2001; Martirosian et al. 2004). Depending on the specific technique used, ASL techniques may be able to yield only perfusion-weighted images (Michaely et al. 2004) or to exactly calculate the renal perfusion (Martirosian et al. 2004).

The clinical relevance of perfusion measurements is underlined by publications showing that reduced renal perfusion is associated with increased rates of morbidity and mortality in different settings (Fan et

H. J. Michaely, MD
Department of Clinical Radiology, University Hospitals – Grosshadern, Ludwig Maximilian University of Munich, Marchioninistr. 15, 81377 Munich, Germany
N. Oesingmann, PhD
Siemens Medical Solutions USA, Inc., MR R&D Collaboration, NYU CBI, 660 First Avenue, New York, NY 10016, USA

al. 1990; Hillege et al. 2000). Interestingly, decreased first-pass perfusion parameters were also found in hypertensive rats without renal artery stenosis and were found to improve under therapy (Lenhard et al. 2003). This may indicate that first-pass perfusion could also be applied to the detection and monitoring of chronic renal failure in the future.

39.2 Arterial Spin-Labeling Perfusion Measurements

ASL techniques are attractive in that they are non-invasive and do not require the administration of contrast agents (Michaely et al. 2004). In addition, many ASL sequences can be acquired within a single breath-hold. Different techniques have been proposed so far in the literature, however mainly animal studies or volunteer studies have been performed (Karger et al. 2000; Roberts et al. 1995; Williams et al. 1994; Wang et al. 1998). The basic idea of ASL is to acquire two images that are post-processed to obtain a perfusion-weighted image without the use of contrast agents. In one image, in-flowing blood is labeled with an RF pulse, while a control image without blood labeling is acquired for subtraction to suppress signal from stationary tissue.

A commonly used technique is the so-called flow-sensitive alternating inversion-recovery method (FAIR) (Michaely et al. 2004). In this technique, first a non-selective global inversion is applied for the labeling image, whereas the control image is acquired with selective inversion only. The stationary tissue is inverted in both images and thus disappears with the subtraction. This completely symmetric inversion scheme has the advantage of reducing magnetization transfer effects. However, no image information is sampled during the delay time, so that FAIR measurements are relatively inefficient and time-consuming.

To overcome this problem a Look-Locker acquisition has been proposed (Gunther et al. 2001) that samples a series of images after each labeling pulse instead of just one image. This technique also overcomes the limitation of many ASL sequences to generate only a single perfusion-weighted slice without the temporal perfusion information and thereby possibly offers quantification of perfusion. Other approaches for ASL perfusion include STAR and EPISTAR techniques (Prasad et al. 1997) with an EPI readout module being implemented into the latter. However, one disadvantage of STAR is the induction of magnetization-transfer contrast (MTC) caused by the specific labeling technique used. Recently, a steady-state free precession TrueFISP-readout for ASL sequences has been presented to increase the signal-to-noise ratio (SNR) and to decrease the susceptibility for artefacts (Martirosian et al. 2004), which allowed absolute quantification of the perfusion.

One major disadvantage of using arterial spin labeling techniques for renal perfusion imaging is the poor signal-to-noise ratio of this approach at 1.5 T. This makes the calculation of semi-quantitative or quantitative parameters of renal perfusion difficult and unreliable, although some authors have presented absolute values of renal perfusion with modified ASL techniques and acceptable reproducibility (Karger et al. 2000). Newer approaches used a FAIR-TrueFISP readout (Martirosian et al. 2004) to yield a higher SNR than with the conventionally used FAIR-HASTE (Michaely et al. 2004) or FAIR-EPI (Gunther et al. 2001) readouts. Also, the transition to higher field strength will surely be beneficial for ASL measurements, as with the longer T1 relaxation times at higher field strength the magnetic labeling will decay more slowly (Michaely et al. 2004; Thulborn 1999). Another major drawback associated with the low inherent SNR of ASL measurements is the sensitivity to susceptibility artefacts. While the application of parallel imaging would be disadvantageous in terms of SNR, it will be helpful in avoiding or reducing susceptibility artefacts, particularly with EPI readouts. Since sufficient SNR for the application of parallel imaging is only available at higher field strengths, ASL will surely profit from the increasing number of high-field scanners. However, no reports on the combination of parallel imaging and ASL exist so far for abdominal applications. In brain perfusion, the feasibility of ASL with parallel imaging has been proven (Wang et al. 2005).

39.3 First-Pass Perfusion

In contrast to the ASL techniques, CE MR perfusion techniques do not suffer from SNR limitations. A bolus of paramagnetic contrast agent such as Gd-DTPA or Gd-BOPTA is administered at a high flow rate of 3 to 4 ml/s to obtain a well-defined bolus. Different reports

have been published about the ideal amount of contrast agent raging from a 2 ml flat dose (Lee et al. 2001) to 0.1 mmol/kg body weight (Michaely et al. 2006a). The first pass of the contrast-agent bolus is imaged with a high temporal resolution to finally obtain a signal-intensity-versus-time curve. Depending on the approach used, a semi-quantitative or quantitative measurement of the perfusion can be achieved with standard, extracellular contrast agents. The applied sequence techniques are characterized by a high temporal resolution, which is required to sample enough data points of the contrast agent bolus passing through the kidneys. In the literature VIBE (Gandy et al. 2003) sequences, TurboFLASH sequences (Michaely et al. 2006a; Trillaud et al. 1993) and fast gradient-echo (GRE) sequences without magnetization preparation (Vallee et al. 2000) are used to visualize the signal increase with standard contrast agents. With the application of intravascular contrast agents, such as investigational drugs including NC 100150 (Nycomed, Oslo, Norway), T2*-based techniques can be applied (Aumann et al. 2003; Schoenberg et al. 2003; Trillaud et al. 1993). Recently approved strongly protein-binding gadolinium chelates with semi-intravascular properties allow the absolute quantification of renal perfusion with T1-weighted saturation-recovery GRE techniques (Prasad et al. 1999).

Perfusion data require intensive postprocessing to determine either semiquantitative parameters such as the mean transit time and the maximum upslope of the signal-intensity-versus-time curve (Fig. 39.1) (Michaely et al. 2006a; Gandy et al. 2003) or absolute parameters of renal perfusion such as blood flow per minute and 100 g of renal tissue. While semiquantitative approaches are more robust, but somewhat limited in their information, absolute quantification requires correction of the data by the arterial input function. For patients with renal artery stenosis (Fig. 39.2) the semiquantitavtive approach revealed significant differences in the mean transit time and the maximal upslope of the signal-intensity-versus-time curve between patients with high-grade renal artery stenosis (>75% diameter) and healthy patients (Michaely et al. 2006a). In a study by Vallee et al. (2000), a significantly decreased absolute renal blood flow in patients with renal artery stenosis or renal failure of 0.51 ml/min/g compared to 2.54 ml/min/g in healthy kidneys was found. Apart from this approach in which the signal intensity was converted into the concentration of the contrast agent, other approaches with deconvolution algorithms for quantification of renal perfusion (Aumann et al. 2003; Dujardin et al. 2004; Johansson et al. 2003) have been published as well. However, none of these techniques have found widespread acceptance as major technical hurdles for fast and reliable deconvolution techniques have to be overcome in the future.

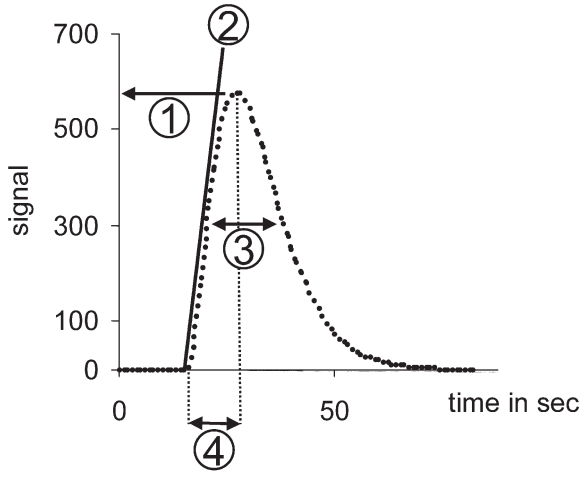

Fig. 39.1. This scheme demonstrates how the perfusion parameters maximal signal intensity (*1*), maximal upslope (*2*), mean transit time (*3*) and the time-to-peak signal intensity are derived based on a Gamma-variate fit from the first pass part of the signal-intensity-versus-time curve. Reprinted with permission from (Michaely et al. 2006b)

Initial results using parallel imaging for semiquantitative assessment of kidneys were presented by Michaely et al. Hereby, the number of slices, which can be measured during the first pass of the contrast agent bolus, could be increased from four to six. The applied TurboFLASH sequence used the GRAPPA algorithm, which led to some increased background noise. However, in an intraindividual comparison study of TurboFLASH without parallel imaging versus TurboFLASH with parallel imaging, the semiquantitative parameters were found to be statistically not different. While at 1.5 T the noise is significantly increased with parallel imaging, imaging at 3.0 T offers sufficient SNR for fast imaging with the application of parallel-imaging techniques. Initial results of perfusion imaging at 3.0 T found superior image quality with a 60% increase in SNR even with the application of parallel-imaging techniques. The semiquantitative perfusion parameters were not statistically significant to 1.5 T again (submitted data). An example for 3.0-T perfusion can be found in Fig. 39.3.

A different methodological approach for the depiction of the renal perfusion is time-resolved MRA tech-

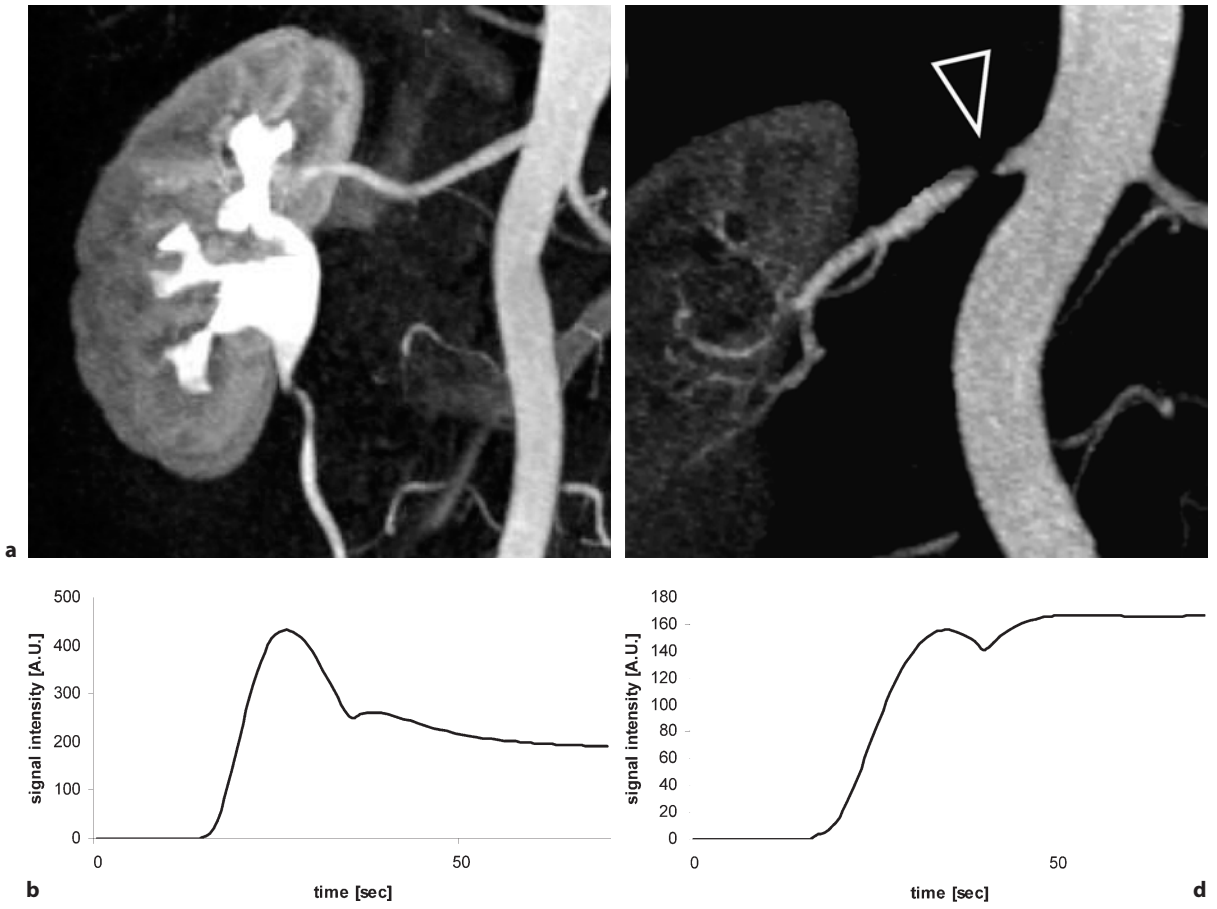

Fig. 39.2. a Thin MIP of an MRA of a patient without renal artery stenosis demonstrating a healthy renal artery. **b** The signal-intensity-versus-time curve of this patient reveals a regular curve with a steep upslope and a marked peak. **c** Thin MIP of a patient with high-grade renal artery stenosis (*arrow*) at the ostium of the renal artery. **d** The signal-intensity versus time curve of this patient demonstrates a markedly slower upslope of the perfusion curve with a less pointed peak (compare to **b**). Reprinted with permission from (Michaely et al. 2006b)

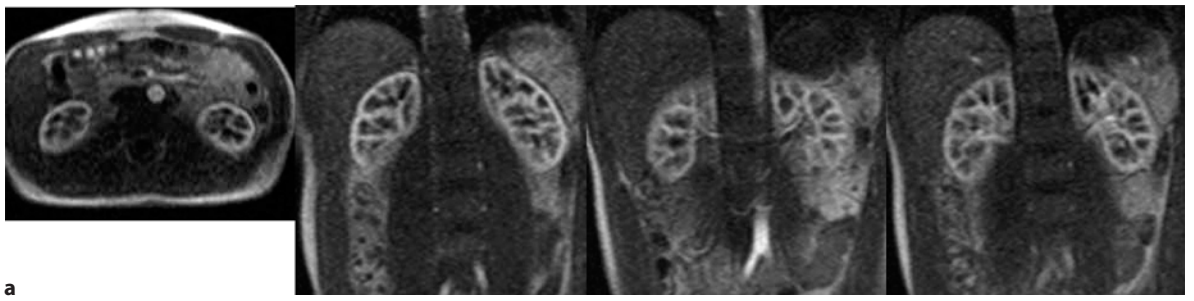

Fig. 39.3. a Exemplary images of a TurboFLASH perfusion measurement in a 29-year-old healthy volunteer. This sequence was acquired without parallel imaging, which allowed acquiring four slices per second. In this early arterial phase, there is marked enhancement in the aorta and the renal cortices. **b** Exemplary images of a TurboFLASH perfusion measurement in the same 29-year-old healthy volunteer as shown in **a**. This sequence was acquired with parallel imaging, which allowed acquiring six slices per second. In this early arterial phase, there is equal enhancement in the aorta and the renal cortices as compared to the images without parallel imaging. Also, the visual assessment does not reveal a lower SNR of the TurboFLASH sequence with parallel imaging. **c** Comparison of the signal-intensity-versus-time curves of the two TurboFLASH sequences of the above volunteer. The curves reveal that using parallel ▷▷

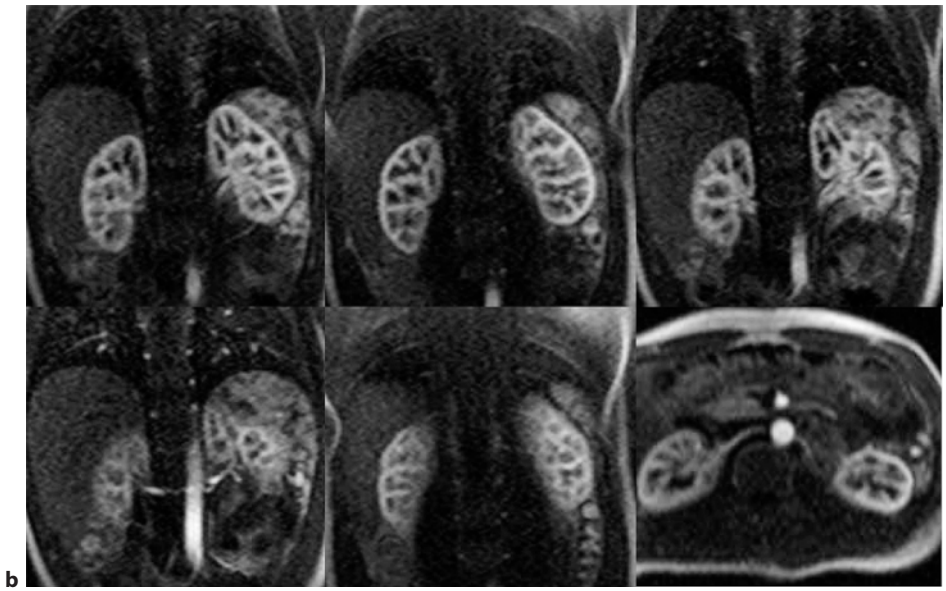

b

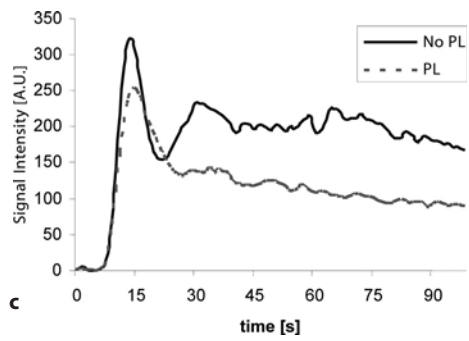

c

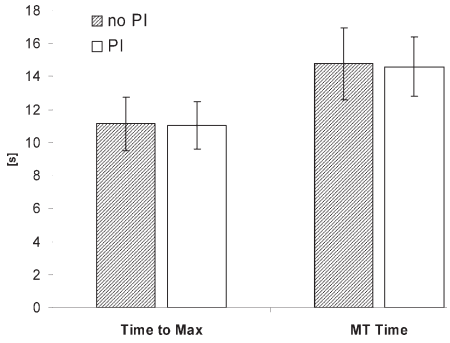

d

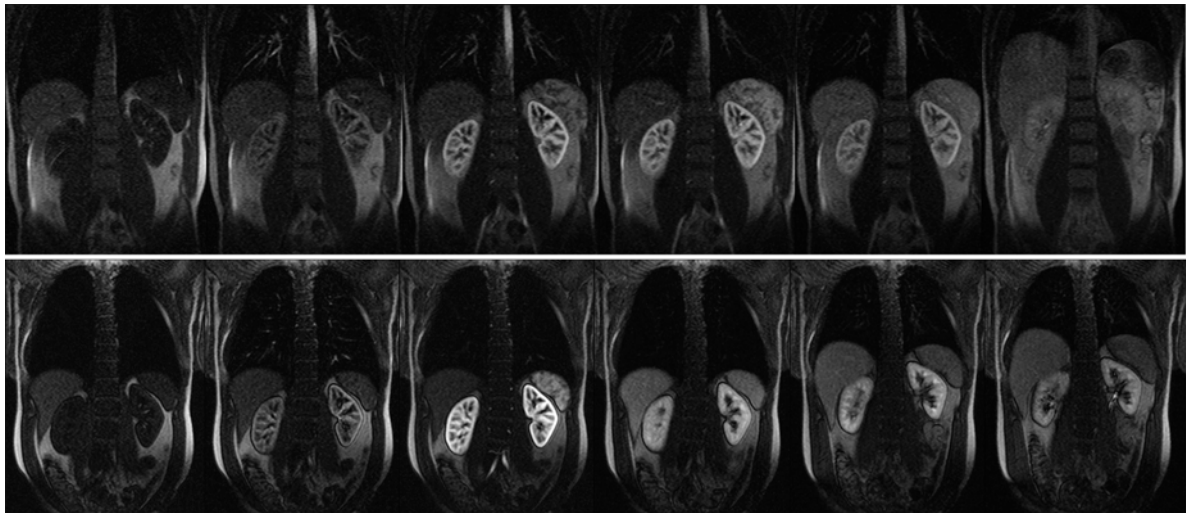

e

imaging (PI) the maximal signal intensity is lowered compared to the non-parallel-imaging sequence. **d** This *box plot* compares the mean transit time and the time to peak measurements of 15 healthy volunteers who underwent renal TurboFLASH perfusion measurements with and without parallel imaging (PI). There is no significant difference between the two different techniques to be seen. **e** Intra-individual comparison of TurboFLASH perfusion measurements at 1.5 T (*upper row*) and 3.0 T (*lower row*). In this volunteer, no parallel imaging was used at 1.5 T; GRAPPA with an acceleration factor of R=2 was used at 3.0 T to increase the number of simultaneously acquired slices. This example demonstrates the significantly increased SNR at 3.0 T. While the first pass can be well visualized at both field strengths, in later phases of the perfusion measurements the demarcation of the kidneys is much better at 3.0 T

niques with high temporal resolution (<2 s/3D frame). The time-resolved echo-shared angiographic technique (TREAT) (Fink et al. 2005),which is based on the TRICKS (Korosec et al. 1996) technique, combines the view-sharing elements with parallel imaging to finally yield a temporal resolution of 1-2 s per entire 3D frame; cf. Chaps. 7 and 11. This temporal resolution is fast enough to follow the arrival of the contrast agent in the kidney, and hence to obtain accurate signal-intensity-versus-time curves from which perfusion parameters can be calculated (Fig. 39.4). In initial reports where this technique was compared to a conventional TurboFLASH sequence, equal values could be obtained for the assessment of perfusion with both techniques (Michaely et al. 2005a). TREAT offers the additional advantage of exact vessel depiction, and the TREAT data can be reformatted in any desired way due to the three-dimensional character of the sequence. However, this property of TREAT also implies that vast amounts of data are acquired, which hinders temporally extended measurements of renal perfusion and filtration.

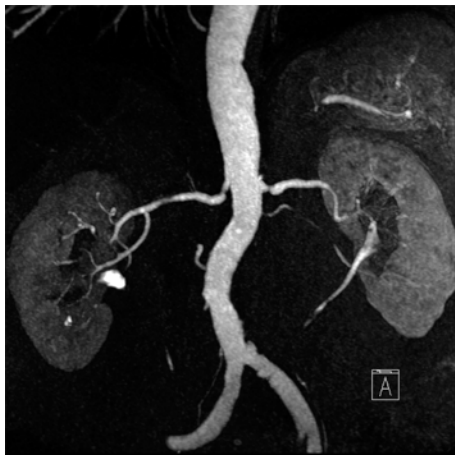

a

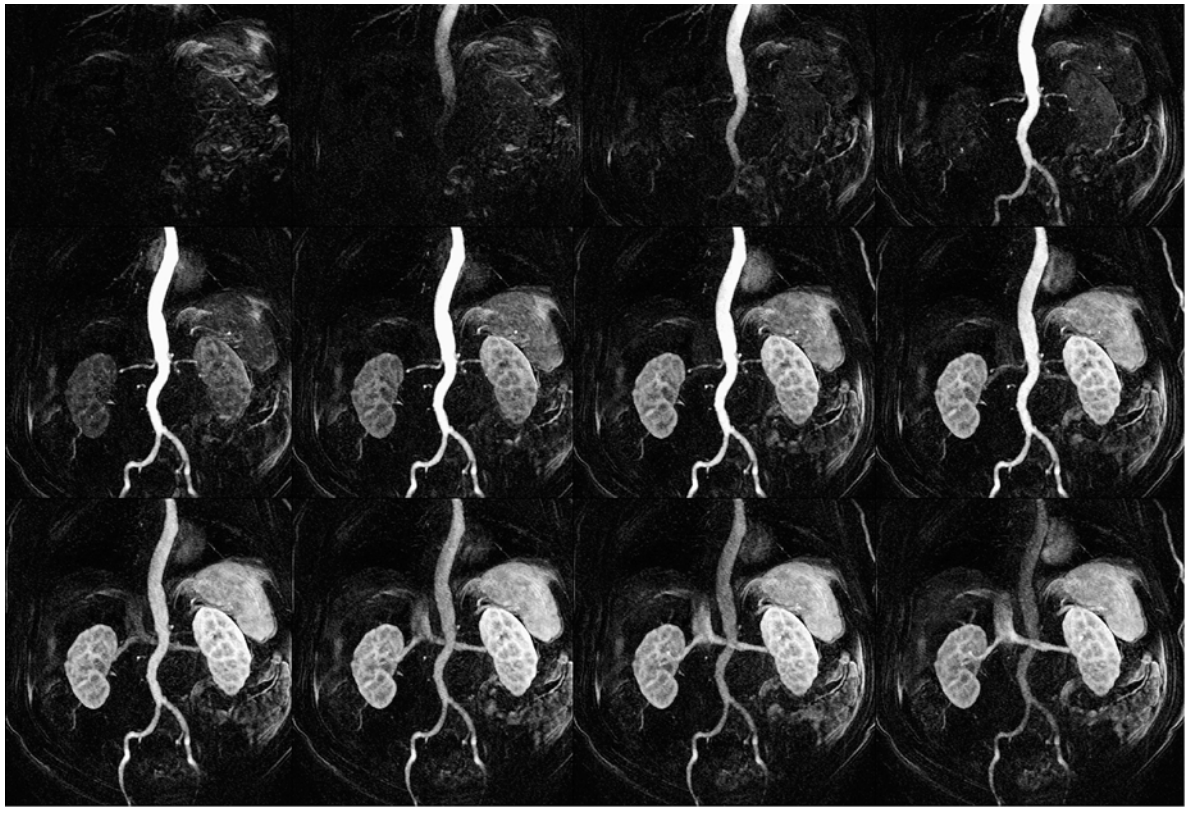

b

Fig. 39.4. a High-spatial-resolution MRA of a patient with bilateral intermediate-grade renal artery stenosis at 3.0 T (0.9×0.6×1.4 mm³; GRAPPA; *R*=2; 22 s acquisition time). **b** TREAT perfusion study of the same patient at 3.0 T (1.5×1.5×3.0 mm³; GRAPPA; *R*=3, 1.4 s/3D frame) reveals bilateral symmetric perfusion of both renal cortices. These time-resolved angiographic data can also be used to determine the renal perfusion parameters, which were only slightly elevated in this patient

Table 39.1. Imaging parameters for perfusion imaging (exemplary for Siemens Magnetom Avanto 1.5-T scanner)

	SR-TurboFLASH (Michaely et al. 2005b)	VIBE (Lee at al. 2003)	TREAT (Michaly et al. 2005a)
Echo time (ms)	1.04	0.8	1.07
Repetition time (ms)	254	2.2	2.21
Flip angle	12°	9°	20°
Bandwidth (Hz/pixel)	980	720	1,300
Field of view (mm^2)	400×350	380×380	370×270
Matrix size	192×154	134×256	320×224
Temporal resolution	4 slices/1 s	1 3D slab/3 s	1 3D slab/1.4 s
Voxel (mm^3)	2.3×2.1×8	2.8×1.5×4	1.7×1.2×5
Parallel imaging	Possible: → 6 slices/1 s	Possible: → improved temp. resolution	GRAPPA, factor 2

References

Aumann S, Schoenberg SO, Just A, Briley-Saebo K, Bjornerud A, Bock M, Brix G (2003) Quantification of renal perfusion using an intravascular contrast agent (part 1): Results in a canine model. Magn Reson Med 49: 276–287

Berr SS, Hagspiel KD, Mai VM, Keilholz-George S, Knight-Scott J, Christopher JM, Spinosa DJ, Angle JF, Matsumoto AH (1999) Perfusion of the kidney using extraslice spin tagging (EST) magnetic resonance imaging. J Magn Reson Imaging 10: 886–891

Bjornerud A, Johansson LO, Ahlstrom HK (2002) Renal T(*)(2) perfusion using an iron oxide nanoparticle contrast agent--influence of T(1) relaxation on the first-pass response. Magn Reson Med 47: 298–304

De Bazelaire C, Rofsky NM, Duhamel G, Michaelson MD, George D, Alsop DC (2005) Arterial spin labeling blood flow magnetic resonance imaging for the characterization of metastatic renal cell carcinoma (1). Acad Radiol 12: 347–357

de Haan MW, Kouwenhoven M, Kessels AG, van Engelshoven JM (2000) Renal artery blood flow: quantification with breath-hold or respiratory triggered phase-contrast MR imaging. Eur Radiol 10: 1133–1137

de Haan MW, van Engelshoven JM, Houben AJ, Kaandorp DW, Kessels AG, Kroon AA, de Leeuw PW (2003) Phase-contrast magnetic resonance flow quantification in renal arteries: comparison with 133Xenon washout measurements. Hypertension 41: 114–118

Dujardin M, Sourbron S, van Schuerbeek P, Luypaert R, Osteaux M (2004) Deconvolution-based MR imaging of renal perfusion and function using dynamic T1 contrast: a feasibility study. Proceedings of the International Society for Magnetic Resonance in Medicine

Fann JI, Sarris GE, Mitchell RS, Shumway NE, Stinson EB, Oyer PE, Miller DC (1990) Treatment of patients with aortic dissection presenting with peripheral vascular complications. Ann Surg 212: 705–713

Fink C, Ley S, Kroeker R, Requardt M, Kauczor HU, Bock M (2005) Time-resolved contrast-enhanced three-dimensional magnetic resonance angiography of the chest: combination of parallel imaging With view sharing (TREAT). Invest Radiol 40: 40–48

Gandy SJ, Sudarshan TA, Sheppard DG, Allan LC, McLeay TB, Houston JG (2003) Dynamic MRI contrast enhancement of renal cortex: a functional assessment of renovascular disease in patients with renal artery stenosis. J Magn Reson Imaging 18: 461–466

Gunther M, Bock M, Schad LR (2001) Arterial spin labeling in combination with a look-locker sampling strategy: Inflow turbo-sampling EPI-FAIR (ITS-FAIR). Magn Reson Med 46: 974–984

Hillege HL, Girbes AR, de Kam PJ, Boomsma F, de Zeeuw D, Charlesworth A, Hampton JR, van Veldhuisen DJ (2000) Renal function, neurohormonal activation, and survival in patients with chronic heart failure. Circulation 102: 203–210

Ichikawa T, Haradome H, Hachiya J, Nitatori T, Araki T (1997) Perfusion-weighted MR imaging in the upper abdomen: preliminary clinical experience in 61 patients. AJR Am J Roentgenol 169: 1061–1066

Johansson LO, Schoenberg SO, Ahlstrom H, Bjornerud A (2003) Comparision of different deconvolution techniques for quantification of renal blood flow using an intravascular contrast agent. Proceedings of the International Society for Magnetic Resonance in Medicine

Karger N, Biederer J, Lusse S, Grimm J, Steffens J, Heller M, Gluer C (2000) Quantitation of renal perfusion using arterial spin labeling with FAIR-UFLARE. Magn Reson Imaging 18: 641–647

Korosec FR, Frayne R, Grist TM, Mistretta CA (1996) Time-resolved contrast-enhanced 3D MR angiography. Magn Reson Med 36: 345–351

Laissy JP, Faraggi M, Lebtahi R, Soyer P, Brillet G, Mery JP, Menu Y, Le Guludec D (1994) Functional evaluation of normal and ischemic kidney by means of gadolinium-DOTA enhanced TurboFLASH MR imaging: a preliminary comparison with 99Tc-MAG3 dynamic scintigraphy. Magn Reson Imaging 12: 413–419

Lee VS, Rusinek H, Johnson G, Rofsky NM, Krinsky GA, Weinreb JC (2001) MR renography with low-dose gadopentetate dimeglumine: feasibility. Radiology 221: 371–379

Lee VS, Rusinek H, Noz ME, Lee P, Raghavan M, Kramer EL (2003) Dynamic three-dimensional MR renography for the measurement of single kidney function: initial experience. Radiology 227: 289–294

Lenhard SC, Nerurkar SS, Schaeffer TR, Mirabile RC, Boyce RW, Adams DF, Jucker BM, Willette RN (2003) p38 MAPK inhibitors ameliorate target organ damage in hypertension. Part 2: Improved renal function as assessed by dynamic contrast-enhanced magnetic resonance imaging. J Pharmacol Exp Ther 307: 939-946

Martirosian P, Klose U, Mader I, Schick F (2004) FAIR true-FISP perfusion imaging of the kidneys. Magn Reson Med 51: 353–361

Michaely HJ, Herrmann KA, Kramer H, Dietrich O, Laub G, Reiser MF, Schoenberg SO (2006) High-Resolution Renal MRA: Comparison of Image Quality and Vessel Depiction with Different Parallel Imaging Acceleration Factors. J Magn Reson Imaging (1): 95–100

Michaely HJ, Schoenberg SO, Ittrich C, Dikow R, Bock M, Guenther M (2004) Renal disease: value of functional magnetic resonance imaging with flow and perfusion measurements. Invest Radiol 39: 698–705

Michaely HJ, Schoenberg SO, Oesingmann N, Ittrich C, Friedrich D, Buhlig C, Struwe A, Rieger J, Reininger C, Samtleben W, Weiss M, Reiser MF (2006a) Functional assessment of renal artery stenosis using dynamic MR perfusion measurements - feasibility study. Radiology 238: 586–596

Montet X, Ivancevic MK, Belenger J, Jorge-Costa M, Pochon S, Pechere A, Terrier F, Vallee JP (2003) Noninvasive measurement of absolute renal perfusion by contrast medium-enhanced magnetic resonance imaging. Invest Radiol 38: 584–592

Prasad PV, Cannillo J, Chavez DR, Pinchasin ES, Dolan RP, Walovitch R, Edelman RR (1999) First-pass renal perfusion imaging using MS-325, an albumin-targeted MRI contrast agent. Invest Radiol 34: 566–571

Prasad PV, Kim D, Kaiser AM, Chavez D, Gladstone S, Li W, Buxton RB, Edelman RR (1997) Noninvasive comprehensive characterization of renal artery stenosis by combination of STAR angiography and EPISTAR perfusion imaging. Magn Reson Med 38: 776–787

Prince MR (1998) Renal MR angiography: a comprehensive approach. J Magn Reson Imaging 8: 511–516

Roberts DA, Detre JA, Bolinger L, Insko EK, Lenkinski RE, Pentecost MJ, Leigh JS, Jr. (1995) Renal perfusion in humans: MR imaging with spin tagging of arterial water. Radiology 196: 281–286

Schoenberg SO, Aumann S, Just A, Bock M, Knopp MV, Johansson LO, Ahlstrom H (2003) Quantification of renal perfusion abnormalities using an intravascular contrast agent (part 2): Results in animals and humans with renal artery stenosis. Magn Reson Med 49: 288–298

Schoenberg SO, Bock M, Kallinowski F, Just A (2000) Correlation of hemodynamic impact and morphologic degree of renal artery stenosis in a canine model. J Am Soc Nephrol 11: 2190–2198

Schoenberg SO, Rieger J, Nittka M, Dietrich O, Johannson LO, Reiser MF (2003) Renal MR angiography: current debates and developments in imaging of renal artery stenosis. Semin Ultrasound CT MR 24: 255–267

Shetty AN, Bis KG, Kirsch M, Weintraub J, Laub G (2000) Contrast-enhanced breath-hold three-dimensional magnetic resonance angiography in the evaluation of renal arteries: optimization of technique and pitfalls. J Magn Reson Imaging 12: 912–923

Tan KT, van Beek EJ, Brown PW, van Delden OM, Tijssen J, Ramsay LE (2002) Magnetic resonance angiography for the diagnosis of renal artery stenosis: a meta-analysis. Clin Radiol 57: 617–624

Thulborn KR (1999) Clinical rationale for very-high-field (3.0 Tesla) functional magnetic resonance imaging. Top Magn Reson Imaging 10: 37–50

Trillaud H, Grenier N, Degreze P, Louail C, Chambon C, Franconi JM (1993) First-pass evaluation of renal perfusion with TurboFLASH MR imaging and superparamagnetic iron oxide particles. J Magn Reson Imaging 3: 83–91

Vallee JP, Lazeyras F, Khan HG, Terrier F (2000) Absolute renal blood flow quantification by dynamic MRI and Gd-DTPA. Eur Radiol 10: 1245–1252

Wang JJ, Hendrich KS, Jackson EK, Ildstad ST, Williams DS, Ho C (1998) Perfusion quantitation in transplanted rat kidney by MRI with arterial spin labeling. Kidney Int 53: 1783–1791

Wang Z, Wang J, Connick TJ, Wetmore GS, Detre JA (2005) Continuous ASL (CASL) perfusion MRI with an array coil and parallel imaging at 3T. Magn Reson Med 54: 732–737

Williams DS, Zhang W, Koretsky AP, Adler S (1994) Perfusion imaging of the rat kidney with MR. Radiology 190: 813–818

Part VII:
Comprehensive Protocols

Cardiovascular Screening

40

Harald Kramer

CONTENTS

40.1 Introduction

In most industrialized countries cardiovascular disease still ranks number one in morbidity and mortality statistics. Until now, Doppler ultrasonography for the greater arterial vessels as well as ECG and ECG stress testing and blood parameters have been the only non-invasive modalities to evaluate these diseases. At the time these diseases get symptomatic, mostly an invasive treatment, such as dilatation and stenting of vessel segments, or even, surgery is necessary; therefore, an exam for early detection of initial, asymptomatic changes seems reasonable (Goyen et al. 2002, 2003; Henschke and Yankelevitz 2000). In the past few years many trials were started to use magnetic resonance imaging (MRI) as a screening modality in this field of disease, but the standards for this type of exam were too low to fulfil the requirements of a fully diagnostic multi-organ evaluation. Spatial and temporal resolution of MRI was too low and the examination time was too long to establish MRI as a new screening modality.

Recent technical developments in hardware and software, as well as the introduction of parallel imaging, have changed this situation (Kramer et al. 2004). Magnetic resonance imaging has become the new standard of reference for the evaluation of global cardiac function and perfusion, and magnetic resonance angiography (MRA) has replaced most of the solely diagnostic digital subtraction angiography exams. Because of the absence of ionizing radiation and nephrotoxic contrast agents (CA), and because of the increased spatial and temporal resolution, MRI now fulfils all conditions of a screening exam.

40.2 Protocol Setup with Parallel-Imaging Techniques

A whole-body cardiovascular screening exam should include a complete state-of-the-art heart examination including functional imaging of the left ventricle (Wintersperger et al. 2003), perfusion imaging of the left-ventricular myocardium as well as delayed contrast-enhanced (DCE) imaging for the detection of infarcted myocardium. It also should include MRA of the complete arterial vascular tree from the skull base down to the feet (Ruehm et al. 2001). In this protocol also imaging of lungs (Biederer et al. 2002), abdominal organs and brain including intracranial vessels is possible.

H. Kramer, MD
Department of Clinical Radiology, University Hospitals – Grosshadern, Ludwig Maximilian University of Munich, Marchioninistr. 15, 81377 Munich, Germany

Protocol setup depends on which kind of MR system is used. When using a commonly available state-of-the-art MR system, which means a 1.5-T system with up to 8 receiver channels and table movement up to 150 cm, the complete exam has to be divided into two steps because of repositioning the patient from head first to feet first into the magnet. The first part includes the complete cardiac exam as well as imaging of the lungs and brain and MRA of the supra-aortic vessels. The second part consists of imaging of the abdominal organs and MRA from the diaphragm down to the feet.

When using a dedicated whole-body MR system, which means a 1.5-T system with up to 32 receiver channels and a large range of table movement of up to more than 200 cm, the patient has not to be repositioned (Fig. 40.1). This is only possible due to the implementation of multi-channel MR systems and parallel-imaging techniques. Prior to the first image acquisition, all necessary coils are placed on the patient, which is only possible if enough receiver channels are available. Parallel imaging is used in nearly every step of the exam. This reduces acquisition time while increasing the spatial and/or temporal resolu-

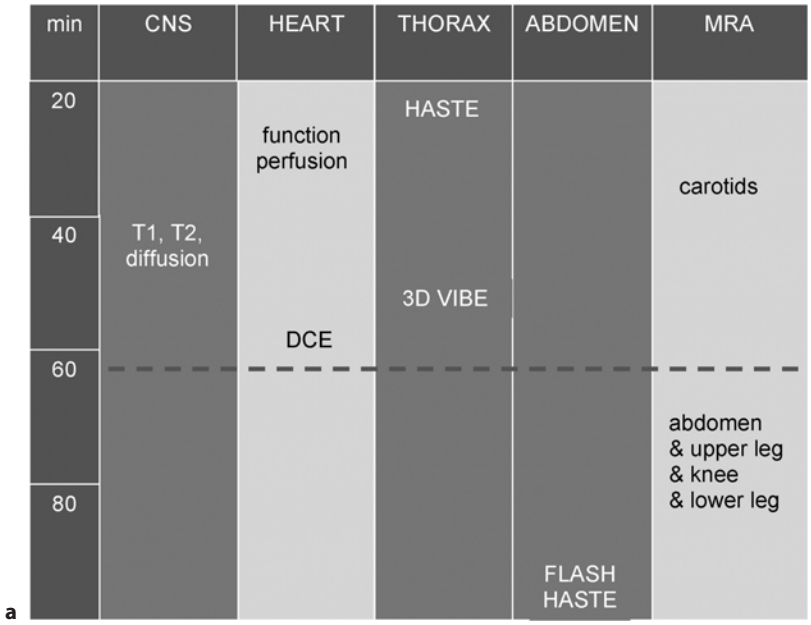

a

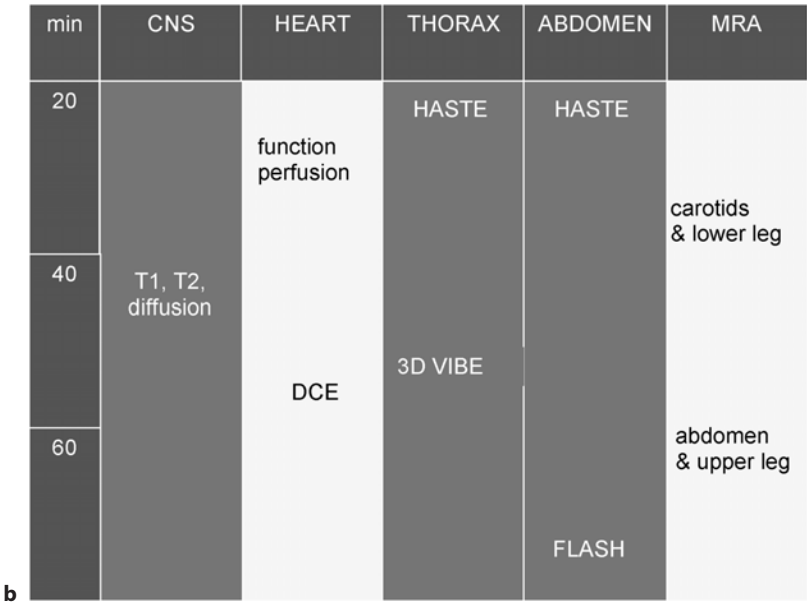

b

Fig. 40.1a,b. Protocol setup for cardiovascular whole-body imaging. **a** Protocol on a standard MR system. *Dotted line* stands for patient repositioning from head first to feet first to the magnet. **b** Protocol on a dedicated whole-body MR system

tion. In particular during the cardiac examination, advantages of parallel acquisition techniques are in the foreground. The thorax has to be covered with multi-element coils to be able to use parallel imaging in anterior–posterior and left–right direction; here, high temporal resolution in combination with short scan times, good signal intensity and spatial resolution are very important. This combination is only possible with parallel imaging, so a complete heart examination with functional and perfusion imaging as well as DCE can be performed within only three breathholds (cf. Chaps. 35 and 36). Spatial resolution of whole-body MRA can be increased to $1\times1\times1$ mm^3 which has been previously only achieved by dedicated MRA exams of a single anatomic area. Quality of lung imaging could be improved due to the increase of signal intensity and decrease of blurring artefacts because of the shorter echo train as described in Chap. 20.

40.2.1 Standard MRI Systems

Standard MRI systems normally have a limited range of table movement. Due to this fact, the patient has to be repositioned during the exam or special table devices have to be used. If the exam is divided into two parts, during the first part the patient is positioned head first into the magnet, and the head coil, two body array coils, and the spine array are used. First axial and coronal images of the lungs before administration of contrast agent (CA) are acquired in a breath-hold technique with a single-shot half-Fourier turbo-spin-echo (HASTE) sequence. This is followed by functional and perfusion imaging of the left ventricular myocardium. After that, MRA of the carotid arteries is performed with a test-bolus technique. Then T1- and T2-weighted images of the brain are acquired, again followed by post-CA imaging of the lungs with a 3D gradient-echo sequence. Thirteen to 17 min after the last CA injection, delayed contrast-enhanced imaging of the left ventricle is performed. In the second part the patient is repositioned feet first into the magnet and MRA of the arterial vascular tree from the diaphragm down to the feet is performed in four steps. At the end of the complete MR exam T1- and T2-weighted images of the abdominal organs are acquired. For this second part of the examination the peripheral-angio array coil, two body-array coils, and again the spine array as well as the large-field-of-view adaptor, are used (Fig. 40.2a). If using special table devices, such as the AngioSURF/BodySURF system (MR-Innovations, Essen Germany), the patient is manually moved between the spine array and a flexible body-array surface coil, which rests on a holder over the examined anatomic area. This holder follows the contours of the patient to minimize the distance between the coil and the patient. Here the patient has not to be repositioned from "head first" to "feet first"; on the other hand, there is less flexibility to use parallel imaging in the left–right direction because of the limitation to just two anterior and two posterior coil elements.

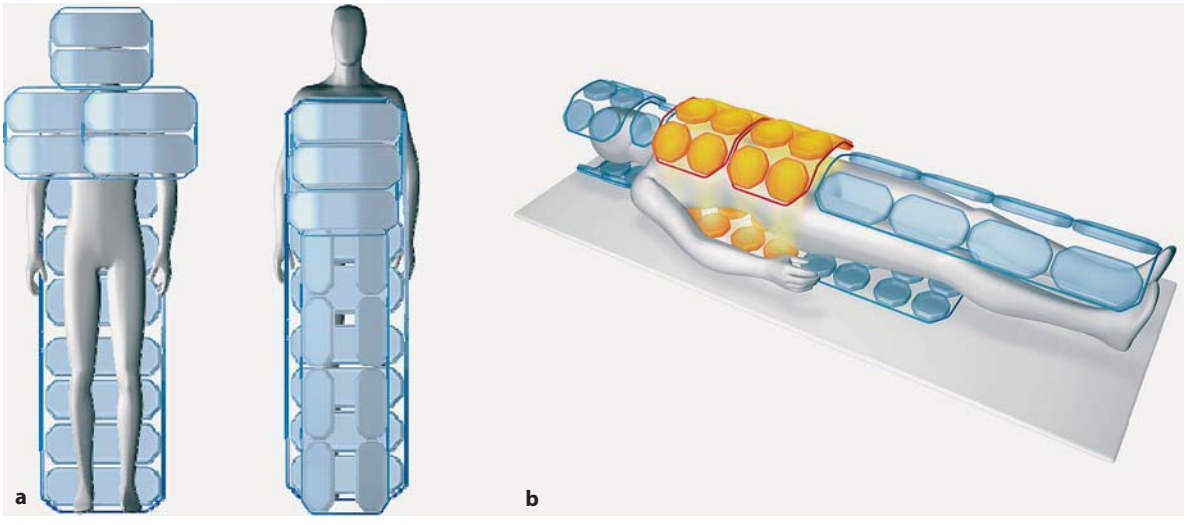

Fig. 40.2a,b. Coil setup for cardiovascular whole-body imaging. **a** Setup on a standard MRI system: *left part* for imaging of the upper body part, *right part* for imaging of the lower body part. **b** Setup on a dedicated whole-body MR system equipped with a matrix-coil system

40.2.2 Whole-Body MRI Systems

When using a dedicated whole-body MR system with a range of table movement of more than 200 cm, the above-described repositioning of the patient during the exam becomes unnecessary. The sequence of the individual exams on these kinds of MRI systems differs from the common MRI systems. On the MRI system described here a special matrix-coil system is available (Fig. 40.2b). Now T1-weighted imaging of the brain and pre-CA HASTE imaging of the thorax and abdomen is performed in the beginning of the exam, followed by a time-of-flight (TOF) angiography of the intracranial vessels. Then functional and perfusion imaging of the heart is performed, followed by a modified MRA protocol. In this protocol, MRA of the supra-aortic vessels is directly followed by MRA of calf and feet with the same CA bolus. This is possible due to the large range of table movement. After the first part of MRA, post-CA, imaging of thorax, abdomen and brain is performed followed by DCE imaging of the left ventricle. The exam is finished by the second part of the MRA protocol, imaging of abdominal aorta and thighs and post-CA imaging of the abdominal organs.

40.3 Design of Screening Studies

In our experience of more than 200 participants in a cardiovascular screening protocol using two different MR systems, cardiovascular whole-body MRI is feasible at high quality and can be implemented to clinical routine. On the other hand, it can be further improved. Due to recent technical developments in hardware and software and the implementation of parallel-imaging techniques cardiovascular MR screening at a high quality and with a high spatial and temporal resolution is possible within a reasonable time. In our institution the first exams were performed on a routinely used 1.5-T 8-channel MRI system (Magnetom Sonata, Siemens, Erlangen, Germany). From participant number 43 onward, all individuals were examined on a 1.5-T 32-channel dedicated whole-body MRI system (Magnetom Avanto, Siemens, Erlangen, Germany). To verify diagnostic accuracy all exams were read by two experienced radiologists and pathological findings as well as functional parameters of the heart were reported. Image quality of the whole-body MRA was judged by two different radiologists blinded to each other in terms of vessel conspicuity, artefacts and venous overlay on a three-point scale. In-room examination time was reported and compared for both MR systems. Reports of the MRI exam were compared with the findings of the conventional exams in the first 60 individuals, and further comparison is still ongoing.

In the literature some other setups for screening studies are described. In one study, whole-body cardiovascular MRI is included in a prospective trial in cooperation with a public health insurance company (Kramer et al. 2005).

40.4 Participants

Presented data show results from individuals participating in a company-based health care program. All of them underwent routine yearly screening for cardiovascular diseases with conventional techniques (e.g. ultrasonography, ECG at rest and stress, echocardiography, etc.). Mean age was 55±8 years, and all participants were referred from their company medical officer. In the above-mentioned other studies participants were referred by their health-insurance company or were self-referring individuals.

40.5 Results

40.5.1 Pathologies

All recently published studies predominantly found manifestations of peripheral vascular disease and ischaemic heart disease, whereas relatively few malignant diseases were found. In the first 180 individuals of our study we detected 19 cardiac pathologies, namely one primary unknown and one known myocardial infarction, 12 cardiac perfusion defects and 5 wall motion abnormalities. The participant with the known infarction suffered from diabetes mellitus and also revealed a perfusion defect and a wall motion abnormality in the infarcted area (Fig. 40.3). Most of these cardiac pathologies were not detected

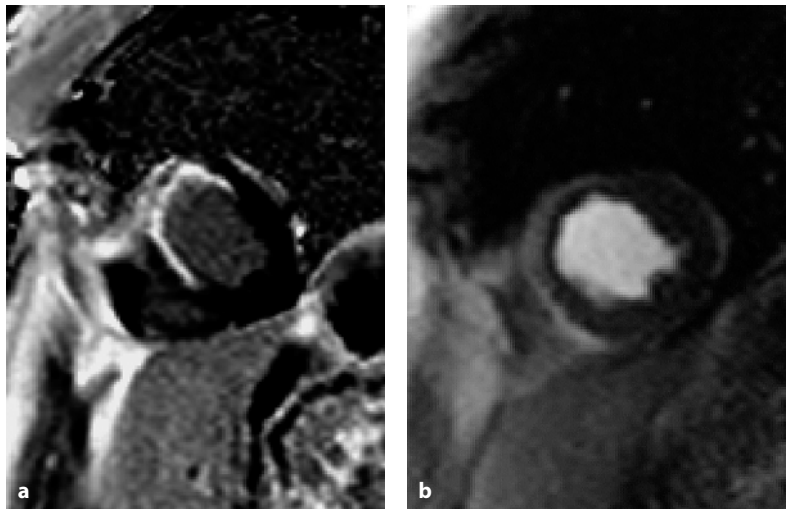

Fig. 40.3. **a** Delayed contrast-enhanced in an infarcted area of the septum and the anterior wall. **b** Corresponding matched perfusion defect

with the conventional modalities such as ECG and echocardiography. The MRA showed 42 pathologies, namely one renal artery stenosis, one jugular glomus tumor, eight ectatic or aneurysmatically dilated aortic segments, 12 pathological changes in the carotid arteries including low- and high-grade stenosis and multiple periphery vessel occlusions (Fig. 40.4). The HASTE imaging of the thorax showed 16 pathological findings, namely four nodules, infiltrates in four and pathological enlarged lymph nodes in 8 patients (Table 40.1). Nodules were not detected in previously existing chest X-rays. The T1- and T2-weighted imaging of the brain showed microangiopathic changes in multiple individuals, and one meningioma was detected. Abdominal imaging showed multiple cysts and haemangiomas in the liver and kidneys; however, one renal cell carcinoma was detected.

Table 40.1. Main pathologies found by whole-body MRI

Cardiac pathologies	19	Others
	WMA	5
	PD	12
	DCE	2
Whole-body MRA	42	
	RAS	1
	JGT	1
	CAST	12
	AE/AA	8
HASTE lung imaging	16	
	Nodules	4

WMA wall-motion abnormality, *PD* perfusion defect, *DCE* delayed contrast enhancement of left-ventricular myocardium, *RAS* renal-artery stenosis, *JGT* jugular glomus tumor, *CAST* carotid artery stenosis, *AE/AA* aortic ectasia/aortic aneurysm

40.5.2 Examination Time

Even though shorter examination times have been reported in the literature, mean room time in our study was 102±23 min on the standard MRI system compared with 80±7 min on the whole-body MRI system (Fig. 40.5). These scan times seem to be very long, but they are needed to realize a high-quality whole-body examination. The MR exams of <60 min for a complete cardiovascular work-up suffer from reduced image quality. The described scan time reduction results from several reasons. A major advantage of a whole-body MRI system is the absence of the need to reposition the patient. But another important point is the possibility to use parallel-acquisition techniques in combination with a matrix-coil system which make the protocol much more flexible. There is no need for makeshift techniques such as the positioning of body-array coils next to each other to implement parallel imaging during the heart examination.

40.5.3 Image Quality: Detection of Pathologies

It is always difficult to judge the quality of an MRI examination. On one hand, one needs good spatial

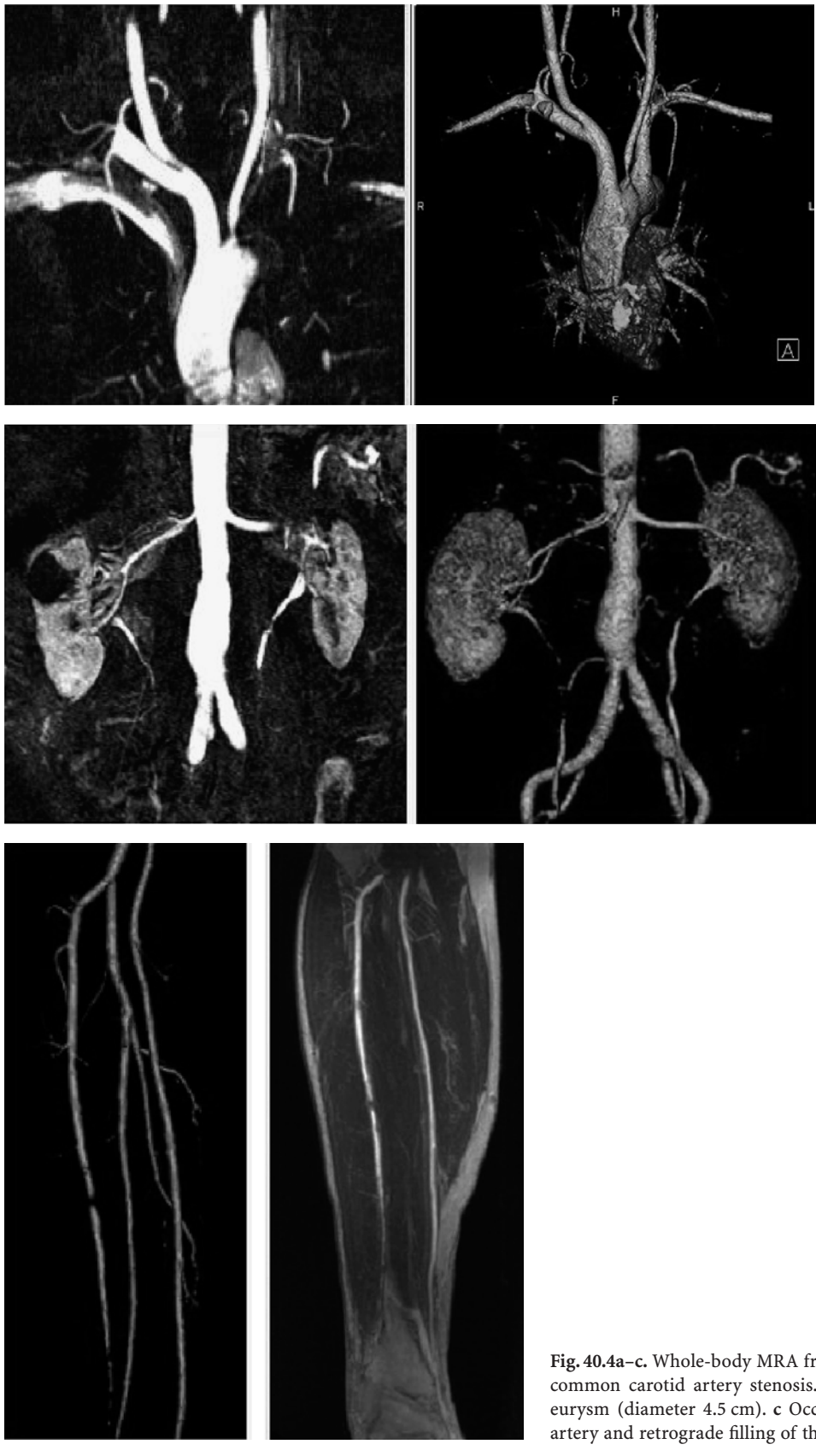

Fig. 40.4a–c. Whole-body MRA from head to toe. **a** A 70% common carotid artery stenosis. **b** Infrarenal aortic aneurysm (diameter 4.5 cm). **c** Occlusion of anterior tibial artery and retrograde filling of the distal tibial artery.

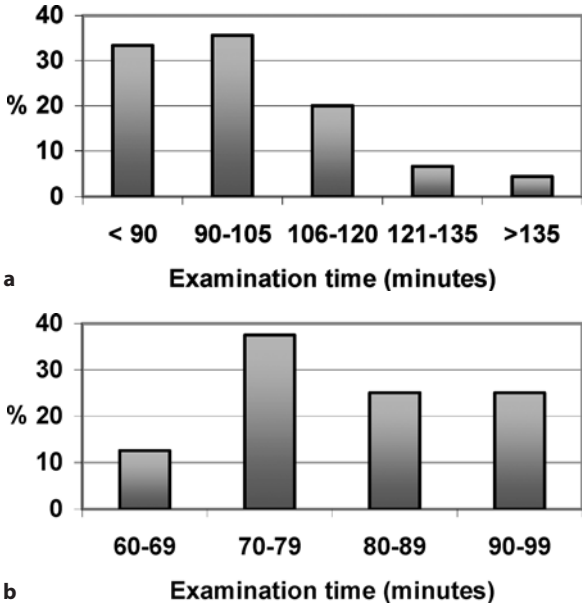

Fig. 40.5a,b. Examination time on both MR systems: 102±23 min on the standard MRI system (**a**) compared with 80±7 min on the whole-body MRI system (**b**)

and in some cases temporal resolution to get a good exam, and on the other hand, one can have excellent resolution but limited image quality in terms of artefacts and low signal-to-noise-ratio (SNR). Good image quality of MR exams is the combination of good spatial and temporal resolution as well as high SNR. Additionally to that, there must not be any artefacts and, in contrast-enhanced examinations, there has to be good vessel conspicuity and no disturbing venous overlay. This kind of image quality has to be rated by readers. The SNR values can be calculated, the readers have to judge occurring artefacts and, in the special case of MRA, vessel conspicuity and venous overlay. In our study, the first 60 examinations were read by two experienced radiologists blinded to each other, and inter-reader agreement was calculated by means of kappa values. Detected pathologies were correlated to the primary existing conventional exams. Inter-reader agreement was good to excellent with kappa values (κ) of 0.66 in the detection of cardiac pathologies, 0.75 in the detection of pathologies of the brain, the lungs or the abdominal organs and 0.91 in the detection of pathological changes of the vascular bed (Table 40.2). Nearly all previously known pathologies from the conventional exams were detected, exclusively intimal thickening of the carotid wall without lumen reduction which was not detected by

Table 40.2. Inter-reader agreement in terms of detection of pathological changes ranging from good to excellent

Region	κ	Range
Angiography	0.905	0.642–1.000
Heart	0.662	0.542–0.789
Lungs	0.650	0.643–0.656
CNS and abdominal organs	0.787	0.486–1.000

CNS central nervous system

MRI but by Doppler ultrasonography. On the other hand, multiple additional pathological findings were detected by MRI, e.g. peripheral artery occlusion, pulmonary nodules, wall motion abnormalities and one myocardial infarction (Table 40.3).

40.5.4 Image Quality: Magnetic Resonance Angiography

Of particular interest is the question of whether a whole-body MRA acquisition accelerated by parallel imaging keeps up with the high-quality standards of the present dedicated high-spatial-resolution MRA of a single vascular territory. In our study 90 whole-body MRA data sets were judged by two different radiologists blinded to each other. Forty-five of these data sets were acquired on a standard MR system, and the other 45 on a dedicated whole-body MR system. Whole-body MRA was divided into 24 vessel segments; each segment was rated on a three-point scale in terms of vessel conspicuity, artefacts and venous overlay. The MRA showed good quality on the standard MR system with good vessel conspicuity in nearly 75% of all vessel segments. Nearly 80% of cases were not affected by artefacts, >85% of all vessel segments had no venous overlay and <1% had major, non-diagnostic venous overlay. Most of the artefacts occurred because of the preliminary suboptimal coil setup. Moderate or poor vessel conspicuity occurred mostly in the calves because of field-of-view limitations requiring a four-station angiography of the lower body part with only one CA bolus or because of mistakes in bolus timing. Inter-reader agreement showed good kappa values with 0.67 in terms of vessel conspicuity, 0.72 in terms of artefacts and 0.76 in terms of venous overlay. On the whole-body MR system, MRA image quality could be further increased.

Here >80% of all vessel segments showed good vessel conspicuity, >92% were not affected by artefacts and >95% showed no venous overlay. Inter-reader agreement could also be increased to excellent kappa values of 0.75 in terms of vessel conspicuity, 0.7 in terms of artefacts and 0.88 in terms of venous overlay (Table 40.4). Vessel conspicuity could be increased due to the new MRA protocol with only four steps because of a field of view of 500 mm and the altered chronological order of scanned regions. Artefacts could be reduced because of the special coil setup using the matrix coil system. Spatial resolution could be reduced to 1×1×1 mm^3 in the carotid arteries and to <1.6×1×1.5 mm^3 in all other regions.

Table 40.3. Comparison between results from conventional exams and whole-body MRI (initial results, first 60 individuals). (Modified from Wintersperger et al. 2005

Standard exams	Pathological findings	MRI exam	Detected in standard exams and in MRI	Additionally detected in MRI	Comments on additional findings in MRI
ECG	0	Cardiac exam			
US heart	4	Functional perfusion/ DCE	2/4	7	Wall motion abnormalities (5), DCE (2)
Chest radiograph	1	Lung: HASTE/VIBE	1/1	3	Pulmonary nodules, partially calcified, confirmed by HRCT (3)
		Abdomen T1, T2			
US liver	0	Liver	0/0	6	Cysts (4), haemangiomas (2)
US gallbladder	5	Gallbladder	5/5	5	
US kidneys	3	Kidneys	3/3/	9	Cysts (9)
US spleen	0	Spleen	0/0	0	
US pancreas	0	Pancreas	0/0	1	Cyst (1)
		MRA			
US carotid arteries	5	Carotid arteries	0/5	2	Abdominal origin (1), low-grade stenosis (1)
US abdominal/renal arteries	1	Abdominal/renal arteries	1/1	1	Low-grade stenosis (1)
		Thigh, calf, feet		5	Occlusion of peripheral arteries (5)

Except for 5 cases of intimal thickening, all conventional diagnosed pathologies were detected by MRI without primary knowledge. On the other hand, multiple additional pathologies were detected by MRI.

Table 40.4. Image analysis of whole-body MRA in terms of vessel conspicuity, incidence of artefacts as well as venous overlay. Whole-body MRA was divided into 24 vessel segments and judged on a three-point scale by two blinded radiologists. Because of increased image quality in all analysed categories inter-reader agreement increased as well.

Magnetom Sonata								
Vessel conspicuity	Percentage	Absolute	Artefacts	Percentage	Absolute	Venous overlay	Percentage	Absolute
Good	73.2	1476	None	79.3	1598	None	86.5	1744
Moderate	22.5	454	Minor	18.4	370	Minor	13.0	261
Poor	4.3	86	Major	2.4	48	Major	0.6	11
κ		0.671	κ		0.716	κ		0.756

Magnetom Avanto								
Vessel conspicuity	Percentage	Absolute	Artefacts	Percentage	Absolute	Venous overlay	Percentage	Absolute
Good	80.6	1624	None	92.9	1873	None	95.6	1928
Moderate	15.3	309	Mild	4.4	89	Mild	4.4	88
Poor	4.1	83	Major	2.7	54	Major	0	0
κ		0.745	κ		0.697	κ		0.881

40.6 Conclusion: Advantages of Parallel Imaging

Due to the introduction of parallel imaging as well as recent technical developments, such as matrix-coil systems and dedicated whole-body MRI systems, cardiovascular whole-body MRI screening seems to be feasible. The introduction of parallel imaging was a major breakthrough to overcome the limitations that had restricted MRI in this field of imaging. One of the most important considerations for screening is to perform imaging with the best possible quality. The introduction of parallel imaging made it possible to combine multiple state-of-the-art exams into one comprehensive protocol within reasonable scan time. Different studies have shown that MR imaging detects the same or even more pathological changes than commonly used conventional techniques when screening for cardiovascular changes. Another very important point in screening is a good to excellent inter-reader agreement, which appears to be the case when using parallel imaging. Parallel acquisition techniques have helped to reduce scan time, to increase spatial and/or temporal resolution. Reduced scan time and increased spatial resolution is very important in MRA. Short scan times are mandatory for whole-body angiography to keep venous overlay to a minimum in the last acquired vessel region. On the other hand, spatial resolution is very important, because for the purpose of cardiovascular screening, asymptomatic early changes should be detected. High temporal resolution is mandatory for functional cardiac imaging.

References

Biederer J, Busse I, Grimm J et al. (2002) Sensitivity of MRI in detecting alveolar infiltrates: experimental studies. Rofo 174:1033–1039 [in German]

Goyen M, Quick HH, Debatin JF et al. (2002) Whole-body three-dimensional MR angiography with a rolling table platform: initial clinical experience. Radiology 224:270–277

Goyen M, Herborn CU, Kroger K, Lauenstein TC, Debatin JF, Ruehm SG (2003) Detection of atherosclerosis: systemic imaging for systemic disease with whole-body three-dimensional MR angiography. Initial experience. Radiology 227:277–282

Henschke CI, Yankelevitz DF (2000) Screening for lung cancer. J Thorac Imaging 15:21–27

Kramer H, Schoenberg SO, Nikolaou K et al. (2004) Cardiovascular whole body MRI with parallel imaging. Radiologe 44:835–843 [in German]

Kramer H, Schoenberg SO, Nikolaou K, Huber A, Struwe A, Winnik E, Wintersperger BJ, Dietrich O, Kiefer B, Reiser MF (2005) Cardiovascular screening with parallel imaging techniques and a whole-body MR imager. Radiology 236:300–310

Ruehm SG, Goyen M, Barkhausen J et al. (2001) Rapid magnetic resonance angiography for detection of atherosclerosis. Lancet 357:1086–1091

Wintersperger BJ, Nikolaou K, Dietrich O et al. (2003) Single breath-hold real-time cine MR imaging: improved temporal resolution using generalized autocalibrating partially parallel acquisition (GRAPPA) algorithm. Eur Radiol 13:1931–1936

Tumor Staging

41

Gerwin P. Schmidt

CONTENTS

41.1 Introduction

Precise tumor staging is a fundamental precondition when assessing the prognosis and therapeutic options in a patient with a neoplastic disease. The TNM-staging system proposed by the American Joint Committee on Cancer (2002) has become the international standard for this purpose. This three-grade system concerns primary tumor growth (T-stage), local lymph-node invasion (N-stage) as well as distant hematogenic metastatic spread (M-stage). Besides interventional and operative procedures (e.g., tumor biopsy or thoracoscopy), particularly diagnostic imaging procedures are necessary to get a clear picture of the total tumor burden. At present, multimodality diagnostic approaches are still widely used in the clinical routine, which can be time consuming, costly and often strain patients. However, whole-body imaging techniques are increasingly applied to give consideration to neoplastic disease as a systemic affection. In principle, MRI with its excellent tissue contrast at a high spatial resolution, detailed morphological information and lack of ionizing radiation seems suitable for tumor staging. With the advent of whole-body scanners covering the patient from head to toe, MRI has become a promising candidate for comprehensive, integrated high-resolution tumor imaging.

G. P. Schmidt, MD
Department of Clinical Radiology, University Hospitals – Grosshadern, Ludwig Maximilian University of Munich, Marchioninistr. 15, 81377 Munich, Germany

41.2 Initial Experience with Whole-Body MRI

In the past, MRI basically has been employed for the assessment of focal pathologies in specific anatomical regions or organ systems, and a key problem for an application in whole-body imaging has been the integration of substantially different requirements in coil setup, contrast-media application, slice positioning and sequence design into one single comprehensive protocol. Various attempts in the past have been made to establish whole-body MRI concepts for tumor staging. Originally, whole-body imaging on a conventional scanner required at least one patient and coil repositioning process, which substantially increased examination time far beyond an hour. The introduction of a rolling platform (AngioSURF/BodySURF, MR-Innovation, Essen, Germany) mounted on top of the scanner table for the first time enabled overcoming field-of-view restrictions and extending the scan on the whole body without repositioning. Here, the patient glides in between a "coil sandwich" comprised

of a body surface coil and the integrated spine coil. Barkhausen et al. (2001) used this system for axial whole-body tumor screening with fast steady-state free precession "TrueFISP" sequences. Although the protocol made examination times possible comparable to a CT scan, considerable compromises in spatial resolution, especially for the detection of lung and liver pathologies, had to be taken into account. Certainly, the application of a body surface coil in the distal extremities or cervical region represents a compromise in spatial resolution.

The introduction of whole-body scanners, using a system of multiple phased-array coils covering the whole body like a matrix, finally allowed whole-body imaging with the use of parallel imaging in all three spatial dimensions; cf. Chap. 13. The combination of parallel imaging with a single-positioning examination has reduced room time substantially and improved spatial resolution. So far, there are only a few experiences in whole-body tumor staging on these scanners. Schlemmer et al. (2005) examined 65 patients with different neoplasms and compared the diagnostic performance with a conventional spiral-CT scanner. More metastases were detected in whole-body MRI, especially in the liver, brain, lymph nodes and musculoskeletal system. Also, findings led to a therapy change in 10% of the patients.

Recently, a combination of continuously-moving-table MRI with parallel imaging has been introduced for whole-body oncological imaging. For this purpose, the SENSE reconstruction algorithm has been successfully applied on stationary receiver coils with arbitrary coil dimensions for continuously 3D gradient-echo imaging from head to toe at an acceleration factor of R=2 without significant constraints in image quality (Keupp et al. 2005).

41.3 Protocol Setup

A whole-body MRI tumor protocol has to cover the different pathways of metastatic spread and at the same time must guarantee a high diagnostic accuracy. Therefore, it should imply state-of-the-art imaging techniques, such as T1-weighted and STIR imaging, which have proved highly efficient for the assessment of soft-tissue and bone structures, fast high-resolution imaging of the lung (e.g., HASTE MRI, cf. Chap. 21), as well as static and dynamic contrast-enhanced studies of the abdominal organs and brain (Metha et al. 1995, Hargaden et al. 2003, Lutterbey et al. 1998, Semelka et al. 2001). However, these sequences are time-consuming and push scan times far beyond an hour, which used to make an economic clinical application impossible. The introduction of parallel imaging techniques has shortened scan times substantially without compromising spatial resolution (Pruessmann et al. 1999, Sodickson et al. 1997, Griswold et al. 2002). Finally, a flexible protocol for high-resolution whole-body MRI with examination times below 60 min seems feasible. So far, at our institution experience on more than 100 patients with whole-body imaging for systemic tumor staging exists. The total scan time of the protocol presented below is 55 min.

The proposed protocol is based on a 1.5-T whole-body MRI system (Magnetom Avanto, Siemens Medical Solutions, Erlangen, Germany) that allows the connection of up to 76 elements from multiple phased-array surface coils (matrix coil system) covering the patient from head to toe with simultaneous signal reception from up to 32 independent receiver channels (Fig. 41.1). The coil setup consists of a head coil (12 elements), neck coil (4 elements), 2 or 3 body coils for imaging of the abdomen and pelvis (12 or 18 elements) and a peripheral-MRA coil for the lower extremities (8 elements). The spine coil consists of 24 elements and is embedded into the scanner table. After one single positioning of the patient (supine, arms beside the body), the system allows parallel imaging in three spatial directions using automatic table motion at a total scan range of 205 cm.

The protocol (Fig. 41.2) begins with coronal STIR imaging of the complete anatomy at five body levels: head/neck, pelvis, thighs, and calves (TR/TE/TI 5,620 ms/92 ms/170 ms; slice thickness 5 mm; matrix 384×269), as well as thorax/abdomen (TR/TE/TI 3,380 ms/101 ms/150 ms) in breath-hold technique with prospective 2D navigator correction of the inspiration phase. A parallel-imaging acceleration factor of R=3 is normally used for coronal whole-body imaging, apart from the calves, which are scanned with an acceleration factor of R=2.

The lung is examined with fast single-shot half-Fourier turbo-spin-echo (HASTE) (TR/TE 1,100 ms/27 ms; slice thickness 6 mm; matrix 320×156) and STIR sequences (TR/TE/TI 3,800 ms/100 ms/150 ms), followed by a navigator-triggered "free-breathing" T2-weighted fat-saturated turbo-spin-echo (TSE) scan of the liver (TR/TE 2,010 ms/101 ms; slice thickness 6 mm; matrix 320×240). In this protocol, an

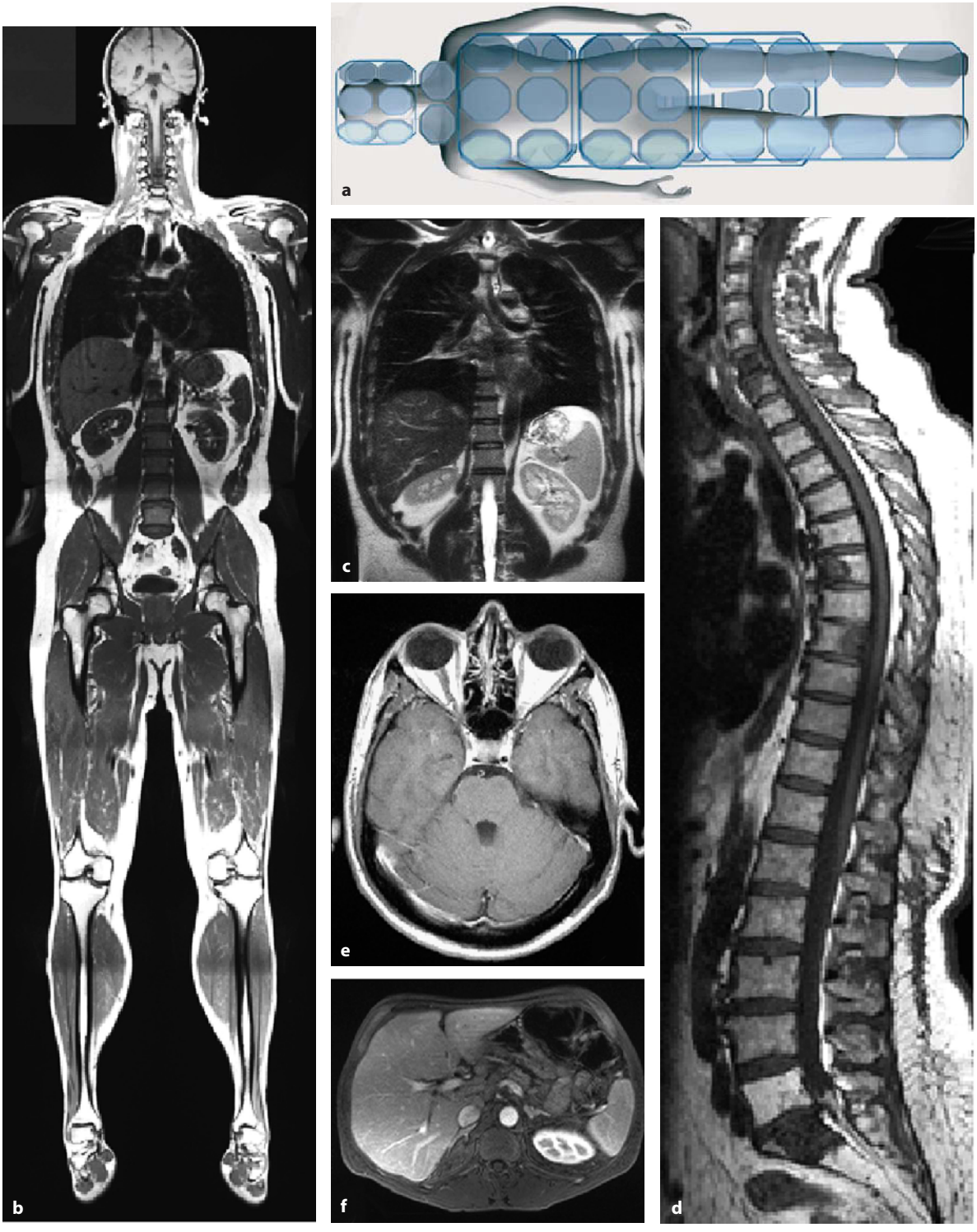

Fig. 41.1. a Matrix coil system for whole-body coverage from head to toe with parallel imaging in all three spatial orientations (courtesy of Siemens Medical Solutions, Erlangen, Germany). **b** T1-weighted whole-body MRI. **c** HASTE MRI of the lung. **d** T1-weighted MRI of the whole spine. **e** Contrast-enhanced T1-weighted MRI of the brain. **f** Fat-saturated T1-weighted gradient-echo sequence of the abdomen/pelvis.

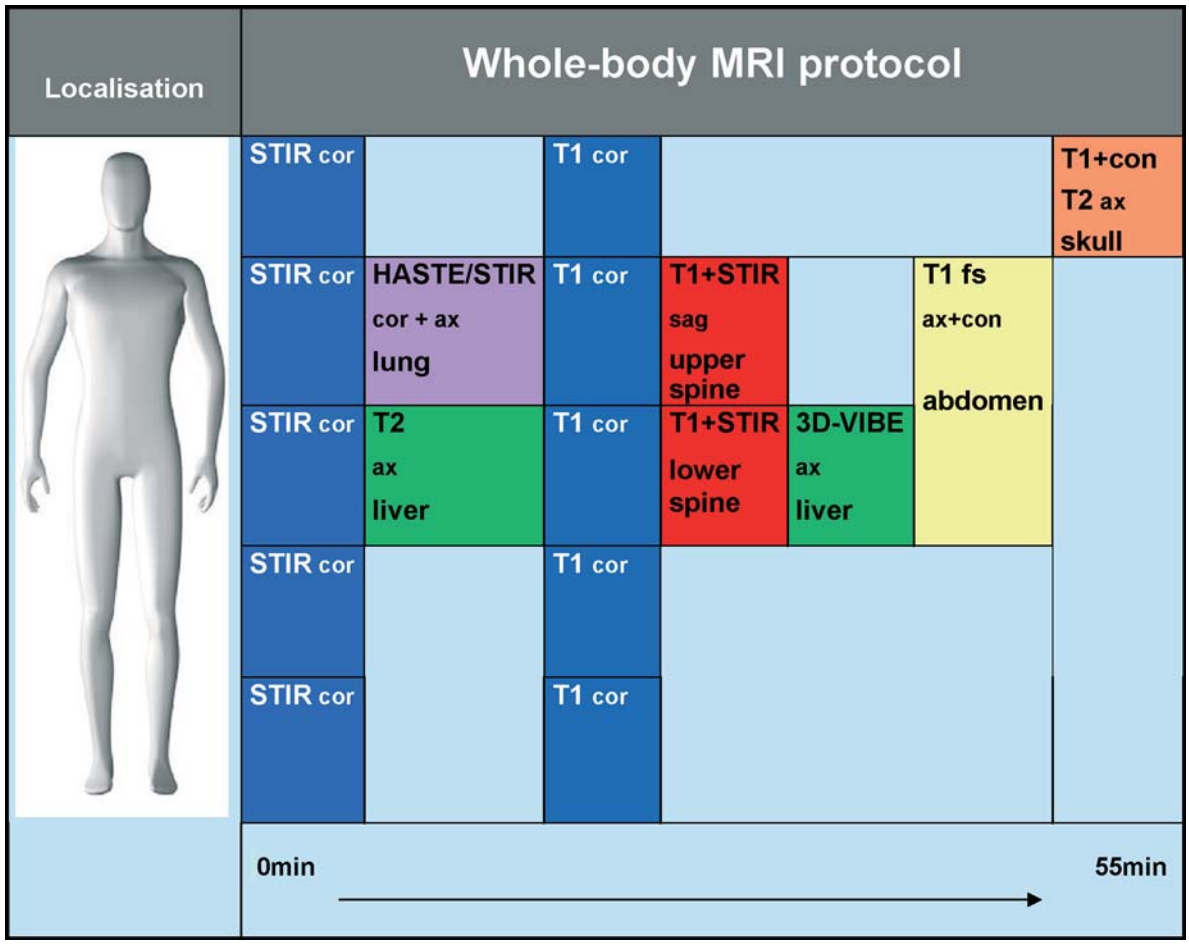

Fig. 41.2. Whole-body MRI protocol on a 32-receiver-channel system (Magnetom Avanto, Siemens Medical Solutions, Erlangen, Germany). Using parallel imaging, a total scan time of below 1 h is possible.

acceleration factor of R=2 is applied on sagittal and axial studies. Then, the five body levels are examined again with T1-weighted spin-echo imaging (TR/TE 79 ms/12 ms, slice thickness 5 mm, matrix 448×385; thorax/abdomen TR/TE 400 ms/8.2 ms), followed by sagittal T1-weighted (TR/TE 849 ms/11 ms; slice thickness 3 mm; matrix 384×384) and STIR imaging (TR/TE/TI 5,700 ms/59 ms/180 ms) of the upper and lower spine.

During contrast-material application, axial dynamic (3D VIBE; TR/TE 4.38 ms/1.61 ms; slice thickness 3 mm) liver scans and a fat-saturated T1-weighted gradient-echo sequence of the complete abdomen (TR/TE 179 ms/3.3 ms; matrix 320×193; slice thickness 6 mm) are performed. In a last examination step, the brain is examined with axial T1-weighted (TR/TE 635 ms/17 ms; slice thickness 5 mm; matrix 320×240) and T2-weighted (TR/TE 1,420 ms/109 ms; matrix 512×250) sequences. The coronal imaging of five body levels is later fused to one whole-body image, along with the studies of the spine (Fig. 41.1b-f, Fig. 41.3).

41.4 Patients and Study Design

Our experiences with patients suffering from different neoplasms are presented in the following. The aim was to compare the potential and performance of a whole-body MRI protocol using parallel imaging with a dual-modality PET-CT scanner (Gemini, Philips Medical systems, Cleveland, OH). For this purpose the examinations were analyzed by two board-

certified radiologists (MRI) and one radiologist/one nuclear medicine physician (PET-CT). The location, size and extent of the primary or recurrent tumor, lymph nodes and distant metastases were described by both reader groups, and the TNM stage was defined according to the criteria of the AJCC (American Joint Committee on Cancer). For all detected lesions, available clinical, histological and radiological data (CT, PET, bone scintigraphy, MRI, radiographs, and ultrasound) were consulted within a period of 5 months as a reference method, especially to verify questionable or discrepant findings. In an initial analysis, 38 individuals (mean age, 56 years; range, 21-81 years; 21 females/17 males) with different histologically proven primary tumor diagnoses were assessed (Fig. 41.4). The patients referred for primary staging, restaging or tumor search were examined with both modalities within a short period of time. Most common primary diagnoses were tumors of the gastrointestinal tract (n=14) and breast carcinoma (n=11) (Fig. 41.4). Patients with tumors that had experienced poor FDG uptake or did not fulfill indications for PET examination (e.g., renal cell carcinoma) were not included in the population (Reske and Kotzerke 2001). The

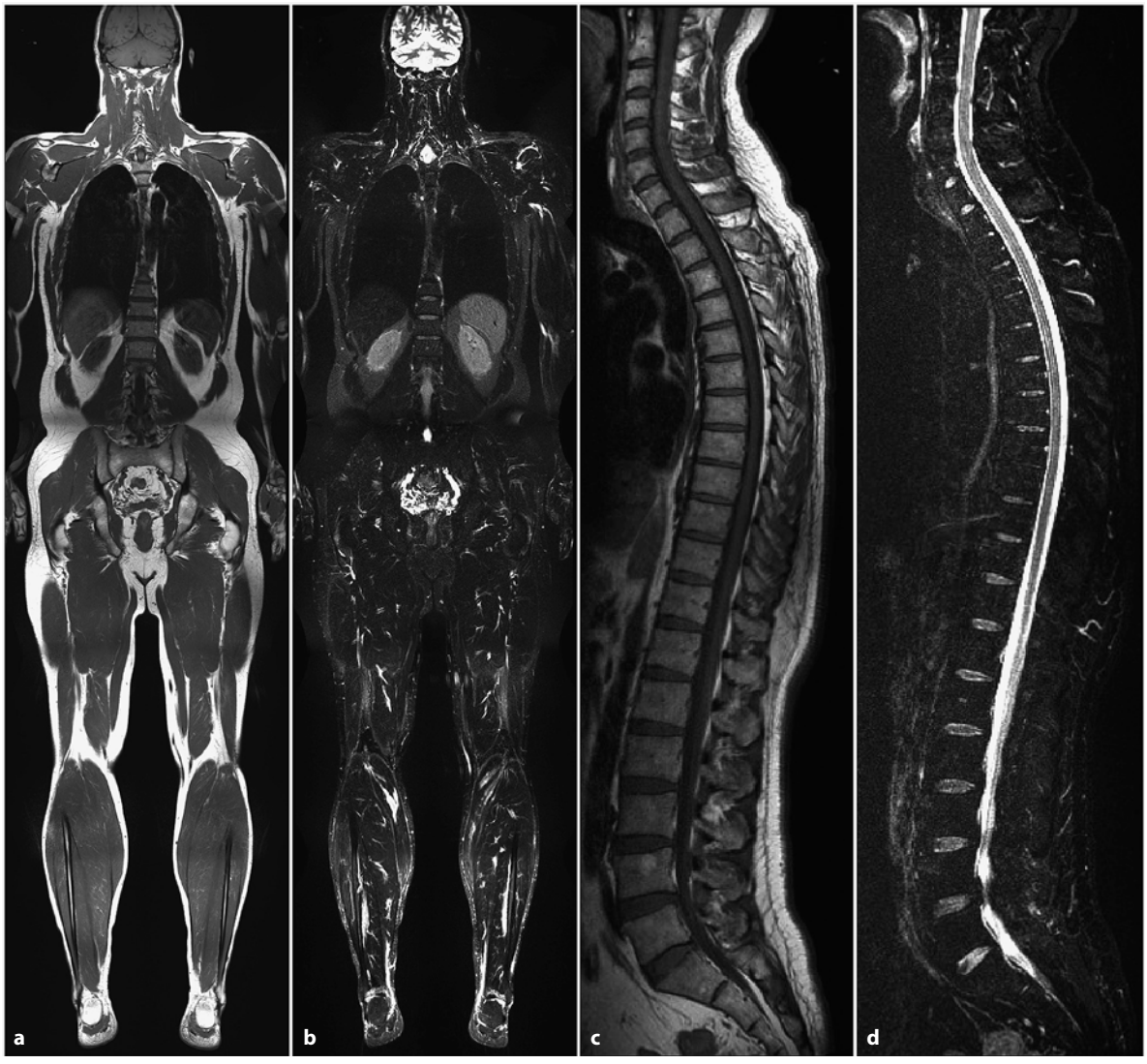

Fig. 41.3a–d. Healthy 40-year-old male. Fused T1-weighted- and STIR-imaging at five body levels in coronal orientation **a** and **b** and of the whole spine in sagittal orientation **c** and **d**. With a parallel-imaging acceleration factor of 3, whole-body STIR imaging is possible within a total scan time of 12:28 min at an in-plane resolution of 1.8×1.3 mm². The matrix coil system guarantees optimal coil geometry for each body part.

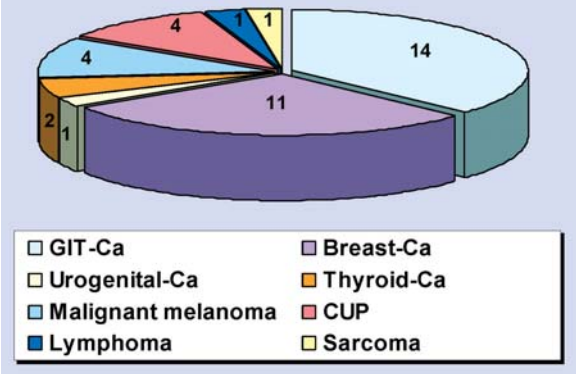

Fig. 41.4 Overview on the primary tumor diagnoses of 38 patients scanned with whole-body MRI and PET-CT within a time period of 2 weeks.

mean room time for whole-body MRI was 70 min (56-76 min; scan time, 55 min) and 103 min for PET-CT (60 min patient preparation; 43 min scan time).

41.5 Results: Image Quality

The substantial reduction of individual scan times due to parallel imaging enables the incorporation of flexible sequence protocols for MRI tumor staging, even when potentially time-consuming sequence types, like STIR imaging, are used. The combination of T1-weighted and STIR sequences guarantees a highly resolved demonstration of bone marrow and soft-tissue structures. Especially tumor-induced edema and the replacement of bone marrow by water-containing tumor cells are readily detected as hyperintense signal in STIR with an excellent contrast to the surrounding normal tissue (Fig. 41.5). Using an acceleration factor of R=3, whole-body STIR imaging is possible within a total scan time of 12:28 min at an in-plane resolution of 1.8×1.3 mm². Additionally, by using the total-imaging-matrix system on our whole-body scanner, optimal coil geometry for each body part is achieved, guaranteeing high spatial resolution with an excellent signal-to-noise ratio. Our data show that bone lesions down to a cut-off size of 2 mm are readily detected with this protocol (Fig. 41.5b and 41.5c).

For the detection of lung pathologies, single-shot half-Fourier turbo-spin-echo sequences (such as HASTE) have proved to be highly efficient (Vogt et al. 2004); cf. Chap. 20. An important profit of parallel imaging is the significant reduction of blurring and increased sharpness of the image when single-shot pulse sequences are used (Eibel et al. 2005); cf. Chap. 10. Additionally, by a shortening of the echo time and length of the echo train in tissue with fast T2 decay, such as lung parenchyma, the loss of the signal-to-noise ratio can be reduced. With a combination of axial HASTE and STIR sequences using 6-mm sections, lung nodules of 7 mm minimum size are reliably visualized, coming close to the resolution and contrast achieved with a conventional spiral-CT scanner (Fig. 41.6).

Dynamic contrast-enhanced studies today are indispensable for the diagnosis of abdominal lesions, especially of the liver, and contrast-uptake behavior gives essential information on the dignity and classification of a lesion (Semelka et al. 2001). Parallel-imaging acceleration enables the incorporation of a dynamic 3D VIBE sequence into the protocol, acquired within 2:17 min, comprising an early arterial, venous and late-phase T1-weighted TSE sequence. An advantage of parallel-imaging acceleration here is the larger anatomical coverage in one image stack during the transit of contrast media. When free-breathing T2-weighted imaging of the liver is performed, parallel imaging reduces scan time by half, from an 8- down to 4-min acquisition time, with higher spatial resolution (Zech et al. 2004). With this protocol, liver pathologies at a cutoff size of 3 mm are reliably localized with a high tissue contrast, revealing lesions invisible in the diagnostic spiral CT of the PET-CT examination in some patients (cutoff size 5 mm, Fig. 41.7).

41.6 Results: Pathologies

In the examined patient population, six of the seven present tumors, of which three were primaries and four were recurrences, were reliably detected by whole-body MRI. The low presence of primary tumors is explained by the fact that many patients were referred to our department for restaging after surgical therapy. One esophageal recurrence in stage T3 was missed with MRI, which hardly showed morphological changes of the esophageal wall and was impossible to delineate due to overlying breathing artefacts. Of 120 lymph nodes present, 60 nodes were

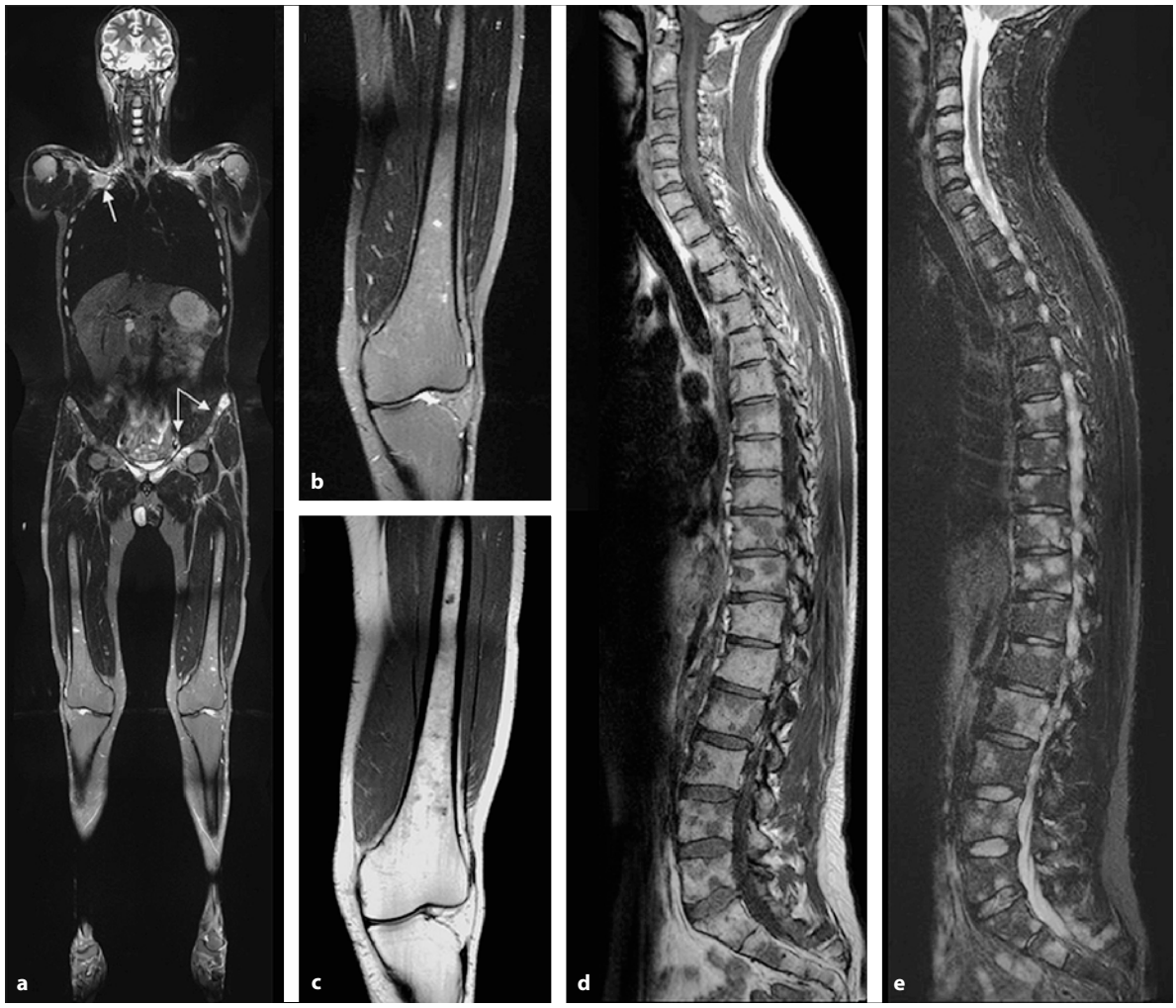

Fig. 41.5a–e. **A** 27-year-old male with non-Hodgkin's lymphoma. **a** STIR whole-body imaging reveals a tumor bulk in the right clavicular groove (*arrow*) and extensive infiltration of the right pelvis (*arrow*). **b, c** Magnification of the distal right femoral shows a multifocal bone infiltration down to a size of 2 mm in STIR- and T1-weighted imaging. **d, e** Sagittal imaging of the spine depicts extensive multifocal boney infiltration.

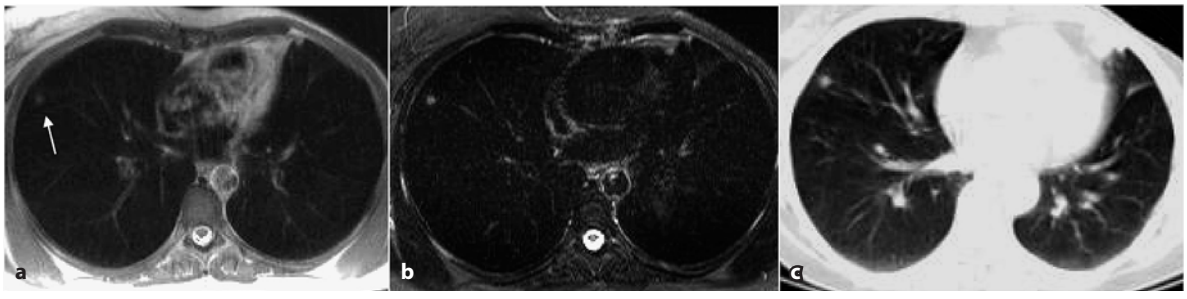

Fig. 41.6a–c A 65-year old female with breast carcinoma. **a** Axial HASTE imaging reveals a singular lung node in the right upper lobe. **b** STIR imaging depicts the node with high contrast comparable to the corresponding spiral CT **c** The node was confirmed as a lung metastasis. The use of parallel imaging leads to a significant reduction of blurring when single shot sequences are used. Additionally, by reducing the echo time and length of echo train, the loss of signal-to-noise ratio in lung tissue is reduced.

confirmed malignant and 60 benign. MRI reached a moderate diagnostic accuracy of 78% in a lesion-by-lesion analysis. Especially when malignant nodes are borderline sized (10±3 mm), the correct classification and localization can cause problems without the metabolic information provided in the PET examination, especially when nodes are located in areas impaired by artefacts, such as the hilar or retrocrural regions. Still, compared to the published literature, diagnostic accuracy is significantly higher for lymph node detection when parallel imaging with a combination of axial HASTE/STIR imaging is used (Antoch et al. 2004). Image analysis revealed 268 distant lesions in 29 patients, of which 191 were malignant and 77 benign, and in the lesion-by-lesion analysis, whole-body MRI reached an excellent accuracy of 92% for the detection of distant metastases.

41.7 Results: Comparison to PET-CT

The introduction of combined PET-CT scanners has made a new modality available for whole-body imaging. PET-CT increases diagnostic accuracy compared to PET and CT alone by providing "anato-metabolic" information through the fusion of data given by pathologic tumor glucose-uptake in the PET examination and accurate delineation of anatomical structures through improved spatial resolution provided by the spiral CT scan (Beyer et al. 2000, Pelosi et al. 2004). Our observations indicate that PET-CT has advantages in the detection of lymph node metastases due to the facilitated localization and classification by the pathological tracer uptake, especially in borderline-sized lymph nodes (Fig. 41.8). Here, PET-CT revealed a diagnostic accuracy superior to MRI (92%). Improving the sensitivity and specificity in lymph node detection obviously represents the key to a further increase in the overall accuracy of whole body MRI in tumor staging. Several concepts have been developed to enhance traceability, e.g., with the use of diffusion-weighted MR imaging, a so-called "MRI PETgraphy" (Takahara et al. 2004). The main strength of whole-body MRI certainly is reflected by the detection of distant metastatic disease: in our study MRI (n=76) detected significantly more bone metastases than PET-CT (n=50), as well as liver metastases (n=71 vs. n=62) and was practically equivalent in the detection of lung pathologies (n=36 vs. n=37). Also due to the larger field of view used in whole-body MRI (PET-CT usually is acquired with a neck-thorax-pelvis CT scan) additional malignant lesions were revealed in the distal femoral bones and cerebrum (Fig. 41.9). Altogether, our data showed an equal and robust performance of both modalities with an excellent overall accuracy of 96% for PET-CT and 91% for whole-body MRI for the correct assessment of the TNM stage.

41.8 Conclusion

With the introduction of whole-body MRI and PET-CT scanners, two modalities for systemic tumor staging and promising alternatives to the established multimodality approach have become more

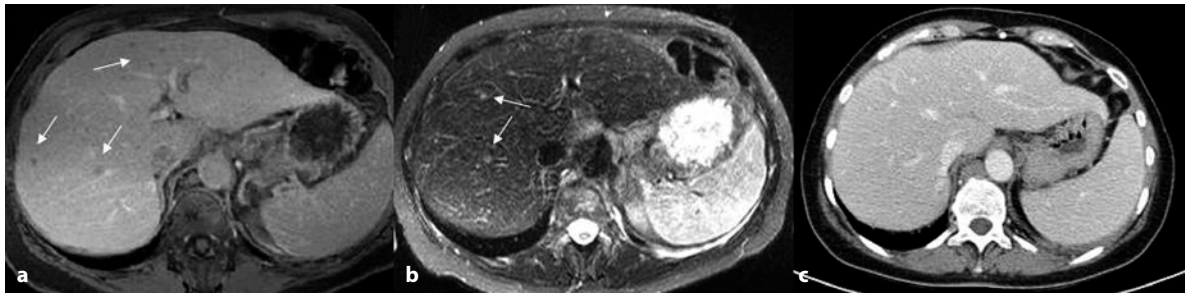

Fig. 41.7a–c. A 70-year-old female with liver metastases. **a** Dynamic contrast-enhanced 3D VIBE imaging of the liver reveals multiple punctual lesions with an indicated ring-like enhancement (*arrows*). Parallel imaging allows larger anatomical coverage in one image stack during transit of contrast media. **b** The lesions are clearly distinguishable in T2-weighted imaging with a hyperintense signal (*arrows*). With the use of parallel imaging, acquisition time is reduced by half without a loss of spatial resolution. **c** Contrast-enhanced spiral CT falsely shows inconspicuous liver parenchyma.

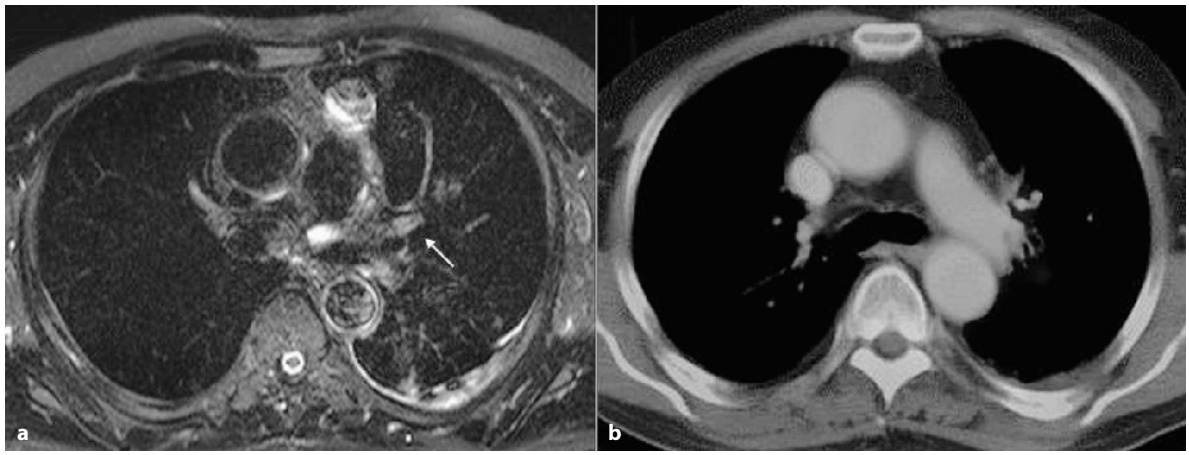

Fig. 41.8a,b. A 66-year-old male with pancreatic carcinoma. **a** Axial STIR imaging of the lung shows a hyperintense structure (8 mm) on the left hilus that is difficult to allocate. **b** Fused axial PET-CT imaging of the same area shows a small hilar lymph node with pathological FDG uptake (SUV=2.8). This lymph node was confirmed as a metastasis.

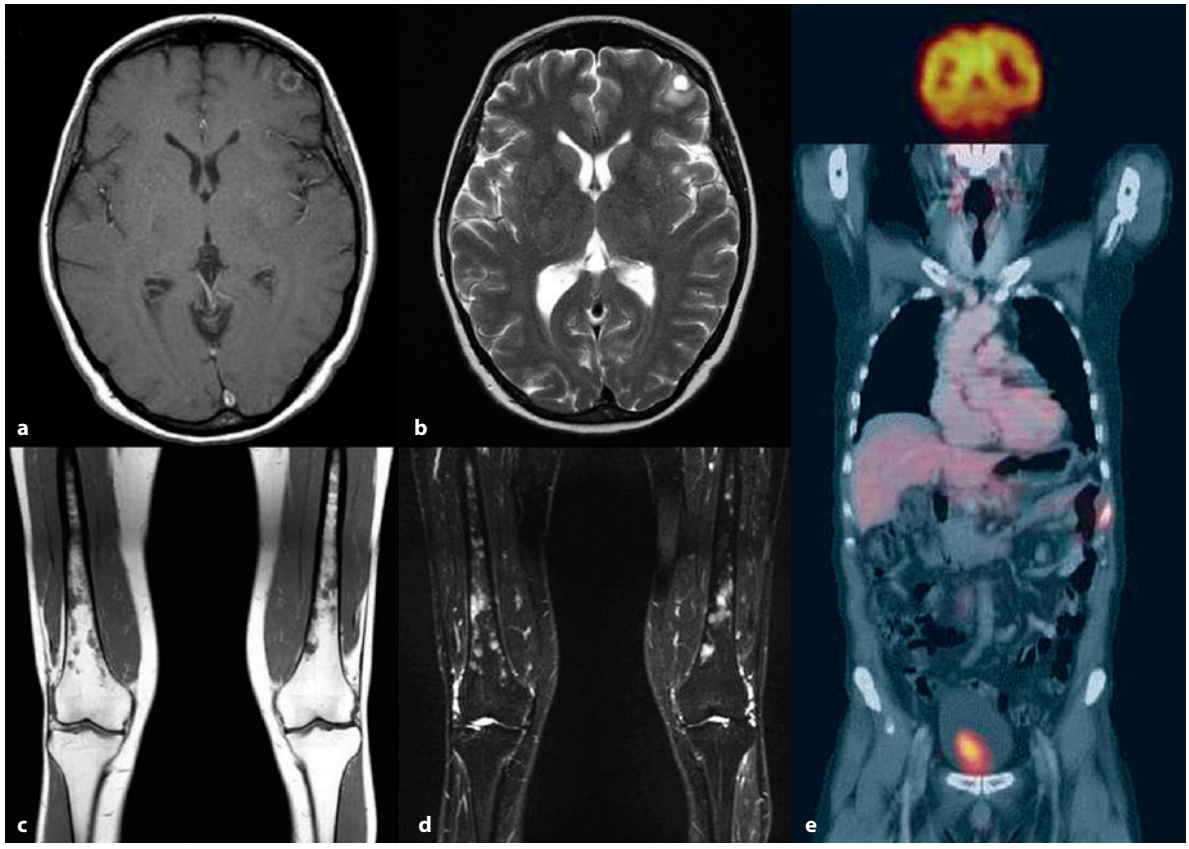

Fig. 41.9a–e. a, b Axial T1-weighted post-contrast and T2-weighted imaging of the brain of a 60-year-old male with carcinoma of the esophagus indicates a brain metastasis in the left frontal lobe. **c, d** Due to the larger field of view compared to PET-CT, coronal T1-weigthed- and STIR-whole-body MRI depicts multifocal metastatic disease to the distal femoral bones in a 45-year-old female with breast carcinoma. **e** Coronal reconstruction of a whole-body PET-CT scan. Due to the high physiological FDG uptake in the brain and the smaller field of view, lesions in the brain and the distal extremities are not identified.

widely available. Although both modalities seem to have their individual pros and cons, first experiences have shown a reliable performance of both modalities for a clinically applicable tumor staging where patients might benefit from early accurate staging and improved therapeutic options. In case of primary tumors with known poor FDG-uptake, (e.g., renal-cell carcinoma) or in patients with counter-indications to ionizing radiation (e.g., young patients) or to the application of iodine-based contrast agents, whole-body MRI is the method of first choice (Reske and Kotzerke 2001). The use of parallel imaging in combination with multi-channel whole-body scanners finally makes a flexible, high-resolution whole-body tumor staging protocol lasting less than an hour feasible. Still, more experiences with these new techniques are needed to assess thoroughly their full potential as a more cost efficient and accurate tumor imaging.

References

American Joint Committee on Cancer (2002) AJCC Cancer Staging Manual, 6th edn. Springer, Berlin Heidelberg New York

Antoch G, Vogt FM, Freudenberg LS et al (2003) Whole-body dual-modality PET/CT and whole-body MRI for tumor staging in oncology. JAMA 290: 3199–3206

Barkhausen J, Quick HH, Lauenstein T et al (2001) Whole-body MR imaging in 30 s with real-time true FISP and a continuously rolling table platform: feasability study. Radiology 220: 252–256

Beyer T, Townsend DW, Brun T et al (2000) A combined PET-CT scanner for clinical oncology. J Nucl Med 34: 1190–1197

Eibel R, Herzog P, Dietrich O et al (2005) Detection of pulmonary abnormalities in immunocompromised patients: fast single-shot MRI with parallel imaging in comparison to thin-section helical CT. Radiology, accepted

Griswold MA, Jakob PM, Heidemann RM et al (2002) Generalized autocalibrating partially parallel acquisitions (GRAPPA). Magn Reson Med 47: 1202–1210

Hargaden G, O'Connell M, Kavanagh E et al (2003) Current concepts in whole-body imaging using turbo short tau inversion recovery MR imaging. AJR 180: 247–252

Keupp J, Boernert P, Aldefeld B (2005) Continuously moving table SENSE imaging with exact reconstruction using a 16-coil array. Proc Intl Soc Magn Reson Med 13: 483

Lutterbey G, Leutner C, Gieseke J et al (1998) Detection of focal lung lesions with magnetic resonance tomography using T2-weighted ultrashort turbo-spin-echo-sequence in comparison with spiral computerized tomography. RöFo Fortschr Geb Röntgenstr Neuen Bildgeb Verfahr 169: 365–369

Mehta RC, Marks MP, Hinks RS et al (1995) MR evaluation of vertebral metastases: T1-weighted short inversion time inversion recovery, fast spin echo, and inversion-recovery fast spin-echo sequences. Am J Neuroradiol 16: 281–288

Pelosi E, Messa C, Sironi S et al (2004) Value of integrated PET/CT for lesion localisation in cancer patients: a comparative study. Eur J Nucl Med Mol Imaging 31: 932–939

Pruessmann KP, Weiger M, Scheidegger MB et al (1999) SENSE: sensitivity encoding for fast MRI. Magn Reson Med 42: 952–962

Reske SN, Kotzerke J (2001) FDG-PET for clinical use. Results of the 3rd German interdisciplinary consensus conference, "Onko-PET III", 21 July and 19 Sept 2000. Eur J Nucl Med 28: 1707–1723

Schlemmer P, Schäfer J, Pfannenberg C et al (2005) Fast whole-body assessment of metastatic disease using a novel magnetic resonance imaging system. Invest Radiol 40: 64–71

Semelka RC, Martin DR, Balci C et al (2001) Focal liver lesions: comparison of dual-phase CT and multisequence multiplanar MR imaging including dynamic gadolinium enhancement. J Magn Reson Imaging 13: 397–401

Sodickson DK, Manning WJ (1997) Simultaneous acquisition of spatial harmonics (SMASH): fast imaging with radiofrequency coil arrays. Magn Reson Med 38: 591–603

Takahara T, Yamashita E, Nasu S et al (2004) "Diffusion PETgraphy": technical breakthrough in body diffusion weighted images with non-breathholding and high resolution display. Proc Intl Soc Mag Reson Med 11

Vogt FM, Herborn CU, Hunold P et al (2004) HASTE MRI versus chest radiography in the detection of pulmonary nodules: comparison with MDCT. AJR 183:71–78

Imaging of Bronchial Carcinoma

42

Stefan O. Schoenberg, Christian Fink and Bastian Fischer

CONTENTS

42.1 Epidemiology

Non-small-cell lung cancer (NSCLC) is still the leading cause of death from a malignancy in men, with a rising incidence in women. In the past decade, the therapeutic options for advanced stages of NSCLC have been substantially improved, including new chemotherapeutic and anti-angiogenic agents for first- and second-line medical treatment, new protocols for neo-adjuvant and adjuvant chemotherapy as well as improved techniques for surgical resection of centrally growing tumors. These developments require improved non-invasive imaging modalities for staging of resectability and operability in order to select the adequate treatment options for the individual patient.

S. O. Schoenberg, MD; C. Fink, MD; B. Fischer
Department of Clinical Radiology, University Hospitals – Grosshadern, Ludwig Maximilian University of Munich, Marchioninistr. 15, 81377 Munich, Germany

42.2 Radiological Staging

The staging of non-small-cell lung cancer has to be performed in an interdisciplinary approach considering all clinical, radiological, nuclear-medicine, and histological results. The radiological staging is done according to the TNM classification with T describing the extent of the primary tumor, N the presence and location of metastatic lymph nodes and M the presence or absence of distant metastases. It is important to remember that the individual stages of the TNM classification have undergone numerous revisions and thus need to be considered in their most recent version (Mountain 1997; Mountain and Dresler 1997). For the radiologist, it is also important to know which therapy the patient is possibly undergoing in order to optimize the imaging strategy. Spiral CT is currently viewed as the backbone of radiological staging. With the new 16- to 64-channel generation of multi-slice CT systems, the entire thorax can be scanned in less the 10 s with 1-mm slice thickness.

42.2.1 T Stage

For the assessment of the tumor extension, special attention has to be drawn to the assessment of chest-wall and mediastinal invasion, since these findings directly affect the tumor stage. The only reliable CT sign is a mass in the chest wall or the presence of rib destruction (Libshitz 1990; Pearlberg 1987). However, these signs have a poor sensitivity of only

20% with moderate specificity. The accuracy can be moderately increased if other findings such as an obtuse angle with the thoracic wall, thickening of the underlying pleura, and presence of chest pain are also considered (Scott et al. 1998). Highest accuracies are found in dynamic expiratory scans that demonstrate a decreased or absent mobility of the ingrown tumor (Murata et al. 1994); however, this technique has not gained wide-spread use in the clinical routine. Due to the oblique course of the left and right main stem bronchus, delineation of an infiltration of the carina is difficult to assess on standard spiral CT with 5-mm-thick slices. Multi-slice CT has advantages compared to standard spiral CT since the course of the entire bronchial tree can be delineated on three-dimensional reconstructions of thin-slice images (Grandy 2001). Multiplanar reconstructions also reduce errors from partial volume effects, particularly in the apex of the lung where the convex surface of the lungs might erroneously cause an impression of superior sulcus infiltration.

Accuracy for the assessment of mediastinal invasion by CT, however, is limited. Definite proof of tracheal invasion is only present in the case of intraluminal or circumferential tumor growth, while the sole contact between the tumor and the trachea does not suffice to make the diagnosis of tracheal invasion. In these cases, mediastinoscopy or endotracheal sonography is necessary to make the diagnosis (Herth and Becker 2000). While tumors with partial encasement can usually be considered resectable, the assessment of the mediastinal fat planes as a criterion for operability is less reliable (Herman et al. 1994) with both false-positive and false-negative findings.

Due to the superior tissue contrast of magnetic resonance imaging, vessels can be delineated from surrounding mediastinal structures without any contrast agents as a result of the black-blood effect. In case of slow flow, however, inflowing blood might still contribute to the signal within the plane, giving the false impression of a thrombosed vessel or solid structure such as a lymph node. With the introduction of fast time-resolved three-dimensional contrast-enhanced MR angiography (3D-CE-MRA), these limitations can be overcome. Several studies have demonstrated the superiority of MRI for delineation of the extrapleural fat plane and detection of tumorous chest wall invasion, particularly on coronal scans (Manfredi et al. 1996). Sensitivity and specificity reach 90% (Padovani et al. 1993). MR imaging should be always performed for tumors with superior sulcus invasion. Invasion of pulmonary arteries and veins is well visualized on the individual 3D-CE-MRA scans (Schoenberg et al. 1998). Sometimes, atelectasis can be differentiated from the primary tumor by the different signal intensity on MR images (Kauczor and Kreitner 1999). These advantages are of importance since nowadays tumors with limited invasion of the pericardium, the mediastinal pleura and fat as well as infiltration of the vagal and phrenic nerve routinely undergo resection. Even advanced tumors with limited invasion of the left atrium or even the carina can be resected in selective cases (Mitchell et al. 1999; Shirakusa et al. 1998). However, the so-called desmoplastic reaction caused by tumor-induced proliferation of benign connective tissue adjacent to the tumor can result in an overestimation of the stage of the tumor (Webb et al. 1991). MR is advantageous for the delineation of the desmoplastic reaction due to the larger differences in signal intensity between the tumor and adjacent connective tissue. On the other hand, MR is inferior to CT for the assessment of endo-bronchial tumor growth due to the poorer spatial resolution and the signal loss in air-containing structures.

In conclusion, the sole use of CT alone is not sufficient for the accurate staging of borderline findings such as tracheal or mediastinal infiltration. In any case, multi-slice CT should be used to reformat the data set in multiple planes for the most accurate determination of the single longest tumor diameter according to the RECIST criteria. Compared to CT, MRI has various advantages for assessment of the T stage. Nevertheless, so far detection of mediastinal invasion has not proved to be superior compared to CT despite the better soft tissue contrast (Manfredi et al. 1996; Webb et al. 1985).

42.2.2 N Stage

Staging of lymph nodes still remains a major challenge to cross-sectional imaging since only 10% to 15% of all patients are found to be stage I, and thus do not reveal any metastatic lymph nodes. Complete resection of these nodes improves the prognosis of the patient (Keller et al. 2000). The key to the accurate staging and resection of lymph nodes is the correct localization of theses nodes along anatomic structures (Mountain and Dresler 1997). Standardized lymph nodes maps should be used to correlate the location of an enlarged lymph node in CT, mediastinoscopy and bronchoscopy; however, not all

enlarged lymph nodes seen on CT can be reached by mediastinoscopy or bronchoscopy. Accuracy of lymph node staging with CT is only moderate with substantial differences in the reported accuracies ranging from 40% to 90% and high interobserver variability (Kiyono et al. 1988). The upper limit of normal lymph node size varies with their position between 10 mm and 12 mm (Guyatt et al. 1995). In addition, metastatic spread can skip regional lymph nodes, thus giving the wrong impression of an N0 stage. The main problem arises from the fact that the criterion of lymph node size has only limited value for the assessment of lymph node metastases. However, even nodes smaller than 10 mm may be affected by metastatic spread. On the other hand, lymph nodes larger than 10 mm may be inflammatory. Thus, the cut-off value of 10 mm for differentiation between normal and metastatic nodes has only an accuracy of 70% to 80% (Dales et al. 1990; Kernstine et al. 1999). With an increasing stage of the primary tumor, the sensitivity for detection of enlarged lymph nodes increases, while the specificity decreases due to benign inflammatory nodes. The negative predictive value of CT for the presence of enlarged lymph nodes is high, thus the predominant role of CT is to exclude metastatic nodes and to confirm an N0 stage. A negative CT scan avoids mediastinoscopy with similar results at surgery (Daly et al. 1993). Another established role is the confirmation of massively enlarged lymph nodes in the N3 position, which usually is considered inoperable.

So far, MR is considered equal to CT for the staging of lymph nodes despite the fact, that different criteria other than size were assessed for differentiation of benign from metastatic nodes. Differentiation by means of different T1 relaxation times or gadolinium-chelate enhancement had only moderate success (Laissy et al. 1994). MR-compatible superparamagnetic iron-oxide contrast agents (USPIO = ultrasmall superparamagnetic iron oxide) are cleared from the blood by normal lymph nodes with subsequent signal loss in the node. Metastatic nodes show a much smaller signal loss due to fewer uptakes. Although remarkable results with accuracy of 85% have been reported in one study, the same authors reported only a sensitivity of less than 70% for nodes smaller than 15 mm due to the limited spatial resolution of the sequences used (Nguyen et al. 1999). Other authors found lower specificities due to overlap of the signal characteristics between benign and metastatic nodes (Pannu et al. 2000). Therefore, at the moment, particularly marginally enlarged lymph nodes in the N3-position need to be confirmed by mediastinoscopy or positron-emission tomography (PET), respectively PET-CT. Several studies have reported sensitivities and specificities for PET exceeding 85% (Schmidt et al. 2004; Wahl et al. 1994). If the functional information of PET is combined with the morphologic information from CT, the overall accuracy can be further increased to over 90% (Vansteenkiste et al. 1998). This trend is further enhanced by modern PET-CT systems, combining even multi-ring PET and multi-slice CT within one single scanner. Due to the high negative predictive value of over 95%, some authors advocate abandoning the need for mediastinoscopy in cases of a normal PET.

42.2.3 M Stage

Staging of distant metastases is of pivotal importance for adequate patient management since 40% of all patients with newly diagnosed bronchial carcinoma already have distant metastases (Boring et al. 1992), 25% of which are outside the thorax, predominately hepatic, adrenal, osseous and intracranial (Sider and Horejs 1988). Patients with stage-T3 tumors, patients with metastatic nodes in N2-position as well as patients with adenocarcinoma and poorly differentiated carcinomas have a higher risk of distant metastases even in the face of negative lymph nodes (Sider and Horejs 1988; Salvatierra et al. 1990). Another indication for extra-thoracic tumor staging holds true for patients with a high morbidity from other underlying diseases for whom the presence of distant metastases would avoid the risk from perioperative mortality. Due to the speed of multi-slice CT, local staging of the primary tumor is often completed with imaging of the entire abdomen, pelvis, and cranium using a slice thickness of less than of equal to 3 mm.

For the individual organs such as the adrenal glands, CNS, and liver, MRI is already considered superior to CT. Special fat-suppressing techniques, so-called in-phase/out-of-phase imaging, allow the subtraction of fatty components within the organ tissue. This has been successfully used to differentiate benign, fat-containing adrenal adenomas from carcinomas (Reinig et al. 1994). MR is the modality of choice to exclude intracranial metastases and is more sensitive than CT. This is particularly important for stage-IIIA patients where even the smallest brain metastases need to be excluded before a risky operation is performed. Opti-

mized imaging strategies with sensitive MR sequences such as fat-suppressed short-tau inversion-recovery (STIR) techniques allow a whole-body staging with equal results compared to standard, clinically used staging procedures that involve multiple modalities (Schmidt et al. 2004). For staging of metastasis, MRI is in competition to FDG-PET, for which the results are extremely good. Prospectively designed studies could show a correct change of the M-stage in 10% of all cases compared to a conventional metastasis search, thus directly influencing therapeutic management (Bury et al. 1996). Unexpected metastases were found in 10% of cases, whereas 10% to 20% of false-positive CT findings were down-staged to M0 (Dietlein et al. 2000; Valk et al. 1995). This change of therapeutic management was found to be cost-effective (Dietlein et al. 2000). In the future, whole-body MRI maybe a competitive technique for systemic metastases screening with fewer upfront costs (Schmidt et al. 2004, 2004). Recent data with dedicated whole-body MRI scanners report almost equal results for metastases screening compared to PET-CT (Schmidt et al. 2004; Antoch et al. 2003).

42.3 Role of Parallel-Imaging Techniques

Image quality of MRI used to be degraded by poorer spatial resolution and long scan times resulting in artefacts from respiratory and cardiac motion. In addition, the scan set-up and re-positioning of the patient in dedicated coils was time-intensive in the past. The flexibility of the MRI systems has changed dramatically within the last 5 years. Techniques of cardiac and respiratory gating can be now routinely applied. Multi-channel MRI systems featuring numerous flexible surface coil systems combined with automated table movement allow covering large areas of the body with maximum signal-to-noise ratio. Faster gradient systems reduce three-dimensional acquisitions to a single breath-hold while maintaining high spatial resolution. All these advances are further enhanced with the introduction of parallel-imaging techniques. In particular, this refers to increases in temporal and spatial resolution, reduction of signal decay from air-filled structures, decrease of blurring in single-shot acquisitions, and reduction of overall acquisition time. In addition, anatomic coverage can be substantially expanded.

42.3.1 Increase of Temporal and Spatial Resolution

During bolus-injection of gadolinium chelates, the pulmonary arteries and veins can be assessed along with the pulmonary perfusion and the systemic vascular supply of the lung, a technique also known as multiphasic time-resolved 3D contrast-enhanced MR angiography (TR-3D-CE-MRA). Compression of vessels or tumor invasion is also reliably seen (Schoenberg et al. 1998). Analysis of the time-resolved 3D MRA data sets allows detecting perfusion defects. In addition, tumor feeding vessels arising from systemic vessels such as bronchial arteries are also seen in later phases of the contrast media transit. The use of parallel imaging allows increasing temporal resolution while preserving spatial resolution. The scan time for an individual time frame of TR-3D-CE-MRA can be decreased to 1.2 s despite a spatial resolution 1.6×3.0×4.0 mm³ if a parallel-imaging acceleration factor of R=2 in combination with the GRAPPA algorithm is applied (Nikolaou et al. 2004). Even higher temporal and spatial resolution can be achieved when parallel imaging is combined with view-sharing techniques, a technique known as TREAT (time-resolved echo-shared angiographic technique) (Fink et al. 2005).

Besides separate visualization of arteries and veins, qualitative as well as quantitative assessment of pulmonary perfusion is feasible. For qualitative assessment, the TR-3D-CE-MRA data sets can be evaluated for segmental and lobar perfusion defects. In addition, the ratio of the relative perfusion between the lung affected by the tumor and the contralateral side can be visually assessed. Data from one study shows that perfusion deficits resulting from tumor infiltration of the lobar or segmental pulmonary arteries can be identified with good correlation to perfusion scintigraphy (Fink et al. 2004). This was confirmed by our own results from a pilot study on patients with central NSCLC (Schoenberg et al. 2005). In addition, tumor infiltration of the lung can be differentiated from atelectasis as the latter reveals a delayed hyper-enhancement on the time-resolved images (Fig. 42.1).

Quantitative perfusion can be calculated based on a single-compartment model. One study of healthy volunteers yielded mean values for the upper lung zones of 7.1±2.3 ml/100 ml for regional blood volume (RBV) and 197±97 ml/min/100 ml for regional blood flow (RBF) and for lower lung zones, 12.5±3.9 ml/100 ml for RBV and 382±111 ml/min/

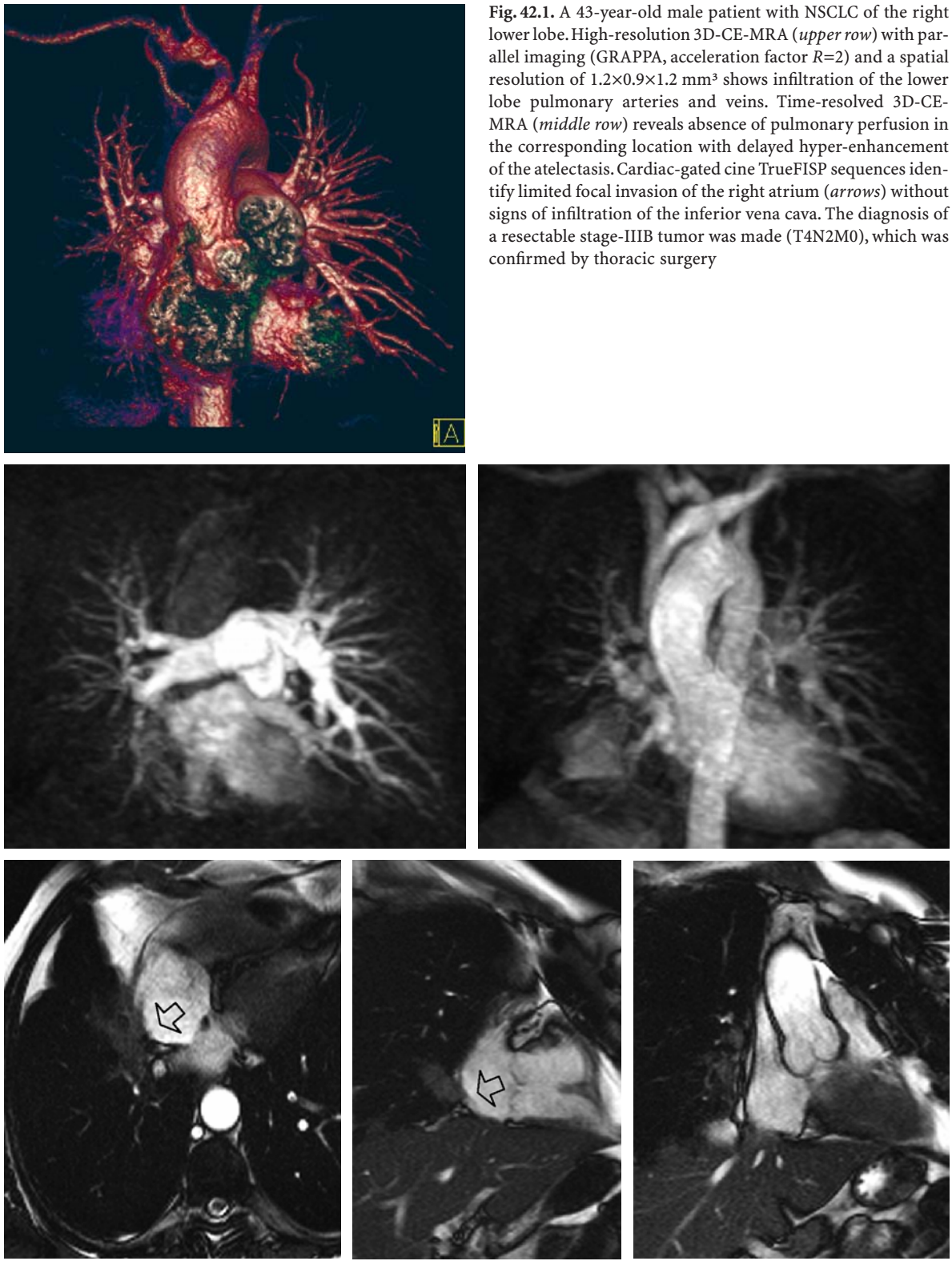

Fig. 42.1. A 43-year-old male patient with NSCLC of the right lower lobe. High-resolution 3D-CE-MRA (*upper row*) with parallel imaging (GRAPPA, acceleration factor *R*=2) and a spatial resolution of 1.2×0.9×1.2 mm³ shows infiltration of the lower lobe pulmonary arteries and veins. Time-resolved 3D-CE-MRA (*middle row*) reveals absence of pulmonary perfusion in the corresponding location with delayed hyper-enhancement of the atelectasis. Cardiac-gated cine TrueFISP sequences identify limited focal invasion of the right atrium (*arrows*) without signs of infiltration of the inferior vena cava. The diagnosis of a resectable stage-IIIB tumor was made (T4N2M0), which was confirmed by thoracic surgery

100 ml for RBF (Nikolaou et al. 2004). These results are in good agreement with reference data from the literature. However, so far, these data have only been verified in volunteer studies.

In regard to high-resolution 3D-CE-MRA, a further gain in spatial resolution is possible with the use of parallel imaging. By application of GRAPPA with an acceleration factor of R=3, the entire pulmonary vasculature can be imaged with a spatial resolution close to 1 mm^3 within a single breath-hold of approximately 20 s (Fig. 42.2).

42.3.2 Reduction of Signal Decay and Blurring in Single-Shot Acquisitions

In theory, single-shot turbo-spin-echo sequences such as HASTE are well suited for imaging the lung since the acquisition of a single slice is completed within a scan time of less than 1 s. This substantially reduces artefacts from cardiac motion or incomplete breath-holds. A disadvantage of this type of sequence is the presence of blurring as a result of long echo trains and off-resonances, which reduces the anatomic delineation of mediastinal structures. In addition, the signal decay due to short T2* relaxation times still substantially reduces the visualization of pulmonary parenchyma. Shortening of the echo trains by parallel imaging improves these limitations to a large degree (Fig. 42.2); cf. also Chap. 10. Small satellite metastases with a size of more than 8 mm can be reliably detected (Fig. 42.3). It is important to locate these metastases on axial, sagittal, and coronal images in order to differentiate lesions within the same lobe (tumor stage T4) from those in abutting lobes (tumor stage M1). Small atelectases resulting from proximal tumor occlusion of bronchi can also be reliably detected.

42.3.3 Reduction of Acquisition Time

Besides assessment of perfusion, MRI is capable of determining pulmonary ventilation. However, this initially required the technically demanding hyperpolarization of helium-3 with the drawback of limited availability (Bock 1997). A much easier promising approach is the use of oxygen-enhanced MR imaging as a surrogate for assessment of ventilation and diffusion (Loffler et al. 2000). So far, the use of this technique was time-intensive, technically demanding and not robust enough for clinical application since the complex sequence scheme required low heart rates and long breathing cycles for adequate cardiac and respiratory gating. With the implementation of parallel imaging, the time for read-out of the MR signal can be substantially decreased, allowing the application of this technique also in patients with fast heart rates and short end-expiratory plateaus (Dietrich et al. 2005); cf. Chap. 38. Although oxygen-enhanced MRI represents a mixture of ventilation, diffusion, and perfusion by detecting the signal of molecular oxygen dissolving in blood, the technique shows good agreement to ventilation scintigraphy (Schoenberg et al. 2005). In cases of complete tumor occlusion of the bronchus in a dependent lung segment or lobe, an absence of signal is noted, while in those cases with a patent bronchus but occluded pulmonary arterial supply, the oxygen signal is preserved (Fig. 42.2). In animal studies of oxygen-enhanced MRI, it was shown that the signal component from ventilation overweighs those of diffusion and perfusion (Keilholz et al. 2002).

Another important field for which reduction of the acquisition time is of key importance is cardiac imaging. Due to improvements of surgical techniques, tumors with focal invasion of the left or right atrium can still undergo resection, whereas those with massive infiltration of the orifices of several pulmonary

Fig. 42.2. A 54-year-old male with a non-resectable stage-IIIB (T4N2M0) NSCLC. On the coronal HASTE sequence with shortened echo train by parallel imaging (external reference scan, GRAPPA, R=2), a large mediastinal invasion of the tumor to the contralateral side is noted (*arrow*). This is confirmed on the sagittal HASTE images (second row) on which the tumor growth along the right upper lobe bronchus and left main stem bronchus into the mediastinum in between the trachea and the large vessels can be clearly identified due to the excellent tissue contrast between the tumor, the fat and the black-blood signal void of the vessels. Also note the sharp delineation of the anatomic structures due to reduced blurring in the images as a result of parallel imaging. No invasion of the bronchi is visible; even the upper lobe bronchus can be clearly delineated surrounded by tumor growth. The color-coded parameter maps of the oxygen-enhanced inversion-recovery HASTE sequence (*third row*) show preserved ventilation in all lung lobes including the right upper lobe. However, the arterial phase of the time-resolved 3D-CE-MRA scan (*lower row*, *left*) demonstrates a lack of perfusion in the right upper lobe due to complete occlusion of the right upper pulmonary artery (*arrow*) by the tumor confirmed on the high-resolution 3D-CE-MRA image (*lower row*, *right*). The combination of oxygen-enhanced MRI and time-resolved MRA correctly identified the ventilation/perfusion mismatch

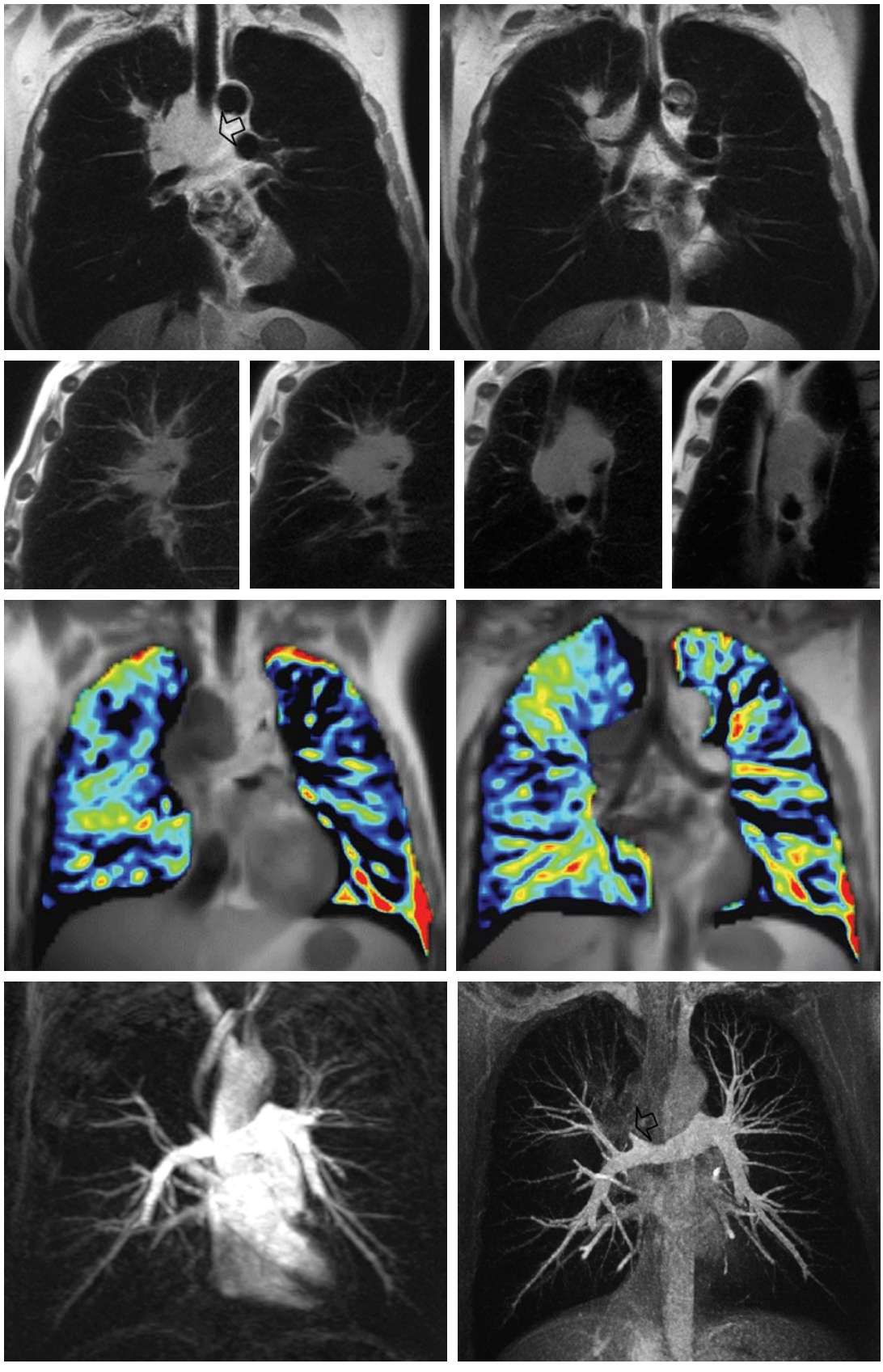

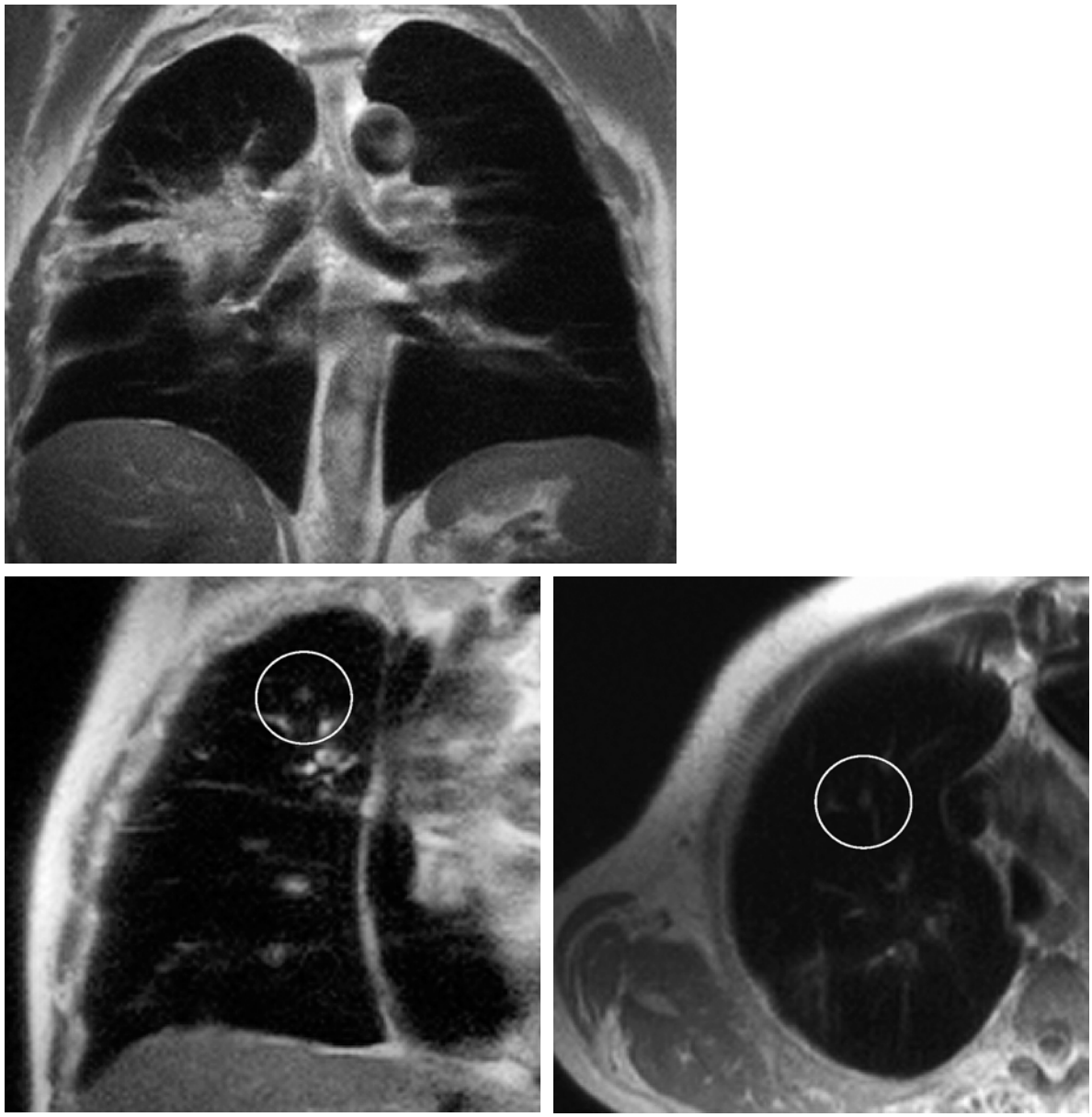

Fig. 42.3. A 56-year-old male with a resectable stage-IIIB NSCLC (T4N2M0). Besides the centrally growing large tumor of the right upper lobe, a small 8-mm metastasis is clearly identified on the HASTE images with parallel imaging (external reference scan, GRAPPA, *R*=2). In the two perpendicular orientations the lesion can be located in the same lobe, consistent with a T4 stage

veins or infiltration of the ventricle are not amenable to surgery. The relationship between the tumor and the adjacent myocardium can be displayed in high detail with time-resolved ECG-gated cine TrueFISP imaging (Fig. 42.1). Without the use of parallel imaging, this approach is time-intensive since only one slice is acquired per breath-hold. It therefore takes total scan times in the order of 10 to 15 min in order to display the complex relationship between the tumor, the heart, and the large vessels of the mediastinum in multiple angulations. The introduction of TSENSE into clinical routine for cardiac MRI allows acquiring four to five slices within a single breath-hold without a noticeable loss of image quality if specially designed multi-channel coils are used (Wintersperger et al. 2006). The total scan time thus can be reduced to less than 5 min for time-resolved evaluation of tumor infiltration in two perpendicular imaging planes.

42.3.4 Increase of Anatomic Coverage

The introduction of multi-channel whole-body MRI systems in combination with highly accelerated parallel imaging allows accurate screening of metastasis with very good agreement to PET-CT. For metastatic involvement of the liver and adrenal glands, bones and central nervous systems, equal or even superior results have been found with sensitivities and specificities exceeding 95% (cf. Chap. 41) (Schmidt et al. 2005). Since metastatic disease in NSCLC most frequently involves these target organs, whole-body MRI with parallel imaging is expected to gain an increasing role for staging of this tumor entity. While at the moment whole-body screening for metastasis by itself requires total scan times of 50 min, further improvements in coil design might enable higher scan acceleration with parallel-imaging factors beyond 3 and thus allow integrating this approach into the MRI scan for local tumor staging.

42.4 Conclusion

The combination of fast T1-weighted and T2-weighted imaging, cardiac MRI, MR angiography, oxygen-enhanced MRI, and perfusion MRI offers a comprehensive, non-invasive, morphologic, and functional assessment of lung cancer (Kauczor and Kreitner 2000). Parallel-imaging techniques improve image quality, robustness, and acquisition speed of this approach, which therefore represents an attractive alternative to a step-wise multi-modality algorithm of multi-slice CT and nuclear-medicine studies for assessment of the operability and resectability of centrally growing advanced tumors.

References

Antoch G et al (2003) Whole-body dual-modality PET/CT and whole-body MRI for tumor staging in oncology. JAMA 290:3199–3206

Bock M (1997) Simultaneous T2* and diffusion measurements with 3He. Magn Reson Med 38:890–895

Boring CC, Squires TS, Tong T (1992) Cancer statistics, 1992. CA Cancer J Clin 42:19–38

Bury T et al (1996) Staging of non-small-cell lung cancer by whole-body fluorine-18 deoxyglucose positron emission tomography. Eur J Nucl Med 23:204–206

Dales RE, Stark RM, Raman S (1990) Computed tomography to stage lung cancer. Approaching a controversy using meta-analysis. Am Rev Respir Dis 141 (5 Pt 1):1096–1101

Daly BD et al (1993) N2 lung cancer: outcome in patients with false-negative computed tomographic scans of the chest. J Thorac Cardiovasc Surg 105:904–910; discussion 910–911

Dietlein M et al (2000) Cost-effectiveness of FDG-PET for the management of potentially operable non-small cell lung cancer: priority for a PET-based strategy after nodal-negative CT results. Eur J Nucl Med 27:1598–1609

Dietrich O et al (2005) Fast oxygen-enhanced multislice imaging of the lung using parallel acquisition techniques. Magn Reson Med 53:1317–1325

Fink C et al (2004) Regional lung perfusion: assessment with partially parallel three-dimensional MR imaging. Radiology 231:175–184

Fink C et al (2005) Time-resolved contrast-enhanced three-dimensional magnetic resonance angiography of the chest: combination of parallel imaging with view sharing (TREAT). Invest Radiol 40:40–48

Grandy M (2001) Multislice-CT of patients with stage IIIa bronchial carcinoma for monitoring of neoadjuvant chemotherapy and presurgical evaluation. In: European Congress of Radiology, Vienna

Guyatt GH et al (1995) Interobserver variation in the computed tomographic evaluation of mediastinal lymph node size in patients with potentially resectable lung cancer. Canadian Lung Oncology Group. Chest 107:116–119

Herman SJ et al (1994) Mediastinal invasion by bronchogenic carcinoma: CT signs. Radiology 190:841–846

Herth F, Becker HD (2000) Endobronchial ultrasound of the airways and the mediastinum. Monaldi Arch Chest Dis 55:36–44

Kauczor HU, Kreitner KF (1999) MRI of the pulmonary parenchyma. Eur Radiol 9:1755–1764

Kauczor HU, Kreitner KF (2000) Contrast-enhanced MRI of the lung. Eur J Radiol 34:196–207

Keilholz SD, Knight-Scott J, Mata J, Fujiwara N, Altes TA, Berr SS, Hagspiel K (2002) The contributions of ventilation and perfusion in oxygen-enhanced pulmonary MR imaging: results from rabbit models of pulmonary embolism and bronchial obstruction. Proc Intl Soc Mag Reson Med 10:409

Keller SM et al (2000) Mediastinal lymph node dissection improves survival in patients with stages II and IIIa non-small cell lung cancer. Eastern Cooperative Oncology Group. Ann Thorac Surg 70:358-365; discussion 365–366

Kernstine KH et al (1999) PET, CT, and MRI with Combidex for mediastinal staging in non-small cell lung carcinoma. Ann Thorac Surg 68:1022–1028

Kiyono K et al (1988) The number and size of normal mediastinal lymph nodes: a postmortem study. AJR Am J Roentgenol 150:771–776

Laissy JP et al (1994) Enlarged mediastinal lymph nodes in bronchogenic carcinoma: assessment with dynamic contrast-enhanced MR imaging. Work in progress. Radiology 191:263–267

Libshitz HI (1990) Computed tomography in bronchogenic carcinoma. Semin Roentgenol 25:64–72
Loffler R et al (2000) Optimization and evaluation of the signal intensity change in multisection oxygen-enhanced MR lung imaging. Magn Reson Med 43:860–866
Manfredi R et al (1996) Accuracy of computed tomography and magnetic resonance imaging in staging bronchogenic carcinoma. Magma 4:257–262
Mitchell JD et al (1999) Clinical experience with carinal resection. J Thorac Cardiovasc Surg 117:39-52; discussion 52–53
Mountain CF (1997) Revisions in the International System for Staging Lung Cancer. Chest 111:1710–1717
Mountain CF, Dresler CM (1997) Regional lymph node classification for lung cancer staging. Chest 111:1718–1723
Murata K et al (1994) Chest wall and mediastinal invasion by lung cancer: evaluation with multisection expiratory dynamic CT. Radiology 191:251–255
Nguyen BC et al (1999) Multicenter clinical trial of ultrasmall superparamagnetic iron oxide in the evaluation of mediastinal lymph nodes in patients with primary lung carcinoma. J Magn Reson Imaging 10:468–473
Nikolaou K et al (2004) Quantification of pulmonary blood flow and volume in healthy volunteers by dynamic contrast-enhanced magnetic resonance imaging using a parallel imaging technique. Invest Radiol 39:537–545
Padovani B et al (1993) Chest wall invasion by bronchogenic carcinoma: evaluation with MR imaging. Radiology 187:33–38
Pannu HK et al (2000) MR imaging of mediastinal lymph nodes: evaluation using a superparamagnetic contrast agent. J Magn Reson Imaging 12:899–904
Pearlberg JL et al (1987) Limitations of CT in evaluation of neoplasms involving chest wall. J Comput Assist Tomogr 11:290–293
Reinig JW et al (1994) Differentiation of adrenal masses with MR imaging: comparison of techniques. Radiology 192:41–46
Salvatierra A et al (1990) Extrathoracic staging of bronchogenic carcinoma. Chest 97:1052–1058
Schmidt GP et al (2004) [Comparison of high resolution whole-body MRI using parallel imaging and PET-CT. First experiences with a 32-channel MRI system]. Radiologe 44:889–898
Schmidt GP et al (2004) [Whole-body MRI and PET/CT in tumor diagnosis.]. Radiologe 44:1079–1087
Schmidt GP et al (2005) High-resolution whole-body magnetic resonance image tumor staging with the use of parallel imaging versus dual-modality positron emission tomography-computed tomography: experience on a 32-channel system. Invest Radiol 40:743–753
Schoenberg SO (2005) Comprehensive pulmonary MR imaging in patients with bronchial carcinoma using parallel acquisition techniques. In: European Congress of Radiology, Vienna
Schoenberg SO et al [Ultrafast MRI phlebography of the lungs]. Radiologe 38:597–605
Scott IR et al (1988) Resectable stage III lung cancer: CT, surgical, and pathologic correlation. Radiology 166(1 Pt 1):75–79
Shirakusa T et al(1998) Extended operation for T4 lung carcinoma. Ann Thorac Cardiovasc Surg 4:110–118
Sider L, Horejs D (1988) Frequency of extrathoracic metastases from bronchogenic carcinoma in patients with normal-sized hilar and mediastinal lymph nodes on CT. AJR Am J Roentgenol 151:893–895
Valk PE et al (1995) Staging non-small cell lung cancer by whole-body positron emission tomographic imaging. Ann Thorac Surg 60:1573–1581; discussion 1581–1582
Vansteenkiste JF et al (1998) FDG-PET scan in potentially operable non-small cell lung cancer: do anatometabolic PET-CT fusion images improve the localisation of regional lymph node metastases? The Leuven Lung Cancer Group. Eur J Nucl Med 25:1495–1501
Wahl RL et al (1994) Staging of mediastinal non-small cell lung cancer with FDG PET, CT, and fusion images: preliminary prospective evaluation. Radiology 191:371–377
Webb WR et al (1985) Bronchogenic carcinoma: staging with MR compared with staging with CT and surgery. Radiology 156:117–124
Webb WR et al (1991) CT and MR imaging in staging non-small cell bronchogenic carcinoma: report of the Radiologic Diagnostic Oncology Group. Radiology 178:705–713
Wintersperger BJ et al (2006) Cardiac CINE MR imaging with a 32-channel cardiac coil and parallel imaging: impact of acceleration factors on image quality and volumetric accuracy. J Magn Reson Imaging 23:222–227

Imaging of Pulmonary Hypertension

43

Konstantin Nikolaou and Armin Huber

CONTENTS

K. Nikolaou, MD; A. Huber, MD
Department of Clinical Radiology, University Hospitals – Grosshadern, Ludwig Maximilian University of Munich, Marchioninistr. 15, 81377 Munich, Germany

43.1 Clinical Background

Pulmonary hypertension (PH) is a devastating disease characterized by the progressive elevation of pulmonary artery pressure leading to right ventricular failure and eventually death. However, it is not a single disease entity, but a common clinical end point for a host of diseases that are still being actively investigated. Traditionally, pulmonary hypertension was classified into primary pulmonary hypertension (PPH) and secondary pulmonary hypertension (SPH). The major difference between these two groups of patients is that patients with SPH have a clear etiology or associated underlying disorder, which directly leads to elevated pulmonary artery pressure, while those with PPH are seemingly without a clear underlying cause. A newer, clinically more useful, treatment-based classification of pulmonary hypertension was put forth by a team of experts in the World Health Organization (WHO) meeting on the diagnostic classification of pulmonary hypertension in 1998 (Rich 1998). Five categories of pulmonary hypertension were recognized, including primary pulmonary arterial hypertension, pulmonary venous hypertension, pulmonary hypertension associated with disorders of the respiratory system and/or hypoxemia, pulmonary hypertension due to chronic thrombotic and/or embolic diseases, and pulmonary hypertension due to disorders directly affecting the pulmonary vasculature. The pathobiology of PPH includes endothelial and smooth muscle cell dysfunction, abnormal activation and release of vasoactive mediators, vascular remodeling, microvascular thrombosis, increased proinflammatory cytokines and abnormal ion channels (Loscalzo 2001). Recurrent pulmonary thromboembolism is one of the secondary etiologies leading to PH, classified as chronic thromboembolic pulmonary arterial hypertension (CTEPH), and may be treated surgically (Fedullo et al. 2001), whereas PPH is typically treated using vasodilating drugs (Rich 2000). Comprehensive workup to differentiate the various etiologies of pulmonary hyperten-

sion and especially CTEPH typically requires a series of clinical examinations and imaging procedures. However, because treatment of CTEPH differs significantly from other causes of pulmonary hypertension, an accurate diagnosis is essential.

The use of MRI in the assessment of cardiovascular diseases is a rapidly growing field. However, detection of chronic occlusive and non-occlusive changes of the pulmonary arteries at a segmental or subsegmental level requires high spatial resolution, which is limited by the scan time of a single breath-hold. Another relatively new potential clinical application of MRI in the diagnostic workup of PH has been the assessment of right-ventricular (RV) dysfunction. Recently, parallel-imaging techniques have become widely available. With implementation of parallel imaging, the temporal and spatial resolution of MR angiographic techniques and cardiac MR can be improved substantially (Griswold et al. 2002), giving magnetic resonance imaging an important role in the comprehensive assessment of the pulmonary circulation and consecutive right-heart changes.

43.2 Methods

43.2.1 MR Angiography and MR Perfusion Imaging with Parallel Acquisition Techniques

43.2.1.1 High-Spatial-Resolution Magnetic Resonance Angiography

Pulmonary MR angiography has been reported to have a high sensitivity and specificity in the diagnosis of acute PE without the need for ionizing radiation or iodinated contrast material (Meaney et al. 1997; Stein et al. 2003). Oudkerk et al. (2002) have reported an excellent sensitivity of MRA in the diagnosis of pulmonary embolism. It could be shown that maximized spatial resolution of MRA is necessary for a reliable diagnosis. To achieve this goal, Oudkerk et al. (2002) used a double-bolus injection protocol and a small field of view with sagittal orientation of the 3D slabs to depict both lungs with a high, sub-millimeter spatial resolution while maintaining a sufficient signal-to-noise ratio. With parallel imaging, a similarly high spatial resolution can be achieved, applying only one contrast injection for MR angiography and covering both lungs with a larger field of view and coronal orientations of the 3D slab; cf. also Chap. 28. This way, a nearly isotropic voxel size of $1.0\times0.7\times1.6\ mm^3$ can be realized (Table 43.1). This should result in a higher overall accuracy of pulmonary MRA for detection of occlusive and non-occlusive changes of the pulmonary arteries as compared to conventional MRA techniques. However, the usefulness of MRA as a sole modality in the diagnostic workup of pulmonary diseases other than PE has not been studied extensively.

43.2.1.2 Magnetic Resonance Perfusion Imaging

MR perfusion imaging might add additional valuable information in the clinical workup of PH, such as demonstration of the exact extent of perfusion defects, and could increase diagnostic accuracy in the differentiation of various PH etiologies, depending on specific patterns of perfusion defects (Fink et al. 2003). First studies on time-resolved, dynamic imaging of the pulmonary circulation have shown promising results (Sonnet et al. 2002). MRI of lung perfusion is realized by rapid imaging of the first pass of contrast material through the lungs after bolus injection into a peripheral vein. Despite substantial improvements of the gradient technique over the past few years, the 3D imaging techniques used have been limited with regard to spatial and temporal resolution (Matsuoka et al. 2002). However, a sufficient temporal resolution is critical in visualizing peak enhancement of the lungs, since the transit time of a contrast bolus through the lungs usually ranges between 3 and 4 s (Fishman 1963). Compared to applications of conventional MRI sequences, parallel-imaging techniques only acquire a fraction of the phase-encoding lines and reconstruct the missing information to a full field-of-view image using the inherent spatial encoding of the different receiver coils (Dietrich et al. 2002); cf. Chap. 2. This way, a temporal resolution of about 1 s per phase can be obtained (Table 43.1). Still, as breath-hold times can add up to 20 to 25 s to acquire a sufficient number of datasets, the readout scheme of MR perfusion scans should be centrically re-ordered. By this type of data acquisition, the central lines of the k-space are read out at the beginning of the scan, attributing to sufficient contrast of the image, and peripheral lines of the k-space are read out towards the end of the scan, attributing to high-resolution data of the images.

To maintain a sufficient signal-to-noise ratio in spite of an improved spatial resolution, the bolus timing has to be optimized. To achieve a sharp bolus

Table 43.1. Comparison of acquisition parameters of MR angiography and MR perfusion imaging with and without parallel imaging

	MR angiography		MR perfusion	
	Without parallel imaging	With parallel imaging	Without parallel imaging	With parallel imaging
TR/TE (ms)	3.3/1.2	2.9/1.2	1.7/0.7	1.7/0.6
Spatial resolution (mm^3)	1.4×0.7×2.0	1.0×0.7×1.6	2.9×1.5×5.0	2.9×1.5×4.0
Slice thickness (mm)	2.0	1.6	5.0	4.0
Number of slices	64	88	16	24
Slab thickness (mm)	128	144	80	96
Number of phases	1	1	24	25
Acquisition time per phase (s)	21	22	1.2	1.1
Total acquisition time(s)	21	22	29	28

[Modified from (Nikolaou et al. 2005), with permission]

profile of the perfusion study, a high injection rate of contrast, e.g., 5 ml/s, should be used. A further improvement of signal-to-noise ratio can be gained from the use of contrast agents with higher relaxivity, either due to a higher gadolinium concentration (Gadobutrol, 1.0 mol/l) (Tombach and Heindel 2002), or due to weakly or strongly protein-binding substances (e.g., Gadobenate Dimeglumine, Multihance, Bracco, Italy, or Gadovosveset Trisodium, Vasovist, Schering AG, Germany). Finally, MRI of lung perfusion has various advantages. Three-dimensional MRI offers a higher spatial resolution and better anatomic information than radionuclide perfusion scintigraphy and offers the advantage of reconstructing the data in any desired imaging plane. Additionally, MRI lacks any radiation exposure.

43.2.1.3 Pulmonary MRA and MR Perfusion: Protocol Parameters

In the following sections, typical protocol parameters for high-spatial-resolution MRA and MR perfusion imaging of the lung with parallel acquisition techniques are given. These protocol parameters have been implemented on a 1.5-T MR system with high-performance gradients (40 mT/m, 200 T/m/s slew rate, 200 µs rise time) and eight receiver channels (Magnetom Sonata Maestro Class, Siemens Medical Solutions, Erlangen, Germany). MR perfusion imaging has to be performed before MRA to avoid residual contrast in the pulmonary parenchyma after MRA. Table 43.1 gives a comprehensive overview of these protocol parameters compared to conventional MRA techniques.

MR Perfusion Protocol

Patients are positioned in the supine position, head first. A special 12-channel receiver coil, dedicated for parallel imaging, is used. Eight of the 12 receiver channels of this coil are combined in pairs of two to fit the eight receiver channels of the MR system. With this coil, the receiver channels are arranged circularly around the patient's chest to optimize the spatial sensitivity profiles of the receiver coils for parallel imaging. After initial localizer sequences, a test-bolus sequence is performed, injecting 2 ml of a 1.0-molar gadolinium-chelate gadobutrol (Gadovist, Schering AG, Berlin, Germany) at a flow rate of 5.0 ml/s, acquiring a series of coronal images of the right heart. For the dynamic perfusion study, an ultra-fast FLASH (fast low angle shot) gradient-echo sequence [repetition time (TR)/echo time (TE), 1.7 ms/0.6 ms; flip angle, 25°] with a generalized auto-calibrating partially parallel acquisition technique (GRAPPA, acceleration factor R=2) (Griswold et al. 2002) is applied. Further sequence parameters for the MR perfusion protocol are: readout bandwidth: 1,220 Hz/pixel; reference k-space lines (auto-calibration signals) for coil calibration: 24; slice thickness: 4.0 mm; partitions: 24; resulting slab thickness: 96 mm; acquisition matrix 133×256 (52% phase resolution); field of view: 400 mm, resulting in a spatial resolution of 1.6×3.0×4.0 mm^3; k-space readout scheme: centrically re-ordered. Acquisition time for one 3D data set of 24 slices is 1.1 s. A total of 25 slabs are acquired for each perfusion study, resulting in a total breath-hold time of 27.5 s (inspiration). Acquisition is started 4 s before the estimated arrival time of the contrast to acquire non-contrast-enhanced studies for subtraction purposes. Injections have to be performed

with a power-injection system, using a contrast-agent dosage of 0.1 mmol/kg body weight of gadobutrol followed by a saline flush of 25 ml. To ensure an optimized bolus profile, a high injection rate of 5.0 ml/s is used in combination with a 16-gauge intravenous catheter, which should be placed into an antecubital vein. For each phase (n=25), maximum intensity projections (MIP) of the subtracted data sets over all 24 slices are performed for three-dimensional display.

MR Angiography Protocol

To determine the exact circulation time of the contrast bolus from the injection site to the pulmonary arteries, the test-bolus study has to be repeated, as different flow rates of the contrast agent are used for the high-spatial-resolution angiography study. The second test bolus for MRA is performed applying identical sequence parameters, plane orientation and contrast agent (2.0 ml of gadobutrol), but using a flow rate of 2 ml/s to ensure a longer, more homogeneous contrast bolus for MRA. Subsequently, a breath-hold contrast-enhanced, three-dimensional FLASH study (TR/TE/flip angle: 2.9 ms/1.2 ms/25°) is performed in coronal slice orientation, using the same parallel imaging technique as for the MR perfusion study (GRAPPA, acceleration factor R=2). Further sequence parameters for the MRA protocol are: readout bandwidth: 650 Hz/pixel; reference k-space lines for coil calibration: 24; slice thickness: 1.6 mm; partitions: 88; resulting slab thickness: 141 mm; acquisition matrix: 410×512 (80% phase resolution); field of view: 400 mm, resulting in a spatial resolution of 1.0×0.7×1.6 mm^3. Acquisition time for one 3D data set of 88 slices is 22 s, acquired during breath-hold (inspiration); the k-space readout scheme is centrically re-ordered. Due to this asymmetric sequential read-out scheme of the k-space, acquisition is started 5 s before the estimated arrival time of the contrast bolus. A non-contrast-enhanced MRA dataset, which is acquired before any administration of contrast at the beginning of the examination, is subtracted from the contrast-enhanced images, and for image analysis, single coronal slices and MIP reconstruction of the complete dataset (88 slices) are stored.

43.2.2 Multi-planar Imaging of the Right Ventricle with Parallel Imaging

Right-ventricular hypertrophy and right-ventricular heart failure are commonly caused by pulmonary hypertension and are a major cause of death in this patient population. Accurate and reproducible assessment of right-ventricular function including ejection fraction as well as chamber volumes during end-diastole and end-systole is important to the care of these patients (Hunt 1997). However, exact right-ventricular volumes are not routinely obtained even in settings in which quantitative data are useful, partly due to the measurement inaccuracy of established modalities such as echocardiography (Bottini et al. 1995; Teichholz et al. 1976). While previous authors have validated the accuracy of cardiac MRI-derived volume and functional data (Bellenger et al. 2000), existing strategies can suffer from measurement variability and decreased clinical robustness in heart-failure patients (Grothues et al. 2002). Current techniques require ill, dyspneic patients to undertake multiple, prolonged breath holds in the exact same diaphragmatic position. They also collect and assemble data over multiple cardiac cycles, causing image degradation during arrhythmias. In addition, the process of complete volumetric imaging of the entire right ventricle (RV) and left ventricle (LV) can take as long as 10 to 15 min, during which time patient motion will compromise image quality and quantitative accuracy.

Current techniques are thus ill-suited for routine application in heart failure patients and have hampered the clinical utility of cardiac MRI. Recently, steady-state free precession (SSFP) sequences have been introduced to cardiac MR imaging (Thiele et al. 2001). While their increased signal-to-noise ratio and blood-to-myocardial contrast have improved image quality, the quantification of cardiac function continues to suffer from prolonged image acquisition times and the need for multiple breath-holds. The incorporation in faster, real-time imaging strategies has been hampered by the relative inefficiency of k-space sampling techniques, with resultant poor temporal and spatial resolution (Hori et al. 2003; Spuentrup et al. 2003). Some investigators have advocated combining real-time techniques with a free-breathing strategy to assess LV and RV volumes quantitatively. Narayan et al. (2005) suggested using a high-resolution spiral sequence that provides efficient k-space sampling for real-time imaging with SSFP. This strategy provides complete coverage of RV and LV function in a single breath hold by employing a multislice strategy in which one slice is imaged every heartbeat. This single-breath-hold strategy was assessed in 20 patients with congestive heart failure and validated with the gold standard: gated, segmented k-space, multiple-breath-hold acquisition. A good correlation for LV and RV parameters between the real-time technique and the segmented-k space technique was found.

An alternative method was used for real-time imaging of ten slices, one per RR cycle, during a single breath hold with sufficient temporal resolution: A shared-echo technique was combined was parallel imaging for improvement of temporal resolution with a time window per frame below 50 ms (Wintersperger et al. 2003). Results for the ventricular parameters EDV (r=0.93), ESV (r=0.99), SV (r=0.83), and EF (r=0.99) of real-time multi-slice SSFP imaging showed a high correlation with results of segmented SSFP acquisitions. Systematic differences between both techniques were statistically non-significant. Single-breath-hold multi-slice techniques using GRAPPA allow for improvement of temporal resolution and for accurate assessment of global ventricular functional parameters (Wintersperger et al. 2003).

This imaging technique can be used in a comprehensive evaluation of patients with pulmonary hypertension to image lung perfusion, lung arteries and the right heart within one examination. A complete coverage of the right and left ventricle can be achieved within one breath hold. With two breath holds, one stack of ten cine slices can be acquired in the short-axis orientation and a second stack of ten slices can be acquired in transverse orientation. Typical imaging parameters of a real-time cine technique including echo-sharing and parallel imaging are shown in Table 43.2. The quantitative assessment with post-processing software can be performed on the short-axis images; the transverse images allow for an additional visual evaluation of typical right-heart changes. Both the short-axis images and the transverse images allow detecting right-heart dilatation, hypertrophy of the myocardium, pathological movement of the septum – flattening or convex shape in relation to the left ventricle – and a jet into the right atrium caused by secondary regurgitation of the tricuspid valve.

Table 43.2. Typical imaging parameters of a real-time cine TrueFISP (GRAPPA, R=2, 12 reference lines) pulse sequence using parallel imaging and echo sharing for assessment of right heart function

TR	0.8 ms
TE	0.9 ms
Flip angle	50°
Temporal resolution	48 ms
Bandwidth	1,395 Hz/pixel
Field of view	350×265 mm²
Acquisition matrix	128×80
Spatial resolution	3.1×3.3 mm²
Slice thickness	8 mm
Inter-slice gap	2 mm

In addition to cine imaging, flow measurements can be carried out with a free-breathing technique to quantify the volume of secondary regurgitation of the tricuspid valve. A flow measurement with coverage of the pulmonary trunk and the ascending aorta can be used to exclude or detect intra- or extra-cardiac shunts and quantify the shunt volume, as the presence of vascular or cardiac shunts can be a reason for secondary pulmonary hypertension. Figure 43.1 demonstrates the diastolic and systolic cine images acquired with a real-time technique during a single breath-hold. With acquisition of one slice per breath-hold, a change of the respiratory position during the duration of the cine examination has a minor impact on image quality. The use of an averaging technique during free breathing for the velocity-encoded phase-contrast measurements in the position of the tricuspid valve and in a transverse orientation including the two large arteries, ascending aorta and pulmonary trunk, does not require breath-holding, and allows for reconstruction of images with adequate temporal resolution of 20 ms. The scan time per flow measurement with retrospective ECG gating is between 1 1/2–2 min. Figure 43.2 shows phase-contrast images of the tricuspid valve and the aorta and the pulmonary trunk.

43.3 Results

43.3.1 Differentiation of Primary and Secondary Pulmonary Hypertension with High-Resolution MRA and Perfusion Measurements Using Parallel Imaging

In the following sections, results from a pilot study are reported (Nikolaou et al. 2005). The purpose of this study was the assessment of a combined approach for the correct differentiation of PPH and CTEPH, subsequently performing time-resolved, dynamic MR perfusion imaging and MR angiography in one study with parallel-imaging techniques (using the protocol parameters given in Sect. 43.2.1.3). During this study, 29 consecutive patients (mean age, 55±16 years; 16 female patients, mean age 54±17 years; 13 male patients, mean age 57±15 years) with known pulmonary arterial hypertension were examined.

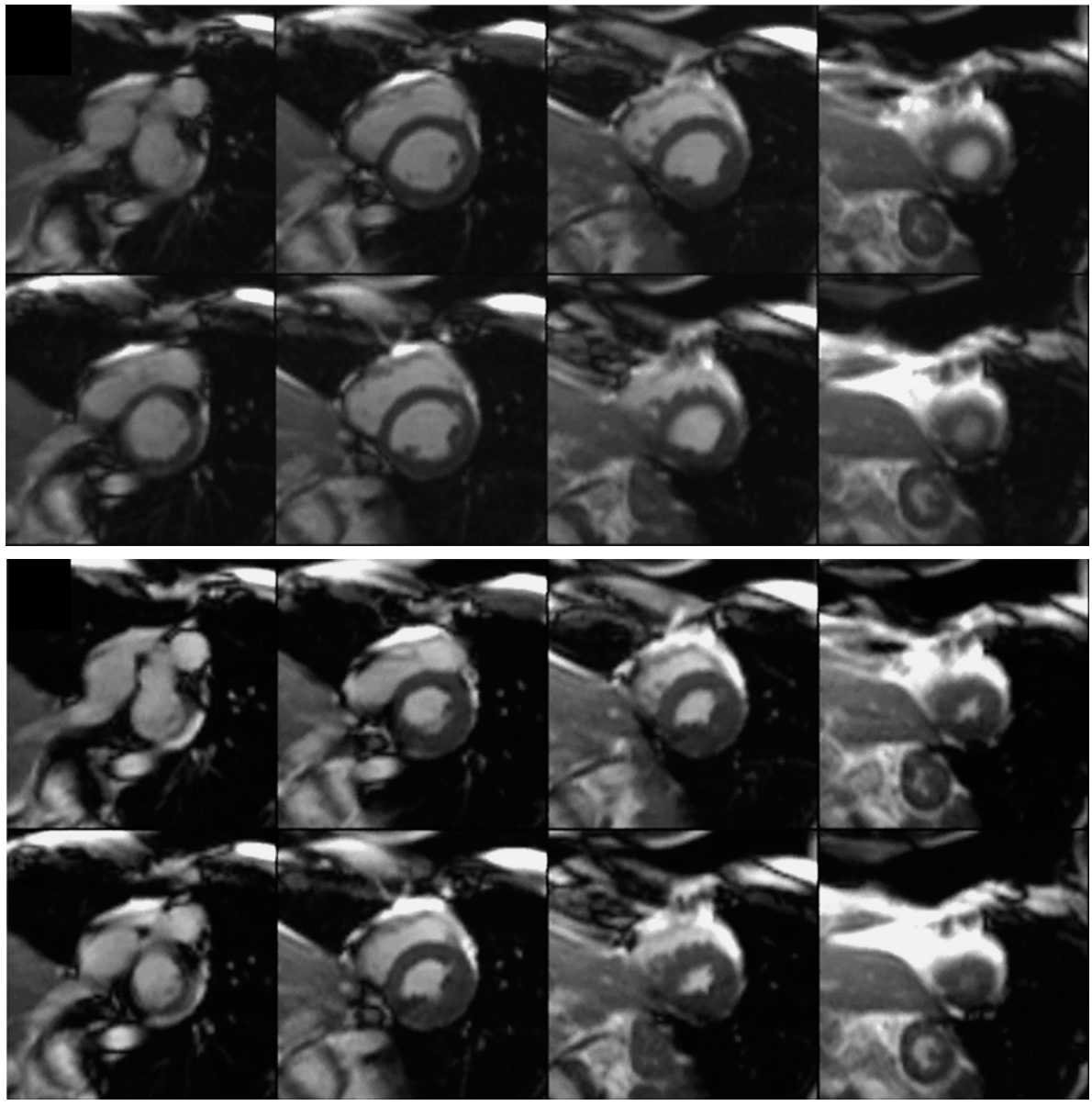

Fig. 43.1. a Eight cine images in a short-axis orientation acquired during the end-diastolic phase with a real-time SSFP pulse sequence. Ten slices can be acquired during a single breath hold with a temporal resolution of 47 ms using parallel imaging and shared-echo technique. **b** Eight cine images in a short-axis orientation acquired during the end-systolic phase with a real-time SSFP pulse sequence. Ten slices can be acquired during a single breath hold with a temporal resolution of 47 ms using parallel imaging and a shared-echo technique

43.3.1.1 Results of MR Angiography

Analysis of the MR angiographic images alone (without knowledge of the MR perfusion results) allowed differentiation of typical obstructive and non-obstructive imaging findings, as compared to digital subtraction angiography (DSA) and/or CT angiography (CTA) as reference modalities. Table 43.3 shows the diagnostic imaging criteria for MRA datasets, differentiating non-occluding and occluding imaging findings. For non-occlusive image criteria, MRA showed high sensitivities for changes of the central pulmonary arteries (dilated main stem, pruned tree, 100% and 94%, respectively), but lower sensitivities for non-occlusive changes involving more peripheral vessels (57%–89%).

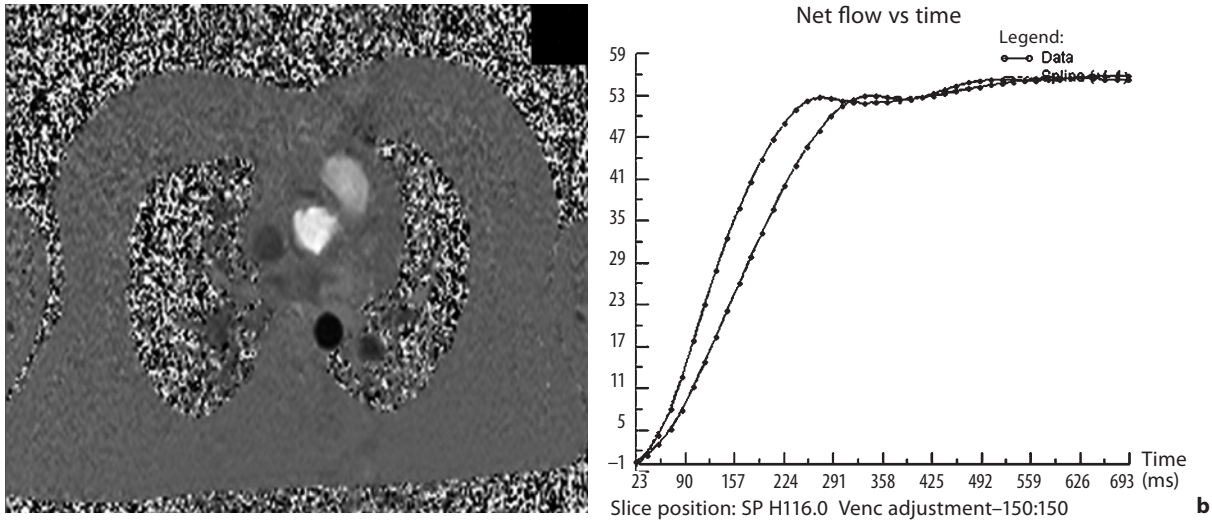

Fig. 43.2a,b. Phase-contrast imaging: **a** The pulmonary trunk and the ascending aorta reveal bright signal. **b** After drawing regions of interests, the forward volumes can be determined

Table 43.3. Imaging criteria in the assessment of MR angiography

Imaging criteria: non-occluding	Imaging criteria: occluding
Dilatation of the pulmonary arterial main stem	Complete vessel occlusion
Proximal caliber changes (pruned-tree sign)	Free-floating thrombus
Peripheral vessel reduction	Wall-adherent/endothelialized thrombus
Focal vessel ectasia	Webs and bands
Presence of the corkscrew phenomenon	

[Modified from (Nikolaou et al. 2005), with permission]

For occlusive image criteria, sensitivities were high for complete vessel occlusion and free-floating thrombi (83% and 86%, respectively), but lower for older and/or organized thrombi (wall adherent thrombi, webs and bands, 71% and 50%, respectively). Accordingly, kappa-values (κ) (inter-observer agreement) ranged from 0.79 to 0.26 and inter-modality agreement ranged from 97% to 72%. Using MRA data alone, correct differentiation of PPH and CTEPH succeeded in 83% of the cases (24/29) (Table 43.4).

43.3.1.2 Results of MR Perfusion Imaging

The analysis of the time-resolved MR perfusion data sets alone (without knowledge of the MRA results) allowed differentiation of perfusion abnormalities from normally perfused lungs in most cases, as compared to perfusion scintigraphy as the reference modality (for n=24 patients). In detail, MRI showed a sensitivity of 77% for the detection of any perfusion defect on a per-patient basis (17 of 22 patients with perfusion abnormalities detected). Two patients with normal findings in perfusion scintigraphy were also assessed as normal in MR. When the results of the MR perfusion data were compared with the conventional perfusion scintigraphy for all 24 patients undergoing both modalities, an inter-modality agreement, i.e., congruent diagnosis on a per-patient basis, of 79% (19/24) was observed. Inter-observer agreement for the detection of perfusion defects was high (κ=0.64, good agreement). For the differential diagnosis of PPH and CTEPH, reviewers had to make the following decision: If a perfusion defect is present, is it:
(1) patchy/diffuse? → indicative for PPH
or
(2) segmental/circumscribed? → indicative for CTEPH

Comparing MR perfusion data of all patients (n=29) with the final reference diagnosis, a correct diagnosis (PPH or CTEPH) was made in 69% of the cases (20/29) (Table 43.4).

43.3.1.3 Results of the Combined MR Perfusion and MRA Approach

While the interpretation of MR-perfusion and MRA data alone led to a correct diagnosis (PPH or CTEPH) in 69% and 83% of the cases, respectively, the combi-

Table 43.4. Diagnostic accuracy of MR angiography, MR perfusion imaging, and the combined assessment of MRA and MR perfusion imaging

Modality	Detection and correct classification of any defect (n=29)	Detection and correct classification of secondary defects (n=10)	Inter-modality agreement	Inter-observer agreement (κ)
MR angiography	83%	60%	Vs. CTA/DSA: 86%	0.70
MR perfusion	69%	70%	Vs. scintigraphy: 86%	0.63
MRA and MR perfusion	90%	80%	Vs. final diagnosis: 90%	0.73

[Modified from (Nikolaou et al. 2005), with permission]

nation of the data led to a correct diagnosis in 90% of the cases, i.e., 26 of 29 patients were diagnosed correctly for suffering from PPH or CTEPH, as compared to the final reference diagnosis (Table 43.4). This way, it was proven that combining the information of MR perfusion and MR angiography in a comprehensive evaluation, the diagnostic information can be used complementarily, increasing the diagnostic value of pulmonary MRI. Figures 43.3 and 43.4 display typical imaging findings of MR angiography and MR perfusion imaging in patients with CTEPH and PPH.

43.3.2 Staging of Pulmonary Hypertension by Comprehensive Protocol of Right-Ventricular Functional Analysis and Flow Analysis Compared to Clinical Staging (Wood Units, Echo, ECG)

The early diagnosis of PAH is difficult because presenting symptoms are often mild and non-specific. By the time patients develop significant dyspnea, the disease is usually advanced. Accurate diagnosis depends on right-heart catheterization; however, this is an invasive and costly test and thus is not appropriate for screening. Right-ventricular dysfunction and pulmonary hypertension often are diagnosed serendipitously by echocardiography; however, echocardiography may not detect pulmonary hypertension unless the diagnosis is specifically sought or if there is not adequate tricuspid regurgitation. The latter scenario may occur in up to 10% of patients with pulmonary hypertension.

The ECG is easily performed, is inexpensive, and is widely available. Its diagnostic utility has been established for ischemic heart disease, but it has not been widely evaluated as a screening tool with which to exclude pulmonary vascular disease associated with PAH. Ahearn et al. (2002) found that ECG parameters do not correlate well with hemodynamic or echocardiographic findings in patients with suspected pulmonary hypertension. The amplitude of the P-wave in lead II had a negative correlation with the cardiac index of 0.3. It correlated poorly with other hemodynamic, echocardiographic, and exercise parameters, with correlation coefficients ranging from 0.26 to 0.39. The frontal QRS axis correlated best of all ECG parameters with hemodynamic and echocardiographic parameters, with a coefficient of –0.46 with the cardiac index.

The pulmonary vascular resistance (PVR) is determined by right heart catheterization and quantified by Wood units. An increased pulmonary vascular resistance can be caused by lung embolism, various parenchymal lung diseases or secondary to cardiac or extra-cardiac shunts and congenital vascular and cardiac anomalies and heart-valve disease.

For cine MRI of the left and right ventricles, gender and age-specific reference values for the functional parameters ejection fraction, end-diastolic and end-systolic volume and ventricular mass have been available since 1999 (Lorenz et al. 1999). However, they are somewhat different depending on the MRI technique that is used. For assessment of right-ventricular functional parameters, MRI is superior compared to echocardiography. A main limitation of echocardiography of the right ventricle is the lack of clear landmarks. Therefore, the most sufficient parameter for quantifying the right-ventricular failure and pulmonary hypertension is assessment of the extent of regurgitation of the tricuspid valve by echocardiography either by direct visualization or determination of the pressure gradient. In contrast to echocardiography, MRI is not only able to visualize the regurgitation jet (Fig. 43.5) and determine the pressure gradient of the jet, but also the regurgitated volume can be determined exactly and quantified in relation to the right ventricular stroke volume. Cine images in the short-axis orientation near the atrioventricular valves demonstrate pathological movement of the septum towards the left ventricle during diastole. Either flattening or inversion of the normal curvature of the septum can be

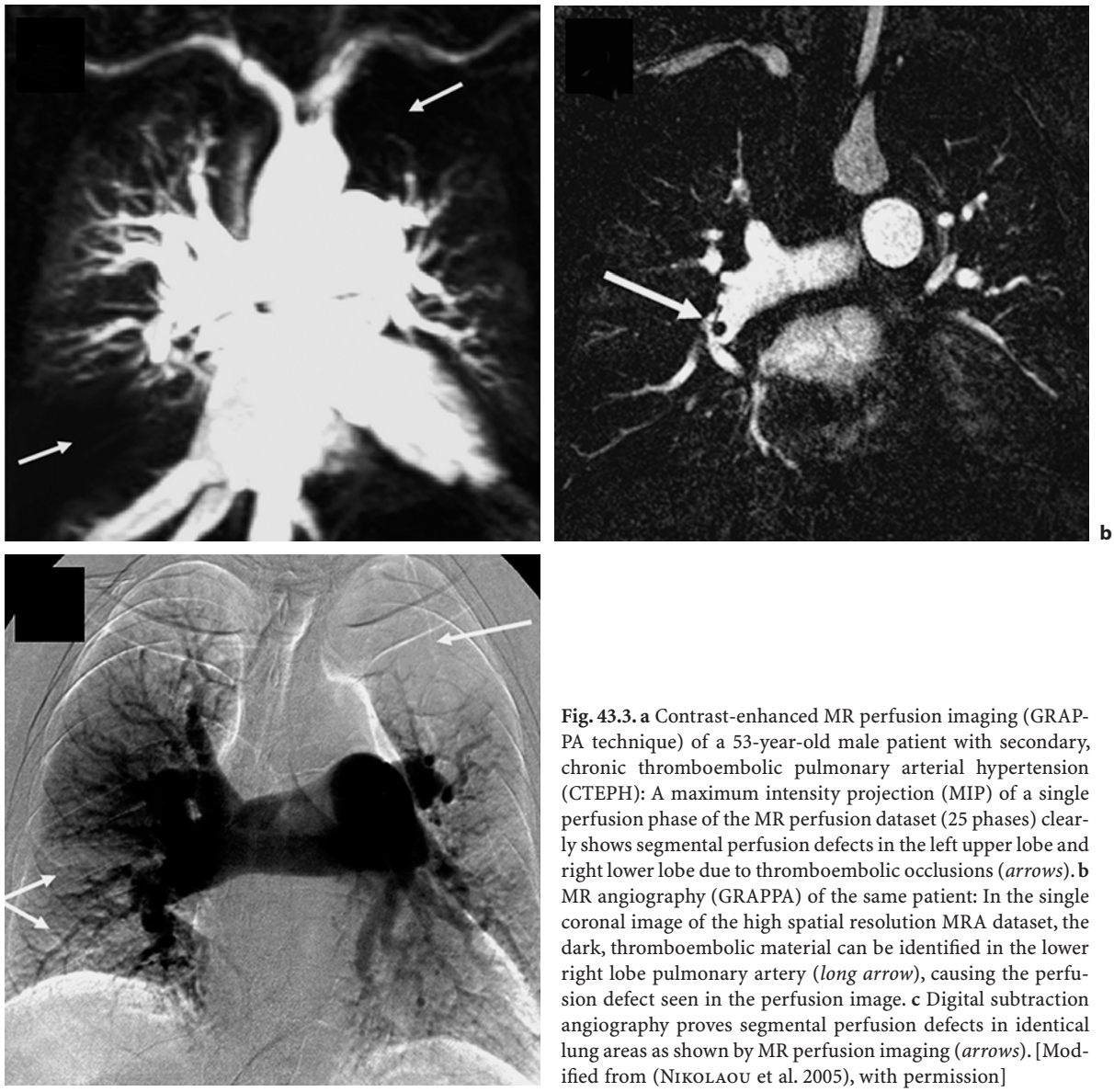

Fig. 43.3. a Contrast-enhanced MR perfusion imaging (GRAPPA technique) of a 53-year-old male patient with secondary, chronic thromboembolic pulmonary arterial hypertension (CTEPH): A maximum intensity projection (MIP) of a single perfusion phase of the MR perfusion dataset (25 phases) clearly shows segmental perfusion defects in the left upper lobe and right lower lobe due to thromboembolic occlusions (*arrows*). **b** MR angiography (GRAPPA) of the same patient: In the single coronal image of the high spatial resolution MRA dataset, the dark, thromboembolic material can be identified in the lower right lobe pulmonary artery (*long arrow*), causing the perfusion defect seen in the perfusion image. **c** Digital subtraction angiography proves segmental perfusion defects in identical lung areas as shown by MR perfusion imaging (*arrows*). [Modified from (Nikolaou et al. 2005), with permission]

observed (Fig. 43.5). In patients with intra- or extracardiac shunts, the shunt volume can be determined in relation to the right-ventricular stroke volume by flow measurements. The percentage of shunt volume (Fig. 43.6) is important for the therapeutic decision of surgical or interventional repair. The most established alternative method for shunt quantification is right-heart catherization, which is an invasive examination. Pulmonary hypertension in intra- or extra-cardiac shunts except for larger ventricular septum defects usually develops slowly when Eisenmenger's reaction is beginning. With a shunt volume of more than 50%, surgical or interventional therapy is indicated.

43.4 Future Perspectives

43.4.1 Oxygen Imaging in PH

A major impact on the comprehensive assessment of PH using MRI might arise from the combination of pulmonary MR angiographic techniques with functional imaging of lung ventilation, using either hyperpolarized gases such as helium-3 (Kauczor et al. 2002; Rizi et al. 2003) or simply oxygen (Muller

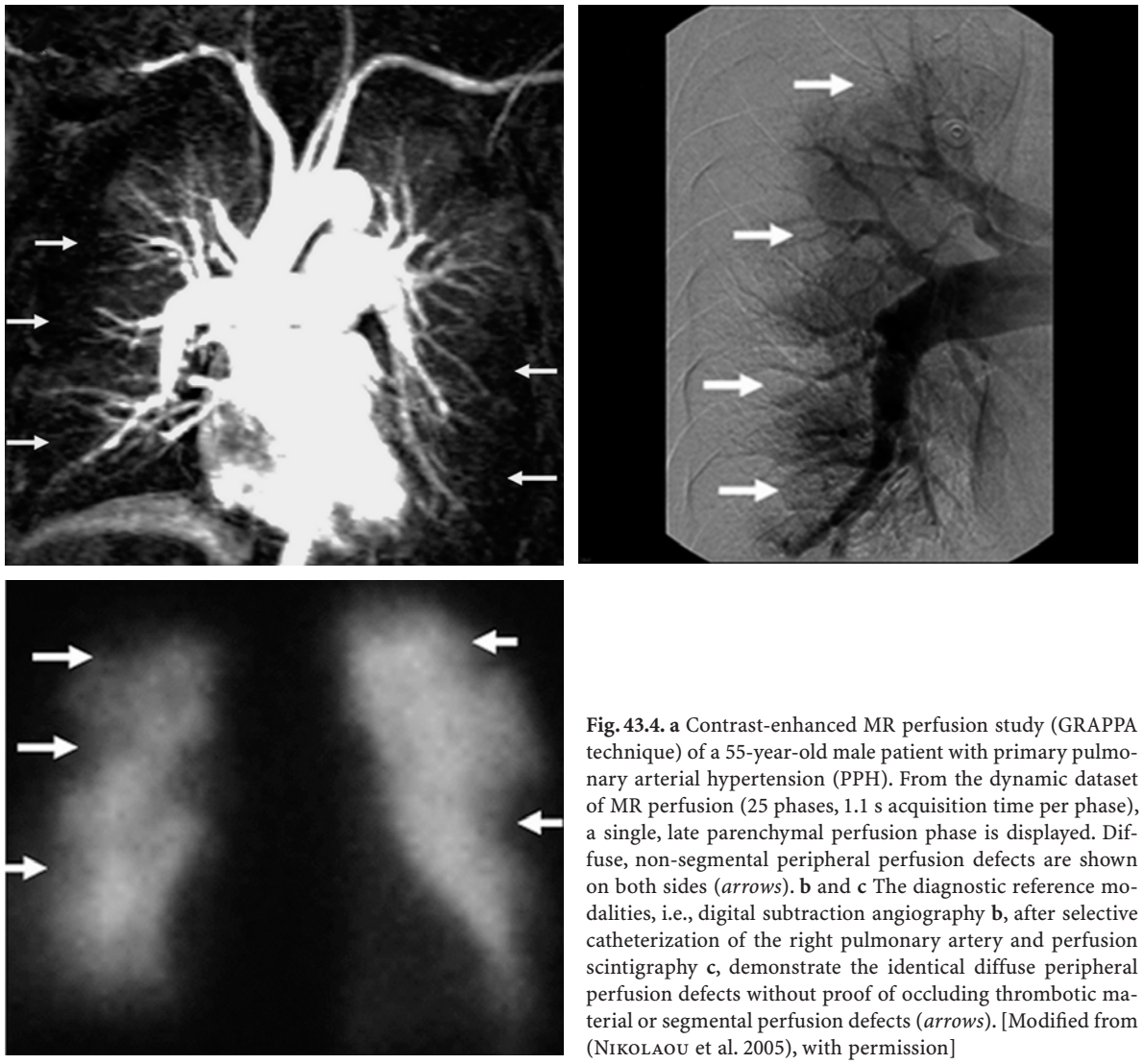

Fig. 43.4. a Contrast-enhanced MR perfusion study (GRAPPA technique) of a 55-year-old male patient with primary pulmonary arterial hypertension (PPH). From the dynamic dataset of MR perfusion (25 phases, 1.1 s acquisition time per phase), a single, late parenchymal perfusion phase is displayed. Diffuse, non-segmental peripheral perfusion defects are shown on both sides (*arrows*). **b** and **c** The diagnostic reference modalities, i.e., digital subtraction angiography **b**, after selective catheterization of the right pulmonary artery and perfusion scintigraphy **c**, demonstrate the identical diffuse peripheral perfusion defects without proof of occluding thrombotic material or segmental perfusion defects (*arrows*). [Modified from (Nikolaou et al. 2005), with permission]

et al. 2002; Dietrich et al. 2005). Using either MR imaging technique of pulmonary ventilation, and combining information with the MR perfusion data, a differentiation of perfusion defects arising from thromboembolic origin or from atelectasis/dystelectasis can be made (Ley et al. 2004), further helping in the complex differential diagnosis of PH. Oxygen imaging of the lung has the advantage of being easier to perform and less expensive than helium imaging. Since oxygen imaging is based on the T1-shortening of molecular oxygen dissolving in blood, it represents the combined physiologic processes of ventilation, diffusion and, to a lesser degree, perfusion. However, the signal-to-noise ratio of oxygen imaging is considerably lower than applying helium, and if respiratory and/or cardiac triggering are employed for optimized image quality, oxygen imaging of pulmonary ventilation has been reported to be very time-consuming (Ohno et al. 2002). With implementation of parallel-acquisition techniques, using slice-selective pulses and combined respiratory and ECG triggering, oxygen-enhanced lung MRI with the acquisition of six slices and 80 repetitions can be performed in 8 to 13 min, depending only on the respiratory frequency of the examined subject (Dietrich et al. 2005); cf. Chap. 38. Thus, using parallel imaging, oxygen-enhanced lung imaging becomes sufficiently fast to be integrated into a clinical routine MRI examination of the lung consisting of other morphologic and functional methods such as lung perfusion MRI and pulmonary MR angiography. Future studies will have to prove if oxygen imaging

with parallel acquisition techniques integrated into a comprehensive MRI protocol will further improve the diagnostic and clinical workup of PH.

43.4.2 Quantitative Assessment of Pulmonary Perfusion in PH

Apart from the distinct determination of the peak enhancement of the lung tissue, the temporal information achieved by parallel imaging could be used for the temporal analysis of tissue perfusion and ultimately for the calculation of semi-quantitative or quantitative parameter maps of parenchymal perfusion (Nikolaou et al. 2004). If a correct contrast-agent dose and fast sequences with high temporal resolution are used, MRI is able to evaluate regional differences in pulmonary perfusion (Fink et al. 2004); cf. Chap. 37. By assessing the arterial input function and the parenchymal response curve, quantitative perfusion parameters can be derived, applying a simplified one-compartment model (Fig. 43.7) (Nikolaou et al. 2004). Such a quantitative MR approach would be of high potential clinical value, because intra- and interindividual differences in pulmonary blood flow and volume would be detectable. In combination with recent MR ventilation/diffusion techniques, such as oxygen-enhanced imaging, it might also be attractive to estimate ventilation/perfusion ratios. Ideally, a quantitative method of perfusion assessment would enable the detailed follow-up of PH patients and help in the assessment of treatment effects of vasodilative drug therapy in patients suffering from PPH.

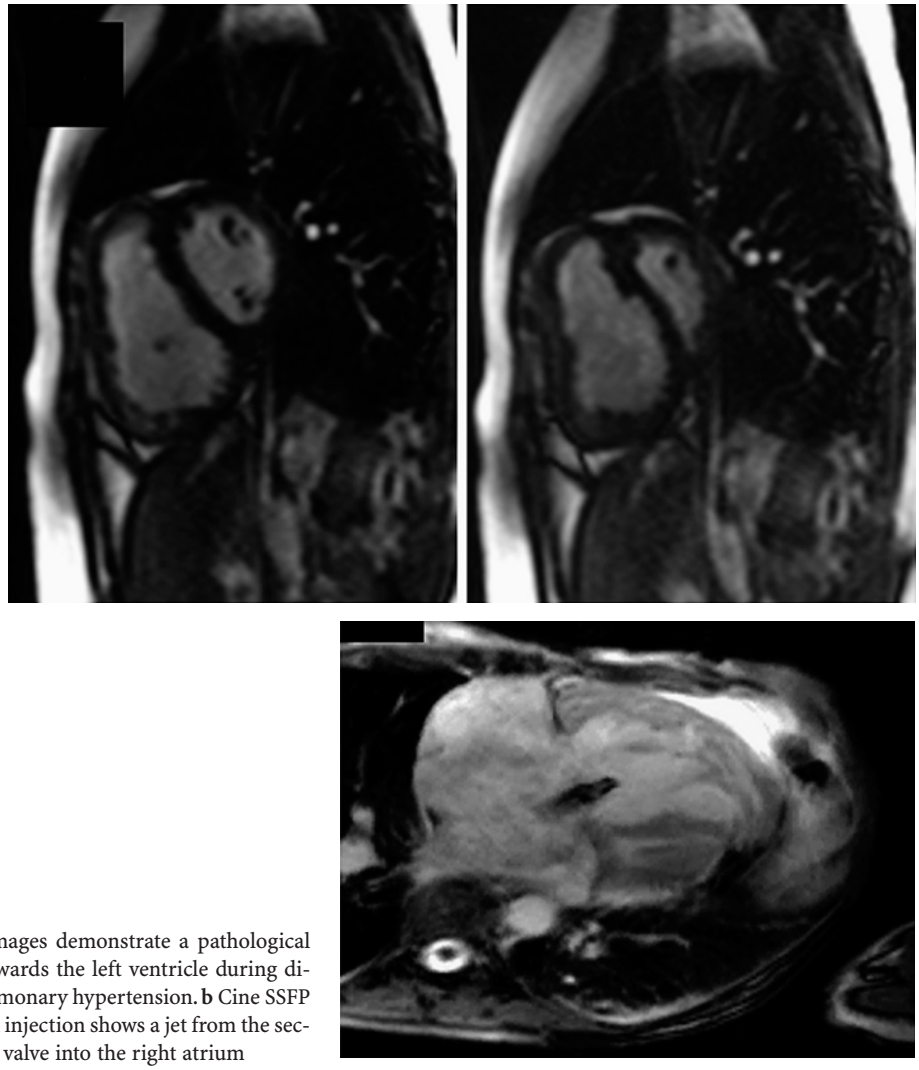

Fig. 43.5. a Real-time cine images demonstrate a pathological movement of the septum towards the left ventricle during diastole caused by primary pulmonary hypertension. **b** Cine SSFP image after contrast-material injection shows a jet from the secondary insufficient tricuspid valve into the right atrium

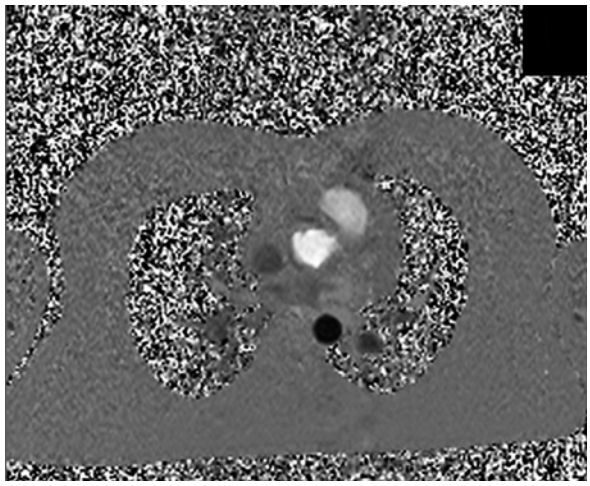

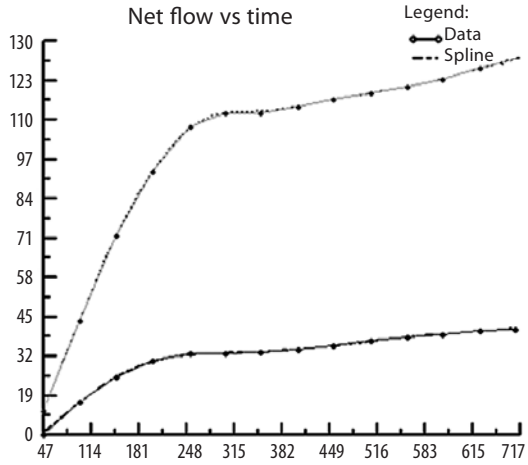

a b

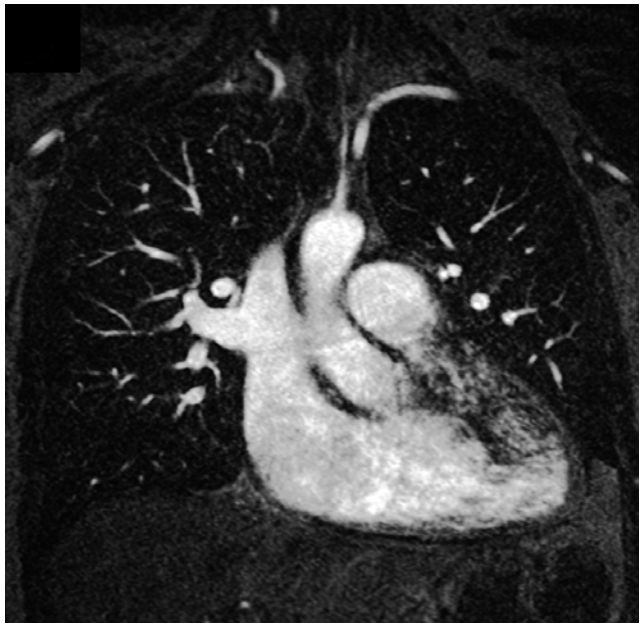

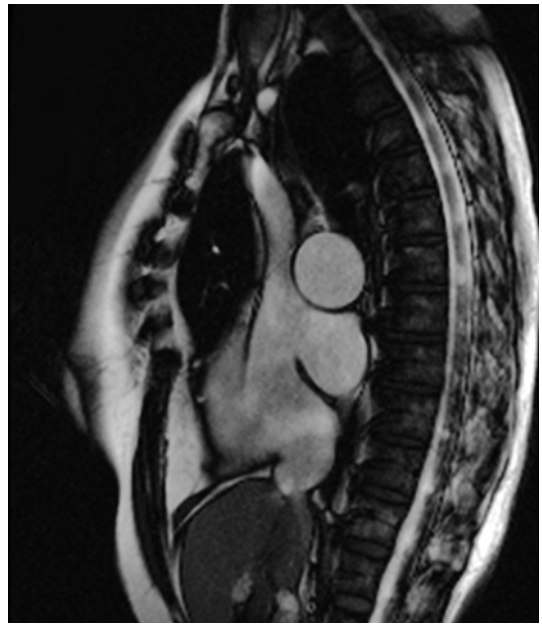

c d

Fig. 43.6. a Phase-contrast images of the ascending aorta and pulmonary trunk. **b** The quantification of the net flow demonstrates a shunt volume of 70%. A secondary pulmonary hypertension is caused by an anomalous return of the right upper lobe vein into the superior vena cava **c** and by a large sinus venous defect **d**. Surgical repair is indicated

43.5 Conclusion

In patients with pulmonary hypertension, MR imaging of the pulmonary circulation using the combination of MR perfusion imaging and MR angiography with parallel-imaging techniques provides a high diagnostic accuracy in differentiating PPH and CTEPH. Further larger-sample studies will be needed for validation. Besides improving temporal and spatial resolution of these techniques, also their required scan time can be substantially reduced from several minutes to even breath-holds. This allows the combined use of different morphologic and functional MRI techniques within a reasonable total scan time. MR angiography of the pulmonary vasculature can be complemented by additional functional measurements such as flow measurements and assessment of right-heart cardiac function. In the future, potential clinical applications of pulmonary MRI in the diagnosis of pulmonary hypertension could include ventilation imaging using oxygen, or quantitative assessment of pulmonary perfusion, enabling a truly comprehensive workup of PH using MRI alone.

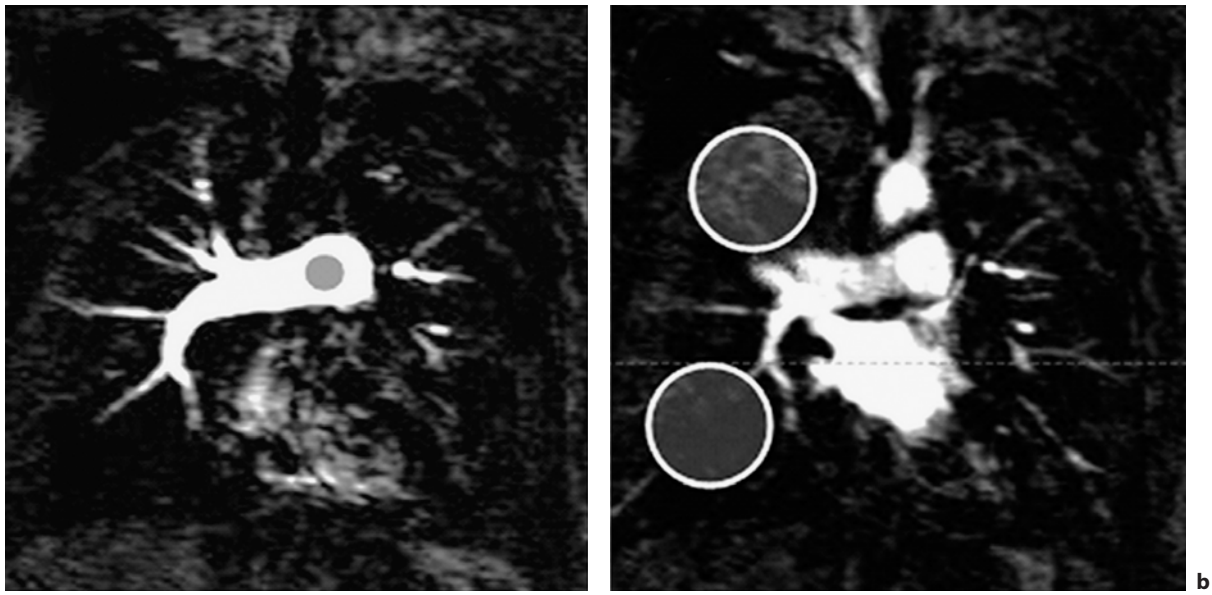

Fig. 43.7. a and **b** Dynamic contrast-enhanced MRI of a healthy volunteer using a fast 3D gradient-echo FLASH sequence. In this examination, 4 ml of the paramagnetic contrast agent gadodiamide (0.5 mol/l; Omniscan, Amersham Health, UK) were administered with a flow rate of 4 ml/s. Shown are two exemplary coronal images, each at the same position, taken from the total of 25 frames acquired with a temporal resolution of 1.1 s. ROIs are placed in the location of the main pulmonary artery for assessment of the arterial input function (**a**, *small circle*) and in the upper and lower region of the right lobe for assessment of the tissue response (**b**, *large circles*). **c** After calculating the arterial input function and the tissue-response curve as shown in **a** and **b**, the concentration-time course from the right lower lung is determined, using a simplified one-compartment model. From this analysis, absolute quantitative values of pulmonary parenchymal perfusion can be derived. [Modified from (Nikolaou et al. 2004), with permission]

References

Ahearn GS, Tapson VF, Rebeiz A, Greenfield JC Jr (2002) Electrocardiography to define clinical status in primary pulmonary hypertension and pulmonary arterial hypertension secondary to collagen vascular disease. Chest 122:524–527

Alfakih K, Plein S, Thiele H, Jones T, Ridgway JP, Sivananthan MU (2003) Normal human left and right ventricular dimensions for MRI as assessed by turbo gradient echo and steady-state free precession imaging sequences. J Magn Reson Imaging 17:323–329

Bellenger NG, Grothues F, Smith GC, Pennell DJ (2000) Quantification of right and left ventricular function by cardiovascular magnetic resonance. Herz 25:392–399

Bottini PB, Carr AA, Prisant LM, Flickinger FW, Allison JD, Gottdiener JS (1995) Magnetic resonance imaging compared to echocardiography to assess left ventricular mass in the hypertensive patient. Am J Hypertens 8:221–228

Dietrich O, Losert C, Attenberger U, Fasol U, Peller M, Nikolaou K, Reiser MF, Schoenberg SO (2005) Fast oxygen-enhanced multislice imaging of the lung using parallel acquisition techniques. Magn Reson Med 53:1317–1325

Dietrich O, Nikolaou K, Wintersperger BJ, Flatz W, Nittka M, Petsch R, Kiefer B, Schoenberg SO (2002) Integrated parallel acquisition techniques (iPAT): applications for fast and cardiovascular MR imaging. Electromedica 70:133–146

Fedullo PF, Auger WR, Kerr KM, Rubin LJ (2001) Chronic thromboembolic pulmonary hypertension. N Engl J Med 345:1465–1472

Fink C, Bock M, Puderbach M, Schmahl A, Delorme S (2003) Partially parallel three-dimensional magnetic resonance imaging for the assessment of lung perfusion - initial results. Invest Radiol 38:482–488

Fink C, Risse F, Buhmann R, Ley S, Meyer FJ, Plathow C, Puderbach M, Kauczor HU (2004) Quantitative analysis of pulmonary perfusion using time-resolved parallel 3D MRI -

initial results. Rofo Fortschr Geb Rontgenstr Neuen Bildgeb Verfahr 176:170–174
Fishman AP (19630 Dynamic of the pulmonary circulation. in: Hamilton WF (ed) Handbook of Physiology, Sect 2. Circulation Washington, DC, American Physiological Society, p 1708
Griswold MA, Jakob PM, Heidemann RM, Nittka M, Jellus V, Wang J, Kiefer B, Haase A (2002) Generalized autocalibrating partially parallel acquisitions (GRAPPA). Magn Reson Med 47:1202–1210
Grothues F, Smith GC, Moon JC, Bellenger NG, Collins P, Klein HU, Pennell DJ (2002) Comparison of interstudy reproducibility of cardiovascular magnetic resonance with two-dimensional echocardiography in normal subjects and in patients with heart failure or left ventricular hypertrophy. Am J Cardiol 90:29–34
Hori Y, Yamada N, Higashi M, Hirai N, Nakatani S (2003) Rapid evaluation of right and left ventricular function and mass using real-time true-FISP cine MR imaging without breath-hold: comparison with segmented true-FISP cine MR imaging with breath-hold. J Cardiovasc Magn Reson 5:439–450
Hunt SA (1997) Pulmonary hypertension in severe congestive heart failure: how important is it? J Heart Lung Transplant 16:13-15
Kauczor HU, Hanke A, van Beek EJ: Assessment of lung ventilation by MR imaging: current status and future perspectives. Eur Radiol 2002;12:1962–1970.
Ley S, Kreitner KF, Fink C, Heussel CP, Borst MM, Kauczor HU (2004) Assessment of pulmonary hypertension by CT and MR imaging. Eur Radiol 14:359–368
Lorenz CH, Walker ES, Morgan VL, Klein SS, Graham TP Jr (1999) Normal human right and left ventricular mass, systolic function, and gender differences by cine magnetic resonance imaging. J Cardiovasc Magn Reson 1:7–21
Loscalzo J (2001) Genetic clues to the cause of primary pulmonary hypertension. N Engl J Med 345:367–371
Matsuoka S, Uchiyama K, Shima H, Terakoshi H, Oishi S, Nojiri Y, Ogata H (2002) Effect of the rate of gadolinium injection on magnetic resonance pulmonary perfusion imaging. J Magn Reson Imaging 15:108–113
Meaney JF, Weg JG, Chenevert TL, Stafford-Johnson D, Hamilton BH, Prince MR (1997) Diagnosis of pulmonary embolism with magnetic resonance angiography. N Engl J Med 336:1422–1427
Muller CJ, Schwaiblmair M, Scheidler J, Deimling M, Weber J, Loffler RB, Reiser MF (2002) Pulmonary diffusing capacity: assessment with oxygen-enhanced lung MR imaging preliminary findings. Radiology 222:499–506
Narayan G, Nayak K, Pauly J, Hu B (2005) Single-breathhold, four-dimensional, quantitative assessment of LV and RV function using triggered, real-time, steady-state free precession MRI in heart failure patients. J Magn Reson Imaging 22:59–66
Nikolaou K, Schoenberg SO, Attenberger U, Scheidler J, Dietrich O, Kuehn B, Rosa F, Huber A, Leuchte H, Baumgartner R, Behr J, Reiser MF (2005) Pulmonary arterial hypertension: diagnosis with fast perfusion MR imaging and high-spatial-resolution MR angiography - preliminary experience. Radiology 236:694–703
Nikolaou K, Schoenberg SO, Brix G, Goldman JP, Attenberger U, Kuehn B, Dietrich O, Reiser MF (2004) Quantification of pulmonary blood flow and volume in healthy volunteers by dynamic contrast-enhanced magnetic resonance imaging using a parallel imaging technique. Invest Radiol 39:537–545
Ohno Y, Hatabu H, Takenaka D, Van Cauteren M, Fujii M, Sugimura K (2002) Dynamic oxygen-enhanced MRI reflects diffusing capacity of the lung. Magn Reson Med 47:1139–1144
Oudkerk M, van Beek EJ, Wielopolski P, van Ooijen PM, Brouwers-Kuyper EM, Bongaerts AH, Berghout A (2002) Comparison of contrast-enhanced magnetic resonance angiography and conventional pulmonary angiography for the diagnosis of pulmonary embolism: a prospective study. Lancet 359:1643–1647
Rich S (1998) Executive summary from the World Symposium on Primary Pulmonary Hypertension 1998, Evian, France, September 6-10, 1998, cosponsored by the World Health Organization. www who int/entity/cardiovascular_diseases/ resources/publications/en/ 1998
Rich S (2000) Primary pulmonary hypertension. Curr Treat Options Cardiovasc Med 2:135–140
Rizi RR, Saha PK, Wang B, Ferrante MA, Lipson D, Baumgardner J, Roberts DA (2003) Co-registration of acquired MR ventilation and perfusion images - validation in a porcine model. Magn Reson Med 49:13–18
Sandstede J, Lipke C, Beer M, Hofmann S, Pabst T, Kenn W, Neubauer S, Hahn D (2000) Age- and gender-specific differences in left and right ventricular cardiac function and mass determined by cine magnetic resonance imaging. Eur Radiol 10:438–442
Sonnet S, Buitrago-Tellez CH, Scheffler K, Strecker R, Bongartz G, Bremerich J (2002) Dynamic time-resolved contrast-enhanced two-dimensional MR projection angiography of the pulmonary circulation: standard technique and clinical applications. AJR Am J Roentgenol 179:159–165
Spuentrup E, Schroeder J, Mahnken AH, Schaeffter T, Botnar RM, Kuhl HP, Hanrath P, Gunther RW, Buecker A (2003) Quantitative assessment of left ventricular function with interactive real-time spiral and radial MR imaging. Radiology 227:870–876
Stein PD, Woodard PK, Hull RD, Kayali F, Weg JG, Olson RE, Fowler SE (2003) Gadolinium-enhanced magnetic resonance angiography for detection of acute pulmonary embolism: an in-depth review. Chest 124:2324–2328
Teichholz LE, Kreulen T, Herman MV, Gorlin R (1976) Problems in echocardiographic volume determinations: echocardiographic-angiographic correlations in the presence of absence of asynergy. Am J Cardiol 37:7–11
Thiele H, Nagel E, Paetsch I, Schnackenburg B, Bornstedt A, Kouwenhoven M, Wahl A, Schuler G, Fleck E (2001) Functional cardiac MR imaging with steady-state free precession (SSFP) significantly improves endocardial border delineation without contrast agents. J Magn Reson Imaging 14:362–367
Tombach B, Heindel W (2002) Value of 1.0-M gadolinium chelates: review of preclinical and clinical data on gadobutrol. Eur Radiol 12:1550-1556
Wintersperger BJ, Nikolaou K, Dietrich O, Rieber J, Nittka M, Reiser MF, Schoenberg SO (2003) Single breath-hold real-time cine MR imaging: improved temporal resolution using generalized autocalibrating partially parallel acquisition (GRAPPA) algorithm. Eur Radiol 13:1931–1936

Part VIII:
Future Developments

New Coil Systems for Highly Parallel MR Acquisition Strategies

44

Lawrence L. Wald and Graham Wiggins

CONTENTS

L. L. Wald, PhD; G. Wiggins, PhD
MGH/MIT/HMS Athinoula A. Martinos Center for Functional and Structural Biomedical Imaging, Charlestown Navy Yard, Building 149, 13th Street (2301), Charlestown, MA 02129-2060, USA

44.1 Introduction

While advances in the "primary" technologies of MR such as increased field strength and improved gradient performance have been substantial, advances in the third component of the triad, RF technology, have also proved to be a valuable and cost-effective way to improve sensitivity and encoding capabilities in MR imaging. Past success in this area will, no doubt, drive substantial future development. In this chapter we examine current limitations in parallel-imaging technology and try to identify future directions for parallel RF hardware. In particular, we wish to explore how parallel-imaging technology might be constructed if the coil designer was unconstrained by the number of RF channels available on the instrument.

With the success of parallel-reconstruction methods, a new criterion has been added to the RF engineers' list of requirements beyond the usual sensitivity, coverage and patient comfort issues: the ability to accelerate the image encoding. While it seems innocuous, it is actually a new role for the detector that has already greatly impacted the type of arrays being constructed. As just one example, the design of a cardiac array for non-accelerated imaging would have little use for coil elements over areas of the chest distant from the heart. But the accelerated image requires localized coil elements in these areas to assist with unaliasing the accelerated image. More extreme acceleration demands such as "single-echo acquisition" (SEA) (McDougall and Wright 2005a), where essentially all of the image encoding in at least one direction is achieved with the array geometry, show that the encoding capabilities of the array are extensive, at least for positions very near the array elements.

In these "detectors of the future," the role of the image encoding is no less important than the role of signal detection. Increased reliance on the array as the primary device for image encoding will likely lead to considerably higher numbers of detectors

than would be contemplated from sensitivity arguments alone. In this scenario, the role of the MR detector array begins to more resemble the electroencephalography (EEG) or magnetoencephalography (MEG) detector where all of the spatial information is derived from the detector geometry. Although there appear to be limits on the ability of the array to encode spatial information distant from the array, the MEG/EEG case can also serve to educate us on the extraction of useful spatial information when faced with an ill-conditioned inverse problem. We are only beginning to explore the potential of these methods of this unusual regime.

In addition to the exciting opportunities, implementation of "large-N" arrays (i.e., arrays with a large number, N, of coil elements) will impose considerable technical challenges for the design, construction and use of the array. The aim of this chapter is to review some of the probable benefits and the system design directions they motivate, as well as the potential problems that may be faced. In addition to the obvious manufacturing and up-time issues of a 128-channel coil and receiver system, there are issues of maintaining body-noise dominance in the small coils, the possibility of considerable sensitivity loss if the array elements are not combined in an optimized fashion, interactions among elements and between the array elements and the excitation coil, cable management between the array and MR system, data-rate limits and reconstruction speed.

44.2 Array Design: Signal and Noise Considerations

44.2.1 Noise Considerations

A principal design goal of a receive coil is to be inductively tightly coupled to the precessing nuclear magnetization. Because the spins in the body lie in an ionic bath (salt water), the coil is also tightly coupled to randomly fluctuating fields produced by ionic currents. The currents that happen to have frequencies within the bandwidth of the RF receiver appear as spatially uniform Gaussian-distributed noise in the complex image. An equivalent picture is produced by a reciprocity argument. Here, the effectiveness of the receive coil is proportional to its efficiency as a transmit coil. The receive noise power is proportional to the power dissipated in the conductive tissue through eddy-current damping (driving the ions with the electric field associated with dB_1/dt) or through electric coupling (direct electric fields originating from the coil). In either picture, the same basic rules of thumb arise. The more effective the receive coil is at detecting the spins, the more effective it will be at receiving the noise. Thus, once "body-noise dominance" has been achieved, gains in SNR can only be achieved by limiting the volume of tissue contributing the noise. For example, the coil should only interact with tissue that is of interest; tissue outside of the imaging field of view but within the region of coil sensitivity produces only unwanted noise.

44.2.1.1 Measuring Body-noise Dominance

Body-noise dominance for a coil can quickly be estimated by measuring the unloaded-to-loaded ratio of the quality factor, Q, of the coil. The Q of a coil is defined as the energy stored in the resonator divided by the energy lost per cycle and can be shown to be $Q=\omega L/R$ for a simple LCR circuit. Here R is the sum of all losses in the coil, $R=R_{body}+R_{other}$, where R_{other} represents all losses not associated with the body. For example, R_{other} could come from resistive losses in the conductor, radiative losses, or losses in the capacitors The Q factor is conveniently measured by making an S12 measurement between two untuned probes loosely coupled to the coil. The Q is the full width at the –3 dB points of the frequency response divided by the resonance frequency. When energy is critically coupled out of the coil using a coupling network to transform the series loss resistance of the coil to 50 Ohms, then the Q drops by a factor of 2 (since critical coupling, by definition, couples half of the stored energy per cycle into the external 50-Ohm load). Thus the Q measurement is usually done without an output coax. Losses in the output coax or associated with the noise figure of the preamplifier can be considered separately.

By measuring the coil with and without the body present, the ratio of R_{body} to R_{other} is determined:

$$\frac{R_{Body}}{R_{Other}} = \frac{Q_{unloaded}}{Q_{loaded}} - 1.$$

Since the detected signal and noise in the image are voltage signals rather than powers, the detected signal-to-noise ratio (SNR) is proportional to the square root of the total resistance in the coil

$\sqrt{R_{body}+R_{coil}}$. Thus we can estimate the ratio of the sensitivity of the imperfect coil (with $R_{body}+R_{other}$) to that of the idealized coil (where $R_{other}=0$):

$$\frac{SNR_{imperfect}}{SNR_{Rother=0}} = \sqrt{\frac{R_{body}}{R_{body}+R_{other}}} = \sqrt{1-\frac{Q_{loaded}}{Q_{unloaded}}}\,.$$

Thus, if the unloaded-to-loaded-Q ratio is 3, then the coil will have achieved 81% of the SNR which could potentially be obtained by completely eliminating the other noise mechanisms. Figure 44.1 shows some sample circular loop coils; their unloaded-to-loaded-Q values measured at 64 MHz are displayed in Table 44.1.

Table 44.1. Unloaded-to-loaded-Q ratio of coils in Fig. 44.1 (from left to right)

	48 mm	48 mm (avg.)	48 mm	60 mm	70 mm
Conductor width	2 mm	2 mm	10 mm	5 mm	7 mm
$Q_{unloaded}/Q_{loaded}$	2.2	2.6	5.0	4.7	6.0
$\frac{SNR_{imperfect}}{SNR_{Rother=0}}$	73.9%	78.4%	89.4%	88.7%	91.3%

44.2.1.2 Improving Unloaded-to-loaded-*Q* Ratio

Although some methods, like cooling the copper or using superconductors, can improve R_{other}, it is usually easier to improve this ratio by increasing R_{body} in a way that also improves the sensitivity of the signal detection (by more tightly coupling to the tissue) and leaves R_{other} relatively unaffected. The exception to this is to address the copper losses by increasing the width of the copper trace. The simplest strategy for increasing the coupling of the coil to the body is to move the receiver coil as close to the body as possible. A second choice is to increase the coupling by adding an additional turn to the coil loop. Going from a single-turn to a two-turn coil increases the inductive coupling to the spins and noise more than copper losses are increased due to the longer conductor.

The equivalent resistance due to losses in the conductive tissue body (R_{body}) can be estimated for a circular surface coil close to a semi-infinite sample of uniform conductivity σ. At low frequencies (roughly up to 50 MHz) this can be shown to scale as the cube of the coil's radius, a, and the square of the frequency (Chen and Hoult 1989).This assumes quasi-static approximations with negligible skin-effect attenuation or current displacement. In a simplistic interpretation, the total body noise is visualized as proportional to the volume of tissue under the coil, thus scales with a^3. Other, more complicated, expressions can be derived for the body noise at higher frequencies (Carlson 1989; Harpen 1988a; Harpen 1988b). Serfaty and colleagues (1995) give a useful analytical approximation, and Wright (2002) provides a frequency-domain calculation method.

44.2.2 Noise in Array Images

The magnitude of the penalty associated with non-optimal combination of the array data is seen to increase with the number of receivers. The implicit assumptions of common array combination methods, such as the "Sum of squares" (SoS) approximation were pointed out from its inception (Roemer et al. 1990). In SoS approximation, where coil i receives signal $S_i(x,y)$, the pixel value from each coil is assumed to be a good approximation of the coil sensitivity for that location, and the noise is assumed to be uncor-

Fig. 44.1. Circular coils evaluated for unloaded-to-loaded-Q ratio at 64 MHz. At 123 MHz the ratio for the 48-mm diameter 2-mm conductor coil nearly doubled to 4.0 and improved to 12.6 at 300 MHz

related among the array elements. Then the signal $S_i(x,y)$ is weighted by itself and combined:

$$S_c(x,y) = \sqrt{\sum_{i=1}^{N_{coils}} S_i(x,y)^2} \,. \tag{44.1}$$

The SoS result derives from the more optimized combination that utilizes a direct measure of the coil sensitivity profile of the coil $C_i(x,y)$ and the noise correlation matrix R_{ij} (noise correlation between coil i and j) (Roemer et al. 1990). The assumption used in the SoS approximation that the image intensity from a coil is a good measure of the coil sensitivity at that location is violated for images with intrinsically poor SNR (such as the component images used to form high-b-value diffusion tensor maps) or for anatomical regions with poor SNR (dark areas such as a cyst or CSF space in a T1-weighted image). Violation of these assumptions will cause loss of sensitivity in the SoS image and has been analyzed in detail for small arrays (Constantinides et al. 1997), but the magnifying effect of a large number of coils merits revisiting this problem.

A quick way to visualize the noise penalties that might be incurred when the assumptions of the SoS approximation break down is to consider the more generalized version of Eq. 44.1. In this case, the coil sensitivity maps C_i are used as the weight functions instead of the signal itself, but the noise correlation matrix for the coil is still assumed to be the identity matrix (uncorrelated and equal noise in the coils). If the normalization of the combination is chosen to produce uniform noise across the image then:

$$S_c(x,y) = \frac{\sum_{i=1}^{N_{coils}} C_i(x,y) S_i(x,y)}{\sqrt{\sum_{i=1}^{N_{coils}} C_i(x,y)^2}} \,. \tag{44.2}$$

Note that if the image signal $S_i(x,y)$ is used as an estimate of the coil sensitivity profile $C_i(x,y)$ then Eq. 44.2 reduces to the SoS formula (Eq. 44.1). If the normalization is chosen to produce uniform signal levels across the image then:

$$S_c(x,y) = \frac{\sum_{i=1}^{N_{coils}} C_i(x,y) S_i(x,y)}{\sum_{i=1}^{N_{coils}} C_i(x,y)^2} \,. \tag{44.3}$$

To visualize the potential for loss of sensitivity in a large array, Fig. 44.2 shows noise images acquired with no RF excitation and combined using Eq. 44.3. The coil sensitivity maps are, however, determined from high SNR reference scans. If these noise images were combined with the SoS methods, a uniform pattern with a noise level comparable to that seen in the air space around the phantom of Fig. 44.2 would be seen. While the difference in these levels is barely visible for the eight-channel array, it becomes quite pronounced for the larger arrays.

Figure 44.3 shows the loss in contrast-to-noise ratio associated with combining low-SNR data from large arrays with the SoS method. Model images with SNR=4 and a low-contrast grid feature were combined with SoS (top row) and Eq. 44.3 (bottom row). The simulation used experimental coil sensitivity maps and noise from 8-channel, 23-channel and 90-channel coils. While the combination method has little effect on the ability to visualize the low-contrast grid in the eight-channel-coil case, significant improvement is seen (especially at the periphery of the phantom) when the measured coil sensitivity profiles are used in conjunction with the larger arrays.

44.2.3 Theoretical Analysis of Sensitivity for Arrays of Small Surface Coils

Three related sensitivity figures of merit for the array coil are of interest: (1) the SNR as a function of position for un-accelerated scans, (2) a similar SNR map for accelerated scans and (3) the maximum acceleration achievable with an acceptable g-factor penalty. General simulations of array coils are challenging since there are a near infinite number of design choices. Nevertheless, analyzing arrays of identical coil elements arranged to cover simple sample geometries (such as spherical or planar regions) can provide insight into more complicated variations. One particularly illuminating approach for understanding the future benefits of larger array configurations is to analyze how the SNR is affected by a larger and larger number of array elements covering the same area (Wright and Wald 1997; Wiesinger et al. 2005a). Studies of this kind have analyzed planar (Wright and Wald 1997) and spherical arrays (Wiesinger et al. 2005a).

44.2.3.1 Planar Array Model

In the planar case (Wright and Wald 1997), a square region was tiled with N=1, 4, 16 and 64 square array

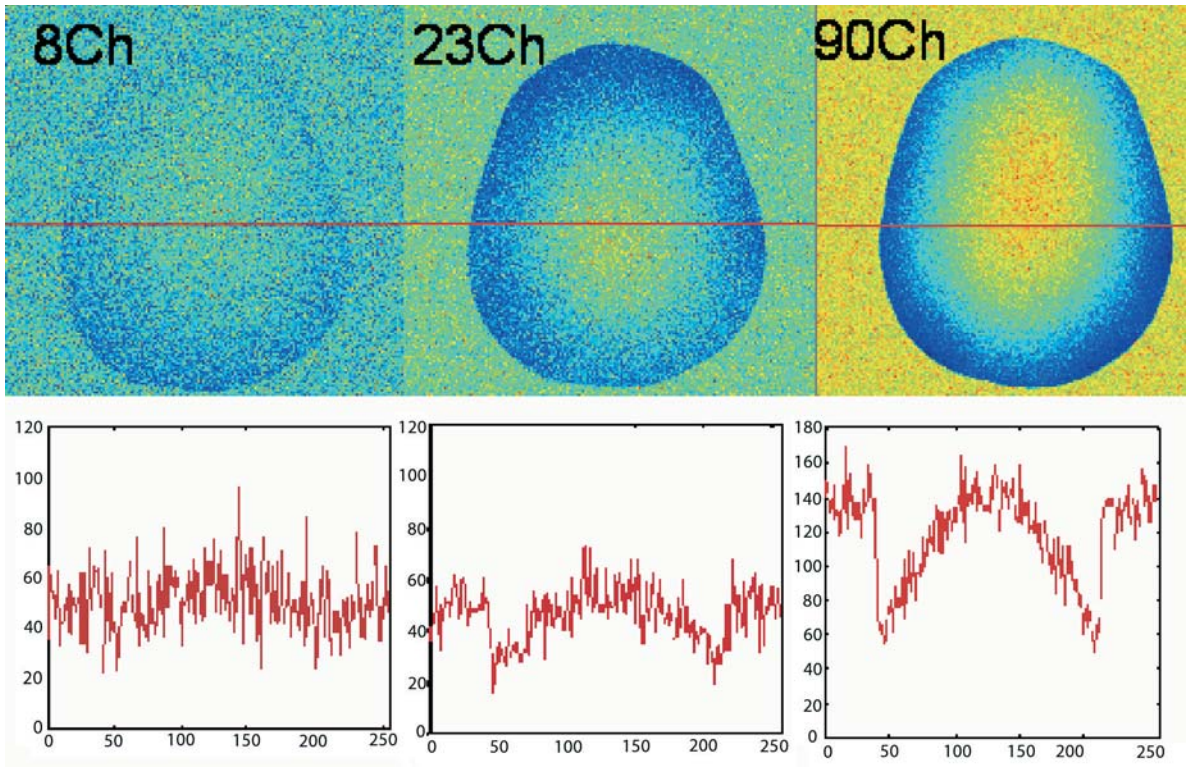

Fig. 44.2. Noise distribution maps for combined images acquired with coils with 8, 23, and 90 elements from the zero-excitation data and profiles at location shown. Axial cut through a head-shaped phantom. Regions outside the phantom are comparable to the SoS reconstruction of low-SNR images since no coil map information is present. The gain in SNR from weighted reconstuction of such data is seen to be about three-fold in the cortex for the 90-channel array. Reconstructions courtesy of C. Triantafyllou, MGH

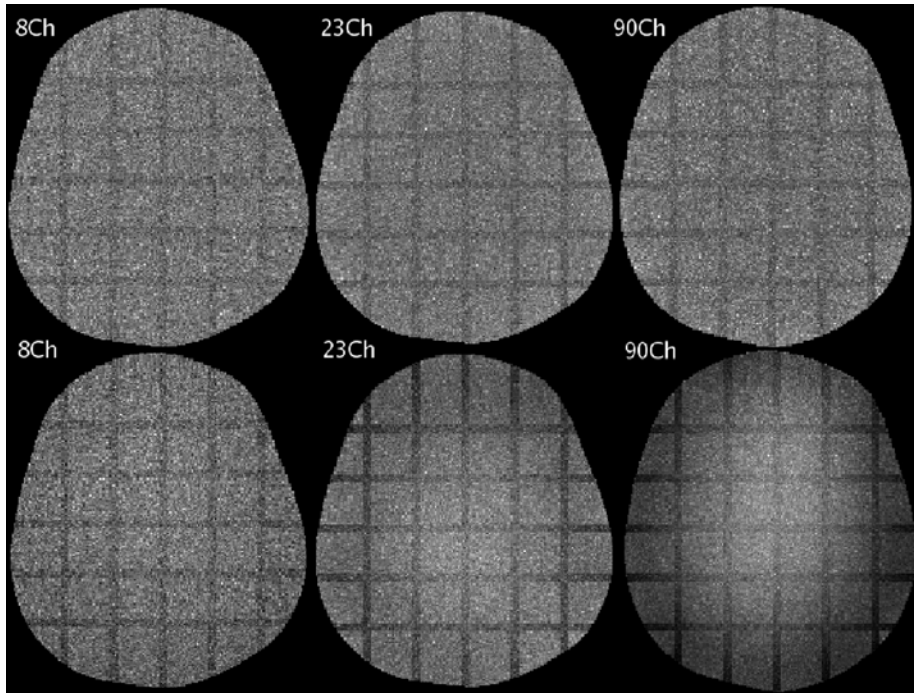

Fig. 44.3. Model data showing the increasing potential to lose contrast-to-noise ratio in low-SNR SoS-combined images. Images with SNR=4 and a low-contrast grid feature were combined with SoS (*top row*) and Eq. 3 (*bottom row*). The simulation used experimental coil sensitivity maps and noise from 8-channel, (*left*), 23-channel (*middle*) and 90-channel (*right*) coils. While the effect on the low-contrast grid is difficult to visualize for the 8-channel data, a substantial difference in the two methods is seen in the 90-channel data. Reconstructions courtesy of C. Triantafyllou, MGH

elements in a 1×1, 2×2, 4×4 and 8×8 configuration. The coils were overlapped by the width of the conductor and were modeled as being 1 cm above an infinite half-space of lossy salt water (σ=0.72 S/m). The coils were assumed to have no inductive coupling (e.g., from perfect preamplifier decoupling or decoupling networks), but the noise correlation from their shared view of the sample noise was calculated using a full-wave analysis. The SNR was then calculated as a function of depth from the center of the array. The SNR near the array was found to scale approximately with the number of array elements per side (i.e., with $\sqrt{N}$). Thus, a four-fold potential sensitivity gain can be expected for tissue near the array by moving from a modest number of array elements (N=4) to a "large-N" array (N=64). This gain is, however, lost for deeper tissue (depths approximately equal to the lateral size of the overall array). But, there is no depth at which the smaller-N arrays outperform the larger ones. Thus, large gains near the surface are potentially achievable at the cost of an added number of receive channels and a less homogeneous sensitivity profile.

44.2.3.2 Spherical Array Model

In a separate modeling study, circular coils were uniformly distributed around a 22-cm diameter sphere of conductive dielectric material modeling biological tissue (Wiesinger et al. 2005a). Circular coils (N=8, 12, 16, 20, 26, and 32) were tiled on the sphere. His presentation extended the calculation to 64 coils and both overlapped and gapped layouts (Wiesinger et al. 2005b). The coils were assigned a non-body-noise resistance determined from typical copper and preamplifier noise contributions. Full wave signal maps were generated using the methods of Keltner et al. (1991). In addition to modeling SNR for un-accelerated scans, this work modeled the additional g-factor penalty incurred in accelerated imaging and examined the SNR as a function of B_0. Furthermore, the authors compared the model results to that expected from the so-called "ultimate" SNR: the highest achievable SNR obtainable with an arbitrarily large array whose individual sensitivity basis set satisfys Maxwell's equations (Wiesinger et al. 2004; Ohlinger et al. 2003; Ocali and Atalar 1998).

In the spherical case, the results were qualitatively similar to the planar case. The largest gains achieved by increasing the number of array elements, N, occurred near the coil elements. At a radius of 9 cm in the 11-cm radius sphere, the SNR of the un-accelerated image at 1.5 T increased 3.5-fold when the number of loops was increased from 8 to 32. In this case, the dependence on N was observed to be closer to linear with N compared with the $\sqrt{N}$ seen near the planar array. Like the planar case, however, the benefits were considerably smaller more distant from the array elements. At the center of the sphere the un-accelerated 1.5-T SNR increased only about 5% with the four-fold increase in N. At higher field strength, the modeled arrays achieved a smaller fraction of the ultimate SNR. At 7.5 T, for example, only a very small region in the center of the phantom was within 10% of the ultimate SNR levels for a 64-channel array (Wiesinger et al. 2005b).

The models of SNR in accelerated imaging showed substantial gains from moving to larger arrays. The largest gains in g-factor performance as a function of N were for high acceleration rates, R. For example at R=3, the g-factor was 1.4-fold larger for the 8-channel array compared to the 32-channel. At R=4, this widened to a factor of 2. An additional finding of this study was an improved SNR for the overlapping array configuration compared to the gapped configuration for the largest-N coils for both un-accelerated and accelerated scans. For the smaller array, the gapped array was beneficial for accelerated scans, a result seen by other studies (Weiger et al. 2001; de Zwart et al. 2002).

44.2.3.3 "Ultimate" SNR of Arrays

Several studies have examined the upper bound on sensitivity and spatial encoding capabilities of coil arrays. The concept of the "ultimate" SNR achievable by an RF coil was introduced by Ocali and Atalar (1998). An arbitrary coil sensitivity profile was generated from a complete set of basis functions satisfying Maxwell's equations and a linear combination was found that maximized the SNR at a given location in the sample. This approach assumes there are no coil elements within the sample region. This work was expanded to include the SNR of accelerated imaging by the groups of Sodickson and Pruessmann (Wiesinger et al. 2004; Ohlinger et al. 2003). The ultimate SNR for accelerated imaging is found by analyzing the performance of the complete basis set. The basis set itself was chosen to be either plane waves (Ohlinger et al. 2003; Ocali and Atalar 1998) or spherical harmonics (Wiesinger et al. 2004).

The first interesting conclusion of this analysis is that the sensitivity of MR detection is intrinsically limited. The significance of this for future array designs, of course, hinges on how close current array designs are to this theoretical ceiling. Comparing actual designs (such has the arrays of circular coils tiling a spherical phantom reviewed above), suggests that a 32-channel array is close to the theoretical limit at the center of the phantom (Wiesinger et al. 2005a). Happily for the array designer, there is substantial room for improvement towards the periphery. At a radial location equal to 80% of the coil radius, there is still a factor of 7 to go before the theoretical limit is achieved (Wiesinger et al. 2005a).

The ultimate limitation of the ability of the array to encode is likely imposed by a fundamental smoothness to the coil sensitivity patterns in regions free of current sources associated with solutions to Maxwell's equations. Both groups point out a steep drop in the SNR for accelerations above about R=4 or 5 (Wiesinger et al. 2004; Ohlinger et al. 2003). For example, after this rate, the g-factor penalty was seen to rise exponentially with acceleration rate for locations near the center of the spherical sample (Wiesinger et al. 2004). As with the un-accelerated SNR, the situation improves as you move closer to the array elements. Here, the proximity to the wires provides more rapidly varying spatial profiles. This proximity effect allowed the 64-element array of McDougall and Wright to achieve credible images with an acceleration rate of 64-fold; considerably higher than the 4 to 5-fold limit suggested by the ultimate sensitivity analysis, which focused on regions far from the array.

Both studies found that moving to higher B_0 field strength postponed the rapid deterioration of SNR for rates above R=4. As the wavelength of the RF becomes shorter compared to the object size, the modeled solutions move into the far-field regime and support more sharply varying solutions. To take an extreme example, consider electromagnetic fields in the optical frequencies that can support tightly focused beams that are quite beneficial for probing small spatial scales. All beams are diffraction-limited; unfortunately, at the RF frequencies available to MRI, the diffraction limit is comparable to the object size. Nevertheless, this phenomenon provides an additional benefit to accelerated high-field imaging, above those brought about by increased equilibrium magnetization and various changes in image contrast.

44.3 Large-N array Coils in Practice

44.3.1 Introduction

Historical experience with array coils quickly showed that signal detection efficiency improved with even a modest number of surface coils and that the reception uniformity and reconstruction burden could be handled with simple post-processing algorithms. The use of surface coils was thus able to expand into the traditional role of volume coil structures. The quest for higher sensitivity and improved encoding acceleration both drive exploration of the logical expansion of the array approach, increasing the number of elements and reducing the size of the receive coils (to cover a fixed anatomical territory). With 32 receive channels appearing to be the new standard on current clinical scanners, multiple groups are developing torso/cardiac (Zhu et al. 2004; Sodickson et al. 2005), and brain (Wiggins et al. 2005a; Moeller et al. 2004; Cline et al. 2004) arrays for these instruments.

Although exploring arrays of N>32 channels clearly risks hitting the limits identified by the studies of the ultimate sensitivity for MR, such important limitations must be extensively experimentally explored. Therefore, a few groups have gone on to build such arrays explicitly to determine the potential capabilities and practical limitations of even larger-N arrays (64 and 90 channels) (McDougall and Wright 2005a; Wiggins et al. 2005b). The overall picture of these two efforts has been to support the case that parallel imaging strategies can receive expanding benefits from these "large-N" arrays.

44.3.2 Close Fitting Brain Arrays with 23, 32 and 90 Channels

Preliminary experience in highly parallel acquisition strategies using helmet-shaped geometries of circular receive coils has concentrated on building and testing brain array prototype for 1.5 T, 3 T, and 7 T. Tests so far include 23- and 90-channel arrays for 1.5 T (Wiggins et al. 2005b) and 32-channel arrays for 3 T (Wiggins et al. 2005a) and 7 T. All of the arrays were built onto a helmet-shaped former that conforms closely to the head. The tiling strategy for the individual circular surface coils was based on

the combination of hexagonal and pentagonal symmetry of the soccer ball or the Buckminster-Fullerene molecule. Coil elements are circular, and employ active PIN diode trap detuning, a cable trap to block common mode currents on the output coax and a commercial preamps designed to provide "preamp decoupling" (Roemer et al. 1990) (Siemens Medical Solutions, Erlangen Germany.)

44.3.2.1 32-Channel Brain Array

Figure 44.4 shows a photo of the 32-channel brain coil without covers as well as SNR maps measured for this coil, the widely used commercial 8-channel dome array (InVivo Corp., Orlando FL) and a commercial quadrature transmit-and-receive birdcage coil. In addition to nearly three-fold higher peripheral SNR, the 32-channel coil was found to have 20-30% higher SNR in the center of the head than the 8-channel array, likely explained by the tighter fit of this coil.

The g-factors as a function of acceleration for the 32-channel coil were obtained by measuring the noise correlation matrix (using an image acquired with no RF excitation) and coil sensitivity maps in a head-shaped phantom (Pruessmann et al. 1999). Figure 44.5 shows the sensitivity of the arrays for accelerated imaging. Shown are the fraction of the maximum obtainable SNR, a measure related to the g-factor penalty (%SNR=1/g) for two through six-fold acceleration in a single direction. For example, the %SNR of approximately 53% seen in the four-fold accelerated image corresponds to the maximum g-factor of 1.9 or a SNR loss of nearly 50% at this location. The maximum g-factor in the slice is also computed and displayed below the map. While the 32-channel coil performs significantly better with acceleration than the 8 and 12-channel coils, it still does not appear to truly push the R=5 intrinsic limit identified in the ultimate g-factor calculations (Wiesinger et al. 2004; Ohlinger et al. 2003).

As pointed out by the ultimate g-factor calculations, significantly higher accelerations can be achieved if the encoding is accelerated in each of two phase-encoding directions in a 3D image (Wiesinger et al. 2004, Ohlinger et al. 2003). Figure 44.6 shows a section of a high-resolution 3D FLASH image accelerated 12-fold (3-fold acceleration in one direction and 4-fold in the other). The 1-mm-spatial-resolution volume acquisition was acquired in 1:20 min.

44.3.2.2 90-Channel Brain Array

The 90-channel preliminary data were taken to (1) determine the feasibility and issues associated with upgrading the standard 32-channel system to 96 channels and (2) to gain experience with the capabilities and design issues of large-N helmet arrays. Preliminary layouts suggested that the helmet could be tiled with 90 coils with each about 5 cm in diameter. Thus, the coil did not use 6 of the available 96 receive channels. The prototype was undertaken at 1.5 T where the clinical system already had 32 channels and could therefore be modularly expanded in blocks of 32 to 96 channels. To increase the number of receivers to accommodate the 90-channel array we supplemented the existing 32 channels with an additional rack of 64

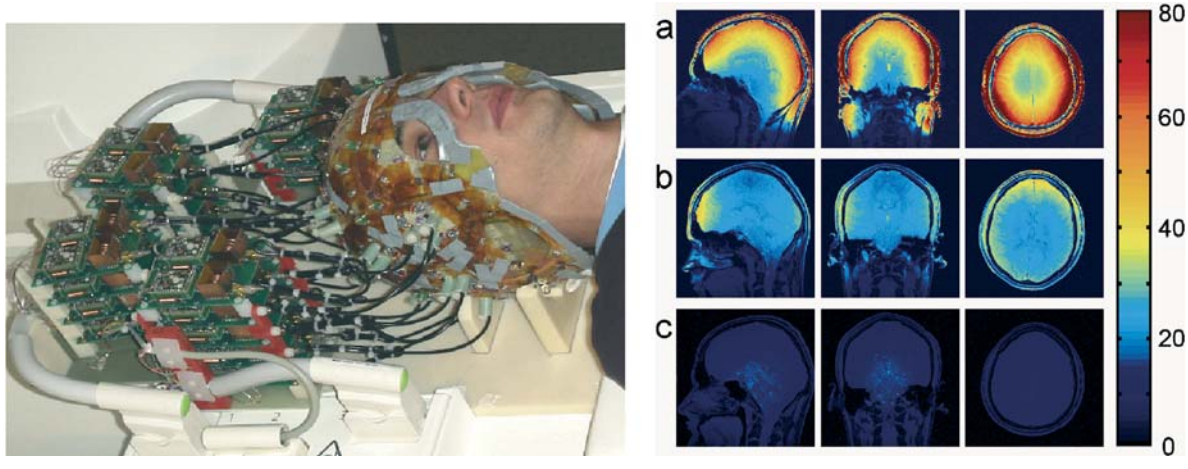

Fig. 44.4. Photo of the 32-channel 3-T coil (*left*) and SoS-generated SNR maps for 32-channel coil (*right*, *top*) compared to a commercial 8-channel dome array coil (*middle*) and a commercial quadrature birdcage coil (*bottom*)

receivers and 2 additional reconstruction PCs (one for each set of 32 channels). We then created the additional copies of the local oscillators and command signals needed to run these devices from the standard cabinet. We also mounted two additional sets of the Siemens second-stage RF amplifiers/switching matrices inside the magnet room. Their fiber-optic controls were also duplicated from the existing signals. The additional reconstruction computers were programmed to simply save the raw data for offline reconstruction.

The preamps were situated in stacks of 16 per board just behind the subject's head as seen in Fig. 44.7. The array consisted of 5.5-cm and 4.5-cm diameter coils laid out in a tiling pattern using the same combinations of hexagonal and pentagonal symmetry. The coils were overlapped between nearest neighbors to minimize mutual inductance. Figure 44.7 also shows images from each of the 90 individual channels demonstrating that the individual receive elements act independently with good decoupling from the combination of overlapped coils and preamplifier decoupling. The coil decoupling is also reflected in the noise correlation matrix for this coil, shown in Fig. 44.8.

While significant gains in SNR were observed with the 90-channel coil compared to an 8-channel array, the array performed less well compared to a similarly shaped 23-channel helmet coil. In the cortex, where an approximate two-fold gain was expected, the 90-channel only produced slightly higher SNR. In the center a 40% lower sensitivity was observed. This is consistent with an overall drop in sensitivity for the array elements, likely due to the poor unloaded-to-loaded-Q ratio of these small loop coils at 64 MHz. With an unloaded-to-loaded-Q ratio of approximately 2, the body noise was approximately equal to the other sources. Improving the Q ratio could thus potentially make up this 40% loss in sensitivity. In addition to strategies for reducing non-body noise sources such as increasing the copper trace width, simply building the coil at 3 T or 7 T should substantially improve the degree of body-noise dominance.

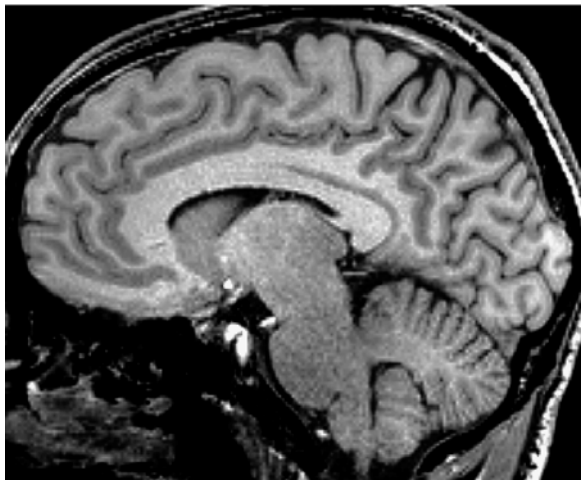

Fig. 44.6. A highly accelerated 3D FLASH scan acquired with the 32-channel 3-T helmet array. Image was accelerated 12-fold, 4-fold in the in-plane phase-encode direction and 3-fold in the through-plane phase-encode direction. Image time 1:20 min, image resolution 1 mm isotropic

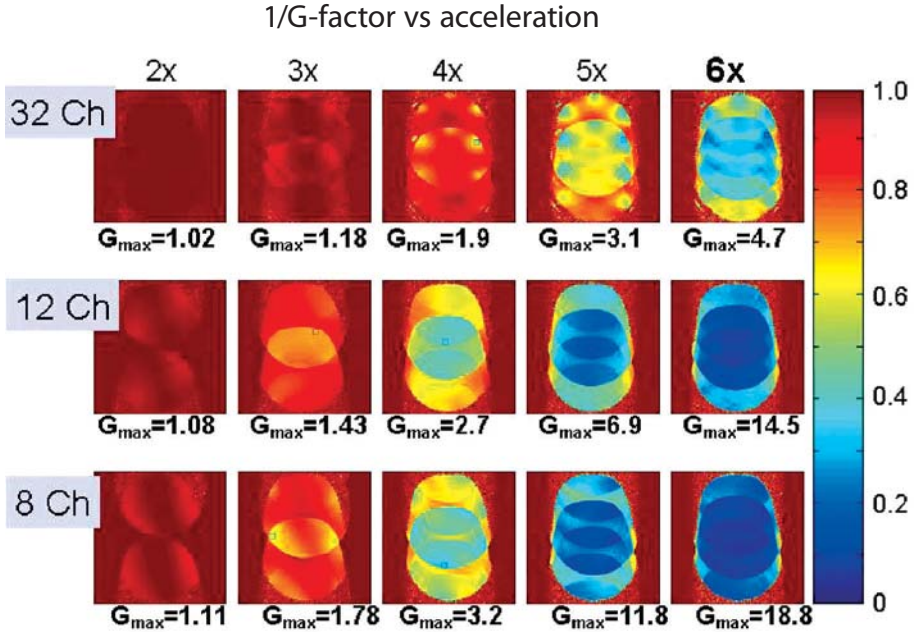

Fig. 44.5. g-factor results for R=2 through R=6 acceleration for 8, 12 and 32-channel brain arrays displayed as 1/g to allow visualization on the same scale

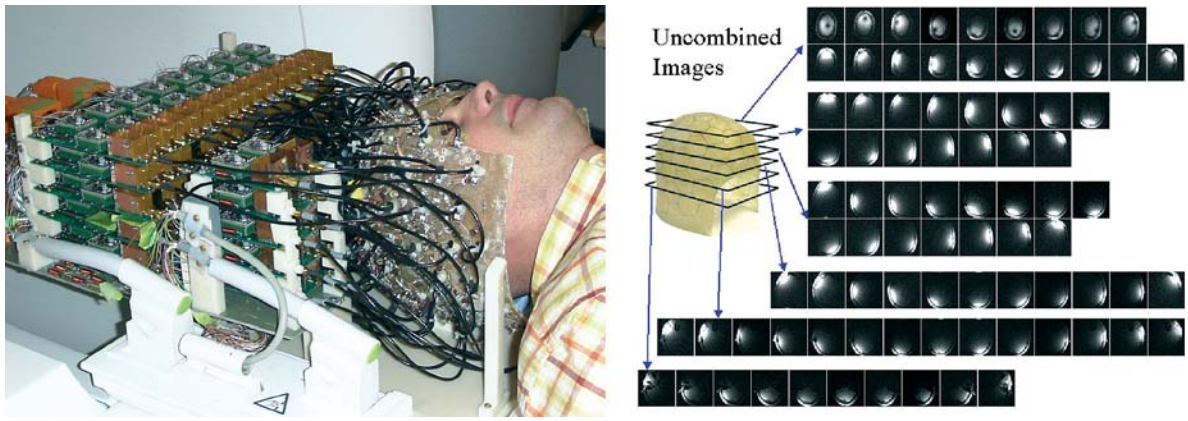

Fig. 44.7. A 90-channel brain array constructed for 1.5 T. The photo shows the 90-channel array and preamplifier, cable trap and bias line assembly. On the right-hand side, the 90 individual images produced by the array are shown. Here the image from each channel is shown from a slice approximately through the coil

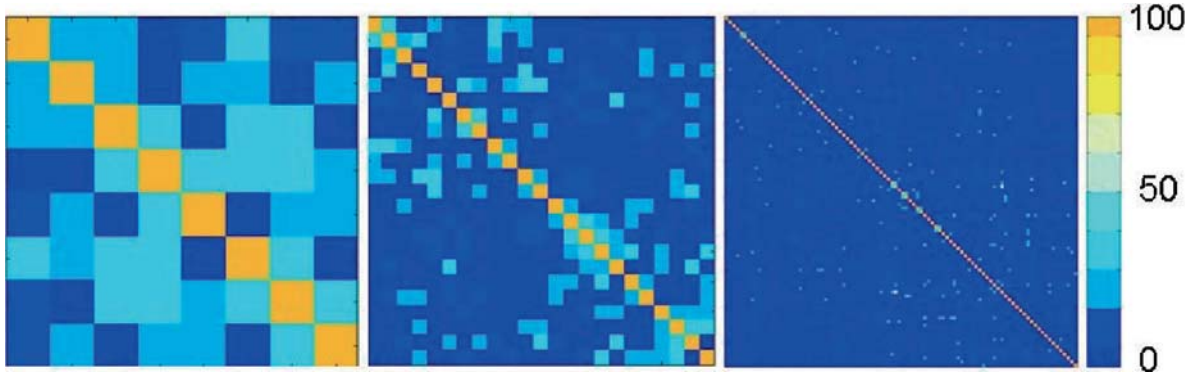

Fig. 44.8. Noise correlation matrices measured from zero RF excitation images for 8-channel commercial dome array (*left*), 23-channel helmet array (*middle*) and 90-channel array (*right*). Average noise correlation of off-diagonal elements is 0.22, 0.11 and 0.062, respectively

The acceleration capabilities of the 90-channel coil showed marked improvements in g-factor penalties compared with 8- and 23-channel coils. Figure 44.9 shows maximum g-factors in a transverse slice with AP acceleration as a function of the acceleration rate. g-factor calculations were based on the measured coil sensitivity profiles and noise correlation matrix. While the g-factors become significant for six-fold acceleration, the array still appears to be operating in a regime not limited by the ultimate g-factor limit. With this possible exception, the overall results at 32 and 90 channels are consistent with the findings of the ultimate SNR studies, but do not reflect the immediate presence of a heavy constraint imposed by the ultimate performance limitations (although they could be close-by).

44.3.3 Technical Problems of Large Arrays of Very Small Coils

In the discussion above, we have touched upon some of the difficulties associated with covering a given array with larger numbers of smaller coils. The poor unloaded-to-loaded-Q ratio of small coils underscores the necessity of maintaining close proximity to the body as the coil gets smaller. Patient safety issues may ultimately dictate how close the conductors can get to the subject. If the body noise cannot be made to dominate, approaches to reducing the other loss sources will have to be utilized to avoid sensitivity losses. Over the years, many such approaches have been taken such as cooling the copper conductors

(Scott et al. 1994) or using superconductors (van Heteren et al. 1994). But these technologies add additional layers of complication to the coil. In either case, it seems likely that if the large-*N* pathway is followed to its extreme of hundreds of elements, coil arrays will benefit from becoming more like articles of clothing (or EEG caps), fitting and very flexible with miniaturized and un-obstructive circuitry.

The interaction between the receive array's output coaxes and the transmit body coil tends to increase with the number of elements if the common mode rejection on each channel is not scaled with the number of elements. Thus, there is the potential for a significant fraction of the RF transmit power to be dissipated among the cabling of the array. At the very least, it must be dissipated safely.

Once an array of body-noise dominated coils free of excessive interaction with the excitation RF is constructed, the manufacturing and quality control issues must be faced. If a 128-channel coil has a 1% failure rate among elements, the user will be faced with the prospect of always having a broken element. Since maintenance is a significant cost over the lifetime of MR equipment, this added expense (in addition to the obvious increased parts and labor costs of construction) cannot be overlooked.

Finally, our current zeal for increasing the number of receiver channels appears to be out-stripping the ability of the reconstruction computer to handle the added data. The data rates can be immense. For example, a 64-matrix EPI sequence will acquire as many as 82,000 *k*-space points per second per coil. For 2× over-sampled readouts and a 128-channel coil, the total data rate is 170 MByte per second. Efficient reconstruction of this data will require improvements in computing, such as 64-bit architectures and massively parallel processing. Despite the daunting reconstruction task, advances in computational power have been quite rapid, and sufficient computational power will likely reach the market before 128-channel MR systems.

44.4 Extreme Encoding with Large-N Arrays

With current clinical systems (e.g., 32-channel), the reduction of a 10-min volume scan to less than 1 min with 12-fold acceleration is possible with a modest increase in noise beyond the standard trade-off between SNR and acquisition time. With even more channels (64 and 96), credible imaging can take place with truly minimal use of the gradients (for example, a single readout to form an image).

44.4.1 Single-Echo Acquisition (SEA)

McDougall and Wright (2005a, 2005b) constructed a specialized 64-element planar array to demonstrate the potential for very high frame rate imaging acquired with no phase-encode steps (all the information in this direction provided by array localization). Since the imaging is performed in a single readout, they refer to the resulting highly accelerated image as a "single echo acquisition" (SEA). Figure 44.10 shows their array. It consists of thin strips, each one designed to provide a pixel in the *y*-direction (conventional frequency encoding provides the second spatial dimension). Because the readout can be performed in a few milliseconds, frame rates of up to 200 fps are potentially achievable. Figure 44.11 shows a SEA image acquired as part of a 125-frame-per-second acquisition of a phantom with a paddle wheel rotating at 60 rpm. In addition to illustrating the excellent image quality (considering the 64-fold acceleration and total acquisition time of 8 ms!), this image shows the extreme robustness of motion possible at these encoding rates.

At first glance, the 64-fold acceleration apparently violates the acceleration limits described in the "ultimate" g-factor and SNR calculations (which predict

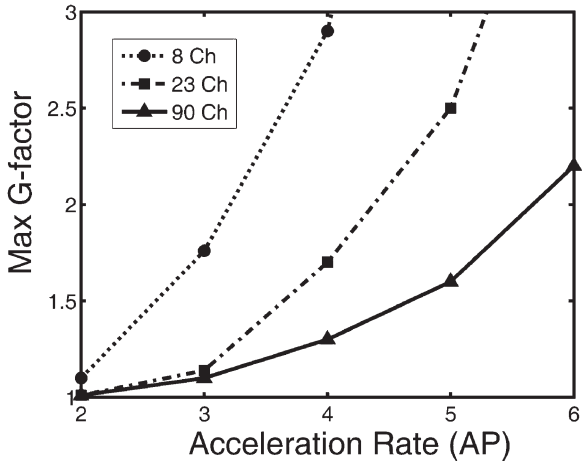

Fig. 44.9. Maximum g-factor in transverse slice for 8, 23 and 90-channel coils at 1.5 T

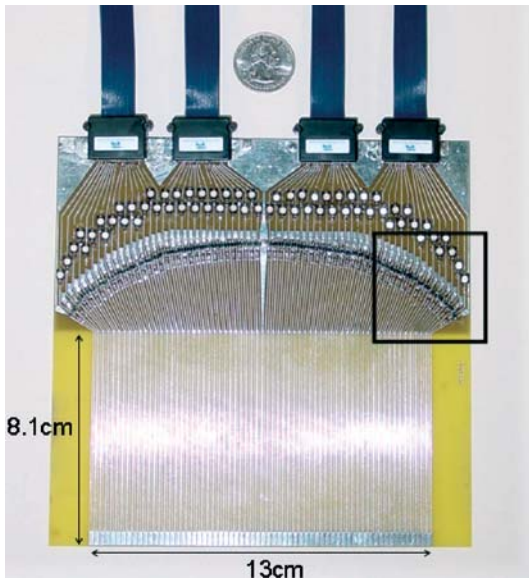

Fig. 44.10. A 64-channel linear array for extreme acceleration in one spatial dimension. Image courtesy of S. Wright, Texas A&M University

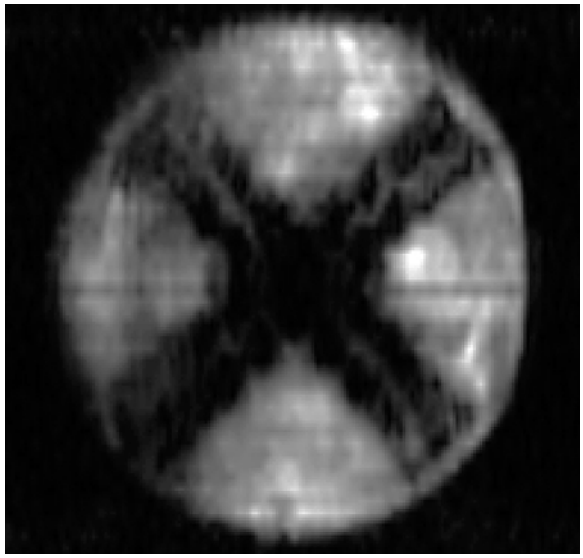

Fig. 44.11. Image from a series taken at a frame rate of 125 fps generated from single readouts (64-fold acceleration. The dark *x* is rotating at 60 rpm. Image courtesy of S. Wright, Texas A&M University

a maximum single direction acceleration of approximately R=5 or 6). However, these R=64 images were acquired for a location that was not the focus of the ultimate SNR studies, i.e., in close proximity to the very thin coil elements. These are the "best case" locations since near the current sources Maxwell's equations support very quickly varying field profiles.

44.4.2 MR Inverse Imaging (MR InI)

Using a completely different reconstruction strategy, SEA imaging was acquired in the brain using the 90-channel brain array described above. The goal was not to detect images per se, but to localize the source regions of dynamic change within the brain during functional activation. In this case the goal of the MR image reconstruction resembles MEG/EEG source localization. We seek statistical best estimates of the source locations and associated time courses given the spatial and temporal information available by applying the inverse solution methods used in MEG/EEG source localization. In the example shown in Fig. 44.12, the temporal information comes from a 50-fps PRESTO sequence acquired with no phase encoding. PRESTO was used at achieve the long TE needed for BOLD fMRI. The spatial information was provided by the readout gradient (LR direction) and the 90-channel array (AP direction). Because of the similarity of the reconstruction to the MEG/EEG inverse problem, this approach was called "MR inverse imaging" (MR InI) (Lin et al. 2006).

Unlike conventional parallel imaging where the lack of sufficient spatial information from the array manifests itself as noise amplification (g-factor), the same problem in MR InI produces reduced ability to localize the changes spatially, namely, a greatly reduced spatial resolution. Here, "sources" refers to the areas of the brain with dynamically altered signal with respect to the user-defined baseline condition. Since spatial locali-

zation is provided in one direction by the array and in the other by conventional frequency encoding, the MR InI method as implemented is a 2D method with slice-select and standard frequency-encoding providing the other spatial dimensions. It could potentially be expanded to 3D. The 2D case is thus a single-echo acquisition, and the 3D case is potentially a single sample of the signal with no use of gradients. For the 90-channel array, the spatial resolution of the activation localization in the 2D case was 3 mm in the readout direction and estimated to vary from just over 1 cm near the array to about 3 cm deep within the head.

Thus, in the MEG-like inverse problem, the reduced ability of the array to provide spatial information in the center of the head (where the coil profiles are too smooth to provide high-spatial-resolution information) translates to a deteriorated spatial resolution in these regions. Since the SNR of MR imaging scales as the cube of the voxel dimensions, a small increase in voxel dimensions may make up for reduced spatial-encoding accuracy since statistical estimates will be more robust due to the higher signal levels in the larger voxels. Thus, the MR InI method can be viewed as coping with the encoding limitations in the center of the head by adjusting the spatial resolution accordingly.

Figure 44.12 shows the InI reconstructed statistical estimates of the stimulus correlated changes associated with a block design visual stimulus. Also shown is the reconstructed time-course for the activated area. At this temporal resolution, many physiological modulations such as the cardiac and respiratory modulations are not temporally aliased (as they normally are) and thus potentially easily removable from the data.

The ability to improve the temporal resolution of fMRI significantly using these extreme parallel acceleration methods offers several exciting possibilities. Firstly, this will be a necessary technology for future attempts to image direct neuronal manifestations of neuronal activation (as opposed to relatively slow and more indirect hemodynamic effects). MEG and EEG show these evoked responses are typically bipolar and of a duration of 30 ms or less. Thus, imaging strategies with order-of-magnitude improvements in the temporal resolution are needed to resolve these events unambiguously. The ability to temporally resolve significant sources of physiological modulation in the data, such as respiratory and cardiac-cycle effects, will also improve statistical inference in BOLD fMRI. Finally, with 3D MR InI there is the potential for truly silent fMRI studies of the auditory system since all gradient waveforms can be eliminated.

44.5 Conclusion

While the technical issues of building arrays with large numbers of receive elements are challenging, both the theoretical simulations and the experimental prototypes suggest the potential for substantial benefits, especially for accelerated image encoding.

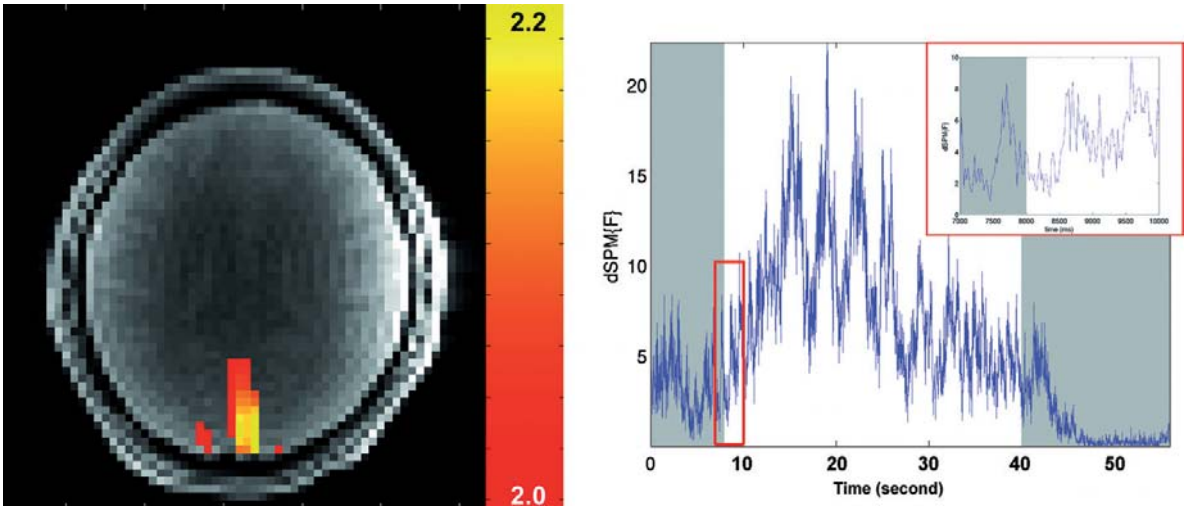

Fig. 44.12. MR-InI-reconstructed statistical estimates of BOLD visual activation acquired with the 90-channel brain array. Spatial maps (*left*) and time series of one epoch. Temporal resolution of 20 ms was achieved with a PRESTO sequence and no phase encoding. Modulation at frequencies corresponding to the respiratory and cardiac rates is clearly visible in the time-course. Result courtesy of Fa Hsuan Lin, MGH

The synergy between large receive arrays and higher-field-strength systems also suggest that these two methods will continue to evolve together in a productive way. This is seen on the theoretical side where the sensitivity gains for accelerated imaging as a function of the number of array elements were seen to improve at higher field, and also on the practical side where constructing a small receive coil which is body-noise dominated is easier at higher field strength.

Perhaps even more intriguing than being able to improve conventional imaging substantially is the ability to perform new types of imaging. Realization of this potential is in its infancy, but will likely have its first and largest implications for encoding-limited imaging such as high-resolution 3D imaging, spectroscopic imaging, and dynamic functional imaging.

Acknowledgements. We would like to thank Andreas Potthast of Siemens Medical Systems for his contribution to the large-N brain array and receiver configurations, Christina Triantafyllou of MGH for her contribution to the studies of noise in the combination of the array elements, Fa Hsuan Lin of MGH for results from the inverse imaging reconstruction method, and Steven Wright of Texas A&M University for results from his 64-channel array. We would like to acknowledge support from the NCRR of the NIH, grant 5P41RR014075-05, and the MIND Institute for Mental Illness and Neuroscience Discovery.

References

Carlson JW (1989) Power deposition and noise correlation in NMR samples. Mag ResonMed 10:339–403

Chen CN, Hoult DI (1989) Biomedical MR technology. Adam Hilger, Bristol, New York

Cline H et al (2004) 32 channel head array for highly accelerated parallel imaging. In: Proc 12th Annual Meeting of ISMRM, Kyoto, Japan

Constantinides CD, Atalar E, McVeigh ER (1997) Signal-to-noise measurements in magnitude images from NMR phased arrays. Magn Reson Med 38:852–857

de Zwart JA et al (2002) Design of a SENSE-optimized high-sensitivity MRI receive coil for brain imaging. Magn Reson Med 47:1218–1227

Harpen MD (1988a) Influence of skin depth on NMR coil impedance. Part II. Phys Med Biol 33:597–605

Harpen MD (1988b) Influence of skin depth on NMR coil impedance. Phys Med Biol 33:329–337

Keltner JR et al (1991) Electromagnetic fields of surface coil in vivo NMR at high frequencies. Magn Reson Med 22:467–480

Lin FH et al (2006) Dynamic magnetic resonance inverse imaging of human brain function. Magn Reson Med, submitted

McDougall MP, Wright SM (2005a) 64-channel array coil for single echo acquisition magnetic resonance imaging. Magn Reson Med 54:386–392

McDougall MP, Wright SM (2005b) Phase compensation in single echo acquisition imaging. Phase effects of voxel-sized coils in planar and cylindrical arrays. IEEE Eng Med Biol Magn 24:17–22

Moeller S et al (2004) Parallel imaging performance for densely spaced coils in phase arrays at ultra high field strength. In Proc 12th Annual ISMRM Meeting, Kyoto, Japan

Ocali O, Atalar E (1998) Ultimate intrinsic signal-to-noise ratio in MRI. Magn Reson Med 39:462–473

Ohliger MA, Grant AK, Sodickson DK (2003) Ultimate intrinsic signal-to-noise ratio for parallel MRI: electromagnetic field considerations. Magn Reson Med 50:1018–1030

Pruessmann KP et al (1999) SENSE: sensitivity encoding for fast MRI. Magn Reson Med 42:952–962

Roemer PB et al (1990) The NMR phased array. Magn Reson Med 16:192–225

Scott G et al (1994) Body noise feasibility limits of PMRI. In: Proc ISMRM

Serfaty S,Darrasse L, Kan S (1995) Patient equivalent resistance in surface coils: a simple analytical expression for the usual MRI frequency range. In: Proceedings of the ISMRM, Nice, France

Sodickson DK et al (2005) Rapid volumetric MRI using parallel imaging with order-of-magnitude accelerations and a 32-element RF coil array: feasibility and implications. Acad Radiol 12:626–635

van Heteren JG, James TW, Bourne LC (1994) Thin film high temperature superconducting RF coils for low field MRI. Magn Reson Med 32:396–400

Weiger M et al (2001) Specific coil design for SENSE: a six-element cardiac array. Magn Reson Med 45:495–504

Wiesinger F, Boesiger P, Pruessmann KP (2004) Electrodynamics and ultimate SNR in parallel MR imaging. Magn Reson Med 52:376–390

Wiesinger F, DeZanche N, Pruessmann KP (2005a) Approaching ultimate SNR with finite coil arrays. In: Proceedings of the ISMRM, Miami FL

Wiesinger F, DeZanche N, Pruessmann KP (2005b) Approaching ultimate SNR with finite coil arrays. In: ISMRM 13th Annual Scientific Meeting, presentation 672, Miami FL

Wiggins G et al (2005a) A 32 channel receive-only phased array head coil for 3T with novel geodesic tiling geometry. In: Proc Int Soc Magn Reson Med, Miami FL

Wiggins G et al (2005b) A 96-channel MRI system with 23- and 90-channel phase array head coils at 1.5 Tesla. In: Proc Int Soc Magn Reson Med, Miami, FL

Wright SM (2002) Full-wave analysis of planar radiofrequency coils and coil arrays with assumed current distribution. Concepts Magn Reson (Magn Reson Eng) 15:2–14

Wright SM, Wald LL (1997) Theory and application of array coils in MR spectroscopy. NMR Biomed 10:394–410

Zhu Y et al (2004) Highly parallel volumetric imaging with a 32-element RF coil array. Magn Reson Med 52:869–877

Parallel-Excitation Techniques for Ultra-High-Field MRI

45

Lawrence L. Wald and Elfar Adalsteinsson

CONTENTS

45.1 Introduction

The success of parallel-imaging methods and their impact on image encoding have sparked a great deal of interest in parallel-excitation arrays and the potential to utilize the spatial information in an array during RF transmission. One of the principal applications of parallel-excitation technology will likely be spatially tailored RF pulses, excitation pulses with a carefully controlled spatially varying flip angle and/or excitation phase. While the benefits of spatially tailored excitation pulses have been known for some time, the potential to decrease the pulse length of spatially tailored excitations to practical durations for clinical imaging using parallel-transmission methods raises the exciting possibility of their routine use. If the technical issues are addressed, this technology will be a timely addition to ultra-high field strength (7 T and above) studies. At these fields, the wavelength effects of the excitation fields in the head or body cause considerable transmit B_1 inhomogeneity. This issue could be addressed with spatially tailored excitation pulses with accelerated gradient trajectories and parallel excitation channels. This chapter will look into the potential needs of this nascence field.

L. L. Wald, PhD; E. Adalsteinsson, PhD
MGH/MIT/HMS Athinoula A. Martinos Center for Functional and Structural Biomedical Imaging, Charlestown Navy Yard, Building 149, 13th Street (2301), Charlestown, MA 02129-2060, USA

45.2 Ultra-High-Field MRI Systems

High-field MRI offers many potential advantages to clinical and scientific studies, including increased sensitivity and in many cases improved image contrast. In synergy, these effects promise improved characterization of brain function and anatomy in health and disease. However, spatially inhomogeneous B_1 transmit fields intrinsic to the shortened RF wavelength in biological tissue present one of the outstanding methodological challenges to bringing ultra-high-field systems from the research to the clinical arena. The spatial homogeneity of the transmit field is especially problematic since tissue contrast is a function of the excitation flip angle for many clinical and research imaging applications. Thus, unlike detection inhomogeneity that manifests primarily as image intensity shading, a non-uniformly transmitted B_1 field results in spatially dependent tissue contrast and therefore reduced diagnostic power.

The problem is quite severe for the human head at 7 T. In this case, the wavelength of the RF in the tissue is approximately 14 cm, comparable to the size of the head. The "dielectric center brightening" is the well-known result of this wavelength effect for most coil types. At 7 T, the transmit B_1 field is peaked at the center of the head, undergoes minima at approximately the location of the insular cortex and then partially recovers toward the scalp. Since the head is not symmetric, the response to the head-coil interaction is also not symmetric, but presents a complex three-dimensional spatial profile in amplitude and phase. While it is tempting to pass this dramatic field variation off as a "coil problem," there are no current coil designs for 7-T brain imaging that produce uniform transmit-field profiles. Figure 45.1 illustrates the center brightening in a 7-T proton-density-weighted image acquired with a "uniform" birdcage coil.

The B_1-field inhomogeneity leads to unwanted spatial variations in the tissue contrast for most pulse sequences. For example, the contrast in a typical T1-weighted pulse sequence will vary within the head from proton-density-weighted to heavily T1-weighted in a simple FLASH image using a "uniform" mode birdcage (BC) or transverse-electromagnetic (TEM) type structure at 7 T. The severity of the effect depends on the contrast's dependence on B_1, and since the problem arises during excitation, it is not easily dealt with in post-processing. Where the intrinsic contrast information is not present locally, no amount of image manipulation can substitute for the missing information. In addition to mitigating the non-uniform transmit B_1 profile at high fields, spatially tailored RF excitation offers the potential to minimize local susceptibility dephasing dropouts in T2*-weighted sequences by pre-phasing the RF excitation to cancel the expected off-resonance effects (Stenger et al. 2003; Stenger et al. 2000; Stenger et al. 2002; Glover and Lai 1998).

45.3 Spatially Tailored RF Excitation

RF excitations appropriately modulated in amplitude and phase during time-varying gradients offers the potential of spatially tailored RF phase and amplitude in the excitation (Pauly et al. 1989). Although these types of pulses have been demonstrated for many years, there are serious engineering challenges to their routine and practical use. First and foremost is the lengthy encoding period needed for these pulses (as long as 50 ms). One of the most promising ways to address this limitation is the extension of parallel reconstruction methods to parallel excitation to accelerate the excitation encoding. A practical goal is

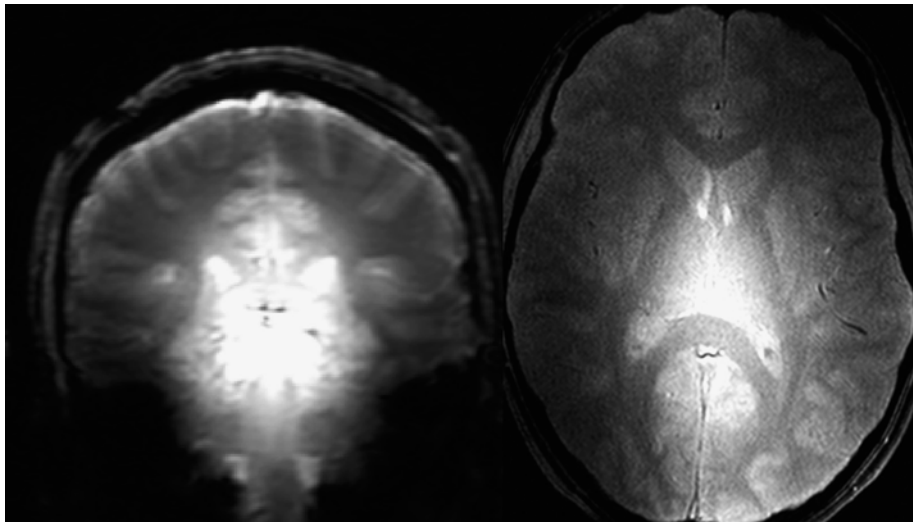

Fig. 45.1. Coronal and axial 7-T proton-density-weighted brain images acquired with a "uniform" band-pass birdcage coil. For a low-flip-angle gradient-echo exam, the image intensity scales as the square of B_1 (one factor of B_1 for the transmit efficiency and one for the receive efficiency). Variations in the transmit efficiency are more problematic than the receive inhomogeneities since they lead to contrast alterations

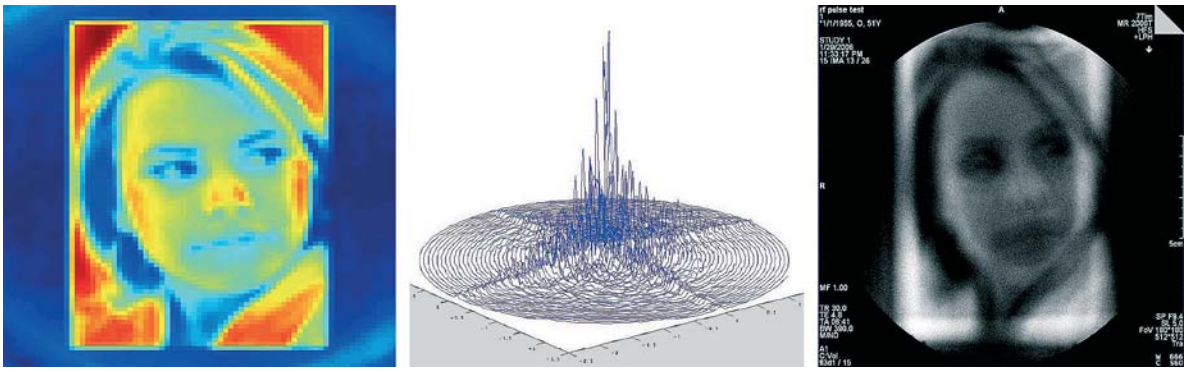

Fig. 45.2. Standard demonstration of a tailored excitation pulse. Target flip-angle profile (*left*) is used to compute the RF pulse phase and amplitude as a function of position in excitation k-space. The amplitude k-space matrix of the pulse along a spiral trajectory is shown (*middle*). The *right-hand image* shows a low flip angle proton-density-weighted image acquired with this pulse at 7 T. A grey-scale target flip-angle map is thus "burned into" an oil phantom at 7 T using a uniform birdcage coil. Single 16-ms spiral readout, 2-mm resolution. Pulse is not slice-selective or encoded in the through-plane direction and is therefore of limited practical value. Pulse design courtesy of K. Setsompop, MIT

to achieve a 5-ms duration 3D excitation pulse with a spatial profile that can mitigate the observed B_1 pattern in the head at 7 T in birdcage-like coils. This short duration is needed to be useful in common anatomical imaging sequences such as MPRAGE and FLASH.

Shaping the 2D spatial flip-angle distribution of an RF excitation requires the use of modulated RF amplitude and phase, while the gradients trace a particular k-space trajectory, typically a spiral or echo-planar path. In practice, we first chose a target magnetization map (which is proportional to the flip-angle map for small flip angles). For example, the target magnetization map might be the inverse of the measured B_1 profile for a given coil in the head. The calculation of the needed RF waveform is greatly simplified in the low-flip angle case where it can be reduced to a k-space analysis (Pauly et al. 1989). The RF excitation during such a gradient traversal is viewed as a series of small flip angle excitations short enough so the gradient can be thought of as constant during these sub-excitations. The phase and amplitude of these small RF pulses is altered so that the deposition of RF energy in the "excitation k-space" matrix is the Fourier transform of the desired spatial flip-angle map. This design method relies on the linear nature of the Bloch equations for small flip angles. Then the Fourier transform of the k-space excitation matrix is a good approximation of the desired excitation profile (Fig. 45.2).

Extending this concept to 3D profiles requires covering k-space in three directions and is therefore considerably more time consuming in addition to requiring additional gradient trajectory designs. Full 3D excitation is required for many applications including a slice-selective excitation with an in-plane tailored flip-angle pattern. In both the 2D and 3D cases, the gradient trajectory is chosen to cover the needed area or volume in k-space, using similar considerations as for image encoding. For our current applications, we constrain the excitation and 3D gradient designs to single-shot applications. Single-shot 3D image encoding is rarely (if ever) performed, and it is plausible for excitation trajectories only because relatively low spatial resolutions are sufficient (1 cm or less) to mitigate dielectric-center-brightening patterns. As in image encoding, there is likely to be one or more spatial direction that is considerably more slowly encoded than the other(s), leaving this direction open to off-resonance artefacts.

Tailored 3D pulses have been pursued to mitigate susceptibility dephasing in fMRI (Stenger et al. 2003; Stenger et al. 2000; Stenger et al. 2002; Glover and Lai 1998). In this case, relatively high spatial resolution is needed in all three spatial directions, requiring very long pulse durations. For example, Stenger and colleagues (2003) utilized four excitations of 20 ms each to achieve a 5-mm slice-selective pulse and 3.7-mm in-plane spatial resolution and 0.1-mm transitions in the slice direction. Recently, Stenger and colleagues have pursued tailored 3D pulses to address B_1 inhomogeneity (Saekho et al. 2005). For this application, they applied the "stack of spirals" trajectory approach, which allowed the relatively slowly vary-

ing B_1 profile to be addressed in all three directions. The excitation resolution was 2×2×1.25 cm^3, and the pulse required 22 ms, which is still unacceptably long for many applications. In addition, this approach is not suitable to 2D imaging since it does not provide a sharp slice profile.

A slice-selective spatial excitation pulse with in-plane B_1 mitigation but retaining sharp slice-select profiles is also a desirable goal for 2D imaging sequences. A method of 3D single-channel excitation to select a 2D slice with in-plane B_1 compensation was demonstrated by Ulloa et al. (2005) and Saekho et al. (2005). In this case, high spatial resolution is needed in the slice-select direction (defined here as the z direction) to achieve thin, well-defined slice profiles, but only 1-cm resolution is needed in the in-plane (x, y) direction to follow the slowly varying B_1 maps. Therefore, the gradient trajectory usually considered consists of lines or "spokes" in the z direction extending far in the k_z direction (for the needed sharpness in the slice select profile). A sinc-like pulse is played out for each of these k_z lines to insure a slice selective pulse. The k_z spokes with differing excitation amplitudes and phases are repeated at a multitude of locations in the k_x, k_y plane. Figure 45.3 shows an image acquired in a low-dielectric oil phantom at 7 T with a uniform mode birdcage coil. This low-dielectric phantom produces uniform images with conventional slice-selective pulses. In this image a "spokes" trajectory pulse was used that imposed a 30% reduction in B_1 in the center of the phantom with a Gaussian profile to reduce dielectric center brightening. Only 13 "spokes" (lines in the k_z directions) were needed spaced to give a 1-cm resolution to the in-plane flip-angle profile. Each spoke used a traditional sinc-shaped excitation to produce a clean slice select in z. The duration of the pulse was only 4.1 ms using the fast head gradients on this 7-T system. Thus, useful pulse durations are potentially feasible for this type of excitation given a modest acceleration with parallel-excitation methods. For example, two-fold acceleration will produce a 2-ms pulse, a short enough duration to substitute for the slice-selective pulse in most 2D sequences without excessive implications for the pulse sequence strategy.

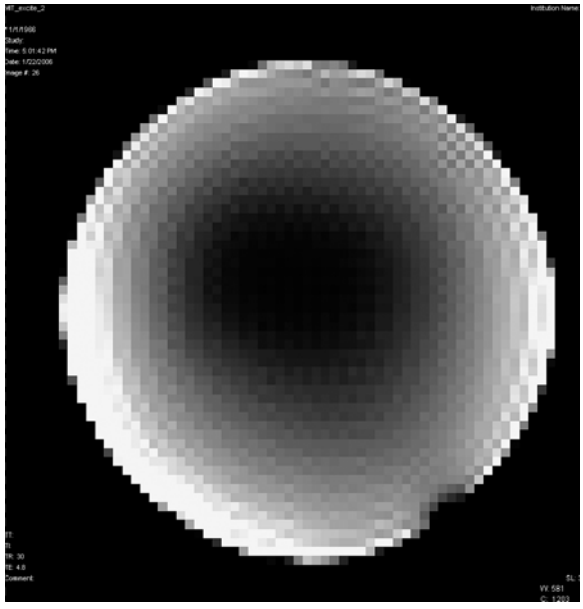

Fig. 45.3. Gaussian dip profile shown in an oil phantom with a uniform BC coil at 7 T. The 4-ms pulse is slice-selective and utilizes the "spokes" trajectory. Pulse design courtesy of K. Setsompop, MIT

45.4 Acceleration of Transmit Pulses with Parallel Excitation

The traversal of transmission k-space can be accelerated in analogy to the under-sampling of k-space in accelerated image encoding (Katscher et al. 2002; Zhu 2002; Katscher et al. 2003; Zhu 2004). Here, the under-sampling of transmission k-space is compensated for by simultaneous transmission from multiple transmit coils. Acceleration of the transmit pulse through parallel excitation has the potential to provide the considerable acceleration needed to bring the duration of the 3D tailored RF pulses to a length useable for common imaging applications. A plausible goal for a slice-selective pulse is a duration of less than 5 ms and accommodation of in-plane spatial B_1 variations on a scale of 1 cm of resolution. Preliminary results suggest that these goals can be met on a state-of-the-art 7-T head-gradient system with a two-fold acceleration from transmit SENSE. With four-fold acceleration, the pulse duration could be potentially reduced to less than 2 ms, making these tailored excitations truly interchangeable with conventional slice-select pulses in most pulse sequences.

For spatially selective RF pulses, the excitation consists of a regular deposition of RF energy as a function of position in the excitation k-space defined by the gradient trajectory being played out during the excitation. Since the concept of k-space in spatially

selective RF pulses is dual to that of image encoding, the principles of parallel acceleration of the excitation gradient trajectory follow by analogy. An array of multiple transmit coils is needed, each of which exhibits a spatially different excitation pattern (flip-angle map) and is driven by an independent RF waveform. The gradient waveform is played out during the excitation and modulates the transverse magnetization created. The amplitude and phases of the excitations as a function of position in the excitation k-space are determined by the Fourier transform of the target flip-angle map for the low-flip-angle case.

Since multiple, spatially differing transmit channels are used, there is the opportunity to undersample in the excitation k-space. This shortens the path to be traversed without sacrificing spatial definition. Since its introduction, transmit SENSE has been further explored by a number of groups, mainly using simulations on single-transmit-channel systems, but also on a three-channel small-bore scanner (Ullmann et al. 2005) and a clinical imager outfitted with eight channels (Zhu et al. 2005). Figure 45.4 shows a spatially tailored 2D excitation, accelerated using a prototype 3-T whole-body system with eight independent transmit channels (Siemens Medical Solutions, Erlangen Germany). The 2D spiral excitation trajectory was accelerated from R=1 to R=8, giving pulse durations ranging from 9.4 ms to 1.2 ms. The data in Fig. 45.4 suggest a potential for transmit SENSE to tolerate considerably more acceleration without degradation than seen with image encoding. This might be possible since a major source of degradation is noise amplification during the inversion of the under-sampled image. In the image-encoding case, we seldom have sensitivity to spare, while the signal-to-noise ratio of the transmit pulses is high since there is relatively little noise in the transmit system (Fig. 45.5).

45.5 Future System Requirements for Parallel-Excitation Techniques

45.5.1 Multiple, Fast Transmit Channels

A key component of parallel-excitation techniques is that the MR system is capable of simultaneously exciting with different RF waveforms on multiple excitation channels. The waveform is carefully calculated with a time-varying phase and amplitude modulation that is synchronized to the gradient traversal. Simply splitting a single RF waveform and exciting multiple

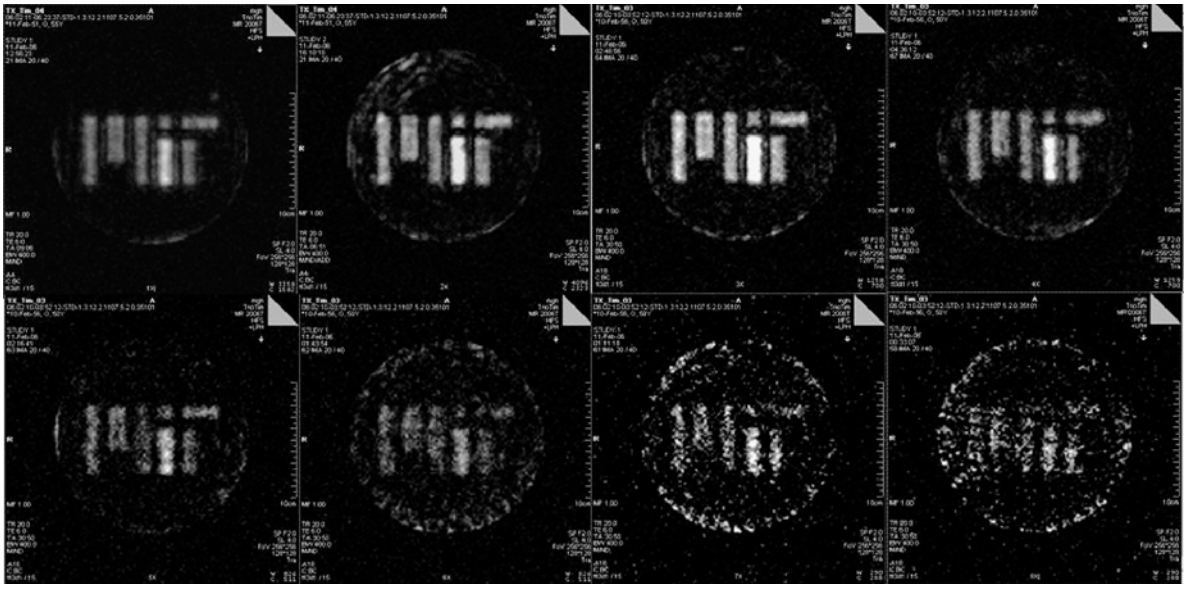

Fig. 45.4. Acceleration of a 2D spiral trajectory spatial-excitation pulse (target profile is the "MIT" logo). Accelerated from R=1 (*top left*) to 8 (*bottom right*) using the eight-channel transmit array of Fig. 45.7. The R=1 pulse has a duration of 9.4 ms, the R=8 pulse 1.2 ms. Some of the noise in the high-acceleration images is due to the pulse-amplitude normalization; the high-rate pulses have a lower flip angle. Pulse design courtesy of K. Setsompop, MIT

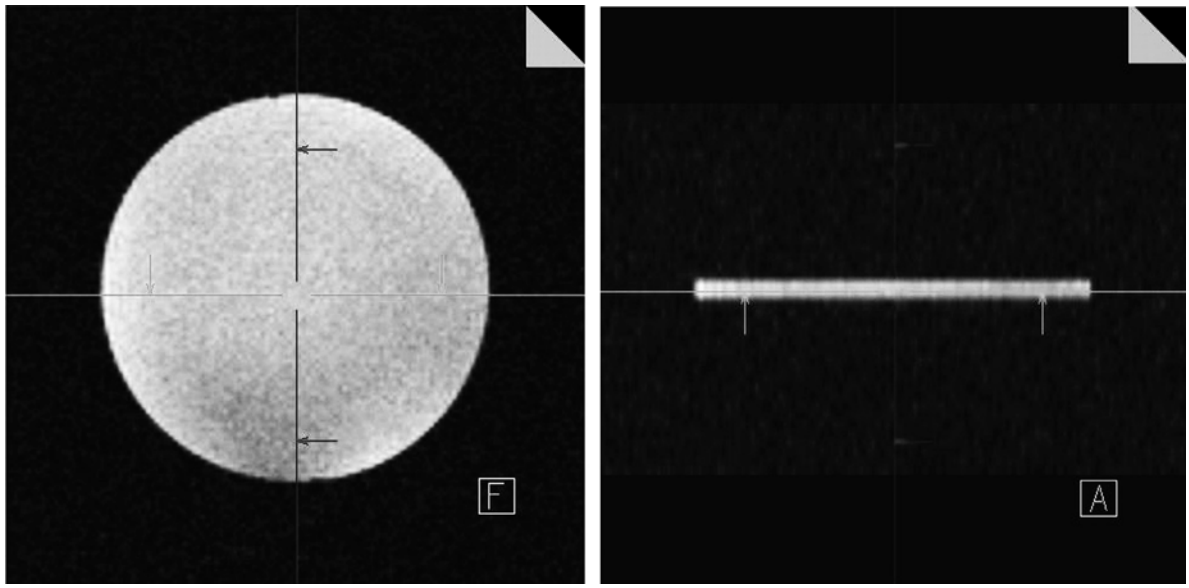

Fig. 45.5. Accelerated five-spoke trajectory at 3 T with eight-channel parallel system (pulse duration: 5.4 ms). In this case, the RF waveforms were calculated to allow a very inhomogeneous array (that of Figs. 45.7 and 45.8) to produce a uniform in-plane excitation (*left image*) with a sharp slice-selective profile (*right image*)

coils with a global phase shift and amplitude alteration is a form of B_1 shimming, but does not provide the required spatial control for accelerating spatially tailored RF pulses. Since the spatial resolution of the excitation pattern needed is low compared to imaging (at least for mitigating B_1 inhomogeneity), the gradient trajectory is expected to be slew-rate limited. This makes fast, low-inductance gradient sets such as a dedicated head-gradient system advantageous. It also requires a finer gradient and RF raster than found on most clinical systems. Ideally, the gradient and RF waveforms should be defined on a 1-μs raster. Although currently only a few experimental systems have more than two independent excitation channels, there are few fundamental barriers to making this technology widespread. However, the benefits of parallel transmission will not be widely explored until more systems are available.

45.5.2 SAR Considerations

Although there are many similarities between parallel-excitaiton techniques such as transmit SENSE and the acceleration of image encoding using parallel-receive coils (regular parallel imaging), there are also some important differences. Firstly, in the receive case, the data acquired from the multiple receive channels can be digitally combined with great flexibility in post-processing. For the parallel-excitation case, the only flexibility is in the pre-calculation of the RF waveforms. These waveforms are based on the target profile, knowledge of the transmit profiles of the individual coils, and knowledge of the gradient trajectory. The B_1 fields from the multiple transmit coils simply superimpose as magnetic fields within the object with no opportunity for adjustment after the excitation. The spatial distribution of the transverse magnetization (and thus the flip-angle map) is modulated by the gradient waveform in concert with the RF waveform allowing cancellation or build-up of the magnetization at certain spatial locations as desired. The electric fields (which govern the SAR distribution) are not affected by the gradients and simply superimpose among the coil elements. Therefore, the SAR distribution, although affected by the transmit pulses and array geometry, is not an explicit part of current RF design. Nevertheless, it is an important consideration for high-field imaging, and future work is needed to include SAR explicitly in the design of the RF pulses to enable a flexible trade off between RF excitation properties (due to the magnetic RF field, B_1) and SAR distribution (due to the electric RF field, E_1). There is potential for the E_1 fields from the coils to superimpose constructively,

creating a local SAR hot spot. Therefore, in addition to monitoring the average power from each channel, the system must make some estimate of how the local E_1 fields will superimpose so that the local SAR limits are not exceeded.

45.5.3 Pulse Calculation

The development of an automated system for calculating tailored RF pulses based on the B_1 profile measured in an individual subject and utilizable by an MR technologist will be required to utilize parallel-excitation techniques fully for B_1-inhomogeneity mitigation. In this scenario, a 3D B_1-field-mapping sequence would be incorporated into an automated pre-scan, and the image reconstruction program would calculate the 3D B_1 map and the RF phase and amplitude waveforms for accelerated RF pulses needed for subsequent studies. Currently, the calculation of accelerated 3D pulses can take several minutes, but substantial speed-ups are anticipated with coding optimization and faster processors such as the new generation of 64-bit machines now available on clinical scanners for image reconstruction.

45.5.4 Large-Flip-Angle Pulses

All work performed to-date has assumed the small-flip-angle approximation. While this approximation provides for elegant and computationally tractable RF designs, large flip-angle pulses are central to many clinical pulse sequences, and the low-flip-angle constraint needs to be addressed. Thus, parallel-excitation methods stand where slice-select pulse design stood 25 years ago when a sinc function was used for slice selection. The non-linearity of the Bloch equations for high flip angles causes the sinc-shape RF pulses to result in an imperfect slice profile for larger flip angles, but it is a good initial guess. More sophisticated calculation methods such as the Shinnar-LeRoux algorithm (Shinnar and Leigh 1989; Shinnar et al. 1989a; Shinnar et al. 1989b; Shinnar et al. 1989c; Pauly et al. 1991), optimal control theory (Mao et al. 1986; Conolly et al. 1989) or simulated annealing (Geen et al. 1989) have emerged to produce pulses that appear sinc-like to first approximation, but provide improved slice-select profiles for large-flip-angle excitations. It remains an open question how to best proceed along these lines for accelerated tailored RF pulses, but the analogous nature of the problem gives hope that similar innovations will be made.

45.6 RF Transmit Arrays for Parallel Excitation

45.6.1 General Considerations

While a great deal of effort has been placed in designing receive-only arrays, until recently the design of arrays for transmitting has been limited to cases where the use of a uniform body RF excitation was not available (Kim et al. 2003; Peterson et al. 2003). More recent work has focused on developing a transmit array based on surface-coil designs, whose excitation field fall-off would partially compensate for the dielectric-center-brightening effect (Pinkerton et al. 2005) or allow flexible excitation and reception in a single array ultimately providing either B_1 shimming approaches or parallel-excitaiton applications (Lee et al. 2001; Lee et al. 2004; Adriany et al. 2005; Adriany et al. 2003). The work toward transmit manipulation has almost exclusively focused on the decoupled lumped-element strip-line array.

A separate receive coil is required to map the B_1 profiles since all phase information in the B_1 field is lost if the same coil is used for both transmit and receive (the complex transmit field scales as B_1 and the receive profile as the complex conjugate, B_1^*; therefore, the detected image from the transmit/receive coil, which is the product, loses all phase information). Since a separate receive coil is needed to measure the complex B_1 maps, the body coil is useful for this purpose due to its uniformity in the oil phantoms we used at 3 T.

A second over-all issue with transmit arrays is the lack of an equivalent of preamplifier decoupling (Roemer et al. 1990) to help reduce inductive coupling between array elements. In preamplifier coupling, the coil is matched to present the impedance needed to optimize the noise figure of the preamplifier (usually 50 Ohm), but the preamplifier itself does not present a 50-Ohm impedance to the coil. Instead, it is configured to present a high impedance in series with the loop of the coil. In practice, this is achieved by having the preamplifier impedance transformed to a low impedance across a PIN-diode trap circuit, which in

turn presents a high impedance in series with the coil. With a high impedance effectively inserted in the coil loop, inductive coupling is reduced since the currents and therefore magnetic fields that mediate the inductive coupling are reduced. It is not possible to extend this concept to the transmit array in a straightforward way since power transmission along a 50-Ohm coax necessitates a 50-Ohm RF source. However, it might be possible to engineer an RF source and transmission line with the needed properties. Some preliminary designs have been discussed (Nam and Wright 2005; Kurpad et al. 2005).

45.6.2 Strip-Line Arrays

In the strip-line approach, each element consists of a linear conductor possibly broken with series capacitors and connected to the ground plane at either end via a capacitor. Thus, the circuit resembles the standard "pi" model of a transmission line. The elements resemble the transmission line element of a TEM coil (Vaughan et al. 1994). The strip-line elements showed a favorable lack of coupling to each-other when used in their original (no-lumped-element) configuration and closely shielded and trimmed to a λ/4 length (Lee et al. 2001). But most work has found it simpler to use the lumped-element approach and either have the elements far from one-another (Lee et al. 2004) or decoupled with capacitive networks (Adriany et al. 2005) or both (Lee et al. 2004) (Fig. 45.6).

The ability of the fields of the strip-line to penetrate into the subject critically depends on the spacing of the line from its ground plane. The closer the line is to the ground plane, the more "bottled up" the fields are (as is desired for a transmission line), and the less inductive coupling to neighboring coils exists. But, this also keeps the fields away from the subject. Relaxing this distance allows more penetration, but also allows the otherwise tight design to resemble more a square surface coil on its side, with the associated element-to-element coupling of this geometry. In fact, it is the inductive coupling between the strip-line elements of the TEM coil that gives the TEM volume resonator its intrinsic mode structure. In the TEM coil, the thinner the coil annulus, the lower the element-to-element coupling (and narrower the mode spacing), and a higher the fraction of the stored energy is held outside of the subject (between the rung and shield). So, at least in their practical implementation, the strip-line approach like the loop approach is not free from coupling issues.

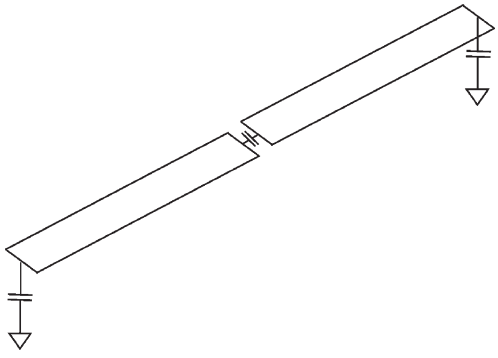

Fig. 45.6. Strip-line geometry for lumped-element configuration (ground plane not shown). After Lee et al. (2004)

Used as a receive coil to make a magnitude image formed in a normal sum of squares fashion, the strip line array shows highest reception sensitivity near the elements similar to other arrays. The transmit fields for a single element are also peaked near the element. But depending on the relative phases, much different spatial patterns can be obtained in the transmit B_1 map due to constructive and destructive interference between the elements (van de Moortele et al. 2005). While the use of these cancellations and super-positions has been theoretically examined for B_1 shimming (Collins et al. 2005; Ibrahim et al. 2001), they are also the basis for the ability of the parallel-excitaiton method to accelerate tailored RF pulses.

45.6.3 Loop-Coil Transmit Arrays

In this configuration, many of the considerations of receive arrays apply to the transmit array. Although the tight design of the stripline is attractive, one potential benefit of a transmit array of loop elements is the ability to minimize nearest neighbor interactions with coil overlap. A second potential benefit is the efficient nature of the loop coil. Figure 45.7 show a prototype eight-channel 3-T transmit array used for the transmit-SENSE experiments shown in Figs. 45.4 and 45.5. Eight circular loops with diameter of 15.6 cm were placed on an acrylic former with outer diameter of 27.6 cm. Figure 45.8 shows B_1 amplitude and phase maps acquired with each coil excited independently. Considerable next-nearest-neighbor coupling and coupling between opposite elements is visible. Nevertheless, as long as the B_1 field maps are accurate, they will be correctly taken into account in the pulse calculation.

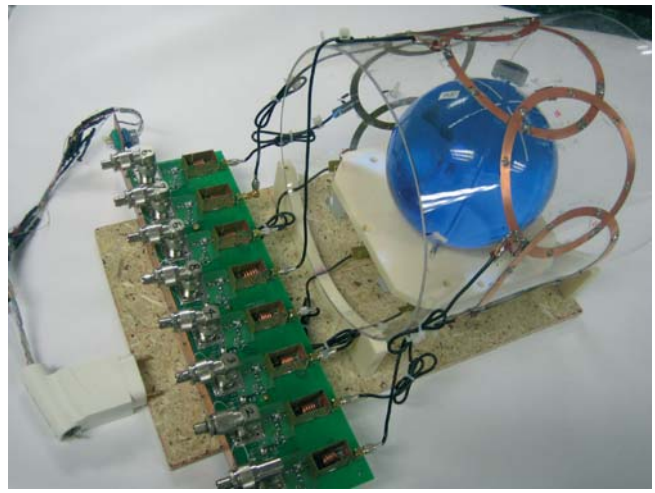

Fig. 45.7. Eight-channel transmit array of overlapping circular loop coils for 3 T. Each element has a transmit/receive switch, cable trap, and PIN-diode coil detuning to allow measurement of the B_1 map with a separate receive-only coil. S12 measures between nearest neighbors were –22 dB and –17 dB between next-nearest neighbors. Coupling between opposite coils on the cylinder was about –15 dB. Coil design and construction courtesy of A. Alagappan, MGH

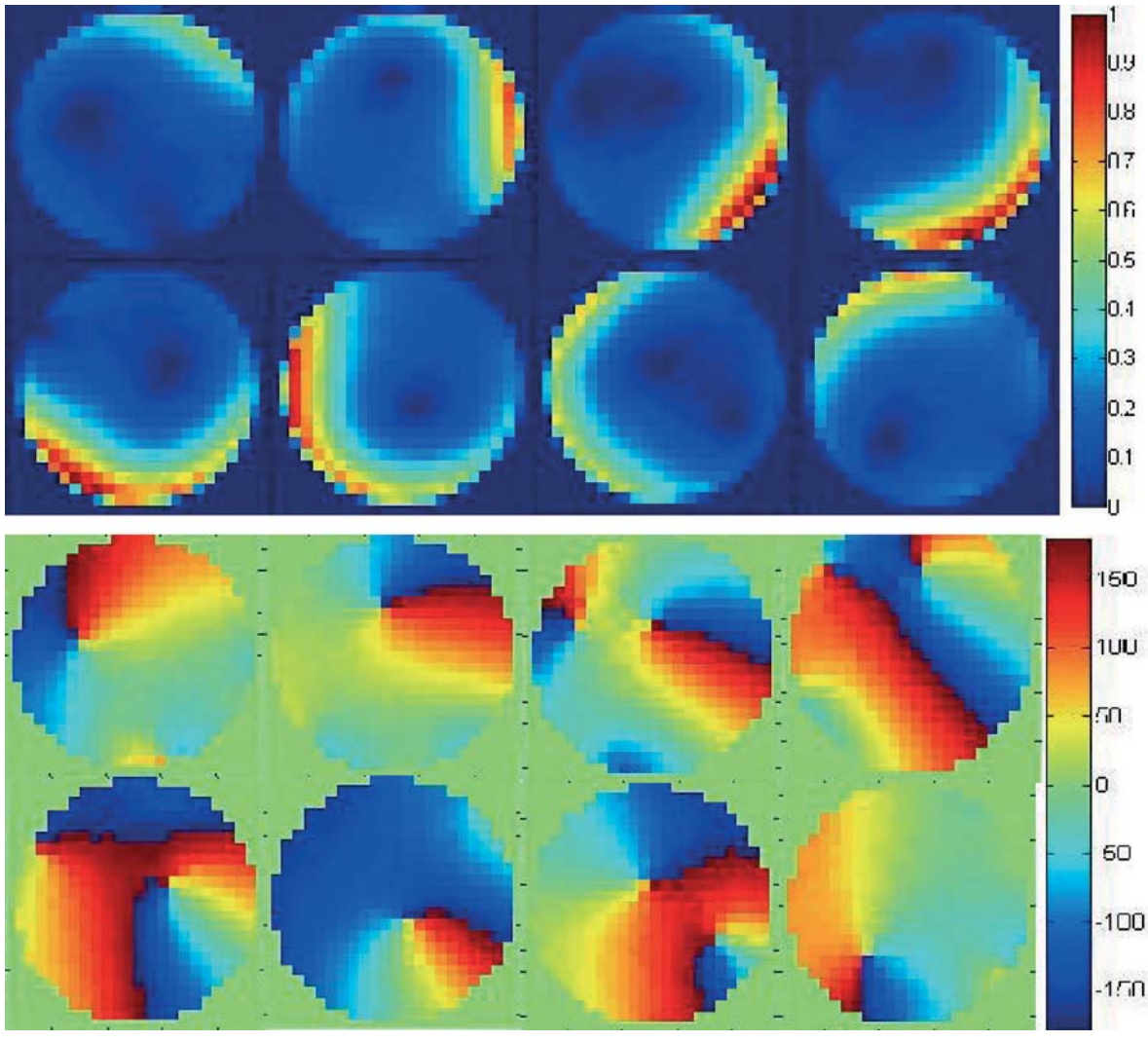

Fig. 45.8. Magnitude (*top*) and phase (*bottom*) maps of the eight-channel transmit overlapping-loop array. Data were acquired with the array coil for RF transmission and the body RF coil for reception. Measurements courtesy of A. Alagappan, MGH

45.7 Conclusion

Theoretical work on parallel RF transmission and recent experimental implementations on prototype systems indicate that parallel excitation has the potential to overcome critical obstacles to robust and routine human scanning at high field strength. As these developments are extended to 16- and 32-channel neuroimaging arrays, it seems likely that very-high-field human brain imaging will be possible with an essentially constant flip angle across the human head with RF pulse durations comparable to current slice-selective pulses. While most work has been concentrated on head-sized transmitters, the problem of B_1 homogeneity in the torso becomes significant at lower B_0 fields. Thus, the first clinical applications might be for body transmit coils at 3 T.

Of course, intriguing research questions remain open in several areas, including optimal coil array designs that minimize element couplings and maximize spatial orthogonality of individual channels, the estimation and real-time monitoring of local SAR during simultaneous application of RF in excitation coil arrays, and the development of rapid and robust RF pulse designs that extend the current low-flip-angle domain to an arbitrary excitation angle, such as spin echoes, saturation, and inversions pulses. However, with continued active research in these areas, progress is likely to accelerate, and one can envision logical additions to the architecture of a current clinical scanner that readily accommodates the requirements of a general parallel RF excitation system. These include coil arrays optimized for parallel transmit and receive, modular blocks of RF synthesis and amplification with individual characterization of amplifier nonlinearities, subject-specific models of local SAR deposition for monitoring, and a rapid B_1-estimation pre-scan that feeds fast RF-pulse-design software capable of incorporating E_1 constraints.

References

Adriany G et al (2003) Transceive stripline array for ultra high field parallel imaging applications. In: 11th annual scientific meeting of the ISMRM, Toronto

Adriany G et al (2005) Transmit and receive transmission line arrays for 7 Tesla parallel imaging. Magn Reson Med 53:434–445

Collins CM et al (2005) Combination of optimized transmit arrays and some receive array reconstruction methods can yield homogeneous images at very high frequencies. Magn Reson Med 54:1327–1332

Conolly S, Nishimura D, Macovski A (1989) Optimal control solutions to the magnetic resonance selective excitation problem. IEEE T Med Imaging MI-5:106–115

Geen H, Wimperis S, Freeman R (1989) Band-selective pulses without phase distortion. A simulated annealing approach. J Magn Reson 85:620–627

Glover G, Lai S (1998) Reduction of susceptibility effects in BOLD fMRI using tailored RF Pulses. In: 6th Scientific Meeting ISMRM

Ibrahim TS et al (2001) Dielectric resonances and B(1) field inhomogeneity in UHFMRI: computational analysis and experimental findings. Magn Reson Imaging 19:219–226

Katscher U et al (2002) Theory and experimental verification of Transmit SENSE. In: 10th Annual Meeting of ISMRM, Hawaii

Katscher U et al (2003) Transmit SENSE. Magn Reson Med 49:144–150

Kim HW et al (2003) In vivo prostate magnetic resonance imaging and magnetic resonance spectroscopy at 3 Tesla using a transceive pelvic phased array coil: preliminary results. Invest Radiol 38:443–451

Kurpad KE, Boskamp, Wright SM (2005) A parallel transmit volume coil with independent control of currents on the array elements. In: Proc ISMRM, Miami FL

Lee RF et al (2001) Planar strip array (PSA) for MRI. Magn Reson Med 45:673–683

Lee RF et al (2004) Lumped-element planar strip array (LPSA) for parallel MRI. Magn Reson Med 51:172–183

Mao JM, Scott K, Andrew E (1986) Selective inversion radiofrequency pulses by optimal control. J Magn Reson 70:310–318

Nam H, Wright SM (2005) Transmit surface coil array using RF current sources. In: Proc ISMRM, Miami FL

Pauly J et al (1991)Parameter relations for the Shinnar-Le Roux selective excitation pulse design algorithm. IEEE Tr Medical Imaging 10:53–65

Pauly J, Nishimura D, Macovski A (1989) A k-space analysis of small-tip angle excitation. J Magn Reson 81:43–56

Peterson DM et al (2003) An MR transceive phased array designed for spinal cord imaging at 3 Tesla: preliminary investigations of spinal cord imaging at 3 T. Invest Radiol 38:428–435

Pinkerton RG, Barberi EA, Menon RS (2005) Transceive surface coil array for magnetic resonance imaging of the human brain at 4 T. Magn Reson Med 54:499–503

Roemer PB et al (1990) The NMR phased array. Magn Reson Med 16:192–225

Saekho S et al (2005) Small tip angle three-dimensional tailored radiofrequency slab-select pulse for reduced B1 inhomogeneity at 3 T. Magn Reson Med 53:479–484

Shinnar M et al (1989a) The synthesis of pulse sequences yielding arbitrary magnetization vectors. Magn Reson Med 12:74–80

Shinnar M, Bolinger L, Leigh JS (1989b) The use of finite impulse response filters in pulse design. Magn Reson Med 12:81–87

Shinnar M, Bolinger L, Leigh JS (1989c) The synthesis of soft pulses with a specified frequency response. Magn Reson Med 12:88–92

Shinnar M, Leigh JS (1989) The application of spinors to pulse synthesis and analysis. Magn Reson Med 12:93–98

Stenger VA, Boada FE, Noll DC (2000) Three-dimensional tailored RF pulses for the reduction of susceptibility artefacts in T(*)(2)-weighted functional MRI. Magn Reson Med 44:525–531

Stenger VA, Boada FE, Noll DC (2002) Multishot 3D slice-select tailored RF pulses for MRI. Magn Reson Med 48:157–165

Stenger VA, Boada FE, Noll DC (2003) Variable-density spiral 3D tailored RF pulses. Magn Reson Med 50:1100–1106

Ullmann P et al (2005) Experimental analysis of parallel excitation using dedicated coil setups and simultaneous RF transmission on multiple channels. Magn Reson Med 54:994–1001

Ulloa J et al(2005) In: Meeting of the ISMRM, Miami.

Van de Moortele PF et al (2005) B(1) destructive interferences and spatial phase patterns at 7 T with a head transceiver array coil. Magn Reson Med 54:1503–1518

Vaughan JT et al (1994) High frequency volume coils for clinical NMR imaging and spectroscopy. Magn Reson Med 32:206–218

Zhu Y (2002) Acceleration of focused exitation with a transmit coil array. In: 10th Annual Meeting of ISMRM

Zhu Y (2004) Parallel excitation with an array of transmit coils. Magn Reson Med 51:775–784

Zhu Y et al (2005) Parallel excitation on an eight transmit channel MRI system. In: 13th Meeting of the ISMRM, Miami

Future Software Developments

46

Philip G. Batchelor

CONTENTS

46.1 Introduction

Future software developments in parallel MRI will certainly be mainly influenced by future, and present, hardware developments. The most likely direction for hardware developments, at least in the short-term future, is toward a higher number of coils. What effect will this have on software? As the software will mainly involve the computational reconstruction and exploitation of images, the question could be restated as, what are the computational issues?

First of all, let us clarify what will be considered as software issues in this chapter. Strictly speaking, the hardware in parallel MRI consists of array coils, providing images of the object modulated by the coil sensitivities. Thus, in theory, any scanner that allows one specific parallel imaging technique could also perform any of the other ones. In that sense, the distinction between parallel MRI techniques (SMASH, SENSE, GRAPPA, etc., see Chap. 2) could be interpreted as a distinction between software implementations. If our scanner has 32 coils, we have the ability to get up to 32 times more data out of it than we would from a single coil, and the role of the software computations is to exploit these data.

Furthermore, physiology and physics limit the speeding up of MR image acquisition by purely technological methods, thus software computations will have to shoulder more and more of future improvements.

P. G. Batchelor, PhD
Medical Physics and Bioengineering, Malet Place Engineering Building, University College London, WC1E 6BT, UK

46.2 Computational Aspects

A crucial distinction in MR is the distinction between k-space and image space. The bridge between the two is the Fourier transform, generally implemented in software by the fast fourier transform (FFT), see (Edelman et al. 1999) for a discussion of future developments in this field. This operation is so standard that we consider it a given, thus we can go back and forth to k-space according to our needs, without prohibitive computational costs.

In parallel imaging, the hardware delivers a wealth of data, one dataset per coil, and the role of the software computation is to reconstruct a clinically useful image. What can we expect in the future from this point of view? Current commercial products offer parallel imaging in general with a Cartesian sampling. Speed up is then achieved by acquiring only a certain fraction $1/R$ of all lines in k-space. The limit on R is the number of coils nc. This gives rise to very specific undersampled images. Artefacts appear as aliases separated by exactly a fraction $1/R$ of the field of view. Computationally, this is reflected in that we

need to solve only a small (in the sense of the potential of modern equation solvers) equation of size R times n_c for each voxel. Thus a failure or imperfect reconstruction will result mostly in residual aliases which preserve an anatomical structure, and may be relatively easily recognised by an experienced radiologist, although g-factor noise (see also Chaps. 3 and 4) may still present for unfavourable coil configurations.

What one may want as future development are first to perfect these reconstructions, thus to be able to manipulate the parameters which affect this reconstruction. This means we need to find these parameters. Furthermore, Cartesian trajectories are often not the best choice, and radial, spiral, etc., are more appropriate in a lot of applications, see, for example (Cashen and Carroll 2005, Liu et al 2005a) and Chap. 6. Even for Cartesian trajectories, some software optimisation is possible, as shown by Xu et al. (2005). But this raises a big difficulty in parallel imaging, as we cannot anymore just jump some lines in k-space, and more importantly, the artefacts are of a totally different nature.

In summary, some of the computational problems of parallel MRI are: we don't normally know the coil sensitivities; even if we know them the reconstruction may be of bad quality; if the subsampling in k-spaces is not regular the reconstruction becomes much harder and slower, with different artefacts. We will now have a closer look at these issues from a computational software point of view.

46.2.1 Coil Sensitivities

In the standard form of parallel imaging, we have as many datasets as coils, but of size reduced by speed up. A linear operation relates these datasets and the unknown clinically useful image. In between, we would have a rectangular matrix whose coefficients depend on the coil sensitivities. To solve the system, we thus need to assume that this matrix is known, in other words, that the coil sensitivities are known.

This normally then makes the reconstruction a two-step process: first, fit a reconstruction operator that can explain the relationship among the data we have, then use this operator to predict the data we have not acquired. When this prediction is perfect, we get a least squares (LS) problem. This implicitly assumes that all the errors due to noise are in the data. In some applications of statistics and numerical linear algebra, a method has been developed to allow errors in the linear reconstruction operator too. These are total least squares problems (TLS, (Gene et al. 1996), p. 595), see Fig. 46.1. As the coil sensitivities are unlikely to be perfectly known, TLS methods seem particularly appropriate in parallel MRI, see Figs. 46.2 and 46.3 from Raj (TL-SENSE), and (Raj 2005; Raj and Zabih 2004; Liang et al. 2002) (maximum likelihood formulation). Note that the difference between these images is due to software.

The standard hardware method to determine coil sensitivities is an additional scan using a body coil. For this reason, computational methods have been developed that should allow to avoid this step. Such methods, self-calibrating or auto-calibrating, in general acquire additional lines near the centre of k-space, thus some extra data [see (Breuer et al. 2005, Kholmovski and Samsonov 2005, Lew et al. 2005)] for recent examples, and Chaps. 2 and 8 for more details). A simple method in SENSE to avoid such a step is to use a sum of squares (SOS) of the coil images.

- Let s_i be the image from coil k. If c_k is the ideal coil sensitivity, we should have the relationship $s_i = c_k\, s$, where s is the ideal image. Thus, the sum of squares is $\mathrm{sos} = \sum_k |s_k|^2 = |s|^2 \sum_k |c_k|^2$, and the estimated coil sensitivities are $\tilde{c}_k = s_k / \sqrt{sos} = c_k / \sqrt{\sum_k |c_k|^2}\, e^{i\varphi}$, where φ is the phase of the ideal image. Thus, the SOS approximation is good if the coils have a good 'coverage' of the field of view, in the sense that the sum of squares of the coil magnitudes is approximately uniform, see also Fig. 46.4 (Bydder et al. 2002).

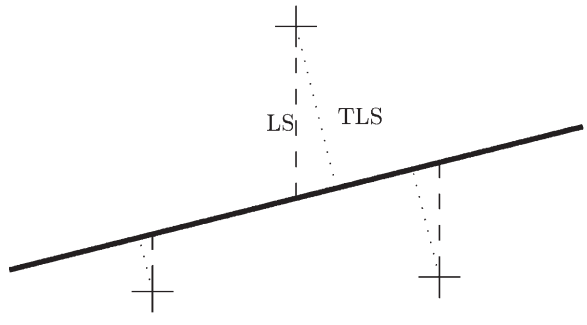

Fig. 46.1. The difference between least squares (*LS*) and total least squares (*TLS*): LS minimises the sum of the lengths of *hyphenated lines*, whereas TLS minimises the sum of the lengths of *dotted lines*

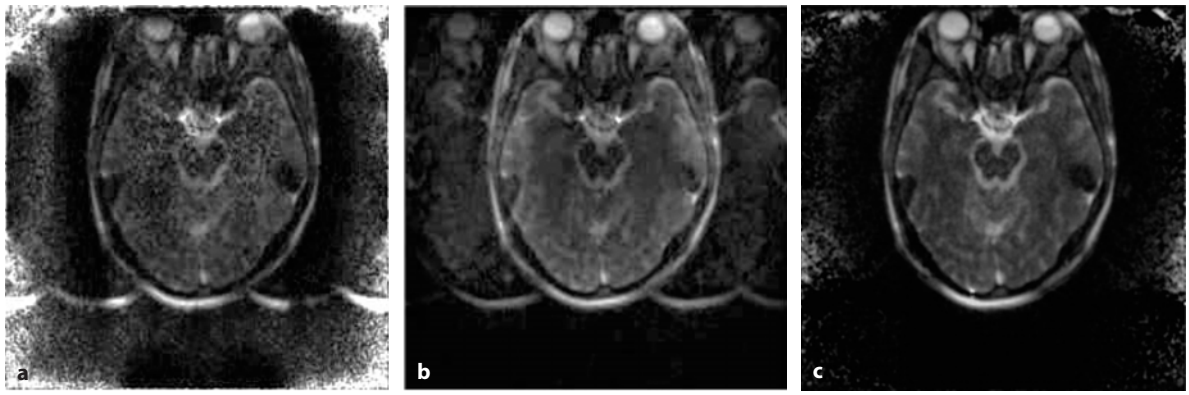

Fig. 46.2a–c. SENSE reconstructions of brains: Note excessive noise amplification suffered by standard SENSE **a**. This noise can be reduced by introducing regularization **b** [see (King and Angelos 2001)], but at the cost of insufficient unfolding performance. TL-SENSE removes the noise without degrading unfolding performance **c**. Images courtesy of A. Raj

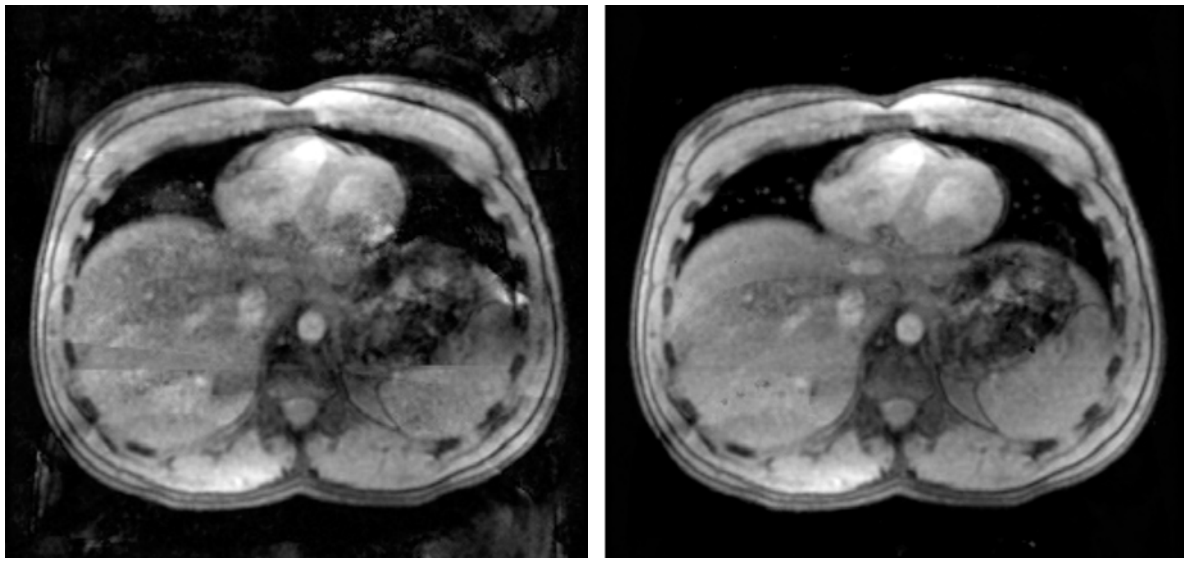

Fig. 46.3. SENSE reconstructions of torso: Note the distortion in heart-stomach boundary introduced by standard regularised SENSE, which was effectively removed by TL-SENSE. Strip artefacts across the liver were also removed by TL-SENSE. Images courtesy of A. Raj

46.2.2 Coil Array Quality

If all the coils were uniform, or simply similar, the n_c images would all be similar, and we would have lost the advantage of multiple information. If on the other hand the coils were not overlapping at all, every coil would simply give information on its own portion of the image (see Chap. 3 for coil design issues). In both cases, with speed up, i.e., loss of information, we end up with not enough data to reconstruct an image. It may be instructive to consider what factors affect this. Computationally, this appears to depend on how well the coils cover the field of view in a sum-of-squares sense.

- Using the above notations, let us compute the condition number of the system defined by $[s_k] = [c_k]\mathrm{s}, \mathrm{k}=1 \ldots n_c$. This is the ratio of maximum to minimum singular value and controls error propagation in linear computations. To simplify the computation, we assume no speed up. With speed up, we expect the computation to get worse, thus our estimate should be seen as

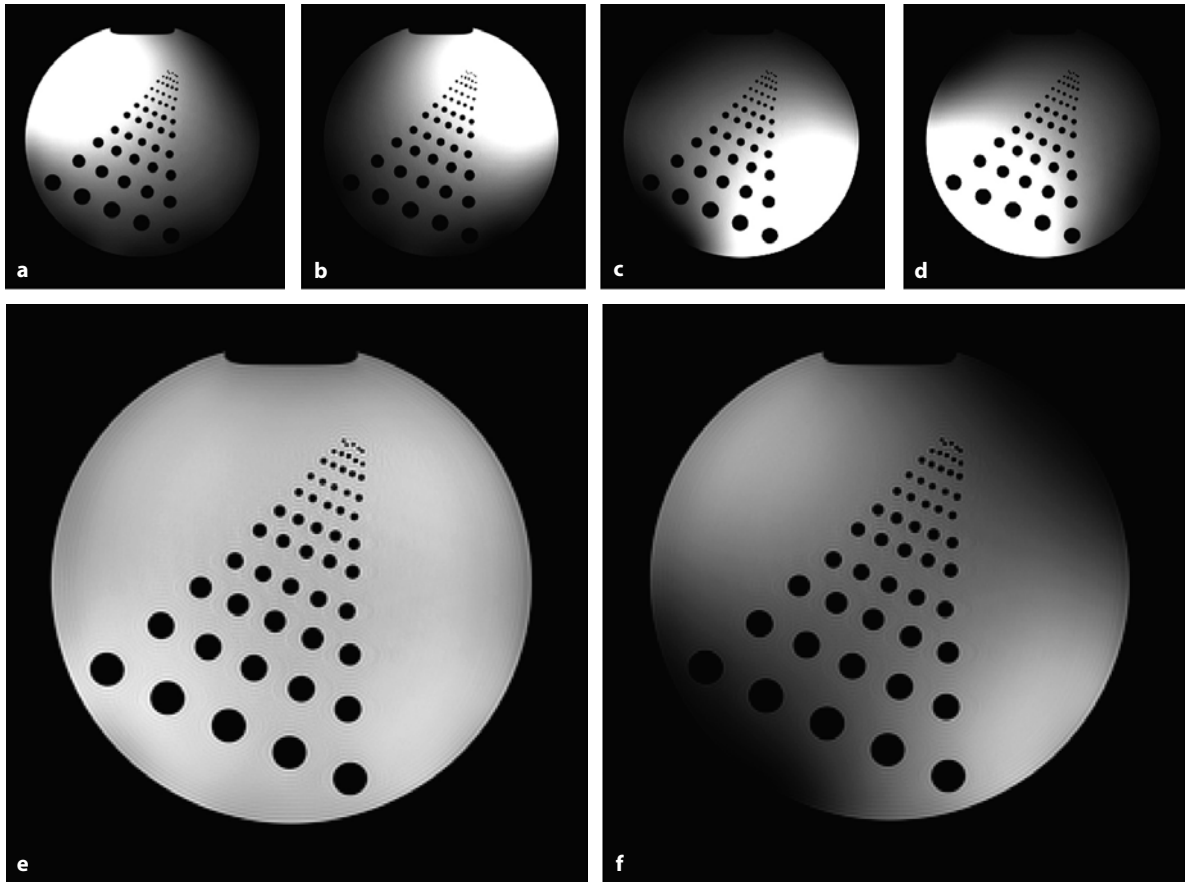

Fig. 46.4a–f. Sum-of-squares reconstruction using image data from four and two coil elements. **a-d** Image data from single coil elements. **e** SOS reconstruction from all four elements with good 'coverage' of the field of view. **f** SOS reconstruction from only two elements with insufficient 'coverage' of the field of view. BYDDER et al. (2002) offer an improvement over this simple scheme

a simple lower bound. It is easy to see that the normal matrix of the system is a square diagonal matrix with as many rows as voxels. The diagonal elements are the sum of squared magnitudes of coil sensitivities for each voxel, thus the condition number is the square root of the ratio of maximum to minimum (over voxels) of these SOSs:

$$\sqrt{\max_x \sum_k \left|c_k(x)\right|^2 / \min_x \sum_k \left|c_k(x)\right|^2}.$$

A higher number of coils will thus have not only the advantage of speed up, but also a better quality of coverage of the field of view. On the other hand, a post-processing question one may ask is: do we need to use all coils in the computation? BUEHRER et al. (2005) have shown that for localized imaging, it may be possible to use down from 32 to 16 coils without significant effect on SNR, by optimising on the coils used.

46.2.3 Image Reconstruction

A speed up of 2 and Cartesian sampling are computationally an entirely different issue from speed up of say 8, with 32 coils, and non-Cartesian sampling. As this chapter is on software, it seems appropriate to offer some code examples. We present a short Matlab (The Mathworks, Inc., Natick, MA) pseudo-code for a SENSE reconstruction.

Here *c* is a 3D array containing the coil sensitivities, *s* a 3D array of coil images with speed up 2, and *r* the 2D reconstructed image

```
[n1 n2 ncoils]=size(c); c1=c(1:n1/2,:,:); c2=c(n1/2+1,:,:);
c11=sum(conj(c1).*c1,3); c22=
    sum(conj(c2).*c2,3); c12= sum(conj(c1).*c2,3);
c21=conj(c12);
c1s=sum(conj(c1).*s,3); c2s=sum(conj(c2).*s,3);
```

```
r=[(c22.*c1s -c21.*c2s);(c11.*c2s -c12.*c1s)]./...
repmat(c11.*c22 -abs(c12).*abs(c12),2,1);
```

The reconstruction is very simple and fast because the sampling induces a half-field-of-view aliasing, and the speed up of 2 means we can use an explicit formula for the inversion of the system. The following piece of code shows the difference when the sampling is at the general k-space positions samples (but here on a Cartesian grid for simplicity):

```
function y = irreg - sense (x,c,samples,tflag)
if strcmp(tflag,'notransp')
for ci = 1:n3
S=fft2(c(:,:,ci).*r); S - samp = O; S - samp(samples) = S(samples);
s - samp = ifft2(S - samples);
y((ci-1)*N+1:ci*N) = s - samples(:);
end
elseif strcmp(tflag,'transp')
s = reshape(x,n1,n2,n3); y = zeros(n1,n2);
for ci = 1:n3
S = fft2(s(:,:,ci)); S - samp =O; S - samp(samples) = S(samples);
y=y+ conj(c(:,:,ci)).*ifft2(S - samp);
end
y = y(:);
end
% Then we can call some CG of NE solver for this linear operation:
r =  lsqr(@(x,tflag) irreg _ sense(x,c,samples,tflag),s);
```

This is just the author's simplistic implementation of the sophisticated approach by Kannengiesser et al. (2000) and Pruessmann et al. (2001), see also (Liu et al. 2005b) for fast reconstructions. This aims to illustrate what may be the single most important development from a computational software point of view in parallel MRI. The essential idea is as follows: we write a function which starting from an ideal image creates an artefacted image (the *forward* operation), taking into account what causes the corruption. Often, this turns out to be linear. However, this is an equation whose size is huge, for a 3D 128×128×128 image the linear operator would be in theory of size $128^6 \approx 4.4 \times 10^{12}$. Thus, the classical approach is to make some simplifying assumptions or approximations. But this is where modern computational techniques come to the rescue: Conjugate gradient-based techniques (so-called Krylov space methods) require *only* the forward operation, and in general in about 10 to 15 iterations, produce the *inverse*. In summary, we only need to be able to describe how artefacts appear, and the solvers can be used as a black-box to get the solutions. This idea obviously generalises to other fields, and shows what parallel MRI software can contribute to MRI [for example, multishot motion correction (Batchelor et al. 2005), and specifically in DWI (Liu et al. 2005a)], also to generate shaped pulses in Transmit SENSE (Graesslin et al. 2005).

46.2.4 Other Artefacts Correction

The standard use of the extra data from multiple coils is for reconstruction of a fully sampled image from undersampled ones. Undersampled images are aliased, that is, they suffer from artefacts caused by the undersampling for speed up. This speed up has the advantage of making images more robust to other artefacts, for example, motion. Different types of corruptions may, however, still be present. For this, more subtle uses of the extra data are possible, in particular for motion correction. Depending on the relative motions of the object relatively to the coils, it may be possible to detect inconsistencies caused by motion and quantify them. This is the idea behind the CARE algorithm (Atkinson et al. 2004), for more details refer to Chap. 5. A very recent paper by Winkelmann et al. (2005) also shows how the information from parallel MRI can be used to remove ghosts. Additionally, most of the classical motion correction techniques have been upgraded to parallel MRI for example Propeller (Chuang et al. 2005) or Pocs (Samsonov et al. 2005).

Specific types of acquisition that suffer particularly from motion are diffusion-weighted ones. This is not surprising as diffusion is a form of motion itself. Parallel imaging has helped in this context, too, to correct for distortions caused by EPI acquisitions (Chuang et al. 2005; Chuang et al. 2004; Liu et al. 2005a; Wang et al. 2005). Another way around distortion effects is to use a multishot acquisition which would be less corrupted by distortions, but more by motion affecting the different shots inconsistently. It is then possible to describe the effects in a linear system and to use a reconstruction method similar to the one used for reconstruction of irregularly sampled SENSE data. This is the idea behind Liu's work, see Fig. 46.5 and (Liu et al. 2005a).

Another clinical field undergoing important changes is dynamic imaging. There speed may be even more important than in other fields, and recently big advances have been made, a combination of very efficient scanning with clever software implementations, as in k-t BLAST, and its parallel imaging coun-

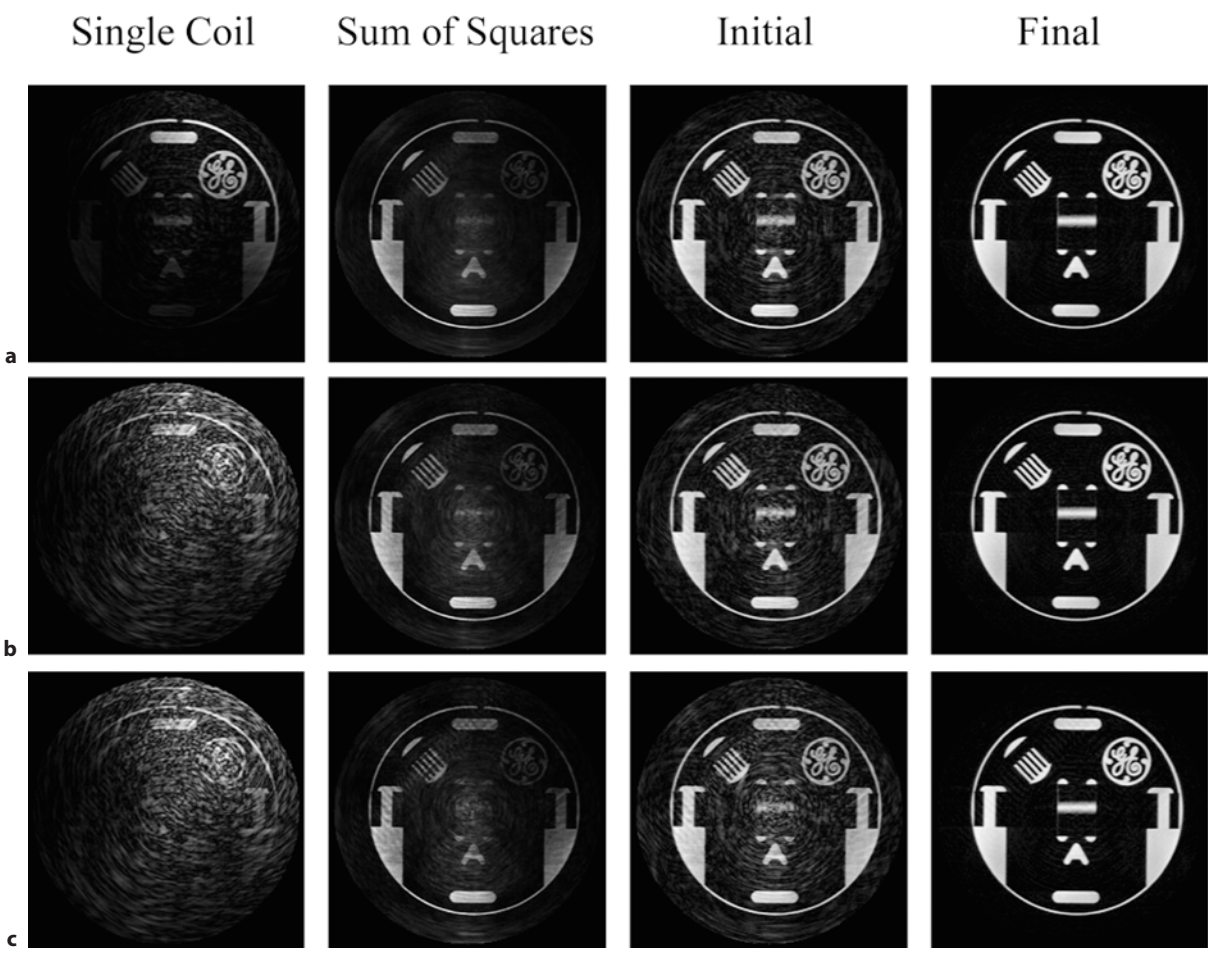

Fig. 46.5a–c. Multi-shot SENSE DWI simulations using SNAILS with reduction factors up to 3. **a** Reduction factor equals 1 (no acceleration); **b** reduction factor equals 2; **c** reduction factor equals 3. From *left* to *right*, images shown are: single coil images, sum-of-squares images, initial images, and final reconstructed images. Figure courtesy of C. Liu

terpart, k-t SENSE (Tsao et al. 2003; Tsao et al. 2005). Functional MRI has also been a beneficiary of parallel MRI, see for example (Lin et al. 2005).

The iterative methods enable fast reconstructions where they would not have been possible otherwise, but may still be slow in general. Another potential for reconstruction is to use a 'direct' method instead of an iterative one, as proposed recently by Sénégas and Eggers (2005). The idea is to use only local information in k-space, thus it is similar in spirit to the GRAPPA method, but is applied to irregular sampling (Fig. 46.6).

46.2.5 Regularization and Preconditioning

Often, the reconstruction equations are badly conditioned. This means that if we solve them using a straightforward method, the errors due to noise will get amplified, sometimes to the point that the solution is useless. Two procedures that can be implemented in software are commonly used to handle this: preconditioning and regularization.

- If the system takes the form $Cr=s$, where s is the coil data, C the reconstruction operator formed from the coil sensitivities and undersampling, and r the unknown ideal image to reconstruct, a preconditioner would be for example another matrix

P, and we would solve instead *PCr=Ps*. It has the same solution as the original system, but if *P* is chosen carefully, the condition number of *PC* can be significantly lower that that of *C*. A regularized solution rμ would be for example the minimum of $||Cr-s||2 + \mu D(r)$, where the operator *D* imposes some condition on *r*. From a clinical point of view, the interest is that although mathematical pre-conditioners and regularisers exist, it is often possible to guess better ones from an intuition of the problem.

Preconditioners have the additional advantage that they will accelerate the iterative algorithms. In general, they are obtained by 'guessing' an approximate answer. A preconditioned system should have exactly the same answer in exact arithmetic as the original system.

The second method is regularisation. A regularisation will compute a solution to a *modified* system, in general so that the solution has some additional desired properties. Thus, the solution we get, even without noise, is different from what we would get without it. In general, there will be a control parameter deciding how much we trust our original equation, and how much we want the solution to have the additional properties. Standard regularisation methods are called Tikhonov regularisation, truncated singular-value decomposition (SVD), or for iterative methods, interrupted iterations, where the control parameter is the number of iterations, see (Qu et al. 2005) and references therein. The different algorithms for parallel imaging reconstruction have different preconditioning and regularisation abilities (Lin et al. 2004). Again, in the future we can expect a wider use of iterative methods for reconstruction, and a discussion of the regularisation issues appeared very recently (Qu et al. 2005) . A rigorous discussion of regularisation in parallel MRI can also be found in (Clayton et al. 2005).

46.3 Practical Aspects

It may be useful to mention some more practical issues. The fragments of code illustrate that the required operations do not necessarily need thousands of lines of code, but what may turn out to slow down the reconstruction is related to the number of

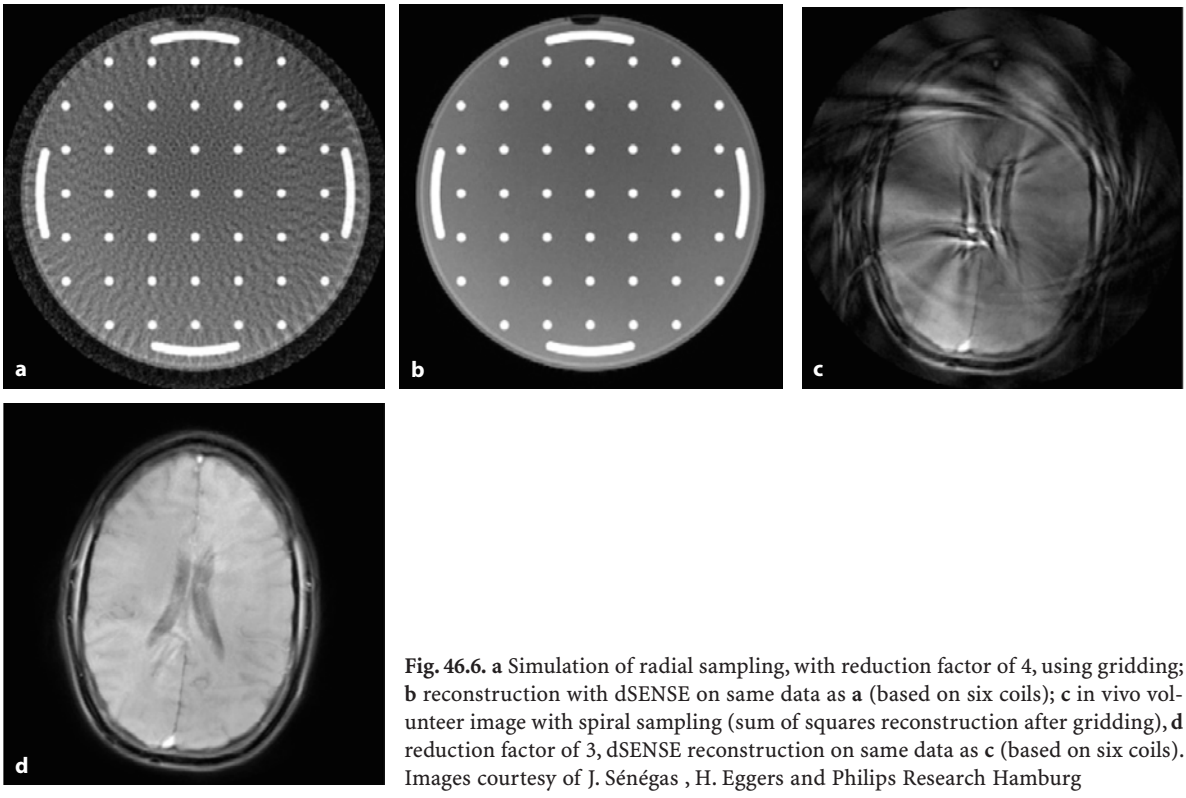

Fig. 46.6. a Simulation of radial sampling, with reduction factor of 4, using gridding; **b** reconstruction with dSENSE on same data as **a** (based on six coils); **c** in vivo volunteer image with spiral sampling (sum of squares reconstruction after gridding), **d** reduction factor of 3, dSENSE reconstruction on same data as **c** (based on six coils). Images courtesy of J. Sénégas , H. Eggers and Philips Research Hamburg

coils. For this reason, Cohen et al. (2004) use an association of parallel imaging with parallel computing in the form of a Beowulf cluster for SMASH reconstructions. Increasing the number of CPUs from 1 to 10, the image reconstruction time could be reduced to about 10 % of the original value. The data is from a 32-channel system, which for relatively small images (128×128×128) generates 262 megabytes of data, with up to 64 additional megabytes of calibration data (Cohen et al. 2004).

46.3.1 Manufacturers

The main manufacturers all offer parallel MRI, and thus some software interfacing to it. Again, their main effort is certainly focused on bringing 32 channels and more to clinical use, but the differentiation between products will be most apparent in the software. As we interpret differences between say GRAPPA and SENSE as mostly software differences, and this book is about clinical applications, it is worth mentioning an explicit comparison of these methods (for spine imaging) on a single manufacturer's MRI unit (Siemens Symphony) (Ruel et al. 2004).

46.3.2 Online Code

A toolbox for parallel MR reconstruction, called PULSAR, is available at http://www.ece.tamu.edu/

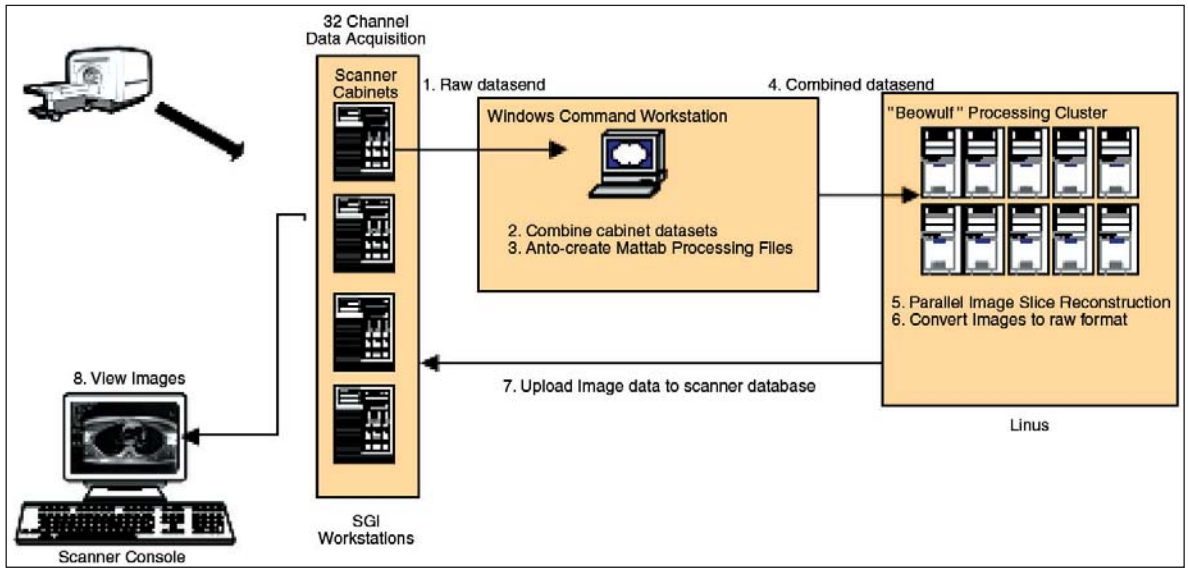

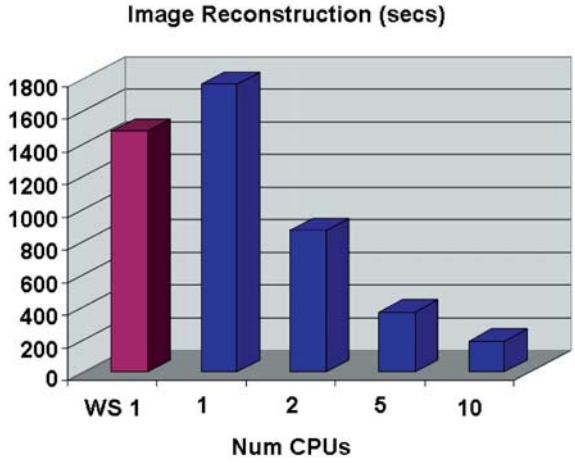

Fig. 46.7. Massively parallel reconstructions using a BEOWULF Linux cluster, computation times. Images courtesy of D. Cohen, D. Sodickson

~mrsl/JIMJI_TAMU/pulsarweb/index.htm. Some additional code from Lin is also: http://www.nmr.mgh.harvard.edu/~fhlin/tool_sense.htm, and at Cornell http://www.cs.cornell.edu/~rdz/SENSE.htm. Reconstruction software is also announced at http://bio.physik.uni-wuerzburg.de/people/mark/ppa.html.

46.4 Conclusion

In summary, software developments are likely to play an increasing role in the exploitation of parallel MRI data, and it is even likely that computational tools as in Sodickson's lab (Cohen et al. 2004) may become more common, and the cost associated to it should be considered. Iterative methods in the spirit of Kannengiesser et al. (2000); Liu et al. (2005a); Pruessmann et al. (2001) are also likely to become more and more common. If we make a distinction between 'classical' parallel MRI and modern developments (regularised, iterative reconstructions), it seems that a much wider range of uses will be possible, and it is up to software flexibility to make such uses available in a day to day clinical practice.

Acknowledgements. I thank R. Bammer, T.-C. Chuang, M. Hansen, F.-H. Lin, C. Liu, A. Raj and D. Sodickson for their contributions.

References

Atkinson D, Larkman D, Hajnal J, Batchelor PG, Hill DLG (2004) Coil-based artefact reduction. Magn Res Med 52:825–830

Batchelor PG, Atkinson D, Irarrazaval P, Hill DLG, Hajnal J, Larkman D (2005) Matrix description of general motion correction applied to multi-shot images. Magn Res Med 54:1273–1280

Breuer FA, Kellman P, Griswold MA, Jakob PM (2005) Dynamic auto-calibrated parallel imaging using temporal GRAPPA (TGRAPPA). Magn Res Med 53:981–985

Buehrer M, Boesiger P, Kozerke S (2005) Considerations for the number of coil elements for 2d-SENSE imaging of localized regions. In: Proc Eur Soc Magn Reson Med Biol, p 190

Bydder M, LarkmanD, Hajnal JV (2002) Combination of signals from array coils using image-based estimation of coil sensitivity profiles. Magn Res Med 47:539–548

Cashen TA, Carroll TJ (2005) Hybrid radial-parallel 3D imaging. In: Proc Int Soc Magn Reson Med, p 288

Chuang T-C, Huang T-Y, Lin F-H, Wang F-N, Chung H-W, Chen C-Y, Kwong KK (2004) Propeller EPI with SENSE parallel imaging using a circularly symmetric phase array RF coil. In: Proc Int SocMagn Reson Med, p 535

Chuang T-C, Huang T-Y, Lin F-H, Wang F-N, Ko C-W, Kwong K, Chung H-W (2005) PROPELLER EPI with parallel imaging on high resolution DTI at 3T. In: Proc Int Soc Magn Reson Med, p 9

Clayton DB, Skare S, Golub GH, Modarresi M, Bammer R (2005) Augmented SENSE reconstruction by an improved regularization approach. In: Proc Int Soc Magn Reson Med, p 2438

Cohen S, Grant AK, Yeh EN, Joshi S, Sodickson DK (2004) A parallel computing solution for rapid reconstruction of highly-accelerated volumtetric parallel MRI data. In: Proc Int Soc Magn Reson Med

Edelman A, McCorquodale P, Toledo S (1999) The future fast Fourier transform? SIAM J Sci Computing 20:1094–1114

Gene H, Golub GH, Van Loan CF (1996) Matrix computations, 3rd edn. John Hopkins University Press

Graesslin I, Markus N, Katscher U, Boernert P (2005) Iterative calculation of transmit SENSE pulses for non-Cartesian trajectories. In: Proc Eur Soc Magn Reson Med Biol, p 187

Kannengiesser SAR, Brenner AR, Noll TG (2000) Accelerated image reconstruction for sensitivity encoded imaging with arbitrary k-space trajectories. In: Proc Int Soc Magn Reson Med, p 155

Kholmovski EG, Samsonov A (2005) GARSE: Generalized autocalibrating reconstruction for sensitivity encoded MRI. In: Proc Int Soc Magn Reson Med, p 2672

King KF, Angelos L (2001) SENSE image quality improvement using matrix regularization. In: Proc Int Soc Magn Reson Med, p 1771

Lew C, Bammer R, Spielman D, Chan F (2005) Challenges with coil calibrations in in-vivo phase contrast SENSE. In: Proc Int Soc Magn Reson Med, p 2442

Liang Z-P, Bammer R, Ji J, Pelc NJ, Glover GH (2002) Making better SENSE: Wavelet denoising, Tikhonov regularization, and total least squares. In: Proc Int Soc Magn Reson Med p 2388

Lin F-H, Huang T-Y, Chen N-K, Wang F-N, Stufflebeam SM, Belliveau JW, Wald LL, Kwong KK (2005) Functional MRI using regularized parallel imaging acquisition. Magn Res Med 54:343–353

LinF-H, Kwong KK, Belliveau JW, Wald LL (2004) Parallel imaging reconstruction using automatic regularization. Magn Res Med 51:559–567

Liu C, Moseley ME, Bammer R (2005a) Simultaneous phase correction and SENSE reconstruction for navigated multi-shot DWI with non-Cartesian k-space sampling. Magn Reson Med 54:1412–1422

Liu C, Moseley ME, Bammer R (2005b) Fast SENSE reconstruction using linear system transfer function. In: Proc Int Soc Magn Reson Med, p 689

Pruessmann KP, Weiger M, Bornert P, Boesiger P (2001) Advances in sensitivity encoding with arbitrary k-space trajectories. Magn Res Med 46:638–651

Qu P, Zhong K, Zhang B, Wang J, Shen GX (2005) Convergence behavior of iterative SENSE reconstruction with non-cartesian trajectories. Magn Res Med 54:1040–1045

Raj A (2005) A signal processing And machine vision approach to problems in magnetic resonance imaging. PhD thesis, Cornell University

Raj A, Zabih R (2004) An optimal maximum likelihood algo-

rithm for parallel imaging in presence of sensitivity noise. In: Proc Int Soc Magn Reson Med, p 2411, see also http://www.people.cornell.edu/pages/ar74/research.html

Ruel L, Brugières P, Luciani A, Breil S, Mathieu D, Rahmouni A (2004) Comparison of in vitro and in vivo MRI of the spine using parallel imaging. AJR 182:749–755

Samsonov A, Kholmovski EG, Johnson C (2005) POCS-enhanced parallel MRI correction of MR image artefacts. In: Proc Int Soc Magn Reson Med, p 690

Sénégas J, Eggers H (2005) Direct k-space reconstruction for non-Cartesian parallel MR imaging. In: Proc Eur Soc Magn Reson Med Biol, p 188

Tsao J, Boesiger P, Pruessmann KP (2003) k-t BLAST and k-t SENSE: Dynamic MRI with high frame rate exploiting spatiotemporal correlations. Magn Res Med 50:1031–1042

Tsao J, Kozerke S, Boesiger P, Pruessmann KP (2005) Optimizing spatiotemporal sampling for k-t BLAST and k-t SENSE: Application to high-resolution real-time cardiac steady-state free precession. Magn Res Med 53:1372–1382

Wang F-N, Huang T-Y, Lin F-H, Chuang T-C, Chen N-K, Chung H-W, Chen C-Y, Kwong KK (2005) PROPELLER EPI: an MR imaging technique suitable for diffusion tensor imaging at high field strength with reduced geometric distortions. Magn Res Med 54:1232–1240

Winkelmann R, Boernert P, Doessel O (2005) Ghost artefact removal using a parallel imaging approach. Magn Res Med 54:1002–1009

Xu D, Jacob M, Liang Z-P (2005) Optimal sampling of k-space with Cartesian grids for parallel MR imaging. In: Proc Int Soc Magn Reson Med, p2450

Future Imaging Protocols

47

Stefan O. Schoenberg and Olaf Dietrich

CONTENTS

47.1 Introduction

Any desired scan protocol in magnetic resonance imaging must range within the magic triangle of spatial/temporal resolution, signal-to-noise ratio, and anatomic coverage. Limitations arising hereof can be exemplarily demonstrated for 3D contrast-enhanced MRA (3D-CE-MRA). In order to become fully the new standard of reference for diagnostic angiographic imaging, 3D-CE-MRA has to meet all the requirements fulfilled by conventional X-ray digital-subtraction angiography. Ideally, a submillimeter spatial resolution with isotropic voxel sizes of 0.3×0.3×0.3 mm^3 should be achieved, while maintaining acquisition times of less than 500 ms for both high temporal resolution and rapid re-positioning of the field of view during automated table movement. One can immediately see that this type of scan performance is not feasible with current designs in scanner hardware and pulse sequences. Therefore, the question arises what strategies may be evolving to overcome these limitations and how this might open new horizons for more a comprehensive use of magnetic resonance imaging in the clinical work-up.

S. O. Schoenberg, MD; O. Dietrich, PhD
Department of Clinical Radiology, University Hospitals – Grosshadern, Ludwig Maximilian University of Munich, Marchioninistr. 15, 81377 Munich, Germany

47.2 Hardware Development and Clinical Protocols

47.2.1 Increasing Number of RF Channels

With the introduction of multi-channel MRI systems with more than eight independent RF channels, the possibilities for accelerated imaging with a more flexible use of parallel acquisition techniques have been substantially improved. As has been elaborated in many chapters of this book, this enables the routine use of parallel-imaging acceleration factors between 2 and 3 for imaging in arbitrary slice orientations for most anatomic regions in the body. While this is a substantial improvement in comparison to non-accelerated imaging, it does not meet by far all requirements in terms of temporal resolution for dynamic imaging or isotropic voxel sizes for three-dimensional reconstructions. Since there is a clear trend in clinical routine for imaging of larger anatomic areas within one single MRI exam, even current high-end MRI systems require up to 32 independent receiver channels to fulfill these requirements for parallel imaging without repositioning the coil arrays. On the other

hand, several studies, of which the results are also in part presented in this book, have clearly shown that dedicated multi-element coils with more than 32 receiver elements can substantially increase the performance of parallel imaging with acceleration factors of up to 64, cf. Chap. 44. The limitation of this type of coils is that their design in terms of shape as well as size, geometric location and penetration of the individual coil elements is highly dedicated to certain anatomic regions of the body. For example, 12-fold (two-dimensional) accelerations are possible for isotropic T1-weighted gradient-echo imaging of the brain with dedicated 32-channel head coils (Wiggins et al. 2005b) as well as for 3D cine steady-state-free-precession (SSFP) imaging of the heart with dedicated 32-channel cardiac array coils (Zhu et al. 2004; Sodickson et al. 2005; Hardy et al. 2006). On the other hand, this type of coils is difficult to integrate into a clinical work flow, where usually more than one anatomic region is imaged during the entire exam.

One possible solution could be the development of MR systems with an even substantially higher number of independent RF channels. First prototypes of 96-channel MR systems exist (Wiggins et al. 2005a) that potentially might allow the combined use of dedicated multi-element coils for anatomic areas with particular requirements for high temporal and spatial resolution in combination with a large number of additional surface coils for complete coverage of the entire body. This would open new horizons for comprehensive disease-specific imaging protocols (see Sect. 47.3.3) that require fast high-resolution imaging of the cardiovascular system in combination with a global assessment of, e.g., musculoskeletal disease. Another advantage of such multi-channel MRI systems would be the synergistic use of "coil-in-a-coil" set-ups, in which a large anatomic area is illuminated by a large coil array with only a few receiver elements in combination with a focused high-resolution display of small anatomic structures by small dedicated coils with a focally high signal-to-noise ratio. This approach, for example, is effectively used for head and neck imaging (cf. Chap. 19) where display of the entire skull base has to be combined with ultra-high-resolution imaging of the cranial nerves.

However, the question arises, if this is entirely the ideal step for the evolution of MR systems in terms of technical feasibility, complexity of set-up, and costs. The integration of multiple independent RF channels into one MR system is highly expensive and may therefore not be affordable for many health-care providers. Also, the set-up time for plug-in of a multitude of different coils might be exponentially increasing, thereby reducing overall patient throughput.

47.2.2 Continuously-Moving-Table Scanning

Recent developments in software and hardware design unrelated to parallel imaging might lead the way to a different approach. The so-called moving-table techniques offer the possibility to scan always in the iso-center of the magnet while the patient is continuously moving through the magnet (Dietrich and Hajnal 1999; Kruger et al. 2002; Shankaranarayanan et al. 2003). In comparison to current approaches, in which a series of predefined fields of view are obtained in fixed steps, now a complete data set of contiguous axial slices is primarily acquired. Though primarily unrelated to parallel imaging, these techniques can be vastly accelerated with parallel imaging, as well (Keupp et al. 2005; Hu et al. 2005). The fundamental difference is that potentially only a single multi-element coil would be necessary to perform acquisitions with highly parallel imaging since the patient could be sliding underneath the coil during the acquisition with continuous table movement. The combination of highly parallel imaging with continuous table movement is of particular appeal also in terms of the general trend for the design of MR systems with substantially larger bore diameter and shorter magnet length. These systems provide a higher patient comfort due to the wider and shorter bore, however at the cost of a further reduction in the field of view in the head-feet direction. Here, contiguous axial acquisitions during automated table movement could be a desirable approach while the patient slides underneath a vast number of fixed independent coil elements. The downside of a single multi-element coil fixed in the iso-center of the magnet is the lack of adaptation to the patient's anatomic dimensions at different levels of the body. The signal-to-noise ratio and g-factor performance greatly depend on the fill factor of the coil, which tremendously varies in the different anatomic areas of interest. One way to overcome this limitation would be the development of more flexible coils that automatically adapt to the surface of a given anatomic area of interest.

One commonly referred to problem of highly parallel imaging is the substantial loss of signal-to-noise ratio (SNR). While multi-element receiver coils provide substantially higher SNR for the periphery of

an object close to the coil surface, the SNR gain in the core of the object is often limited. Here, the move to higher field strengths is clearly beneficial. Already at this point, the first 32-channel MR systems with a field strength of 3 T are clinically available. This trend towards 3 T and ultimately to even higher field strengths for clinical routine imaging is expected to be further enhanced in the near future.

47.3 Acquisition Technique, Pulse Sequences, and Protocols

Regardless which of the software and hardware designs ultimately succeed, there will be a shift of paradigm for clinical MRI protocols with a more comprehensive assessment of disease.

47.3.1 Blood-Pool Contrast Agents

For magnetic resonance angiography, a synergistic diagnostic value of parallel-imaging techniques and recently approved strongly protein-binding intravascular MR contrast agents is expected. These contrast agents have a high relaxivity during first-pass imaging (Rohrer et al. 2005; Caravan et al. 2002) and have already been shown to allow dynamic contrast-enhanced MRI with high spatial resolution in the first pass (Prasad et al. 1999), which may be further improved with the use of dedicated multi-element coils. To keep up with the requirements in spatial resolution, this first-pass imaging can be combined with ultra-high-resolution imaging in the steady state since this type of contrast agent remains in the vascular system for a long imaging window of about 1 h (Grist et al. 1998; Kroft and de Roos 1999). To maintain reasonable scan times, parallel-acquisition techniques are necessary for acquisition of these high-resolution data sets in the steady state (Nikolaou et al. 2006). These techniques can be ideally combined with continuous table movement since the acquisition is largely independent from the highly varying speed of the contrast-media travel during first pass, which at the moment is still considered to be a problem for this type of acquisition. While artery-vein separation was considered a major drawback for steady-state acquisitions, further enhancement of spatial resolution will surely overcome this problem. Already at this point, acquisitions with high SNR and acceleration factors of R=3 are feasible at voxel sizes of less than 0.1 mm^3. This can be further improved by the use of 3-T systems with more dedicated coil designs. This approach for vascular imaging is expected to substantially reduce the complexity of magnetic resonance angiography for the operating technicians. Whereas currently multiple bolus-timing scans are required for whole-body dynamic first-pass MRA (cf. Chaps. 32 and 40), high resolution 3D-CE-MRA with intravascular contrast agents in the steady state would more or less require a continuous data acquisition during table movement accelerated by parallel-imaging techniques.

47.3.2 Cardiac MRI

Another area of high complexity of data acquisition despite multiple improvements is cardiac imaging. Here the limitations are threefold. First, many techniques related to cardiac imaging such as cine SSFP imaging for assessment of cardiac function or first-pass perfusion imaging require both cardiac gating as well as suspension of breathing (cf. Chaps. 35 and 36). Thus, image quality is substantially decreased in cases of severe arrhythmia or reduced breath-hold capacity of the patient. Second, due to the complex orientation and anatomy of the heart, special care is required for exact positioning of short-axis slices perpendicular to the long axis of the heart for assessment of cardiac function and perfusion. Third, in-detail assessment of the cardiac chambers in the four-chamber view, two-chamber view and short axis is time intensive particularly when combined with imaging of perfusion and delayed contrast enhancement.

The arising potential for highly accelerated parallel imaging might overcome these limitations by real-time acquisitions with high temporal and spatial resolution that obviate the need for cardiac gating or breath-hold or navigator-corrected imaging. Given the fact that for functional analysis of the heart a temporal resolution of 50 ms and a spatial resolution of at least 1.5 mm in-plane is mandatory, acceleration factors of at least 6 or higher will be required to fulfill this task. Initial experience with dedicated 32-element coils and TSENSE algorithms for parallel imaging has shown the principal feasibility of this approach (Wintersperger et al. 2006). A further step towards a substantial reduction of the complex-

ity of cardiac imaging will be the change from 2D to 3D acquisitions, allowing the reconstruction of any deliberate plane in the heart after the data has been acquired. Here, acceleration factors of at least 16 are necessary to maintain adequate spatial and temporal resolution. However, given the high intrinsic SNR of SSFP sequences and the better SNR performance of dedicated multi-element coils at higher field strength, this endeavor is certainly to be realized in the near future. These high acceleration factors would not only be useful for real-time and 3D imaging, but also for implementation of hybrid techniques that allow both functional and tissue-specific imaging. For example, imaging of delayed contrast enhancement is already today the new standard of reference for detection and measurement of the transmural extent of myocardial infarction. The current drawback is that the wall motion abnormality of the infarcted tissue cannot be directly visualized within the static contrast-enhanced scans, thus requiring the separate acquisition of time-resolved cine SSFP images. With massive acceleration of image acquisition, time-resolved inversion-recovery 3D imaging might be feasible, allowing the exact delineation of the wall-motion abnormality on the delayed-contrast-enhancement images. Overall, a massive acceleration of image acquisition might reduce a cardiac imaging protocol to a few 3D time-resolved breath-hold acquisitions without any need for cardiac gating or time-intensive anatomic scan positioning.

47.3.3 Disease-Specific and Disease-Dependent Imaging

The introduction of parallel-imaging techniques along with dedicated whole-body MRI systems has tremendously changed the role of radiology in the clinical workflow of the patient. Traditionally, radiological imaging was performed on clinicians' requests for a dedicated anatomic area in regard to a highly circumscribed clinical question. Usually a stepwise diagnostic algorithm was then pursued, adding further diagnostic exams by different imaging modalities to sequentially complete the imaging work-up and narrow down the list of differential diagnoses. Accelerated scanning with parallel imaging on whole-body MRI scanners initiated a trend to a more comprehensive assessment of not only a single organ, but organ systems within a single exam, thereby integrating different morphological and functional imaging sequences.

Two representative examples are the assessment of pulmonary arterial hypertension (PAH) and non-small-cell lung cancer as shown in Chaps. 42 and 43 of this book, for which functional techniques such as oxygen-enhanced and perfusion imaging as well as imaging of cardiac function are combined with high-resolution imaging of the mediastinum and angiographic assessment of the pulmonary arteries and veins. Thereby, multiple clinical questions for a given disease are addressed such as the presence of right-heart failure in pulmonary arterial hypertension, differentiation between primary causes of PAH from embolic causes as well as staging of the severity of vasoconstriction of the peripheral pulmonary vascular bed.

This type of comprehensive assessment is only feasible since many of the individual acquisitions are reduced to a few breath holds due to the acceleration by parallel-imaging techniques. A further step in this trend is the introduction of disease-specific imaging. In the presence of a systemic disease with typical disease manifestations in different organs, such as for example diabetes with macro- and microangiopathy, the dedicated clinical question can be combined with imaging of all organ systems with frequent disease involvement. Although the clinical focus may be on one target organ due to acute presentation of the patient with symptoms, other organ systems might be even more severely involved, causing major complications for the patient in the near future. If all these disease manifestations are addressed in a single disease-specific exam, a time-intensive, costly and potentially invasive multi-step diagnostic algorithm can be avoided. For example, one study (Weckbach et al. 2006) showed that in diabetics presenting with suspicion of acute osteomyelitis of the feet, a number of potentially more life-threatening vascular complications including high-grade renal and carotid artery stenosis as well as silent myocardial infarction can be detected when a comprehensive diagnostic algorithm of whole-body MR angiography, cardiac imaging, and musculoskeletal imaging is combined with the use of parallel-acquisition techniques.

A next step in this direction is the so-called disease-dependent imaging in which a specific constellation of laboratory and clinical findings automatically pre-selects the various functional and morphological imaging sequences tailored to the individual risk profile of the patient. Again, this might open new horizons for imaging of multi-morbid patients suffering from a systemic disease. Adhering to the example of diabetes, this scan could be automatically adapted

to the most urging clinical questions, such as renal-artery MR angiography combined with renal perfusion imaging in the case of rising creatinine, assessment of myocardial perfusion for suspected ischemic heart disease and dedicated musculoskeletal imaging for detection of osteomyelitis.

Another clinical example for this kind of disease-dependent imaging is the use of whole-body MRI for assessment of rheumatologic joint diseases. Here, assessment of synovialitis by time-resolved MRA is focused on the most painful joint of the patient followed by a complete evaluation of all joints of the entire body with fat-suppressed T1-weighted sequences (Fig. 47.1). Of course, these types of scans are only feasible if each of the acquisitions can be performed with minimal scan times, thus requiring fast acceleration of the image acquisition, for example with the use of parallel imaging.

Lastly, the question arises if this type of highly accelerated scan from head to toe could be useful for preventive imaging. While the medical value of whole-body MR imaging for secondary prevention in the general asymptomatic population is still highly debated, this could be valuable again in patients with underlying diseases predisposing them to serious complications such as stroke, myocardial infarction, or malignancies. Examples again could be patients with longstanding diabetes mellitus in which sev-

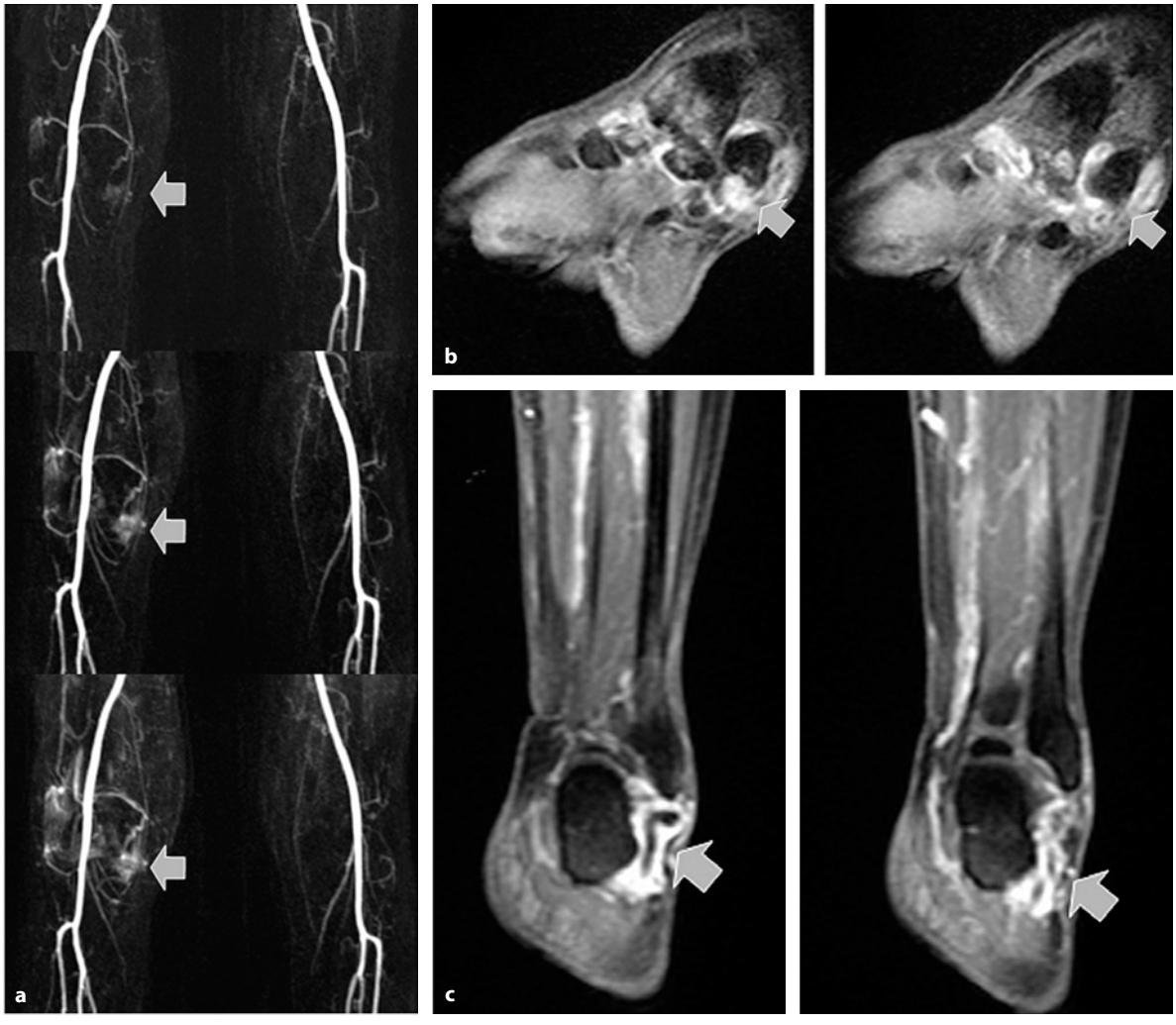

Fig. 47.1a–c. Whole-body MRI of a 55-year-old female with chronic rheumatoid polyarthritis and leading symptoms of knee pain. The time-resolved MRA of these most painful joints shows a severe synovialitis on the right (**a**). In addition, whole-body T1-weighted fat-suppressed gradient-echo images reveal additional manifestations of rheumatoid joint disease in the carpus (**b**) and ankle (**c**).

eral studies have clearly demonstrated a more than tenfold higher risk of stroke or myocardial infarction as well as cured cancer patients or transplant patients in which the risk for secondary malignancy is increased. However, this will require a massive increase in acquisition speed to allow scanning of the entire patient from head to toe in less than 20 min to integrate this imaging concept into a clinically useful routine follow-up algorithm.

It can be expected that parallel-imaging techniques do not fulfill these tasks alone. In the last decade a number of other techniques for substantial acceleration of image acquisition have arisen, including spiral echo-planar imaging, view-sharing algorithms, and radial imaging; cf. Chaps. 6, 7, and 11. The appeal of parallel imaging, however, is that in principle this technique can be combined with any of the other techniques named, thus allowing a synergistic use for even further acceleration of image acquisition. One example is the introduction of TREAT (time-resolved echo-shared angiographic technique) for dynamic contrast-enhanced MR angiography with acceptable temporal and spatial resolution. Here, the view-sharing algorithms of the TRICKS techniques are combined with parallel imaging for further gain in acquisition speed. Promising results have been shown for time-resolved assessment of tumors of the skull base, for which both adequate spatial resolution is required for assessment feeding arteries as well as short acquisition times to visualize arterial enhancement and venous drainage separately (Fig. 47.2) (Michaely et al. 2006).

Fig. 47.2. Time-resolved contrast-enhanced 3D MRA with view-sharing and parallel imaging (TREAT); spatial resolution: 2.1×1.3×3 mm³; temporal resolution: 2.3 s/3D data set. This sequence integrates morphological and functional information within a single acquisition. In this 59-year-old patient with a left-sided glomus tumor, the arterial feeders from the internal and external carotid artery, the vascularized tumor, and the venous drainage can be separately visualized on the individual time frames allowing detailed surgical planning.

47.4 Pre- and Post-Processing

While parallel imaging can be expected to reduce the complexity of magnetic resonance imaging in terms of bolus timing, anatomical orientation (due to isotropic resolution) and physiologic gating, the technique on the other hand introduces new technical complexities by itself. One major consideration is the choice of the optimal relationship among the arrangement of coil elements, coil positioning, and desired orientation of the imaging plane, since these factors directly influence the g-factor of the acquisition. This is of particular importance for imaging protocols that require complex double-oblique positioning of scan planes such as in short-axis imaging of the heart with high acceleration factors where increasing g-factors might exponentially enhance noise and reconstruction artefacts. Due to the different angles of the long axis of the heart varying from patient to patient, not every scan orientation might optimally exploit the properties of the coil for parallel imaging. Here, the number of fruitless attempts for artefact-free double-oblique imaging could be substantially reduced if scout acquisitions would interactively determine g-factor maps for the optimum selection of the maximum acceleration factor depending on the slice orientation and in-plane rotation in the given coil set-up. As a consequence of these g-factor maps, the maximum acceleration factor could be reduced if too many artefacts occur, the slice position could be slightly altered, or the coil could be repositioned on the patient depending on the patient's individual anatomy.

Another challenge for massively accelerated image acquisition addresses the exponential time for post-processing and reading of the acquired data by the radiologist. Already current whole-body MRI scans used for comprehensive assessment of cardiovascular or oncologic diseases include more than 1,000 images, which need to be independently evaluated and read (Fig. 47.3). From a legal point of view, imaging data acquired outside the specific region of interest to which the diagnostic question was primarily referred to do not exempt the radiologist from carefully evaluating that data, even when unrelated to the clinical question. Already, there have been litigations for overlooked pathologies that were completely outside the primary area of interest as well as the dedicated clinical question. Therefore, the major question arises how these continuously increasing data sets can still be handled.

A promising solution could be the fusion of morphologic and functional information in a single data set. One current example is the recent development of whole-body diffusion-weighted MRI for a better visualization of lymph nodes (Takahara et al. 2004), which is sometimes referred to as "MR PETography". While the resolution and anatomic information of this whole-body diffusion scan is very low, the contrast between lymph nodes and surrounding tissues is high. On the other hand, whole-body STIR images, already used in clinical routine for tumor staging (Schmidt et al. 2005), have an exquisite spatial resolution as well as soft-tissue contrast; however, lymph nodes are easily overlooked if they are positioned in between other structures of high-signal intensity such as veins with low flow, fluid-filled structures, such as small or large bowel, or fluid collections, such as cysts. Here, image fusion of the whole-body diffusion scans containing high-contrast information with the high anatomic information of the STIR images could be extremely beneficial to reduce the amount of reading time for the radiologist despite doubling the number of acquired images. This approach would be similar to the use of combined positron-emission tomography and computed tomography (PET-CT) where a high-contrast low-resolution PET scan for imaging of lymph nodes or other malignant, highly FDG-avid structures is combined with the high-resolution, high-detail, low-contrast information of the CT scan (Fig. 47.3).

While this in principle is a very appealing approach, the practical use has so far been substantially limited by the fact that the scan protocols for different soft-tissue contrast substantially vary in terms of in-plane spatial resolution, slice thickness, geometric distortions, and scan orientation, making an anatomically precise image fusion virtually impossible. A promising solution could be the primary acquisition of 3D data sets vastly accelerated by parallel imaging. This strategy could then be applied within a clinical exam for all individual scans that inherit different soft-tissue contrast or different morphologic and functional information.

At 3 T, this has been already realized for the stereotactic radiation treatment planning of patients with arteriovenous malformations (AVM) using a 12-element head coil. Here, the use of 3D turbo-spin-echo sequences with variable flip angle restores pulses, and parallel-acquisition techniques with an acceleration factor of $R=3$ allows acquiring a completely isotropic $1\times1\times1$ mm³ data set of the brain with T2 weighting. The TREAT sequence allows acquiring time-resolved MR angiographic data sets at a temporal resolution of 700 ms and an isotropic spatial resolution of $2\times2\times2$ mm³. In a fused image using commercially available image fusion software, the morphologic fea-

tures of the AVM on the T2-weighted scan can now be combined with the early arterial phase of the time-resolved MRA displaying the arterial feeder and the nidus of the AVM. The fused image, although arising from a large number of source data, now represents a substantial reduction of images while enhancing the diagnostic content (Fig. 47.4). Thus, although further increasing the amount of acquired data, parallel imaging may actually be helpful to reduce the number of images to be assessed by the radiologist by offering more consistent data for image fusion of scans with different morphologic and functional contents.

47.5 Conclusion

In summary, parallel-imaging techniques not only provide improved spatial and temporal resolution as well as the reduction of image artefacts, but also increase the diagnostic capabilities of magnetic resonance imaging through more comprehensive imaging protocols. This will allow a better evaluation of systemic diseases as well as more consistent detection and communication of pathologic findings.

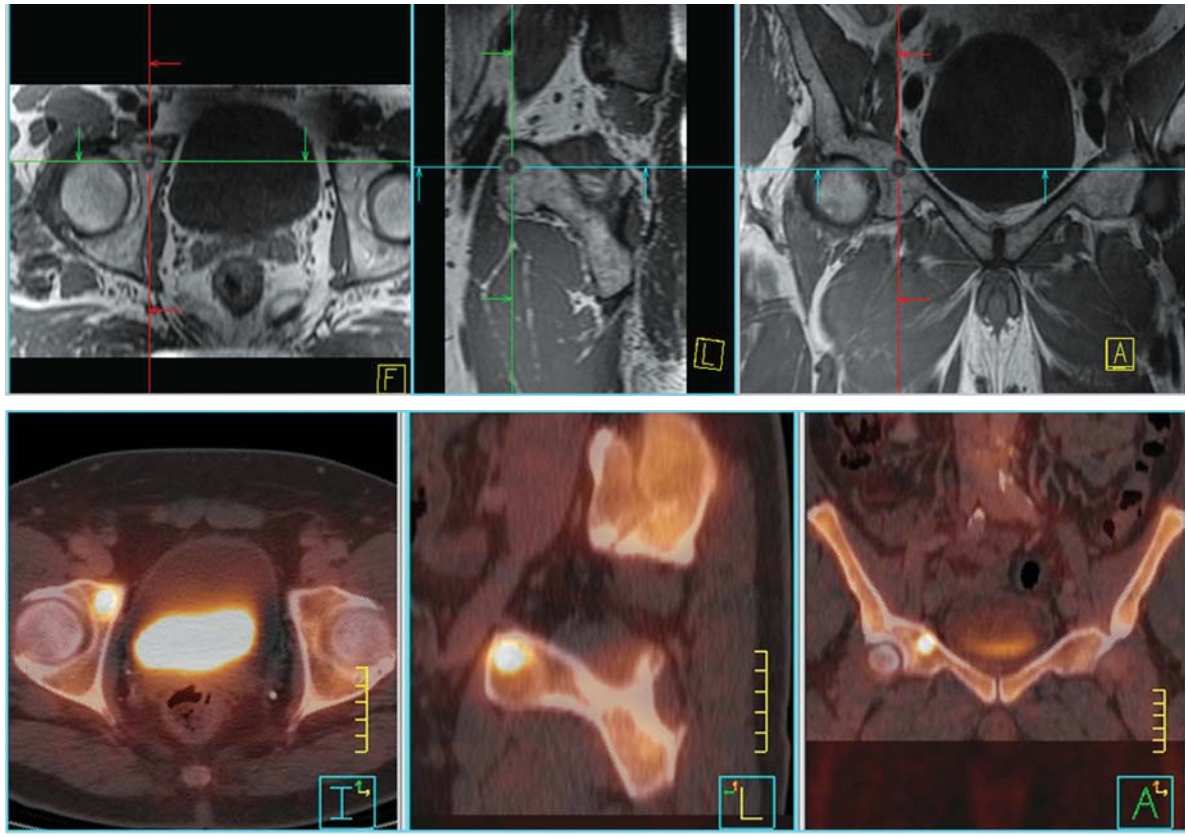

Fig. 47.3. Diagnostic challenge of large data volumes for detection of subtle pathology. A 58-year-old patient with a neuroendocrine tumor and osseous metastases. On PET-CT (*lower row*) with ^{18}F-Fluoride the metastases are easily visible due to the high lesion-to-background contrast from uptake of the tracer in the PET and can be three-dimensionally located using the additional CT information. In magnetic resonance imaging (*upper row*), this lesion can also be accurately detected using a recently developed T1-weighted 3D turbo-spin-echo sequence with parallel imaging, variable flip-angle distribution, long echo trains, and magnetization restore pulses (SPACE = Sampling Perfection with Application-optimized Contrasts using different flip-angle Evolutions) on a 3-T whole-body MRI scanner (Magnetom Tim Trio, Siemens Medical Solutions). With this sequence, a T1-weighted 3D data set of the entire pelvis with an isotropic spatial resolution of 1 mm³ can be acquired, which allows to reformat the osseous structures in any desired imaging plane. However, the time for data post-processing and reading increases exponentially to identify the subtle hypointense lesion within the large data set.

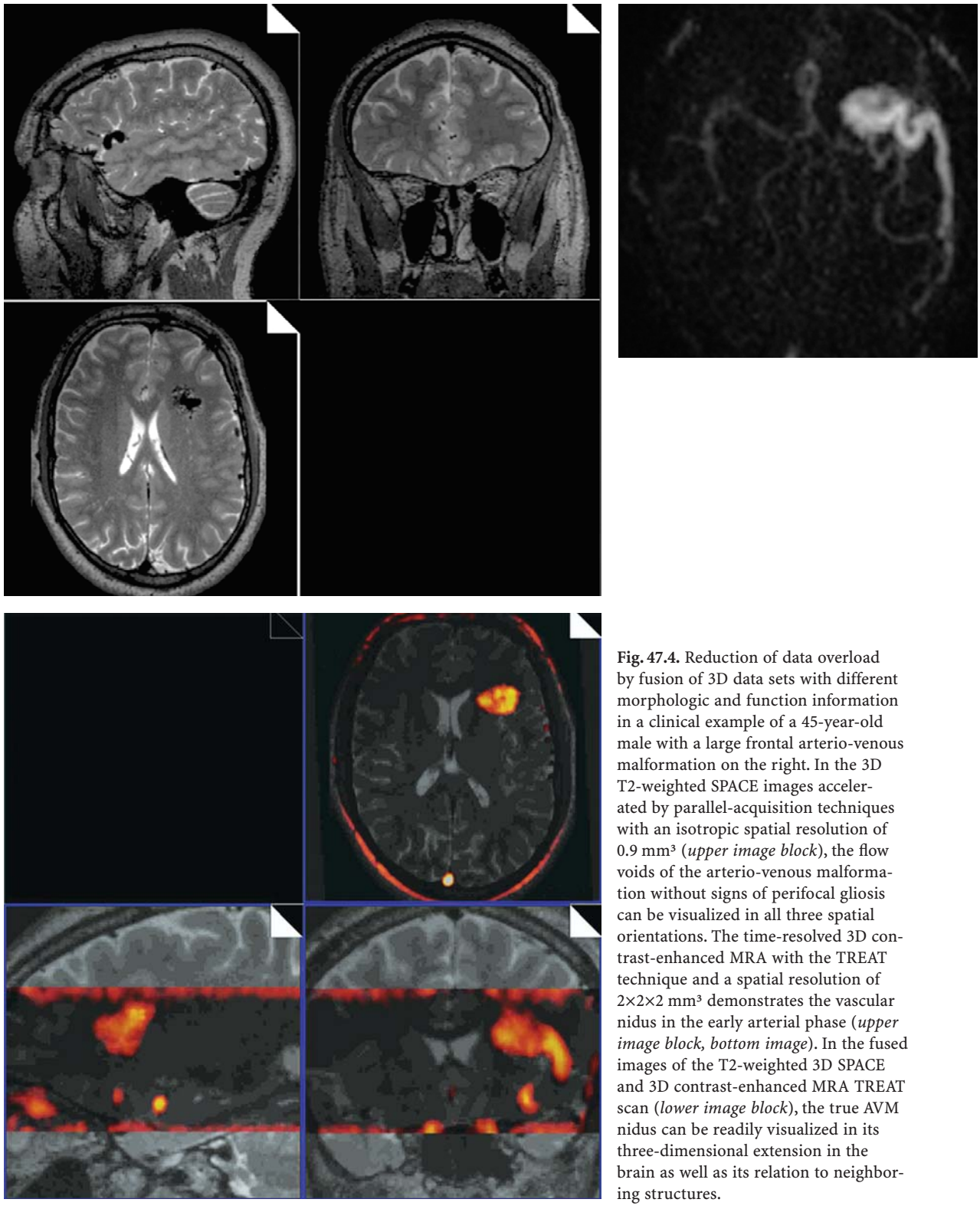

Fig. 47.4. Reduction of data overload by fusion of 3D data sets with different morphologic and function information in a clinical example of a 45-year-old male with a large frontal arterio-venous malformation on the right. In the 3D T2-weighted SPACE images accelerated by parallel-acquisition techniques with an isotropic spatial resolution of 0.9 mm³ (*upper image block*), the flow voids of the arterio-venous malformation without signs of perifocal gliosis can be visualized in all three spatial orientations. The time-resolved 3D contrast-enhanced MRA with the TREAT technique and a spatial resolution of 2×2×2 mm³ demonstrates the vascular nidus in the early arterial phase (*upper image block, bottom image*). In the fused images of the T2-weighted 3D SPACE and 3D contrast-enhanced MRA TREAT scan (*lower image block*), the true AVM nidus can be readily visualized in its three-dimensional extension in the brain as well as its relation to neighboring structures.

References

Caravan P, Cloutier NJ, Greenfield MT, McDermid SA, Dunham SU, Bulte JW, Amedio JC Jr, Looby RJ, Supkowski RM, Horrocks WD Jr, McMurry TJ, Lauffer RB (2002) The interaction of MS-325 with human serum albumin and its effect on proton relaxation rates. J Am Chem Soc 124:3152–3162

Dietrich O, Hajnal JV (1999) Extending the volume of true volume scans by continuous movement of the subject. Proc Intl Soc Mag Reson Med 7:1653

Grist TM, Korosec FR, Peters DC, Witte S, Walovitch RC, Dolan RP, Bridson WE, Yucel EK, Mistretta CA (1998) Steady-state and dynamic MR angiography with MS-325: initial experience in humans. Radiology 207:539–544

Hardy CJ, Cline HE, Giaquinto RO, Niendorf T, Grant AK, Sodickson DK (2006) 32-element receiver-coil array for cardiac imaging. Magn Reson Med 55:1142–1149

Hu HH, Madhuranthakam AJ, Kruger DG, Glockner JF, Riederer SJ (2005) Continuously moving table MRI with SENSE: application in peripheral contrast enhanced MR angiography. Magn Reson Med 54:1025–1231

Keupp J, Aldefeld B, Bornert P (2005) Continuously moving table SENSE imaging. Magn Reson Med 53:217–220

Kroft LJ, de Roos A (1999) Blood pool contrast agents for cardiovascular MR imaging. J Magn Reson Imaging 10:395–403

Kruger DG, Riederer SJ, Grimm RC, Rossman PJ (2002) Continuously moving table data acquisition method for long FOV contrast-enhanced MRA and whole-body MRI. Magn Reson Med 47:224–231

Michaely HJ, Herrmann KA, Dietrich O, Reiser MF, Schoenberg SO (2006) Quantitative and qualitative characterization of vascularization and hemodynamics in head and neck tumors with 3D magnetic resonance angiography – time-resolved echo-shared angiographic technique (TREAT) – initial results. Eur Radiol (in press)

Nikolaou K, Kramer H, Grosse C, Clevert D, Dietrich O, Hartmann M, Chamberlin P; Reiser MF, Schoenberg SO (2006) High-resolution whole-body MRA using parallel imaging on a 32-channel MR system and a blood-pool contrast agent: protocol optimization and clinical implementation. Radiology (in press)

Prasad PV, Cannillo J, Chavez DR, Pinchasin ES, Dolan RP, Walovitch R, Edelman RR (1999) First-pass renal perfusion imaging using MS-325, an albumin-targeted MRI contrast agent. Invest Radiol 34:566–571

Rohrer M, Bauer H, Mintorovitch J, Requardt M, Weinmann HJ (2005) Comparison of magnetic properties of MRI contrast media solutions at different magnetic field strengths. Invest Radiol 40:715–724

Schmidt GP, Baur-Melnyk A, Herzog P, Schmid R, Tiling R, Schmidt M, Reiser MF, Schoenberg SO (2005) High-resolution whole-body magnetic resonance image tumor staging with the use of parallel imaging versus dual-modality positron emission tomography-computed tomography: experience on a 32-channel system. Invest Radiol 40:743–753

Shankaranarayanan A, Herfkens R, Hargreaves BM, Polzin JA, Santos JM, Brittain JH (2003) Helical MR: continuously moving table axial imaging with radial acquisitions. Magn Reson Med 50:1053–1060

Sodickson DK, Hardy CJ, Zhu Y, Giaquinto RO, Gross P, Kenwood G, Niendorf T, Lejay H, McKenzie CA, Ohliger MA, Grant AK, Rofsky NM (2005) Rapid volumetric MRI using parallel imaging with order-of-magnitude accelerations and a 32-element RF coil array: feasibility and implications. Acad Radiol 12:626–635

Takahara T, Imai Y, Yamashita T, Yasuda S, Nasu S, Van Cauteren M (2004) Diffusion weighted whole body imaging with background body signal suppression (DWIBS): technical improvement using free breathing, STIR and high resolution 3D display. Radiat Med 22:275–282

Weckbach S, Schoenberg SO, Kramer H, Parhofer KG, Spitzweg C, Kessler S, Reiser MF (2006) Comprehensive diabetes imaging with whole-body MRI at 1.5 and 3.0 T in patients with long-standing diabetes. Eur Radiol 16:259 [Suppl 1]

Wiggins GC, Potthast A, Triantafyllou C, Lin F, Benner T, Wiggins CJ, Wald LL (2005a) A 96-channel MRI system with 23- and 90-channel phase-array head coils at 1.5 Tesla. Proc Intl Soc Mag Reson Med 13:671

Wiggins GC, Triantafyllou C, Potthast A, Reykowski A, Nittka M, Wald LL (2005b) A 32-channel receive-only phased-array head coil for 3T with novel geodesic tiling geometry. Proc Intl Soc Mag Reson Med 13:679

Wintersperger BJ, Reeder SB, Nikolaou K, Dietrich O, Huber A, Greiser A, Lanz T, Reiser MF, Schoenberg SO (2006) Cardiac CINE MR imaging with a 32-channel cardiac coil and parallel imaging: impact of acceleration factors on image quality and volumetric accuracy. J Magn Reson Imaging 23:222–227

Zhu Y, Hardy CJ, Sodickson DK, Giaquinto RO, Dumoulin CL, Kenwood G, Niendorf T, Lejay H, McKenzie CA, Ohliger MA, Rofsky NM (2004) Highly parallel volumetric imaging with a 32-element RF coil array. Magn Reson Med 52:869–877

Subject Index

C

D

E

H

I

J

K

L

M

N

Q

R

S

T

List of Contributors

Elfar Adalsteinsson, PhD
Athinoula A. Martinos Center for Biomedical Imaging
Department of Radiology
Massachusetts General Hospital
Harvard Medical School and Harvard-MIT Division of Health Sciences and Technology
Charlestown, MA 02129-2060
USA
and
Department of Electrical Engineering and Computer Science
Massachusetts Institute of Technology
Cambridge, MA
USA

Murat Aksoy, MSc
Department of Radiology
Lucas Center
Stanford University
1201 Welch Road
Stanford, CA 94305-5488
USA

David Atkinson, PhD
University College London
Department of Medical Physics
London, WC1E 6BT
United Kingdom

Roland Bammer, PhD
Assistant Professor of Radiology
Stanford University
Department of Radiology
Lucas Center
1201 Welch Road
Stanford, CA 94305-5488
USA

Philip G. Batchelor, PhD
Medical Physics and Bioengineering
Malet Place Eng. Building
University College London
London WC1E 6BT
UK

Thomas Benner, PhD
MGH/MIT/HMS Athinoula A. Martinos Center for Functional and Structural Biomedical Imaging
Charlestown Navy Yard
Building 149 13th Street (2301)
Charlestown, MA 02129-2060
USA

Michael Bock, PhD
Deutsches Krebsforschungszentrum (dkfz)
Abt. Medizinische Physik in der Radiologie (E020)
Im Neuenheimer Feld 280
69120 Heidelberg
Germany

Jan W. Casselman, MD, PhD
Chairman of the Department of Radiology
AZ St-Jan Brugge AV
Ruddershove 10
8000 Brugge
Belgium

Olaf Dietrich, PhD
Department of Clinical Radiology
University Hospitals – Grosshadern
Ludwig Maximilian University of Munich
Marchioninistrasse 15
81377 Munich
Germany

Randy Duensing, PhD
Department of Diagnostic Imaging
Invivo Corporation
3545 SW 47th Avenue
Gainesville, FL 32608
USA

Roger Eibel, MD
Department of Clinical Radiology
University Hospitals – Innenstadt
Ludwig Maximilian University of Munich
Ziemssenstrasse 1
80336 Munich
Germany

Marco Essig, MD
Abt. Radiologische Diagnostik und Therapie
Deutsches Krebsforschungszentrum Heidelberg
Im Neuenheimer Feld 280
69120 Heidelberg
Germany

Christian Fink, MD
Department of Clinical Radiology
University Hospitals – Grosshadern
Ludwig Maximilian University of Munich
Marchioninistrasse 15
81377 Munich
Germany

J. Paul Finn, MD
Professor of Radiology
David Geffen School of Medicine
UCLA Radiol Sci
BOX 957206, 3371 PVUB
Los Angeles, CA 90095-7206
USA

Bastian Fischer
Department of Clinical Radiology
University Hospitals – Grosshadern
Ludwig Maximilian University of Munich
Marchioninistrasse 15
81377 Munich
Germany

Mark A. Griswold, PhD
Department of Radiology
Case Center for Imaging Research
Case Western Reserve University School of Medicine
11100 Euclid Ave
Cleveland, OH 44106
USA

Karin A. Herrmann, MD
Department of Clinical Radiology
University Hospitals – Grosshadern
Ludwig Maximilian University of Munich
Marchioninistrasse 15
81377 Munich
Germany

Romhild M. Hoogeveen, PhD
Philips Medical Systems, Clinical Scientist,
QR0113 - PO Box 10000
5680 DA Best
The Netherlands

Armin Huber, MD
Department of Clinical Radiology
University Hospitals – Grosshadern
Ludwig Maximilian University of Munich
Marchioninistrasse 15
81377 Munich
Germany

Peter Kellman, PhD
Laboratory of Cardiac Energetics
National Institutes of Health/NHLBI
NIH Building 10/B1D-416
10 Center Drive, msc-1061
Bethesda, MD 20892-1061
USA

Harald Kramer, MD
Department of Clinical Radiology
University Hospitals – Grosshadern
Ludwig Maximilian University of Munich
Marchioninistrasse 15
81377 Munich
Germany

Karl-Friedrich Kreitner, MD
Department of Diagnostic and
Interventional Radiology
Johannes-Gutenberg-University of Mainz
Langenbeckstrasse 1
55131 Mainz
Germany

David J. Larkman, PhD
Magnetic Resonance Physics and Engineering Group
Robert Steiner MRI Unit
Imaging Sciences Department
Clinical Sciences Centre, Faculty of Medicine
Imperial College of Science
Technology and Medicine
Hammersmith Hospital Campus
Du Cane Road
London W12 0NN
UK

Tim Leiner, MD, PhD
Maastricht University Hospital
Department of Radiology
Peter Debijelaan 25
NL-6229HX
Maastricht
The Netherlands

Chunlei Liu, PhD
Stanford University
Department of Radiology
Lucas Center
1201 Welch Road
Stanford, CA 94305-5488

Charles A. McKenzie, PhD
Department of Radiology,
Beth Israel-Deaconess Medical Center
Boston, MA
USA

Henrik J. Michaely, MD
Department of Clinical Radiology
University Hospitals – Grosshadern
Ludwig Maximilian University of Munich
Marchioninistrasse 15
81377 Munich
Germany

Kambiz Nael, MD
Department of Radiological Sciences
David Geffen School of Medicine at UCLA
10945 LeConte Ave, Suite 3371
Los Angeles, CA 90095
USA

Scott Nagle, MD, PhD
Lucas MRS/I Center
Department of Radiology
Stanford University
Stanford, CA 94305-5488
USA

Konstantin Nikolaou, MD
Department of Clinical Radiology
University Hospitals – Grosshadern
Ludwig Maximilian University of Munich
Marchioninistrasse 15
81377 Munich
Germany

Mathias Nittka, PhD
Siemens AG
Medical Solutions MREA
Karl-Schall-Strasse 6
91052 Erlangen
Germany

Niels Oesingmann, PhD
Siemens Medical Solutions USA, Inc.
MR R&D Collaboration NYU CBI
660 First Avenue
New York, NY 10016
USA

Scott B. Reeder, MD, PhD
Departments of Radiology and Medical Physics
E3/311 CSC
University of Wisconsin
600 Highland Avenue
Madison, WI 53792-3252
USA

Maximilian F. Reiser, MD
Director of the Department of Clinical Radiology
University Hospitals
Ludwig Maximilian University of Munich
Marchioninistrasse 15
81377 Munich
Germany

Wolfgang Reith, MD
Professor, Radiologische Universitätsklinik
Abt. für Neuroradiologie
Kirrbergerstrasse 1
66421 Homburg/Saar
Germany

Arne Reykowski, PhD
Invivo Corporation
3545 SW 47th Ave
Gainesville, FL 32608
USA

Johannes Rieger, MD
Department of Clinical Radiology
University Hospitals – Innenstadt
Ludwig Maximilian University of Munich
Pettenkoferstrasse 8a
80336 Munich
Germany

Bernd Romaneehsen, MD
Department of Diagnostic and
Interventional Radiology
Johannes-Gutenberg-University of Mainz
Langenbeckstrasse 1
55131 Mainz
Germany

Gerwin P. Schmidt, MD
Department of Clinical Radiology
University Hospitals – Grosshadern
Ludwig Maximilian University of Munich
Marchioninistrasse 15
81377 Munich
Germany

Stefan O. Schoenberg, MD
Department of Clinical Radiology
University Hospitals – Grosshadern
Ludwig Maximilian University of Munich
Marchioninistrasse 15
81377 Munich
Germany

Bram Stieltjes, MD
Abt. Radiologische Diagnostik und Therapie
Deutsches Krebsforschungszentrum Heidelberg
Im Neuenheimer Feld 280
69120 Heidelberg
Germany

Lawrence L. Wald, PhD
MGH/MIT/HMS Athinoula A. Martinos Center
for Functional and Structural Biomedical Imaging
Charlestown Navy Yard
Building 149 13th Street (2301)
Charlestown, MA 02129-2060
USA

Ruopeng Wang, MS
MGH/MIT/HMS Athinoula A. Martinos Center
for Functional and Structural Biomedical Imaging
Charlestown Navy Yard
Building 149 13th Street (2301)
Charlestown, MA 02129–2060
USA

Astrid M. Wallnoefer, MD
Department of Clinical Radiology
University Hospitals – Grosshadern
Ludwig Maximilian University of Munich
Marchioninistrasse 15
81377 Munich
Germany

Van J. Wedeen, MD
MGH/MIT/HMS Athinoula A. Martinos Center
for Functional and Structural Biomedical Imaging
Charlestown Navy Yard
Building 149 13th Street (2301)
Charlestown, MA 02129–2060
USA

Oliver Wieben, PhD
Depts. of Medical Physics & Radiology
University of Wisconsin-Madison, J5/150 CSC
600 Highland Ave
Madison, WI 53792-1590
USA

Graham Wiggins, PhD
MGH/MIT/HMS Athinoula A. Martinos Center
for Functional and Structural Biomedical Imaging
Charlestown Navy Yard
Building 149 13th Street (2301)
Charlestown, MA 02129-2060
USA

Bernd J. Wintersperger, MD
Department of Clinical Radiology
University Hospitals – Grosshadern
Ludwig Maximilian University of Munich
Marchioninistrasse 15
81377 Munich
Germany

Christoph J. Zech, MD
Department of Clinical Radiology
University Hospitals – Grosshadern
Ludwig Maximilian University of Munich
Marchioninistrasse 15
81377 Munich
Germany

Medical Radiology Diagnostic Imaging and Radiation Oncology

Titles in the series already published

Diagnostic Imaging

Innovations in Diagnostic Imaging
Edited by J. H. Anderson

Radiology of the Upper Urinary Tract
Edited by E. K. Lang

The Thymus - Diagnostic Imaging, Functions, and Pathologic Anatomy
Edited by E. Walter, E. Willich, and W. R. Webb

Interventional Neuroradiology
Edited by A. Valavanis

Radiology of the Pancreas
Edited by A. L. Baert, co-edited by G. Delorme

Radiology of the Lower Urinary Tract
Edited by E. K. Lang

Magnetic Resonance Angiography
Edited by I. P. Arlart, G. M. Bongartz, and G. Marchal

Contrast-Enhanced MRI of the Breast
S. Heywang-Köbrunner and R. Beck

Spiral CT of the Chest
Edited by M. Rémy-Jardin and J. Rémy

Radiological Diagnosis of Breast Diseases
Edited by M. Friedrich and E.A. Sickles

Radiology of the Trauma
Edited by M. Heller and A. Fink

Biliary Tract Radiology
Edited by P. Rossi, co-edited by M. Brezi

Radiological Imaging of Sports Injuries
Edited by C. Masciocchi

Modern Imaging of the Alimentary Tube
Edited by A. R. Margulis

Diagnosis and Therapy of Spinal Tumors
Edited by P. R. Algra, J. Valk, and J. J. Heimans

Interventional Magnetic Resonance Imaging
Edited by J. F. Debatin and G. Adam

Abdominal and Pelvic MRI
Edited by A. Heuck and M. Reiser

Orthopedic Imaging
Techniques and Applications
Edited by A. M. Davies and H. Pettersson

Radiology of the Female Pelvic Organs
Edited by E. K.Lang

Magnetic Resonance of the Heart and Great Vessels
Clinical Applications
Edited by J. Bogaert, A.J. Duerinckx, and F. E. Rademakers

Modern Head and Neck Imaging
Edited by S. K. Mukherji and J. A. Castelijns

Radiological Imaging of Endocrine Diseases
Edited by J. N. Bruneton in collaboration with B. Padovani and M.-Y. Mourou

Trends in Contrast Media
Edited by H. S. Thomsen, R. N. Muller, and R. F. Mattrey

Functional MRI
Edited by C. T. W. Moonen and P. A. Bandettini

Radiology of the Pancreas
2nd Revised Edition
Edited by A. L. Baert. Co-edited by G. Delorme and L. Van Hoe

Emergency Pediatric Radiology
Edited by H. Carty

Spiral CT of the Abdomen
Edited by F. Terrier, M. Grossholz, and C. D. Becker

Liver Malignancies
Diagnostic and Interventional Radiology
Edited by C. Bartolozzi and R. Lencioni

Medical Imaging of the Spleen
Edited by A. M. De Schepper and F. Vanhoenacker

Radiology of Peripheral Vascular Diseases
Edited by E. Zeitler

Diagnostic Nuclear Medicine
Edited by C. Schiepers

Radiology of Blunt Trauma of the Chest
P. Schnyder and M. Wintermark

Portal Hypertension
Diagnostic Imaging-Guided Therapy
Edited by P. Rossi
Co-edited by P. Ricci and L. Broglia

Recent Advances in Diagnostic Neuroradiology
Edited by Ph. Demaerel

Virtual Endoscopy and Related 3D Techniques
Edited by P. Rogalla, J. Terwisscha Van Scheltinga, and B. Hamm

Multislice CT
Edited by M. F. Reiser, M. Takahashi, M. Modic, and R. Bruening

Pediatric Uroradiology
Edited by R. Fotter

Transfontanellar Doppler Imaging in Neonates
A. Couture and C. Veyrac

Radiology of AIDS
A Practical Approach
Edited by J.W.A.J. Reeders and P.C. Goodman

CT of the Peritoneum
Armando Rossi and Giorgio Rossi

Magnetic Resonance Angiography
2nd Revised Edition
Edited by I. P. Arlart, G. M. Bongratz, and G. Marchal

Pediatric Chest Imaging
Edited by Javier Lucaya and Janet L. Strife

Applications of Sonography in Head and Neck Pathology
Edited by J. N. Bruneton in collaboration with C. Raffaelli and O. Dassonville

Imaging of the Larynx
Edited by R. Hermans

3D Image Processing
Techniques and Clinical Applications
Edited by D. Caramella and C. Bartolozzi

Imaging of Orbital and Visual Pathway Pathology
Edited by W. S. Müller-Forell

Pediatric ENT Radiology
Edited by S. J. King and A. E. Boothroyd

Radiological Imaging of the Small Intestine
Edited by N. C. Gourtsoyiannis

Imaging of the Knee
Techniques and Applications
Edited by A. M. Davies and V. N. Cassar-Pullicino

Perinatal Imaging
From Ultrasound to MR Imaging
Edited by Fred E. Avni

Radiological Imaging of the Neonatal Chest
Edited by V. Donoghue

Diagnostic and Interventional Radiology in Liver Transplantation
Edited by E. Bücheler, V. Nicolas, C. E. Broelsch, X. Rogiers, and G. Krupski

Radiology of Osteoporosis
Edited by S. Grampp

Imaging Pelvic Floor Disorders
Edited by C. I. Bartram and J. O. L. DeLancey
Associate Editors: S. Halligan, F. M. Kelvin, and J. Stoker

Imaging of the Pancreas
Cystic and Rare Tumors
Edited by C. Procacci and A. J. Megibow

High Resolution Sonography of the Peripheral Nervous System
Edited by S. Peer and G. Bodner

Imaging of the Foot and Ankle
Techniques and Applications
Edited by A. M. Davies, R. W. Whitehouse, and J. P. R. Jenkins

Radiology Imaging of the Ureter
Edited by F. Joffre, Ph. Otal, and M. Soulie

Imaging of the Shoulder
Techniques and Applications
Edited by A. M. Davies and J. Hodler

Radiology of the Petrous Bone
Edited by M. Lemmerling and S. S. Kollias

Interventional Radiology in Cancer
Edited by A. Adam, R. F. Dondelinger, and P. R. Mueller

Duplex and Color Doppler Imaging of the Venous System
Edited by G. H. Mostbeck

Multidetector-Row CT of the Thorax
Edited by U. J. Schoepf

Functional Imaging of the Chest
Edited by H.-U. Kauczor

Radiology of the Pharynx and the Esophagus
Edited by O. Ekberg

Radiological Imaging in Hematological Malignancies
Edited by A. Guermazi

Imaging and Intervention in Abdominal Trauma
Edited by R. F. Dondelinger

Multislice CT
2nd Revised Edition
Edited by M. F. Reiser, M. Takahashi, M. Modic, and C. R. Becker

Intracranial Vascular Malformations and Aneurysms
From Diagnostic Work-Up to Endovascular Therapy
Edited by M. Forsting

Radiology and Imaging of the Colon
Edited by A. H. Chapman

Coronary Radiology
Edited by M. Oudkerk

Dynamic Contrast-Enhanced Magnetic Resonance Imaging in Oncology
Edited by A. Jackson, D. L. Buckley, and G. J. M. Parker

Imaging in Treatment Planning for Sinonasal Diseases
Edited by R. Maroldi and P. Nicolai

Clinical Cardiac MRI
With Interactive CD-ROM
Edited by J. Bogaert, S. Dymarkowski, and A. M. Taylor

Focal Liver Lesions
Detection, Characterization, Ablation
Edited by R. Lencioni, D. Cioni, and C. Bartolozzi

Multidetector-Row CT Angiography
Edited by C. Catalano and R. Passariello

Paediatric Musculoskeletal Diseases
With an Emphasis on Ultrasound
Edited by D. Wilson

Contrast Media in Ultrasonography
Basic Principles and Clinical Applications
Edited by Emilio Quaia

MR Imaging in White Matter Diseases of the Brain and Spinal Cord
Edited by M. Filippi, N. De Stefano, V. Dousset, and J. C. McGowan

Diagnostic Nuclear Medicine
2nd Revised Edition
Edited by C. Schiepers

Imaging of the Kidney Cancer
Edited by A. Guermazi

Magnetic Resonance Imaging in Ischemic Stroke
Edited by R. von Kummer and T. Back

Imaging of the Hip & Bony Pelvis
Techniques and Applications
Edited by A. M. Davies, K. J. Johnson, and R. W. Whitehouse

Imaging of Occupational and Environmental Disorders of the Chest
Edited by P. A. Gevenois and P. De Vuyst

Contrast Media
Safety Issues and ESUR Guidelines
Edited by H. S. Thomsen

Virtual Colonoscopy
A Practical Guide
Edited by P. Lefere and S. Gryspeerdt

Vascular Embolotherapy
A Comprehensive Approach
Volume 1
Edited by J. Golzarian. Co-edited by S. Sun and M. J. Sharafuddin

Vascular Embolotherapy
A Comprehensive Approach
Volume 2
Edited by J. Golzarian. Co-edited by S. Sun and M. J. Sharafuddin

Head and Neck Cancer Imaging
Edited by R. Hermans

Vascular Interventional Radiology
Current Evidence in Endovascular Surgery
Edited by M. G. Cowling

Ultrasound of the Gastrointestinal Tract
Edited by G. Maconi and G. Bianchi Porro

Imaging of Orthopedic Sports Injuries
Edited by F. M. Vanhoenacker, M. Maas, J. L. M. A. Gielen

Parallel Imaging in Clinical MR Applications
Edited by S. O. Schoenberg, O. Dietrich, and F. M. Reiser

MR and CT of the Female Pelvis
Edited by B. Hamm and R. Forstner

Ultrasound of the Musculoskeletal System
S. Bianchi and C. Martinoli

Radiology of the Stomach and Duodenum
Edited by A. H. Freeman and E. Sala

Springer

Medical Radiology Diagnostic Imaging and Radiation Oncology

Titles in the series already published

Radiation Oncology

Lung Cancer
Edited by C.W. Scarantino

Innovations in Radiation Oncology
Edited by H. R. Withers
and L. J. Peters

Radiation Therapy
of Head and Neck Cancer
Edited by G. E. Laramore

Gastrointestinal Cancer –
Radiation Therapy
Edited by R.R. Dobelbower, Jr.

Radiation Exposure
and Occupational Risks
Edited by E. Scherer, C. Streffer,
and K.-R. Trott

Radiation Therapy of Benign Diseases
A Clinical Guide
S. E. Order and S. S. Donaldson

Interventional Radiation
Therapy Techniques – Brachytherapy
Edited by R. Sauer

Radiopathology of Organs and Tissues
Edited by E. Scherer, C. Streffer,
and K.-R. Trott

Concomitant Continuous Infusion
Chemotherapy and Radiation
Edited by M. Rotman
and C. J. Rosenthal

Intraoperative Radiotherapy –
Clinical Experiences and Results
Edited by F. A. Calvo, M. Santos,
and L.W. Brady

Radiotherapy of Intraocular
and Orbital Tumors
Edited by W. E. Alberti and
R. H. Sagerman

Interstitial and Intracavitary
Thermoradiotherapy
Edited by M. H. Seegenschmiedt
and R. Sauer

Non-Disseminated Breast Cancer
Controversial Issues in Management
Edited by G. H. Fletcher and S.H. Levitt

Current Topics in
Clinical Radiobiology of Tumors
Edited by H.-P. Beck-Bornholdt

Practical Approaches to
Cancer Invasion and Metastases
A Compendium of Radiation
Oncologists' Responses to 40 Histories
Edited by A. R. Kagan with the
Assistance of R. J. Steckel

Radiation Therapy in Pediatric Oncology
Edited by J. R. Cassady

Radiation Therapy Physics
Edited by A. R. Smith

Late Sequelae in Oncology
Edited by J. Dunst and R. Sauer

Mediastinal Tumors. Update 1995
Edited by D. E. Wood and C. R. Thomas, Jr.

Thermoradiotherapy
and Thermochemotherapy
Volume 1:
Biology, Physiology, and Physics
Volume 2:
Clinical Applications
Edited by M.H. Seegenschmiedt,
P. Fessenden, and C.C. Vernon

Carcinoma of the Prostate
Innovations in Management
Edited by Z. Petrovich, L. Baert,
and L.W. Brady

Radiation Oncology
of Gynecological Cancers
Edited by H.W. Vahrson

Carcinoma of the Bladder
Innovations in Management
Edited by Z. Petrovich, L. Baert,
and L.W. Brady

Blood Perfusion and
Microenvironment of Human Tumors
Implications for Clinical Radiooncology
Edited by M. Molls and P. Vaupel

Radiation Therapy of Benign Diseases
A Clinical Guide
2nd Revised Edition
S. E. Order and S. S. Donaldson

Carcinoma of the Kidney and Testis,
and Rare Urologic Malignancies
Innovations in Management
Edited by Z. Petrovich, L. Baert,
and L.W. Brady

Progress and Perspectives in the
Treatment of Lung Cancer
Edited by P. Van Houtte,
J. Klastersky, and P. Rocmans

Combined Modality Therapy of
Central Nervous System Tumors
Edited by Z. Petrovich, L. W. Brady,
M. L. Apuzzo, and M. Bamberg

Age-Related Macular Degeneration
Current Treatment Concepts
Edited by W. A. Alberti, G. Richard,
and R. H. Sagerman

Radiotherapy of Intraocular
and Orbital Tumors
2nd Revised Edition
Edited by R. H. Sagerman,
and W. E. Alberti

Modification of Radiation Response
Cytokines, Growth Factors,
and Other Biolgical Targets
Edited by C. Nieder, L. Milas,
and K. K. Ang

Radiation Oncology for Cure and Palliation
R. G. Parker, N. A. Janjan,
and M. T. Selch

Clinical Target Volumes in Conformal and
Intensity Modulated Radiation Therapy
A Clinical Guide to Cancer Treatment
Edited by V. Grégoire, P. Scalliet,
and K. K. Ang

Advances in Radiation Oncology
in Lung Cancer
Edited by Branislav Jeremić

New Technologies in Radiation Oncology
Edited by W. Schlegel, T. Bortfeld,
and A.-L. Grosu

Technical Basis of Radiation Therapy
4th Revised Edition
Edited by S. H. Levitt, J. A. Purdy, C. A.
Perez, and S. Vijayakumar

Springer

Printing and Binding: Stürtz GmbH, Würzburg